# Material Science and Environmental Engineering

Edited by
Ping Chen

TRANS TECH PUBLICATIONS

# Material Science and Environmental Engineering

Edited by
Ping Chen

# Material Science and Environmental Engineering

Selected, peer reviewed papers from the
2014 International Conference on
Material Science and Environmental Engineering
(MSEE 2014),
March 21-23, 2014, Changsha, Hunan, China

*Edited by*

**Ping Chen**



**Copyright** © 2014 Trans Tech Publications Ltd, Switzerland

All rights reserved. No part of the contents of this publication may be reproduced or transmitted in any form or by any means without the written permission of the publisher.

Trans Tech Publications Ltd
Kreuzstrasse 10
CH-8635 Durnten-Zurich
Switzerland
http://www.ttp.net

Volume 937 of
*Advanced Materials Research*
*ISSN print 1022-6680*
*ISSN cd 1022-6680*
*ISSN web 1662-8985*

Full text available online at *http://www.scientific.net*

***Distributed** worldwide by*

Trans Tech Publications Ltd
Kreuzstrasse 10
CH-8635 Durnten-Zurich
Switzerland

Fax: +41 (44) 922 10 33
e-mail: sales@ttp.net

*and in the Americas by*

Trans Tech Publications Inc.
PO Box 699, May Street
Enfield, NH 03748
USA

Phone: +1 (603) 632-7377
Fax: +1 (603) 632-5611
e-mail: sales-usa@ttp.net

# Preface

The 2nd International Conference on Material Science and Environmental Engineering (MSEE2014) was successfully held in Changsha, China on March 21-24, 2014. MSEE2014 provided an excellent international Academic forum for sharing knowledge and results in theory, methodology and applications of Material Science and Environmental Engineering. The MSEE2014 aims to cover the recent research and application in the area of chemical material, Mechanical Engineering Materials, Biomaterials, Electronic Materials, Structural Material, Metal Material, Nano Material and Environmental Protection and Sustainable Development, Environmental Science and Engineering.

The MSEE2014 has attracted more than 300 submissions. More than 100 participants attended this conference. The MSEE2014 provided a platform to bring not only researchers but also governmental agents, industrial professionals in Material Science and Environmental Engineering. With this platform, the ideas and results from the conference will embarks whole process of making new discoveries and translating them into products and service for the marketplace.

I believe many of you will benefit in many ways in this conference either as speakers or as participants. I also hope this conference is a good platform to build research network in many fields and open for great opportunity of cooperation in future.

Finally, I wish all of you good luck and all the best at this conference.

Dr. Ping Chen

MSEE2014 General Chair

# Organizing Committee

General chair

Dr. Ping Chen, Boise State University, USA

Technical Committee Chair

Dr. Yun Li, Shanxi Normal University, China

Technical Committee

Dr. Y. R. Ghodasara Anand Agricultural University, India

Dr. Zhigang Lian Shanghai DianJi University, China Dr Jinzhuo Liu, Henan University, China

Dr. Zi Tao, Industry and Information Technology Department of Hebei Province, China

Dr. Shengde Li, Anhui Science and Technology University, China

Dr. Zhao Jiakui, China Electric Power Research Institute, China

Dr. Zhongming Yao, Qiqihar University, China

Dr. Xiaohong Zhang, Jinan University, China

Dr. Wen Quan, Nanjing University of Science and Technology, China

Dr. Yanyan Liu, Lanzhou University, China

Dr. Qing He, North China Electric Power University, China

Dr. Wang Yunyin, XinJiang University, China

Dr. Shuang Hu, Fuzhou University, China

Dr. Dang He, Hunan Agricultural University, China

Dr. Bian Qian, Hunan University of Science and Technology, China

Dr. Xianju Shu, Wuhan Textile University, China

Dr. Tao He, Yunnan University, China

Dr. Yingzhi Fu, Qinghai University, China

Dr. Wenbei Bai, Guangxi University for Nationalities, China

Dr. Jiang Pan, Wuhan Polytechnic University, China

Dr. Meiji Cai, Hainan University, China

Dr. Ke Guan, Henan Normal University, China

Dr. Da Zeng, Hubei Normal University, China

Dr. Langqi Liu, Lanzhou Jiaotong University, China

Dr. Fei Qian, Jianghan University, China

**Organizer**

Advanced Information Science Research Center (AISRC)

**Sponsors**

Chengdu University, Hunan University of Science and Technology

# Table of Contents

**Preface, Organizing Committee and Sponsors**

## Chapter 1: Chemical Materials

**The Effects of Electroplating Conditions on the Morphology and Glucose Oxidation Performance of $Cu_2O/TiO_2$**
M. Long, L. Tan and A.D. Tang 3

**Synthesis, Adsorption Behavior of a Maleamic Acid Cross-Linked *β*- Cyclodextrin Polymer for Removal of Basic Fuchsin in Aqueous Solution**
X.M. Zhang, H.Z. Li, M.L. Cao and C.Y. Chen 9

**Electrosyntheses of Poly(selenophene-co-3-methylthiophene) with Improved Thermoelectric Property in Boron Trifluoride Diethyl Etherate**
S.T. Wang, B.Y. Lu, J.K. Xu and W.Q. Zhou 17

**Electrodeposition of Novel Cross-Linked Poly(methacrylic acid) Functionalized Poly(9-aminofluorene) Network Films**
D. Cheng, B.Y. Lu, W.Q. Zhou and J.K. Xu 23

**3D-Braided Thick Composites Made by Simultaneous Outside-in and Inside-out Resin Infusion**
R. Chen, Z.D. Shan and F. Liu 29

**The Effect of Acetate on the Electrodeposition of Manganese on Polycrystalline Au without $SeO_2$ Additives**
W.P. Li, X.L. Zuo, J.Y. Yang and S.T. Zhang 34

**Numerical Analysis for Cavitation Intensity's Effects on the Extend Angle of Convergence-Divergence Nozzle**
F.H. Zhang, X. Su, C.L. Tang and L.W. Shan 41

**Experimental Application of Salt Slurry in Talimu High Density Drilling Fluid Composed of KCl-Saturated Brine and Polybasic Alcohol**
L.J. Zhou and J.M. Feng 46

**Preparation of 2,2-Dimethylol Propionic Acid**
J.W. Zhang and J.W. Liu 51

**Reaction Routes for the Electro-Deoxidation of Ilmenite in Molten Salt**
X.L. Zou, X.G. Lu, W. Xiao and C.Y. Lu 58

**A Study on Relationship between Orientation Evolution and Coarsening Behavior of $Cu_6Sn_5$ Grains Formed on Polycrystalline Cu Substrate**
M. Yang, X. Ma and M.Y. Li 64

**Glass-Ceramics Obtained from Sewage Sludge and its Characteristics Affected by Alkalinity**
D. Wu, Y. Tian, X.W. Wen and H.L. Liu 70

**Experimental Study of Urea Depositions in Urea-SCR System**
S.Z. Bai, S.G. Lang, K.P. Yuan, Y. Liu and G.X. Li 74

**Synthesis and Characterization of $A_2$+$B_4$ Hyperbranched Polyesters with Hydroxyl End Groups**
H.A.M. Saeed, Y.A. Eltahir, Y.M. Xia and Y.M. Wang 80

**Preparation of Polyamide 5,6 (PA56) Fibers and its Mechanical Properties**
Y.A. Eltahir, H.A.M. Saeed, Y.M. Xia and Y.M. Wang 86

**Inhibition and Recovery of Nitrification during the Process of Sludge Reduction Induced by a Metabolic Uncoupler, 2,6-Dichlorophenol (2,6-DCP)**
D. Wu, Y. Tian, X.W. Wen and H.L. Liu 92

**Influence of Ethanol on the Interactions and Physical Properties of Binary Mixtures of 1-Ethyl-3-Methylimidazolium Based ILs at 298.15 K**
H.N. Saba, Y.M. Zhang and H.P. Wang 99

**The Corrosion Evaluation Methodology of the Lock Gate**
C.H. Jiang, K. Fan, X.Y. Luo and L. Qian 105

**Adsorption Behavior and Corrosion Inhibition of *S*-Benzyl *o*-Phenylenedioxydithiophosphate for Carbon Steel in Hydrochloric Acid Solution**
X.L. Zhang, X. Lin, B. Xie, L.K. Zou, S.S. Zhu, Y. Lu, J.S. Feng and Y.L. Li 109

**First-Principles Study on the Surface Energies of Rutile $TiO_2$(110) vs (011)-2×1 Surfaces**
F. Yuan, S.X. Lu, W.G. Xu, H.F. Zhang and T. Ning 113

**Optimization of Preparation Process of Essential Oil of Baokening Granule-β-Cyclodextrin Inclusion by Orthogonal Test**
F. Luo and S.B. Qiao 118

## Chapter 2: Metal Materials and Alloys

**Research and Empoldering of High Strength Weathering Steel S450EW**
J.S. Wang, P.Y. Shi, C.J. Liu and M.F. Jiang 125

**Simulation of the Yield Strength of Mo Alloys at Both Room and Elevated Temperatures**
J.L. Fan, H.C. Cheng and M. Song 130

**Preparation and Photocatalytic Properties of Iron Titanate Compounds**
X.F. Lei, X.X. Xue and H. Yang 136

**Study on Laser Brazing for Copper**
X.H. Wu 141

**Expansion Behavior and Microstructures of Hypereutectic Al-Si Alloys Subjected to Thermal Cycling**
X.W. Zhu, R.C. Wang and J. Peng 145

**Fatigue Damage Evaluation Research of Aluminum Alloy Based on Energy Degradation**
X.D. Li, L. Zou, Z.T. Mu and G.M. Kong 150

**Comparative Study of Copper Brazing with Ag-Cu-Zn and Ag-Cu-P Filler in Heat Treatment Furnace**
R. Wang and Y.J. Jin 154

**The Research of Fatigue Properties of Steel Q235 Butt Welded Joint**
W.P. Ouyang, J. Zhang and X.D. Xu 158

**Analysis of the Grain Refinement Mechanism for Commercial Pure Titanium by ECAP and SMAT**
X.M. He, S.S. Zhu and C.H. Zhang 162

**Corrosion Behavior of 13Cr Steel in Different Temperature**
Z.C. Qiu, X. Liu and N. Zhang 168

**Microstructure and Properties of AZ31B Magnesium-LY12 Aluminum Alloys Diffusion-Bonded Joint**
S.M. Du and Q. Qin 172

**Research Progress of Mg-Re Alloys**
Q.A. Li, W.C. Liu and X.J. Song 178

**Effect of Solution Treatment on Microstructures and Hardness of Mg-Gd-Y-Zr Alloy**
Q.A. Li, L.L. Chen, W.C. Liu, X.Y. Zhang and H.Z. Jiang 182

**Basic Properties of Iron and Steel Making Dust**
X.B. Li, W. Wang, D.H. Zhang and L. Xiong 187

## Chapter 3: Electronic Materials

**Effect of Acetate on Electrodeposition of Manganese from Chloride Electrolyte with $SeO_2$ Additives**
W.P. Li, X.L. Zuo, J.H. Liang, J.H. He and S.T. Zhang 193

**Molecular Dynamics Simulations of the Conductivity of Aqueous NaCl in the Presence of Sucrose and Electric Fields**
X.G. Li, S.A. Yang, M.J. Tang, J. Lei, H. Hu, H. Hou and B.S. Wang 200

**Electron Transport in Zigzag Graphene Nanoribbons with a Tetra-Vacancy Complex: A Perfect Spin Filter**
W. Lu and S.H. Ke 207

**An Effective N, N-Diethylthiourea as Accelerator for Microvia Filling via Copper Electrodeposition**
W.W. Ma and Y. Wang 214

**Adsorption Mechanism Study of Magnetic EDTA-Chitosan on Cu (II) Ions of Solution**
R.H. Qin, F.S. Li, W. Jiang and L.Y. Hao 218

**Preparation, Characterization and Conductivity of Solid High-Proton Conductor $Na_7[CoW_{11}O_{39}Cd(H_2O)]\cdot 12H_2O$**
L.Q. Chen, X.M. Lin, M.X. Zhu and L.M. Dai 224

## Chapter 4: Nano-Scale and Amorphous Materials

**Synthesis of $Co_3O_4$ Multilayer Nanosheet Material and its Promising Gas Sensing Property**
M.L. Yin and S.Z. Liu 231

**Influence of Ultrasonic Time on the Preparation and Properties of $LaCoO_3$ Nanoparticles**
J. Dong, H.F. Shen, Y.M. Wang, Y.J. Lu and G.L. Fang 237

**Avoidance of Forbidden DNA Nanorobots Configurations in Patterned Immobilization of other Materials**
V. Popov 244

**Preparation of Carbaryl-Imprinted Capillary Monolithic Column for Screening of Carbaryl from Three Carbamates Mixture**
C. Zhang, J.R. Cai, Y.Q. Duan and L. Xu 248

**Methylthiouracil-Templated Formation of the Fluorescent Silver Nanocluster and its Application to Bioimaging**
X.Q. Xu 256

**A Facile and Efficient Method to Prepare Exfoliated and Reduced Graphene Nanosheets by Detonation**
Y.H. Guo, D.X. Zhuo, L.X. Wu, L. Ma, Z.X. Weng and R. Wang 260

## Chapter 5: Biomaterials and Healthcare

**Drug Sustained Release Multiple-Component Polymeric Microparticles Fabricated Using an Electrospray Process**
X.Y. Li, D.G. Yu, F.P. Jiang, K.J. Deng, Z. Du and X. Wang 269

**Adsorption Behavior of Rhodamine B and Methylene Blue by Chemical Modified Cornstalk Biomass**
Q.L. Cao, Y.M. Zhao, X.Y. Wei and F. Luo 276

**Pathogenic Fungi Induce the Expression of *Trichoderma asperellum* Cell Wall Degrading Enzymes in the Process of Mycoparasitism**
P. Yang 282

**Prevalence of Allergy and Complications Caused by Jewelry among Higher Vocational College Students**
J.P. Yuan, D.D. Chen and P. Wan 286

**The Effect of Food-Microorganism(F/M)Ratio on Gas Properties in Batch Biogas Fermentation with Walnut Peel**
J.H. Liu, W.D. Zhang, S.Q. Liu, X.L. Zhao, F. Yin, J. Liu, L. Xu, Y.B. Chen and H. Yang 291

**Diversity and Distribution of Sulfate-Reducing Bacteria in Jilin Oilfield**
W.F. Song, D.S. Ma, Y.Y. Zhu, X.F. Wei and J. Wu 297

**Cultivation and Regulation of Sulfate-Reducing Bacteria in Oilfield**
W.F. Song, D.S. Ma, Y.Y. Zhu, X.F. Wei and J. Wu 303

**Application of Neural Network in Bioactive Prediction of Inhibitor of Thymidylic Acid-Based Synthetase**
X.H. Du and X.H. Wang 308

## Chapter 6Mechanical Materials and Engineering

**Study on Fault Rule Prediction of Hydraulic System and its Accessories of Shipborne Aircraft**
L. Li, C.Y. Wang, P.Z. Zhao, X.D. Li and H.Q. Zhao 315

**Analysis of Welding Residual Stress on Cracked Vessels with X-Ray Diffraction Method**
J.M. Zhou and Y.L. Zhang 318

**Energy Consumption Performance Study of New S-Shaped Hysteretic Damper**
C. Xu, Y.F. Niu and Y.X. Zhao 324

**Adhesive Mechanism and Experimental Study on Shear Adhesive Strength of Impact Ice**
R.R. Wu, C.L. Zhu, C.X. Zhu and B. Miao 330

**Design of the Hydraulic System of Lead Plate Coiling Machine**
H. Sen, R.B. Yuan and R. Li 336

**Influence of Vibration on Thermomechanical Property and Transformation Behavior of TiNi Shape Memory Alloy**
A.S. Zheng, R.H. Li, P.S. Zheng and G.Y. Fu 341

**The Design and Development of a Single-Axle Parallel Hybrid Powertrain Test Platform**
Q. Sun, C.C. Ma, Q. Miao and G.X. Li 346

**The Research of the Rolling Element Bearing Fault Signal Frequency Domain Feature Extraction Method Based on the Wavelet Packet Decomposition**
S.Y. Qiu and R.B. Yuan 351

**The Influence of the Diameter Ratio between Rigid Body and Particle on the Impact Strength Exerted on the Rigid Body Impacting Particles**
J.D. Lu, L.H. Li and G.M. Zhang 357

**Research on Perovskite Catalysis for Diesel Engine Exhaust Removal**
P. Liang, Q.Y. Chen and H.B. Long 363

**Research on Operation Mechanism and Application in Engineering of UNITANK Process**
D.J. Bao, J. Li and P. Zhang 370

**Thermodynamic Analysis of the Internal Melt-Ice-on-Tube during Melting under Natural Convection**
Y. Liu and X. Chen 375

**Introduction of a Thermal Response Test (TRT) Apparatus Used for Measuring Underground Heat Exchanger Characteristics**
Y. Liu, Y. Shi and Y.N. Zhang 381

**The Application of Paste Tailing Technology in High Latitude Cold Area**
B. Zhou, X.W. Zhou, Y. Chen and Z. Chen 386

**Elastic Modulus Influence on the Forming Precision of Grinding Tool Bended for the Aspherical Surface Grinding**
C.M. Shang, D.M. Zhang and J.D. Yang 391

**Rotating Angle Error Influence to Grinding Aspheric Optical Component**
C.M. Shang, D.M. Zhang and X.M. Zhang 396

**Effect of Carding Plate Gauge under the Licker-in of Carding Machine on Polyester Yarn Hairiness**
X.Z. Yu and P.Z. Sun 400

**Design and Trial-Production of Emergency Power Supply System Battery Based on Chemical Hydrogen Production**
C.H. Xiong, Y.J. Zhou, F. Zheng, G. Wang and F. Wang 404

**Complex Image Recognition Method of Train Wheels Based on Contour Feature**
D.Y. Jia and P. Hu 409

## Chapter 7: Structural Materials and Civil Engineering

**Study on the Effect Evaluation of Spinescence Application on Segregating Gratings of Expressway - Taking Wu (Ding) – Kun (Ming) Expressway as Example**
Y.W. Li, Y. Shen and Q. Meng 419

**Comparison Study of Structural Stabilities for H-Section Columns Built with Ordinary Grade Strength Structural Steels According to Boundary Conditions and Lengths at High Temperature**
I.K. Kwon 424

**Bridge with Lead Rubber Bearing Finite Element Analysis Based on ANSYS**
Y.X. Chen 428

**Numerical Simulation on a Deep-Foundation Pit of Shenzhen Holiday Plaza Project**
Y. Zheng 433

**Piled Raft Structure Finite Element Analysis of Composite Foundation Settlement in Da XI Passenger Dedicated Line**
X.T. Ma and G.L. Liu 438

**Fluctuations Response of Tall Building to Change of Aspect Ratio in Interference Building**
K.P. You, Y.M. Kim, J.Y. You and S.Y. Paek 444

**Performances of Manganese Slag Cement**
Q.Z. Chen and D.Q. Liang 450

**Historical and Cultural Connotation of the Architectural Wood Carving Ornament in the Ancestral Temple of Chen Family - With "Feast in Bronze Sparrow Terrace Held by Cao Cao" and "Jiantu Conference" as Examples**
Y.N. Chen 456

**Lost Wax Casting Process Design of Artificial Jade Cup Basing on Blast Furnace Slag**
W. You, Y.M. Jiang, Q. Lin, X.X. Yu, P.F. Li and Y.G. Wang 462

**Analysis of Sound Absorption Properties of Three-Leaf Microperforated Panel Absorbers without a Rigid Backing**
X.L. Gai, X.H. Li, R. Wu, B. Zhang and J.J. Zhao 465

**Influence of Alkaline Activator on the Strength of Fly Ash-Cement Gel Sand Material**
H.Y. Huang, A.M. Gong and K. Yuan 472

**Moulding Process Design of Artificial Purple Jade Ship Basing on Blast Furnace Slag**
W. You, S.S. Wang, Y.G. Wang, Q. Lin, X.X. Yu and P.F. Li 476

**The Construction of City Complex Intelligent System**
Y. Liu 479

## Chapter 8: Environment Protection and Sustainable Development

**Nitrogen Oxides Reduction by Zeolite Sorbents in Manufacturing Use**
I. Pandová 487

**Study on the Effect of Streambed Substrate on Invertebrate Diversity**
Z.W. Luo, W.Y. Wu and K. Le 491

**An Extended-Range Hybrid Solar-Cell and Battery Powered Bicycle**
C.H. Chao 495

**Experimental Study on Biogas Production by Mesophilic Fermentation with Dimocarpus Longan Pericarp**
L.J. Zhang, W.D. Lin, W.D. Zhang, F. Yin, X.L. Zhao, J. Liu, L. Xu, Y.B. Chen, S.Q. Liu and H. Yang 502

**Research on Environmentally Friendly Water-Based Covering Ink and its Application in Scratch-Type Invoice Printing**
Y. Gong, B.Q. Huang and X.F. Wei 508

**Study on Reuse of Power Lithium Ion Battery Recycling**
Y.X. Li, R.L. Guo, Y.Q. Zhang and D.S. Zhou 515

**Safety, Heath, and Environment (SHE) Case for Oil & Gas Operating Company**
W.J. Yuan 520

**Design and Development of the Environmental Protection Mobile Enforcement System**
Y.Q. Wang and Y.J. Zhao 526

**Energy Consumption Performance Study of New Box-Shaped Hysteretic Damper**
C. Xu, Y.F. Niu and Y.X. Zhao 531

**Assessment and Characteristics of Heavy Metal Contaminated Soil in the Vicinity of a Zinc Mine Dump Heaps**
H. Wang, H.B. Li, X.D. Lv, P.F. Wang and J.F. Ma 537

**Application of the Head-Tail Method to Determine Irrigation Coefficient in Hongguang Irrigation District**
F.L. Zuo, W.H. Zhang, J. Gao, X.L. Bai, J.H. Nong, H.Q. Zhao and M.Q. Zhong 543

**Calculation of Parameters of Crop Water Production Function of Jensen Model Based on Stochastic Particle Swarm Optimization Algorithm**
S.H. Chang and Z.H. Qie 548

**Effects of Grazing on Reproductive Allocation of Elm in Horqin Sandy Land, Northeastern China**
Y. Tang and X.J. Wang 554

**Water Resources Optimal Allocation in Middle Line of South to North Water Diversion Project of Hebei, China Using AHP-LP**
T.Z. Gao, C.C. Zhang and H.C. Pang 559

**Study of the Differences between Vegetation and Soil Spectrum about Alpine Wetland Ecosystem**
J.M. Wang, K.L. Chen, X. Zhang and Z.X. Luo 565

**Toxicity of Three Heavy Metal Pollutants of the Pharmaceutical Wastewater to Paramecium Caudatum**
Z.L. Gong, Y. Chen, Y. Yan, S.Y. Pei, D. Wu, M. Zhang and Q. Wang 571

**Responses of Water Holding Characteristic of Crown Debris and Litter in a Cunninghamia Lanceolata Stand to Ice-Snow Damage**
Q.J. Li, Y.T. Hao, L. Xue and X.L. Hou 578

**Study on Particle Breakage of Coarse-Grained Soil Based on Large-Scale Triaxial Test**
F.Y. Chu 585

**The Research of Slope Stability Based on Unsaturated Soil Theory**
C.Q. Shao, N. Zhang and F.L. Lv 590

## Chapter 9: Environmental Science and Engineering

**Comparative Researches on the Provenances of Suspended Sediments in Different Reaches of Dongtiaoxi and Xitiaoxi Watershed**
Z.P. Lu, X.Y. Yuan, H. Wang, H.L. Chen and W.W. Xu 597

**Introduction to Midas GTS Software Application in Design of Deep Foundation Pit**
X.L. Dong 604

**An Overview of Different Distillation Technologies for Drinking Water Preparation**
L. Liu and H.L. Wang 607

**Erosion Experiment of Self-Excited Oscillation Pulsed Jet**
C.L. Tang, J. Pei, D. Hu and X.T. He 614

**Ozon/Hydrogen Peroxide System for Degradation of Humic Acid in Water**
K.W. Kim and D.S. Rhee 620

**Experimental Study on Dynamic Characteristics of Self-Excited Oscillation Pulsed Jet**
C.L. Tang, J. Pei and D. Hu 624

**The Study of Groundwater Modeling of Plain Area in Shiyang River Basin - I Groundwater System Conceptual Model Construction**
Y.F. Cheng, Y.H. Li, X.Q. Hu, J.D. Wang and S.C. Lu 632

**The Study of Groundwater Modeling of Plain Area in Shiyang River Basin - II Groundwater Modeling and Validation**
Y.F. Cheng, J.D. Wang, Y.H. Li, X.Q. Hu and S.C. Lu 639

**Removal of Heavy Metals from Contaminated Soils by Washing with Citric Acid and Subsequent Treatment of Soil-Washing Solutions**
L. Sun, H.Q. Liu, G.X. Wei, Z.H. Wu and W. Yang 646

**Preparation of Calcium Silicate Using Hazardous Solid Wastes and its Application in Treatment of Phosphate-Containing Wastewater**
X.H. Zhu, Z. Zhang and J. Shen 652

**Multi-Scale Analysis of Marine Environmental Situation in the Caofeidian Nearshore District**
Y.J. Zhao, M.C. Li and Y.Y. Cao 659

**Garden Plants under Global Climate Change**
Q.J. Li, X.L. Hou, L. Xue, H.Y. Chen and Y.T. Hao 663

**The Nutritional Status of Waters and Origin Analysis of the Xitiaoxi Tributaries**
H. Wang, X.Y. Yuan, Z.Y. Li, H.Y. Xu and H.L. Chen 669

## Chapter 10: Computation and Management Engineering Application

**The Evaluation in Fuzzy Matter-Element Theory Based on Hybrid Weight**
D.Y. Jia and S.X. Zou 679

**ALB: A Methodology for the Simulation of the Producer-Consumer Problem**
C.A. Xu 686

**Analysis of Relaxation and Relaxation Training on Sprint Performance Impact**
P. Wang 691

**A New Method and Applications of the Boundary Value Problem of Differential Equation**
H.E. Li, X.X. Dong, S.C. Li, D.D. Gui and C.Y. Fan 695

**Changchun College of Architecture Electrical Design for Sheling Campus Library**
T.T. Li 700

**Optimized Research for Mobile Communication Strategy Based on Parallel Computing**
J.W. Zhang and Y.L. Yao 703

**The Stochastic Imperfection Method of Sheet Space Structure Based on Truncated Univariate Normal Distributions**
T.J. Jin and X.M. Guo 707

# CHAPTER 1:

# Chemical Materials

*Advanced Materials Research Vol. 937 (2014) pp 3-8*
*© (2014) Trans Tech Publications, Switzerland*
*doi:10.4028/www.scientific.net/AMR.937.3*

# The Effects of Electroplating Conditions on the Morphology and Glucose Oxidation Performance of $Cu_2O/TiO_2$

Mei LONG[1], Lin TAN[1], Ai-dong TANG*[1, 2]

School of Chemistry and Chemical Engineering, Central South University, Changsha, 410083, P.R.China;

tangaidong@126.com

**Keywords:** $Cu_2O$ nanoparticles, $TiO_2$ nanotube arrays, Non-enzymatic glucose oxidation, Electrocatalysis.

**Abstract:** A series of $Cu_2O/TiO_2$ electrodes for the enzyme-free glucose oxidation have been fabricated by secondary anodic oxidation combined electroplating method. The obtained nanocomposites were characterized by scanning electron microscopy (SEM), X-ray diffraction (XRD) and their electrochemical behaviour measured by cyclic voltammetry (CV). The effects of preparation conditions on the morphology and performance of $Cu_2O/TiO_2$ for enzyme-free oxidaton of glucose were studied. For the electrochemical deposition at the potential range of −0.4 to −0.8 V, $Cu^{2+}$ was electrochemically reduced to polyhedral $Cu_2O$, accompanied by the simultaneous formation of Cu with a nanoparticle morphology. It was found that the reduced particles with Cu cooperated onto the $Cu_2O$ were completely covered on the top surface of $TiO_2$ nanotubes and showed a highest response current with a lower overpotential 0.5 V. The results indicate that the incorporation of Cu nanoparticles favors to improve the response current, which might find promising applications in biosensor and biological fuel cells.

## Introduction

Electrocatalytic oxidation of glucose has been investigated extensively in the field of biosensor because of its importance for glucose determination[1, 2]. Moreover, utilisation of biofuel cells with glucose as a power source has also attracted increasing attention. Glucose fuel cell has been reported for development of implantable power supply source [3, 4]. And this device uses enzyme such as glucose oxidase as catalyst. Although enzyme as catalyst shows high sensitivity, selectivity to glucose and power density, their disadvantages are obvious, such as low stability, complication of immobilization procedure and high price. In order to overcome these drawbacks, many efforts have been made to develop non-enzymatic electrode.

Direct electro-oxidation of glucose on non-enzymatic noble metal such as Au, Pt, Ag electrode has been explored in both biosensor and biofuel cell[5, 6]. Besides, with ongoing technical development, nanostructured mediating metal (Ni, Cu) or metal oxidation materials (NiO, $Co_3O_4$, $Cu_xO$) have already been verified as nonenzymatic glucose sensor for determining the amount of trace glucose[7-10]. Among these materials, copper-based materials exhibited high catalytic oxidation ability for glucose and lower price. However, the catalytic activities of the nanoscaled materials are closely related to their morphology. And the synthesized $Cu_xO$ nanoparticals are easily agglomerated, which greatly limits their application. Well-aligned $TiO_2$ nanotube arrays (TNT) fabricated by anodization of Ti substrate with large specific surface area and many active sites has attracted extensive interest. Recently, Luo et al.[11] have prepared a novel $TiO_2$ nanotube arrays modified with CuO nanofibers for sensitive nonenzymatic glucose detection, which showed excellent stability and repeatability. However, to the best of our knowledge, no successful reports about $Cu_2O$/TNT array for nonenzymatic glucose oxidation are available and the potential application of these nanostructures for glucose sensing and biofuel cell is of great interest. Moreover, it is still necessary to study the controllable growth of the $Cu_2O$ particles deposited onto $TiO_2$. In this work, we fabricated a helical TNT electrode modified by $Cu_2O$ nanoparticles for nonenzymatic oxidation of glucose. The effects of preparation conditions on the morphology and performance of $Cu_2O/TiO_2$ for oxidaton of glucose were studied.

## Experimental

$TiO_2$ nanotube arrays were fabricated via the anodization process through two steps. Ti foils (purity >99.6%, 100×10mm) were anodized at 20 V for 1 hour in a two-electrode electrochemical cell with a Pt foil as a cathode in a glycerol electrolyte containing 0.5 wt % $NH_4F$. After that, the pre-anodized Ti foil was ultrasonically cleaned in deionized water to remove the formed $TiO_2$ film. The cleaned Ti foil was used for the secondary anodization in the used electrolyte at 20 V for 4 hour. The as-prepared $TiO_2$ nanotubes were calcined in atmosphere at 500 ° C for 2 h.

The $Cu_2O$/TNT film was fabricated by employing a three-electrode system. The sample was used as the working electrode. A platinum foil and a saturated calomel electrode (SCE) were used as the counter electrode and the reference electrode, respectively. The electrolyte was prepared by dissolving 0.4 M $CuSO_4$ in a 3 M lactic acid solution. And then the pH value was adjusted to 11 using 5 M NaOH aqueous solution. The electrolyte was kept at 30 ºC during the deposition progress. A CHI 660B electrochemical working station (ChenHua Instruments Co. Ltd., Shanghai, China) worked as the power source, where constant potential was the working mode.

The obtained nanocomposites were characterized by SEM, XRD. Electrochemical measurements were performed on a CHI 660B electrochemical workstation with a conventional three-electrode setup, consisting of the prepared sample as working electrode, a Pt foil as the counter electrode, and a SCE as the reference electrode. The CV experiments was measured in a mixture of 2 mM glucose and 0.1 M NaOH solution at scan rate 50 mV/s ranging from 0 to 0.8 V versus SCE.

## Results and Discussion

The effects of deposition potential on the morphology and glucose oxidation performance of the $Cu_2O$/TNT electrodes were presented in Fig. 1. Figure 1A (a) showed the classic TNT with helical uniform outer diameter of about 100 nm and wall thickness of 10 nm. When the applied potential was -0.4 V, few $Cu_2O$ particles deposited on TNT were observed (b), although the deposition time extended to 2 h. when the applied potential increased to -0.5 V for 1 h, the wall of $TiO_2$ nanotube arrays was thicken (c). As the deposition potential increased, and the preparation time of the samples kept 5 min, it can be observed that some crystals with octahedral shape were uniformly embedded into the TNT structure including both the surface and internal, external walls of TNT ((d) and (e)). When the electroplating potential was –0.8 V, under the same electrochemical conditions, the dimension of $Cu_2O$ particles diminished. And polyhedral $Cu_2O$ particles clearly covered mainly the nanotubular surface (f). These results indicated that -0.4 V and -0.5 V were too low to deposite $Cu_2O$ on TNT at short time; when the deposition potential reached to -0.6 V, there were $Cu_2O$ particles that embedded into the TNT structure clearly. As the deposition potential increased, the size of $Cu_2O$ nanocrystals decreased, and the load increased.

Figure 1B showed the XRD patterns of the $Cu_2O$/TNT electrodes that prepared at different potentials. The substrate showed well-crystallized anatase $TiO_2$ phase (JCPDS file: 21-1272) on Ti. The $Cu_2O$ phase (JCPDS 65-3288) became quite evident when the deposition potential increased to –0.6 V. The characteristic reflection peaks at 36.5 ° and 29.6 ° assigned to the (111) and (110) crystal planes of $Cu_2O$. No peaks assigned to CuO or Cu phase were detected in the as-prepared materials. As the applied potential increased, the peak intensity of $Cu_2O$ became stronger for the increasing of the load. The results matched well with the SEM images.

Figure 1C showed the effect of the $Cu_2O$/TNT electrodes deposited at different potential on the catalytic oxidation activity of glucose. There was no obvious catalytic oxidation current on the $Cu_2O$/TNT electrode prepared at -0.4 V (b) and –0.5 V (c) in the presence of 2.0 mM glucose due to the low amount of $Cu_2O$ particles. With the increasing of the applied potential, there was a broad wide peak at 0.3 V-0.7 V and the oxidation current became larger (e and f).

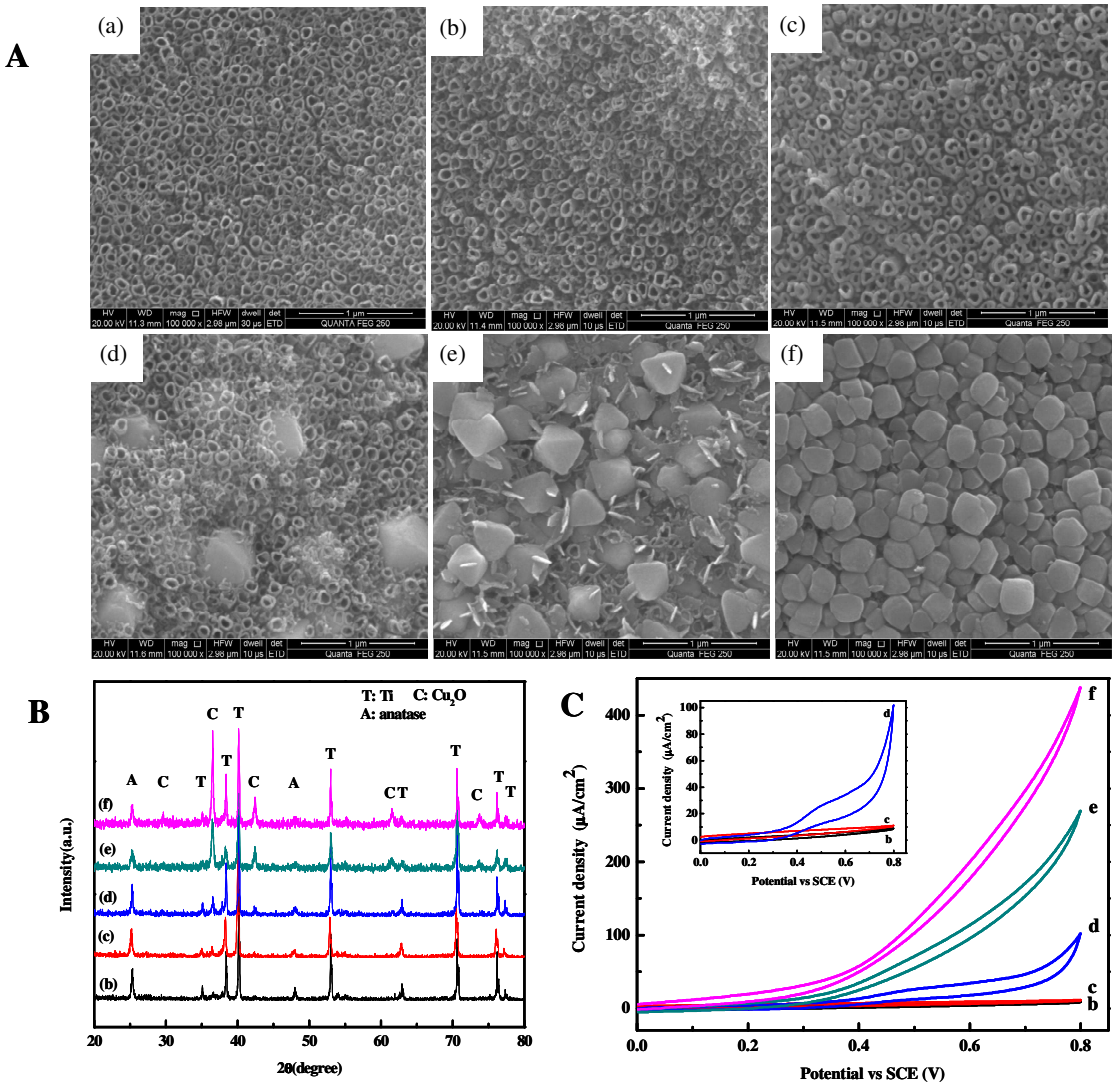



Fig. 1. (A) SEM images of the top view of the $TiO_2$ nanotube arrays (a), (B) XRD patterns and (C) CVs of the as-prepared $Cu_2O$/TNT electrode prepared at different potentials: –0.4 V (b), –0.5 V (c), –0.6 V (d), –0.7 V (e), –0.8 V (f).

The effects of $CuSO_4$ concentration on the morphology and glucose oxidation performance of the $Cu_2O$/TNT electrodes were presented in Fig. 2. A constant potential 0f -0.7 V was applied and the deposition time was controlled in 3 min. When the concentration of $CuSO_4$ in the electrolyte was 0.04 M, some small sheet-like $Cu_2O$ coated on the surface of TNT in Fig. 2A(a). For 0.1 M, a few large $Cu_2O$ particles were observed on the surface and internal and external walls of the TNT (b). For 0.4 M, the TNT surface was extensively covered by the octahedral $Cu_2O$ particles and some particles were inserted into the internal tubes (c). Figure 2B showed the XRD patterns of the $Cu_2O$/ TNT electrodes prepared at different concentrations of $CuSO_4$. As the concentration of $CuSO_4$ increased, the peak intensity of $Cu_2O$ became stronger indicating that the increasing of the $Cu_2O$ load, which matched well with the SEM images.

The effect of $CuSO_4$ concentration on the property of glucose enzyme-free oxidation was compared in Fig. 2C. It was found that the large of response current was obtained at the $CuSO_4$ concentration 0.04 and 0.4M due to the large $Cu_2O$ load on the surface of TNT.

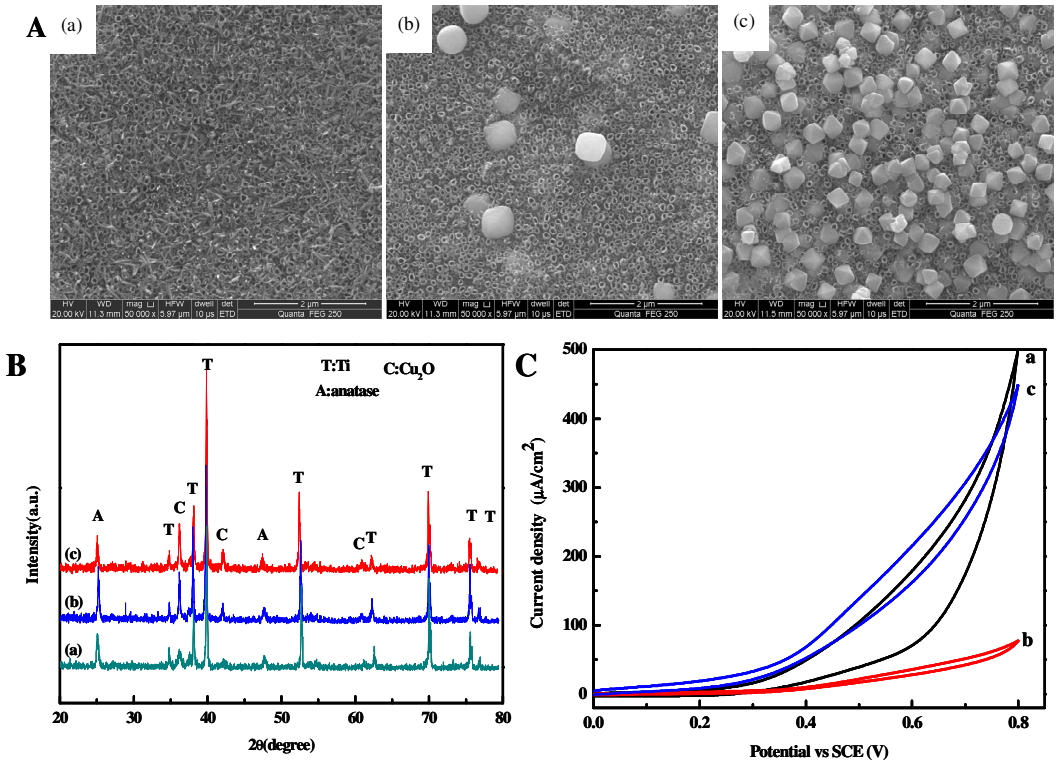



Fig. 2. (A) SEM images, (B) XRD patterns and (C) CVs of the as-prepared $Cu_2O$/TNT electrodes prepared in the electrolyte with different concentration of $CuSO_4$: 0.04 M (a), 0.1 M (b), 0.4 M (c).

The morphology and glucose oxidation performance of the Cu/$Cu_2O$/TNT electrode prepared by continuous electroplating method were presented in Fig. 3. The electrode was prepared at a constant potential of –0.6 V with 0.4 M $CuSO_4$ for 5 min twice by the electrodeposition method. Figure 3A presented the SEM image of the as-prepared sample. Compared with the once electrodeposition for 5 min (Fig. 1A(d)), the deposited layer clearly covered on the entire nanotubular surface. The crystal structure was shown in Fig.3B. Besides of the characteristic peaks of anatase $TiO_2$ and Ti substrate, there were strong characteristic peaks of $Cu_2O$ and Cu. A series of peaks at 43.2 °, 50.44 ° and 74.14 ° were assigned to the (111), (200) and (220) crystal planes of Cu (JCPDS 04-0836). The results confirmed that $Cu_2O$ and Cu were crystallized on the surface of the TNT.

The CV measurements of the bare TNT electrode and Cu/$Cu_2O$/TNT electrode were conducted in the absence and presence of 2 mM glucose in 0.1 M NaOH solution to investigate the electrocatalytic avctives. As shown in Fig. 3C, the Cu/$Cu_2O$/TNT electrode showed obvious catalytic oxidation current (c) in the presence of glucose as compared with that in the absence of glucose (b). The oxidation current increaseed rapidly, starting at about 0.3 V with the appearance of an oxidation peak at around 0.5 V and completing at about 0.7 V. In contrast, no oxidation peak was found on the bare TNT electrode (a) in the presence of 2 mM glucose. This indicated that there was a strong electrocatalytic function of Cu/$Cu_2O$ layer towards glucose oxidation. Moreover, with the increasing of glucose concentration, the catalytic currents increased gradually on the Cu/$Cu_2O$/TNT electrode (Fig. 3D). The wide oxidation peak at about 0.4-0.7 V was atrributed to the oxidation of Cu (Ⅱ) into Cu (Ⅲ) [1, 9, 12]. The peak potential and the peak current of the Cu/$Cu_2O$/TNTs electrode which was detected in the presence of 2 mM glucose were about 0.5 V and 6.4 mA/$cm^2$. Compared with other previous reported glucose sensors, the Cu/$Cu_2O$/TNT electrode showed lower responsing potential and higher peak current[10, 11]. The results indicated that the coorporation of Cu nanoparticles favors to improve the response current due to the synergistic effect of the highly dispersed Cu and $Cu_2O$ layer and large surface area of $TiO_2$ nanotubes arrays in electrocatalytic reaction as well as the fast electron transfer in the Cu/$Cu_2O$ /TNT electrode. The synergistic effect and controlled growth of Cu and $Cu_2O$ still need to further study.

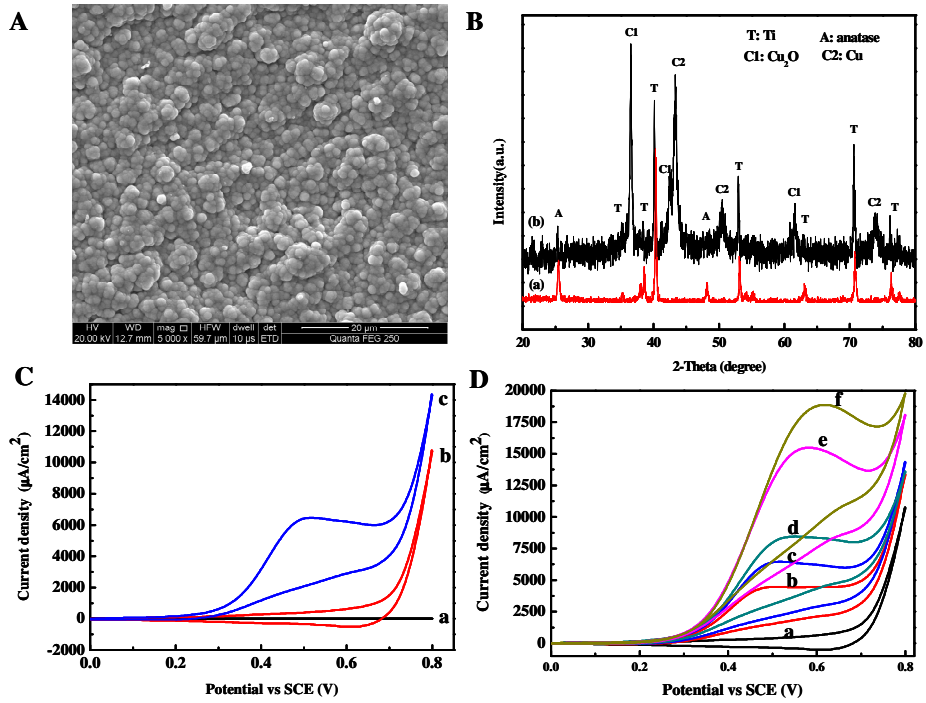



Fig. 3 (A) SEM image of the as-prepared Cu/$Cu_2O$/TNTs; (B) XRD patterns of bare TNT substrate (a) and the Cu/$Cu_2O$/TNT (b); (C) CVs of the bare TNT electrode (a) and the as-prepared Cu/$Cu_2O$/TNT electrode (b and c) in the absence (b) and presence (a and c) of 2 mM glucose in 0.1 M NaOH; (D) CVs of the Cu/$Cu_2O$/TNT electrode in 0.1 M NaOH in different concentration of glucose: 0 (a), 1.0 (b), 2.0 (c), 3.0 (d), 4.0 (e) and 5.0 (f) mM. Note: the applied potential and time to prepared Cu/$Cu_2O$/TNT electrode was −0.6 V and 10 min.

## Conclusions

(a) The effects of the detail fabricate condition such as deposition potential and $CuSO_4$ concentration on the crystal structure, morphology and property of $Cu_2O$/TNT electrode were investigated. (b) The Cu/$Cu_2O$/TNT electrodes showed a higher response current for nonenzymatic glucose oxidation. The good electrocatalytic oxidation of glucose performance, low cost and simple preparation method makes this novel electrode material promising for the development of effective glucose nonenzymatic glucose sensor or glucose biofuel cell.

## Acknowledgements

This research was financially supported by the National Science Foundation of China (No. 51374250) and Hunan Provincial Natural Science Foundation for Innovative Research Groups.

## References

[1] M.M. Rahman, A. Ahammad, J.-H. Jin, J. Sen. 10 (2010) 4855-4886.

[2] G. Wang, X. He, L. Wang, J. Microchim Acta. 180 (2013) 161-186.

[3] M. Rasmussen, R.E. Ritzmann, I. Lee, J. JACS. 134 (2012) 1458-1460.

[4] L. Halámková, J. Halámek, V. Bocharova, J. JACS. 134 (2012) 5040-5043.

[5] Y.-Y. Song, Z. Gao, K. Lee, J. Electrochem Commun. 13 (2011) 1217-1220.

[6] P. Schechner, E. Kroll, E. Bubis, J. Electrochem. 154 (2007) B942-B948.

[7] X. Li, J. Yao, F. Liu, J. Sens Actuators B Chem. 181 (2013) 501-508.

[8] C. Wang, L. Yin, L. Zhang, J. J. Phys. Chem. C. 114 (2010) 4408-4413.

[9] A. Pop, F. Manea, C. Orha, J. Nanoscale Res Lett. 7 (2012) 1-4.

[10] X. Zhou, H. Nie, Z. Yao, J. Sens Actuators B Chem. 168 (2012) 1-7.

[11] S. Luo, F. Su, C. Liu, J. Talanta. 86 (2011) 157-163.

[12] S.T. Farrell and C.B. Breslin, J. Electrochim Acta. 49 (2004) 4497-4503.

*Advanced Materials Research Vol. 937 (2014) pp 9-16*
*© (2014) Trans Tech Publications, Switzerland*
*doi:10.4028/www.scientific.net/AMR.937.9*

# Synthesis, Adsorption Behavior of a Maleamic Acid Cross-linked *β*-Cyclodextrin Polymer for Removal of Basic Fuchsin in Aqueous Solution

Xiao-mei ZHANG*, Hong-zhan LI, Man-li CAO, Chao-yue CHEN

Department of Chemical and Engineering, Anhui University of Science and Technology, Shungeng Middle Road 168, Huainan 232001, Anhui, People's Republic of China.

xmzhang6289@163.com

Xiaomei Zhang

**Keywords** maleamic acid cross-linked *β*-cyclodextrin polymer.adsorption.basic fuchsin.kinetics. thermodynamics

**Abstract.** A crosslinked *β*-cyclodextrin (β-CD) polymer (PCD) was synthesized by using maleamic acid as a crosslinked agent, and its adsorption behavior for basic fuchsin in aqueous solution was investigated. The adsorption isotherms could be well fitted by the Langmuir adsorption equation. On the basis of the Langmuir analysis, the maximum adsorption capacities were determined to be 33.56 $mg \cdot g^{-1}$ at 308K. The kinetics of adsorption followed the pseudo-second-order model.

## Introduction

Widespread contamination of groundwater by organic pollutants including dye-containing effluents has been recognized as an issue of growing seriousness in recent years. Some dyes at very low concentrations (less than $1mg \cdot L^{-1}$) in the effluent are highly visible and can be harmful to human and animals [1-4]. *β*- cyclodextrin (*β*-CD) is a torus-shaped cyclic oligosaccharide made up of seven a -1,4- linked-D- glucopyranose units with an internal hydrophobic cavity [5] which gives rise to a remarkable capacity to form inclusion complexes in solution with organic molecules through host-guest interactions. Hence, *β*-CD complexation is a procedure of choice for depollution techniques [6]. As a kind of potential efficient adsorption material used to remove organic pollutants from water, water-insoluble *β*-cyclodextrin (*β*-CD) based polymers have developed fast in the pass two decades [6-16], due to their properties of forming inclusion complexes with a wide variety of organic compounds in *β*-CD hydrophobic cavity and existing non-inclusion binding sites within framework of the polymers [17]. Water-insoluble *β*-CD polymer, which is synthesized by crosslinking the hydroxyl groups of *β*-CD with diacid to form a stable crosslinked network, have already been used to remove dyes from wastewater [9,18], but little is known about the adsorption kinetics and isotherm of the *β*-CD polymer for dyes. The aim of this paper is to prepare the maleamic acid *β*-CD cross-linked polymer (PCD, chemical structures see Fig.1 ) as an adsorbent for removal of basic fuchsin (BF) from aqueous solutions through the batch experiments while the adsorption kinetics and isotherm of the adsorption process were studied for better understanding of the adsorption behavior.

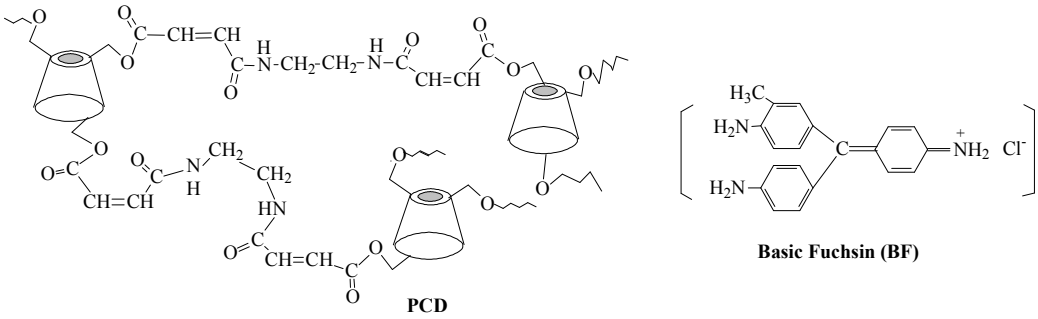



Fig. 1. Chemical structures of PCD and BF

## Experimental

### Reagents

*β*-cyclodextrin (*β*-CD) purchased from Anhui Shanhe Co., Ltd, China was recrystallized in water and dried overnight under vacuum at 100 °C. The cross-linked agent maleamic acid was synthesized according to report [19]. The analytical pure reagents used in the study were purchased from guaranteed manufacturers in China. The water used in all experiments was purified by Ultrapure Water system.

### Instruments

$^1$H NMR spectra were recorded on a Bruker DPX 300 in DMSO-$d_6$ with TMS as internal standard. FT-IR spectra were performed on a Bruker Vector 33 FT-IR spectrometer. All the UV-Vis experiments were carried out using a Shimadzu UV-Vis 2550 spectrophotometer. A ZD-2A automatic potentiometric titration apparatus (Shanghai DaPu Instrument Co., Ltd.) was used to measure the pH of solutions.

### Preparation of Maleamic Acid- *β*-CD Cross-linked Polymer (PCD)

5.0 g maleamic acid were dissolved in 60 mL dry toluene, then, 20mL thionyl chloride were added and the mixture stirred at 60°C for 7 h. The solvent was evaporated under reduced pressure, and the residue was dissolved in dry DMF followed by adding 50 mL dry DMF solution containing 5.7g *β*-CD. The resulting solution was stirred at 65 °C for 12h. The mixture was poured into deionized water after cooled down, and the precipitate was filtered off and then washed with 95% alcohol for three times. Dried in vacuum cabinet dryer at 80°C overnight and then passed through a 80 mesh sieve to ensure a uniform particle size, 6.7g yellowish powder PCD were obtained.

### Adsorption Studies

Accurately weighted amount (50 mg) of PCD were suspended in 15mL BF solution with initial concentrations ranging from 20 -180 mg·L$^{-1}$ in a tightly closed flask. The suspensions were stirred at 260rpm and kept thermostatic at a defined temperature (10- 35°C). After 2.5h, the mixtures were filtrated, and the concentrations were determined by UV-Vis spectrophoto- -meter at 543.0 nm after the pH values of the filtrates were adjusted to 6.1 ±0.1 to exclude the influences of pH on dye itself using NaOH or HCl solution. The adsorption capacity was calculated and expressed in equilibrium adsorption quantity $Q_e$ (mg·g$^{-1}$) or % sorption by equation (1) or (2):

$$Q_e = \frac{V(C_0 - C_e)}{W} \tag{1}$$

$$Sorption\% = \frac{100(C_0 - C_e)}{C_0} \tag{2}$$

Where $C_0$ is the initial concentration (mg·L$^{-1}$), $C_e$ the equilibrium concentration(mg·L$^{-1}$); $V$ is the volume of the solution used (L); and $W$ is the weight of adsorbent used (g).

In kinetic studies, the adsorption quantity of the adsorbate at time $t$, $Q_t$ (mg·g$^{-1}$), was calculated by equation (3):

$$Q_t = V\frac{C_0 - C_t}{W} \tag{3}$$

Where $C_t$ is the concentration of adsorbate in solution at time $t$.

## Results and Discussion

### Characterization of PCD

Fig.2 illustrated the $^1$H NMR spectra for *β*-CD and PCD in DMSO-$d_6$. In comparison with *β*-CD, the $^1$H NMR spectra of PCD showed some line broadening and upfield shifts for the resonance lines

of $\beta$-CD. The relative composition of PCD were calculated from the integration ratio of the $H_1$ nuclei of $\beta$-CD (1/7 area) and the -CH=CH- nuclei in maleamic acid (1/4 area). The number of substituents for PCD was estimated 11.42 maleamic acid units, indicating of 29.0% $\beta$-CD in the polymer.

Fig.3 showed the FT-IR spectra of the synthesized PCD and its native $\beta$-CD. The observable absorption bands in PCD at 1695 $cm^{-1}$ and 1651 $cm^{-1}$ (both were absent in $\beta$-CD) could be assigned to C=O stretching vibration of esther carboxyl and amide carboxyl groups, respectively, which appeared at lower frequency zone due to conjugation effect of carboxyl groups with double bonds. The strong and broad band at 3388 $cm^{-1}$ in $\beta$-CD corresponded to O-H stretching vibration of the hydroxyl groups in $\beta$-CD, and the similar bands observed at 3404$cm^{-1}$ in PCD to the integrated O-H, N-H stretching vibration. The C-H asymmetric stretching vibration of $>CH_2$ at 2927 $cm^{-1}$, the C-OH stretching vibration at 1030 $cm^{-1}$, and the other absorption bands including 1162 $cm^{-1}$ and 578 $cm^{-1}$ in $\beta$-CD also appeared nearly at the same wave numbers in PCD, indicating that the structural characteristics of $\beta$-CD were essentially maintained in PCD.

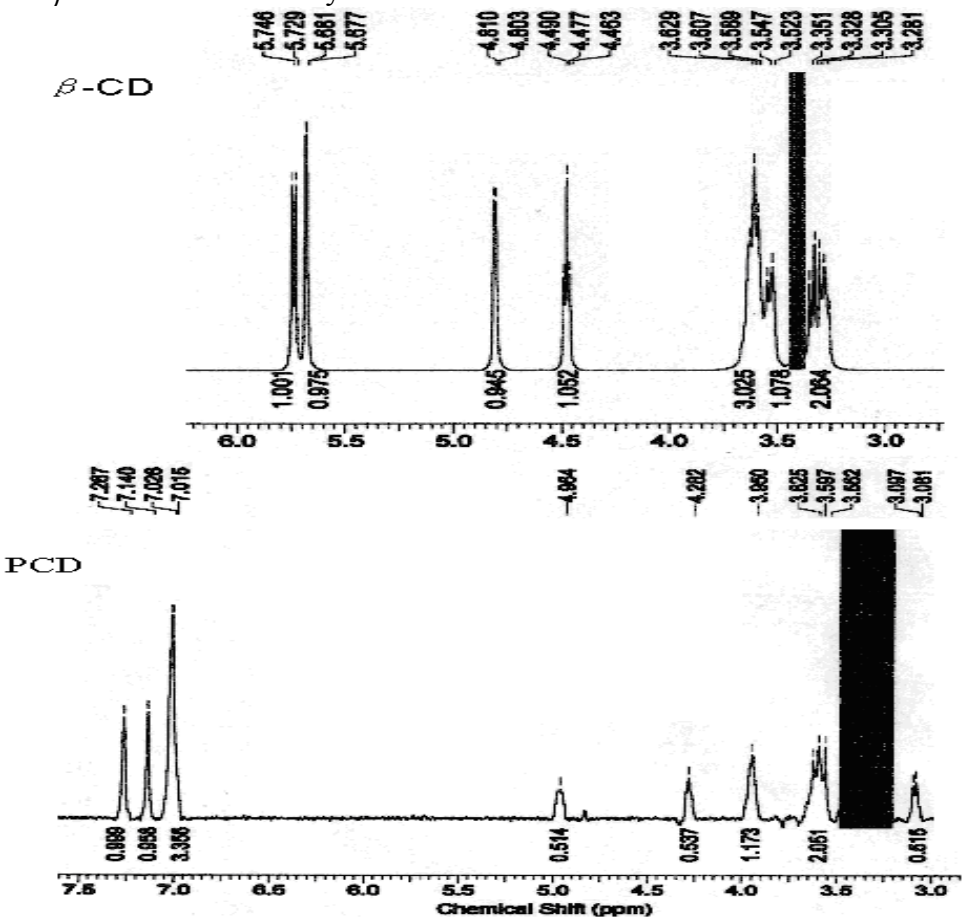



Fig. 2. IH NMR spectra of $\beta$-CD and PCD (DMSO-$d_6$)

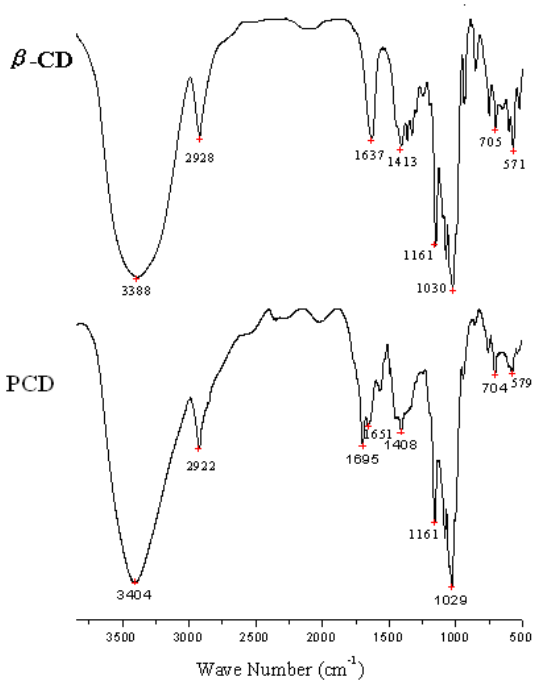



Fig. 3. IR spectra of $\beta$-CD and PCD (KBr)

## Adsorption of BF on to PCD

### Effects of Initial Concentration at Different Temperatures

The effects of initial concentrations on the adsorption capacities $Q_e$ of BF onto PCD at different temperatures were showed in Fig.4. As Fig.4 indicated, $Q_e$ increased with the increase of $C_0$, and then maintained almost constant while $C_0$ exceeded 140 mg·L$^{-1}$. 95% sorption of BF displayed an effective adsorption capacity of PCD to remove BF from water under 40 mg·L$^{-1}$. It is possible that the initial concentration of dyes molecules provide the necessary driving force to overcome the resistances to mass transfer of dyes molecules between the aqueous phase and the solid phase [20]. Moreover, Fig. 4 also showed that $Q_e$ increased with the increase of temperature, and the effect of temperature on $Q_e$ was not obvious until $C_0$ exceeded 60 mg·L$^{-1}$.

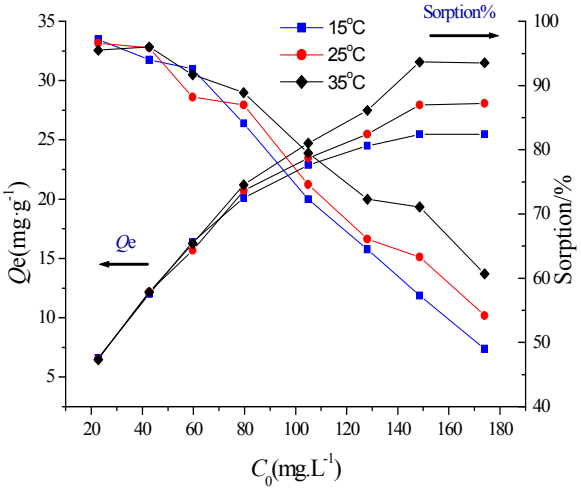



Fig. 4. Effects of $C_0$ on $Q_e$ at different temperatures

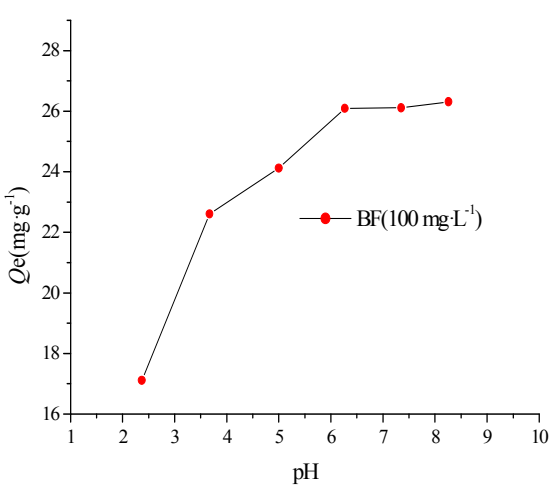



Fig. 5. Effect of pH on $Q_e$ (25°C)

### Effect of pH

Fig. 5 showed the influences of pH on $Q_e$ within pH 2 -9. As shown in Fig.5, the adsorption capacity of PCD increased with the increase of pH, then reached to maximum value and maintained nearly constant over pH 6.5. The PCD contained both hydroxyl and carboxylic groups (at pH 8, these groups are deprotonated) and it was demonstrated that these carboxylic sites were also responsible for dye binding through electrostatic interactions [21]. In acidic medium, hydroxyl and carboxylic groups on PCD were protonated, positively charged BF molecules were difficult to include with $\beta$-CD units and to interact with framework in PCD. So, BF was adsorbed on PCD mainly by van der waals' force and hydrogen bond, which resulted in the low values of $Q_e$. Increasing pH of solution to 6-7, protonated functional groups in PCD and BD were deprotonated gradually, which increased interactions between BF molecules and sorption sites, inclusion and non- inclusion binding sites, which made values of $Q_e$ improved obviously. At higher pH (pH>8.5), BF was precipitated in alkaline solution.

### Adsorption Isotherm

The experimental data were analyzed using tow well-known and widely applied isotherm models of Langmuir and Freundlich [22,23]. The linear equations are given below:

$$\ln Q_e = \ln K_F + \frac{\ln C_e}{n} \tag{4}$$

$$\frac{Ce}{Qe} = \frac{Ce}{Qm} + \frac{1}{QmK_L} \tag{5}$$

Where $Q_e$ (mg·g$^{-1}$) and $C_e$ (mg·L$^{-1}$) are the solid phase concentration of adsorbate and liquid phase concentration at equilibrium, respectively; $K_F$ (L$^{-1}$·mg) is the Freundlich constant, 1/n is the heterogeneity factor; $Q_m$ (mg·g$^{-1}$) is the saturation adsorption quantity and $K_L$ (L·mg$^{-1}$) is the Langmuir isotherm constant.

The plot of ln $Q_e$ versus ln$C_e$ was employed to generate the intercept value of $K_F$ and the slope 1/ n (Fig.6)**.** The $K_F$ relates to adsorption capacity and 1/n is related to the surface heterogeneity. When 0 < 1/n < 1, the adsorption is favorable; 1/ n =1, the adsorption is homogeneous and there is no interaction among the adsorbed species; 1/n > 1, the adsorption is unfavorable [24]. By plotting $C_e/Q_e$ against $C_e$ ( Fig.7), it was possible to obtain the values of $Q_m$ and $K_L$ from the slope and intercept. A higher value of $K_L$ indicates a favorable adsorption process [25]. The Freundlich and Langmuir isotherm parameters for the adsorption of BF onto PCD were listed in Table 1. The criterion of the best-fit between the experimental and calculated sorption data according to the Freundlich and Langmuir isotherm was determined by the correlation coefficients ($R^2$) along with equilibrium adsorption capacities ($Q_m$) .

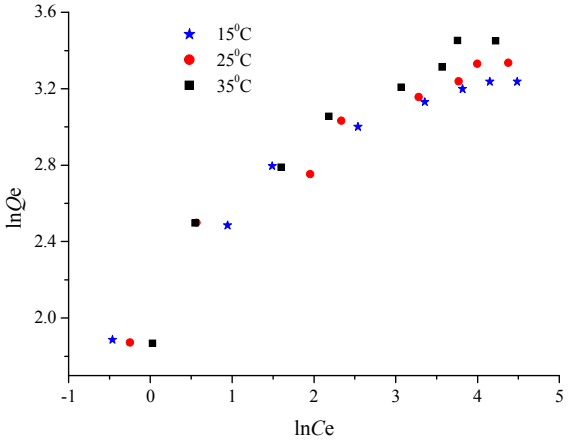



Fig. 6. ln $Q_e$ versus ln$C_e$ for BF

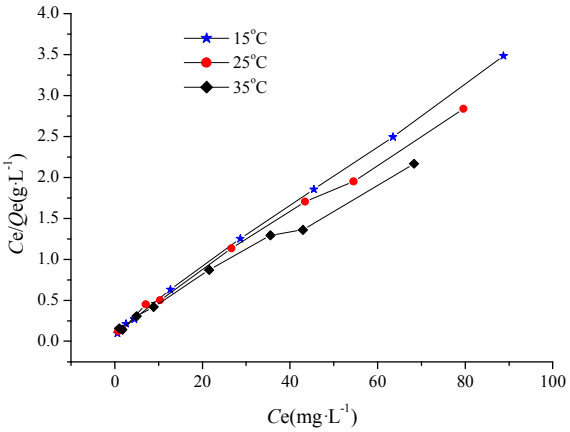



Fig. 7. $C_e/Q_e$ versus $C_e$ for BF

Table 1. The adsorption parameters for Freundlich and Langmuir's isotherm at different temperatures

| Model | Parameters | Temperature /K | | |
|---|---|---|---|---|
| | | 288 | 298 | 308 |
| Freundlich | $K_F$ | 9.090 | 8.736 | 8.535 |
| | 1/n | 0.2616 | 0.2932 | 0.3412 |
| | $R^2$ | 0.922 | 0.931 | 0.920 |
| Langmuir | $Q_m{}^a$ /mg.g$^{-1}$ | 26.34 | 29.33 | 33.56 |
| | $K_L$/L·mg$^{-1}$ | 0.326 | 0.229 | 0.200 |
| | $R_L$ | 0.133 | 0.179 | 0.200 |
| | $R^2$ | 0.999 | 0.995 | 0.993 |
| $Q_m{}^b$ /mg.g$^{-1}$ | | 25.47 | 28.08 | 31.51 |

$Q_m{}^a$ : calculated values ; $Q_m{}^b$ : experimental data

As displayed in Fig.6, Fig.7 and Table 1, adsorption equilibrium data of BF at different temperatures under the concentration range studied fitted the Langmuir's model well, with the correlation coefficients of $R^2 > 0.993$ and the small deviation of $Q_m$ between calculated and tested data, which suggested that some homogeneity in the surface of PCD would play a key role in BF adsorption and the adsorption of BF on to PCD would be a monomolecular layer adsorption.

From the value of Langmuir isotherm constant $K_L$, a dimensionless parameter called separation factor $R_L$ can be calculated through following equation:

$$R_L = \frac{1}{1 + K_L C_0} \tag{6}$$

Where $K_L$ is the Langmuir constant (L·mg$^{-1}$) and $C_0$ is the initial concentration (mg·L$^{-1}$). The value of $R_L$ indicates the type of the isotherm to be unfavorable ($R_L$ >1), linear ($R_L$ =1), favorable (1>$R_L$ >0), or irreversible ($R_L$ =0) [26]. It was observed that the values of $R_L$ in the range of 0 -1(see Table 1) confirmed the favorable uptake of the dyes process.

**Adsorption Kinetics**

The non-linear forms of the pseudo-first-order and pseudo-second-order [27,28] can be expressed by the following equations, respectively:

$$Q_t = Q_e(1 - e^{-K_1 t}) \tag{7}$$

$$Q_t = \frac{Q_e{}^2 K_2 t}{(1 + Q_e K_2 t)} \tag{8}$$

Where, $Q_e$ and $Q_t$ refer to the adsorption quantity (mg·g$^{-1}$) at equilibrium and at any time $t$ (min), respectively, and $k_1$ (min$^{-1}$) and $k_2$ (g·mg$^{-1}$·min$^{-1}$) are the pseudo-first-order and pseudo- second-order rate constants which can be determined by plotting of $Q_t$ versus $t$ using the non-linear regression analysis, respectively. The criterion of the best-fit between the experimental and calculated sorption data according to the two models is determined by correlation coefficient ($R^2$), also along with equilibrium adsorption capacities ($Q_e$). The kinetic data at 10°C,20°C and 30°C were analyzed using pseudo-first-order and pseudo-second-order models, showen in Fig.8, and the kinetics parameters mentioned above at three temperatures were summarized in Table 2.

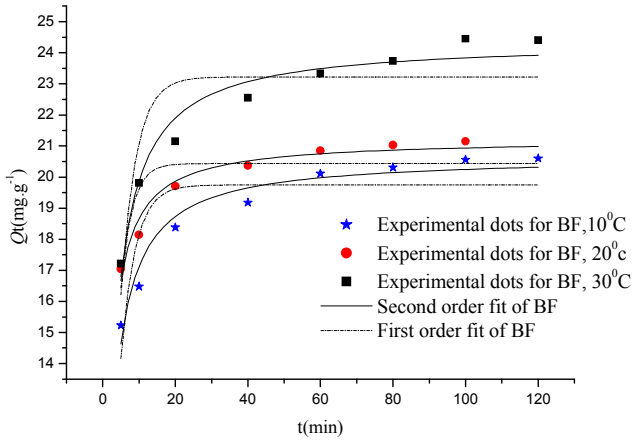



Fig. 8. Kinetic models for adsorption of BF onto PCD ($C_{0,BF}$=102 mg.L$^{-1}$)

Table 2. Pseudo-first and second order kinetics parameters for adsorption of BF onto **PCD**

| | T/K | First order: $Q_t = Q_e(1-e^{-K1t})$ | | | Second order: $Q_t = \frac{Q_e^2 K_2 t}{1+Q_e K_2 t}$ | | | $Q_e^b$ / mg·g$^{-1}$ |
|---|---|---|---|---|---|---|---|---|
| | | $K_1$/min$^{-1}$ | $Q_e^a$/mg·g$^{-1}$ | $R^2$ | $K_2$/g·min$^{-1}$·mg$^{-1}$ | $Q_e^a$/mg·g$^{-1}$ | $R^2$ | |
| BF(102 mg·L$^{-1}$) | 283 | 0.2527 | 19.75 | 0.733 | 0.0235 | 20.66 | 0.95 | 20.60 |
| | 293 | 0.3257 | 20.44 | 0.724 | 0.0345 | 21.22 | 0.96 | 21.15 |
| | 303 | 0.2398 | 23.22 | 0.783 | 0.0182 | 24.37 | 0.96 | 24.45 |

$Q_e^a$ : calculated values ; $Q_e^b$ : experimental data

From Fig.8 and Table 2, kinetics data fitted the pseudo-second order model better than pseudo-first-order, with regression coefficients $R^2$ higher than 0.95, and the calculated $Q_e$ values from the model were also in good agreement with the experimental values. Rsults also showed that the adsorption capacities increased with the increase of temperature at the same initial concentration of 102 mg·L$^{-1}$. This confirmed that adsorption of BF onto PCD took place probably via surface adsorption firstly, then BF molecules diffused from the surface into the interior of PCD for further interactions (including inclusion, hydrophobic interactions and chemical reactions), and high temperature was favorable to those interactions.

## Conclusion

A maleamic acid cross-linked *β*-cyclodextrin polymer PCD was synthesized and its adsorbtion behavior to BF from water was investigated. Results showed that 95% sorption of BF from water displayed a good adsorption capacity of PCD at initial concentration under 40 mg·L$^{-1}$ using dosage of 3.3 g·L$^{-1}$. Equilibrium isotherm data were analyzed according to Freundlich and Langmuir equations. The Langmuir isotherm gave the best correlation for the adsorption of BF on PCD, indicating a monomolecular layer adsorption. The kinetic data were analyzed using pseudo-first order kinetics, pseudo-second order kinetics models . It was found that kinetics followed a pseudo-second order equation.

## Acknowledgement

This work was supported by a grant from natural science research projects for universities in AnHui province (No. KJ2011A091)

**References**

[1] I.M.Banat, P.Nigam, D.Singh, R.Marchant. *Bioresour. Technol.* 58, 217-227 (1996)

[2] T.Robinson, G.McMullan, R.Marchant, P.Nigam. *Biresour. Technol.* 77, 247- 255 (2001)

[3] M.Rafatullah, O.Sulaiman, R.Hashim, A.Ahmad. *J. Hazard. Mater.* 177, 70-80 (2010)

[4] M.Doˇgan, H.Abak, M.Alkan. *J. Hazard. Mater.* 164, 172-181 (2009)

[5] J.Szejtli. *Chem Rev.* 98, 1743-1754 (1998)

[6] G.Crini. *Dyes Pigments.* 77, 415-426 (2008)

[7] Crini, G. *Bioresour Technol.* 90, 193-198 (2003)

[8] G.Crini, H.N.Peindy. *Dyes Pigments.* 70, 204-211 (2006)

[9] D.Zhao, L.Zhao, C.S.Zhu, W.Q.Huang, J.L.Hu. *Inclusion Phenom. Macrocycl. Chem.* 63, 195-201(2009)

[10] E.Yilmaz, S.Memon, M.Yilmaz. *J. Hazard. Mater*. 174, 592 -597(2010)

[11] B.B.Mamba, R.W.Krause, T.J.Malefetse, E.N.Nxumalo. *Environ. Chem. Lett.* 5, 79-84 (2007)

[12] E.Y.Ozmen, M.Yilmaz. *J. Hazard. Mater.* 148, 303-310 (2007)

[13] H.Yamasaki, Y.Makihata, K.Fukunaga. *J. Chem. Technol. Biotechnol.* 83, 991-997 (2008)

[14] A.Romo, F.J.Peñas, I.J. R.sasi, I.X. García-Zubiri, G. González-Gaitano. *React. Funct. Polym.* 68, 406-413 (2008)

[15] X.M.Zhang, C.S.Peng, G.C.Xu. J. *Incl. Phenom. Macrocycl. Chem.* 72, 165-171 (2012)

[16] L.L.Fan, Y.Zhang, C.N.Luo, F.G.Qiu, H.M.Lu, M.Sun. *Int. J. Biol. Macromo.* 50, 444-450 (2012)

[17] W.L.D.ilson, M.H.Mohamed, J.V.Headley. *J. Colloid Interf. Sci.* 357, 215-222 (2011)

[18] L.D.Wilson, R.Guo. *J. Colloid Interf. Sci.* 387(1), 250-261 (2012)

[19] H.Z.Li, C.Ma, X.M.Zhang, G.C.Xu, C.Y. Chen. *Petrochemical Technology*. 41(12) 1424 -1428 (2012) (in Chinese)

[20] Y.S.Ho, T.H.Chiang, Y.M.Hsueh. *Process Biochem.* 40, 119-124 (2005)

[21] G.Crini, H.N.Peindy, F.Gimbert, C.Robert. *Sep. Pur. Technol.* 53, 97 -110 (2007)

[22] H.M.F.Freundlich. *Z. Physi. Chem.* 1906, *57,* 385-470

[23] I.Langmuir. *J. Am. Chem. Soc. 8*, 2221-2295(1916)

[24] M.A.Rauf, S.B.Bukallah, F.A.Hamour, A.S.Nasir. *Chem. Eng. J.* 137, 238-243 (2008)

[25] Y.S.Al-Degs, M.I.El-Barghouthi, A.H.El-Sheikh, G.M.Walker. *Dyes Pigments.* 77, 16-23 (2008)

[26] A G.nnadurai, L.Y.Ling, J.F.Lee.*J. Hazard Mater*. 152, 337-346 (2008)

[27] S. Lagergren.*Kungliga Svenska Vetenskapsakademiens, Handlingar*. 24, 1 -39 (1898)

*Advanced Materials Research Vol. 937 (2014) pp 17-22*
*© (2014) Trans Tech Publications, Switzerland*
*doi:10.4028/www.scientific.net/AMR.937.17*

# Electrosyntheses of Poly (selenophene-co-3-methylthiophene) with Improved Thermoelectric Property in Boron Trifluoride Diethyl Etherate

Sheng-Tao WANG[1], Bao-Yang LU[2], Jing-Kun XU[1,*] and Wei-Qiang ZHOU[1]

[1]Jiangxi Key Laboratory of Organic Chemistry, Jiangxi Science and Technology Normal University, Nanchang 330013, China

[2]School of Pharmacy, Jiangxi Science and Technology Normal University, Nanchang 330013, China

*Corresponding author: xujingkun@tsinghua.org.cn; Tel.: +86-791-88537967; fax: +86-791-83823320

**Keywords:** Conducting polymers, Electrochemical copolymerization, Poly(3-methylthiophene); Polyselenophene, Thermoelectric property

**Abstract.** Novel poly(selenophene-co-3-methylthiophene) was successfully achieved by directly electrochemical oxidation of the monomer mixtures of selenophene and 3-methylthiophene (3MeT) in boron trifluoride diethyl etherate. The effect of monomer concentration ratios on the copolymerization were investigated by cyclic voltammetry. The structures of as-prepared copolymers were characterized by UV-vis and infrared spectroscopy. The conductivity and thermoelectric measurements revealed the incorporation of 3MeT into the polyselenophene (PSe) chain improved significantly the conductivity and thermoelectric property of PSe.

## Introduction

Conducting polymers have been attracting considerable attention owing to their potential applications in rechargeable batteries, electrochromic devices, supercapacitors, antistatic coating, biosensors, etc [1,2]. Compared to polythiophene, polyselenophene (PSe) with lower LUMO level has the reduced optical band gap, enhanced photostability, lower oxidation and reduction potentials, greater polarizability of the selenium atom compared with the sulfur atom, and improved interchain charge transfer [3]. Therefore, PSe and its derivatives are a promising class of organic semiconductors for applications in optoelectronic devices such as light-emitting field-effect transistors.

It is surprising that little attention was paid to PSe and its derivatives due to their low conductivity and lack of well-defined electrochemical behavior [4]. Although many modifications by chemical methods have improved the qualities of PSe and its derivatives, the preparation of the initial substituted selenophene monomers was very complex [5,6]. Electrochemical polymerization is one of the most useful approaches for one-step syntheses of conducting polymer. However, the high oxidation potential of selenophene in common organic solvents resulted in the damage of conjugated PSe backbone, leading to powdery PSe formation with low conductivity of $3.7\times10^{-2}$ S/cm [2]. Previously, our group has prepared free-standing PSe by low potential anodic oxidation of selenophene in boron trifluoride diethyl etherate [7]. Although as-formed PSe from BFEE had better properties than that from common organic solvents, PSe exhibited still low conductivity ($2.8\times10^{-1}$ S/cm) and poor thermal stability. Therefore, it will be necessary to further improve the electrical conductivity and thermal stability of PSe for its future applications in some specific and sophisticated domains.

Electrochemical copolymerization can modify the properties of conducting polymers. In order to further improve the properties of PSe, a proper copolymerized-partner should be found out. Presently, 3-methylthiophene (3MeT) as an important derivative of thiophene is popular to be used as copolymerized-partner because poly (3-methylthiophene) (PMeT) has many advantages such as outstanding electrical conductivity, high tensile strength, good environmental stability, and high thermal stability [8]. The incorporation of 3MeT can improve the electrochemical activity, electrical conductivity, mechanical property and thermal stability of polymers. Additionally, the

electron-donating group (-$CH_3$) at thiophene ring can increase the HOMO level of thiophene [9]. The incorporation of selenophene with the low LUMO and3MeT with high HOMO level will produce a novel compound with lower optical band gap. Therefore, it would be interesting to copolymerize selenophene with 3MeT electrochemically so that as-formed copolymer may have high conductivity and other improved properties. However, to the best of our knowledge, the electrochemical copolymerization of selenophene with 3MeT has not been reported so far.

Here, selenophene and 3MeT were successfully copolymerized by direct anodic oxidation of monomer mixtures in BFEE. The electrochemical properties and spectroscopic properties, electrical conductivity and thermoelectric properties of as-formed copolymers were studied, which were in comparison with those of PSe and PMeT homopolymers.

## Experimental

### Chemicals

Boron trifluoride diethyl etherate (BFEE, Beijing Xin'ao Chemical Plant) was distilled and stored at −20 °C before use. Selonophene (98%; Tokyo Chemical Industry, Tokyo, Japan) and 3MeT (99%, Acros Organics, Fair Lawn, New Jersey) were used directly.

### Electrochemical Experiments

Electrochemical experiments were carried out in a one-compartment glass cell using a Model 263A potentiostat-galvanostat (EG&G Princeton Applied Research) connected to a computer. The working electrode and counter electrode were two platinum (Pt) wires. All the potentials mentioned follow were versus the Ag/AgCl electrode. The polymer films deposited on an indium-tin-oxide (ITO) coated glass were used for the ultraviolet–visible (UV–vis) spectral measurements. After polymerization, all the PSe, PMeT, and copolymers were rinsed repeatedly with ethyl ether to remove the electrolyte, monomers, and oligomers. All polymers were dried at 60 ºC under vacuum for 2 days.

### Characterization

The electrical conductivity of as-formed polymer and copolymer films was determined by applying the conventional four-probe technique with the films of the samples. UV–vis spectra were measured with a Perkin-Elmer Lambda 900 UV–vis-near-infrared spectrophotometer. Infrarde spectra were recorded on a Bruker Vertex 70 Fourier transform infrared (FTIR) spectrometer with KBr pellets.

## Results and Discussion

### Electrochemical Copolymerization

Fig. 1 shows the successive cyclic voltammograms (CVs) of selenophene, 3MeT, and the corresponding monomer mixtures with different feed ratios (selenophene/3MeT = 1:1, 1:5, 1:10) in BFEE. As the cyclic potential scan continued, conducting polymer films were formed on the working electrode surface. The increase in the redox wave current densities implied that the amount of conducting polymers deposited on the electrode was increasing. Moreover, the obvious potential shift of the wave current density provided information about the increase in the electrical resistance in the polymer film and the overpotential needed to overcome the resistance [10]. For the CVs recorded in the solution of selenophene (Fig. 1a), their redox peaks were unsymmetrical and located at about 0.75 V and -0.03 V. On the contrary, the CVs of 3MeT was quite plump (Fig. 1e), and its oligomer or polymer could be oxidized and reduced at the range of 0.57 to -0.25 V. For comparison, the CVs of the monomer mixtures with the feed ratio of selenophene/3MeT=1:1, 1:5, and 1:10 were also recorded (Fig. 1b-d), respectively. When the monomer feed ratio of selenophene/3MeT was 1:1, the mixtures could be oxidized and reduced from 0.67 to 0 V. When the concentration of 3MeT was dominated in the monomer mixtures, the CVs were much more similar to those of pure 3MeT,

indicating that more 3MeT units were incorporated into the copolymer film. As the feed ratio of the monomer mixtures changed, new redox peaks of the CVs of the copolymer appeared compared with those of homopolymers, which indicated that a copolymer of selenophene and 3MeT might be formed in the system.

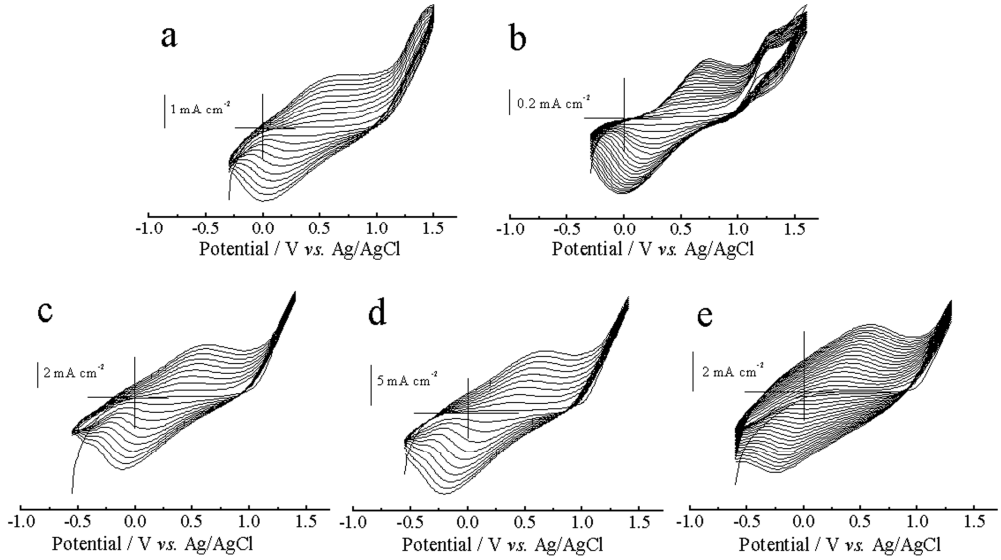



Fig. 1. CVs of 5 mmol $L^{-1}$ selenophene (a), the monomer mixtures with the feed ratios of selenopnene/3MeT=1:1 (b), 1:5 (c), 1:10 (d), and 5 mmol $L^{-1}$ 3MeT (e) in BFEE at 100 mV $s^{-1}$.

**Electrochemistry of the Copolymer Films**

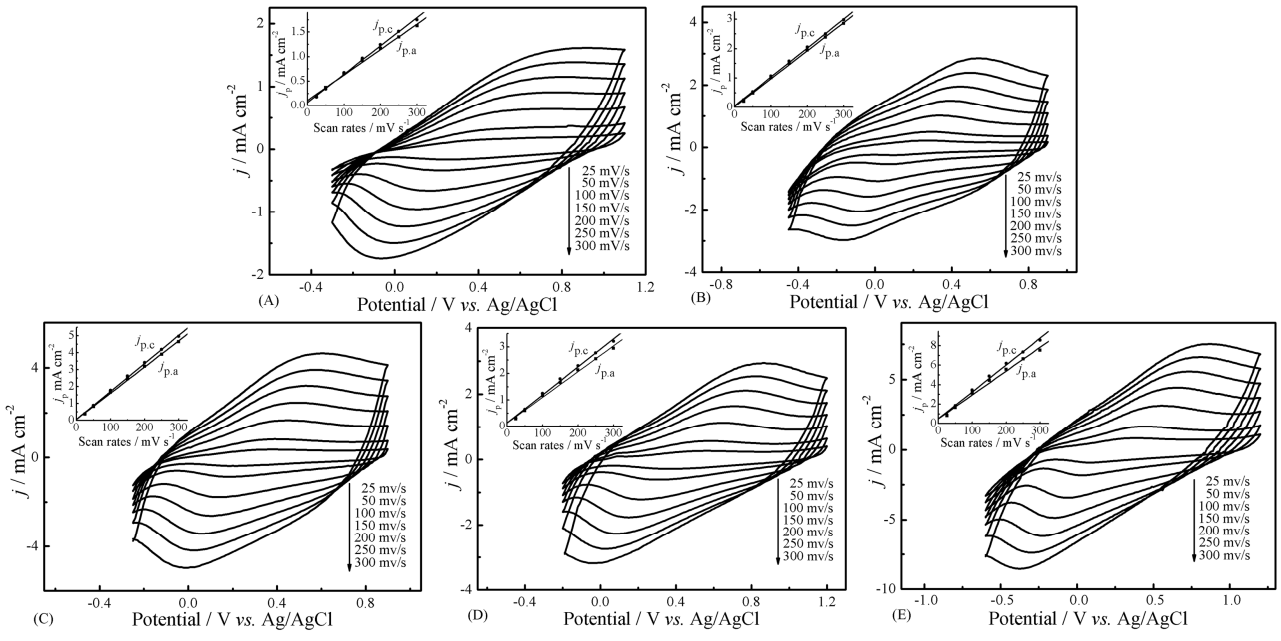



Fig. 2. CVs of PSe (A), PMeT (B), and copolymers prepared by the feed ratios of selenophene/3MeT= 1:1 (C), (1:5) (D), (1:10) (E) in BFEE.

The electrochemical properties of these films were characterized by CVs in BFEE (Fig. 2). Obviously, these polymer films were cycled repeatedly between conducting and insulating states without significant decomposition. In the insets of Fig. 2, the current densities were proportional to the potential scan rates, indicating a redox couple fixed on the electrode. As-synthesized PSe from BFEE was oxidized and reduced from 0.90 to -0.06 V. For PMeT, it was oxidized and reduced at a

lower and narrower potential range from 0.53 to -0.16 V (Fig. 2B). However, as-prepared copolymers exhibited different electrochemical activity. For example, the copolymer prepared from the feed ratio of selenophene/3MeT=1:1 could be oxidized or reduced from 0.56 to -0.01 V (Fig. 2C), the copolymer prepared from the feed ratio of selenophene/3MeT=1:5 showed a couple of redox waves at 0.86 and -0.02 V (Fig. 2D), when the feed ratio changed to 1:10, the redox peaks of copolymer located at around 0.85 and -0.36 V (Fig. 2E). Based on the comparison described above, it was reasonable to draw the conclusion that selenophene and 3MeT were oxidized together and the copolymer chain was composed of both selenophene and 3MeT units.

**Structural Characterization**

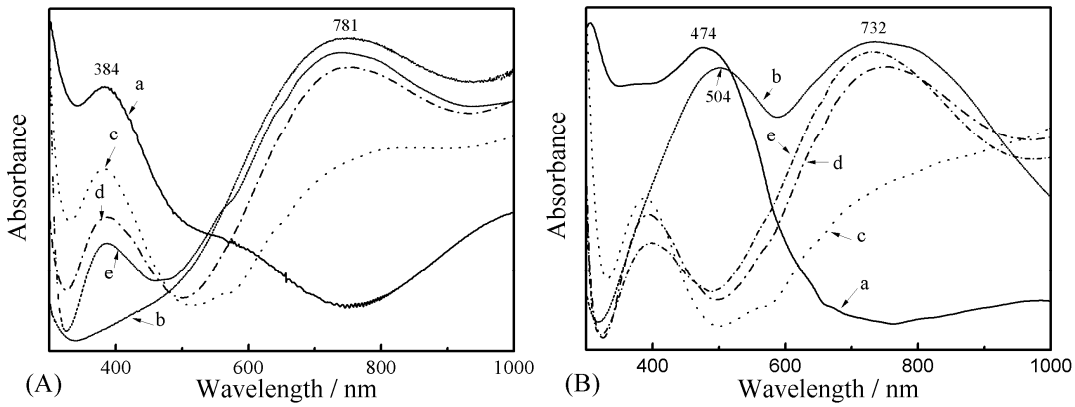



Fig. 3. UV–Vis spectra of doped (A) and dedoped (B) PSe (a), P3MeT (b), and copolymers prepared by the feed ratios of selenophene/3MeT=1:1 (c), 1:5 (d), 1:10 (e) deposited on ITO glasses.

Fig. 3 shows the UV–vis spectra of the doped (A) and dedoped (B) homopolymers and copolymer films. The spectrum of as-formed PSe film showed a characteristic absorption peak at 384 nm and a shoulder at about 600 nm [Fig. 3A(a)], which could be assigned to the valence band–conductive band ($\pi$-$\pi^*$) transition [26]. The broad bands from 750 nm to near-infrared region are the characteristic of the existence of conducting species. For PMeT film, there was a strong broad absorbtion at 500-950 nm and a very weak shoulder peak at about 470 nm, which are ascribed to the characteristic of conducting species and $\pi$-$\pi^*$ transition, respectively [Fig. 3A(b)]. For these doped copolymers, their spectra showed the characteristic absorptions of both PSe and PMeT [Fig. 3A(c-e)]. At the same time, the band intensity of about 384 nm weakened and the band of 500-950 nm intensified with increasing 3MeT concentration. However, the spectra of dedoped homopolymers show greatly difference from those of corresponding doped polymers. That is, the characteristic peaks of conducting species and $\pi$-$\pi^*$ transition, respectively, were weakened and intensified for the both dedoped homopolymers [Fig. 3B(a,b)], which indicated the dedoped PSe and dedoped PMeT were changed into neutral or nonconductive state from their conductive state. Surprisedly, the spectra of copolymers in dedoped state all were similar to those in doped state. This indicated that copolymers had stable doped state.

Fig. 4 shows the vibrational spectra of PSe, PMeT and copolymers. The PSe film shows aromatic stretching bands at 1630, 1430, and 1081 $cm^{-1}$ (Fig. 4A). A strong absorption at 782 $cm^{-1}$ can be assigned to the C-H out-of-plane vibration of the 2,5-disubstituted selenophene ring (due to $\alpha$, $\alpha'$ polymerization). The very weak band at 682 $cm^{-1}$ is ascribed to the C-H out-of-plane vibration of the monosubstituted selenophene rings. The lack of characteristics absorption band of $\alpha$, $\beta$ coupling at 824 $cm^{-1}$ confirms that selenophene units are coupled by $\alpha$,$\alpha'$ places. The above-mentioned characteristics absorption band could also be found in the spectra of copolymers. For PMeT (Fig. 4E), the bands at 1643 and 1202 $cm^{-1}$ are ascribed to the stretching modes of C=C in the thiophene ring. The band at 820 $cm^{-1}$ is ascribed to the out-of-plane C-H bands, which could be found in the spectra of the copolymers (Fig. 4B-D). The bands at 1445 and 1379 $cm^{-1}$ were assigned to the deformation of the

methyl group. The weak absorption band at about 614 $cm^{-1}$ was the characteristic absorption of the C-S bond.

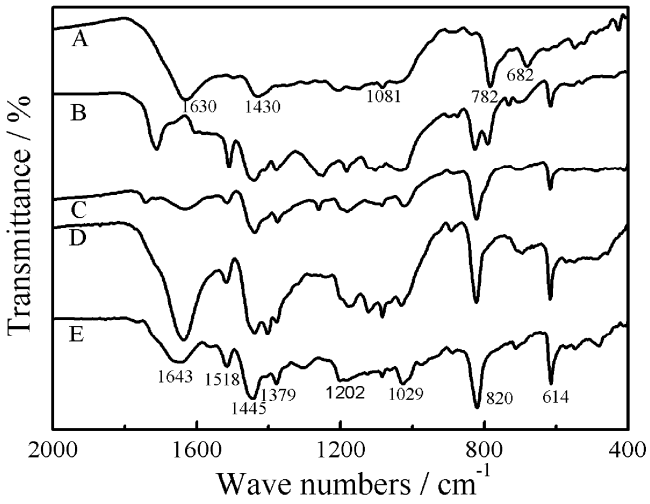



Fig. 4. FT-IR spectra of PSe (A), copolymers prepared in BFEE by the feed ratios of selenophene/3MeT=1:1 (B), 1:5 (C) and 1:10 (D), and PMeT (E) at 1.2 V.

**Electrical Conductivity and Thermoelectric Property**

The film quality of PMeT prepared from BFEE was quite good, which can be peeled off the electrode into freestanding state. After the copolymerization of selenophene and 3MeT, the copolymer films can also be peeled from the electrode surface as freestanding films. The electrical conductivities of freestanding PSe, PMeT, and their copolymers were investigated. The electrical conductivity of PSe was about $1.6\times10^{-1}$ S $cm^{-1}$, whereas PMeT showed higher electrical conductivity, up to 69 S $cm^{-1}$. The electrical conductivities of the copolymers were between PSe and PMeT. When the feed ratios of selenophene/3MeT=1:10, the electrical conductivities of as-prepared copolymers reached 9.3 S $cm^{-1}$.

Table 1. Electrical conductivities and thermoelectric properties of copolymers prepared by the feed ratios of selenophene/3MeT=1:1 (A), 1:5 (B) and 1:10 (C) at 1.2 V.

| Polymers | Conductivity (S $cm^{-1}$) | Seebeck coefficient ($\mu$V $K^{-1}$) | $\sigma S^2$ / 10000 ( mW $K^{-1}$) |
|---|---|---|---|
| PSe | 0.16 | 17 | 0.0046 |
| Copolymer (A) | 0.37 | 36 | 0.048 |
| Copolymer (B) | 6.68 | 20.89 | 0.29 |
| Copolymer (C) | 9.3 | 17.79 | 0.29 |
| PMeT | 69 | 38 | 9.96 |

Thermoelectric property of polymers were also investigated, the results are shown in Table. 1. Note that $\sigma S^2$ is the power factor. The higher power factor indicated that the polymers had better thermoelectric property. In Table 2, PMeT showed good power factor, up to 9.96 mW $K^{-1}$, which is much higher than that of PSe (0.0046 mW $K^{-1}$). The power factors of the copolymers were between those of PSe and PMeT. When the feed ratios of selenophene/3MeT≤1:5, the power factors of as-prepared copolymers can reach 0.29 mW $K^{-1}$. From the above results of conductivity and thermoelectric property, the insertion of 3MeT units into PSe was greatly helpful for the property improvements of PSe.

## Conclusions

The electrochemical copolymerization of selenophene and 3MeT was successfully realized in BFEE by direct anodic oxidation of selenophene and 3MeT monomer mixtures. Electrochemical and structural studies indicated high quality copolymer films were formed. The electrical conductivities of as-prepared copolymers reached 9.3 S $cm^{-1}$, and the power factor of thermoelectric was 0.29 mW $K^{-1}$. Therefore, the successful electrochemical copolymerization of selenophene and 3MeT in BFEE would be greatly helpful for the further study of novel conducting polymers containing selenophene units.

## Acknowledgements

NSFC (50963002, 51073074), Jiangxi Provincial Department of Education (GJJ11590, GJJ10678, GJJ12595), Natural Science Foundation of Jiangxi Province (2010GZH0041) are acknowledged for their financial support.

## References

[1] H. Shirakawa, E. Louis, A.G. Mac Diarmid, C.K. Chiang, A.J. Heeger, J. Chem. Soc. Chem. Commun. 16 (1977) 578-580.

[2] J. Roncali, Chem. Rev. 92 (1992) 711-738.

[3] U. Salzner, J.B. Lagowski, P.G. Pickup, R.A. Poirier, Synth. Met. 96 (1998) 177-189.

[4] S. Glenis, D.S. Ginley, A.J. Frank, J. Appl. Phys. 62 (1987) 190-194.

[5] Y.H. Wijsboom, A. Patra, S.S. Zade, Y. Sheynin, M. Li, L.J.W. Shimon, M. Bendikov, Angew. Chem. Int. Ed. 48 (2009) 5443-5447.

[6] S. Haid, A. Mishra, C. Uhrich, M. Pfeiffer, P. Bäuerle, Chem. Mater. 23 (2011) 4435-4444.

[7] S.Z. Pu, J. Hou, J.K. Xu, G.M. Nie, S.S. Zhang, L. Shen, Q. Xiao, Mater. Lett. 59 (2005) 1061-1065.

[8] L. Zhou, S. Jin, G. Xue, Macromol. Chem. Phys. 197 (1996) 3309-3315.

[9] H.A.M. Van Mullekom, J.A.J.M. Vekemans, E.E. Havinga, E.W. Meijer, Mater. Sci. Eng. R 32 (2001) 1-40.

[10] T.F. Otero, E.D. Larreta-Azelain, Polymer 29 (1988) 1522-1527.

*Advanced Materials Research Vol. 937 (2014) pp 23-28*
*© (2014) Trans Tech Publications, Switzerland*
*doi:10.4028/www.scientific.net/AMR.937.23*

# Electrodeposition of Novel Cross-linked Poly(methacrylic acid) Functionalized Poly(9-aminofluorene) Network Films

Dan CHENG[1], Bao-yang LU[2], Wei-qiang ZHOU[1] and Jing-kun XU[1,*]

[1]Jiangxi Key Laboratory of Organic Chemistry, Jiangxi Science and Technology Normal University, Nanchang 330013, China

[2]School of Pharmacy, Jiangxi Science and Technology Normal University, Nanchang 330013, China

xujingkun@tsinghua.org.cn

*Corresponding author

**Keywords:** Conducting polymer, Poly(9-aminofluorene), Poly(methacrylic acid), Secondary polymerization, Fluorescence

**Abstract.** Four novel cross-linked network conjugated poly(methacrylic acid) functionalized poly (9-aminofluorene) films were prepared by a precursor polymer approach, i.e., poly { poly [ N - (9H-fluoren-9-yl) methacrylamide ] } (P1), poly { poly [ N - (9H-fluoren-9-yl) methacrylamide-*co*-methacrylic acid ] } (P3), poly { poly [ N - (9H-fluoren-9-yl) methacrylamide] -*co*-9-aminofluorene } (P2) and poly { poly [ N - (9H-fluoren-9-yl) methacrylamide-*co*-methacrylic acid ] -co-9-aminofluorene } (P4). As-prepared polymer films had good redox activity and structure stability in concentrated sulfuric acid. Fluorescence spectra indicated that the soluble cross-linked polymers were good blue light emitters and in solid state they were blue-green light emitters.

## Introduction

The precursor polymer approach has attracted significant attention because it is a method to prepare high quality optical ultrathin films of conjugated polymers in microelectronics devices [1-3]. For the approach, the first step is to design and synthesize a polymer containing pendant active groups as precursor polymer. Then a cross-linked network polymer can be formed by the electropolymerization or chemical oxidation polymerization due to the inter- and intra-molecular cross-linking between pendant active units. The process is of high interest for incorporating functional groups with specific electroactive properties to fine-tune structure-property relationships. Using the secondary polymerization of the conjugated precursor polymer, flat network ultrathin films has been deposited and patterned by electrochemical methods [1-3].

Polyfluorene and its derivatives (PFs) have been considered promising candidates as blue-light-emitting materials in polymer light emitting diode [4]. Among PFs, poly (9-aminofluorene) (P9AF) is a valuable polymer because amino group substitution on polyfluorene has obvious advantages, i.e., the amino group is a very good functionalized group, and amino group as electron donor can enhance the fluorescence of polyfluorene. However, P9AF is difficult to obtain in conventional electrolytes by electrochemical polymerization [5]. Using a middle strong Lewis acid as electrolyte, P9AF has been successfully electrodeposited in boron trifluoride diethyl etherate (BFEE) [5]. Unfortunately, it is difficult to form a uniform thin film due to the poor film-forming property of P9AF itself. In order to improve the film-forming property of P9AF, P9AF may be further functionalized by $NH_2$ group to graft other functional groups, such as polymethylsiloxane, poly(cyclic ether) and poly(acrylic acid). Poly (acrylic acid) and its derivatives are widely used for the formulation of paints because they possess excellent film-forming property and good mechanical property [6]. At present, cross-linked conjugated polymers functionalized with polyacrylate have also been developed by our group, such as polyacrylate-functionalized poly (3,4-ethylenedioxythiophene) polymer [7] and polyacrylate-functionalized polycarbazole polymer [8]. Polyacrylate backbone on as-prepared polymers had great positive effect on their mechanical, optical and electrochemical

properties. Methacrylic acid rich in reactive carboxyl (–COOH) can easily bond with amino group at the 9-position of fluorene, forming N - (9H-fluoren-9-yl) methacrylamide. N - (9H-fluoren-9-yl) methacrylamide failed for its electrochemical polymerization in different electrolyte systems. However, the electropolymerization of poly (N-vinylcarbazole) formed through free radical polymerization of alkene can be easily realized [9]. It should be supposed that the precursor polymers based on poly [ N - (9H-fluoren-9-yl) methacrylamide] can also be polymerized. If so, it will be interesting to prepare the cross-linked network poly (methacrylic acid)-functionalized P9AF films through precursor polymer route. Up to now, there have been no reports on the cross-linked conjugated poly (methacrylic acid) functionalized P9AF films.

Here, we reported four cross-linked network poly (methacrylic acid) -functionalized P9AF films by precursor polymer approach, namely, poly { poly [ N - (9H-fluoren-9-yl) methacrylamide ] } (P1), poly { poly [ N - (9H-fluoren-9-yl) methacrylamide-*co*-methacrylic acid ] } (P3), poly { poly [N - (9H-fluoren-9-yl) methacrylamide ] -*co*-9-aminofluorene } (P2) and poly { poly [N - (9H-fluoren-9-yl) methacrylamide-*co*-methacrylic acid ] -co-9-aminofluorene } (P4). Meanwhile, poly [ N - (9H-fluoren-9-yl) methacrylamide ] (PFMA) and poly [ N - (9H-fluoren-9-yl) methacrylamide – *co* - methacrylic acid ] (PFAA) as precursor polymers were synthesized through the free radical homo- and co-polymerization of N-(9H-fluoren-9-yl)methacrylamide (FMA) and methacrylic acid, respectively; P1, P3 and P2, P4 were obtained by the electrochemical homo- and co-polymerization of precursor polymers and 9-aminofluorene, respectively. The electrochemical properties, structures, fluorescent properties, and morphology of the as-prepared polymer films were studied in detail.

## Experimental

### Chemicals

9-Aminofluorene hydrochloride (99%; Alsa Aesar), 4-dimethylaminopyridine (DMAP, 99%; Aladdin), N,N'-dicyclohexylcarbodiimide (DCC, 99%; Aladdin), azobisisobutyronitrile (AIBN, 95%; Tianjin Damao Chemical Plant, Tianjin, China). BFEE (Changyang Chemical Plant, Beijing, China) was distilled before use. Other reagents were all analytical grade and used as received.

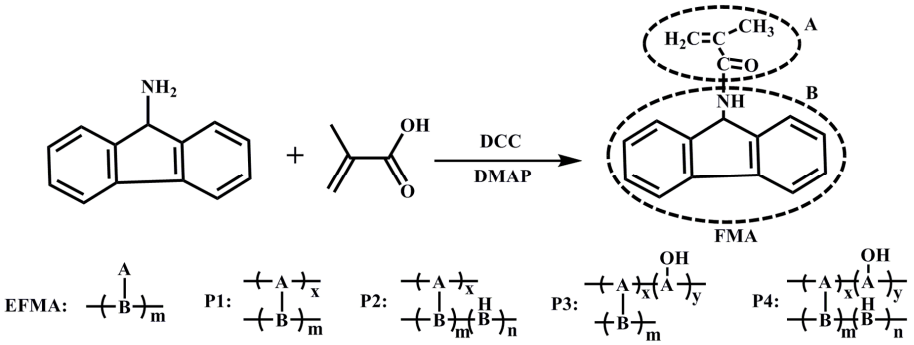
### Synthesis of FMA

0.10 g 9-aminofluorene hydrochloride (0.46 mmol) was dissolved in 20 mL deionized water. The pH was adjusted to 8.0 with $NaHCO_3$. A mixture of 9-aminofluorene, methacrylic acid (MAA, 0.51 mmol/L) and DMAP (0.046 mmol/L) in anhydrous $CH_2Cl_2$ was stirred under nitrogen at 0 ºC for 15 min. Then 0.1 g DCC pre-dissolved in $CH_2Cl_2$ was added dropwise into the mixture. After then, the reaction was stirred at room temperature for 24 h, after then, the filtrate was washed with 1 mol $L^{-1}$ HCl, saturated $NaHCO_3$ and $H_2O$, and dried over $MgSO_4$. After the solvent was evaporated, the residue was recrystallized with $CH_2Cl_2/C_6H_{14}$ (yield 90%). $^1H$ NMR (400 MHz, $CDCl_3$, δ, ppm): 7.72 (d, J = 7.6 Hz, 2H), 7.59 (d, J = 7.6 Hz, 2H), 7.42 (t, J = 14.8 Hz, 2H), 7.32 (t, J = 14.8 Hz, 2H), 6.31 (d, J = 8.8 Hz, H), 6.04 (d, J = 7.6 Hz, H), 5.76 (s, H), 5.40 (s, H), 2.02 (s, 3H).

### Synthesis of PFMA and PFAA

PFMA and PFAA were synthesized by conventional free radical polymerization using azobisisobutyronitrile(AIBN) as the initiator in THF. The detailed procedure is that, 0.1 g FMA and 1.3 mg AIBN dissolved in distilled THF were poured into a Schlenk flask under nitrogen. The monomers were polymerized under nitrogen at 60 ºC for 2 days. The reaction solution was cooled at room temperature. The polymer was obtained by filtration and purified by reprecipitation from THF into methanol and dried in a vacuum oven for 2 days. The copolymerization was carried out at ratio of FMA:MAA=10:1 to form the PFAA by free radical polymerization. The preparation of PFAA was the same as that of PFMA except for polymers precipitated with hexane. The number average molecular weights of PFMA and PFAA were 5900 and 3358, respectively, relative to polystyrene standards.

**Electrosynthesis of P1, P2, P3 and P4**




Scheme 1. Structures of N-(9H-fluoren-9-yl)methacrylamide (FMA) and its polymers.

Scheme 1 shows the structures of polymer bearing 9-aminofluorene moieties. The electropolymerization of precursor polymers were performed in a one-compartment cell using a potentiostat-galvanostat (model 263A, EG&G Princeton Applied Research) under computer control. The working and counter electrodes were Pt wire and stainless steel wire, respectively. An Ag/AgCl electrode served as the reference electrode. The electrolyte was $CH_2Cl_2$-BFEE (1:2, by volume). All the solutions were deaerated by a dry nitrogen stream and maintained under a slight overpressure through all the experiments. All obtained polymers were dried at 60 ºC under vacuum for 24 h.

**Characterization**

UV-vis spectra were taken by using an Agilent 8453 UV/VIS spectrophotometer. FT-IR spectra were recorded by using KBr pellets of the monomer and polymers on a Bruker Vertex 70 FT-IR spectrometer. All fluorescence experiments were carried out using a Hitachi F-4500 spectrophotometer.

**Results and Discussion**

**Electrodeposition of P1, P2, P3 and P4 Films**

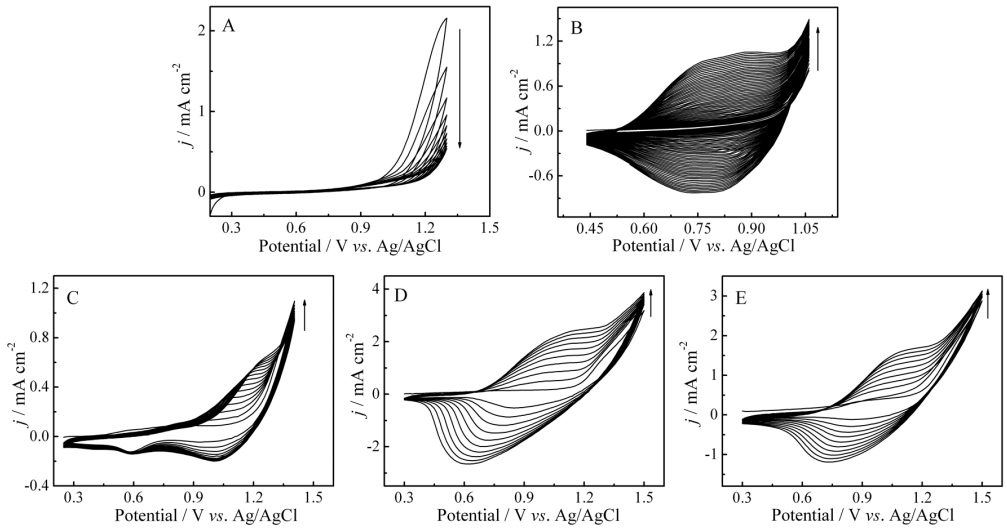



Fig. 1. Cyclic voltammograms of 0.01 M FMA (A), 0.01 M PFMA (B), 0.01 M PFAA (C), 0.01 M 9AF and 0.01 M PFMA (D), 0.01 M 9AF and 0.01 M PFAA (E) in the mixed electrolyte of $CH_2Cl_2$-BFEE (1:2, by volume). Potential scan rate: 100 mV $s^{-1}$.

Fig. 1 shows the electropolymerization of FMA and precursor polymers. The cyclic voltammograms (CVs) of FMA showed no reductive wave, and the current densities decreased quickly with increasing CV scan numbers (Fig. 1A). After successive potential scans, no polymer film was formed on the electrode, implying that electropolymerization of FMA is infeasible. As seen from Fig. 1B&C, the CVs of PFMA and PFAA had a couple of good redox waves, their onset oxidation potentials ($E_{ox}$ onset) were about 1.0 V and 1.13 V, respectively. For the CVs of PFMA and PFAA, the current densities of well-defined redox wave increased gradually as the potential scanning continued, indicating that the amount of polymers was increased on the surface of working electrode. Flat polymer films were observed on the surface of working electrode in the process of electrosynthesis. It was concluded that the poly(methacrylic acid) backbone facilitates the electropolymerization of fluorene units on the precursor polymers.

The CVs of the blends of precursor polymers (PFMA, PFAA) and 9AF were shown in Fig. 1D&E, respectively. For the electrochemical copolymerization of PFMA and 9AF, the $E_{ox}$ onset was about 1.15 V, while the $E_{ox}$ onset was about 1.24 V for the copolymerization of PFAA and AF. Their redox wave current densities per cycle were higher than those of PFMA and PFAA homopolymerization, which implied the rate of copolymerization was faster in the $CH_2Cl_2$-BFEE solution. The broad redox waves of the polymer films may be ascribed to the wide distribution of the polymer chain length. The potential shift of the current wave maximum provided information about the increase of the electrical resistance of the polymer film and the overpotential needed to overcome this resistance. Compared with figures 1B-E, the redox wave is different from each other, implying the formation of homopolymers and copolymers.

**Electrochemistry of P1, P2, P3 and P4 films**

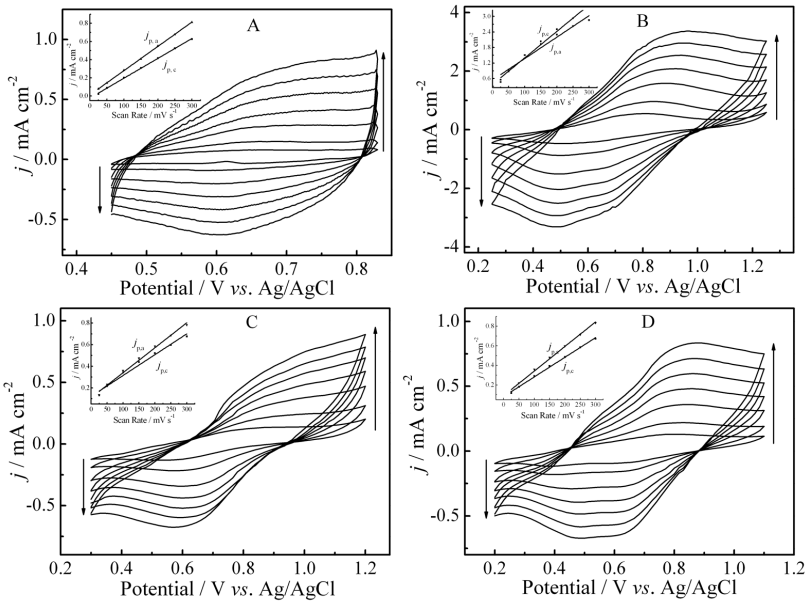



Fig. 2. Cyclic voltammograms of P1 (A), P2 (B), P3 (C) and P4 (D) in free-monomer SA at potential scan rates of 25, 50, 100, 150, 200, 250, 300 mV $s^{-1}$. Inset: plots of redox peak current densities *vs.* potential scan rate.

Fig. 2 shows the cyclic voltammetry of P1, P2, P3 and P4 films in concentrated sulfuric acid (SA). It can be clearly seen that steady-state CVs of these films represented broad anodic and cathodic peaks in SA. The peak current densities were proportional to potential scanning rates (insets of Fig. 2), indicating that the redox process is nondiffusional and the electroactive polymers were well adhered to the working electrode surfaces. Furthermore, these films could be cycled repeatedly between the conducting (oxidized) and insulating (neutral) state without significant decomposition of the materials, indicating their good electroactivity and structural stability.

**Structural Characterization**

Fig. 3 shows FT-IR (A), UV-vis (B) and fluorescence (C, D) spectra spectra spectra of the monomer, precursor polymers and dedoped polymer films. In Fig. 3A, the absorption bands in the spectra of polymers were obviously broadened in comparison with those of the monomer and precursor polymers. This phenomenon is mainly due to the wide chain distribution of the resulting product consisting of oligomers/polymers. In the spectrum of FMA (Fig. 3A-a), the strong and narrow peak at 3269 $cm^{-1}$ is the characteristic absorption of the N-H bond, which was broadened and shifted to 3445 $cm^{-1}$ for PFMA and 3441 $cm^{-1}$ for PFAA (Fig. 3A-b and Fig. 3A-c), respectively. The characteristic bands at 739 $cm^{-1}$ and 764 $cm^{-1}$, which are typical of the out-of-plane bend vibration of ortho-substituted benzene, exist in the spectra of P1, P2 and P4. Additionally, P1, P2 and P4 appeared a new peak at 826 $cm^{-1}$, 818 $cm^{-1}$ and 816 $cm^{-1}$, respectively (Fig. 3A-d and Fig. 3A-f), which suggested that the benzene ring on the resultant polymers were 1,2,4-trisubstitution. This result implied that the electropolymerization occurred on the fluorene units and mainly coupled at C(2) and C(7) positions on fluorene units.

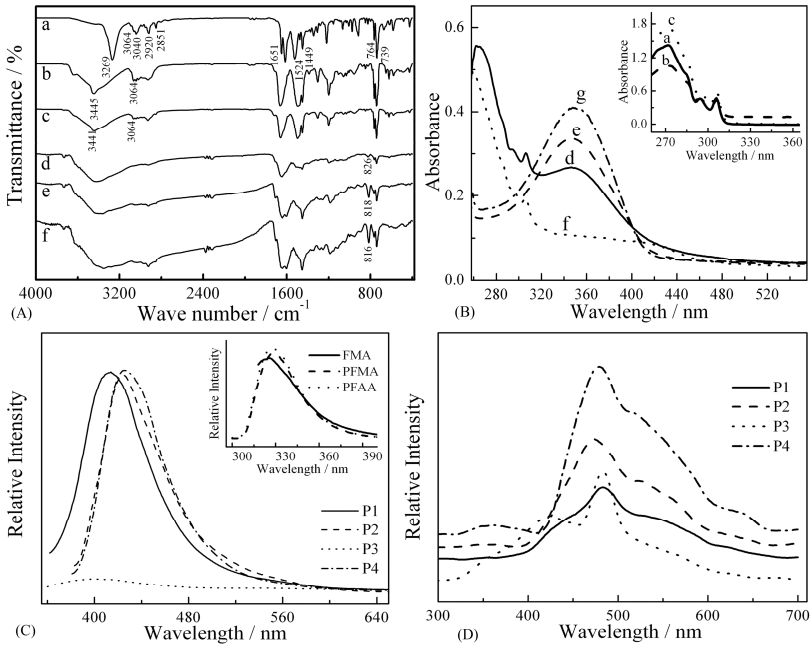



Fig. 3. (A) FT-IR spectra of FMA (a), PFMA (b), PFAA (c), P1 (d), P2 (e) and P4 (f) films; (B) UV-vis spectra of FMA (a), PFMA (b), PFAA (c), doped P1 (d), doped P2 (e), doped P3 (f), doped P4 (g) in DMSO; Fluorescence spectra of FMA, PFMA, PFAA, P1, P2, P3 and P4 in DMSO (C) and in solid state (D), respectively.

In Fig. 3B, monomer and precursor polymers showed three characteristic absorption peaks at 273, 295, and 306 nm, which is ascribed to the single electron π-π* transition. The doped P1, P2 and P4 showed stronger and broader absorption with peak absorption at 350 nm, which was red-shift compared with P9AF (339 nm) [5]. This reflects the higher conjugation length of the backbone. However, the doped P3 exhibited relative weak and broad absorption at 350 nm, indicating that its same conjugated chain length as P1, P2, and P4 is fewer. Generally, conducting polymer shows a characteristic broadband of conducting species such as polarons and bipolarons at about 500 nm above in the doped state and the band in dedoped state disappeared. However, these polymers had no the characteristic broadband of conducting species due to their autodedoping in DMSO solvent.

In Fig.3C, FMA exhibited a strong emission peak at 326 nm under excitation at 308 nm, and it is observed that the emission of PFMA and PFAA centered at 328 nm when excited at 290 nm. It was revealed that the fluorene group is stable during free radical polymerization of vinyl group. In DMSO solvent, the dedoped P1 showed a maximum emission at 413 nm when excited at 352 nm, the

maximum emission peak of dedoped P2 appeared at 425 nm when excited at 374 nm and the emission of dedoped P4 centered at 426 nm when excited at 371 nm. All the emission spectra emerged in the blue region. However, the P3 had a very weak emission peak at 403 nm, which is consistent with the result of its UV-vis spectrum. Large red shifts about 97 nm between the monomer (or precursor polymers) and polymers is mainly attributed to the elongation of the polymer's delocalized π-electron chain sequence. In DMSO, the fluorescence quantum yields ($Ø_{overall}$) of P1, P2 and P4 were calculated to be 0.16, 0.40 and 0.48, respectively. From above results, P1, P2 and P4 in DMSO solvent still retained excellent blue light-emitting properties. It should be noted that the emission wavelengths and Øoverall of P1, P2 and P4 were somewhat different from those of P9AF (418 nm, $Ø_{overall}$=0.44) [5], and the order of fluorescence is P4 > P9AF > P2 > P1 > P3, implying that the incorporation of poly(methacrylic acid) into P9AF can tune the fluorescence of P9AF. The emission spectra of polymer films in solid state showed one sharp peak and several broad shoulder peaks in the blue-green region (Fig. 3D). The result demonstrated that P1, P2 and P4 films in solid state were good blue-green light emitters and the insoluble part films had higher conjugation length.

## Conclusions

Four novel cross-linked network polymers P1, P2, P3 and P4 were synthesized by a precursor polymer route based on pendant fluorene group onto a polymethacrylic acid backbone. It was found that P1, P2 and P4 can be successfully deposited from direct anodic oxidation while P3 can only form oligomers. P1, P2 and P4 exhibited good redox activity and stability. The order of their thermal stability was P4 > P2 > P1. Fluorescence spectra indicated that the soluble cross-linked polymers were good blue light emitters and in solid state they were blue-green light emitters, and the order of fluorescent quantum yields is P4 > P9AF > P2 > P1 > P3.

## Acknowledgements

The authors thank NSFC (51073074), Jiangxi Provincial Department of Education (GJJ11590, GJJ10678, GJJ12595), Natural Science Foundation of Jiangxi Province (2010GZH0041) for providing financial support.

## References

[1] P. Taranekar, X.W. Fan, R. Advincula, Langmuir 18 (2002) 7943-7952.

[2] S.X. Deng, R.C. Advincula, Chem. Mater. 14 (2002) 4073-4080.

[3] C.J. Xia, X.W. Fan, M. Park, R.C. Advincula, Langmuir 17 (2001) 7893-7898.

[4] B.Y. Lu, S. Chen, J. Wang, J.K. Xu, X.M. Duan, M.S. Pei, Chin. J. Chem. 30 (2012) 1177-1184.

[5] C.L. Fan, J.K. Xu, W. Chen, B. Dong, J. Phys. Chem. C 112 (2008) 12012-12017.

[6] L.J. Borthakur, S. Konwer, R. Das, S.K. Dolui, J. Polym. Res. 18 (2011) 1207-1215.

[7] L.Q. Qin, J.K. Xu, B.Y. Lu, Y. Lu, X.M. Duan, G.M. Nie, J. Mater. Chem. 22 (2012) 18345-18353.

[8] Z.J. Zhu, B.Y. Lu, C.C. Liu, L.Y. Wang, J.K. Xu, M.S. Pei, Chem. J. Chinese Universities 31 (2010) 2102-2109.

[9] J.K. Xu, W.Q. Zhou, H.P. Peng, S.Z. Pu, J.W. Wang, L.S. Yan, Polymer J. 38 (2006) 369-375.

*Advanced Materials Research Vol. 937 (2014) pp 29-33*
*© (2014) Trans Tech Publications, Switzerland*
*doi:10.4028/www.scientific.net/AMR.937.29*

# 3D-braided Thick Composites Made by Simultaneous Outside-in and Inside-out Resin Infusion

Rui CHEN [1,a], Zhong-de SHAN [1,b,*] and Feng LIU [1,c]

[1] Advanced Manufacture Technology Center China Academy of Machinery Science & Technology

[a]869727808@qq.com, [b]Shanzd@cam.com.cn, [c]Liufeng@cam.com.cn

*Zhongde Shan/ E-mail: shanzd@cam.com.cn, TEL: +86-13801092495, FAX: +86-10-8241-5078

**Keywords:** 3D-braided thick composites, simultaneous inside-out and outside-in infusion

**Abstract.** Thick composites made with traditional impregnation and with simultaneous resin infusion from the inside and outside were studied to compare two methods for optimizing permeability, dipping time, and structural organization. Permeability was greater, the dipping time was shorter, the impregnated resin was more uniformly distributed, and blow hole defects were fewer when infusion was performed simultaneously from the inside and outside of the braided structure. The resin flow channel was preset in the precast body, allowing simultaneous outside-in and inside-out dipping.

## Introduction

Due to their excellent mechanical properties, 3D-braided composites have drawn a great deal of attention and have been applied in many important fields, including aviation, space exploration, national defense, and the military, for sustainable development in new material[1,2,3,4].

The traditional RTM process is restricted by resin flow time and flow length. In fiber composites, the molding process, fiber drying, non-uniform dipping, and bubble formation can significantly reduce the mechanical properties of the final parts [5, 6]. This process is therefore not suitable for forming large wall-type parts and requires improvements to the mold design and the permeability of the reinforcement.

An alternate strategy that makes use of simultaneous infusion from both the inside and outside of a 3D-braided reinforcement is presented herein.

## Experimental

### Theory of Simultaneous Resin Infusion

To facilitate simultaneous infusion from both the inside and outside of a fiber reinforcement, guide sleeves with micro-porous hollow tubes were used to provide resin flow channels from the inside to the outside of the composite. The principle of operation is illustrated in Figure 1, and a corresponding model is shown in Figure 2.

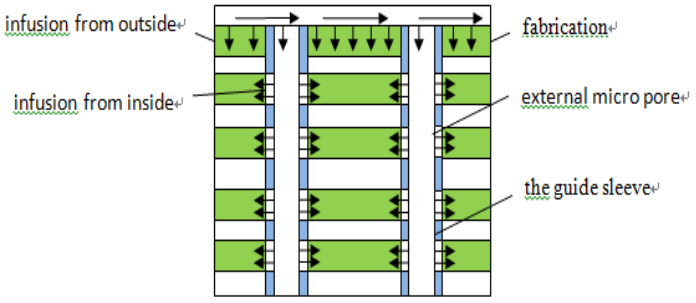



Fig. 1. The principle of simultaneous resin infusion from the inside and outside of a fiber reinforcement is shown.

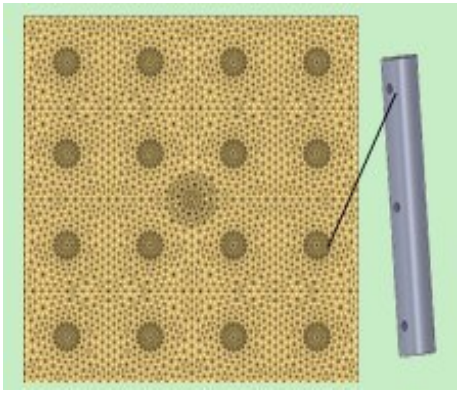


Fig. 2. A model shows a system with simultaneous resin infusion from the inside and outside of the material.

**Selection of Guide Sleeve Diameter and Spacing**

The guide sleeves were perforated with micropores along the primary, vertical axis at intervals of 10 mm and at every 90$^{o}$ around the sleeve circumference. The spacing between sleeves and the length of each sleeve were 25 and 24 mm, respectively. The guide sleeves were fragile and tended to break with pore sizes larger than 2 mm. Pore sizes of 1, 1.2, 1.5, 1.8, and 2 mm were assessed in order to find the optimal pore size. Simulated results of mold filling times using these various pore sizes are shown in Table 1.

Table 1. Simulated mold filling times are given as a function of pore diameter.

| Pore diameter | Mold filling time |
|---|---|
| 1 mm | 134 s |
| 1.2 mm | 133 s |
| 1.5 mm | 128 s |
| 1.8 mm | 124 s |
| 2 mm | 117 s |

The data in Table 1 show that the shortest molding time was 117 s when the micropore diameter was 2 mm.

**Measurements of Primary Permeability**

The device used to measure primary permeability is shown in Figure 3. A sealing film was fixed onto a metal base plate measuring 170 × 30 mm. Both ends were open vacuum orifices for use as the resin outlet and inlet. The periphery of the film was sealed.



Fig. 3. Primary permeability was determined using the above device during the one-way flow of resin.

## Analysis of the experimental results

### Determination of primary permeability

Primary permeability was measured assuming the simple, ideal case of one-way resin flow in which the flows in the *y* and *z* directions are considered negligible [7]. According to Darcy's law and the law of conservation of mass and after substituting boundary conditions, the formula for calculating permeability is

$$K = \frac{\mu L^2}{2P_0 \mathrm{T}} \quad [8]$$

where K is the permeability, $\mu$ is the fluid viscosity, $P_0$ is the initial pressure, and L is the resin flow forward position at time T.s

The relationship between $L^2$ and T, calculated as the average of five independent measurements, is shown in Figure 4. The correlation coefficient of $R^2 > 0.99$ indicates a highly linear relationship.

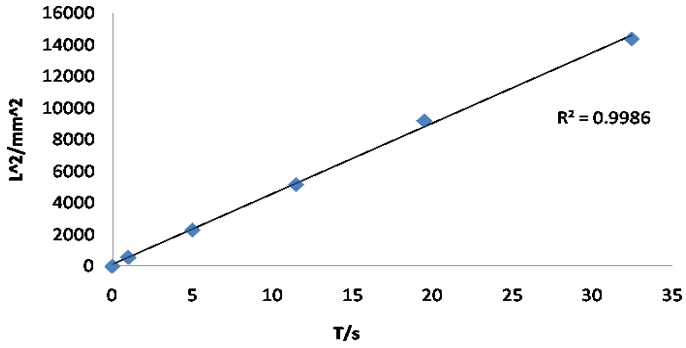



Fig. 4. The relationship between $L^2$ and T.

The data in Figure 4 indicate a K of 0.0135 mD ($\mu$ was assumed as 1 cP), which is significantly greater than traditional permeability values for this system. In general, resin flows more easily at higher permeability.

### Simulation of Mold Filling Time

Permeability is one of the most important parameters for simulating filling time [9, 10]. Figure 5 compares the simulated results of mold filling times using a traditional RTM process with those obtained using the simultaneous infusion method presented herein.

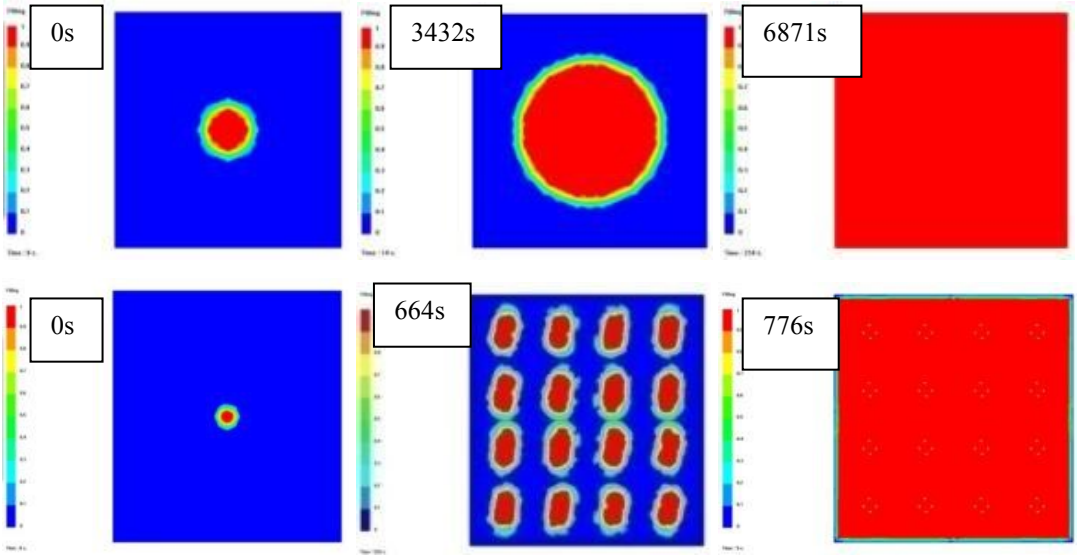



Fig. 5. Simulation results of the mold filling times using a traditional RTM process (top) and simultaneous infusion from the inside and outside of the reinforcement (bottom).

The images in Figure 5 demonstrate that the filling time when using the simultaneous infusion method described herein is approximately an order of magnitude shorter than the filling time required with the tradition RTM process.

**Microstructural Observations**

Specimens measuring 50 × 50 × 40 mm (length × width × thickness) were cut from the edges of the fabricated parts, and cross sections were imaged under a microscope along both the longitudinal and transverse axis after polishing. Both macro- and micro-structural details were observed at a magnification of 50×. Slices from parts fabricated using a traditional RTM process and the simultaneous infusion process are shown in Figures 6 and 7, respectively.

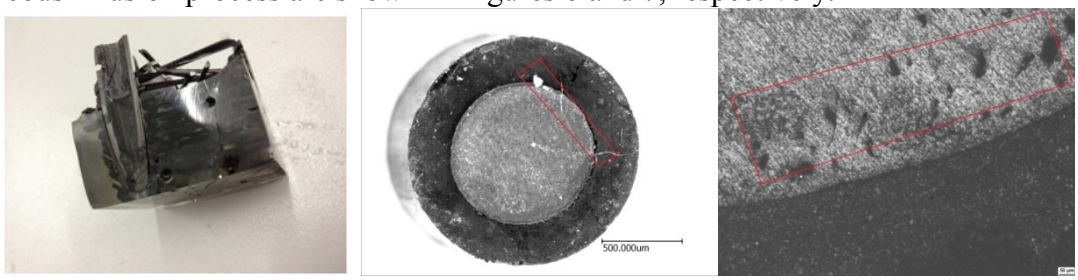



Fig. 6. Microscopic images of a slice from a part fabricated using a traditional RTM process.

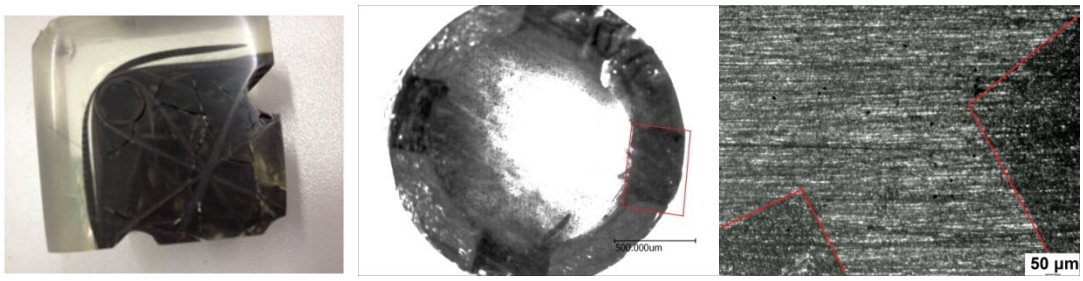



Fig. 7. Microscopic images of a slice from a part made with simultaneous resin infusion from the inside and outside of the reinforcement material.

The center of the slice in Figure 6 contains several bubbles, although the fiber did not break. These bubbles or blow holes may be due to thermal stresses induced by exothermic resin curing or by internal organizational stress [11].

In contrast, Figure 7 shows that resin impregnation via the guide sleeves resulted in relatively defect-free material. No blow holes, bubbles, or cracks were observed along the entire longitudinal cross section.

**Summary**

Relative to traditional RTM processes, the results of simultaneous infusion from the inside and outside of a fiber-braided reinforcement showed greater permeability, shorter fill times, and more uniform impregnation with fewer defects.

**Acknowledgements**

The study is supported by National Nature Science Foundation of China, key project (Grant No: 51035003), and Development Special Funds of Research Institutes of China, Grant No: 2011EG119107.

**References**

[1] Mouritz A.P.Review of applications for advanced three dimensional fiber textile composites[J].Composites:Part A,1999,30:1445-l46.

[2] Crane R.M.,Macander A.B.[J].Naval engineers journal,1984,96(6):52—56.

[3] Tao xiaoming, Xi xingjuan, Gao guanxu, The textile structural composites [M].Science press.2001,1~9. (In Chinese)

[4] Zhongde Shan, Shaoyan Qin, Qian Liu, Feng Liu, Key Manufacturing Technology & Equipment on Energy Saving and Emissions Reduction in Mechanical Equipment Industry. International Symposium on Green Manufacturing and Applications.2011.

[5] Ghiorse S R. . Effect of Void Content on The Mechanical Properties of Carbon/ Epoxy Laminates SAM PE Q. , 1993, 24( 2) : 54~ 59.

[6] Bow ies K J. Frimpong S J. Void Effects on the Inter laminar Shear Strength of Unidirectional Graphite- Fiber- Reinforced Composites. Composite Mater. , 1992, 26(10) : 1487~ 1509.

[7] A G Every,Y Tzou,D P H Hasselman,R Raj.The Effect of particle size on the thermal conductivity of ZnS/diamond composites[J].Acts Metall Mater,1992,40:123.

[8] TrPvino L,Rupei K,Young W B,et al. Analysis of resin injection moulding in moulds with preplaced fiber mats I:permeability and compressibility measurements[j]. Polymer Composites,1991,12(1):20-29.

[9] Ahn K J, Letterman L. Braided to net section graphite/epoxy composite shapes [J]. 1985(6):589-607.

[10] Blest D C, McKee S. Resin infusion technology for the autoclave process. P. Marshall [J]. Compos Sci, 1999,59:2297.

[11] N. Patel and L.. James Lee. Modeling of Formation and Removal in Liquid Composite Molding. Part I:Wet ability Analysis. Polymer Composites. 1996, 17(1):104.

*Advanced Materials Research Vol. 937 (2014) pp 34-40*
*© (2014) Trans Tech Publications, Switzerland*
*doi:10.4028/www.scientific.net/AMR.937.34*

# The Effect of Acetate on the Electrodeposition of Manganese on Polycrystalline Au without $SeO_2$ Additives

Wen-po LI[1,a,*], Xiu-li ZUO[2,b], Jun-ying YANG[1,c] and Sheng-tao ZHANG[1,d]

[1]School of Chemistry and Chemical Engineering, Chongqing University, Chongqing, China

[2]Department of Oil Application & Management Engineering, Logistic Engineering University, Chongqing, China

[a]wpli@cqu.edu.cn, [b]zuoxiuli009@163.com, [c]ceciliayjy@gmail.com, [d]stzhang@cqu.edu.cn

*Corresponding author

**Keywords:** Manganese, Electrodeposition, Acetate, Electrochemical Quartz Crystal Microbalance, Spectroscopic Ellipsometry.

**Abstract.** The influence of acetate additives on the mechanism of manganese electrodeposition from chloride-based acidic solution was investigated by electrochemical quartz crystal microbalance and spectroscopic ellipsometry. The EQCM data were represented as plots $\Delta$m versus *E*. Because they are not affected by interference from the hydrogen evolution reaction, they clearly show the manganese reduction and oxidation processes. The in situ spectroscopic ellipsometry ( SE) data were analyzed with a single-layer model ( substrate Au - deposition Mn layer) and the thicknesses of Mn layer were obtained by fitting experimental data with the model. Morphology, chemical composition and structure of the manganese deposits were analyzed by scanning electron microscopy (SEM), energy dispersion spectroscopy (EDS), and X-ray diffraction (XRD). The results showed that in the absence of acetate additives, $Mn(OH)_2$ is formed. In the presence of acetate additives, the formation of α-Mn was observed and the deposition rate of Mn electrodeposition on the Au electrode slowed down.

## Introduction

Metallic manganese (Mn) is used in certain types of steel, particularly low-carbon steels, and in nonferrous alloys. Little work has been done on the mechanism of electrodeposition of pure metallic manganese. Diaz-Arista and Antano-Lopez[1] electrodeposited manganese from a chloride-based electrolytic solution with ammonium thiocyanate ($NH_4SCN$) as an additive. They found that the adding ammonium thiocyanate to the electrolytic solution increased the reduction of manganese. They obtained the formation of α-and γ- manganese, and when the potential was≤-1.8V and [$NH_4SCN$]exceeded 0.3M, the α-manganese phase was favored. In other work in this area, Fink and Kolodney[2] electrodeposited manganese from a sulfate-based electrolytic solution containing glycerol as an additive. The manganese coatings obtained were easily oxidized when they were exposed to air, forming a dark oxide film on the surface. When the fresh manganese coating was submerged in dichromate solution, the white and shiny appearance of the coatingwas maintained indefinitely.

In the present study, we used electrochemical quartz crystal microbalance (EQCM) and in-situ spectroscopic ellipsometry to investigate the influence of acetate additives on the mechanism of manganese electrodeposition from a chloride-based acidic solution. The EQCM data were represented as graphs of $\Delta$m versus *E*. The graphs have certain advantages over the conventional approaches to representing EQCM data.By comparing they with their corresponding voltammograms, it was possible to differentiate mass changes due to faradaic processes(mass changes that are coupled to charge transfer at the electrode surface) from those due to non-faradaic processes(mass changes that are not associated with charge transfer processes).The in-situ spectroscopic ellipsometry (SE) data were analyzed with a single-layer model ( substrate Au-deposition Mn layer) and the thicknesses of Mn layer were obtained by fitting experimental data with the model. In the present work, electrochemical quartz crystal microbalance and in-situ

spectroscopic ellipsometry are presented as alternative approaches to the study of systems in which there is interference from the hydrogen evolution reaction. The morphology, chemical composition, and structure of the manganese deposits were analyzed using scanning electron electron microscopy (SEM), energy dispersion spectroscopy (EDS), and X-ray diffraction (XRD).

## Experimental

### Electrolyte and Electrode

The electrodeposition of manganese was studied in chloride- and acetate-based electrolytic solutions with different additives in this work. The chloride-based solutions (*S*0) without $SeO_2$ additives were used: 0.2 M $MnCl_2$ + 0.3 M $NH_4Cl$ + 0.1 M NaCl + 0.25 M KCl, and the acetate-based solutions (*S*1) without $SeO_2$ additives were used: 0.2 M $(CH_3COO)_2Mn$ + 0.3 M $HCOONH_4$ + 0.1 M $NaOOCCH_3$ + 0.25 M KCl. The solution was made from analytic grade reagents and ultrapure water (18.2MΩ cm in resistivity). All tests were conducted at room temperature (~22 °C). The substrate material for the specimens used in this work is gold (99.9%). The specimens for SE were fabricated into disc-shaped electrode with 1cm in diameter, and then embedded in epoxy resin leaving a working area of 0.785$cm^2$. Prior to test, the electrode was subsequently ground with 120 grit, 320 grit, 600 grit, 800 grit and 1200 grit emery papers, and ultrasonic cleaned in ultrapure water and ethanol for 5min. The specimens for EQCM were purchased from Shanghai Chenhua Co. (Shanghai, China), and cleaned in ultrapure water and ethanol for 5min.

### SE Measurement

In order to perform the SE and electrochemical test simultaneously, a three-electrode cell as previously described was used in this work[3] . Electrochemical measurements were performed using a CHI 660B electrochemical workstation (Shanghai Chenhua, China) through the self-designed three-electrode cell, where the disc-shaped gold was used as working electrode, a platinum foil as counter electrode, and a saturated calomel electrode (SCE) as reference electrode. Spectroscopic ellipsometry (SE) is an optical method for surface analysis, which is based on measuring the change of the polarization state of a light beam during reflection[4] .The spectroscopic ellipsometry of gold/solution interface during electrodeposition was measured by M22000U Automatic Ellipsometer (Woollam Corporation, USA). The wavelength range of incident light is 246–999nm with the incident angle of 70◦. The strong absorption of light at wavelength 246–400nm or 900–999nm causing the little reflected light intensity, the collected signal was rather noisy. So the optical data analyzed by the software WVASE32 used for fitting is among wavelength range 400–900nm.

### Electro-gravimetric Tests

The electrochemical and electrogravimetric study of the reduction of Mn(II) was performed in a conventional three-electrode cell.Electro-gravimetric tests were performed using a CHI 440A EQCM (Shanghai Chenhua, China). AT-cut quartz crystal ($f_0$ = 7.995MHz) covered with a gold film(Shanghai Chenhua, China) was used as the working electrode (Au-EQCM) (geometrical area 0.196 $cm^2$). Because the manganese deposited during the cathodic scan could not be completely dissolved anodically, a new Au-EQCM electrode was used for each experiment. Before each experiment, the electrode was cleaned with degreasing solution. A platinum wire electrode was used as the counter electrode and a saturated calomel electrode (SCE) was used as the reference electrode, all potential values cited in the text are referred to SCE.To minimize iR-drop effects, a Luggin capillary was employed to connect the reference electrode compartment to the working electrode one. The EQCM signal was registered as $\triangle f$ (Hz) ($=f-f_0$), the experimental frequency change, which can be expressed as :

$$\Delta f=-2\Delta m f_o^2/(\mu\rho)^{1/2} \quad (1)$$

where $f_0$ is the natural frequency of the quartz crystal ($f_0$ = 7.995 MHz), $\mu_q$ the shear modulus of the quartz crystal($\mu_q = 2.947\times10^{11}$ g $cm^{-1}$ $s^{-2}$) and $\rho_q$ is the density of the quartz crystal ($\rho$q =2.684 g $cm^{-3}$). Eq.(1) is the Sauerbrey term[5], which represents the total mass change at the electrode

surface. $\triangle m=\triangle m_{dep}+\triangle m^*$. $\triangle m_{dep}$ is the mass change due to the deposition /dissolution of the metal, and$\triangle m^*$ includes the contributions from adsorption and from trapped solvent molecules[6]. Other possible contributions to the frequency change include changes in the solution viscosity[7] and thesurface roughness [8-10]. In the present work, the use of polished Au-EQCM electrodes should minimize the effects of surface roughness, and the effects of viscosity variations are expected to be negligible. The surface morphology and chemical composition of the deposits were evaluated using a scanning electron microscopy (SEM) (Jeol, Led,Japan. JSM-6490LV) coupled to an Energy Dispersion Spectrometer (EDS). Crystal structures were determined by X-ray diffraction (shimadzu,Japan,XRD-6000).

## Results and Discussion

### Voltammetric and EQCM Study

To determine the effect of acetate additives on the reduction of Mn(II) on a Au-EQCM electrode, we carried out voltammetric and EQCM studies in the potential range-1.65V to −0.4 V using solutions *S*0 and *S*1. The potential scans were initiated in the cathodic direction with a potential scan rate ($v$) of 10 $mVs^{-1}$. The manganese deposits obtained from solution *S*0 and *S*1 were dried in a nitrogen atmosphere for analysis by SEM, EDS and XRD.

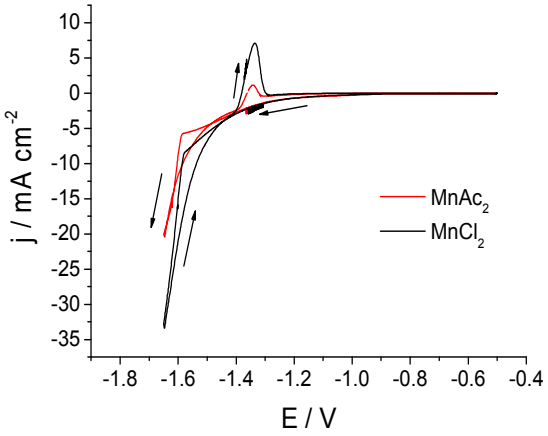



Fig. 1. Cyclic Voltammetry for a Au-EQCM electrode in solution *S*0(black) and *S*1(red), $v$=10 $mVs^{-1}$.

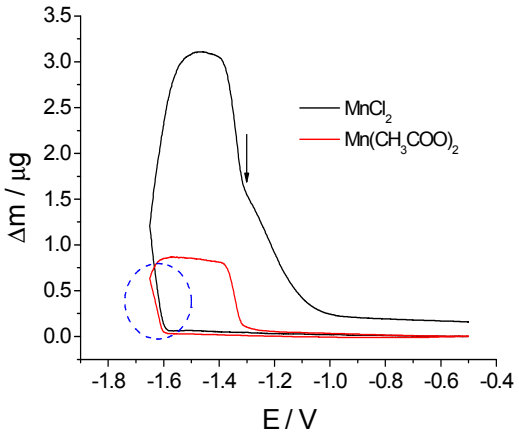



Fig. 2. $\triangle m$ vs. E plot for a Au-EQCM electrode in solution *S*0(black) and *S*1(red), $v$=10$mVs^{-1}$.

Fig. 1 shows typical voltammograms obtained from solution *S*0 and *S*1. The black line (line a) is the voltammogram obtained from solution *S*0, and the red one (line b) is obtained from solution *S*1. In the voltammogram(line a) a slow increase is observed in the cathodic current density in the range −1.58V to−0.4Vduring the potential scan in the cathodic direction. At the same time,we can see bubbles braving from the surface of the electrode. Similar behavior was reported by Casanova et al. [11], who attributed this to the hydrogen evolution reaction. At more cathodic potentials, a rapid increase is observed in the cathodic current density, which is associated with two processes, the reduction of $Mn^{2+}$ ions and the reduction of $H_2O$ (hydrogen evolution). On switching the potential scan to the anodic direction from −1.65V, the absolute value of the current density is greater than was observed during the potential scan in the cathodic direction, leading to a crossover characteristic of the formation of a new phase [12]. The behavior of the voltammogram(line b) was discussed above in relation to the voltammogram(line a). Comparing the area of oxidation peak of line a to that of line b, we can conclude that the quantity of the deposit obtained from solution *S*0 is larger than that from solution *S*1.

Fig. 2 shows mass changes ($\triangle m$) obtained from solution *S*0 and *S*1, and their associated voltammograms showed in Fig. 1. The mass response (line a) associated with its voltammogram shows a slight increase in $\triangle m$ in the potential range −1.58V to −0.4V during the cathodic potential scan. This increase can be attributed to the formation of the insoluble species $Mn(OH)_2$ on the electrode surface due to hydrogen evolution in this potential region and to the resulting increase in pH in the vicinity of the working electrode. At more cathodic potentials (<−1.58V) , a rapid increase in $\triangle m$ is observed, associated with the reduction of Mn(II) ions. It is possible that the observed increase in $\triangle m$ contains a contribution from the incorporation of manganese hydroxide ( $Mn(OH)_2$) during the growth of the deposit. On switching the potential scan to the anodic direction, $\triangle m$ continues to increase until it reaches a maximum value and forms a plateau in the potential range−1.55V to−1.4 V. At more positive potentials, $\triangle m$ shows a decreasing. It is important to note that there is a turning point at the potential of −1.3V during the potential scan in the anodic direction,which meams there are two processes during the anodic potential scan. The first part (−1.4 V to −1.3V) should be the oxidation of manganese. And in the second part (>−1.3V), The decrease in $\triangle m$ observed during the potential scan in the anodic direction is not accompanied by an oxidation current in the corresponding voltammogram (line a, Fig. 1), suggesting that the dissolution process is non-faradaic (without charge transfer associated).This decrease in $\triangle m$ can be attributed to the dissolution of manganese, which is unstable and tends to dissolve easily in acidic media [13.14]. In addition, dissolution of $Mn(OH)_2$ may contribute to the decrease in $\triangle m$, given that in this potential region hydrogen evolution does not occur and the pH returns to its value in the bulk solution. At the end of the scan, the value of $\triangle m$ does not return to its initial value of zero, indicating that a quantity of material remains on the electrode surface.The mass response (line b) was discussed above in relation to that of line a.

Comparing the line a and line b in Fig. 2, we can conclude that the mass of the deposit obtained from solution *S*0 is larger than that from solution *S*1, which is in accordance with the conclusion of voltammograms in Fig. 1. And it is important to note that the speed of the growth of the deposit in solution *S*0 is quicker than that in solution *S*1 during the potential scan in the cathodic direction.

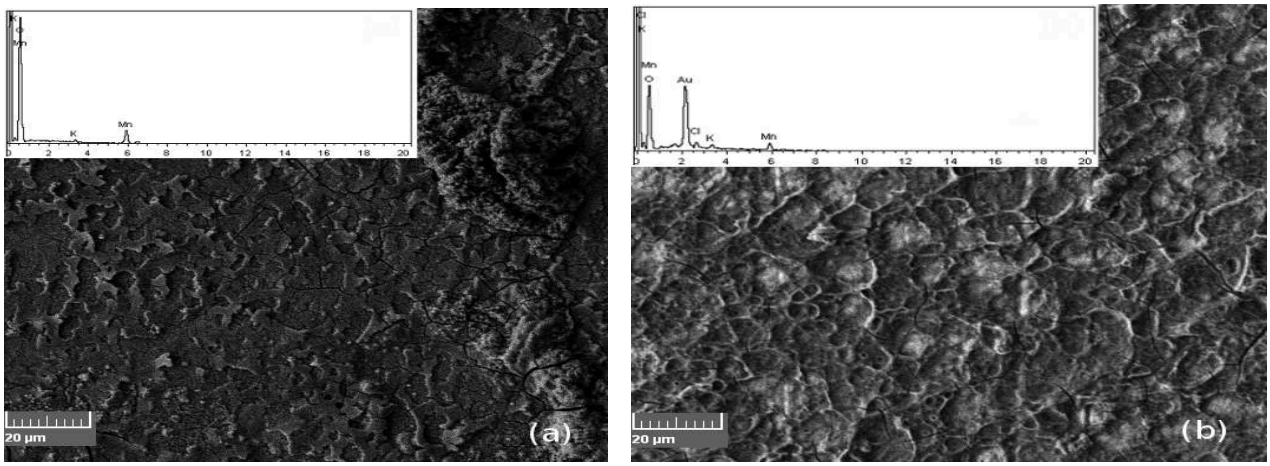



Fig. 3. SEM images (analysis EDS is also shown in the inset) of a manganese coating electrodeposited at $E$ =−1.60V, $t$ = 80 s from solution *S*0(a) and *S*1(b).

Manganese deposits were obtained by holding the potential scan at −1.6 V for 80s in solution *S*0 and *S*1. An SEM image of the deposit obtained from solution *S*0 (Fig. 3a) shows a nonuniform deposit covering some parts of the substrate, EDS analysis (inset) showed the presence of manganese and oxygen. And an SEM image of the deposit obtained from solution *S*1(Fig. 3b) shows the deposit is uniform. EDS analysis (inset) showed the presence of manganese and oxygen. Gold, the substrate material, was also detected due to the thinness of the coating.

Fig. 4 shows the X-ray diffraction(XRD) pattern of Manganese deposits. A XRD image of the deposit obtained from solution *S*0 (Fig. 4a) shows that $Mn(OH)_2$ and other kempite are formed on the electrode surface due to hydrogen evolution and to the resulting increase in pH in the vicinity of the working electrode. These results indicate mass change correspond to the non-faradaic dissolution of

the species formed during the cathodic scan, that is, $Mn(OH)_2$. A XRD image of the deposit obtained from solution *S*1 (Fig. 4b) shows that the deposit is the α-manganese phase. In the acetate-based solutions(*S*1), it is better for the deposit to grow because of the buffer function of the acetate additives and the main deposit is the α-manganese phase.

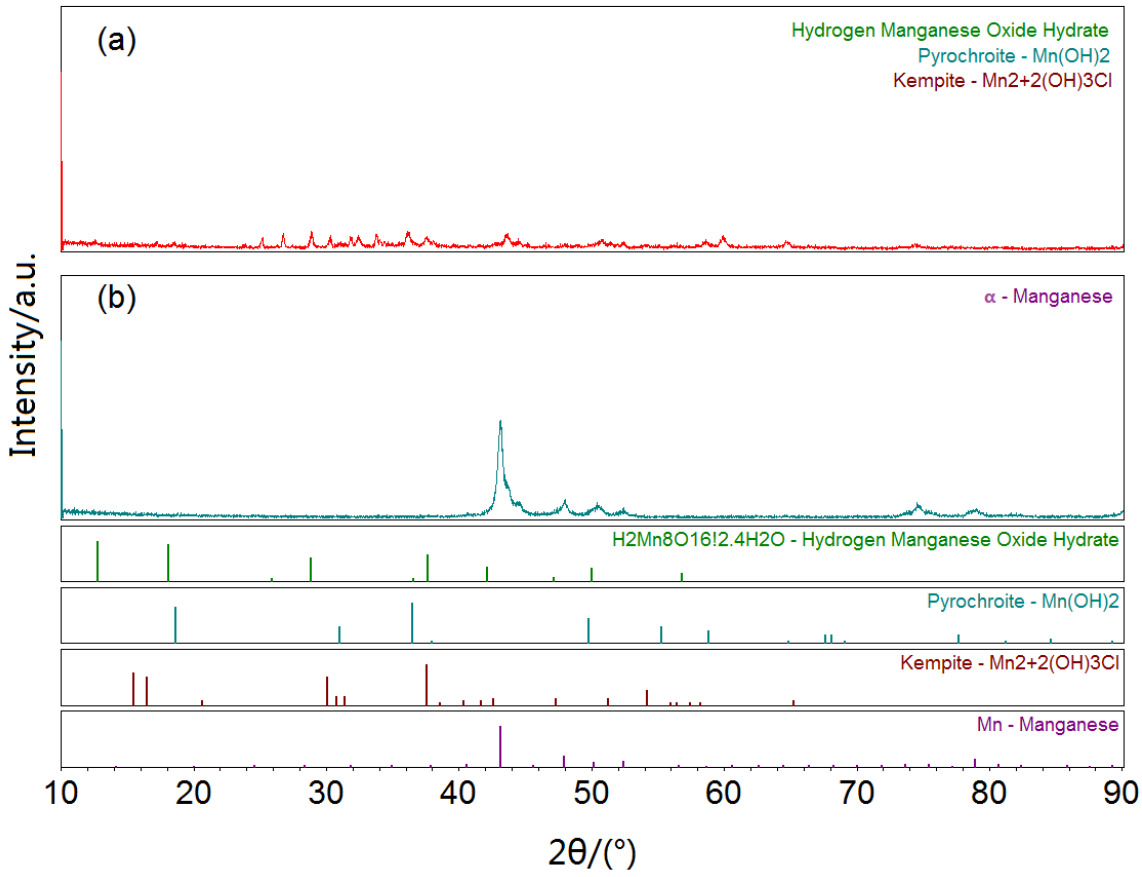



Fig. 4. X-ray diffraction (XRD) pattern, of a manganese coating electrodeposited at $E$ =−1.60V, $t$ = 180 min from*S*0(a) and *S*1(b).

**Spectroscopic Ellipsometry Study**

There are two ways to measure the thickness including indirect method (gravity method, which transforms into oxidation film thickness by calculation) and direct method (spectroscopic ellipsometry), where using ellipsometric measurement is relatively less in the domestic now.

The influence of acetate additives on the mechanism of manganese electrodeposition from chloride-based acidic solution was investigated by using in-situ spectroscopic ellipsometry. By fitting data from ellipsometric measurements with a single-layer model ( substrate Au - deposition Mn layer), the evolution of the refractive indices and the thickness of Mn layer was obtained. Suppose the Mn layer deposited on the substrate Au is a single-layer with stable optical properties. And the refractive index and absorbance of substrate Au can be got by using spectroscopic ellipsometry. Fig. 5 shows the single-layer model in this SE test. The parameters (Δ and Ψ) are defined by mean square error (MSE),which can be expressed as[3]:

$$\mathrm{MSE} = \frac{1}{n-1} \sum_{i=1}^{n} [(\Psi^{c}_{i} - \Psi^{e}_{i})^{2} + (\Delta^{e}_{i} - \Delta^{e}_{i})^{2}] \quad (2)$$

where $n$ is the total nunber of the experimental data, c is the calculated value and e is the experimental value.

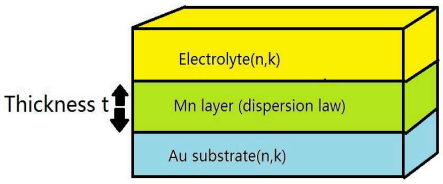



Fig. 5. The single-layer model (substrate Au - deposition Mn layer).

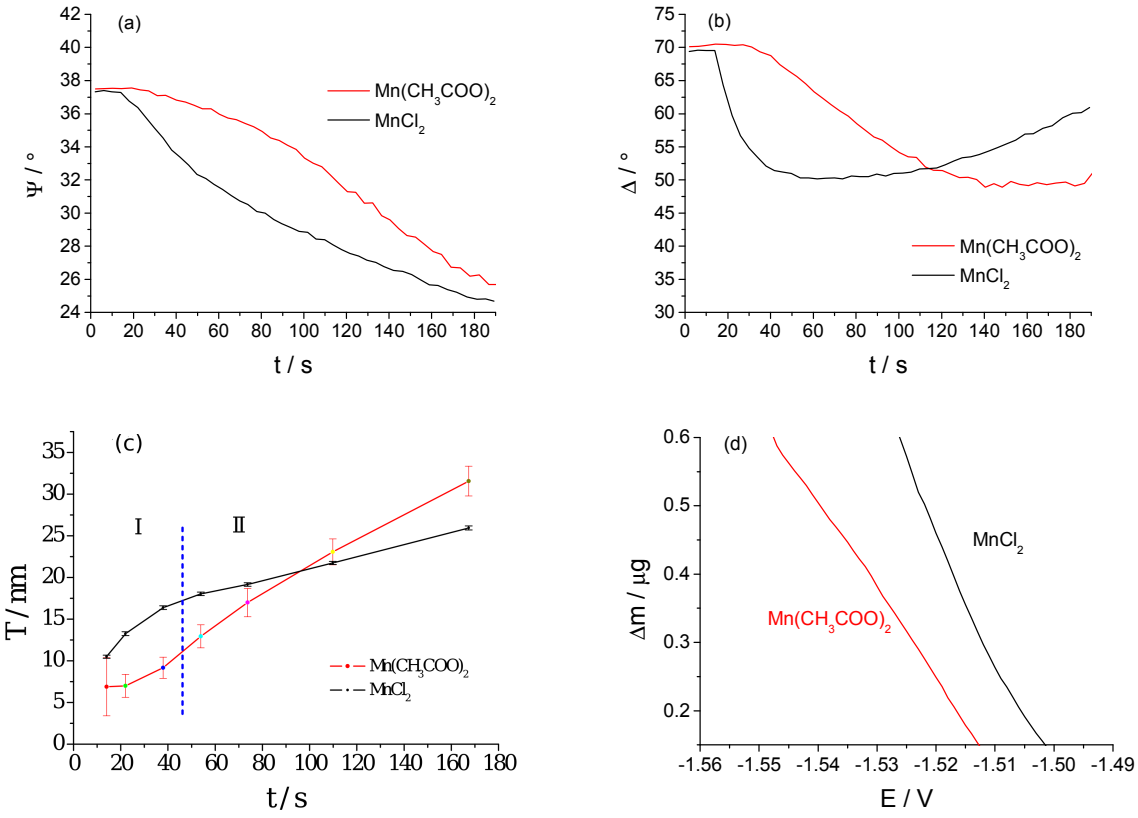



Fig. 6. Plots of in-situ ellipsometer parameters Ψ(a) , Δ(b) and the thickness of the deposits (c) vs time, with the cathode-current density of -8 mAcm$^{-2}$ for 180s in the solution *S*0(black line) and *S*1(red line). (d) shows the partial enlargement of Fig. 2.

Mn layer of electrodeposition on Au electrode is regarded as a studied model. The content of the topic is studied with chronopotentiometry. Plots of in-situ ellipsometer parameters Ψ and Δ vs time were given in Fig. 6a and Fig. 6b, with the cathode-current density of -8 mA/cm$^2$ for 180s in the solution *S*0(black line) and *S*1(red line). From the initial time 0s to 12s, the current density is 0 and the values of ellipsometer parameters were rather high and almost did not change. After 12s, the galvanostatic polarization took place, So the ellipsometer parameter (Ψ) decreased sharply not only in the solution *S*0 but also *S*1. The ellipsometer parameter (Δ) in the solution *S*0 decreased sharply from 12s to 40s, and the value of ellipsometer parameter (Δ) were rather low and hardly changed from 40s to 100s, then it began to rise again. While the value of ellipsometer parameter (Δ) in the solution *S*1 decreased sharply and then hardly changed.

By fitting data from ellipsometric measurements with a single-layer model, the thickness of Mn layers was obtained (Fig. 6c). We can conclude that the thickness of the deposits growing in solution *S*0 and solution *S*1 increased from 12s to 180s. What interests us is that there was a crossover between black line and red line, which indicated the change in the speed of the growth of the deposits. Fig. 6d is the drawing of partial enlargement of Fig. 2. And the slope of the line indicated the speed of the growth of the deposit. The I part in Fig. 6c shows that the speed of the growth of the deposit in solution *S*0 is quicker than that in solution *S*1, which is in accordance with the analysis of EQCM data.

But the II part shows the speed of the growth of the deposit in solution *S*1 is quicker. And the thickness of the deposits is almost the same at 100s. The reason for this phenomenon is the main deposit in solution *S*0 is $Mn(OH)_2$ and other kempite, whose electrical conductivity is bad. So the speed of the growth of the deposit slowed down.

## Conclusions

(a)In this study we use electrochemical quartz crystal microbalance and spectroscopic ellipsometry to investigate the influence of acetate additives on the mechanism of manganese electrodeposition from chloride-based acidic solution. The EQCM data were represented as plots △ m versus E. Use of the mass change (as well as the change in thickness) allowed us to eliminate the contribution of the hydrogen evolution reaction and thus it shows the manganese reduction and oxidation (dissolution) processes with greater clarity.

(b)The results showed that in the absence of acetate additives, $Mn(OH)_2$ is formed. In the presence of acetate additives, the formation of α-Mn was observed and the deposition rate of Mn electrodeposition on the Au electrode slowed down.

## Acknowledgement

This research was financially supported by the National Natural Science Funds of China(21003163) and Fundamental Research Fund for the Central Universities(CQDXWL-2013-025).

## References

[1] P.Diaz-Arista, R.Antano-Lopez,Y.Meas, R.Ortega,E.Chainet, P.Ozil, G.Trejo.Electrochimica Acta 51(2006)4393-4004.

[2] C.G. Fink, M. Kolodney, Trans. Electrochem. Soc. 71 (1937) 287.

[3] LI W, ZHANG S.[J]. Applied Surface Science, 2011, 257(8): 3275-80.(in chinese)

[4] H. FUJIWARA, Spectroscopic ellipsometry. Principles and Applications, 2007,

[5] G. Sauerbrey, Z. Phys. 155 (1959) 206.

[6] D.A. Butry, in: A.J. Bard (Ed.), Electroanalytical Chemistry, vol. 17,Marcel Dekker, New York, 1991, p. 1.

[7] K.K. Kanazawa, J.G. Gordon, Anal. Chim. Acta 175 (1985) 99.

[8] M. Urbakh, L. Daikhin, Langmuir 10 (1994) 2836.

[9] L. Daikhin, M. Urbakh, Faraday Discuss. 107 (1997) 27.

[10] R. Schumacher, G. Borges, K.K. Kanazawa, Surf. Sci. 163 (1985) L621.

[11] T. Casanova, F. Soto, M. Eyraud, J. Crousier, Corr. Sci. 39 (1997) 529.

[12] G. Gunawardena, G. Hills, I. Montenegro, B. Scharifcker, J. Electroanal.Chem. 138 (1982) 225.

[13] D. Sylla, J. Creus, C. Savall, O. Roggy, M. Gadouleau, Ph. Refait, Thin Solid Films 424 (2003) 171.

[14] M. Gonsalves, D. Pletcher, J. Electroanal. Chem. 285 (1990) 185.

*Advanced Materials Research Vol. 937 (2014) pp 41-45*
*© (2014) Trans Tech Publications, Switzerland*
*doi:10.4028/www.scientific.net/AMR.937.41*

# Numerical Analysis for Cavitation Intensity's Effects on the Extend Angle of Convergence-Divergence Nozzle

Feng-hua ZHANG [1,a], Xin SU[1,b,*] , Chuan-lin TANG[1,c],Li-wei SHAN[1,d]

[1]Hunan University of Technology , Zhuzhou, China

[a]fenghua387@126.com, [b]273416742@qq.com, [c]TCL5608@126.com, [d]shan1666@qq.com

*Corresponding author

**Keywords:** Style. Numerical analysis, cavitation , extend Angle

**Abstract.** The one of technical key of the convergence-divergence nozzle is extend Angle. To use applies continuity equation, momentum equation and Rayleigh-Plesset equation, bubbly liquid through different extend angles of converging-diverging nozzle were simulated. The results show that it is helpful to increase the vibrating width of cavitate bubble when enlarge appropriately the exit taper of nozzle, that is the convergence-divergence nozzle with extended angle is more conducive to cavitation.

## Introduction

The size and structure of cavitating nozzle has significant effect on the cavitation[1-6],according to the erosion volume of material by angular nozzle which is several times when using non-angled one in cavitating jet erosion test[1]. The author had once attended the research of steady-state solution of high-speed bubble flow through convergence-divergence nozzle, and the result shows that: the flow properties are affected dramatically even though the void fraction in cavitating flow is very small, when the dimensionless length of convergence-divergence nozzle L=100. When the void fraction is critical value, the bifurcation of steady-state solutions of cavitation flows is presented[4]. And the study of effect of the convergence-divergence nozzle length on cavitation shows that: with the increasing of nozzle length, the critical value of the void fraction at nozzle entrance drops exponentially, and the bubble radius rises linearly. This article is further research which was based on the literature[4] and[5], and discussed when the convergence-divergence nozzle extend changes, the influence of nozzle cavitation effect.

## Fundamental Equation

A schematic representation of the physical model of convergence-divergence nozzle has been given in Fig.1. Choose the coordinate system showed in fig.1, length of convergence-divergence nozzle as L, cross-sectional area as A(x) and extend angle asθ.

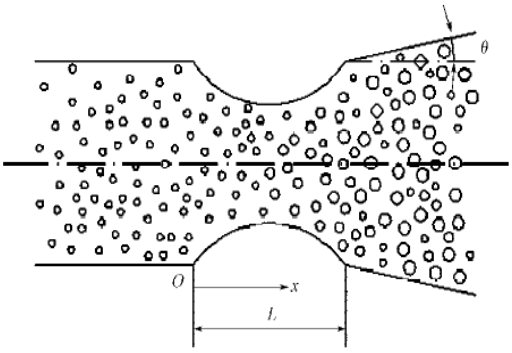



Fig. 1. Physical model of the convergence-divergence nozzle

Before analyse, we make the flowing assumptions:1)the Liquid is incompressible. The relative motion between gas and liquid phase, and the friction between the fluid and pipe's wall has been

ignored. So it can be analysed and calculated according to one-dimensional fluid. 2) The number of bubbles in the inlet liquid per unit volume is uniform, and there is no bubble cohesion or burst when liquid is flowing;3)The quality of liquid's evaporation and condensation can be neglected.

The continuity equation and the momentum equations of the bubbly fluid flow can be showed as:

$$\frac{\partial}{\partial t}\left[(1-\alpha)A\right]+\frac{\partial}{\partial x}\left[(1-\alpha)\mu A\right]=0 \tag{1}$$

$$\frac{\partial u}{\partial t}+\mu\frac{\partial u}{\partial x}=-\frac{1}{2(1-\alpha)}\frac{\partial C_p}{\partial x} \tag{2}$$

Where $u=u^*/u_s^*$ is non-dimensional velocity, $A = A^*/A_s^*$ is Dimensionless cross-sectional area of the nozzle, $X=x^*/R_s^*$ is Dimensionless coordinates,and $t=t^*u_s^*/R_s^*$ is the dimensionless time.

The preferences with '*' are dimensional, and with 's' are the preferences measured in entrance of nozzle, for example $R_s^*$ is the bubble radius at the entrance of the nozzle. Because of liquid's density much greater than steam's, dimensionless fluid density in Eq.(1) and Eq.(2) is: $\rho = (1 - \alpha)$.

The void fraction $\alpha(x,t)$ can be related to dimensionless radius R(x, t):

$$\alpha(x,t)=\frac{4\pi\eta R^3(x,t)/3}{1+4\pi\eta R^3(x,t)/3} \tag{3}$$

where:$\eta = \eta^* R_s^{*3}$is the dimensionless numbers of bubbles per unit liquid, which is constant according to assumptions 2).

The liquid pressure coefficient is:

$$C_p(x,t)=\frac{p^*(x,t)-p_s^*}{p^* u_s^{*2}/2} \tag{4}$$

Simulateing interaction between bubbles and the flow field with Rayleigh-Plesset equation[6] and connecting with the pressure coefficient Cp (x, t) and bubble radius R (x, t), we can get Eq.(5):

$$R\frac{D^2R}{Dt^2}+\frac{3}{2}\left(\frac{DR}{Dt}\right)^2+\frac{\sigma}{2}(1-R^{-3y})+\frac{4}{\mathrm{Re}}\frac{1}{R}\frac{DR}{Dr}+\frac{2}{We}(R^{-1}-R^{-3y})+\frac{C_p}{2}=0 \tag{5}$$

**Steady-state Solution**

Hypothesis that Eq. (1), Eq. (2) and Eq. (5) have the steady-state solutions, the mass flow which determined by the condition of entrance of nozzle is a constant. After removel all the partial derivative of time, the governing equation becomes a the ordinary differential equation system of the single independent variables.

$$(1-\alpha)uA=1-\alpha_s=\text{constant}, \tag{6}$$

$$u\frac{du}{dx}=-\frac{1}{2(1-\alpha)}\frac{dC_p}{dx}, \tag{7}$$

$$R\left(u^2\frac{d^2R}{dx^2}+u\frac{du}{dx}\frac{dR}{dx}\right)+\frac{3}{2}u^2\left(\frac{dR}{dx}\right)^2+\frac{4}{\mathrm{Re}}\frac{u}{R}\frac{dR}{dx}+\frac{2}{We}(R^{-1}-R^{-3y})+\frac{\sigma}{2}(1-R^{-3y})+\frac{C_p}{2}=0 \tag{8}$$

The condition of initial (or inlet ) x=0 is:

$$R_0=1,\ \ u_0=1,\ \ C_{p0}=0,\ \ (\mathrm{d}R/\mathrm{d}x)_0=0 \tag{9}$$

The shape function of the nozzle is:

$$A(x)=\begin{cases}\left\{1-\dfrac{1}{2}C_{p\min}[1-\cos(\dfrac{2\pi x}{L})]\right\}^{-1/2} & 0\le x\le L\\ \pi[\tan\theta(x-L)+\pi^{-1/2}]^2 & x>L\end{cases} \tag{10}$$

Using 2-3 order Runge-Kutta solve the Eq. (7) and Eq.(8). The initial value is : adiabatic index of gases $\gamma$ =1.4, bubble radius at entrance $R_s^*$ =100 μ m,water temperature 20ºC, $\rho^*$ =1000 kg/m3, $\mu_L^*$ =0.001N·s/m$^2$,$S^*$=0.073N/m,the flow velocity at the entrance of nozzle $\mu_L^*$ =100m/s,Minimum pressure coefficient Cpmin=1,Cavitation Number at the entrance σ=0.8,Reynolds number Re=333,equivalent liquid viscous $\mu_e^*$=0.03N/m$^2$ istead of practical liquid viscosity[6], We=13 699.

Given nozzle length L=100, solve the steady-state solutions of dimensionless fluid velocity u, the pressure coefficient Cp, the void fraction and dimensionless bubble radius R for each of the nozzle. The results show in Fig.2~4.

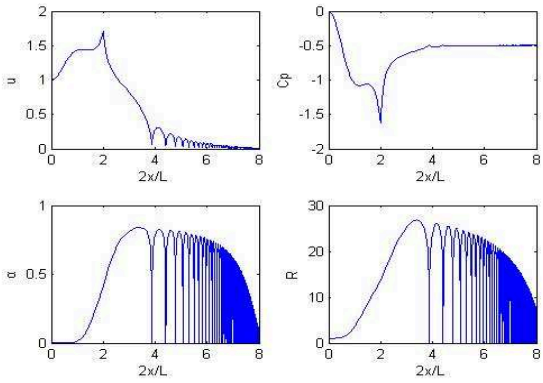



Fig. 2. The numerical solution when $\theta$ = 1º,entrance void fraction $\alpha_s$ =2.70×10$^{-4}$

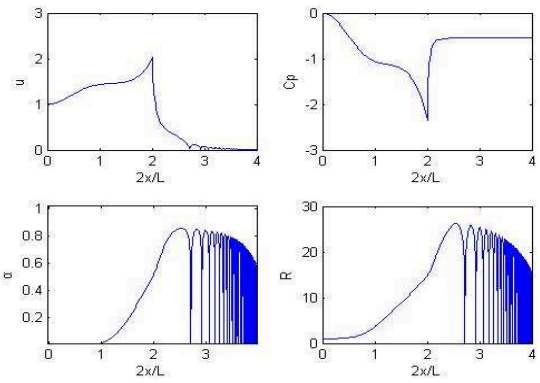



Fig. 3. The numerical solution when $\theta$ = 5º,entrance void fraction $\alpha_s$ =3.2×10$^{-4}$

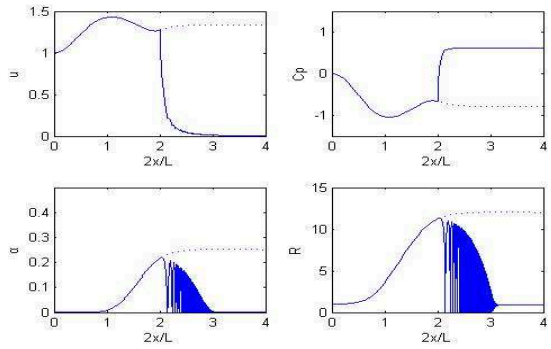



Fig. 4. The numerical solution when $\theta$ =0º(dot line), $\theta$ =5º(solid line)

**Analysis of Result**

Because of mathematical model in this paper does not take external fluid outer of the nozzle into account to the influence of flow field in nozzle, when the extended angle increases to certain degree, external flow would enter in nozzle, which would influence internal flow field of nozzle, so continuity equation no longer hold. Thus, this paper focus on small scale change of extend angle (1~5º).

The calculation results shown that When the extend angle θ changed from 1º to 5º, the steady-state solution have similar distribution ( Fig.2 and Fig.3). With the increasing of the void fraction of entrance $\alpha_s$, the oscillating scope of both of the steady-state solution of the void fraction

α and bubble radius R gradually reduce, and the oscillating frequency also gradually decrease. When $\alpha_s$ is more than 3.3999×10-4, both of α and R stop oscillating and back to 0. For influence of extended angle, the steady-state solution in this paper does not appear to the bifurcate phenomenon as literature [4].

With the expanded angle , the dimensionless flow velocity u tend to 0 at outlet of nozzle when the void fraction is critical value(Fig.4). When the flow is constant, due to the existence of expanded angle, with the expansion of flow section velocity reduces, according to the law of mass conservation. And dimensionless pressure coefficient $C_p$ rapidly tend to a certain value. That is because: when outlet velocity reduces and fluid dynamic pressure decrease, according to Bernoulli equation, the fluid hydrostatic pressure will definitly increase, therefore, the value of dimensionless pressure coefficient $C_p$ increase to positive one, which means the outlet pressure is greater than inlet one. Moreover, along with the flow section further increasing, dimensionless velocity tends to be 0, and the dimensionless pressure coefficient $C_p$ tends to be fixed value. When the extend angle changes, both of the steady-state solution of u and $C_p$ make a little change.

Bubble radius violently oscillate, so as to the void fractionα (Fig. 2-Fig. 4). It can be explained that the flow velocity and pressure mutations which at outlet of nozzle strongly influence the form of bubble. By this time, bubbles' growth experience repetitive process of inflating-deflating-reinflating-redeflating. The high-ampllitude and high-frequency oscillation of bubbles near the critical value will certainly induce to new cavitate bubbles. It can be foreseed that the process of bubbles' repeatedly breaking will be beneficial to release more cavitate energy.

With the increasing of extenden angle θ, the maximum of bubbles' radius decreases in general at the vibrating section. But the decline of R is merely 0.63% even when θ is at the biggest drop range(θ=1°-5°), so the author think that the change of extended angle has little influence on vibration of bubbles' radius.

With the increasing of extenden angle θ, the vibrating width of bubbles, radius is decreasing(Fig. 5), which decreases by 38% when θ=1~5° and declines slowly when θ=5~8° .

As previously discussing, In the real environment, when extended angle becomes large, there will lead to considerable error about the steady-state solution because of the influence of the external fluid to the internal flow field in the nozzle. However, that does not affect the forecast to the trend of the steady-state solution. we can forecast that: it is helpful to increase the vibrating width of cavitate bubble when enlarge appropriately the exit taper of nozzle, that is the convergence-divergence nozzle with extended angle is more conducive to cavitation.

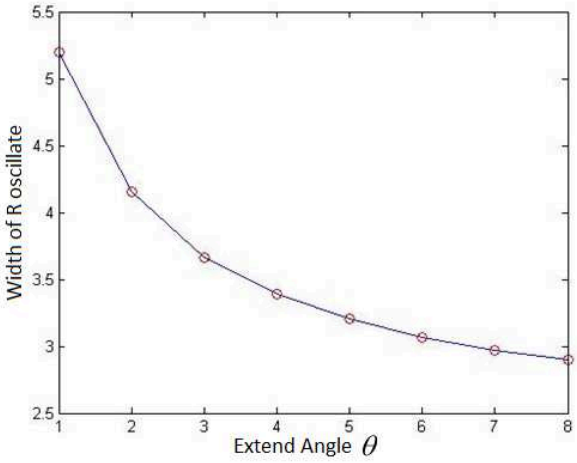



Fig. 5. The interpolate curve of the extend angle θ and fluctuated width *d* of the bubble radius

## Conclusion

This paper has comparatively analysied the steady-state solution of convergence-divergence nozzle between extended-angle and no-exended-angle. The steady-state solution of fluid vilocity, the pressure coefficient, the void fraction and the bubble radius will change when the extend angle

exists. Firstly, flow speed will quickly tend to 0 at the outlet of nozzle and the pressure coefficient quickly reached a plateau, and both of their steady-state solution do not change when extend angle changes. Secondly, for the existance of extenden angle, both void fraction and bubble radius violently oscillate at outlet of nozzle. bubbles' growth experience repetitive process of inflating-deflating-reinflating-redeflating. The high-ampllitude and high-frequency oscillation of bubbles near the critical value will certainly induce to new cavitate bubbles. So repeative process of bubble's growth and collapse will release more cavitate energy than single one. Finally, with the increasing of extended angle $\theta$, the vibrating width of bubbles' radius and void fraction is decreasing, which decreases by 38% when $\theta$=1~5$^{o}$, but both of the vibrating amplitude are almost independent of the change of the extended angle. In the end, an appropriate increase in extended angle of convergence-divergence nozzle will be more conducive to cavitation.

**Acknowledgement**

This work was financially supported by the National Science Foundation of China (Grant No. 51374101). The Natural Science Foundation of Hunan Province (Grant No. 13JJ9013) and the Projects of Hunan Province Science and Technology Department (Grant No. 2013SK3165).

**References**

[1] Katsuya Yanaida.Water Jet Cavitation of Submerged Horn Shaped Nozzles[A]. Proc.third U.S.Water Jet Conference[C]. May, 1985:103-110.In Chinese

[2] Liao zhenfang, Tang chuanlin, Zhang fenghua. Experiments of the Self-excited Oscillation Pulsed Jet Nozzle[J].Journal of Chongqing University,2002,25(2):28-32. In Chinese

[3] Yi can, Li gensheng, Shen zhonghou. Experimental Study of Self-resonating Cavitating Jet to Improve drilling speed[J].Gas Industy,2006,26(5): 52-54. In Chinese

[4] Zhang Fenghua, Tang Chuanlin, Yang Lin, Liao Zhenfang. Bifurcation of Steady-State Solution of Cavitation Flow Through Converging-Diverging Nozzle[J]. Mechanical Science And Technology, 2004, 23(8): 979-981. In Chinese

[5] d'Agostino L, Brennen C E. Linearized dynamics of spherical bubble clouds[J].J. Fluid Mech., 199, 1989, 155~176

[6] Plesset M S, Prosperetii A P. Bubble dynamics and cavitation[J].Ann. Rev. Fluid Meth., 1977,9:145~185

*Advanced Materials Research Vol. 937 (2014) pp 46-50*
*© (2014) Trans Tech Publications, Switzerland*
*doi:10.4028/www.scientific.net/AMR.937.46*

# Experimental Application of Salt Slurry in Talimu High Density Drilling Fluid Composed of KCl-saturated Brine and Polybasic Alcohol

Li-ju ZHOU [1, a], Jia-man FENG [2]

[1]College of Environmental Engineering, Wuhan Textile University, Wuhan 430073, China

[2]Jianghan Salt & Chemical Complex, Qianjiang, Hubei 433121, China

[a]fengzhouliju@163.com (Zhou Liju)

**Keywords:** Salt slurry; Application; High density; KCl-saturated brine; Drilling fluid

**Abstract** Salt slurry is the semi-solid waste of the salt industry. The study object was the salt slurry before filter in Jianghan Salt & Chemical Complex. In laboratory, this study investigated the application of the salt slurry in Talimu high density drilling fluid which composed of KCl-saturated brine and polybasic alcohol. It indicates that on the premise of the same density and pH value as the basic drilling fluid recipe, when the salt slurry dosage is less than 500 kg/m$^3$, all the salt slurry application-based recipes measure up both the rheology behavior and the filtrate loss of the drilling fluid. This investigate will reduce the cost of the drilling fluid with the salt slurry as a resource.

## Introduction

The salt industry is an important basic chemical industry. The salt production in China was 81.98 million tonnes in 2011 [1]. The salt industry produces large quantities of salt slurry which is the semi-solid waste that results from brine purification [2]. At present, the recycling methods of the salt slurry are generally still pilot-scale projects, and their problems include high investment costs, high operating costs, complicated processes, high energy consumption, secondary pollution, erosion of equipment by salt, and a low market price for the recycled product.

The saturated brine-based drilling fluid is one of the efficient techniques which are used in the complicated salt drilling in Talimu Oilfield, China [3]. But this drilling fluid system has the problem of high cost. Investigating the application of the salt slurry in high density drilling fluid which composed of KCl-saturated brine and polybasic alcohol, will have important significance for both reducing the cost of salt drilling and the recycling of the salt slurry.

## Laboratory Study

### Salt Slurry Component

This study object is the salt slurry before the rotary-drum vacuum filter in Jianghan Salt & Chemical Complex. The brine used as an input to the Salt Factory of JSCC is from well and rock salt. The first brine purification process is adding $NaCO_3$, NaOH to remove harmful ions (e.g., $Ca^{2+}$, $Mg^{2+}$, respectively), and adding sodium polyacrylate as accelerating agent. Salt slurry is the sediment that results from this process. The filter is used to reduce the volume of the salt slurry which need to disposal.

The Density of the salt slurry before filter is 1633 kg/m$^3$, pH value is 11.24, moisture is 34.84%, water soluble matter is 11.08%, acid soluble matter is 53.98%.

Table 1 is the chemical constituents of the salt slurry (dry basis) before filter.

Table 1. Chemical constituents of the salt slurry (dry basis) /% (in weight)

| Constituent | NaCl | $Na_2SO_4$ | NaOH | $Na_2CO_3$ | CPA | $CaCO_3$ | $Mg(OH)_2$ | $Al_2O_3$ | MnO | $Fe_2O_3$ | ZnO |
|---|---|---|---|---|---|---|---|---|---|---|---|
| Salt slurry | 12.59 | 4.11 | 0.07 | 0.23 | 3.83 | 68.37 | 7.41 | 0.132 | 0.008 | 0.048 | 0.028 |

### Recipe Design of Salt Slurry Application

Salt slurry application is on the basis of the drilling fluid recipe which is efficient. In this study, the recipe of the high density drilling fluid which composed of KCl-saturated brine and polybasic alcohol in Talimu Oilfield [3] is referred. Under the condition of the ingredients which were on hand in the laboratory, to determine the basic drilling fluid recipe through experiment. The special drilling fluid recipe is: 1.5% bentonite + 0.15% NaOH + 6% SMP-2 + 1.5% SMC + 1% RH102 + 3% polybasic alcohol + 1.5% $Na_2SiO_3$ + 0.2% $XY_2$ + 0.2% PAC + 7% KCl +25% NaCl + 3% FT-388, the density of the drilling fluid is 2000 kg/m$^3$. This basic drilling fluid recipe is recipe 0.

On the basis of the salt slurry component and the basic drilling fluid recipe, under the premise of the same density and pH value as the basic drilling fluid, to design the recipe of the salt slurry in the high density drilling fluid which composed of KCl-saturated brine and polybasic alcohol in Talimu Oilfield. In the recipe 1 to the recipe 5, the dosage of salt slurry is 100 kg/m$^3$, 200 kg/m$^3$, 300 kg/m$^3$, 400 kg/m$^3$ and 500 kg/m$^3$ respectively.

### Results Analysis

The salt slurry, especially those resulted from the brine purification of well and rock salt, has similar characteristics with the brine-based drilling fluid in constituents, compatibility with the geology environment, and also the process of salt slurry formation and the drilling fluid madeup. There are firm theory bases for salt slurry application in brine-based drilling fluid [2].

### Effect of Salt Slurry on Solid Concentration of Drilling Fluid

Solid concentration is one of the important property indexes of drilling fluid [4], generally, solid concentration in volume is required by less than 30% [3].

On the premise of the same density and pH value as the basic drilling fluid recipe 0, with the increasing of the salt slurry, the solid concentration of the high density drilling fluid which composed of KCl-saturated brine and polybasic alcohol increased (Figure 1).

The density of the salt slurry before filter is 1633 kg/m$^3$, and the density of barite is 4210 kg/m$^3$. To madeup drilling fluid with the same density, it will need more salt slurry to take the place of barite, thus, the solid concentration of the drilling fluid increased. In this way, the salt slurry dosage should be confined in a certain range.

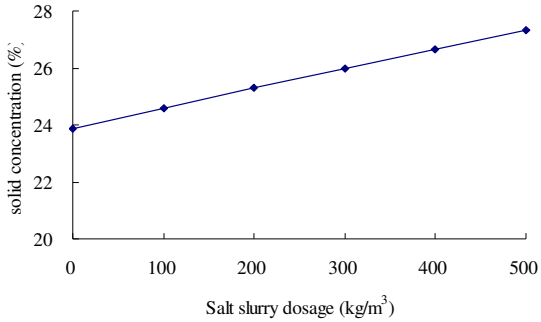



Fig. 1. Relationship between salt slurry dosage and solid concentration of drilling fluid

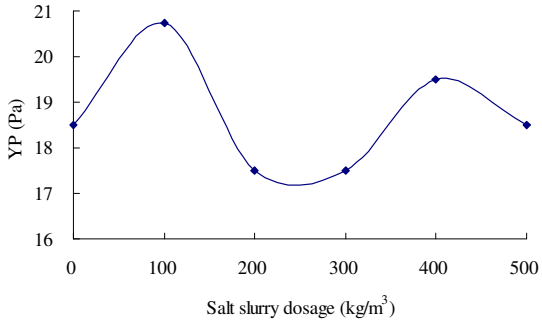



Fig. 2. Relationship between the salt slurry dosage and the YP value

### Effect of Salt Slurry on Rheology Behavior of Drilling Fluid

On the premise of the same density and pH value as the basic drilling fluid recipe 0, when the salt slurry dosage was less than 500 kg/m$^3$, all the salt slurry application-based recipes measured up the rheology behavior of the drilling fluid.

With the increasing of the salt slurry, when the salt slurry dosage was 0~100 kg/m$^3$, the YP value increased; when the salt slurry dosage was 100~200 kg/m$^3$, the YP value decreased; when the salt

slurry dosage was 300~400 kg/m$^3$, the YP value increased; when the salt slurry dosage was 400~500 kg/m$^3$, the YP value decreased. All YP value of the salt slurry application dosages fluctuated to that of recipe 0 (Figure 2).

When the salt slurry dosage was 0~100 kg/m$^3$, with the salt slurry increasing, the concentration of the solid, CPA increased, led to yield point increased.

On the other hand, with the increasing of the salt slurry, when the salt slurry dosage was 100~200 kg/m$^3$, $Na_2SO_4$ concentration increased, led to yield point decreased. When added small amount of electrolyte, the negative sulfate ion would be adsorbed by the clay particles, the zeta potential of the clay colloid particles would increase. The drilling fluid property of YP, PV and filtrate loss would decrease. Hence, when the salt slurry dosage was 100~200 kg/m$^3$, the YP value decreased.

When the salt slurry dosage was 300~500 kg/m$^3$, the YP value fluctuated to that of recipe 0, this phenomenon indicated that in this drilling fluid system, the effect of solid, CPA, and $Na_2SO_4$ on YP value was interactional and interdependent.

With the increasing of the salt slurry, when the salt slurry dosage was 0~100 kg/m$^3$, the PV value increased; when the salt slurry dosage was 100~200 kg/m$^3$, the PV value decreased; when the salt slurry dosage was 300~400 kg/m$^3$, the PV value increased; when the salt slurry dosage was 400~500 kg/m$^3$, the PV value decreased somewhat (Figure 3).

In this drilling fluid system, with the increasing of the salt slurry, the solid, CPA and the positive colloid concentration increased, led to PV value increased; on the other hand, $Na_2SO_4$ concentration increased, led to PV value decreased. When the salt slurry dosage was 0~100 kg/m$^3$, the effect of the solid, CPA and the positive colloid on PV value was stronger than that of $Na_2SO_4$, so the PV value increased. When the salt slurry dosage was 100~200 kg/m$^3$, the effect of $Na_2SO_4$ on PV value was enhanced. When the salt slurry dosage was 200~300 kg/m$^3$, the increased effect of the solid, CPA and the positive colloid on PV value was relatively balanced with the decreased effect of $Na_2SO_4$ on PV value, as a result, the PV value kept unchanged.

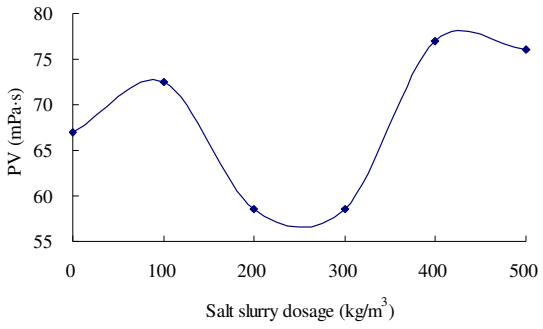



Fig. 3. Relationship between the salt slurry dosage and the PV value

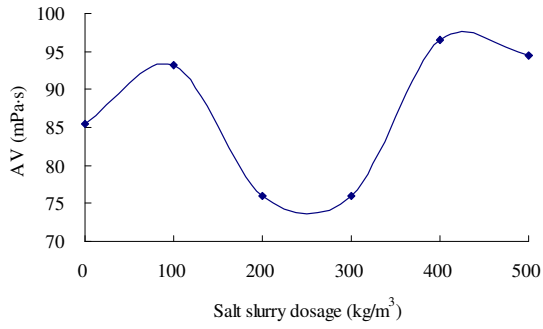



Fig. 4. Relationship between the salt slurry dosage and the AV value

With the increasing of the salt slurry, when the salt slurry dosage was 0~100 kg/m$^3$, the AV value increased; when the salt slurry dosage was 100~200 kg/m$^3$, the AV value decreased; when the salt slurry dosage was 300~400 kg/m$^3$, the AV value increased; when the salt slurry dosage was 400~500 kg/m$^3$, the AV value decreased somewhat (Figure 4).

From the above analysis of the salt slurry effect on YP, PV value, the effect of salt slurry on AV value could be deduced.

With the increasing of the salt slurry, when the salt slurry dosage was 0~300 kg/m$^3$, the YP/PV value increased; when the salt slurry dosage was 300~500 kg/m$^3$, the YP/PV value decreased (Figure 5).

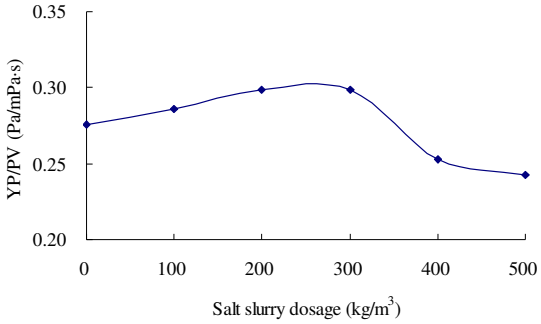



Fig. 5. Relationship between the salt slurry dosage and the YP/PV value

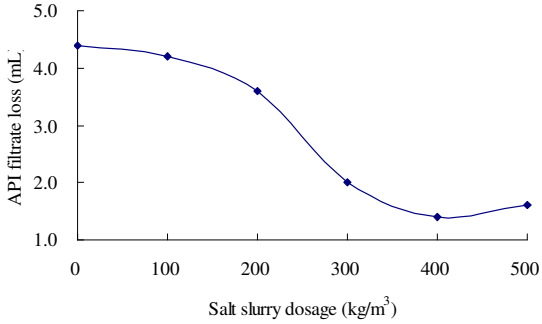



Fig. 6. Relationship between the salt slurry dosage and the API filtrate loss

**Effect of Salt Slurry on API Filtrate Loss of Drilling Fluid**

The filtrate loss is principally determined by the viscosity of the filtrate and the quality of the mud-cake (fluid permeability) [4]. The latter is principally determined by the distribution of the solid particles in the drilling fluid. Proper particles distribution is related to the coagulation stability of the particles [4].

On the premise of the same density and pH value as the basic drilling fluid recipe 0, when the salt slurry dosage was less than 500 kg/m$^3$, The filtrate losses of the salt slurry based drilling fluid were all less than that of the basic drilling fluid recipe 0 (Figure 6).

(1) With the increasing of the salt slurry, $CaCO_3$ concentration increased.

In drilling practice, $CaCO_3$ with proper particles size is generally used to control filtrate loss. It is used as bridge additive to enhance the well building property of the drilling fluid, to improve the compact ability of the mud-cake. Because $CaCO_3$ is acid soluble, it is convenient to unseal by adding acid when the well will be on production [3]. The mud-cake is formed when the solid particles bridge on the surface of the multi-pore medium. The above process is go by the principle of "bridge in 1/3 diameter", that is, the diameter of the solid particles is required more than 1/3 of the pore diameter of the sand. Generally, the diameter of the bridge additive is required as 2~200μm. The concentration of the solid particles whose diameter are more than 1/3~1/2 of the medium pore diameter of the strata is required no less than 5% (in volume) [4].

(2) With the increasing of the salt slurry, CPA concentration increased.

CPA is the ingredient to control filtrate loss [3]. It can resist salt, calcium and high temperature. In this study, it is resulted from the reaction of calcium ion and sodium polyacrylate in the process of brine purification. It has relative large molecular weight, strong hydrophilcity, and proper cross-linking reticulated structure. The clay particles in the reticulated structure are uneasy to adhere and setting, thus, CPA has strong capability to decrease the filtrate loss.

(3) With the increasing of the salt slurry, $Na_2SO_4$ concentration increased.

Adding small amount of electrolyte may increase the zeta potential of the colloid particles, uneasy to collide each other and adhere, the colloid will be more stability, as a result, the filtrate loss decrease to form thin, plastic and compacted mud-cake.

**Conclusions**

On the premise of the same density and pH value as the basic drilling fluid recipe, when the salt slurry dosage was less than 500 kg/m$^3$, all the salt slurry application-based recipes measured up both the rheology behavior and the filtrate loss of the drilling fluid. The application of the whole components of the salt slurry in the madeup of the Talimu high density drilling fluid which composed of KCl-saturated brine and polybasic alcohol can be realized through special prescription.

**Acknowledgements**

Financial and technical supports from Jianghan Salt & Chemical Complex, and technical supports from Jianghan Drilling Company in China are gratefully acknowledged.

**References**

[1] Bu Z.F., The salt production in China has kept the first in the world, Information on http://www.cnsalt.cn/d.asp?id=10781 (In Chinese).

[2] Zhou L.J., Feng J.M., Lei J.J., Zhao Y.C., Feasibility study of applying salt slurry in brine drilling fluids, Petroleum Drilling Techniques. 1 (2008) 33-37 (In Chinese).

[3] Tang J.P., Wang S.Q., Chen M., Theory and Practice of Salt Drilling, Petroleum Industry Press, Beijing, 2004 (In Chinese).

[4] Zhang K.Q., Chen Y.L., Drilling Technique Handbook, Volume 2, Drilling Fluid, Petroleum Industry Press, Beijing, 1988 (In Chinese).

*Advanced Materials Research Vol. 937 (2014) pp 51-57*
*© (2014) Trans Tech Publications, Switzerland*
*doi:10.4028/www.scientific.net/AMR.937.51*

# Preparation of 2,2-Dimethylol Propionic Acid

Jian-Wei ZHANG [a,*], Ji-Wei LIU [b]

[1,2]Provincial Key Laboratory of Oil and Gas Chemical Technology, College of Chemistry and Chemical Engineering, Northeast Petroleum University, Daqing, Heilongjiang, China

[a]benbenbao@163.com, [b]liujiwei0706@163.com

*Corresponding author

**Keywords:** 2,2- Dimethylol propionic acid, orthogonal design, propionaldehyde, formaldehyde

**Abstract.** 2,2- Dimethylol propionic acid was synthesized by two steps using sodium hydroxide as the catalyst in this article. The influence of various factors on the yield of 2,2-Dimethylol propionic acid were studied by single factor experiment that included condensation temperature, condensation time, propionaldehyde -formaldehyde ratioetc.. On the basis of this foundation, the orthogonal design was carried out in order to confirm the preferable synthesis conditions of 2,2-Dimethylolpropanoic. The results show that the optimal synthesis conditions are as follows: condensation time is 8 hours, condensation temperature is 35°C, propionaldehyde-formaldehyde ratio is 2.2, sodium hydroxide-formaldehyde ratio is 0.03, the oxidation temperature is 90°C, oxidation time is 6 hours. The product yield can reach to 71.35% under these reaction conditions that is higher than the value reported in references.

## Introduction

2,2- Dimethylol propionic acid (DMPA) that is an ideal kind of hydrophilic monomer can be used in synthesis resin, polyester, printing ink, chemical intermediates, photographic chemicals, electrodeposition coating, epoxy coating, food additives etc.[1-6]. It has a very broad market prospect. The synthesis methods have been reported in many references, but the yield are not very high which is nearly 50%-60%[7,8]. In order to improve the product yield greatly, 2,2- Dimethylol propionic acid was synthesized by two steps using sodium hydroxide as the catalyst in this article. The influences of various factors on the yield were also investigated.

## Materials

The main materials used in the paper were formaldehyde, propionaldehyde, hydrogen peroxide and sodium hydroxide. All the above were AR.

## Experiment methods

2,2-Dimethylolpropanoic was prepared by two steps. Firstly, formaldehyde and sodium hydroxide were mixed on a certain ratio adequately, and then propionaldehyde was added to the above reaction system that the dropping speed could be two drop per second. The solution with 2,2-Dimethylol propionaldehyde was prepared at last through aldol reaction. The partly water and by-products were removed by the first reduced pressure distillation. Secondly, Hydrogen peroxide was added to the mother liquor contained 2,2-Dimethylol propionaldehyde purified preliminary in temperature-rise period in which oxidizing reaction occurred. After the second reduced pressure distillation, water and by-products in the products were removed again and at last the solution containing 2,2- Dimethylol propionic acid was prepared.

The solution containing 2,2-Dimethylol propionic acid was cooling to separate out the crude product. Then the crude product was dried, filtered under reduced pressure, washed by absolute ethyl alcohol and dried again. After that the pure 2,2-Dimethylol propionic acid product was prepared as white crystal.

The FTIR spectra (4000-400 $cm^{-1}$) was measured with Spectrum One Fourier Transform-Infrared Spectroscopy (PerkinElmer, American). The melting point of 2,2-Dimethylol propionic acid was measured by S-6 Micro Melting Point Apparatus (Beijing Tech Instrument Co. LTD., China).

## Results and Discussion

### Single Factor Experiment

#### The Influence of Condensation Reaction Temperature on Product Yield

The effects of reaction temperature on product yield in condensation reaction is shown in Fig.1 that the reaction time was 6h, propionaldehyde-formaldehyde ratio was 2.2 and sodium hydroxide-formaldehyde ratio was 0.03. The yield increases firstly and then decreases when the temperature is from 25 °C to 45 °C. The yield reaches a maximum at 35 °C. This may have occurred because that high temperature benefits the initial aldol reaction but when the temperature is higher than 35 °C the disproportionation reaction occurs and the by-products greatly increase and then the field decreases. The proper reaction temperature in condensation reaction is 35 °C.

#### The Influence of Condensation Reaction Time on Product Yield

When the reaction temperature was 35 °C, propionaldehyde-formaldehyde ratio was 2.2 and hydrogen peroxide- formaldehyde ratio was 0.03, the influence of condensation reaction time on product yield was researched, as shown in fig. 2. It could be seen that the yield increases with the increase of reaction temperature before 8h and then remains unchanged. It appears that the condensation reaction may stop after 8h and the yield could not increase more. The proper reaction time in condensation reaction is from 6h to 8h.

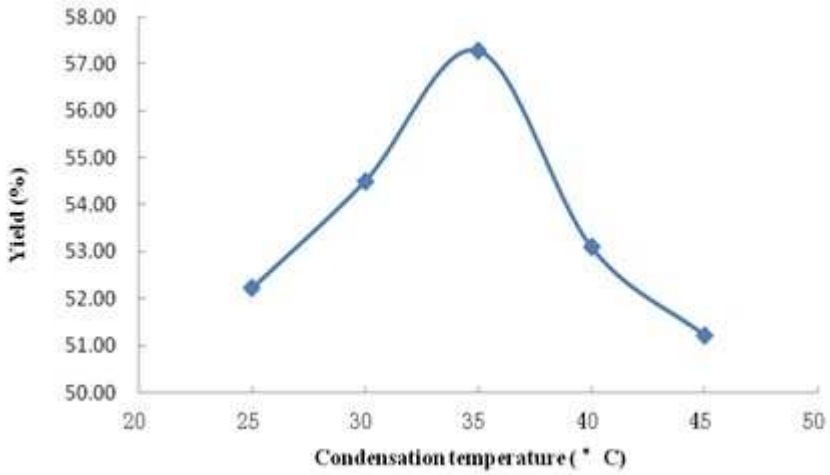



Fig. 1. The effect of condensation temperature on the yield

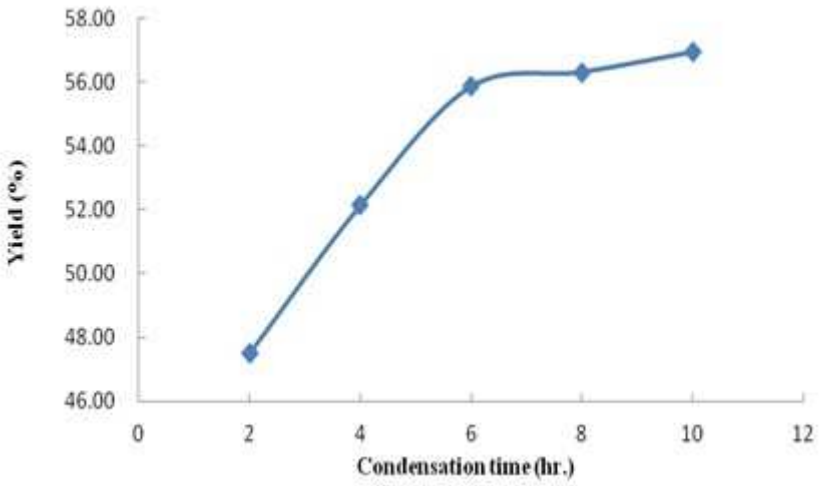



Fig. 2. The effect of condensation time on the yield

**The Influence of Propaldehyde-formaldehyde Ratio on Product Yield in Condensation Reaction**

The effects of propaldehyde-formaldehyde ratio on product yield in condensation reaction is shown in Fig. 3. that the reaction time was 6h, reaction temperature was 35 °C and sodium hydroxide-formaldehyde ratio was 0.03. The result shows that the yield increases when the propaldehyde-formaldehyde ratio is from 2 to 2.2 and decreases when the propaldehyde-formaldehyde ratio is from 2.2 to 2.4. The yield reaches a maximum at 2.2. A possible explanation for this is that if formaldehyde is excessive it can occur disproportionation reaction with the product and if propaldehyde is excessive it can occurre condensation reaction with itself. The proper propaldehyde-formaldehyde ratio could be 2.2.

**The Influence of Catalyst Dosage on Product Yield in Condensation Reaction**

Sodium hydroxide was used as the catallyst. When the reaction time was 6h, reaction temperature was 35 °C and propionaldehyde-formaldehyde ratio was 2.2, the influence of sodium hydroxide-formaldehyde ratio on product yield in condensation reaction was researched, as shown in fig. 4. It could be seen that the yield increases with the increase of sodium hydroxide-formaldehyde ratio before 0.03 and then decreases. The yield reaches a maximum when propionaldehyde-formaldehyde ratio is 0.03.The proper explanation for this is that the pH of the reaction system increases when the dosage of sodium hydroxide increases. The higher pH could not be benefit for condensation reaction because disproportionation reaction can occur easily in high pH system that decreases the product yield. The proper sodium hydroxide-formaldehyde ratio in condensation reaction is 0.03.

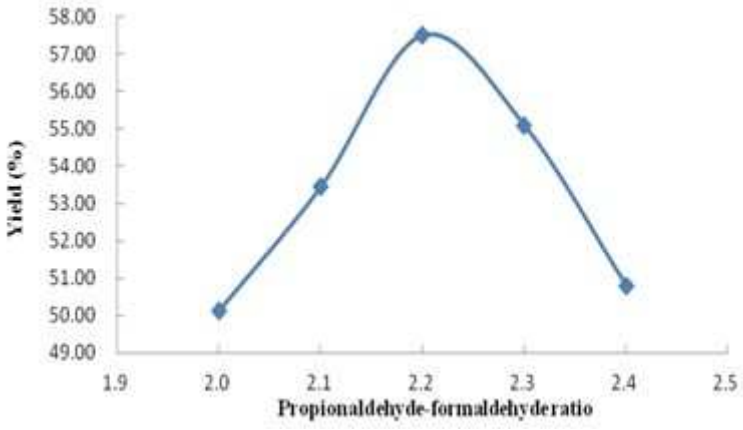



Fig. 3. The effect propionaldehyde-formaldehyde ratio on the yield

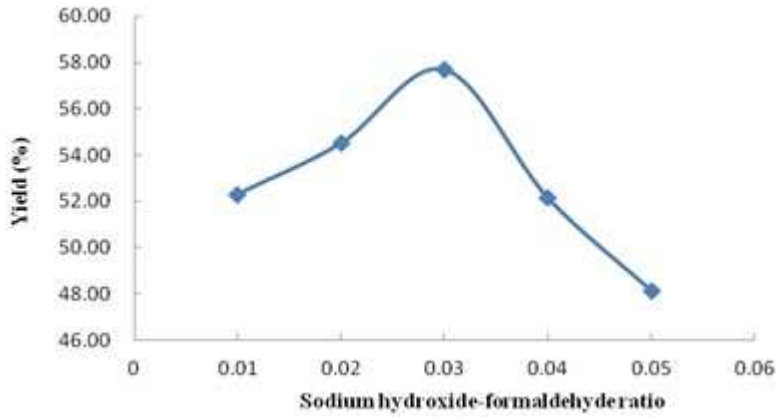



Fig. 4. The effect of sodium hydroxide-formaldehyde ratio on the yield

**The Influence of Oxidation Reaction Time on Product Yield**

When the reaction time was 6h, reaction temperature was 35 °C, propionaldehyde-formaldehyde ratio was 2.2 in condensation reaction, sodium hydroxide-formaldehyde ratio was 0.03 and the temperature in oxidation reaction was 35 °C, the influence of oxidation reaction time on product yield was researched, as shown in fig. 5. Fig. 5 shows that the yield increases with the increase of oxidation reaction time which is from 2h to 8h but then increases less obviously when the time is greater than 8h. This is may be that when the time increases to 8h, the reaction materials have been oxidized sufficiently and thus the yield will not increases when the time is greater than 8h. The proper oxidation reaction time is from 6h to 8h.

**The Influence of Oxidation Reaction Temperature on Product Yield**

The influence of oxidation reaction temperature on product yield was researched, as shown in fig. 6, that the reaction time was 6h, reaction temperature was 35 °C, propionaldehyde-formaldehyde ratio was 2.2 in condensation reaction, sodium hydroxide-formaldehyde ratio was 0.03 and oxidation reaction time was 6h. Fig. 6 shows that the yield increases with the increase of oxidation reaction temperature which is from 75 °C to 90 °C but does not increase obviously when the temperature is greater than 90 °C. The proper oxidation reaction temperature is from 85 °C to 90 °C.

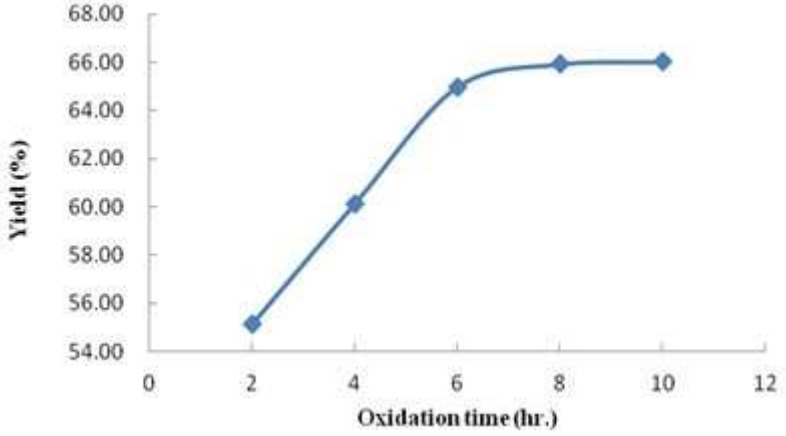



Fig. 5. The effect of oxidation time on the yield

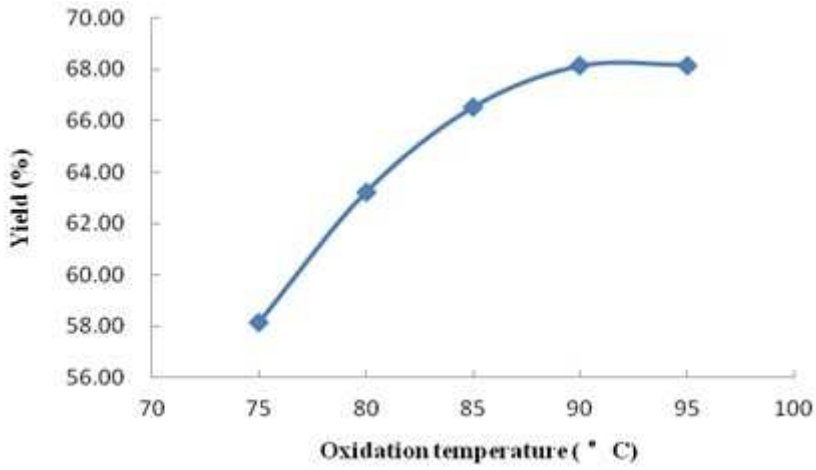



Fig. 6. The effect of oxidation temperature on the yield

**Orthogonal Experiment**

Through the above research it is could be seen that condensation reaction time, condensation reaction temperature, propionaldehyde-formaldehyde ratio, sodium hydroxide-formaldehyde ratio, oxidation reaction temperature and oxidation reaction time all play a significant part in product yield. In order to determine the optimal synthetic conditions for 2,2-Dimethylol propionic acid production, the orthogonal method and the error analysis method were used. All of the factors affecting product yield and stoichiometric numbers were shown in Table 1. The best optimum synthesis condition was identified according to the yield of 2,2- Dimethylol propionic acid. The orthogonal design test results were shown in Table 2. The average of the yield of 2,2- Dimethylol propionic acid at *i* level was represented by *Ki*. The variance was the value that the maximum yield minus the minimum yield.

Table 1. Levels and factors

| | A | B | C | D | E | F |
|---|---|---|---|---|---|---|
| Level | Condensation reaction temperature(°C) | Condensation reaction time(hr.) | NaOH/ $C_2H_5CHO$ | $C_2H_5CHO$ /$CH_3CHO$ | Oxidation reaction time(hr.) | Oxidation reaction temperature (°C) |
| 1 | 30 | 6 | 0.02 | 2.2 | 6 | 85 |
| 2 | 35 | 8 | 0.03 | 2.3 | 8 | 90 |

Table 2. $L_8(2^5)$ Orthogonal design test results

| Sample | A | B | C | D | E | F | Yield(%) |
|---|---|---|---|---|---|---|---|
| 1 | 1 | 1 | 1 | 1 | 1 | 1 | 42.50 |
| 2 | 1 | 1 | 1 | 2 | 2 | 2 | 43.21 |
| 3 | 1 | 2 | 2 | 1 | 1 | 2 | 60.29 |
| 4 | 1 | 2 | 2 | 2 | 2 | 1 | 52.64 |
| 5 | 2 | 1 | 2 | 1 | 2 | 1 | 68.55 |
| 6 | 2 | 1 | 2 | 2 | 1 | 2 | 65.73 |
| 7 | 2 | 2 | 1 | 1 | 2 | 2 | 69.42 |
| 8 | 2 | 2 | 1 | 2 | 1 | 1 | 62.51 |
| $k_1$ | 49.62 | 54.97 | 49.87 | 60.15 | 59.70 | 56.47 | |
| $k_2$ | 66.50 | 61.15 | 61.75 | 55.97 | 57.98 | 59.63 | |
| Variance | 16.88 | 6.18 | 11.56 | 4.18 | 0.72 | 3.16 | |
| Optimal solutions | $A_2$ | $B_2$ | $C_2$ | $D_1$ | $E_1$ | $F_2$ | |

A technical condition for the reaction by orthogonal test was investigated. By experiment and calculation, the best optimum synthesis conditions for the reaction are as follows: condensation reaction temperature 35°C, condensation reaction time 8h, oxidation reaction time 6h, oxidation

reaction temperature 90 °C, NaOH/ $C_2H_5CHO$ 0.03, $C_2H_5CHO$ /$CH_3CHO$ 2.2. It is confirmed that the yield is 71.35% under the best optimum synthesis conditions. The variance of condensation reaction temperature which is 16.88 is the largest in all the variances, so condensation reaction temperature has great influence in total factors on the yield of 2,2- Dimethylol propionic acid.

**FTIR and Melting Point Analysis of 2,2- Dimethylol Propionic Acid**

Figure 7 shows the FTIR spectra of 2,2- Dimethylol propionic acid which was synthesized under the best optimum synthesis condition. The spectrum shows a broad band in the range of 1600-3700$cm^{-1}$, which is attributed to the typical absorption band of 2,2- Dimethylol propionic acid, including the following characterization: 3420 $cm^{-1}$ (-OH stretching band), 2560 $cm^{-1}$ and 2980 $cm^{-1}$ (-$CH_3$ and -$CH_2$ stretching band), 1690$cm^{-1}$ (-C=O stretching band).

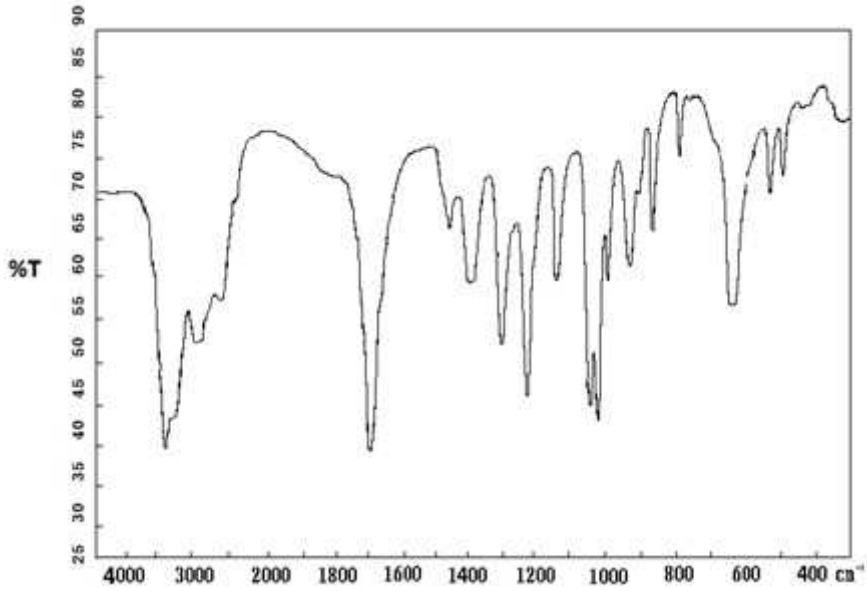



Fig. 7. FTIR of 2,2- Dimethylol propionic acid

In the melting point analysis of 2,2- Dimethylol propionic acid, it was found that the melting point of the product was 190.2°C in accordance with the value from the reference 189°C-191°C[8]. From the above we can infer the product is 2,2- Dimethylol propionic acid.

**Conclusions**

The 2,2- Dimethylol propionic acid was synthesized through condensation reaction and oxidation reaction. Besides it was characterized using the FTIR spectroscopy method and melting point analysis. The best optimum synthesis condition identified according to the product yield. The conclusions are summarized as follows:

[1] Through the single factor experiments it could be find that the product yields increases firstly and then decrease with the increasing of condensation reaction temperature, propaldehyde-formaldehyde ratio and sodium hydroxide-formaldehyde ratio.

[2] When condensation reaction time, oxidation reaction temperature and oxidation reaction time increase, the product yield increase firstly but does not increase obviously later.

[3] Condensation reaction temperature and sodium hydroxide-formaldehyde ratio can influence the yield of 2,2- Dimethylol propionic acid greatly in the total factors.

[4] The optimum synthesis condition for 2,2- Dimethylol propionic acid are confirmed through the orthogonal test that condensation reaction temperature is 35°C, condensation reaction time is 8h, sodium hydroxide-formaldehyde ratio is 0.03, propaldehyde-formaldehyde ratio is 2.2, oxidation reaction time is 6h and oxidation reaction temperature is 90 °C . The yield can reach to 71.35% under the best optimum synthesis conditions.

**Acknowledgement**

The authors are grateful to the Provincial Key Laboratory of Oil and Gas Chemical Technology of Northeast Petroleum University in China for financial support.

**References**

[1] Luciani A,Plummer C J G, Nguyen T, et al . Rheological and physical properties of aliphatic hyperbranched polyesters [J]. Journal of Polymere (SciencePartB). 2004, 42(7): 1218-1225.

[2] Zagar E, Zigon M. Characterization of a commercial hyperbranched aliphatic polyester based on 2,2-Bis (methylol)prop ionic acid[J]. Macromolecules. 2002, 35(27): 9913-9925.

[3] Komber H, Ziemer A, Voit B. Etherification as side reaction in the hyperbranched polycondensation of 2,2-Bis (hydroxymethyl) prop ionic acid [J]. Macromolecules. 2002, 35 (9): 3514-3519.

[4] Busson P, Ortegren J, Ihre H. Ferroelectric liquid crystalline dendrimers: synthesis, thermal behavior and electrooptical characterization [J]. Macromolecules. 2001,34(5):1221-1229.

[5] Magnusson H , Hult A , Malmstrom E. Structure buildup in hyperbranched polymers from

2,2-Bis(hydroxymethyl) propionicacid [J]. Macromolecules. 2000, 33(8): 3099-3104.

[6] Ren Z; Ma D; Wang Y; Zhao G, Molecular structure and hydrogen bonds in solid dimethylol propionic acid (DMPA). Spectrochimica Acta. Part A: Molecular and Biomolecular Spectroscopy. 2003, 59(12): 2713-2722.

[7] Jin Zhao, Zuliang Huang, et al. Synthesis of 2, 2- dimethylolbutyric acid [J]. Fine Chemical Intermediates.2012, (6): 44-46.(In Chinese)

[8] Zhongyuan Chen. Novel process on preparation of 2, 2- Bis( hydroxymethyl) propionic acid [J]. China Leather . 2011,(9):47-45. (In Chinese)

*Advanced Materials Research Vol. 937 (2014) pp 58-63*
*© (2014) Trans Tech Publications, Switzerland*
*doi:10.4028/www.scientific.net/AMR.937.58*

# Reaction Routes for the Electro-deoxidation of Ilmenite in Molten Salt

Xing-Li ZOU[1,a,*], Xiong-Gang LU[1,b,*], Wei XIAO[1,c] and Chang-Yuan LU[1,d]

[1]Department of Materials Science and Engineering, Shanghai University, Shanghai 200072, China

[a]zouxingli@shu.edu.cn, [b]luxg@mail.shu.edu.cn, [c]shawway@126.com, [d]luchangyuan2006@163.com

*Corresponding author

**Keywords:** Electro-deoxidation, Reaction mechanism, Titanium alloy, Ilmenite, Molten salt.

**Abstract.** The reaction mechanism of electrochemical extraction of $Fe_xTi$ alloys direct from natural ilmenite in molten $CaCl_2$ has been investigated. The electrochemical deoxidation experiment process was carried out at 1000 °C and 3.8 V, and a solid oxide oxygen-ion-conducting membrane (SOM) filled with carbon-saturated liquid metal was served as the inert anode of the electrolytic cell. The macro-/micro-structure variations of the samples during electrolysis were investigated. The reaction routes from natural ilmenite to $Fe_xTi$ alloys are proposed and discussed. It is found that element Fe is reduced firstly from ilmenite and thus serves as electronic conductor to accelerate subsequent deoxidation, $Fe_xTi$ alloys can be produced directly from natural ilmenite by electrolysis in molten salt. It is suggested that $Fe_xTi$ phase can be formed directly from $Fe_xTiO_y$ compounds and/or from deoxidation-generated Ti and Fe through various reaction routes.

## Introduction

The dominant mineral form of titanium is natural ilmenite and its derivatives, which is the main source for production of metal titanium. Natural ilmenite is commonly expressed as $FeTiO_3$, however, it usually accommodates CaO, MgO, $Al_2O_3$ and $SiO_2$ in its structure [1]. Therefore, the production of titanium from natural ilmenite generally involves high processing cost and complicated procedures [1,2]. In recent years, the technologies which have the potential for extracting of titanium and/or titanium alloys directly from the multicomponent natural ilmenite have received considerable attention. Such as the electrochemical deoxidation technology, i.e. the Fray-Farthing-Chen (FFC) Cambridge process [2,3], the SOM process [4-8] and Ono-Suzuki (OS) process [9,10], etc. These processes have been extensively studied and successfully used to deoxidize metal oxides and mixtures thereof directly into their parent metals and alloys. Moreover, the direct electro-deoxidation of ilmenite has been attempted [6,11,12]. It is interesting to find that some of the metallic impurities contained in the natural ilmenite such as Ca, Mg and Al can be removed during electrolysis, and $Fe_xTi$ alloys can be obtained as final product [6,11,12]. In our recent work [7,8], we have reported the mechanisms of electro-deoxidation of mixed oxides ($TiO_2/Fe_2O_3$) and complex multicomponent titanium/silicon-containing compounds using the SOM process in molten $CaCl_2$. However, the reaction routes related to the electro-deoxidation of natural ilmenite in molten salt is still unclear.

In this paper, we present the detailed reaction routes for the electro-deoxidation of natural ilmenite in molten $CaCl_2$. In addition, the current features during electrolysis process, the morphology variations and the phase composition evolutions of the samples were investigated.

## Experimental

### Preparation of Cathode

The chemical composition of the natural ilmenite used in this experiment is tabulated in Table 1. The ilmenite was ball-milled with anhydrous alcohol for 10~15 h, and then about 1.0 g of the milled ilmenite powder was pressed under 5~8 MPa to form a porous pellet. The pressed pellet was then annealed in air for 2 h at 1150 °C. The annealed pellet was first sandwiched between two porous Ni films and then tightened using Mo or Fe-Cr-Al wire to form a cathode.

Table 1. Chemical composition of the natural ilmenite [wt%]

| Composition | $TiO_2$ | Total Fe | $SiO_2$ | CaO | MgO | $Al_2O_3$ | MnO |
|---|---|---|---|---|---|---|---|
| Natural ilmenite | 45.74 | 36.17 | 2.67 | 2.32 | 0.15 | 0.51 | 1.16 |

## Preparation of Anode

The key feature of the SOM process is that an inert membrane-based anode system was introduced to control the electrochemical experiment. The membrane-based anode system includes an yttria-stabilized zirconia (YSZ) tube filled with carbon-saturated liquid metal (Cu or Sn), and a Mo or Fe-Cr-Al wire was inserted into the YSZ tube as electronic conductor. The YSZ tube used in this experiment is fabricated in our laboratory. Details about the SOM process can be found in our previous work [6-8].

## Electro-deoxidation Experiments and Characterization of Products

The fabricated anode and cathode were placed in a graphite crucible, and $CaCl_2$ was filled in the crucible as electrolyte. The electrochemical experiments were carried out at 1000 °C and 3.8 V under highly purified argon atmosphere. The experiments were controlled by a HCP-803 electrochemical workstation linked to a computer. More details of the experimental procedure are described elsewhere [6-8]. The morphology and phase composition of the samples were characterized by JSM-6700F scanning electron microscope (SEM) and by D/Max-2550 X-ray diffractometer (XRD), respectively.

## Results and Discussion

### Current Features

The electro-deoxidation experiments were carried out systematically in molten $CaCl_2$ at 1000 °C and 3.8 V. The schematic of the SOM process is shown in Fig. 1a. The oxygen component contained in the natural ilmenite precursor is ionized to oxygen ions, then the oxygen ions dissolve in molten salt and migrate through the SOM and to be oxidized at the anode (as shown in Fig. 1a). The typical current/charge-time curves recorded during electro-deoxidation process are shown in Fig. 1b, and its partial details are shown in Fig. 1c. It should be noted that due to the SOM membrane having selective permeability for only oxygen ions, the current passed through the SOM electrolytic cell is therefore deemed to be mainly corresponds to the oxygen ions oxidized at the anode or the metal ions reduced at the cathode [13]. In this experiment, the applied potential of 3.8 V creates current of ~1000 mA at the beginning (period i as shown in Fig. 1b and 1c), and then the current declines gradually to about 800 mA (period ii as shown in Fig. 1c). With the increasing of electrolysis time, the whole surface of the porous pellet is metallized. Therefore, the reactions propagate from the pellet exterior to its interior, and the mass transfer becomes slow due to the deoxidation-generated metallic layer blocking the electromigration of oxygen ions [14]. As a result, the current decreases gradually to a constant level of ~400 mA (corresponding to the periods iii and iv as shown in Fig. 1b). When the current keeps at a constant small level, it means the pellet has been electrolyzed almost completely. The total charge passed through the electrolytic cell during the electro-deoxidation process is calculated to be ~2.0 A.h in 4 h electrolysis (as shown in Fig. 1b).

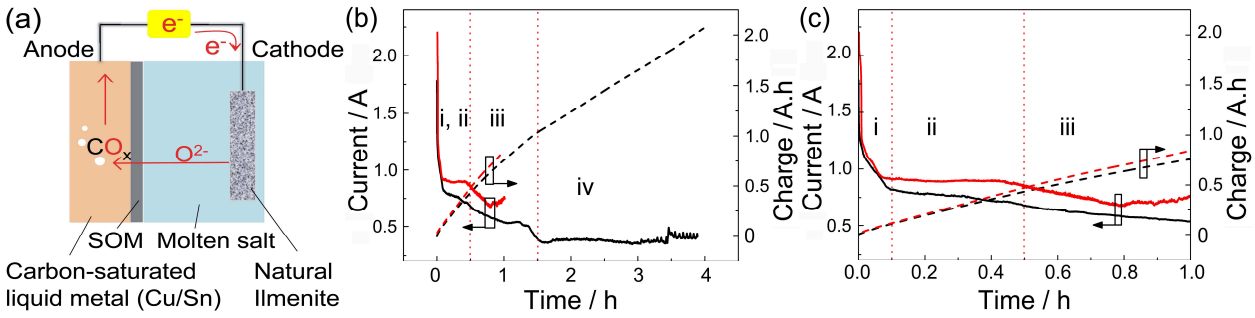



Fig. 1. (a) Schematic of the SOM process, (b) typical current/charge-time curves of the electro-deoxidation of ilmenite at 1000 °C and 3.8 V for 1 h and 4 h, (c) partial details of the current/charge-time curves in (b).

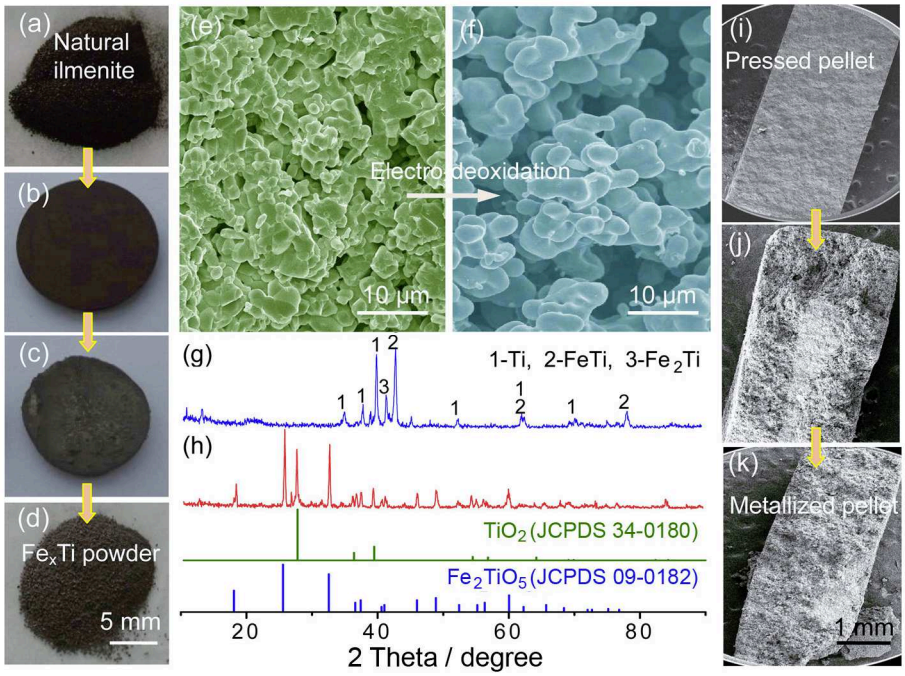



Fig. 2. (a) The natural ilmenite powder, (b) pressed porous ilmenite pellet, (c) electrolyzed pellet, (d) produced $Fe_xTi$ powder, (e) SEM image of the sintered natural ilmenite pellet, (f) SEM image of the electrolyzed pellet, (g) XRD pattern of the electrolyzed pellet, (h) XRD pattern of the natural ilmenite precursor, (i)-(k) are the SEM images of the cross-section of the pressed pellet (i) and the pellet electrolyzed incompletely (j) as well as the pellet electrolyzed completely (k).

**Morphology and Phase Composition Variations**

The Photos of the appearance of natural ilmenite powder as well as its pressed porous pellet are shown in Fig. 2a and 2b. Fig. 2c and 2d are the photos of the ilmenite pellet electrolyzed completely and its corresponding final $Fe_xTi$ alloys powder, respectively. It clearly shows that the morphology of the ilmenite pellet changes during deoxidation process. The electrolyzed pellet shrinks slightly and also changes in color, it can be grinded easily to powder. Fig. 2e and 2f are the SEM images of the sintered natural ilmenite precursor and its corresponding electrolyzed product, respectively. The sintered pressed ilmenite pellet exhibits irregular particles. In contrast, the deoxidized sample possesses interconnected smooth nodular particles with the size of approximately 5 μm. Fig. 2g and 2h are the XRD patterns of the obtained $Fe_xTi$ alloys and its corresponding sintered ilmenite precursor [6], respectively. It is obvious that the sintered natural ilmenite (it mainly consists of $Fe_2TiO_5$ and $TiO_2$) has been deoxidized to $Fe_xTi$ alloys and metal titanium. The oxygen contained in the precursor has been removed completely during the SOM electro-deoxidation process. It should be mentioned that, the SOM deoxidation process also complies with the three-phase-interlines (3PIs) deoxidation mechanism [14,15]. The reactions first occur on the contact point of ilmenite pellet/initial electronic conductor/molten salt. In this experiment, the nickel films provide plenty of uniformly distributed initial electronic contacts to the surface of the pellet, which means the surface of the pellet can be metallized quickly. The reaction area/3PIs then extends gradually into the pellet interior, as shown in Fig. 2j. The porous pellet electrolyzed completely becomes thinner (as shown in Fig. 2i-k), which should be, to some extent, mainly attributes to the removal of oxygen and the sintering effect during electrolysis.

The XRD pattern of the product obtained from electrolysis for 1 h is shown in Fig. 3. It clearly shows that the intermediate product contains $CaTiO_3$, Fe, $Fe_xTiO_y$ and $Fe_xTi$. $CaTiO_3$ can be generated from $Fe_xTiO_y$ and/or $TiO_2$ by chemical/electrochemical reactions [6,12]. Element Fe is deoxidized firstly from ilmenite and thus may serve as electronic conductor to accelerate subsequent deoxidation. Meanwhile, $Fe_xTiO_y$ such as $FeTiO_3$ and $Fe_2TiO_4$ are generated as intermediate products during the electro-deoxidation process. The inset in Fig. 3 shows the micro-structure of the intermediate product is different from the ilmenite precursor and final $Fe_xTi$ product (Fig. 2e and 2f).

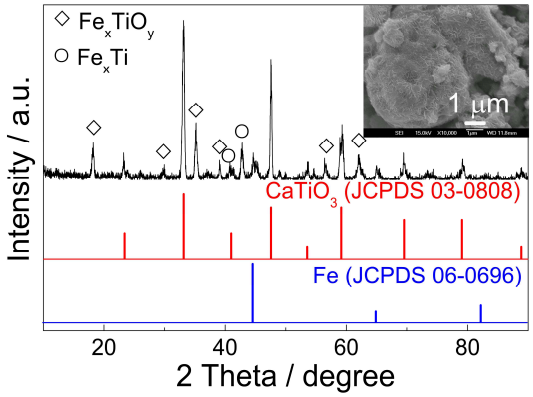



Fig. 3. XRD pattern of the natural ilmenite electrolyzed at 1000 °C and 3.8 V for 1 h, the inset shows a SEM image of the intermediate product.

## Reaction Routes

Based on our previous work [6-8], thermodynamic analysis and previous report [11,12,16,17]. The reaction routes from ilmenite to Fe$_x$Ti alloys by electrolysis are proposed and shown in Fig. 4. It is obvious that all routes presented in Fig. 4 are possible while the applied potential in the SOM electro-deoxidation process is 3.8 V. The reaction mechanism can be generally summarized as four routes.

Route i: $Fe_2TiO_5 \rightarrow Fe_2TiO_4 \rightarrow Fe, TiO_2, Fe_xTi, FeTiO_3, CaTiO_3 \rightarrow Fe, Ti, Fe_xTi \rightarrow Fe_xTi$.
Route ii: $Fe_2TiO_5 \rightarrow Fe, TiO_2 \rightarrow Fe, Ti, CaTiO_3 \rightarrow Fe, Ti \rightarrow Fe_xTi$.
Route iii: $Fe_2TiO_5 \rightarrow Fe, FeTiO_3 \rightarrow Fe, TiO_2, Fe_xTi, CaTiO_3 \rightarrow Fe, Ti, Fe_xTi \rightarrow Fe_xTi$.
Route iv: $Fe_xTiO_y \rightarrow Fe_xTi$.

It should be noted that the four reaction routes occur simultaneously during electro-deoxidation due to the theoretical decomposition voltages of these relevant reactions are lower than 3.8 V. It is suggested that the three routes, i.e. $Fe_2TiO_5 \rightarrow Fe_2TiO_4 \rightarrow Fe, TiO_2/CaTiO_3 \rightarrow Fe, Ti \rightarrow Fe_xTi$; $Fe_2TiO_5 \rightarrow Fe, TiO_2/CaTiO_3 \rightarrow Fe, Ti \rightarrow Fe_xTi$; and $Fe_2TiO_5 \rightarrow Fe, FeTiO_3 \rightarrow Fe, TiO_2/CaTiO_3 \rightarrow Fe, Ti \rightarrow Fe_xTi$ are the dominate routes coexist in the electro-deoxidaton process (as shown in Fig. 4).

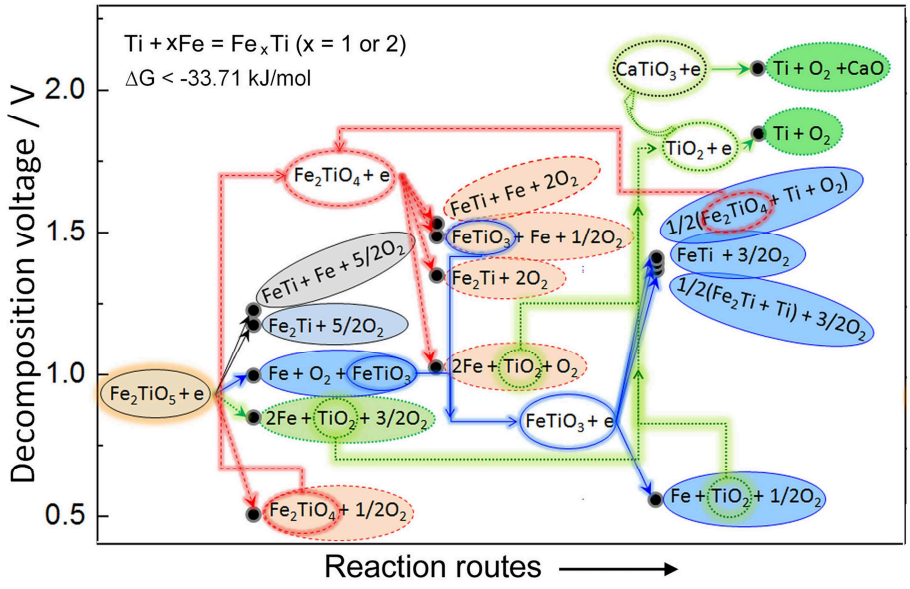



Fig. 4. Reaction routes for the electro-deoxidation of natural ilmenite in molten $CaCl_2$, the black spots labeled in the figure show the decomposition voltages of these reactions.

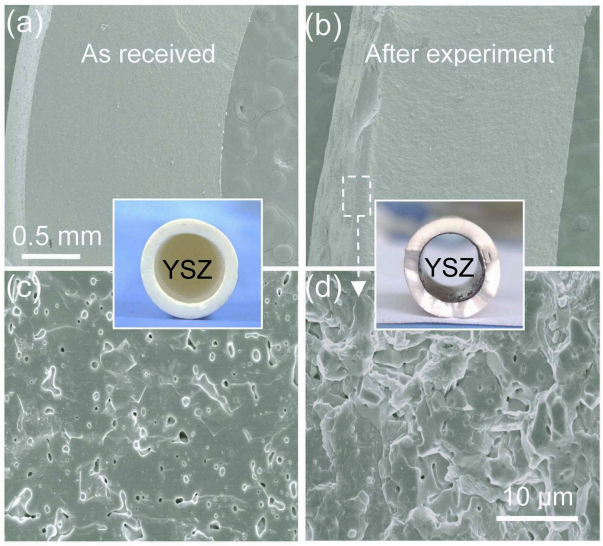



Fig. 5. SEM images of the SOM before experiment (a) (c) and after experiment (b) (d), the insets are the photos of the YSZ tubes before experiment and after experiment, respectively.

## Stability of the SOM

The SEM images of the SOM before experiment and after experiment are shown in Fig. 5, and the insets are the photos of the cross-section of the YSZ tubes. It shows that the electro-deoxidation experiment process has a slight influence on the outer surface (molten salt/YSZ) of the YSZ tube. In contrast, the inner surface (YSZ/carbon-saturated liquid metal) is not influenced by the experiment. The micro-structure of the outer surface changes slightly during electrolysis which may attribute to the corrosion of molten $CaCl_2$. However, the strength of the SOM tube still keeps good during the whole electro-deoxidation process. It should be noted that the stability of the membrane depends on the molten salt system, temperature and applied voltage, the details have been discussed in an earlier study [5]. In this experiment, the YSZ tube manufactured in our laboratory has considerable and sufficient stability for the SOM electro-deoxidation process.

## Conclusions

The reaction mechanism involved in the electro-deoxidation of natural ilmenite in molten $CaCl_2$ has been proposed based on our experimental data and thermodynamic analysis. It is suggested that the complex multistep reaction routes including $Fe_2TiO_5 \rightarrow Fe_2TiO_4 \rightarrow Fe$, $TiO_2/CaTiO_3 \rightarrow Fe$, $Ti \rightarrow Fe_xTi$; $Fe_2TiO_5 \rightarrow Fe$, $TiO_2/CaTiO_3 \rightarrow Fe$, $Ti \rightarrow Fe_xTi$; $Fe_2TiO_5 \rightarrow Fe$, $FeTiO_3 \rightarrow Fe$, $TiO_2/CaTiO_3 \rightarrow Fe$, $Ti \rightarrow Fe_xTi$; and $Fe_xTiO_y \rightarrow Fe_xTi$ coexist in the electro-deoxidation process. The morphology and phase composition of the obtained $Fe_xTi$ alloys were investigated. The results show that $Fe_xTi$ alloys powder can be produced directly from natural ilmenite by the SOM electro-deoxidation process in molten salt.

## Acknowledgements

This research was financially supported by the National Natural Science Foundation of China (Nos. 51304132; 51225401), China Postdoctoral (Special) Science Foundation (Nos. 2012M520873; 2013T60436), the Foundation of State Key Laboratory of Advanced Metallurgy (No. KF12-05) and the Science and Technology Commission of Sichuan Province (No. 2013GZ0146).

**References**

[1] C.S. Kucukkaragoz and R.H. Eric: Miner. Eng. Vol. 19 (2006), p. 334

[2] G.Z. Chen, D.J. Fray and T.W. Farthing: Nature Vol. 407 (2000), p. 361

[3] A.M. Abdelkader, K. Tripuraneni Kilby, A. Cox and D.J. Fray: Chem. Rev. Vol. 113 (2013), p. 2863

[4] U.B. Pal, D.E. Woolley and G.B. Kenney: JOM Vol. 53 (2001), p. 32

[5] A. Krishnan, X.G. Lu and U.B. Pal: Metall. Mater. Trans. B Vol. 36 (2005), p. 463

[6] X.G. Lu, X.L. Zou, C.H. Li, Q.D. Zhong, W.Z. Ding and Z.F. Zhou: Metall. Mater. Trans. B Vol. 43 (2012), p. 503

[7] X.L. Zou, X.G. Lu, Z.F. Zhou, C.H. Li and W.Z. Ding: Electrochim. Acta Vol. 56 (2011), p. 8430

[8] X.L. Zou, X.G. Lu and W.Z. Ding: Rare Met. Mater. Eng. Vol. 40 (2011), p. 169 (in Chinese)

[9] R.O. Suzuki: J. Phys. Chem. Solids Vol. 66 (2005), p. 461

[10] K. Ono and R.O. Suzuki: JOM Vol. 54 (2002), p. 59

[11] M. Ma, D.H. Wang, W.G. Wang, X.H. Hu, X.B. Jin and G.Z. Chen: J. Alloys Compd. Vol. 420 (2006), p. 37

[12] M. Panigrahi, E. Shibata, A. Iizuka and T. Nakamura: Electrochim. Acta Vol. 93 (2013), p.143

[13] X.Y. Yan and D.J. Fray: Adv. Funct. Mater. Vol. 15 (2005), p. 1757

[14] W. Xiao, X.B. Jin, Y. Deng, D.H. Wang, X.H. Hu and G.Z. Chen: ChemPhysChem Vol. 7 (2006), p. 1750

[15] Y. Deng, D.H. Wang, W. Xiao, X.B. Jin, X.H. Hu and G.Z. Chen: J. Phys. Chem. B Vol. 109 (2005), p. 14043

[16] S. Tan, T. Örs, M.K. Aydınol, T. Öztürk and İ. Karakaya: J. Alloys Compd. Vol. 475 (2009), p. 368

[17] G.M. Li, X.B. Jin, D.H. Wang and G.Z. Chen: J. Alloys Compd. Vol. 482 (2009), p. 320

*Advanced Materials Research Vol. 937 (2014) pp 64-69*
*© (2014) Trans Tech Publications, Switzerland*
*doi:10.4028/www.scientific.net/AMR.937.64*

# A Study on Relationship between Orientation Evolution and Coarsening Behavior of $Cu_6Sn_5$ Grains formed on Polycrystalline Cu Substrate

Ming YANG [1,a], Xin MA [2,b,] and Ming-yu LI [1,c*]

[1]Shenzhen Key Laboratory of Advanced Materials, Shenzhen Graduate School, Harbin Institute of Technology, Shenzhen 518055, People's Republic of China

[2]Yik Shing Tat Industrial Co., Ltd., Shenzhen 518101, People's Republic of China

[a]yangming@hitsz.edu.cn, [b]maxin@yikst.com, [c]myli@hit.edu.cn

*Corresponding author

**Keywords:** Crystal orientation, Coarsening, Interfacial Reaction, Polycrystalline Cu

**Abstract** The coarsening behavior of $Cu_6Sn_5$ grains formed at the Sn37Pb/Polycrystalline Cu interface is investigated in terms of their orientation evolution during solid-state aging. The results show that the coarsening behavior of the interfacial $Cu_6Sn_5$ grains during solid-state aging are quite different from that during liquid-state soldering. The occurrence of the coarsening in the solid-sate reaction is caused by the different surface energies between two adjacent grains. In addition, the texture morphologies of the interfacial grains affect their coarsening rates. In particular, the interfacial $Cu_6Sn_5$ grains formed at 200 ºC exhibit a texture with the [0001] direction normal to the interface after 16 days of aging at 150 ºC, and the formation of this texture accelerates the coarsening process of the interfacial $Cu_6Sn_5$ grains.

## Introduction

Due to the environmental and health concerns, the European Union enacted legislation that bans the use of lead (Pb) and several other substances in electronic products commencing July 1, 2006. However, it is well recognized in certain electronic products, specifically servers, storage and storage array systems, network infrastructure equipment and network management for telecommunication equipment referred to as high-performance electronic products, where perform tasks so important to modern society that their operational integrity had to be maintained, the introduction of new and unproven materials would pose a significant potential reliability risk [1-3]. Accordingly, the European Commission (EC) granted an exemption permitting the continued use of Pb in solders, independent of concentration, for high-performance equipment applications [1, 2]. In such applications, the SnPb solders usually react with Cu to form two interposing layers of Cu-Sn intermetallic compounds (IMCs), e.g., $Cu_3Sn$ and $Cu_6Sn_5$ at the interface [1-4]. These layers tend to grow with time by solid state diffusion even at ambient temperatures. Due to the excessive growth during storage and service, these IMC layers may adversely affect the reliability of solder joints. They can be sources of mechanical weakness in solder joints due to the brittle nature of the IMCs. Therefore, an understanding of the growth behaviors of IMCs formed at the SnPb/Cu interface during solid-state aging is necessary. In addition, because SnPb solders have been used on Cu over several decades and many studies have been done on the ternary system of Sn-Pb-Cu, it is helpful to figure out the solder reactions of SnPb on Cu as the background references for Pb-free solders [2-4].

To date, numerous studies of the solid-state IMC growth have been reported [5-10]. However, an important issue, i.e., the coarsening mechanism, has not been attracted much attention. The trend toward the miniaturization of electronic products leads to the need for a shrinkage of joint size, resulting in a high volume fraction of $Cu_6Sn_5$ intermetallic compounds (IMCs) generated at the Sn-based solders/Cu interface. Due to the coarsening phenomenon, only several $Cu_6Sn_5$ grains exist in such small joint after solid-state aging. Such the few-grain IMC joints would have a potential threat on the joint thermal and electronic reliability because of the anisotropy of electronic mobilities and atomic diffusivities along various crystal orientations. Therefore, understanding the coarsening behaviors of interfacial $Cu_6Sn_5$ grains are necessary.

In addition, recently, some studies found that the interfacial IMC exhibit a textured growth during solid-state aging [10]. The electronic mobilities and atomic diffusivities are different along various crystal orientations. As a result, this textured growth may have an influence on the interfacial IMC's coarsening behavior. The aim of this study is, therefore, to investigate the relationship between crystal orientation and coarsening behavior of $Cu_6Sn_5$ grains formed at the Sn37Pb/Cu (polycrystalline Cu unless otherwise specified) interface under solid-state reaction condition.

## Experimental

### Preparation of Samples

For the sample preparation, 150±5 mg of eutectic Sn37Pb beads were placed on polycrystalline Cu foil (5 mm × 5 mm × 0.3 mm) and then reflowed using hot air at peak temperatures of 200 ºC±2 ºC or 280 ºC±2 ºC, respectively, for durations of 2 min. The samples were cooled in water after soldering and then placed in an oven at a constant temperature of 150 ºC and aged for 1 day to 81days. Two samples were prepared to study each parameter: one was mounted in epoxy and polished to reveal the cross-sectional microstructures; the other was immersed in 10 vol.% $HNO_3$ solution with ultrasonic waves to dissolve away the excess solder and expose the IMC film. The IMC grain morphology was studied in top view and then the sample were used for X-ray diffraction (XRD) and electron backscattering diffraction (EBSD) analyses.

### Identification and Thickness Measurement of IMCs

Scanning electron microscopy (SEM), together with energy-dispersive X-ray spectroscopy (EDX), was employed to characterize the IMC microstructure. As presented below, the IMCs formed in the Sn37Pb/Cu system include η-phase ($Cu_6Sn_5$) that grew at the solder side and ε-phase ($Cu_3Sn$) that grew at the Cu side. To study the coarsening behaviors of the interfacial $Cu_6Sn_5$ grains, the top view of the interfacial grains was first recorded by SEM as a function of the reaction time. The mean equivalent spherical radius and size distributions of the interfacial $Cu_6Sn_5$ grains were then determined using the program ImageJ; 500-800 grains were measured for each experimental condition.

### $Cu_6Sn_5$ Growth Orientation Measurement

EBSD analyses were conducted to reveal the interfacial $Cu_6Sn_5$ orientations. To facilitate EBSD characterization, the samples with exposed interfacial $Cu_6Sn_5$ were mounted, and the tips of interfacial $Cu_6Sn_5$ grains were carefully ground and polished to faceted surfaces [11]. Orientation data were collected from the selected area using an SEM equipped with a fully automatic EBSD analysis system; pole figures were then obtained using the program Orientation Imaging Microscopy (OIM). To obtain more statistically reliable orientation distributions, many grains that covered an area of at least 500 μm × 500 μm were analyzed. During the EBSD acquisition, a step size of 0.8~2 μm was chosen.

## Results and Discussion

Figure 1 presents the morpholoies of the interfacial $Cu_6Sn_5$ grains in top view. It can be seen that the interfacial grains become bigger but fewer with prolonged aging time. In addition, compared with the joint formed at 200 and 280 ºC, the coarsening rates of the interfacial grains are different during solid-state aging.

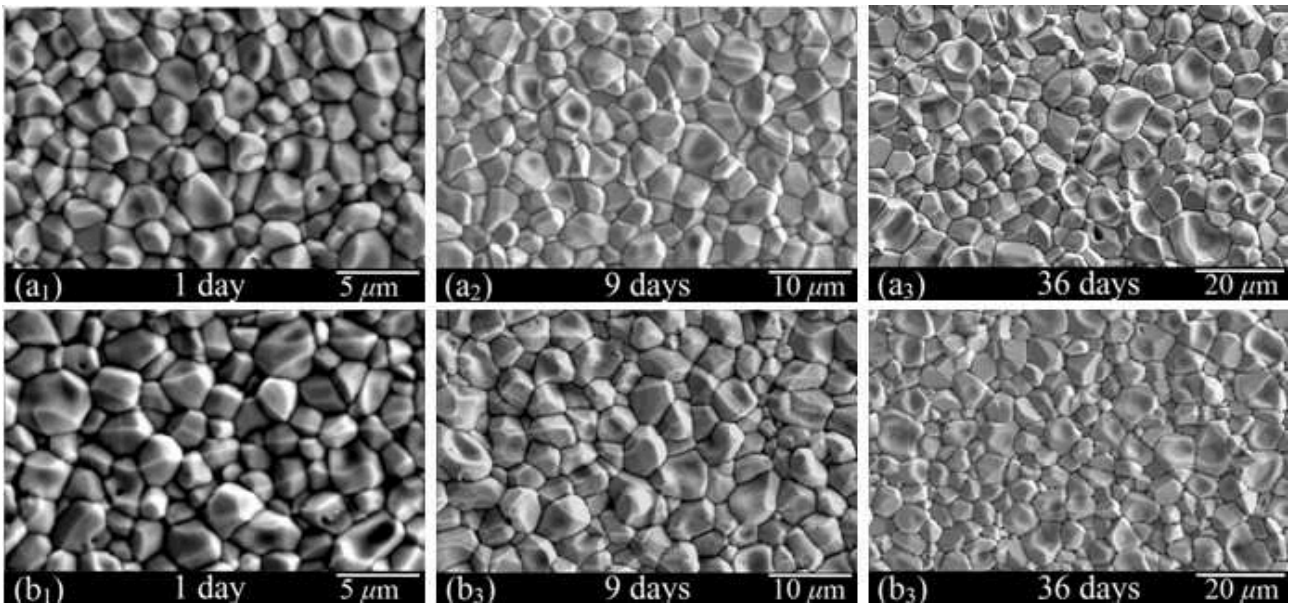



Fig. 1. Representative SEM images showing the morphologies of $Cu_6Sn_5$ formed at the Sn37Pb/Cu interfaces at 150 ºC for different aging times. The initial joints formed at (a) 200 ºC and (b) 280 ºC for 2 min, water-cooling condition.

To clarify the coarsening behavior, the interfacial $Cu_6Sn_5$ grains are analyzed by plotting the mean size versus the storage time on log-log coordinates (Fig. 2). Obviously, the relationship between mean radius of $Cu_6Sn_5$ grains and aging time is exponential:

$$R = Ct^k \tag{2}$$

where $R$ is the mean radius of $Cu_6Sn_5$ grains, C and k are two constants, and t is the aging time. The exponent $k$ listed in Fig. 2 are 0.294 for the samples formed at 200 ºC over all experimental temporal scales, whereas 0.247 for those formed at 280 ºC.

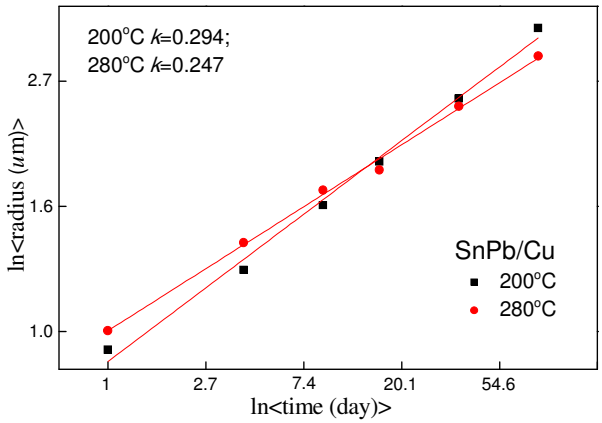



Fig. 2. Plots of $Cu_6Sn_5$ mean radius versus storage times at 150 ºC on log-log coordinates.

Recently, Zou et al.[10] have studied the coarsening behaviors of interfacial $Cu_6Sn_5$ grains under solid-state condition. In their study, the exponent k was calculated as 0.28, close to 1/3, the value predicted by of flux-driven ripening (FDR) theory [12, 13], proposed by Tu et al. to reveal the coarsening mechanisms of the $Cu_6Sn_5$ grains formed at molten solder/solid Cu interface. Therefore, they declared that the coarsening mechanism of $Cu_6Sn_5$ grains has no obvious variation for the Sn-based/Cu under solid-state condition. However, it should be pointed out that, in FDR model, $Cu_6Sn_5$ grains are assumed to be hemispherical, and they grow at the expense of their nearest neighbors. Due to Gibbs-Thomson effect, the Cu concentration near the surface of smaller grains is

higher, and therefore the Cu atoms in the smaller grains are prone to dissolve into molten solder and diffuse to the bigger ones. This Cu flux dominates the coarsening of interfacial $Cu_6Sn_5$ grains during liquid-state soldering. In solid-state aging, however, the hemispherical grains turn to layer-type, and the diffusion path for Cu atoms is very different from that in liquid-state soldering. Therefore, it is not appropriate to recognize the coarsening mechanism of interfacial IMCs under solid-state condition are similar with that under liquid-state condition just because of k close to 1/3. In addition, for the samples formed at 280 ℃, the values of k is only 0.247, greatly deviating from 1/3. This result further implies that the coarsening mechanisms of interfacial $Cu_6Sn_5$ grains in solid- and liquid-state reactions arequite different.

The drivening force for the coarsening of interfacial $Cu_6Sn_5$ during solid-state aging should derive from the difference of energies between the two adjacent surfaces of interfacial grains [14]. The interfacial $Cu_6Sn_5$ grains transform to layered grains with vertical and flat grain boundaries with aging time[3], as shown in Fig. 3. Due to the anisotropy of the $Cu_6Sn_5$ crystal, the energies for side surface of $Cu_6Sn_5$ grains with different orientations are different. To minimize the surface energy, the atoms are prone to diffuse from the grain with higher energy to that with lower energy. Consequently, the interfacial $Cu_6Sn_5$ grains become bigger but fewer with prolonged aging time.

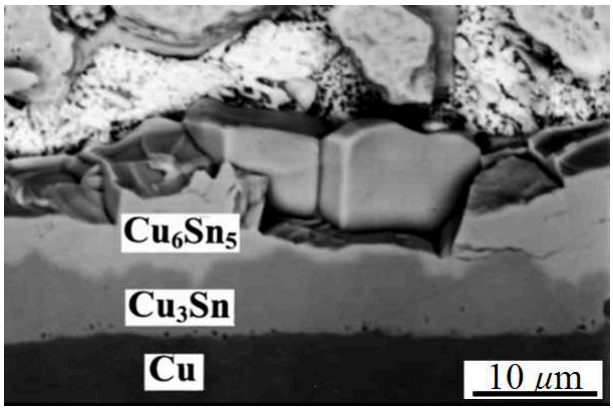



Fig. 3. SEM image of the cross section of a sample of Sn37Pb on Cu aged at170 ℃ for 960hrs[3]

Hillert [15] and Bruke et al. [16] have analyzed the grain coarsening in two-dimensional systems without consideration of the anisotropy of interfacial energy, and remarkably, the growth is expected to follow a 1/2 power law in time, which is higher than our experiment results. One likely reason would be the inhibition of impurity at the grain boundary, in this case that of Pb. In solid Sn37Pb/Cu reaction, Pb will inevitably exist in the grain boundary [8], which may act as second-phase particles to inhibit the migration of grain boundary and therefore induce the reduced coarsening rate.

Another problemic issue is why the coarsening rates in the joints formed at different temperatures are different during solid-state aging. We assume that the difference should derive from the growth orientation of the interfacial $Cu_6Sn_5$ grains in the two sets of the joints. As mentioned above, the driving force for the coarsening derives from the difference surface energies between the two adjacent grains. Different orientations in the interfacial IMC grains would induce a difference in the surface energy due to the crystal anisotropy. To confirm this assumption, we determined the growth orientation of interfacial $Cu_6Sn_5$ grains. Unsurprisingly, the interfacial $Cu_6Sn_5$ grains formed at different temperatures exhibit clear different texture morphologies after 16 days of aging. As shown in Fig. 4 the $\theta$ for near 80% of the interfacial grains formed at 200℃ falls within 30° after 81 days of aging, and that for about 70% of the interfacial grains formed at 280 ℃ falls anywhere between 25° and 45°. These results show that the texture morphologies of the interfacial $Cu_6Sn_5$ grains have a great influence on their coarsening behaviours.

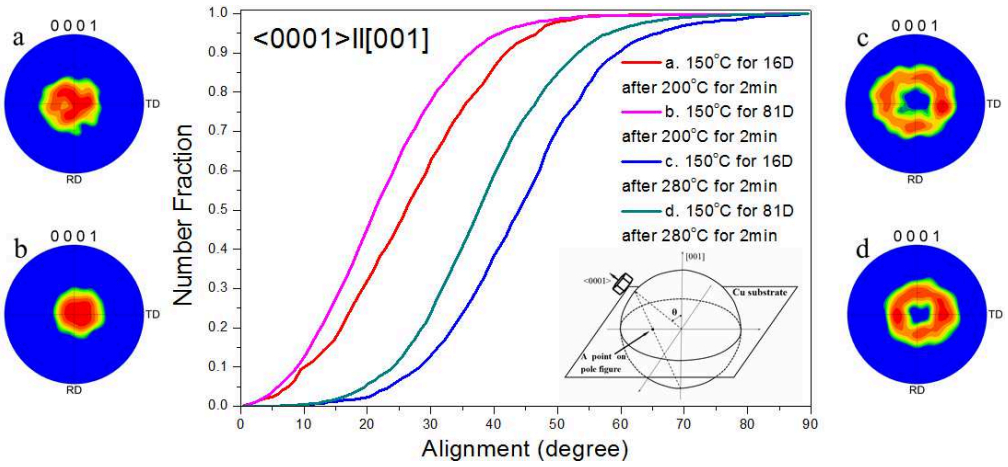



Fig. 4. Pole figures and misorientation of $Cu_6Sn_5$ layer with polycrystalline Cu substrate toward [001] direction.

## Summary

In this study, the coarsening behavior of $Cu_6Sn_5$ grains formed at the Sn37Pb/ Polycrystalline Cu interface is investigated. The results show that the coarsening behavior of the interfacial $Cu_6Sn_5$ grains during solid-state aging are quite different from that during liquid-state soldering. The occurrence of the coarsening in the solid-sate reaction is caused by the different surface energies between two adjacent grains. In addition, the coarsening rates are affected by the texture morphologies of the interfacial grains. In particular, the interfacial $Cu_6Sn_5$ grains formed at 200 ºC exhibit a texture with the [0001] direction normal to the interface after 16 days of aging at 150 ºC, and the formation of this texture accelerates the coarsening process of the interfacial $Cu_6Sn_5$ grains.

## Acknowledgement

This work was supported by National Nature Science Foundation of China under Grant No. 51175116, and Shenzhen Special Funds for Development of Strategic Emerging Industries (No. CXZZ20120829103358067).

## References

[1] K.J. Puttlitz, G.T. Galyon, Impact of the ROHS Directive on High-Performance Electronic Systems , J. Electron. Mater. 18 (2007) 331-346.

[2] K.N. Tu, Solder Joint Technology Materials, Properties and Reliability, seconded., Springer, New York, 2007.

[3] K.N. Tu, K. Zheng, Six Cases of Reliability Study of Pb-free Solder Joints in Electronic Packaging Technology, Mater. Sci. Eng. R. 34 (2001) 1-58.

[4] T. Tian, K. Chen, A.A. Macdowell, D. Parkinson, Y.S. Lai, K.N. Tu. Quantitative X-ray microtomography study of 3-D void growth induced by electromigration in eutectic SnPb flip-chip solder joints, Scripta Mater. 65 (2011) 646-649.

[5] K.N. Tu, T.Y. Lee, J.W. Jang, L. Li, D.R. Frear, K. Zeng, Wetting reaction versus solid state aging of eutectic SnPb on Cu, J. Appl. Phy. 89 (2001) 4843-4849.

[6] T.Y. Lee, W.J. Choi, K.N. Tu, J.W. Jang, S.M. Kuo, Morphology, Kinetics, and Thermodynamics of Solid-State Aging of Eutectic SnPb and Pb-Free Solders (Sn-3.5Ag, Sn-3.8Ag-0.7Cu and Sn-0.7Cu) on Cu, J. Mater. Res. 17 (2002) 291-301.

[7] D. Yao, J.K. Shang, Effect of aging on fatigue crack growth at Sn-Pb/Cu interfaces, Metal. Mater. Metal. Trans. A 26 (1995) 2677-2685.

[8] J.W. Yoon, J.H. Lim, H.J. Lee, J. Joo, S.B. Jung, Interfacial Reactions and Joint Strength of Sn-37Pb and Sn-3.5Ag Solders with Immersion Ag-plated Cu Substrate during Aging at 150ºC, J. Mater. Res. 21 (2006) 3196-3204.

[9] M. Yang, M. Li, L. Wang, Growth behavior of Cu6Sn5 grains formed at an Sn3.5Ag/Cu interface, Mater. Lett. 65 (2011) 1506-1509.

[10] H.F. Zou, H.J. Yang, Z.F. Zhang, A Study on the Orientation Relationship Between the Scallop-Type $Cu_6Sn_5$ Grains and (011) Cu Substrate Using Electron Backscattered Diffraction. Journal of Applied Physics, 106 (2009) 113512.

[11] M. Yang, M. Li, C.Q. Wang, Interfacial reactions of eutectic Sn3.5Ag and pure tin solders with Cu substrates during liquid-state soldering, Intermetallics 25 (2012) 86-94.

[12] J.O. Suh, K.N. Tu, G.V. Lutsenko, A.M. Gusak, Size distribution and morphology of $Cu_6Sn_5$ scallops in wetting reaction between molten solder and copper, Acta Mater. 56 (2008) 1075-1083.

[13] A.M. Gusak, K.N. Tu, Kinetic Theory of Flux-Driven Ripening, Phys. Rev. B 66 (2002) 115403.

[14] D. Feng, (1990) Metal physics (Volume 2) The phase transition, firsted. Science Press, Beijing, 1990.

[15] M. Hillert, On the Theory of Normal and Abnormal Grain Growth, Acta Metall. 13 (1965) 227-238.

[16] J.E. Bruke, D. Turnbull, Recrystallization and grain growth, Progr. Met. Phys. 3 (1952) 220-292.

*Advanced Materials Research Vol. 937 (2014) pp 70-73*
*© (2014) Trans Tech Publications, Switzerland*
*doi:10.4028/www.scientific.net/AMR.937.70*

# Glass-ceramics Obtained from Sewage Sludge and its Characteristics Affected by Alkalinity

Di WU[1,a], Yu TIAN[2,b,*], Xing-wang WEN[3,c] and Hui-ling LIU[4,d]

[1] School of Municipal and Environmental Engineering, Harbin Institute of Technology, Harbin, 150090, China

[2] State Key Laboratory of Urban Water Resource and Environment, Harbin Institute of Technology (SKLUWRE, HIT), Harbin 150090, China; School of Municipal and Environmental Engineering, Harbin Institute of Technology, Harbin, 150090, China

[3] FAW Jiefang Automotive Company Ltd., Changchun 130400, China

[4]School of Municipal and Environmental Engineering, Harbin Institute of Technology, Harbin, 150090, China

[a]angel523116@126.com, [b]hittianyu@163.com, [c]wen-sevenyy@163.com, [d]hlliu2002@163.com

**Keywords:** Glass-ceramics, Sewage sludge, Alkalinity.

**Abstract.** Sewage sludge was tested as component for producing glass-ceramics with the addition of analytic reagent CaO to solve the sewage sludge disposal problems. The effect of alkalinity (Ak=mCaO/m$SiO_2$) on the characteristics of the glass-ceramics was investigated. Differential scanning calorimetry (DSC) and X-ray diffraction (XRD) were used to investigate thermal behavior and crystalline phase of the samples. It was found that the degree and characteristics of crystals in vitrified sludge significantly correlate to the alkalinity of the raw materials. The glass-ceramics with Ak = 0.36 possessed the best physical and chemical properties.

## Introduction

The production of sewage sludge from domestic and industrial waste water treatment plants is in constant increase. The severe impact on human health and the environment drives us to find methods that enable its reduction or convert it into more environmental friendly products. Considering the great amount of $SiO_2$, $Al_2O_3$ and CaO in the sewage sludge, it can be a good candidate as a raw material source for the glass-ceramics production [1-3]. The production of glass-ceramic seems to be a promising method due to the immobilization and stabilization of hazards materials, volume reduction [4-6]. In addition, the formed novel materials possessing attractive mechanical and chemical properties can be utilized extensively in the building industry[7].

Sewage sludge glass-ceramics not only realized the resource utilization of sewage sludge, but also implemented the high added value in the process. It is generally believed that the characteristics of crystalline phase were affected by the alkalinity of the raw sludge. In this work, glass-ceramics were prepared from water treatment sludge with added CaO and the present research focused on: (1) investigating the effect of alkalinity on the thermal behavior of the sewage sludge glass-ceramics; (2) investigating the effect of alkalinity on the crystalline phases; (3) investigating the effect of alkalinity on the properties of the glass-ceramics.

## Materials and Methods

Sewage sludge used in experiments was collected from urban wastewater treatment plants in Harbin, China. The sewage sludge was treated by air-dry method and was ground at sizes below 100 mm that are sufficiently fine to be mixed homogeneously. Components of sewage sludge examined by X-ray fluorescence spectroscopy (XRF) were shown in table 1.

Three batches of experimental samples were prepared by mixing sewage sludge with analytic reagent CaO(Table2). Parent glasses were prepared by melting the well-mixed powder in an alumina crucible at 1500 ℃ for 2 h after which melts were preheated at 600 ℃ to reduce thermal shock.

Table 1. The major chemical composition of sewage sludge

| Composition | $SiO_2$ | $Al_2O_3$ | CaO | MgO | $Fe_2O_3$ | Others |
|---|---|---|---|---|---|---|
| (%) | 47.62 | 18.34 | 7.91 | 2.50 | 8.29 | 15.34 |

Table 2. Ratios of CaO/ $SiO_2$ in the Mixtures (wt.%)

| Samples | CaO | sewage sludge | Alkalinity |
|---|---|---|---|
| S1 | 8.1 | 91.9 | 0.18 |
| S2 | 14.6 | 85.4 | 0.36 |
| S3 | 20.5 | 79.5 | 0.54 |

DSC (STA449C, NETZSCH) was used to investigate the thermal behavior of the parent glass samples, including the glass transition temperatures ($T_g$) and the crystallization peak temperatures ($T_c$). The experiments were performed in Ar atmosphere by heating 25mg glass powder in an $Al_2O_3$-crucible and using α-$Al_2O_3$ as the reference material in the temperature range between 20 and 1500 ℃ at a heating rate of 10 ℃/min. The heat-treatment was determined according to the results of DSC.

The amount and type of crystalline phases existed in a sample after heat treatment was determined by X-ray radiation (XRD: Plmax-γβ, Rigaku, Japan). XRD measurements were carried out by a rotating anode X-ray diffraction apparatus using Cu Kα radiations generated at 40 kV and 50 mA at 5°/min scanning speed with scanning angle for 10 ~ 90° and a step size of 0.02°.

The morphology of the crystalline phases was investigated using a scanning electron microscope (SEM, S-4700, HITACHI). For SEM investigations, specimens were etched with HF solution (5 vol.%) after grinding and polishing for 1.5 min, immediately rinsed with excess distilled water and then cleaned in ethanol for 2 min. The samples were coated with gold prior to examination.

Density was measured by the Archimedes' method using water as a medium. Hardness was measured by an indentation method using the Vickers indenter. Vickers hardness was measured with loads of 100-1000g with loading times of 10 s. Bending strength was obtained from a four-point method with spans of 20 and 40 mm at a cross-head speed of 100 μm/min. The chemical durability of glass-ceramics samples were tested as flowing: twenty grams of the powder were immersed into 100 ml of 10% $H_2SO_4$ and 10% NaOH solutions and boiled at 373K for 2 h. The resistance was estimated by measuring the weight loss of dehydrated powders.

## Results and Discussion

### Thermal Analysis

The glass transition temperature(Tg) and crystallization temperature(Tn) were determined by DSC. The results were shown in table 3, vitrification processes occurred around at $Tg_1$ = 788 ℃, $Tg_2$ = 774 ℃ and $Tg_3$ = 762 ℃, respectively. Crystallization temperatures of three parent glass samples were respectively identified as $Tc_1$ = 990 ℃, $Tc_2$ = 978 ℃ and $Tc_3$=965℃. Results showed that the glass transition and crystallization temperatures all decreased with the increase of alkalinity, because the alkali metal oxides CaO led to lower energy input in crystalline phase transition.

Tn was an important factor on nucleus formation. Previous studies showed that the optimum nucleation temperature usually occurred in the range from 50 ℃ to 100 ℃ above Tg [8]. Because higher temperature was helpful for fast particle migration, in our study, the nucleation temperatures of S1, S2 and S3 samples were identified as $Tn_1$=838 ℃, $Tn_2$=820 ℃ and $Tn_3$= 812℃, respectively.

Table 3. The results of DSC for sewage sludge glass

| Samples | Tg(ºC) | Tc(ºC) | Alkalinity |
|---|---|---|---|
| S1 | 788 | 990 | 0.18 |
| S2 | 770 | 978 | 0.36 |
| S3 | 762 | 965 | 0.54 |

**Effect of Alkalinity on the Crystalline Phases**

To identify the crystalline characteristics in the glass-ceramics with different alkalinity, X-ray diffraction analysis(XRD)was carried out and the results were shown in Fig.1.

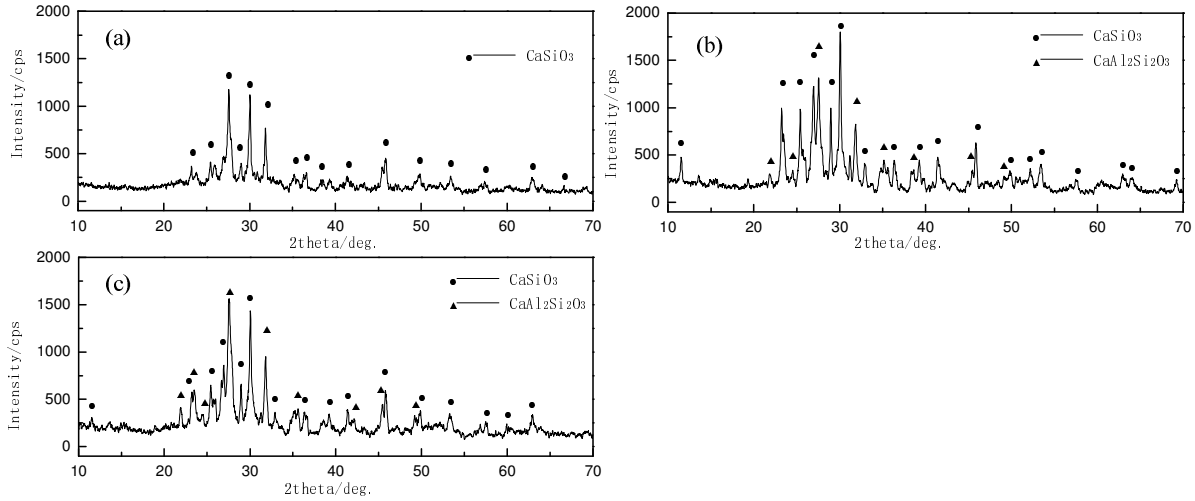



Fig.1. XRD patterns of produced glass-ceramics samples with different alkalinity ($Ak_a$=0.18, $Ak_b$=0.36, $Ak_c$=0.54 )

When the glass batch was in low alkalinity (0.18), the prepared sample was predominantly composed of residual glassy phase with a little wollastonite, the result implied that only a few glassy amorphous articles were converted into crystals. As the alkalinity increased from 0.18 to 0.36, the peak intensity of glass-ceramics increased obviously and the major crystalline phase was wollastonite and anorthite, indicating that the increased alkalinity promoted the transformation of glassy amorphous articles into crystalline ones. While when the alkalinity increased to 0.54, the peak intensity decreased, the major crystalline phase was still wollastonite and anorthite. From the results, it would be concluded that the species and quantities of crystalline phases in glass-ceramics strongly depended on the alkalinity of the original specimen. When the alkalinity of the raw materials was lower (0.18 in this study), the higher content of [$SiO_4$] units formed by $SiO_2$ made the transformation to crystalline state much difficult. With the increase of alkalinity, CaO unite $SiO_2$ to form more wollastonite , and the structure unit [$AlO_4$]Ca[$AlO_4$] was forced to rearrange and unite [$SiO_4$] to form anorthite during crystallization. While with the alkalinity increased to 0.54, the superfluous hindered the formation of crystals.

**Effect of Alkalinity on the Properties of Sewage Sludge Glass-ceramics**

Various properties of the glass-ceramics with different alkalinity were summarized in Table 4. Density of S2 was higher than that of the other two samples. The bending strength of S2 (76MPa) was the highest compared with S1(70MPa) and S3(72MPa). The Vickers hardness of S2 was5.32 GPa, which was the highest of all. It was the most crystalline phases conduced S2 to possess the best physical properties.

Chemical durability of glass-ceramics is of importance in terms of potential application of the product and environmental aspect. It could be seen that all samples showed acceptable chemical resistance behavior. Furthermore, the glass-ceramics samples in the present study showed good

stability in NaOH solution. The relatively higher weight losses in the HCl durability tests might be due to that the glassy matrix was more easily leached in the acidic solutions.

Table 4. Physical and chemical properties of produced glass-ceramics samples with different alkalinity

| Property | S1 | S2 | S3 |
|---|---|---|---|
| Density(g/cm3) | 2.38 | 2.67 | 2.47 |
| Bending strengths (MPa) | 70.0 | 76.0 | 72.0 |
| Vickers hardness (GPa) | 5.14 | 5.32 | 5.28 |
| Acid weight loss (%) | 0.067 | 0.039 | 0.045 |
| Alkali weight loss (%) | 0.0010 | 0.00076 | 0.0008 |

## Conclusions

1. Tg and Tn were all decreased with the increase of alkalinity because the alkali metal oxides CaO led to lower energy input in crystalline phase transition.
2. The type and degree of crystalline phases was affected by the alkalinity. The degree of crystalline phases increased with the increase of alkalinity within a certain range (from 0.18 to 0.36), while the higher alkalinity will hinder the formation of crystals.
3. The produced glass-ceramics possessed excellent properties, which were more related to the amount and type of generated crystalline phases.

## Acknowledgement

This study was supported by the Major Science and Technology Program for Water Pollution Control and Management (No. 2013ZX07201007), the State Key Laboratory of Urban Water Resource and Environment, Harbin Institute of Technology (No. 2011DX01) and the Specialized Research Fund for the Doctoral Program of Higher Education (No. 20112302110060). The authors also appreciate the Funds for Creative Research Groups of China (No. 51121062).

## References

[1] E. Bernardo, R. Dal Maschio, Glass–ceramics from vitrified sewage sludge pyrolysis residues and recycled glasses, Waste Management 31 (11) (2011) 2245-2252.

[2] M. Erol, S. Küçükbayrak, A. Ersoy-Meriçboyu, Production of glass-ceramics obtained from industrial wastes by means of controlled nucleation and crystallization, Chemical engineering journal 132 (1) (2007) 335-343.

[3] Y.J. Park, S.O. Moon, J. Heo, Crystalline phase control of glass ceramics obtained from sewage sludge fly ash, Ceramics international 29 (2) (2003) 223-227.

[4] T. Cheng, Effect of additional materials on the properties of glass-ceramic produced from incinerator fly ashes, Chemosphere 56 (2) (2004) 127-131.

[5] E.G. Pan, A.A. Ravaev, Microwave synthesis of advanced dental ceramic–alloy materials, Materials Letters 58 (21) (2004) 2679-2683.

[6] M. Garcia-Valles, G. Avila, S. Martinez, R. Terradas, J. Nogués, Heavy metal-rich wastes sequester in mineral phases through a glass–ceramic process, Chemosphere 68 (10) (2007) 1946-1953.

[7] T. Toya, A. Nakamura, Y. Kameshima, A. Nakajima, K. Okada, Glass-ceramics prepared from sludge generated by a water purification plant, Ceramics international 33 (4) (2007) 573-577.

[8] F. Peng, K.-m. Liang, A.-m. Hu, Nano-crystal glass–ceramics obtained from high alumina coal fly ash, Fuel 84 (4) (2005) 341-346.

*Advanced Materials Research Vol. 937 (2014) pp 74-79*
*© (2014) Trans Tech Publications, Switzerland*
*doi:10.4028/www.scientific.net/AMR.937.74*

# Experimental Study of Urea Depositions in Urea-SCR System

Shu-zhan BAI [,2,a], Shuai-guo LANG[1,2,b], Ke-ping YUAN [,c], Yang LIU [,2,d], Guo-xiang LI [1,f*]

[1]School of Energy and Power Engineering, Shandong University, Jinan 250061, China;

[2]Weifu Lida Catalytic Converters Co., Ltd., Wuxi 214177, China

[a]peter.baishzh@gmail.com, [b]shuaiguo.lang@wfld.com.cn, [c]keping.yuan@wfld.com.cn, [d]yang.liu@wfld.com.cn, [e]renlin.wen@wfld.com.cn, [f]liguox_baishzh@163.com

**Key word:** Urea depositions; Urea-SCR system; Structural optimization

**Abstract:** Avoiding the urea deposition in the exhaust stream is one of the basic requirements for SCR system normal application. Unreasonable structure design, machining and installation position all could lead to urea crystallization on the wall of exhaust pipe and the front end surface of the catalyst, in addition, unreasonable control strategy also could deteriorate this phenomenon. The components of the urea depositions are the urea and cyanuric acid analyzed by thermogravimetry - FTIR technology. The integrated injector mounting is designed to alleviate the urea crystallization based on analysis results. The engine test and the vehicle road test are all shown that the optimal structural design and calibration strategies could avoid crystallization and sedimentation effectively in the exhaust system.

## Introduction

Urea-SCR technology is one of the effective methods for diesel engines to meet Europe Ⅳand Europe Ⅴ emission standards [1,2]. It can reduce the emission of NOx and effectively decrease the fuel consumption using 32.5% urea solution and matching with the optimal combustion. However, one problem that threatens the life and performance of the urea SCR system is urea deposits. The atomization, breakup and evaporation of the urea droplets are all included in the SCR system. The atomization and the temperature after the urea's injection vary with the work condition of the diesel engine, the Urea droplets decompose into the ammonia, at the same time, they produce intermediate products(byproducts), such as cyanic acid, biuret, cyanuric acid, which cause the urea crystallization and deposition[3]. Gao Junhua[4] and Lifeng Xu[5] analyzed the urea sediments using gas phase chromatography mass spectrum linking, infrared spectrum, nuclear magnetic resonance. Guanyu Zheng[6] illustrated the influence of the SCR system layouts, the different exhaust pipe wall temperatures and the multiple urea mixers on the urea deposits by engine dyno test. In addition, Gabriel Salanta[7] published a study on the effect of entirely urea SCR system layout to urea-related deposits by CFD analysis and test.

The phenomenon of urea depositions of SCR system is studied in this paper, and provides improvement measures based on the analysis of the formation conditions for the urea crystallization. This study not only analyzes the urea crystallization, edimentation phenomenon and constituents, but also explores proprietary methods to decrease the urea sediments the SCR system.

## The Urea Sedimentation and Crystallization

Urea depositions were found in several locations of downstream: between the nozzle and the injector connection boss, the injection housing, the inner surface of the exhaust pipe, and the surface of the catalyst.

### Urea Sedimentation and Crystallization on the Nozzle

The urea sedimentation and crystallization on the nozzle was shown in Figure 1. The deposition located near the hole of the injector mounting base, the injection housing was blocked eventually.



(a) Injector boss (b) Injection housing

Fig. 1. Urea deposition on injection housing after test

**Urea Deposition and Crystallization under the Injector Mounting Base**

Figure 2 shows the urea crystallization phenomenon under the injector mounting base, the white sediments gathered at the injector mounting base. The urea deposits have been crystallized because the sediments can't be eliminated by heating. The main reasons are the unreasonable arrangement of the urea injector mounting base at the exhaust pipe and the long connecting sleeve.

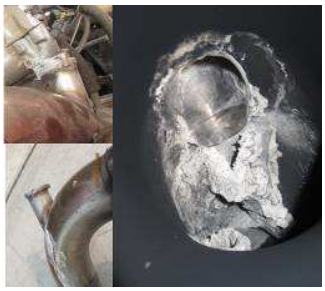


Fig. 2. Urea depositions under the injector mounting base



Fig. 3. Urea depositions on exhaust pipe

**Urea Sedimentation and Crystallization in the Exhaust pipes**

The urea crystallization in the exhaust pipes is given in Fig. 3. The deviation of the fixing angle for the injector mounting base in the exhaust pipe makes it easier to inject the urea on the wall of the exhaust pipe. In the real exhaust system, because the exhaust temperature is relatively low under certain load, and the diameter of the exhaust pipe is smaller, when the droplets splashed onto the wall, the liquid film will form and the crystallization and sedimentation will deposit. The evaporation of the liquid film will decrease the temperature of the pipe wall, which increases the formation of the crystal.

**Components Analysis of the Urea Crystallization and Sedimentation**

The constituents of the urea crystallization were analyzed by means of the TGA-FIIR technology.

**Thermo Gravimetric Analysis**

The thermo gravimetric analysis of the sampled urea deposition and pure urea were compared in this study. The rising rate of the temperature is 10°C/min. The comparison of the urea deposition at different position and the thermo gravimetric analysis of the pure urea are shown in Figure 4, about 90% depositions have been decomposed when the temperature rises to 410°C. The thermolysis results show that the components of the urea are the same at the nozzle position and the injector mounting base. The quality of the urea deposition begin to decrease at 190°C gradually, and the quality continued reduce quickly until to 350°C. And the quality drops to 10% of the original quality at 420°C, 5% at 500°C and 1.5% at 700°C, after which it remains the same.

The thermolysis proves that the urea deposition inside the exhaust pipe is similar to the pure urea, so the components at this position are similar with urea.

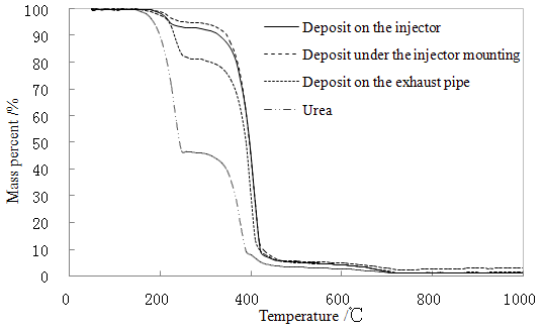
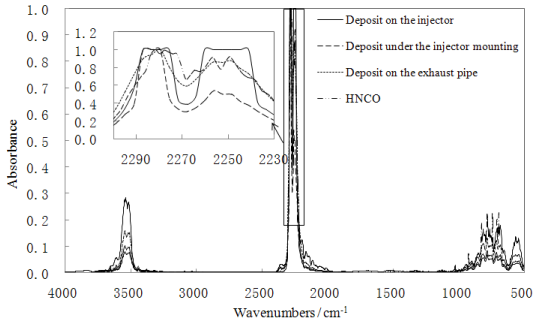


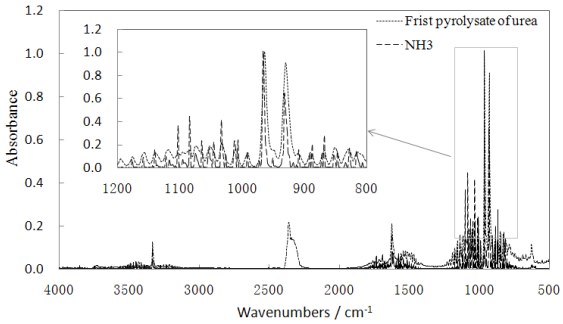

Fig. 4. Comparison of the thermolysis process among the urea depositions and pure urea

**Infrared Spectruman Analysis of the Thermolysis Decompositions**

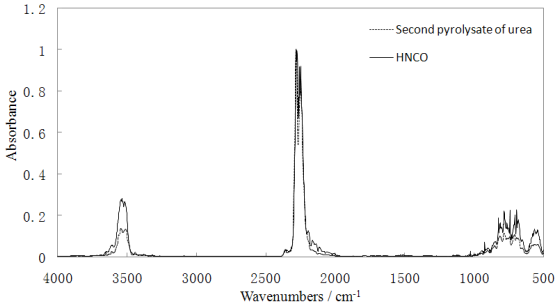
Thermal decomposition products of sample crystallization were analyzed using the thermal gravimetric analysis and the infrared spectrum, the results compared with the standard infrared absorption spectrum of the ammonia and the isocyanic acid are shown in Figure 5. There is only one peak value during the thermolysis process of the urea depositions from three positions, and two peak values of the absorption spectrum during the thermolysis process of the pure urea. The peak spectral absorption map of the thermal decomposition products of the deposition is similar to that of the isocyanic acid, so the main thermal decomposition products of deposition is the isocyanic acid. The peak spectral absorption map of the decomposition products of the pure urea is similar to those of the ammonia and the isocyanic acid, so that we can infer the main thermolysis products of urea respectively are the ammonia and the isocyanic acid, but the first decomposition product is the ammonia.




(a) Comparison of deposits and HNCO




(b) Comparison of frist pyrolysate of urea and $NH_3$




(c) Comparison of second pyrolysate of urea and HNCO

Fig. 5. Comparison of the infrared absorption spectrum

TGA-FTIR results show that the main decomposition products of the urea deposition are the ammonia gas and the isocyanic acid, and the main products of the pure urea is the ammonia gas. $NH_3$ comes from urea and the isocyanic acid is produced by cyanuric acid when the temperature is more than 350°C. So the main components of crystallization and deposition are solid urea and cyanuric acid.

### Analysis to Thermal Decomposition Products

There are a serial of chemical reactions from urea to $NH_3$[8],as shown in Figure 6, producing several byproducts such as biuret, cyanuric acid and so on. The crystallization of urea, which is on the exhaust pipe or the surface of catalyst, can produce biuret, cyanuric acid even melamine by condensation reaction, named as deposition. However the deposition can be decomposed at high temperature. But if decomposing speed and temperature is not high enough, the deposition can still be get worse.

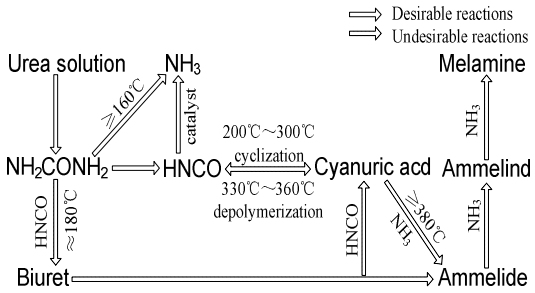



Fig. 6. Reactions involved in urea thermolysis

### Solution and the Improvement of the Design

### mprovement of the Structural Design

In order to promote the atomization and decomposition, and to avoid the formation of the crystallization and sedimentation, this study provides the integrated injector mounting which arranges the injector at the inlet of the SCR catalyst, as shown in Figure 7.

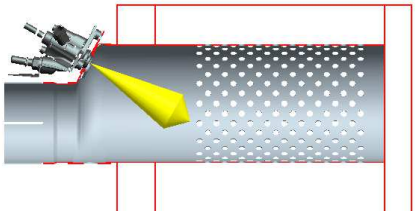


Fig. 7. The integrated injector mounting

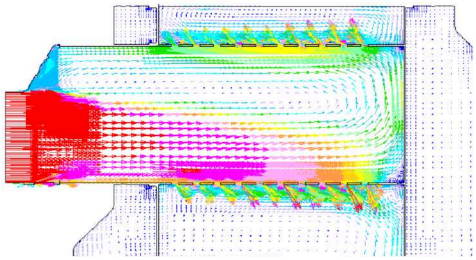


Fig. 8. CFD result for the injection atomization

To ensure urea to atomize and decompose sufficiently, the diameter of the down-stream pipe should satisfy the atomization space for the urea, and the distance from injection point to opposite pipe wall should be larger than the penetration distance of the urea spray. Therefore the wide atomization space weakens the swirl around the nozzle, and eliminates the risk of the crystallization and sedimentation at the injector mounting base. In addition, the atomization pipe inside the catalysis silencer can prevent the heat lose, and avoid the urea crystallization and sedimentation on the pipe as a result of the temperature difference.

The result of CFD simulation about the integrated injector mountings is given in Figure 8. The design can not only prevent the urea deposit accumulation around the nozzle effectively, but also avoid the crystallization and sedimentation of the urea solution at the injector position and inside the exhaust pipe.

### Calibration Strategy of the Urea Injection

Unreasonable calibration strategy is one of the reasons for urea deposits. Urea spray rate is calculated by the NOx and the NSR strategies, and the influence of exhaust temperature should be taken into account. Lower exhaust temperature will cut down the decomposition rate. Both the lower injection temperature and more injection volume at low exhaust temperature all will accelerate crystallization and deposition on the internal wall of exhaust pipe and the surface of the catalyst. So the NSR calibration based on the exhaust temperature is crucial, at the same time the

combustion of engine and the character of SCR should be considered. The calibration strategy should meet the engine performance, conversion efficiency, and avoid the urea deposits. So the main means to solve the problem include reasonable injection temperature and optimal injection calibration strategy.

## Experimental Verification

### Integrated Injector Mountings

To verify the influence of the structure to the prevention of the urea crystallization and deposition, The engine bench early 200h durability test and the 5000km road verification were carried out. The experimental results found that there are no urea depositions, as shown in Figure 9. So this design layout can prevent the urea crystallization and sedimentation effectively.



Fig. 9. Deposit placed at SCR inlet and injiector

## The Calibration Strategy of the urea Injection

### Influence of the Exhaust Temperature on urea Deposition

The influence of the exhaust temperature on the urea deposition was researched on the engine test bench. The results indicate that the urea deposition is reduce along with increasing exhaust temperature, as shown in Figure10, there will be no urea deposition if the exhaust temperature is higher than 272°C.

### Influence of the Urea Injection rate on Urea Deposition

The influence of the urea injection rate on urea deposition was studied with the same exhaust temperature and flow rate on the engine test bench. The results show that the urea solution injection rate has a great influence on the urea deposition, as shown in Figure 11, there will be no urea deposition when the injection rate drops to 5 g/min.

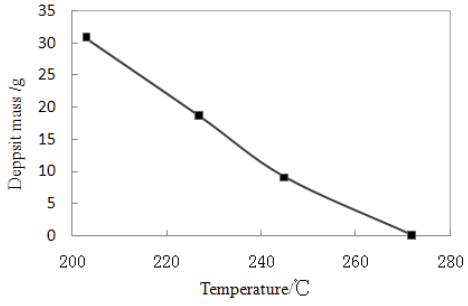



Fig.10. Influence of the exhaust temperature

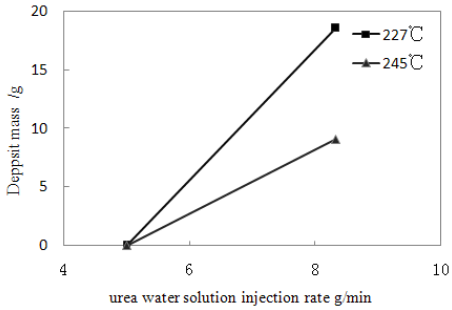



Fig. 11. Influence of the urea injection rate

## Conclusion

The reasons and components of urea depositions are analyzed in this paper, and experimental studies show that the optimized pipe layout and injection calibration strategies could prevent the formation of urea crystallization and other deposition effectively. The conclusions are as follows:

(1) TGA-FTIR results show the urea and the pyrolithic acid are the main components of the urea crystallization and deposition which can be almost eliminated if heated to 500°C.

(2) The integrated injector mountings could prevent the urea crystallization and deposition effectively.

(3) The optimized calibration strategies of the urea injection, including the higher injection temperature and the correction of the injection amount, all can reduce the urea deposition effectively.

**Acknowledgment**

This work is financially supported by the Youth scientist foundation of Shandong Province (BS2013NJ012).

**References**

[1] Johnson T V. Review of diesel emissions and control [C]. SAE 2010-01-0301

[2] Tao Jianzhong. Study on DeNOx Technology by Selective Catalytic Reduction (SCR) for Heavy-Duty Diesel Engines:[D].Jinan:Shandong University,2008

[3] Vadim O.Strots, Shyam Santhanam, Brad J.Adelman, Gregory A.Griffin and Edward M.Derybowski. Deposit Formation in Urea-SCR Systems. SAE paper 2009-01-2780, 2009

[4] Gao Jun-hua, Kuang Jian Song Chong-lin et al. Componets of Crystal from SCR System of a Diesel Engine Compliant with China Stage Ⅳ Emission Standard. [J].Journel of Combustion Scinece and Technology,2010,16(6):547-552

[5] Lifeng Xu, William Watkins, et al. Laboratory and Engine Study of Urea-Related Deposits in Diesel Urea-SCR After-Treatment Systems. SAE paper 2007-01-1582

[6] Guanyu Zheng, Adam Fila, Adam Kotrba, and Ryan Floyd. Investigation of Urea Deposits in Urea SCR Systems for Medium and Heavy Duty Trucks [C]. SAE paper, 2010-01-1941

[7] Gabriel Salanta, Guanyu Zheng, Adam Kotrba, Leonardo Bergantim, Rafael Rampazzo. Optimization of a Urea SCR System for On-highway Truck Applications [C]. SAE paper, 2010-01-0094

[8] Peter M. Schaber, James Colson, Steven Higgins, Daniel Thielen, Bill Anspach, Jonathan Brauer. Thermal Decompisiton (Pyrolysis) of Urea in an Open Reaction Vessel [J]. Thermochimica Acta,2004:131-142

*Advanced Materials Research Vol. 937 (2014) pp 80-85*
*© (2014) Trans Tech Publications, Switzerland*
*doi:10.4028/www.scientific.net/AMR.937.80*

# Synthesis and Characterization of $A_2$ +$B_4$ Hyperbranched Polyesters with Hydroxyl end Groups

Haroon A. M. SAEED[1,2 ,a], Yassir A. ELTAHIR[1,2, b], Yumin XIA[1, c] and Wang YIMIN[1, d*]

[1]College of Materials Science and Engineering, State Key Laboratory for Modification of Chemical Fibers and Polymer Materials, Donghua University, Shanghai 201620, P.R. China.

[2]Faculty of Textiles,University of Gezira, Wad-medani,P.O. Box 20, SUDAN.

[a] haroonsaeed75@gmail.com [b] yassir_eltahir@yahoo.com [c] xym@dhu.edu.cn [d]ymw@dhu.edu.cn

*Corresponding author

**Keywords:** Synthesis, pentaerythritol, $A_2$+$B_4$ approach, hyperbranched polyester, polycondensation.

**Abstract.** Hydroxyl-terminated hyperbranched polyesters (HBPET) with aromatic-aliphatic structure were synthesized by melt polycondensation of isophthalic acid and pentaerythritol via $A_2$+ $B_4$ approach, at three different monomer mole ratios ($A_2/B_4$ =1:1, 1.5:1, 2:1, respectively). Fourier transform infrared (FTIR) spectroscopy indicated that the expected HBPET. The degree of branching of the HBPET was estimated to be between 0.39–0.45 by $^1$H-NMR and $^{13}$C-NMR measurement. The thermogravimetric analysis ( TGA ) measurement revealed that HBPET had a 10 % weight-loss at 350°C in $N_2$.

## Introduction

Over the past two decades, hyperbranched polymers (HBPs) have received much attention because of their unique chemical structures with a large number of terminal groups which are easily functionalized according to requirements. Therefore, many novels HBPs have been synthesized for various applications [1-6].

Numerous HBPs, such as polyamides, polyesters, poly (ether sulfones), polyurethanes, and polycarbosilanes, were prepared through condensation reaction, addition reaction, ring-opening reaction or click chemistry. The synthetic strategies can be mainly divided into two categories; the first one is the "$AB_n$" ($n \geq 2$) route, the second one is well-known as "$A_2 + B_n$" ($n \geq 3$) strategy, based on two monomers containing multifunctional groups, namely $A_2$ and $B_n$, generating highly branched polymers [7, 8]. However, most of the $AB_n$ type monomers are unavailable commercially; they are either expensive or have to be synthesized prior to polymerization. Recently, the $A_2$+$B_3$ type of polymerization has been demonstrated to be an alternative route to fabricate HBPs, which provides a more facile approach to several families of HBPs. In addition, $A_2$ and $B_3$ monomers are more readily obtained than $AB_2$ type monomers.[8-10] The low cost of synthesizing HBPs allows them to be produced on a large scale, giving them an advantage over dendrimers in applications involving large amounts of material, although the properties of HBPs are intermediate between those of dendrimers and linear polymers [5, 11, 12]. Because of their highly functioned globular structures, HBPs exhibit different properties from those of linear polymers of the same molar mass, such as less entanglement in the solid state, high solubility in various solvents, and low melt viscosity [13-18].

Among numerous types of HBPs the family of hyperbranched polyesters (HBPET) has been studied in detail. HBPET with all-aliphatic and all- aromatic structure has been investigated in many publications [10, 19].

Several HBPET based on the $A_2$+$B_3$ synthetic strategy has already been reported. Lusic and Fossum presented the $A_2$+$B_3$ HB aliphatic polyesters prepared by reaction of fumaric acid and trimethylolpropane, and the ratio of these two reagents was varied [7, 8]. Other HB aliphatic

polyester was synthesized by an $A_2$+$B_3$ approach using glycerol and adipic acid [7]. Many investigations on the $A_2$+$B_3$ routes to HB polyesters were also done in the group of Long and several $A_2$+$B_3$ HBPET was reported by them [10, 20, 21]. Furthermore, the theoretical investigations of the kinetics of HB $A_2$+$B_3$ systems by polycondensation reactions were carried out by Schmaljohann and Voit [10], but all of these polymers with aliphatic structures [7, 19, 21]. Recently, Saeed and Yimin [6] synthesized aliphatic- aromatic HBPET based on adipic acid phloroglucinol via $A_2$+$B_3$ approach. However, until now, no work has been released on treating of hyperbranched aromatic-aliphatic polyesters prepared according to the $A_2$+$B_4$ method.

In the present work, hydroxyl-terminated HBPET with aromatic−aliphatic structure was synthesized via $A_2$+$B_4$ method by melting polymerization of isophthalic acid ($A_2$) and pentaerythritol ($B_4$) at 150°C in the presence of p-toluene sulfonic acid (p-TSA) as a catalyst. The structure of the resulting HBPET and their properties were investigated.

## Experimental

### Materials and Instrumentation

Isophthalic acid, pentaerythritol and p-Toluenesulfonic acid (p-TSA) were purchased from Sinopharm chemical reagent Co. Ltd (China). Acetone and hexane were obtained through Donghua university chemical store. All reagents and solvents were of commercial grade and used as received. The structure of the resulting HBPET and their properties were investigated by Nicolet 5700 FTIR, (Netzsch TG209F1) theromgravimetric analysis (TGA), a Bruker DRX-400 spectrometer for $^{13}C$ NMR and $^{1}H$ NMR analysis and diffractometer Rigaku Mini Flex II for X-ray diffraction measurements.

### Synthesis of HBPET

The HBPET was prepared in a single-step, melt polycondensation reaction of isophthalic acid and a pentaerythritol as the core. The molar ratios of pentaerythritol to isophthalic acid were (1:1, 1:1.5, 1:2) respectively. The pentaerythritol was charged with isophthalic acid kept in a 250 ml four-necked, round-bottom flask placed over an oil bath and equipped with a thermometer, mechanical stirrer, nitrogen inlet, and Dean–Stark apparatus. The reaction mixture was slowly heated to 160°C. After the reactants were completely melted, the temperature was maintained at 150°C with a continuous nitrogen flow for about 9 h. p-Toluene sulfonic acid (p-TSA) (0.05 weight % on the basis of the weight of isophthalic acid) was used as the catalyst for the esterification. The HBPET samples were collected at different intervals, 3, 6, and 9 h, to investigate the structural buildup of HBPET with different techniques. Usually, gelation is encountered during the synthesis of these polyesters, but with proper control of the temperature and catalyst concentration, we prepared these polyesters without gelation. The crude product was collected as pale gray color, and was purified and precipitated from acetone in ethyl ether to remove the un-reacted materials and the catalyst, then was dried at 50°C under vacuum.

## Results and Discussion

### Synthesis of HBPET

In this work, HBPET was synthesized by single step-melt polycondensation of isophthalic (as $A_2$ monomer) and pentaerythritol (as $B_4$ monomer) via $A_2$+$B_4$ approach. In contrast to classical hyperbranched polymers synthesized according to the $AB_2$ strategy, the structures of hyperbranched polyesters prepared via the $A_2$+$B_4$ approach do not display just one focal reactive group but present two different types of functional end groups, as can be seen on a scheme 1. Indeed, OH groups arising from pentaerythritol units, and COOH groups arising from isophthalic acid units can coexist within the same macromolecule in different ratios according to the molar ratio of the monomers prior to reaction and, to a certain extent, to the degree of conversion. Both two monomers are commercially available, and their properties are very suitable for preparing hyperbranched polyester.

As an ordinary dibasic acid, the esterification difficulty degree of isophthalic acid is situated between terephthalic acid and phthalic acid, but polyesters formed from isophthalic acid have good chemical stability, mechanical properties, and thermal deformation. pentaerythritol is a polyol which has four high reactive hydroxyl groups with the structure-like neopentane; the unique structure endows its excellent stability, and polyesters prepared from pentaerythritol has good chemical stability, and weather resisting property. The reaction was maintained at 150°C for 9 h. It was driven toward high conversion as the water formed was removed continuously under reduced pressure with an optimized reaction time to avoid gelation. The composition and structure were analyzed by $^{1}$H-NMR, $^{13}$C-NMR spectroscopy and XRD. Hydrogen-bonding information was obtained from FTIR spectroscopy.

**NMR Analysis**

In order to further confirm the chemical structure and calculate the DB values of HBPET, the $^{1}$H NMR and $^{13}$C NMR measurements were performed.

DB for different pseudo-generations of HBPET were calculated using the following Eq:

$$DB_{(Fretchet)} = (D + T)/ (D + T + L) \quad (1)$$

Where, D, T and L refer to the numbers of dendritic, terminal, and linear units in the polymer, respectively [4, 9, 22]. Experimentally, DB is usually determined from $^{1}$H NMR or $^{13}$C NMR spectroscopy by comparing the integration of peaks for respective units in HBPET.

The data of $^{1}$H NMR confirmed the structure of the HBPET. In the $^{1}$H NMR spectrum of HBPET in fig.1. the signals at 8.3-8.7 ppm indicate the presence of hydroxyl protons. Proton signals for aromatic rings at 3.5-4.5 ppm. Carboxyl protons were appeared at 2.4-2.6 ppm. Hydrogyn protons of aromatic were observed at 7.6 ppm.

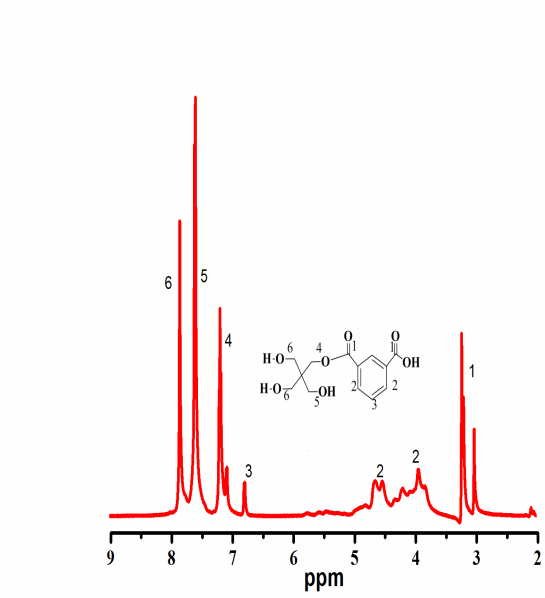



Fig. 1. $^{1}$H NMR spectra of HBPET.

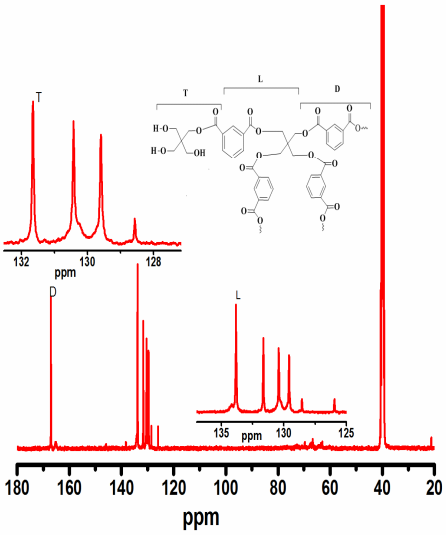



Fig. 2. $^{13}$C NMR spectra of HBPET.

The $^{13}$C NMR spectra of HBPET in fig. 2. showed that the resonances from the carbons in the T, L, and D units had different shifts due to the difference in their chemical environments. The peak at 170 ppm could be attributed to the carbonyl carbon of acid or ester. The peaks at 134.5 ppm are due to the aromatic carbons in the benzene ring; the peak at 130 ppm is due to the methylene carbon of ester and alcohol unit; and the peak at 98 ppm arises from quaternary carbons of isophthalic acid. The percentage of T, L and D units present in HBPET, are calculated from the integral area ratios of methylene and the quaternary carbon zone of $^{13}$C-NMR spectra, as a result, DB can be determined by using equ.1. The degree of branching of the HBPET was estimated to be between 0.39–0.45 percent.

## FTIR Analysis

Fig.3. shows the FTIR spectra of the synthesized hyperbranched polyester. Broad peaks around 3083–2971 $cm^{-1}$ are associated to adsorbed water and un-reacted –OH groups from pentaerythritol, confirmed a high concentration of hydroxyl groups in HBPET molecules. The peak at 2686 $cm^{-1}$ was the characteristic absorption of methyl, and the peak at 2540 $cm^{-1}$could be attributed to the absorptions from methylene groups, as well as a peak at 723 $cm^{-1}$ which is due to the presence of the aromatic group originated from isophthalic, the peaks at 1705 $cm^{-1}$(C=O in ester bond), 1287 $cm^{-1}$ (C-O symmetric stretching) and 1286 $cm^{-1}$ (asymmetric stretching), these being the characteristic absorption bands of polyesters. These data indicated that the polymers contained hydroxyl groups, ester bonds, benzene ring, methyl and methylene groups, which were in agreement with our objective polymers.

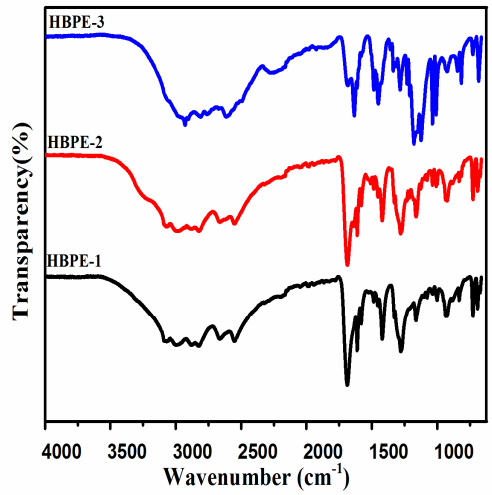
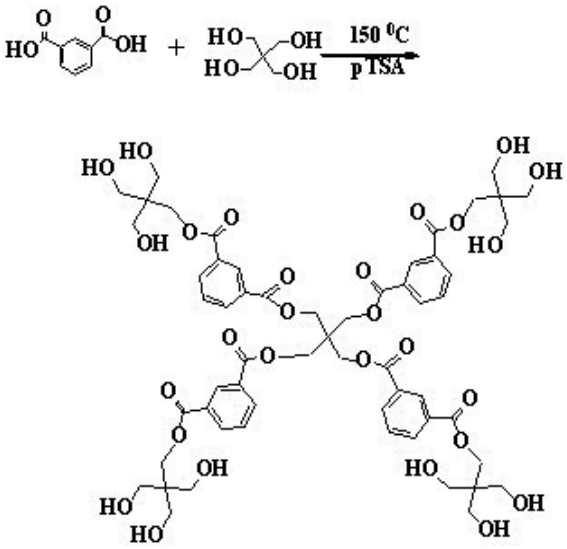



Fig. 3. FTIR spectra of HBPET.




Scheme 1. The possible structure of HBPET.

## Thermal Properties of HBPET

The thermal stability of a polymer can provide an important guidance for its application. The studies of thermal behavior not only can explain the behavior of a polymer at the high temperatures, but also provide assistance for the establishment of selection criteria for specific applications of polymer materials [23, 24].

TGA technique was used to study the thermal behaviors and thermal properties of HBPET. These HBPET show similar decomposition behavior and good thermal stability in N2 because they have the same structures. According to the TGA curves in fig. 4. the initial decomposition temperatures (T5) were about 311°C and the temperature for 10% gravimetric loss (T10), which is an important evidence for thermal stability, was about 350°C. The maximum decomposition temperature (Tmax) was about 370°C and also char yields of the HBPET at 600°C were 7-19%.

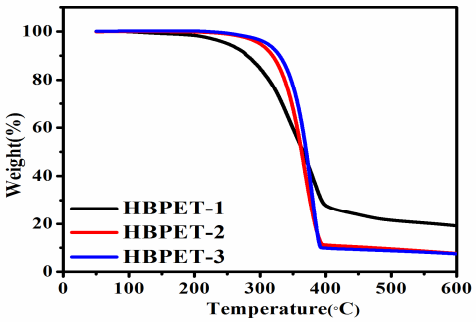



Fig. 4. TGA curves of the synthesized HBPET.

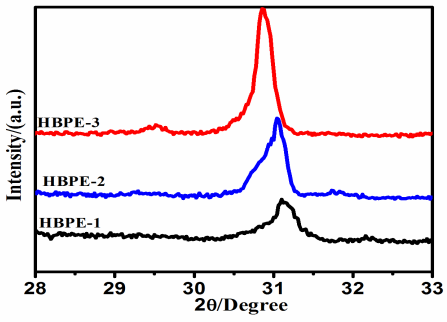



Fig. 5. XRD curves of the synthesized HBPET.

**X ray Powder Diffraction (XRD):**

The crystallinity of HBPET was examined by X-ray diffraction scans with 2θ ranging from 28 to 33 and the results were shown in fig.5. The crystallinity of the polymers was determined by bisecting the experimental plot into crystalline domain and amorphous domain by curve fitting. The crystallinity obtained from the XRD data were 40.5, 42.4 and 46.5% for HBPE-1, HBPE-2 and HBPE-3 respectively. The XRD pattern of HBPET suggests that the presence of rigid aromatic rings, stemmed from isophthalic, lead to more rigid structures, which should be more prone to crystallize than fully aliphatic hyperbranched polyesters. From the XRD pattern of HBPET the peaks at a 2θ value of 31° for HBPE-3 and 31.2° for HBPE-2 and HBPE-3 have been observed, and according to the literature these polymers are semi-crystal.

**Conclusion**

In this work, three generations of aromatic- aliphatic (HBPET) via the $A_2$+$B_4$ methods were synthesized, based on isophthalic acid ($A_2$ monomer) and pentaerythritol ($B_4$ monomer) as a core molecule via melt condensation procedure with p-Toluene sulfonic acid (p-TSA) as a catalyst. The HBPET had good thermal stability up to 350°C. The DB of HBPE-1, HBPE-2 and HBPE-3 were 0.39, 0.42, and 0.45%, respectively. These HBPET had a 10% weight-loss at 350°C in $N_2$, which render them, particularly attractive in industrial applications.

**References**

[1] H. Miao, F. Bao, L. Cheng, W. Shi, Fluorinated modification of hyperbranched polyesters used for improving the surface property of UV curing coatings, J. Fluorine Chem. 131 (2010) 1356-1361.

[2] E. Žagar,M. Žigon, Aliphatic hyperbranched polyesters based on 2,2-bis(methylol)propionic acid—Determination of structure, solution and bulk properties, Prog. Polym. Sci. 36 (2011) 53-88.

[3] S. Wang, S. Tateyama, D. Kaneko, S.Y. Ohki, T. Kaneko, Synthesis of well-defined hyperbranched polymers bio-based on multifunctional phenolic acids and their structure–thermal property relationships, Polym. Degrad. Stab. 96 (2011) 2048-2054.

[4] A. Khalyavina, F. Schallausky, H. Komber, M. Al Samman, W. Radke, A. Lederer, Aromatic−Aliphatic Polyesters with Tailored Degree of Branching Based on AB/$AB_2$ and ABB*/$AB_2$ Monomers, Macromolecules, 43 (2010) 3268-3276.

[5] A. Khalyavina, L. Haeussler, A. Lederer, Effect of the degree of branching on the glass transition temperature of polyesters, Polymer, 53 (2012) 1049-1053.

[6] H.A.M. Saeed,W. Yimin, Synthesis and characterization of $A_2$+$B_3$ type hyperbranched aromatic-aliphatic polyester with carboxyl end groups, Russ. J. Appl. Chem. 86 (2013) 1569-75.

[7] X. Zhang, Synthesis and Characterization of Hyperbranched Polyesters Based on Isophthalic Acid and Trimethylolpropane, J. Macromol. Sci., Pure Appl. Chem. 48 (2010) 128-134.

[8] H. Chen, J. Kong, W. Tian, X.D. Fan, Intramolecular Cyclization in $A_2$ + $B_3$ Polymers via Step-Wise Polymerization Resulting in a Highly Branched Topology: Quantitative Determination of Cycles by Combined NMR and SEC Analytics, Macromolecules, 45 (2012) 6185-6195.

[9] S. Shabbir, S. Zulfiqar, Z. Ahmad, M.I. Sarwar, Synthesis and characterization of hyperbranched aromatic polyester-imides with good thermal properties based on 1,3,5-tris(3′,4′-carboxyphenyl)benzene trianhydride, Polym. Degrad. Stab. 95 (2010) 1251-1259.

[10] Z. Fan, A. Lederer, B. Voit, Synthesis and characterization of $A_2$+$B_3$-type hyperbranched aromatic polyesters with phenolic end groups, Polymer, 50 (2009) 3431-3439.

[11] T. Murakami, S. Uchida, K. Ishizu, Architecture of hyperbranched polymers consisting of a stearyl methacrylate sequence via a living radical copolymerization, J. Colloid Interface Sci. 323 (2008) 242-246.

[12] X. Zhai, S. Peleshanko, N.S. Klimenko, K.L. Genson, D. Vaknin, M.Y. Vortman, V.V. Shevchenko, V.V. Tsukruk, Amphiphilic dendritic molecules: Hyperbranched polyesters with alkyl-terminated branches, Macromolecules, 36 (2003) 3101-3110.

[13] T. Zeiner,S. Enders, Phase behavior of hyperbranched polymer solutions in mixed solvents, Chem. Eng. Sci. 66 (2011) 5244-5252.

[14] X. Li, C.Y. Hong, C.Y. Pan, Preparation and characterization of hyperbranched polymer grafted mesoporous silica nanoparticles via self-condensing atom transfer radical vinyl polymerization, Polymer, 51 (2010) 92-99.

[15] D. Foix, A. Serra, L. Amparore, M. Sangermano, Impact resistance enhancement by adding epoxy ended hyperbranched polyester to DGEBA photocured thermosets, Polymer, 53 (2012) 3084-3088.

[16] D. Foix, M.T. Rodríguez, F. Ferrando, X. Ramis, A. Serra, Combined use of sepiolite and a hyperbranched polyester in the modification of epoxy/anhydride coatings: A study of the curing process and the final properties, Prog. Org. Coat. 75 (2012) 364-372.

[17] K.K. Jena, R. Narayan, K.V.S.N. Raju, Hyperbranched polyester based on the core + $AB_2$ approach: Synthesis and structural investigation, J. Appl. Polym. Sci. 118 (2010) 280-290.

[18] J.T. Sun, C.Y. Hong, C.Y. Pan, Surface modification of carbon nanotubes with dendrimers or hyperbranched polymers, Polym. Chem. UK. 2 (2011) 998-1007.

[19] Z. Fan, K. Jaehnichen, P. Desbois, L. Haeussler, R. Vogel, B. Voit, Blends of different linear polyamides with hyperbranched aromatic $AB_2$ and $A_2$ + $B_3$ polyesters, J. Polym. Sci., Part A: Polym. Chem. 47 (2009) 3558-3572.

[20] K.C. Cheng, T.H. Chuang, T.H. Tsai, W. Guo, W.F. Su, Model of hyperbranched polymers formed by monomers $A_2$ and $B_g$ with end-capping molecules, Eur. Polym. J. 44 (2008) 2998-3004.

[21] X. Zhang, Hyperbranched aromatic polyesters: From synthesis to applications, Prog. Org. Coat. 69 (2010) 295-309.

[22] S. Boye, H. Komber, P. Friedel, A. Lederer, Solution properties of selectively modified hyperbranched polyesters, Polymer, 51 (2010) 4110-4120.

[23] I.V. Dolbin, A.I. Burya, G.V. Kozlov, The structure and thermal stability of polymer materials: A fractal model, High Temp. 45 (2007) 313-316.

[24] T. Vlad-Bubulac,C. Hamciuc, Aliphatic-aromatic copolyesters containing phosphorous cyclic bulky groups, Polymer, 50 (2009) 2220-2227.

*Advanced Materials Research Vol. 937 (2014) pp 86-91*
*© (2014) Trans Tech Publications, Switzerland*
*doi:10.4028/www.scientific.net/AMR.937.86*

# Preparation of Polyamide 5,6 (PA56) Fibers and Its Mechanical Properties

Yassir A. ElTAHIR[1,2,a], Haroon A. M. SAEED[1,2,b], Yu-min XIA[1,c] and YI-min Wang [1, d,*]

[1]State Key Laboratory for Modification of Chemical Fibers and Polymer Materials, Donghua University, 2999 North Renmin Road, Songjiang, Shanghai 201620, P.R. China

[2]Faculty of Textiles, University of Gezira, Wad-Medani, P.O. Box 20, Sudan

[a]yassir_eltahir@yahoo.com, [b]haroonsaeed75@gmail.com, [c]xym@dhu.edu.cn, [d]ymw@dhu.edu.cn

*Corresponding author

**Keywords:** Polyamide 5,6, Fibers, Draw ratio, Tenacity, Tensile modulus.

**Abstract.** Polyamide 5,6 (PA56) fibers were successfully prepared by melt-spinning technique. PA56 fibers were subjected to hot drawing process at different draw ratio and temperature. The effect of the drawing conditions on their mechanical properties such as tenacity, tensile modulus and breaking elongation were investigated by means of tensile test measurements. The results revealed that the tenacity and tensile modulus were found to be increased, while the elongation at break decreased with the draw ratio. The improvements of the mechanical properties could be attributed to the enhanced of the molecular orientation along the fiber axis and an increase in crystallinity. On the other hand, the PA56 fibers mechanical properties do not show significant difference with the drawing temperatures.

## Introduction

Since the pioneering work of Carothers in 1932 [1], many kinds of polyamide have been developed and a number of them have been commercialized in the past 80 years. Aliphatic polyamides commonly referred as nylons are semi-crystalline polymers that can be used as fibers and engineering thermoplastics because of their outstanding properties such as a relatively high modulus, good temperature resistance, excellent toughness and strength, and are also excellent resistant to abrasion [2]. The attractive matrix of properties of polyamides originates mostly from the strong hydrogen bonds which are formed by –NH– and –CO– in the amide groups [3]. Therefore, the properties of polyamides vary with the density of the amide groups in their molecular chains.

Melt spinning is a continuous deformation process and the most commonly used method for manufacturing commercial synthetic fibers. It has been an important manufacturing process since its commercialization for production of nylon 66 fibers in 1940 [4]. Most relevant features of the influence of melt spinning and drawing variables were noted by Carothers and Hill [1] including the effect of take-up velocity on crystalline orientation and mechanical properties. Since this work, numerous researches have been carried out to investigate the effect of melt spinning variables and drawing conditions on the mechanical properties of melt spun fibers [5-9]. Bankar et al. [5] studied the structure development and mechanical properties of nylon 6 fibers produced at various spinning speeds. They reported that the modulus and tensile strength increase while elongation at break decreased with increasing take-up speed and spin-line stress. Rahbar and Mojtahedi [8] has investigated the effect of multistage drawing on the structure and mechanical properties of nylon 6 fibers. However, up to now only a few studies have been reported on the polyamide 5,6 (PA56). Puiggalí, et al. [10] studied the crystal structures of PA56 and reported the lattice of the mono-clinic unit cell with a = 0.512 nm, b = 0.868 nm, c (chain axis) =3.133 nm and β = 125.70. Morales-Gámez, et al. [11], investigated the Brill transition and melt crystallization of PA56 by optical microscopy and reported that the spherulites of PA56 had different optical properties comparing to the sheet structures of the conventional polyamides. It is obvious that the preparation of PA56 fibers

has not been investigated in depth and reported so far. The objective of this study is to prepare PA56 fibers by melt spinning process at take-up speed of 3200 m/min and study the influence of drawing process such as draw ratio and drawing temperature on the mechanical properties of PA56 fibers.

## Material and Methods

### Material

Polyamide 56 with an intrinsic viscosity of 0.68 dL/g (measured in dichloroacetic acid at 25 °C), which was kindly supplied by Guangdong Xinhui Meida Nylon Co. Ltd, China. Melt flow index (MFI) was 15.65 g/10 min (ASTM D1238, 275 °C and 0.325 kg as recommended for nylon 66).

### Melt Spinning

Melt spinning of PA56 was carried out using a lab melt-spinning (Polymer ABE Engineering MATE-V, Co. Tokyo, Japan) spinning machine at spinning temperature of 285 °C and a take-up speeds of 3200 m/min. The pellets were extruded through a spinneret with 36 holes each with a diameter of (D=0.3 mm) and the spinneret hole length to diameter ratio (L/D) of 3. Prior to processing the PA56 pellets were dried in a vacuum oven first at a temperature of 50 °C for 60 min then 75 °C for 60 min, and finally at a constant temperature 110 °C for 8 h before being cooled to room temperature.

### Drawing Process of PA56 Fibers

To investigate the effect of the drawing conditions on properties of the PA56 fibers, drawing process was performed at various draw ratio and temperature. Drawing of PA56 fibers were carried out using a Parallel drawing machine type TF-100, made in Suzhou, China, between two rolls at different speeds and temperatures. The draw ratio was calculated by the ratio of the speed of feed roll to that of take-up roller. The diameter of feed and take-up roller was the same for both rollers.

### Linear Density

Linear density of all samples was determined by measuring the weight of 100 m long yarns. Five reading were taken for each sample, and then the average has been reported.

### Mechanical Properties Measurements

Mechanical properties of the PA56 fibers such as tensile strength, modulus, and breaking elongation were measured using ASTM D 3822 with a XL-2 Yarn Elongation Tester, from Shanghai New Fine Instrument Co. Ltd. with a crosshead speed of 400 mm/min and a gauge length of 250 mm. The results reported were the average of at least 20 measurements.

## Results and Discussion

### Fiber Linear Density

Fig.1 shows the effect of draw ratio and temperature on PA56 fibers linear density. PA56 fibers linear density decreased continuously with the increase of the draw ratio as shown in Fig. 1(a). For instance, the linear density decreased from 92.9 dtex to 60.6 dtex, 54.3 dtex, 51.1 dtex and 49.1 dtex, respectively, with the increase of the draw ratio from 1.0 to 1.6, 1.8, 1.9 and 2.0. Increase in a draw ratio leads to more drawing of the fiber and hence decreases the fiber linear density. On the other hands, the fiber linear density decreased slightly with the drawing temperature.

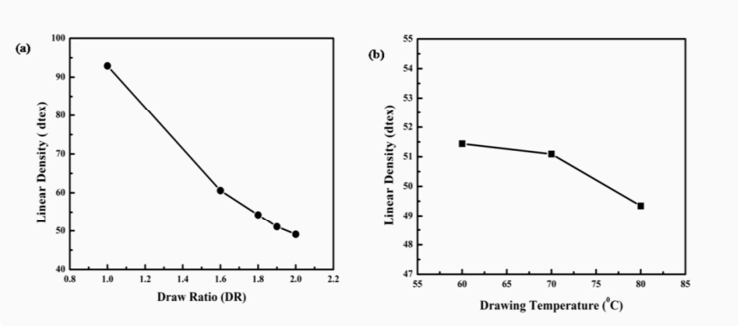



Fig. 1. PA56 fibers linear density (a) at different draw ratio and (b) at different drawing temperatures.

**Effects of Draw Ratio on the Mechanical Properties of PA56 Fibers**

It is well known that the tenacity, Young's modulus and elongation at break are the main characterizes of the fibers mechanical properties. Fig.2 shows the PA56 fibers tenacity and elongation at break obtained at various draw ratios at temperature of 70 °C As shown in Fig. 2, the tenacity rises sharply from 3.6cN/dtex to 3.8, 4.5 and 5.2cN/dtex, respectively, with increasing draw ratio from 1.6 to 1.8, 1.9 and 2.0, and the highest tenacity is obtained for the fibers at DR=2 (i.e. 5.2cN/dtex). It should be noted that the fiber morphological characteristics such as crystallinity, degree of crystalline perfection and orientation of crystalline and amorphous regions are probably the most parameters influence the performance of the fibers [9, 12]. It may suggest that the improvements on fibers tenacity may be attributed to the increased of crystallinity, molecular orientation in a non-crystalline regions and crystal perfections. On the other hand, the elongation at break drops rapidly from 40.5% to 24.6%, 19.4% and 16.7%, respectively, with the draw ratio from 1.6 to 1.8, 1.9 and 2.0. This may be attributed to the structural and morphological changes occur during drawing process, which could be leads to decrease in fibers elongation.

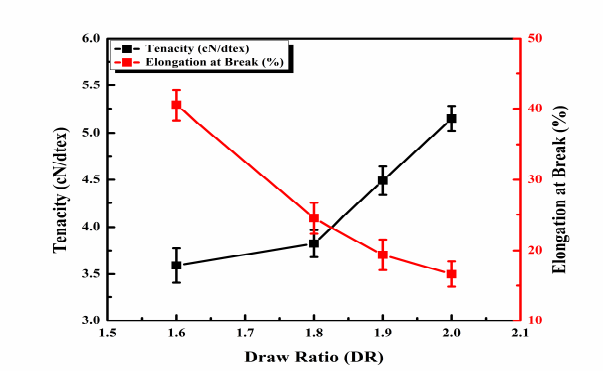



Fig. 2. Effect of draw ratio on PA56 fibers tenacity

Fig. 3 shows the tensile modulus of PA56 fibers at various draw ratios. It is clearly that the tensile modulus of PA56 fibers increases steadily from 24.8 cN/dtex to 30.3, 44.3 and 44.6 cN/dtex with the increasing the draw ratio from 1.6 to 1.8, 1.9 and 2.0, respectively. These results demonstrate that the tensile modulus can be markedly improved by drawing. Increased the draw ratio facilitates extension and alignment along the fiber axis of molecular chains in the non-crystalline regions [13], as well as enhance the orientation of crystallites. All these effects of the drawing process improve the overall orientation and hence increase the tensile modulus of PA56 fibers.

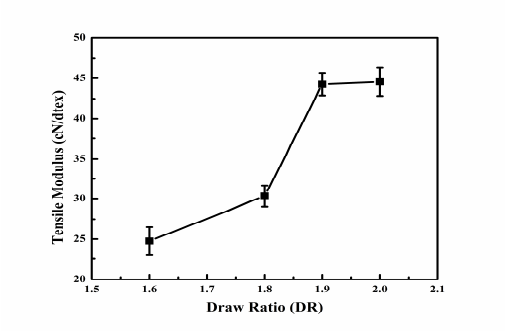



Fig. 3. Effect of draw ratio on tensile modulus of PA56 fibers

**Effect of Drawing Temperature on the Mechanical Properties of PA56 Fibers**

The optimum drawing temperature to cause a noticeable morphological change and the increase in overall molecular orientation lies between the glass transition and the melting point temperatures of semi-crystalline polymers [14]. Fig.4 shows the effect of drawing temperature on the tenacity and elongation at break of PA56 fibers with the draw ratio (DR)= 1.9. It is seen from Fig.4, the tenacity increase from 4.4cN/dtex to 4.5 and 4.7cN/dtex when the drawing temperature increased from 60 °C to 70 °C and 80 °C, respectively. On the other hand, the elongation at break was observed to increase slightly from 17.5% to 19.4% and 21.8% as the drawing temperature increase from 60 °C to 70 °C and 80 °C, respectively. The increase of drawing temperatures, cause existing entanglement molecules to disentangle and become mobile, get orients along the fiber axis under the influence of stresses, and tend to crystallize.

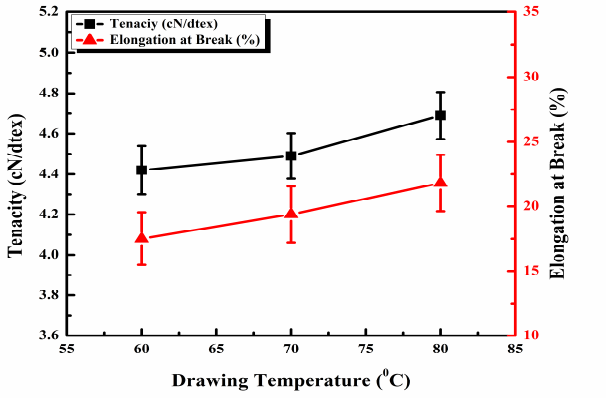



Fig. 4. Effect of drawing temperatures on the tenacity of PA56 fibers.

Fig. 5 shows the tensile modulus of PA56 fibers prepared at various draw ratios. From Fig. 5, the tensile modulus of PA56 fibers increased gradually from 40.3cN/dtex to 44.3 cN/dtex and 45.3cN/dtex, respectively, when the drawing temperatures increased from 60°C to 70 and 80°C. Despite the variation in drawing temperature, these fibers do not show a significant difference in the mechanical properties. This result indicates that the drawing temperature affects the amorphous region to a greater extent compared to the crystalline regions.

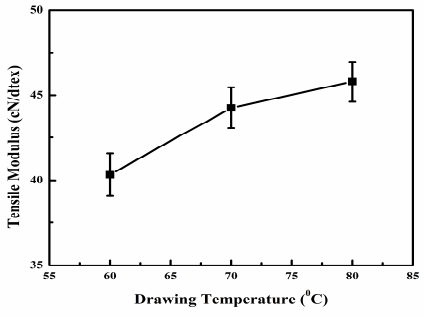



Fig. 5. Effect of drawing temperatures on the tensile modulus of PA56 fibers.

## Conclusion

Polyamide 56 fibers were successfully prepared at take speed of 3200 m/min. The effects of the drawing conditions on their mechanical properties were investigated by tensile test measurements. The results showed that the tenacity and tensile modulus were found to be increased while the elongation at break decreased with the draw ratio. On the other hand, the PA56 fibers mechanical properties do not show significant difference with the drawing temperatures. The results showed that the important process parameters affecting the mechanical properties are a draw ratios and drawing temperatures.

## References

[1] W.H. Carothers, J.W. Hill, STUDIES OF POLYMERIZATION AND RING FORMATION. XV. ARTIFICIAL FIBERS FROM SYNTHETIC LINEAR CONDENSATION SUPERPOLYMERS, J. Am. Chem. Soc. **54** (1932) 1579-1587.

[2] M.I. Kohan, Nylon Plastics Handbook. Vol. 378. 1995: Hanser Publishers Munich, Germany.

[3] P.W. Morgan, Condensation Polymers, Interscience Publishers New York, 1965.

[4] E.K. Bolton, Chemical Industry Medal. Development of Nylon*,* Ind. Eng. Chem. **34** (1942) 53-58.

[5] V.G. Bankar, J.E. Spruiell, J.L. White, Melt spinning of nylon 6: Structure development and mechanical properties of as-spun filaments, J. Appl. Polym. Sci. **21** (1977) 2341-2358.

[6] M.D. Danford, J.E. Spruiell, J.L. White, Structure development in the melt spinning of nylon 66 fibers and comparison to nylon 6, J. Appl. Polym. Sci. **22** (1978) 3351-3361.

[7] T.F. Meyabadi, M.R.M. Mojtahedi, S.A.M. Shoushtari, Melt spinning of reused nylon 6: structure and physical properties of as-spun, drawn, and textured filaments, J. Tex. Inst. **101** (2010) 527-537.

[8] R.S. Rahbar, M.R.M. Mojtahedi, Influence of Hot Multistage Drawing on Structure and Mechanical Properties of Nylon 6 Multifilament Yarn, J. Eng. Fibers Fabr. **6** (2011) 7-15.

[9] N.S. Murthy, R.G. Bray, S.T. Correale, R.A.F. Moore, Drawing and annealing of nylon-6 fibres: studies of crystal growth, orientation of amorphous and crystalline domains and their influence on properties, Polymer. **36** (1995) 3863-3873.

[10] J. Puiggalí, L. Franco, C. Alemán, J.A. Subirana, Crystal Structures of Nylon 5,6. A Model with Two Hydrogen Bond Directions for Nylons Derived from Odd Diamines, Macromolecules. **31**(1998) 8540-8548.

[11] L. Morales-Gámez, D. Soto, L. Franco, J. Puiggalí, Brill transition and melt crystallization of nylon 56: An odd–even polyamide with two hydrogen-bonding directions, Polymer. **51** (2010) 5788-5798.

[12] R.S. Rahbar, A. Haji, Use of D-optimal design to model and the analysis of the effect of the draw ratio on some physical properties of hot multistage drawn nylon 6 fibers, J. Appl. Polym. Sci. **130** (2013) 1337-1344.

[13] D.C. Prevorsek, G.A. Tirpak, P.J. Harget, A.C. Reimschuessel, Effects of thermal contraction on structure and properties of PET fibers, J. Macromol. Sci., Part B. **9** (1974) 733-759.

[14] A. Suzuki, M. Ishihara, Application of $CO_2$ laser heating zone drawing and zone annealing to nylon 6 fibers, J. Appl. Polym. Sci. **83** (2002) 1711-1716.

*Advanced Materials Research Vol. 937 (2014) pp 92-98*
*© (2014) Trans Tech Publications, Switzerland*
*doi:10.4028/www.scientific.net/AMR.937.92*

# Inhibition and Recovery of Nitrification During the Process of Sludge Reduction Induced by a Metabolic Uncoupler, 2,6-dichlorophenol (2,6-DCP)

Di WU[1,a], Yu TIAN[2,b,*], Xing-Wang WEN[3,c] and Hui-Ling LIU[4,d]

[1] School of Municipal and Environmental Engineering, Harbin Institute of Technology, Harbin, 150090, China

[2] State Key Laboratory of Urban Water Resource and Environment, Harbin Institute of Technology (SKLUWRE, HIT), Harbin 150090, China; School of Municipal and Environmental Engineering, Harbin Institute of Technology, Harbin, 150090, China

[3] FAW Jiefang Automotive Company Ltd., Changchun 130400, China

[4]School of Municipal and Environmental Engineering, Harbin Institute of Technology, Harbin, 150090, China

[a]angel523116@126.com, [b]hittianyu@163.com, [c]wen-sevenyy@163.com, [d]hlliu2002@163.com

**Keywords:** Metabolic uncoupler 2,6-DCP, Sludge reduction, Nitrification Inhibition, Nitrification recovery

**Abstract.** 2,6-DCP was found to be an efficient metabolic uncoupler to reduce sludge production. 20mg/L 2,6-DCP could reduce sludge production about 34.62%, however, it also affected nitrification seriously, the nitrification inhibition was about 76.17% compared to control. Environmental factors, temperature and pH, were varied to repair nitrification. The nitrification inhibition was decreased to 45.7% at 28±1 ˚C and pH=8.5±0.2. Nitrification inhabitation was further decreased to 30% when the 2,6-DCP concentration reduced to 10 mg/L, the sludge reduction also decreased to17.9%. The 30-day operation data indicated that 10mg/L 2,6-DCP can also effectively reduced the sludge production about 17.9% with the COD removal efficiency decreased about 6.99% and nitrification inhabitation was about 30.91%. It shouldn't only consider the sludge reduction when selecting the concentration of metabolic uncoupler. The application of metabolic uncoupler for sludge reduction should be cautious and need further study.

## Introduction

The widely adapted activated sludge processes in treating wastewaters generates a large quantity of excess sludge daily as a byproduct, the management of which presents many challenges[1]. At present, most sewage sludge is disposed by means of landfill or incineration, both of which are of drawbacks[2]. Minimization of excess sludge may be an ideal solution[3]. Hence, some technologies to minimize sludge generation in the activated sludge process have been explored and developed, such as inducing cell lysis to form autochthonous substrate on which cryptic growth occurs, prolonging aeration to promote conversion of organic pollutants to respiration products, or encouraging microbial predation by bacteriovirus[4-8]. However, they are difficult to control, have a low efficiency, or have higher costs. During the last decades, uncoupling metabolism was developed as an alternative to reduce excess sludge generation in the activated sludge process [9-13].

Catabolism is coupled tightly with the anabolism under normal conditions and energy uncoupling does not occur. However, energy uncoupling can be brought about when microbes are under some abnormal conditions such as high temperature, nutrients limitation, and the presence of metabolic uncouplers[14-16]. In view of the engineering feasibility of utilizing the above abnormal conditions to encourage energy uncoupling, the main advantage of chemical uncoupler was that it can reduce excess sludge production effectively without modification of conventional wastewater treatment processes[17].

In previous studies, research concentrated mainly on the comparison and screening of effective chemical uncouplers[14, 18-20], also some about the effect of pH on the biomass reduction[10, 21]. Besides the chlorinated and nitrated phenols, TCS was effective in reducing the production of both batch and continuous activated sludge cultures, addition of 0.8–1.0mg/l TCS could reduce sludge production by 40% without affecting COD removal efficiency [12, 22]. However, there was a paucity of information concerning the impact of chemical uncouplers on nutrient removal and the sludge reduction induced by 2,6-DCP. In our previous study, 2,6-DCP was selected as the metabolic uncoupler for sludge reduction, its distribution variation and its effect on sludge reduction were investigated[23]. Therefore, the present research focused on: (1) investigating the impact of 2,6-DCP addition on nitrification; (2) examining the effect of the variation of operating conditions (temperature and pH) on recovery of nitrification; (3) reducing the concentration of 2,6-DCP to establish a balance between the sludge reduction and nitrification.

## Materials and Methods

The activated sludge used as initial seed was taken from a local municipal wastewater treatment plant in Harbin, China. After screened through a 2 mm sieve, activated sludge was cultivated in a 70 L batch reactor and operated in a batch mode (in 8 h cycle with 6 h of aeration, 2 h settling) at a mean room temperature of 20±1°C. The dissolved oxygen (DO) level was kept above 5 mg/L. Excess sludge withdrawing did not start until the mixed liquor suspended solids (MLSS) level exceeded 2000 mg/L. The MLSS level was then maintained at this level throughout the remaining period of cultivation. Sodium bicarbonate was employed to maintain the pH at around 7.0±0.2.

Tap water was used to prepare feed solutions throughout SBR operation. Synthetic wastewater, composed of glucose (final concentration equal to 400 mg COD/L), ammonium chloride and carbamide (final concentration 40 mg N/L), phosphate (final concentration 8 mg P/L), and other minerals ($MgSO_4$, $CaCl_2$, $MnSO_4$, $FeSO_4$, $CoCl_2$, $ZnSO_4$, and $CuSO_4$ with the final concentrations 40, 5, 1.25, 1.25, 0.3, 1.25, and 0.25 mg/L, respectively) were fed to the reactor three times a day.

In order to identify the effect of 2,6-DCP on nitrification, batch tests using the above activated sludge and the operating conditions were conducted in 7L reactors.

As important environmental factors affecting nitrification, temperature and pH were varied to do the research in the interest of repairing nitrification. Considering the practical application, T=18±1, 23±1, 28±1 °C, pH=6.5±0.2, 7.5±0.2, 8.5±0.2 were selected. When test the temperature, the pH was fixed at 7.0±0.2. To test the pH effect, sodium hydroxide of 1mol/L was used to control pH, while the temperature was fixed from the above tests, which slightly affected nitrification and guaranteed sludge reduction. The rest procedure experimental were the same as above mentioned.

All of the above batch experiments were carried out for 6 days with a sampling interval of 24 h. There were two reactors, one reactor was run as control reactor, the other reactor received a dose of 2, 6-DCP at a 20 $mg \cdot L^{-1}$ level once a cycle (the optimal dosage for sludge reduction observed in our previous study).

In order to identify the effective concentration of 2,6-DCP on sludge reduction, batch tests was conducted in 7L reactors at various initial concentrations of 2,6-DCP ranging from 1 to 20mg/L. The concentration which guarantee sludge reduction and slightly inhibit nitrification was selected. Then a month long experiment was done to investigate the effect of 2,6-DCP on the activated sludge system.

For components analyses, samples were taken from the batch reactors at the end of aeration time and immediately filtered through 0.45μm membranes. COD, $NH_4$-N, $NO_2$-N, $NO_3$-N, and MLSS were measured according to Standard Methods[24]. PH and DO were measured by pH meter and DO meter. The sludge decay may affect sludge yield which reflects a potential growth ability of sludge. The observed growth yield was actually determined from the increase in MLSS divided by the decrease in COD during the batch tests.

Calculation of the inhibition of nitrification of activated sludge by the test substance was made using the following formula:

$$\% \text{ Inhibition}=100-[\frac{S_1 - S_0}{C_1 - C_0} \times 100]$$

where $S_1$ is the concentration of oxidised nitrogen (mg N/L) in the reactor with 2,6-DCP after 2 h of incubation; $S_0$, the initial concentration of oxidised nitrogen (mg N/L) in the reactor with 2,6-DCP; $C_1$ is the concentration of oxidised nitrogen (mg N/L) in the control, after 2 h of incubation; $C_0$, the initial concentration of oxidised nitrogen (mg N/L) in the control.

All of the experiments were repeated 3 times, and the average values of these results were taken as final results. The experimental errors were not greater than 5%.

## Results and Discussion

### The Effect of 2,6-DCP on Nitrification

Fig. 1a showed the effect of 2,6-DCP on the observed growth yield of the activated sludge cultures at T=20±1°C and pH=7.0±0.2. The effect of 2,6-DCP on the sludge yield was obvious, the average sludge yield in the 2,6-DCP reactor was 0.306 mg MLSS/mg COD and the sludge reduction was about 34.6% compared to the control reactor.

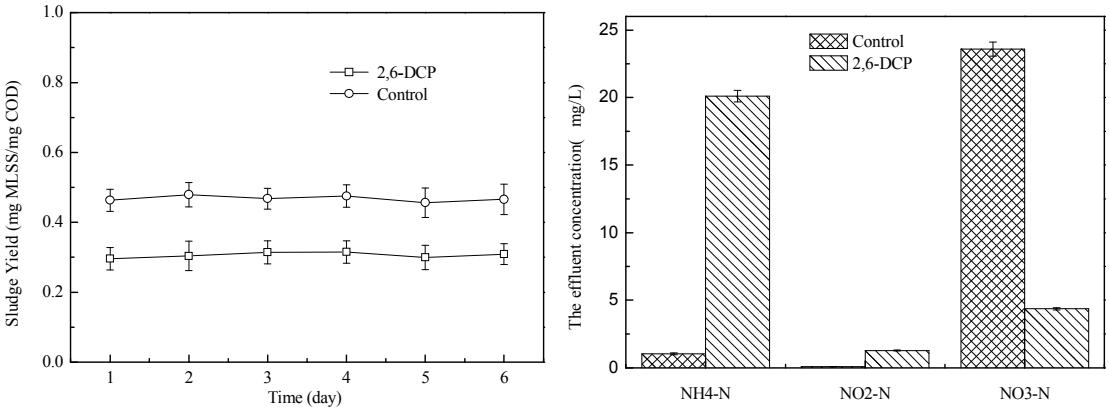



Fig. 1. Effect of 2,6-DCP on sludge yield and nitrification

Nitrification is the biological oxidation of ammonia with oxygen into nitrite followed by the oxidation of these nitrites into nitrates. The effect of 2,6-DCP on nitrification was illustrated in Fig. 1b, The average $NH_4$-N effluent concentration of the control reactor was about 1.04 mg/L, the $NH_4$-N removal efficiency was about 95.85%. It was apparent that the $NH_4$-N removal efficiency in the batch cultures was affected seriously by the presence of 2,6-DCP. In the 2,6-DCP reactor, the $NH_4$-N removal efficiency was only about 19.56%, $NO_2$-N was accumulated(1.28 mg/L), $NO_3$-N effluent concentration was 4.36 mg/L, nitrification was affected seriously, with the nitrification inhibition was about 76.17%. The destruction of nitrification may be caused by the inhibition of 2,6-DCP to ammonia oxidizing bacteria (AOB) and nitrite oxidizing bacteria (NOB).

### Recovery of Nitrification

Based on the above experimental results, 20mg/L 2,6-DCP could effectively reduce the sludge production and also affected the nitrification adversely. It has been reported that temperature and pH were important environmental factors affecting nitrification, so it is expected to repair nitrification through varying temperature and pH [25].

Table 1 showed the effect of 2,6-DCP on sludge reduction and nitrification of the activated sludge culture at 18±1, 23±1 and 28±1 °C. The sludge reduction was increased with the increase of temperature, which was 15.01% at 18±1°C, 34.62% at 23±1 °C and 35.67% at 28±1°C. $NH_4$-N removal efficiency in the control and 2,6-DCP reactors was also increased with the increase of temperature. The average $NH_4$-N removal rate was 97.4% and 46.8% in the control and 2,6-DCP

reactor at 28±1°C, respectively. Nitrification inhibition was also catabatic with the increase of temperature, from 83.68% to 49.36%. The increase of temperature was beneficial to nitrification, but which was still very inefficient in comparison with that of the control.

Table 1. Effect of 2,6-DCP on sludge and nitrification at various temperature (pH=7.0±0.2)

| Temperature (ºC) | | 18±1 | 23±1 | 28±1 |
|---|---|---|---|---|
| Sludge reduction (%) | | 15.01 | 34.62 | 35.67 |
| $NH_4$-N effluent concentration (mg/L) | control | 2.02±0.16 | 1.04±0.08 | 0.64±0.12 |
| | 2,6-DCP | 20.28±0.26 | 20.11±0.32 | 17.60±0.24 |
| $NO_2$-N effluent concentration (mg/L) | control | 0.07±0.01 | 0.08±0.01 | 0.07±0.01 |
| | 2,6-DCP | 0.23±0.03 | 1.28±0.12 | 2.27±0.13 |
| $NO_3$-N effluent concentration (mg/L) | control | 22.33±0.34 | 23.59±0.23 | 25.80±0.31 |
| | 2,6-DCP | 3.43±0.12 | 4.36±0.15 | 6.58±0.12 |
| Nitrification Inhibition (%) | | 83.68 | 76.17 | 49.36 |

Table 2 showed that the average sludge yield was 0.517, 0.541 and 0.539 mg MLSS/mg COD, which varied slightly when the pH increased from 6.5±0.2 to 8.5±0.2. The sludge yield decreased immediately with the addition of 2,6-DCP and the sludge reduction was 30.94%, 35.67 and 38.2%, respectively. There was no significant difference in the sludge yield in the control reactor among the certain pH, while the sludge yield in the 2,6-DCP reactor was reduced obviously and decreased with the increase of pH. This showed that the sludge reduction effect of 2,6-DCP depended greatly on pH.

The effect of pH on nitrification recovery was illustrated in Table 2. It could be concluded that $NH_4$-N removal efficiency in the control was 56.7%, 97.7% and 99.6% at pH=6.5±0.2, 7.5±0.2 and 8.5±0.2, respectively. While in the 2,6-DCP reactor, $NH_4$-N removal efficiency increased with pH increase from 6.5±0.2 to 8.5±0.2, it was 17.8%, 28.8% and 45.4%, respectively. Nitrification inhibition was also decreased with the increase of pH. It could be concluded that the increase of pH alleviated the deterioration of 2,6-DCP on nitrification to a certain extent.

Table 2. Effect of 2,6-DCP on sludge yield and nitrification at various PH (T=28±1ºC)

| pH | | 6.5±0.2 | 7.5±0.2 | 8.5±0.2 |
|---|---|---|---|---|
| Sludge reduction (%) | | 30.94 | 35.67 | 38.22 |
| $NH_4$-N effluent concentration (mg/L) | control | 10.83±0.14 | 0.64±0.08 | 0.09±0.02 |
| | 2,6-DCP | 20.55±0.34 | 17.60±0.23 | 13.64±0.17 |
| $NO_2$-N effluent concentration (mg/L) | control | 0.09±0.02 | 0.07±0.01 | 0.60±0.11 |
| | 2,6-DCP | 3.30±0.08 | 2.27±0.12 | 2.61±0.14 |
| $NO_3$-N effluent concentration (mg/L) | control | 24.92±0.35 | 25.80±0.37 | 27.43±0.42 |
| | 2,6-DCP | 11.86±0.23 | 6.58±0.16 | 12.41±0.34 |
| Nitrification Inhibition (%) | | 60.36 | 49.36 | 45.7 |

**Balance Between the Sludge Reduction and Nitrification**

The variation of temperature and pH alleviated the deterioration of 2,6-DCP on nitrification, however, the nitrification inhibition was still 45.7%. So it is necessary to reduce the concentration of 2,6-DCP.

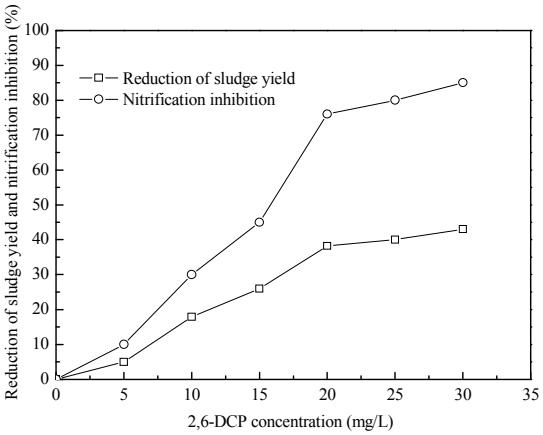



Fig. 2. Effect of 2,6-DCP on sludge reduction and nitrification inhibition

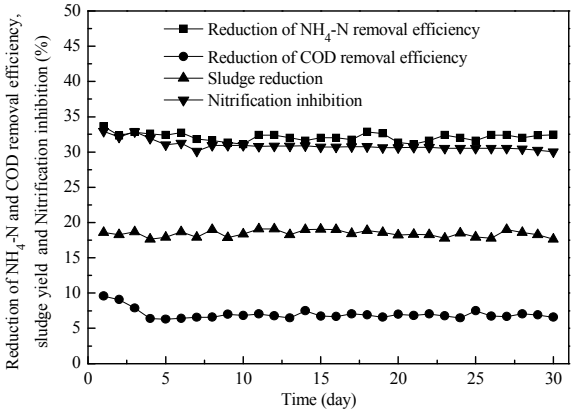



Fig. 3. Reduction of $NH_4$-N, COD removal efficiency and sludge yield and nitrification inhibition

Fig. 2 showed the effect of 2,6-DCP concentration on the reduction of sludge yield and nitrification inhibtion. It was apparent that a high 2,6-DCP concentration was in favor of a reduction in the sludge yield. This effect became more significant when the 2,6-DCP concentration was beyond 15mg/L, however, the nitrification was affected seriously. So 10mg/L was selected in the 30-day experiment. The sludge reduction was about 17.9% and the nitrification inhibition was about 30%.

These 30-day operation data in Fig. 3 had further confirmed that 10 mg/L 2,6-DCP can effectively cut down the sludge production. It was also clear that the activated sludge microorganisms would not establish resistance to the 2,6-DCP function and the nitrification inhibitation was acceptable. The reduction of COD removal efficiency (6.99%) was lower than the reduction of $NH_4$-N removal efficiency (31.78%), which indicated that autotrophic microorganisms were more sensitive to 2,6-DCP than heterotrophic microorganisms. It was possible to establish a balance between the sludge reduction and the nitrification inhibitation. It should be comprehensively considered the sludge reduction and removal of substrates and nutrients rather than the consideration of sludge reduction only when selecting the concentration of uncouplers.

**Conclusions**

1. Nitrification was affected adversely with the addition of 20mg/L 2,6-DCP, nitrification inhibition was about 76.17% compared to the control.

2. pH played an important role in the process of sludge reduction, which increased from 30.94% to 38.22% when the pH increased from 6.5±0.2 to 8.5±0.2 with the addition of 20mg/L 2,6-DCP.

3. Nitrification inhibition was recoveried to 45.7% with the the variation of operating conditions to T=28±1ºCand pH=8.5±0.2.

4. Nitrification inhibition reduced to 30% with the sludge reduction reduced to 17.9% by decreasing the concentration of 2,6-DCP to 10 mg/L.

5. A 30-day operation with the addition of 10mg/L 2,6-DCP indicated that the systerm was stable, the nitrification inhibition was about 30.91% and the sludge reduction about 18.41%.

**Acknowledgement**

This study was supported by the Major Science and Technology Program for Water Pollution Control and Management (No. 2013ZX07201007), the State Key Laboratory of Urban Water Resource and Environment, Harbin Institute of Technology (No. 2011DX01) and the Specialized Research Fund for the Doctoral Program of Higher Education (No. 20112302110060). The authors also appreciate the Funds for Creative Research Groups of China (No. 51121062).

**References**

[1] Y. Wei, R.T. Van Houten, A.R. Borger, D.H. Eikelboom, and Y. Fan, Minimization of excess sludge production for biological wastewater treatment, Water Research. 37 (2003) 4453-4467.

[2] J. Werther, and T. Ogada, Sewage sludge combustion, Progress in energy and combustion science. 25 (1999) 55-116.

[3] T. Mahmood, and A. Elliott, A review of secondary sludge reduction technologies for the pulp and paper industry, Water Research. 40 (2006) 2093-2112.

[4] G. Chen, S. Saby, M. Djafer, and H. Mo, New approaches to minimize excess sludge in activated sludge systems, Water Science & Technology. 44 (2001) 203-208.

[5] J. Wagner, and K.-H. Rosenwinkel, Sludge production in membrane bioreactors under different conditions, Water Science and Technology. (2000) 251-258.

[6] S. Rosenberger, U. Krüger, R. Witzig, W. Manz, U. Szewzyk, and M. Kraume, Performance of a bioreactor with submerged membranes for aerobic treatment of municipal waste water, Water Research. 36 (2002) 413-420.

[7] W. Ghyoot, and W. Verstraete, Reduced sludge production in a two-stage membrane-assisted bioreactor, Water Research. 34 (2000) 205-215.

[8] S. Yan, K. Miyanaga, X.-H. Xing, and Y. Tanji, Succession of bacterial community and enzymatic activities of activated sludge by heat-treatment for reduction of excess sludge, Biochemical Engineering Journal. 39 (2008) 598-603.

[9] M. Mayhew, and T. Stephenson, Low biomass yield activated sludge: a review, Environmental technology. 18 (1997) 883-892.

[10] E.W. Low, H.A. Chase, M.G. Milner, and T.P. Curtis, Uncoupling of metabolism to reduce biomass production in the activated sludge process, in Water Research, 2000, pp. 3204-3212.

[11] Y. Liu, Chemically reduced excess sludge production in the activated sludge process, Chemosphere. 50 (2003) 1-7.

[12] G.-H. Chen, H.-K. Mo, S. Saby, W.-K. Yip, and Y. Liu, Minimization of activated sludge production by chemically stimulated energy spilling, Water Science and Technology. (2000) 189-200.

[13] G.-H. Chen, and Y. Liu, Modeling of energy spilling in substrate-sufficient cultures, Journal of Environmental Engineering, 125 (1999) 508-513.

[14] S.E. Strand, G.N. Harem, and H.D. Stensel, Activated-sludge yield reduction using chemical uncouplers, Water Environment Research. (1999) 454-458.

[15] E.W. Low, and H.A. Chase, Reducing production of excess biomass during wastewater treatment, Water Research. 33 (1999) 1119-1132.

[16] M. van Loosdrecht, K. Dircks, J. Beun, J. Heijnen, G.-H. Chen, and Y. Liu, Modeling of Energy Spilling in Substrate-Sufficient Cultures, Journal of Environmental Engineering. 126 (2000) 979-980.

[17] Y. Liu, and J.-H. Tay, Strategy for minimization of excess sludge production from the activated sludge process, Biotechnology Advances. 19 (2001) 97-107.

[18] R.W. Okey, and H.D. Stensel, Uncouplers and activated sludge—the impact on synthesis and respiration, Toxicological & Environmental Chemistry. 40 (1993) 235-254.

[19] X.-F. Yang, M.-L. Xie, and Y. Liu, Metabolic uncouplers reduce excess sludge production in an activated sludge process, Process Biochemistry. 38 (2003) 1373-1377.

[20] C. Aragon, J. Quiroga, and M. Coello, Comparison of four chemical uncouplers for excess sludge reduction, in Environmental technology. 30 (2009) 707-714.

[21] E.W. Low, and H.A. Chase, The use of chemical uncouplers for reducing biomass production during biodegradation, Water Science and Technology. 37 (1998) 399-402.

[22] M. Mayhew, and T. Stephenson, Biomass yield reduction: Is biochemical manipulation possible without affecting activated sludge process efficiency?, Water Science and Technology. 38 (1998) 137-144.

[23] Y. Tian, J. Zhang, D. Wu, Z. Li, and Y. Cui, Distribution variation of a metabolic uncoupler, 2, 6-dichlorophenol (2, 6-DCP) in long-term sludge culture and their effects on sludge reduction and biological inhibition, Water Research. 2012.

[24] A.P.H. Association, Standard methods for the examination of water and wastewater, American Public Health Association. 1955.

[25] J.-H. Kim, X. Guo, and H.-S. Park, Comparison study of the effects of temperature and free ammonia concentration on nitrification and nitrite accumulation, in Process Biochemistry. 43 (2008) 154-160.

*Advanced Materials Research Vol. 937 (2014) pp 99-104*
*© (2014) Trans Tech Publications, Switzerland*
*doi:10.4028/www.scientific.net/AMR.937.99*

# Influence of Ethanol on the Interactions and Physical properties of Binary Mixtures of 1-ethyl-3-methylimidazolium Based ILs at 298.15 K.

Hina SABA[1,a], Yu-Mei ZHANG [1,b,*] and Hua-Ping WANG [1,c]

[1] State Key Laboratory for Modification of Chemical Fibers and Polymer Materials, Donghua University, Shanghai 201620, China

[a]xinashah@gmail.com, [b] zhangym@dhu.edu.cn, [c]wanghp@dhu.edu.cn

*Corresponding author

**Keywords:** Ionic liquid mixtures, Density, Refractive index, Conductivity, Viscosity, Ethanol.

**Abstract.** Density (ρ), refractive index (n), conductivity (κ) and viscosity (η) measurements have been carried out for binary mixtures of imidazolium based ionic liquids with ethanol at 298.15 K. Excess molar volumes have been calculated from experimental data and was fitted by Redlich-Kister equation. The density and refractive index increase with increasing ionic liquid (IL) concentration. Addition of IL leads to increased conductivity initially within these mixtures, which is subsequently followed by gradual decrease in IL-rich region showing the restricted ion mobility and enhanced interactions within these mixtures. Viscosity was found to be increase gradually with increasing IL concentration. It has been observed that solubility parameters, dielectric constant and nature of anions of ILs being used play a vital role in determining the fate of resultant properties.

## Introduction

Ionic liquids (ILs) are a class of solvents that have shown great potential in different technological processes due to their unique properties such as extremely low vapor pressure [1, 2]. Immidazolium based ionic liquids have found great applicability especially in the processing of polymers, mainly focusing on the dissolution and further processing of lignocellulosic biomass. As it is known that ILs are quite expensive and also exhibit high viscosity in certain cases which could hinder their applicability in certain fields. In order to fully exploit the potential of ionic liquids as solvent and recovery medium in various applications, it would be crucial to investigate certain binary systems of ILs with organic solvents. As the competence of such ILs systems is strongly dependent on the molecular interactions between ILs and organic solvents [3], the studies of various physical properties could definitely provide an insight into the extent of interactions monitoring the resultant properties of the mixtures. Previously, various studies focusing on the mixtures of ILs with organic solvent have been reported [4-8]. The ILs being used in our studies comprise of 1-ethyl-3-methylimidazolium acetate ([EMIM]OAc), 1-ethyl-3-methylimidazolium formate ([EMIM]COOH) and 1-ethyl-3-methylimidazolium methyl phosphate ([EMIM][$PO_2(CH_3)H$]). Immidazolium based ILs have received much more attention due to their applicability in polymer processing most importantly, cellulose [9]. Ethanol is one of the versatile solvents used in various chemical and technological processes and is relatively cheap [10]. Conductivity, density, viscosity and refractive index measurements have been carried out in order to discuss the effect of the underlying interactions on the mass and transport properties of these mixtures.

## Experimental

### Materials and Instrumentation

[EMIM]OAcand [EMIM]COOH were purchased from Chengjie chemical. Ethanol has been bought from Shanghai chemicals.[EMIM][$PO_2(CH_3)H$] has been prepared in laboratory following the procedure mentioned by Fukaya et al. [9]. The details of the chemicals being used with their

percentage purity and water fraction have been illustrated in Table 1. The purity of ILs was verified in terms of NMR analysis. The water mass fraction of ILs was determined by the Karl Fisher titration (ZSD-2 KF Cany Precision Instruments Co, Ltd.). A 2WAJ Abbe refractometer has been used for the measurements of the refractive index. Calibration of the instrument has been done by means of deionized water.

Table 1. Purity grades with experimental and theoretical values for properties of the pure ILs and ethanol along with Hildebrand, Hansen solubility parameters and dielectric constants at 298.15 K

| Purity Grades and physical data for pure components | | | | | | | | |
|---|---|---|---|---|---|---|---|---|
| Component | Purity [%] | Water Mass Fraction | n | | ρ [g.mL$^{-1}$] | | η [mPa.s] | |
| | | | Exp. | Lit. | Exp. | Lit. | Exp. | Lit. |
| [EMIM][$PO_2(CH_3)H$] | >98 | 0.19 | 1.489 | - | 1.191 | - | 43.14 | - |
| [EMIM]OAc | 99.3 | 0.12 | 1.49 | - | 1.135 | - | 32.13 | - |
| [EMIM]COOH | 99.1 | 0.15 | 1.466 | - | 1.229 | - | 6.734 | - |
| Ethanol | >99.5 | - | 1.359 | 1.35[20] | 0.786 | 0.785[20] | 1.094 | 1.09[20] |

| Solubility Parameters and Dielectric constants | | | | | |
|---|---|---|---|---|---|
| Solvent | Hildebrand Solubility parameters [MPa$^{1/2}$] | Hansen solubility parameters [MPa$^{1/2}$][19] | | | Dielectric constants |
| | Δ | $\delta_d$ | $\delta_p$ | $\delta_h$ | ε |
| Ethanol | 12.92 | 15.8 | 8.8 | 19.4 | 24.20[19] |

The conductivity measurements were made with a DDSJ-308A conductometer (Shanghai Optical Instrument Factory, cell constant=1.0 cm$^{-1}$); uncertainty was found to be 0.5 %. The viscosity was determined by an Ubbelohde viscometer (inner diameter=1.5 mm). The temperature of the sample was maintained at 298.15±0.01K with an external temperature controller (SYP Electro-thermostatic water cabinet). The uncertainty was found to be 2.0+10$^{-3}$ mPa.s. Before measuring the densities, DA-130N Density Specific Gravity Meter was calibrated with pure water at298.15±0.01 K. The uncertainty in density was estimated to be 5×10$^{-4}$ g.cm$^{-3}$. Repetition of all the data was carried out three times.

**Results and Discussions**

Various models have been used for describing the underlying interactions between ILs and ethanol. In order to elucidate the extent of interaction within solute-solvent molecules, the excess molar volumes ($V^E$) were calculated for all the systems by Eq. 1 [11]:

$$V^E = \frac{x_1M_1 + x_2M_2}{\rho} - \left(\frac{x_1M_1}{\rho_1} + \frac{x_2M_2}{\rho_2}\right) \quad (1)$$

Where ρ depicts density of mixtures; x and M represents mole fractions and molar masses. Subscripts 1 and 2 correspond to pure ionic liquid and ethanol, respectively. All values of excess molar volume have been fitted by using Redlich-Kister polynomial equation:

$$V^E = x_1(1 - x_1)\sum_{i=0}^{k} A_i\,(2x_1 - 1)^i \quad (2)$$

Where ($A_i$) is adjustable parameter. The standard deviations (σ) have been calculated by using Eq. 3:

$$\sigma = \left[\sum \frac{(V^E_{exp} - V^E_{calc})^2}{n - p}\right]^{1/2} \quad (3)$$

For viscosity measurements, data has been fitted by empirical equations suggested by Seddon *et al.* [4] as shown below:

$$\eta = \eta_{IL} \exp(A x_s) \quad (4)$$

Here, $\eta$ and $\eta_{IL}$ denote the viscosities of mixtures and pure ILs, respectively. $x_s$ is the mole fraction of ethanol in the mixtures; and A is a constant.

**Density and refractive index of ILs+ethanol binary mixtures**

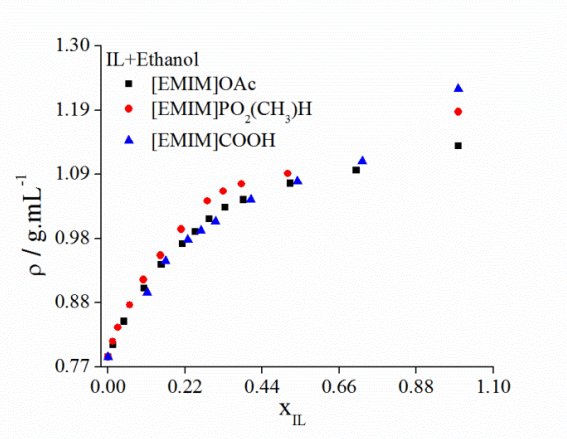



Fig. 1. Relationship between density and mole fraction of IL ($x_{IL}$) of ethanol with ILs at 298.15 K

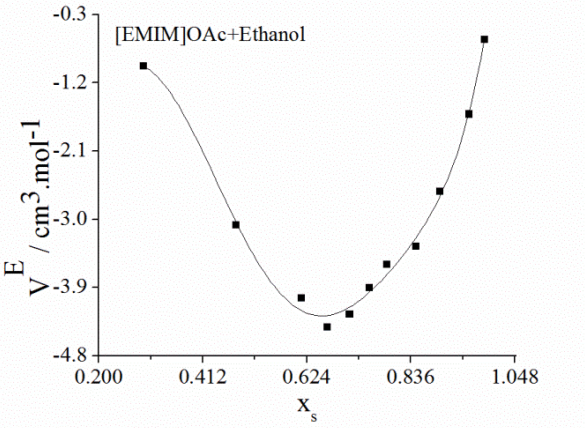



Fig. 2. Plot of excess molar volumes against mole fractions of ethanol ($x_s$) for the mixture of [EMIM]OAc with ethanol at 298.15 K. Solid line represents the Redlich-Kister fit.

The relationship of densities and mole fractions (x) of different ILs with ethanol has been shown in Fig. 1. It is clearly indicated that density of the mixtures increase with increasing concentration of IL [12, 13]. In order to elucidate further interactions, excess molar volumes ($V^E$) have been calculated by means of Eq. 1. The data has been fitted by Redlich-Kister equation and has been shown in Fig.2.

Table 2. Coefficients of Redlich Kister Equation for $V^E$ of Different ILs/organic solvents at 298.15 K.

| Systems | $A_0$ | $A_1$ | $A_2$ | $A_3$ | $A_4$ | σ |
|---|---|---|---|---|---|---|
| [EMIM]OAc +ethanol | -12.97 | -24.23 | 13.58 | 33.10 | -53.65 | 0.045 |
| [EMIM]$PO_2(CH_3)$H +ethanol | -3.798 | -16.39 | -243.7 | 603.403 | -407.6 | 0.139 |
| [EMIM]COOH +ethanol | 7.805 | -24.94 | -3.765 | -52.310 | 74.11 | 0.515 |

The negative values of $V_E$ are due to the chemical intermolecular interactions which lead to volume decrease, and include charge transfer type forces and complex forming interactions among the molecules of ILs and ethanol. For [EMIM]COOH system, certain positive values could be observed for excess molar volumes especially at higher concentrations of IL. It could be suggested that as $COOH^-$-anion is known to make dimmers within solvent system; it's quite obvious that the ethanol moieties failed to disrupt this strong network of dimmers of IL molecules with eachother. This dominant behavior of the IL molecules leads to weak interactions in the IL-rich region. The relationship of refractive index with mole fraction has shown a gradual increase with increasing mole fraction (Fig.3) for all the ILs+ethanol systems as being suggested by many studies reported in literature [14]. Generally, polar and dipolar solvents of high dielectric constants show better miscibility with ILs indicating polar solvents have stronger molecular interactions with ILs [4]. Deetlefs et al. [15] and Brocos et al. [16] reported that the larger the reduced molar free volume of the substance, the smaller would be its refractive index. So it could be suggested that in case of ILs with

anions, $[PO_2(CH_3)H]^-$ and $OAc^-$; increasing concentration within solution would lead to more interactions and hence more aggregate formation. But in case of [EMIM]COOH+ethanol, the mixture still show aggregates formation or more interactions. Hereby, it is necessary to suggest that absence of free volume in this case is more due to interactions in ILs molecules itself rather than IL-ethanol molecule's interactions.

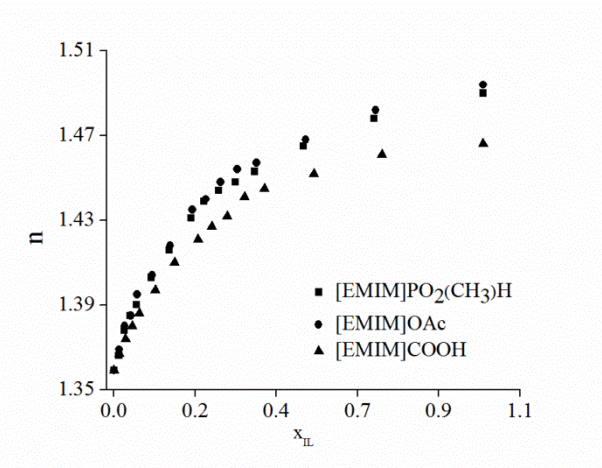



Fig.3. Relationship between refractive index and mole fraction of IL ($x_{IL}$) of ethanol with ILs at 298.15 K

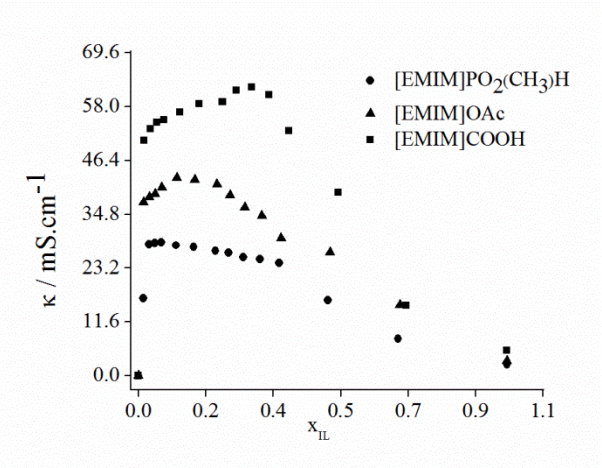



Fig. 4. Relationship between conductivity and mole fraction of IL ($x_{IL}$) of ethanol with ILs at 298.15 K.

**Conductivity and viscosity on ILs+ethanol binary mixtures**

Conductivity measurements are quite crucial in liquid systems as it depends on the extent of associations and dissociations within solvent molecules in mixtures. For ethanol+ILs mixtures, it follows the general trend (Fig. 4) i.e. the conductivity increase rapidly in the organic solvent-rich region and then gradually decreases IL-rich region. Related data has been shown in Table 2.
The increase of conductivity in high organic rich-region could be attributed to the rapid and free movement of ions more easily as compared to IL-rich region which can obstruct the motion of ions due to aggregates formation/association [17].

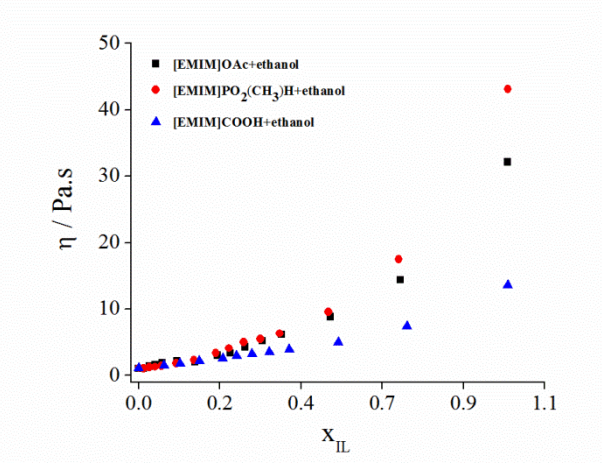



Fig. 5. Relationship between viscosity and mole fraction of ILs ($x_{IL}$) with different organic solvents at 298.15 K.

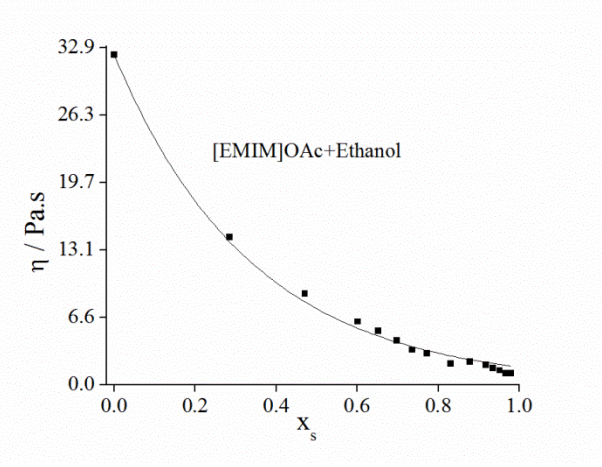



Fig. 6. Relationship between viscosity and mole fraction of ethanol ($x_s$) with ILs at 298.15 K.

Viscosities of binary mixtures, ILs+ethanol; has been measured as shown in Fig.5. For each IL, ethanol was found to interact in same manner. The data was fitted with Seddon equation (Eq. 4) as shown in Fig. 6. It has been observed that the viscosity of mixtures is decreased with increasing

concentration of organic solvent and vice versa. Due to occurrence of diverse interactions and aggregation within pure ILs, their addition in certain mixture will lead to enhanced viscosities and therefore hindered mobilities of ions. Similar behavior has been observed previously for different mixtures of ILs with organic solvents [18]. The A values along with their standard deviations have been listed in Table 3. It is quite evident that parameter A varies for all the systems. The values show variation depending on the nature of the ILs. The experimental data fit accurately by using Eq. 6.

Table 3. The A values and the standard deviations of the fit for the viscosities of ILs+ethanol.

| Systems | A | σ |
|---|---|---|
| [EMIM]OAc+Ethanol | -2.877+0.052 | 0.347 |
| [EMIM]COOH+Ethanol | -2.172+0.031 | 0.137 |
| [EMIM][PO2(CH3)H] +Ethanol | -3.185+0.051 | 0.402 |

## Conclusions

The density, refractive index, viscosity and conductivity measurements for the mixtures of [EMIM]-based ILs with ethanol have been reported. All mixtures have shown ideal behavior for the density, and refractive index measurements i.e. increase with increasing IL concentration. Excess molar volumes studies showed the existence of considerable interactions and aggregates formation within these mixtures. This behavior was further confirmed by refractive index measurements by the unavailability of free volume within these mixtures as the concentration of IL is increased. Conductivity measurements have shown enhanced electrical conductivity and ion mobility in organic-rich region. Viscosity was found to be increased by the addition of ILs. It was evaluated that the molar mass and hydrogen bonding ability of anion, solubility parameters and dielectric constants of ethanol play an important role in determining the extent of solute-solvent interactions within these mixtures.

## Acknowledgements

This work is supported by a grant from National Natural Science Foundation of China (51273041).

## References

[1] E.J. Gonzalez, B. Gonzalez, N. Calvar, A. Dominguez, Physical properties of binary mixtures of the ionic liquid 1-ethyl-3-methylimidazolium ethyl sulfate with several alcohols at T = (298.15, 313.15, and 328.15) K and atmospheric pressure, J. Chem. Eng. Data. 52(2007) 1641-1648.

[2] R. Bernini, A. Coratti, G. Provenzano, G. Fabrizi, D. Tofani, Oxidation of aromatic aldehydes and ketones by H2O2/CH3ReO3 in ionic liquids: a catalytic efficient reaction to achieve dihydric phenols, Tetrahedron. 61 (2005) 1821-1825.

[3] P. Attri, P. Venkatesu, T. Hofman, Temperature dependence measurements and structural characterization of trimethyl ammonium ionic liquids with a highly polar solvent, J. Phys. Chem. B. 115 (2011) 10086-10097.

[4] K.R. Seddon, A. Stark, M.-J. Torres, Influence of chloride, water, and organic solvents on the physical properties of ionic liquids, Pure Appl. Chem. 72 (2000) 2275-2287.

[5] Ciocirlan, O. Croitoru, O. Iulian, Densities and viscosities for binary mixtures of 1-butyl-3-methylimidazolium tetrafluoroborate ionic liquid with molecular solvents, J. Chem. Eng. Data. 56 (2011), 1526-1534.

[6] S. Sarkar, R. Pramanik, C. Ghatak, P. Setua, N. Sarkar, Probing the interaction of 1-ethyl-3-methylimidazolium ethyl sulfate ([emim][etso4]) with alcohols and water by solvent and rotational relaxation,J. Phys. Chem. B. 114 (2010)2779-2789.

[7] S. Singh, M. Aznar, N. Deenadayalu, Densities, speeds of sound, and refractive indices for binary mixtures of 1-butyl-3-methylimidazolium methyl sulphate ionic liquid with alcohols at T = (298.15, 303.15, 308.15, and 313.15) K, J. Chem. Thermodynamics. 57 (2013) 238-247.

[8] D. Matkowska, T. Hofman, Volumetric properties of the ionic liquids: [C6mim][MeSO4], [C6mim][EtSO4], [C4mim][EtSO4] and their mixtures with methanol or ethanol, J. Mol. Liq. 177 (2013) 301-305.

[9] Y. Fukaya, K. Hayashi, M. Wada, H. Ohno, Cellulose dissolution with polar ionic liquids under mild conditions: required factors for anions, Green Chem. 10 (2008) 44-46.

[10] K.A. Kurnia, B. Ariwahjoedi, M.I. Abdul Mutalib, T. Murugesan, Density and excess molar volume of the protic ionic liquid bis(2-hydroxyethyl)ammonium acetate with alcohols, J. Solution Chem. 40 (2011) 470-480.

[11] Redlich, A.T. Kister, Algebraic Representation of Thermodynamic Properties and the Classification of Solutions, Ing. Eng. Chem. 40 (1948) 345-348.

[12] D. Wu, B. Wu, Y.M. Zhang, H. Wang, Density, viscosity, refractive index and conductivity of 1-allyl-3-methylimidazolium chloride+water mixture,J. Chem. Eng. Data. 55 (2010) 621-624.

[13] Iulian, O. Ciocirlan, Volumetric properties of binary mixtures of two 1-alkyl-3-methylimidazolium tetrafluoroborate ionic liquids with molecular solvents, J. Chem. Eng. Data. 57 (2012) 2640-2646.

[14] M. Anouti, A. Vigeant, J. Jacquemin, C. Brigouleix, D. Lemordant, Volumetric properties, viscosity and refractive index of the protic ionic liquid, pyrrolidiniumoctanoate, in molecular solvents,J. Chem. Thermodynamics. 42 (2010) 834-845.

[15] M. Deetlefs, K.R. Seddon, M. Shara, Predicting physical properties of ionic liquids, Phys. Chem. Chem. Phys. 8 (2006) 642-649.

[16] P. Brocos, A. Pin˜eiro, R. Bravo, A. Amigo, Refractive indices, molar volumes and molar refractions of binary liquid mixtures: Concepts and correlations, Phys. Chem. Chem. Phys. 5 (2003) 550-557.

[17] H. Every, A.G. Bishop, M. Forsyth, D.R. MacFarlane, Ion Diffusion in Molten Salt Mixtures Electrochim. Acta . 45 (2000) 1279-1284.

[18] M.T.Z.-Moattar, R.M.-Cegincara, Viscosity, density, speed of sound, and refractive index of binary mixtures of organic solvent + ionic liquid, 1-butyl-3-methylimidazolium hexafluorophosphate at 298.15 K, J. Chem. Eng. Data. 52 (2007)2359-2364.

[19] A.F.M. Barton, Handbook of Solubility Parameters, CRC Press, 1983.

[20] H.A. Zarei, M.Z. Lavasani, H. Iloukhani, Densities and volumetric properties of binary and ternary liquid mixtures of water (1) + acetonitrile (2) + dimethyl sulfoxide (3) at temperatures from (293.15 to 333.15) K and at ambient pressure (81.5 kPa), J. Chem. Eng. Data. 53 (2008) 578-585.

*Advanced Materials Research Vol. 937 (2014) pp 105-108*
*© (2014) Trans Tech Publications, Switzerland*
*doi:10.4028/www.scientific.net/AMR.937.105*

# The Corrosion Evaluation Methodology of the Lock Gate

Chao-hua JIANG[A], Ke FAN[B,*], Xiang-yun LUO[C], Liang QIAN[D]

No.1 Xikang Road, College of Harbour, Coastal and Offshore Engineering, Hohai University, Nanjing 210098, China

jiangnjhhu@sina.com,fanke200890@126.com,q156411098@126.com, qianliang_1340@126.com

Corresponding author email: fanke200890@126.com

**Keywords**: lock gate, corrosion, evaluation, indicator, dispose

**Abstract**: Influenced by surrounding environment, performance load and eroded by all kinds of media, the structure of lock gate prone to corrosion phenomena. Therefore, aimed at the situation of gate corrosion, to carry out the appraisal method for gate, a gate corrosion detection rating method is established. Based on the environment characteristics, taking corrosion appearance, coating thickness, the residue corrosion depth and corrosion pit depth as the index to evaluate,provides the judgment and evaluation basis for the lock gate is in need of repair.

## Introduction

It exists some different extent corrosion phenomenonon the lock gate running for many years. It may lead to reduce the cross section area, increase the stress, reducing the strength and the stiffness of the whole structure, and affect the safe operation of the structure directly. Thus according to the corrosion condition of the lock gate, carried out the study of gate evaluation technique, is to meet the daily efficiency of the gate lock and it is necessary measures to ensure the safe and efficient operation of the lock gate structure.

## Research on the Situation of the Lock Gate Corrosion Evaluation Methodology

In the existing specifications only "Scrapping standard of metallic structure of hydraulic and hydropower engineering " (SL-98) hasregulations. Corrosion of steel lock gate evaluation is generally based on the thickness after corrosion and the corrosion rate forstructural stress computation and safety assessment of structure analysis. Zhou [1] used metal thickness gauge to measure the virtual thickness after corrosion as the basis of repair or replacement for the lock gate through checking local bending stress intensity. Wang etc. [2] used corrosion situation, bending resistance, shearing resistance and deflection of the four indicators to evaluate the safety of hydraulic structure and to forecast the service life on the basis of current specification. Su [3] evaluated the lock gate of control sluice is based on the analysis of instrument testing and data processingthrough adopting its structural strength and rigidity with spatial static finite element. Duan [4] checked the stress of components, calculating the remaining useful life and determined when to change or by reinforcing measures according to the thickness after corrosion.

The current specification for steel lock gate of evaluation is lack of specificity and comprehensiveness. There is no special specification to follow for the lock gate corrosion evaluation. Thus according to the operation condition and the structural features of the lock gate, established a lock gate evaluating system correspondingly and a comprehensive evaluation research aimed at structure corrosion characteristics of the lock gate, and provided a basis for judgment and evaluation for repairment.

## Selection of Evaluation Indicators

There are varying degrees of corrosion in most of lock gates; the corrosion speed and the degree of corrosion of the lock gate are closely related to the operation condition, surrounding environment, water quality, the quality of the steel and the anti-corrosion measures. Based on the environment characteristics, we take corrosion appearance, the thickness of the coating thickness, the corrosion residue depth and corrosion pit depth as the index to evaluate.

Corrosion appearanceevaluations include pulverization, discoloration, cracks, blistering, peeling and rust on the surface of the steel structure, as well as the surface erosion, corrosion, pitting, or perforation and distribution are included.

Coating thickness is the thickness of dry film in the steel structure surface of lock gate, which is compared with the original design thickness, on this basis for safety assessment and corresponding treatment measures.

Corrosion residual thickness plays an important role in safety assessment. According to the corrosion residual thickness, the parameters such as corrosion rate and section size after corrosion can be received, which can providesthe safety evaluation of the gate. Therefore this research formulates erosion thickness conversion into grade corrosion rate in accordance with therelevant standards and literature [5] as formula (1)

$$\varepsilon = \frac{A_1}{A} \tag{1}$$

In the formula: $A_1$—the decrease section area of component caused by different kinds of corrosion

A—the section area of component before corrosion

Corrosion pit depth can evaluate the hidden danger and destructiveness of the lock gate. The evaluation content includes the depth of pit corrosion or hole depth, size, location, and the density of the pit or hole corrosion etc.

**The Corrosion Evaluation Methodology for Lock Gate**

There is no corresponding specification for the lock hydraulic structures, the result of testing will be divided into A,B,C and D four levels(Table 1)reference to “Technical Code of Safety Inspection for Hydraulic Steel Gate and Hoist Machinery”(DL/T 835-2003), “Technical Specification for Detection an Assessment of Harbour and Marine Structures”(JTJ302-2006) and “Standard for Abolition of Hydraulic and Hydropower Metal Structure”(SL-98), then requirements for the processing of repair and reinforcement processing can be done by relevant specification (Table 1).

Table 1. Grade estimation for lock gate testing project

| Test items | Grade | |
|---|---|---|
| Corrosion appearance | A | No pulverization discoloration or mild pulverization discolora tion, no crack, blistering and peeling rust; Slight corrosion. Surface coating in mainly good condition, the local has a bi t of plaques or unconspicuous corrosions, no pitted phenome non or only a small amount of scattered corrosion pit. |
| | B | Obvious pulverization discoloration, decentralized crack, blist ering and peeling rust area is not greater than 0.3%. Partial coating peeling, obvious plaque, corrosion pits, corrosion pi t depth is less than 0.5 mm, or deeper pits, depth between 1.0 mm and 2 mm, but relatively scattered |
| | C | More serious pulverization discoloration, crack foaming and rust area is greater than 0.3%. Large area of surface coatings fall off, loss area is not less than 100 mm×100 mm, or the coating separate from metal or there are corrosion scales between them. There are dense patches of corrosion pits, 1.0 mm to 2.0 mm in depth range. |
| | D | Severe pulverization discoloration, a wide range of crack, bl ister and the fall off and rust area is more than 1.0%. Corr |

| | | |
|---|---|---|
| | | osion pits deepand dense slices, there are deep pits which d epth more than 3.0 mm in local component, appearing the phenomenon such as holes etc.. |
| Coating thickness | A | The coating dry film thickness is not less than 90% of the thickness of the original design. |
| | B | The coating dry film thickness is not less than 90% of the thickness of the original design and not less than 75%. |
| | C | The coating dry film thickness is less than 75% of the thic kness of the original design. |
| | D | The coating dry film thickness is less than 75% of the thic kness of the original design, and easy to peel by knife. |
| the residue corrosion depth | A | Coating in good condition, few rusty spot, a small amount of scattered shallow rust pit, corrosion rate $\varepsilon < 2\%$. |
| | B | Coating disbonding,appearing dispersed rust pit, component i s not significantlyweaken, corrosion rate $2\% \leq \varepsilon < 6.5\%$. |
| | C | Coating on large area of disbonding,large area of dense patc hes of rusts or textured severely in surface,deep rust pit in local component, the component has a certain degree weake n, corrosion rate $6.5\% \leq \varepsilon < 12\%$. |
| | D | Dense patches of deep rust pits, severe deep pits in local c omponent, component severely weakened, corrosionrate $12\% \leq \varepsilon < 20\%$. |
| | remark | When the corrosion residual thickness less than 6 mm, the component of lock gate must be scrapped. |
| corrosion pit depth | A | Few scattered corrosion pits on the surface of metal. 1 or 2 corrosion pits within the scope of 300 mm×300 mm, no more than 4 in intensive place. |
| | B | Obvious corrosion pits, corrosion pit depth is less than 0.5 mm, or deeper pits, depth between 1.0 mm and 2 mm, but scattered. No more than 30 corrosion pits within the scope of 300 mm×300 mm, no more than 60 in intensive place. |
| | C | Corrosion pit depth is between 1.0 mm and 2.0mm, more than 60 corrosion pits within the scope of 300 mm×300 mm, or with heavier textured phenomenon , no more than 60 corrosion pits within the scope of 300 mm×300 mm, but more than 2.5 mm in depth. |
| | D | Dense patches of deep rust pits, severe deep pits above 3.0 mm in local component,appearing deterioration phenomenon such as holes. |

Contraposed 4 indicators above for the lock gate, the test results can be obtained on the basis of Table 2.

Table 2. Structure evaluation classification and processing requirements for lock gate

| Grade | The classification standard | Processing requirements |
|---|---|---|
| A | The deterioration degree conforms to grade A standard requirement | Do not take measures |
| B | The deterioration degree conforms to grade B standard requirement | Repair measures in a timely manner |
| C | The deterioration degree conforms to grade C standard requirement | Take immediate repair and reinforcement measures |
| D | The deterioration degree conforms to grade D standard requirement | Repair and reinforcement measures depending on the condition or scrapped |

## Conclusion

In this paper,based on the environment characteristics, taking corrosion appearance, coating thickness, the residue corrosion depth and corrosion pit depth as the index to evaluate, according to the criterion of evaluation and processing, provides the judgment and evaluation basis for the lock gate is in need of repair. The corrosion evaluation methodology has a strong operability for the evaluation for the lock gate.

## References

[1] Zhou Li. The inspection and strength calculation of hydraulic steel gate[J]. China rural water and hydropower,2007,1:97~99

[2] Wang Bin,Li Jun.The hydropower engineering software development of steel structure evaluation.[J]. Water resources and hydropower engineering,2003,34(3):5~8

[3] Su Jianming,Chen Fei,Ye Xiaoqiang.Detection and safety appraisal for the lock gate in operation.[J],Journal of Yangtz River Scientific Research Institute,2011,23(8):24~27

[4] DuanHongqin,BaiYunfeng.Test and life prediction of aging lock gate.[J]. Water Resources and Hydropower of Northeast China,2004,22(234):17~19

[5] GuoJianbin,Zhang Qingwu.Corrosion of steel gate component and safety diagnosis research.[J]. Corrosion and Protection,2004,25(12):513~517

*Advanced Materials Research Vol. 937 (2014) pp 109-112*
*© (2014) Trans Tech Publications, Switzerland*
*doi:10.4028/www.scientific.net/AMR.937.109*

# Adsorption Behavior and Corrosion Inhibition of *S*-benzyl *o*-phenylenedioxydithiophosphate for Carbon Steel in Hydrochloric Acid Solution

Xiu-lan ZHANG[1, a,*], Xiao LIN[2] , Bin XIE[1, 3, b], Li-ke ZOU[1,3], Sha-sha ZHU[2], Yan LU[1] ,Jian-shen FENG[1,3] and Yu-long LI[1]

[1]Institute of Functional Materials,Sichuan University of Science & Engineering,China

[2]School of Material and Chemical Engineering, Sichuan University of Science & Engineering,China

[3]Material Corrosion and Protection Key Laboratory of Sichuan Province, China

[a,*]zxlsuse@sina.com, [b]xiebinqhg@sina.com.cn

**Keywords:** *O,O'*-dialkyldithiophosphates, Corrosion inhibitor, Carbon steel, Adsorption

**Abstract.** The corrosion inhibition of *S*-benzyl *o*-phenylenedioxydithiophosphate(BPOTP), for carbon steel in hydrochloric acid solution was studied by electrochemical measurements and weight loss measurements. Polarization curves indicate BPOTP is a mixed-type inhibitor, and the effects of temperature, hydrochloric acid concentration and immersion time were also studied. The studies of weight loss measurement show that the inhibition efficiency was up to 92.82 % at the BPOTP concentration of 40 $mg \cdot L^{-1}$ in 1.0 M hydrochloric acid solution at 30°C. The adsorption of BPOTP on carbon steel surface obeys the Langmuir isotherm.

## Introduction

Acid solutions are often used in industry for cleaning, decaying and pickling of steel structures, processes which are normally accompanied by considerable dissolution of the metal, A useful method to protect metals and alloys deployed in service in aggressive environments against corrosion is addition of species to the solution in contact with the surface in order to inhibit the corrosion reaction and reduce the corrosion rate. Inhibitor is a chemical additive that can effectively inhibit the corrosion of a metal in a corrosive environment with only a small amount of addition[1-4]. Compared with other corrosion protection technologies, using inhibitors has some advantages, such as no special equipment required, low cost and easy operation.

*O*,*O*'-dialkyldithiophosphates and their complexes have been explored extensively in the past decades because of their potential use as anti-oxidants, insecticides, flotation reagents, additives to lubricating oils[5-6]. There were no studies have investigated the corrosion inhibition of *S*-alkyl *O,O'*-dialkyldithiophosphate for ferrous alloys and steels. The present study is to investigate the inhibitive action of *S*-benzyl *o*-phenylenedioxydithiophosphate(BPOTP) on corrosion of carbon steel in hydrochloric acid solution.

## Experimental

### Materials Preparation

Carbon steel was used in electrochemical, weight loss measurement. The solution of hydrochloric acid was used for all studies. All of the electrochemical measurements were carried out using a conventional three-electrode cell consisting of a carbon steel working electrode, a saturated calomel electrode (SCE) as reference and a graphite counter-electrode. The working electrode was prepared by embedding the carbon steel plate in epoxy resin and exposing a flat surface.The electrochemical measurements(polarization curves) were obtained by changing the electrode potential automatically from (E±150 mV) at open circuit potential with a scan rate 0.5 mV/s to study the effect of BPOTP on carbon steel corrosion.

The electrochemical measurements. The inhibition efficiency was determined using Eq. 1:

$$IE\ (\%) = \frac{I_0 - I_1}{I_0} \times 100 \quad (1)$$

Where $I_0$ and $I_1$ are the corrosion current densities in absence and presence of BPOTP, respectively.

Weight loss measurements. The inhibition efficiency IE% and surface coverage (θ) was determined using Eq. 2-3:

$$IE(\%) = \frac{W_0 - W_1}{W_0} \times 100 \quad (2)$$

$$\theta = \frac{W_0 - W_1}{W_0} \quad (3)$$

Where $W_0$ and $W_1$ are the weight loss values in absence and presence of BPOTP, respectively.

## Results and Discussion

### Type of Inhibitor

As seen in Fig.1, both anodic and cathodic reactions on carbon steel electrode were inhibited in the presence of BPOTP. The results reveal that the BPOTP is a mixed-type inhibitor.

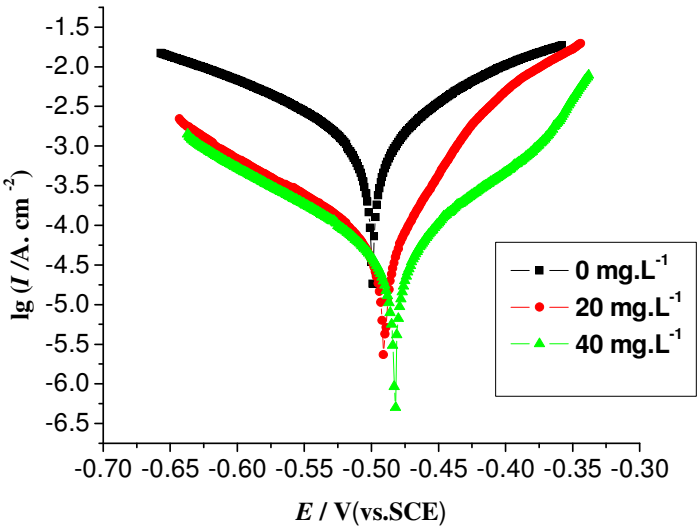



Fig. 1. Polarization curves for carbon steel in 1.0M hydrochloric acid solution with different concentration range of BPOTP at 30°C

### Electrochemical Measurements

The effect of temperature, hydrochloric acid concentration, and immersion time on corrosion behavior of carbon steel in the presence of 40mg·$L^{-1}$ BPOTP concentration was studied and the results were shown in Fig. 2(a), 2(b) and 2(c), respectively. The inhibition efficiency of BPOTP remained stable as acid concentration, temperatures and immersion time increasing.

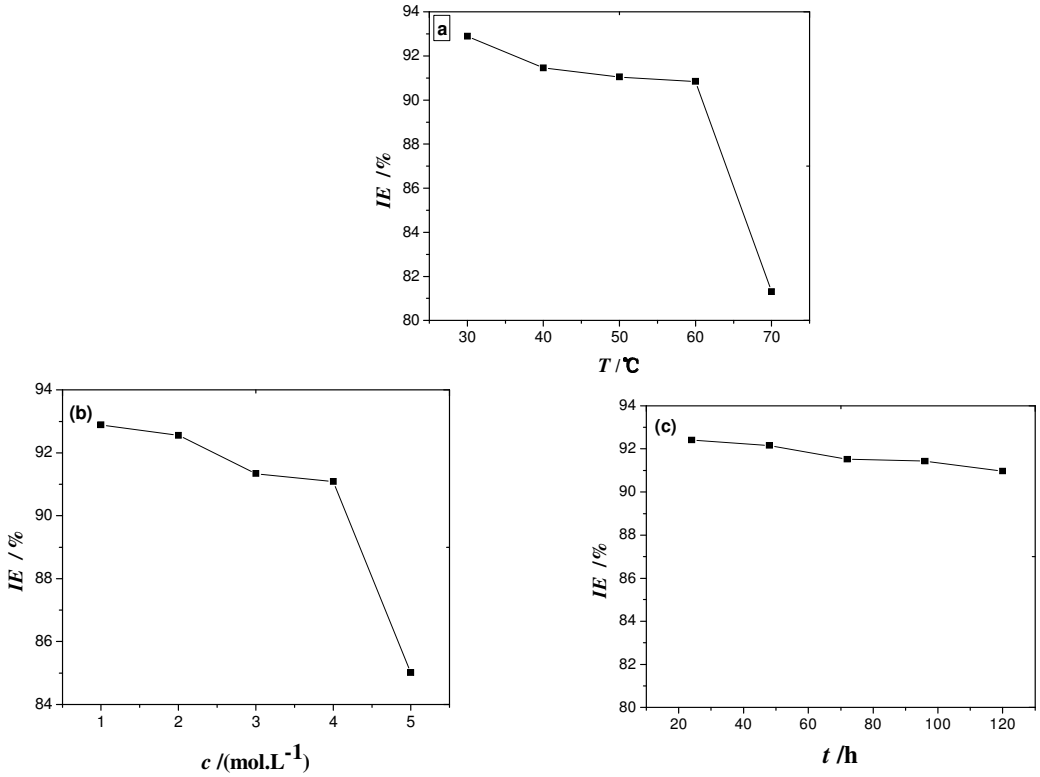



Fig. 2. Variation of inhibition efficiency with (a) different temperatures, (b) different concentration of hydrochloric acid solution and (c) different immersion time.

## Weight Loss Measurements

Study results of weight loss measurements for carbon steel in 1.0 M hydrochloric acid solution at 30°C (in absence and presence of different concentrations of BPOTP ) are shown in Fig. 3(a). With the increasing of BPOTP concentration, the inhibition efficiency increases. That is up to 92.89% at the BPOTP concentration of 40 mg·$L^{-1}$. The results indicate that the BPOTP acts as a good inhibitor for the corrosion of carbon steel in 1.0 M hydrochloric acid solution.

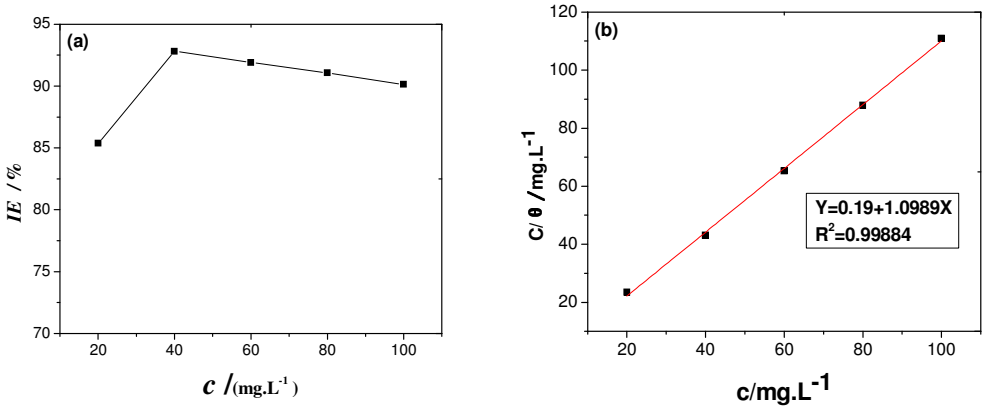



Fig. 3.(a) Study results of weight loss measurements for carbon steel in 1.0 M hydrochloric acid solution at 30°C (in absence and presence of different concentrations of BPOTP ) (b) Langmuir isotherm for adsorption of BPOTP on the carbon steel surface in 1.0 M hydrochloric acid solution at 30°C

## Adsorption Isotherm.

In order to gain more information about the adsorption mode of BPOTP on the surface of carbon steel, the data of weight loss measurements had been tested using Frumkin, Freundlich, Temkin and Langmuir isotherms. The adsorption of BPOTP on carbon steel was found to be consistent with

Langmuir isotherm ($R^2$=0.99884) and the relationship between $C/\theta$ and $C$ is shown in Fig. 3 (b). The equilibrium constant for adsorption process was related to the free energy of adsorption ($\Delta G^0_{ads}$) and can be expressed by Eq. 4:

$$K_{ads} = \frac{1}{55.5}\exp\left(-\frac{\Delta G^0_{ads}}{RT}\right) \quad (4)$$

Where 55.5 is the molar concentration of water in the solution expressed in molarity units ($mol \cdot L^{-1}$), R and T are gas constant (8.314 $J \cdot K^{-1} \cdot mol^{-1}$) and absolute temperature (K) respectively. The $\Delta G^0_{ads}$ values of -37.67 $KJ \cdot mol^{-1}$ indicates that the physisorption and chemisorption of BPOTP molecule takes place spontaneously on the carbon steel surface.

## Conclusions

(1) BPOTP acts as a good corrosion inhibitor in different concentration of hydrochloric acid solution.

(2) BPOTP is a mixed-type inhibitor.

(3) The adsorption of BPOTP on the carbon steel surface obeys Langmuir adsorption isotherm.

(4) The physisorption and chemiorption takes place spontaneously by BPOTP molecule on the carbon steel surface.

(5) The inhibition efficiency of BPOTP remained stable as immersion time increasing and reduced as acid concentration and temperatures increasing.

## Acknowledgment

This work is supported by the Education Department of Sichuan Province, China (No.13ZB0134), Sichuan University of Science & Engineering,China (No.2009xjkPL004, No.y2012017), Material Corrosion and Protection Key Laboratory of Sichuan Province, China (No.2011CL03), Science and Technology Office of Zigong City, China(No.2012H04).

## Reference

[1] M. A. Hegazy, A. M. Badawi , S. S. A E. Rehim and W. M. Kamel: Corr. Sci. Vol. 69(2013): p. 110

[2] E. E. Oguzie: Corros. Sci. Vol. 50(2008): p. 2993

[3] M. Bobina, A. Kellenberger, J. P. Millet, C. Muntean and N. Vaszilcsin Corr. Sci. Vol. 69(2013): p. 389

[4] I. Ahamad and M. A. Quraishi: Corros. Sci. Vol. 52(2010): p. 651

[5] L. K. Zou, B. Xie, J. Q. Xie, J. S. Feng, X. L. Chang and X. L. Zhang. Transition Metal Chem. Vol. 34 (2009):p.395

[6] G. Bereket, E.Hur and C.Ogretir. J. Mol. Struc. Vol. 578(2002): p. 79

*Advanced Materials Research Vol. 937 (2014) pp 113-117*
*© (2014) Trans Tech Publications, Switzerland*
*doi:10.4028/www.scientific.net/AMR.937.113*

# First-principles Study on the Surface Energies of Rutile $TiO_2$(110) vs (011)-2×1 Surfaces

Feng YUAN[A], Shi-xiang LU[B,*], Wen-guo XU[C,*], Hai-feng ZHANG and Tao NING

School of Chemistry, Beijing Institute of Technology, Beijing 100081, PR China

[a]fyuan80@126.com, [b]shixianglu@bit.edu.cn, [c]xuwg60@bit.edu.cn

**Keywords:** Density functional theory, Surface energy, $TiO_2$(110) surface, $TiO_2$(011)-2×1 surface.

**Abstract:** First-principles calculations based on density functional theory have been used to study the surface energies of the rutile $TiO_2$(110) and (011)-2×1 surfaces. We investigate the effect of the slab thickness on the predicted surface energy and find that slab thicknesses of at least 5 layers are necessary to converge the surface energy to within 0.01 J/m$^2$ for both rutile $TiO_2$(110) and (011)-2×1 surfaces. For the rutile $TiO_2$(110) surface, it should be noted that the surface energy oscillates with the number of layers (odd-even oscillations). However, the calculated surface energies of the rutile $TiO_2$(011)-2×1 surface are closer to the linear relationship for the number of layers larger than 4. Finally, our calculated results indicate that the rutile $TiO_2$(011)-2×1 surface has a significantly higher surface energy than the rutile $TiO_2$(110) surface.

## Introduction

Titanium dioxide as a photocatalyst is one of the most widely studied compounds in material science and its surfaces play a key role in the photocatalytic properties of this transition metal oxide [1,2]. Of the low index surfaces of titania, the rutile $TiO_2$(110) surface is the thermodynamically most-stable form for fundamental surface science studies, and most experimental surface science techniques can be applied without difficulties. The structure of the rutile $TiO_2$(110) surface is made of alternating horizontal and vertical polymers [3], which makes the surface at the same time reactive and stable [4]. The second most stable facet of the rutile $TiO_2$ surface is the recently proposed rutile $TiO_2$(011)-2×1 surface, and it provides us with the first opportunity to study a more complicated oxide surface with a significant reconstruction. This has led to most of these studies focused on the reconstructed structure of rutile $TiO_2$(011)-2×1 surface. Unlike the rutile $TiO_2$(110) surface, which still exhibits a bulk truncation in the top layer, the rutile $TiO_2$(011)-2×1 surface forms a 2×1 reconstruction at the vacuum interface and exhibits a distorted square pyramidal structure rather than the "ideal" bulk-terminated structure.

Surface energy is one of the most fundamental surface properties of a solid, since it depends directly on the binding forces of a given material. Indeed, the surface energy is a measurement of separating a material into two parts along a plane. The determination of the surface energy of a material is of great importance in the understanding of a wide range of surface phenomena, such as the crystal growth, the form of crystallites, catalytic behavior, surface segregation, and the adsorption. The surface energy defined as the surface excess free energy per unit area of a particular crystal facet and is one of the basic quantities in surface physics. At the same time, the surface energy depends on the crystallographic orientation, i.e., the surface facet, of the surface under consideration. In general, very few measurements have been made of this quantity and these by indirect means, because of the difficulties of measurement and interpretation. It is for this reason that many theoretical treatments have been made to calculate this parameter. The aim of the present paper is to present the first-principles density functional theory calculations to estimate the surface energies of the rutile $TiO_2$(110) and (011)-2×1 surfaces. At the same time, the obtained results of the rutile $TiO_2$(110) and (011)-2×1 surfaces with different number of layers are compared.

## Computational Details

First-principles calculations based on the density functional theory were carried out utilizing the Vienna ab initio simulation package (VASP 5.2) [5]. The generalized gradient approximation (GGA) of the Perdew-Burke-Ernzerhof (PBE) functional was employed [6], and the kinetic cutoff energy for the electron plane-wave expansion was set to 400 eV. For *k*-point sampling regime, 4 × 4 × 4 Monckhorst-Pack grids for the bulk rutile $TiO_2$, 4 × 4 × 1 Monckhorst-Pack grids for the rutile $TiO_2$(110) surface, and 2 × 4 × 1 Monckhorst-Pack grids for the rutile $TiO_2$(011)-2×1 surface were used for geometry optimizations. Both atomic positions and cell parameters were optimized until the residual forces were below 0.01 eV/Å.

## Results and Discussion

### Geometric Structure

To evaluate the reliability of the present computational settings above, we first optimized the lattice parameters of the bulk rutile $TiO_2$. The obtained equilibrium lattice constants are a = 4.555 Å, c = 2.924 Å, and c/a = 0.642, in good agreement with the experimental values of a = 4.584 Å, c = 2.953 Å, and c/a = 0.644 [7], and the deviations are only -0.63%, -0.98%, and -0.31%, respectively. It indicates that the employed method is suitable for the rutile $TiO_2$ calculations.

Based on the optimized rutile $TiO_2$ unit cell, both rutile $TiO_2$(110) and (011)-2×1 surfaces [see Figs. 1 and 2] were constructed as periodic slabs with 3, 4, 5, and 6 layers. For the complicated rutile $TiO_2$(011)-2×1 surface, a theoretical simulation with forming from bulk truncation to the 2×1 reconstruction has been mentioned in our previous work [8]. A vacuum space of 18 Å above the slab was chosen to eliminate the influence from the adjacent bottom layer.

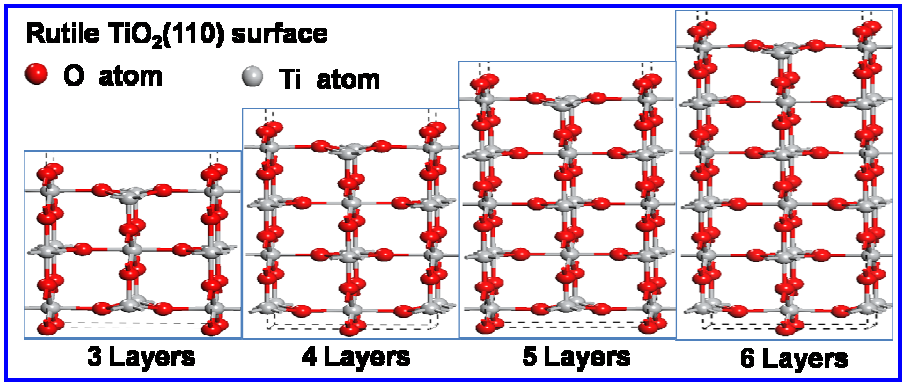



Fig. 1. Calculated structures of the rutile $TiO_2$(110) surface (side views) for slab thicknesses with 3, 4, 5, and 6 layers.

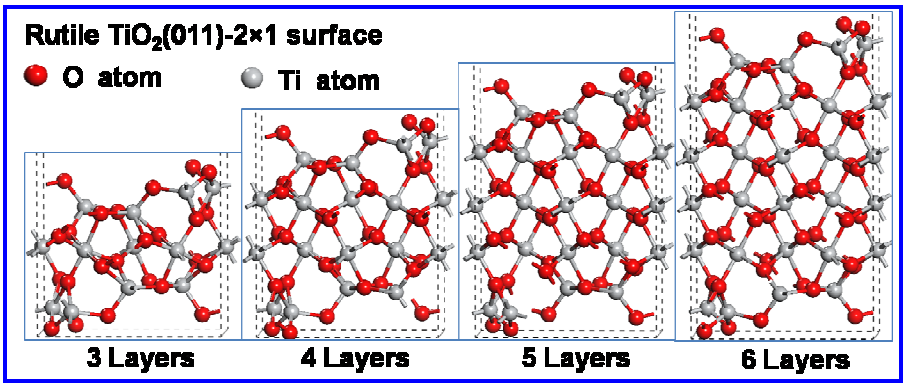



Fig. 2. Calculated structures of the rutile $TiO_2$(011)-2×1 surface (side views) with the number of layers 3, 4, 5, and 6.

The rutile $TiO_2$(110) surface contains titanium atoms with two different coordination environments, five-fold and six-fold coordinated, forming alternating rows [see Fig. 1]. All oxygen atoms are three-fold coordinated as in the bulk except those ones in the outermost plane called bridging atoms, which lose one bond when the upper layer is removed. From a more covalent point of view, the rutile $TiO_2$(110) surface is created by a cleavage of the crystal in which the minimum possible number of bonds has been broken. An entirely unanticipated geometric structure for the rutile $TiO_2$ surface, as shown in Fig. 2, is the recently proposed rutile $TiO_2$(011)-2×1 surface. The rutile $TiO_2$(011)-2×1 surface with a significant 2×1 reconstruction at the vacuum interface has a corrugated profile along the [100] direction. There are two inequivalent surface two-fold oxygen atoms, the top ones and the ones at either side of the hillocks. The exposed five-fold titanium atoms in the valleys do not extend a dangling bond towards the vacuum, and the ridge five-fold titanium atoms at the top can be regarded as a distorted square pyramidal structure rather than the usual octahedral symmetry in bulk. As illustrated in Figs. 1 and 2, the rutile $TiO_2$(110) surface is terminated with the "dangling" bond of the twofold-coordinated top oxygen, while the reconstructed rutile $TiO_2$(011)-2×1 surface already minimizes unsaturated bonds.

**Surface Energy**

Surface energies ($E_{surf}$) for both rutile $TiO_2$(110) and (011)-2×1 surfaces were estimated from total energy calculations using the following formula [9]:

$$E_{surf} = (E_{slab} - nE_{bulk}) / 2A, \quad (1)$$

where $E_{slab}$ is the total energy of the calculated slab, $E_{bulk}$ is the total energy of a bulk unit cell, $n$ is the number of the bulk unit cells in the calculated slab, and $A$ is the exposed area of one side of the calculated slab. As illustrated in Figs. 1 and 2, we used symmetric slab so the two sides are equivalent. The treatment of which can eliminate the unnecessary influence from the bulk and give reliable properties similar to that present in many real-life applications.

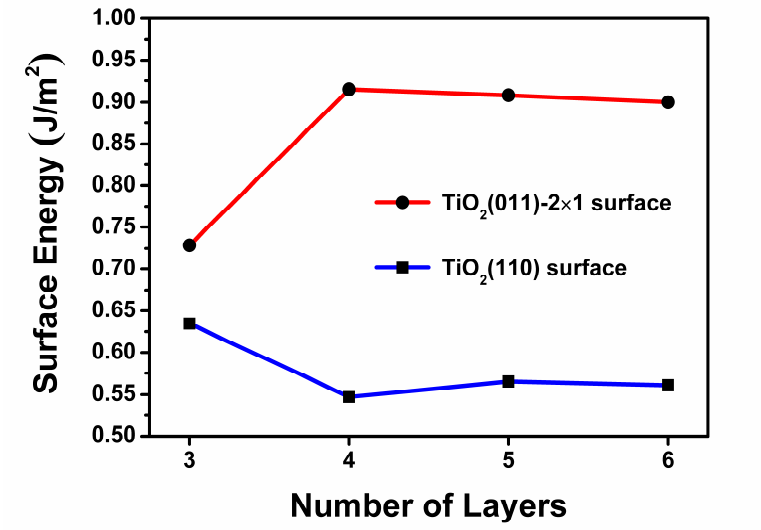



Fig. 3. The variation of surface energy as a function of slab thickness of the rutile $TiO_2$(110) and (011)-2×1 surfaces.

Surface energy calculations have been performed for slab thickness with 3, 4, 5, and 6 layers of the rutile $TiO_2$(110) and (011)-2×1 surfaces. The thickness of the slab is usually expressed in terms of the number of layers, where a layer is defined as a [110] plane for the rutile $TiO_2$(110) surfce and [011] plane for the rutile $TiO_2$(011)-2×1 surface that contains both Ti and O atoms. The variation of $E_{surf}$ as a function of the number of layers of the rutile $TiO_2$(110) and (011)-2×1 surfaces is shown in Fig. 3. For the rutile $TiO_2$(110) surface, this is clear from Fig. 3 where the odd-even oscillation of the surface energy is shown. The surface energy of the rutile $TiO_2$(110) surface is converged to within 0.01 J/m$^2$

for the number of layers larger than 5, which presents a surface energy with 0.57 J/m$^2$. It is quite close to the results of the previous calculations, 0.58 J/m$^2$ with GGA [10], indicating that the employed method is suitable for $TiO_2$ surface calculations. These oscillations have also been noted previously [11,12], and the odd–even oscillations arise from the different symmetry of the slabs which leads to a significant change in the hybridization of the O 2*p* and Ti 3*d* states in the direction of the surface normal [12]. In the slabs with an even number of layers, which do not contain a symmetry plane normal to the [110] direction, the O-Ti hybridization causes the formation of a series of tightly bound $TiO_2$ bi-layers with weaker interactions between a bi-layer and the following one. The slabs with an odd number of layers, on the contrary, have a symmetry plan at the center of the film and develops O(2*p*)-Ti(3*d*) hybrid orbitals which extend along the entire thickness of the film, thus reducing the tendency to form weakly interacting bi-layers [12]. The surface energy of the slabs with an odd number is higher and the convergence to the limit of infinite slab thickness is slower than when using an even number of layers. For the rutile $TiO_2$(011)-2×1 surface, the calculated surface energy is closer to the linear relationship for the number of layers larger than 4. As one can see, the surface energy convergence as the number of layers tends to infinity is clear, and for both slab thicknesses $E_{surf}$ is converged to within 0.01 J/m$^2$ for the number of layers larger than 5, which presents a surface energy with 0.91 J/m$^2$. It is worth to note that the rutile $TiO_2$(011)-2×1 surface has a significantly higher surface energy than the rutile $TiO_2$(110) surface. In the case of semiconductor surfaces, the surface energy mainly comes from the unsaturated dangling bonds that are left on the surface [13]. The rutile $TiO_2$(110) surface is terminated with the “dangling” bond of the twofold-coordinated top oxygen. While, the reconstructed rutile $TiO_2$(011)-2×1 surface already minimizes unsaturated bonds and causes a large distortion in the surface and subsurface layers, which may lead the surface energy to be large (energetically less stable).

## Conclusions

This work makes appealing to test the effect of the slab thickness on the predicted surface energies of the rutile $TiO_2$(110) and (011)-2×1 surfaces using first-principles density functional theory calculations. For both rutile $TiO_2$(110) and (011)-2×1 surfaces, the surface energy is converged to within 0.01 J/m$^2$ for the number of layers larger than 5 at a vacuum width of 18 Å above the slab. There are pronounced oscillations in both surface energies as a function of slab thickness of the rutile $TiO_2$(110) surface compared with the rutile $TiO_2$(011)-2×1 surface with a linear relationship for the large number of layers. In addition, the rutile $TiO_2$(011)-2×1 surface has a significantly higher surface energy than the rutile $TiO_2$(110) surface. Hence, our theoretical calculations provide evidence that the rutile $TiO_2$(011)-2×1 surface is energetically less stable than the rutile $TiO_2$(110) surface.

## Acknowledgements

We gratefully thank the National Natural Science Foundation of China (No. 21271027) and the 863 Project of China (No. 20140AA065103-1) for their support of this work.

## References

[1] M. Grätzel, Nature 414 (2001) 338-344.

[2] A. Fujishima, X.T. Zhang, D.A. Tryk, Surf. Sci. Rep. 63 (2008) 515-582.

[3] A. Fahmi, C. Minot, Surf. Sci. 304 (1994) 343-359.

[4] J. Ahdjoudj, A. Markovits, C. Minot, Catal. Today 50 (1999) 541-551.

[5] G. Kresse, J. Furthmüller, Phys. Rev. B 54 (1996) 11169-11186.

[6] J.P. Perdew, K. Burk, M. Ernzerhof, Phys. Rev. Lett. 77 (1996) 3865-3868.

[7] U. Diebold, Surf. Sci. Rep. 48 (2003) 53-229.

[8] F. Yuan, S.H. Lu, W.G. Xu, H.F. Zhang, Surf. Sci. 621 (2014) 88-93.

[9] X.Q. Gong, A. Selloni, M. Batzill, U. Diebold, Nat. Mater. 5 (2006) 665-670.

[10] B.J. Morgan, G.W. Watson, Surf. Sci. 601 (2007) 5034-5041.

[11] K.J. Hameeuw, G. Cantele, D. Ninno, F. Trani, G. Iadonisi, J. Chem. Phys. 124 (2006) 024708.

[12] T. Bredow, L. Giordano, F. Cinquini, G. Pacchioni, Phys. Rev. B 70 (2004) 035419.

[13] H. Lüth, Surfaces and Interfaces of Solid Materials, Springer, New York, 1995.

*Advanced Materials Research Vol. 937 (2014) pp 118-121*
*© (2014) Trans Tech Publications, Switzerland*
*doi:10.4028/www.scientific.net/AMR.937.118*

# Optimization of Preparation Process of Essential Oil of Baokening granule-β-cyclodextrin Inclusion by Orthogonal Test

Fang LUO[a], Shun-Bin QIAO[b]

Experimental and Training Center of Guizhou Industry Polytechnic College, China

[a]email:luofang71@sina.com.cn, [b]email:hafcd@163.com,

**Keywords:** Baokening granule,Orthogonal test, Inclusion, Essential oil.

**Abstract.** To study optimum inclusion process conditions for essential oil from perilla and Pericarpium Citri Reticulatae in Baokening granule,the utilization ratio of volatile and the inclusion rate were determined to evaluate process conditions, and the condition was optimized with orthogonal design by the liquid-phase method in aqueous solution. The experiment results showed that the optimum preparation conditions for inclusion were established as: oil: ß -CD was 1:8, and ratio of amount of water to ß –CD was 10. The inclusion temperature and time were at 40°C and for 180 min. The yield is high in such optimum process condition and the inclusion effect is good.

## Introduction

Baokening granules prescription by Perilla leaf 30g, leaf 30g, 60g, 30g, root of Fritillaria thunbergii ephedra 30g, Platycodon grandiflorum 30g, Arisaema (system) 60g, orange peel 30g, bitter almond (fried) 60g, 60g, 21g, baicalin, indigo naturalis trichosanthin 60g, Fructus aurantii (stir fried with bran) 60g, hawthorn (fried). 45g, licorice 15g, artificial bezoar 3G total of 16 traditional Chinese medicines.With heat clearing and table, the effectiveness of cough and phlegm. For pediatric exogenous cold, heat and stopping headache body burn, cough with profuse sputum, shortness of breath, dyspnea, throat swelling and pain, restlessness[1-2] .The preparation method is as follows: extracting volatile oil from perilla leaf, dried tangerine peel, water solution is collected after the distillation of the other; the remaining leaves of thirteen kinds of decocting two times, the first 2.5 hours, second hours 1.5 times, merging the decoction, filtration, the filtrate and the merging of aqueous solution, concentrated into a relative density of 1.32 ~ 1.35 (50 °C) clear paste. The clear paste, add sugar and dextrin, and artificial bezoar powder for grinding, granulating, drying, volatile oil, add the basil leaves and dried tangerine peel, mix, made of 900g, which was[1] .Perilla leaf perilla Labiatae [Perilla frutescens (L.) Britt.] (dried leaves or twigs). The volatile oil of perilla leaves contain more, there are divergent cold, Qi and stomach effective component[3,4]. Dried tangerine peel (Periarpium Citri Retiulatse) mature fruits: orange and planting varieties of plants, mainly in Sichuan, Zhejiang, Fujian, Jiangxi etc.. Citrus aroma, pungent, bitter[5,6].

At present, traditional Chinese medicine preparations of two kinds of volatile oil in coordination with the volatile oil, volatile oil seal packaging, easy loss, smell bad and not easy to store. Cyclodextrin inclusion of new technology is widely used in traditional Chinese medicine preparations. Cyclodextrin has a hydrophobic cavity structure, inclusion and cavity can be similar to the size of the guest molecules or some group [1]. The inclusion, can be isolated from the drug molecules with the surrounding environment, contact to a certain extent, to avoid the affected by light, oxygen and other factors, so as to improve the drug stability and reduce the volatilization, and increases the stability of the preparation.

The perilla leaf and peel a volatile oil beta cyclodextrin inclusion process have been reported to [3-6], while the perilla leaf and peel mixed volatile oil inclusion process and experiment not reported in the literature. This experiment using orthogonal test method, preferably beta cyclodextrin perilla leaf and peel of mixed volatile oil of optimum process conditions, will be on baokening granules and other forms in disposal of embedding volatile oil has reference function.

## Instruments and Reagents

### Instruments

Volatile oil extractor, East China Medical Apparatus Co. Ltd.; DZF-6050 type vacuum drying box, Shanghai Jinghong Experimental Equipment Co., Ltd.; D40-2F type electric blender, Hangzhou Instrument Motor Co. Ltd; W201B constant temperature water bath, Shanghai Shen Sheng Biotechnology Co., ltd..

### Reagents

Perilla leaf, dried tangerine peel purchased from Qingping medicine market; reagents were analytically pure; beta cyclodextrin powder, more than 99% purity, Shanghai Boao Biological Technology Co., ltd..

## Methods and Results

### Mixed Volatile oil Extraction

According to the mass ratio of 1:1 from perilla leaf, dried tangerine peel mixed coarse powder mixed with 12 times amount of water, soaking 1H, according to the "Chinese Pharmacopoeia" 2010 Edition appendix XD determination of volatile oil (Jia Fa) essential oils were extracted from 6h, with anhydrous sodium sulfate can be obtained after dehydration, perilla leaf and Pericarpium Citri Reticulatae volatile oil were prepared by mixing.

### Study on Inclusion Technology of Volatile Oil

#### The preparation methods of the inclusion complex

According to each experimental condition, precision that take the right amount of beta - cyclodextrin amount, the conical flask, adding 10 times amount of distilled water, heating and stirring to dissolve into a clear solution, constant temperature, to the inclusion temperature. The stirring speed drop adding mixed volatile oil 1.00mL at time 200r/min, the refrigerator 48h, filtration, inclusion complex with a small amount of oil washing two times (volatile oil wash not inclusion), and no smell, vacuum drying at 40 deg.c to obtain 4h, powder white powder inclusion.

#### Index Determination

According to pharmacopoeia method to determine the content of volatile oil in inclusion complex. The reduced 1mL containing volatile oil inclusion compound, the 250mL round bottom flask, add 100mL distilled water and zeolite, were determined by volatile oil extractor, read the volatile oil, the yield of inclusion compound and the oil yield were calculated.

#### The Orthogonal Test Design

Through pre experiment research to determine the beta - cyclodextrin and volatile oil ratio, stirring time, the inclusion temperature influence the inclusion of the main factors, see table 1. According to the experimental conditions to determine the three levels for each factor, using $L_9(3^4)$orthogonal experiment, with the inclusion of oil content and yield of inclusion compound as the evaluation index, the results in table 2 and table 3.

Table 1. Factors and levels of orthogonal test

| Levels | β-CD:Volatile oil (g:ml) | Inclusion time(min) | Inclusion temperature(°C) |
|---|---|---|---|
| 1 | 8 | 60 | 30 |
| 2 | 6 | 120 | 40 |
| 3 | 4 | 180 | 50 |

Table 2. Orthogonal test and results

| Experiment number | A | B | C | D (deviation) | Oil content /% | Yield /% | Comprehensive evaluation /% |
|---|---|---|---|---|---|---|---|
| 1 | 1 | 1 | 1 | 1 | 76.01 | 53.11 | 59.98 |
| 2 | 1 | 2 | 2 | 2 | 87.20 | 60.14 | 68.26 |
| 3 | 1 | 3 | 3 | 3 | 92.41 | 64.25 | 72.70 |
| 4 | 2 | 1 | 2 | 3 | 70.22 | 45.67 | 53.04 |
| 5 | 2 | 2 | 3 | 1 | 74.27 | 50.59 | 57.69 |
| 6 | 2 | 3 | 1 | 2 | 60.23 | 38.32 | 44.89 |
| 7 | 3 | 1 | 3 | 2 | 41.98 | 20.09 | 26.66 |
| 8 | 3 | 2 | 1 | 3 | 39.02 | 17.98 | 24.29 |
| 9 | 3 | 3 | 2 | 1 | 60.25 | 35.34 | 42.81 |
| k1 | 200.93 | 139.67 | 129.16 | 160.49 | | | |
| k2 | 155.63 | 150.24 | 164.11 | 139.81 | | | |
| k3 | 93.76 | 160.40 | 157.05 | 150.02 | | | |
| R | 107.17 | 20.73 | 34.95 | 20.68 | | | |

Note: The inclusion of oil content and yield as the evaluation index,the weight coefficients were 0.3,0.7.

Table 3. The results of variance analysis

| Sources of variance | Sum of squares of deviations | Variance | F value | Conspicuousness |
|---|---|---|---|---|
| A | 1929.71 | 2 | 27.07 | <0.05 |
| B | 71.62 | 2 | 1.01 | |
| C | 227.65 | 2 | 3.19 | |
| D | 71.27 | 2 | | |

Analysis of the results of orthogonal experiments, effects of beta - cyclodextrin and volatile oil ratio on the experimental results the most significant. The best inclusion technology for A1B3C2, namely the beta - cyclodextrin and volatile oil ratio is 8:1, the inclusion temperature 40 °C, inclusion time is 180min.Three copies of the volatile oil of previously orthogonal consistent, verified by optimizing process conditions, the recovery of inclusion complex is 93.11%, rate of oil was 64.32%. To determine the final optimization of process of Portfolio: ß - cyclodextrin and volatile oil ratio is 8:1, the inclusion temperature 40 °C, inclusion time is 180min.

**Inclusion Test**

**Sample Preparation**

Take purple perilla leaf, orange peel volatile oil 0.2mL, and absolute alcohol solution of 20mL, as the test a; the inclusion amount, recovery of volatile oil, remove the 0.2mL plus ethanol solution of 20mL, as the test B; respectively, the blank of cyclodextrin and inclusion of the 2G, adding anhydrous alcohol, 20mL, vibration shake the static 1H, centrifugation, the supernatant, as the test C, D.

### Inclusion of Thin Layer Chromatography Test

Thin-layer chromatography ("the people's Republic of China Pharmacopoeia" 2005 version of an appendix VIB) experiment: respectively from samples a, B, C, D solution is 10 μ L, respectively, on the same silica gel G plate (105E activated 1hr), ethyl acetate hexane chloroform (1:9:5) as expansion agent, expansion, removed, dried, spraying with $50g \cdot L^{-1}$ vanillin sulfuric acid solution chromogenic agent, chromogenic clear heating at 105 °C to spot, TLC comparison of four samples. The inclusion of the volatile oils extracted with the inclusion of the volatile oil in the TLC conditions, all spots at the corresponding position in the same color, thin layer chromatography of identical composition, that does not change. Beta - cyclodextrin and inclusion of washing liquid are not spotted, showed that volatile oil inclusion after it has formed inclusion rather than physical mixture.

### Conclusions

The best package selected by orthogonal experiments of mixed oil process, beta - cyclodextrin and volatile oil ratio is 8:1, the inclusion temperature 40 °C, inclusion time is 180min, beta - cyclodextrin and water ratio of 1:10. Verifying test results found that the process is reproducible, stable quality, the yield of inclusion compound and oil inclusion rate.With beta cyclodextrin inclusion process of volatile oil is feasible, can improve the stability of volatile components of liquid, solid, and the inclusion of effectively masking volatile oil smell, keep the physiological activity and stability of volatile oil.

### Acknowledgment

This research was financially supported by the Guizhou province science and technology Foundation.

### References

[1] Chinese Pharmacopoeia Commission . Pharmacopoeia of the People’s Republic of China,China Medical Science Press, Beijing,1(2010)854.

[2] State Food and Drug Administration,The local standard of Chinese traditional patent medicine rise of national standards,China Medical Science Press, Beijing,(2005)9-13.

[3] Wu DZ,Wu PJ,Yang M,Optimization preparation of Complex of Perilla Leaf Oil-β-cyclodextrin by Box-behnken Design and Response Surface Method. Journal of Chengdu University of Traditional Chinese Medicine,32(2009)81-87.

[4] Qiu JY，Yang XD，Du HJ, et al. . Preparation of β-Cyclodextrin Inclusion Compound of Volatile Oil of Perilla,Acta Academiae Medicinae Jiangxi,45(2005)39-40.

[5] Cai Z,Wu LX,Zhong GL.Technological studies of effects of inclusion of Pericarpium Citri Reticulatae volatile oil-beta-cyclodextrin, China Journal of Chinese Material Medica, 20(1995)603-605.

[6] Yao FY,Wang BZ,Shi Q,et al.,Optimizing the Inclusion Process of Pericarpium Citri Reticulatae Volatile Oil of Jiangzhi Jianfei Capsules with β-CD by Orthogonal Design.Journal of Liaoning University of Traditional Chinese Medicine,11(2009)177-178.

# CHAPTER 2:

# Metal Materials and Alloys

*Advanced Materials Research Vol. 937 (2014) pp 125-129*
*© (2014) Trans Tech Publications, Switzerland*
*doi:10.4028/www.scientific.net/AMR.937.125*

# Research and Empoldering of High Strength Weathering Steel S450EW

Jun-shan WANG[1,2], Pei-yang SHI[1,a], Cheng-jun LIU[1] and Mao-fa JIANG[1]

[1]Key Laboratory for Ecological Metallurgy of Multimetallic Ores (Ministry of Education), Northeastern University,Shenyang 110819, China

[2]Anshan Iron and Steel Group Corporation, Anshan 114014, China

[a]shipy@smm.neu.edu.cn

**Keywords:** S450EW high strength weathering steel; Organization; Microstructure.

**Abstract.** According to the characteristics of high strength weathering steel, this paper designs to develop anexperimental steel S450EW with yield strength higher than 450MPa.Through the study,it has been found that with decreasing cooling rate, the organizational changed largely, while ferrite and pearlite gradually transformed to martensite and a small amount of ferrite, then finally tomartensite organization.It has also been found that the crystal size decreased, and the experimentalsteel also precipitated a rectangular second phase particles of (NbTi) CN phase and TiC, which were sparsely distributed with the size of 100 ~ 300nm and below 30nm, while some phases were distributedasa number of strips in the grain boundary which mainly are C, Fe, Cr.

## Introduction

Organizatio Weathering steel as a low-alloy structural steel, not only has good resistance to atmospheric corrosion, but also has excellent overall performance, such as mechanics, welding, etc., therefore much attention are paid[1-4]. Since the rapid development of industry andintensifying pollution of environment, general weathering steel can not meet the requirements of such circumstances, and developing of high strength weathering steel is urgent need. The second phase particles that precipitatesin the steel has a pinning effect on the grain boundary, thushinder the grain boundary migration and suppress the grain growth, for which, on purpose of grain refinement and improving material properties, the particles of the second phase are introduced into as an effective control method[5-8]. In this paper, the structure changes of experimental steel with yield strength of 450MPa and the second phase precipitation behaviorwere researched, while some amount of alloying elements Cr, Ni, Ti and Nbwere added to the steel. A theoretical basis for the development of high strength weathering steel wasprovided.

## Experiment

### Preparation of Experimental Steel

The experimental steel weresmelted 6Kg or so in a 10Kg vacuum induction furnace on a domestic mills. The main chemical compositions of experimentalsteel are shown in Table 1.

Table 1. S450EW weathering steel main chemical component(mass%)

| Elements | C | Si | Mn | P | S | Ni | Cr | Cu | Als | Nb | Ti | N |
|---|---|---|---|---|---|---|---|---|---|---|---|---|
| Content | 0.043 | 0.40 | 0.73 | 0.018 | 0.0025 | 0.40 | 1.08 | 0.44 | 0.011 | 0.030 | 0.017 | 0.0044 |

### Rolling of Weathering Steel

The experimental steel was rolledin the testing mill in Northeastern University, and under the existing equipment capacity conditions, all ingots were separated intofive experimental rolling of tests. The ingots were heated at temperature of 1230 °C, insulated for 60min, with finishing thickness of 6mm, finishing rolling temperature controlled at 750 °C, the final cooling temperature controlled at 600 °C.

## Analysis

(1) High-resolution microscopyanalysis

The rolled steel was cut by wire-electrode cuttinginto samples of 10×10mm , grinded, polished and thenetched with 4% nital,the microstructure was observed with the microscope of Olympus .

(2) TEM analysis

Carbon extraction replica sample was observed and precipitation behavior of weathering steel second phase particles was analyzed with the Use of TEM. Process of preparing the carbon extraction replica specimen was as follows: A well-polished metallographic sample was etched with 4% nitric acid solution with absolute ethanol,deposited on the surface layerwith carbonwith the carbon injection instrument, after that, the carbon film was divided into the grid of 31T11TI × 3mlTl, and then placed in 10 % nitaland etched , till carbon was mustered off, sample was gained with copper mesh, washed by alcohol , and then placed in distilled water till the carbon film fully expanded, finally, was drained to with a copper mesh .

(3) Thermal simulation analysis

With the Gleeble-3800 thermal simulation tester,invacuum , the sample was heated with the rate of 20°C/S till 1150°C, then keep the temperature for 5min, after that was cooled with 5°C/S to 1000 °C. The sample was compressed with deformation of 15 %,then cooledto 700°C with the speed of 15°C/S, then heated again with the rate of 20°C/S to 780°C, then 5°C/S to 850°C, after that the sample was compressed one more time with deformation of 30%, kept warm for 10 seconds, finally cooledwith the speed of 0.5°C/S, 1°C/S, 5°C/S, 10°C/S, 15°C/S, 20°C/S, 30°C/S, 40°C/S respectively. The Temperature - transverse strain expansion curves were tested while the tests were cooling down.

## Experimental Results and Discussion

The experimental steels CCT curve test results wereshown inFigure 1. As can be seen from the figure, temperature Ac3 of the test steel was 932°C, temperature Ac1 is 732°C, Ms temperature was 430°C, the cooling rate is less than 3°C/s when the pearlite transformation occurs, when the cooling rate is less than 40°C/s or less ferrite transformation occurred, and when the cooling rate was greater than 1°C/s varying degrees of bainite transformationoccured, specific content of the changingorganization and hardness was shown in Figure 1 as followed.

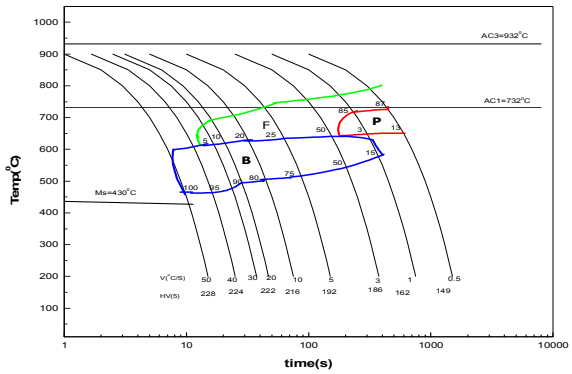



Fig. 1. CCT curves of the experimental steel

The organizational structure of the experimental steel under different cooling rate of 0.5°C/s,50°C/s, 20°C/s, 5°C/s were shown in Fig. 2. As can be seen from Fig. 2, with the decrease of the cooling rate, the structure of the experimental steel changeslargely,ferrite and pearlite transformed gradually to martensite and a small amount of ferrite, then the former less left ferrite, pearlite and the martensite turned into whole martensite, and meanwhile the crystal size decreases. When the cooling rate was 0.5°C/S, the experimental steel structure was mainly pearlite and ferrite and the ferrite

structure was equiaxed; When the cooling rate was 2°C/S, a little amount of needle-like ferrite showed up besides of the equiaxed structure although the organization did not significantly change, and ferrite microstructure size has been reduced; when the cooling rate was 5°C/S, small amounts of ferrite and martensite tissue and residual pearlite were left; when the cooling rate was 10°C/S, the steel structure in the experiment appeared in a small amount of bainite, martensite and ferrite structure, the crystal size further decreased; when the cooling ratewas 15°C/S, the bainitedisappearedin the experiment steel, small amounts of ferrite and martensitewas the main for organization; when the cooling rate was 20°C/S, the ferritictissue disappears from the experimental steels which had thetypical stripsmartensite left; when the cooling speed was further decreased,the microstructure did not changed any more, but the crystal size is further reduced. Generally the martensitic can enhaunce the strength and the hardness largelyof steel, but weaken the plasticity and toughness of steel. Therefore, it's critical of controlling the cooling rate to the performance of the experimental steels.

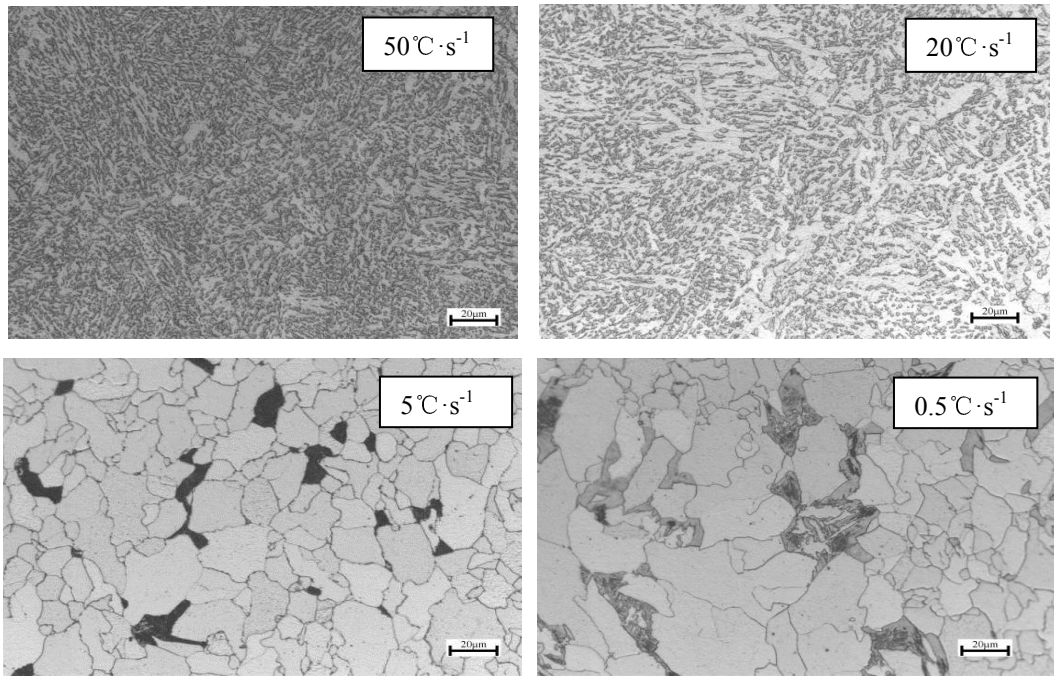



Fig. 2. Microstructure of Experimental steel under different cooling rates

The replica TEM sample picturesof the experimental steel were shown in Fig. 3. As can be seen from the pictures, the second phases precipitate in the sample in square or rectangular ,which could be divided into twokinds by sizes, one with the size of 100~300nm was precipitated by the phase (NbTi)CN and TiC which were determinedthrough spectrum analysis, and has the amount was not much; the other is 30nm or less in size, the sparse distribution of the precipitates was spectrum analyzed of mainly Ti carbonitride. It could be considered thatthe precipitates those were 100~300nm were castedprecipitates,and the fine depositsin size of 30~30nm were precipitated during tempering.

Impeding the in-situ dislocation motion by solid solution strengthening produced by alloying elements was unstable, thus, stable second phase precipitation were requiredto effectively prevent the movement of dislocations, it was because the second phase can provide high solution temperature to protect the second-phase particles which produced an important factor in strengthening precipitates at high temperatures.Because of the TiNbCN and TiC phase precipitatedin experimental steels, which played a role in precipitation hardening, and the melting points of such phases were high and with good hardness, when it begun to precipitate, the semi-coherent interfacestarted to be producedwith the substrate, which would increase the resistance to dislocation motion. Furthermore, due to the large intensity of the second phase particles ,bending of dislocation motion resultedquite large.According

to the dislocation bypass mechanism, the yield strength of the experimental steel would undoubtedly increased. Therefore, under the experimental conditions the composite tissue of TiNb(CN) andTiCprecipitation producedmarkedhardening .

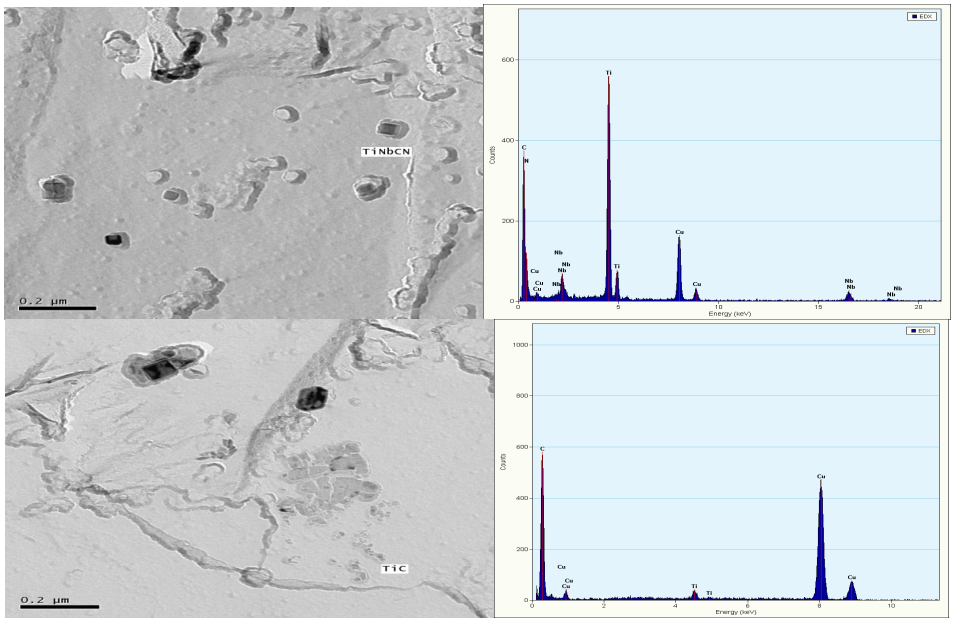



Fig. 3. TEM specimens tested steel replica image and EDS analysis

The TEMpicturesof the experimental steel film samplewere shown in fig. 4. As can be seen from the picture, some strips wereon the internal grain boundary of theexperimental steelmicrostructure, which analyzedby EDS was main component of component C, Fe, Cr, while the matrix was also C, Fe, Cr, but the C, Cr peak is significantly higher of grain boundariesthan that of the substrate.

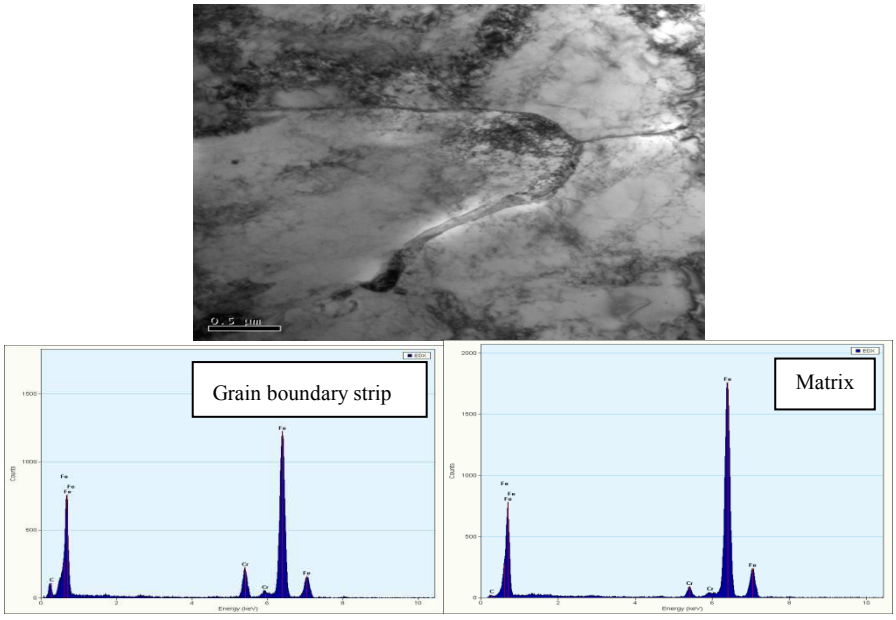



Fig. 4. Samples of experimentalsteel film TEM and EDX

## Conclusion

(1) Under the experimental conditions, with decreasing cooling rate, the organizational changed largely, while ferrite and pearlite gradually transformed to martensite and a small amount of ferrite, then finally to martensite organization. It has also been found that the crystal size decreased.

(2) Under the experimental conditions, the experimental steel also precipitated a rectangular second phase particles of (NbTi) CN phase and TiC, which were sparsely distributed with the size of 100 ~ 300nm and below 30nm, while some phases were distributed as a number of strips in the grain boundary which mainly are C, Fe, Cr.

**Acknowledgement**

This research was financially supported by the National Science Foundation.

**References**

[1] Chunling Zhang, CaiDayong, Zhang Keqin, et al, Microstructure and mechanical property of hot-rolled dual- phase weathering steel Cu-P-Cr-Ni-Mo, J.Transactions of Materials and Heat Treatment. 33(2012)33-37.

[2] Qingjun Chen, Yonglin Kang, HairongGu, et al, Effect of Nb-Ti on Structure and Properties of High StrengthWeathering Steel, J.Special Steel. 26(2005) 30-33.

[3] Qiuyue Jiang, Kunning Jia. Structure transformation of HAZ for high strength weathering steel , J. Heat Treatment of Metals. 38(2013) 28-30.

[4] Chunling Zhang, Dayong Cai, Bo Liao. Study on the dual-phase treatment of steel 09CuPCrNi, J. Steel and Iron.39(2004) 50-53.

[5] Qingyou Liu, Dong Han,Weng Yu, et al. New Ultra-fine Grained Weathering Steel in Grade of 450 MPa, J. IRON AND STEEL. 39(2004) 45-48.

[6] Dillmann P, Balasubramaniam R, Beranger G. Characterization of protective rust on ancient Indian iron using microprobe analyses, J. CorrosSci. 44(2002) 2231-2234.

[7] Guoping Zhou, Zhenyu Liu, Yiqing Qiu, et al. The Improvement of Weathering Resistance by Increasing P Contentsin Cast Strips of Low Carbon Steels, J. Materials & Design.30(2009) 43-42.

[8] Hui Feng, Feng Liu, Benxian Wang, et al. Effects of Cu and Cr content on mechanical properties and corrosion resistance of weathering steels, J. Transactions of Materials and Heat Treatment. 33(2012) 110-116.

[9] Masao T, Tamaki S, Genichi S, et al. Characterization of Nanostructure of Rusts Formed on Weathering Steel, J. ISIJ International. 42(2012) 1534-1540.

*Advanced Materials Research Vol. 937 (2014) pp 130-135*
*© (2014) Trans Tech Publications, Switzerland*
*doi:10.4028/www.scientific.net/AMR.937.130*

# Simulation of the Yield Strength of Mo Alloys at Both Room and Elevated Temperatures

Jing-lian FAN[1, a], Hui-chao CHENG[1, b], Min SONG[1, c,*]

[1]State Key Laboratory of Powder Metallurgy, Central South University, Changsha 410083, China,

[c]fjl@csu.edu.cn, [b]chc26@sina.com, [c]msong@csu.edu.cn

*Corresponding author

**Keywords:** Mo alloy, Yield strength, Constitutive model.

**Abstract.** In this paper, the yield strength of a kind of carbide strengthened molybdenum (Mo) alloy has been investigated at both room and elevated temperatures. OM image showed that the sintered Mo alloy has an average grain size of ~20 μm. SEM image of the fracture surface of the sintered Mo alloy after tensile deformation to facture showed that intergranular fracture is the dominant mechanism at room temperature. A constitutive model has been developed to simulate the yield strength of Mo alloys at both room and elevated temperatures. It has been shown that the evolution trend of the yield strength predicted by the constitutive model broadly agrees with the experimental counterparts. The simulation indicated that creep dominates the deformation when the temperature is above 1200 K, while dislocation overcoming the obstacles through thermal activation dominates the deformation when the temperature is below 1200 K.

## Introduction

Owing to the outstanding properties such as high melting point, low thermal-expansion coefficient, good abrasive resistance, high thermal conductivity and high temperature strength, molybdenum (Mo) alloys have shown extensive applications as structural parts in aerospace and defense industries, especially at high temperatures[1-3]. However, the intrinsic brittleness, grain boundary segregation of N and O interstitials, high ductile to brittle transition temperature (DBTT) and high room-temperature brittleness inhibit the wide applications of Mo alloys[4-5]. Without improving the ductility by plastic deformation, such as forging, extrusion and rolling, and post heat treatments, the elongation of most Mo alloys under tensile deformation was normally below 5%[6]. Currently, the improvements of high-temperature strength, ductility and toughness become the research focuses for Mo alloys[7-9].

It is generally accepted that high temperature strength is the leading parameter determining the possible applications of the structural material used at elevated temperature[10]. However, most investigations (both experimentally and theoretically) concentrated on the room temperature strength of Mo alloys[4,5]. Thus, the aim of this paper is to develop a constitutive model to calculate yield strength of Mo alloys at both room and high temperatures. Experimental results were used to verify the accuracy of the model.

## Model Development

### Yield Strength at Room Temperature

In general, the yield strength ($\sigma_r$) of a material at room temperature can be calculated by considering the contributions of intrinsic yield strength of the pure material ($\sigma_{in}$, without impurities or solute atoms), solid solution strengthening ($\Delta\sigma_{ss}$) and second phase particle strengthening ($\Delta\sigma_p$), in the form of

$$\sigma_r = \sigma_{in} + \Delta\sigma_{ss} + \Delta\sigma_p \quad (1)$$

In equation (1), the solid solution strengthening can be expressed as

$$\Delta\sigma_{ss} = \sum k_j C_j^{2/3} \tag{2}$$

where $C_j$ is the concentration of one type ($j$) of the solute atom, and $k_j$ is the distribution parameter.

Since most second phase particle in Mo alloys are unshearable, the second phase particle strengthening in equation (1) can be calculated by considering the Orowan mechanism, with the form of

$$\Delta\sigma_p = \Delta\sigma_{or} = KM(1-\upsilon)^{-1/2}(Gb/\lambda)\ln(r/b) \tag{3}$$

where $M$ is Taylor factor, $\upsilon$ is the Poisson's ratio, $G$ is the shear modulus of the matrix, $b$ is the matrix Burgers vector, $K$ is a constant related to the granularity of the strengthening particles, $r$ is the average particle size on the dislocation slip plane and $\lambda$ is the effective particle interspacing on the dislocation slip plan.

Assuming that $\varphi$ is the volume fraction of the second phase particles and $S$ is the shape factor ($S$ equals one for spherical particles), then we have

$$\varphi = 2\pi S r^3 / \lambda^3 \tag{4}$$

Put equation (4) into (3), then it can be obtained

$$\Delta\sigma_p = \Delta\sigma_{Or} = KM(1-\upsilon)[Gb\varphi^{1/3}/r(2\pi S)^{1/3}]\ln(r/b) \tag{5}$$

Thus, the yield strength of Mo alloys at room temperature can be expressed as

$$\sigma_r = \sigma_{in} + \sum k_j C_j^{2/3} + KM(1-\upsilon)[Gb\varphi^{1/3}/r(2\pi S)^{1/3}]\ln(r/b) \tag{6}$$

**Yield Strength at Elevated Temperature**

Generally the yield strength of most materials (including Mo alloys) decreases with increasing the temperature, due to three possible reasons: (1) the softening of the matrix can help dislocations overcome the Peierls-Nabarro stress (lattice friction) due to the thermal activation at elevated temperature, (2) thermal activation can help decrease the energy required by the dislocations to overcome the obstacles (second phase particles) at elevated temperatures, and (3) creep deformation dominates at temperature above a critical value. Thus, to accurately predict the yield strength of Mo alloys, all the above mentioned three factors should be considered.

**Softening of the Matrix at Elevated Temperature**

For solid solution alloys, the evolution of the yield strength with temperature can be expressed as

$$\sigma_s(T) = \alpha\left[1-\exp(\frac{-Q_s}{RT})\right] \tag{7}$$

where $\alpha$ is the yield strength of the solid solution alloy at room temperature, $Q_s$ is the softening activation energy, $R$ is the gas constant and $T$ is the absolute temperature. For Mo alloys, the evolution of the yield strength with temperature can thus be expressed as：

$$\sigma_s(T) = (\sigma_{in} + \Delta\sigma)\left[1-\exp(\frac{-Q_s}{RT})\right] \tag{8}$$

**Effect of Second Phase Particles on Yield Strength at Elevated Temperature**

Considering that thermal activation at elevated temperature can help dislocation overcome the obstacles (second phase particles) through climbing, increasing temperature decreases the Orowan strengthening effect. The contribution of the second phase particles on the yield strength of Mo alloy at elevated temperature can thus be expressed as

$$\Delta\sigma_p^T = KM(1-\upsilon)[Gb\varphi^{1/3}/r(2\pi S)^{1/3}]\ln(r/b)\left[1-\exp(\frac{-Q_p}{RT})\right] \quad (9)$$

where $Q_P$ is the activation energy for dislocation bypassing the second phase particles.

Thus, the yield strength of Mo alloys at elevated temperature can be calculated as

$$\sigma(T) = \sigma_s(T) + \Delta\sigma_p^T = (\sigma_{in} + \Delta\sigma)\left[1-\exp(\frac{-Q_s}{RT})\right] + KM(1-\upsilon)[Gb\varphi^{1/3}/r(2\pi S)^{1/3}]\ln(r/b)\left[1-\exp(\frac{-Q_p}{RT})\right] \quad (10)$$

**Contribution of Creep on the Yield Strength at Elevated Temperature**

Creep deformation usually happens under a stress field for materials at elevated temperature. Normally the creep strain increases with the temperature. Considering that if the stress required for creep is less than that required for transient deformation, the dominant deformation mechanism is thus creep and the yield strength of the materials is determined by the creep resistance. For Mo alloys containing second phase particles, the constitutive equation for creep can be expressed as

$$\dot{\varepsilon} = A\left(\frac{\sigma-\sigma_p-\sigma_{bo}}{E}\right)^n \exp\left(\frac{-Q_c}{RT}\right) \quad (11)$$

where $\sigma_p$ is the inverse stress caused by the second phase particles inside the grains, $\sigma_{bo}$ is the obstacle stress at boundaries, $E$ is the Young's modulus and $Q_c$ is the activation energy for creep. The obstacle stress at boundaries, $\sigma_{bo}$, can be calculated by

$$\sigma_{bo} = m(2KGb/d)^{1/2}\sigma^{1/2}(1-\sigma_p/\sigma) \quad (12)$$

where m is the density of second phase particles. For edge dislocations K=1-υ, and for screw dislocations K=1.

**Experimental Validation of the Simulations**

**Experimental Details**

Mo-0.2%Ti-0.1%Zr-0.2%TiC alloy (in weight percentage) was used to verify the model accuracy. The alloy were fabricated using a similar method to that reported previously[11]. In brief, proper Mo (99.9% in purity and ~3 μm in size), Ti (99.5% in purity and ~80 μm in size) and TiC (99% in purity and ~1.1 μm in size) powders were mechanically mixed for 3 hours, followed by compression to compacts under a pressure of 250 MPa. Then the compacts were heated from room temperature to 1000 °C. At 1000 °C, the compacts were sintered for 2 hours. Then the compacts were heated to 1920 °C. At 1920 °C, the compacts were further sintered for 2 hours. During the whole sintering process, the compacts were protected by $H_2$ atmosphere.

The microstructures of the sintered Mo-0.2%Ti-0.1%Zr-0.2%TiC alloy were studied using optical microscope (OM) and JSM-5600LV scanning electron microscope (SEM). The dog-bone shaped tensile specimens with a gage size of 5 mm in diameter and 40 mm in length, were served in the tensile test at a constant strain rate of $5\times10^{-4}$ $s^{-1}$ on an Instron-8802 testing machine to determine the stress/strain curves at both room and elevated temperatures. The yield stress was determined as the 0.2% offset. Note that Each point of the yield strength values has been measured on three specimens.

**Validation of the Simulations by Experimental Results**

Fig. 1 shows the OM image of the sintered Mo alloy, showing that the alloy has an average grain size of ~20 μm. It can also be seen from Fig. 1 that some pores and second phase particles, with the size of 1~2 μm, distribute uniformly in the matrix. Our previous study indicated that the second phase particles are Ti, Zr, O, C contained strengthening phase, which substantially improves the

mechanical properties of the alloy by inhibiting dislocation movements[12]. Fig. 2 shows the SEM image of the sintered Mo alloy after tensile deformation to facture at room temperature, indicating that intergranular fracture is the dominant mechanism during deformation at room temperature. The Ti, Zr, O, C contained strengthening particles and pores can also be clearly observed on the fracture surface, similar to Fig. 1.

Fig. 3 shows both the model-predicted and experimental determined data for the yield strength of the Mo alloy at both room and elevated temperatures. Both experimental data and model predictions show that the yield strength of the Mo alloys decreases with increasing the temperature. It can be seen from Fig. 3 that the evolution trend of the yield strength predicted by the model broadly agrees with the experimental counterparts, although some predicted values at high temperature are higher than the experimental data. The higher the temperature, the large the discrepancy between the experimental data and model predictions. It is believed that the relatively lower experimental data might be due to the pores in the Mo alloy, as shown in Figs. 1 and 2. In the model, it is assumed that the alloy has a dense structure. However, since the Mo alloy was fabricated through a powder metallurgy process, which might leave some pores in the structures. The existence of the pores will decrease the yield strength of the alloy, because the pores can be easily collapsed under a low stress during deformation. One should be noted that creep dominates the deformation when the temperature is above 1200 K, while dislocation overcoming the obstacles through thermal activation dominates the deformation when the temperature is below 1200 K (see Fig. 3 for detailed information)). The investigation indicated that the developed model has a relatively high accuracy, and can thus be used to predict yield strength of the Mo alloys at both room and elevated temperatures.

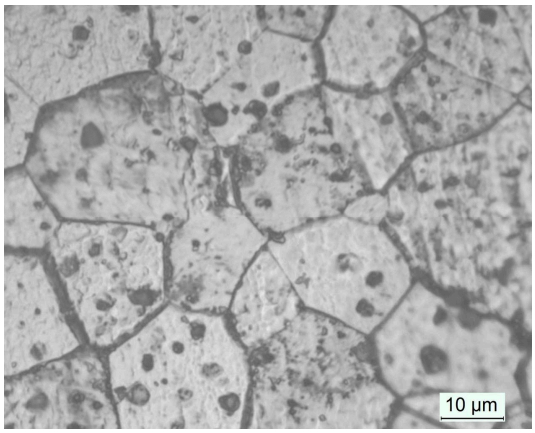



Fig. 1. OM image of the sintered Mo alloy.

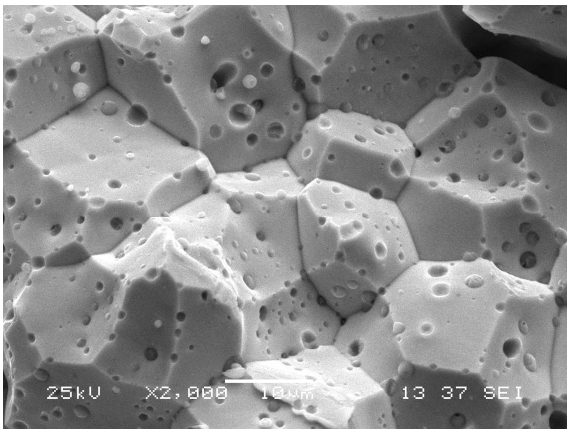



Fig. 2. SEM image of fracture surface of the sintered Mo alloy.

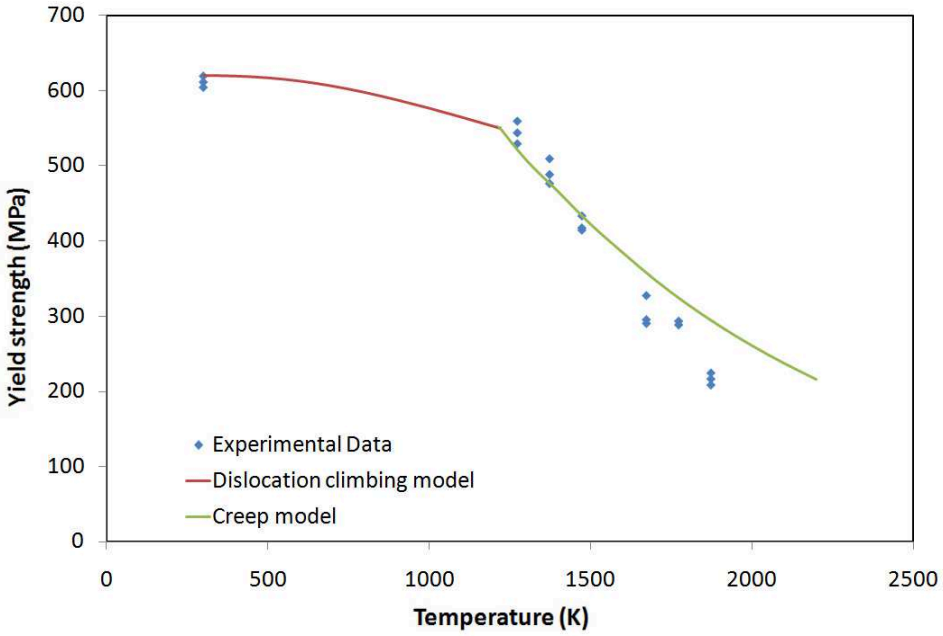



Fig. 3. Experimentally determined and simulated yield strength of the Mo alloy at both room and elevated temperatures.

## Conclusions

In this paper, the yield strength of a sintered Mo alloy has been investigated at both room and elevated temperatures. OM image showed that the sintered Mo alloy has an average grain size of ~20 μm, with some pores and second phase particles (Ti, Zr, O, C contained strengthening phase) distributing uniformly in the matrix. SEM image of the fracture surface of the sintered Mo alloy after tensile deformation to facture showed that intergranular fracture is the dominant mechanism at room temperature. A constitutive model has been developed to simulate the yield strength of Mo alloys at both room and elevated temperatures. It has been shown that the evolution trend of the yield strength predicted by the constitutive model broadly agrees with the experimental counterparts. The simulation indicated that creep dominates the deformation when the temperature is above 1200 K, while dislocation overcoming the obstacles through thermal activation dominates the deformation when the temperature is below 1200 K.

## Acknowledgements

This work is financially supported by the Program for New Century Excellent Talents in University (NCET-10–0842), Fundamental Research Funds for the Central Universities (2011JQ021), Distinguished Young Scholars of National Natural Science Foundation of China (50925416) and Ph.D. Programs Foundation of Ministry of Education of China (20090162110032).

## References

[1] B.V. Cockeram, The mechanical properties and fracture mechanisms of wrought low carbon arc cast (LCAC), molybdenum-0.5pct titanium-0.1pct zirconium (TZM), and oxide dispersion strengthened (ODS) molybdenum flat products, Mater. Sci. Eng. A 418 (2006) 120-136.

[2] T. Xiang, Molybdenum metallurgy, first ed., Central South University Press, Changsha, 2002.

[3] J.H. Schneibel, E.J. Felderman, E.K. Ohriner, Mechanical Properties of Ternary Molybdenum-Rhenium Alloys at Room Temperature and 1700 K, Scr. Mater. 59 (2008) 131-134.

[4] Y. Hiraoka, T. Noda, M. Okada, Embrittlement of sintered molybdenum predoped with carbon in high temperature oxygen-contaminated helium, J. Less Common Metals 91 (1983) 167-176.

[5] Y. Hiraoka, S. Yoshimura, Low-temperature tensile behavior of powder-metallurgy Mo-Ti alloys, Inter. J. Refra. Metal. Hard Mater. 12 (1994) 211-216.

[6] Z. Cai, J. Jin, H. Chen, Analysis of the strengthening mechanism of TZM molybdenum alloy, J. Shanghai Iron and Steel Research 3 (1993) 56-58.

[7] S. Yoshimura, Y. Hiraoka, Influence of heating in vacuum on low-temperature fracture behavior of carburized Mo-Ti alloys, Inter. J. Refra. Metal. Hard Mater. 14 (1996) 325-333.

[8] J. Fan, H. Cheng, M. Liu, B. Huang, J. Tian, Effect of Alloyed Elements Ti,Zr on the Property and Microstructure of Mo Alloy, Rare Metal Mater. Eng. 37 (2008) 1471-1474.

[9] T. Inoue, Y. Hiraoka, E. Sukedai, M. Nagae, J. Takada, Hardening behavior of dilute Mo-Ti alloys by two-step heat treatment, Inter. J. Refra. Metal. Hard Mater. 25 (2007) 138.

[10] W.L. Johnson, K. Samwer, A universal criterion for plastic yielding of metallic glasses with a $(T/Tg)^{2/3}$ temperature dependence, Phys. Rev. Lett. 95 (2005) 195501(1-4).

[11] H. Cheng, J. Fan, M. Song, Simulation of the elastic modulus of Mo alloys at both room and high temperatures, Advanced Materials Research 785-786 (2013) 81-85.

[12] H. Cheng, J. Fang, M. Liu, P. Li, J. Tian, Preparation, performance and structure of high tenacious Mo-0.1Zr alloy, The Chinese J. Nonfer. Metals 22 (2012) 114-120.

*Advanced Materials Research Vol. 937 (2014) pp 136-140*
*© (2014) Trans Tech Publications, Switzerland*
*doi:10.4028/www.scientific.net/AMR.937.136*

# Preparation and Photocatalytic Properties of Iron Titanate Compounds

Xue-fei LEI[1, 2, a], Xiang-xin XUE[3, 4, b], He YANG[4, 5, c]

[1] School of Resources and Materials, Northeastern University at Qinhuangdao, Qinhuangdao 066004, PR China

[2]Institute of Metallurgical Resource and Environmental Engineering, Northeastern University, Shenyang 110819, PR China

[3]Liaoning Key Laboratory of Metallurgical Resource Recycling Science, Shenyang 110819, PR China

[4]Liaoning Engineering and Technology Research Center of Boron Resource, Comprehensive Utilization, Shenyang 110819, PR China

[5]Liaoning Provincial Universities Key Laboratory of Boron Resource Ecological, Utilization Technology and Boron Materials, Shenyang 110819, PR China

[a] leixuefei69@163.com, [b] xuexx@mail.neu.edu.cn, [c] yangh@smm.neu.edu.cn,

**Keywords:** Iron titanate; Heat treatment; Photocatalytic activity; Methyl orange

**Abstract:**Iron titanate photocatalysts were synthesized by the high-energy ball milling method with titanium ore as the starting material. X-ray diffraction (XRD), Fourier transform infrared spectra (FTIR), thermal gravity and differential thermal analysis (TG-DTA), UV-visible diffuse reflectance absorption spectra (UV-Vis), photoluminescence emission spectra(PL) and photocatalytic degradation measurement were conducted to characterize the structure, surface status, UV-visible light response and performance of the obtained sample. After low temperature calcination (above 400 oC), the photocatalytic activity of iron titanate catalyst decreased gradually, which was mainly due to the decrease of surface hydroxyls and reactant adsorption capability.

## Introduction

$TiO_2$ has attracted intensive interests in the field of photocatalysis because of high catalytic activity, nontoxicity and excellent stability, etc. However, nanosize $TiO_2$ particles in suspension are difficult to handle and remove after their application in water and wastewater treatment. The separation step can be a tedious and costly process. On the other hand, a new series of photocatalysts containing complex $ABO_3$-type perovskite structure have been studied recently. These perovskite compounds as photocatalysts are particularly attractive because of their higher activities which can be easily excited under visible light or UV light irradiation. However, it is an expensive photocatalyst for application in large scale. Consequently, there is a need to search for more economical and effective photocatalyst for application in catalysis and separations. As illustrated by our recent works, our groups have reported that the whole of titanium dioxide-bearing blast furnace slag (TBBFS) as photocatalysts show UV-vis light photocatalytic activity to some extent[1-3]. The obvious advantages of the whole of TBBFS as photocatalysts are the lower costs involved and easy to be isolated.

In this paper, iron titanate photocatalysts were prepared by a simple but powerful approach through the high energy ball milling method with titanium ore as the starting material at different calcination temperature. The photocatalytic activities of iron titanate photocatalysts were evaluated by oxdating methyl orange under UV-vis light irradiation. The experimental results in this study can supply some theoretical guidance for the optimization of preparation conditions and further industrial use of iron titanate photocatalysts.

## Experimental Procedure

### Materials

In the process of preparing iron titanate photocatalysts, massive titanium ore was broken into pieces; the resulting shatters were then comminuted by disintegrator; subsequently, the powders were ground in the high-energy ball mill for 5 days. The average particle size of prepared samples was 10μm. After pulverization, titanium ore powders were calcined in air at a heating rate of 10°C/min up to 200, 300, 400 and 500°C and held for 3 h，then cooled down by natural; The resulting catalysts were labeled as $TO_{x,}$ where $x$ denoted the calcination temperature (°C).

### Experimental Procedure and Analytical Methods

Photocatalytic irradiations were carried out in a multi-tube mixing reaction apparatus equipped with a quartz immersion well, where a 500 W mercury lamp was placed as radiation source.

The X-ray diffraction patterns of $TO_x$ powders were obtained by using Philips X'pert X-ray diffractormeter with Cu Kα radiation. Fourier transform infrared spectrum of $TO_x$ powders was recorded on a Nexus-670 instrument. The optical absorption spectra were recorded on a Shimazu UV-2500 spectrophotometer. The thermal gravity and differential thermal analysis was conducted on a Shimadzu, DTG-60H apparatus to characterize the weight change and endothermal–exothermal status of $TO_x$ powders. The photoluminescence emission spectra of $TO_x$ powders were measured on a Hitachi FL-4500 spectrophotometer. Average particle diameter of $TO_x$ powders was got by using BT-1600 image analyzer.

## Results and Discussion

### Phase Analysis

As illustrated in Fig.1 (a-d), increasing the calcination temperature from 200 to 500°C led to the increase of the diffraction peak intensity. It can be observed that the similar patterns were obtained for all $TO_x$ catalysts, which were identified to be a mixture of titanomagnetite ($Fe_{2.75}Ti_{0.25}O_4$), iron titanate ($FeTiO_3$), titanium dioxide ($TiO_2$) and iron oxide.

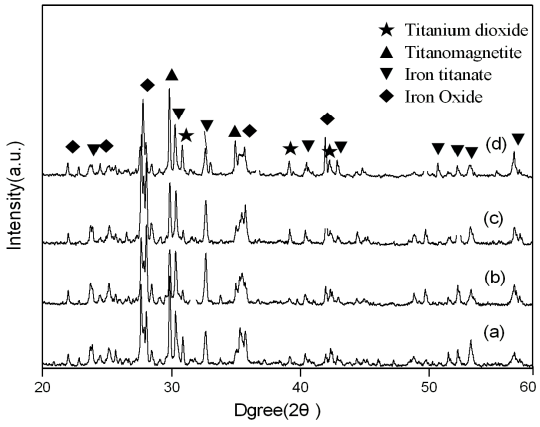



Fig. 1. XRD patterns of (a) $TO_{200}$, (b) $TO_{300}$, (c) $TO_{400}$, (d) $TO_{500}$ catalysts

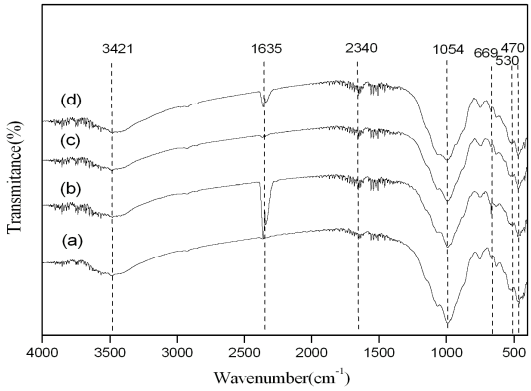



Fig. 2. FTIR absorption spectroscopy of (a) $TO_{200}$, (b) $TO_{300}$, (c) $TO_{400}$, (d) $TO_{500}$ catalysts

Fig. 2 shows the FTIR absorption spectroscopy of $TO_x$ catalysts calcined at different temperature, which can supply more information about the microstructure of $TO_x$ serial catalysts. As we can see, all samples showed the FTIR absorption bands at 3421 and 1635$cm^{-1}$, which are attributed to the stretching vibrations of surface hydroxyls and bending vibrations of adsorbed molecular water, respectively. With the increasing of calcination temperature, especially to 400 and 500 ˚C, the band intensity of O-H stretching vibration mode at 3421$cm^{-1}$ showed some decrease, implying the occurrence of dehydroxylation effect and thus the decrease of surface Brønsted acid sites, which is in well accordance with the TG-DTA results. In the fundamental vibration region, the bands at 470 $cm^{-1}$ was attributed to the fundamental vibrations of Titanomagnetite[4], the band at 530 $cm^{-1}$ was attributed to the fundamental vibration of Fe-O-Ti group in iron titanate ($FeTiO_3$)[5], the band at 669 $cm^{-1}$ was attributed to the fundamental vibrationof Ti-O group in $TiO_2$[6], and the band at 1054 $cm^{-1}$ was attributed to the fundamental vibrationof Fe-O group in $Fe_2O_3$[6], which are in well accordance with XRD results.

Fig. 3 shows the TG-DTA curve result of $TO_x$ catalysts. Combining the DTA and TG results we can see that, the endothermal peak below 150 ºC corresponded to the desorption of physisorbed $H_2O$. The exothermal peak in the range of 100-400°C corresponded to the desorption of $H_2O$ produced by the acid-base neutralization reaction between basic hydroxyls in $Fe(OH)_x$[7] and acidic hydroxyls in $Ti(OH)_x$[7], in which process the iron titanate crystallite with specific Fe-O-Ti structure was formed. The endothermal peak in the range of 400-450°C was due to the desorption of surface hydroxyls from iron titanate crystallite, which means that further increasing the calcination temperature could result in the decrease of surface Brønsted acid sites and thus the decrease of methyl orange adsorption amount in the photocatalytic experiments[5]. Above 450°C, there was no $H_2O$ desorption peak detected as been reported elsewhere[5], and only an unobvious exothermal peak was observed possibly due to the catalyst crystallization or phase transformation.

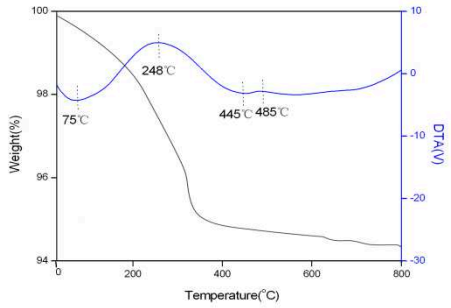



Fig. 3. TG-DTA curve result of $TO_x$ catalysts

The light absorbance characteristics of $TO_x$ catalysts calcined at different temperatures are depicted in Fig. 4. It is demonstrated in the UV-visible diffuse reflectance absorption spectra that $TO_x$ catalysts have higher absorbance in the UV-visible region. It is evident from the Fig that

UV-absorption edge of prepared $TO_x$ catalysts extended to longer wavelength, which is beneficial for improving the photoabsorption and photocatalytic performance of $TO_x$ catalysts under visible light. With increasing calcination temperature, the visible absorption capacity(>400 nm) of $TO_x$ catalysts increased obviously. The different light absorption capacity might be attributed to the difference in the surface microstructure, composition and phase structure in $TO_x$ catalysts[8].

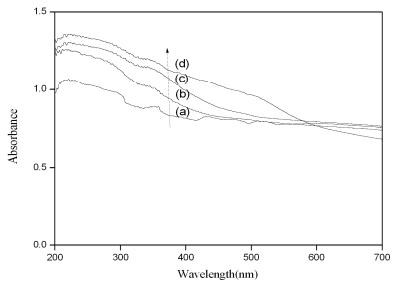



Fig. 4. UV-visible diffuse reflectance absorption spectra of (a) $TO_{200}$, (b) $TO_{300}$, (c) $TO_{400}$, (d) $TO_{500}$ catalysts

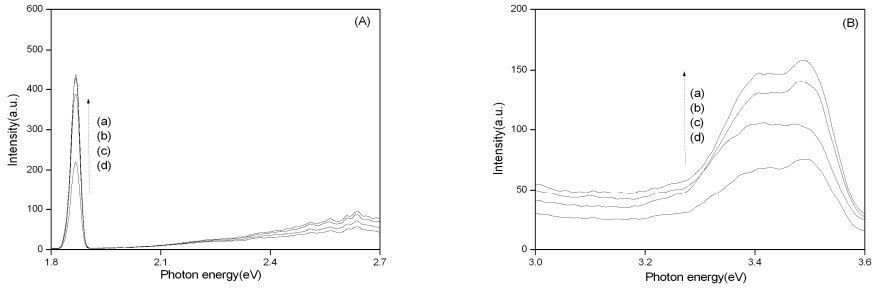



Fig. 5. Photoluminescence emission spectra of (a) $TO_{200}$, (b) $TO_{300}$, (c) $TO_{400}$, (d) $TO_{500}$ catalysts

The photoluminescence emission spectra of $TO_x$ catalysts calcined at different temperatures, as shown in Fig. 5, revealed that several peaks appeared at 1.87, 3.4, and 3.49 eV, which were equivalent to the 663.1, 364.7 and 355.3 nm wavelengths. The photoluminescence intensity of $TO_x$ catalysts calcined at the lower temperatures was significantly higher than that of $TO_x$ catalysts calcined at the higher temperatures. If it is agreed that the photoluminescence emission mainly results from the recombination of excited electrons and holes, then a lower photoluminescence intensity might indicate a lower recombination rate of those electrons and holes under light irradiation[9].

**Photocatalytic Activity**

The decolorization rate of methyl orange in the presence of different catalysts is illustrated in Fig. 6. The results in Fig. 6 indicate that the decolorization rate of methyl orange increased with the increase of calcination temperature when it was below 400°C, and decreased with the increase of calcination temperature when it was higher than 400°C. This suggests that an optimum calcination temperature was 400°C and any higher calcination temperature was detrimental to the enhancement of photoactivity of $TO_x$ catalysts.

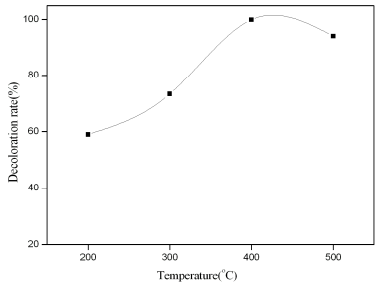



Fig. 6. Decolorization rate of methyl orange in the presence of different catalysts

## Conclusions

$TO_x$ catalysts were prepared by a simple but powerful approach through the high energy ball milling method at different calcination temperature. $TO_x$ catalysts were identified by XRD to be a mixture of titanomagnetite, iron titanate, titanium dioxide and iron oxide. The absorption edge of $TO_x$ catalysts appeared at about 500 nm. With increasing calcination temperature, the visible absorption capacity of $TO_x$ catalysts increased obviously. The photoluminescence intensity of $TO_x$ catalysts calcined at the lower temperatures was significantly higher than that of $TO_x$ catalysts calcined at the higher temperatures. The order of the activities of $TO_x$ catalysts is $TO_{400}$ >$TO_{500}$ >$TO_{300}$ >$TO_{200}$. Through comparing the photocatalytic activities of $TO_x$ catalysts calcined at different temperatures, the higher value depicts that methyl orange oxidation can be enhanced under low temperature calcination due to the higher absorbance in UV-visible region, surface hydroxyls and reactant adsorption capability, and the lower recombination rate of electron-hole pairs. Consequently, $TO_{400}$ catalyst is promising candidates for the photocatalytic oxidation of organic dyes wastewater with higher photocatalytic activity under UV-vis light irradiation.

## Acknowledgements

The authors wish to thank “the Natural Science Foundation-Steel and Iron Foundation of Hebei Province (E2012501012) and Basic Scientific Research costs of Central Colleges (No. N110423003)” for the financial support for the study.

## References

[1]H. Yang, L.L. Bai and E.J. Bu. Adv. Mater. Res. Vol. 113-114 (2010), p. 2105

[2]X.F. Lei, X.X. Xue. Mater. Sci. Semicond Process Vol. 11 (2008), p. 117

[3]X.F. Lei, X.X. Xue. Mater. Chem. Phys. Vol. 112 (2008), p. 928

[4]S.J. Yang, H. P. He, D.Q. Wu, et al. Env. Chem. 28 (2009), p. 697

[5]F. D. Liu, K. Asakurab, H. He, and Y. C. Liu, Catal. Today 164 (2011), p.520

[6]W. S. Peng, G. K. Liu, Editor, Infrared spectra of inorganic and coordination compounds, Science Press, Beijing (1982).

[7]J. Baltrusaitis, J.H. Jensen, V.H. Grassian, J. Phys. Chem. B 110 (2006), p.12005

[8]D. Jiang, Y. Xu, D. Wu, and Y. H. Sun, J. Solid State Chem. 181 (2008), p. 593

[9]F. B. Li and X. Z. Li, Chemosphere, 48 (2002), p. 1103

*Advanced Materials Research Vol. 937 (2014) pp 141-144*
*© (2014) Trans Tech Publications, Switzerland*
*doi:10.4028/www.scientific.net/AMR.937.141*

# Study on Laser Brazing for Copper

Xiao-hong WU

College of Electronic Information Engineering,Wuhan Polytechnic,Wuhan 430074,Chian

wxh-19671229@126.com

**Keywords**：laser brazed; copper;stainless steel ;tensile strength

**Abstract.** The power at 400 Watts Nd: YAG laser is used for laser brazing on copper. By improving the process parameter,a good joint will be achieved. Because of the stainless steel material, more lasers will be absorbed, which can actualize the small power laser weld the thicker red copper. The test of the joint pull shows that the tensile strength of the copper brazing joint can reach more than 80% of its base mental.

## Introduction

Copper has good characteristics of heat and electrical conduction, extension and corrosion resistance.It is widely used in the fields of petrochemical industry,marine machinery, communication, power and air system[1]. The traditional ways of connecting copper joint mainly including gas welding, manual electric arc-welding and TTG welding, then electron beam welding,plasma arc-welding and friction welding also followed. The main characteristics of laser welding are efficient, non-connect and average heat input, and it has been widely used in stainless steel welding, carbon steel welding and nickel alloy welding. As copper has a strong heat conduction and low absorption of laser wavelength(YAG laser is 1064 m, CO2 laser is 10.60μm),it needs a large laser output power to reach its target value[2]. There is still no report about the copper laser welding. Stainless steel has good heat conduction and welding character, and its laser absorption is much larger than the copper[3]. In this article, stainless steel is used as an adding solder, and through improving the process parameter to achieve a better welding result.

## Experimental Conditions and Methods

### Experimental Equipments

Average power output at 400 watts Nd: YAG laser welding is used in the test. The solder is 0.2 mm thick stainless steel [304].

Table 1. The main parameters of the welding system

| Parameter | Laser wavelength λ(nm) | Maximum average power output (W) | Electric pulse output energy(J) | Pulse repetition frequency (Hz) | Pulse width (ms) | Energy stability |
|---|---|---|---|---|---|---|
| Index | 1064 | 400 | 80 | 1-200 | 0.2-20 | 3% |

### Experimental Material

Red copper was used as test material; welding test piece size is 20mmX10mmX1mm. Before the test, use alcohol and deionizer water ultrasonic clean the surface to remove oil and impurities. The solder is stainless steel [304] (Standard 20mm*1mm*0.2mm). Argon was used as protective gas (protect on one side), and the gas-flow rate is 15L/min. After the welding, the tensile sample would be tested on MTS 810 tensile test machine.

## Experimental Methods

Using fixture fixes the copper piece, and tiles the stainless steel piece on the weld line. Using small power laser fix the stainless steel on the weld line which needs to be welded, every weld line needs to keep 10mm distances so that the stainless steel piece would not be shaped or perked by the heat during the persistent welding process. During the pulse laser welding process ,many factors can influence the welding effect, such as peak power, pulse width, pulse waveform, pulse frequency, welding speed and defocusing amount(the distance between Laser beam focusing focus and work piece surface).On the foundation of early stage feasible experiment, and in order to save more material and decrease experimental times, this paper keep the speed(2mm/s), defocusing amount(0.5mm) and pulse waveform(square wave)unchanged, and have test on the three parameters(welding electricity , pulse width, frequency), the factors can be seen in the table 2, besides, the paper also analyzes their influences on the welding quality.

Table 2. Factors and levels table

| Level | factor | factor | factor |
|---|---|---|---|
| | A welding electricity/A | B pulse width/ms | C pulse frequency/Hz |
| 1 | 260 | 6 | 2 |
| 2 | 280 | 9 | 4 |
| 3 | 300 | 15 | 8 |

## Experimental Results, Discussions and Analysis

### Orthogonal Experiment Result and Analysis

According to the design principle of three factors and three levels orthogonal test, there are nine ways to organize the process parameters in table 2. Then nine groups laser welding test will be tested on the flat, and the experimental numbers are listed in table 3.

Table 3. Analysis of orthogonal experiment

| number | A welding electricity /A | B pulse width /ms | C pulse frequency /Hz | welding surface, shaped characterization numerical value |
|---|---|---|---|---|
| 1 | 260 | 6 | 2 | 65 |
| 2 | 260 | 9 | 4 | 85 |
| 3 | 260 | 15 | 8 | 85 |
| 4 | 280 | 6 | 8 | 65 |
| 5 | 280 | 9 | 4 | 100 |
| 6 | 280 | 15 | 2 | 65 |
| 7 | 300 | 6 | 8 | 85 |
| 8 | 300 | 9 | 2 | 75 |
| 9 | 300 | 15 | 4 | 65 |

During the process of pulse laser welding on the red copper, laser's peak power plays a vital role. The peak power is directly controlled by electricity, so in this paper electricity is used to control laser's peak power. When the laser's peak power is low, the single laser pulse power is also low, and then the welding work piece can't be heated and melted efficiently. When the pulse width remains, with the increasing of the pulse peak electricity, laser's unit peak power increased gradually. Picture 1 is the appearance effect at different welding power. As the experimental numbers are 1, 2, 3, the peak electricity is 240A, the peak power is a little low, so the copper appearance can't be melted, and most of the laser will be reflected. The laser just welds the solder and stainless steel together; the weld line is not completely welded, picture 1a is the detail. While the peak power level can melt the copper appearance instantly, the absorption of laser will be increased a lot, which will contribute to the two copper's welding. When the peak electricity is 260A, the experimental numbers are 4, 5, 6; the welding effect can be seen from 1b. After scissoring the stainless steel, we can see obvious

copper weld line. However, with the continual increasing of the laser beam, for example, the experimental numbers 7, 8, 9, whose peak electricity is 280 A, one laser pulse may heat the welding part excessively, and even cause some following welding material melted and evaporated, and then form empty holes so that get through base metal, the test result can be seen in picture 1c.

The pulse width of the pulse laser also plays a vital role in welding quality. When the pulse width is 6ms, even the laser's peak power increases, the copper still can't be welded completely. When the pulse width is 15ms, it will cause the stainless steel solder spurt, and the welding consistency will be influenced at the end, the detail can be seen in picture 1d. Laser welding is using laser as heat source melt the material, the pulse width of the pulse laser directly control the work time between the single laser and material, so when the pulse width is small, that is to say when the work time between the single pulse and material is short, the material start to solidify before melt, and both the weld line width and depth are low. When the pulse width is too big, the work time between the single pulse and material will be too long, which will cause the low melting point alloy element in the material turn to gasification quickly, the quickly gasification function will splash the melting shape material in the melting pond. For this experiment, because of taking different low melting point stainless steel as solder, when the pulse width is big, the stainless steel is easier to make a splash and then influence the welding effect. From the analysis of pulse width's influence on welding effect, we can see that when the pulse width is 9ms, it can not only ensure the stainless steel not make a big splash but also can have the copper completely welded.

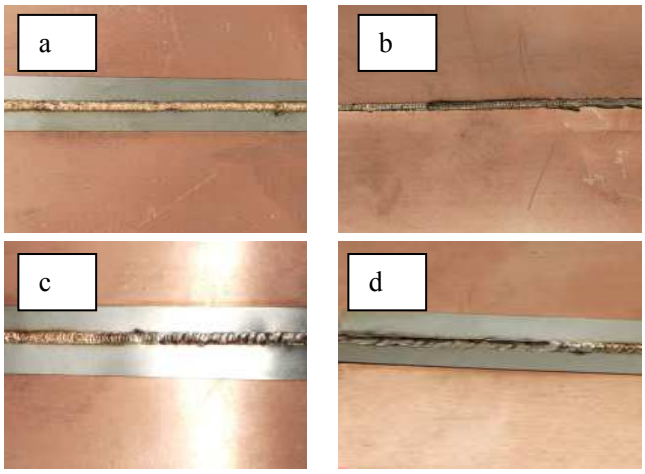



Fig. 1. The appearance of the weld

The pulse frequency of the laser is also one of the most important reasons that influence welding effect, but it mainly matches with the welding speed. When the speed is low, in order to avoid too much heat accumulation during the continual welding, the welding frequency should also be low. In order to ensure the single weld's continuation and suitable overlapping density,with the increasing of the speed, the welding frequency should also be increased.

We can conclude from the orthogonal experiment that when the electricity of the laser process parameter is 280A, pulse width is 9ms, frequency is 4Hz, the best welding appearance can be achieved, and it is ensured to be welded completely.

**Analysis of the Tensile Test**

Table3 is the result of the tensile test, the tensile strength of the base mental is 400MPa. If not taking stainless steel padding, the best process parameter can only make a 100MPa tensile strength, the reason is that the red copper has a low absorption on laser (wavelength of 1064nm), and most of the parts have been reflected, the laser can't melt the work piece efficiently, which makes the welding depth very low, and directly crack on the weld. Because the welding sample 1, 2, 4 haven't enough laser energy density or not inputting enough heat to the copper, the welding joint isn't welded completely, and then the tensile strength is low. While in sample 3, 8, 9, the laser inputs excessive heat to the work piece, so there is a lot of splash , and the defects of the weld such as hole and collapse cause the welding joint's tensile strength low. In sample 6, 8, because the pulse

frequency, welding facula's overlap rate and the melting rate on the horizontal direction are low, the welding joint's tensile strength is low. In sample 5, at the best process parameter, the biggest tensile strength is 326MPa, which can reach 80% of the base metal.

Table 4. Result of tensile test

| Sample | Tensile strength /MPa | Sample | Tensile strength /MPa |
|---|---|---|---|
| Base metal | 400 | 5 | 326 |
| Not padding | 100 | 6 | 282 |
| 1 | 256 | 7 | 310 |
| 2 | 268 | 8 | 275 |
| 3 | 285 | 9 | 285 |
| 4 | 265 | | |

**Analysis of the Weld Line**

In figure.2, the welding width is 1mm and the melting depth is 1mm, so this is a copper with 1mm thick welding head. There is no obvious layered phenomenon, which implies the stainless steel might haven't melted enough into the weld, it is just help the copper absorb more laser, this promise the welding quality and high tensile strength. The welding process may like this, when the laser can't work on the stainless steel's appearance, the stainless steel absorb lots of laser, the heat is conducted to the copper, with the copper's temperature increasing, the absorption also increase, and then the whole welding process can continue working.

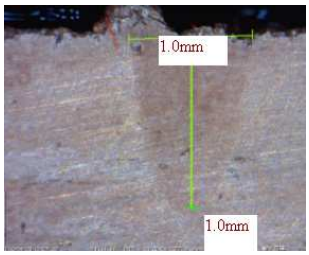



Fig. 2. The cross section of the weld line

**Conclusions**

(1)Stainless steel can be a solder and within its high absorption on laser, the low power laser can weld 1mm thick copper.

(2)Through optimizing the parameters, the best welding process parameters are: electricity 280A, pulse width 9ms, frequency 4Hz.

(3)The stain relief test shows that at the best process parameter, the tensile strength can reach 80% of the base metal.

**Reference**

[1] Wang.B.W, Wang.T,et al.Copper alloy and its processing technology[M].Beijing:Chemical Industry Press,2007:1-2(in Chinese)

[2] Ihor Mys,Manfred GEIGER.Using of pre-pulse in laser spot welding of materials with high optical reflection[J].Fourth international symposium on laser Precision micro. 2003, 5063: 314-319

[3] Y.S.Yang et a1.J.Materials Processing Technology.1999,94:l51

*Advanced Materials Research Vol. 937 (2014) pp 145-149*
*© (2014) Trans Tech Publications, Switzerland*
*doi:10.4028/www.scientific.net/AMR.937.145*

# Expansion Behavior and Microstructures of Hypereutectic Al-Si alloys Subjected to Thermal Cycling

Xue-wei ZHU[a], Ri-chu WANG[b], Jian PENG[c]

[a,b,c] School of Materials Science and Engineering, Central South University, Changsha 410083, Hunan, China

[a]zxw_83614@163.com; [b]wrc@csu.edu.cn; [c]pengjian365@163.com

**Keywords**: Hypereutectic Al-Si alloys; Coefficient of thermal expansion (CTE); Microstructure; Thermal cycling

**Abstract:** The effects of the thermal cycling on the coefficient of thermal expansion (CTE) and microstructure of the hypereutectic Al-Si alloys were investigated. The hypereutectic Al-Si alloy was produced by spray-forming and extruding process. Experiment results showed that the distribution of Si in Al matrix is uniform for the Al-Si alloy. The primary Si phase grew gradually during the thermal cycle. There is no remarkable change of CTE during thermal cycling for both materials at the same temperature range. The CTE of Al-Si alloy decrease with increasing on thermal cycling temperature up to 300°C due to the compressive thermal stress in the alloys.

## Introduction

Hypereutectic Al-Si alloys have been developed for electronic packaging applications due to their attractive properties such as high thermal conductivity, low weight and compatible coefficient of thermal expansion (CTE) with microelectronic systems [1-4]. In electronic packaging applications, the thermal expansion coefficient of the thermal material becomes a critical property parameter which many researchers have focused on [5-8]. The thermal materials served in electronic packaging often work in a harsh thermal environment, such as repeated heating and cooling. The mismatch of CTE between thermal materials and electronic packaging system could influence the overall performance of the component.

The purpose of this article is to discuss the effect of thermal cycling on Al-Si alloy. CTE of Al-Si alloy versus thermal cycling counts and temperatures was investigated. The microstructure evolution of the Al-Si alloys with thermal cycling counts and temperature has also been studied, in order to reveal the influence mechanism of the thermal cycling insight on the damage of the Al-Si alloys.

## Experimental Procedures

The Al-Si alloys containing 27wt.%Si were fabricated by spray-forming and extruding process. Al-Si alloy samples for experiment (diameter 5 mm×25 mm) were cut from bulk materials using a wire electrical discharge machine. Pure Al specimens with same dimension were also prepared for the purposed of comparison. The microstructures of the Al-Si alloys were observed by SEM (FEI QUANTA-200).

A thermo-mechanical tester (NETZSCH DIL 402 PC) was employed to obtain thermal response curves from which the CTE value could be derived. Specimens were polished with 1μm alumna slurry before experiment for native oxide film removal. Thermal cycling was performed in temperature range of 20~170°C, 20~235°C and 20~300°C. Heating and cooling rate is 5 K/min.

In this work, average CTE from temperature T1 to T2 was calculated using the following equation:

$$\alpha = \frac{l_{T_2,n} - l_{T_1,n}}{l_{T_1,n}(T_2 - T_1)}$$

Here, $\alpha$ is CTE, $n$ denotes cycling counts, $l_{T2,n}$ and $l_{T1,n}$ denotes the length of specimen at temperatures $T_2$ and $T_1$ in thermal cycling $n$.

## Results and Discussion

### Microstructures of the Al-Si alloys

Fig.1 presents the SEM images of the hypereutectic Al-Si alloys for thermal cycling during different temperatures range for 10 times. It can be seen that the distribution of Si is relatively uniform in the as-extruded alloy, and the thermal cycling process has not changed the tiny crystal Si phase particles uniform dispersion in Al matrix, and few gas porosity was observed. The primary Si phase particles are grew up characteristic to various extents at different temperatures. However, the Si particulates remain nearly spherical shape during thermal cycling process. Considering as the uniform distribution and fine size of the primary Si phase, the best microstructure of hypereutectic Al-Si alloys was obtained after thermal cycling treatment at 235°C for 10 times.

Fig.2 presents the microscopy images of hypereutectic Al-Si alloys after thermal cycling for different times. It can be seen that the primary Si phase remains uniform distribution and fine, like particulate in shape after thermal cycling for 10 times(as shown in Fig.2(a)). However, the primary Si phase grew slightly with the cycling count of 20 and 40(as shown in Fig.2(b) and (c)). In the thermal cycling process, the microstructure evolution is composed of the supersaturated Al matrix desolventizing, primary Si phase particles further coarsening, and the number of Si particles declining. It suggests that the growth mechanism of the primary Si phase under the thermal aging effect is agglomeration growth, resulting in the non-uniform distribution of the Si phase. On the other hand, the largest Si phase particle size is remained less than 10 μm at 300°C thermal cycling for 40 times, which is generally accepted as a fine microstructure alloy.

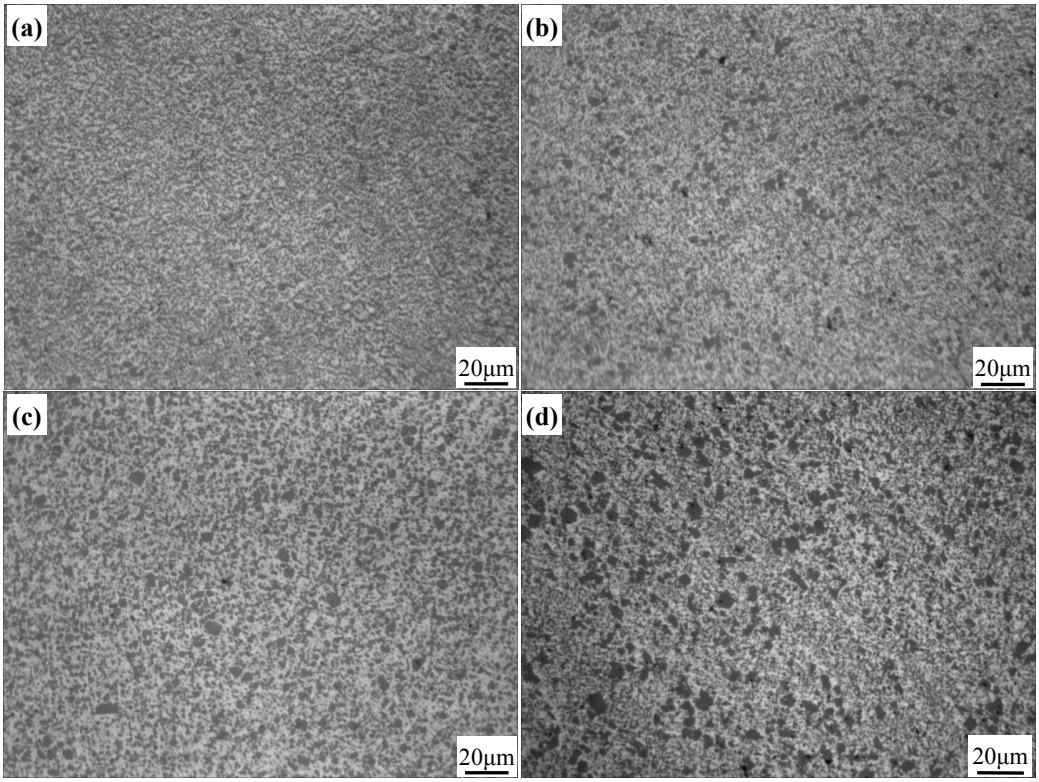



Fig. 1. Microstructures of extruded spray-deposited Al-27%Si alloy before and after thermal cycling under different temperatures: (a) as-extruded; (b) 170°C; (c) 235°C; (d) 300°C

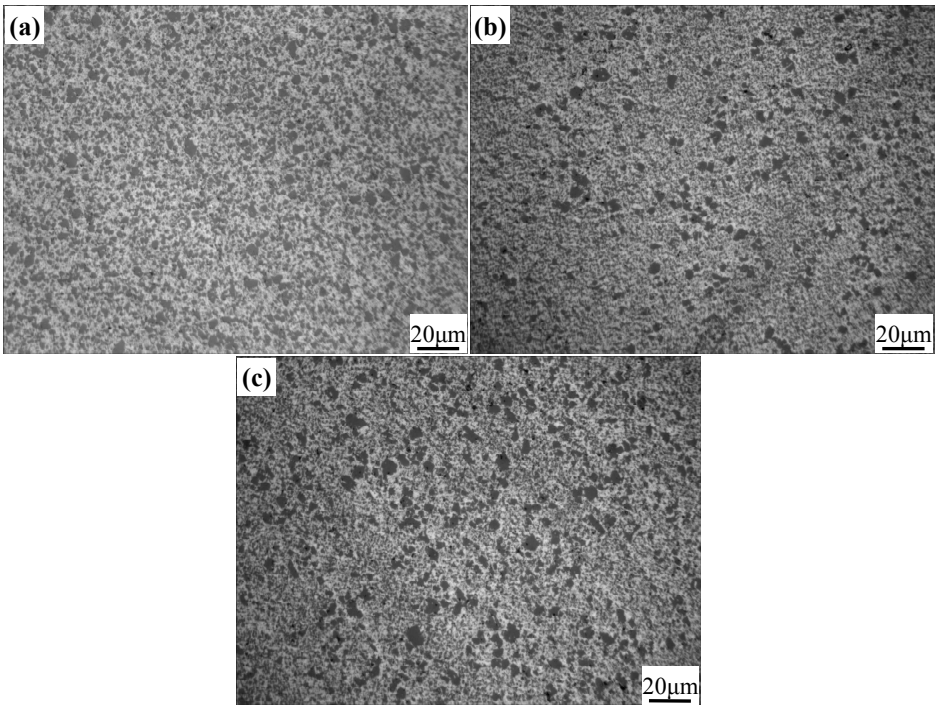



Fig. 2. Microstructures of spray-deposited Al-27%Si alloy between 20°C and 235°C for different times: (a) 10 times; (b) 20 times; (c) 40 times

Fig.3 presents the fracture surfaces of the Al-Si alloys after thermal cycling at different temperatures. It can be seen that dimple fracture surface formed at the Al matrix, while cleavage fracture surface formed in the primary Si phases. It suggests that the Al matrix fracture with a ductile model, and the Si phase fracture with a brittle model. Furthermore, the primary Si phases are encompassed by the Al matrix, the Al/Si interface coheres well in the hypereutectic Al-Si alloys. With the ascending of the temperature, the fracture model is unchanged, but the area fraction of the cleavage fracture surface increases slightly. This result is consistent with the SEM analysis of the microstructure. In a word, the hypereutectic Al-Si alloys have a stable thermo-mechanical property.

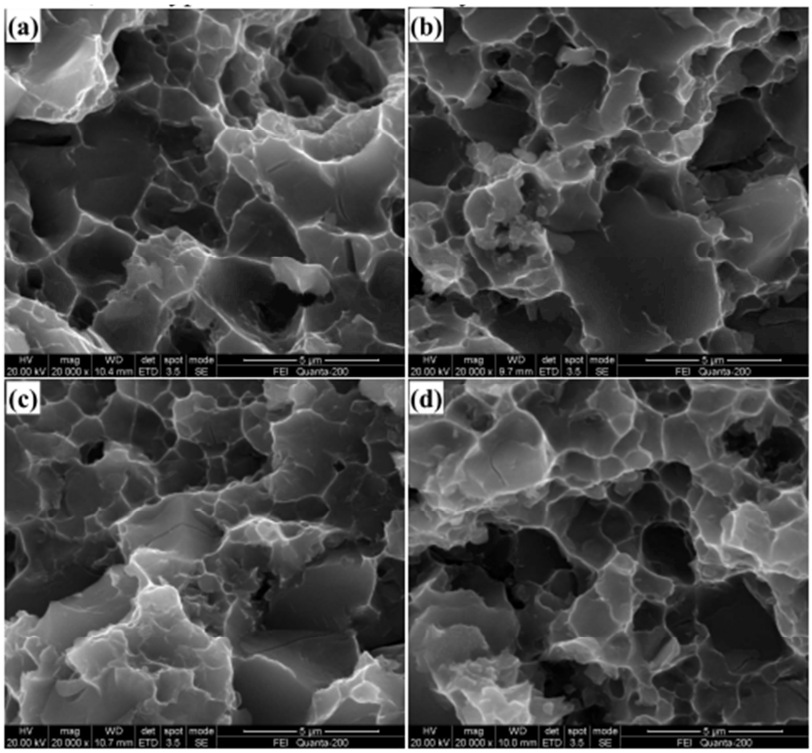



Fig. 3. Microstructures of hot extruded spray-deposited Al-27%Si alloy before and after thermal cycling under different temperatures for 10 times: (a) hot extruded; (b) 170°C; (c) 235°C; (d) 300°C

## CTE of Al-Si alloys

The average CTE within different temperature range versus thermal cycling counts for both pure Al and hypereutectic Al-Si alloys are shown in Fig.4. It could be seen that the addition of Si can significantly decrease the CTE of aluminum. There is no remarkable change of CTE during thermal cycling for both materials at the same temperature range. This result demonstrates that the Al-Si alloy have good thermo-stability under 300°C.

Furthermore, the CTE of Al-Si alloy decrease with increasing on thermal cycling temperature. The mainly effect of this variation tendency is the compressive thermal stress. At the beginning of the thermal cycle, the residual tensile stress is relaxed elastically, and CTE keep higher due to the lower constraint force. With the ascending of the temperature, the residual stress is completely relaxed, the compressive stress is gradually developed during further heating and that will also constrain the lattice expansion, resulting in the decreasing of the CTE.

## Conclusions

(1) The distribution of Si in Al matrix is uniform for the hypereutectic Al-Si alloy produced by spray forming and extruding process. The primary Si phase grew gradually during the thermal cycle, but the largest Si phase particle size is still less than 10 μm at 300°C thermal cycling for 40 times, which is generally accepted as a fine microstructure alloy.

(2) There is no remarkable change of CTE during thermal cycling for both materials at the same temperature range. The CTE of Al-Si alloy decrease with increasing on thermal cycling temperature up to 300°Cdue to the compressive thermal stress in the alloys.

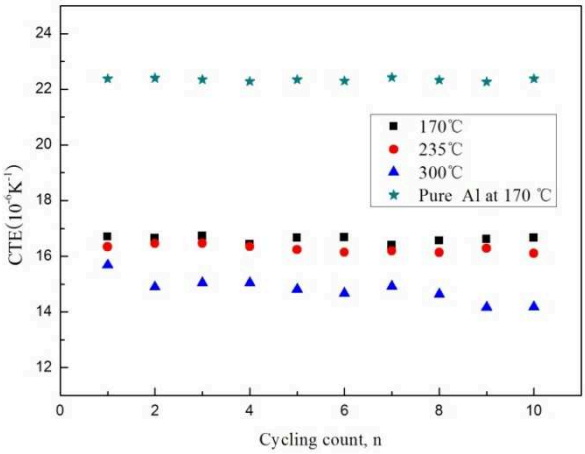



Fig. 4. CTE of pure Al and Al-Si alloys vs. thermal cycling counts.

## Acknowledgement

This work was financially supported by ‘‘Ministry of Science and Technology of China (JPPT-125-GH-039)’’.

## References

[1] C. Cui, A. Schulz, K. Shimanski. Spray forming of hypereutectic Al-Si alloys. J.Mater. Pro. Tech., 209(2009) 5220-5228.

[2] C.M. Chen, C.C. Yang, C.G. Chao. A novel method for net-shape forming of hypereutectic Al–Si alloys by thixocasting with powder performs, J.Mater. Pro. Tech., 167(2005) 103–109.

[3] H.S. Dai, X.F. Liu. Refinement performance and mechanism of an Al-50Si alloy. Mater. Character., 59(2008) 1559-1563.

[4] K. Yu, C. Li, J. Yang. Production and properties of a 90%Si-Al alloy for electronic packaging applications. Mater. Sci. Forum, 610/613(2009) 542–545.

[5] N. Chen, H. Zhang, M.Y. Gu. Effect of thermal cycling on the expansion behavior of Al/SiC composite. J Mater. Pro. Tech., 209(2009) 1471-1476.

[6] A. Arpon, J.M. Molina, R.A. Saravanan. Thermal expansion behaviour of Al/SiC composites with bimodal particle distributions. Acta Metall., 51(2003) 3145-3156.

[7] B.G. Kim, S.L. Dong, S.D. Park. Effect of thermal processing on thermal expansion coefficient of a 50vol.%SiC/Al composite. Mater. Chem. Phys., 72(2001) 42-47.

[8] Q. Zhang, G.H. Wu, L.T. Jiang. Dimensional stability of Al-Si matrix composite reinforced with high content SiC. Mater.Chem.Phys., 82(2003)780-785.

*Advanced Materials Research Vol. 937 (2014) pp 150-153*
*© (2014) Trans Tech Publications, Switzerland*
*doi:10.4028/www.scientific.net/AMR.937.150*

# Fatigue Damage Evaluation Research of Aluminum Alloy Based on Energy Degradation

Xu-dong LI[1, a *], Lan ZOU[2,b], Zhi-tao MU[1,c] Guang-ming KONG[1,d]

[1] Naval Aeronautical Engineering Academy Qingdao Campus, Qingdao, 266041, People's Republic of China

[2] Qingdao University, Qingdao,266061, People's Republic of China

[a] xdli236415064@163.com, [b]236415064@qq.com, [c] mzt63@163.com, [d] kgm@163.com

**Keywords:** fatigue crack, aluminum alloy, prior corrosion, microstructure, SEM in-situ technology.

**Abstract.** Experimental investigations of fatigue cracking behavior of LC9 aluminum alloy (AA LC9) subjected to elevated temperature were conducted with scanning electron microscope (SEM). Results indicate elevated temperature is important for the fatigue crack growth of AA LC9. Based on small crack growth, crack growth rate for AA LC9 is characterized.

## Introduction

Fatigue is of great concern in aircraft structure, and for the important engineering value, attracts interests of many researchers [1-3]. Fatigue damage is caused as a result of damage accumulation of cyclic mechanical load, and will result in great disaster if left without concern. How to choose proper parameter to characterize damage accumulation which will lead proper residual fatigue life estimation has become a crucial research area. Lots of researchers put great efforts, and proposed various quantitative characterization methods include cycling plasticity response methods, ultrasonic wave method and electric resistance method etc. There is one shortcoming for the above mentioned methods are that these parameters are hard to acquire and are not so sensitive to material damage. The present thesis proposed a method that is easy to manipulate which is also sensitive to damage accumulation based on the mechanism of fatigue damage accumulation, and is promising for engineering application [4-7].

## Theoretical Analysis

From viewpoint of energy, material absorbs energy from external cyclic mechanical load during fatigue process, which will cause irreversible damage to material. The total energy material absorb before final fracture represent the toughness of material. The more energy absorbed, the better toughness material owns. After damage, the ability of material absorbing energy will decrease. So it is reasonable to choose toughness as parameter to characterize damage revolution of material.

Considering a uniform section specimen subjecting to single direction fatigue loading, damage is accumulating in the specimen. The present study made a supposition that unit volume material will absorb energy $w$ which maintains constant during whole fatigue process. The pristine and damaged specimen will absorb energy of $W_0$ and $W$ until fracture. So the toughness variation can be expressed as $(W_0\text{-}W)/ W_0$, which is defined as damage variable $D$ as Eq. (1).

$$D = \frac{W_0 - W}{W_0} = 1 - \frac{W}{W_0} \tag{1}$$

where $W_0$ represent the original toughness, while $W$ represent the residual toughness when damaged. Based on physical meaning of the material single direction tensile curve, $W_0$ and $W$ can be easily acquired by integrating the area below the single direction tensile curve of pristine and damaged material, which are quite easy to manipulation in engineering application. Establishing an equivalent relationship between damage variable $D$ and fatigue damage will be of help in evaluating fatigue damage revolution of material.

## Experiments Setup and Results

### Experiment Material

Aero LY12CZ aluminum alloy is used for the experimentation, which is made into dog-bone specimen in the rolling direction, whose shape, composition, and mechanical property is shown in Fig.1 and Table.1 respectively.

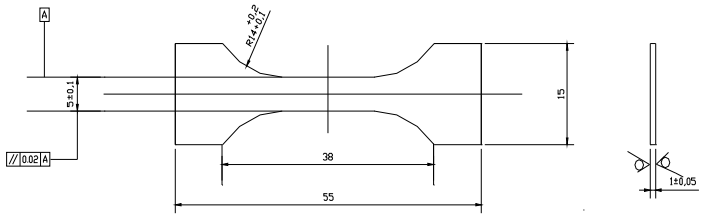



Fig.1. Specimen dimension (Unit: mm)

Table 1. Chemical constitution of LY12CZ

| Composition | Si | Fe | Cu | Mn | Mg | Zn | Ti | Al |
|---|---|---|---|---|---|---|---|---|
| Content (Wt. %) | 0.5~1.2 | 0.5 | 0.3 | 0.2 | 0.75 | 0.2 | 0.15 | Bal. |

### Experiment Procedure

The whole experiments are accomplished in MTS 880 fatigue test machine. The procedure is as follows:

(1) Single direction tensile test is executed on pristine specimen to get original stress-strain curve, which is used to calculate original toughness $W_0$.

(2) Fatigue test is executed on pristine specimen under condition of maximum stress of 150, 200, 250MPa respectively with stress ratio $R$=-1 without changes until fracture occurred to obtain the fatigue life $N_f$ under above mentioned three fatigue stress.

(3) Fatigue test is executed on pristine specimen with the same fatigue test condition as in (2), but the specimen is only subjected to several different load cycles lower than fatigue life $N_f$ without fracture in order to introduce different fatigue damage to specimen, after which single direction tensile test is executed on the damaged specimen to get stress-strain curve of damaged specimen with the aim to calculate residual toughness $W$.

### Results and Discussion

Damage variable changes with fatigue ratio, which is shown in Fig.2. It can be inferred that damage variable increases rather slowly in low fatigue ratio, while it boosts rapidly in high life ratio, which indicates that the defined damage variable $D$ is very sensible fatigue damage, and is suitable for fatigue damage revolution characterization.

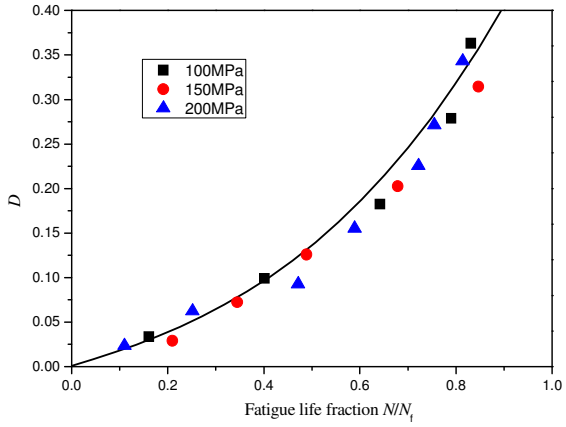



Fig. 2. Relationship of damage variable $D$ versus fatigue life fraction

A damage model were proposed by reference [2] and [3]

$$\frac{\mathrm{d}D}{\mathrm{d}N}=\left(\frac{\alpha\sigma_a+(1-\alpha)\sigma^{'}}{R(1-D)}\right)^{-n(R)} \tag{2}$$

Where $R$ represent stress ratio, $n(R)$ is constant related to material property. $\sigma_a$ is maximum applied stress, $\sigma^{'}$ is average applied stress. $\alpha$ refers to the damage contribution ratio of stress amplitude to average stress. When $R$=-1, $\sigma^{'}=0$, $\sigma_a=\sigma_{\max}$, $\alpha=1$. Integrating Eq. (2) will lead to Eq. (3).

$$D=1-(1-\frac{N}{N_f})^{\frac{1}{n(R)+1}} \tag{3}$$

From Eq.(1) and Eq.(3), we can get Eq.(4).

$$\lg(1-D)=\frac{1}{n(R)+1}\lg(1-\frac{N}{N_f}) \tag{4}$$

Suppose

$$k=\frac{1}{n(R)+1} \tag{5}$$

From Eq. (4), it can be inferred that in double log coordinate system $\lg(1-D)\sim\lg(1-\frac{N}{N_f})$, the slope of the fitting straight line is $k$, then

$$n(R)=\frac{1}{k}-1 \tag{6}$$

The fitting result of data appeared in Fig.2 is shown in Fig.3, of which the slope is $k=0.2344$. Then $n(R)$ can be calculated as 3.2662 from Eq.(6). Compared to reference [4] which indicates that $n(R)$ for 45# steel is 5.66, it can be inferred that LY12CZ is more sensible to fatigue damage than 45# steel.

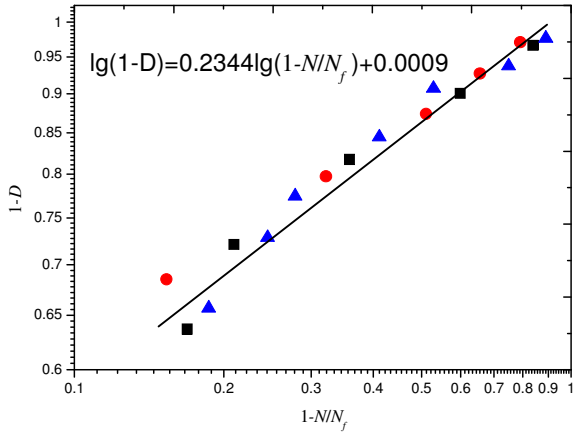



Fig.3. $\lg(1-D)$ versus $\lg(1-\frac{N}{N_f})$

From Eq.(1) and (3), we get Eq.(7)

$$N_f = \frac{N}{(1-\frac{W}{W_0})^{n(R)+1}} \tag{7}$$

From Eq.(7), residual life of damaged specimen can be estimated by single direction tensile test of the pristine and damaged specimen.

## Conclusions

(1) The present paper proposes a damage variable based on energy degradation, which is quite sensible to metal fatigue damage evolution and easy to acquire, making it very promising for engineering application.

(2) The thesis get the relationship between the damage variable and residual life of damaged aluminum alloy, which is valuable in aluminum structure safety evaluation of aircraft.

(3) For only a few tests has been conducted for the experiment is time and money consuming, the general validity of the obtained conclusion in this paper need to be examined furthermore.

## References

[1] Lemmatize J and Caroche J L. Mechanics of solid Materials. Cambridge University Press, London, 1990, pp. 15-20

[2] Wang J. Low cycle fatigue and cycle dependent creep with continuum mechanics. Int. J. Damage Mech. 1(2) (1992) 237-244

[3] Jiang Jusheng, Xu jinquan, Resistence based fatigue damage chrecterization of metallic materials. Mechanical strength. 21 (3) (1999) 232-234.

[4] Jiang Jusheng, Guo Yimu. The quantitative research of fatigue damage for metallic materials. Materials science and Engineering. 18(1) (2000) 43-46.

[5] Li Xu-Dong, Wang Xi-Shu, Ren Huai-Hui, Chen Yin-Long, Mu Zhi-Tao. Effect of prior corrosion state on the fatigue small cracking behaviour of 6151-T6 aluminum alloy. Corros. Sci. 55(2) (2012) 26-33.

[6] X.D. Li, Z.T. Mu, Z.G. Liu. SEM In-situ study on pre-corrosion and fatigue cracking behavior of LY12CZ aluminum alloy. Advances in Fracture and Damage Mechanics XI. Trans Tech Publications, Switzerland. (2012) 81-84.

[7] Xi-Shu Wang, Xu-Dong Li, Huai-Hui Ren, Hai-Yan Zhao , Ryosuke Murai, SEM in-situ study on high cyclic fatigue of SnPb-solder joint in the electronic packaging. Microelectronics Reliability. 51(2011) 1377-1384

*Advanced Materials Research Vol. 937 (2014) pp 154-157*
*© (2014) Trans Tech Publications, Switzerland*
*doi:10.4028/www.scientific.net/AMR.937.154*

# Comparative Study of Copper Brazing with Ag-Cu-Zn and Ag-Cu-P Filler in Heat Treatment Furnace

Rong WANG[1,a,*], Ya-juan JIN[2,b]

[1]The Department of Science and Technology, Jiangsu University of Science and Technology, Zhenjiang Jiangsu 212003, P. R. China

[2]Provincial key Lab of Advanced Welding Technology, School of Materials Science and Engineering, Jiangsu University of Science and Technology, Zhenjiang Jiangsu 212003, P. R. China

[a]13905280125@163.com, [b]1103029064@qq.com

*Corresponding author

**Keyword:** Furnace brazing, Copper, Ag-Cu-Zn filler, Ag-Cu-P filler

**Abstract:** Wetting and spreading ability of Ag-Cu-Zn filler and Ag-Cu-P filler on copper surface under heat treatment furnace was studied. The microstructures of brazed joints of Ag-Cu-Zn and Ag-Cu-P filler under the same parameter were also observed. The microstructure shows that the wetting ability of Ag-Cu-Zn filler on the copper surface is better than Ag-Cu-P and its structure is uniformed and regulated. It is founded that there were obvious dissolution and diffusion between base metal and filler for the copper/Ag-Cu-Zn/copper joint, there were white and black eutectic structure formed in the joint interface.

## Introduction

Copper has many desirable properties for thermally efficient and durable heat exchangers. First and foremost, copper is an excellent conductor of heat. This means that copper's high thermal conductivity allows heat to pass through it quickly. Other desirable properties of copper in heat exchangers include its corrosion resistance, biofouling resistance, maximum allowable stress and internal pressure, creep rupture strength, fatigue strength, hardness, thermal expansion, specific heat, antimicrobial properties, tensile strength, yield strength, high melting point, alloyability, ease of fabrication, and ease of joining. Brazing process is used in joining most of copper heat exchangers.

The melting point of silver-based solder is not very high and can be used in joining many metals. It has many properties which contains good strength, ductility, thermal conductivity and corrosion resistance to various medium[1-3]. Introducing Zn can reduce the melting point of silver-copper alloy. From the phase diagram of silver-copper-zincalloys, the zinc in the alloy cannot pass a certain value. Otherwise, it may appear the brittle phase[4,5]. Therefore, the zinc content should not more than 35%. The melting point of copper-phosphorus brazing is low and liquidity of it is very good. This kind of brazing temperature is close to silver brazing. It also has advantages of self-fluxing and low price. Adding silver into the sliver-copper can improve its workability, plasticity, tensile strength and electrical conductivity. And also improve the metallic wettability of the copper-phosphorus filler.

In this paper, the wettability and gap filling of silver-copper-zinc brazing filler and silver-copper-phosphorus brazing filler in the heat treatment furnace was studied. It is benifit to choose a suitable brazing filler metal for joining red copper pipes.

## Experimental Materials and Methods

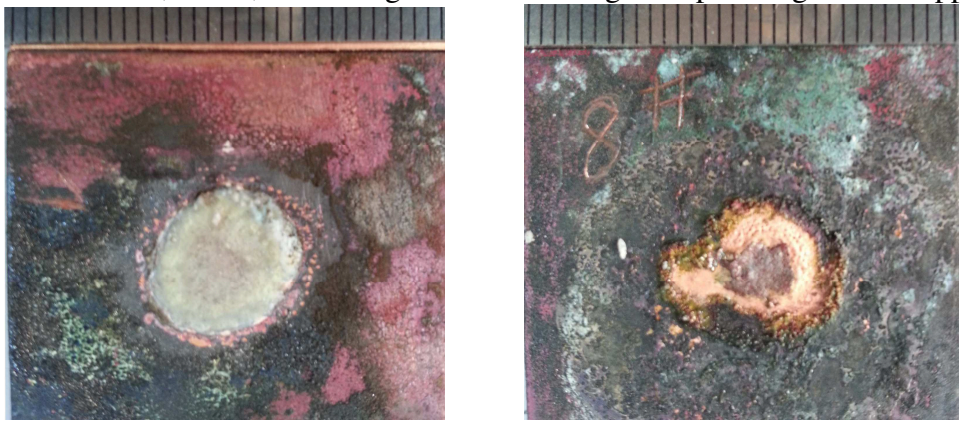
The chemical compositions of the brazing filler metals are shown in table 1. The base metal is red copper. The brazing tests were performed in traditional heat treatment furnace. The parameters of the tests contain temperature and time. We set the temperature at 810 °C and keep heating for 3 minutes and 5 minutes. Then, spreading area and wetting angle of brazing filler metals on the red copper were measured after the test. And the cross-sectional microstructure of the joint is observed by optical microscope. By comparing the size of the wetting angle and structure, we can choose more suitable filler for red copper.

Table 1. Compositions of the brazing filler metals

| Brazing filler | Chemical components wt.% | | | |
|---|---|---|---|---|
| | Ag | Cu | Zn | P |
| BAg45CuZn, HL303 | 45 | 30 | remain | — |
| BCu80PAg, HL204 | 15 | remain | — | 5 |

## Experimental Results and Analysis

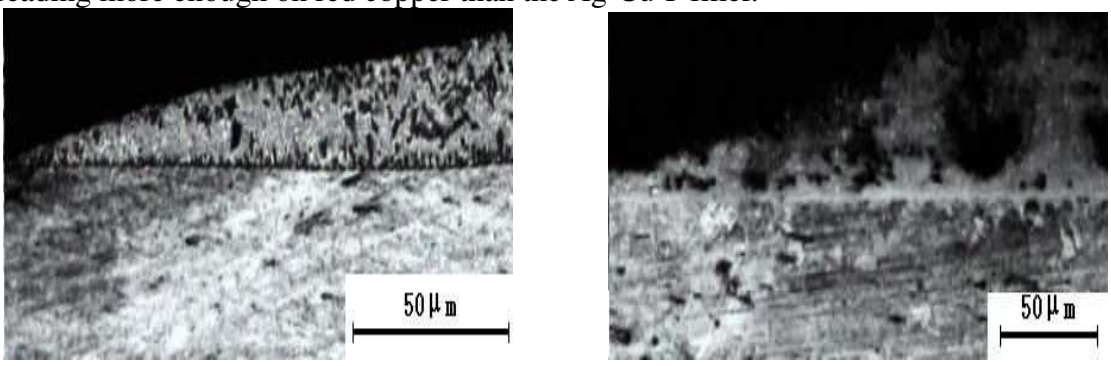
Fig.1 shows the macrophotograph of Ag-Cu-Zn and Ag-Cu-P filler after wetting and spreading on the red copper surface with flux at 810 °C for 3 minutes. From Fig.1, It can be seen that the two kinds of fillers wet and spread on the red copper, but they are obviously different. The Ag-Cu-Zn filler forms the better wetting and spreading property on red copper, so the wetting and spreading areas is bigger than the Ag-Cu-P filler on red copper. Because of the elements of zinc in the Ag-Cu-Zn filler, it can reduce the melting point. The melting point of the Ag-Cu-Zn filler is between 665°C and 745 °C. However, the brazing temperature of 810 °C is much more than the melting point of the filler, hence, the filler gets better wetting and spreading on red copper.



(a)Ag-Cu-Zn filler (b) Ag-Cu-P filler

Fig. 1. Wetting and spreading macro-photograph of Ag-Cu-Zn and Ag-Cu-P filler at 810 °C for 3 minutes

Fig.2 shows the microstructure of wetting tip of Ag-Cu-Zn and Ag-Cu-P filler on red copper. The brazing temperature is both at 810 °C for 3 minutes. The microstructure of Ag-Cu-Zn filler is much uniform. While some pores were formed in the Ag-Cu-P filler. The reasons maybe that the fluidity of melted Ag-Cu-Zn filler is much better that that of Ag-Cu-P filler. The micro-pores formed during wetting process is easier escape from Ag-Cu-Zn filler. The wetting angle of the Ag-Cu-Zn filler is 13° and the wetting angle of the Ag-Cu-P filler is14°. That is to say, the Ag-Cu-Zn filler is wetting and spreading more enough on red copper than the Ag-Cu-P filler.



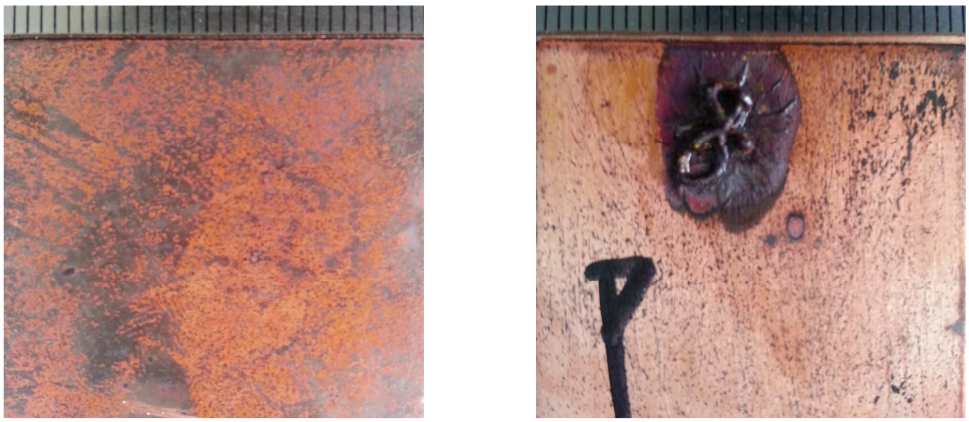

(a) Ag-Cu-Zn filler (b) Ag-Cu-P filler

Fig. 2. Microstructure of wetting tip of Ag-Cu-Zn and Ag-Cu-P filler on red copper at 810 °C for 3 minutes.

Fig.3 shows the macro-photograph of Ag-Cu-Zn and Ag-Cu-P filler after wetting and spreading on the red copper without flux. The filler in the Fig.3(b) is Ag-Cu-P filler. The Ag-Cu-P filler is an air self-fluxing brazing alloy which is widely used in the industry. The copper with phosphorus has two effects. On the one hand, the phosphorus can decrease the melting point of the alloy. While adding a certain amount of phosphorus, the phosphorus and the copper form the low-melting equilibrium which is composed of the α+$Cu_3P$ whose melting point is 714 °C.The brittleness which the $Cu_3P$ brings to the cooper-phosphorus filler, comparing with the silver based filler in the Fig3(a), and the plasticity is also lower. On the other hand, when the red copper is brazed by the filler, phosphorus works as a self-fluxing. Because of phosphorus, CuO is restored in brazing[6,7], the reactions during brazing process is shown as equation (1).

$$5CuO+2P=P_2O_5+5Cu \quad (1)$$

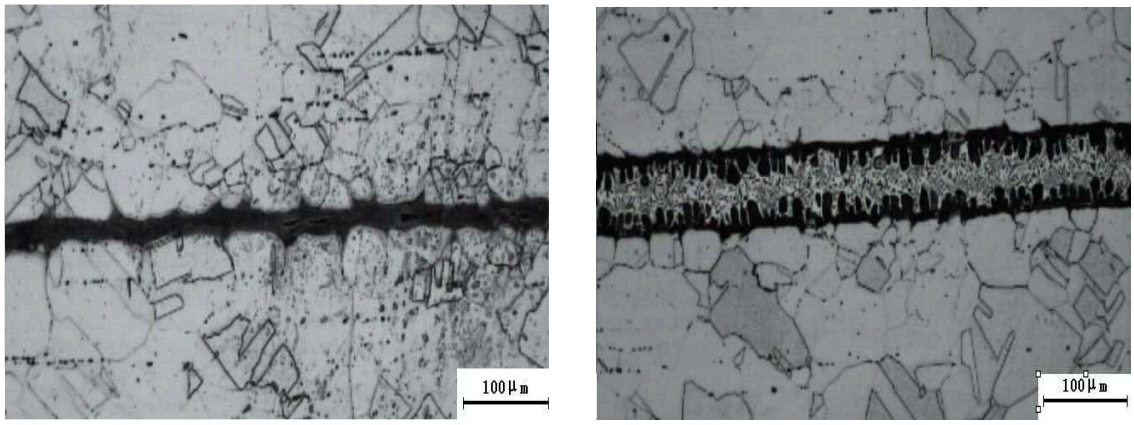
It forms the composite compound which is constituted of CuO on the red copper's surface and $P_2O_5$ which is restored. Under the brazing temperature, it presents the liquidus and covers in the parent metal surface. Thereby, it can vent the base material and filler oxidizing and promote wetas shown in Fig.3.



(a)Ag-Cu-Zn filler (b) Ag-Cu-P filler

Fig. 3. Macro-photograph of Ag-Cu-Zn and Ag-Cu-P filler after wetting and spreading on the red copper without flux

Fig.4 shows the cross-sectional morphology of Ag-Cu-Zn filler and Ag-Cu-P filler brazed red copper joint at 810 °C for 5 minites During brazing process, the parent material dissolves and flows to the filler and the filler diffuses to the parent material usually occur. Suitable dissolution and diffusion between base metal and filler can lead to the elements at brazing seam alloying. Not only can it form the good brazing seam, but also improve the strength of the joint[8]. From fig.4, it can be concluded that parent materials spread and dissolve to brazing seam, but different fillers have different dissolving capacity. Ag-Cu-Zn filler diffuses evidently enough. α-Cu solid solution structure which contains Ag and Zn was formed on the interface of base material and filler. While in the middle of the brazing seam is mainly Ag-Cu-Zn eutectic structures. On the contrary, dissolution and diffusion are not obvious between the Ag-Cu-P filler and parent material. Thus, we prefer to select the Ag-Cu-Zn filler than Ag-Cu-P filler during brazing.




(a) Ag-Cu-Zn filler (b) Ag-Cu-P filler

Fig.4. Cross-sectional morphology of Ag-Cu-Zn filler and Ag-Cu-P filler brazed red copper joint at 810 °C for 5 minutes

## Conclusions

1.Under the same experimental parameters, the wetting abilities of Ag-Cu-Zn filler are better than that of Ag-Cu-P filler on the red copper surface.

2.Without adding any brazing flux, wetting and spreading behavior can be seen for Ag-Cu-P filler on red copper surface.

3.By the analysis of the joint microstructure, there were obvious dissolution and diffusion between base metal and Ag-Cu-Zn filler, and the solid solution structure which includes the Ag and Zn elements were formed.

## References

[1] Mel M. Schwartz. Brazing. ASM International, Materials Park, Ohio, 2003.

[2] Timmins P. F.. The development of nontoxic Ag-based brazing alloys. Welding, Journal, 1994, 73(9): 31s-33s.

[3] L. Sisamouth, M. Hamdi, T. Ariga. Investigation of gap filling ability of Ag-Cu-In brazing filler metals. Journal of Alloys and Compounds, 2010, 504: 325–329.

[4] Zhang, L. X., Feng, J. C. and He, P. Brazing temperature and time effects on the mechanical properties of TiC cermet/Ag-Cu-Zn/steel joints. Mater. Sci. Eng. A, 2006, 428, 24–33.

[5] Zhang, L., Feng, J., Zhang, B. and Jing, X. Ag-Cu-Zn alloy for brazing TiC cermet/steel. Mater. Lett., 2005, 59, 110–113.

[6] Liu Huijie, Feng Jicai, Vacuum brazing TiAl-based alloy to 40Cr steel using Ag-Cu-Zn filler metal, Journal of Materials Science Letters 21, 2002, 9–10.

[7] P. L. Zhang, S. Yao, M. Ding, F. G. Lu, S. N. Lou. Microstructural analysis in the vacuum brazing of copper to copper using a phosphor–copper brazing filler metal. International Journal of Materials Research, 2010, 101(11): 1436-1440.

[8] Phlip C. W ing ert, Ch i- Hung Leung. The development of silver-based cadmium-free contact materials. Journal of Alloys and Compounds, 2004, 72(3): 148-157.

*Advanced Materials Research Vol. 937 (2014) pp 158-161*
*© (2014) Trans Tech Publications, Switzerland*
*doi:10.4028/www.scientific.net/AMR.937.158*

# The Research of Fatigue Properties of Steel Q235 Butt Welded Joint

*Wei-ping OUYANG[A], Jin Zhang[b] and Xiu-dong XU[C]

Shanghai City special equipment supervision and Inspection Institute of Technology, Shanghai, China

[a]ouyangweipingvi@163.com

*Weiping Ouyang

**Keyword:** Q235 butt welded joint; improved linear equivalent structural stress method; master S-N curve; fatigue life

**Abstract.** The research on the fatigue life of butt welded joint has important significance to hoisting equipment's design, development and using safety. This paper conducted a study on fatigue properties of the most widely used joint at hoisting equipment-steel Q235 butt welded joint's, based on the improved linear equivalent structural stress method, the stress of the weld joint can be obtained, and the master S-N curve of Q235 weld joint be acquired through fatigue test, thus the joints stress distribution under different stress environment can be gained through improved linear equivalent structural stress calculation and the fatigue life of the joint can be realized at the master S-N curve. The stress distribution situation and the fatigue life of butt welded joint can be calculated by integrated finite element software, this have profound reference significance to hoisting machinery industry.

## Introduction

The wide using of welding structure at hoisting equipment for its apparent advantages like: can endure alternating stress, preferable force transfer property and the high connection reliability etc. According to statistics, the fatigue failure is the main failure mode of weld structure and the accident caused by this brings relatively serious loss usually. For its complex stress distribution which brought by geometry variety ,welding technology and the changing of physical properties of materials after welding etc, conduct a study on weld structure become very difficult to the traditional fatigue property research method. Detail-classification method is the main method of traditional fatigue property research measures for weld structure, this method demands geometry strictly of determined specific joint, the nominal stress under load mode and the corresponding fatigue resistant force data, this leads the scope of application and the convenience on engineering application very limited. In recent years, researchers carried on some study on fatigue mechanism of weld joint, relevant theories are proposed [1-2]. The equivalent structural stress theory is the relatively mature technique among these proposed theories, detailed introduction of the equivalent structural stress theory was conducted by relevant scholar [3]. For consideration of stress concentration of weld toe, equivalent structural stress theory own high calculation accuracy. Simultaneously, it can be applied conveniently to finite element stress analysis and could avoid the selection of the fatigue design S-N curve. It was recommended by the Standard of 2007 AWME containers and pressure boiler and the evaluation Standard of API/ASME for fatigue analysis of weld beam [4]. It is relatively difficult that the insensitivity of the finite element grid require be overcome in the finite element application of the equivalent structural stress theory, related reports of application of the equivalent structural stress theory on hoisting equipment have not found yet. The butt welded joint is the major joint form of hoisting equipment, the base material of weld structure is relative stable, steel Q235 is the most common material, therefore, the improved linear equivalent structural stress theory was intend to adopted to the study of fatigue property of steel Q235 weld joint.

**The Improved Linear Equivalent Structural Stress Theory**

The stress distribution of the thickness direction of the plate near the weld toe gap area is nonlinear usually, the normal stress of the gap is formed by the film normal stressσp along the thickness t of the plate, the bending normal stressσm and the peak value nonlinear normal stressσp [5], equivalent structural stress $\sigma_s$ is defined the summation of the normal stress of surface weld toe and the bending normal stress.

$$\begin{aligned}\sigma_{\mathrm{m}} &= \frac{1}{t}\int_{x=0}^{x=t}\sigma(x)dx \\ \sigma_{\mathrm{b}} &= \frac{1}{t^2}\int_{x=0}^{x=t}\sigma(x)(\frac{t}{2}-x)dx \\ \sigma_{\mathrm{s}} &= \sigma_{\mathrm{m}}+\sigma_{\mathrm{b}}\end{aligned} \tag{1}$$

Eq (1) can not be used to calculate the structural stress usually at the actual application for the geometrical discontinuity of the weld toe front area. The stress concentration during this area is controlled mainly by the self-balancing nonlinear stress distribution, and this area is the singular point in the ideal finite element model, therefore, element type, grid shape and size etc impose immense influence to the result of stress analysis. The shell element model is the most common one in welded structures engineering analysis, the stress at the geometric discontinuity area accord with the convergence solution of shell theory, the local stress of the weld toe area compelled be identical to the shell theory that the stress distribution at the plate thickness direction is linear. Differ from the structural stress calculated by Eq1, the improved linear equivalent structural stress theory (mainly be applied to three dimensional model) is introduced to reducing or eliminating the grid sensitivity of structural stress analysis results. The film normal stress and the bending normal stress can be calculated by Eq(2) and Eq(3).

$$\sigma_{\mathrm{m}} = \frac{1}{t}\int_{y=0}^{y=t}\sigma_x(y)dy \tag{2}$$

$$\sigma_m\frac{t^2}{2}+\sigma_b\frac{t^2}{6} = \int_{y=0}^{y=t}\sigma_x(y)ydy+\delta\int_{y=0}^{y=t}\tau_{xy}(y)dy \tag{3}$$

The required line force and line torque at finite element structural stress analysis obtained from the calculation which be based on the principle of energy equivalency. That means the consume energy value of node displacement for node force and torque equals the value of line force or line torque. Eq(4) and Eq(5) can be applied to calculate the line force and line torque of three dimensional two order shell element model.

$$\begin{aligned}\mathrm{f}_1 &= 3(6NF_1+2NF_3-NF_2)/(2\omega) \\ \mathrm{f}_2 &= -3(2NF_1+2NF_3-3NF_2)/(4w) \\ \mathrm{f}_3 &= 3(2NF_1+6NF_3-NF_2)/(2\omega)\end{aligned} \tag{4}$$

$$\begin{aligned}\mathrm{m}_1 &= 3(6NM_1+2NM_3-NM_2)/(2\omega) \\ \mathrm{m}_2 &= -3(2NM_1+2NM_3-3NM_2)/(4w) \\ \mathrm{m}_3 &= 3(2NM_1+6NM_3-NM_2)/(2\omega)\end{aligned} \tag{5}$$

The $\mathrm{f}_i$, $\mathrm{m}_i$, $\mathrm{N}F_i$, $\mathrm{N}M_i$ indicate the line force, line torque, internal force and internal torque which parallel to element width ω and perpendicular to the hypothesis the crack surface of weld toe respectively (i=1,2,3).

**The Master S-N Curve**

108 Q235 butt welded joints which have two geometric dimensions were made for fatigue test. These joints were divided into 18 test groups for symmetric tension compression test (as shown in Fig1).



Fig. 1. Fatigue test of steel Q 235 butt welded joint

Via the linear regression analysis of test data, the master S-N curve under constant amplitude, circulation characteristic value R=-1, average force value S m=0 can be obtained, Eq(6) is the mathematical expressions.

$$\log N = 11.422309 - 3.055853 \log \Delta S \tag{6}$$

N is the cycle number, $\Delta S$ is the stress value. In according to the Goodman equation, when the circulation characteristic value R and the average stress value S m are changeable, the numerical relationship between force range Sa and average force Sm can be expressed as Eq(7):

$$(S_a / S_{-1}) + (S_m / S_u) = 1 \tag{7}$$

$S_{-1}$, $S_u$ are force range and the yield stress when R=-1, S m=0. Therefore, the stress under changeable R and Eq(7) could be converted to the stress value of master S-N curve, and the corresponding cycle number N could be calculated too.

**Finite Element Calculation**

The finite element software-MSC has powerful calculation and rewriting function which can be applied to integrating fatigue calculation of weld structure. The sub software MSC-Patran could be employed to geometry modeling and the element meshing, and the MSC-Nastran own good ability of mechanic analyzing and calculation which could be used for stress distribution calculation of the model. Through the rewriting the software MSC-fatigue based on improved linear equivalent structural stress theory and the master S-N curve, the fatigue life of the Q235 butt welded structure can be gained by the software. It is apparent that the weld property calculation of the weld structure is convenient by software, this brings great significance to the research, development, manufacture and the maintenance of hoisting industry.

**Conclusion**

The following conclusions can be reached through research on fatigue property of steel Q235 butt welded joint:

(1) The wide using and large harmfulness of fatigue failure of weld structure makes the fatigue property study becoming necessary.

(2) the stress value of the weld structure can be calculated accurately by recommended the improved linear equivalent structural stress method, and the master S-N curve of Q235 weld structure achieved through fatigue test, the fatigue life of the joint can be obtained by calculation.

(3) the stress distribution and the fatigue life can be acquired by integrated finite element software-MSC, this have significant meaning to design, development and using safety of hoisting equipment.

**References**

[1] LOTSBERG I.SIGURDSSON G.Hot Spot Stress S-N Curve for Fatigue Analysis of Plated Structures [J]. Journal of Offshore Mechanics and Arctic Engineering,2006,128(4):330-336.

[2] DONG P,HONG J K,CAO Z. A New Mesh-Insensitive Procedure for Characterizing Stress Concentration at welds[C]//200l ASME Pressure Vessels and Piping Conference.Atlanta:The American Society of Mechanical Engineers,2001:85—103.

[3] ZHOU ZHANGYI, LI DI, AN QI. The latest progress of fatigue strength analysis techniques of steel structure weld [J].Chinese Railway Science,2009,30(4).

[4] APL. API 579-1/ASME FFS-1 Fitness-for-Service[s].Washington:The American Petroleum Institute,2007.

[5] ASME. 2007 ASME Boiler and Pressure Vessel Code Section Ⅷ Division 2 Part 5:Design by Analysis Requirements[s].New York:The American Society of Mechanical Engineers,2007.

*Advanced Materials Research Vol. 937 (2014) pp 162-167*
*© (2014) Trans Tech Publications, Switzerland*
*doi:10.4028/www.scientific.net/AMR.937.162*

# Analysis of the Grain Refinement Mechanism for Commercial Pure Titanium by ECAP and SMAT

Xiao-Mei HE[1,a], Shan-Shan ZHU[2*,b], Cong-Hui ZHANG[3,c]

[1, 2, 3]Shool of Metallurgical Engineering, Xi'an University of Architecture & Technology, Xi'an 710055, China

[a]85554949@qq.com

[b]mumaxiaowai@126.com

[c]jiandazhang2010@hotmail.com

*Corresponding author

**Key words:** commercial pure titanium (CP-Ti);equal channel angular pressing (ECAP); surface mechanical attrition treatment (SMAT)**;** grain refinement mechanism.

**Abstract.** Equal Channel Angular Pressing (ECAP) and Surface Mechanical Attrition (SMAT) are the two Severe Plastic Deformation (SPD) processes that have been used to process ultrafine grained (UFG) materials. These two kinds of processes have been used to refine the grain size of coarse-grained commercial pure titanium (CP-Ti). The development of microstructure during equal channel angular pressing (ECAP) and surface mechanical attrition (SMAT) of commercial pure titanium (CP-Ti) is investigated to establish the mechanisms of grain refinement. Based on the various experimental results and analysis, it has been found that the high-strain-rate and many direction loading is conducive to the formation of nanograins and also the grains with less than 100 nm cannot be obtained by the single equal channel angular pressing (ECAP).

## Introduction

Recently, ultrafine grained (UFG) materials with sub-micrometer order grain size have received much attention due to their excellent mechanical properties [1]. Severe plastic deformation(SPD) techniques, such as equal channel angular pressing(ECAP)[2], high pressure torsion(HPT)[3], accumulative roll-bonding(ARB)[4], cyclic extrusion and compression(CEC)[5], repetitive corrugation and straightening(RCS) [6] have been developed to fabricate ultra-fine grained materials with mean grain sizes ranging from 10 to 200 nm.

In this case study, different microstructure and grain refinement mechanism of the commercially pure titanium (CP-Ti) by ECAP and SMAT has been analyzed. The reason that the grains with less than 100 nm cannot be obtained by the single equal channel angular pressing (ECAP) has been discussed.

Surface mechanical attrition treatment (SMAT)[7] is a recently developed technique that can result in surface grain refinement down to the nanometer scale without changing the chemical composition of the material. The SMAT has been successfully applied in various kinds of materials including pure metals, steels, and alloys, in which a nano-structured surface layer up to 50 μm thick has been obtained [8]. After applied SMAT treatment [9] enhanced overall properties and performance of the material is observed.

## Experiment Procedures

An annealed CP-Ti plate with a grain size of 15–25 μm is being referred for the detailed study. The chemical composition of the material in term of percentage of weight is 0.12% Fe, 0.04% C, 0.01% $N_2$, 0.004% $H_2$ and 0.13% $O_2$. It is being treated by ECAP and SMAT respectively.

The size of the sample piece for ECAP was 15 mm×15 mm×80 mm, used as experimental billets. A die-set with an internal angle of 120° and an outer curvature angle of 20°.All billets were processed at room temperature 4 passes with BC route, in which the sample is rotated by 90° in the

same sense in each pass. A composite lubricant is used; here in graphite was the main component as a lubricant. After each ECAP pressing, the billets were annealed immediately at 200°C for 1 h to remove residual stress [10].

A specimen for SMAT process was also prepared from CP-Ti plate with a dimension of 100mm×100mm×10mm. A cleaning-up procedure using ethanol and acetone was carried out to remove the impurities at the surface prior to the SMAT. The SMAT is performed in Vacuum at room temperature with stainless steel balls 3 mm in diameter. This stainless steel ball is fed with vibration of magnitude of 50 Hz for 30 min.

The micro structural features of the treated specimens are systematically observed by cross-sectional scanning electron microscopy observations(SEM), transmission electron microscopy (TEM) and high-resolution transmission electron microscopy (HRTEM) investigations.

## Experimental Results

### ECAP

ECAP of CP-Ti via rout BC was processed to four passes at room temperature. The equivalent strain was up to 2.54. Fig.1 (a) shows TEM images of the microstructure of CP-Ti after four ECAP pass. It can be seen that there are few dislocations in subgrains, and the subgrain boundaries consist of high dislocation density walls. After four ECAP pass, the grains are refined to about 250 nm. The corresponding SAED pattern shows diffraction arranged in circles, attesting to the existence of high angle grain (Fig.1(b)) [10].

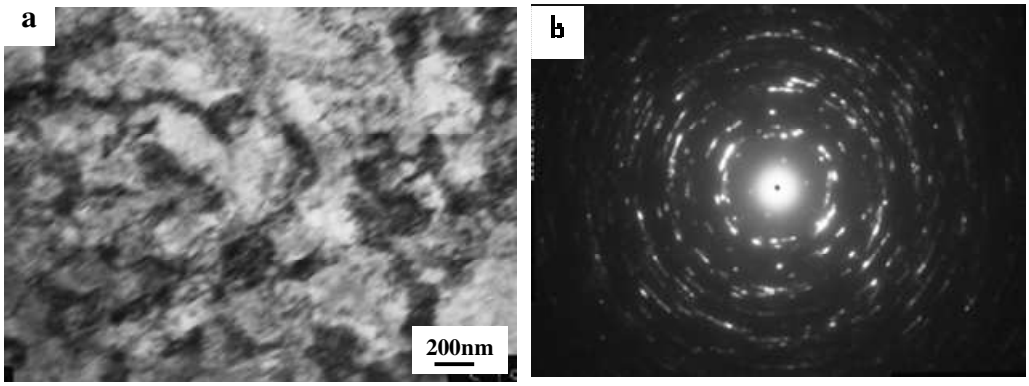



Fig. 1. TEM micrographs of CP-Ti after the fourth ECAP pass at room temperature
(a) Fine grains; (b) corresponding SAED pattern

### SMAT

Fig. 2(a) shows a cross-sectional observation of the CP-Ti sample after the SMAT processing for 30 min. The microstructure morphology of the treated surface layer differs from that in the matrix. Evidence of severe plastic deformation is seen in the surface layer, in which grain boundaries cannot be clearly identified in SEM observations (as shown in Fig. 2(b)), as they can be in the matrix. It can be seen that the deformation layers can be observed consisting of many mechanical twins which become more and more dense as they approach the treated surface. Intersections of twins are also visible in the top layer of the sample. It can be noted that the gradient structure resulting from a gradual decrease in the applied strain and strain rate as the depth of the treated surface layer of specimens increases, from very high (top surface) to zero (substrate), represents the complete range of structural changes which occur during treatment.

(a) show a HRTEM image and the selected area electron diffraction (SAED) pattern of the top surface layer in the SMAT CP-Ti sample (about 0–15 μm below the treated surface). The corresponding SAED patterns of areas with a diameter of 50 nm exhibit rings (Fig. 3(b)), which illustrates the formation of finer grains with a more random orientation on the top treated surface. The average grain size of the top layer is about 10 nm.

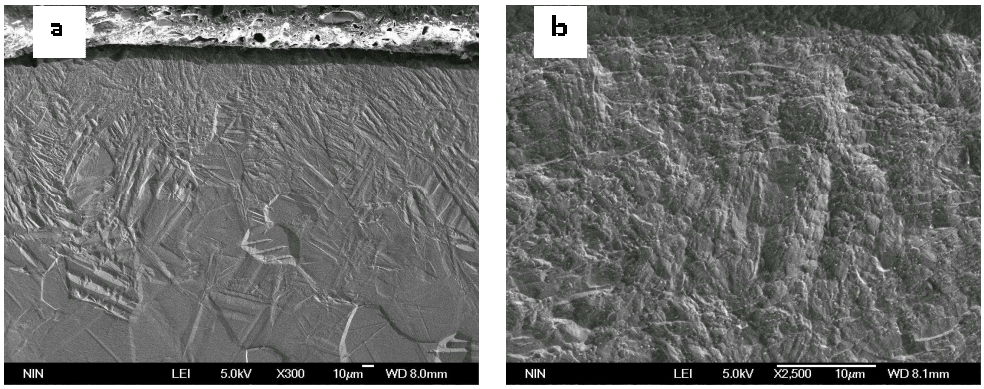



Fig. 2. A cross-sectional optical microstructures observation of the SMAT 60min

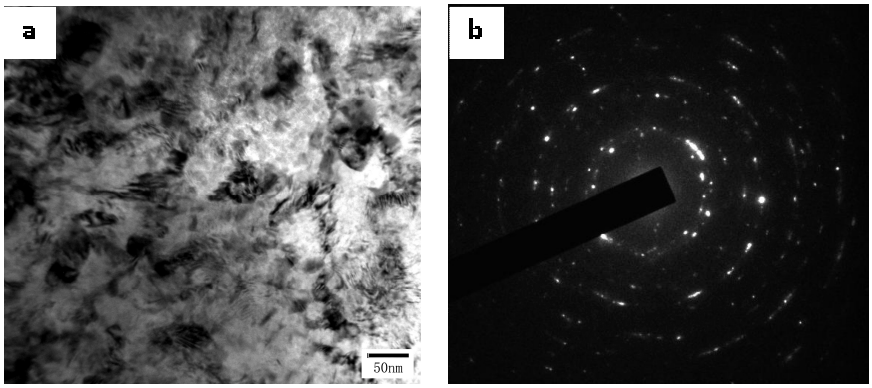



Fig. 3. HRTEM image and corresponding SAED of the top surface treated by SMAT 30min

## Discussion

The results show that the minimum grains size are refined to about 250 nm after four ECAP pass [10], and the grain are refined to nanometer scale with the minimum grains size 10 nm after SMAT for 30 min.

Comparing the SMAT with other SPD techniques, the essential cause resulting in nanocrystallization is that the high strain rate (about $10^{2\text{-}3}$ $s^{-1}$) and random directional impacts of the balls onto sample. Table 1 is comparisons of strain, strain rate and the final grain size among severe plastic deformation techniques. One may find obvious difference that the strain rate of ball mill (BM) and SMAT is much higher than the strain rate of ECAP, HPT and ARB. Moreover, BM and SMAT can obtain ultrafine crystallites of about 10 nm. It shows that the strain rate plays a very important role in nanocrystallines.When dislocation multiplication rate is balanced by the annihilation rate, the increase of strains could not reduce the subgrain size any longer, and a stabilized grain size is resulted [11]. For materials that the twins is main grain refining mechanism, it was found that increasing strain rate leads to smaller twin layer thickness[12].

Table 1. Comparisons of strain, strain rate and the final grain size among severe plastic deformation techniques

| SPD techniques | strain | strain rate | final grain size(nm) |
|---|---|---|---|
| ECAP | large | small to medium | 100-200 |
| HPT | large | small to medium | 100-200 |
| ARB | large | small to medium | 100-200 |
| BM | large | large | ~10 |
| SMAT | large | large | ~10 |

In addition, the randomly multidirectional repeated loads of ball milling and surface mechanical attrition to promote the activation of different slip system and twin deformation systems, which is favorable to the refinement of original coarse grains (as shown in Fig. 4).

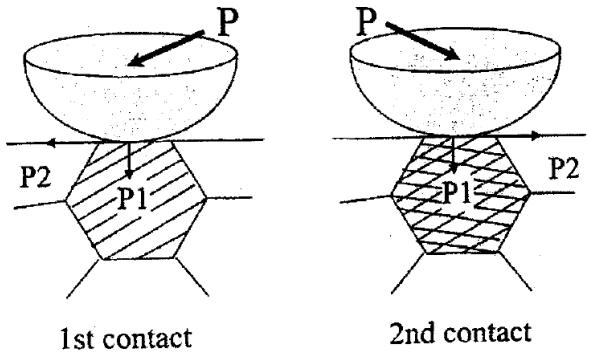



Fig. 4. Repeated multidirectional impacting leading to deformation microstructures with a high density of dislocation arrays or mechanical twins

The lath microstructure generated by slipping can be seen from the TEM observations in the ECAP samples during the first several passes. Most of the dislocation in SMAT sample located along twin and intersection boundaries. The microstructure of the subsurface layer of SMAT sample is twin as shown in Fig.5-6, moreover dislocation cell were generated. In literature [10], it is considered that the grain refinement mechanism of the CP-Ti processed by ECAP at room temperature as follows: the grain fragmentation is the result of interaction and intersection of lath microstructures formed by dislocation slip and deformation twins.

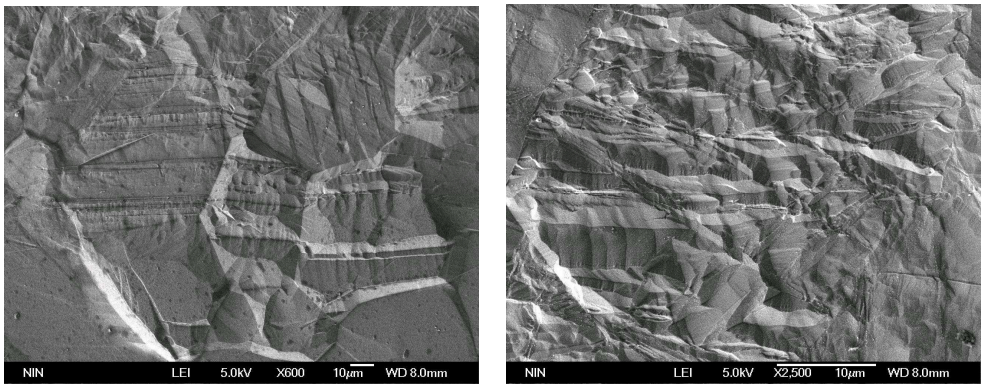



Fig. 5. SEM images of twining structures after SMAT

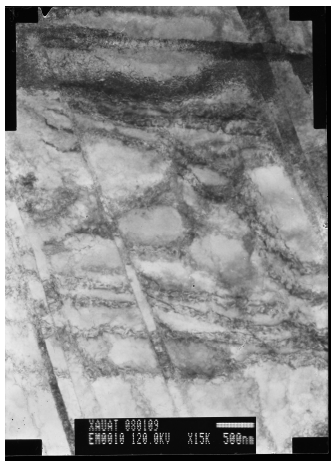


Fig. 6. TEM image of 150μm cross-section after SMAT

The difference of the microstructure and morphology is caused by different strain rate. At room temperature, the plastic deformation patterns of h.c.p commercial pure Ti are slipping and twinning, as there are fewer slip systems within CP-Ti [13].

CHICHILI[14] found that the density of twins increased with increasing strain rate when he studied the influence of the strain rate on the deformation mechanism and model. In general, the critical resolved shear stress of slip is smaller than that of twin deformation, therefore the plastic deformation is dominated by slip deformation.

Slip critical resolved shear stress is more sensitive to strain rate and temperature, it increases with the increase of strain rate and temperature decreases, while the twin critical resolved shear stress is generally less sensitive to strain rate and temperature. For Cp-Ti, the critical resolved shear stress of slip increases with the strain rate increasing, but dislocation slip need more stress, once the stress reaches to the critical resolved shear stress of the twin, twin deformation will play a major role[15]. Strain increases with the depth of the treated surface layer of SMATD specimens decreases. Twin deformation was dominated when the value of strain is small, and the grain refinement was caused by the intersections of twin.

When the train reached a certain extent, the movement of dislocations played a major role. The movement of dislocation was hindered by lots of high density of twin and its intersection at beginning, furthermore, these dislocation aggregated along twin boundary to form dislocation wall and dislocation tangle. As a result, the slice twin was broke up into sub-grain with low angle [16]. With the further increase of the strain, high density dislocation tangles appeared in the sub-grains with low angle grain boundary, sub-grains structure with large angle grain boundary emerged because of dynamic recovery, shown in Fig.7.

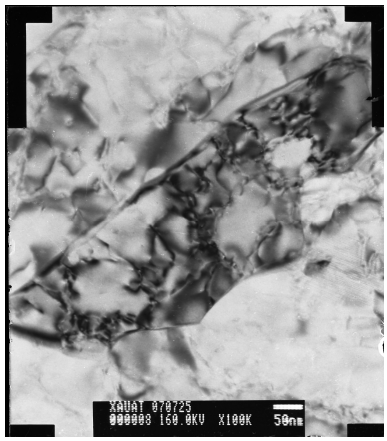



Fig. 7. TEM image of submicron grains

Dynamic re-crystallization of material generally occurs under high temperature plastic deformation, dynamic re-crystallization takes place after strain accumulated to definite value at room temperature.

Therefore, the dynamic re-crystallization occurred at room temperature on the condition of high strain and high strain rate during the SMAT process. The formation of the re-crystallized grain not only dissipated deformation energy, reduced the dislocation density, and then released the stress concentration caused by uneven deformation. The grain disorientation improved through the mergence and recombinant of dislocations, and large angle grain boundary formed. Finally, the equaled re-crystallized grains formed based on the migrating of partial random grain boundaries.

## Conclusions

Through comparison and analysis of ECAP and SMAT deformation means of CP-Ti, it can be summarized that it is the different strain rate and loading direction that led to the grain size of ECAP is an order of magnitude higher than that of SMAT.

Higher strain rate raised the critical shear stress of dislocation slip so as to facilitate the twin deformation under SMAT at room temperature, and dynamic re-crystallization plays an important role in grain refinement of SMAT, which differed from the mechanism of grain refinement under ECAP.

**Acknowledgement**

This research was financially supported by the Key Project of Chinese Ministry of Education (211178), the Technologicial Project of Bledu city xi'an Province (GX1314) and Scientific Research Project of Shannxi Education Department (2013JK0903).

**References**

[1] R.Z. Valiev, R.K. Islamgaliev, I.V. Alexandrov. Bulk nanostructured materials from severe plastic deformation[J].Progress in Materials Science, 2000, 45(2):103-189.

[2] D.P. DeLo, S.L. Semiatin. Hot working of Ti-6Al-4V via equal channel angular extrusion[J]. Metall. Mater. Trans. 1999,30A(9):2473-2481.

[3] R.Z. Valiev, A.K. Mukherjee. Nano structures and unique properties in intermetallic subjected to severe plastic deformation[J].Scr.Mater.,2001,44 :1747-1750.

[4] Y. Saito, H. Utsunomiya, N. Tsuji, et al. Novel ultra-high straining process for bulk materials: development of the accumulative roll-bonding (ARB) process[J].Acta Mater., 1999, 47(2):579-583.

[5] M. Richert, Q. Liu, N. Hansen..Microstructural evolution over a large strain range in aluminium deformed by cyclic-extrusion–compression Original Research Article[J].Materials Science and Engineering: A, 1999, 260(1-2):275-283.

[6] J.Y. Huang, Y.T. Zhu, H. Jiang, T.C. Lowe. Microstructures and dislocation configurations in nanostructured Cu processed by repetitive corrugation and straightening[J].Acta Materialia, 2001, 49(9):1497-1505.

[7] K. Lu, J. Lu. Surface Nanocrystallization (SNC) of metallic materials-presentation of the concept behind a new approach[J]. Mater Sci Technol,1999, 15:193-197.

[8]J. HAN, G. M. SHENG, G. X. HU. Nanostructured surface layer of Ti-4Al-2V by means of high energy shot peening[J]. ISIJ International, 2008, 48 (2):218-223.

[9] K. Lu, J. Lu. Nanostructured surface layer on metallic materials induced by surfacemechanicalattrition treatment[J]. Materials Science and Engineering: A,2004,375-377:38-45.

[10] X.R. Yang, X.C. Zhao, W.J. Fu. Deformed Microstructures and Mechanical Properties of CP-Ti Processed by Multi-Pass ECAP at Room Temperature[J]. Rare Metal Materials and Engineering.2009,38(6): 0955-0957.

[11] K. Lu, J. Lu. Nanostructured surface layer on metallic materials induced by surface mechanical attrition treatment[J].Mater Sci&Eng A,2004, 375/377(7):38-45.

[12] G. H. Xiao, N.R. Tao,K. Lu.Effects of strain, strain rate and temperature on deformation twinning in a Cu–Zn alloy [J]. Scripta Materialia.2008, 59: 975–978.

[13] N. Munroe, X.L. Tan, H.C. Gu.Orientation dependence of slip and twinning in HCP metals [J]. Scripta Materialia, 1997,36 (12):1383.

[14] D.R. Chichili, K.T. Ramesh, K.J. Hemker. The high-strain-rate response of alpha-titanium: Experiments deformation mechanisms and modeling [J].Acta Mater,1998,46 (3): 1025-1043.

[15] L.Q. Gao, J.H. Zhu, L. Hui, et al. Effects of High Strain Rate and Low Temperature on Mechanical Properties of TA2[J]. Rare Metal Materials and Engineering.2008,37(6):1051-1054.

[16] J.Han, G.M. Sheng, G.X. Hu. Mechanism of grain refinement for TA17 near α Ti alloy by high energy shot peening[J].The Chinese journal of nonferrous metals. 2008,15(5): 799-804.

*Advanced Materials Research Vol. 937 (2014) pp 168-171*
*© (2014) Trans Tech Publications, Switzerland*
*doi:10.4028/www.scientific.net/AMR.937.168*

# Corrosion Behavior of 13Cr Steel in Different Temperature

Zhi-Chao QIU[1,a,*], Xiang LIU[1,b] and Na ZHANG[1,c]

[1]Oil Production Department of RIPED P.O.Box 910, 20# Xueyuan Road Beijing 10083, P.R.China

[a]qiuzhichao@petrochina.com.cn, [b]liuxiang69@petrochina.com.cn,
[c]zhangna01@petrochina.com.cn

**Keywords:** 13Cr steel; corrosion behavior; $CO_2$; electrochemical corrosion

**Abstract:** Corrosion experiments were applied for 13Cr steel. Through the experiments, the corrosion rate of 13Cr steel in different temperature was tested. The corrosion rate of 13Cr steel was increased with the increase of temperature. Moreover X-ray diffraction analysis and scanning electron microscope analysis were applied to understand the corrosion behavior of 13Cr in micro-scale.

## Introduction

In the practice use of steel, such as oil pipeline, oil well etc, electrochemical corrosion induced by the sour gas (such as $CO_2$) would be an important problem which the corrosion engineers should concern[1-4]. In the field application, two anti-corrosion methods also were used. One was carbon steel with corrosion inhibitor, another was high alloy steel such as 13Cr steel. If carbon steel with corrosion inhibitor was applied, corrosion inhibitor which was suitable for filed corrosive environment should be selected. However with the change of corrosive environment, corrosion inhibitor should be changed or updated. In this paper, the corrosion rate of 13Cr was tested in different temperature to understand the corrosion behavior of 13Cr steel in this corrosive environment.

## Experimental Parts

### Material

The material used in corrosion test was 13Cr stainless steel. This steel is used for oil and gas wells with high $CO_2$ gas. The chemical compositions are shown in Table 1 and the test specimens were machined to 50 × 10 × 3 mm.

Table 1. The chemical composition of 13Cr

| Material | C | Si | Mn | P | S | Cr | Ni | Cu |
|---|---|---|---|---|---|---|---|---|
| 13Cr | 0.18 | 0.85 | 0.95 | 0.02 | 0.01 | 13.10 | 0.18 | 0.17 |

### The Medium for Corrosion Test

All corrosion experiments were carried out in a closed container that rotated in a roller heating furnace. A container with volume of 100 $cm^3$ was used for the conditions with $CO_2$ while the other volume for the conditions with oil-water mixture. The corrosion medium was prepared from the de-ionized water, reagent grade chemicals and purity gases. The test conditions were shown in Table 2.

Table 2. The medium composition for corrosion test

| No. | T/°C | $P_{H2S}$/MPa | $P_{CO2}$/MPa | $Cl^-$/mg•$L^{-1}$ | $H_2O$/% | Material |
|---|---|---|---|---|---|---|
| 1 | 60 | 0 | 0.12 | 100000 | 30 | 13Cr |
| 2 | 85 | 0 | 0.12 | 100000 | 30 | 13Cr |
| 3 | 110 | 0 | 0.12 | 100000 | 30 | 13Cr |

### The Specimen Treatment

First, the test specimens were machined to 50 × 10 × 3 mm from the raw metal material of 13Cr stainless steel. Second, the surface of the specimen was polished by sand paper with grid degree of 300#-1000#, cleaned with alcohol and dried in hot air. Finally the specimens were weighed and stored in desiccators until the corrosion test.

### Experimental Processing

(1) A certain quality of required chemicals was added into a container.

(2) Put a supporter with required specimens hung on into the certain container that prepared in procedure, and sealed the container with the designed cover.

(3) The down-pressure value and flow counter were open, and the gas of $H_2S$ and $CO_2$ were inserted into the container. The input value of the container and down-pressure value of the vessel were shut down when the pressure of $H_2S$ and $CO_2$ was up to the design value.

(4) The heater and stirrer were open to mix the medium and make the test temperature up to the need.

(5) The corrosion test was started. The temperature fluctuation range was controlled to ±1°C and the test time was continued to 168h during the test.

(6) Firstly, the power of heater was shut off, and the sample was taken out from the container after the container was cooled to room temperature by the way of nature cool. Secondly, the corrosion production on the specimen surface was treated in according to the standard of "GB/16545-1996 corrosive product on the corrosive sample of metal and alloy", and the sample was cleaned and got rode of water using alcohol and acetone. Finally the mass of sample was weighed and recorded after the sample cleaned was kept in a desiccator for at least 24h.

## Experimental Result Analysis

### Corrosion Weight Loss

The corrosion rate of 13Cr steel is 0.0045mm/a, 0.0290mm/a and 0.1746mm/a in different temperature respectively. Fig.1 showed the corrosion rate for 13Cr specimens after the 168-hour test. As was shown in the figure, corrosion rate was ranked as 110°C>85°C>60°C, which was owing to the accelerated active-dissolution while temperature rise. Particularly, while temperature changed from 85°C to 110°C, corrosion rate greatly increased from 0.0290mm/a to 0.1746mm/a.

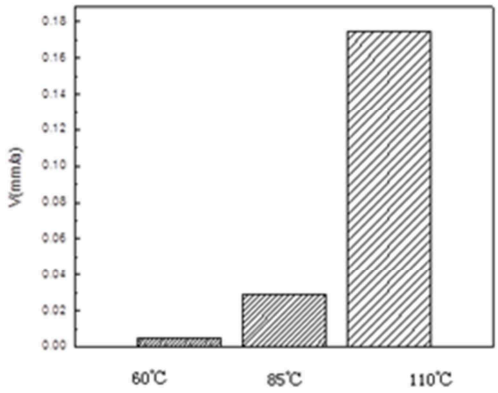



Fig. 1. Corrosion rate of 13Cr after 168-hours test in different temperature

### Macro-Morphology Analysis

Fig.2 showed the appearance of 13Cr specimen after corrosion test of 168 hours in different temperature. As Fig.2 showed, corrosion was hardly happened on 13Cr that specimen surface was still light and smooth after experiment. Only a little trace of corrosion would be found on the steel, however, more corrosion trace appeared with the increase of experiment temperature.

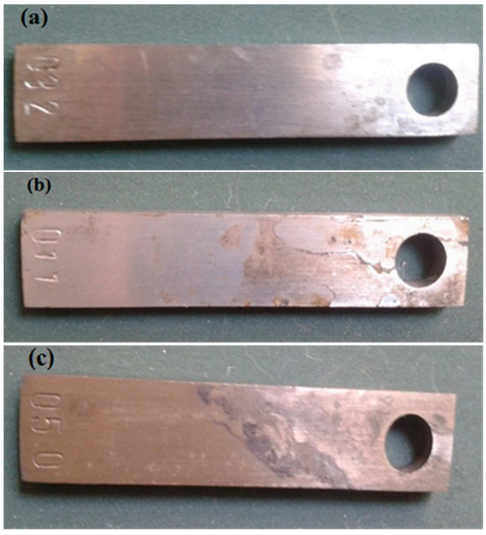
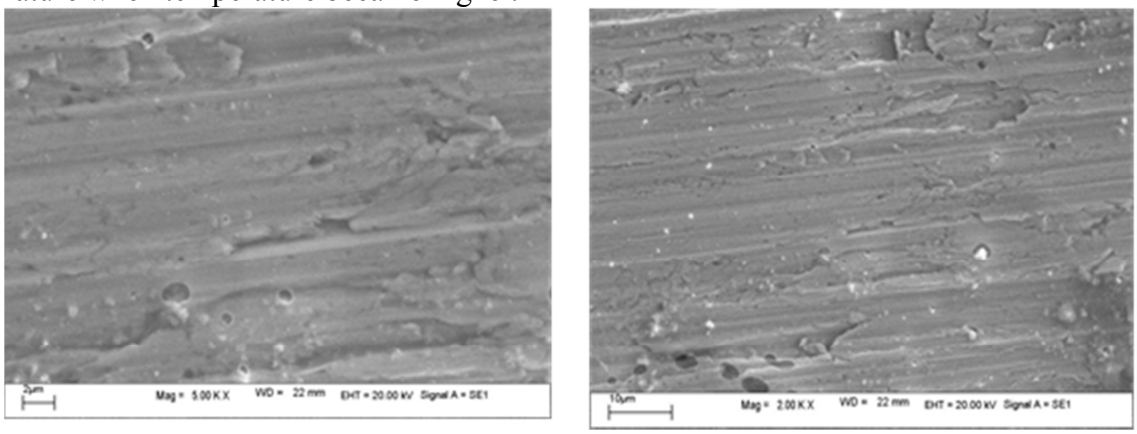


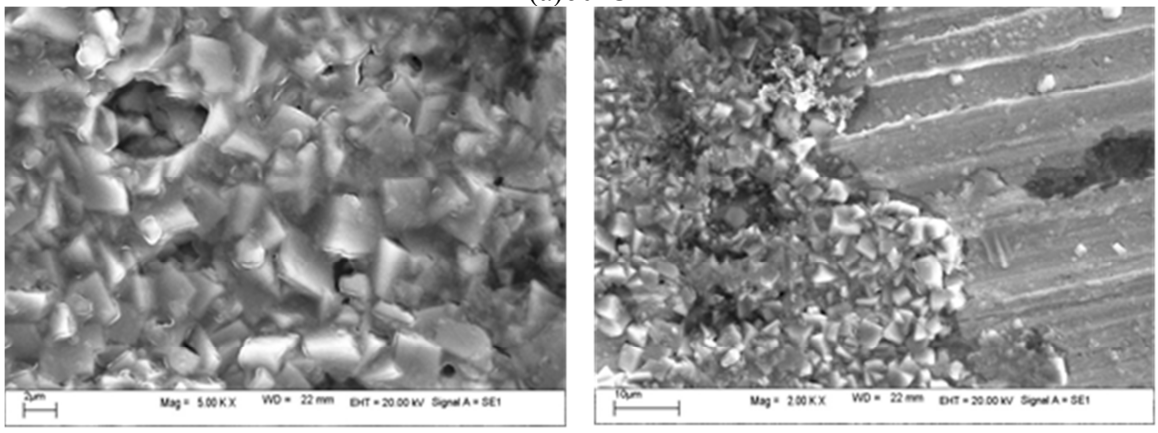

Fig. 2. The macro-morphology of 13Cr specimens after 168-hours test

**SEM Analysis**

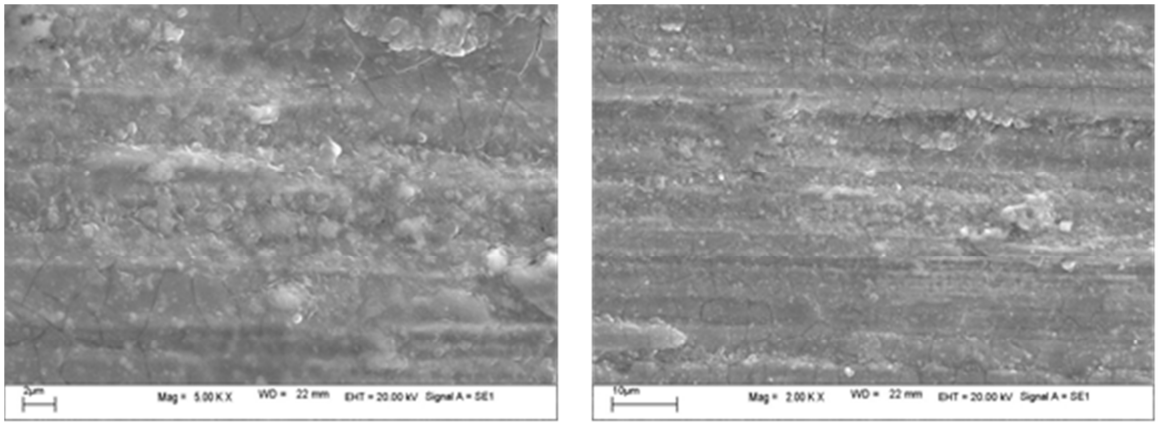
Fig.3 showed the surface morphologies of the 13Cr specimens at 60 °C, 85 °C and 110 °C. Left picture was the surface SEM magnified 5.00k times, while the right was that magnified 2.00k times. It was concluded from Fig.3 that temperature had a great impact on micro-morphology of 13Cr specimen surface. At 60°C, surface of 13Cr specimen was smooth with little polygonal crystalline corrosion product and polygonal crystalline corrosion product appeared at 85°C. In the other side, the complete corrosion scale and appearance of polygonal crystalline corrosion product could prevent steel from severe corrosion. However, when it was up to 110°C, a complete corrosion scale with much more crackles showed less protection for steel, and caused severe corrosion of the steel. From Fig.3, it could be found that the corrosion of the steel was more and more sensitive to temperature when temperature became higher.



(a)60°C



(b)85°C

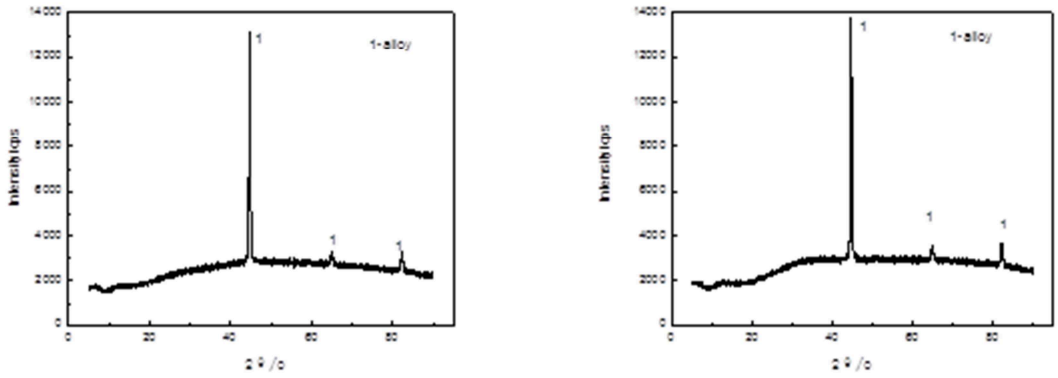


(c)110°C

Fig. 3. The SEM analysis of 13Cr specimens after 168-hours test

**XRD Analysis**

Fig.4 showed the XRD analysis of 13Cr specimen after 168-hours corrosion test. From Fig.4, the corrosion product on the steel was only a little and would not be detected by XRD analysis. From Fig.4, the chemical composition of steel could be detected, and further analysis, such as EDS, XPS and so on should be down to detect the chemical. These are owing to passivation film on the surface controlled corrosion medium pass it through, which severe corrosion would hardly happen.




(a)60°C (b)85°C

Fig. 4. The XRD analysis of 13Cr specimens after the 168-hours test

**Conclusion**

13Cr had a much better corrosion resistance. At 110°C, the corrosion rate was only 0.1746mm/a and the corrosion trace was not appear. But corrosion of 13Cr specimens was more sensitive to temperature. When temperature increased per 25°C, corrosion rate of 13Cr specimens increased about six times. However, with the presence of passivation film on 13Cr, the value of its corrosion rate should be considerately low.

**Acknowledgement**

This research was financially supported by the National Science and Technology Major Project(2011ZX05059).

**References**

[1] Masakatsu Ueda, Akio Ikeda. Effect of microstructure and Cr content in steel on $CO_2$ corrosion[A].Corrosion, 1996, 13.

[2] Binder Singh, Tom Folk, Paul Jukes, et al. Engineering pragmatic solutions for $CO_2$ corrosion problems[A]. NACE, 2007, 07310.

[3] E.Dayalan, F.D.de Moraes, J.R.Shadley, et al. $CO_2$ corrosion prediction in pipe flow under $FeCO_3$ scale-forming conditions[A]. Corrosion, 1998, 51.

[4] J.H.Cai, J.Y.Yan, J.Yan, et al. Carbon dioxide corrosion of a casing steel-effect of environments and temperature[A]. Canadian International Petroleum Conference, 2006-194.

*Advanced Materials Research Vol. 937 (2014) pp 172-177*
*© (2014) Trans Tech Publications, Switzerland*
*doi:10.4028/www.scientific.net/AMR.937.172*

# Microstructure and Properties of AZ31B Magnesium-LY12 Aluminum Alloys Diffusion-bonded Joint

Shuang-ming DU and Qian QIN

College of material science and engineering, Xi'an University of Science and Technology, Xi'an 710054, China

College of material science and engineering, Xi'an University of Science and Technology, Xi'an 710054, China

shuangmingdu@163.com, qianqincl@163.com

Qian QIN

**Keywords:** AZ31B/LY12, Diffusion bonding, Microstructure, Mechanical properties.

**Abstract.** In this paper, AZ31B magnesium alloy/LY12 aluminum alloy were bonded together with copper foil as interlayer by vaeuum diffusion bonding technology at different temperature for holding time 60 min and pressure 2.5MPa. Analysis the microstructure of the joint under the condition of 450°C,and the effects of heating temperature on the shear thrength , microhardness and the width of the interface zone were studied. The results showed that under the condition of 450°C in holding time 60 min and pressure 2.5MPa, the microstructure at interface zone of diffusion brazing joint includes α-Mg solid solution, $Mg_2Cu$, $Cu_2Mg$, γ-Cu solid solution, CuAl, $CuAl_2$ and β-Al solid solution. The width of the interface increases with brazing temperature increasing, and the microhardness gradient of interface zone in the side of aluminum alloy is much higher than that in magnesium alloy side. As the welding temperature increases, the shear strength shows an increasing trend at first and then decreases. When the welding process is 460°C keeping for 60 min, welding pressure is 2.5Mpa, the highest shearing strength of the joint can reach 35 MPa.

## Introduction

With many commonly used metal mineral resources are exhausted, rich reserves of magnesium resources is to being paid more and more attention. Magnesium alloy have advantages such as possess higher specific strength, higher specific modulus, good heat dissipation, strongly damping and noise reduction capacity, acceptable electromagnetic radiation shielding and easy to recycling, et al; And aluminum alloy have the properties of lower density, good electrical conductivity, good thermal conductivity and strongly corrosion resistance. In order to give full play to their respective performance advantages of Mg /Al dissimilar metals, it is necessary to combine magnesium alloy and aluminum alloy for the welded joints with firmly interface bonding, and to further extend the application of magnesium alloys as structural components in the field of high-tech [1-3].

Diffusion welding is a kind of welding method, which expands physical contact of the awaiting weld surface by micro plastic deformation, and then realize the combination by the interdiffusion of atoms. The heating temperature of it is generally much lower than the parent material and heating uniformly, which avoids adverse impact on physical and chemical properties of the parent material from the conventional welding method, Thus which causes the small stress deformation, and is suitable for connecting the occasion with large area and high dimensional precision [4]. So the vacuum diffusion welding have received more attention in the welding of dissimilar materials, but it forms a series of $Mg_xAl_y$ brittle intermetallic compound at the joint due to the very small mutual solubility of the two materials while welding Mg/Al by diffusion welding directly, which deteriorates the microstructure and mechanical properties of welding joint [5]. Research shows that, the middle layer of suitable material has a positive effect on inhibiting formation of brittle intermetallic compound between dissimilar metals, and is an important way to improve the welding properties of diffusion welding about dissimilar materials [6,7].

This paper has studied on welding AZ31B/LY12 dissimilar metal by vacuum diffusion welding with the Cu foil of 50 μ m as intermediate layer, and has analyzed elemental composition, microscopic structure, phase composition and micro hardness of diffusion zone of diffusion welding joint, which is in order to lay the foundation for achieving Mg/Al welding of dissimilar metals.

## Experimental Work

Square shaped specimens (50mm×50mm) were machined from rolled plates of 2mm thickness magnesium (AZ31B) and aluminum (LY12) alloys. The chemical compositions of the base metals are shown in Table 1. The interlayer material is copper foil of 99.9% purity used in the navigation. The thickness of copper foil is 50μm.

Table 1. Chemical constitutions of the base metals (wt.%)

| alloy | Mg | Al | Zn | Mn | Si | Fe | Cu | Cr | Ti |
|---|---|---|---|---|---|---|---|---|---|
| AZ31B | Bal. | 2.5-3.5 | 0.5-1.5 | 0.2-0.5 | 0.10 | 0.005 | 0.05 | - | - |
| LY12 | 1.2-1.8 | Bal. | 0.25 | 0.3-0.9 | 0.5 | 0.5 | 3.8-4.9 | 0.1 | 0.15 |

Before welding ,the surface of samples were polished by Particle size $800^{\#}$,$1000^{\#}$ and $1200^{\#}$ SiC sandpaper and the oxide film was degreased by a powerful solvent (acetone) on the both surfaces of the Mg and Al plate. used Ultrasonic cleaning of 5 min in ethanol, And then folded together and placed in a self-made mold, using ZR-45 type vacuum diffusion bonding equipment for vacuum diffusion bonding. The diffusion bonding technology adopted the step heating in the test. The technological parameters were: the heating temperature T=450-480 °C, the pressure P=2.5 Mpa, the holding time t=60 min and the vacuum degree 0.1 Pa. The specimens were heated up to the bonding temperature in an induction furnace at a heating rate of 10 °C/min. After bonding, the samples were cooled to room temperature before removal from the chamber.

The soldered joint was cross-sectioned by a cutting machine, and prepared into a series of metallographic samples. The series of metallographic samples prepared were polished by means of mechanical polishing,and then the samples were ground and etched using the reagent ( 4ml oxalic acid, 2ml $HNO_3$, 94ml $H_2O$ ) corrosion 20s. After the samples were polished and etched, the microstructure near the welded joint interface region was observed by means of SEM. The element distribution determination was tested by EDS. The phase constitution in the soldering region was analyzed by XRD. The microhardness of the formed phases in the soldering region was measured by means of a microhardness tester with a load of 0.25 N for 5 s.

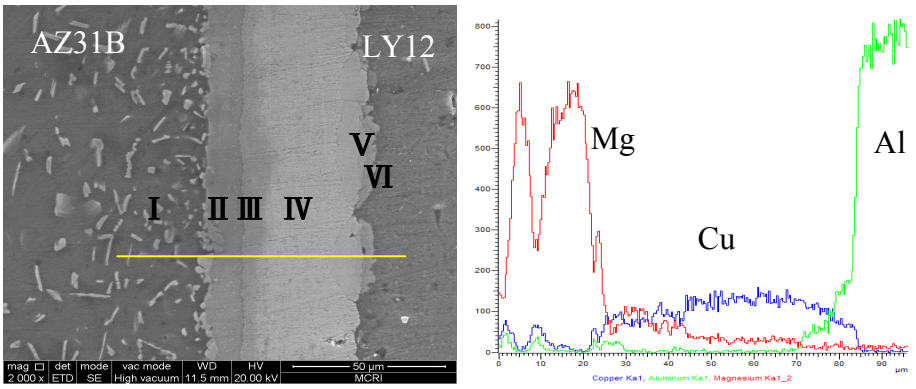
## Results and Discussion

### Microstructures of Joints

The microstructure and element diffusion of AZ31B/Cu/LY12 diffusion bonded joint was observed by means of SEM (see Fig. 1). It can be seen that the joint is combined well without defects such as cracks, holes and inclusion (see Fig. 1a). The interface of AZ31B/Cu/LY12 diffusion bonded joint produced the obvious diffusion and formed the layered structure diffusion zone between the AZ31B substrate and the LY12 substrate. The interface zone is mainly composed of the transition region on AZ31B/Cu side and the transition region on Cu/LY12 side. Three layers can be clearly observed near AZ31B/Cu side (Layer Ⅰ, Ⅱ, Ⅲ), two layers are formed near Cu/LY12 side (Layer Ⅴ, Ⅵ), and the residual copper foil is apparently visible (Layer Ⅳ).

Fig. 1b is the interface line analysis result of AZ31B/Cu/LY12 diffusion bonded joint by scanning electronic microscope. It was found that obvious diffusion occurred at the interface as shown in the line analysis of Mg, Cu and Al element. In the layer Ⅰ, the content of Mg element is very large, Al-rich phase and Cu-rich phase are shown in the white net part. The content of Mg element in layer

Ⅱ is changed into stable, and the contents of Al and Cu elements in layer Ⅵ are quite adjacent. The ratio of Al and Cu contents in layer Ⅴ far from LY12 substrate is 1:2. The diffusion of Al and Cu elements in the V and VI layer are more gently, no obvious ups and downs. The content of Al element is higher than that of Mg and Cu elements on LY12 matrix (grey organization) side, no segregation of Cu element in LY12 matrix.




(a) Microstructure (b) Interface line analysis result

Fig.1. Microstructure and Element diffusion of AZ31B/Cu/LY12 diffusion bonding joints at 450°C with 60min

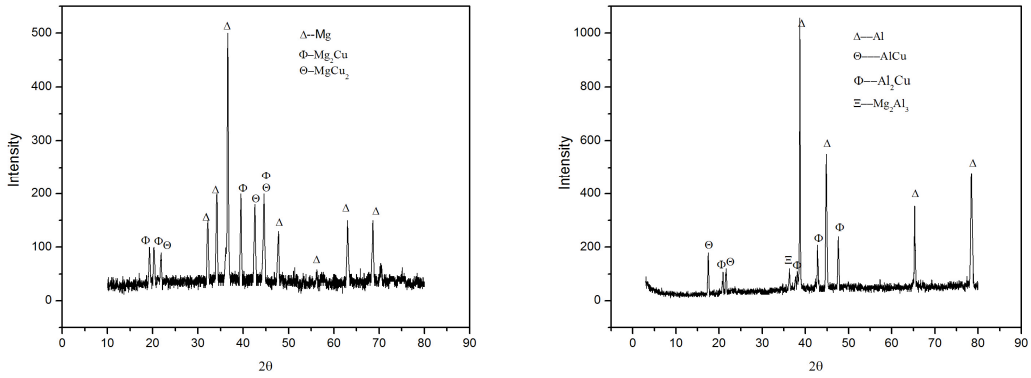
In order to search the dispersal behavior of Mg, Cu, Al elements near AZ31B/Cu and Cu/LY12 interface reaction zone further, the EDS analysis results obtained from different characteristic layers shown in Fig. 1 are illustrated in Table 2. From the results, near the diffusion reaction layer on AZ31B side, layer Ⅰ and Ⅱ are mainly composed of Mg and Cu elements,which explains that there are a great quantity Mg elements diffuse into copper foil on this region. The atomic ratio of Mg and Cu contents is 2:1, and the atomic ratio of Mg and Cu contents in layer Ⅲ is 1:4. Combined with Mg-Cu binary alloy phase diagrams, the organization of layer Ⅰ and layer Ⅱ is $Mg_2Cu$, and layer Ⅲ is mainly consists of α-Mg solid solution and Mg-Cu intermetallic compounds. The diffusion reaction layer Ⅳ is consists of much Cu element and a few Mg and Al elements, suggesting that Mg element in AZ31B matrix and Al element in LY12 matrix could diffuse into Cu interlayer to form γ-Cu solid solution. Layer Ⅴ is mainly composed of Cu and Al elements, which suggests that Al element could dissolve into copper foil. The atomic ratio of Cu and Al contents in layer Ⅴ is 1.8:1, and that in layer Ⅵ is 1:2. Combined with Al-Cu binary alloy phase diagrams, indicating that layer Ⅴ is composed of $Cu_2Al$ and layer Ⅵ is composed of $CuAl_2$.

Table 2. EDS results on area in Fig. 1

| characteristic layers | Mg | | Cu | | Al | |
|---|---|---|---|---|---|---|
| | (Wt.%) | (At.%) | (Wt.%) | (At.%) | (Wt.%) | (At.%) |
| Ⅰ | 40.77 | 57.47 | 45.90 | 25.25 | 13.34 | 17.28 |
| Ⅱ | 42.76 | 66.13 | 57.24 | 33.87 | - | - |
| Ⅲ | 8.96 | 20.46 | 91.04 | 79.52 | - | - |
| Ⅳ | 1.30 | 3.28 | 97.77 | 94.59 | 0.93 | 2.12 |
| Ⅴ | - | - | 81.05 | 64.49 | 18.95 | 35.51 |
| Ⅵ | - | - | 54.70 | 33.89 | 45.30 | 66.11 |

Figure 2 shows the XRD result from layer Ⅱ and layer Ⅴ in Fig. 1. It is shown that near the transition region on AZ31B side, layer Ⅱ contains α-Mg solid solution and $Mg_2Cu$, $MgCu_2$ intermetallic compounds phases. Near the transition region on LY12 side, layer Ⅴ is eventually formed by β-Al solid solution and CuAl, $CuAl_2$, $Mg_2Al_3$ intermetallic compounds.

Based on the above analysis, the microstructure of AZ31B/Cu/LY12 diffusion bonded joint according to the order was α-Mg, $Mg_2Cu$, $Cu_2Mg$, γ-Cu, CuAl, $CuAl_2$ and β-Al, there is also a trace amount of $Mg_2Al_3$ phase.




(a) Layer Ⅱ on AZ31B side (b) Layer Ⅴ on LY12 side

Fig.2. XRD result from transition zone of AZ31B/Cu/LY12 diffusion bonded joint at 450°C with 60min

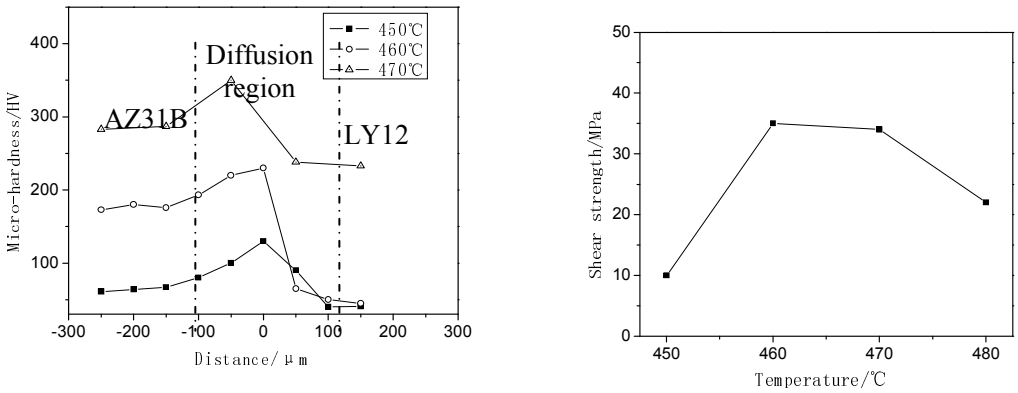
**Elements Diffusion Process of Joints**

The elements diffusion process of AZ31B/Cu interface: According to the diffusion flux ratio in diffusion theory [8], the constitution and proportion of the diffuse reaction created new phases should be produced first. Because there is a concentration gradient of Mg and Cu elements in both sides of the AZ31B/Cu interface, and the diffusion rate of Mg element is bigger than that of Cu element, the reaction primary phase of AZ31B/Cu interface is $Cu_2Mg$. When the diffusion flux ratio of Mg and Cu atoms is bigger than 1:2, new phase $Cu_2Mg$ will start nucleation in both γ-Cu solid solution and the interface of Mg matrix. The process of nucleation need Mg atoms get into activation point to displace Cu atom lattice, and form $Cu_2Mg$ crystal structure. Cu atoms are substituted and then stay in the interface of Mg substrate to form new activation points. With the increase of Mg atoms content around $Cu_2Mg$, new reaction is occurred ($Cu_2Mg+3Mg\rightarrow 2Mg_2Cu$), finally the phase constitution of the diffusion region is α-Mg, $Mg_2Cu$ and $Cu_2Mg$.

The elements diffusion process of Cu/LY12 interface: During the initial stage of the Cu/LY12 interface contacting, surface atoms transferred each other to form β-Al solid solution and γ-Cu solid solution in both sides of the interface. According to the flux-energy principle, because the diffusion rate of Al element is much bigger than that of Cu element, the reaction primary phase of Cu/LY12 interface is $Cu_2Al$. When the diffusion flux ratio of Al and Cu atoms is bigger than 1:2, new phase $Cu_2Al$ will start nucleation in both γ-Cu solid solution and the interface of Al matrix [9]. Because the diffusion velocity of Al atoms is faster, when the concent of Al atoms around $Cu_2Al$ increase significantly, new reaction is occurred ($Cu_2Al+3Al\rightarrow 2CuAl_2$), and finally the phase constitution of the diffusion region is β-Al and $CuAl_2$.

**Microhardness and Shear Strength of Joints**

Figure 3 is the microhardness and shear strength of AZ31B/Cu/LY12 diffusion bonded joint. According to Fig. 3a, as the welding temperature increases, the width from substrate to diffusion center region and the microhardness show an increasing trend. The microhardness gradient of interface zone in the side of magnesium alloy is much lower than that in aluminum alloy side. However, the width of hardness area in the side of magnesium alloy substrate is obviously bigger than that in aluminum alloy substrate. It suggests that under the same technology condition, Mg element will diffusion more fully in the copper foil interlayer than Al element. When the welding temperature is 450°C, 460°C and 470°C, microhardness reaches the highest value of 130HV, 230HV and 350HV.




(a) Microhardness (b) Shear strength

Fig.3. Microhardness and shear strength of AZ31B/Cu/LY12 diffusion bonding joints at different temperature with 60min

The shear strengths of the joints at different welding temperature are shown in Fig. 3b. As the welding temperature increases, the shear strength shows an increasing trend at first and then decreases. When the welding temperature is 450°C, the shear strength reaches the lowest value. The reason is that when the interface elements interdiffuse inadequate, solid solusion diffusion is formed in the LY12 side of Cu/LY12 interface, and the bonding force is weak. At 460°C, the highest shearing strength of the joint can reach 35 MPa. Because the interface elements interdiffuse adequate and the elements diffuse reaction is clearly, shear strength of the joint rises obviously. With the welding temperature continues to increase, the shear strength of the joint descend to the contrary, this is because increasing temperature promotes the proliferation ability of the interface elements. Excessive interface reaction makes copper foil lose the function, which can prevent Mg and Al substrate contact directly. A series of MgxAly intermetallis compounds appear at the interface due to the shear strength decrease.

## Conclusions

1. When the bonding temperature is 450°C, holding time is 60min and bonding pressure is 5M, AZ31B/Cu/LY12 diffusion bonded joint is combined well without defects such as cracks, holes and inclusion. The microstructure of AZ31B/Cu/LY12 diffusion bonded joint according to the order was α-Mg, $Mg_2Cu$, $Cu_2Mg$, γ-Cu, CuAl, $CuAl_2$ and β-Al, there is also a trace amount of $Mg_2Al_3$ phase.

2. The interface of AZ31B/Cu/LY12 diffusion bonded joint presents the layered structure, and it is mainly composed of AZ31B/Cu interface zone and Cu/LY12 interface zone. The AZ31B/Cu interface region is close to AZ31B side and the phase composition of the diffusion region is α-Mg + $Mg_2Cu$ + $Cu_2Mg$. The Cu/LY12 interface region is close to LY12 side and the phase composition of diffusion region is β –Al + CuAl + $CuAl_2$.

3. As the welding temperature increases, the width from substrate to diffusion center region and the microhardness show an increasing trend. The microhardness gradient of interface zone in the side of magnesium alloy is much lower than that in aluminum alloy side. However, the width of hardness area in the side of magnesium alloy substrate is obviously bigger than that in aluminum alloy substrate.

4. As the welding temperature increases, the shear strength shows an increasing trend at first and then decreases. When the welding process is 460°C keeping for 60 min, welding pressure is 2.5Mpa, the highest shearing strength of the joint can reach 35 MPa.

**References**

[1] Kun Yu, Wenxian Li, Richu Wang, et al. Research on the development and application of wrought magnesium alloys [J]. Chinese Journal of Nonferrous Metals,2003,13 (2) :277-286

[2] Wanqun Huang, Lijun Ma, Xin Wang. Welding of magnesium alloy with other metal and alloy [J]. Aerospace Materials and Technology In Chinese, 2010, 4:1 - 4

[3] Ying Chen, Gaofeng Quan, Changbin Shen, et al. Research status and Prospect of welding method for magnesium alloy [J]. Journal of Materials In Chinese, 2008, 12 (22): 346 - 348

[4] Hongzhou Fang, Jicai Feng. The behavior of the interface material joining process [M]. Harbin: Harbin Institute of Technology Press In Chinese, 2005

[5] Peng Liu. Study on the microstructure and element diffusion in the interface of Mg/Al activity of dissimilar metal welding [D]. Shandong University, Ji Nan, china

[6] WU Ming-fang, SI Nai-chao, CHEN Jian. Contact reactive brazing of Al alloy/Cu/ stainless steel joints and dissolution behaviors of interlayer [J]. Trans. Nonferrous Met. Soc. China 2011 (21) 1035-1039

[7] Shuangming Du, Gang Liu, Mingjing Wang. Properties and microstructure of AZ31/Cu dissimilar metal transition liquid phase diffusion welded joint [J]. Chinese Journal of Nonferrous Metals, 2013 (5) 1255-1264

[8] Xiaonong Chen, Qixun Dai, Honghong Shao. Solid phase transformation and diffusion of material [M]. Chemical Industry Press In Chinese, 2006

[9] G. MAHENDRAN, V. BALASUBRAMANIAN, T. SENTHILVELAN. Influences of diffusion bonding process parameters on bond characteristics of Mg-Cu dissimilar joints [J]. Trans. Nonferrous Met. 2010 (20) 997 - 1005

*Advanced Materials Research Vol. 937 (2014) pp 178-181*
*© (2014) Trans Tech Publications, Switzerland*
*doi:10.4028/www.scientific.net/AMR.937.178*

# Research Progress of Mg-RE alloys

Quan-an LI[1,2,a], Wen-chuang LIU[1,b] , Xiao-jie SONG[1,c]

[1]School of Materials Science and Engineering, Henan University of Science and Technology, Luoyang 471023, China

[2]Collaborative Innovation Center of Nonferrous Metals, Henan Province, Luoyang, 471023, China

[a]q-ali@163.com, [b]hkalwc1987@163.com,[c] song_xiaojie@foxmail.com

**Keywords:** elevated temperature properties, Mg-RE alloys, alloying elements

**Abstract:** Magnesium alloys as the emerging commercial metal structure material have excellent specific properties, low density, and stability, which are more and more vital for researchers. This paper reviews the behavior of rare earth in magnesium alloy and the way to enhance the elevated temperature properties of Mg-RE alloys. The current Mg-RE alloys are summarized. The future development direction is pointed.

## Introduction

Magnesium alloys have been identified as ideal materials in automotive, aerospace and railway industries because of their low density, high specific and stiffness, and good machine-ability[1].Light weighting transport is one of the easiest ways to improve energy efficiency. The magnesium alloys can be the replacement of Fe-based alloys resulting in substantial reductions of energy usage.The greatest benefits are achieved with the use of cast magnesium[2-4].The legislation limiting emission requirement by reducing the weight of car has triggered the interest in magnesium. The growth rate in the next 10-12 years has been forecast to be 7.5% per year[5].Most of the rare earth elements' atomic sizes are close to the magnesium's. The RE element has solid solution strengthening and precipitation strengthening effect, it can improve tensile strength, creep properties at elevated temperature. In addition, RE elements get rid of hydrogen deoxidation to improve the casting performance [6].

## The Main Functions of RE in the Magnesium Alloys

### The Melt Protection and Purification Effect

Rare earth elements in magnesium alloy melt have the functions of removal of hydrogen, oxygen, sulfur ,iron, and the inclusion to degassing and purification. It is very easy for magnesium to oxidation in melting process. Magnesium alloys are protected by flux or gas protecting at present.But there are many disadvantages, If they can be improved the ignition temperature of magnesium alloy melt, they are likely to achieve the direct smelting process of magnesium alloys in atmosphere. It is so vital for magnesium alloys in the further application. Rare earths are the surface active elements in magnesium alloy melt, they can form the dense composite oxide film at the melt surface to effectively prevent the melt and air contact, greatly improve the melt temperature of the magnesium alloys[7-9].

### Strengthening Effect

Rare earth elements have solid solution strengthening，fine grain strengthening，solid solution strengthening and dispersion strengthening in magnesium alloys.The solid solubility of rare earth element is high in magnesium. Rare earth atoms dissolve in the magnesium matrix,enhance the binding force of atomic ask, and distort the matrix lattice. The solid solution strengthening effect of rare earth elements have the slow diffusion rates to block dislocation movement.Rare earth elements are enriched in the solid-liquid interface to constitutional supercooling. The supercooled region can form the new nuclear stripe and the fine equiaxed grains.Rare earth enrichment can impede Mg grain growth,and further promote the grain refinement[10-12].

## Research and Development of Rare Earth Magnesium Alloys

### Mg-Y-based Alloys

The solid solubility of Y in the magnesium is as high as 12%, and Y atom size is so huge difference with magnesium atomic size, and its solubility gradually reduces with the temperature decreases. So Y can produce the excellent effect of solid solution strengthening and aging strengthening in magnesium alloy. In the rare earth elements of all, Y is considered to be the most effective element to improve elevated temperature properties of magnesium alloy , thus it has developed a series of Mg-RE-based heat resistant magnesium alloys.WE54 and WE43 are the most successful development of magnesium alloys, they have very high strength at room and elevated temperature, and they can be up to 300°C of heat resistant temperature. And after the heat treatment, the corrosion resistance is better than that of other magnesium alloys[13-14].

The effects of 2-12 wt.%Y addition on the microstructure and mechanical properties of as-cast Mg-Y binary alloys have been investigated. The results show that proper content of rare earth Y addition can obviously refine the grains and form high melting point $Mg_{24}Y_5$ phases in the matrix, and improve the microstructure and mechanical properties of the alloys. At room temperature, the optimum combination of ultimate tensile strength and elongation, 195MPa and 7.5%[15].The Microstructures and mechanical properties of the Mg-4Y-2.5Nd-0.6Zr (wt%) alloy in the as-cast, as-rolled, and rolled-T5 conditions have been investigated. Results show that the as-cast sample mainly consisted of the α-Mg matrix, network-like $Mg_{41}Nd_5$ phase, and cuboid-shaped $Mg_{24}Y_5$ particles. For the as-rolled sample, the thermally stable $Mg_{24}Y_5$ particles locat at both grain boundaries and matrix, and the average grain size is greatly refined to about 15 μm. Yield strength, ultimate tensile strength, and elongation of as-rolled samples are 290 MPa, 235 MPa, and 10%, respectively[16].

### Mg-Gd-based Alloys

Mg-Gd-based alloy is one of the candidates for novel Mg-based preciptatation-hardened alloys having high creep resistance and specific strength at elevated temperature,thus it plays an vital role in their mechanical properties. Mg-Gd binary alloys exhibit a three-stage precipitation sequence.When the mass contents of Gd are up to 20%, it can greatly enhance the hardness and strength.Mg-Gd-Zn,Mg-Gd-Y-Zr,and other alloys have been widely investigated[17].

In Mg-Gd-Zn alloy,as the test temperature increases to 230°C, the YS, UTS reduces significantly and the elongation to failure increased correspondingly. The overall strength properties are much higher with Mg-10Gd–xZn base alloys compared with Mg-2Gd-xZn alloys. The YS of Mg-10Gd-2Zn alloy at 230°C is 92.17 MPa, which is higher than the room temperature.[18] In Mg-Gd-Y-Zr alloy made by high cycle fatigue extrusion, the uniaxial tensile and compressive stress–strain curves of GW123K alloy are around 250 MPa (given for 0.2% offset). It is noted that the present GW123k alloy does not exhibit an obvious asymmetry in its tensile and compressive yield strengths[19].

### Mg-Sm-based Alloys

The main characteristics of Mg-Sm diagram is the existence of five kinds of binary intermetallic phases, where Mg2Sm and Mg-Sm are stable intermetallic compounds. As a rare element, Sm is added to strength the matrix and grain boundary, and enhance the mechanical properties, The maximum solubility of Sm in solid Mg is 5.8wt.%, which is lower than Y and Gd. Thus, addition of small amount Sm could lead to the formation of semi-continuous grain-boundary eutectics, and strength the grain boundary. The maximum solid solubility is higher than Ce. It can form dense dispersion of five precipitates during creep to retard dislocation motion[20-21].

The effects of heat treatment on the microstructure and mechanical properties of Mg-Sm extruded alloy are investigated by tensile test and hardness measurement. The results show that the hardness of the alloy after T5 treatment is higher that after T6 treatment. After T5 treatment, the tensile strength, yield strength and elongation of the Mg-Sm alloy reaches the peak 217.4MPa, 162.1MPa and 13.1%, respectively[22].

**Other Mg- RE Alloys**

Sc is a kind of potential alloy elements to enhance the properties of magnesium alloys at elevated temperature (300°C). It has many advantages, its melting point is very high that can be up to 1541 °C, and it diffuses slowly in the magnesium to improve solid melting point of magnesium, and its density is only 3g/cm$^3$. Comparing with the other added elements, such as, Y, Nd, Ce, Ho, it can surely improve the strength of magnesium alloy at room temperature and elevated temperature[23-24].

**Conclusion**

To meet the needs of aerospace, automobile, electronic communications, it should be to purse high-strength. Comparing with other alloys, it is seen that alloys have still existed poor comprehensive mechanical properties at elevated temperature, thus it should not be widely used in commercial production. How to solve these problems, the methods should be considered as below:

(1)According to the raw material characteristics, the novel manufacture methods should be put forward and applied.

(2) The formation mechanism of RE elements added to the magnesium should be widely studied in the future.

**Acknowledgement**

The project is supported by the National Natural Science Foundation of China (Project No. 51171059), and Basic and Frontier Technologies Research Plan of Henan Province (Project No. 102300410018), and by Program for Innovative Research Team (in Science and Technology) in University of Henan Province (Project No. 2012IRTSTHN008), and Collaborative Innovation Center of Nonferrous Metals of Henan Province.

**References**

[1] J.X. Song, Q.A. Li,L.S. Fu,et al. Advanced Materials Research. 750-752(2013) 583-586.

[2] CH Ca'ceres. Metal Mater Trans, A. 38( 2007) 1649-1662.

[3] JF King. Mater Sci Technol. 23(2007) 1-14.

[4] M. Hakamada, T. Furuta, Y. Chino, et al. Energy. 32(2007) 1352-1360.

[5] B. L. Mordike, T. Ebert. Materials Science and Engineering, A. 302(2001) 47-52.

[6] Y. F.Wu, W.B.Du, Z.J.Yan, et al. Rare Metals. 29(2010) 55-61(in Chinese).

[7] H.J. Zhang, X.D. Tang, J.H. Zhang, et al. Chinese Journal of Rare Metals. 32(2008) 20-24.

[8] H.G. Wu, M.H. Song, Y.Z. Xiu, et al. J. Mater. Sci. Technol. 25(2009) 423.

[9] M.W. Zhao, Y. Sun, P.H. Li, et al. Materials Science and Engineering, B. 127(2006) 105-107.

[10]K.S. Tian, F.X. Guo, B.H. Cui, et al. Foundry Technology. 32(2011) 1174-1177(in Chinese).

[11] T. Li, W.Z. Du, K. Zhang, et al. Material Review. 26(2012) 96-100(in Chinese).

[12] S.Y. Chang, Y.L. Kim. J. Mater. Sci. Technol. 24(2008) 38.

[13]A. Luo,M.O. Pekguleryuz. Journal of Materials Science. 29(1994) 525-527.

[14] M. Suzuki, T. Kimura, et a1. Mater Sci Forum.419-422(2003) 473—478.

[15] A.Q. Li, Q. Zhang, Q.C. Li, et al. Advanced Materials Research..352(2011) 239-242.

[16] X. Wang, M.C. Liu, X. Lu, et al. Journal of Materials Research. 28(2013) 1386-1393.

[17] M.Sun, H.G. Wu, W.Wang, et al. Material Review. 23(2009) 98-103(in Chinese).

[18]A. Srinivasan, Y. Huang, C.L. Mendis, et al. Mater. Sci. Eng. A 559(2014) 224-234.

[19] F. Yang, F. Lv, X.M. Yang, et al. Mater. Sci. Eng. A. 528(2011) 2231-2238.

[20] L.L. Rokhlin, Magnesium alloys containing rare earth metals, London, Talyor and Francis, 2003.

[21] D.Q. Li, Q.D. Wang, W.J. Ding. Mater. Sci. Eng A. 448(2007) 165-170

[22] R, Zhen, Z.Z. Wang, S.Y. Sun, et al. Material and Heat Treatment. 40(2011) 157-159

[23] B. L. Mordike. Mater. Sci. Eng A. 224(2002) 103-112.

[24] F.V. Buch, J. Lietzau, B.L. Mordike, et a1.Mater Sci Eng A. 263(1999) 1-7.

*Advanced Materials Research Vol. 937 (2014) pp 182-186*
*© (2014) Trans Tech Publications, Switzerland*
*doi:10.4028/www.scientific.net/AMR.937.182*

# Effect of Solution Treatment on Microstructures and Hardness of Mg-Gd-Y-Zr Alloy

Quan-an LI[1,2,a], Lei-lei CHEN[1,b], Wen-chuang LIU[1], Xing-yuan ZHANG[1] and Hui-zhen JIANG[1]

[1]School of Materials Science and Engineering, Henan University of Science and Technology, Luoyang 471023, China

[2]Collaborative Innovation Center of Nonferrous Metals, Henan Province, Luoyang, 471023, China

[a]email:q-ali@163.com, [b]email: cll19880623@163.com

**Keywords:** Mg-Gd-Y-Zr alloy, solution treatment, microstructures, Vickers hardness.

**Abstract.** The influence of the solution treatment (at the temperature of 500-520°C for 4-12 h) on microstructures and mechanical properties of Mg-Gd-Y-Zr alloy was investigated by means of optical microscopy, scanning electron microscopy (SEM), X-ray diffraction (XRD) and Vickers hardness measurement. The as-cast alloy contains a microstructure consisting of α-Mg matrix, $Mg_5Gd$ phase and $Mg_{24}Y_5$ phase. With increasing solution temperature and time, the quantity of the primary particles ($Mg_5Gd$ and $Mg_{24}Y_5$) in the alloy continually decreased, and the degree of recrystallization gradually increased, which result in the gradual decrease of the Vickers hardness of the solution-treated alloys.

## Introduction

Recently, there have been constantly increasing uses of light-weight and high-strength materials as structural materials in engineering applications such as automobile industry, 3C (Computer, Communication, Consumer Electronic) and electron industry [1,2]. However, due to the low strength and poor heat resistance, the widespread applications of magnesium and its alloys are limited [3,4]. Thus, developing a new kind of Mg alloys with high mechanical performance is a significant issue [5,6].

The equilibrium solid solubility of Gd in Mg matrix is fairly high (4.53 at.% or 23.49 wt.%) at 548 °C. And, as the temperature decreases, the solubility quickly drops to 0.61 at.% (3.82 wt.%) at 200°C, forming an ideal system for precipitation hardening, which is beneficial to improve the mechanical properties of the magnesium alloys[7].Meanwhile, it was also found that the addition of other RE (Dy, Nd and Y) elements into the Mg−Gd based alloys is an very effective method to improve the strength and creep resistance of the Mg alloys at elevated temperatures[8]. Rokhlin [9] and He Shangming [10] have developed Mg–Gd–Y–Zr alloys which show higher strength at both room and elevated temperature and better creep resistance than WE54 and QE22. And they also have investigated the relationship between mechanical properties and microstructures of these high gadolinium-containing magnesium alloys.

The precipitation sequence of these high gadolinium-containing Mg–Gd–Y–Zr alloys have been clearly reported, which contains α-Mg supersaturated solid solution (S.S.S.S.)→ metastable β' (D019)→metastable β'(cbco)→metastable β'(fcc)→stable β (fcc)[11-12]. However the formation and evolution of α-Mg supersaturated solid solution and the low gadolinium-containing Mg–Gd–Y–Zr alloys not yet well understand. Determining the most suited solution treatment conditions is one of the major considerations in the reseach of Mg–Gd–Y–Zr alloys; therefore the present study was conducted to report the behavior of solution heat treatment on the microstructures and the hardness of Mg–5Gd–3Y–0.5Zr alloys from 500 to 520 °C for 4-12 hours.

## Experimental Procedures

Mg-30Gd (wt.%) and Mg-25Y (wt.%) master alloys were made first by melting high purity Mg (N99.95%), Gd (N99.9%) and Y (N99.9%) in a vacuum medium- frequency induction furnace under an argon atmosphere. Then, the Mg–5Gd–3Y–0.5Zr alloy ingots were prepared from high purity Mg (99.95%), the Mg-30Gd (wt.%), Mg-Y (wt.%) and Mg-25Zr (wt.%) master alloys in a medium-frequency induction furnace with a graphite(99.99%) crucible under a mixed atmosphere of $CO_2$ and SF6 with the ratio of 100:1.

Before the melting started, all the materials should be dried at 200°C for 1-2 hours. Firstly, the Mg-30Gd (wt.%), Mg-Y (wt.%) and Mg-25Zr (wt.%) master alloys were putted into the bottom of the furnace, however the high purity Mg was above. Secondly, the metals were heated to melt. Then, the melt was held at 740°C for 5min to obtain a uniform alloy, which was stirred at the same time. Finally, when the temperature was reduced to 710-720°C, the melt was slowly poured into a permanent metallic mold which was preheated to 200~250°C.

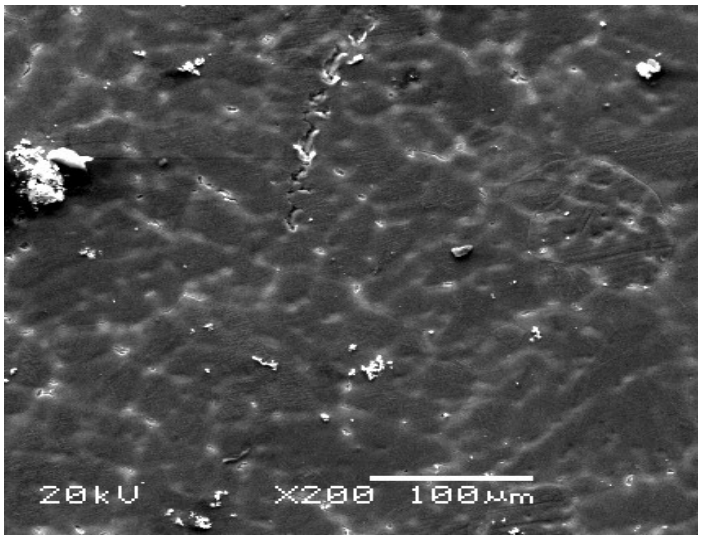



Fig. 1. SEM image of as-cast Mg–5Gd–3Y–0.5Zr alloy.

After casting , specimens were solution treatment from 500 to 520 °C in the time range 4–12 h and then quenched into water at about 60°C. Cast specimens and cast-T4 specimens were etched in a 4 vol.% nital. Vickers hardness testing was taken using 980.7mN load and holding time of 10s. Microstructural examination was performed in an optical microscope (OM), scanning electron microscopy (SEM, JSM 5610LV) and X-ray diffraction (XRD).

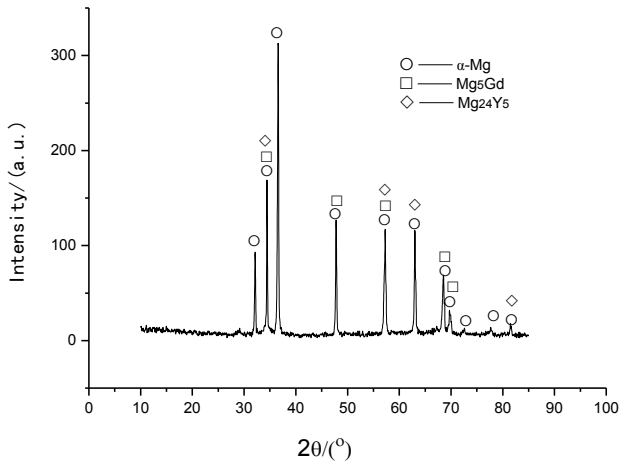
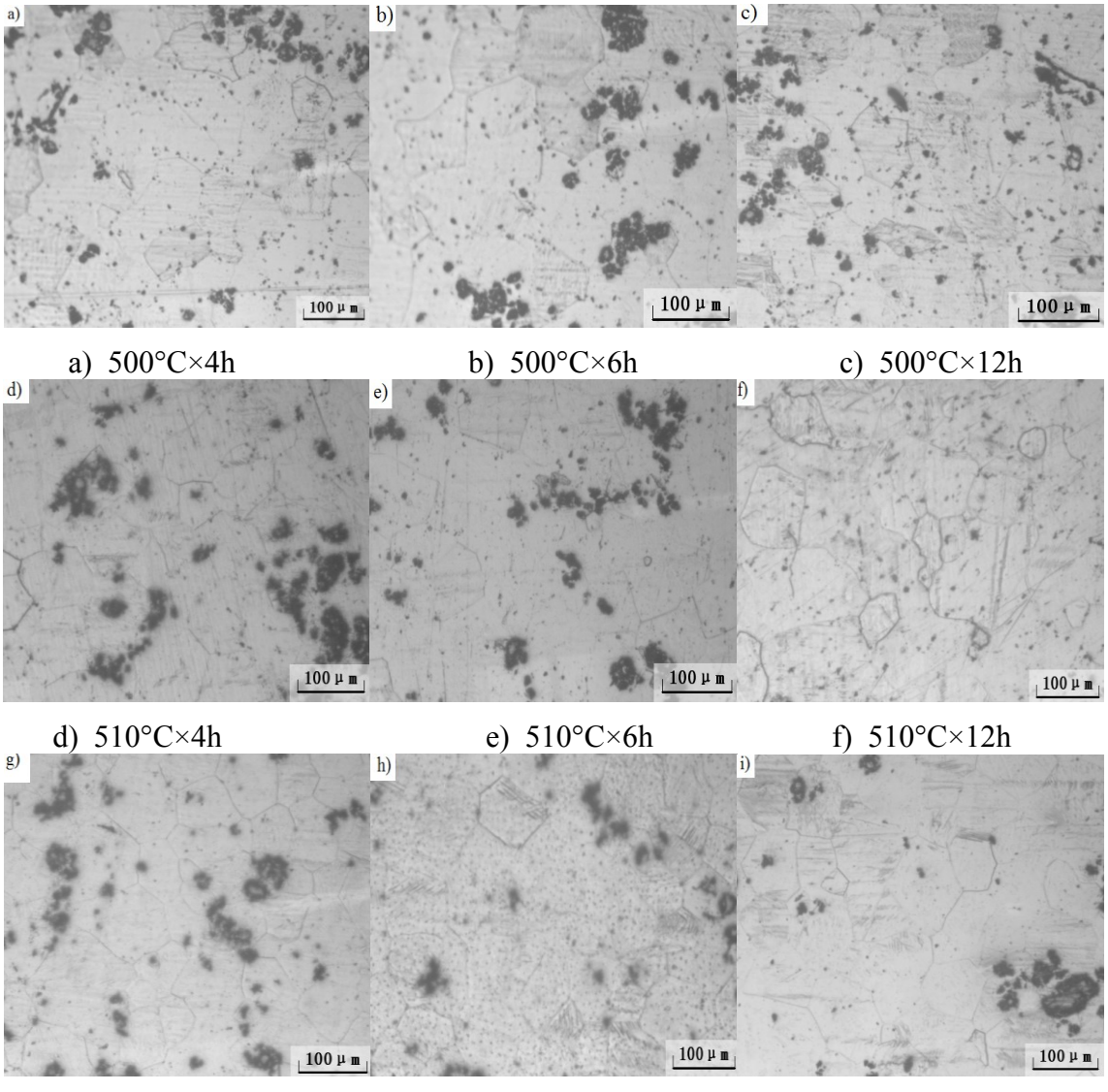



Fig. 2. XRD pattern of as-cast Mg–5Gd–3Y–0.5Zr alloy.

**Results and Discussion**

The SEM image of as-cast Mg–5Gd–3Y–0.5Zr alloy is shown in Fig. 1. In the SEM image, it was observed that one phase solid solution with a white cellular and net-work of second phase which is mostly disposed between the dendrite branches of α-Mg solid solution, and there are many dark petal-like Zr-rich regions were diffuse in the -Mg basal body. The average grain size is very fine. The phase compositions of the as-cast alloy by XRD analysis are shown in Fig. 2. It indicates that Mg–5Gd–3Y–0.5Zr alloy mainly consists of α-Mg solid solution, $Mg_5Gd$ and $Mg_{24}Y_5$ eutectic compounds.

The microstructure evolutions of Mg–5Gd–3Y–0.5Zr alloy with different solution temperature and time are list in Fig. 3. It was found that both grain size and the dendrite arm spacing as well as their shapes were obviously changed with the time and temperature going on.




a) 500°C×4h b) 500°C×6h c) 500°C×12h

d) 510°C×4h e) 510°C×6h f) 510°C×12h

g) 520°C×4h h) 520°C×6h i) 520°C×12h

Fig. 3. Effect of different solution temperature and time on the microstructures of Mg–5Gd–3Y–0.5Zr alloy

At 500 °C for 4 h, the morphology of the phase became thinner and the amount decreased (Fig. 3a) compared with that in the as-cast specimen shown in Fig. 1. After heating for 6 h (Fig. 3b), the Mg5Gd and $Mg_{24}Y_5$ net-work of second phase were fused into disconnected and fragmentized island morphology. With the time prolong, Mg5Gd and $Mg_{24}Y_5$ particles were further decrease and

dissolved into α-Mg matrix after 12 h at 500°C(Fig. 3c), however the average size of the grains was much bigger than that after 4 h and 6h. And in this temperature and time, the eutectic phases have not dissolved into the Mg basal body, it is obviously that the temperature of 500 C is so lower. About 6 h solution treatment at 510°C, the Mg5Gd and $Mg_{24}Y_5$ network of second phase was nearly dissolved (Fig. 3e), and the grain growth was not obvious and still thin. When the solution treatment time was 12 h. Although the second phases were completely dissolved, but the average grain size grown up clearly (Fig. 3f). At 520°C for 4 h, there are some remnant eutectic compound in the grain-boundaries, but their shape have been changed into spheroid congeries and the average grain size grown up rapidly (Fig. 3g). At 540°C solution treatment (Fig. 3h and Fig. 3i), the spheroid congeries was completely dissolved. Because at so high temperature, the element Mg, Gd and Y diffuse rapidness and the average grain size grown up very obviously.

Fig. 4 shows the hardness cures for the alloy solution-treated at 500-520°C for 4 to 12h. The three kinds of curves show similar regular pattern. The hardness of all the alloys greatly decreases abruptly within the first 8 h, then its decreasing slightly. Because, at the beginning of solid solution, there were the $Mg_5Gd$ and $Mg_{24}Y_5$ eutectic compound dissolved. After reaching 8 h, the hardness decreased due to the average grain size grown up. The conclusion is in agreement with the microstructures results shown in Fig. 4.

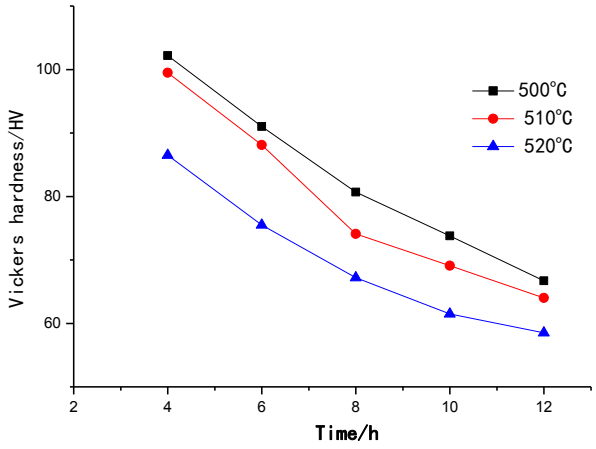



Fig. 4. Effect of solution temperature and time on the hardness of Mg–5Gd–3Y–0.5Zr alloy.

## Conclusions

1) The as-cast Mg–5Gd–3Y–0.5Zr alloy mainly consists of α-Mg solid solution, $Mg_5Gd$ and $Mg_{24}Y_5$ phases.

2) With the increase of solution temperature and/or time, the second phases $Mg_5Gd$ and $Mg_{24}Y_5$ were gradually dissolved into the α-Mg matrix.

3) As the result of these microstructures changes, the Vickers hardness of the solution-treated alloys decreases continually.

## Acknowledgement

In this paper, the research was sponsored by the National Natural Science Foundation of China (51171059),Basic and Frontier Technologies Research Plan of Henan Province 102300410018) and by Program for Innovative Research Team (in Science and Technology) in University of Henan Province(2012IRTSTHN008).

**References**

[1] Zhenyan Zhang, Liming Peng, Xiaoqin Zeng, Penghuai Fu and Wenjiang Ding, Characterization of phases in a Mg-6Gd-4Sm-0.4Zr (wt.%) alloy during solution treatment, Materials Characterization, (60) 2009 555-559.

[2] Aghion E, Bronfin B, Eliezer D, The role of the magnesium industry in protecting the environment, Journal of Materials Processing Technology. (117) 2001 381-385.

[3] Zhanhui Wang, Wenbo Du, Xudong Wang, Ke Liu and Shubo Li, Microstructure evolution of Mg−9Gd−2Er−0.4Zr alloy during solid solution treatment, Transactions of Nonferrous Metals Society of China. (23) 2013 593-598.

[4] Bayani, Hossein, Effect of rare earth elements addition on thermal fatigue behaviors of AZ91 magnesium alloy, Journal of Rare Earths. (27) 2009 255-258.

[5] Jilin Li, Rongshi Chen, Wei Ke, Microstructure and mechanical properties of Mg−Gd−Y−Zr alloy cast by metal mould and lost foam casting, Transactions of Nonferrous Metals Society of China. (21) 2011 761−766.

[6] Mingbo Yang, Caiyuan Qin, Fusheng Pan and Tao Zhou, Comparison of effects of cerium, yttrium and gadolinium additions on as-cast microstructure and mechanical properties of Mg−3Sn−1Mn magnesium alloy, J Rare Earth. (29) 2011 550−557.

[7] Yan Gao, Qudong Wang, Jinhai Gu, Yang Zhao and Yan Tong, Behavior of Mg–15Gd–5Y–0.5Zr alloy during solution heat treatment from 500 to 540 °C, Materials Science and Engineering A. (459) 2007 117-123.

[8] Jie Wang, Yuansheng Yang and Wen-hui Tong, Effect of purification treatment on corrosion resistance of Mg−Gd−Y−Zr alloy, Transactions of Nonferrous Metals Society of China. (21) 2011 949−954.

[9] L.L. Rokhlin, Advance Light Alloys and Composites, in: Proceedings of NATO Advanced Study Institute, Kluwer, 1998, pp. 443.

[10] S.M. He, X.Q. Zeng, L.M. Peng, X. Gao, J.F. Nie and W.J. Ding, Microstructure and strengthening mechanism of high strength Mg-10Gd-2Y-0.5Zr alloy, Journal of Alloys and Compounds. (427) 2007 316-323.

[11] L.M. Peng, S.M. He, J.F. Nie, X. Gao, X.Q. Zeng and W.J. Ding, in: B.S. You (Ed.), Proceeding of the 1st Asian Symposium on Magnesium Alloys, Jeju, Korea, 2005, pp. 55–60.

[12] S.M. He, X.Q. Zeng, L.M. Peng, X. Gao, J.F. Nie and W.J. Ding, Precipitation in a Mg-10Gd-3Y -0.4Zr (wt.%) alloy during isothermal ageing at 250°C, Journal of Alloys and Compounds . (421) 2006 309-313.

*Advanced Materials Research Vol. 937 (2014) pp 187-190*
*© (2014) Trans Tech Publications, Switzerland*
*doi:10.4028/www.scientific.net/AMR.937.187*

# Basic Properties of Iron and Steel Making Dust

Xue-Bing LI[1,a], Wei WANG[1,b*], Dong-Hai ZHANG[1,c], Li XIONG[1,d]

[1]Key Laboratory for Ferrous Metallurgy and Resources Utilization of Ministry of Education, Wuhan University of Science and Technology, Wuhan, China

[a]727729638@qq.com, [b]30389194@qq.com, [c]1214219703@qq.com, [d]969097674@qq.com

*Corresponding author

**Keywords:** Dust, Iron, Property.

**Abstract.** A large amount of dust can be produced in iron and steel making process. This paper analysis the chemical composition, particle size distribution and microscopic characteristics of those iron and steel making dust. Some dust with high iron content, some dust with much CaO and some dust with carbon, those indicate that the iron and steel making dust can be used as iron making raw material. But the size of the iron and steel making dust is very small, which will make it harder to deal with those dust.

## Introduction

The iron and steel making dust including blast furnace dust, sinter dust, BOF sludge, mill scale, and EAF dust are hard to deal with [1]. Since they all contain iron and other valuable minerals, there are two benefits to recycle steel making wastes: one is to recycle valuable resources such as iron and carbon, and the other is to reduce environmental pollution. Many steel companies are searching for appropriate methods to recycle those iron and steel making dust[2].

The properties of those dust must be made clear before use those dust. This paper analysis the chemical composition, particle size distribution and microscopic characteristics of those iron and steel making dust.

## Basic Properties of Iron and Steel Making Dust

### Chemical Composition of the Iron and Steel Making Dust

The chemical composition of the iron and steel making dust from a steel plant is shown in Table 1. The chemical composition of the iron and steel making dust has following characters:

(1) BF discharge yard dust and BOF sludge are utilizable iron mineral resource with high iron content.

(2) Sinter dust, BOF Sludge and BOF dust are utilizable mineral resource with CaO.

(3) The carbon content of the BF dust is about 49%.

(4) The impurities content, such as S, P, Pb of the iron and steel making dust is higher than iron ore.

These characters indicate that the iron and steel making dust can be used as iron making raw material.

### Particle Size Distribution of the Iron and Steel Making Dust

The particle size distribution of the iron and steel making dust from a steel plant is shown in Table 2. Table 2 indicate that the size of the iron and steel making dust is very small. For example, particles smaller than 74um in the BOF dust account for 75%.

The small size of the iron and steel making dust would cause problems as ironmaking raw.

Table 1. Chemical Composition of the Iron and Steel Making Dust

| | TFe | FeO | CaO | $SiO_2$ | $Al_2O_3$ | MgO | $K_2O$ | $Na_2O$ | Pb | Zn | P | S | C | R |
|---|---|---|---|---|---|---|---|---|---|---|---|---|---|---|
| Sinter Dust 1 | 45.85 | 3.99 | 14.30 | 5.28 | 2.27 | 2.50 | 0.31 | 0.030 | 0.009 | 0.005 | 0.054 | 0.12 | 3.78 | 2.7 |
| Sinter Dust 2 | 54.47 | 4.58 | 9.116 | 5.41 | 2.31 | 2.05 | 0.18 | 0.034 | 0.005 | 0.005 | 0.065 | 0.078 | 1.18 | 1.68 |
| Sinter Dust 3 | 27.58 | 2.81 | 5.38 | 3.08 | 1.33 | 1.11 | 21.05 | 0.97 | 1.30 | 0.048 | 0.034 | 1.93 | 1.62 | 1.75 |
| Sinter Dust 4 | 50.22 | 3.10 | 9.81 | 6.00 | 2.74 | 2.03 | 0.38 | 0.050 | 0.01 | 0.008 | 0.056 | 0.20 | 2.34 | 1.63 |
| Blast Furnace Dust 1 | 49.41 | 5.32 | 7.48 | 5.87 | 2.46 | 1.71 | 0.12 | 0.020 | 0.005 | 0.005 | 0.056 | 0.066 | 9.47 | 1.27 |
| Blast Furnace Dust 2 | 49.07 | 5.62 | 7.10 | 5.99 | 2.46 | 1.61 | 0.13 | 0.042 | 0.005 | 0.005 | 0.059 | 0.072 | 10.07 | 1.18 |
| Blast Furnace Dust 3 | 19.13 | 7.10 | 2.32 | 6.10 | 3.15 | 0.75 | 5.39 | 1.27 | 0.17 | 0.59 | 0.096 | 0.77 | 37.00 | 0.38 |
| Blast Furnace Dust 4 | 20.30 | 4.88 | 2.59 | 4.90 | 3.26 | 0.72 | 0.33 | 0.097 | 0.016 | 0.025 | 0.060 | 0.20 | 49.00 | 0.53 |
| BF Discharge Yard Dust | 63.43 | 11.68 | 0.59 | 1.92 | 0.73 | 0.17 | 0.44 | 0.065 | 0.005 | 0.061 | 0.083 | 0.31 | 3.82 | 0.31 |
| BOF Sludge | 71.48 | 92.8 | 8.41 | 3.98 | 0.85 | 1.86 | 0.15 | 0.12 | 0.007 | 0.006 | 0.13 | 0.042 | 1.32 | 2.11 |
| BOF Dust | 47.92 | 7.69 | 11.45 | 3.48 | 1.45 | 3.30 | 1.39 | 0.48 | 0.022 | 0.16 | 0.079 | 0.33 | 2.73 | 3.29 |

Table 2. Particle Size Distribution of the Iron and Steel Making Dust

| Size | +0.5mm | 0.5~0.25mm | 0.25~0.2mm | 0.2~0.125mm | 0.125~0.098mm | 0.098~0.074mm | −0.074mm |
|---|---|---|---|---|---|---|---|
| Sinter Dust 1 | 0.2 | 0.5 | 1.02 | 3.67 | 13.3 | 16.47 | 64.85 |
| Sinter Dust 2 | 1.54 | 3.7 | 3.21 | 10.28 | 28.79 | 13.91 | 38.58 |
| Sinter Dust 3 | 18.93 | 12.05 | 3.02 | 8.27 | 10.01 | 11.18 | 36.54 |
| Sinter Dust 4 | 0.99 | 7.63 | 1.13 | 5.67 | 5.15 | 11.24 | 68.19 |
| Blast Furnace Dust 1 | 4.85 | 5.53 | 2.56 | 8.74 | 7.52 | 14.42 | 56.38 |
| Blast Furnace Dust 2 | 6.22 | 7.42 | 1.2 | 11.03 | 5.72 | 13.74 | 54.66 |
| Blast Furnace Dust 3 | 12.77 | 11.85 | 4.32 | 13.33 | 5.7 | 14.6 | 37.43 |
| Blast Furnace Dust 4 | 17.59 | 20.8 | 6.39 | 20.2 | 10.47 | 14.64 | 9.92 |
| BF Discharge Yard Dust | 17.91 | 7.2 | 3.51 | 7.4 | 3.79 | 5.31 | 54.88 |
| BOF Sludge | 11.5 | 19.92 | 7.62 | 25.13 | 9.27 | 16.33 | 10.22 |
| BOF Dust | 2.93 | 3.2 | 4.34 | 3.58 | 0.31 | 4.89 | 80.75 |

## Microscopic Characteristics of the Iron and Steel Making Dust

(1) SEM Analysis of BF Discharge Yard Dust. The SEM micrograph of BF discharge yard dust is shown in Fig.1. Fig.1 indicates that the size of the BF discharge dust is very small. EDS spectra shows that iron oxide particle can be found in BF discharge yard dust.

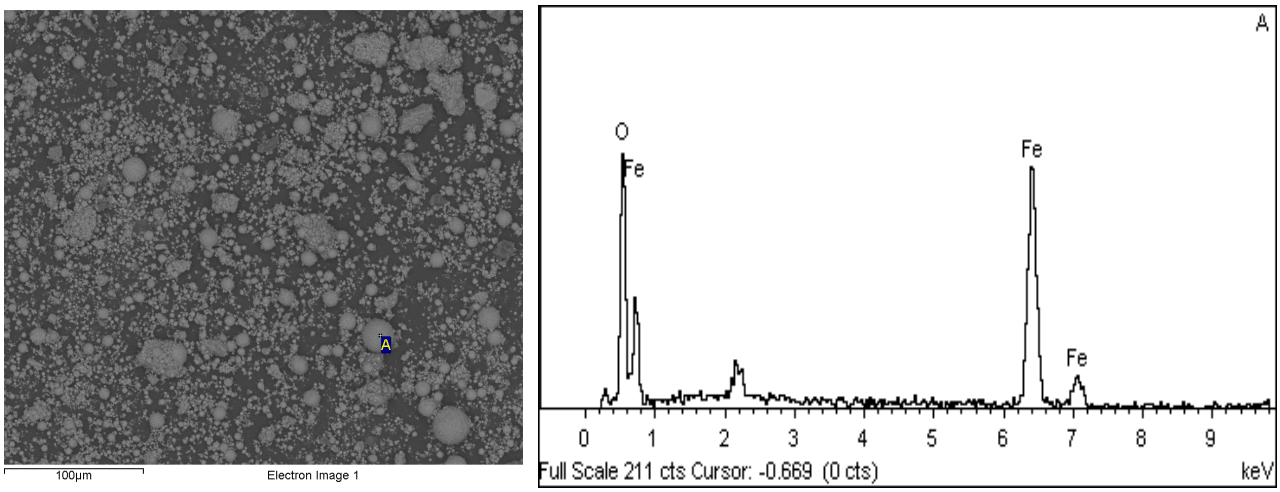



Fig. 1. SEM micrograph of BF discharge yard dust

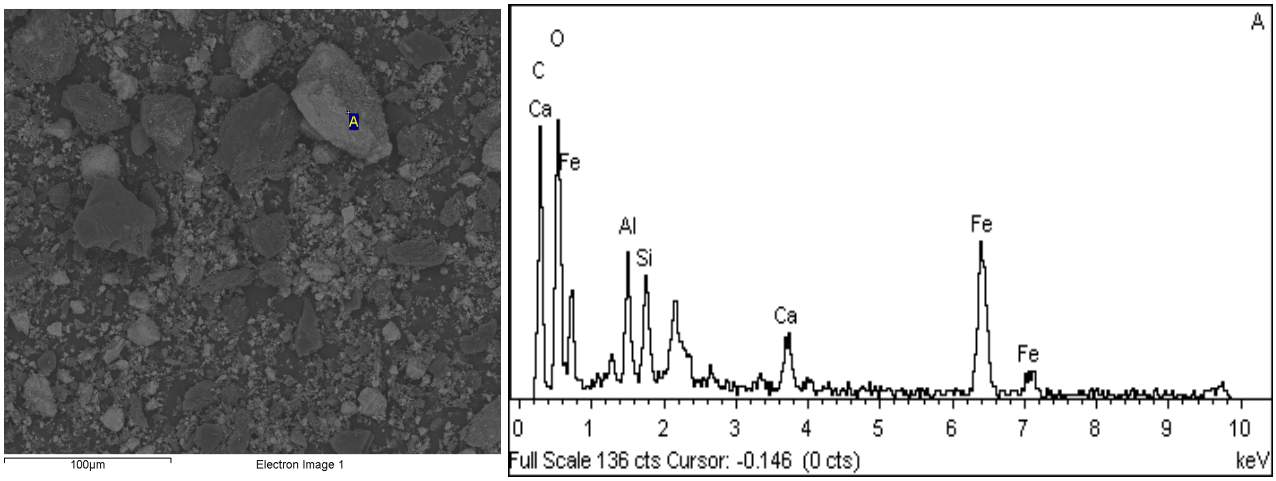



Fig. 2. SEM micrograph of BF dust

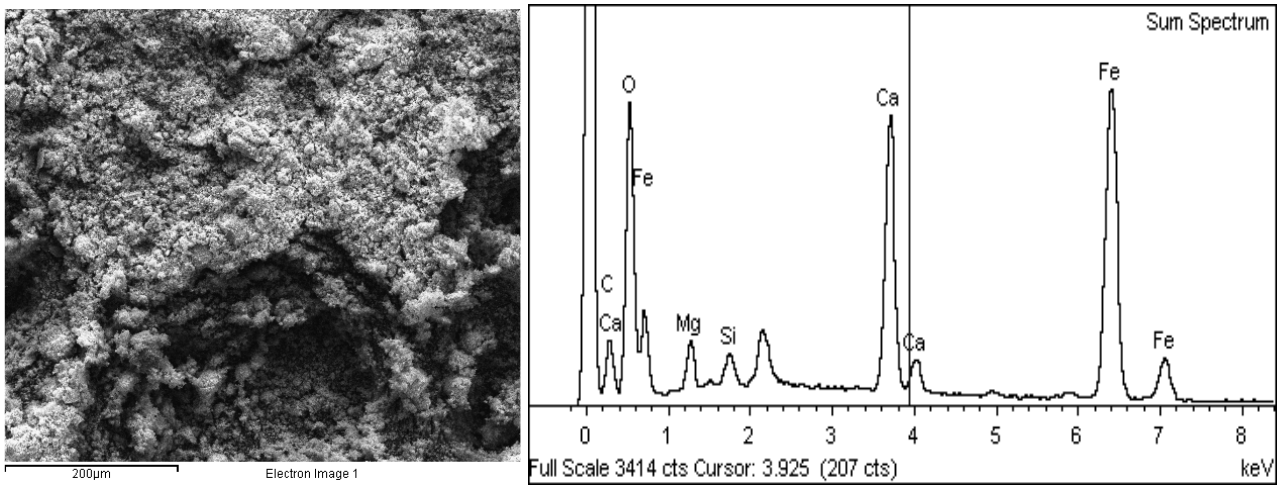



Fig. 3. SEM micrograph of BOF sludge

(2) SEM Analysis of BF Dust. The SEM micrograph of BF dust is shown in Fig.2. Fig.2 indicates that the size of the BF dust is larger than the BF discharge yard dust. EDS spectra indicates that iron oxide, CaO, $SiO_2$ and C can be found in BF dust.

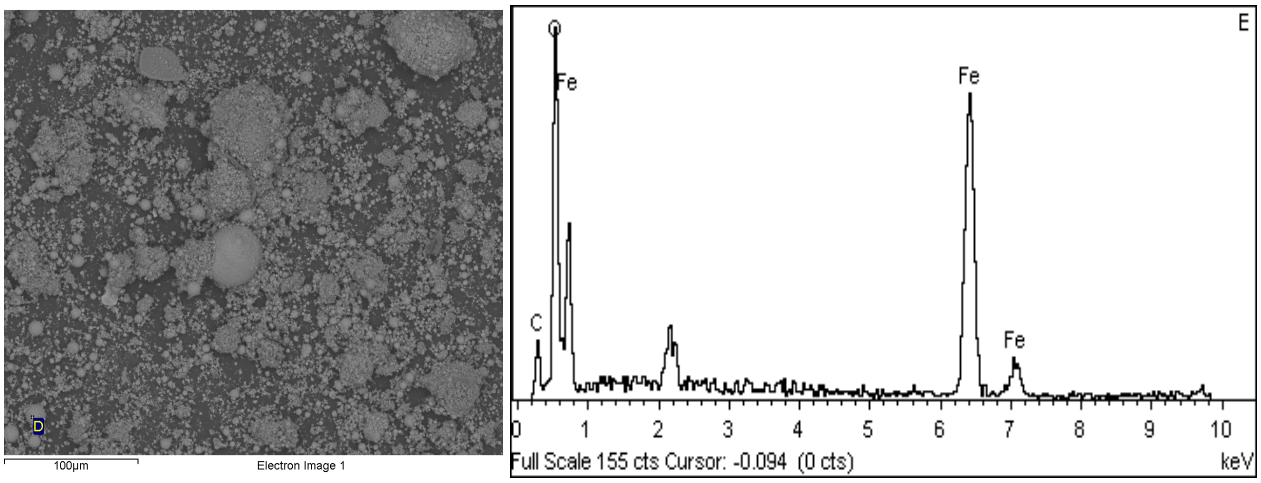



Fig. 4. SEM micrograph of BOF dust

(3) SEM Analysis of BOF sludge. The SEM micrograph of BOF sludge is shown in Fig.3. Fig.3 indicates that the size of the BOF sludge is very small. EDS spectra indicates that iron oxide, CaO, SiO2 and MgO can be found in BOF sludge.

(4) SEM Analysis of BOF dust. The SEM micrograph of BOF dust is shown in Fig.4. Fig.4 indicates that the size of the BOF dust is very small. Some particles is smaller than 1um, some particles is about 20um to 40um. EDS spectra indicates that iron oxide can be found in BOF dust.

## Summary

The iron and steel making dust contain iron, which can be used as iron making raw material. But the size of the iron and steel making dust is very small, which will make it harder to deal with those dust.

## Acknowledgement

This research was financially supported by the National Training Programs of Innovation and Entrepreneurship for Undergraduates (201210488021).

## References

[1] J. He . TREATM ENT AND APPLICATION OF STEEL MAKING AND IRON MAKING SLUDGE AT JISTEEL. IRON AND STEEL, Vo1. 38(5), 2003.

[2] James M. McClelland, Jr. P.E.. FASTMET Dust Pellet Reduction Operations Report on the First FASTMET Waste Recovery Plant, 60th Ironmaking Conference Proceedings, Baltimore, Maryland, March 25-28, 2001.

# CHAPTER 3:

# Electronic Materials

*Advanced Materials Research Vol. 937 (2014) pp 193-199*
*© (2014) Trans Tech Publications, Switzerland*
*doi:10.4028/www.scientific.net/AMR.937.193*

# Effect of Acetate on Electrodeposition of Manganese from Chloride Electrolyte with $SeO_2$ Additives

Wen-po LI[1,a,*], Xiu-li ZUO[2,b], Jin-hu LIANG[1,c], Jia-hong HE[1,d] and Sheng-tao ZHANG[1,e]

[1]School of Chemistry and Chemical Engineering, Chongqing University, Chongqing, China

[2] Department of Oil Application & Management Engineering, Logistic Engineering University, Chongqing, China

[a]wpli@cqu.edu.cn, [b]zuoxiuli009@163.com, [c]liangjinhu19870325@126.com, [d]hjh6118@163.com, [e]stzhang@cqu.edu.cn

*Corresponding author

**Keywords:** Manganese, Acetate, Electrodeposition, Spectroscopic ellipsometry, Corrosion

**Abstract.**This paper deals with manganese electrodeposition from an chloride electrolyte without and with acetate and the resultant deposit properties. The addition of acetate to the plating bath reduces the rate of manganese deposition observed under cyclic voltammetry and in situ Spectroscopic ellipsometry. The addition of acetate improves the corrosion resistance of the manganese deposits. The XRD pattern obtained for electrodeposited manganese show a pure α-Mn with polycrystalline nature no matter with or without acetate. A uniform and pore free surface was observed under SEM analysis in the two plating baths.

## Introduction

Metallic manganese (Mn) is used in certain types of steel, particularly low-carbon steels, and in nonferrous alloys. Coatings of Mn as well as Zn-Mn[1-3], Co-Mn[4] and Ni-Mn[5] alloys are potentially useful as sacrificial coatings for protecting ferrous substrates against corrosion. The electrodeposition of manganese has been studied in chloride- and sulfate-based electrolytic solutions, both with and without additives[6, 7]. However, there are very few studies concentrating on the issue of grain refinement and defect structure formation during manganese deposition in presence of acetate.

Spectroscopic ellipsometry (SE) is an optical method for surface analysis, which is based on measuring the change of the polarization state of a light beam during reflection[8]. The complex-reflectivity ratio is defined by $\rho=r_\rho/r_s=\tan\Psi\exp(j\Delta)$, where $r_\rho$ and $r_s$ are the complex-amplitude reflection coefficients. The angles $\Psi$ and $\Delta$ are the conventional ellipsometic parameters. The ratio $\rho$, as well as $\Psi$ and $\Delta$, explicitly depend on the wavelength $\lambda$ and the angle of incidence. Prior to measurement, it is experimentally proved that the hydrogen evolution has no influence on SE measurements[9].

In this paper results on cyclic voltammetry of manganese ions in chloride electrolyte with and without acetate and deposit characteristics such as deposition rate, reflectivity, corrosion resistance, crystal structure and surface morphology are reported in an attempt to contribute to the better understanding of the more complex Mn-Me(metal) alloys electrodeposition process.

## Experimental

Two chloride-based solutions with or without acetate were used in this work, solution $S_0$: 0.2 M $MnCl_2$ + 0.3 M $NH_4Cl$ + 0.1 M NaCl + 0.25 M KCl + 0.8 mM $SeO_2$ and solution $S_0$ + 0.3M $CH_3COONa$. The solution was made from analytic grade reagents and ultrapure water (18.25MΩ cm in resistivity). All tests were conducted at room temperature (25°C).

In order to perform the spectroscopic ellipsometry and electrochemical test simultaneously, a self-designed three-electrode cell was used, which is made of polytetrafluoroethylene, and transmittance window is made of optical glass with high light transmission coefficient. Electrochemical measurements were performed using a CHI 660B electrochemical workstation (Shanghai Chenhua, China) through the self-designed three-electrode cell, where the disc-shaped

gold (0.785cm$^2$) was used as working electrode, a platinum foil as counter electrode, and a saturated calomel electrode (SCE) as reference electrode. Prior to test ,the Au electrode was subsequently ground with 800 grit, 2000 grit and 4000 grit emery papers, and utrasonic cleaned in ultrapure water and ethanol for 5 min.

The spectroscopic ellipsometry of gold/solution interface during electrodeposition was measured by M22000U Automatic Ellipsometer (Woollam Corporation, USA). The wavelength range of incident light is 246–999nm with the incident angle of 70°. The strong absorption of light at wavelength 246–400nm or 900–999nm causing the little reflected light intensity, the collected signal was rather noisy. So the optical data analyzed by the software WVASE32 used for fitting is among wavelength range 400–900nm.

The surface morphology of the electrodeposited manganese was characterized by scanning electron microscope (SEM) (JEOL JSM-6490LV, Japan). X-ray diffraction (Shimadzu, XRD-7000X, Japan) was carried out on the manganese deposits, thus produced to analyze the phases prensent withou and with acetate.

## Results and Discussion

### Cyclic Voltammetry

CV experiments were performed on gold electrodes in deaerated solutions $S_0$ and $S_0$ + 0.3M CHCOONa. Figure 1 shows the obtained results. The voltammogram main features are the sharp cathodic peak C and the corresponding anodic stripping peak A no matter with or without acetate($Ac^-$). The onset of the cathodic current is observed at approximately -1.30 V, irrespective of the solution, is attributed to hydrogen evolution. In the absence of acetate, the forward cathodic sweeps shows the abrupt increase of the current density(peak C) at -1.53 V ($E_D$, solid line), which is associated with two processes, the manganese bulk deposition and the reduction of $H_2O$ (hydrogen evolution). When the potential scans reversely from -1.60V to -1.20V, a current cross ring (nuclear loop) appears on cathode branch at the potential -1.48V($E_c$), indicating the formation of a new phase[10]. An anodic current peak(peak A) is observed at potential about -1.40V, corresponding to manganese stripping. This potential values agree fairly well with the reported value for the reduction of $Mn^{2+}$ to metallic manganese from chloride electrolyte[11]. Beyond anodic peak the current approaches to zero, indicating that the majority of the deposited manganese been removed from the substrate surface.

In the presence of acetate, a clear negative shift of the Mn-reduction potential ($E_D$, about -1.55V) and a negative shift of the crossover potential ($E_c$, about -1.50V) are observed(dot dash line). Also, a decrease in the cathodic currents (peak C) is observed. Thus, the slower manganese bulk deposition occurs in acetate solutions when the current is governed by charge transfer. The deposition rate of Mn depend on the nature of the anions in the electrolyte. These could be explained by the decrease in the manganese deposition rate induced by the formation of different Mn-Ac complexes and the adsorption of $Ac^-$. Because the potential of cathodic current onset remained constant (-1.30V) no matter with or without $Ac^-$, the formation of the Mn-Ac complexes might be a major parameter that explains the differences in the rate of Mn deposition[12, 13].

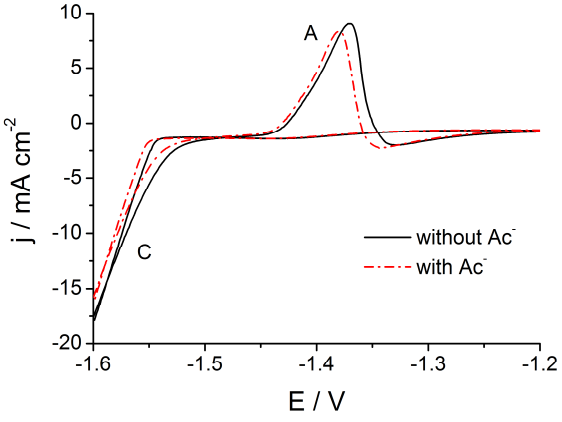



Fig. 1. Current-potential scan on gold electrodes in aqueous solutions $S_0$ (solid line) and $S_0$ +0.3M $CH_3COONa$ (dot dash line). The scan rate is set at 10mV/s.

**Spectroscopic Ellipsometry Measurement**

In our previous study, we have reported that spectroscopic ellipsometry is an ideal tool to in situ study the electrodeposition of manganese owing to it is immune to hydrogen evolution[9]. In the present study, in situ spectroscopic ellipsometry was performed on the study solutions to analyze the rate of manganese deposition (Fig.2). All parameters were kept constant over a period of 20s before the elctrodeposition process. The values of Ψ and Δ corresponded to a gold surface. The manganese deposition began when j=-8mA/cm$^2$ was applied(t=20s, Fig.2). The polarization potential E dropped and the progressively reached a plateau of -1.56V for solution $S_0$ and a plateau of -1.58V for solution $S_0$ +acetate (not presented in this paper). It is indicat that complex species of Mn in acetate electrolyte are more stable as compared to the corresponding species in chloride electrolyte[14]. Concerning the ellipsometric angles Ψ and Δ, a first strong variation was observed up to 40s in the solution without acetate(solid line) and up to 60s in the solution with acetate(dot dash line). Subsequently, the optical parameters vary slowly and continuously whatever the wavelenth in the rang 400-900 nm. Figure 2 just shows the variation of the optical parameters at λ=532nm.

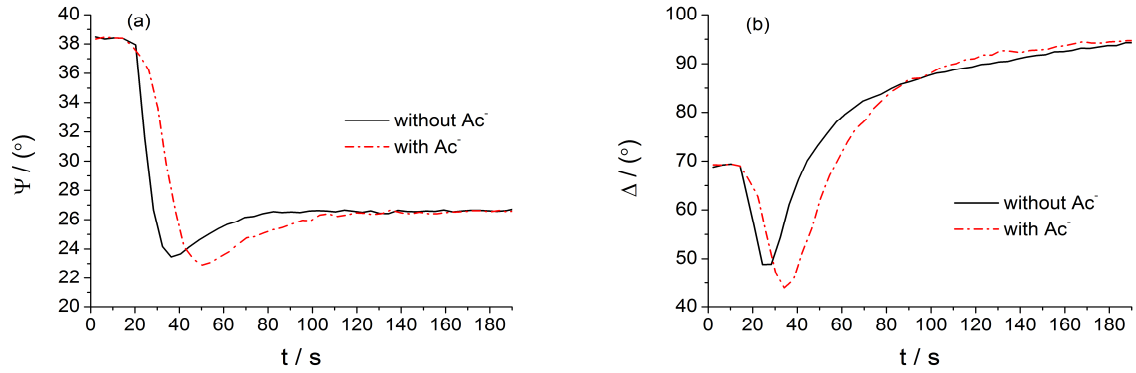



Fig. 2. In situ ellipsometric angles (a) Ψ(°) and (b) Δ(°) during Mn electrodeposite at a constant cathodic current (j=-8mA/cm$^2$) in solution $S_0$(solid line) and solution $S_0$ +acetate(dot dash line) (λ=532nm).

The construction of an optical model is one of the most important steps in ellipsometry data analysis. The layers used in this study model include Au substrate, Mn layer and ambient medium. The details of the model were showed in our previous study[9]. The model was introduced to analyze the spectroscopic ellipsometry data(Fig.2) in terms of Ψ and Δ at different deposition time. The parameters of the model were determined by minimizing the mean square error(MSE) defined in the reference[15]. Figure 3 shows the variation of deposited Mn film thickness with time fitted by Lorentz oscillator. Good values of MSE are obtained throughout this process. It is seen that the trend of electrodeposition thickness vary with the deposition time. Values of fitted thickness increase linearly with deposition time from 20 s to 40 s in chloride electrolyte and from 20 s to 50 s in acetate electrolyte. The values of the slope are 1.57 nm/s and 1.18 nm/s in chloride electrolyte and acetate electrolyte, respectively. It is indicated that the rate of manganese deposition is slowed by the formation of Mn-Ac complex. Beyond linear variation, the observed plateau is not physically coherent, as proven by the following points. First, manganese is absorbent in the visible range with a high absorption coefficien[16].Consequently the gold substrate is optically ignored as soon as the Mn film thickness exceeds a certain value. Secondly there is no published maximal thickness of an electrodeposited Mn layer. Thirdly, the potential of the working electrode is constant during the entire process, indicating continuous formation of Mn film. To conclude, the thickness of the Mn film can be evaluated by ellipsometry in the first stages of electrodeposition but the data have to be ignored for longer deposition time.

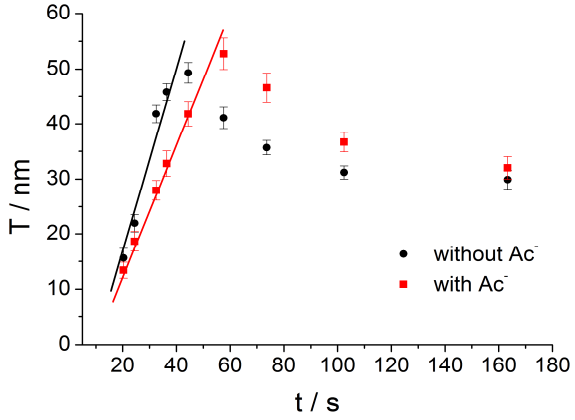



Fig. 3. Fitted values of film thickness (nm) during the first 180 s of electrodeposition in solution $S_0$ (●)and solution $S_0$+acetate(■) with error bars(data from Fig. 2).

**Corrosion-resistance Measurements**

On a manganese electrodeposit anodic and cathodic polarization experiments were carried out upto ±300 mV away from open circuit potential at 1 mV/s. From the electrochemical theory of corrosion, corrosion current densities can be obtained by extrapolating the linear segments of cathodic and anodic Tafel plots[17]. Figure 4 presents the typical potentiodynamic curves for deposits obtained at j=-8 mA/cm$^2$ from solution $S_0$ and $S_0$+acetate of 10 µm thickness, named film $F_0$ and $F_1$. There is a significant change in corrosion potential for the two films $F_0$ and $F_1$. The corrosion current was lower for the deposits produced from the solution containing acetate whereas the corrosion current is high for the deposit produced from the bath without acetate.

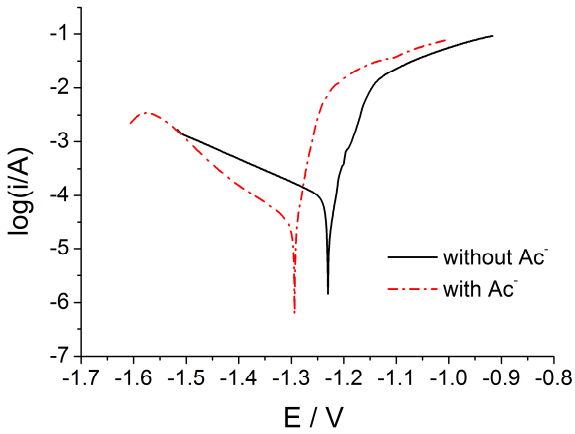



Fig. 4. Typical potentiodynamic polarization curves for (10µm) manganese films deposited at -8mA/cm$^2$ from solution $S_0$ (solid line) and $S_0$+acetate(dot dash line) in 5%NaCl solution.

The Nyquist impedance plots and Bode plots for manganese films $F_0$ and $F_1$ in 5%NaCl solution is shown in Fig. 5. It seems that the Nyquist curves are composed of one semicircle at middle frequencies(Fig. 5a). However, Bode plots show clearly that there are two time constants present in the impedance spectra, which are independent of the deposition solution. The first time constant is observed at middle frequencies, and the second at the highest frequency values, as shown in Fig. 5b. The two time constants at high and medium frequency could be associated with pore resistance of corrosion product film and charge transfer resistance, respectively[3]. The shape of impedance plots at high frequencies is similar for the two Mn films $F_0$ and $F_1$. Contrary, at medium and low frequency values, the shape of Nyquist plots changes rapidly for different Mn films, i.e. the extension of middle-frequency semicircle loop is different for various deposition solution. For the film $F_0$, an inductive loop can be clearly seen in Nyquist plot. For the film $F_1$, the inductive loop

disappears, but it but it can also be seen that the middle-frequency loop in Nyquist plots does not have the shape of regular semicircle, related to simple Randles type time constant. Contrary, the shape of this loop at low frequencies reveals the coupling of semicircle loop with a line related to diffusion processes.

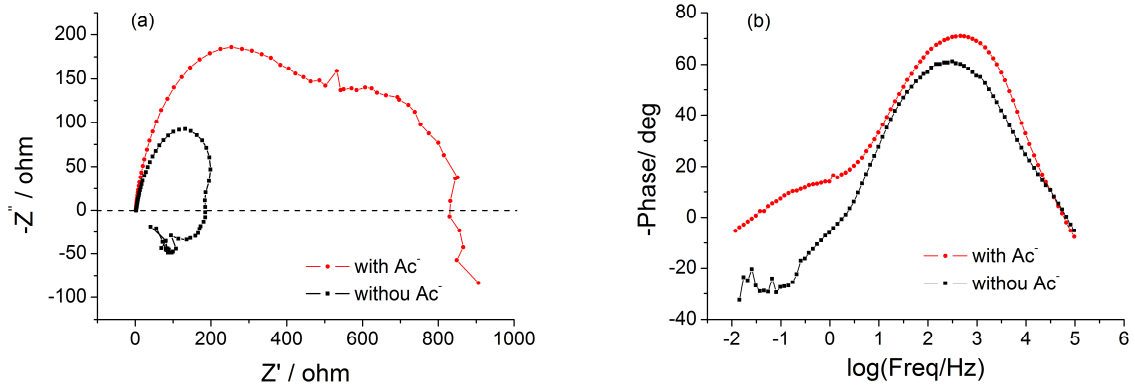



Fig. 5. (a)Nyquist plot and (b) Bode plot (phase angle vs. logf) for (10μm )manganese films deposited at -8mA/cm$^2$ from solution $S_0$ (■) and $S_0$+ acetate(●) in 5%NaCl solution.

**Morphology and Crystalline Structure**

XRD was performed to determine the crystalline structure of the deposits. XRD patterns (θ-2θ scans) of the deposits $F_0$ and $F_1$ are shown in Fig. 6. Pure α-Mn is obtained at j=-8mA/cm$^2$ no matter with or without acetate. Contrary, it is reported that only γ-Mn could be observed for the freshly deposited coating at low current densities(<100mA/cm$^2$)[6]. The observation indicate a transition to α-Mn structure because of the high chemical activity of freshly deposited manganese. The transformation rates are dependent on the growth conditions of the Mn deposits. The defects of the deposits are responsible for the transformation[6]. In the region of the limiting current density for manganese deposition, the γ-Mn lattice structure is highly distorted due to hydrogen incorporation. A large amount of hydrogen is evolved during Mn electrodeposition, and it is reasonable to assume that the hydrogen content in manganese deposits is always at its saturation level and does not change with acetate. The observed no shift of the α-Mn diffraction peaks for the two deposits $F_0$ and $F_1$ can be related to no effect of acetate on the hydrogen evolution. It is in agreement with potentiodynamic polarization evidence from CV data(Fig. 1).

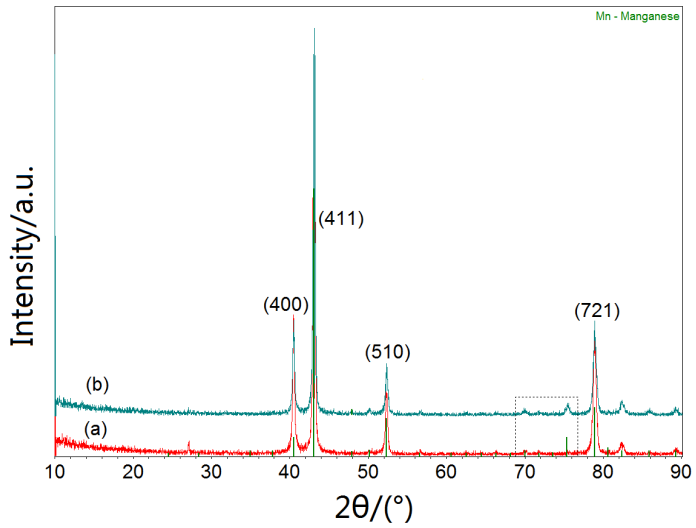



Fig.6. XRD patterns of (10μm )manganese films deposited at -8mA/cm$^2$ in solution $S_0$ (a, the $F_0$ film) and $S_0$+ acetate(b, the $F_1$ film).

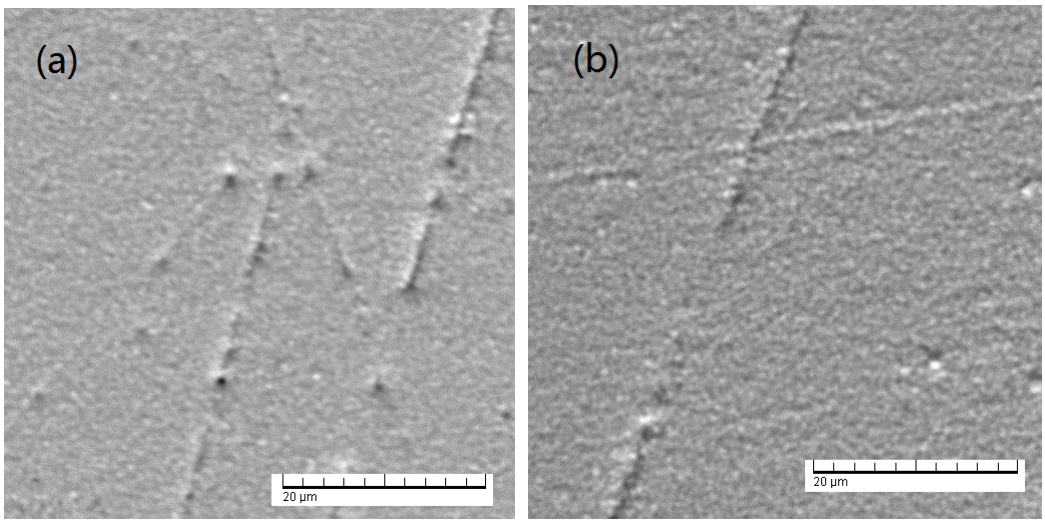



Fig. 7. SEM of (10μm )manganese films deposited at -8mA/cm$^2$ in solution $S_0$ (a, the $F_0$ film) and $S_0$+ acetate(b, the $F_1$ film).

Both $F_0$ and the $F_1$ films were visually uniform and adhered well to the gold substrate. To probe the morphology of the electrodeposited material at the micrometre scale, we employed scanning electron microscopy (SEM) (Fig. 7). Both Mn films cover completely the surface of the electrode. The morphologies of the $F_0$ film(Fig. 7a)and the $F_1$ film(Fig. 7b) do not differ clearly. This implies that the difference in corrosion-resistance is not explainable by the difference in morphology.

## Conclusions

(a) The addition of acetate to the plating bath reduces the rate of manganese deposition by the formation of Mn-Ac complexes.

(b) The additive of acetate improves the corrosion resistance of the manganese deposits.

(c) Electrodeposited manganese show a pure α-Mn with polycrystalline nature no matter with or without acetate. The morphologies of manganese deposition do not differ clearly obtained in acetate electrolyte.

## Acknowledgement

This research was financially supported by the National Science Foundation of China (no. 21003163).

## References

[1] D. Sylla, C. Rebere, M. Gadouleau, C. Savall, J. Creus, P.H. Refait, J. Appl. Electrochem., 35 (2005) 1133-1139.

[2] N. Boshkov, Surf. Coat. Technol., 172 (2003) 217-226.

[3] M. Bucko, J. Rogan, B. Jokic, M. Mitric, U. Lacnjevac, J.B. Bajat, J. Solid State Electrochem., 17 (2013) 1409-1419.

[4] A.M. Dayaghi, M. Askari, H. Rashtchi, P. Gannon, Surf. Coat. Technol., 223 (2013) 110-114.

[5] S. Penttila, I. Betova, M. Bojinov, P. Kinnunen, A. Toivonen, Corr. Sci., 53 (2011) 4193-4203.

[6] J. Gong, G. Zangari, J. Electrochem. Soc., 149 (2002) C209-C217.

[7] Y. Sun, X.K. Tian, B.B. He, C. Yang, Z.B. Pi, Y.X. Wang, S.X. Zhang, Electrochim. Acta, 56 (2011) 8305-8310.

[8] H. Fujiwara, Spectroscopic ellipsometry: principles and applications, John Wiley & Sons, 2007.

[9] W. Li, S. Zhang, Appl. Surf. Sci., 257 (2011) 3275-3280.

[10] G. Gunawardena, G. Hills, I. Montenegro, B. Scharifker, J. Electroanal. Chem. & Interf. Electrochem., 138 (1982) 225-239.

[11] M. Gonsalves, D. Pletcher, J. Electroanal. Chem., 285 (1990) 185-193.

[12] C.C. Hu, P.Y. Chuang, Y.T. Wu, J. Electrochem. Soc., 152 (2005) C723-C729.

[13] B. Benfedda, N. Benbrahim, A. Kadri, E. Chainet, F. Charlot, S. Coindeau, Electrochim. Acta, 56 (2011) 1275-1282.

[14] M. Bucko, J. Rogan, S.I. Stevanovic, S. Stankovic, J.B. Bajat, Surf. Coat. Technol., 228 (2013) 221-228.

[15] A. Zimmer, N. Stein, L. Johann, R. Beck, C. Boulanger, Electrochim. Acta, 52 (2007) 4760-4766.

[16] P.B. Johnson, R.W. Christy, Phy. Rev. B, 9 (1974) 5056-5070.

[17] R. Sekar, S. Jayakrishnan, J. Appl. Electrochem., 36 (2006) 591-597.

*Advanced Materials Research Vol. 937 (2014) pp 200-206*
*© (2014) Trans Tech Publications, Switzerland*
*doi:10.4028/www.scientific.net/AMR.937.200*

# Molecular Dynamics Simulations of the Conductivity of Aqueous NaCl in the presence of Sucrose and Electric Fields

Xiao-gang LI[1], Shu-ai YANG[2], Ming-jun TANG[3], Jing LEI[3], Hui HU[4, a], Hua HOU[4] and Bao-shan WANG[4]

[1]Guangzhou Yueneng Power Technology Development Co. Ltd., Guangzhou, China

[2]School of Electrical Engineering, Wuhan University, Wuhan, China

[3]Guangdong Power Grid Electric Power Research Institute, Guangzhou, China

[4]College of Chemistry and Molecular Sciences, Wuhan University, Wuhan, China

[a]email: h_hu@whu.edu.cn

**Keywords:** Insulator, Flashover, Sucrose, NaCl, Molecular Dynamics

**Abstract.** Various natural contamination components distributed on the surface of high-voltage insulators play important roles on the flashover hazard. Under the low humidity condition, the flashover voltage could be affected considerably by the sucrose contaminations. Molecular dynamics simulations have been carried out in order to reveal the microscopic mechanisms for the sucrose-involved flashover uptake. It is found that the diffusion of ions decreases significantly and thus the conductivity of aqueous medium is lowered apparently. In the presence of sucrose, the contact ion pairs formed between $Na^+$ and $Cl^-$ ions are enhanced because both ions are less coordinated to water molecules. The influence of the external electric fields on the diffusion and conductivity were investigated as well. It is suggested that the sucrose contamination might lead to the uneven electric fields on the insulator surface.

## Introduction

High-voltage insulators play a critical role on the safety of power transmission. Although various advanced material and coating techniques have been employed to improve the performance of the insulators, the contamination flashover hazards of insulators are hard to be avoided completely particularly for the ultrahigh voltage power networks. It is well known that the natural contamination components, including cations (e.g., $Ca^{2+}$, $Na^+$, $K^+$, etc.) and anions (e.g., $SO_4^{2-}$, $Cl^-$, $CO_3^{2-}$, etc.), determine the flashover voltage, and the major contamination is inorganic salt $CaSO_4$ [1]. The solvable organic species accounts for about 30% of the overall natural contaminations. However, there is little study on the influence of the organic contamination on the performance of insulators [2].

In a 500 kV power station, the strong discharge occurs on the insulator surface even in sunny days while the relative humidity is only around 70%. Increasing the safety distance between insulators and normal cleaning cannot stop the discharge event until the insulator surface are coating with PRTV. A large amount of organic contaminations, mainly sucrose, have been found in the surface dust. Therefore, it is speculated that the sucrose contaminations might contribute the uptake of the flashover voltage of the insulator surface and the understanding of the corresponding mechanism at molecular level is highly desirable.

Since the solubility of $CaSO_4$ is about 180 times lower than that of NaCl, it is conceivable that only the aqueous NaCl is capable of contributing to the conductivity of the surface under the very dry conditions. For simplicity, in the present work the NaCl solution has been employed to simulate the surface conductivity of insulators. The influence of the sucrose contamination on the solvation structures of the ion pairs and diffusion behaviors are investigated using the force-field based classical molecular dynamics simulation techniques. Moreover, the effect of the applied external electric fields is studied to gain an insight on the distribution of the surface conductivity.

## Computational Methods

All the simulations were carried out in cubic boxes with periodic boundary conditions. In the starting configurations, 512 water molecules, 10 $Na^+$ and 10 $Cl^-$ ions were located with random orientations in the cell with the lattice length of 25.35 Å. The density is 1.0 g/cm$^3$. The concentration of NaCl is 1 M, which corresponds to the equivalent salt deposit density (ESDD) of 0.05 mg/cm$^2$, as observed experimentally on the surface contamination [3]. To simulate the effect of sucrose, 10 sucrose molecules are added to the initial cell and the lattice length increases to 28.0 Å in order to keep the experimental density of 1.0 g/cm$^3$.

In this work, we have used a well-established COMPASS force field as implemented in the Discover program, in which the potential parameters and partial charges were obtained from either *ab initio* quantum chemistry calculations or fitting to the experimental data [4]. The Ewald method was applied for treatment of long-range electrostatic interactions and the cutoff distance for the van der Waals interaction is half of the cell length. Firstly, the cells were fully optimized to eliminate any possible close contacts. Subsequently, the systems were equilibrated during 500 - 1000 ps with the time step of 1 fs using a constant-temperature/constant-pressure molecular dynamics algorithm. In all our simulations, the temperature was 300 K and the pressure was 1 bar. Finally, 500 ps production run has been performed for analysis to obtain the structures and diffusion properties. The external electric field was considered as an additional force along the z-direction into the MD simulations, namely, F = qE, where F is the force induced by the electric field and q is the charge of each atom. The strength of electric field ranges from $10^2$ to $10^7$ V/m. Note that the strongest electric fields on the insulator surface could be in the range (3.4 - 5.4) $\times 10^6$ V/m.

A standard model for studying the structure of solution is to calculate the radial distribution functions $g_{ij}$ between different interaction sites such as ion-ion, ion-water, and water-water. The coordination number is calculated by Eq. 1,

$$N_{ij} = 4\pi\rho_j \int_{r_1}^{r_2} r^2 g_{ij}(r) dr \tag{1}$$

which gives the mean number of particles ($j$) contained in a volume defined by two concentric spheres of radii $r_1$ and $r_2$ centered on a particle $i$. The translational motion of the constituent species are analyzed in terms of the self-diffusion constant D, which can be calculated from the mean-square displacement by Eq. 2,

$$D = \lim_{t\to\infty} \frac{\left\langle \left| \mathrm{r}(t) - \mathrm{r}(0) \right|^2 \right\rangle}{6t} \tag{2}$$

The ionic conductivity could be determined using the interdiffusion constant $D_{12}$. Usually $D_{12}$ could be obtained from the time integration of the current correlation function J(t) using the Green-Kubo formula. However, the significant contributions from the long tail of the J(t) makes such a calculation unreliable. Therefore, the ionic conductivity of the aqueous NaCl solution is calculated by the mean-square displacement of the "center of charge" as follows Eq. 3

$$\lambda = \frac{e^2}{Vk_BT} \lim_{t\to\infty} \frac{\left\langle \left| \mathrm{R}(t) - \mathrm{R}(0) \right|^2 \right\rangle}{6t} \tag{3}$$

where $\mathrm{R}(t) = \sum_i z_i \mathrm{R}_i(t)$, and $z_i$ is the charge of the ions.

## Results and Discussion

### Structure Properties

The calculated radial distribution functions for the structure of $Na^+$-$Cl^-$ pairs are depicted in Fig. 1. Two peaks could be seen from the plots. For the NaCl+water system, the first peak is centered at

~2.67 Å corresponding to the distance of contact ion pair (CIP), and the second peak is centered at ~ 5.0 Å corresponding to solvent-separated ion pair (SSIP). The coordination number of CIP is 0.0746, which is in good agreement with the previous estimations [5-8]. For the NaCl+sucrose+water system, the Na-Cl radial distribution function is evidently enhanced. The CIP peak is at ~ 2.64 Å and the peak intensity increases by a factor of 3. The coordination number increases to 0.17, which is about twice of that for the NaCl+water system. Apparently, more $Na^+$-$Cl^-$ CIP pairs are formed in the presence of sucrose. It is well accepted that the coordination numbers of both CIP and SSIP increase as the concentrations of NaCl increase. Therefore, the sucrose molecules appear to have the similar effect as increasing the concentration of NaCl solution. When the external electric field is applied, the radical distribution functions for the $Na^+$-$Cl^-$ pairs change marginally, as shown in Fig. 1. Both intensities and coordination numbers are lowered slightly.

The interaction between $Na^+$, $Cl^-$ ions and water molecules are shown using the radial distribution function of $Na^+$-$O_w$ and $Cl^-$-$O_w$, respectively (see Fig. 2). The first peak for the $Na^+$-$O_w$ function, representing the structure of the first solvation shell, is always located at ~2.27 Å. However, the coordination number decreases from 5.22 in the NaCl+water system to 4.69 in the NaCl+sucrose+water system. The similar results could be obtained for the first $Cl^-$ solvation shell, in which the coordination number decreases from 6.61 to 6.19. It implies that both $Na^+$ and $Cl^-$ ions become less coordinated to the solvent molecules with the sucrose molecules added. This result is consistent with the increasing of CIP.

It is interesting to note that there are two peaks in the radial distribution functions of the NaCl+sucrose+water system, as shown in Fig. 2. For the first $Cl^-$ solvation shell, the two peaks are centered at 3.12 Å and 3.21 Å, respectively. The former corresponds to the interaction of $Cl^-$ anion with the free water molecules and the later represents the interaction of $Cl^-$ with the water molecules bonding to the sucrose additives. In fact, the structure of water is only slightly affected by the sucrose molecules and the coordination number deceases from 3.76 to 3.32.

The interaction between water and sucrose are demonstrated in Fig. 3 by various radical distribution functions for various possible hydrogen bonding modes. Apparently, the water molecules prefer to be proton acceptors to form hydrogen bonding with the HO group of sucrose. The $O_w$...$HO_s$ distance is centered at ~1.71 Å and the corresponding coordination number is 0.6, that is, a total of about five $O_w$...$HO_s$-type hydrogen bonds could be formed between water and sucrose. In contrast, the hydroxyl O atom of sucrose is a much weaker proton acceptor than the water O atom. On the other hand, significant interaction between sucrose molecules could be seen from the radial distribution function for the intermolecular hydrogen bonding. The peak is centered at ~1.71 Å, which is essentially the same as the $O_w$...$HO_s$ distance. After monitoring the time-dependent trajectories of the NaCl+sucrose+water system, it is very clear that the sucrose molecules form clusters in solution via intermolecular hydrogen bonds.

It is worth noting that the applied electric fields have only marginal influence on the structures of the aqueous NaCl solution, no matter the sucrose contamination is absent or not.

**Dynamical Properties**

The electric field dependent self-diffusion constants for water, $Na^+$, $Cl^-$ and sucrose are shown in Fig. 4 for comparison. For the pure NaCl+water system at zero field, the calculated self-diffusion constants for water, $Na^+$ and $Cl^-$ are 2.78, 1.00 and 1.43 in unit of $10^{-5}$ $cm^2/s$, which are in good agreement with the experimental data and previous theoretical simulations [8]. Moreover, the diffusion constants of $Cl^-$ anions are always larger than those of $Na^+$ cations, in accordance with the experimental observations [5-8]. For the sucrose molecules, the calculated self-diffusion constant is $2.33\times 10^{-6}$ $cm^2/s$ in the aqueous NaCl solution, which is only half of the value as reported for the pure sucrose solution [9].

When the external electric fields are applied, the diffusion of water molecules appears to become slower. This is in agreement with the previous finding for the pure water where the viscosity of water increases as the electric fields because the rotational motion of water molecules could be disturbed considerably [10]. Moreover, the diffusions of both $Na^+$ and $Cl^-$ decrease along with the increasing electric fields.

In the presence of sucrose contaminations, the diffusion of water, $Na^+$ and $Cl^-$ species are reduced significantly. For example, the self-diffusion constants of water, $Na^+$ and $Cl^-$ are lowered by about (28±8)%, (20±9)%, and (13±4)%, respectively. Moreover, the self-diffusion constants become almost independent on the applied electric fields. The change of diffusion behavior of $Na^+$ and $Cl^-$ can be easily understood in view of the fact that the ions prefer to form CIP and thus diffuse together in the presence of sucrose. Therefore, it is expected that the conductivity of the sucrose-added NaCl aqueous should be reduced to some extent because the motion of CIP does not contribute to the conductivity.

The calculated conductivity of the NaCl aqueous solution is shown in Fig. 5. For the pure NaCl+water system without electric field, the estimated conductivity is (7.56±0.63) S/m, which is in good agreement with the experimental value of 7.43 S/m [11], indicating the good reliability of the current theoretical results. Although the calculated conductivities become relatively scattered, it could be seen that the conductivity of the NaCl+water system is almost field-independent up to $10^7$ V/m, that is, the homogeneous electric fields should always present on the surface of the insulators if only NaCl contamination exists. However, with the sucrose molecule being presented as contaminations in any local area of the insulator surface, the conductivity of the solution is lowered by about 24%, that is, the sucrose contaminated area will become less conductive and thus the homogeneous distribution of electric fields might be destroyed. Moreover, such a disturbance to the even electric fields on the insulator surface could be enhanced by the negative field-dependence of the conductivities of the solution.

## Conclusions

Structures and diffusion dynamics of the NaCl aqueous solution in the presence of both sucrose molecules and electric fields have been investigated extensively using molecular dynamics simulations. It is revealed that both $Na^+$ and $Cl^-$ solvation shells are affected significantly by the sucrose contaminations as indicated by the more profound contact ionic pair formed between $Na^+$ and $Cl^-$. The self-diffusion constants of water, $Na^+$ and $Cl^-$ ions are all reduced. The local conductivity due to the sucrose contaminations is lowered significantly and thus the normal homogeneous electric fields distribution on the insulator surface disappears. Such an uneven electric field on the surface is thought to be the dominant factor that leads the uptake of flashover under the low humidity environment. Our theoretical calculations present new insights into the flashover hazards due to organic contamination components at molecular level.

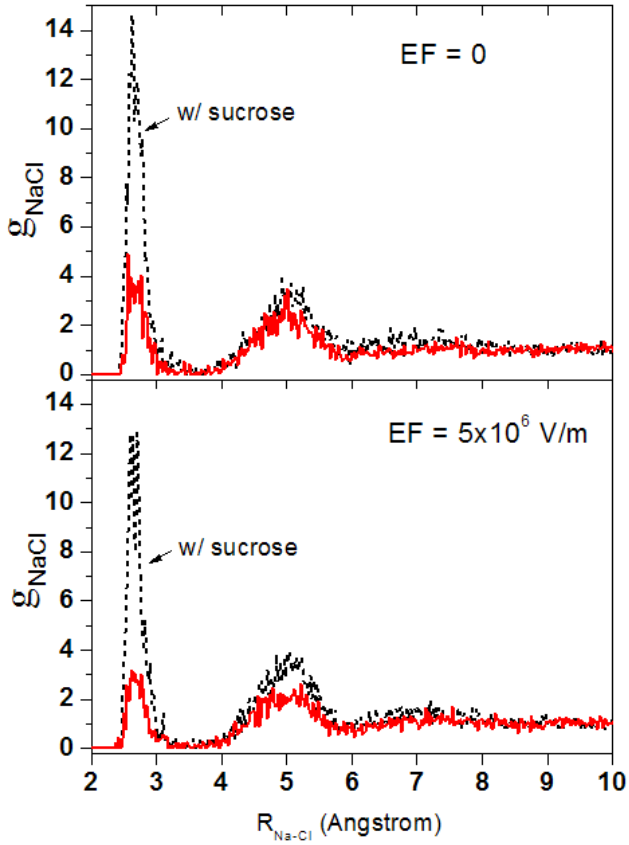



Fig. 1. Radial distribution functions for the $Na^+$-$Cl^-$ pairs. Upper panel: zero electric field. Lower panel: with the electric field of $5\times10^6$ V/m. Red solid lines: NaCl+water. Black dashed lines: NaCl+sucrose+water.

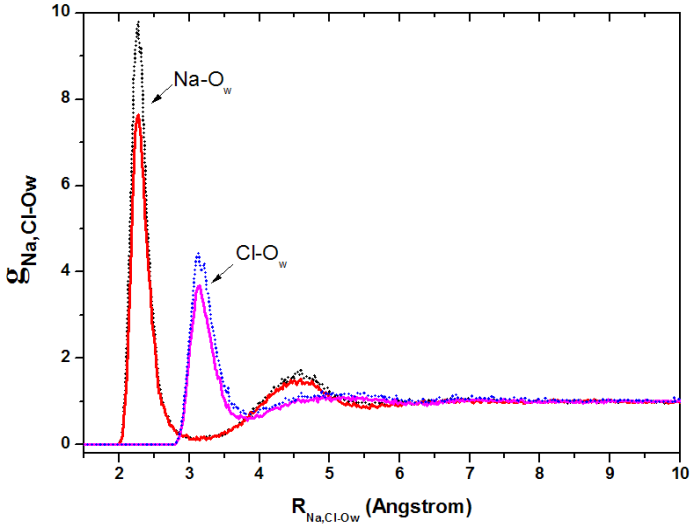



Fig. 2. Radial distribution functions for the $Na^+$-$O_w$ and $Cl^-$-$O_w$ solvation shells. Solid lines and dashed lines correspond to the NaCl+water and NaCl+sucrose+water systems, respectively.

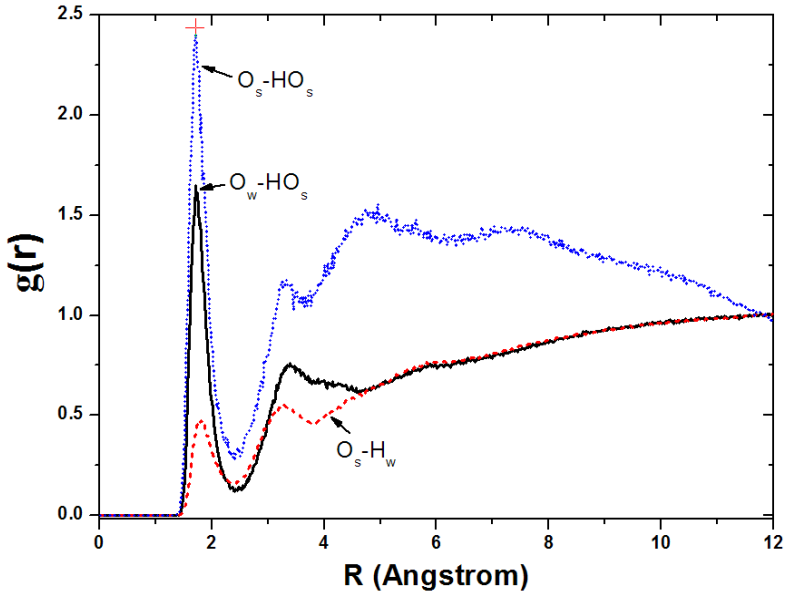



Fig. 3. Radial distribution functions for the sucrose-water interactions.

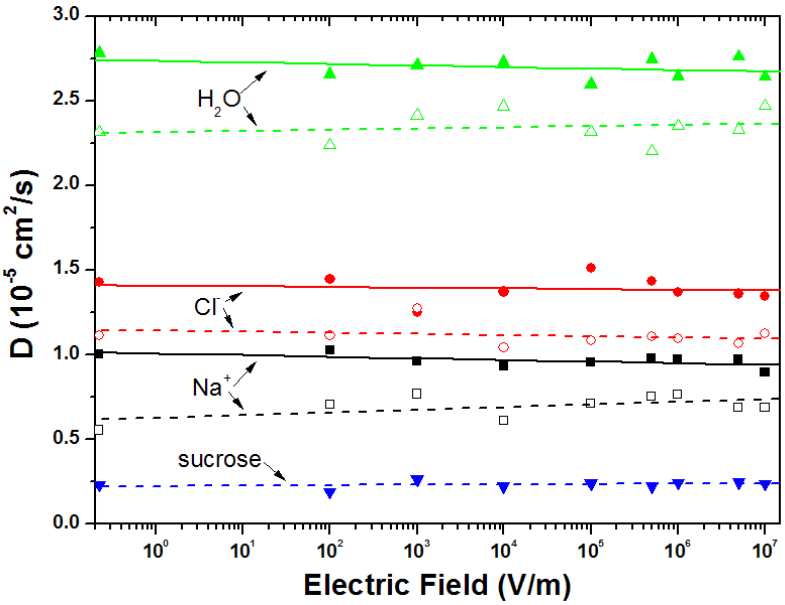



Fig. 4. The calculated self-diffusion constants (D) for water, $Na^+$ $Cl^-$ and sucrose as functions of the applied electric fields. Solid lines: the NaCl+water system. Dashed lines: the NaCl+sucrose+water system.

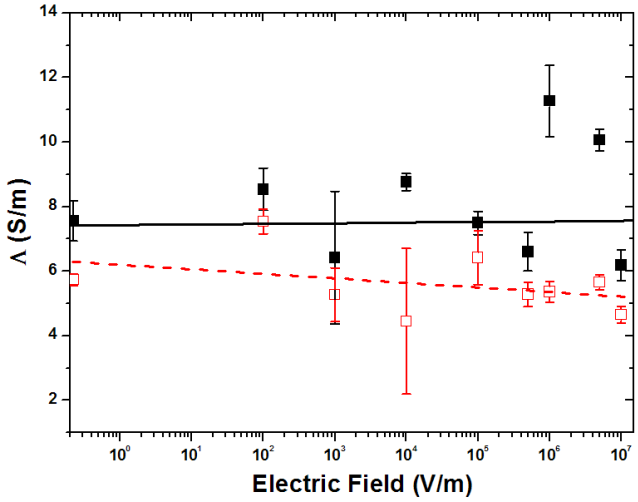



Fig. 5. Theoretical conductivities of the NaCl+water system (solid squares) and the NaCl+sucrose+water system (open squares). The solid and dashed lines represent the apparent fitting to the scattered data.

**Acknowledgement**

This work is partially supported by National Science Foundation of China Grant 21073135, 21073134, and 21273166.

**References**

[1] N. G. Ramos, R. M. T. Campillo, K. Naito: IEEE Transactions on Power Delivery, Vol. 8 (1993), p. 1842-1850

[2] Z. Su: Annual Conference Proceedings of High Voltage Special Committee of Chinese Society for Electrical Engineering (2007), p. 281-290

[3] H. Li, G. Liu, L. Li: Proceedings of the CSEE, Vol. 31 (2011), p. 128-137

[4] H. Sun: J. Phys. Chem. B Vol. 102 (1998), p. 7338

[5] H. Uchida, M. Matsuoka: Fluid Phase Equilibria, Vol. 219 (2004), p. 49-54

[6] J. Timko, D. Bucher, S. Kuyucak: J. Chem. Phys. Vol. 132 (2010), p. 114510

[7] S. Bouazizi, S. Nasr, N. Jaidane, M. Bellissent-Funel: J. Phys. Chem. B, Vol. 110 (2006), p. 23515-23523

[8] A. P. Lyubartsev, A. Laaksonen: J. Phys. Chem. Vol. 100 (1996), p. 16410-16418

[9] S. B. Engelsen, C. H. Penhoat, S. Perez: J. Phys. Chem. Vol. 99 (1995), p. 13334-13351

[10] H. Hu, H. Hou, B. Wang: J. Phys. Chem. C, Vol. 116(2012), p. 19773-19780

[11] J. A. Dean, in: Lange's Handbook of Chemistry; edited by McGraw-Hill Publishing, NY (1985)

*Advanced Materials Research Vol. 937 (2014) pp 207-213*
*© (2014) Trans Tech Publications, Switzerland*
*doi:10.4028/www.scientific.net/AMR.937.207*

# Electron Transport in Zigzag Graphene Nanoribbons with a Tetra-vacancy Complex: A Perfect Spin Filter

Wei LU[1,a], San-huang KE[1,2,b,*]

[1]Key Laboratory of Advanced Microstructured Materials, MOE, Department of Physics, Tongji University, 1239 Siping Road,Shanghai 200092, P. R. China

[2]Beijing Computational Science Research Center, 3 Heqing Road, Beijing 100084, P. R. China

[a]lu_wei07@126.com, [b]shke@tongji.edu.cn

*San-Huang Ke

**Keywords**:graphene nanoribbon, electronic transport, spin polarization.

**Abstract.** A novel doping scheme for graphene was recently realized experimentally by creating different vacancy complexes doped with a transition metal (TM) atom [Nano Lett. **12**, 141 (2012)]. This provides a new reliable way to modifying the electronic structure and transport property of graphene. Here, we show, by performing first-principles calculations, that the defect complex of TM@$V_4$ (a TM atom doped tetra-vacancy) in zigzag graphene nanoribbons (ZGNRs) can lead to a 100% spin-polarized electron transport in a wide energy range around the Fermi energy. Analyses show that this is due to the particular atomic structure of the TM@$V_4$ complex regardless of the species of the TM atom.

## Introduction

Graphene nanostructures, like graphene nanoribbons (GNRs), are playing more and more important role in the development of nanoelectronics[1], possibly leading to an era of carbon-based electronics. The electronic properties of GNRs are determined by their edge geometry and width, and have shown promise for future generation of transistor[3]. Zigzag-edged GNRs (ZGNRs) are particularly intriguing because of their spin-polarized edge states which are localized around the two edges, as have been observed in monoatomic step edges of graphite by scanning probe techniques[5]The resulting spin-dependent transport may make them as promising candidates for applications in spintronics.

For practical applications, it is most desirable to be able to modify the electronic structures of GNRs to realize a specific function. In this regard, different schemes have been proposed so far. One way is to make use of native defects, including vacancies[7], extended di-vacancy lines[11], heptagon-pentagon pairs[12] and Thrower-Stone-Wales (TSW) defects[13]. Indeed, while native defects are usually inevitable in real experimental conditions, they can, however, be used to modify the electronic properties of the sample if one can fully control their structure and location. This may be theoretically possible but is difficult to achieve in practice. Another way is to dope graphene, especially with transition metal (TM) atoms (like Au, Pt, Cr, Fe, Ni and Cu[14]). Doping may be a more effective way to tailoring the electronic properties of graphene because TM atoms can inject charge to and/or bring novel magnetic properties to graphene samples leading to a significant modification of graphene band structure[16].

Combination of these two ways (using native defects and doping) has also been studied. For example, the energy and structure of a single TM atom embedded in a single vacancy (ie., single atom substitution) or a di-vacancy of graphene have been studied theoretically[15]. It was found that the binding energies of different TM atoms are in the range of 2-8 eV [17]showing a good chemical stability, which is stronger than direct chemical adsorption on graphene. Furthermore, the migration barriers of the TM atoms is also found to be high enough so that they cannot move at room temperature, indicating that they can be used in real life. A possible issue is that to have a full control of the size and location of these TM@vacancy complexes in GNRs is still a challenge.

Very recently, a novel doping scheme was realized in two steps[24], in which vacancies of different sizes are first created by high-energy atom/ion bombardment, and then they are filled with different TM atoms (Co, Pt, and In). In this way, it is possible to control the size and location of the vacancies created. The large binding energy of the TM atoms in the vacancies indicates a very good stability[24]. This technique provides a well defined way to modifying the electronic structure and transport property of GNRs.

Theoretically, the electronic transport in GNRs with different native defects have been studied extensively, for instance, GNRs with a single vacancy[7], ZGNRs with TSW defects[13] and GNRs with an extended di-vacancy lines[11]. However, the transport property of GNRs with defects of TM@vacancy complexes have not been reported in the literature.

In this work, we investigate the electron transport in ZGNRs with a defect of TM@vacancy complex by using the nonequilibrium Green's function method combined with density function theory calculations. Two different complexes are considered: Pt- and Co-doped tetra-vacancies (denoted by Pt@$V_4$ and Co@$V_4$, respectively). Different widths of ZGNRs and different locations of complexes (from the middle to the edge of the ZGNRs) are investigated. It is found that a complete spin polarization in a large energy range around the Fermi energy is present when the complex is located in the middle of the ribbon. This energy range of complete spin polarization increases with the decreasing width of the ribbon. It is also found that this complete spin polarization stems mainly from the particular structure of the complexes instead of the TM atoms: It will remain when the TM atom is taken away with the dangling bonds saturated by H atoms. However, when only the $V_4$ defect is present, the significant spin polarization disappears.

**System Investigated and Computational Details**

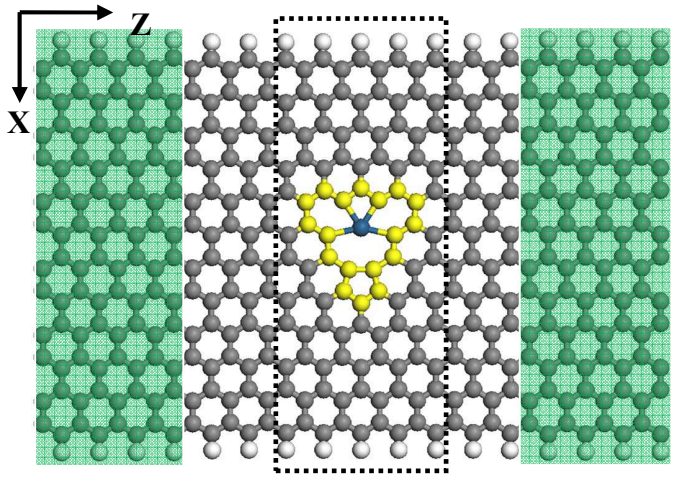



Fig. 1. Structure of a 12-ZGNR with a Pt@$V_4$ complex (indicated by the yellow C atoms plus the green Pt atom) created in the middle of the ribbon. The two shadowed parts are used as electrodes in our transport calculation and the area between them is the scattering region. The location of the complex may change in the dotted-lined box.

We mainly consider a ZGNR consisting of 12 zigzag carbon chains (12-ZGNR). ZGNR of different width (8-ZGNR) is also considered to check the effect. The edges of the ZGNRs are terminated by H atoms. Because of the localized spin-polarized edge states, there are two spin configurations for the ZGNRs: The ferromagnetic (FM) configuration with the two edges being α-spin and the anti-ferromagnetic (AFM) one with one edge being α-spin and the other being β-spin. Two TM@$V_4$ complexes are studied: Pt@$V_4$ and Co@$V_4$ . Pt@$V_4$ at different locations from the middle to the edge of the 12-ZGNR are specific studied. The structure of a 12-ZGNR with a Pt@$V_4$ complex located in the middle is shown in Fig.1. For transport calculation, the scattering region around the complex is seamlessly connected to two semi-infinite ZGNR leads, as shown in Fig.1.

To investigate electron transport through the lead-scattering region-lead system, we adopt the nonequilibrium Green's function method combined with *ab initio* density functional theory (DFT) calculations[25]. The self-consistent Kohn-Sham Hamiltonian of the scattering region and the self-energies of two semi-infinite ZGNR leads are used to construct a single-particle Green's function from which the transmission coefficient at any energy is calculated. The computational techniques have been described in details previously[25]. Briefly, for the DFT electronic structure calculation, we employ a double-zeta plus polarization (DZP) numberical basis set for all atomic species[26]. The optimized Troullier-Martins pseudopotentials[28] are adopted to describe the atomic cores and the PBE version of the generalized gradient approximation (GGA)[29] is used for the electron exchange and correlation. The atomic structures of the systems studied are fully optimized by minimizing the forces on atoms to be smaller than 0.02 eV/Å.

**Result and Discussion**

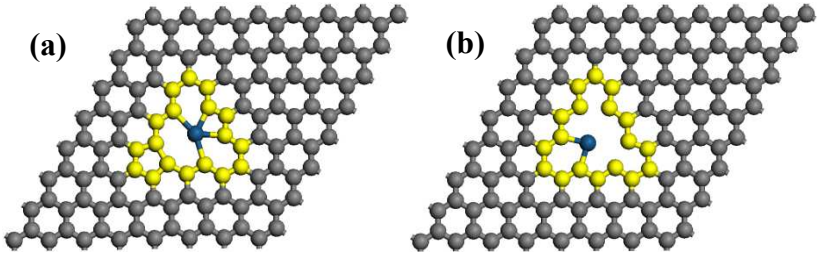



Fig. 2. (a) The optimized structure of Pt@$V_4$ complex in a graphene sheet. (b) The metastable structure. The indication of the complex is the same as in Fig.1.

Let us start with the optimized structure of the Pt@$V_4$ complex in ZGNRs with the FM and AFM spin configurations. Firstly, we put the Pt@$V_4$ complex into an infinite large graphene sheet. Because the complex is quite complicated, we need to try different initial Pt positions to get the global minimum. The most stable structure is shown in Fig.2(a). The binding energy of the Pt atom to the $V_4$ in graphene is 4.7 eV indicating that the complex is very stable in the graphene. In addition, we get a metastable structure shown in Fig.2(b). We denote two structures as $S_A$ and $S_B$, respectively, with $S_A$ being lower in energy than $S_B$ by 0.24 eV. We note that the $S_B$ is just the same as the structure found by Wang *et al*[24]. Next we will only discuss the $S_A$ since it is more energy favored. Secondly, we tailor the graphene sheet introduced with $S_A$ into ZGNRs, there will be two cases (denoted by $S_{A1}$ and $S_{A2}$, respectively) due to the symmetry of the ZGNRs as shown in the Figs.3. Moreover, it is found that the relative stability of $S_{A1}$ and $S_{A2}$ can be control by using external strain. The results are graphically summarized in Fig.4. With the introduction of the Pt@$V_4$ complexes the FM and AFM spin configurations have almost the same total energy (The difference is only about 0.01 eV). Besides the nonmagnetic Pt atom, we also consider a magnetic Co atom doped into $V_4$, as was also realized in the experiment[24].

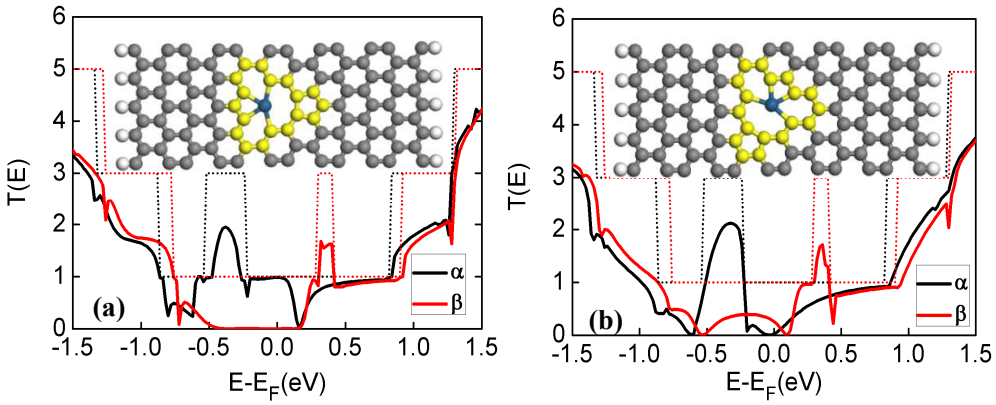



Fig. 3. The structures and the transmission function of 12-ZGNRs doped by (a) $S_{A1}$ and (b) $S_{A2}$ which are placed around the middle. The dotted lines indicated the transmission function of a pristine 12-zGNR with FM spin configuration.

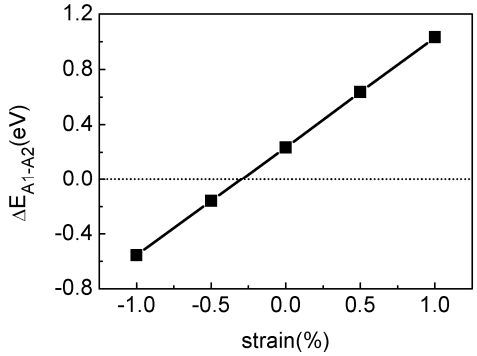



Fig. 4. The energy difference between the $S_{A1}$ and $S_{A2}$ varying with the strain.

Next, let us look at the transport behavior of ZGNRs with a Pt@ $V_4$ complex. We first introduce the Pt@$V_4$ complexes into the 12-ZGNR with both FM and AFM spin configurations. We find that spin polarization effect is much more significant in the FM system than in the AFM system. This is consistent with a previous study about transport in ZGNRs with adatoms and vacancies, where systems with FM configuration was found to have more significant spin-polarization effects[30]. Considering that the FM and AFM configurations are almost degenerate in energy and the FM configuration may be stabilized by applying an external magnetic or electric field [31], in this work, we will only discuss the transport behavior for the FM case. Also, it is found that the transmission function scarcely changes under an external strain from -1% to 1%.

For the Pt@$V_4$ complexes introduced in the middle region of the 12-ZGNR, the calculated transmission functions (*T(E)*) are given in Fig.3. The first thing to note is the overall reduction in the transmission spectrum due to the scattering from the defects in both cases. Most importantly, from Fig.3(a) we find that the spin degeneracy around the Fermi energy is significantly destroyed: The minority channel (β-spin) is near completely blocked while the majority channel (α-spin) is affected much less, producing a complete (100%) spin polarization in a energy range from -0.48 to 0.18 eV as can be measured by

$$P = \frac{T_\alpha - T_\beta}{T_\alpha + T_\beta}. \tag{1}$$

However, the phenomenon doesn't appear in Fig.3(b). So next we will only discuss the $S_{A1}$ since we are more curious about the perfect spin filter phenomenon.

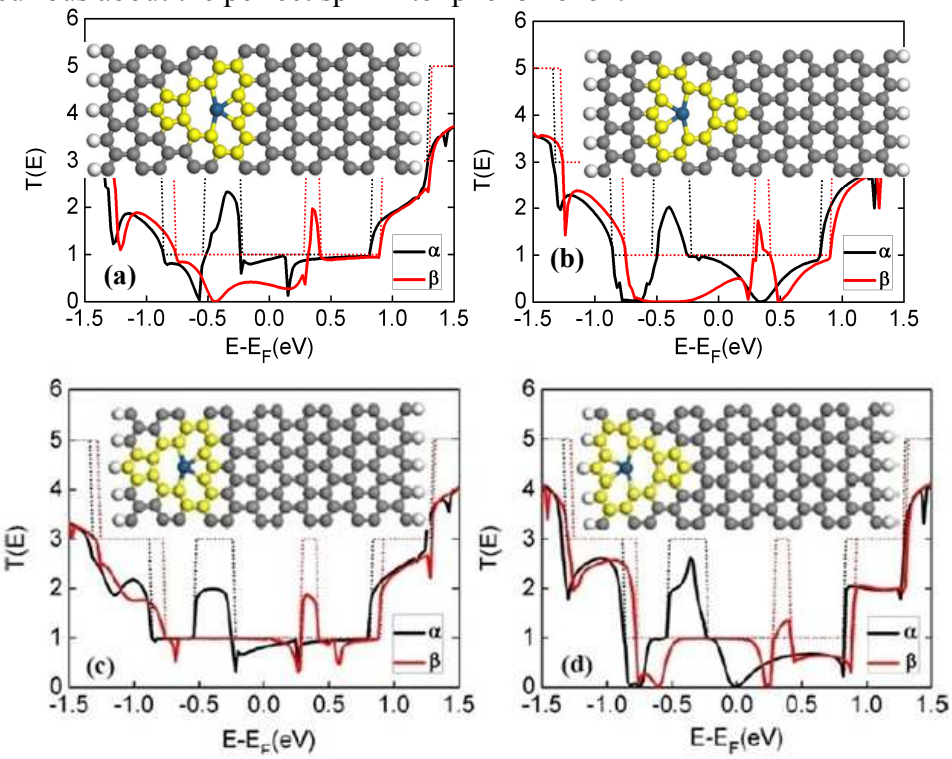



Fig. 5. The structures and the transmission function of 12-ZGNRs doped by Pt@$V_4$ which are placed in the different positions from the middle to the edge of the ribbon.

To investigate the effect from the Pt@$V_4$ position, we place the Pt@$V_4$ complex at various positions from the middle to the edge of the 12-ZGNR (see Fig.5(a) - (d)). It turns out that with the Pt@$V_4$ complex moving towards the edge, the scattering of β-spin channel becomes weaker (see Figs.5(a) - (b)), leading to a decreased ratio *P* around the Fermi energy, though a large value still remains around the energy window of the occupied edge state (-0.50 to -0.25eV). However, when the Pt@$V_4$ complex touches the edge with its 'apex' (see Fig.5(c)), the transmission function around the Fermi energy (from -0.7 to 0.7eV) is largely recovered to that of the ideal ZGNR except for the suppression of the two edge states. On the other hand, when the Pt@$V_4$ complex touches the edge with its 'bottom' (see Fig.5(d)) the majority α-channel has a dip at the Fermi energy while the minority β-channel is little affected. The different behavior with different positions of the Pt@$V_4$ complex can be understood qualitatively by considering the spatial distribution of the α- and β-spin states. In the FM spin configuration, the α-spin state (majority) distributes more near the edges. When the defect complex is in the middle region, the β-spin states will be more significantly scattered while the α-spin states still have some space to pass through, as appears in Figs.4(a). Contrarily, when the defect complex is right at the edge, the α-spin states will be largely scattered while the β-spin states will be affected less, as it appears in Figs.5(d). To further check effects from the width of ZGNRs, we consider a narrower ZGNR, 8-ZGNR (see the insets in Fig.6(a)). From the calculated transmission functions, one can see that the narrowing of the ribbon enhances the scattering for both the α- and β-spin channels, while the large spin polarization ratio still remains around the Fermi energy. In the 8-ZGNR system, the range of complete spin polarization becomes even larger (from -0.50 to 0.28 eV). These findings are just consistent with our previous analyses for different defect positions.

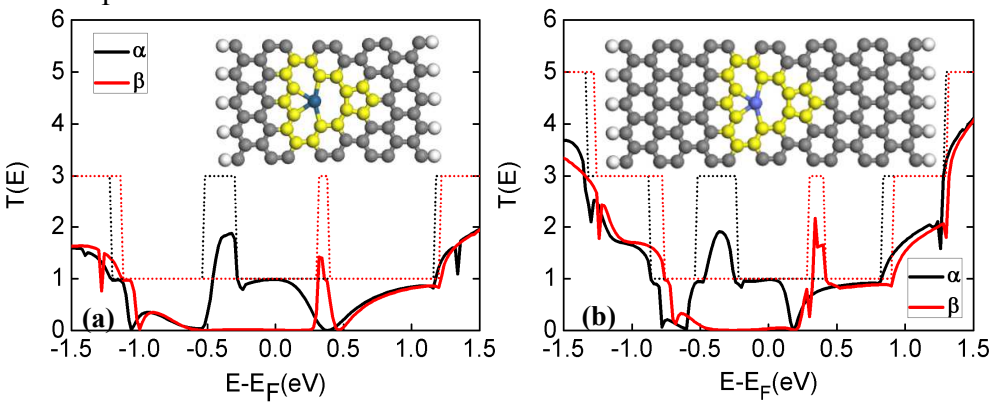



Fig. 6. (a) The transmission for 8-ZGNRs doped by Pt@$V_4$. (b) The transmission for 12-ZGNRs doped by Co@$V_4$ in the middle of ZGNRs.

Now, an interesting question arises: What is the main factor leading to the 100% spin polarization? Is it determined by the TM doping atom or by the particular complex structure? To check this, we replace the nonmagnetic atom Pt with a magnetic atom Co in the 12-ZGNR system. The calculated transmission function is given in Fig.6(b). Surprisingly, the result is almost the same as in the case of Pt@$V_4$, indicating that the transport property is basically independent of the doping TM atom. To confirm this idea, we take away the TM atom and use H atoms to saturate the dangling bonds, as shown in Fig.7(a). From the calculated *T(E)* function one can see that the 100% spin polarization is still remained though its energy range decreases a bit. At last, we simply take away the TM atom and relax the structure, that is, only a $V_4$ is introduced (see Fig.7(b). One can see that now the significant spin polarization around the Fermi energy disappears, confirming that it is the particular structure of TM@$V_4$ that causes the 100% spin polarization. The underlying physics for the totally different behavior between $V_4$ and TM@$V_4$ can be understood by considering the integrity of the global π-bond network of the system. The pure $V_4$ defect introduces only a perturbation to the local π-bond network but does not destroy it while the TM@$V_4$ structure destroys the local π-bond network, and therefore, creates localized defective states which will act as scattering centers around the Fermi energy.

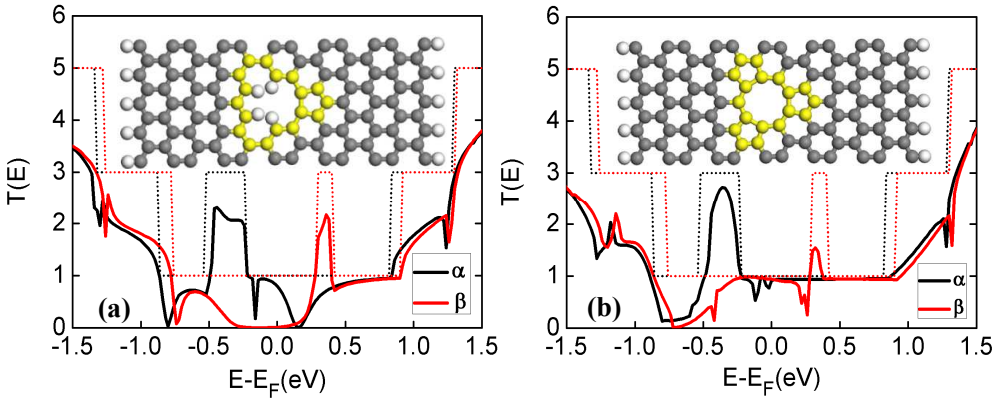



Fig. 7. The defect structure and the transmission function of the doped 12-ZGNRs: (a) Pt or Co are substituted by H, (b) pristine tetra-vacancy.

## Summary

In summary, by performing first-principles calculations we have investigated the transport properties of ZGNRs doped with a defect of TM@$V_4$ complex, which can be now fabricated in experiment. A 100% spin polarization has been found in a large energy rang around the Fermi energy, indicating that this kind of defect can be used to realize perfect spin filters. Our analyses have shown that this 100% spin polarization stems from the particular atomic structure of TM@$V_4$ complex regardless of the species of the TM atom. However, a pure $V_4$ defect will not lead to such a transport behavior because it does not destroy the local π-bond network.

## Acknowledgments

This work was supported by the National Natural Science Foundation of China under Grants No. 11174220 and 11374226, and by the MOST 973 Project 2011CB922204, as well as by King Abdulaziz University (KAU) under Grant No.49-3-1432/HiCi.

## References

[1] J. C. Meyer, A. K. Geim, K. S. Novoselov, T. J. Booth, and S. Roth, Nature 446(2007) 60-63.

[2] S. Morozov, K. S. Novoselov, M. I. Katsnelson, F. Schedin, D. J. L. A. Ponomarenko, and A. K. Geim, Phys. Rev. Lett. 97(2006) 016801.

[3] H. Terrones, R. Lv, M. Terrones, and M. S. Dresselhaus, Rep. Prog. Phys 75, 062501 (2012).

[4] K. S. Novoselov, Rev. Mod. Phys 83 (2011) 837-849.

[5] Y. Kobayashi, K.-I. Fukui, T. Enoki, K. Kusakabe, andY. Kaburagi, Phys. Rev. B 71(2005) 193406.

[6] Y. Niimi, T. Matsui, H. Kambara, K. Tagami, M. Tsukada, and H. Fukuyama, Phys. Rev. B 73 (2007) 085421.

[7] J. Haskins, A. Knac, C. Sevik, H. Sevincli, G. Cuniberti, and T. Cagin, ACS Nano 5(2011) 3779-3787.

[8] T. C. Li and S.-P. Lu, Phys. Rev. B 77 (2008) 085408.

[9] N. Gorjizadeh, A. A. Farajian, and Y. Kawazoe, Nanotechnology 20 (2009) 015201.

[10] I. Deretzis, G. Fiori, G. Iannaccone, and A. L. Magna, Phys. Rev. B 81(2010) 085427.

[11] A. R. Botello-Mendez, X. Declerck, M. Terrones, H. Terronesa, and J.-C. Charlier, Nanoscale 3 (2011) 2868-2872.

[12] J. C. Meyer, C. Kisielowski, R. Erni, M. D. Rossell, M. F. Crommie, and A. Zettl, Nano Lett. 8 (2008), 3582-3586.

[13] Y. Ren and K. Q. Chen, J. Appl. Phys. 107 (2009) 044514.

[14] Y. Gan, L. Sun, and F. Banhart, Small 4(2008) 587-591.

[15] M. F. Chisholm, G. Duscher, andW.Windl, Nano Lett. 12 (2012) 4651-4655.

[16] S. Lisenkov, A. N. Andriotis., and M. Menon, Phys. Rev. Lett. 108(2012) 187208.

[17] A. V. Krasheninnikov, P. O. Lehtinen, A. S. Foster, P. Pyykkö, and R. M. Nieminen, Phys. Rev. Lett. 102 (2009) 126807.

[18] E. J. G. Sántos, A. Ayuela, and D. Sánchez-Portal, New J.Phys 12 (2010) 053012.

[19] G. Giovannetti, P. A. Khomyakov, G. Brocks, V. M. Karpan, J. van den Brink, and P. J. Kelly, Phys. Rev. Lett. 101 (2008) 026803.

[20] K. T. Chan, J. B. Neaton, and M. L. Cohen, Phys. Rev. B 77 (2008) 235430.

[21] V. V. Nelayev and A. I. Mironchik, Mater. Phys. Mech. 9 (2010) 26-34.

[22] D. W. Boukhvalov and M. I. Katsnelson, Appl. Phys. Lett. 95 (2009) 023109.

[23] F. Banhart, J. Kotakoski, and A. V. Krasheninnikov, ACS Nano 5(2011) 26-41.

[24] H. Wang, Q. Wang, Y. Cheng, K. Li, Y. Yao, Q. Zhang, C. Dong, P. Wang, U. Schwingenschlögl, W. Yang, et al., Nano Lett. 12 (2012) 141-144.

[25] S.-H. Ke, H. Baranger, andW. T. Yang, Phys. Rev. B70 (2004) 085401.

[26] D. Sánchez-Portal, P. Ordejon, E. Artacho, and J. M. Soler, Int. J. Quantum Chem. 65(1997) 453-461.

[27] J. M. Soler, E. Artacho, J. D. Gale, A. Garcia, J. Junquera, P. Ordejón, and D. Sónchez-Portal, J. Phys.:Condens. Matter 14 (2002) 2745.

[28] N. Troullier and J. L. Martins, Phys. Rev. B 43 (1991) 1993.

[29] J. P. Perdew, K. Burke, and M. Ernzerhof, Phys. Rev. Lett. 77 (1996) 3865.

[30] S.M.-M.Dubois, Z.Zanolli, X.Declerck, and J-C.Charlier, Eur. Phys. J. B 72 (2009) 1.

[31] Y. Son, M. Cohen, and S. Louie, Nature 444 (2006) 347-349.

*Advanced Materials Research Vol. 937 (2014) pp 214-217*
*© (2014) Trans Tech Publications, Switzerland*
*doi:10.4028/www.scientific.net/AMR.937.214*

# An Effective N, N-diethylthiourea as Accelerator for Microvia Filling Via Copper Electrodeposition

Weiwu Ma*, Yan Wang

Sciences of college, Lishui University, Zhejiang Provence, China

Sciences of college, Lishui University, Zhejiang Provence, China

symaww@163.com, wy8805@126.com

**Keywords**: accelerator, printed circuit board, filling

**Abstract.** The effect of N, N-diethylthiourea (DET) upon the microvia filling by Cu electrodeposition was investigated by cross-sectional images using optical microscopy. The bottom-up filling of the electroplating bath was achieved with an addition of DET. The electrochemical study indicated that the polarisation on the cathode was increased with an addition of DET. The results present DET as an accelerator which is beneficial for microvias filling for high density interconnections printed circuit board.

## Introduction

With the progress of development of electronic devices, the number of electronic devices on the chip and circuit densities has increased significantly; Cu electrodeposition in the damascene process for the metallisation of semiconductor interconnects has been used widely for fabricating printed circuit boards (PCBs).[1–3] This is a fabrication process for integrated circuits, including formation of the diffusion barrier, formation of copper seed layer, plating copper and CMP process. However, because the microvias for PCBs are approximately 103 times larger than those for ultra large scale integration interconnects, it is difficult for the Cu electrodeposition solution used in the damascene process to obtain a void-free filling for PCBs.[4] A complete filling of microvias by Cu electroplating is a challenge in the fabrication of Cu interconnects of PCB with high density interconnections. In order to guarantee good quality interconnects of PCB, void-free filling, or the so called bottom-up filling, in which the Cu deposition rate at the bottom of the microvia is faster than that at the top, must be achieved.[5] Several additives, such as chloride ions ($Cl^-$), polyethylene glycol (PEG) as a suppressor, and bis(3-sulphopropyl)disulphide (SPS) as an accelerator, are incorporated in the Cu electroplating bath and assist in the direct current plating of Cu to accomplish bottom up filling for PCBs.[6,7] Although there are many reports in the literature focused on understanding superfilling for fabricating Cu interconnects in ultra large scale integration,[8] the research in bottom-up filling for PCBs is slim. Only Honma et al.[2] and Dow et al.[5–7] have reported via-filling using electroplating for PCBs.

For the electroplating Cu solution in the damascene process, the additives PEG and $Cl^-$ adsorb preferentially on the outside of microvias and inhibit the Cu electrodeposition, and SPS adsorbs at the bottom of microvias and accelerates the Cu electrodeposition in the superfilling of Cu electrodeposition [9,10] . The bottom up filling of copper electroplating was achieved with an addition of triblock copolymer as an inhibitor to fill 100-nm microvias [11], but the bottom up filling of copper electroplating was not obtained with an addition of triblock copolymer with propylene oxide terminal blocks termed EPE as an inhibitor to fill 50 μm microvias.

Triblock copolymers EPE had strong inhibition for Cu electrodeposition and were used as suppressor in the superfilling of Cu electrodeposition [12, 13], but the copper filling of EPE as suppressor of a three-additive system has not been reported.

In this work, microvia filling performance of the copper plating solution using N,N-diethylthiourea (DET) as an accelerator is investigated by means of extensive electrochemical methods.

## Experimental

The electroplating solution used for microvia filling experiments was composed of 220g/L $CuSO_4 \cdot 5H_2O$, 55g/L $H_2SO_4$, 300 ppm PEG-8000, 4 ppm Janus Green B (JGB) as well as Cl−(added as NaCl), N,N-diethylthiourea (DET) with varying concentration. Temperature of the plating solution was controlled at 25℃. The filling performance of the plating bath was evaluated by cross-sectional views of the microvias using optical microscopy (DFC290, Leica) at a magnification of 200×.

Linear sweep voltammetry(LSV) was wereperformed on an electrochemical workstation (CHI 760D) in athree-electrode cell at 25℃. A platinum electrode with a diameter of 5 mm and a copper electrode were employed as the counter electrode and working electrode, respectively. A saturated Ag/AgCl electrode was used as the reference electrode.

## Results and Discussion

3.1. Effects of DET concentration on microvia filling capability

In order to achieve a complete bottom-up filling of electroplating copper, the effects of the inhibitor on the bottom-up filling of microvias should be first investigated.

Figure 1 shows cross-sectional OM images of 50 μm microvias filled by electrodeposition of Cu in the bath. Figure 1A shows the cross-sectional OM image of the hole before electrodeposition. After plating for 30 min (Fig. 1B) a somewhat conformal filling was obtained, and 80 min (Fig. 1C), a significant bottom-up filling of electroplated Cu in the microvia was observed. Further to that, void-free filling of Cu was completed after electroplating for 200 min (Fig. 1D), and a bottom-up filling was obtained.

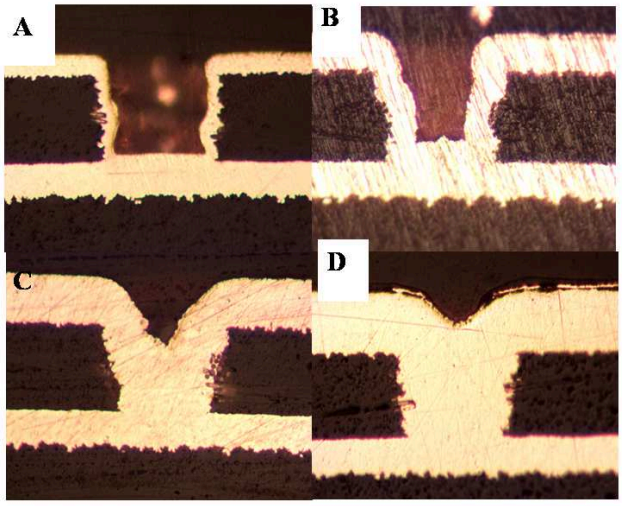



Fig. 1 Cross-sectional OM images of microvias with different plating times
Plating times: (A) 0 min, (B) 30 min, (C) 80 min, (D)200 min

It was noted that thickness of Cu on the top surface changes significantly over plating time. The deposition rate of Cu on the top surface was very small before microvias had been filled by plated Cu. After the microvias were almost filled with Cu, the thickness of Cu on the top surface started to increase noticeably. This was attributed to PEG-$Cl^-$ suppressing mainly Cu deposition on the surface of the substrate, and the acceleration of DET-$Cl^-$ acting at the bottom of microvias before they had been filled in plating of Cu. When the microvias were almost filled with Cu, the combined effects of DET-$Cl^-$ and PEG-$Cl^-$ cause the deposition rate of plating of Cu on the surface of the substrate to increase.

This result may be explained by the following: According to the filling mechanism, the inhibition of copper deposition by the suppressor (PEG-$Cl^-$ ) at the board surface was inadequate. Suppressor (PEG-$Cl^-$) has a large molecular weight and low diffusion rate in electroplating solution, and it is adsorbed onto a copper surface of substrate in the form of monolayer. Though the molecular

weights of DET-$Cl^-$ were near 400, the diffusion coefficients of DET-$Cl^-$ should be larger than that of PEG-$Cl^-$ because of large molecular weight of PEG. The acceleration of copper deposition by the accelerator (DET-$Cl^-$) at the microvia bottom was strong under the plating condition, and so bottom-up filling of copper was accomplished.

3.2 Effect of DET concentration on polarisation behaviour of electroplating Cu solution

In order to explore the effect of DET for copper deposition, linear sweep voltammetry measurement was used to investigate the effects of DET on the polarization curves of the electroplating solution (Fig.2).

Effects of DET on the cathodic polarisation of the electroplating bath were investigated by linear sweep voltammetry, and the results are shown in Fig. 2. From Fig. 2, it was found that copper reduction current changed with addition of DET. The reduction peak current and peak potential were about -5.75 Am cm-2 and -0.63 V without addition of DET, it shifted to -5.43 Am cm-2 and –0.62 V with 12 mg L-1 DET addition. It may be attributed to the strength of DET adsorption on the Cu surface with addition of DET.

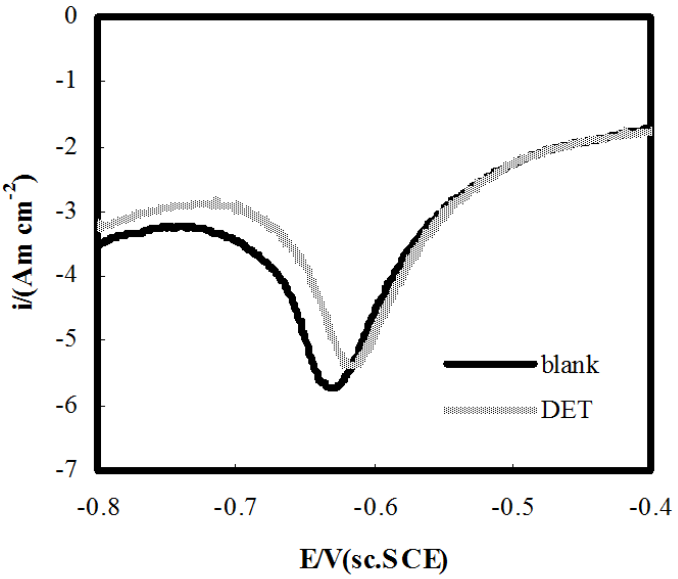



**Fig. 2 Effect of DET on the cathodic polarization behavior of electrolyte for copper plating**

## Conclusions

The effect of DET as an additive on bottom-up filling characteristics in copper deposition was investigated. Bottom-up fillings with microvias of 50 μm and aspect ratio of one were obtained in the electroplating Cu bath with addition of DET. Linear sweep voltammetry measurement indicated that DET accelerated on Cu deposition, which is in agreement with the results of cross-sectional OM observation. From the results obtained in this study, it is concluded that DET was highly effective for void-free filling of microvias.

## References

[1] P. C. Andricacos, C. Uzoh, J. O. Dukovic, J. Horkans and H.Deligianni, Damascene copper electroplating for chip interconnections, IBM J. Res. Dev., 42(1998) 567-574.

[2] Q. X. Shen, X. Wang, H. P. Zhu, Effect of additive triblock copolymer EPE-8000 on bottom-up filling in copper electroplating, Int. J. Electrochem. Sci., 9 (2014) 365-370.

[3] W. P. Dow, H. S. Huang and Z. Lin,Interactions Between Brightener and Chloride Ions on Copper Electroplating for Laser-Drilled Via-Hole Filling, Electrochem. Solid State Lett., 6(2003) C134-C136.

[4] S. Miura and H. Honma, Advanced copper electroplating for application of electronics, Surf. Coat. Technol., 169(2003) 91-95.

[5] W. P. Dow, M. Y. Yen, W. B. Li, and S. W. Ho, Influence of Molecular Weight of Polyethylene Glycol on Microvia Filling by Copper Electroplating, J. Electrochem.Soc., 152(2005) C769-C775.

[6] W. P. Dow, H. S. Huang, M. Y. Yen and H. C. Huang, Influence of Convection-Dependent Adsorption of Additives on Microvia Filling by Copper Electroplating, J. Electrochem. Soc., 152( 2005) C425-C434.

[7] W. P. Dow, M. Y. Yen, C. W. Liu and C. C. Huang, Enhancement of filling performance of a copper plating formula at low chloride concentration, Electrochim. Acta, 53(2008) 3610-3619.

[8] S. K. Kim and J. J. Kim, Superfilling Evolution in Cu Electrodeposition: Dependence on the Aging Time of the Accelerator, Electrochem. Solid State Lett., 2004, 7,C98-C100.

[9] K. Kondo, T. Matsumoto and K. Watanabe, Role of Additives for Copper Damascene Electrodeposition: Experimental Study on Inhibition and Acceleration Effects, J. Electrochem. Soc.,, 151( 2004) C250-C255.

[10] A. Pohjoranta and R. Tenno, A Method for Microvia-Fill Process Modeling in a Cu Plating System with Additives, J. Electrochem. Soc., 154(2007) D502-C509.

[11] J. W. Gallaway, M. J. Willey, A. C. West, Acceleration Kinetics of PEG, PPG, and a Triblock Copolymer by SPS during Copper Electroplating,J. Electrochem. Soc., 156 (2009)D146-D154.

[12] J. W. Gallaway ,M. J. Willey, A. C. West, Copper Filling of 100 nm Trenches Using PEG, PPG, and a Triblock Copolymer as Plating Suppressors, J. Electrochem. Soc., 156(2009) D287-D295.

[13] J. W. Gallaway, A. C. West, PEG, PPG, and Their Triblock Copolymers as Suppressors in Copper Electroplating, J. Electrochem. Soc., 155(2008) D632-D639.

*Advanced Materials Research Vol. 937 (2014) pp 218-223*
*© (2014) Trans Tech Publications, Switzerland*
*doi:10.4028/www.scientific.net/AMR.937.218*

# Adsorption Mechanism Study of Magnetic EDTA-Chitosan on Cu(Ⅱ) Ions of Solution

Run-Hua QIN[1,a] , Feng-Sheng LI[2,b], Wei JIANG [2,c] and Ling-Yun HAO[1,d,*]

[1]School of Materials Engineering, Jinling Institute of Technology, Nanjing 211169, China

[2] National Special Superfine Powder Engineering Research Center, Nanjing University of Science & Technology, Nanjing 210094, China

[a]qinrunh@126.com, [d]hly@jit.edu.cn

*Corresponding author

**Keywords:** Magnetic adsorbent, Adsorption mechanism, Cu (Ⅱ) ions, Chelation.

**Abstract.** A novel magnetic adsorbent, magnetic EDTA/chitosan nano-beads was synthesized. The adsorption mechanisms of magnetic EDTA/chitosan nano-beads for removal of Cu(Ⅱ) ions from aqueous solution were investigated in this paper. The interaction mechanisms of $Cu^{2+}$ adsorption onto magnetic EDTA/chitosan nano-beads and active sites were interpreted by fourier transform infrared spectroscopy (FTIR) and X-ray photoelectron spectroscopy (XPS) analysis. Uniting the analysis results of FTIR and XPS, the functional groups of participating in chelating were confirmed, and the results indicated that $Cu^{2+}$ adsorption was mainly through interactions with electron donating atom N and O. This adsorption property was similar to N·O-type chelating agent and the adsorption mechanism was put forward. This work was very significant to control adsorption influence factor and improve adsorption capacity of magnetic EDTA-chitosan nano-beads, and then succeed to apply to magnetic adsorption fields.

## Introduction

The presence of heavy metals in the environment has been of great concern because of their increased discharge, toxic nature and other adverse effects on receiving waters. Various methods exist for the removal of toxic metals from aqueous solution such as ion-exchange, reverse osmosis, adsorption, complexation and precipitation [1-4]. Adsorption process, as the most effective and widely used method, has been extensively examined for the elimination of the organic substances or heavy metal ions from water and waste water. Bio-sorption or sorption of biological material is recognized as an emerging technique for the treatment of wastewater containing heavy metals.

Among various biopolymer available, chitosan has the highest sorption capacity for several metal ions, was described as a suitable natural polymer for the collection of metals ions, possibly due to presence of primary amine at C-2 position of the glucosamine residues [5-8]. Some researchers have applied chitosan to the separation and adsorption [9]. Due to the presence of both amino groups and hydroxyl groups in its structure, chitosan can be chemically modified to be used as drug delivery or separation media.

Whereas, ethylenediaminetetraacetate (EDTA) [10-11], the polyamine polycarboxylate chelator is known for its capacity to form complexes with metal ions [12-13]. Moreover, in comparison with other chelating agents, EDTA presents a high level of complexing capacity with respect to heavy metals. The molecule configuration of EDTA was shown in Fig.1.

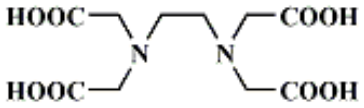



Fig. 1. The molecule configuration of EDTA

The as-prepared magnetic EDTA/chitosan is a predominance integration of chitosan and EDTA. The most notable property of magnetic EDTA/chitosan is that its two functional groups (amino and carboxyl) can serve as chelating sites and form complexes with metal ions. Thus, the as-prepared magnetic EDTA/chitosan nano-beads yield a novel method for magnetic adsorption. However, the mechanisms responsible for these properties have so far not been well studied and explained.

In this work, we report the removal of copper ions from aqueous solution with magnetic EDTA/chitosan nano-beads. The aim is to understand the mechanisms of copper binding to magnetic EDTA/chitosan nano-beads. FTIR and XPS spectra were used to identify the adsorption mechanisms. This information will be useful for further application in the treatment of waste effluents.

## Experimental

### Preparation of $Cu^{2+}$ Solution and Adsorption Experiments

$Cu^{2+}$ solutions were prepared by diluting $CuCl_2 \cdot 6H_2O$ in deionized water. Typically, 0.02g magnetic EDTA/chitosan nano-beads were added to 25ml of 0.1mol/L $Cu^{2+}$ solution. Then this mixture was dispersed with the help of ultrasonic cleaning to ensure sufficient interaction between magnetic EDTA/chitosan nano-beads and $Cu^{2+}$. Batch adsorption experiments were conducted in a thermostatic shaker under shaking speed of 100 rpm for 2h to attain the equilibrium of adsorption. The initial concentration of $Cu^{2+}$ in the solution and samples after adsorption treatment were determined using ultraviolet-visible spectrophotometer (JH-752N). After reaching equilibrium, the magnetic EDTA/chitosan nano-beads were separated easily from the solution with the help of an external magnetic force. Then, the separated magnetic EDTA/chitosan nano-beads were treated with deionized water to neutralize and measured using FT-IR and XPS, respectively.

### Analysis Methods

FTIR spectra of magnetic EDTA/chitosan nano-beads before and after adsorption Cu(Ⅱ) ions were recorded with KBr discs in the range of 4000-400$cm^{-1}$ on MB154S Fourier transfer infrared. X-ray photoelectron spectroscopy (XPS) of magnetic EDTA/chitosan nano-beads before and after adsorption Cu(Ⅱ) ions were carried out with an ESCALAB 250 electron spectrometer from Thermo of USA. The concentrations of Cu(Ⅱ) ion in solution were analyzed using an ultraviolet-visible spectrophotometer (JH-752N).

## Results and Discussion

The structural formula of as-prepared magnetic EDTA-chitosan was shown in Fig.2.

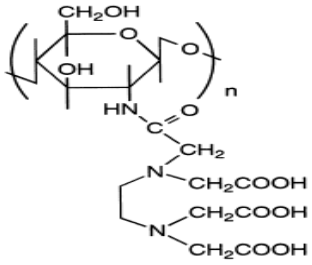



Fig. 2. The tructural formula of as-prepared magnetic EDTA-chitosan

For the magnetic EDTA/chitosan nano-beads used in this study, it may be expected that the adsorption sites for copper are at the nitrogen atoms and oxygen atoms. To further prove the possible sites of $Cu^{2+}$ binding to the magnetic EDTA/chitosan nano-beads, FTIR and XPS spectra were obtained for the magnetic EDTA/chitosan nano-beads before and after Cu(Ⅱ) ions adsorption.

### FT-IR Analysis

FT-IR spectra of magnetic EDTA-chitosan (a) before Cu(Ⅱ) ions were loaded and (b) after Cu(Ⅱ) ions were loaded were shown in Fig.3. As was shown in Fig.3, the 3420$cm^{-1}$ overlapping peak of —$NH_2$ and —OH stretching vibration shifted to high frequency, which indicated that both —$NH_2$ and —OH participated in chelating reaction. Compared with the spectra of magnetic EDTA-chitosan,

the 1554cm$^{-1}$ peak of —NH disappeared in magnetic EDTA-chitosan-$Cu^{2+}$, and the 1636cm$^{-1}$ peak of amide □C=O shifted to low frequency, which indicated that both —NH and C=O participated in chelating reaction for Cu(Ⅱ). The 1316cm$^{-1}$ peak of —OH in carboxyl group and the 1067cm$^{-1}$ peak of C—O in alcoholic hydroxyl group shifted to low frequency, which indicated that both —COOH and —OH also possibly participated in chelating reaction for Cu(Ⅱ).

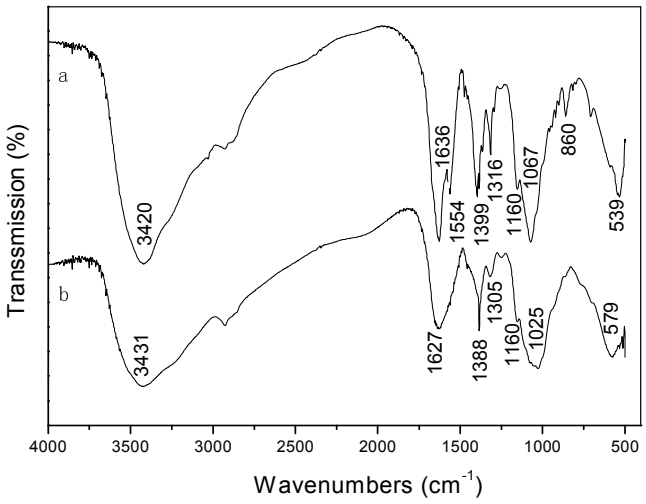



Fig. 3. FT-IR spectra of magnetic EDTA-chitosan (a) before Cu(Ⅱ) ions were loaded and (b) after Cu(Ⅱ) ions were loaded

**XPS Analysis**

Fig.4 showed XPS spectra of (a) N1s and (b) O1s of magnetic EDTA-chitosan before $Cu^{2+}$ adsorption, respectively.

Fig.5 showed XPS spectra of (a) N1s, (b) O1s and (c)Cu2p of magnetic EDTA-chitosan after $Cu^{2+}$ adsorption, respectively.

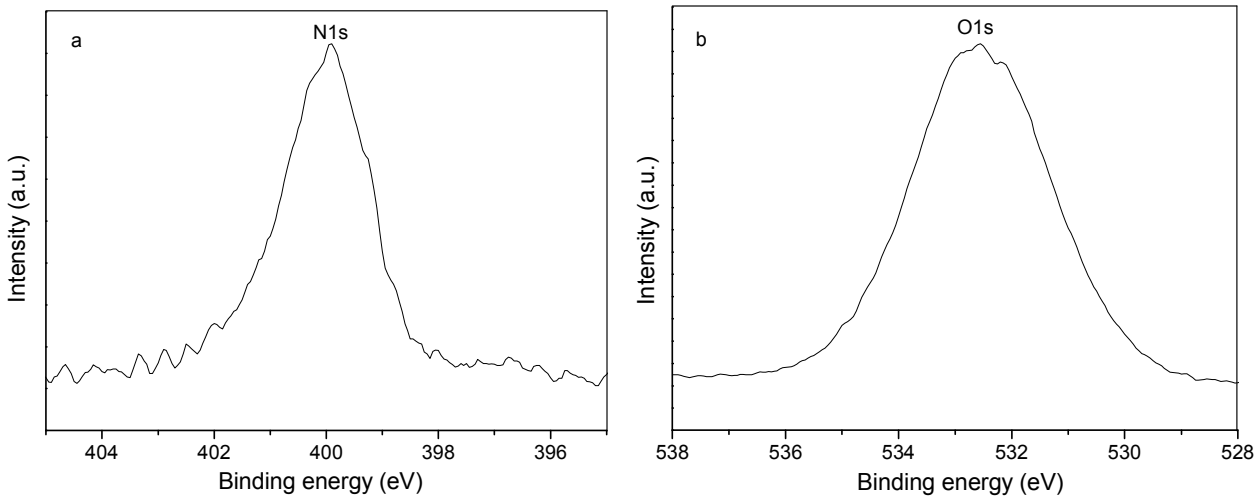



Fig. 4. XPS spectra of (a) N1s and (b) O1s of magnetic EDTA-chitosan before $Cu^{2+}$ adsorption

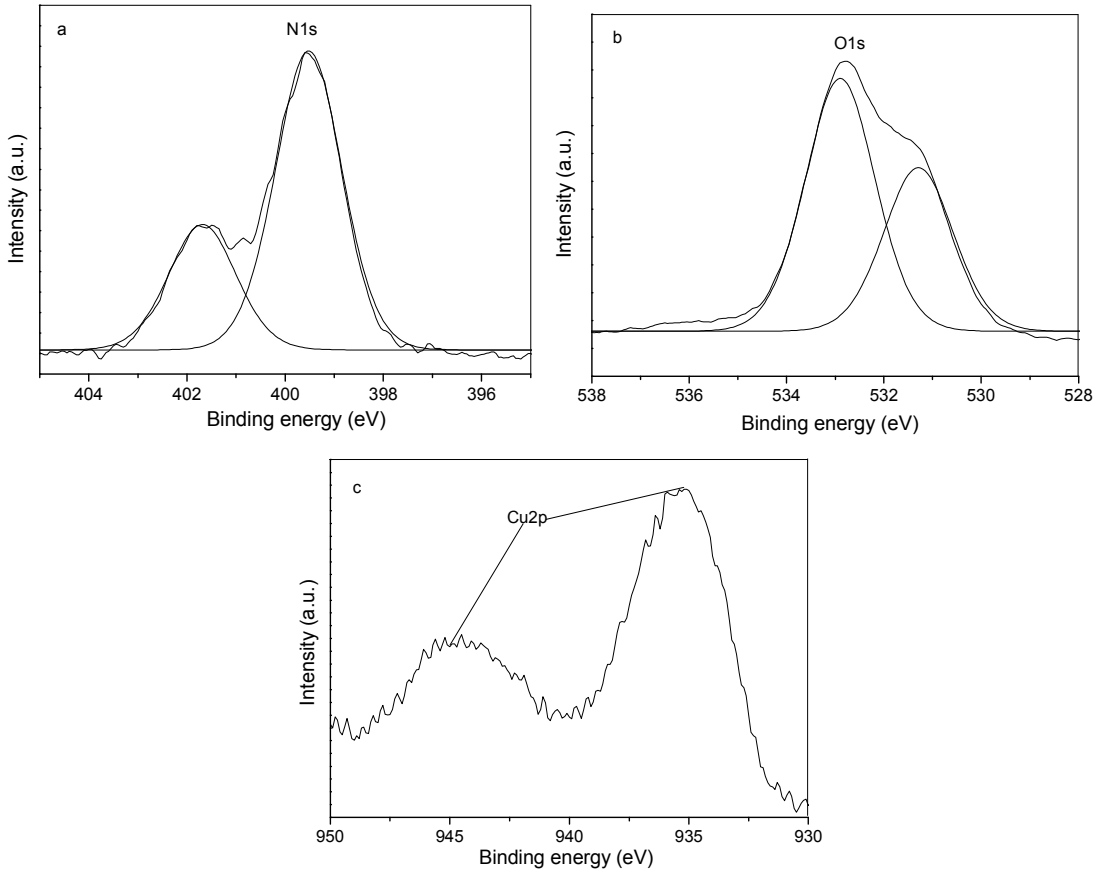



Fig. 5. XPS spectra of (a) N1s,(b) O1s and (c)Cu2p of magnetic EDTA-chitosan after $Cu^{2+}$ adsorption

Compared with two graphs, there was a peak at magnetic EDTA-chitosan before $Cu^{2+}$ adsorption, in which the photoelectron lines at binding energy of about 399.9 and 532.6eV were attributed to N1s and O1s, resectively. After $Cu^{2+}$ adsorption, there were two peaks located at 399.5 and 401.7eV correspond to N1s, and there were two peaks located at 532.9 and 531.3eV correspond to O1s. Which indicated that chemical environment of N and O atom changed, i.e. N and O atom participated in chelating. Thereinto N can be from unreacted completely —$NH_2$, or from amide Ⅱ—NH, also form tertiary nitrogen of EDTA. While O can be from unreacted completely —COOH of EDTA, or from alcohol —OH groups, also form amide Ⅰ C=O, which furter proved the IR results.

The two peaks located at 935.4 and 945.1eV correspond to Cu2p3/2, thereinto the binding energy of 935.4eV attributed to Cu2p3/2 of $CuCl_2$, which conformed $Cu^{2+}$ was adsorbed on magnetic EDTA-chitosan via physical adsorption. The Cu binding energy of 945.1eV was adsorbed via chelating reaction, and the binding energy increased, which indicated that Cu possessed a trend for obtaining and sharing electrons after chelating reaction.

## Adsorption Mechanism Analysis

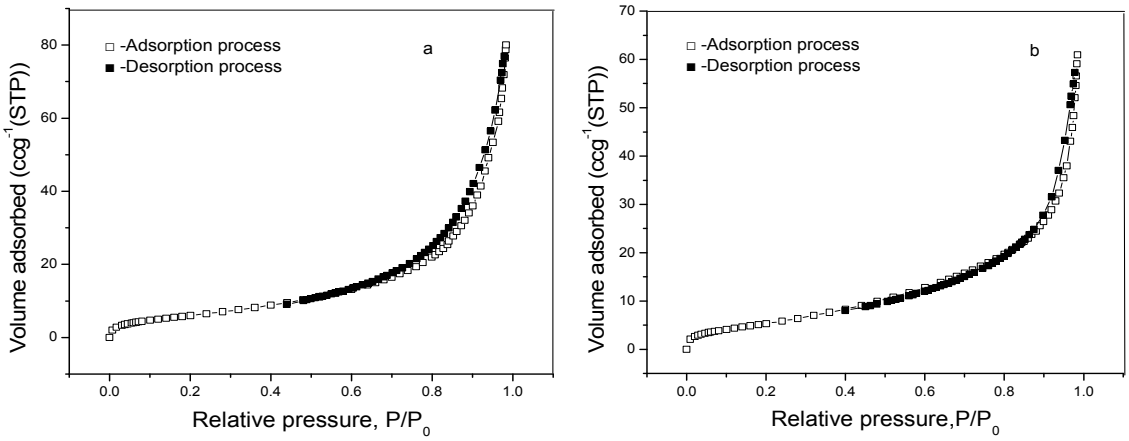



Fig. 6. $N_2$ adsorption-desorption isotherms of magnetic EDTA-chitosan at different conditions

$N_2$ adsorption-desorption isotherms of magnetic EDTA-chitosan at different conditions were shown in Fig.6. As showin in Fig.6, the isotherms belong to type Ⅲof the BET classification, adsorption and desorption route coincide with each other, no hysteresis loop. Which indicated that the as-prepared magnetic EDTA/chitosan nano-beads were imperforate, and the adsorption of magnetic EDTA/chitosan on Cu(Ⅱ) ions was not commonly physical adsorption.

Uniting the analysis results of FTIR, XPS and BET, the functional groups of participating in chelating were involved —$NH_2$, ═NH,═N<,═COOH, C=O and $CH_2$═O, and the results indicated that $Cu^{2+}$ adsorption was mainly through interactions with electron donating atom N and O.

So many possibilities of reaction with Cu(Ⅱ) ions that the as-prepared magnetic EDTA/chitosan nano-beads have very excellent potential of adsorption application.

## Conclusions

In this work, the as-prepared magnetic EDTA/chitosan nano-beads were used to adsorb Cu(Ⅱ) ions from aqueous solution. The analysis of BET indicated that the as-prepared magnetic EDTA/chitosan nano-beads were imperforate, and the adsorption of magnetic EDTA/chitosan on Cu(Ⅱ) ions was not commonly physical adsorption. The adsorption mechanisms of magnetic EDTA/chitosan nano-beads for removal of Cu(Ⅱ) ions were studied using FTIR and XPS. The analysis showed that —$NH_2$, ═NH, ═N<,═COOH, C=O and $CH_2$═OH groups were involved in the adsorption of Cu(Ⅱ) ions onto magnetic EDTA/chitosan beads, and the possible adsorption mechanisms were proposed. This also explained the reasons that the as-prepared magnetic EDTA/chitosan nano-beads had the good potentials of adsorption. This work was very significant to control adsorption influence factor such as pH, temperature, time as so on, and improve adsorption capacity of magnetic EDTA/chitosan nano-beads.

## Acknowledgements

This research was financially supported by the National Science Foundation No. 50972060 and Doctor Initial Foundation of Jinling Institute of Technology No. jit-b-201309.

## References

[1] Zouboulish A I, Loukidou M, Matis K A. Biosorption of toxic metals from aqueous solutions by bacteria strains isolated from metal polluted soils [J]. Process Biochemistry, 2004, 39: 909-916

[2] Ghinwa Naja, Bohumil Volesky. The mechanism of metal cation and anion biosorption[J]. Microbial Biosorption of Metals, 2011, 1: 19-58

[3] Çabuk A, Akar T, Tunalı S, et al. Biosorption characteristics of Bacillus sp.ATS-2 immobilized in silica gel for removal of Pb(Ⅱ)[J]. Journal of Hazardous Materials, 2006 136: 317-323

[4] Vieira RHSF, Volesky B. Biosorption: a solution to pollution [J]. International Microbiology, 2010, 3(1): 17-24

[5] Yi H, Wu L, Bentley W E, et al. Biofabrication with chitosan[J]. Biomacromol, 2005, 9: 2881-2894

[6] Cheung W H, Szeto Y S, McKay G. Enhancing the adsorption capacities of acid dyes by chitosan nano particles[J]. Bioresource Technology, 2009, 100: 1143-1148

[7] Ding P, Huang K L, Li G Y. Kinetics of adsorption of zn(Ⅱ) ion on chitosan derivatives [J]. International Journal of Biological Macromolecules, 2006, 39: 222-227

[8] Pillai C K S, Paul W, Sharma C P. Chitin and chitosan polymers: Chemistry, solubility and fiber formation [J]. Progress in Polymer Science, 2009, 34(7): 641-678

[9] Elwakeel K Z, Atia A A, Donia A M. Removal of Mo(VI) as oxoanions from aqueous solutions using chemically modified magnetic chitosan resins [J]. Hydrometallurgy, 2009, 97: 21-28

[10] Lee J W, Lee S M, Huh Y D, et al. EDTA surface capped water-dispersible ZnSe and ZnS: Mn nanocrystals [J]. Bulletin of Korean Chemical Society, 2010, 31(7): 1997-2002

[11] Hinck M L, Ferguson J. Resistance of EDTA and DTPA to aerobic biodegradation [J]. Water Science and Technology, 1997, 35 (2): 25~31

[12] Zhou Z L, Qiu R L, Zhang W H, et al. The study of operating variables in soil washing with EDTA [J]. Environmental Pollution, 2009, 157(1): 229-236

[13] Zaier H, Ghnaya T, Rejeb K B, et al. Effects of EDTA on phytoextraction of heavy metals (Zn, Mn and Pb) from sludge-amended soil with Brassica napus [J]. Bioresource Technology, 2010, 101(11): 3978-3983

*Advanced Materials Research Vol. 937 (2014) pp 224-228*
*© (2014) Trans Tech Publications, Switzerland*
*doi:10.4028/www.scientific.net/AMR.937.224*

# Preparation , Characterization and Conductivity of Solid High-proton Conductor $Na_7[CoW_{11}O_{39}Cd(H_2O)]\cdot 12H_2O$

Li-qiang CHEN , Xiu-mei LIN, Ming-xia ZHU, Li-mei DAI*

Department of Chemistry, Heihe University, Heihe, Heilongjiang 164300, People's Republic of China

First author email, chlq_314101@sina.com

*Corresponding author, Tel: +86-18704563385, Fax: +86-0456-6840239,

E-mail: dlm1155@163.com

**Keywords:** Heteropoly compounds, Keggin structure, cadmium, Conductivity.

**Abstract.** A new solid high-proton conductor $Na_7[CoW_{11}O_{39}Cd(H_2O)]\cdot 12H_2O$ has been synthesized for the first time. The percentage composition of the product were determined by Inductively coupled plasma (ICP) and X-ray photoelectron spectroscopy (XPS). The product was characterized by infrared spectroscopy (IR) and X-ray diffraction (XRD), which indicate it possesses the Keggin structure. The TG-DTA curve shows the sequence of water loss in the compound, the amount of the loss, as well as the thermostability. Conductivity of the compound was investigated by four-electrode method at room temperature and different measuring temperatures, the results reveal that its proton conductivity is $4.87\times10^{-4}$ S·cm$^{-1}$ at 27ºC and the activation energy for proton conduction is 15.31 kJ/mol.

## Introduction

Heteropoly compounds are a fascinating class of inorganic metal-oxygen cluster compounds [1]. They are important because of their potential applications such as catalysis, biology, magnetism, photochemistry, medicine [2–4] and good proton conductivity at room temperature [5]. The heteropoly compounds belong to low temperature proton conductors generally [6]. Nowadays, many solid high-proton conductor of heteropoly compounds have been reported, such as $H_7[In(H_7O)CoW_{11}O_{39}]14H_2O$ [7], which show that this field continues to have a prominent place at the forefront of heteropoly compounds chemistry. We try to synthesize a heteropoly compound containing element cadmium to investigate the conductivity with the change of heteroatoms. In this paper, we originally report the preparation of undeca tungsto cobalto cadmic heteropoly acid $Na_7[CoW_{11}O_{39}Cd(H_2O)]\cdot 14H_2O$ by the acidification and the stepwise addition of solution of the component elements. In addition, we report our result on its conductivity.

## Experimental

### Instruments and Reagents

The infrared spectroscopy (IR) was recorded by KBr (S.P. grade) pellets on a 1730-FTIR (P.E. U.S.A.) spectrophotometer in the range of 400–4000 cm$^{-1}$. X-ray diffraction (XRD) patterns were measured using a D/MAX-3C diffractometer with a Cu target, Cu $K_a$ radiation ($\lambda$ = 0.15405 nm). The elemental analysis was performed by a P1 ASMA-SPEC (1) ICPAES (Leeman Labs, U.S.A.) quantometer. The X-ray photoelectron spectroscopy (XPS) was executed on an ESCA LAB MARKII XPS spectroscopy. Thermal analysis was carried out on diamond TG-DTA P-E thermo-analysis system (U.S.A), the rate of rising temperature was 10 ºC·min$^{-1}$.The conductivity was obtained on a KEITHLEY2400 Digital Multimeter (U.S.A.). All the reagents used were of analytical reagent (AR) grade.

### Preparation of $Na_7[CoW_{11}O_{39}Cd(H_2O)]\cdot 12H_2O$

$Na_2WO_4\cdot 2H_2O$ (36.30 g, 0.11 mol) was dissolved in 300 ml of water and the pH of the solution was adjusted to 6.3 with the acetic acid. After heating this solution to boiling, a solution of Co $(NO_3)_2\cdot 3H_2O$ (2.19 g, 0.01 mol $Co^{2+}$) dissolved in 100 ml of water was added dropwise while stirring, the stirring was continued for 45 min, and the temperature was kept 95ºC.A solution of $CdSO_4\cdot 8H_2O$

(2.85 g, 0.01 mol $Cd^{2+}$) dissolved in 100 ml of water was added, the stirring was continued for 1 h, and the temperature was kept at 75ºC.The mixture was cooled at room temperature. A green oily liquid was obtained after adding the absolute alcohol into the above mixture. The green oily liquid was added the absolute alcohol for several times repeatedly, it turned into fine grained shapes finally and kept in a vacuum desiccator. The final yield was about 65%.

**Elemental Analysis**

Cobaltum, cadmium, and tungsten were analyzed by inductively coupled plasma (ICP) spectrometry. The water content was determined by thermogravimetry. Anal. Calc (in %). for $Na_7[CoW_{11}O_{39}Cd(H_2O)]\cdot 12H_2O$: Na, 5.80; Co**,** 1.83; Cd, 3.50; W, 62.95; $H_2O$, 7.28. Found : Na, 5.82; Co, 1.84 ; Cd , 3.49; W, 62.70 ; $H_2O$, 7.12.

**Results and Discussion**

**IR**

Fig.1 shows characteristic peaks of the sample in the range of 400–1000 $cm^{-1}$. These peaks can be assigned to $\nu_{as}$（W=Od）923 $cm^{-1}$, $\nu_{as}$（W–Ob–W）861 $cm^{-1}$, $\nu_{as}$(W–Oc–W) 786 $cm^{-1}$, 684 $cm^{-1}$ and $\nu_{as}$（Co–Oa）415 $cm^{-1}$, respectively. These datas indicate that the compound anions have the Keggin cage structure [8–10]. we can see the sample has two obvious absorption peaks in 3437 $cm^{-1}$ and 1627 $cm^{-1}$, they are treated as the stretching vibration of O–H bonds and the bending vibration of H–O–H bonds, respectively [11,12], these results can illustrate that the sample has water molecules existing.

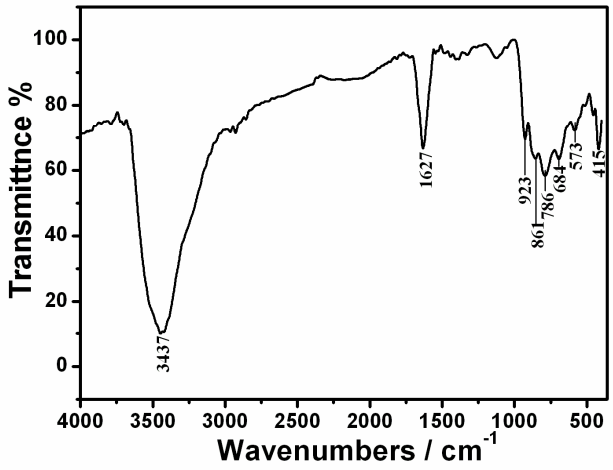



Fig. 1. IR spectrum of $Na_7[CoW_{11}O_{39}Cd(H_2O)]\cdot 12H_2O$.

**XRD**

X-ray diffraction pattern of $Na_7[CoW_{11}O_{39}Cd(H_2O)]\cdot 12H_2O$ powdered Sample obtained at room temperature is shown in Fig.2. The compound has distinct characteristic diffraction peaks at the 2θ angle of $7^o$–$10^o$,$16^o$–$22^o$,$25^o$–$30^o$,$32^o$–$38^o$, The positions and intensities of the main peaks are similar to those expected for the Keggin structure. Combined with IR, it can be considered that $Na_7[CoW_{11}O_{39}Cd(H_2O)]\cdot 12H_2O$ possesses the Keggin structure [13–15].

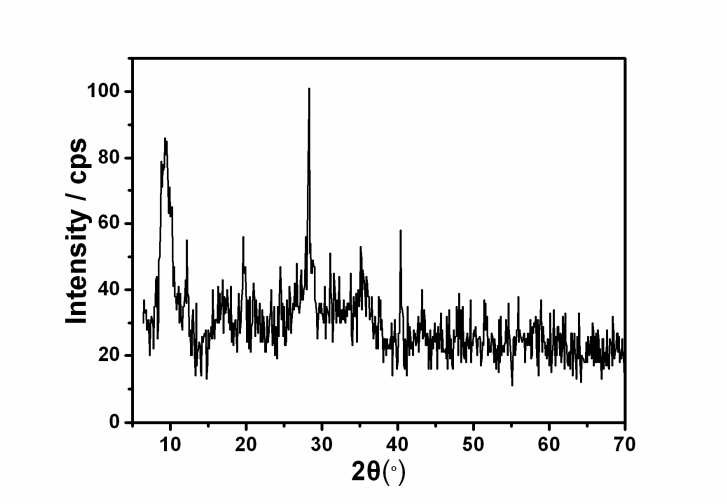



Fig. 2. XRD pattern of $Na_7[CoW_{11}O_{39}Cd(H_2O)]\cdot 12H_2O$.

**Thermal Stability**

TG-DTA curves of $Na_7[CoW_{11}O_{39}Cd(H_2O)]\cdot 12H_2O$ is shown in Fig. 3. The TG curve can show the weight loss process of a heteropoly compound. The TG curve shows that the total percent of weight loss is 7.12%, which illustrates that there is three steps of weight loss. The first is the loss of 10 molecules of zeolite water from room temperature to 180ºC, the second is the loss of 2 molecules of composition water from 181ºC to 308ºC, the third is the loss of 1 molecule of structural water from 308ºC to 726ºC. Furthermore, a strong exothermic peak appears at 370ºC in the DTA curve, which is considered to be the decomposition temperature of the compound [16–18]. A prominent endothermic peak appears at 726ºC in the DTA curve, which indicates the decomposition product melted.

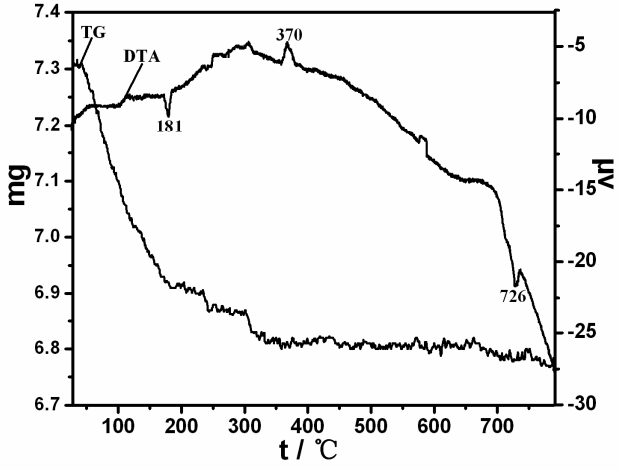



Fig. 3. TG-DTA curve of $Na_7[CoW_{11}O_{39}Cd(H_2O)]\cdot 12H_2O$.

**XPS**

XPS is one of common techniques on surface analysis, which can determine the elements of the materials and also can give the information of the elements' chemical states [19]. To understand the elements consisting of the samples,XPS analysis are conducted on the the sample. The XPS total spectra of $Na_7[CoW_{11}O_{39}Cd(H_2O)]\cdot 12H_2O$ is shown in Fig. 4. It can be seen that , there are characteristic peaks of tungsten, Cobaltum, cadmium, sodium, and Oxygen in the spectral graph. The calculation result of percentage composition of the product is consistent with ICP result.

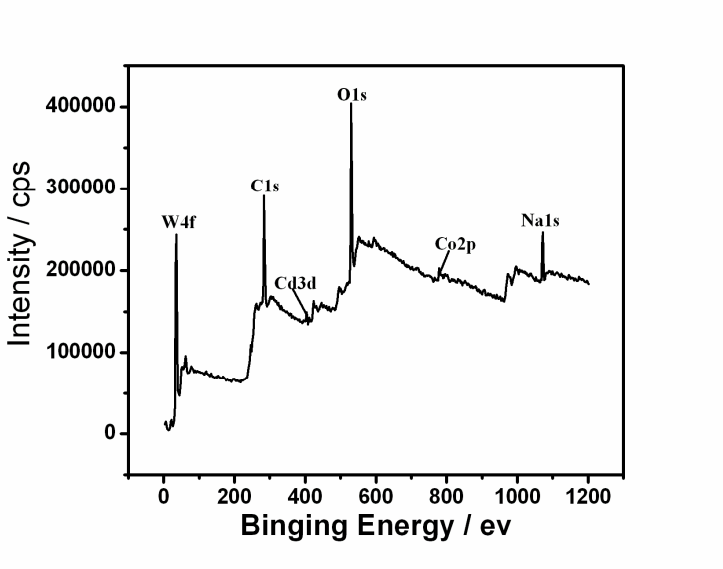



Fig. 4. XPS total spectra of $Na_7[CoW_{11}O_{39}Cd(H_2O)]\cdot 12H_2O$

**Conductivity**

The conductivity of the compound is measured by four-probe method at room temperature and different measuring temperatures. The electric conductivities of the sample are $\sigma = 4.87\times10^{-4}$ S·cm$^{-1}$ at room temperature. The compound of $Na_7[CoW_{11}O_{39}Cd(H_2O)]\cdot 12H_2O$ is a new solid high-proton conductor. And the conductivity of the compound depends on the number of water molecules. The changes of the electrical con ductivity with the increased temperatures meet the Arrhenius equation $\ln\sigma = -Ea / RT$ [20]. Fig.5 shows the Arrhenius plot. From the slope, we can calculate the activation energy of proton conduction, By using a curve-ftting algorithm, the activation energies (Ea) of the compound is 15.31 kJ·mo1$^{-1}$, In the range of 20ºC–58ºC, the conductivity of $Na_7[CoW_{11}O_{39}Cd(H_2O)]\cdot 12H_2O$ is increased with an increase in temperature.

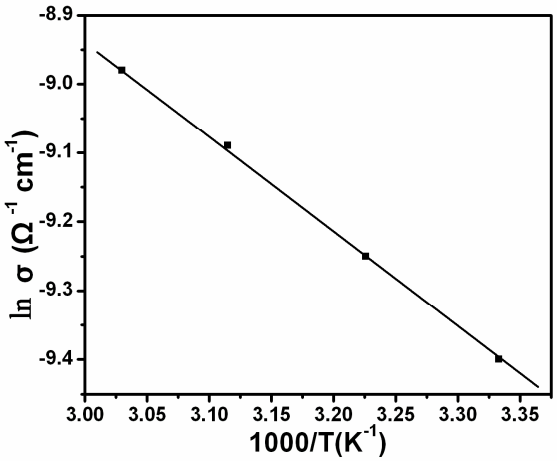



Fig .5. Arrhenius plot for $Na_7[CoW_{11}O_{39}Cd(H_2O)]\cdot 12H_2O$.

**Conclusion**

In this paper, we report $Na_7[CoW_{11}O_{39}Cd(H_2O)]\cdot 12H_2O$, a new excellent solid high-proton Conductor , was prepared and characterized for the first time. The IR and XRD indicate that its structure is Keggin structure. TG curve shows that there are three steps of weight loss. DTA curve shows that the thermal stability of the compound is higher than that of $H_6CoW_{12}O_{40}$ (320ºC).We

determined the conductivity of $Na_7[CoW_{11}O_{39}Cd(H_2O)]\cdot 12H_2O$ by four-electrode method, its proton conductivity is $4.87\times10^{-4}$ $S\cdot cm^{-1}$ at room temperature (27ºC), and in the range of 20ºC–58ºC, the conductivity of $Na_7[CoW_{11}O_{39}Cd(H_2O)]\cdot 12H_2O$ is increased with an increase in temperature.

**Acknowledgements**

This work was financially supported by the Science and Technology Foundation of Office of Education of Heilongjiang Province (No. 12521360).

**References**

[1] U. Kortz, M.G. Savelieff, F.Y.A. Ghali, L.M. Khalil, S.A. Maalouf, D.I. Sinno, Angew. Chem. Int. Ed. 41 (2002) 4070–4073.

[2] L.C.W. Baker, D.C. Glick, Chem. Rev. 98 (1998) 3–49.

[3] P. Gouzerh, A. Proust, Chem. Rev. 98 (1998) 77–111.

[4] P.J. Hagrman, R.C. Finn, J. Zubieta, Solid State Sci. 3 (2001) 745–774.

[5] E.B.Wang, C.W. Hu, Introduction of Polyacid Chemistry, Chemical Industry Press, Beijing, 1998, pp. 215–226.

[6] G.Alberti, M.Casciola, Solid State Ionics. 145(2001)249–255.

[7] Q.Y. Wu, X.G. Sang, F.Shao, W.Q. Pang, Mater. Chem. Phys. 92(2005)16–20

[8] Q.Y. Wu, E.B. Wang, J.F. Liu, Polyhedron. 12 (1993) 2563–2568.

[9] P.A. Jalil, N. Tabet, M. Faiz, N.M. Hamdan, Z. Hussain, Appl. Catal. A: Gen. 257 (2004) 1– 6.

[10] B.B. Zhou, Y.D. Wei, Z.H. Li, Y.R. Guo, J. Chin. Rare Earth Soc.20 (2002) 83– 87.

[11] V.P. Tolstoy, L.B. Gulina, G.S. Korotchenkov, V.I. Brynsari, Appl. Surf. Sci. 221 (2004) 197–202.

[12] Q.Y. Wu, G.Y. Meng, Mater. Res. Bull. 35 (2000) 85–91.

[13] Z.H. Li, Y.D. Wei, B.B. Zhou, J.Meng, Y.R.Guo, Z..Lv, J. Chin. Inorg. Chem. 19 (2003) 1053–1058.

[14] Y.P. Wang, B.B. Zhou,Y.L. Liu, J. Alloys Compd. 463 (2008) 333–337

[15] Q.Y. Wu, X.G. Sang, Y.C. He, X. Li, Mater. Lett. 57 (2003) 4028–4032.

[16] Z.P. Wang, J.Y. Nu, L.Xu, Acta Chim. Sin. 53 (1995) 757–764.

[17] A.V.Ivanov, T.V.Vasina,V.D. Nissenbaum, L.M.Kustov, M.N. Timofeeva, J.I. Houzvicka, Appl. Catal. A: Gen. 259 (2004) 65–72.

[18] Q.Y.Wu, S.K.Wang, D.N. Li, X.F.Xie,I norg. Chem. Commun. 5(2002) 308–311

[19] Z.F. Li, J. Sun, L.P.You,Y.X.Wang, J.H. Lin, J. Alloys Compd. 379 (2004) 117–121.

[20]A.S. Nowick, in: G.E.Murch, A.S.Nowick(Eds.), Diffusionin Crystalline Solids, Academic Press, New York, 1984, pp. 143–151.

# CHAPTER 4:

# Nano-Scale and Amorphous Materials

*Advanced Materials Research Vol. 937 (2014) pp 231-236*
*© (2014) Trans Tech Publications, Switzerland*
*doi:10.4028/www.scientific.net/AMR.937.231*

# Synthesis of $Co_3O_4$ Multilayer Nanosheet Material and Its Promising Gas Sensing Property

Ming-Li YIN[1,2,a]*, Sheng-Zhong LIU[2,b]

[1]School of Science, Xi'an Technological University, Xi'an 710032, PR China

[2]School of Materials Science & Engineering, Shaanxi Normal University, Xi'an 710062, China

[a]xatuyml@whu.edu.cn, [b]email:liusz@snnu.edu.cn

*Corresponding author:Ming-Li YIN

**Keywords:** $Co_3O_4$, p-type, nanosheet, gas sensor.

**Abstract.** $Co_3O_4$ multilayer nanosheets were synthesized by a hydrothermal method and a post annealing treatment process. The effect of solution concentration and ratio on the morphology of $Co_3O_4$ precursor was studied. The crystalline structure, morphology and elemental composition of $Co_3O_4$ multilayer nanosheets were characterized by X-ray diffraction, scanning electron microscopy and X-ray photoelectron spectroscopy technologies. When exposed to reducing gas such as ethanol, resistance of $Co_3O_4$ multilayer nanosheet sensor increases quickly, demonstrating that the $Co_3O_4$ multilayer nanosheets are p-type conductivity. For 100 ppm alcohol at 240 ° C, the sensor response is as high as 32, indicating that the powder of $Co_3O_4$ multilayer nanosheets is a very promising low-powder gas sensing material.

## Introduction

$Co_3O_4$, as an important p-type semiconductor oxide material with excellent electronic, optical and magnetic properties, is expected to find applications in catalysis [1], Li-ion rechargeable batteries [2], supercapacitors [3], black ceramic pigments [4], electrochromic device [5], data storage [6] and solid-state sensors [7], etc. A range of techniques have been attempted in synthesis of $Co_3O_4$ micro/nanomaterials. Among them, successful ones include thermal-decomposition [8], hydrothermal or hydrothermal [9-10], electrospinning [7], micro-emulsion [11] and sol–gel processes [12]. Resultant products have exhibited variety of micro/nanostructures including nanowire [2], nanorods [13], nanotubes [14], nanosphere [15], nanosheets [16] and nanofibers [7], and so on.

In a p-type semiconductor material, holes are accumulated at surface as electrons are preferentially extracted by oxygen acceptor [7]. When exposed to reducing gas atmosphere, sensor resistance increases due to recombination of electrons and holes. This gas sensing characteristic is exactly opposite to its n-type counterpart. Yoon et al. reported their study on highly sensitive and selective $Co_3O_4$ nanofiber sensors [9]. They found that upon annealing at 500 °C, $Co_3O_4$ nanofibers demonstrated high response of 85.3 to 100 ppm ethanol at a fairly low temperature of 267 °C. Using $Co_3O_4$ nanorods, Patil et al. prepared a highly sensitive and fast responding carbon monoxide (CO) sensor, showing very high gas response of ca. 6.55 toward 50 ppm CO gas at 250 °C [17]. Park et al. synthesized $Co_3O_4$ hollow nanospheres using a hydrothermal synthesis method and fabricated sensors for volatile organic compounds (VOC) with a response of 6.3 to 1000 ppm ethanol vapor [18].

We present a hydrothermal synthesis and post annealing treatment process for $Co_3O_4$ multilayer nanosheets. It was found that morphology of the $Co_3O_4$ precursors could be tailored by varying the nutrient concentrations. The $Co_3O_4$ multilayer nanosheets show p-type conductivity. The sensors fabricated exhibit relatively high gas response, fast response and recovery, taking into account that $Co_3O_4$ is p-type semiconductor materials.

## Experimental

All major chemicals used are AR grade from Beijing Chemicals Co. Ltd. Multilayer sheet-like $Co_3O_4$ precursors were prepared by a hydrothermal synthesis process. In a typical procedure, nutrient solutions were prepared by mixing 200 ml $Co(NO_3)_2$ and 200 ml hexamethylene tetramine (HMTA) aqueous solutions with different mole ratio (1:1, 2:3 and 1:2). For each nutrient, 400 ml starting solution, in 500 ml beaker covered with plastic wrap, was put into a blast oven at 90 °C. After reaction for 4 hours, the solution was cooled down to room temperature. Pink precipitate was collected from the beaker, washed using distilled water and anhydrous ethanol for 5 times. Finally, the precipitates ($Co_3O_4$ precursors) were dried at 70 °C for 12 hours. Black $Co_3O_4$ powders were obtained after the precursors annealed at 300 °C for 1 hour.

Crystal structure of the samples were characterized by a DX-2700 X-ray diffractometer (XRD) using Cu Kα radiation (λ = 0.15418 nm) with 2θ range of 10–70°. The morphologies of the samples were characterized on a FEI Quanta 200 scanning electron microscopy (SEM) operated at 20 kV. Surface elemental analysis was performed on an AXIS ULTRA X-ray photoelectron spectroscopy (XPS) instrument using monochromatic Al Kα X-ray source.

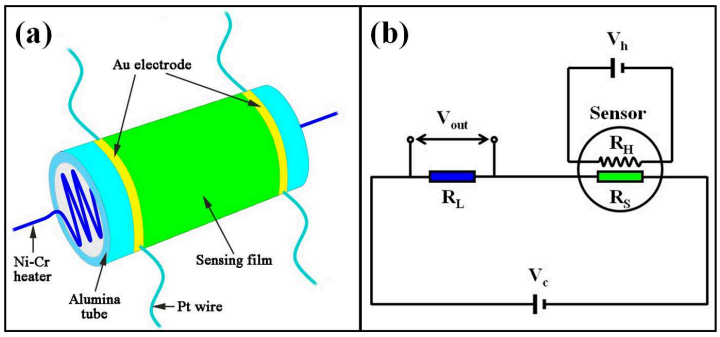



Fig. 1. (a) An illustration of gas sensor structure and (b) a scheme of measuring electric circuit with photograph of a sensor.

For device fabrication, a proper amount of $Co_3O_4$ powder was ground with a few drops of terpineol in an agate mortar to form slurry. The slurry was then coated onto an alumina tube with an Au terminal incorporated with two Pt wire leads on each end. The coating was dried by a hair dryer for a few minutes and then was put into a Muffle furnace for 20 hours of aging at 300 °C. A Ni–Cr wire coil, set in the tube, was employed as a heater to control working temperature. Sensor performance was tested on a WS-30A gas sensitivity instrument (Wei Sheng Electronics Co., Ltd., China) with a test chamber of 30L in volume and the circuit voltage ($V_c$) was set at 5 V. Out voltage ($V_{out}$) signal was recorded at the terminal of a standard resistor ($R_L$: 470 KΩ) connected in series with the gas sensor. Fig. 1(a) shows an illustration of the sensor, and Fig. 1(b) is the measuring circuit. The sensor response (S) is defined as Rg/Ra in reducing gas atmosphere, where Ra and Rg are resistance of the gas sensor in air and in testing gas atmosphere, respectively. The response and recovery time were defined as the time taken by the gas sensor to achieve 90% of the entire voltage change for target gas adsorption and desorption, respectively.

## Results and Discussion

Fig. 2 shows XRD patterns of the $Co_3O_4$ precursors prepared using 10 and 15 mM of $Co(NO_3)_2$ and HMTA solutions in 1:1 volume ratio and the corresponding $Co_3O_4$ multilayer nanosheets (labeled as a1). All diffraction peaks of a1 can be indexed to pure cubic $Co_3O_4$ (JCPDS card no. 76-1802). No impurities peaks were observed from the XRD pattern of a1, indicating the single-phase of $Co_3O_4$. The peak intensity of a1 is significantly weaker than its precursor, which possibly because the crystal structure of the precursor was damaged by the annealing process. Fig. 3 shows low and high magnification of SEM images of the $Co_3O_4$ precursors in Fig. 2. The precursors were composed of multilayer nanosheets and have monodisperse size of about 4.2 μm in diameter.

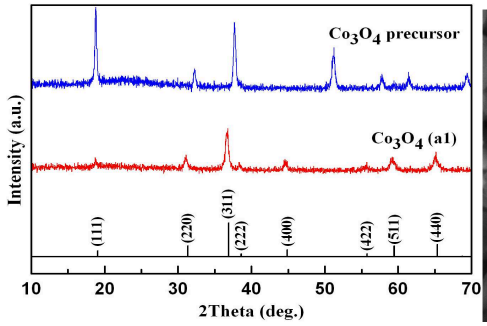



Fig. 2. XRD patterns of $Co_3O_4$ precursors using 10 and 15 mM of $Co(NO_3)_2$ and HMTA solutions in 1:1 volume ratio and the corresponding $Co_3O_4$ multilayer nanosheets (a1).

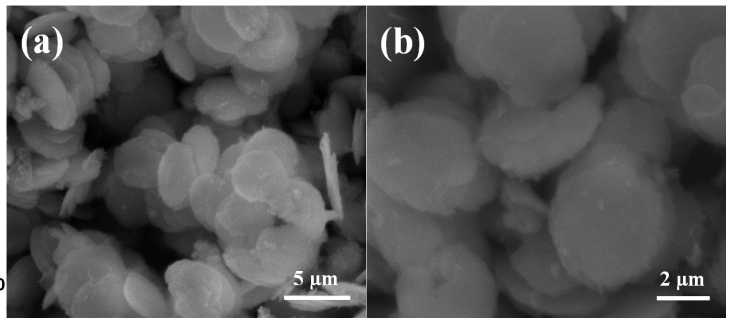



Fig. 3. Low (a) and high (b) magnification of SEM images of $Co_3O_4$ precursors prepared using 10 and 15 mM of $Co(NO_3)_2$ and HMTA solutions in 1:1 volume ratio.

When concentration of the nutrients ($Co(NO_3)_2$ and HMTA) doubled from that of $Co_3O_4$ precursors in Fig. 3, the resultant sample displays a multi-layer microstructure with an average diameter of 4.7 μm (Fig. 4a), moreover, the layer spacing is significantly larger and some floc were mixed in the sample. When concentration of the nutrients increased to 5 times, the resultant sample shows more complicated structures with apparent size distribution and flower-like morphology (Fig. 4b).

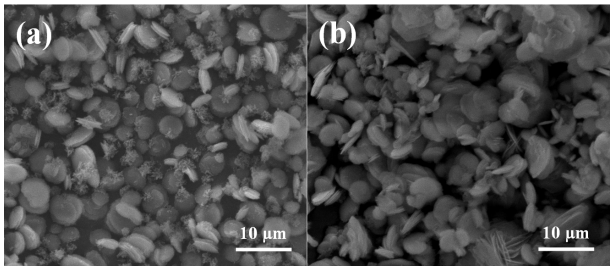



Fig. 4. SEM images of $Co_3O_4$ precursors prepared using (a) 20 and 30 mM and (b) 50 and 75 mM of $Co(NO_3)_2$and HMTA solutions in 1:1 volume ratio.

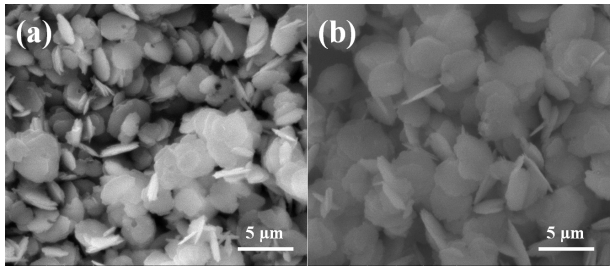



Fig. 5. SEM images of $Co_3O_4$ precursors prepared using (a) 10 and 10 mM and (b) 10 and 20 mM of $Co(NO_3)_2$and HMTA solutions in 1:1 volume ratio.

The influence of the HMTA solution concentration on the morphology of the $Co_3O_4$ precursors was also studied. Fig. 5(a) shows SEM images of $Co_3O_4$ precursors prepared using 10 and 10 mM of $Co(NO_3)_2$ and HMTA solutions in 1:1 volume ratio. The resultant sample also shows apparent size distribution. Non-circular morphology and agglomeration phenomena were observed. When the HMTA solution concentration increased to 20 mM while keeping other conditions unchanged, the resultant sample exhibited similar morphology with the sample prepared with 10 mM of HMTA solution (Fig.5b). However, the agglomeration phenomena significantly reduced.

Fig 6(a) shows Co 2p XPS spectra of a1. As can be seen, there are two main photoelectron peaks centered at 779.8 and 794.8 eV, corresponding to electron states of Co $2p_{3/2}$ and Co $2p_{1/2}$, respectively, of the $Co_3O_4$ phase [19]. Each main peak has a shake-up satellite peak, centered at 790.2 and 804.5 eV, respectively, which further confirmed the formation of $Co_3O_4$ [20-21]. The O 1s spectra of a1 and its deconvoluted peaks using Gaussian distribution were shown in Fig. 6(b). The peak centered at 529.9 eV is in good agreement with $O^{2+}$ in $Co_3O_4$, which is attributed to Co-O bond of pure $Co_3O_4$ [22]. The peak centered at 531.2 eV is associated with –OH (hydroxyl) adsorbed on the surface of the sample [23] . The later peak has a relatively large area, indicating that there are abundant adsorption sites on the surface of the sample.

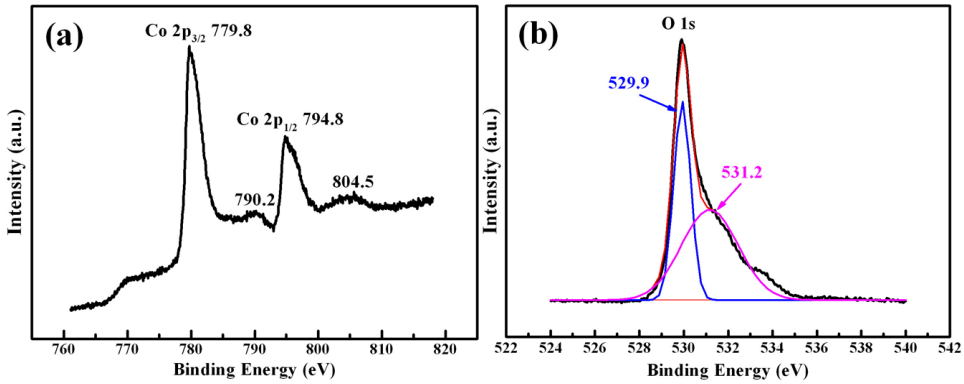



Fig. 6. XPS of a1: (a) Co 2p and (b) O 1s spectra.

Working temperature has great impact on the sensor response. The transient response and recovery curves of $Co_3O_4$ multilayer nanosheet sensor (labeled as S1) toward 100 ppm ethanol at different working temperature were shown in Fig. 7(a). The optimum working temperature was determined to be 240 °C. Fig. 7(b) shows response of S1 toward different concentrations of alcohol at the optimum working temperature. The response is 22, 32 and 42 for 50, 100 and 200 ppm alcohol, respectively, fairly high among p-type sensors, indicating that $Co_3O_4$ multilayer nanosheets can be a good candidate material in gas sensors. The inset shows a photograph of S1.

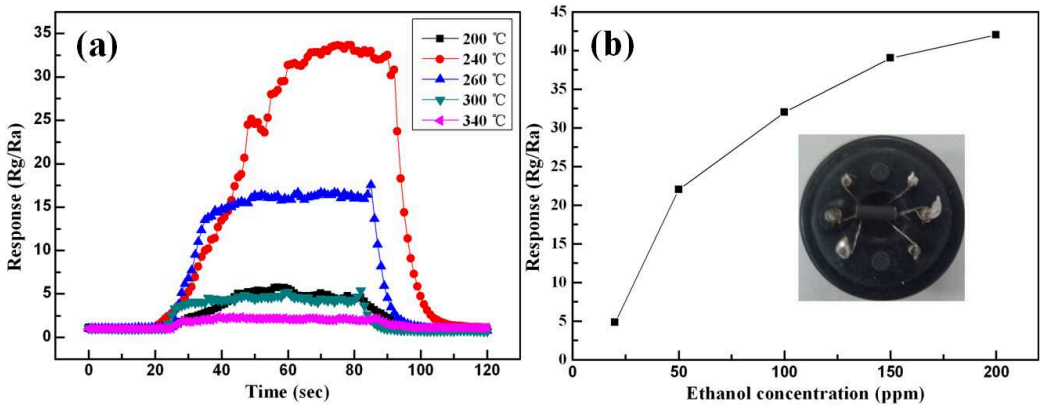



Fig. 7. (a) Transient response and recovery curves of S1 toward 100 ppm ethanol at different working temperature; (b) response of S1 toward different concentrations of ethanol at the optimum working temperature of 240 °C. The inset in Fig. 7(b) is a photograph of S1.

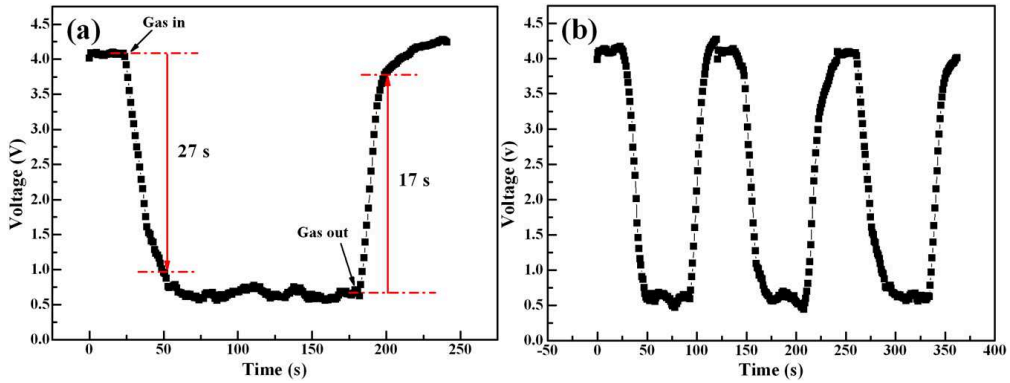



Fig. 8. Transient voltage response and recovery curves of S1 toward 100 ppm ethanol at the optimum working temperature of 240 °C: (a) single and (b) multiple testing.

Fig. 8(a) and (b) show single and multiple tests of transient voltage response curves of S1 toward 100 ppm alcohol at the optimum working temperature. As can be seen, the partial voltage of the sensor increased quickly when alcohol was introduced into the testing chamber, indicating that

resistance of the sensor increased. This is a characteristic for p-type conductivity sensor. It is well known that oxygen can be adsorbed on the surface of the sensing materials by capturing surface electrons. As a result, holes accumulated near the surface of p-type materials [7]. Upon exposed to reducing gas, oxidation reaction occurs, leading to release of the captured electrons to the conduction of the sensing materials. The released electrons then recombine with holes, leading to the increased resistance of p-type materials. The sensor response and recovery time are measured to be 27 and 17 seconds respectively (Fig. 8a), comparable to that of other groups [7, 17-18]. It was also found that the on and off response of S1 could be repeated. The sensor shows good stability and repeatability, and has no obvious decline after multiple tests, as can be seen in Fig. 8(b). The above results clearly verify that, as a p-type oxide semiconductor, $Co_3O_4$ multilayer nanosheet powder is a promising gas sensing material. It is well known that $Co_3O_4$ is a good candidate for detecting the flammable and explosive CO and $H_2$ gases [24-25]. The relatively low operation temperature is in favor of reducing the energy consumption and improving the suitability of $Co_3O_4$ multilayer nanosheet sensor in some particular situations.

## Conclusion

$Co_3O_4$ multilayer nanosheets were synthesized by a hydrothermal method and the subsequent annealing processing. It was found that the nutrient concentrations have great impact on morphologies of $Co_3O_4$ precursors. Upon exposed to reducing gas atmosphere, $Co_3O_4$ multilayer nanosheet sensor shows p-type conductivity. The sensor showed a fast response and recovery process with good stability and repeatability at low temperature of 240 °C. Its response reached 22, 32 and 42 toward 50, 100 and 200 ppm ethanol gas, respectively. These results demonstrate that $Co_3O_4$ multilayer nanosheet is a good candidate material for gas sensors.

## Acknowledgement

We acknowledge financial support from Chinese National University Research Fund (GK261001009), Shaanxi Normal University, Xi'an, China and China Postdoctoral Science Foundation (No. 2013M542324).

## Reference

[1] X. W. Xie, Y. Li, Z. Q. Liu, M. Haruta, W. J. Shen, Low-temperature oxidation of CO catalysed by $Co_3O_4$ nanorods, Nature 458 (2009) 746–749.

[2] X. Y. Yao, X. Xin, Y. M. Zhang, J. Wang, Z. P. Liu, X. X. Xu, $Co_3O_4$ nanowires as high capacity anode materials for lithium-ion batteries, J. Alloys. Compd. 521 (2012) 95–100.

[3] G. Wang, H. Liu, J. Horvat, B. Wang, S. Qiao, J. Park, H. Ahn, Highly Ordered Mesoporous Cobalt Oxide Nanostructures: Synthesis, Characterisation, Magnetic Properties, and Applications for Electrochemical Energy Devices, Chem. Eur. J. 16 (2010) 11020–11027.

[4] W. Y. Li, L. N. Xu, J. Chen, $Co_3O_4$ nanomaterials in lithium-ion batteries and gas sensors, Adv. Funct. Mater. 15 (2005) 851–857.

[5] T. Maruyama, S. Arai, Electrochromic properties of cobalt oxide thin films prepared by chemical vapor deposition, J. Electrochem. Soc. 143 (1996) 1383-1386.

[6] Q. Yuanchun, Z. Yanbao, W. Zhishen, Preparation of cobalt oxide nanoparticles and cobalt powders by solvothermal process and their characterization, Mater. Chem. Phys. 110 (2008) 457–462.

[7] J. W. Yoon, J. K. Choi, J. H. Lee, Design of a highly sensitive and selective $C_2H_5OH$ sensor using p-type $Co_3O_4$ nanofibers, Sens. Actuators B 161 (2012) 570–577.

[8] F. Mohandes, F. Davar, M. Salavati-Niasari, Preparation of $Co_3O_4$ nanoparticles by nonhydrolytic thermolysis of $[Co(Pht)(H_2O)]_n$ polymersJ. Magn. Magn. Mater. 322 (2010) 872-877.

[9] H. J. Yan, X. H. Xie, K. W. Liu, H. M. Cao, X. J. Zhang, Y. L. Luo, Facile preparation of $Co_3O_4$ nanoparticles via thermal decomposition of $Co(NO_3)_2$ loading on $C_3N_4$, Powder Technol. 221 (2012) 199–202.

[10] J. Ma, S. Zhang, W. Liu, Y. Zhao, Facile preparation of $Co_3O_4$ nanocrystals via a solvothermal process directly from common $Co_2O_3$ powder, J. Alloys Compd. 490 (2010) 647-651.

[11] G. M. Bai, H. X. Dai, J. G. Deng, Y. X. Liu, F. Wang, Z. X. Zhao, W. G. Qiu, C. T. Au, Porous $Co_3O_4$ nanowires and nanorods: Highly active catalysts for the combustion of toluene, Appl. Catal. A 450 (2013) 42– 49.

[12] N. R. E. Radwan, M. S. El-Shall, H. M. A. Hassan, Synthesis and characterization of nanoparticle $Co_3O_4$, CuO and NiO catalysts prepared by physical and chemical methods to minimize air pollution, Appl. Catal. A 331 (2007) 8.

[13] F. Teng, M. D. Chen, G. Q. Li, Y. Teng, T. G. Xu, Y. C. Hang, W. Q. Yao, S. Santhanagopalan, D. D. Meng, Y. F. Zhu, High combustion activity of CH4 and catalluminescence properties of CO oxidation over porous $Co_3O_4$ nanorods, Appl. Catal. B 110 (2011) 133–140.

[14] J. Xu, L. Gao, J. Y. Cao, W. C. Wang, Z. D. Chen, Preparation and electrochemical capacitance of cobalt oxide ($Co_3O_4$) nanotubes as supercapacitor material, Electrochim. Acta 56 (2010) 732-736.

[15] N. Jayaprakash, W. D. Jones, S. S. Moganty, L. A. Archer, Composite lithium battery anodes based on carbon@$Co_3O_4$ nanostructures: Synthesis and characterization, J. Power Sources 200 (2012) 53–58.

[16] S. S. Lu, X. Y. Jing, J. Y. Liu, J. Wang, Q. Liu, Y. H. Zhao, S. Jamil, M. L. Zhang, L. H. Liu, Synthesis of porous sheet-like $Co_3O_4$ microstructure by precipitation method and its potential applications in the thermal decomposition of ammonium perchlorate, J. Solid State Chem. 197 (2013) 345–351.

[17] D. Patil, P. Patil, V. Subramanian, P. A. Joy, H. S. Potdar, Highly sensitive and fast responding CO sensor based on $Co_3O_4$ nanorods, Talanta 81 (2010) 37–43.

[18] J. Park, X. P. Shen, G. X. Wang, Solvothermal synth esis and gas-sensing performance of $Co_3O_4$ hollow nanospheres, Sens. Actuators B 136 (2009) 494–498.

[19] M. Oku, Y. Sato, In-situ X-ray photoelectron spectroscopic study of the reversible phase transition between CoO and $Co_3O_4$ in oxygen of $10^{-3}$ Pa, Appl. Surf. Sci. 55 (1992) 37–41.

[20] X. Yao, X. Xin, Y. Zhang, J. Wang, Z. Liu, X. Xu, $Co_3O_4$ nanowires as high capacity anode materials for lithium ion batteries, J. Alloys Compd. 521 (2012) 95–100.

[21] T. He, D. R. Chen, X. L. Jiao, Y. L. Wang, Y. Z. Duan, Solubility-controlled synthesis of high-quality $Co_3O_4$ nanocrystals, Chem. Mater. 17 (2005) 4023–4030.

[22] K. G. Chandrappa, T. V. Venkatesha, Generation of $Co_3O_4$ microparticles by solution combustion method and its Zn–$Co_3O_4$ composite thin films for corrosion protection, J. Alloys Compd. 542 (2012) 68–77.

[23] Z. Dong, Y. Fu, Q. Han, Y. Xu, H. Zhang, Synthesis and Physical Properties of $Co_3O_4$ Nanowires, J. Phys. Chem. C 111 (2007) 18475–18478.

[24] U. S. Choi, G. Sakai, K. Shimanoe, N. Yamazoe, Sensing properties of $SnO_2$–$Co_3O_4$ composites to CO and $H_2$, Sens. Actuator B 98 (2004) 166–173.

[25] R. J. Wu, C. H. Hu, C. T. Yeh, P. G. Su, Nanogold on powdered cobalt oxide for carbon monoxide sensor, Sens. Actuator B 96 (2003) 596–601.

*Advanced Materials Research Vol. 937 (2014) pp 237-243*
*© (2014) Trans Tech Publications, Switzerland*
*doi:10.4028/www.scientific.net/AMR.937.237*

# Influence of Ultrasonic Time on the Preparation and Properties of $LaCoO_3$ Nano Particles

Jie DONG[1,a],Hong-fang SHEN[1,2,b,*],Yan-min WANG[2,c], You-jun LU[1,d], Guo-li FANG[1,e]

[1]Materials Science and Engineering, Beifang University of Nationalities, Yinchuan, Ningxia, 750021, China

[2]Materials Science and Engineering, South China University of Technology, Guangzhou, Guangdong, 510641, China

[a]jiedongdj@gmail.com, [b]wenzishen@gmail.com, [c]wangym@scut.edu.cn, [d]youjunlu518@hotmail.com, [e]fangguoli999@163.com

*Corresponding author

**Keywords:** Ultrasonic assistance, perovskite structure, $H_2$-TPR, decolorization efficiency

**Abstract:** Ultrasonic assisted citrate sol-gel is used to synthesis $LaCoO_3$ (LCO) ultrafine particles. The influence of ultrasonic time on the properties of the samples was investigated. TG-DSC is applied to determine the phase transition of LCO gel precursor. XRD, FESEM and $H_2$-TPR were applied to characteristic crystalline phase structure, morphology, thermal-stability of LCO samples. The results indicated that LCO particles exhibit a well-formed polycrystalline rhombohedral distorted perovskite structure, and their particles are well-decentralized, in a smaller size and better dispersivity as the increasing of ultrasonic time ranged from 0min to 60min. $H_2$-TPR implied that ultrasonic assistance can lower the reduction temperature of the product in the zone of low temperature and raise the temperature in the zone of high temperature. Ultrasonic assistance is not conductive to increase organic dye decolorization efficiency of LCO powders in darkroom when taking methyl orange and gold orange II as targeted dye.

## Introduction

Kubo and his group member proposed quantum confinement theory of ultrafine particle in 1962 [1], which promoted experimental physicists to seek after nano-scale micro particle. Since nano materials have the fundamental characteristics of small-size effect, surface effect, quantum size effect and quantum tunneling effect et al, which cause that nano particles and nano bulk materials exhibit many unique physical and chemical properties followed with some abnormal phenomenon. For example, following with the size of gold particles decreasing to nano-scale, the melting point of the gold will also reduce. Just because of the special natures of nano materials, they exhibit wide application prospects in the fields of electronic information, bio-medicine, energy environmental, military and outer space et al.

Among nano materials, perovskite compound oxide is one kind of very important materials because of its unique crystal structure, which decides that it exhibits many special physiochemical properties, can be widely used as superconducting material, ferroelectrics, piezoelectrics, thermistance and oxygen electrode et al, and occupies a high place in the area of material science and catalysis [2]. $LaCoO_3$ (LCO) is one member of the family of perovskite compound oxides and displays excellent natures of catalytic combustion [3, 4] and photocatalysis redox reaction [5-7], especially as its size reduces to the range of ultrafine. Many synthesis methods were commonly used to prepare perovskite-structure compound oxide, such as high temperature solid phase combustion, sol-gel [8-10], co-precipitation [4, 11, 12] et al. However, when using these preparation methods, targeted products will appear a certain degree of agglomeration, followed with the particle size growth. Ultrasonic cavitation is one of very effective methods for solving the phenomenon of particle agglomeration [13], and gradually developed into a novel nanofabrication technique [14, 15].

The aim of this paper is to prepare $LaCoO_3$ (LCO) nanopowders through ultrasound-assisted sol-gel method. The influence of different ultrasonic time on the characteristics of $LaCoO_3$ nanoparticles, such as structure, morphology, performance, and other effects, were also studied in the presence of ultrasonic field.

## Experimental

### Preparation of Powders

Ultrasonic assisted citrate-complex sol-gel method was used to prepare LCO nanoparticles. All the raw materials are analytically pure, obtained from Aladdin Industrial Corporation (Shanghai, China) and direct-used without further treated. Firstly, $La(NO_3)_3 \cdot 6H_2O$ and $Co(NO_3)_2 \cdot 6H_2O$ were dissolved in ultrapure water with 18.2MΩ.cm of resistivity respectively. The molar ratio of La/Co was remained at 1:1. And solution concentration was 0.5mol/L. Then two kinds of solution were mixed together and citric acid was added under magnetic stirring and mixed thoroughly. The dosage of citric acid was 1.5 times of metal ions. Next, the solution was put in an ultrasonic generator, maintained at 40 KHz, 240W; 20min. Thirdly the mixture was shifted in water-bath and stirred to react at 70ºC continuously until wet-gel was formed. Fourthly, the wet-gel was dried at 103ºC under infrared irradiation for 12h. Finally, the precursor was precalcined at 400ºC for 2h, to let the product self-ignite and burn off the organic compound in the precursor, and then calcined at 700ºC for another 4h in air muffle furnace to form perovskite compounds. For comparison, other samples of LCO were synthesized by the same method described above except for the ultrasonic assistance time, such as 0min, 40min, 60min and 80min.

### Characterization

The thermogravimetry-differential scanning calorimetry (TG-DSC) of dry gel precursor powder was performed using a NETZSCH STA 449F3 thermal analyzer, with temperature rate of 20ºC/min in $N_2$, referenced to $\alpha$-$Al_2O_3$. The crystalline phase structure was determined on the Shimadzu XRD-6000 X-ray diffractometer at 40kV, 30mA with Cu Kα radiation (1.5406Å) at a scanning rate of 0.02°/s in the 2θ range of 20-80°. $H_2$ temperature programmed reduction ($H_2$-TPR) was finished on TP-5080 full-automatically adsorption instrument (Tianjin Xianquan Industry and Trade Development Co., Ltd., China) and dosage of the sample was 50mg. The sample was pre-treated 2h. at 300ºC in $N_2$ atmosphere firstly, and then decreased to room temperature, $H_2$ with the pressure of 0.2MPa was piped in, when base line ascribed to stable, the sample was heated up to 850-900ºCat the rate of 10ºC/min. The morphology and microstructure were determined by scanning electron microscopy using a JSM-6700F (JEOL) microscope equipped with energy dispersive spectrometer (EDS).

### Decolorization Test of Organic Dye

Methyl orange and gold orange (Sinopharm Chemical Reagent Co., Ltd, Shanghai, China) was chosen as targeted dye to evaluate the decolorizing efficiency of LCO nano powder in dark room. The decolorization of targeted pollutants was carried out in XPA-7 photochemistry reaction instrument (Xujiang electromechanical plant, Jiangsu, Nanjing, China) at room temperature, in which 50mg of LCO samples was suspended in 50mL of targeted dye aqueous solution (10mg/L) without further treatment. The dispersions of LCO oxide were magnetically stirred during the decolorization process. At designated intervals, 5mL of liquid samples were withdrawn, centrifuged and filtered to remove LCO particles. The concentration of methyl orange and gold orange II was analyzed by measuring the absorbance at 464nm and 485nm respectively using a Shimadzu UV-2700 UV-Vis spectrophotometer.

## Results and Discussion

Fig. 1 shows the TG-DSC curves of the dried gel precursor powders of LCO produced by 40 min. ultrasonic assisted sol-gel. It can be seen that the mass loss is composed of four different steps with

the total mass loss of 55.31% between room temperature ($T_R$) and 463.9ºC. At $T_R$-161.8ºC, the mass loss is 4.15% due to the evaporation of water or release of some substances included in the gel, such as physically adsorbed water and some organic molecules. The exothermic reaction with a sharp weight loss of 17.56% at 161.8ºC could be due to the collapse of gel network and combustions of most of the organic materials [16].

The endothermic peak at 434.9ºC results from the decomposition of the oxygen group carbonate, which is incomplete combustion production of the citric acid and the combustion of the La citrates and Co citrates [17]. There is a slight loss process at the temperature higher than 463.9ºC, which is mainly caused by the desorption of residual hydroxyl (OH) group. During this course, the slight exothermic process can be seen, which is possibly attributed to the gradual crystallization of LCO.

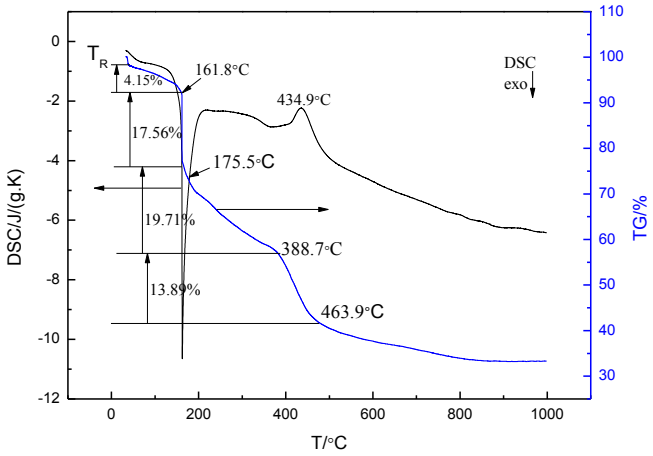



Fig. 1. TG-DSC of the $LaCoO_3$ gel precursor ultra-sounded for 40 min

Fig. 2 presents the XRD patterns of LCO ultrafine particles synthesized under different ultrasonic time and reveals a well-formed polycrystalline rhombohedral distorted perovskite structure for all the samples regardless of the length of the ultrasonic-assisted time. No other parasitic phase or impurity phase or second phase was detectable in all of the samples. The XRD patterns also showed that the increased ultrasonic-assisted time did not have a noticeable negative effect on the crystallization of LCO, and was indexed to correspond with rhombohedral perovskite LCO phase (JCPDS No. 48-0123). When investigating the X-ray diffraction patterns, it was found that every diffraction peak of the LCO shifted to a slightly higher angle with the increasing of ultrasonic assisted time range from 0-60min (Fig. 3 (b)), and however the phenomenon was not detected when the ultrasonic assisted time was raised to 80min.

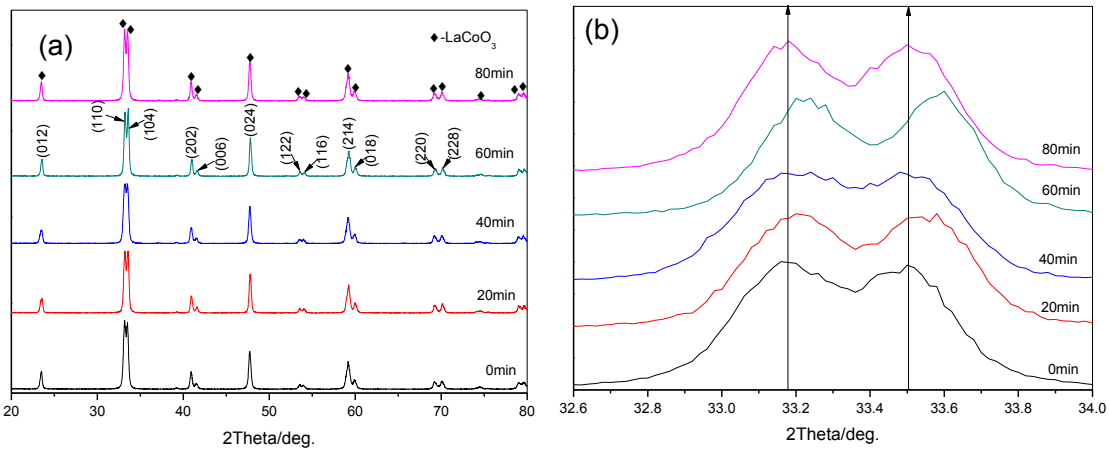



Fig. 2. XRD patterns of $LaCoO_3$ oxides ultra-sounded for different time

The unit cell data of LCO was calculated by Jade. 5 and the average lattice constants obtained are listed in table 1. It was found that the lattice constants of LCO prepared under different ultrasonic

time were a little smaller than those of the traditional thermal decomposition product (a=5.4445 Å, c=13.0936Å) (JCPDS No. 48-0123).

Table 1. Average Lattice constant of the $LaCoO_3$ sample with different Ultrasonic time

| Ultrasonic time [min] | d(110) [Å] | d(104) [Å] | Average lattice constants a [Å] (ESD) | Average lattice constants c [Å] (ESD) | Crystal Volume [$Å^3$] |
|---|---|---|---|---|---|
| 0 | 2.7100 | 2.6791 | 5.42002(0.005595) | 13.05136(0.015679) | 332.04 |
| 20 | 2.7081 | 2.6765 | 5.41624(0.006377) | 13.03644(0.016123) | 331.20 |
| 40 | 2.7104 | 2.6790 | 5.42078(0.006462) | 13.04948(0.016845) | 332.08 |
| 60 | 2.7083 | 2.6732 | 5.41668(0.007483) | 13.01250(0.017491) | 330.64 |
| 80 | 2.7109 | 2.6770 | 5.42183(0.005987) | 13.03342(0.015022) | 331.80 |

The entire datum was calculated from Jade.5, and ESD represents the echo-standard deviation.

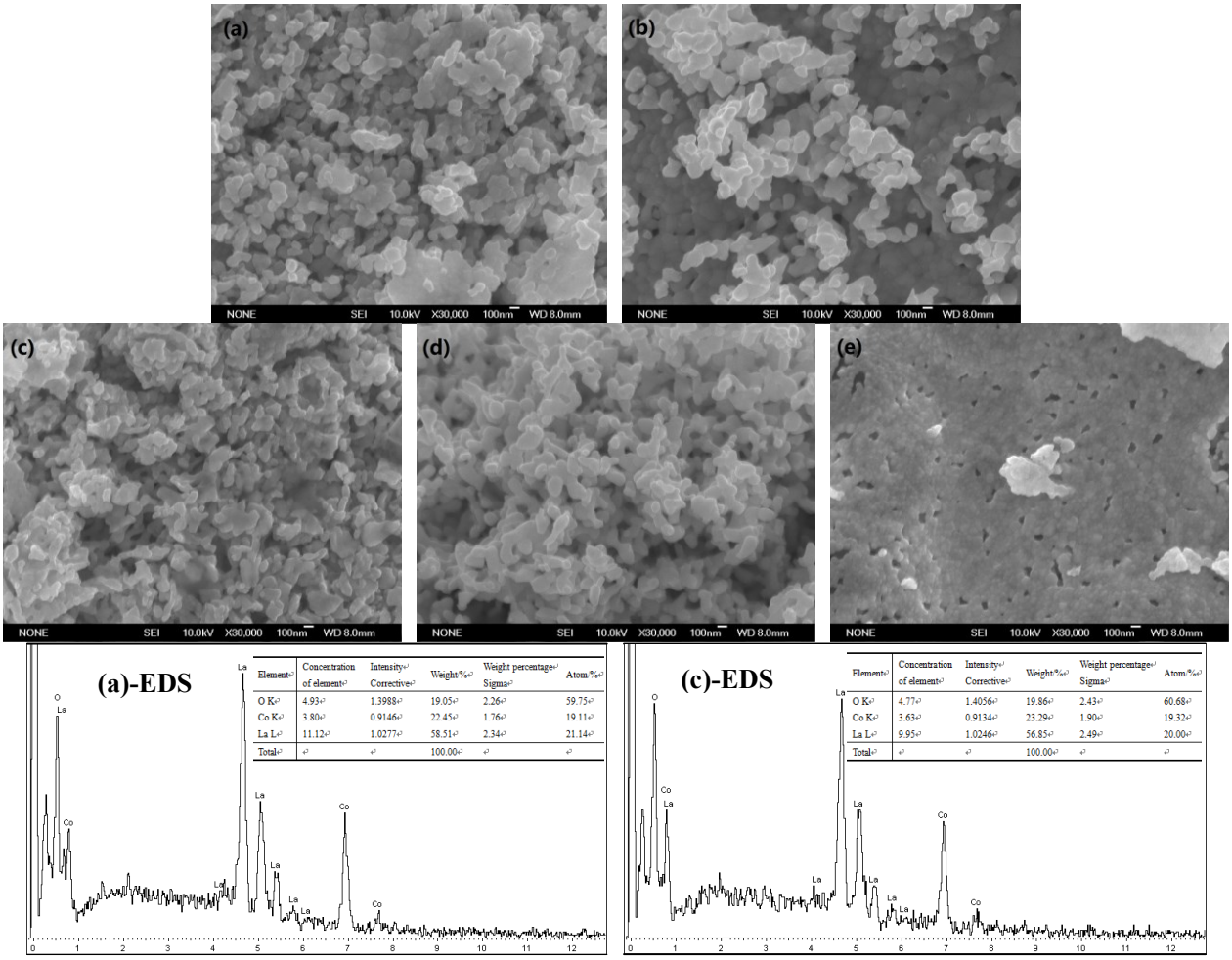



Fig. 3. SEM for $LaCoO_3$ Ultrafine particles with different Ultrasonic time ((a) 0min; (b) 20min; (c) 40min; (d) 60min; (e) 80min)

Fig. 3 is the SEM images of LCO nano particles prepared under different ultrasonic time. It showed that without ultrasonic treatment the particles appeared severe agglomeration (Fig. 3 (a)) with larger particle size after calcining, resulting in decreasing of specific surface area of the powder. With the increasing ultrasonic time from 20 min to 60 min (Fig. 3 (b-d)), particle agglomeration is significantly reduced, followed with smaller particle size and more uniform particle size distribution. When the ultrasonic time was extended to 80min (Fig. 3 (e)), particles appeared serious reunion, accompanied by sintering phenomenon, the particle size was increased, the specific surface area was significantly reduced, but the single particle size is still very small. It

implies that ultrasound not only helps to reduce the particle size and its distribution, can also cause severe particle agglomeration and coarsening [18]. Ultrasonic cavitation contribute to reduce particle size, when the ultrasonic time is too long, the particle size will be extremely small, in the subsequent sintering process, if sintered at the same temperature will be bound to cause excessive grain growth and severe sintering phenomenon. Lowering calcining temperature can effectively avoid seriously growing up together of small particles. In other words, long time ultrasonic cavitation help reduce synthesis temperature of fine particles. To a certain extent, this result has correspondence with the above XRD result. EDS patterns also show that ultrasonic assistance did not affect composition of the products.

Fig. 4 displays the $H_2$-TPR curves of LCO synthesized under different ultrasonic assisted time and reveals that all $H_2$-TPR curves of LCO samples were composed with a low temperature reduction peak and a high temperature reduction peak. The low temperature reduction peak appears at 370-405ºC and the high temperature reduction peak appears at 600-655ºC, which is showed in table 2. Low temperature reduction peaks can be identified as the peak of $Co^{3+}$ reduced to $Co^{2+}$, as well as partial $Co^{2+}$ reduced to $Co^0$, and then high temperature reduction peak is identified as the peak of $Co^{2+}$ reduced to $Co^0$ i.e. elemental cobalt [19, 20]. Reduction peak area and temperature of the $H_2$-TPR curve can reflect oxidative capacity of the sample. Larger reduction peak area and lower reduction temperature is correspondence with stronger oxidizing ability of the sample. From the $H_2$-TPR curve, we can find that at low temperature reduction zone, the ultrasonic treated samples required much more hydrogen consumption and the reduction temperature overall decreased, which implied that ultrasonic assistance can effectively decrease reduction temperature of the samples in the zone of low temperature. It is quite the opposite in the zone of high temperature. With the increase of ultrasonic assisted time, the peak temperature of the high temperature zone generally shows a rising trend. Reduction peak of all of the ultrasonic treated samples comes with a peak shoulder, and reduction temperature range expanded significantly when ultrasonic assisted time was 40min and 60min.

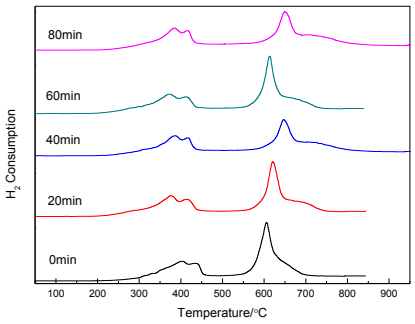



Fig. 4. $H_2$-TPR of $LaCoO_3$ prepared under different ultrasonic time

Table 2 $H_2$ consumptions of $LaCoO_3$ samples prepared under different ultrasonic assisted time

| Sample No. | 1# | | 2# | | 3# | | 4# | | 5# | |
|---|---|---|---|---|---|---|---|---|---|---|
| Ultrasonic time/min | 0 | | 20 | | 40 | | 60 | | 80 | |
| Peak Temperature/ºC | 403 | 605 | 374 | 619 | 385 | 648 | 374 | 617 | 385 | 650 |
| $H_2$ consumption /mmol/g | 2.478 | 4.241 | 2.730 | 4.155 | 2.342 | 3.616 | 2.667 | 4.050 | 2.508 | 3.900 |
| Total $H_2$ consumption /mmol/g | 6.719 | | 6.885 | | 5.958 | | 6.717 | | 6.408 | |

The decolorization efficiency of LCO samples was evaluated by decolorization experiment of methyl orange (MO) and gold orange II (GOII) under darkroom. Fig. 5 shows the decolorization curve of methyl orange taking LCO samples as decoloring agent. It can be seen that the concentration of MO decreases with the increasing of reaction time when LCO is added in MO solution. The sequence of the influence of ultrasonic time on the decolorization efficiency is 0min >

20min > 60min > 40min > 80min, i.e., decolorization efficiency of LCO samples decreased significantly at the same reaction time in the darkroom as the increasing of ultrasonic time. The result implies that ultrasonic assistance is not conductive to increase decolorization efficiency of LCO powders to MO.

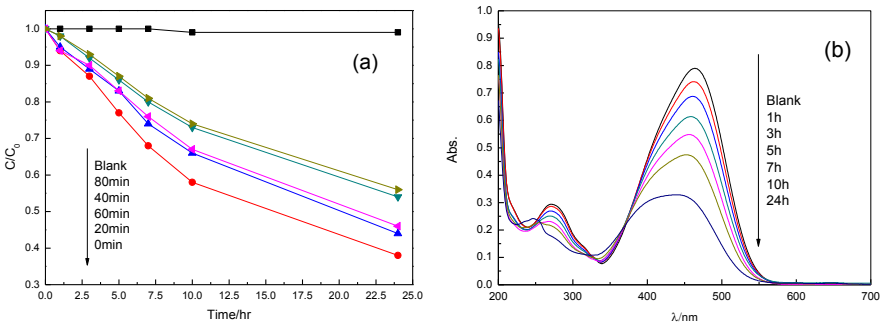



Fig. 5. (a) Darkroom decolorization efficiency of MO as a function of treatment time in the presence of the as-prepared $LaCoO_3$ under different ultrasonic time; (b) Absorbance of MO solution as a function of treatment time in the presence of $LaCoO_3$ particles without ultrasonic

In order to further study the characteristics of LCO samples, gold orange II was also chosen as targeted dye to determine its decolorization efficiency. And the trend of the influence of ultrasonic time on the decolorization efficiency of GOII in the presence of LCO samples as the function of the reaction time (Fig. 6) is as same as that of MO, i.e. 0min > 20min > 60min > 40min > 80min. In contrast, gold orange II is much easier decolorized in the presence of LCO powders in darkroom. Taking LCO powders without ultrasonic as example, the decolorization efficiency of GOII can reach to 56% after 6h treatment in the presence of LCO. However, it is 24h treatment (62% of decolorization efficiency) for MO to achieve the same decolorizing effect. The possible reason for the above phenomenon is that methyl orange and gold orange II have different surface chemical structures (Fig. 7). For gold orange II, (-OH) may be more likely to be adsorbed on the surface of LCO powders and much easier to decolorize. The optimum decolorization efficiency of GOII is 76% after 12h treatment, which implies that as the increasing of the treatment time, decolorizing speed became more and more slowly because of the saturation of dyes molecule absorbed on the surface of LCO powders.

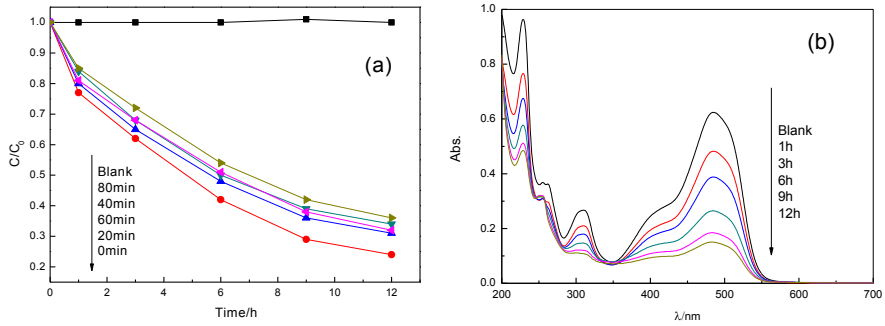
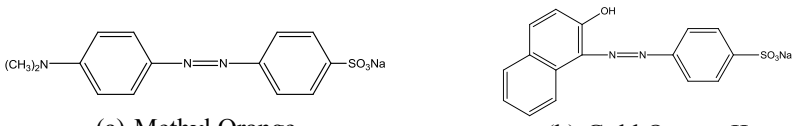



Fig. 6. (a) Darkroom decolorization efficiency of GOII as a function of treatment time in the presence of the as-prepared $LaCoO_3$ under different ultrasonic time; (b) Absorbance of GOII solution as a function of treatment time in the presence of $LaCoO_3$ particles without ultrasonic




(a)-Methyl Orange (b)-Gold Orange II

Fig. 7. Chemical formula of methyl orange and gold orange II

## Conclusion

In the conclusion, ultrasonic assisted citric sol-gel can be used to synthesis $LaCoO_3$ ultrafine particles and the XRD pattern of the samples reveals a well-formed polycrystalline rhombohedral distorted perovskite structure. Ultrasonic time does not only impact the morphology of the product but also impact the surface features of the products. As the increasing of the ultrasonic time ranged from 0min to 60min, $LaCoO_3$ particle size became smaller and dispersion became more uniform. As the ultrasonic time increased to 80min, particles appeared agglomeration and the single particle size is still very small. $H_2$-TPR implied that ultrasonic assistance can lower the reduction temperature of the product in the zone of low temperature, and raise the temperature in the zone of high temperature. Ultrasonic assistance is not conductive to increase organic dye decolorization efficiency of LCO powders when taking methyl orange and gold orange II as targeted dye.

## Acknowledgment

This work was financially supported by the National Students' Innovative Experiment (201211407007), Ningxia Scientific Research Projects (NGY2012095), the National Nature Science Funding (51262001) and the Western Light' of CAS for the talent cultivation project (Liquid microwave assisted synthesis of $Si_3N_4$-SiC-$Re_2O_3$ nano ceramic composite).

## Reference

[1] Ryogo Kubo. Journal of the Physical Society of Japan, 17, (1962): 975-986
[2] Yuanyuan Li. Huazhong University of Science & Technology, 2010 (In Chinese)
[3] ZHANG Xu-xia, XU Yan-hui, et al. Chinese Rare Earths, 2010, 31 (6): 22-26 (In Chinese)
[4] ZHOU Ying, LU Han-feng, et al. China Environmental Science, 2012, 32 (10): 1772-1777 (In Chinese)
[5] Bo Dong, Zhicheng Li, et al. Rapid Communications of the American Ceramic Society, 2010, 93 (11): 3587-3590
[6] Chunqiu Zhang, Hongcai He, et al. Ceramics International, 2013(39) : 3685-3689
[7] YANG Qiu-hua, FU Xi-xian, et al. Journal of Fuel Chemistry and Technology, 2002, 30(4): 368-371
[8] Shudan Li, Liqiang Jing, et al. Materials Resarch Bulletin, 2007 (42): 203-212
[9] ZOU Wen-jing, HAN Hui, et al. Modem Chemical Industry, 2010, 30 (Suppl.2): 144-146, 148
[10] Xinshu Niu, Honghua Li, et al. Journal of Molecular Catalysis A: Chemical, 2005 (232): 89-93
[11] Yao Genyou, Li Yanbin, et al. Chinese Journal of Rare Metals, 2007, 31 (2): 192-196 (In Chinese)
[12] Wei Zhixian, Ou Haifeng, et al. Journal of The Chinese Rare Earth Society, 2006, 24 (Suppl.): 41-44
[13] ZHU Yan-feng, LIU Wei-liang et al. Journal of Synthetic Crystals, 2013, 42(1): 172-176
[14] JIA Chao, TANK Bingtao, et al. Acta Materiae Compositae Sinica, 2012, 29 (1): 85-90
[15] YANG Qiang, HUANG Jianfeng. Chemical Industry and Engineering Progress, 2010, 29 (6): 1091-1095, 1101
[16] Hongyan Liu, Yiping Guo, Bing Guo, et al. Solid state sciences 19 (2013): 69-72.
[17] Shudan Li, Liqiang Jing, Wei Fu, et al. Materials Research Bulletin, 42 (2007): 203-212
[18] Jun Geng, Liping Jiang, et al. Science China: Chemistry, 2012, 55 (11): 2292-2310
[19] Wensheng Yao, Rijie Wang, et al. Catal. Lett., 2009 (130): 613-621
[20] Fei Ma, Lihong Huang, et al. Chinese Journal of Catalysis , 2011, 32 (6): 970-977 (In Chinese)

*Advanced Materials Research Vol. 937 (2014) pp 244-247*
*© (2014) Trans Tech Publications, Switzerland*
*doi:10.4028/www.scientific.net/AMR.937.244*

# Avoidance of Forbidden DNA Nanorobots Configurations in Patterned Immobilization of other Materials

Vladimir Popov[1,a,*]

[1] Ural Federal University, 620083, Ekaterinburg, Russia

[a]Vladimir.Popov@usu.ru

*Corresponding author

**Keywords:** Smart materials, DNA, Nanorobot, Patterned immobilization.

**Abstract.** DNA nanorobots can be applied for patterned immobilization of other materials. However, for successful patterned immobilization, we need to design the self-organization process so that some shapes of DNA nanostructures are avoided. In this paper, we consider an approach to solve the problem of the avoidance of forbidden shapes of DNA nanorobots in patterned immobilization of other materials.

## Introduction

It is well known that synthetic biology allows us to design and assemble synthetic systems that mimic biological systems. There are a number different approaches to create synthetic DNA. In particular, we can mention the works on the development of self-assembled DNA nanostructures (see [1-5]).

Note that properly designed synthetic DNA can be considered as a programmable smart glue. In particular, synthetic DNA can reliably self-organize to form various structures. Therefore, self-assembly of DNA tiles can be used to create different smart materials. In particular, synthetic DNA can be used in nanofabrication as a means of creating patterned structures for use as templates or scaffolds (see e.g. [6-8]). Also, DNA arrays can be applied for patterned immobilization of other materials (see e.g. [9-11]). For instance, metal nanoparticles, peptides, proteins, other nucleic acids, and carbon nanotubes can be immobilized. In general, we can use DNA nanorobots (see e.g. [12-14]) for creation of some pattern and for patterned immobilization of other materials.

It should be noted that the ability of DNA nanostructures to immobilize some material depends on current shape of the nanostructure. Therefore, for successful patterned immobilization, we need to design the self-organization process so that some shapes of DNA nanostructures are avoided. In this paper, we consider an approach to solve the problem of the avoidance of forbidden shapes of DNA nanorobots in patterned immobilization of other materials.

## DNA Nanorobots Representations

Note that we can consider DNA nanorobots as modular robots (see e.g. [15]). Therefore, we can consider shapes of DNA nanorobots as modular robots configurations. In this case, we can use a graph model for representation of DNA nanorobots. In particular, a special graph has been introduced for representing robot's configurations (see [16]). It is called C-graph (see [16]).

It should be noted that the C-graph is an extension of a graph with connection points. Each vertex has a finite number of connection points corresponding to connectors of different types. We consider vertices of C-graphs as modules of some DNA nanorobot. A connection between connector i of module u and connector j of module v is made to correspond to edge (i, j) between vertices u and v.

The notion of C-graphs can be used for motion planning for modular robots. In particular, there are a number of algorithms for the problem of optimal reconfiguration planning for modular self-reconfigurable robots (see [16,17]).

## The Problem of S-avoided Reconfiguration Planning

The self-organization process can be represented by a sequence of elementary reconfiguration actions. In particular, we can consider two types of elementary reconfiguration actions for C-graphs: creation of a new connection and disconnection of a current connection between modules [16].

We say that there exists a reconfiguration plan for two given connected C-graphs H = (V, E[1]) and G = (V, E[2]) if and only if there exists a sequence of elementary reconfiguration actions such that, starting from H, we obtain G. It is easy to see that a reconfiguration plan for two given connected C-graphs H = (V, E[1]) and G = (V, E[2]) can be represented as a sequence of connected C-graphs G[1], G[2], ..., G[r+1], where G[1] = H, G[r+1] = G, and G[i+1] can be obtained from G[i] by some elementary reconfiguration action, for any $0 < i < r+1$.

It is clear that we can use reconfiguration planning to control the self-organization process of patterned immobilization. However, a reconfiguration plan can contain some forbidden configuration. Therefore, we need to consider reconfiguration plans with a set of avoided C-graphs.

Let S = {P[1],P[2],...,P[t]} be a set of connected C-graphs where P[j] = (V,Q[j]) for any $0 < j < t+1$. Given two connected C-graphs H = (V, E[1]) , G = (V, E[2]) and the set S, we say that there exists a S-avoided reconfiguration plan with at most k reconfiguration steps if and only if there exists a sequence of elementary reconfiguration actions of length $r < k+1$ such that the sequence can be represented as a sequence of connected C-graphs G[1], G[2], ..., G[r+1], where G[1] = H, G[r+1] = G, G[i+1] can be obtained from G[i] by some elementary reconfiguration action, and $G[i] \notin S$, for any i such that $0 < i < r+1$.

*Optimal S-avoided reconfiguration planning problem (S-AORP):*

Instance*:* Two C-graphs H = (V, E[1]) and G = (V, E[2]), S = {P[1],P[2],...,P[t]} such that P[j] = (V,Q[j]) for any $0 < j < t+1$, and an integer k.

*Question:* Find out whether there exists a S-avoided reconfiguration plan for H and G with at most k reconfiguration steps?

## Experimental Setup

We consider different test sets for S-AORP problem. In particular, we use random real world DNA sequences (EMBL - EBI database) of $10^5$ - $2\times10^5$ base pairs (TSR1) and $10^6$ - $2\times10^6$ base pairs (TSR2). Also, we consider random real world DNA sequences with various regularities:

- DNA sequences with large approximate periods (see [18]), sequences of $10^5$ - $2\times10^5$ base pairs (TSAP1) and $10^6$ - $2\times10^6$ base pairs (TSAP2);
- DNA sequences with large number of swaps and element duplications (see [19]), sequences of $10^5$ - $8\times10^5$ base pairs (TSSD1) and $10^6$ - $8\times10^6$ base pairs (TSSD2);
- DNA sequences with parameterized k-covers for different values of k (see [20]), sequences of $10^5$ - $8\times10^6$ base pairs (TSC);
- DNA sequences that can be used for DNA sequencing by hybridization (see [21]), sequences of $10^6$ base pairs (TSH).

## Experimental Results

In our experiments, we consider different artificial physics optimization algorithms for solution of S-AORP problem. In particular, we use the artificial physics optimization with negative exponential force law (NEFL), unimodal force law (UFL), linear force law (LFL), and general force law predicted by a Runge Kutta neural network (RKFL). Let D be the average number of reconfiguration steps for optimal solutions. Let D[X] be the average number of reconfiguration steps for solutions that obtained by an artificial physics optimization with force law X.

It is clear that we can consider N[X]=D[X]/D as a measure of the quality of the artificial physics optimization with force law X. Selected experimental results for different force laws are given in Table 1.

Table 1. Experimental results for different force laws

| X | NEFL | UFL | LFL | RKFL |
|---|---|---|---|---|
| N[X] for TSR1 | 2.4322 | 6.4442 | 9.0043 | 1.2171 |
| N[X] for TSR2 | 2.5213 | 6.5631 | 9.1205 | 1.2344 |
| N[X] for TSAP1 | 3.9215 | 8.4420 | 9.5944 | 1.3715 |
| N[X] for TSAP2 | 3.9706 | 8.7116 | 9.9821 | 1.3811 |
| N[X] for TSSD1 | 1.9203 | 5.5513 | 8.8897 | 1.1009 |
| N[X] for TSSD2 | 1.9306 | 5.8209 | 8.9914 | 1.1024 |
| N[X] for TSC | 4.2208 | 9.2005 | 9.3376 | 1.3991 |
| N[X] for TSH | 1.6311 | 4.8992 | 8.5302 | 1.0107 |

**Summary**

In this paper, we have considered synthetic DNA as a programmable smart glue that can be used to create different smart materials. In particular, we have presented an approach to usage of DNA glue for patterned immobilization of other materials. We have proposed the optimal S-avoided reconfiguration planning problem. The problem can be used for planning of patterned immobilization. We have considered different intelligent algorithms for solution of the problem. We have presented experimental results for different test sets. It is easy to see from our experimental results that the artificial physics optimization algorithm with general force law that predicted by a Runge Kutta neural network gives us the best solutions. It is clear that the quality of solution not essentially depends from the length of DNA. However, the quality of solution depends essentially from different regularities in DNA. In particular, we have obtained better solutions for DNA sequences that can be used for DNA sequencing by hybridization and DNA sequences with large number of swaps and element duplications. Also, it is clear that DNA sequences with large approximate periods and DNA sequences with parameterized k-covers for different values of k are hard to solve. This results give us important information for proper design of DNA nanorobots for patterned immobilization.

**Acknowledgement**

This research was partially financially supported by Analytical Departmental Program ”Developing the scientific potential of high school”, RFBR, research project No. 13-01-00048 a, and under the Agreement 02.A03.21.0006 of 27.08.2013 between the Ministry of Education and Science of the Russian Federation and Ural Federal University.

**References**

[1]R. Amin, S. Kim, S. Park, T. LaBean, Artifically designed DNA nanostructures, NANO 4 (2009) 119-139.

[2] T. LaBean, K. Gothelf, J. Reif, Self-assembling DNA nanostructures for patterned molecular assembly, in: C.A. Mirkin, C.M. Niemeyer (Eds.), Nanobiotechnology II: More Concepts and Applications, John Wiley & Sons, Weinheim, 2007, pp. 79–97.

[3] N. Seeman, Nanotechnology and the double helix, Sci. Am. 290 (2004) 64-75.

[4] K. Lund, B. Williams, Y. Ke, Y. Liu, H. Yan, DNA Nanotechnology: A rapidly evolving field, Curr. Nanosci. 2 (2006) 113-122.

[5] Z. Deng, Y. Chen, Y. Tian, C. Mao, A fresh look at DNA nanotechnology, in: J. Chen, N. Jonoska, G. Rozenberg (Eds.), Nanotechnology: Science and Computation, Springer-Verlag, Berlin - Heidelberg, 2006, pp. 23-34.

[6] T. LaBean, H. Yan, J. Kopatsch, F. Liu, E. Winfree, J. Reif, N. Seeman, The construction, analysis, ligation and self-assembly of DNA triple crossover complexes, J. Am. Chem. Soc. 122 (2000) 1848-1860.

[7] E. Winfree, F. Liu, L. Wenzler, N. Seeman, Design and self-assembly of two-dimensional DNA crystals, Nature 394 (1998) 539-544.

[8] X. Yang, L. Wenzler, J. Qi, X. Li, N. Seeman, Ligation of DNA triangle containing double crossover molecules, J. Am. Chem. Soc. 120 (1998) 9779-9786.

[9] A. Alivisatos, K. Johnsson, X. Peng, T. Wilson, C. Loweth, M. Bruchez Jr., P. Schultz, Organization of 'nanocrystal molecules' using DNA, Nature 382 (1996) 609-611.

[10] J. Mbindyo, B. Reiss, B. Martin, C. Keating, M. Natan, T. Mallouk, DNA directed assembly of gold nanowires on modified gold surface, Adv. Mater. 13 (2001) 249-254.

[11] R. Mucic, J. Storhoff, C. Mirkin, R. Letsinger, DNA-directed synthesis of binary nanoparticle network materials, J. Am. Chem. Soc. 120 (1998) 12674-12675.

[12] H. Chandran, N. Gopalkrishnan, J. Reif, DNA Nanorobotics, in: C. Mavroidis, A. Ferreira (Eds.), Nanorobotics, Springer, New York, 2013, pp. 355-382.

[13] M. Hagiya, DNA nanorobotics and sequence design, in: SICE 2004 Annual Conference, 2004, pp. 2774-2778.

[14] A. Nishikawa, S. Yaegashi, F. Tanaka, K. Ohtake, M. Hagiya, Multi-fueled approach to DNA nano-robotics, Nat. Comput. 7 (2008) 371-383.

[15] N. Brener, F. Ben Amar, P. Bidaud, Characterization of lattice modular robots by discrete displacement groups, in: IROS, 2010, 1133-1139.

[16] F. Hou and W. Shen, On the complexity of optimal reconfiguration planning for modular reconfigurable robots, in: ICRA, 2010, 2791-2796.

[17] A. Gorbenko, V. Popov, Programming for modular reconfigurable robots, Program. Comput. Soft. 38 (2012) 13-23.

[18] V. Popov, The approximate period problem for DNA alphabet, Theor. Comput. Sci. 304 (2003) 443-447.

[19] V. Popov, Multiple genome rearrangement by swaps and by element duplications, Theor. Comput. Sci. 385 (2007) 115-126.

[20] A. Gorbenko, V. Popov, The set of parameterized k-covers problem, Theor. Comput. Sci. 423 (2012) 19-24.

[21] V. Popov, Computational complexity of problems related to DNA sequencing by hybridization, Dokl. Math. 72 (2005) 642-644.

*Advanced Materials Research Vol. 937 (2014) pp 248-255*
*© (2014) Trans Tech Publications, Switzerland*
*doi:10.4028/www.scientific.net/AMR.937.248*

# Preparation of Carbaryl-imprinted Capillary Monolithic Column for Screening of Carbaryl from Three Carbamates Mixture

Can ZHANG[1,a*], Jian-rong CAI[1], Yu-qing DUAN[1], Liang XU [2,b,*]

[1] School of Food & Biological Engineering, Jiangsu University, Zhenjiang, Jiangsu 212013, China

[2]Tianjin Key Laboratory on Technologies Enabling Development Clinical Therapeutics and Diagnostics (Theranostics), School of Pharmacy, Tianjin Medical University, Tianjin 300070, China

[a]email: zhangcan@ujs.edu.cn, [b]email: xuliang@tmu.edu.cn

*Corresponding author: Can Zhang[1,a*]

Liang Xu[1,b*]

**Keywords:** Organic-inorganic hybrid, Carbaryl-imprinted capillary monolith, Separate.

**Abstract.** A carbaryl molecularly imprinted capillary monolith was prepared by organic-inorganic hybrid approach. Methacrylic acid (MAA) as functional monomer, γ-methacryloxypropytrimethoxysilane (γ-MAPS) as crosslinker, carbaryl as template molecule, and acetonitrile/dichloromethane mixture (v/v, 1:4) were used as porogen. The molar ratio of 1:6:8 (carbaryl:MAA: γ-MAPS, for which the retention factor k was 7.57, was expected to be highest for carbaryl on the optimum capillary monolith. The condition of 20 mmol/L phosphate buffer with pH value 3.5 containing 30% acetonitrile favored the carbaryl separation from three carbamates (carbaryl, fenobucarb and metocarb) through the effective imprinted length of the column which was 15 cm. As far as the screening of carbaryl from a group of structural analogs, the MIP monolith combined with capillary electrochromatography was preferred.

## Introduction

Capillary electrochromatography (CEC) is an exciting miniaturized separation technique that combines the advantage of the high separation efficiency of CE, and the various retention mechanisms and selectivity of HPLC. The further coupling of molecularly imprinted polymer (MIP) and CEC (or HPLC) has already shown good promise in the separation of target compound from its analogs with good selectivity and high efficiency [1-7]. Among various MIP structures studied, only monolithic columns have the following advantages: Good permeability and easy pore structure tuning. Therefore, the combination of MIP monolithic column with CEC might be very promising to recognize and separate small molecules and biomacromolecules efficiently. Both organic-polymer- and silica-based monoliths have been widely used in CEC. Organic-polymer-based monolith have such advantages as the availability of various monomers and excellent stability in different pH environment. However, it may shrink or swell when exposed to different organic solvents, which causes considerable deformation of the MIP receptors and decreases its recognition ability towards the template. Although, the silica-based MIP monolith can offer excellent mechanical strength and good solvent resistance, the drawback is the cracking and shrinking of the bed during its drying process. Organic-inorganic hybrid technology combines the advantages of the above techniques and avoids the shortcomings of organic and inorganic matrix monoliths. Recently, organic-inorganic hybrid MIP-monolith has been applied for the chiral separation and the screening of target from structural analogs by CEC. For example, Yan et al. recently had reported the molecularly imprinted silica monolithic column from the non-hydrolysis of organic-inorganic hybrid for chiral CEC separation of (S)-naproxen [8] and (S)-zolmitriptan [9] with excellent chiral recognition ability and high resolution. Wang et al. [10] had prepared a molecularly imprinted capillary monolithic column through organic-inorganic hybrid approach with four ractopamine isomers as templates, and the prepared MIP capillary monolithic column had high selectivity to the four ractopamine isomers in CEC. Wang et al [11] had prepared a molecularly imprinted silica monolithic column via a two-step

approach and applied it in CEC for the selectively recognization of sulfamethazine from the sulfonamide mixtures with improved selectivity and good stability. And the sulfamethazine was successfully screened from a group of structural analogs with a CEC mode.

Furthermore, several quantitative and qualitative methods, including the chromatographic assay [12], enzyme-linked immuno-sorbent assay (ELISA) [13], biosensor [14], or capillary electrophoresis-based immunoassay (CEIA) [15], have been used for detecting and screening carbaryl (1-naphthol-N-methylcarbamate) that was the first successful carbamate insecticide due to its broad-spectrum efficacy. Because anti-carbaryl antibody was used as the sensing material in some assays, such as ELISA and CEIA, carbaryl can be recognized rapidly and sensitively. However, with these assays mentioned previously, the mixture of three carbamate insecticides (carbaryl, fenobucarb and metolcarb) cannot be separated simultaneously without the aid of anti-carbaryl antibody. With the development of molecular imprinting technology, one of the most interesting and promising methods is to apply molecular imprinted technology to prepare biomimetic antibody that can imitate the molecular recognition ability of biological antibodies. In this study, carbaryl was used as template to prepare molecularly imprinted capillary monolithic column through organic-inorganic hybrid approach. The CEC, with carbaryl-MIP monolith, not only had good recognition capability for carbaryl, but also could separate the three carbamate insecticides mixture (carbaryl, fenobucarb and metolcarb) completely. Therefore, combined with CEC, carbaryl-MIP monolith could be used to screen carbaryl from structurally similar compounds efficiently and to avoid the clean-up steps that were usually mandatory to analyze complicate samples.To the best of our knowledge, there was no report on the separation and screening of carbaryl from its structurally similar compounds with the combination of organic-inorganic hybrid MIP monolith and CEC.

## Materials and Methods

### Materials

Carbaryl, fenobucarb and metolcarb were purchased from Sigma (St Louis, MO, USA). Methacrylic acid (MAA), 2, 2/-azobisisobutyronitrile (AIBN) and γ-methacryloxypropyltrimethoxysilane (γ-MAPS) were purchased from Shanghai Chemical Plant (Shanghai, China). The MAA was distilled under vacuum and AIBN was re-crystallized in ethanol before use. Fused-silica capillary (100 μm × 375 μm) was purchased from the Yongnian Optic Fiber Plant (Hebei, China). Acetonitrile was HPLC grade and other reagents were all analytical grade. Doubly deionized water (DDW, 18.2 MΩ cm-1) was obtained from WaterPro system (Labconco Corporation, Kansas City, MO, USA).

### Instruments and Methods

CEC experiments were performed on a P/ACE MDQ CE system (Beckman-Coulter, Fullerton, CA, USA) with a UV detector (220 nm). The monolith column was rinsed under pressure (60 psi) and further electro-kinetically conditioned at 15 kV in the instrument with the separation buffer solution until a stable current was obtained. All the phosphate buffers were made in doubly deionized water and filtered through a 0.22 μm filter before use. The UV adsorption spectra of carbaryl was measured on Varian Cary 100 UV spectrometer (Varian, CA, USA). Scanning electron microscopy (SEM) images of the synthesized monoliths were taken at 15.0 kV on a JSM-7001F scanning electron microscope (Joel, Tokyo, Japan). FTIR spectra (4000–400 cm–1) in KBr were recorded on a Magna-560 spectrometer (Nicolet, Madison, WI, USA).

### Preparation of Carbaryl Molecularly Imprinted Capillary Monolithic Column

Before the preparation of monolithic, fused-silica capillary was pretreated as the following: the capillary was rinsed with 1.0 mol/L of NaOH for 12 h, with water for another 30 min, with 0.1 mol/L of HCl for additional 30 min, then washed with water again until pH value of the outflow reached to 7.0. Finally, the capillary was blew with nitrogen and dried at 110 ℃ in a gas chromatographic oven overnight.

The pre-polymerization mixture, including 100.5 mg of carbaryl and 0.258 mL of MAA, was dissolved in 5 mL of acetonitrile/dichloromethane mixture (v/v, 1:4). After 1 h, 0.95 mL of γ-MAPS and 30 mg of AIBN were added and dissolved homogeneously with stirring. The mixture was purged with nitrogen for 5 min and sonicated for 5 min to remove the oxygen. Then, the obtained transparent solution was carefully introduced into the activated capillary to fill about 20 cm with a 0.5 mL disposable syringe. After both ends of the capillary were plugged with silicon rubber, the capillary was submerged into a water bath at 50ºC for 12 h for polymerization. After the polymerization, the prepared capillary monolith was eluted with acetonitrile by a high performance liquid chromatography pump to remove the template molecule and un-reacted monomers, dried with nitrogen, then dried at 80 ºC in a vacuum oven for 10 h. A detection window after the monolith section was created by burning off a 2 mm segment of the polyimide coating. The distance from detection window to the outlet end of capillary was 10 cm. Once fabricated, the capillary was installed in the cartridge with 15 cm of monolith from the inlet to the detection window. The total length of capillary was 30.2 cm. A non-imprinted capillary monolith without template was also prepared with the same procedure.

The imprinted factor (IF) (IF = kMIP/kNIP) was defined as the ratio of the retention factor of template in MIP monolith and that in NIP monolith, which was adopted to evaluate the imprinting ability in this study.

## Results and Discussion

### The Molecular Interaction between Template and Functional Monomer

The template to functional monomer ratio had a significant influence on the preparation of MIPs. In order to successfully prepare highly selective affinity sites, the formation of stable complexes in the early phase of polymerization is essential, thus it is important to study the intermolecular interaction between the template and functional. The impact of different ratios of carbaryl over MAA on the UV absorption spectra of carbaryl had shown in Fig.1 that the carbaryl absorption had obvious blue-shift with the increase of MAA concentration. When the ratio of carbaryl over MAA was 1:6, the maximum blue-shift was reached from 220 nm to 203 nm. The peak was not further changed when the ratio of carbaryl and MAA was above 1:6, which could be due to the formation of hydrogen bonds between carbaryl and MAA . Therefore, the template to monomer ratio was kept at 1:6 in the polymerization of this study.

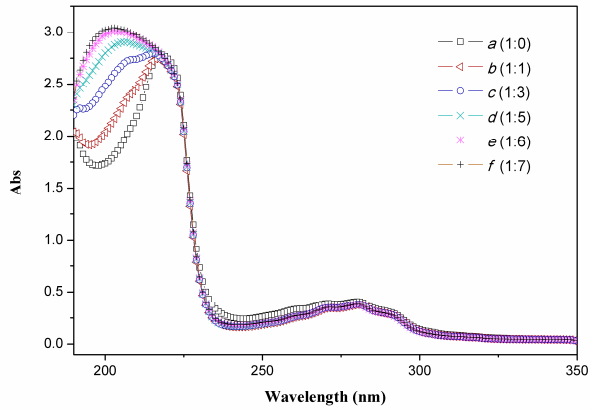



Fig. 1. UV-spectra of carbaryl under the conditions of the different ratio of carbaryl to MAA in acetonitrile.

### Preparation of the Carbaryl Molecularly Imprinted Capillary Monolithic Column

Porogenic solvent plays a dual role in MIP preparation. First, the porogen should produce large pores to assure good flow-through properties of the resultant MIP. Second, the porogenic solvent governs the strength of non-covalent interactions in addition to its influence on the polymer

morphology. The best imprinting porogens, for accentuating the binding strengths, are solvents of very low dielectric constant, such as toluene and dichloromethane. Acetonitrile was also selected as the solvent/porogen because of its good solubility for a large number of polar template molecules and its wide use as a component of electrolyte buffers. It was observed that low polymerized temperature (below 40ºC) or high polymerized temperature (above 60ºC) might induced to incomplete-polymerized or over-polymerized. Therefore, the impacts of different ratio of acetonitrile and dichloromethane (v/v, mL) (0:5, 1:4, 2:3, 3:2) and temperature (40ºC, 50ºC, 60ºC) on the permeability were studied and the following conditions were described by Wang[10]. It was also found that, if the columns prepared by polymerization at higher temperature or with a longer time, its flow-through property became lower. Based on the permeability and affinity, the porogenic solvent of acetonitrile/dichloromethane (1:4) and temperature of 50ºC were chosen to prepare the capillary monolith.

## Characterization of Carbaryl Molecularly Imprinted Capillary Monolithic Column

### FTIR Spectra of Carbaryl Molecularly Imprinted Capillary Monolithic Column

To further determine the characteristics of the silica-based network, FTIR spectra of carbaryl MIP monolith (before and after the extraction of template) were compared, and non-imprinted monolith were also used as the control to verify the complete removal of template molecules. as shown in Fig.2. The peaks at 3300 cm-1 (N-H stretch), 1418 cm-1 (C-N stretch), 1541 cm-1 (C=C skeleton vibration in naphthalene), 3061 cm-1 (C-H stretch in naphthalene) of carbaryl were present in the molecularly imprinted capillary monolithic column only before washed, which indicated that the template was completely removed from the MIP. And the disappearance of 1635 cm-1 (C=C stretch in MAA) in MIP indicated that the double bonds of MAA participated the polymerized reaction. The peaks at 1299 cm-1 (C-O stretch) and 947 cm-1 (O-H bending) in MAA had red-shifts in the MIP, and changed to 1270 cm-1and 913 cm-1, respectively, possibly due to interaction of MAA and carbaryl or the formation of polymers. The peaks near 1088 cm-1 and 820 cm-1 could be assigned to the Si–O–Si asymmetric stretch and symmetric stretch, respectively. The peak at 3447 cm-1 was due to the –OH vibration in the bulk gels.

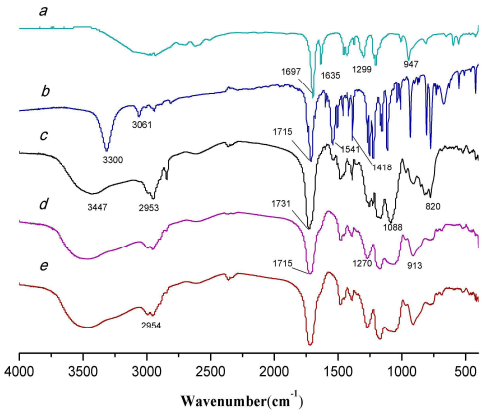



Fig. 2. FTIR spectra of : (a) methacrylic acid, (b) carbaryl, (c) carbaryl-imprinted polymers before extraction, (d) carbaryl-imprinted polymers after extraction, (e) non-imprinted polymers.

### Effects of Functional Monomer and Cross-linker

A number of MIP monolith-based capillary columns were produced under the conditions with different ratios of monomer over cross-linker. It was found that small percentage of γ-MAPS could not react with MAA completely to form the stable matrix because only high percentage of γ-MAPS could induce its self-hydrolysis to form the dense polymer. As shown in Fig.3, with the increase of γ-MAPS, the pore size became smaller and the flow-through property diminished slowly, which could further affect the selectivity of the capillary monolithic column.

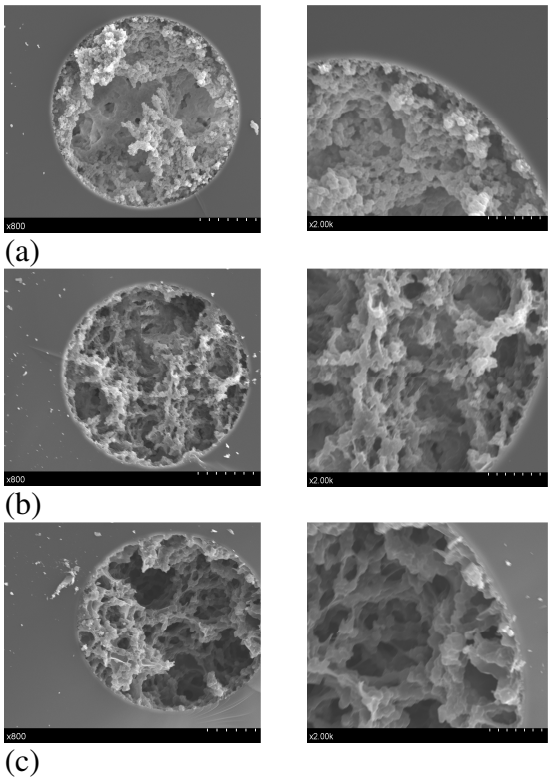



Fig. 3. SEM images of molecularly imprinted capillary monolithic columns prepared with different amounts ofγ-MAPS: (a) 1.0 mL, (b) 0.75 mL and (c) 0.5 mL.

Additionally, two ratios, 1:6:6 and 1:6:8, of carbaryl : MAA : γ-MAPS were compared as shown in Fig.4 and their ability to recognize carbaryl in CEC mode was recorded. It was found that the ratio of 1:6:8 was the highest for carbaryl with the kMIP/kNIP of 7.57 for the optimum capillary.

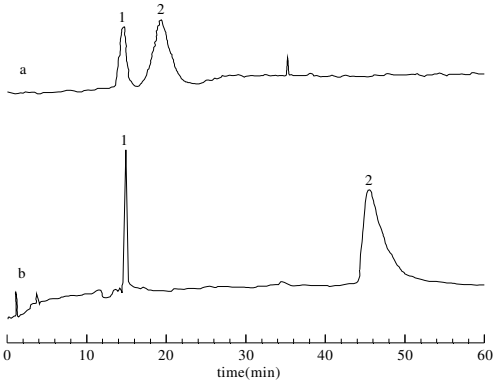



Fig. 4. The chromatograms of carbaryl-imprinted capillary monolith at different ratios of monomer to cross-linker by CEC. (1: thiourea, 2: carbaryl. a: carbaryl : MAA: γ-MAPS = 1:6:6, b: carbaryl : MAA: γ-MAPS = 1:6:8).

**Impact of pH Value of the Separation Buffer on the Carbaryl Identification and Separation in the Prepared Molecularly Imprinted Capillary Monolithic Column**

The pH of the separation buffer is important since it can alter the charges of both the analyte and the polymer, thus to affect the molecular recognition of the MIP and the electrophoretic mobility of the analyte. The Electroosmotic flow (EOF) was generated by the ionization of the surface groups of the stationary phase. Analytes are moved through the column by the mobile phase driven with the EOF as well as the self-electrophoretic mobility of analytes. The impact of pH value on the separation of carbaryl on the prepared monolith column at 3.0, 3.5, 4.0, 4.5 and 5.0 of pH values were

investigated. It was found that the migration time of carbaryl was decreased with the increase of pH value, which might be ascribed to the higher EOF generated by the carboxyl groups of MAA and the silanol groups on the surface of MIP-monolith because the surface of the silica monolith could not be completely covered by the MIP film.

**Effect of Acetonitrile Concentration in Separation Buffer**

Acetonitrile, as an organic modifier in the separation buffer, was the most extensively used electrolyte due to its low viscosity. CEC results showed that the recognition ability of MIPs was a function of acetonitrile concentration (from 10 to 40% v/v) in the mobile phase (20 mM phosphate buffer containing acetonitrile with pH value of 3.5). It was also found that increasing the acetonitrile concentration could reduce the retention time of carbaryl, possibly because the retention of carbaryl was mainly determined by the hydrophobic interaction except the hydrogen bonding interaction with the imprinted cavities in the polymer. Additionally, the configuration of carbaryl peak became more symmetrical and the width of peak became narrower with the increase of acetonitrile concentration in the separation buffer. However, too high concentration of acetonitrile in the buffer (above 50%) could easily result in bubbles in CEC, which could disrupt the separation. All of these results suggested that, during the preparation of MIP monolith, 30% acetonitrile content should be chosen to favor the recognition and separation of carbaryl.

**Comparison of Carbaryl Recognition Capacity of MIP Monolithic Column with NIP Monolithic Column**

The carbaryl-imprinted capillary monolith was used to separate three carbamate insecticides (carbaryl, fenobucarb and metolcarb) in a mixture. As shown in Fig.5, on NIP monolith column, the mixture of three carbamates could not be well separated; however, they could be separated completely on MIP monolith column with kMIP/kNIP of 7.57, 1.27 and 1.64 for three carbamates (carbaryl, fenobucarb and metolcarb), respectively. Additionally, carbaryl was separated after fenobucarb and metolcarb because of the specific recognition of molecular imprinted cavity for carbaryl. For MIP monolith column, the separation factors (α = kcarbaryl/kanalogs) were kcarbaryl/kfenobucarb 5.96 and kcarbaryl/kmetolcarb 4.62, respectively. For effective separation of the mixture of the three insecticides (carbaryl, fenobucarb and metolcarb) and screening of carbaryl with CEC, the MIP-capillary monolith column was preferred because of the molecularly designed cavities showed an special affinity for carbaryl over other structurally similar compounds.

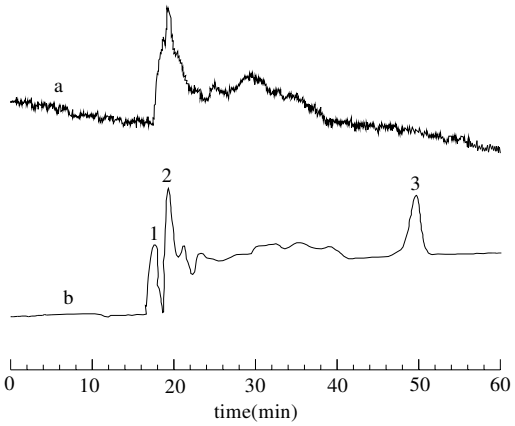



Fig. 5. The comparison of MIP monolith and NIP monolith for the separation of fenobucarb (1), metolcarb (2) and carbaryl (3) by CEC. a: NIP column, b: MIP column. The CEC separations were performed at 15 kV with 20 mM phosphate buffer (pH = 3.5) which contained 30% of acetonitrile (V/V). The analyte solution was injected under pressure (10 psi) for 5 s and detected at 220 nm with a UV detector.

### Repeatability and Reproducibility

The repeatability of the MIP monolith column was assessed in terms of the migration times of carbaryl, fenobucarb and metolcarb and the separation factors under the same conditions as that in Fig.5. The reproducible migration time for all analytes was not more than 2.1% RSD (run-to-run, n=3), and no general trend in the migration time change was observed. The RSD values of the separation factors were smaller than 5.1%. The column-to-column reproducibility was also examined (n=3). The RSD values of the migration times and separation factors were not higher than 4.5% and 10.3%, respectively.

### Conclusions

In this experiment, carbaryl-imprinted capillary monolithic column was prepared with the organic-inorganic hybrid method. The preparation method was simple, and the prepared MIP capillary monolithic column has high selectivity for carbaryl. The mixtures of carbamates (carbaryl, fenobucarb and metolcarb) could be separated effectively through the combination of MIP monolith with CEC, which also was good for the screening of carbaryl from a group of structural analogs. This method also could be used to separate the analyte directly from matrix components, thus to avoid the clean-up steps that were usually mandatory to analyze complicate samples. The combination of monolithic MIP column with CEC would be very useful in the screening and development of insecticides and medicines, in particular, during the initial screening of large libraries.

### Acknowledgement

This research was financially supported by the National Natural Science Foundation of China (No. 31000783, 31201456, ), Jiangsu Planned Projects for Postdoctoral Research Funds (1202010B) and the Talent Foundation of Jiangsu University (09JDG052).

### References

[1]P. Spégel, L.Schweitz, S.Nilsson, Molecularly imprinted microparticles for capillary electrochromatography: Studies on microparticle synthesis and electrolyte composition, Electrophoresis. 22(2001) 3833-3841.

[2] F. Priego-Capote, L. Ye, S. Shakil, S A. Shamsi, S. Nilsson, Monoclonal Behavior of Molecularly Imprinted Polymer Nanoparticles in Capillary Electrochromatography, Anal. Chem. 80(2008) 2881-2887.

[3] P. Spégel, L. Schweitz, S. Nilsson, Selectivity toward Multiple Predetermined Targets in Nanoparticle Capillary Electrochromatography, Anal. Chem. 75(2003) 6608-6613.

[4] Y C. Huang, C C. Lin, C Y. Liu, Preparation and evaluation of molecularly imprinted polymers based on 9-ethyladenine for the recognition of nucleotide bases in capillary electrochromatography, Electrophoresis. 25(2004)554- 561.

[5] S A. Zaidi, W J. Cheong, Preparation of an open-tubular capillary column with a monolithic layer of S-ketoprofen imprinted and 4-styrenesulfonic acid incorporated polymer and its enhanced chiral separation performance in capillary electrochromatography, J. Chromatogr. A. 1216 (2009) 2947-2952.

[6] C. Cacho, L. Schweitz, E.Turiel, C. Perez-Conde, Molecularly imprinted capillary electrochromatography for selective determination of thiabendazole in citrus samples, J. Chromatogr. A. 1179(2008) 216-223.

[7] Z S. Liu, C.Zheng, C.Yan, R Y.Gao, Molecularly imprinted polymers as a tool for separation in CEC, Electrophoresis. 28(2007)127-136.

[8] H F.Wang, Y Z. Zhu, X P.Yan, R Y.Gao, J Y. Zheng, A Room Temperature Ionic Liquid (RTIL)-Mediated,Non-Hydrolytic Sol–Gel Methodology to Prepare Molecularly Imprinted, Silica-Based Hybrid Monoliths for Chiral Separation, Adv. Mater. 18(2006)3266-3270.

[9] H F.Wang, Y Z.Zhu, X P.Yan, J P.Lin, Fabrication of molecularly imprinted hybrid monoliths via a room emperature ionic liquid—mediated nonhydrolytic sol-gel route for chiral separation of zolmitriptan by capillary electrochromatography, Electrophoresis. 29(2008)952-959.

[10] J X.He, G Z.Fang, Q L.Deng, S.Wang, Preparation, characterization and application of organic —inorganic hybrid ractopamine multi—template molecularly imprinted capillary monolithic column, Anal. Chim. Acta. 692(2011) 57-62.

[11] J X.He, G Z.Fang , Y C.Yao, S.Wang, Preparation and characterization of molecularly imprinted silica monolith for screening sulfamethazine, J. Sep. Sci. 33(2010) 3263-3271.

[12] J. Zhang, H K.Lee, Application of liquid-phase microextraction and on-column derivatization combined with gas chromatography–mass spectrometry to the determination of carbamate pesticides, J. Chromatogr. A. 1117(2006)31-37.

[13] B.Mickova, T.Kovalczuk, P.Rauch, M J.Moreno, A.Abad, A.Montoya, E.Ferri, F. Fini, S.Girotti, Analytical performances of validated chemiluminescent enzyme immunoassays to detect N-methylcarbamate pesticides, Anal. Chim. Acta. 528(2005)243-248.

[14] E.Mauriz, A.Calle, A.Abad, A.Montoya, A.Hildebrandt, D.Barceló, L M.Lechuga, Determination of carbaryl in natural water samples by a surface plasmon resonance flow-through immunosensor, Biosen. Bioelectron. 21(2006)2129-2136.

[15] C.Zhang, GP.Ma, GZ.Fang, Y.Zhang, S.Wang, Development of a Capillary Electrophoresis-Based Immunoassay with Laser-Induced Fluorescence for the Detection of Carbaryl in Rice Samples, J. Agric. Food Chem. 56(2008) 8832-8837.

*Advanced Materials Research Vol. 937 (2014) pp 256-259*
*© (2014) Trans Tech Publications, Switzerland*
*doi:10.4028/www.scientific.net/AMR.937.256*

# Methylthiouracil-templated Formation of the Fluorescent Silver Nanocluster and its Application to Bioimaging

Xiao-qing XU[1,a*]

[1]College of Chemistry & Environmental Science, Inner Mongolia Normal University, Hohhot, 010022, China

Lby0649@sina.com

*Corresponding author

**Keywords:** silver nanocluster bioimaging fluorescence

**Abstract:** Herein, we report a novel approach to Methylthiouracil-templated formation of fluorescent Ag nanoclusters and its application to bioimaging. We used fluorescence assay and TEM to characterize the silver nanocluster. The complex can be directly employed into bioimaging HeLa cells. The cell toxicity (3-[4,5-dimethylthiazolyl-2]-2,5-diphenyltetrazolium bromide, MTT) assay demonstrated that the silver nanocluster has only little affect on the cytotoxicity to the cells, which further proves the applicability of the method in tumor cell imaging. This work successfully develops the capping Methylthiouracil scaffolds of silver nanoclusters.

## Introduction

Few-atom noble-metal (gold, silver and platinum) nanoclusters have been developed as a new class of fluorophores in the past decade. The size of nanocluster is gap of between nanometer and atom.Due to special size ,nanocluster have size-dependent, strong fluorescent emission. Especially silver nanoclusters attracted more attention in synthesis using DNA in aqueous solution(1-5). Among the various kinds investigated up to now, silver nanoclusters encapsulated by the single-stranded oligonucleotide dC12 form the most proficient system thanks to their very high photoemission rates and their excellent photostability(6).The UV/Vis absorption spectrum of an aqueous solution of the in situ formed dC12-stabilized silver species shows a narrow maximum of $\lambda max$=440 nm and smaller peaks at 350, 570, and 650 nm(7).Therefore, the development of a facile and convenient procedure is needed for making fluorescent Ag nanoclusters using a small molecule as a template. Herein, Methylthiouracil was selected to template.

## Materials and Methods

### Chemicals and Materials

Silver nitrate ($AgNO_3$, (Sigma-Aldrich, 99.9999%)), sodium borohydride (AF granules, 10–40 mesh, 98%, Sigma-Aldrich), and all chemicals of analytical grade were used as received without further purification. 3-[4,5-dimethylthiazolyl-2]-2,5-diphenyltetrazolium bromide (MTT) were obtained from Sigma-Aldrich (USA). Phosphate Buffered Saline (PBS) [10 mM phosphate ($NaH_2PO_4$ and $Na_2HPO_4$), pH 7.4] was also prepared. The PBS buffer is used to rinsing suspension of HeLa cells. All the solutions were prepared by using distilled water and stored at 4 ◦C before use. HeLa cells were obtained from the American Type Culture Collection (Manassas, VA) and maintained in DMEM supplemented with 10% standard Fetal bovine serum (Defined FBS) (HyClone Laboratories, UT) at 37 ◦C and in 5% CO2. Glass chamber slides (14 mm bottom well) were purchased from Hangzhou Sanyou Biotechnology Co. Ltd. (Hangzhou, China).

### Bioimaging

HeLa cells incubated with Methylthiouracil encapsulated silver nanocluster. HeLa cells were plated onto 35 mm glass chamber slides. Stock solutions of Methylthiouracil encapsulated silver nanocluster dissolved in TE buffer were prepared at concentrations of 10 μM. Diluted solutions in

complete growth medium were then freshly prepared and placed over the cells for 2–3 h. All cells were washed with PBS buffer (3×) at room temperature. After that, cells were scanned by LEICA TCS SP2 laser scanning confocal microscope.

**MTT Assay**

In order to evaluate the silver nanocluster dose on cellular toxicity, the complex treated cells were illuminated for a serial concentration. After treatment, cells were incubated in fresh medium for 24 h. The culture medium was replaced by 100μL fresh medium containing 0.5 mg/mL 3-[4,5-dimethylthiazol-2-yl]- 2,5-diphenyl tetrazolium bromide assays reagent (MTT assay), andthen incubated at 37 ◦C and 5% CO2 for 4 h. Then, the MTT containing medium was added with 100 μL of acid/isopropanol solution, in which the concentration of HCl was 0.04 M to dissolve the MTT product, formazan. Viability of non-silver nanocluster-treated control cells was arbitrarily defined as 100%. Finally, the absorption at 490 nm of each well was measured by an EL808 ultramicroplate reader (Bio-TEK Instrument, Inc., Winooski, VT, USA). The relative cell viability was recorded and shown (Fig. 3).

**Results and Discussion**

The fluorescence detection is based on silver nanocluster. Fig. 1A depicts the fluorescence emission and excitation spectra of silver nanoclusters dissolved in water. From the figure, we can conclude that the intensity of excitation at 580 nm is strong while the ones of 670 nm (Fig. 1A) is relatively weak. Using confocal fluorescence microscopy, the bioimaging of adding silver nanocluster to the HeLa cells was investigated. Fig. 1B shows confocal fluorescence images of HeLa cells incubated with 10 μM of the silver nanocluster complexes.

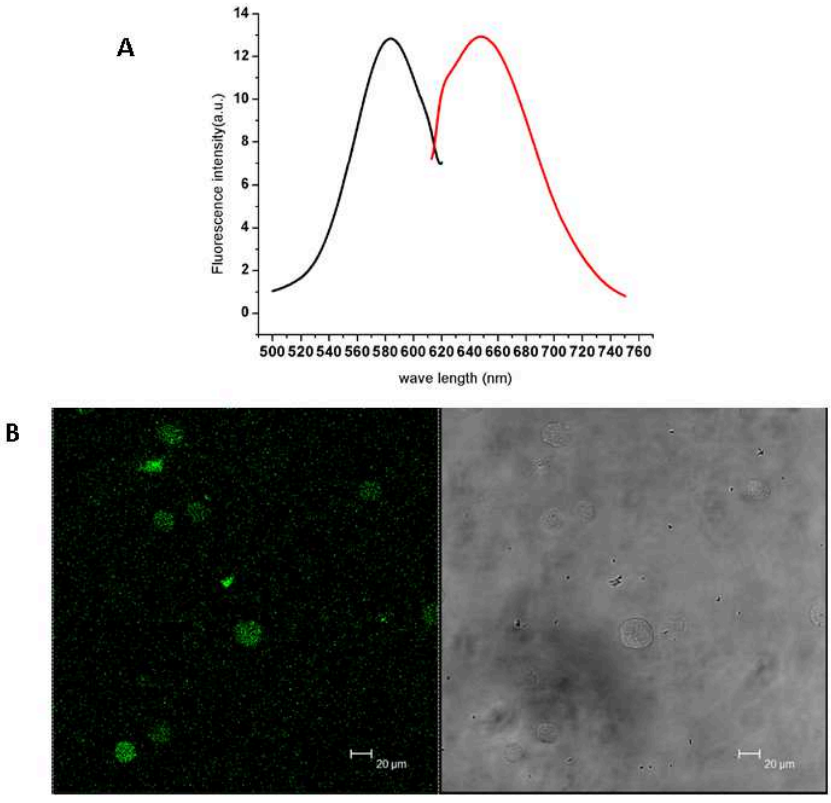



Fig. 1. (A) Fluorescence excitation/emission of Methylthiouracil encapsulated silver nanocluster. (B) Fluorescence image of HeLa cell incubated with silver nanocluster on glass chamber slides. Confocal spectroscopy scanning image obtained on collecting fluorescence of silver nanocluster upon excitation at 563 nm

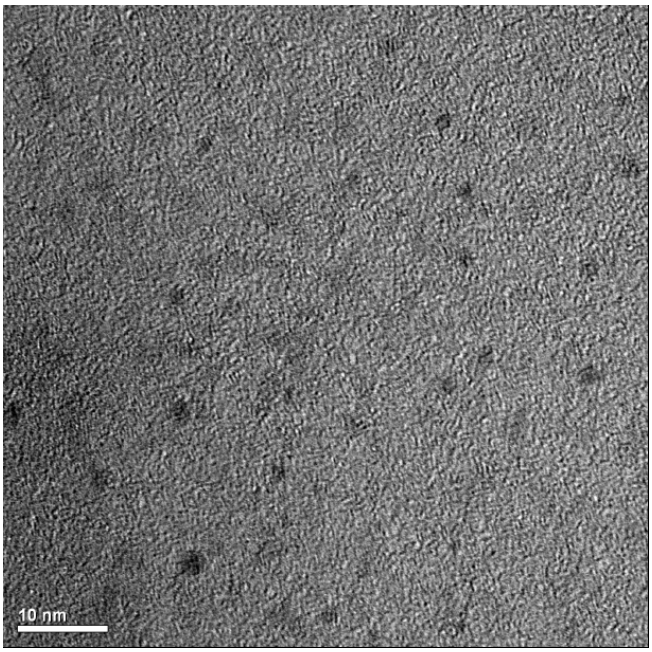



Fig. 2. TEM spectrum of silver nanocluster.

In order to assay particle size of silver cluster, TEM was performed. As shown in Fig. 2, we concluded that Methylthiouracil encapsulated silver nanoclusters were smaller than 2nm. TEM analysis (Fig.2) established that 97% of the water-soluble Methylthiouracil -encapsulated silver nanoclusters ranged between 1.3 and 2.5 nm in diameter with a distribution peak at 1.8 nm. TEM images of Methylthiouracil templated silver nanocluster solutions show entities with sizes smaller than 2 nm in diameter. HeLa cell incubated with Methylthiouracil -encapsulated silver nanocluster.

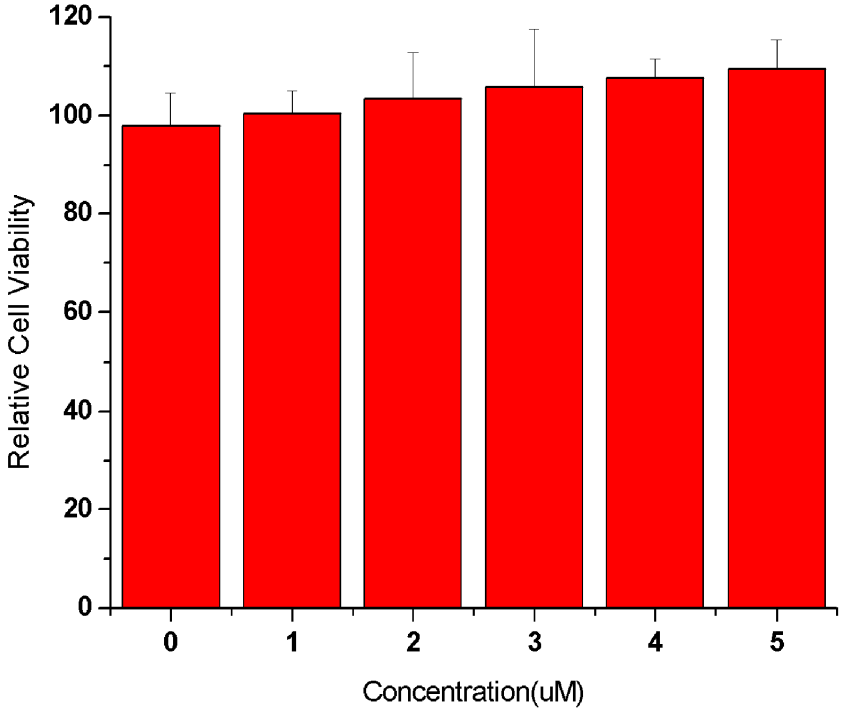



Fig. 3. Cytotoxicity of the silver nanocluster on HeLa cells was measured by MTT assays (n = 8, mean±S.D.). The result showed the relative cell viability of the cells accompany with silver nanocluster with the final concentrations of 0, 5, 8, 10, 15 and 20 μM. The viability of positive control that treated with same volume of water was taken as 100%.

The cytotoxicity of the silver nanocluster on the cell proliferation used in our system was investigated by MTT assay. Fig.3 showed the data of cell viability of the HeLa cells after 24 h of incubation with the transfection complexes. Non-transfected cells were severed as the control and the cell viability of which were set as 100%. It was found that the silver nanocluster for the transfection had hardly any toxicity to the cells. In the presence of silver nanocluster, the cell viabilities increased to be more than 10% for both of the transfection systems. With addition of silver nanocluster at the concentration of 30 μM, the cell viabilities for silver nanocluster did not decrease.

## Conclusions

In summary, we demonstrate the novel method of generating Methylthiouracil -encapsulated silver nanoclusters in aqueous solution. Although fluorescence signal of the Methylthiouracil -encapsulated silver nanocluster in aqueous solution is weak, however, the signal of silver nanocluster incubated with cells is very strong. The data of TEM verified that size of silver atoms are below to 2nm. This work develops successfully the capping Methylthiouracil scaffolds of silver nanoclusters, and the high photobleaching may have great potential in early detection of cancer and bioanalysis field. A mechanism of generating fluorescence signal is accordingly proposed. These new insights into the Methylthiouracil -encapsulated silver nanoclusters will help us to further extend their applications in the bioanalytical field, especially single-molecule studies faster and in longer time scales.

## Acknowledgement

This work was supported by the Inner Mongolia Natural Science Foundation of China: 2011MS0206 and The Inner Mongolia Science and Technology Project:2013.

## References

[1] T. Vosch, Y. Antoku, J.C. Hsiang, C.I. Richards, J.I. Gonzalez, R.M. Dickson, PNAS 104 (2007) 12616–12621.

[2] J.P. Wilcoxon, B.L. Abrams, Chem. Soc. Rev. 35 (2006) 1162–1194.

[3] J. Zheng, P.R. Nicovich, R.M. Dickson, Annu. Rev. Phys. Chem. 58 (2007) 409–431.

[4] S. Link, S. FitzGerald, M.A. El-Sayed, T.G. Schaaff, R.L. Whetten, J. Phys. Chem. B 106 (2002) 3410–3415.

[5] K. Koszinowski, K. Ballweg, Chem-Eur J, 16 (2010) 3285-3290. 5207–5212

[6] N. Nishida, E. S. Shibu, H. Yao, T. Oonishi, K. Kimura, T. Pradeep, Adv. Mater. 2008, 20, 4719–4723.

[7] J.T. Petty, J. Zheng, N.V. Hud,.R. M. Dickson, J. Am. Chem. Soc, 126 (2004) 5207-5212.

*Advanced Materials Research Vol. 937 (2014) pp 260-266*
*© (2014) Trans Tech Publications, Switzerland*
*doi:10.4028/www.scientific.net/AMR.937.260*

# A Facile and Efficient Method to Prepare Exfoliated and Reduced Graphene Nanosheets by Detonation

Yan-hua GUO[1,a] Dong-xian ZHUO[1,b], Li-xin WU[1,*], Lin MA[1,c], Zi-xiang WENG[1,d], Rui WANG[1,e]

[1]State Key Laboratory of Structural Chemistry, Fujian Institute of Research on the Structure of Matter, Chinese Academy of Sciences, Fuzhou 350002, China

[a]guoyanhua28@fjirsm.ac.cn, [b]dxzhuo@fjirsm.ac.cn, [c]ling@fjirsm.ac.cn, [d]wzx@fjirsm.ac.cn, [e]wangrui@fjirsm.ac.cn

*lxwu@fjirsm.ac.cn

**Keywords:** Low-temperature exfoliation, Few-layered graphene nanosheets, Detonation.

**Abstract:** A facile, efficient, and low energy consumption detonation method to prepare few-layered graphene nanosheets has been developed using graphite oxide as a precursor at detonation induced temperature as low as 100 °C . The composition and structure of as-produced few-layered graphenes were characterized by X-Ray Diffraction (XRD), Scanning Electron Microscope (SEM), Fourier Transform Infrared (FTIR), Specific Surface (BET), Transmission Electron Microscopy (TEM), Raman Microscope, and Atomic Force Microscope (AFM). Results showed that the as-produced graphenes were transparent and few-layered with a high specific surface area (225.9 $m^2/g$). The investigation opens a new road to prepare few-layered graphene nanosheets at low exfoliation temperature in a low-cost and facile way.

## Introduction

First prepared almost 150 years ago, graphite oxide (GO) has re-emerged as an intensive research interest in recent years due to its role as a precursor for the affordable and industrial production of graphene-based materials [1]. GO consists of a two-dimensional sheet of covalently bonded carbon atoms bearing various oxygen functional groups (e.g. hydroxyl, epoxide, and carbonyl groups) on the basal planes and edges. The typical GO derived materials include chemically functionalized [2] or reduced [3] graphene oxide (exfoliated from GO) sheets, assembled paper-like forms [4], and graphene-based composites [5].

Due to the attached oxygen functional groups, GO is electrically insulating and various reduction methods have been developed to restore its electrical conductivity. It is well known that several reduction approaches, such as microwave exfoliation [6], thermal exfoliation [7], and sonication plus chemical reduction [8], have been successfully used to convert insulating GO to conducting graphene-like layers. Among these approaches, thermal exfoliation of dry GO by rapid heating treatment at high temperature is the most promising one for large-scale production of graphene-based materials without using potentially hazardous reducing agents [7]. McAllister et al. [7] had proven that high temperature (1050 $^oC$) and rapid heating (>2000 $^oC$/min) were required to ensure the complete exfoliation of GO. It was also reported that a critical temperature of 550 $^oC$ must be exceeded for complete exfoliation to occur. When the decomposition rate of the epoxide and hydroxyl groups of GO surpassed the diffusion rate of the evolved gases, the generated pressure would be high enough to counteract the van der Waals force that holds the graphene sheets together, and thereby enable the complete exfoliation to occur. However, thermal treatment at such a high temperature with the fast heating rate involves huge energy consumption and difficulties in operation, and then hard to achieve. Therefore, it is necessary to develop a facile and efficient approach which can simultaneously achieve high temperature and rapid heating for thermal exfoliation of GO.

It is known that the fast decomposition of explosives can produce high temperature and powerful shock wave, and thus making use of detonation technology to thermal exfoliation of GO is a highly effective approach. Ling et al. [9] reported a new approach to successfully prepare graphene

nanosheets through detonation of GO and explosive compound (picric acid) under sealed stainless steel pressure vessel. This supplies an efficient approach to transform GO to graphene-like layers. However, this approach is limited in application by its high pressure (20MPa). In addition, high pressure was thought to exert an inward force on the expanding graphene layers and inhibit the expansion of graphene layers, ultimately hard to yield complete exfoliated graphite oxide [10,11].

In this paper, a novel approach was proposed to prepare exfoliated and reduced graphene nanosheets (ER-GO) by a controlled detonation, involving complete oxidation of natural graphite (NG), rapid decomposition of explosives, and exfoliation and reduction of GO. The stucture of as-produced ER-GO were analyzed by mutil-testings. the exfoliation mechanism of GO was proposed. This investigation opens a new road to prepare few-layered graphene nanosheets at low exfoliation temperature in a low-cost and facile way.

## Experimental

### Materials

Natural graphite (NG) was bought from Aladdin Reagent Ltd in China. Sulfuric acid ($H_2SO_4$), hydrochloric acid (HCl), potassium permanganate ($KMnO_4$), acetone, and hydrogen peroxide were commercial products in analytical grades and used without further purification; distilled water was produced in our lab.

### Preparation of Graphene Oxide (GO)

The preparation of graphite oxide (GO) completely follows the modified Hummers's method [12]. Typically, 0.25 g graphite and 0.125 g $NaNO_3$ were added into the 100 ml flask filled with 12 ml $H_2SO_4$ (98 %) in the ice bath under stirring. Next, 0.75 g $KMnO_4$ was added slowly to the solution, keeping the temperature below 15 °C. After adding $KMnO_4$, the ice bath was removed and the flask was heated to 50 °C, followed by the slow addition of 12 ml deionized water. The temperature of the solution was increased to 98 °C and the solution was maintained at this temperature for 15 min. Next, the 50 ml deionized water with 10% $H_2O_2$ was added to the solution until the cessation of gas evolution. The solution was left at room temperature for one night and then centrifuged at 11000 rpm. Finally, the precipitation was then dried at 40 °C under vacuum for three days to obtain GO powers.

### Exfoliation and reduction of GO

Appropriate amount of dried GO precipitation was immersed in acetone in a short time, and then placed in a blast drying oven under open environment. Here, GO was thermally exfoliated at 100 ºC for 5 min under atmosphere pressure, and then was transferred to ER-GO.

### Measurements

Fourier Transform Infrared (FTIR) spectra were recorded using a PerkinElemer Spectrum One spectrometer (USA) from 400 to 4000 $cm^{-1}$ with a resolution of 2 $cm^{-1}$ (KBr pellet technique).

Raman Microscope (Renishaw, Invia, 514 nm) is used to determine the Raman scattering characteristics of the samples. The laser power used is 1 mW.

A Scanning Electron Microscope (SEM) (JEOL JEM-2010, Japan) was employed to observe the morphologies of samples. The resolution of the secondary electron image is 1.5 nm under 15 kV. All samples should be dried at 50 °C for 24 h before test.

Transmission Electron Microscopy (TEM) was recorded on a JEM-2010 (JEOL, Japan) at a 200 kV accelerating voltage. The samples were prepared by mounting a drop of the micelle solution (0.05 mL) on a copper EM grid covered with a thin film of formvar.

AFM measurements were performed to characterize the sheet thickness and dimensions using the Scanning Probe Microscopy (Veeco Instruments, Nanoscope Multimode IIIa, USA) operated in contact mode.

Thermogravimetric analyses (TGA) were performed on a Netzsch Instruments STA449C (USA) in the range from 25-800 °C under a nitrogen atmosphere with a flow rate of 100 ml/min and a heating rate of 10 °C /min.

X-ray Diffraction (XRD) analyses were carried out on a MERCURY CCD X-ray diffractometer (RIGAKu, Japan, λ=0.15mm) with CuKα radiation. The 2θ angle ranged from 5 ° to 60 °, and the scan rate was 2 °/min.

The Specific Surface (BET) was performed with ASAP2020M (USA) automatic surface analyzer.

## Results and Discussion

### XRD Patterns

The interlayer spacing of NG, graphite oxide (GO), and as-produced graphene (ER-GO) were characterized by XRD, and the corresponding spectras are shown in Fig. 1. NG showed a sharp and intensive (002) peak at 26.3 º, indicating a highly ordered crystal structure with an interlayer spacing of 0.330 nm. After oxidation, the 002 diffraction peak of NG disappeared, and then the XRD pattern of GO shows a small and wide peak at 7.9 °, corresponding to an interlayer spacing of 1.089 nm. This indicates that graphite is transformed into graphite oxide.Most of oxygen atoms and functional groups are bonded to the planar surface of Go sheet. These atoms and groups, plus the wrinkles of Go enlarge the d-spacing betweein GO layers. Moreover, the interlayer spacing of as-prepared GO (1.089 nm) is larger than that of typical GO (0.7-0.9 nm) [13], which can be attributed to the existence of intercalated hydrogen peroxide and sulfuric acid [14]. In contrast, after detonation, the peak at 7.9 ° disappears completely and a broad peak at 23.1 ° appears in the pattern of EP-GO, indicating that graphite was exfoliated into single-layered or few-layered sheets. and with the formation of a new lattice structure which is significantly different from the graphite a complete elimination of stacked layers to high degree of exfoliation. This feature is similar to that of chemically reduced graphene [15].

### SEM, TEM, and AFM

The structural feature of EP-GO was further characterized with high resolution SEM, TEM and AFM. Fig. 2a and 2b show the SEM images of EP-GO. Generally, due to the low electric conductivity of GO, a thin gold layer is sputtered onto the surface of the GO is neccessary to get clear SEM images. However, after detonation, high resolution imaging can be easily achieved without any pretreatments, suggesting that the EP-GOs have an enhanced conductivity. In addition, the EP-GO sheet resembles a transparent ultrathin film with a few thin ripples within the plane, quite different from the opaque and smooth feature of typical natural graphite. It is known that the perfect two-dimensional graphene sheets are thermodynamically unstable, and thus corrugations and ripples are formed on the sheet for thermodynamic stability. Thereby, the transparency and rippled features of the EP-GO sheet, in turn, suggest that graphene sheets prepared with the detonation are wafer-thin and mainly consist of few layered nanosheets.

The structural feature of EP-RO was further characterized with high resolution TEM and AFM. As shown in Fig. 2c, the samples are homogeneous micrometer-sized flakes, with low contrast, indicating the small thickness. The corrugation is intrinsic to EP-RO, which results from the fact that the two-dimensional membrane structure becomes thermodynamically stable via bending. Consistent with the SEM result, these results indicate that the obtained material is few layered sheets. AFM was also used to determine the thickness of graphene sheets, and many sheets were measured to get an average thickness. As shown in the AFM image of Fig. 2d, EP-RO has a lateral dimension of several micrometres with an average thickness of approximately 1.1 nm, which is very close to the reported apparent thickness of two-layer graphene. Therefore, it is clear that high degree of exfoliation is achieved and few-layered graphene sheets were produced, which is consistent with the absence of the characteristic peaks in the XRD pattern.

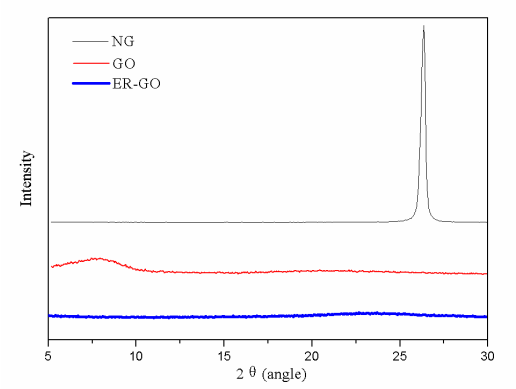



Fig. 1. XRD patterns of NG, GO, and ER-GO

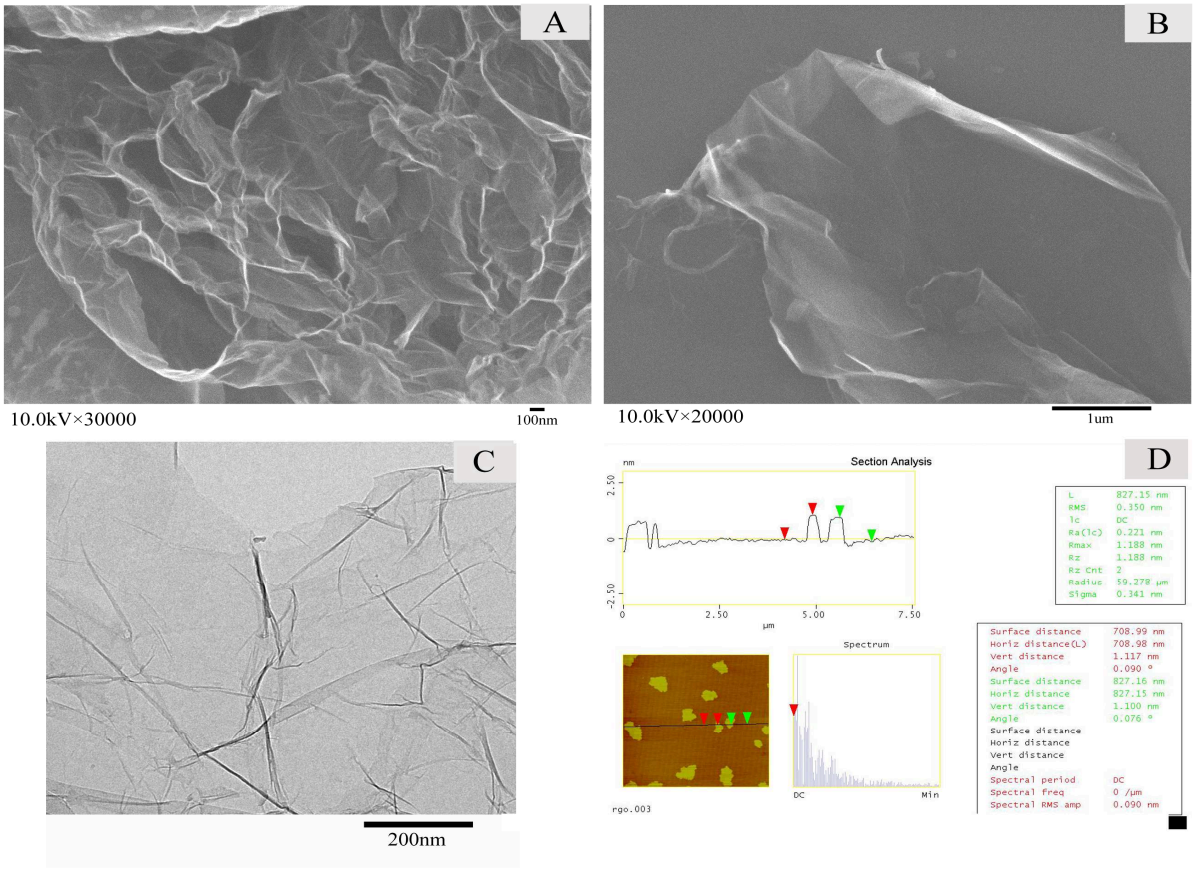



Fig. 2. Optical photos of ER-GO (A) and (B) Typical SEM images of as-prepared ER-GO. (C) Typical TEM image of as-prepared ER-GO. (D) Typical AFM image of as-prepared ER-GO

## Raman Spectroscopy

Raman scattering is strongly sensitive to the electronic structure and proves to be an essential tool to characterize graphite and graphene materials. As shown in Fig. 3, pristine graphite demonstrates a strong band at 1577 $cm^{-1}$ (G band) and a weak band at 1312 $cm^{-1}$ (D band). The G band and D band are attributed to the first-order scattering of the $E_{2g}$ vibrational mode in the graphite sheet and structure defects, respectively. For the Raman spectrum of GO, the D band becomes prominent and shifts to 1347 $cm^{-1}$. Additionally, the G band broadens and shifts to 1607cm $^{-1}$, indicating the reduction in size of the in-plane $sp^2$ domains, possibly due to the extensive oxidation. After detonation, both G and D bands becomes sharp in the Raman spectrum of ER-GO, and shifts back to 1591 $cm^{-1}$ and 1312 $cm^{-1}$, respectively; however, with an increased D/G intensity ratio compared to

that in GO. This change suggests a decrease in the average size of the $sp^2$ domains upon reduction of the exfoliated GO [16], and can be explained if new graphitic domains were created that are smaller in size to the ones present in GO before reduction, but more numerous in number.

**TGA and BET**

To confirm the reduction effect, TGA was used to study the thermal stability of GO and ER-GO, as shown in Fig. 4. In agreement with previous reports, there is a small mass loss (6 wt %) around 100 °C and a major mass loss (25 wt %) around 250 °C for the GO due to the loss of adsorbed water and pyrolysis of the unstable oxygen functionalities, respectively. Compared to GO, however, ER-GO exhibit clearly increased thermal stability without significant mass loss between 200-400 °C. Additionally, the residual char yield of ER-GO are still 76.1 wt%, much higher than 53.4% of GO at 800 °C, further confirming that the GO was reduced after detonation due to the gradual removal of the labile oxygen functionalities. A $N_2$ adsorption Brunauer–Emmett–Teller measurement on the as-prepared ER-GO powders showed a specific surface area of 225.9 $m^2/g$, 2.5-6.5 times higher than the typical values (33-87 $m^2/g$) obtained from the EG prepared by treatment of GICs with microwave irradiation or rapid heating to 1000 °C [17,18]. The high specific surface area is an indication of the high degree of GO exfoliation after detonation, and is consistent with the XRD, SEM, TEM, and AFM results.

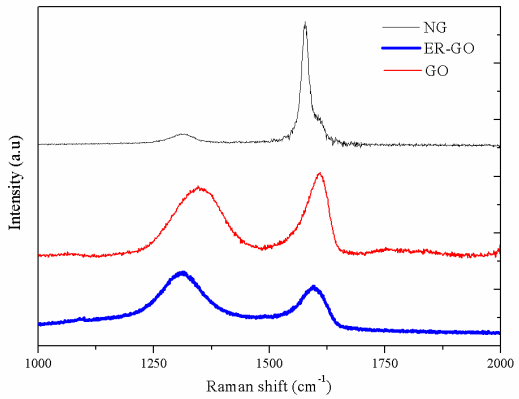



Fig. 3. The Raman spectra of NG, GO, and ER-GO

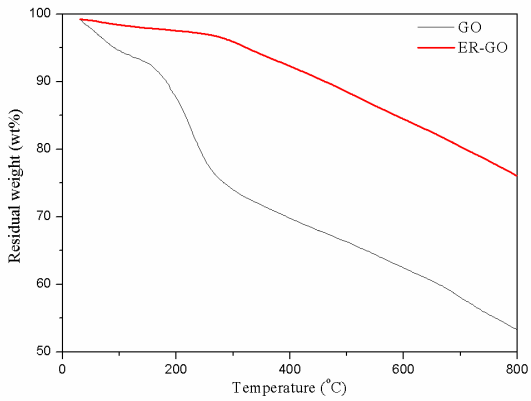



Fig. 4. Normalized TGA plots of GO and the obtained ER-GO

**Mechanism of Exfoliation**

Based on the above analysis, the exfoliation mechanism of GO is proposed in Fig. 6. First, NG was completely oxidized into GO, resulting in abundant oxygen-containing functional groups bonded to the basal planes of the graphite structure; meanwhile, proper hydrogen peroxide and sulfuric acid were intercalated in the planar surface of graphite. Second, the existence of hydrogen peroxide and sulfuric acid reacted with acetone to form explosive compound. Third, the detonation of explosive compound was induced by an external heating, the self-generated enormous thermal energy, and a powerful shockwave at a microsecond scale. Lastly, GO was rapidly heated to high temperature and its oxygen functionalities decomposed into $CO_2$ and $H_2O$. The expansion of the gases evolved into the interstices between the adjacent graphite sheets, resulting in the exfoliation of GO. The reduction of GO was simultaneously completed accompanied with the decomposition of oxygen-containing groups; meanwhile, the outward drawing force formed during the instantaneous decomposition of oxygen functionalities and detonation of explosive compound sheared GO exfoliation into few-layered graphene sheets.

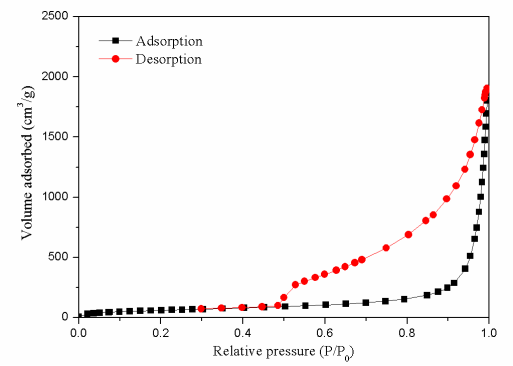



Fig. 5. Nitrogen adsorption and desorption isotherms of ER-GO at 77 K

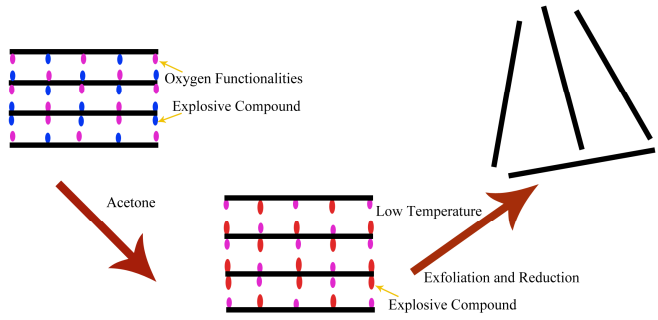



Fig. 6. Schematic Representation of the exfoliation and reduction of GO

## Conclusion

Few-layered graphenes have been produced by a detonation approach at an induced temperature as low as 100 °C. Exfloliated and reduced graphenes were produced and comfirmed by XRD, SEM, TEM, AFM, Raman spectroscopy, TGA, and BET tests. This approach is facile, efficient, and opens a new road to prepare few-layered graphene nanosheets at low cost and low exfoliation temperature .

## Acknowledgement

This research was financially National Natural Science Foundation of China (Grant No.: U1205114), Science Foundation of Fujian province (Grant No.: 2013H0062), and the "Strategic Priority Research Program" of the Chinese Academy of Sciences (Grant No.: XDA09020301).

## References

[1] S. Park, R.S. Ruoff, Nat. Nanotechnol.4 (2009) 217-224.

[2] S. Stankovich, R.D. Piner, S.T. Nguyen, R.S. Ruoffm, Carbon. 44 (2006) 3342-3347.

[3] Z.J. Fan, W. Kai, J. Yan, T. Wei, etal., ACS. Nano. 5 (2011) 191-198.

[4] D.A. Dikin, S. Stankovich, E.J. Zimney, etal., Nature. 448 (2007) 457-460.

[5] S. Stankovich, D.A. Dikin, G.H.B. Dommett, K.M. Kohlhaas, E.J. Zimney, E.A. Stach, etal, Nature. 442 (2006) 282-286.

[6] Y.W. Zhu, S. Murali, M.D. Stoller, A. Velamakanni, R.D. Piner, R.S. Ruoff, Carbon. 48 (2010) 2106-2122.

[7] M.J. McAllister, J.L. Li, D.H. Adamson, H.C. Schniepp, A.A. Abdala, J. Liu, M. Herrera-Alonso, D.L. Milius, R. Car, R.K. Prud'homme, I.A. Aksay, Chem. Mater. 19 (2007) 4396-4404.

[8] X. Fan, W. Peng, Y. Li, X. Li, S. Wang, G. Zhang, F. Zhang, Adv. Mater. 20 (2008) 4490-4493.

[9] C. Wang, L. Zhan, W.M. Qiao, L.C. Ling, New. Carbon. Mat er. 26 (2011) 21-25.

[10] W. Lv, D.M. Tang, Y.B. He, C.H. You, Z.Q. Shi, X.C. Chen, C.M. Chen, P.X. Hou, C. Liu, Q.H. Yang, ACS. Nano. 3 (2009) 3730-3736.

[11] H.B. Zhang, J.W. Wang, Q. Yan, W.G. Zheng, C. Chen, Z.Z. Yu, J. Mater. Chem. 21 (2011) 5392-5397.

[12] S. Stankovich, D. Dikin, G. Dommett, K. Kohlhaas, E. Zimney,E. Stach, R. Piner, S. Nguyen, R. Ruoff, Nature, 2006, 442, 282.

[13] T.N. Zhou, F. Chen, K. Liu, H. Deng, Q. Zhang, J.W. Feng, Q. Fu, Nanotechnology. 22 (2011) 045704.

[14] C. Nethravathi, M. Rajamathi, Carbon. 46 (2008) 1994-1998.

[15] H.M.A Hassan, V. Abdelsayed, A.E.R.S. Khder, etal, J. Mater. Chem. 19 (2009) 3832-3837.

[16] S. Stankovich, D.A. Dikin, R.D. Piner, K.A. Kohlhaas, A. Kleinhammes, Y. Jia, Y. Wu, S.T. Nguyen, R.S. Ruoff, Carbon. 45 (2007) 1558-1565.

[17] B. Tryba, A.W. Morawski, M. Inagaki, Carbon. 43 (2005) 2397-2429.

[18] E.H.L. Falcao, R.G. Blair, J.J. Mack, L.M. Viculis, C.W. Kwon, M. Bendikov, R.B. Kaner, B.S. Dunn, F.Wudl, Carbon. 45 (2007) 1364-1369.

# CHAPTER 5:

# Biomaterials and Healthcare

*Advanced Materials Research Vol. 937 (2014) pp 269-275*
*© (2014) Trans Tech Publications, Switzerland*
*doi:10.4028/www.scientific.net/AMR.937.269*

# Drug Sustained Release Multiple-component Polymeric Microparticles Fabricated Using an Electrospray Process

Xiao-yan LI, Deng-guang YU*, Fa-ping JIANG, Kong-jing DENG, Zhi DU, Xia WANG*

School of Materials Science & Engineering, University of Shanghai for Science and Technology, Shanghai 200093, China.

E-mail: ydg017@usst.edu.cn, wangxia@usst.edu.cn

**Keywords:** Electrospraying, Sustained drug release, Multiple-component, Polymeric Microparticles, Microcomposites

**Abstract.** The present study investigates the preparation of ferulic acid (FA) sustained-release cellulose acetate (CA) microparticles, in which a third component, polyvinylpyrrolidone (PVP), was included into the microcomposites for an improved sustained drug release profile. An electrospraying process was exploited for the fabrication of multiple-component microparticles. Under an applied voltage of 18 kV, FA/PVP/CA composite microparticles were successfully generated. Field emission scanning electron microscopic observations demonstrated that these microparticles had an indented surface morphology with an average diameter of 1.71 ± 0.56 μm. The drug presented in the polymeric microparticles in an amorphous state due to the favorable secondary interactions among the components, as verified by the X-ray diffraction (XRD) patterns and attenuated total reflectance Fourier transform spectra. The triple-component microparticles could provide a fine sustained release profiles with full release completeness and small tailing-off release time period. The electrospraying process is a useful tool for developing sustained release microparticles and multiple-component co-existence in the microparticles can be taken to adjust the sustained drug release profiles.

## Introduction

Polymeric microparticles are particles in size range of 1~1000 μm, usually with solid, porous, or compartmental polymeric interiors. Polymeric microparticles with advanced functions, such as targeted delivery and controlled encapsulation or capture and release, show great importance in numerous applications, including drug delivery, diagnostic imaging, and confined micro-reaction [1].

Microparticles have been prepared most frequency by the following methods: 1) dispersion of preformed polymers; 2) polymerization of monomers; and 3) ionic gelation or coacervation of hydrophilic polymers; 4) supercritical fluid technology; 5) particle replication in non-wetting templates and 6) microfluidic emulsions [2]. Because of many advantages of using micro/nanoparticles as a drug delivery system, new methods for preparing drug-loaded nanoparticles are highly sought after. Especially those that can overcome some limitations associated with traditional preparation methods, such as particle aggregation, difficulty of physical handling of micro/nanoparticles, limited drug loading and burst release. In general, the overall functions of microparticles can be manipulated through their structures and their shapes. However, the mainstream is to take advantage of the properties of their component materials to achieve the desired functions.

Electrohydrodynamic atomization (EHDA), a simple and straightforward process for the preparation of particulate polymeric micro- and nano- particles, fibers and thin films, is now becoming more and more popular recently. A significant feature of this technique is its ability to generate particles and fibers with a mean diameter that can be varied between hundreds of micrometers and tens of nanometers by varying the processing parameters for a particular system such as flow rate, needle diameter, applied voltage, as well as the chemical composition and concentration of the polymer solution [3,4]. And another feature is that electrospraying can be taken for generating microparticles from a wide variety of different types materials, including polymer, inorganic materials

and little chemical molecules, whereas the electrospinning can be exploited for the treatment of over 100 polymers with suitable molecular weights and several types of little molecules [5]. Electrosprayed microparticles have found applications in a wide range of fields including in the pharmaceutics, ceramics, cosmetics and food industries. In the biomedical and drug delivery area, the Edirisinghe group has successfully prepared hollow microspheres, porous films, drug-loaded micro- and nano-particles, and microbubbles using this technology [6-8]. All their researches have demonstrated that electrospraying is a useful tool for developing novel biomaterials and drug delivery systems.

Building on the developments discussed thus far, this study investigates the preparation of drug-loaded cellulose acetate (CA) microparticles with an additional component, polyvinylpyrrolidone (PVP), for facilitating the complete exhaustion of drug and diminishing the "tailing-off" time period, as a means of improving the profile of sustained drug release. An electrospraying process was used to generate the multiple-component microparticles. CA, the acetate ester of cellulose, has been widely investigated for a variety of potential applications in the form of electrospun nanofiber mats, because of its advantageous properties, such as good biocompatibility, biodegradability, regenerative properties, and high affinity with other substances, and hence was used as the filament-forming polymer matrix [9]. Ferulic acid (FA, 4-hydroxy-3-methoxycinnamic acid), an antioxidant capable of scavenging free radicals, was used as the model active ingredient [10]. PVP has a wide variety of applications in medicine, pharmaceutics and cosmetics, and has been widely used as a template for preparing functional nanofibers for applications such as drug-containing nanofibers, inorganic–organic composites, inorganic nanofibers, precursors for organic peroxide nanofibers and liposomes. In drug delivery, PVP is widely used as a binder in tableting (wet granulation, dry granulation, direct compression and effervescent tablets), in film coatings and adhesive gels, and is particularly used as an excipient to prepare solid dispersions for improving the dissolution rates of poorly water-soluble drugs [11].

## Materials and Methods

### Materials

CA (white powder; $M_w$ = 30,000 Da ) was purchased from Acros (NJ, USA) and used as received. FA was purchased from Shanghai Winherb Medical Sci & Tech Development Co., Ltd. (Shanghai, China). PVP K25 ($M_w$ =30,000) was obtained from Shanghai Yunhong Pharmaceutical Aids and Technology Co., Ltd. (Shanghai, China). Methylene blue, *N*,*N*-dimethylacetamide (DMAc), acetone and anhydrous ethanol were purchased from Sinopharm Chemical Reagent Co., Ltd. (Shanghai, China). All reagents were analytical grade and used without further purification. Water was double distilled just before use.

### Electrospraying

The spraying fluids were prepared by dissolving 4.0 g of CA, 1.0 g of FA and 1.0 g PVP K25 in 100 mL of a solvent mixture of acetone: ethanol: DMAc with a volume ratio of 4:1:1. A syringe pumps (KDS100, Cole-Parmer, IL, USA), a high-voltage power supply (ZGF 60 kV/2 mA, Shanghai Sute Corp., Shanghai, China), and a spray head made of G21 stainless steel tube were used to conduct the electrospraying process under a fixed voltage of 18 kV and a particle-accepted distance of 20 cm. All processes were carried out under ambient conditions (23 ± 2 °C; relative humidity, 59% ± 4%). The electrospraying process was recorded using a digital video recorder (PowerShot A490, Canon, Tokyo, Japan).

## Characterization

### Morophology

The morphology of the microparticles was assessed using a Quanta FEG450 scanning electron microscope (SEM) (FEI Corporation, Netherlands). Prior to the examination, the samples were rendered electrically conductive by gold sputter coating under a nitrogen atmosphere. The average diameter was determined by measuring diameters in the SEM images at more than 100 different particles using Image J software (National Institutes of Health, MD, USA). The topography of the FA particles and also the sprayed microparticles were observed under cross-polarized light using an XP-700 polarized optical microscope (Changfang Optical Instrument Co., Ltd. Shanghai, China).

### Physical Status of Components and Compatibility

X-ray diffraction (XRD) patterns were obtained on a D/Max-BR diffractometer (RigaKu, Tokyo, Japan) with CuK$\alpha$ radiation within the $2\theta$ range of 5°-60° at 40 mV and 30 mA. Attenuated total reflectance (ATR-) Fourier transform infrared (FTIR) analyses were performed on a Nicolet-Nexus 670 FTIR spectrometer (Nicolet Instrument Corporation, WI, USA) from 500 $cm^{-1}$ to 4000 $cm^{-1}$ at a resolution of 2 $cm^{-1}$.

### In Vitro Dissolution Tests In Vitro

Dissolution tests were carried out according to the Chinese Pharmacopoeia (2005 ed.) Method II, a paddle method in which an RCZ-8A dissolution apparatus (Tianjin University Radio Factory, Tianjin, China) was used. About 200 mg of drug-loaded microparticles were placed in 900 mL of physiological saline (PS; 0.9 wt%) at 37 ± 1 °C. The instrument was then set to 50 rpm, providing sink conditions in which $C < 0.2C_s$. At predetermined time points, 5.0 mL samples were withdrawn from the dissolution medium and replaced with fresh medium to maintain a constant volume. After filtration through a 0.22 μm membrane (Millipore, MA, USA) and appropriate dilution with PS, the samples were analyzed at $\lambda_{max}$ =322 nm using a UV-vis spectrophotometer (UV-2102PC, Unico Instrument Co. Ltd., Shanghai, China). The cumulative amount of FA released at each time point was reverse calculated from the data obtained against a predetermined calibration curve. Experiments were carried out six times and the results are presented as mean values.

## Results and Discussion

### Electrospraying

A schematic diagram of the electrospraying process is shown in Fig. 1a. An electrospraying system comprises four major components: a fluid driving device-syringe pump, a power supply, a grounded collector and a capillary for introducing the sprayed fluid.

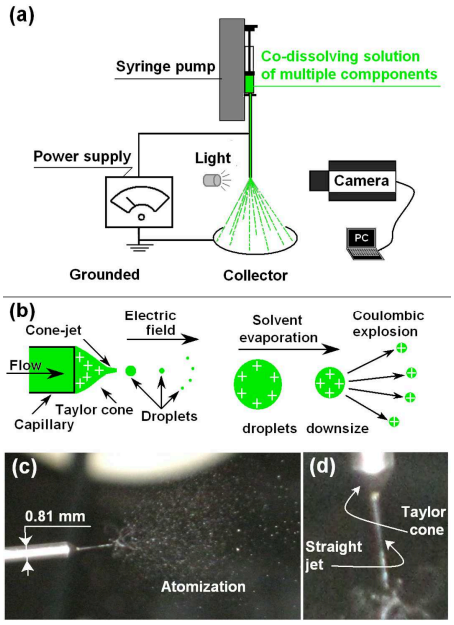



Fig. 1. Electrospraying process and atomization mechanisms: (a) a schematic diagram of the electrospraying process, (b) the formation of the Taylor cone, the cone-jet at the spraying head, and the Coulombic fission of the charged liquid droplet into smaller droplets, (c) a photograph of the actual electrospraying process taken *in situ* and (d) the Taylor cone.

During the electrospraying process, a fluid is fed to a capillary at the end of which a droplet is formed. When the droplet is exposed to a strong electric field, a charge is induced on its surface. Provided the liquid has sufficient electrical conductivity, there will be a range of combinations of the liquid flow rate and the applied voltage for which the drop will assume a conical shape (the Taylor cone). At the apex of this cone, a narrow jet is formed (cone-jet mode) which subsequently breaks up into fine droplets (Fig. 1b and d). Electrospraying first generates near-monodisperse droplets whose size can be varied between a few to hundreds of micrometers. Later, the droplets rapidly shrink due to the fast evaporation of solvents resulting from the Coulombic explosion (Fig. 1b and c). The huge surface areas of the micro-droplets provide the possibility for complete of the solvents and the solidification of products. The facile interactions of electrons with fluid solvents accelerate their evaporation.

**Microparticulate Morphology**

FESEM images of the microparticles are shown in Fig. 2. Figs. 2 (a) to (c) show FESEM images of the microparticles at different magnifications. These microparticles exhibited a flat morphology with indented surface and also some satellites on them. They have an average diameters of 1.71 ± 0.56 µm (Fig. 1d). During the electrospraying process, the fast evaporation of the solvent from the charged droplets made their surface first solidify. Later when the droplets were shrunk into microparticles, there were still some solvents trapped in the them. When these solvents finally escaped, the barometric pressure would flatten the microparticles.

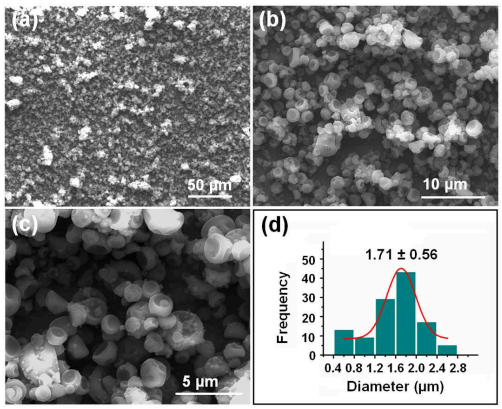



Fig. 2. FESEM images: (a) to (c) the composite microparticles with different imaginations, (d) diameter distributions of the microparticles.

**Physical Status of FA in the Microparticles**

FA, a slight yellow powder to the naked eye, comprised polychrome crystals in the form of prisms or needles, and revealed a rough surface under cross-polarized light (Fig. 3). The presence of many distinct peaks (Fig. 3) in the XRD pattern of pure FA similarly verified that FA was present as a crystalline material. The diffraction patterns of raw CA powders exhibit a diffuse background pattern with one diffraction halo, indicating that the polymer is amorphous. The spectrum of amorphous PVP K25 was characterized by the complete absence of any diffraction peak. From Fig. 5, it is clear that the characteristic diffraction peaks of crystalline FA are completely absent for the composite microparticles. The result suggest that all the FA in the triple-component microparticles was amorphous.

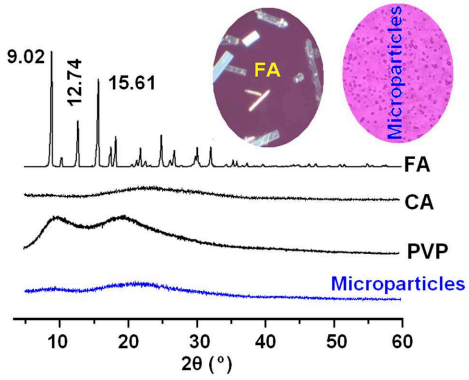



Fig. 3. XRD patterns of the microparticles and their components.

The molecular structures of the three components are shown in Fig. 4. FA and CA molecules possess free hydroxyl groups (-OH) and these could act as potential proton donors for hydrogen bonding. CA, FA and PVP molecules have carbonyl groups (-C=O) and so could act as proton acceptors. Therefore it can be speculated that hydrogen bonding interactions can occur within the composite microparticles through interactions between these groups. ATR-FTIR spectra are included in Fig. 4. A different type of hydrogen bonding between FA molecules in the FA crude particles is possible because FA molecules have both -OH groups and -C=O groups. This can be verified by the ATR-FTIR spectra in which sharp peaks were visible for pure crystalline FA at 1689, 1663 and 1619 $cm^{-1}$, representing the stretching vibration of –C=O groups in the different structure of the crystal lattice. However, all the peaks for FA disappeared in the ATR-FTIR spectra of the composite microparticles. Only one large peak at 1728 $cm^{-1}$ for composite microparticles was noted. Meanwhile, numerous peaks at the finger region of the FA spectra were absent in the spectra of microparticles. These results jointly suggest that there are fewer interactions between the FA

molecules, but extensive hydrogen bond formation between the CA and FA molecules and also between PVP and FA molecules. The hydrogen bonding, combined with the possible electrostatic and hydrophobic interactions, should provide an environment that stabilizes the structure so giving a high degree of compatibility between the components that make up the microparticles, and made them a homogeneous structure.

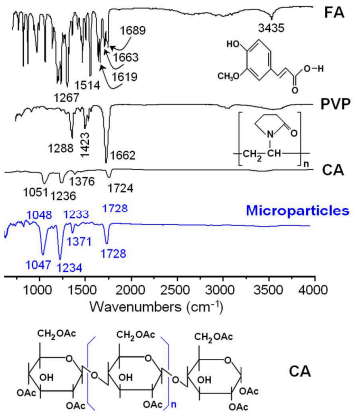



Fig. 4. ATR-FTIR spectra of the microparticles and their components.

### In Vitro Dissolution Properties

The *in vitro* release profiles of FA from the composite microparticles are shown in Fig. 5. Just as anticipated, there was an initial burst effect of FA from the polymeric microparticles, which should be attributed to the hydrophilic properties and easy dissolution of PVP, the huge surface of microparticles, the amorphous state of FA and its uniform distributions in the microparticles. However, this multiple-component microparticles showed advantages over the traditional double-component polymeric microparticles in that: 1) they could completely release all the contained drugs without residue trapped in the un-soluble polymer matrix, and 2) they eliminated the long time period "tailing-off" release to some extent, which is an unfavorable phenomenon during sustained release [12].

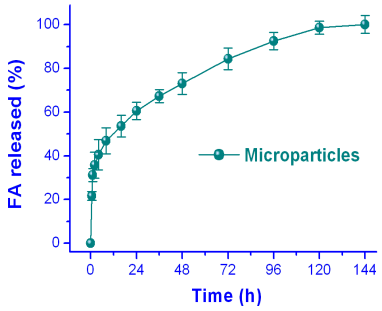



Fig. 5. *In vitro* dissolution profiles

### Summary

Triple-component FA-loaded CA microparticles were fabricated through an electrospraying process. FESEM observations demonstrated that these microparticles had an indented surface morphology with an average diameter of 1.71 ± 0.56 μm. The drug presented in the polymeric microparticles in an amorphous state due to the favorable secondary interactions among the components, as verified by the XRD patterns and ATR-FTIR spectra. The triple-component microparticles could provide a fine sustained release profiles with full release completeness and small tailing-off release time period. The electrospraying process is a useful tool for developing sustained release microparticles and multiple-component co-existence in the microparticles can be taken to adjust the sustained drug release profiles.

**Acknowledgement**

This work was supported by the National Science Foundation of China (Nos. 51373101 and 51373100), the Natural Science Foundation of Shanghai (Nos. 13ZR1428900), the Key Project of the Shanghai Municipal Education Commission (No.13ZZ113) and the Innovation Project of the College Student Fund Committee (No. SH2013167).

**References**

[1] A. A. Moshfeghi and G. A. Peyman, Adv. Drug Del. Rev. 57 (2005) 2047.

[2] W. Wang, M. J. Zhang, and L. Y. Chu, Acc. Chem. Res. (2013) Doi: 10.1021/ar4001263.

[3] D. G. Yu, J. H. Yang, X. Wang, and F. Tian, Nanotechnology 23 (2012) 105606.

[4] D. G. Yu, G. R. Williams, J. H. Yang, X. Wang, J. M. Yang, and X. Y. Li, J. Mater. Chem. 21 (2011) 15957.

[5] X. Wang, W. J. Zhang, D. G. Yu, X. Y. Li, and H. Yang, Macromol. Mater. Eng. 298 (2013) 664.

[6] M.W. Chang, E. Stride, and M. Edirisinghe, Langmuir 26 (2010) 5115.

[7] M. Enayati, Z. Ahmad, E. Stride, and M. Edirisinghe, J. Roy. Soc. Interf. 7 (2010) 667.

[8] E. Stride and M. Edirisinghe, Soft Matter 4 (2008) 2350.

[9] Y. Tian, M. Wu, R. Liu, Y. Li, D. Wang, J. Tan, R. Wu, and Y. Huang, Carbohydr. Polym. 83 (2011) 743.

[10] X. Li, L. Lin, Y. Zhu, W. Liu, T. Yu, and M. Ge, Polym. Compos. 34 (2013) 282.

[11] V. Bühler, Kollidon®:Polyvinylpyrollidone for the Pharmaceutical Industry, 2nd edn. Ludwigshafen: BASF Aktiengesellschaft Feinchemie (1998).

[12] L. Y. Huang, D. G. Yu, C. Branford-White, and L. M. Zhu, J. Mater. Sci. 47 (2012) 1372.

*Advanced Materials Research Vol. 937 (2014) pp 276-281*
*© (2014) Trans Tech Publications, Switzerland*
*doi:10.4028/www.scientific.net/AMR.937.276*

# Adsorption Behavior of Rhodamine B and Methylene Blue by Chemical Modified Cornstalk Biomass

Qilin CAO[1,a], Yuan-meng ZHAO[2,b], Xiang-yan WEI[3,c] and Fang LUO[4,d]*

[1]Changchun Normal University, College of Chemistry, Changchun, 130032, China

[1]Duoluoshan Sapphire Rare Metal Co. Ltd. of Zhaoqing, Sihui, 526200, China

[2,3,4]Key Laboratory of Polyoxometalates Science of Ministry of Education, College of Chemistry, Northeast Normal University, Changchun, 130024, China

[a]email: caoql243@163.com

[b]email: zhaoym243@nenu.edu.cn

[c]email: weixy436@nenu.edu.cn

[d]email: luof746@nenu.edu.cn

*Corresponding author

**Keywords:** Adsorption, Cornstalk, Methylene blue, Rhodamine B, Kinetics, Equilibrium.

**Abstract.** Cornstalk, a cellulosic agricultural waste material, was modified by citric acid to improve the adsorption of rhodamine B (RB) and methylene blue (MB) from aqueous media. Characterization of SEM and FTIR spectra confirmed that the surface morphology of adsorbent changed and carboxylic groups were introduced into the raw cornstalk by chemical modification. The effects of pH, contact time, initial concentration and the amount of dried adsorbent were studied in batch experiments. There was no significant difference in the dye concentration remaining when the pH was increased from 4.0 to 10.0. Several models were used to fit experimental data and the results showed that experimental data fitted the Langmuir model and pseudo-second order model best. Compared with 58.71 and 81.71 mg $g^{-1}$ obtained by CS (raw cornstalk), the maximum adsorption capacities for RB and MB were 203.0 and 245.6 mg $g^{-1}$ by using CCS (cornstalk modified with citric acid), respectively.

## Introduction

Dyes are colorful organic compounds, which can make other substances obtained the distinctive and stable colors. It produces huge economic efficiency to many industries, but also releases considerable amount of colored wastewater into nature water [1,2]. A number of methods are available for dyes removal from liquid effluents, such as photocatalytic degradation, membrane separation process, filtration, ion-exchange, electrokinetic coagulation, precipitation etc [3.4]. However, these processes are generally ineffective in dye removal, high cost and less adaptable to a wide range of dye wastewaters [5]. Adsorption techniques have proved to be an effective and attractive process for pollutants from water and wastewater. In recent years, more prominence has been gained by the biomaterials which are byproducts or the wastes of large-scale industrial processes and agricultural waste materials. A range of adsorbents such as rice husk, baker's yeast, wheat shell, chlorella, coconut coir pith and cottonseed hull have been reported to be used to remove dyes from aqueous solutions [6-8]. Effective use of biomass wastes has become one of the promising fields of the treatment of dyes due to the low cost as well as their environmentally friendly nature.

Corn abounds in northeast of China, therefore, cornstalk has been considered as a very abundant, inexpensive, and easily-available agricultural waste [9]. Cellulose cornstalk as a biosorbent exhibits macroporous network structure, high surface area, good mechanical stability and various functional groups (hydroxyl and carboxyl). Therefore, cationic dyes such as rhodamine B and methylene blue can be adsorbed into cornstalk. Since little is known on the biosorption of dyes to cornstalk biomass, adsorptive properties of the agricultural waste for dyes should be investigated.

## Experiments

### Reagents and Measurements

The stock solutions of 1000 mg/L were prepared by dissolving an appropriate quantity of RB and MB in a liter of distilled water. Initial pH of each solution was adjusted with 0.1 mol L-1 HCl or NaOH and measured with a pHs-3C model acidity meter. The concentration of the dyes was determined by measuring their characteristic absorbance using UV-vis spectrometer, and the characteristic absorbance of RB and MB are 554 and 679 nm, respectively.

### Surface Modification

Cornstalk was obtained from a farm in Changchun city, China. After dried in a convection oven at 60 ºC for 12 h, the dried cornstalk was milled with a muller and sieved to a smaller particle by a boult with the diameter of 0.25 mm. Cornstalk powder was washed three times with distilled water to remove mud, sand and the other contaminants, and then dried in oven for 12 h at 60 ºC. 4 g raw cornstalk powder (CS) was directly mixed with 100 mL 1.0 mol L-1 citric acid and stirred for 2 h at 80 ºC and then filtered and dried in a convection oven at 60 ºC for 12 h, in succession the temperature was increased up to 120 ºC for 3 h. After that, the product was washed repeatedly with distilled water until pH was neutral. Finally, it was dried in oven at 60 ºC for 12 h and hereafter abbreviated as CCS [10, 11].

### Bach Sorption Experiments

Batch adsorption tests were carried out at room temperature and used to investigate the effects of various parameters on RB and MB adsorption by adsorbents. 20 mg of each adsorbent was mixed with 15 mL of dye solution in Erlenmeyer flask, and then shaken for 3 h in a rotary shaker except kinetics experiment. In the adsorption isotherm experiments, the concentration range of dye was 10-500 mg $L^{-1}$. Effect of pH on dye removal was studied over a pH range of 2–10. For the optimization of adsorbent dose, a 15 ml dye solution was contacted with different quantities of adsorbent (5–30 mg). The dyes solutions were centrifuged at 5000 rpm for 5 min and then residual concentration of RB and MB were estimated using the UV-vis spectrophotometer.

## Results and Discussion

### Adsorption Characterization

SEM analysis is a useful tool for analysis of the structure and surface morphology of adsorbents. SEM images of CS and CCS are shown in Fig. 1. As compared with CS, the surface roughness of cornstalk changed significantly after treatment with citric acid. The heterogeneous pores and cavities observed on the CCS surface provide the larger surface area and pore volume, which are essential to enhance uptakes of RB and MB.

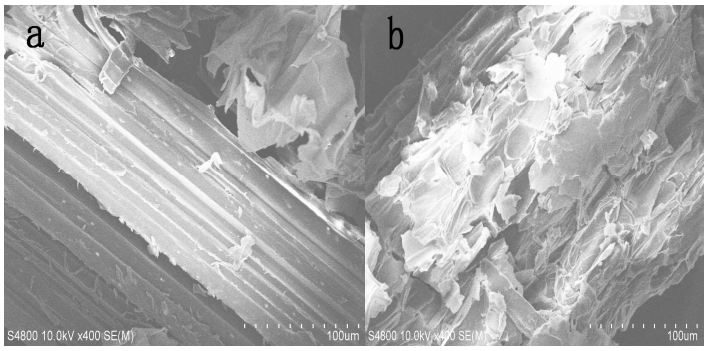



Fig. 1. SEM images of CS (a) and CCS (b).

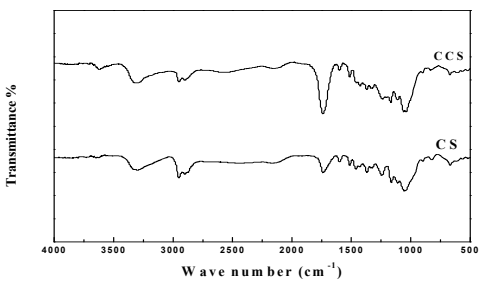



Fig. 2. The FTIR spectra of CS and CCS.

To better understand the modification of citric acid into cornstalk biosorbent, comparison of the FTIR spectra between CS and CCS were performed in Fig. 2. The IR spectra of the CS exhibits doublet peaks at 2952 (strong, sharp) and 2900 $cm^{-1}$ attributed to the asymmetric and symmetric

stretching modes of aliphatic CH groups. The double bonds at 1738 and 1590 $cm^{-1}$ are the absorption band of carbonyl (C=O) stretching and hydroxyl (–OH) deformation vibration of carboxylic groups. The band at 3287 $cm^{-1}$ may be due to the O–H stretching vibration of polymeric compounds. The peak at 1513 $cm^{-1}$ corresponds to the amide and the peak at 1429 $cm^{-1}$ is the symmetric C=O stretching. For CCS, it is observed that the peak at 1738 $cm^{-1}$ stayed in position, but the peak at 1590 $cm^{-1}$ shift to 1608 $cm^{-1}$. The carbonyl stretching vibration shift a little from 1429 to 1421 $cm^{-1}$. The O-H stretching vibration of CCS shifts from 3287 $cm^{-1}$ to 3309 $cm^{-1}$. The position change of different peaks indicated that some functional groups have been successfully introduced into the surface of biomaterial cornstalk after chemical modification.

**Effect of pH on Pb(II) Adsorption**

Acidity of a solution has many effects on any adsorption process. Such as charge of adsorbent surface, the degree of ionization of the material present in the solution, the dissociation of functional groups on the action sites of the adsorbent and the solution dye chemistry. Therefore, pH of a solution is the first parameter to be optimized. Fig. 3 shows the two dyes adsorption on the modified and unmodified biomass at different pH values. It could be seen that the adsorbed amount of two dyes increased initially with an increase in pH, after which it was approximately constant. RB and MB exist in aqueous solution in the form of positively charged ions because they are cationic dye. There was not any adsorption of dyes under highly acidic conditions because binding sites on the biosorbent were tightly associated with $H^+$ and restricted the approach of cationic dyes as the result of repulsive forces. With the solution acidity decreased, the dye cation uptake was improved due to the increase of the negative charge density on the adsorbent surface. As shown, CCS is more excellent adsorption capacities for RB and MB than CS. This observation confirmed that the modified method on cornstalk is feasible and effective to remove RB and MB from aqueous solution.

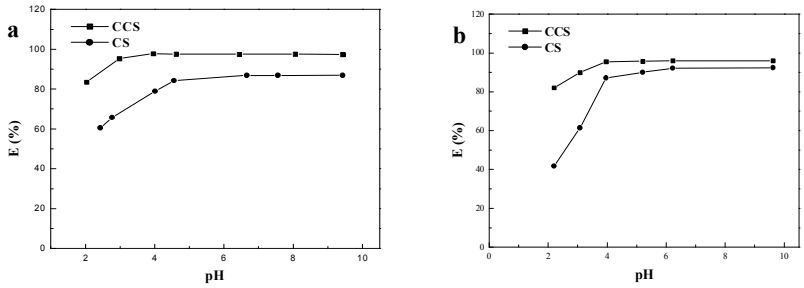



Fig. 3. Adsorption of RB and MB at different pH by cornstalk biosorbents: (a) RB and (b) MB.

**Biosorption Kinetics**

In order to analyze biosorption kinetics of RB and MB, pseudo-first-order [12,13] and pseudo-second-order [14] kinetics models were applied to the biosorption data and non-linear fitting was performed to determine the model parameters. Fig. 4 showed contact time profiles of the modified cornstalk adsorbents on RB and MB adsorption. From the figure, it is clearly that the adsorption rate of dye increased rapidly with the increase of contact time at first, then becomes slower until equilibriums were achieved (50 min). The higher initial adsorption rate of dye was attributed to the surface of the biomass had a high density of active sites for dyes adsorption, which then reduced with increasing coverage of the biosorbent surface. Thereafter, dye ions had to traverse farther and deeper into the active intra-particular sites in overcoming much larger resistances. This slowed down the rate of dye adsorption during later period of adsorption process.

Kinetic model parameters were presented in Table 1. It was determined that pseudo-second-order kinetic model provided much better $R^2$ values than that of pseudo-first-order kinetic model. Moreover, the q values ($q_e$, cal) calculated from the pseudo-second-order model were more consistent with the experimental q values ($q_e$, exp) than those calculated from the pseudo-first-order model (Table 1). This implied that the adsorption processes in this study is due to chemisorption [15].

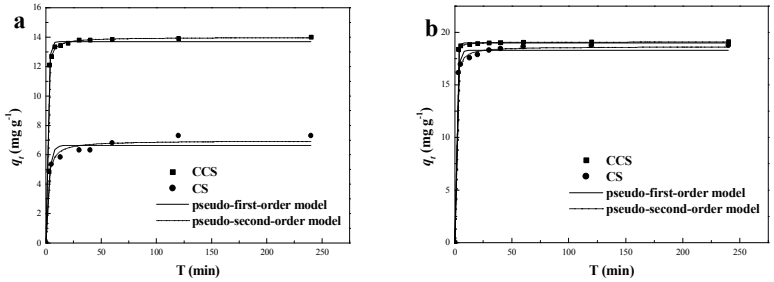



Fig. 4. Effects of contact time on RB and MB uptakes by cornstalk adsorbents: (a) RB and (b) MB.

Table 1. The pseudo-first and second-order kinetics models for RB and MB adsorption

| Sorbent type | *dyes* | The pseudo-first-order model | | | The pseudo-second-order model | | |
|---|---|---|---|---|---|---|---|
| | | $R^2$ | $q_e$ (mg g$^{-1}$) | $K_1$ (min$^{-1}$) | $R^2$ | $q_e$ (mg g$^{-1}$) | $K_2$ (g mg$^{-1}$min$^{-1}$) |
| CS | RB | 0.9536 | 6.647 | 0.3837 | 0.9807 | 6.954 | 0.09517 |
| | MB | 0.9937 | 18.28 | 0.6732 | 0.9988 | 18.63 | 0.1089 |
| CCS | RB | 0.9959 | 13.69 | 0.6706 | 0.9998 | 13.98 | 0.1527 |
| | MB | 0.9997 | 18.99 | 1.127 | 0.9999 | 19.08 | 0.4659 |

**Adsorption Isotherms**

The relationships between initial concentration and adsorbed amount of RB and MB by modified and unmodified adsorbents were studied and presented in Fig. 5. It showed that the adsorption uptakes of dyes improved with increasing the equilibrium concentration, then reached a plateau at higher concentration. It was attributed to the surface active sites of adsorbents had become saturated.

Studying adsorption isotherm is a prerequisite to understand adsorbate-adsorbent interaction and important in adsorption system. In this study the two common isotherm models, the Langmuir [16] and Freundlich [17] isotherms were used to fit the experimental data for RB and MB adsorption in aqueous solution onto CS and CCS. The essential features of Langmuir adsorption isotherm can be expressed as a dimensionless separation factor $R_L$, which is derived as follows:

$$R_L = \frac{1}{1 + bC_O} \tag{1}$$

The non-linear forms of two isotherm models were applied to fit experimental data and the obtained corresponding parameters were listed in Table 2. The initial isotherm gradient indicated the sorbent affinity at low metal concentrations. The $R_L$ value indicates the type of Langmuir isotherm to be irreversible ($R_L = 0$), favorable ($0 < R_L < 1$), linear ($R_L = 1$) or unfavorable ($R_L > 1$) [18]. The calculated $R_L$ values of CCS and CS for RB at initial concentrations of 10–500 mg L$^{-1}$ were found to be $5.035\times10^{-2}$ to 0.726 and $8.953\times10^{-2}$ to 0.831, while that for MB were found to be $1.316\times10^{-2}$ to 0.398 and $1.318\times10^{-2}$ to 0.400, which confirm that the used biosorbents are favourable for RB and MB biosorption. The n values for Freundlich of CS and CCS were found to be 3.176 and 2.912 for RB adsorption, 4.384 and 4.459 for MB biosorption. They were all between 1 and 10, indicating that the adsorption performance of two dyes onto cornstalk biomass was favorable at studied conditions. A comparison of two isotherm models with the correlation coefficients $R^2$ revealed that Langmuir isotherm model gave better fits than the Freundlich isotherm model, indicated that the adsorption on the CCS and CS adsorbents was monolayer adsorption. The maximum uptake capacities ($q_m$) of CCS for RB and MB were 203.0 and 245.6 mg g$^{-1}$, while that of CS were 58.71 and 81.71 mg g$^{-1}$, the increases were about 3.5 and 3 times for RB and MB, respectively. It was found that the cornstalk adsorbent exhibited higher MB adsorption than RB. Higher molecular weight and large ionic size were the probable reasons for the lower sorption of RB.

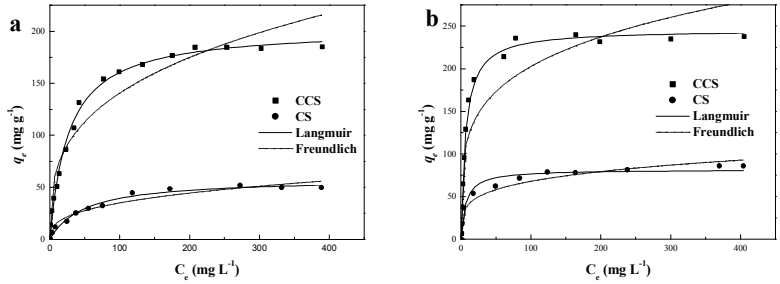



Fig. 5. Adsorption isotherms of RB and MB by cornstalk biosorbents: (a) RB and (b) MB.

Table 2. Langmuir and Freundlich models parameters for RB and MB adsorption

| dyes | Sorbent types | Langmuir | | | Freundlich | | |
|---|---|---|---|---|---|---|---|
| | | $q_m$ (mg g$^{-1}$) | $b$ | $R^2$ | $K_f$ | $n$ | $R^2$ |
| RB | CS | 58.71 | $2.034\times10^{-2}$ | 0.9818 | 7.215 | 2.912 | 0.9471 |
| | CCS | 203.0 | $3.772\times10^{-2}$ | 0.9940 | 32.99 | 3.176 | 0.9434 |
| MB | CS | 81.71 | 0.1497 | 0.9715 | 24.19 | 4.459 | 0.9435 |
| | CCS | 245.6 | 0.1515 | 0.9929 | 70.86 | 4.384 | 0.85403 |

**Effects of Solid/Liquid Ratio on Dyes Adsorption**

The effect of solid/liquid ratio (abbreviated as s/l) on RB and MB adsorption was investigated in the range of 0.3-2 g L$^{-1}$. The results showed that increase initially in the s/l ratio resulted in a rapid increase in the uptake of dye, and then the removal percent changed a little. It may be concluded from these observations that at lower cornstalk adsorbents dosage, the dye was competing for sorption at limiting sorption sites. Therefore, as the s/l ratio increased, the availability of sorption sites eased resulting in greater percentage removal of the dye. The insignificant increase in the uptake of dye at the higher s/l ratio may be attributed to the presence of excess/surplus sorption sites on adsorbents than the available dye present in the solution.

**Conclusion**

The study showed that cornstalk modified through a simple way, can be used as an adsorbent for effectively removal of RB and MB from aqueous solution. It is demonstrated that the adsorption exhibits higher adsorption capacity for MB than RB due to the difference in molecular weight and ionic size. The isotherm experiments indicated that the adsorption capacity of modified biomass (CCS) for RB and MB showed a significant increase compared with that of unmodified biomass (CS) due to the presence of large number functional groups. Langmuir model could describe well the adsorption isotherm, revealed that the adsorption on cornstalk adsorbents was monolayer adsorption. The kinetics of adsorption would be better described by pseudo-second-order model. The modified cornstalk could be an alternative economic material used for dye removal in wastewater.

**References**

[1] J.R. Easton, B.D. Waters, J.H. Churchley, J. Harrison, in: P. Cooper (Ed.), Colour in Dyehouse Effluent, Society of Dyers and Colourists, The Alden Press, Oxford, 1995, p. 9.

[2] J.W. Lee, S.P. Choi, R. Thiruvenkatachari, W.G. Shim, H. Moon, Evaluation of the performance of adsorption and coagulation processes for the maximum removal of reactive dyes, Dyes Pigments 69 (2006) 196–203.

[3] M.R. Sohrabi, M. Ghavami, Photocatalytic degradation of Direct Red 23 dye using UV/TiO2: effect of operational parameters, J. Hazard. Mater. 153 (2008)1235–1239.

[4] J.S. Wu, C.H. Liu, K.H. Chu, S.Y. Suen, Removal of cationic dye methyl violet 2B fromwater by cation exchange membranes, J. Membr. Sci. 309 (2008) 239–245.

[5] Banat, I.M., Nigam, P., Singh, D., Merchant, R., 1996. Microbial decolorization of textile dye containing effluents: a review. Bioresour. Technol. 58, 217-227.

[6] Shamik Chowdhuru, Rahul Mishra, Papita Saha, Praveen Kushwaha, Adersoption thermodynamics, kinetics and isosteric heat of adsoption of malachite green onto chemically modified rice husk, Desalination 265 (2011) 159-168.

[7] W.T. Tsai, H.R. Chen, Removal of malachite green from aqueous solution using low-cost chlorella-based biomass, J. Hazard. Mater. 175 (2010) 844-849.

[8] Q. Zhou, W.Q. Gong, C.X. Xie, D.J. Yang, X.Q. Ling, X. Yuan, S.H. Chen, X.F. Liu, Removal of Neutral Red from aqueous solution by adsorption on spent cottonseed hull substrate, J. Hazard. Mater. 185(2011)502-506

[9] Park, D., Yun, Y., Park, J.M., 2006. Comment on ‘‘Chromate ion adsorption by agricultural by-products modified with dimethyloldhydroxylethylene urea and choline chloride” by Wartelle and Marshall. Water Res. 40, 1501–1504.

[10] T. Vaughan, C.W. Seo, W.E. Marshall, Removal of selected metal ions from aqueous solution using modified corncobs. Bioresour. Technol. 78 (2001) 133-139.

[11] R. Leyva-Ramos, L.A. Bernal-Jacome, I. Acosta-Rodriguez, Adsorption of cadmium(II) from aqueous solution on natural and oxidized corncob, Sep. Purif. Technol. 45 (2005) 41-49.

[12] C.W. Cheung, J.F. Porter, G. McKay, Sorption kinetic analysis for the removal of cadmium ions from effluents using bone char, Water Res. 35 (2001) 605-612.

[13] G. Bayramoglu, A. Denizli, S. Bektas, M.Y. Arica, Entrapment of Lentinus sajor-caju into Ca-alginate gel beads for removal of Cd(II) ions from aqueous solution: preparation and biosorption kinetics analysis, Microchem. J. 72 (2002) 63-76.

[14] Y.S. Ho, G. McKay, Pseudo second order model for sorption process, Process Biochem. 34 (1999) 451-465.

[15] V. Vadivelan, K.V. Kumar, Equilibrium, kinetics, mechanism, and process designfor the sorption of methylene blue onto rice husk, J. Colloid Interf. Sci. 286 (2005) 90–100.

[16] I. Langmuir, The adsorption of gases on plane surfaces of glass, mica and platinum, J. Am. Chem. Soc. 40 (1918) 1361–1403.

[17] M. Kilpatrick, L.L. Baker Jr., C.D. Mckinney Jr., Studies of fast reactions which evolve gases, The reaction of sodium-potassium alloy with water in the presence and absence of oxygen, J. Phys. Chem. 57 (1953) 385–390.

[18] V.J.P. Vilar, C.M.B. Botelho, R.A.R. Boaventura, Methylene blue adsorption by algal biomass based materials: biosorbents characterization and process behaviour, J. Hazard. Mater. 147 (2007) 120–132.

*Advanced Materials Research Vol. 937 (2014) pp 282-285*
*© (2014) Trans Tech Publications, Switzerland*
*doi:10.4028/www.scientific.net/AMR.937.282*

# Pathogenic Fungi induce the Expression of Trichoderma Asperellum Cell Wall Degrading Enzymes in the Process of Mycoparasitism

Ping YANG*

College of food engineering, Harbin University of Commerce, Tongda Street No. 138, Harbin City, Heilongjiang province, China.

Email: ping8434@163.com

**Keywords:** *T. asperellum,* mycoparasitism, cell wall degrading enzymes, Pathogenic fungi.

**Abstract.** *Trichoderma asperellum* is an important biocontrol fungus which has been shown to control plant soil-borne pathogens, such as: *Pythium ultimum*, *Fusarium oxysporum*, *Cytospora chrysosperma* and *Sclerotinia sclerotiorum*. The goal of this research is to study whether the cell wall degrading enzymes genes were induced by pathogens or not in the process of *T. asperellum* mycoparasitism. The results suggest that chitinase gene *ech42*, β-1,3 glucanase gene *bgn13.1*, and β-1,6 glucanase gene *bgn16.1* can be induced by pathogens. However, two N-acetyl-amino glycosidase *nag1* and *nag2* can not be induced by pathogens.

## Introduction

Plant disease serious threat to crop production, although the use of chemical pesticides effectively control the disease, improve the crop production environment, but using those chemical materials throughout the year has led to increase disease and insect resistance, environmental pollution problems and even threaten human health [1]. The emergence of these problems has attracted widespread attention,so many people put forward the method of biological control in alternative synthetic pesticides to the prevent crop diseases, and caused the attention of governments around the world [2-4].

*Trichoderma* is an important biological control fungi, the biocontrol mechanisms of it include competition, antibiosis, mycoparasitism, induction of plant disease resistance; promote plant growth and collaborative antagonism[5]. The mycoparasitism is considered a major role biocontrol mechanism of *Trichoderma*, which is a complex process involving recognition, contact, winding, penetrating and parasitism of pathogen. In this process, pathogenic fungi secrete some substances that identified by *Trichoderma*. after identifying host fungi, *Trichoderma* parallel or spiral wound grow along the host hyphae, through the secrete cell wall degrading enzymes to dissolve host fungal cell wall, thus penetrate and parasitize in pathogens, absorb nutrition and ultimately kill pathogenic fungi.

*Trichoderma* produces a large number of cell wall hydrolases during parasitic process including chitinase, glucanase and cellulose [6]. Chitinase includes endochitinase, exochitnase and N-acetyl-beta-D-amino glycosidase. Glucanase consists of β-1,6 glucanase and β-1,3 glucanase. Cellulase contains endo-1,4-β-D-glucanase, exo-1,4-β-D-glucanase and β-glucosidases. The two chitinase genes *chit42*and *chit33* were studied by Szabó which were proved to be the crucial gene in the process of *Trichoderma* mycoparasitism [7]. N-acetyl-beta-D-amino glycosidase *nag1* was cloned from *T. harzianum* P1 [8].

At present, the research of biocontrol function genes from *T. asperellum* mainly involved three kinds of cell wall degrading enzymes: chitinase, exo-β-1,3-glucanase and N-acetyl-beta-D-amino glycosidase. The clone and expression of chitinase from *T. asperellum* were studied by Song [9]. The antifungi activity of chitinase from was researched by Nguyen; it turned out that chitinase from *T. asperellum* has a strong function of hydrolyzing the fungal cell walls [10]. The exochitinase and exo-β-1,3-glucanase gene were cloned respectively from *T. asperellum* by Kumar and Marcello [11-12]. Two N-acetyl-beta-D-amino glycosidase were separated from *T. asperellum*[13]. Whether those cell wall degrading enzymes and antibiotic gene were induced by pathogens or not is not clear. The goal of this research was whether the cell wall degrading enzymes genes were induced by pathogens or not in the process of *T. asperellum* mycoparasitism.

## Materials and Methods

### Strains and Culture Conditions

*Trichoderma asperellum* T4 (CGMCC3.14975) and the plant phytopathogens *Rhizoctonia solani*, *Fusarium oxysporum*, *Alternaria alternata* and *Cytospora chrysosperma* were all cultured at 28 °C on PDA media until sporulation.

### Plate Confrontation Experiment.

The biocontrol fungus *T. asperellum* and pathogenic fungi *R. solani*, *F. oxysporum*, *A. alternata* and *C. chrysosperma* were inoculated on PDA medium covered with cellophane respectively, cultivated 5d at 28 °C. Cut hyphae pieces at the edge of colony after preincubate and set aside. The preculture 5d hyphae pieces of *T. asperellum* and four kinds of pathogen hyphal block were respectively inoculated on new PDA plates at the symmetrical two points that is 6cm from the center, confrontation culture at 28 °C.

### Real-time Reverse Transcriptase-polymerase Chain Reaction

*T. asperellum* mycelium was collected, RNA was extracted and then reverse transcribed into cDNA for real-time quantitative analysis. The actin was used as control, PCR primers of *T. asperellum* metabolites are shown in Table 1, the reaction system 10μL:SYBR® Premix Ex TaqTM II 5μL,Forward Primer(10μM) 0.4μL,Reverse Primer(10μM)0.4μL,ROX Reference Dye II(50×)0.6μL,DNA 1μL,Sterilized distilled water 2.6μL。The reaction conditions for PCR:95°C initial denaturizing 30s;95°Cdenaturizing 5s,60°C annealing 34s,40cycles;95°C 15s,60°C 60s,95°C 15s.

Table 1. Primers of real-time quantitative PCR for expression of *T. asperellum* hydrolase

| Gene | Primer | Primer sequence 5' → 3' |
|---|---|---|
| actin(*act*) | act-F | CAACGCTCCCGCTTTCTA |
| | act-R | GGACAACGTGGGTAACAC |
| chitinase(*ech42*) | ech42-F | AGTACCCTGCCGATGACA |
| | ech42-R | TAGCCTGGAGCGTATTGC |
| N-acetyl-amino glycosidase1(*nag1*) | nag1-F | TCATTGGCGGTGAACTCG |
| | nag1-R | TCGTCCCGACCACCAGAT |
| N-acetyl-amino glycosidase2(*nag2*) | nag2-F | CAAGAGGACCATTGACGC |
| | nag2-R | GCTTAGGCAGTGAAGGGA |
| β-1,3-glucanase(*bgn13.1*) | bgn13.1-F | GCAGCCCTCAACAAGGTG |
| | bgn13.1-R | AGAGCCAACGGGAACCAC |
| β-1,6-glucanase(*bgn16.1*) | bgn16.1-F | ATGAGTCTCCTGGAATGG |
| | bgn16.1-R | GTTGGGATGTAGTTGAGG |

## Result and Discussion

### The Induction of Pathogens on *T. asperellum* Chitinase Gene

Set a piece of cellophane on PDA plate, confrontation culture *T. asperellum* and *R. solani*, the cDNA of biocontrol fungi before and after contact with pathogenic fungi as template, using real-time quantitative PCR analysis chitinase gene expression before and after the two fungi contact and determine *T. asperellum* chitinase gene is in the process of mycoparasitism whether induced by pathogens or not.

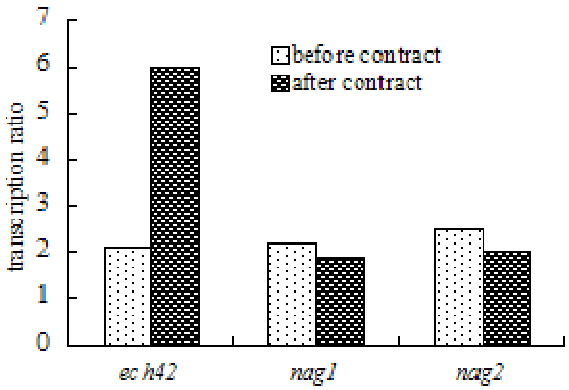



Fig. 1. Real-time quantitative analysis of chitinase gene expression from *T. asperellum*

The expression of chitinase gene *ech42* after *T. asperellum* contact with pathogen is higher than before contact obviously, the expression of N-acetyl-amino glycosidase *nag1* and *nag2* nearly equal before and after *T. asperellum* contact with pathogen from Fig. 1 we can see. Those suggest that gene *ech42* can be induced by pathogens and *nag1* and *nag2* can not.

**The Induction of Pathogens on *T. asperellum* Glucanase Gene**

A piece of cellophane was placed on PDA plate, confrontation culture *T. asperellum* and *R. solani*, the cDNA of biocontrol fungi before and after contact with pathogenic fungi as template, using real-time quantitative PCR analysis glucanase gene expression before and after the two fungi contact and determine *T. asperellum* glucanase gene is in the process of mycoparasitism whether induced by pathogens or not.

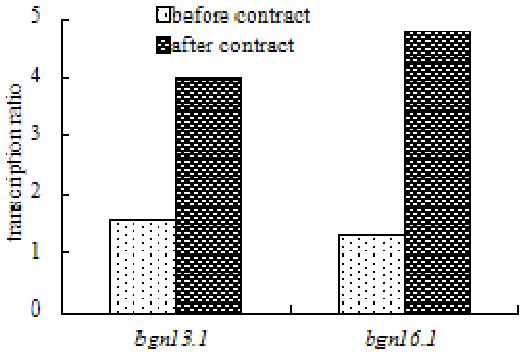



Fig. 2. Real-time quantitative analysis of glucanase gene expression from *T. asperellum*

Fig. 2 showed that the expression of β-1,3 glucanase gene *bgn13.1* and β-1,6 glucanase gene *bgn16.1* after *T. asperellum* contact with pathogen is higher than before contact obviously, Those data suggest that both β-1,3 glucanase gene *bgn13.1* and β-1,6 glucanase gene *bgn16.1* can be induced by pathogens.

**Conclusions**

Whether the cell wall degrading enzymes and antibiotic gene were induced by pathogens or not were studied, the data suggest that chitinase gene *ech42*, β-1,3 glucanase gene *bgn13.1*, and β-1,6 glucanase gene *bgn16.1* can be induced by pathogens. However, two N-acetyl-amino glycosidase *nag1* and *nag2* can not be induced by pathogens.

**Acknowledgement**

This project was financially supported by the natural science foundation of Heilongjiang province (C201118).

**References**

[1] Zhou R X,Dong K J.Talk about pesticide pollution and environmental protection, Xinjiang environmental protection, 1 (1999) 31-33.

[2] Anjaiah V, Thakur R P, Koedam N, Evaluation of Bacteria and *Trichoderma* for Biocontrol of Pre-harvest Seed Infection by *Aspergillus flavus* in Groundnut, Biocontrol Science and Technology, 16 (2006) 431-436.

[3] Schubert M, Fink S, Schwarze F, Evaluation of *Trichoderma* spp. as a Biocontrol Agent against Wood Decay Fungi in Urban Trees, Biological Control, 45 (2008) 111-123.

[4] Larralde-corona C P, Santiago-mena M R, Sifuentes-rincón A M, et al, Biocontrol Potential and Polyphasic Characterization of Novel Native *Trichoderma* Strains against *Macrophomina phaseolina* Isolated from Sorghum and Common Bean, Applied Microbiology and Biotechnology, 80 (2008) 167-177.

[5] Francesco V, Sivasithamparam K, Ghisalberti E L, et al. *Trichoderma*-Plant-Pathogen Interactions. Soil Biology and Biochemistry, 40 (2008) 1-10.

[6] López-mondéjar R, Ros M, Pascual J A. Mycoparasitism-related Genes Expression of *Trichoderma harzianum* Isolates to Evaluate Their Efficacy as Biological Control Agent. Biological Control, vol. 56, pp. 59-66, January 2011

[7] Szabó M, Csepregi K, Gálber M, et al. Control Plant-parasitic Nematodes with *Trichoderma* Species and Nematode-trapping Fungi: the Role of chi18-5 and chi18-12 Genes in Nematode Egg-parasitism. Biological Control, 63 (2012) 121-128.

[8] Peterbauer C K, Matteo L, Christopher K H, et al. Molecular Cloning and Expression of the nag1 Gene (N-acetyl-β-D-glucosaminidase-encoding Gene) from *Trichoderma harzianum* P1. Current Genetics, 30 (1996) 325-331.

[9] Song Jin-Zhu, Yang Qian, Liu Bei-Dong, et al. Expression of the Chitinase Gene from *Trichoderma aureoviride* in *Saccharomyces cerevisiae*. Applied Microbiology and Biotechnology, 69 (2005)39-43.

[10] Nguyen N V, Young-ju K, Kyung-taek O, et al. Antifungal Activity of Chitinases from *Trichoderma asperellum* DY-59 and *Rhizopus microsporus* VS-9. CURR Microbiol, 56 (2008) 528-532.

[11] Kumar D P, Rajesh K S, Anupama P D, et al. Studies on Exo-Chitinase Production from *Trichoderma asperellum* UTP-16 and its Characterization. Indian Journal of Microbiology, 52 (2012). 388-395.

[12] Marcello C M, Andrei S S, Silvana Petrofeza da Silva, et al. Expression Analysis of the Exo-β-1,3-glucanase from the Mycoparasitic Fungus *Trichoderma asperellum*. Microbiological Research, 165 (2010) 75-81.

[13] Ramot O, Viterbo A, Friesem D, et al. Regulation of Two Homodimer Hexosaminidases in the Mycoparasitic Fungus *Trichoderma asperellum* by Glucosamine. Current Genetics, 45 (2004) 205-213.

*Advanced Materials Research Vol. 937 (2014) pp 286-290*
*© (2014) Trans Tech Publications, Switzerland*
*doi:10.4028/www.scientific.net/AMR.937.286*

# Prevalence of Allergy and Complications Caused by Jewelry among Higher Vocational College Students

Jun-Ping YUAN[1,a], De-Dong CHEN[1,b] and Peng WAN[1,c]

[1]Jewelry Institute of Guangzhou Panyu Polytechnic, Guangzhou, China

[a]yuanjp@gzpyp.edu.cn, [b]chendd@gzpyp.edu.cn, [c]864947158@qq.com

**Keywords:** Higher vocational college students, Jewelry, Piercing, Allergy, Complications.

**Abstract:** Allergy and complications caused by jewelry are prevalent among overseas college students, while there has no relevant study in China. To survey the prevalence of this problem among college students, questionnaire was designed and students randomly from three higher vocational colleges in south China joined this survey. The results show that 32.3% students have ever worn jewelry. The proportion of wearing jewelry is different for various specialties, which shows business students rank the highest, Arts and science &engineering students follow successively, while medical students keep in the last. Necklace, ring and bracelet are the main jewelry types worn by students. 1.3% boys and 10.2% girls have ever worn piercing jewelry, and ear is the dominant piercing site, which accounts for 93.1% overall. Among those students who have ever worn metal jewelry, 3.6% boys and 13.7% girls have ever suffered jewelry allergy or complications, which is mainly caused by costume jewelry and piercing jewelry.

## Introduction

With the development of economy and the progress of the times, people pay more attention to the pursuit of fashion and personality, the phenomenon of college students wearing jewelry is increasingly prevalent, even the body piercing accessories, which was viewed as nonconformity art in the past, are quite common nowadays and received by the mainstream culture to some extent[1-2]. However, more and more cases about jewelry allergies have been reported, especially for various complications caused by body piercing. Some researchers abroad have paid high attention to this problem and carried out extensive investigation[3-5].

However, few reliable estimates about jewelry allergy and complications caused by body piercing are available so far in China, therefore, with the aim of providing the necessary basis for college students' health education and health care, the prevalence of wearing ornaments and the related complications among higher vocational college students were surveyed.

## Subjects and Methods

The questionnaire was designed to figure out the percentage of having worn jewelry among vocational college students, the difference between male and female students, the main jewelry types, the attitudes towards body piercing, the period of healing, and the prevalence of jewelry allergy and complications, etc.

Students were randomly selected as respondents from three different higher vocational colleges in south China, their age are similar, which most of them are between 18 to 20 years old, but they have different professional fields.

## Results of Questionnaire and Discussion

There were all together 1,002 students voluntarily joined the survey, among them, 988 questionnaires were valid, the other 14 questionnaires were rejected as invalid because their answers were incomplete or self-contradictory.

**Effects of Gender**

Of 988 valid respondents, 67.6% were female students and 32.4% were male. To our surprise, the percentage of having ever worn or being wearing jewelries for vocational college students was quite high. The total percentage was 32.3%, it showed that with the rapid development of Chinese economics and society in recent years, young college students in China pursue fashion and personality more and more similarly as those in western countries.

There was some difference on wearing jewelry for different genders, just as our expectation, the percentage of wearing jewelry for female students were obviously higher than male, which can be shown in Table 1.

Table 1. Difference from respondent's gender

| Subjects | Number of respondents | Number of having ever worn jewelry | Percentage of having ever worn jewelry |
|---|---|---|---|
| Male students | 320 | 56 | 17.5% |
| Female students | 668 | 263 | 39.4% |
| Total students | 988 | 319 | 32.3% |

**Effects of Professional Field**

The results also showed some difference on wearing jewelry for different professional fields, the respondents' profession fields in our survey can be classified as medical, Arts, science and engineering, business, and others, as shown in Table 2. It is seen that business students rank the first by percentage of having worn jewelry, art, science & engineering and other specialty students follow successively, while medical students rank in the last, their percentage is about 10% lower than that of business students.

It can be inferred that professional education would impose student's life interest and aesthetics to some extent, business students have more opportunities to contact with outer society, they are prone to pursue fads, sometimes they are implied or induced to some extent that their personal appearance be so important in marketing and promotion, therefore it is not difficult to understand the percentage of wearing jewelry takes the lead. For Arts students, they are inclined to liberty and make their individual character public, perhaps jewelry is one of suitable media to meet their inclinations. While for science and engineering students, generally many of them are relatively more rational, they are often preached that practical skill will be really essential to keep a foothold in their future career, it will more or less affect their attitude to jewelry. As for medical students, on the one hand they are educated in similar mode as science and engineering students, on the other hand the medical professional knowledge make them learn about the possible harm of wearing jewelry, which perhaps help to keep some of them away from jewelry.

Table 2. Difference from professional field

| Professional field | Number of valid respondents | Number of having ever worn jewelry | Percentage of having ever worn jewelry |
|---|---|---|---|
| medical | 104 | 27 | 26.0% |
| Arts | 332 | 106 | 31.9% |
| Science and engineering | 169 | 51 | 30.1% |
| business | 324 | 118 | 36.4% |
| others | 58 | 17 | 29.2% |
| total | 988 | 319 | 32.3% |

**Jewelry Categories**

Jewelry can be classified into several categories according to their contour, structure and wearing position, the common categories are finger ring, necklace, bracelet, bangle, piercing jewelry, etc. Table 3 is the quantity and percentage of main jewelry types worn by respondents, it shows that

necklace and finger ring are the main jewelry categories for total respondents, bracelet/bangle and piercing jewelry follow closely, while there is some obvious difference between male and female, necklace and finger ring are the most prevalent for male, piercing jewelry is relatively less, while for female students the percentage of piercing jewelry is quite high, nearly close to bracelet/bangle.

Table 3. The quantity and percentage of main jewelry types worn by students

| Jewelry category | Male | | Female | | Total | |
|---|---|---|---|---|---|---|
| | number of respondents | percentage | number of respondents | percentage | number of respondents | percentage |
| finger ring | 18 | 32.1% | 63 | 24.0% | 81 | 25.4% |
| necklace | 21 | 37.5% | 75 | 28.5% | 96 | 30.1% |
| bracelet/bangle | 16 | 28.6% | 57 | 21.7% | 73 | 22.9% |
| piercing jewelry | 4 | 7.1% | 68 | 25.9% | 72 | 22.6% |
| others | 1 | 1.8% | 16 | 6.1% | 17 | 5.3% |

(Note: some students have ever worn multi-type jewelry)

**Piercing Jewelry Types**

Of all 988 valid respondents, 765 respondents claimed they could not accept body piercing, the reasons for not accepting body piercing were too unorthodox, fear of causing other's antipathy, too pain, fear of wound infection and other reasons.

72 respondents have really ever been pierced, including 4 male and 68 female, which accounted for 1.3% and 10.29% of total male and female respondents respectively. The main piercing jewelry types are showed in Table 4. As can be seen, ear rings/studs are overwhelmingly predominant for both male and female students, other types are relatively few. But there is some obvious difference between two genders.

Table 4. The main types of piercing jewelries worn by students

| Piercing jewelry types | Male | | Female | | Total | |
|---|---|---|---|---|---|---|
| | Number of respondents | percentage | Number of respondents | percentage | Number of respondents | percentage |
| ear rings/studs | 4 | 100% | 63 | 92.6% | 67 | 93.1% |
| navel ring/stud | 0 | 0.0% | 5 | 7.4% | 5 | 6.9% |
| nose ring/stud | 0 | 0.0% | 1 | 1.5% | 1 | 1.4% |
| tongue ring/stud | 0 | 0.0% | 2 | 2.9% | 2 | 2.8% |
| eyebrow ring/stud | 0 | 0.0% | 1 | 1.5% | 1 | 1.4% |
| lip ring/stud | 0 | 0.0% | 1 | 1.5% | 1 | 1.4% |

**Healing Time**

Piercing itself is a kind of trauma, it will form a tunnel without epithelium peridium in the tissue, and the tunnel is then supported by implanted jewelry to prevent surrounding tissue from contacting and adhering. As it were, the whole healing process is that the epithelial tissues on bilateral surface gradually form a fistula along the tunnel wall and ultimately shape an epithelial pipeline. Healing time after piercing may vary according to people and placement, Table 5 is the general healing time reported by respondents, it can be seen that most piercing can heal within 1 month, and there is no claim that the healing time more than 1 year, however the scale of healing time between 1 month and 1 year also keeps a considerable scale. A variety of factors may result in poor healing, and one of the most common factors is infection.

Table 5. General healing time after piercing

| healing time | Number of respondents | percentage |
|---|---|---|
| 2 weeks~1 month | 56 | 71.8% |
| 1~3 months | 13 | 16.7% |
| 3~6 months | 7 | 9.0% |
| 6 months~1year | 2 | 2.6% |
| more than 1 year | 0 | 0.0% |

**Allergy and Complications**

According to the statistics data, 38 respondents have ever encountered allergic reaction or complications to metal jewelry, which accounted for 11.9% of all 319 respondents who have ever worn metal jewelries, it showed that jewelry allergy was very prevalent among vocational college students. Of these 38 allergic subjects, 2 were male and 36 were female, which respectively counted for 3.6% and 13.7% for each gender.

Fig. 1 shows several common symptoms, including redness, eczema, itching, ulceration, etc. As can be seen, although the actual values are not exactly same for different sex, the basic rule is consistent. Itching is the most prevalent allergy symptom, while eczema and redness also reach considerably high proportion.

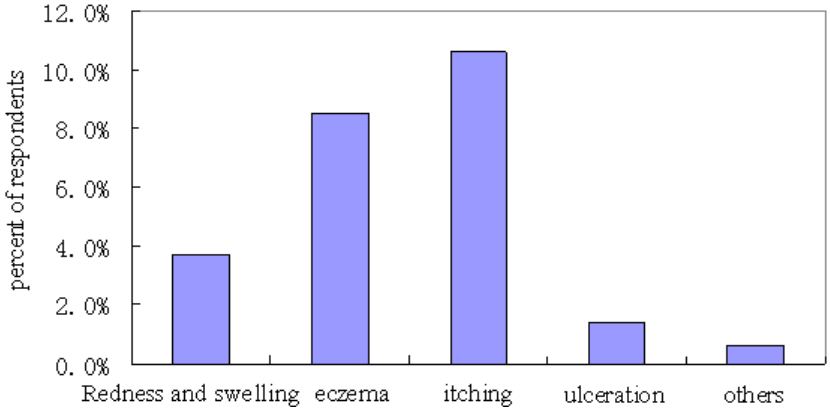



Fig. 1. Common symptoms caused by jewelry

Among all subjects who claimed allergic to jewelry, there is an obvious characteristic that most of them have ever worn fashion jewelry or piercing accessories which contain nickel mostly. Many foreign research results show that nickel is a prevalent allergen, amounts of people suffer allergic reaction from it[3,6]. In jewelry production, nickel has been widely used as the raw material since it is cheap and can significantly change jewelry' physics, chemistry or mechanics properties, it can be used as an alloy element to constitute jewelry alloys, such as cupronickel, white gold alloy, stainless steel; nickel is also often used as the base plating layer of jewelry or surface decorative coating. Compared with the precious metal materials for jewelry, fashion jewelry materials use nickel more extensively and their corrosion resistances are weaker, which make the greater probability of nickel ions releasing and nickel allergies[7]. In addition, piercing is prone to causing infection since the injured local tissues keep constant contacting with the piercing jewelry and suffering from its friction, they are apt to be contaminated by dust, mould or bacteria and consequently infected, resulting in pruritus, red, swollen, papula or bleb around the earlobe hole, even causing fester or anabrosis[8-9]. Especially some students' health concepts are not clear and care the puncture wound improperly, thus the wound is prone to infection and will directly affect the healing time.

Therefore, it is advised that if someone is vulnerable to allergic reaction, he (she) should better avoid wearing fashion jewelries or piercing accessaries. However, limited to the power of consumption, college students often choose cheap fashion jewelry, leading to the overall proportion of jewelry allergy and complications caused by body piercing at a higher level.

## Conclusions

(1) The proportion of wearing or having ever worn jewelry among the higher vocational college students is as high as 32.3%.

(2) The proportion of wearing jewelry is different for various specialties, business students rank the highest, Arts and science &engineering students follow successively, and medical students keep in the last.

(3) Necklace, ring and bracelet are the main jewelry types for students. 1.6% of male students and 10.2% of female students have ever worn piercing jewelry, and stud earrings are the main type, which accounts for 93.1% of overall piercing jewelry types.

(4) Among the students who have ever worn metal jewelry, 3.6% of male students and 13.7% of female students have suffered jewelry allergy and complications, fashion jewelry and piercing accessories are the major incentives.

## Acknowledgements

This work was financially supported by Technology Development Center for Jewelry Engineering, Guangzhou Panyu Polytechnic, Guangzhou, 511483, China(Y.E.R[2012]131).

## References

[1] M.L. Armstrong, A.E. Roberts and D.C. Owen, Contemporary college students and body piercing, J. Adolescent Health, 35(2004), p.58

[2] C.M. Schorzman, M.A. Gold and J.S. Downs, Body Art: Attitudes and Practices Regarding Body Piercing Among Urban Undergraduates. J. Am. Osteopath. Assoc., 107(2007), p.432

[3] M. Mahmoudi, Nickel and Metal-Based Allergic Contact Dermatitis(Eds.), Challenging cases in allergic and immunologic diseases of the skin, CA, 2010, p.153

[4] A.Ehrlich, M.Kucenic and D.V. Belsito, Role of body piercing in the induction of metal allergies, Am. J. Cont. Derm., 12(2001), p.151

[5] T.S. Sivertsen, L.K. Dotterud and E.Lund, Nickel allergy and its relationship with local nickel pollution, ear piercing, and atopic dermatitis: A population-based study from Norway, J.Am. Acad. Derm., 40(1999), p.726

[6] S.E. Jacob, J.N. Moennich and B.A. McKean, Nickel allergy in the United States: A public health issue in need of a ‘‘nickel directive’’, J. Am. Acad. Derm., 6(2009), p.1067

[7] J.P. Thyssen, H.I. Maibach, Nickel release from earrings purchased in the United States: the San Francisco earring study, J. Am. Acad. Derm., 58(2008): p.1000

[8] A.P. Carver, L. Morphis. Body Piercing and Its Complications: A Case Study, J. Nurse Pract., 2(2006): p.46

[9] G..E. Bartlett, T.C.B. Pollard and K.E. Bowker, Effect of jewellery on surface bacterial counts of operating theatres, J. Hosp. Infect., 52(2002), p.68

*Advanced Materials Research Vol. 937 (2014) pp 291-296*
*© (2014) Trans Tech Publications, Switzerland*
*doi:10.4028/www.scientific.net/AMR.937.291*

# The Effect of Food-microorganism(F/M)Ratio on Gas Properties in Batch Biogas Fermentation with Walnut peel*

Jing-hui LIU[1,a], Wu-di ZHANG[1], Shi-qing LIU[1,b], Xing-ling ZHAO[1], Fang YIN[1], Jing LIU[1], Ling XU[1], Yu-bao CHEN[1], Hong YANG[1]

[1]Yunnan Normal University, Kunming 650092, P. R. China

[a] smileoffortune@sina.cn, [b] bcliushiqingwooti@yahoo.com.cn

**Key words:** Walnut peel; food-microorganism(F/M)ratio; biogas fermentation; gas properties

**Abstract.** In order to study the effect of food-microorganism(F/M)ratio on gas properties in batch biogas fermentation experiments with walnut peel, by batch fermentation under the condition of 30°C, with walnut peel as fermentation raw materials, and respectively choose F/M(vs/vs)=0.20, 0.15, the effect of food-microorganism(F/M)ratio on the gas properties was studied in biogas fermentation with walnut peel. The experimental results showed that in the fermentation with walnut peel as raw materials, the potential of TS and VS, the total volume and the time reaching to 80% gas production volume of the time of experimental group F/M(vs/vs)=0.20 were respectively 202ml/gTS, 226ml/gVS, 2840ml, 19d. However, the values of experimental group F/M(vs/vs)=0.15 were respectively 152ml/gTS, 170ml/gVS, 2140ml, 24d. Therefore, food-microorganism(F/M)ratio has a great influence on batch biogas fermentation with walnut peel as the fermentation raw material.

Food-microorganism(F/M)ratio is the ratio of the TS or VS of the raw material to the TS or VS of inoculums in the liquid of the fermentation. In order to maintain the normal operation of the batch reactor, we must add materials into the reactor and a certain amount of inoculums. Some studies show that food-microorganism(F/M)ratio has a certain influence on the performance of anaerobic digestion gas. Wudi Zhang, etc[1] choosing human excrement as fermentation materials and under the condition of the same dosing quantity, adding different proportions of inoculums found that the quality and quantity of inoculums is close to startup and the gas production in the operation of the pool. Lopes, etc[2] found that, when studying the anaerobic digestion of urban organic waste with the cow stomach as its inoculums, it was very important to select the appropriate quality ratio of substrate and inoculums (F/M) for maintaining the stability of the system whose inoculums was cow stomach and urban organic waste was raw material. Guangqing Liu, etc[3] proved that the values of F/M have significant impact on gas production rate of the two kinds of materials, when they studied the batch anaerobic digestion of food waste, grass and their mixture, at the medium temperature (35±2°C) and the high temperature (50±2°C), and respectively controlling F/M at the value of 1.6, 3.1, 4.0 and 3.1. F. Raposo etc[4]found that the values of F/M which were 1/3, 1/2, 2/3 and 1 had a little effects on methane production rate in the anaerobic digestion process study of corn at the medium temperature. Walnut production of our country is the largest in the world. Walnut industry is one of the focus industries in China. However, the study of walnut peel is less. The effect of food-microorganism(F/M)ratio on gas properties in batch biogas fermentation experiments with walnut peel is not studied yet. This experiment by batch fermentation under the condition of 30°C, with walnut peel as fermentation raw materials, and respectively choose F/M(vs/vs)=0.20, 0.15, the effect of food-microorganism(F/M)ratio on the gas properties was studied in biogas fermentation with walnut peel.

## Materials & Methods

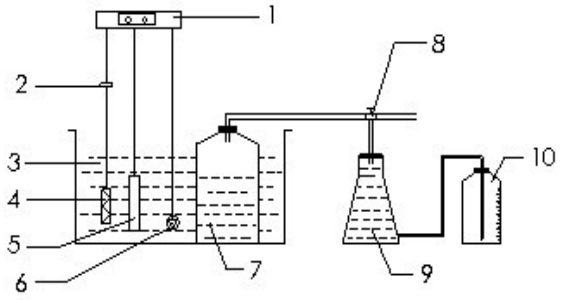
### Material & Inoculums

Fermentation Materials. Fermentation feedstock is walnut peel from Shanxi Province. The determination of TS value was 93.50% and VS value was 84.01%, pH value was 7.0.

Fermentation Inoculums. Inoculums are domesticated by the laboratory long-term mixed anaerobic activated sludge and inoculums from biogas fermentation whose raw materials respectively were walnut peel. The values of TS were 8.32%, 4.46%, and VS values were 50.23%, 69.81%, pH values were all 7.0.

**Experimental Device**

Experiment device as shown in Figure 1[5], the experiment device composed by fermentation bottle, gas storage bottle, metering bottle and temperature control system, etc. Fermentation bottle is 500 ml jar, sealed with rubber stopper with glass tubes. Gas storage bottle adopts the 500 ml triangle bottle mouth with three-way pipe sealed rubber stopper. Metering bottle is 500 ml jar, and it is connected by latex tube with fermentation bottle and gas collection bottle. Temperature control system by the temperature controller (XMT-121 type), type of thermocouple (WCZT-10), a.c. contactor (CJT1-10), a circulating water pump (AP1200 type), galvanothermy tube and iron sink.




1.Monitor;2.AC contactor;3.Sink;4.Heater;5.Thermocouple;6.Circulating pump;7.Fermentation bottle;8.Glass tee;9.Set of cylinders;10.Metering bottle

Fig. 1. Experimental equipment for biogas fermentation

**Experiment Method**

**Experimental Design**

(1)Fermentation pattern: All mixed batch fermentation.

(2)Fermentation temperature: Mesophilic fermentation at 30°C.

(3)Fermentation mixture preparation:

Group 1: Using food-microorganism ratio($F/M_{VS/VS}$=0.20), 120ml laboratory long-term domestication inoculums+14.99g walnut peel + water = 400ml, adjusting the pH to 7.0, setting up three parallels;

Group 2: Using food-microorganism ratio($F/M_{VS/VS}$=0.15), 120ml domestication inoculum from walnut peel biogas fermentation liquid+14.99g walnut peel+water=400ml, adjusting the pH to 7.0, setting up three parallels;

Control group 1:120ml laboratory long-term domestication inoculum+water=400ml, adjusting the pH to 7.0, setting up three parallels;

Control group 2:120ml domestication inoculum from walnut peel biogas fermentation liquid +water=400ml, adjusting the pH to 7.0, setting up three parallel.

**Measuring & Methods**

TS, VS: By conventional analysis, TS, VS of the raw material, the inoculums and the feed liquid before and after fermentation are determined.

TS: Materials are placed in the thermostat at the temperature 105±5°C, drying to constant weight.

VS: Materials are placed in the muffle furnace at the temperature 550±20°C, burning to constant weight.

PH: The precise pH test papers determinate pH values of the raw material, the inoculums and the feed liquid before and after fermentation.

Gas production: This experiment adopts the hydraulic pressure type to collect gas, and the gas production of a day is recorded regularly from the next day when the experiment started.

$CH_4$ content: By igniting to combust methane, the color of the flame and the combustion state are recorded by observation. The color of the gas flame decides methane content[6].

## Results & Analysis

### Results

**The Influence of Different Food-microorganism(F/M) Ratio to Daily Gas Production in Biogas Fermentation with Walnut Peel as Raw Material**

The experimental group and control group were launched on June 1, 2013 and ended on July 4, 2013. The time of fermentation was 34d in total. In the process of fermentation to produce methane, the fermentation time and gas production of different handles are shown in Figure 2.

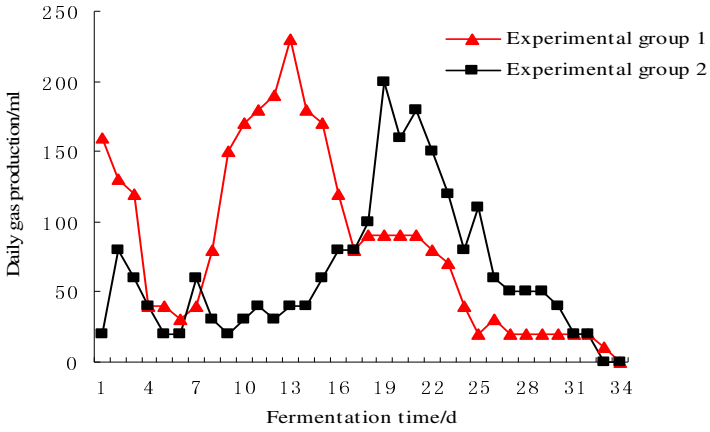



Fig. 2. The influence of different food-microorganism ratio to daily gas production in biogas fermentation with walnut peel as raw material

As can be seen from Figure 2, for experimental group 1, the starting time was shorter and the gas productions reached to 140ml on the average in the first three days, and gradually the gas production reduced. But from the 8th to 13th day which was in the stage of gas exuberant, gas production began to rise again, the methane content was higher (about 70%) and combustion condition was well and continuous, in which flames of the fire was orange. From the 14th to 29th day gas production began to reduce gradually, the methane content was still higher (about 70%), and the combustion condition was continuous and orange flames of the fire. From the 30th day on, the gas production was fairly small. But for experimental group 2, it also produced gas quickly after launched, but the gas production and methane content was both lower than experimental group 1, it did not reach the gas-producing peak until the 19th day and its gas production was only 200ml. The control group in the fermentation process only produced less gas.

**The Influence of Different Food-microorganism Ratio to Total Volume of Biogas Fermentation with Walnut Peel as Raw Material**

As can be seen from table 1, in experimental group 1 because the initial gas production rate is higher and the 8th day is in the gas vigorous stage which lasted to the 16th day. Reaching to the 20th day, the accumulative gas production is 83.8% of the total volume. In experimental group 1 the total volume was 2840ml. However, because of the initial gas production of the experimental group 2 is less and it is not reaching producing gas vigorous stage until the 15th day. The accumulative gas production of the 20th day only accounts for 56.5% of the total volume. Until the 25th day, the accumulative gas production amounted for 86.4% of the total volume. In experimental group 2 the total volume was only 2140ml. Food-microorganism ratio has a grate impact to the time of reaching gas producing peak in biogas fermentation process of walnut peel.

Table1. The influence of different food-microorganism ratio to total volume of biogas fermentation with walnut peel as raw material

| $F/M_{(VS/VS)}$ | Fermentation time(d) | | | | | | |
|---|---|---|---|---|---|---|---|
| | 5 | 10 | 15 | 20 | 25 | 30 | 34 |
| 0.20 | 490 | 960 | 1910 | 2380 | 2670 | 2790 | 2840 |
| 0.15 | 220 | 380 | 590 | 1210 | 1850 | 2100 | 2140 |

**Analysis**

**Analysis of Gas Properties with Different Food-microorganism Ratio in the Experiments with Walnut Peel as Raw Material**

According to the results above, we can get total volume of gas production, TS gas rate and VS gas rate of walnut peel through statistical analysis, and the results are shown in Table 2.

Table 2. Analysis of gas properties with different food-microorganism ratio in the experiments with walnut peel as raw material

| material | $F/M_{(VS/VS)}$ | Total volume (ml) | The time reaching to 80% gas volume(d) | TS gas rate (ml/gTS) | VS gas rate (ml/gVS) |
|---|---|---|---|---|---|
| walnut | 0.20 | 2840 | 19 | 202 | 226 |
| peel | 0.15 | 2140 | 24 | 152 | 170 |

As can be seen from Table 2, total volume, TS gas rate, VS gas rate of experimental group 1 are all higher than experimental group 2. And the time reaching to 80% gas volume is shorter than experimental group 2. Therefore, in an actual application of biogas engineering, experimental group 1 can have littler investment cost than experimental group 2.

**Gas Potential of Different Fermentation Raw Materials.**

To further analysis the biogas production potential of walnut peel in the fermentation with different food-microorganism ratios, they are compared with other raw materials, the results are shown in Table 3. "Multiples" in Table 4 refers to biogas yield (TS) of walnut peel relative to other raw materials.

Table 3. Potential of various materials for biogas production

| Fermentation materials | Biogas yield (ml/g TS) | References | Biogas yield of Walnut peel($F/M_{VS/VS}$=0.20) relative to various raw materials | Biogas yield of Walnut peel($F/M_{VS/VS}$=0.15) relative to various raw materials |
|---|---|---|---|---|
| Walnut peel ($F/M_{VS/VS}$=0.20) | 202 | — | 1.00 | 0.75 |
| Walnut peel ($F/M_{VS/VS}$=0.15) | 152 | — | 1.33 | 1.00 |
| Horse Bean Hull | 161 | [6] | 1.25 | 0.94 |
| Pea Hull | 208 | [7] | 0.97 | 0.73 |
| *Jatropha curcas* Hull | 429 | [8] | 0.47 | 0.35 |
| Peanut Hull | 323 | [9] | 0.63 | 0.47 |
| *Ginkgo biloba* Leaf | 374 | [10] | 0.54 | 0.41 |
| Pineapple Peel | 239 | [11] | 0.84 | 0.64 |

Table 3 shows that TS gas potential of walnut peel with food-microorganism ratio $F/M_{(VS/VS)}$=0.20 was obviously higher than that of walnut peel with food-microorganism ratio $F/M_{(VS/VS)}$=0.15 and that of the hull of horse bean. The highest is 1.25 times of the hull of horse bean. And it is almost equal to the TS gas potential of the hull of pea. And its TS gas potential is only less than the Hull of Jatropha *curcas* and peanut hull. The minimum times is 0.47 times of the Hull of *Jatropha curcas*. However, the TS gas potential of walnut peel with food-microorganism ratio $F/M_{(VS/VS)}$= 0.15 is significantly lower than that of walnut peel with food-microorganism ratio $F/M_{(VS/VS)}$=0.20,the hull of peas and *Jatropha curcas*,Ginkgo biloba leaf,and pineapple peel. It is 0.94 times of hull of horse bean which is the highest times and it is 0.35 times of the hull of *Jatropha curcas* which is the minimum times. Therefore, food-microorganism ratio has a significant effect on TS gas potential of walnut peel.

## Conclusion

(1) The gas potential of TS and VS, the total volume and the time reaching to 80% gas production volume of experimental group F/M(vs/vs)=0.20 were respectively 202ml/gTS, 226ml/gVS, 2840ml, 19d. However, the values of experimental group F/M(vs/vs)=0.15 were respectively 152ml/gTS, 170ml/gVS, 2140ml, 24d.

(2) Food-microorganism(F/M) ratio has a great influence on batch biogas fermentation with walnut peel as the fermentation raw material.

## Acknowledgement

Foundation Item: Science and Technology Condition Platform Construction Project of Yunnan Province (2010DH012)

Author: Jinghui Liu(1985- ), female, Master Degree, engaged in the biomass & environmental engineering research direction. E-mail: smileoffortune@sina.cn

Corresponding author: Shiqing Liu(1964- ), male, Associate Professor, engaged in biomass energy research and teaching work. E-mail: bcliushiqingwooti@yahoo.com.cn

## References

[1] Wudi Zhang, Hongchuan Song, Fang Yin, et al. Biogas Fermentation & Comprehensive Utilization. Kunming: Yunnan Science Press, 2004, p. 109-110. (In Chinese)

[2] W.S. LOPES, V.D.LEITE, S.PRASAD. Influence of inoculum on performance of anaerobic reactors for treating municipal solid waste[J]. Biores Technol, 2004, No.94, p.261-266.

[3] Guangqing Liu, Ruihong Zhang, Metal Hamed, et a1. Effect of feed to inoculum ratios on biogas yields of food and green wastes[J]. Bioresource Technology, 2009, Vol.100, p.5103-5108. (In Chinese)

[4] F.RAPOSO, C.E.BANKS, I.SIEGERT, et a1. Influence of Inoculum to Substrate Ratio on The Biochemical Methane Potential of Maize in Batch Tests[J]. Process Biochemistry, 2006, Vol.41, p.1444-1450.

[5] Yunhua.Jiang, Xiaohua Xu. Flame Color to Determine the Methane Content of the Biogas. China Biogas, 1983, Vol. 3, p. 28. (In Chinese)

[6] Fang Yin, Qingyu Ru, Shiqing Liu, et al. The Study of Biogas Fermentation from the Hull of Horse Bean[J]. Application of Biomass Power, 2006, No. 2, p. 57-58. (In Chinese)

[7] W.W. LIU, Fang Yin, Wudi Zhang. The Study of Biogas Fermentation on the Hull of Pea[J]. Yunnan Normal University, 2005, Vol.25, No.6, p.28-30. (In Chinese)

[8] Shimin. Zhang, Fang Yin, Wudi Zhang. The Study of Biogas Fermentation on the Hull of *Jatropha curcas* [J]. Practical forestry technology, 2009, No. 2, p.51-52. (In Chinese)

[9] Liang Liu. Experiments on Biogas Production from Peanut Hull by Anaerobic Fermentation[D]. Henan Agricultural University, 2005. (In Chinese)

[10] Qiumin. Li, Lichun Liu, Wudi Zhang, et al. Experimental Study on Biogas Fermentation of the *Ginkgo biloba* Leaf[J]. Journal of Anhui Agricultural Sciences, 2013, Vol.41, No.1, p.266- 267. (In Chinese)

[11] Yuanqiang Ruan, Lichun Liu, Defang Guo, et al. Study on Pineapple Peel Waste Biogas Generation by Anaerobic Digestion[J]. Yunnan Normal University, 2013, Vol.33, No.3, p.22-25. (In Chinese)

*Advanced Materials Research Vol. 937 (2014) pp 297-302*
*© (2014) Trans Tech Publications, Switzerland*
*doi:10.4028/www.scientific.net/AMR.937.297*

# Diversity and Distribution of Sulfate-reducing Bacteria in Jilin Oilfield

Wen-feng SONG[1,a,*], De-sheng MA[1,b], You-yi ZHU[1,c], Xiao-fang WEI[1,d], Jie WU[1,e]

[1]State Key Laboratory of Enhanced Oil Recovery, Research Institute of Petroleum Exploration and Development, CNPC, Beijing 100083, China

[a]songw2@hotmail.com, [b]mads6@petrochina.com.cn, [c]zhyy@petrochina.com.cn, [d]xiaofangwei@petrochina.com.cn,[e]wujie317@petrochina.com.cn

*Corresponding author

**Key words:** SRB, sulfate, distribution, oil reservoir, phylogenetic, *Proteobacteria*, OTUs, PCR

**Abstract.**To better understand the roles of microorganisms in oil production, diversity and distribution of microbes in Jilin oilfield was studied. Firstly, chromosomal DNA wassuccessfully extracted directly from crude oil samples. Diversity and distribution of microbes was then analyzed based on 16S rDNA libraries. There were totally 21 OTUs were obtained through 16S rDNA sequencing. Of those OTUs, 13 are bacteria in which *Proteobacteria* is the major family, while 8 are archaea in which *Methanomicrobia* is the dominant. Finally, SRB was found in all samples by amplifying the *apsA* gene using PCR. SRB found in Jilin oil samples belong to *δ-Proteobacteria*.

## Introduction

Biodegrade oils resulting from the action of microorganisms that destroyed hydrocarbons and other oil components have been a problem for the petroleumindustry. Different studies have already demonstrated the existence of large and diverse populations of microbes with different metabolic activities in petroleum systems [1-4]. Based on difficulties in sampling and in the efficiency of DNA extraction from oily samples, little is known about the bacterial diversity in crude oil [5-7]. It is also challenging to work with samples with low indigenous biomass as well as a high, oily, and viscous emulsion.

Sulfate-reducing bacteria (SRB) are a group of bacteria that use sulfate ($SO_4^-$) instead of oxygen as a final electron acceptor [1]. SRB could utilize a very wide spectrum of different low molecular organic compounds (e.g. lactate, acetate, proprionate, succinate, pyruvate, ethanol, sugars, etc.) for growth, with $SO_4^-$ being reduced to hydrogen sulfide ($H_2S$) [1-7]. SRB is well known as strongly harmful microbes in the productive process of oilfields that might cause serious problems in oilfield water systems, including corrosion of iron in anaerobic conditions (mainly by $H_2S$) and reduction of the injectivity of water injection wells by precipitation of amorphous ferrous sulfide [8].

In order to reduce risks of SRB in productive process of oil industry, the distribution and diversity of microorganisms in target oil reservoir was studied. Thus, the features of SRB could be better understood.

## Methods and Materials

### Chemicals

All reagents (media and buffers) used were prepared gravimetrically using aSartorius A200S analytical balancer, and made up to volume with roomtemperaturesterile distilled water ($dH_2O$).All chemicals used in this paper were reached the analytical standard.

### Distribution and Diversity Study of SRB in the Target Oil Reservoir

Four different crude oil samples were randomly collected from four different oil wells (named J-3031, J-2827, J-2625 and J-1709) separately by using a 2 L of thermal-resistant plastic bottles (Nalgene, USA) in Jilin oilfield. All four bottles were autoclaved at 121°C for 15 minutes (mins) before sampling.

Microorganisms were directly extracted from oil samples by using Winogradsky buffers (0.25 g of $K_2HPO_4$, 0.25 g of $MgSO_4 \cdot 7H_2O$, 0.125 g of NaCl, 2.5 mg of $Fe_2(SO_4)_3 \cdot 3H_2O$, 2.5 mg of $MnSO_4 \cdot 4H_2O$ made up with 1 L of $dH_2O$) [14]. 200 ml of oil sample was mixed with the same volume of Winogradsky solution. The mixed liquid was then incubated in hot-water both at 80 °C for 10 mins. The mixture would divide into two layers (oil on the top and buffer on the bottom). Recover the buffer layer (microorganisms contained) into a new bottle. The oil was left to mix with another 200 ml of Winogradsky solution and repeated the above procedure for five times. Finally, 1 L of microorganisms-contained solution was collected in total.

Cells were harvested by centrifuge (Eppendorf 5810Rcentrifuge) at 10, 000 × g for 5 mins at room temperature, and followed by concentrating within 10 ml of phosphate buffer (0.05 M $K_2HPO_4/KH_2PO_4$ pH 7.4, 0.1 M KCl). The total chromosome DNA was isolated subsequently by using Genome DNA isolation kits (Purelink™, Invitrogen, and Carlsbad, USA).

Polymerase chain reaction (PCR) amplification of 16S rDNA gene fragments was performed using the primers 27F [15] and 1401R [16], homologus to conserved regions of the 16S rRNA gene of the bacteria Domain. PCR for amplification was by High Fidelity DNA polymerase (Invitrogen) as per manufacturer's instructions. PCR reactions were: 94° C for 3 mins followed by 35 cycles of: 94° C for 30 seconds (s); 60° C for 1 min and 72° C for 3 mins followed by one step at 72° C for 7 mins. PCR-amplified DNA fragments were purified with PCR purification kit (Purelink™, Invitrogen, Carlsbad, USA), and quantified by nano-drop ND-1000 (100 W. Rockland RD, Montchanin, DE, USA), measuring the absorbance at 260 nm (A260).

The PCR fragments were introduced into pGEM-T easy vector (Promega, Madison, WI, USA) followed by transferring into *Escherichia coli* (*E. coli*) competent cells. The cloned fragments were then selected based on blue/white colour assay. Subsequently those fragments were sequenced at Sangon Biotech Limited Company in Shanghai by using ABI Prism3730xl DNA analyzer. 16S rDNA clone libraries were constructed.

The sequences were grouped in OTUs (operational taxonomic units), assuming that one OTU included sequences with identity values equal to or higher than 97% [17]. A total of 47 valid 16S rDNA gene sequences was analyzed and for the closet match to sequences in the GenBank database by BLASTN [18]. The phylogenetic tree was then drawn by using software "MEGA 5.0". SRB were finally identified by using PCR reaction with primers DSR-1F and DSR-R [19, 20].

## Results and Discussions

### Distribution and Diversity Study of SRB in the Target Oil Reservoir

DNA was successfully extracted from crude oil samples. However, a low amplicon yield was obtained with both pairs of 16S rDNA gene primers used, probably due to the less efficiency of DNA extraction from oil samples. As expected, no amplicons were obtained from the blank tubes (control). The PCR products were cloned, and a total of 47 valid 16S rDNA sequences were obtained and carried on the further analysis.

Table 1. Frequency of clones affiliated with different bacterial families found in each oil sample.

| Bacterial families | Frequency of clones in each oil sample | | | |
|---|---|---|---|---|
| | J-3031 | J-2827 | J-2625 | J-1709 |
| **α-Proteobacteria** | 2 | 2 | 3 | 3 |
| **δ-Proteobacteria** | 1 | 1 | 3 | 3 |
| **γ-Proteobacteria** | 3 | 2 | 2 | 2 |
| **Bacilli** | 1 | - | - | - |

Of those cloned sequences, 28 belong to bacteria (59.6%) (Table 1), whereas the rests were archaea (40.4%) (Table 2). The bacterial colonies were divided into four different types, including

*alpha (α)-Proteobacteria*, *delta (δ)-Proteobacteria*, *gamma (γ)-Proteobacteria*, and *Bacilli*. Among these, *Proteobacteria* is the dominant (96.4%) bacterial group in tested samples (Table 1). Bacteria contained in sample J-3031 had the greatest diversity compared to other three.

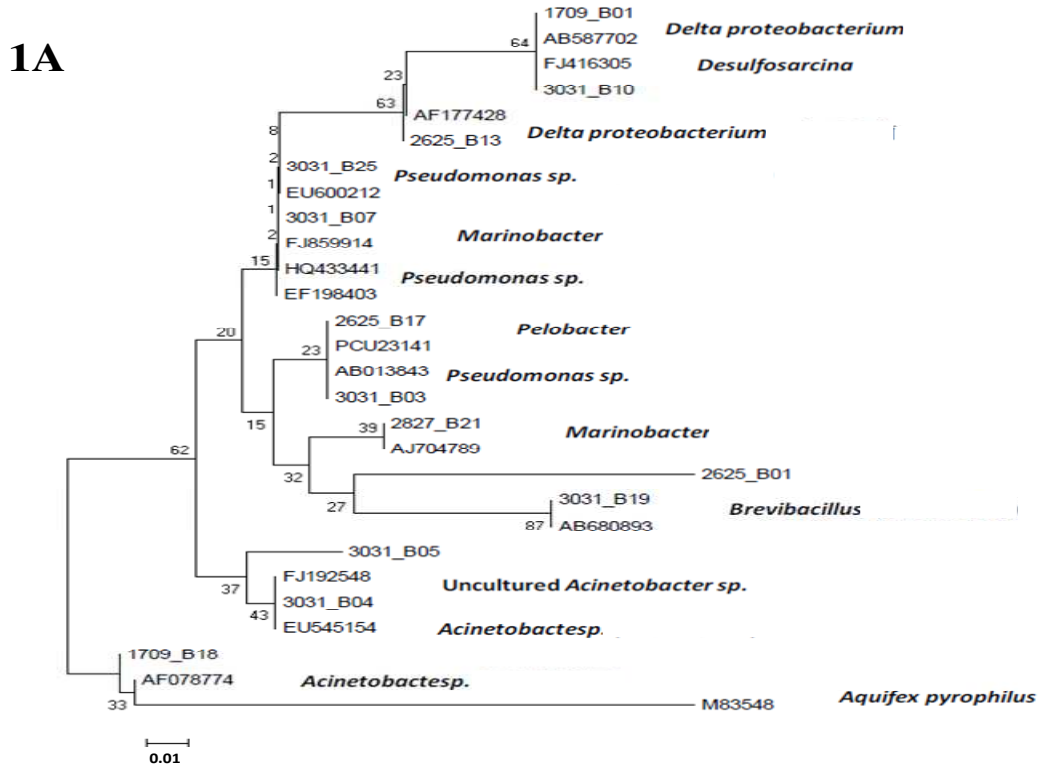
Table 2. Frequency of clones affiliated with different archeal families found in each oil sample.

| Archeal families | Frequency of clones in each oil sample | | | |
|---|---|---|---|---|
| | J-3031 | J-2827 | J-2625 | J-1709 |
| **Euryarchaeota** | 2 | - | 1 | 1 |
| **Methanomicrobia** | 2 | 4 | 3 | 3 |
| **Methanobacteria** | 3 | - | - | - |

In contrast, there was only three different families has been found in archeal group, involving*Euryarchaeota*, *Methanomicrobia* and *Methanobacteria* (Table 2). Of those, Methanomicrobia is the main group. Furthermore, *Methanobacteria* was only found in sample J-3031.

As shown in above results, all of detected families of microorganisms (bacteria and archaea) in this study could be found in sample J-3031, rather than other three. The reason is not very clear. It might be that J-3031 has relatively higher water content (about 30% v/v). In contrast, there was extremely low water content (less than 2% v/v) in the other three. Extraction of chromosome DNA was less efficient from oil than that from water.

All 16S rDNA sequences were then clustered as OTUs. There were totally 21 OTUs were obtained. A phylogenetic tree was constructed subsequently with closely related sequences that were recovered from GenBank database (Fig. 1).



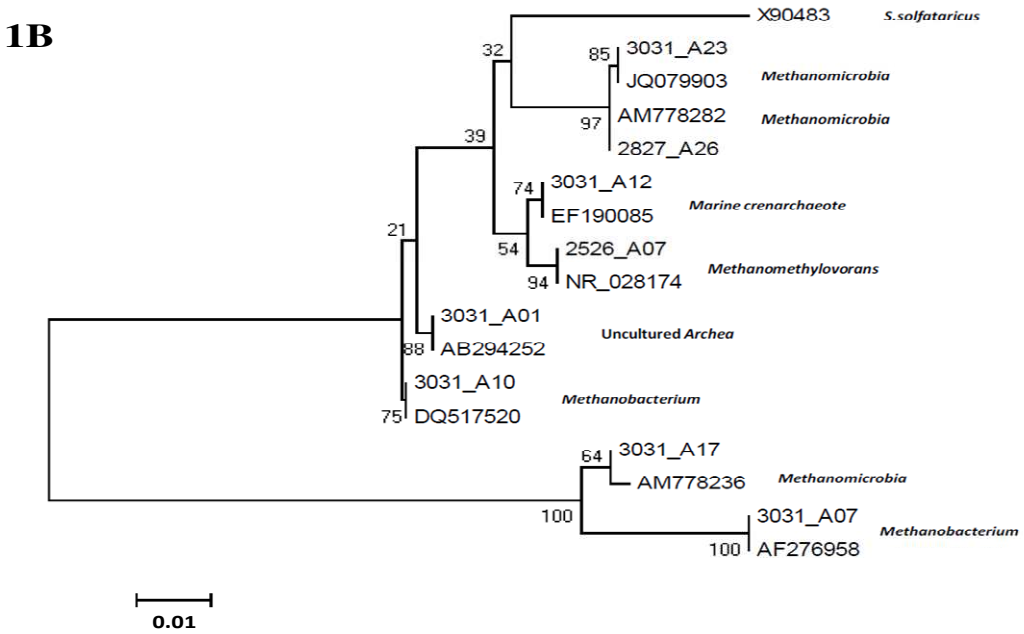



Fig.1. Phylogenetic tree of 16S rDNA gene-based libraries obtained from four crude oil samples. OTUs were defined by MEGA 5.0 using the further neighbor algorithm with a distance level of 1%. A: represents the bacterial phylogenetic tree of 16S rDNA sequences; B: is the archeal phylogenetic tree of 16S rDNA sequences.

The majority of bacterial OTUs were*δ-Proteobacteria* (30.8%) and γ-Proteobacteria (30.8%) (Fig. 1A). However, the dominant OTUs of archaea were *Methanomicrobia* (Fig. 1B). This result is a little bit different with the previous study. It has been reported that the dominant bacteria groups in Chinese oilfields (nationwide) are *Proteobacteria* (75.8%), in which *α-Proteobacteria* and *γ-Proteobacteria* are the major groups [23]. The difference might be caused by inefficient DNA extraction.

The SRB was subsequently identified by amplifying the target structural gene *apsA* gene in PCR reaction. The *apsA* gene is known to encode protein sulfate dissimilatory reductase subunit (SDRS) [24], which plays an important role in the reaction of dissimilatory reduction of sulfate. Therefore, *apsA* could be used as an indicator to prove the presence of SRB in gene level.

The presence of SRB was then determined by using PCR with primers DSR-1F and DSR-R [19, 20]. SRB has been found in all four oil samples. However, all of SRB 16S rDNA sequences were affiliated into one OTU. The poor diversity of SRB in Jilin oilfield might be because of insufficient DNA extraction from oil samples. As our known, SRB are varied and widely distributed under oil reservoir. Moreover, all SRB found in Jilin oil samples belonged to *δ-Proteobacteria*. This result might be partially proved that SRB are mostly like to be a member of *δ-Proteobacteria* family. It is also demonstrated by a previous study [19].There was no SRB found in archaea in Jilin oil samples.

## Conclusions

(1) DNA was successfully extracted from crude oil samples. However, a low amplicon yield was obtained with both pairs of 16S rDNA gene primers used, probably due to the less efficiency of DNA extraction from oil samples.

(2) Major bacteria found in Jilin samples belong to *Proteobacteria*, whereas dominant archaea was *Methanomicrobia*.

(3) SRB found in all samples belongs to *δ-Proteobacteria*. The result proved that SRB were widely distributed in oil reservoir.

**References**

[1] M. Magot, B. Ollivier, and B.K.C. Patel, Microbiology of petroleum reservoir, Anton. Van. Lee. 77 (2000) 103-116.

[2] J.D. Van Hamme, A. Singh, and O.P. Ward, Recent adcances in petroleum microbiology, Microbiol. Mol. Biol. Rev. 67 (2003) 503-549.

[3] C.M. Aitken, D.M. Jones, and S.R. Larter, Anaerobic hydrocarbon biodegradation in deep subsurface oil reservoirs, Nature. 431 (2004) 291-294.

[4] J.C. Philp, A.S. Whiteley, L. Ciric, M.J. Bailey, Monitoring bioremediation, in R.M. Atlas and J.C. Philp (Eds), Bioremediation: Applied Microbial Solutions for Real-World Environmental Cleanup, ASM Press., Washington, DC, USA, 2005, pp. 237-268.

[5] V.M. Oliveira, L.D. Sette, K.C.M. Simioni, E.V. doa Santos Neto, Bacterial diversity characterization in petroleum samples from Brazilian reservoirs, Braz. J. Microbiol. 39 (2008) 445-452.

[6] I. von der Weid, E. Korenblum, D. Jurelevicius, et al. Molecular diversity of bacterial communities from subseafloor rock samples in a deep-water production basin in Brazil, J. Microbiol. Biotechnol. 18 (2008) 5-14.

[7] E. Korenblum, E. Valoni, M. Penna, L. Seldin, Bacterial diversity in water injection systems of Brazilian offshore oil platforms, Appl. Microbiol. Biotechnol.85 (2010) 791-800.

[8] G. Muyzer and A.J.M. Stams, The ecology and biotechnology of Sulphate-reducing bacteria, Nat. Rev. Microbiol. 6 (2008) 441-454.

[9] S.M. Keith, R.A. Herbert, C.G. Harfoot, Isolation of new types of Sulphate-reducing bacteria from estuarine and marine sediments using chemostat enrichments, J. Appl. Bacteriol. 53 (1982) 29-33.

[10] R.J. Parkes, G.R. Gibson, I. Mueller-Harvey, W.J. Buckingham, R. Herbert, Determination of the substrates for Sulphate-reducing bacteria within marine and estuarine sediments with different rates of Sulphate reduction, J. Gen. Microbiol. 135 (1989) 175-187.

[11] F. Bak and N. Pfennig, Sulfate-reducing bacteria in littoral sediment of Lake Constance, FEMS Microbiol. Ecol. 85 (1991) 43-52.

[12] P. Caumette, Ecology and physiology of phototrophic bacteria and Sulphate-reducing bacteria in marine salterns, Experientia. 49 (1993) 473-481.

[13] J.R. Postgate, The Sulphate-Reducing Bacteria, Cambridge U. Press. London (1984).

[14] F. Widdel, and N. Pfennig, Bergey's Manual of Systematic Bacteriology, Williams & Wilkins, Baltimore 1 (1984) 663-679.

[15] R. Cord-Ruwisch, W. Kleinitz, and F. Widdel, Sulfate-Reducing Bacteria and Their Activities in Oil Production, J. Pet. Technol. 39 (1987) 97-106.

[16] V.D.W. Irene, E. Korenblum, D. Jurelevicius, A.S. Rosado, R. Dino, G.V. Sebastian, L. Seldin, Molecular diversity of bacterial communities from subseafloor rock samples in a deep-water production basin in Broazil, J. Microbiol. Biotechnol. 18 (2008) 5-14.

[17] D.J. Lane, 16S/23S rRNA sequencing, In: Stackebrandt E, Goodfellow M (Eds.), Nucleic acids techniques in Bacterial systematics, John Wiley & Sons, Chichester, 1991, pp. 115-147.

[18] H. Heuer, M. Krsek, P. Baker, K. Smalla, E.M. Wellington, Analysis of actinomycete communities by specific amplification of genes encoding 16S rRNA and gel-electrophoretic separation in denaturing gradients, Appl. Environ. Microbiol. 63 (1997) 3233-3241.

[19] M. Zaballos, A. Lopez-Lopez, L. Ovreas, et al. Comparison of prokaryotic diversity at offshore oceanic locations reveals a different microbiota in the Mediterranean Sea, FEMS. Microbiol. Ecol. 56 (2006) 389-405.

[20] J.D. Thompson, T.J. Gibson, F. Plewniak, F. Jeanmougin, D.G. Higgins, The CLUSTAL X windows interface: flexible strategies for multiple sequence alignment aided by quality analysis tools, Nucleic. Acids.Research. 25 (1997) 4876-4882.

[21] R. Kondo, D.B. Nedwell, K.J. Purdy, S.Q. Silva, Detection and enumeration of Sulphate-reducing bacteria in estuarine sediments by competitive PCR, Geomicrobiol. J. 21 (2004) 145-157.

[22] J. Leloup, A. Loy, N.J. Knob, C. Borowski, M. Wagner, B.B. Jorgensen, Diversity and abundance of sulfate-reducing microorganisms in the sulfate and methane zones of a marine sediment, Black Sea, Environ. Microbiol. 9 (2007) 131-142.

[23] L. Zhao, T. Ma, M. Gao, P. Gao, M. Gao, X. Zhu, G. Li, Characterization of microbial diversity and community in water flooding oil reservoirs in China, World. J. Microb. Biot. 28 (2012) 3039-3052.

[24] K. Mori, H. Kim, T. Kakegawa, S. Hanada, A novel lineage of sulfate-reducing microorganisms: Thermodesulfobiaceae fam. Nov., Thermodesulfobiumnarugense, gen. nov., sp. Nov., a new thermophilic isolate from a hot spring, Exremophiles. 7 (2003) 283-290.

*Advanced Materials Research Vol. 937 (2014) pp 303-307*
*© (2014) Trans Tech Publications, Switzerland*
*doi:10.4028/www.scientific.net/AMR.937.303*

# Cultivationand Regulation of Sulfate-reducing Bacteria in Oilfield

Wen-feng SONG[1,a,*], De-sheng MA[1,b], You-yi ZHU[1,c], Xiao-fang WEI[1,d], Jie WU[1,e]

[1]State Key Laboratory of Enhanced Oil Recovery, Research Institute of Petroleum Exploration and Development, CNPC, Beijing 100083, China

[a]songw2@hotmail.com, [b]mads6@petrochina.com.cn, [c]zhyy@petrochina.com.cn, [d]xiaofangwei@petrochina.com.cn,[e]wujie317@petrochina.com.cn

*Corresponding author

**Key words:** SRB, sulfate, hydrogen sulfide, EOR, nitrate, nitrite

**Abstract.** To better regulate(up and down) the activation of SRB thereby contributing to EOR, efficiency of growth and inhibition of SRB was studied in this paper.Six different growth media were tested in total.The optimal growth media were selected based on growth rate and variations of pH between the start and end point of growth. Of the six media, complex I was selected as the best medium in which SRB grew to stationary-phase in less than 8 days with the highest cells' concentration. Finally, the effects of $NO_3^-$ on growth and persistence of SRB were studied by using abroad range concentrations of $NO_3^-$. The result indicated that SRB growth could be significantly inhibited at $NO_3^-$ of 80 mM.

## Introduction

Sulfate-reducing bacteria (SRB) are a group of bacteria that use sulfate ($SO_4^-$) instead of oxygen for respiration. The main property of those either obligate or facultative anaerobic bacteria populations is their active use of $SO_4^-$ as a final electron acceptor [1]. SRB could utilize a very wide spectrum of different low molecular organic compounds (e.g. lactate, acetate, proprionate, succinate, pyruvate, ethanol, sugars, etc.) for growth, with $SO_4^-$ being reduced to hydrogen sulfide ($H_2S$) [1-7].

SRB is well known as strongly harmful microbes in the productive process of oilfields. They might cause serious problems in oilfield water systems, including corrosion of iron in anaerobic conditions (mainly by $H_2S$) and reduction of the injectivity of water injection wells by precipitation of amorphous ferrous sulfide [8]. Furthermore, $H_2S$ is extremely toxic if inhaled. $H_2S$ could easily escape from contaminated liquids and might accumulate under poorly ventilated conditions. Therefore, billions of US dollars might be lost in oilfields each year around worldwide due to corrosions of SRB.

SRB might also play a role in enhancing oil recovery(EOR) [9], even if they are recognized ashazards. For example, SRBcould diminish oil viscosity, replenish thedeclining pressure of reservoir, and change heavy oil to light oil through yields of bio-generated acids, gas ($H_2S$) and degradation ofhydrocarbons(Aliphatic and Aromatic).Moreover, different types of SRB are widely distributed in global oil reservoirs. Actually, SRB could be a great target that used for further improving oil recovery, if they can be well regulated.

In order to find a way for efficientlyregulating(up and down) the activation of SRB, the entire research was divided into two parts. In the first part, six different culture media were tested. The optimal culture medium was then selected according to the growth rate and variations of pH during growth. It is known that the accumulation of bio-production could low the pH thereby leading to inhibit further growth of SRB [10].

In the second part, growth inhibition of SRB was studied by using nitrate ($NO_3^-$). The presence of $NO_3^-$ may pose a specific stress to SRB as $NO_3^-$ has been observed to suppress sulfate reduction activity *in situ* [11, 12]. Furthermore, $NO_3^-$ is a broadly available electron acceptor that could be readily used by a large number of microorganisms in natural environments. Therefore, $NO_3^-$ reduction as an ecologically more competitive process could have major impacts on the survival and persistence of SRB in microbial communities [13].

## Methods and Materials

### Chemicals

All reagents (media and buffers) used were prepared gravimetrically using aSartorius A200S analytical balancer, and made up to volume with roomtemperaturesterile distilled water ($dH_2O$).All chemicals used in this paper were reached the analytical standard.

### SRB Growth Study

In the pre-culture, 1 ml of SRB-contained water sample was inoculated (collected directly from oil wells in Jilin oilfield) and cultured by using agar shaking techniques [14] with ATCC medium 1249 [15]. 10 ml screw capped tubes were employed, and filled with nitrogen ($N_2$) to create an anaerobic environment. The cultures were then placed into an incubator at 40°C for 14 days. After incubation, single colony was picked up and transferred into liquid-medium contained 50 ml of screw capped tubes for the secondary culture.

In the secondary culture, six different growth media were tested, including molasses, degradable forming agent (DFA), and complex I – IV. SRB were cultured under anaerobic conditions at 40°C for 8 days in 50 ml of crewed tubes (filled with $N_2$). SRB growth rate and pH value between start and end point were measured within each medium.

### SRB Growth Inhibition Study

To find out the optimal concentration of $NO_3^-$ that would significantly reduce the growth rate of SRB, a range of concentrations (0, 20, 40, 60 and 80 mM) of $NaNO_3$ was used in this study. SRB were cultured by using an optimal medium (determined in *SRB growth study section*) with varied levels of $NO_3^-$ under anaerobic condition at 40°Cfor 8 days. Different growth rates of SRB were then compared.

## Results and Discussions

### SRB Growth Study

In order to shorten the cultural cycle, growth rate of SRB was measured with six different media (molasses, DFA and complex I-IV). The efficiency of different growth media was then compared.

SRB gained a higher growth rate and grew into stationary-phase within8 days by using three media, including molasses, complex I and complex IV (Fig. 1). Of the three, SRB had the fastest growth rate within medium complex I. Moreover, the highest cell concentration of SRB was also obtained by using medium complex I. In contrast, DFA gave the lowest growth rate among all six media. The carbon sources of DFA might be too hard to be degraded. Cells probably need to spend more time on digestion of the carbon source but not for growth.

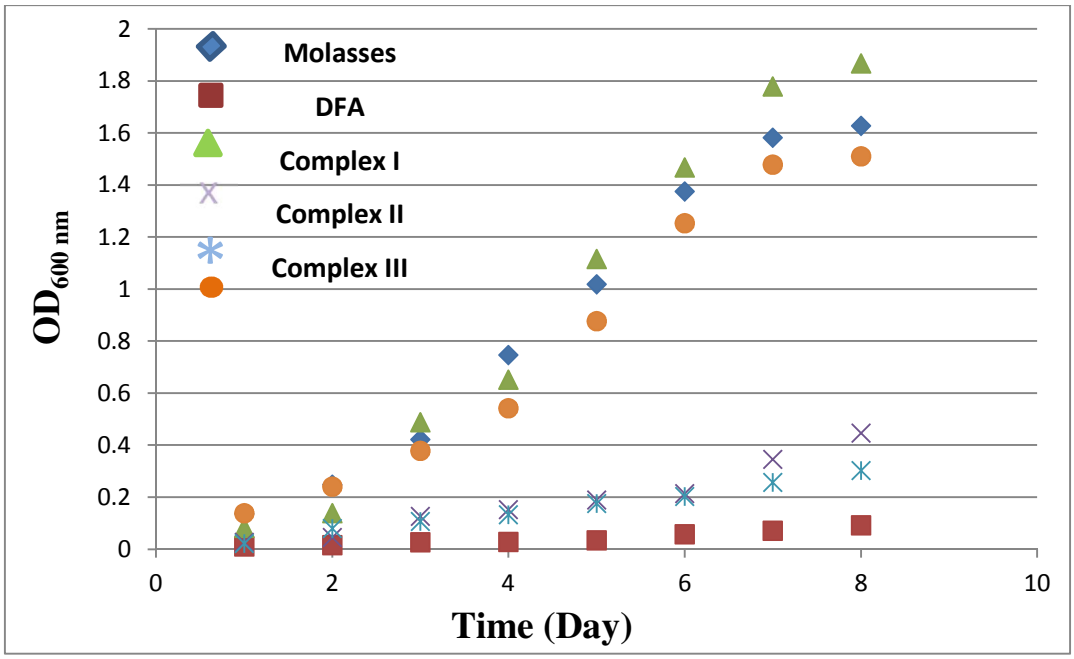



Fig. 1. Comparison of SRB growth rates by using six different growth media.

The pH value is well known to play a significant role in growth and persistence of microorganisms including SRB [10]. To find out an optimal growth media for SRB, difference of pH between start and end point of growth was also determined within these six media. The optimal pH condition for SRB growth was obtained by using medium complex II (Fig. 2). Unfortunately, complex II showed a significantly lower growth rate. Therefore, complex I was selected as an optimal growth medium of SRB due to its fastest growth rate and a small-scale of variations in pH during growth (Fig. 2).

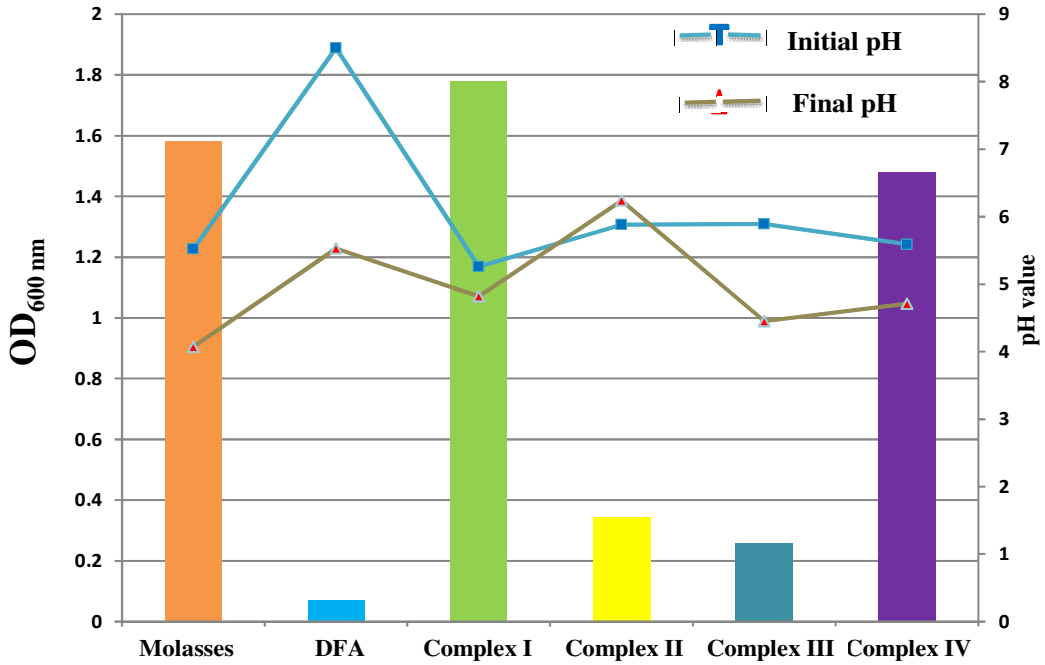



Fig. 2. Comparisons of pH values between initial and final states of SRB growth by using six different growth media. Bars represent the final concentrations of SRB; Lines show the differences of pH between different media.

## SRB Growth Inhibition Study

To find out an efficient way to reduce risks of SRB, growth inhibition study of SRB was conducted by using medium complex I with aboard range concentrations of $NaNO_3$. As shown in results (Fig. 3), cell concentrations were inproportional to $NO_3^-$levels. The growth of SRB was significantly inhibited (still in lag-phase) at $NO_3^-$ of 80 mM. It is well known that the inhibitory effect is not only caused by osmotic stress (a non-specific inhibitory mechanism), but also caused by a specific inhibitory mechanism of $NO_3^-$ [13].

$NO_3^-$ inhibition of metal-reducing microbial populations, such as the SRB, hinders bioremediation efforts exploiting these microbial biocatalysts [16-18]. Owing to the specificity of nitrite ($NO_2^-$) toxicity to sulfate reduction [19, 20], $NO_2^-$(a key intermediate during microbial $NO_3^-$ reduction) derived from $NO_3^-$ could represent a major stress condition for SRB [13]. SRB are lack of $NO_3^-$ reductase genes [20]. Therefore, SRB cannot use $NO_3^-$as electron acceptor. However, $NO_3^-$ is a common electron acceptor readily used by many other microorganisms. The growth of SRB might be further suppressed due to the limited nutrients caused by food competition.

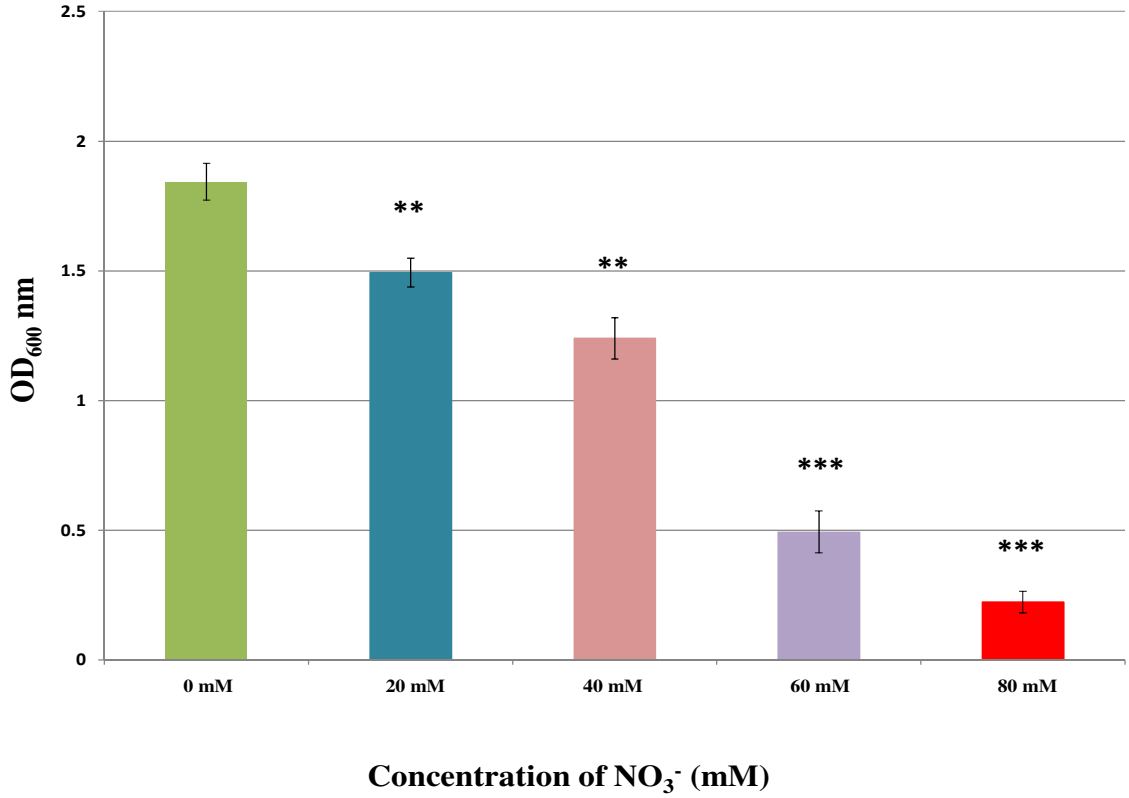



Fig. 3. Effects on SRB growth when exposed to abroad range concentrations of $NO_3^-$. *: significantly different from control assay (0 mM). The number of stars (*) indicates the significance level. *: P<0.05; **: P<0.01; ***: P<0.005. The significant difference was determined in paired test. n=4, error bars are standard error.

## Conclusions

(1) Complex I was chosen as the optimal growth medium of SRB because of its best growth rate and small-scale variations of pH value during the growth.

(2) $NO_3^-$ could significantly affect the growth and persistence of SRB due to both of osmotic stress and the specific inhibitory mechanism of $NO_3^-$.

**References**

[1] G. Muyzer and A.J.M. Stams, The ecology and biotechnology of Sulphate-reducing bacteria, Nat. Rev. Microbiol. 6 (2008) 441-454.

[2] S.M. Keith, R.A. Herbert, C.G. Harfoot, Isolation of new types of Sulphate-reducing bacteria from estuarine and marine sediments using chemostat enrichments, J. Appl. Bacteriol. 53 (1982) 29-33.

[3] R.J. Parkes, G.R. Gibson, I. Mueller-Harvey, W.J. Buckingham, R. Herbert, Determination of the substrates for Sulphate-reducing bacteria within marine and estuarine sediments with different rates of Sulphate reduction, J. Gen. Microbiol. 135 (1989) 175-187.

[4] F. Bak and N. Pfennig, Sulfate-reducing bacteria in littoral sediment of Lake Constance, FEMS Microbiol. Ecol. 85 (1991) 43-52.

[5] P. Caumette, Ecology and physiology of phototrophic bacteria and Sulphate-reducing bacteria in marine salterns, Experientia. 49 (1993) 473-481.

[6] J.R. Postgate, TheSulphate-Reducing Bacteria, Cambridge U. Press. London (1984).

[7] F. Widdel, and N. Pfennig, Bergey's Manual of Systematic Bacteriology, Williams & Wilkins, Baltimore 1 (1984) 663-679.

[8] R. Cord-Ruwisch, W. Kleinitz, and F. Widdel, Sulfate-Reducing Bacteria and Their Activities in Oil Production, J. Pet. Technol. 39 (1987) 97-106.

[9] A. Suarez-Suarez, A. Lopez-Lopez, A. Tovar-Sanchez, P. Yarza, A. Orfila, J. Terrados, J. Arnds, S. Marques, H. Niemann, P. Schmitt-Kopplin, R. Amann, R. Rossello-Mora, Response of sulfate-reducing bacteria to an artificial oil-spill in a coastal marine sediment, Environ. Microbiol. 13 (2011) 1488-1499.

[10] M. Rzeczycka, and M. Blaszczyk, Growth and activity of Sulphate-reducing bacteria in media containing phosphogypsum and different sources of carbon, Pol. Environ. Stud. 14 (2005) 891-895.

[11] G.E. Jenneman, M.J. McInerney, and R.M. Knapp, Effect of nitrate on biogenic sulfide production, Appl. Environ. Microbiol. 51 (1986) 1205-1211.

[12] I. Davidova, M.S. Hicks, P.M. Fedorak, J.M. Duflita, The influence of nitrate on microbial processes in oil industry production waters, J. Ind. Microbiol. Biotechnol. 27 (2001) 80-86.

[13] Q. He, Z. He, D.C. Joyner, M. Joachimiak, M.N. Price, Z.K. Yang, H.C.B. Yen, C.L. Hemme, W. Chen, M.M. Fields, D.A. Stahl, J.D. Keasling, M. Keller, A.P. Arkin, T.C. Hazen, J.D. Wall, J. Zhou, Impact of elevated nitrate on sulfate-reducing bacteria: a comparative study of *Desulfovibrio vulgaris*, ISME. J. 4 (2010) 1-12.

[14] R.J. Parkes, N.J.E. Dowling, D.C. White, R.A. Herbert, G.R. Gibson, Characterization of sulphate-reducing bacterial populations within marine and estuarine sediments with different rates of sulphate reduction, FEMS. Microbiol. Ecol. 102 (1993) 235-250.

[15] D. Shao, Y. Kang, A. Wu, M.H. Wong, Effects of sulfate reducing bacteria and sulfate concentrations on mercury methylation in freshwater sediments, Sci. Total. Environ. 424 (2012) 331-336.

[16] K.T. Finneran, M.E. Housewright, and D.R. Lovley, Multiple influences of nitrate on uranium solubility during bioremediation of uranium-contaminated subsurface sediments, Environ. Microbiol. 4 (2002) 510-516.

[17] J.D. Istok, J.M. Senko, L.R. Krumholz, et al. *In situ* bioreduction of technetium and uranium in a nitrate-contaminated aquifer, Environ. Sci. Technol. 38 (2004) 468-475.

[18] J.L. Nyman, T.L. Marsh, M.A. Ginder-Vogel, M. Gentile, S. Fendorf, C. Criddle, Heterogeneous response to biostimulation for U (VI) reduction in replicated sediment microcosms, Biodegradation. 17 (2006) 303-316.

[19] E.A. Greene, C. Hubert, M. Nemati, G.E. Jenneman, G. Voordouw, Nitrite reductase activity of sulfate-reducing bacteria prevents their inhibition by nitrate-reducing, sulfide-oxidizing bacteria, Environ. Microbiol. 5 (2003) 607-617.

[20] S.A. Haveman, E.A. Greene, C.P. Stilwell, J.K. Voordouw, G. Voordouw, Physiological and gene expression analysis of inhibition of Desulfovibrio vulgaris Hildenborough by nitrite, J. Bacteriol. 186 (2004) 7944-7950.

*Advanced Materials Research Vol. 937 (2014) pp 308-312*
*© (2014) Trans Tech Publications, Switzerland*
*doi:10.4028/www.scientific.net/AMR.937.308*

# Application of Neural Network in Bioactive Prediction of Inhibitor of Thymidylic Acid-Based Synthetase

Xi-Hua DU[1, a], Xiao-Hui WANG[1,b]

[1]School of Chemistry Engineering, Xuzhou Institute of Technology, Xuzhou, Jiangsu, 221111, China

[a] dxh12@hotmail.com, [b] wxh2116@163.com

**Keywords:** Thymidylic acid-based synthetase, Inhibitor, Biological activity, The electrical topology state index, Neural network, Quantitative structure -activity relationship.

**Abstract.** Based on the molecular topology information and adjacency matrix, the 38 electrical state indices of molecules of inhibitor of thymidylic acid-based synthetase as five-membered heterocyclic pyrimidine derivatives were calculated to provide theoretical basis for molecular design of new drugs. By using variable regression method, the best subset of structural parameters of $E_1$, $E_2$, $E_7$, $E_{16}$ and $E_{31}$ were optimized. When the five structural parameters were used as the BP neural network input neurons and the neural network structure of 5:3:1 was used, an ideal prediction model of biological activity was obtained. Its total correlation coefficient $r$ and average relative error were 0.972 and 2.13%, respectively. The result showed that the biological activity and $E_1$, $E_2$, $E_7$, $E_{16}$ and $E_{31}$ have a good non-linear relationship with the biological activity, and the results predicted by neural networks was better than that by multiple regression method. The test proved that the model had good robust and predictive capabilities. Our research would provide theoretical guidance for the development of new drugs of inhibitor of thymidylic acid-based synthetase with efficient and low toxicity.

## Introduction

Thymidylic acid-based synthetase (TS) inhibitors can inhibit the synthesis of DNA and the growth of tumor cells which even lead to the death of tumor cells. Therefore, the chemotherapy drug was used in treating a wide variety of tumor diseases, such as breast cancer, ovarian cancer, colon cancer, colorectal cancer, liver cancer, bladder cancer and so on. The inhibitors based pyrimidine were widely used in clinic, and were relatively effective antitumor drugs [1]. Because the drugs were also toxicity to normal cells, and it has side effects such as blood toxicity, syndrome of hand and foot, neutropenia, thrombocytopenia, and gastrointestinal tract reaction. Therefore, they were limited in clinical use. Thymidylic acid-based synthetase and their clinical research of the inhibitors had related literature reports [2-6], but using the quantitative structure - activity relationship (QSAR) method to study antitumor activity of inhibitors of hymidylic acid-based synthetase was relatively less [7, 8].

In recent years, the quantitative structure-activity relationship QSAR method was widely used in pharmaceutical chemistry and toxicology research field[9-12], the results of the research work have also been fully recognized. By quantum chemistry method, this paper studied the inhibitor of thymidylic acid-based synthetase as five-membered heterocyclic pyrimidine derivatives and their space, electronic structure, and toxicity mechanism of antitumor activity of these kinds of compounds were analyzed in theory, in order to obtain the activity parameters of drug molecular design of these kinds of compounds. On the basis of previous work[13, 14], 38 electrical topology state indices of molecules $E_m$ were calculated by using the MATLAB programs[15, 16] with similar aromatic heterocyclic molecules of inhibitor of thymidylic acid-based synthetase as five-membered heterocyclic pyrimidine derivatives. By using MINITAB software application in the optimal subset regression method the five best variables were screened to analyze the inhibitory activities of these compounds on human TS by regression methods and a good correlation was founded between the electrical topology status index and inhibitory activity. According to the model to forecast the biological activity, we found the predicted values were consistent with the experimental values. The model test with one by one had good stability and the ability of prediction. The research work has important significance to the design of drug molecules of the new type high-efficiency antitumor.

## Methodology

### Molecular Structure of Thymidylic Acid-based Synthetase.

Common structure of inhibitors of thymidylic acid-based synthetase were shown in Fig. 1, mainly for pyrrolo [2,3-d] pyrimidines, pyrrolo [3,2-d] pyrimidine, thieno[2,3-d] pyrimidine compounds and so on. All 38 molecular structures are shown in Table 1.

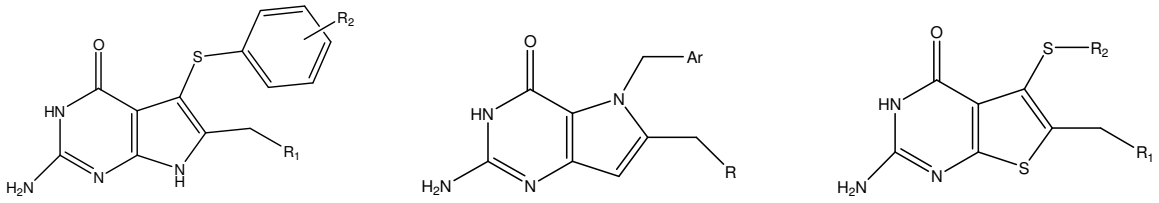



Fig. 1. Molecular Structure of Inhibitors of Thymidylic Acid-Based Synthetase

### The Calculation of Electrical Topology Status Index

Electrical topological index was presented by the Kier and Hall [17] and it is a kind of symbols could show the electronic structure of atoms and spatial topological properties of molecular structure descriptors. Using Chem3D Ultra 9.0, we built structures of 38 molecules of inhibitor of thymidylic acid-based synthetase as five-membered heterocyclic pyrimidine derivatives. Electrical topological indices were calculated by MATLAB. MINITAB 14 software was adopted to improve the optimal variable subset analysis. We chose the best correlation with activity index of the compounds as optimal variables. The data were listed in Table 1, and the best subset regression analysis results were shown in Table 2.

### Analysis of Statistical Regression

We used $E_m$ of the 38 electrical state indices of molecules of inhibitor of thymidylic acid-based synthetase as independent variables, and the inhibitory activity of human's TS ( $pIC_{50}$, the minus paired-domination number of $IC_{50}$ (50% inhibitory concentration)) as dependent variables. We have chosen the best variables of relativity with inhibitory activity by MINITAB 14 software, and then built up the mathematical model between these indexes and biological activity. We have also used leave-one-out (LOO) to check all the models for the robustness and the prediction ability.

Table 1. The E-state Indices and Predicted Values of Inhibitory Activity of Thymidylic Acid-Based Synthetase

| Series | Team | | Groups | $E_1$ | $E_2$ | $E_7$ | $E_{16}$ | $E_{31}$ | $pIC_{50}$ | | |
|---|---|---|---|---|---|---|---|---|---|---|---|
| | | | | | | | | | Exp. | Pre. | Err. |
| 1 | | $R_1$ | $R_2$ | | | | | | | | |
| | 1 | H | 4'-CO-L-glu | 1.838 | -0.594 | 6.415 | 46.580 | 1.356 | 7.27 | 6.97 | -4.15 |
| | 2 | $CH_3$ | 4'-CO-L-glu | 1.960 | 0.079 | 6.463 | 46.793 | 1.380 | 7.05 | 7.20 | 2.10 |
| | 3 | H | 3', 4'-$Cl_2$ | 1.914 | 0 | 5.379 | 12.147 | 1.476 | 6.89 | 6.86 | -0.38 |
| | 4 | H | 4'-$NO_2$ | 1.876 | 0 | 6.407 | 22.917 | 1.414 | 6.82 | 6.91 | 1.29 |
| | 5 | H | 3', 4'-$(OCH_3)_2$ | 5.119 | 0 | 5.654 | 12.252 | 1.509 | 5.62 | 5.62 | 0.02 |
| | 6 | H | 4'-Cl | 1.940 | 0 | 7.519 | 12.106 | 1.546 | 6.00 | 6.17 | 2.90 |
| | 7 | $CH_3$ | 3', 4'-$Cl_2$ | 2.028 | 0.777 | 5.417 | 12.263 | 1.501 | 6.64 | 6.50 | -2.12 |
| | 8 | $CH_3$ | 4'-$NO_2$ | 1.995 | 0.737 | 6.455 | 23.079 | 1.439 | 6.62 | 6.57 | -0.72 |
| | 9 | $CH_3$ | 4'-F | 2.010 | 0.763 | 6.217 | 12.183 | 1.463 | 5.57 | 5.74 | 3.08 |
| | 10 | $CH_3$ | 4'-$OCH_3$ | 3.694 | 0.814 | 7.780 | 12.269 | 1.584 | 4.80 | 4.80 | -0.02 |
| | 11 | $CH_3$ | 4'-Br | 2.062 | 0.828 | 8.040 | 12.235 | 1.609 | 6.00 | 5.84 | -2.62 |
| | 12 | $CH_3$ | 3'-Br | 2.062 | 0.825 | 8.028 | 12.246 | 1.605 | 5.96 | 5.83 | -2.10 |
| | 13 | $CH_3$ | 3'-Cl | 2.045 | 0.804 | 7.587 | 12.230 | 1.550 | 5.59 | 5.60 | 0.20 |
| | 14 | $CH_3$ | 2', 3'-$(CH)_4$ | 2.078 | 0.822 | 14.529 | 12.452 | 1.650 | 5.25 | 5.25 | -0.01 |

| | | | | | | | | | | | |
|---|---|---|---|---|---|---|---|---|---|---|---|
| 2 | | R | Ar | | | | | | | | |
| | 15 | H | 4-CO-L-glu-Ph | 1.836 | -0.246 | 8.189 | 46.533 | 0 | 7.34 | 7.26 | -1.06 |
| | 16 | H | 4-F-Ph | 1.890 | 0.476 | 7.997 | 12.022 | 0 | 5.43 | 5.24 | -3.58 |
| | 17 | H | 4-Cl-Ph | 1.938 | 0.584 | 9.395 | 12.061 | 0 | 5.54 | 5.69 | 2.78 |
| | 18 | H | 4-Br-Ph | 1.955 | 0.622 | 9.885 | 12.074 | 0 | 5.89 | 5.94 | 0.92 |
| | 19 | H | 4-$NO_2$-Ph | 1.874 | 0.439 | 8.220 | 22.870 | 0 | 5.85 | 5.64 | -3.64 |
| | 20 | H | 4-Ome-Ph | 3.578 | 0.591 | 9.615 | 12.108 | 0 | 5.83 | 5.86 | 0.48 |
| | 21 | H | 4-$OCF_3$-Ph | 1.804 | 0.302 | 7.188 | 12.093 | 0 | 5.89 | 5.80 | -1.55 |
| | 22 | H | 3,5-di-Br-Ph | 1.949 | 0.585 | 7.886 | 12.143 | 0 | 5.00 | 5.23 | 4.57 |
| | 23 | H | 3,4-di-Cl-Ph | 1.912 | 0.501 | 7.228 | 12.101 | 0 | 5.27 | 5.44 | 3.16 |
| 3 | | $R_1$ | $R_2$ | | | | | | | | |
| | 24 | H | 4-$C_6H_4$-CO-L-glu | 1.912 | -0.586 | 6.479 | 46.621 | 2.875 | 7.40 | 7.39 | -0.12 |
| | 25 | H | 4-Cl-Ph | 2.014 | 0 | 7.583 | 12.133 | 3.180 | 6.59 | 6.46 | -1.94 |
| | 26 | H | 4-$NO_2$-Ph | 1.950 | 0 | 6.472 | 22.950 | 2.981 | 6.96 | 7.20 | 3.38 |
| | 27 | $CH_3$ | 4-$C_6H_4$-CO-L-glu | 2.002 | 0.162 | 6.527 | 46.833 | 2.944 | 7.27 | 7.27 | -0.04 |
| | 28 | $CH_3$ | Ph | 2.107 | 0.912 | 10.114 | 12.215 | 3.322 | 5.25 | 5.25 | 0.07 |
| | 29 | $CH_3$ | 4-Cl-Ph | 2.090 | 0.885 | 7.632 | 12.248 | 3.249 | 6.12 | 6.20 | 1.26 |
| | 30 | $CH_3$ | 4-$NO_2$-Ph | 2.037 | 0.811 | 6.520 | 23.112 | 3.050 | 6.65 | 6.78 | 1.89 |
| | 31 | $CH_3$ | 2,5-di-OMe-Ph | 5.333 | 0.842 | 5.632 | 12.437 | 3.149 | 5.34 | 5.61 | 5.10 |
| | 32 | $CH_3$ | 3,4-di-Cl-Ph | 2.070 | 0.851 | 5.468 | 12.289 | 3.150 | 6.64 | 6.31 | -4.95 |
| | 33 | $CH_3$ | 3,5-di-Cl-Ph | 2.066 | 0.844 | 5.371 | 12.297 | 3.124 | 6.16 | 6.40 | 3.92 |
| | 34 | $CH_3$ | 4-F-Ph | 2.051 | 0.837 | 6.281 | 12.210 | 3.093 | 5.89 | 5.85 | -0.62 |
| | 35 | $CH_3$ | 4-Br-Ph | 2.104 | 0.902 | 8.104 | 12.262 | 3.304 | 6.41 | 6.27 | -2.18 |
| | 36 | $CH_3$ | 3-Cl-Ph | 2.087 | 0.878 | 7.648 | 12.256 | 3.223 | 6.42 | 6.19 | -3.52 |
| | 37 | $CH_3$ | 3,5-di-OMe-Ph | 5.318 | 0.851 | 5.692 | 12.412 | 3.179 | 5.92 | 5.65 | -4.62 |
| | 38 | $CH_3$ | 2-Cl-Ph | 2.081 | 0.868 | 7.652 | 12.267 | 3.180 | 5.96 | 6.19 | 3.78 |

Table 2. The Results of $E_m$ and *pIC50* with Regression of the Best Subset

| Team | Subset of variables | *r* | $r^2$ | *F* | *S* | *FIT* |
|---|---|---|---|---|---|---|
| 1 | $E_{16}$ | 0.722 | 0.521 | 39.133 | 0.467 | 1.004 |
| 2 | $E_{16}$,$E_{31}$ | 0.770 | 0.593 | 25.546 | 0.455 | 1.214 |
| 3 | $E_1$,$E_7$,$E_{16}$ | 0.819 | 0.671 | 23.162 | 0.415 | 1.475 |
| 4 | $E_{16}$,$E_{17}$,$E_{31}$ | 0.826 | 0.682 | 24.344 | 0.408 | 1.551 |
| 5 | $E_1$,$E_7$,$E_{16}$,$E_{31}$ | 0.849 | 0.721 | 21.267 | 0.388 | 1.579 |
| 6 | $E_1$,$E_7$,$E_8$,$E_{16}$ | 0.847 | 0.717 | 20.858 | 0.391 | 1.548 |
| 7 | $E_1$,$E_2$,$E_7$,$E_{16}$,$E_{31}$ | 0.867 | 0.751 | 19.314 | 0.372 | 1.532 |
| 8 | $E_1$,$E_2$,$E_7$,$E_8$,$E_{16}$ | 0.862 | 0.743 | 18.524 | 0.378 | 1.468 |
| 9 | $E_1$,$E_2$,$E_7$,$E_8$,$E_{16}$,$E_{18}$ | 0.871 | 0.759 | 16.290 | 0.372 | 1.319 |

In Table 2, *r* is the correlation coefficient, *F* is the test value of Fischer, *S* is standard error, *FIT* is the function of Kubinyi [18], that the calculation formula is

$$FIT = \frac{r^2 (n - b - 1)}{(n + b^2)(1 - r^2)} \tag{1}$$

In the formula, *n* is the sample size of the compounds, *b* is the number of variables. The bigger is *FIT*, the more stable is the model, and the better is the ability of prediction. When we choose the five variables of $E_1$, $E_2$, $E_7$, $E_{16}$, and $E_{31}$, we can obtain the best results by the data in Table 2.

## Results and Discussion

### Relevance of the Activity to the Inhibition Models

In general multiple regression analysis, there is a requirement that N/M≥5 (N is the number of samples, and M is the number of variables). The structures of molecules of inhibitor of thymidylic acid-based synthetase as five-membered heterocyclic pyrimidine derivatives have 38 samples within 7 of the variable number of desirability. Therefore, the use of MINITAB software is to screen optimal

electrical state indices. The inhibitory activity of the compounds listed in the literature [7] to the human TS was analyzed by regression equation. Between the $E_1$, $E_2$, $E_7$, $E_{16}$, and $E_{31}$ in the electrical state indices and activity have a good correlation. Equation is obtained as follows:

$$pIC_{50} = -0.218\ E_1 - 0.415\ E_2 - 0.0997\ E_7 + 0.0259\ E_{16} + 0.168\ E_{31} + 6.811 \quad (2)$$

$$n = 38,\quad r = 0.867,\quad r^2 = 0.751,\quad S = 0.372,\quad F = 19.314$$

where $n$ is the sample size, $r$ is the correlation coefficient, $S$ is a standard error, $F$ values is for the fischer test.

According to Equation (2), we predicted the inhibitory activity, speculative values and experimental values. The relative average error was 4.80%. Inspection of the model analysis used the software MINITAB by leave-one-out(LOO). Cross-validation correlation coefficient was also obtained. As $R_{cv}^2 = 0.656$. $R_{cv}^2$ was greater than 0.5, and the *FIT* value was also big, which showed a good stability and capability of predictability of the model.

**Mathematical Models of Neural Networks**

In recent years, artificial neural networks in many areas had extensive researches and applications [19-21], based on its excellent nonlinear function approximation ability, which can achieve a high degree of match between the mapping of input and output in line with targets relationships. The merit-based selection of the five parameters $E_1$, $E_2$, $E_7$, $E_{16}$, and $E_{31}$ in the electrical state indices as the input layer BP neural network, and the biological activity *pIC50* as variables of output layer, and number of hidden layer unit in accordance with the proposed rule of *Xu.* et al [22] .

$$2.2 > \rho\ (=\mathrm{N/M}) \geq 1.4 \quad (3)$$

where N, and M are the total number of samples and the total weight of the network respectively. M value is calculated by the following formula

$$\mathrm{M}=(\mathrm{I}+1)\mathrm{H}+(\mathrm{H}+1)\mathrm{Q} \quad (4)$$

In the formula, I, H, and Q are the number of input layer neurons, hidden layer and an output layer respectively. Here we took the hidden layer H=3, the 38 sample data into a training set (n = number 2, 4, and 5 in the data respectively), the test set (n = 1 in the data respectively) and validation set (n = 3 in the data respectively), the correlation coefficient of the models were obtained, in them, $r = 0.980$ of training set, $r = 0.943$ of the test set, $r = 0.981$ of the test set, $r = 0.972$ of the total correlation coefficient. The model is stable. Goodness of fit of the predicted values and experimental values is very ideal, and relative average error is 2.13%, and the relevant data is also included in Table 1. The neural network and multiple regression method were compared, the results showed that prediction model of using neural network method established better forecast ability than multiple regression method.

**Conclusion**

Electrotopological state indices contain the electronic structure of atoms and molecular space structure topological information, so there is a good correlation between the inhibitory activity indexes and inhibitor of thymidylic acid-based synthetase as. Established mathematical model by cross validation has a good robustness and prediction ability. The indexes of $E_1$, $E_2$, $E_7$, $E_{16}$, and $E_{31}$ contained main factors of five-membered heterocyclic pyrimidine derivatives that inhibited the activity of pyrimidine compounds, and mainly reflected contributions of the 5 groups of $-CH_3$, $-CH_2$, -CH=, =O and -S- in the molecules. As can be seen, in the sub due to atomic oxygen (especially containing double bond) or sulfur atomic absorbing ability of electron strongly, and have a big influence on $R_2$ group connected to improve the inhibitory activity of the compounds. When the $R_2$ group is connected in the 4 location, the bigger group, with the stronger inhibitory activity.

Prediction ability of neural network method is superior to multiple regression prediction model. The errors of prediction results obtained by the method are bigger as the molecules of the number of 22, 31, 32, 37. When the 2, 3 or 5 location of the benzene ring is connected with 2

electron-withdrawing groups, the mutual influence of the $R_2$ group and parents' groups were increased, and this would lead to reduced activity, increase the error.

**Acknowledgement**

This work was financially supported by Natural Science Foundation of Jiangsu Province (09KJD150012) and Xuzhou City Green Key Laboratory Project (SYS2012009).

**References**

[1] C.J. Zhang, G.P. Ouyang: Chin. Pharm. 20 (2009)2469-2470 (In Chinese)

[2] K. akoto, A. Emiko, Y. Junko: Brit. J. Oral. Max. Sur. 48 (2010)88-93

[3] F. Stefania, I. Marco, S. Fabrizia: Bio Med. Chem. Lett. 23 (2013)663-668

[4] C. Li, Y. Guo, C. Tian: J. Chin. Pharm. Sci. 22 (2013)173-176

[5] X. Zhang, X. l. Zhou, R. L. Kisliuk: Bio. Med. Chem. 19 (2011)3585-3594

[6] Y.Chen,C. L. Droumaguet, K. Li: J. A. S. Mass. Spec. 21 (2010)403-410

[7] C. M. Kang, X. H. Zhao, X.Y. Wang: Acta. P. Chim. Sin. 29 (2013)431-438(In Chinese)

[8] V. Srivastava, S P Gupta, M I Siddiqi: Euro. J. Med. Chem. 45 (2010)1560-1571

[9] A.A Frid, E. J. Matthews: Regul. Toxi. Pharm. 56 (2010)276-289

[10] J. Liu, X. Guan, J. Q. Peng: Acta. Chim. Sin. 70 (2012)83-91 (In Chinese)

[11] C. Y. W. Nina, V. Raghuraman, M. B. Robert: Reg. Toxic. Pharm. 59(2011)215-226

[12] Y. L. Liu, Y. T.Li, B.Z.Shi: Sci. Sin. Chim. 43 (2013)198-208 (In Chinese)

[13] X. H. Du, Y. Chen, J. R. Wei: J. Wuhan. Uni. 59 (2013)66-70 (In Chinese)

[14] X. H. Du: J. Chem. Ind. Eng. 61 (2010)3059-3066 (In Chinese)

[15] Q. N. Hu, Y. Z. Liang, Y. L.Wang: Comp. App. Chem. 20 (2003)386-390 (In Chinese)

[16] T. Zhang, Y.Z. Liang, C.X. Zhao : Chin. J. Anal. Chem. 34(2006)1607-1610 (In Chinese)

[17] L. H. Hall, L. B.Kier: J. Chem. Inform. Mod. 35 (1995)1039-1045

[18] U. L. Saiz, M. P. Gonzalez, M. Teijeira: Bio. Med. Chem. 15(2007)3565-3571

[19] O. Prakash, F. Khan, R. S. Sangwan: Com. Chem. H. Screen. 16 (2013)57-72

[20] A. J. Wilczyńska, P. Sławomir, F. Jerzy: J. Environ. Sci. Heal. 47 (2012)155-166

[21] C. J. Feng, L. L. Mu, W. H. Yang : Acta. Chim. Sin. 66 (2008)2093-2098 (In Chinese)

[22] L. Xu, X. G. Shao. Methods of Chemometrics, Science Press, Beijing, 2004 (In Chinese)

# CHAPTER 6:

# Mechanical Materials and Engineering

*Advanced Materials Research Vol. 937 (2014) pp 315-317*
*© (2014) Trans Tech Publications, Switzerland*
*doi:10.4028/www.scientific.net/AMR.937.315*

# Study on Fault Rule Prediction of Hydraulic System and its Accessories of Shipborne Aircraft

Ling LI, Chao-yong WANG, Pei-zhong ZHAO, Xu-dong LI, Hong-qiang ZHAO

Faculty of Aviation Machinery Repairing,Qingdao Branch,Naval Aeronautical Engineering Institute,Qingdao 266041,China

**Keywords:** shipborne aircraft hydraulic system and its accessories fault rule prediction

**Abstract:** With the increase of the service time of shipborne aircraft, the overlarge impact load can affect the life of the hydraulic system accessories. At the same time, the vibration and the corrosion of the ser water will also affect negatively the accessories' life. The accessories are the important composition of the hydraulic system. Therefore, it is necessary to study the possible faults and their rules. This paper aims to establish the suitable model to predict the faults by use of the FEM and experiments.

## Introduction

During the launching and arresting of the shipborne aircraft, all the mechanical systems and equipments will bear the longitudinal and vertical over loading. The landing rate of the shipborne aircraft is 215 times of the land-based aircraft's. The vertical kinetic energy which is absorbed by the landing gear is more than 6 times of that of the land-based aircraft's. The overlarge vibration and impact will affect the hydraulic systems of brake system, landing gear system and front wheel swerve system and their accessories. At the same time, the service environment of the shipborne aircraft is harsh. According to the studies, one of the important faults of the shipborne aircraft is induced by the hydraulic system.

Based on the experience of the using of the land based aircraft, 40% faults of the hydraulic and pneumatic equipments is induced by the vibration and impact. Moreover, the effect of the vibration and impact under condition of the over loading is especially serious. At present, the study of the maintenance of the shipborne aircraft is still on starting processing. Therefore, it is necessary and important to study the fault rule of the hydraulic system accessories.

## Predicting Method of the Fault Rule of the Hydraulic System and its Accessories

Generally, there are two hydraulic systems in shipborne aircraft. The hydraulic system works to control the front wheel swerve, main frame wheel brake, landing gear retraction and extension, and so on. Therefore, the hydraulic system is very important for the safety of the shipborne aircraft.

In this paper, the FEM was used to model the vibration and impact load during takeoff and landing. At the same time, corrosion of the sea water was also considered. The fault prediction was performed consequently.

## Calculation of the Over Loading of the Hydraulic System Accessories

The main hydraulic systems, including brake system, landing gear retraction and extension system, front wheel swerve control system, was modeled by using of the commercial FEM code. The vibration and impact under longitudinal and vertical overloading were considered simultaneously. The stress and strain of the accessories were obtained under the different states. The obtained dada were used to predict accessories'life.

## Experimental Confirmation of Bearing Ability of Accessories

The bearing ability of the hydraulic accessories depends on the flight state. That is to say, the over loading, flight rate, environment temperature and the working state of the aeroengine can

affect the accessories. Of all the factors, the most important factors include pressure, pulsation and temperature of the oil in the pipelines. Obviously, the flight state of the shipborne aircraft will affect the performance parameters of the hydraulic system. During the launching and arresting, the pressure and pulsation in the pipeline can increase quickly because of the great vibration and impact. As a result, the accessories can be affected. The performance parameters of the accessories can be tested by the comprehensive test bench.

**Corrosion Effect of the Sea Water**

Beside of the effect of the flight state, the corrosion of the sea water is also an important factor. The shipborne aircraft will suffer negative effect caused by the high-temperature, high-humidity and high-salt content in the marine environment. Therefore, it is necessary to study the accessories' performance in the simulated seawater. According to the corrosion experiment, the related data can be obtained to predict the life of the accessories.

**Prediction of Fault Rule**

The predicting steps are as followings considering the over loading, ability of bearing the pressure and corrosion of the sea water.

**Foundation of the FEM Model**

The FEM model can be founded by use of the commercial code. The main models include the brake system, landing gear retraction and extension system and front wheel swerve system. Based on the FEM calculation, the stress and strain can be obtained.

**Effect of the Flight State on the Performance Parameters of the Hydraulic System**

The flight state can affect not only the pressure and pulsation in the pipeline but also the working properties. According to the flight dada, the fault caused by the pressure fluctuation and vibration can be investigated. The overloading is very great during the takeoff and arresting of the shipborne aircraft. Under these conditions, the brake system, landing gear retraction and extension system and front wheel swerve system and their accessories are affected greatly. Therefore, the two conditions are the important factors which must be considered. Of course, the fault rule can also be found by experimental studies.

**Effect of the Seawater on the Accessories' Performance**

The Simulated seawater corrosion of accessories can be carried out to study the change of the performance. The corrosion effect when the shipborne aircraft is on the deck or in the air should all be studied.

**Calculation of the Fatigue Life of the Accessories**

According to the experimental and FEM calculation results, the main accessories of the brake system, landing gear retraction and extension system and front wheel swerve system can be obtained by local stress and strain method.

**Foundation of the Inspection and Repair Scheme**

Based on the calculation results, the accessories bearing the greatest stress concentration can be found. At the same time, the serious corroded position can be found, too. Based on the results, the key accessories should be paid more attention. The inspection and repair scheme can be founded.

Because of the differences of the shipborne aircraft and land-based aircraft, the faults of the accessories of the hydraulic system are easier to be caused by the marine environment. It is necessary and important to study the fault rule and predict the life of the accessories. According to the results, the key accessories can be found. It will be good to the daily maintenance and periodic inspection.

## Conclusions

The norm work of the hydraulic system and its accessories is very important for the safety of the shipborne aircraft. The complex service environment of the shipborne aircraft leads to the complexity of the fault rule of the accessories. The FEM calculation and related experimental studies are very important to help the prediction of the fault and life. Based on the studies, the reasonable inspection and repair scheme can be founded scientifically.

## References

[1] Wang Wenliang Chen Ming .Thought on Establishment and Characteriscs of Deck-landing Aircraft Support System. [J] TRAINER AVIC 2012.NO.1 (60-63)

[2]Feng Qing.Ceng Shengkui.Kang Rui.Multiagent-based modeling for integrated logistic support of the carrier aircrsft. [J] System Engineering and Electronics.Jan.2010 (212-215). (in Chinese)

[3]LiLing. Zhao Hongqiang.Wang Guohua. Frequently Problem and Replace About Typical Attanchment Seal Ring of A Certain of aircraft. [J] Hydraulics Pneumatics & Sesls2013,06(6):78-80. (in Chinese)

[4]Tan Xu.Song Zhenyu.Xu Peng.Fei Chen.Analysis of Carrier-based Helicoper's Flight Material Maintenance Modle. [J] Value Engineering 2012.03 (113). (in Chinese)

[5]ZhangHui.Review of research on ship integrated logistics support. [J]Ship Science and Yhchnology.Sep,2010, (128-132). (in Chinese)

*Advanced Materials Research Vol. 937 (2014) pp 318-323*
*© (2014) Trans Tech Publications, Switzerland*
*doi:10.4028/www.scientific.net/AMR.937.318*

# Analysis of Welding Residual Stress on Cracked Vessels with X-ray Diffraction Method

Jun-ming ZHOU[A], Yi-liang ZHANG[B]

(College of Mechanical Engineering and Applied Electronics Technology ,Beijing University of Technology , Beijing 100124,China)

[a]zhoujunming@emails.bjut.edu.cn, [b]zhangyil@bjut.edu.cn

**Key words:**welding residual stress,X-ray diffraction,heat affected zone

**Abstract**:A large number of cracks are found in the 1500m$^3$ Liquefied Light hydrocarbons vessel during the inspection after two years of running．In totally，six vessels being fully heated treated is made of 15MnNbR. Researchers used X-ray stress analyzer measured the welding residual stress of vessels that have been cracked and uncracked. The results show that, residual stress of uncracked spherical vessels are in good condition, while those value of cracked is high, the value of the highest is 1.05σs. It indicates that the possible reason for the separation is the residual stress in the high state. Through welding and heat treated for the second time, the welding residual stress decreased obviously. It indicates the impact of this measure is good.

## Introduction

A petrochemical company put into use six light hydrocarbon vessels which are made of 15MnNbR in 2009. This six vessels are undertaken separately by the two companies . In the routine examination, the three vessels of a company are found of a large number of cracks in the final assembly weld. And the cracks appear in the weld and the heat affected zone (fig 1). While the three vessels of another company did not appear such a situation. Based on residual stress measurements of the vessels inner by X-ray diffraction, author analyze the reasons of this simulation.



Fig. 1. Liquefied Light hydrocarbons



Fig. 2. Test site

The scholars at home and abroad did a lot to study the X-ray measurement of residual stresses. Residual stress is one of key factors that affect safe operation of pressure vessels and pipes, the measurement of which has become an important means for effective safety evaluation. In 2010,Torigoe Masaki studied the welding residual stress effects for high- strength steel[1]. The Beijing University of technology has done a lot of work to research the measurement by X-ray diffraction. And use this method to analyze the failure. With the advance of this method, it has found wider applications in engineering field. What is more, it not only is used in the lab, but also is used in the project[2].

In this paper, the residual stress is measured by X-ray diffraction. There is a cracked vessel A and an uncracked one B measured the welding residual stress. Then after repairing A(weld and heat treated ), the measurement for A is taken for the second time. The result indicated that the value of residual stress of weld I in vessel A larger than those of weld II in vessel B, but the welding residual stress in weld I of vessel A clearly decreased after repaired.

## Residual Stress Measurements

These are the main Parameter of vessels. Media: Light hydrocarbons. Material: 15MnNbR. Diameter: 14200mm. Volume: 1500$m^3$. Yield strength: 370MPa.

## X-ray Diffraction and Testing Equipment

The diffraction of X-ray is based on bragg's law deducted from crystal diffraction. The test principle of the device of $2\theta \sim \sin^2\Psi$ conforming to GB7704－2008[3]. There is a linear relationship between $2\theta$ and $\sin^2\Psi$ , and the slope of line can be calculated if more than three points are determined. Based on this point the device finally calculates and exports the stress $\sigma_x$ by measuring four different $\theta_{\Psi x}$.

In the examined regions coating on the vessels should be removed and measured points should be polished before residual stress is measured. All points are 8mm in diameter and about 0.1mm in polishing depth. the aim to polish is to eliminate surface processing stress.The points are measured by PSF-2M X-ray stress gauge(Rigaku) improved in 2008 after polishing.

The main parameters of the instrument are: α-Fe as the crystal sample, α-Fe (211) as the measured crystal face,0.4° step of $2\theta$ varying from 150° to 162°, 0.8s scanning time at per angle and 10,000 maximum count.

## Measured Points Placement

Stress of vessels include work stress, weight, welding residual stresses and other external stress. Mainly,the cracks appeared around the weld. In order to reflect the stress of vessels accurately, positions with higher stresses are given more attention. Measured points are in the Weld and heated affected zone. Test site as fig.2.

Stresses were measured in two different directions:.vertical and parallel to the weld. And the placement of measured points is shown in fig. 3.

## Results

For vessel A and B, stresses were measured with two directions, direction X is parallel to the weld ,direction Y is vertical to the weld. In total,there is 36 points are measured. The relationship of all points and test value of vessel A is shown in table 1 and table 3, The relationship of all points and test value of vessel B is shown in table 2.

## Analysis and Discussion

For each vessel,three regions are considered: they are base metal zone,weld zone and weld heat affected zone.

## Stress characteristics in Vessel A

Table.1 shows that the residual stresses in weld zone and in heat affected zone are in high level of vessel A. While the residual stresses are small in the zone which are away from the weld(point 6, 7, 8and9). The maximum stress occur in uncracked weld in the vertical direction,which is 393 MPa($1.06\sigma_s$). The minimax stress is 130MPa.

To contrast to the cracks, the residual stresses are in high level. Obviously, The stress of crackers are released.

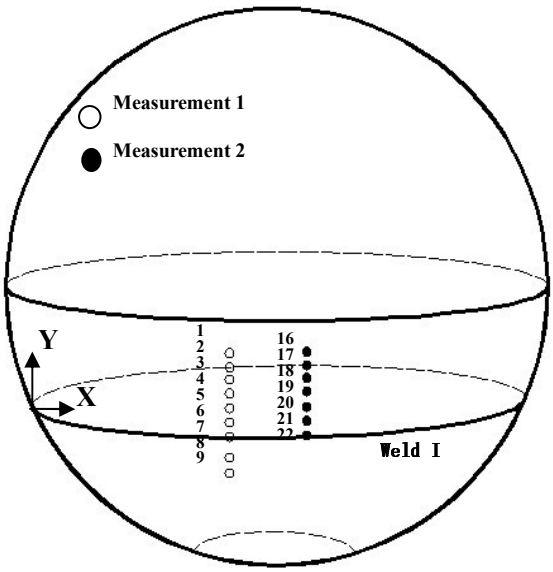



Fig 3a. placement of vessel A

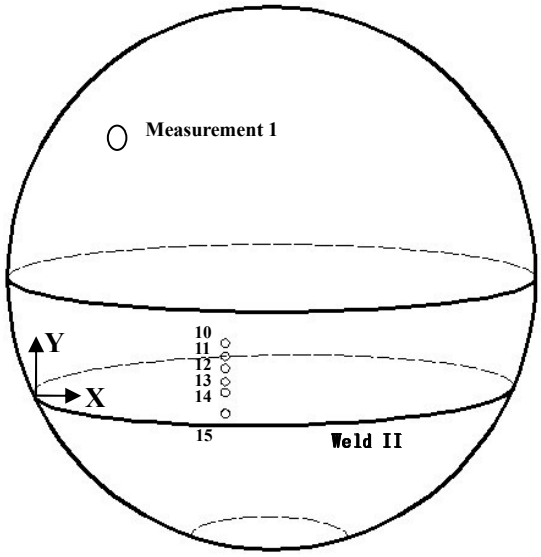



Fig 3b. placement of vessel A

Fig. 3. Measured points placement of vessels

Table 1. Result of measurement 1 of vessel A

| Measurements zone | number | Distance of weld centerline/mm | $\sigma_y$ /MPa |
|---|---|---|---|
| Weld I | 1 | -25 | 205 |
| | 2 | 0 | 393 |
| | 3 | 25 | 268 |
| | 4 | 35 | 218 |
| | 5 | 50 | 216 |
| | 6 | 65 | 135 |
| | 7 | 85 | 149 |
| | 8 | 120 | 176 |
| | 9 | 250 | 130 |

Table 2. Result of measurement 1 of vessel B

| Measurements zone | number | Distance of weld centerline/mm | $\sigma_y$ /MPa | $\sigma_x$ /MPa |
|---|---|---|---|---|
| Weld II | 10 | -25 | 150 | 175 |
| | 11 | 0 | 165 | 138 |
| | 12 | 25 | 208 | 174 |
| | 13 | 40 | 112 | 159 |
| | 14 | 50 | 100 | 170 |
| | 15 | 240 | 168 | 173 |

Table 3. Result of measurement 2 of vessel A

| Measurements zone | number | Distance of weld centerline/mm | $\sigma_y$ /MPa | $\sigma_x$ /MPa |
|---|---|---|---|---|
| Weld I | 16 | -25 | 85 | 130 |
| | 17 | 0 | 100 | 173 |
| | 18 | 25 | 112 | 141 |
| | 19 | 40 | 70 | 147 |
| | 20 | 65 | 77 | 139 |
| | 21 | 85 | 152 | 208 |
| | 22 | 100 | 165 | 172 |

**Stress Characteristics for in Vessel B**

Table.2 shows the result of measurement of vessel B. It indicated that the residual stress of vessel B in a good condition,which is from 100 to 200 MPa. Vessel B is stand for the three uncracked vessels which work well. The maximum stress occur in heat affact zone in the vertical direction,which is 208 MPa. The minimax stress is 70MPa.

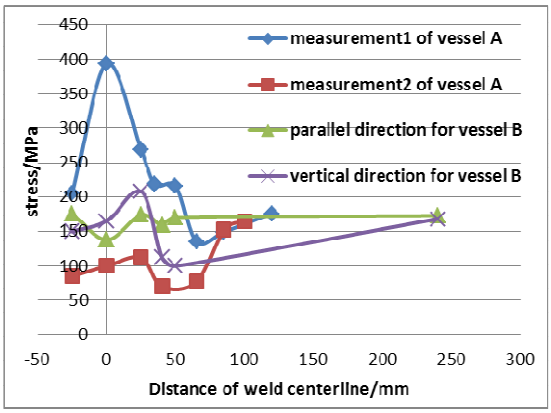



Fig. 4. Comparison of residual stress of two vessels

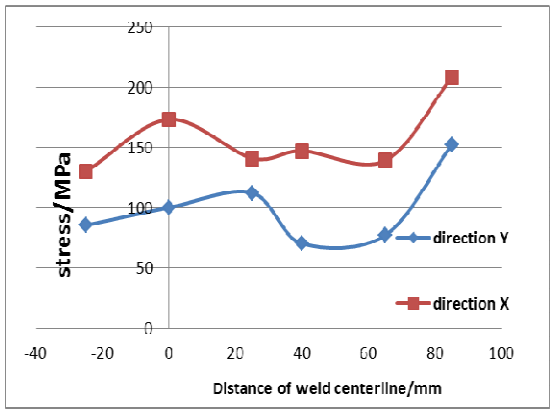



Fig. 5. Vessel A(repaired) stress distribution

**Stress Characteristics in Vessel A after Repaired**

Table.3 shows that the stress in the weld zone and heat affected zone are smaller than the base zone. In total, the stress in X direction are higher than the stress in Y direction,The phenomenon is showed in fig.5. The stress in vertical direction is the first principal stress, this result comply with the law of conventional welding stress distribution[5].The maximum stress appear in uncracked weld in the vertical direction,which is 208MPa. The minimax stress is 70MPa.

**Comparison of Residual Stress of Two Vessels**

Before Vessel A was heat treatment ,the residual stress comparison of Vessel A and Vessel B is shown in fig.4. Fig.4 shows that the residual stress in weld zone of Vessel A higher than that of Vessel B. While the stress of the base zone are in the same state. It is indicated that the possible reason for the separation is the residual stress in the high state. In another word, first heat treatment was failure for the Vessel A.

After vessel A was be heat treatment ,the residual stress comparison of Vessel A and Vessel B is shown in fig.4. The stress of vessel A is smaller than that of in vessel B. The maximum stress is just $0.56\sigma_s$. So we think this phenomenon reveal that Vessel A work in good condition after repaired.

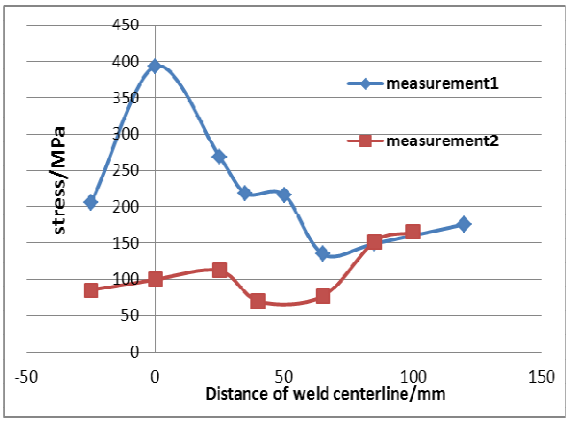



Fig. 6. Comparison of two measurement in vessel A

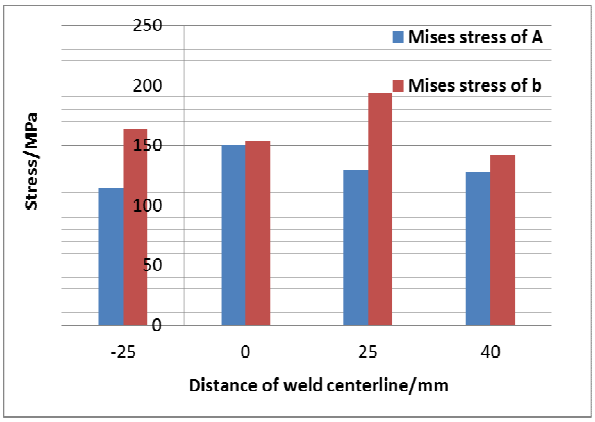



Fig. 7. Mises stress of two vessels

## Comparison of two Measurement in Vessel A

According to GB150-2011, the Temperature of heat treatment is 560±20℃. The company used electric heating treatment in 540℃. Due to test the accuracy of National Standards in engineering, take the results of two measurements to comparison(see fig.6).

Fig.6 shows that the stress of base zone are in the same state for the two measurements. After repaired, the stress of weld zone and heat affected zone decreased apparent. The maximum stress decreased from 392MPa($1.06\sigma_s$)to 200MPa($0.54\sigma_s$). It reveals that the effect of the heat treatment is good and achieve their goal.

## Theoretical Analysis

Mises equivalent stress consider the results of tensile and compression and fully reflect the state of stress,as 1.

According to the law of weld residual stress: parallel to the weld is $\sigma_1$ , vertical to the weld is $\sigma_2$, $\sigma_3$=0. The Mises stress is:

$$\sigma_{r4}=\frac{1}{\sqrt{2}}\sqrt{(\sigma_1-\sigma_2)^2+(\sigma_2-\sigma_3)^2+(\sigma_3-\sigma_1)^2}=\frac{1}{\sqrt{2}}\sqrt{(\sigma_1-\sigma_2)^2+\sigma_2^2+\sigma_1^2} \quad (1)$$

Particularly, compare the mises stress of Vessel A(repaird) to Vessel B, as fig.7. The result was found that the stress of vessel A is little smaller than that of vessel B. It indicate that vessel A work well after repaired.

## Conclusions

1. It is apparent from the analysis, the quality of vessel B is higher than vessel A.
2. The residual stress of Vessel B is in a good condition, the maximum stress is just $0.56\sigma_s$. It indicate that the effect of the heat treatment for B is good.
3. The maximum stress of vessel A is $1.05\sigma_s$. It indicate that the reason for it is effect of first heat treatment is bad. But after repaired for Vessel A, the maximum stress decreased to $0.54\sigma_s$. It reveal that the second heat treatment is good.

**References**

[1] Torigoe Masaki,Yamashita, Yoichi, Yamada, Takehisa. Effect of welding residual stress and plastic constraint on brittle fracture of a high strength steel. Proceedings of the ASME Pressure Vessels and Piping Conference 2009, part B, 1321-1329.

[2]Zhang Zhuwu, Yao Qin, Wu Aiping, Gong Liangzhu. Surface treatment effect on measurement of welding residual stress using X-ray stress analyzer, Materials Engineering for Advanced Technologies,2013,617-621.

[3]GB7704-2008,Non-DestructiveTesting-Practice for Residual Stress Measurement by X-ray[s].

[4] ZhangYL,XuXD,SunYF,ZhangYJ.Stress analysis of a large spherical vessel with X-ray diffractometer and strain gauge measurements.Proceedings of SPIE—The Society of Photo-optical Instrumentation Engineers 2002b;4537:198–201.

[5] Ruibin Gou, Yiliang Zhang, Xuedong Xu, Liang Sun, Yong Yang. Residual stress measurement of new and in-service X70 pipelines by X-ray diffraction method. NDT&E International ,44( 2011),387–393.

*Advanced Materials Research Vol. 937 (2014) pp 324-329*
*© (2014) Trans Tech Publications, Switzerland*
*doi:10.4028/www.scientific.net/AMR.937.324*

# Energy Consumption Performance Study of New S-shaped Hysteretic Damper

Chao XU [1, a], Yong-feng NIU [1,b] and Yong-xie ZHAO [1,c]

[1]School of Civil Engineering,Jilin Jianzhu University,Changchun,China

[a]tianya880217@126.com, [b] yongxiezhao@163.com, [c]1140416324@qq.com.

*Corresponding author: Yongfeng Niu, tianya880217@126.com

**Keywords:** S-shape low yield steel damper; analytical model;ABAQUS; hysteretic loop

**Abstract:** This paper supposes a S-shape low yield steel damper. Based on the mechanical behaviors of the damper, its analytical model is established. Meanwhile, the damper's hysteretic characteristics are numerically simulated by the FEM ABAQUS to obtain the main mechanical parameters of this damper. These parameters are compared with the results from the established analytical model. Results indicate that the analytical model is a-greeable to the FEM analysis. In addition, Analytical results also show that the S-shape low yield damper pos-sesses superior mechanical behaviors and hysteretic characteristics to fit extremely for mitigating the vibrationof engineering structures.

## Introduction

Earthquake disaster since ancient severely threat to human's survival and development. For example the Tangshan earthquake in 1976, and after 32 years later, the Wenchuan earthquake in 2008, even the Yushu earthquake in 2010, has caused serious personal and property losses. With the improvement of science and technology and people's living standard, the ability of prevent earthquake disasters has been improved, the structure of the damping control technology has get more and more researchers' attention both at home and abroad due to its characteristic of economy applicable energy consumption, simple structure, convenient maintenance, and the better damping effect. so the technology has become an effective method to dissipate earthquake energy.

The method of Earthquake energy dissipation and vibration is controlling the structure expected deformation by setting energy dissipation devices, so that the structure of subject does not occur serious damage under the severe earthquake, in which , the mild steel damper as a reasonable energy dissipater because of its low yield point, the higher flexibility and ductility, the better deformation tracking ability, the lesser effect on its performance by environment and the temperature, and it can absorb a lot of energy in the elastic-plastic deformation process, also low steel cost etc., has on the agenda gradually.

## Mechanical Model of Mild Steel Damper

### Sngle Degree of Freedom System Equivalent Curve

Based on full hysteresis curve in shape of fusiform and smooth , the curve is recommended fitting as a line model , the model fitting curve should be based on the following two principles:

1) Area within the range of concerns, surrounded by broken line and the horizontal axis are equal to the original ones

2) The "strength" of the elastic phase intersection of a line and the original model curve is equal to 60% of the" yield strength ". The principle of equivalence is shown in Fig. 1.

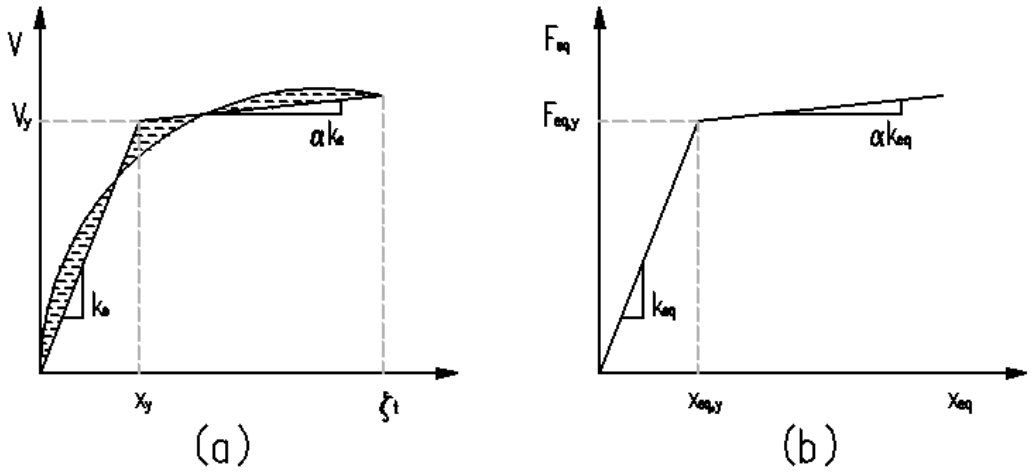



Fig. 1. Sngle degree of freedom system equivalent curve
(a prototype system (b) the equivalent system

**Bilinear Model Analysis**

In this paper, mild steel damper mechanical model used for the bilinear model , In Fig.2. Pmax is the maximum shear force , Py is the yield strength , d is the displacement ;

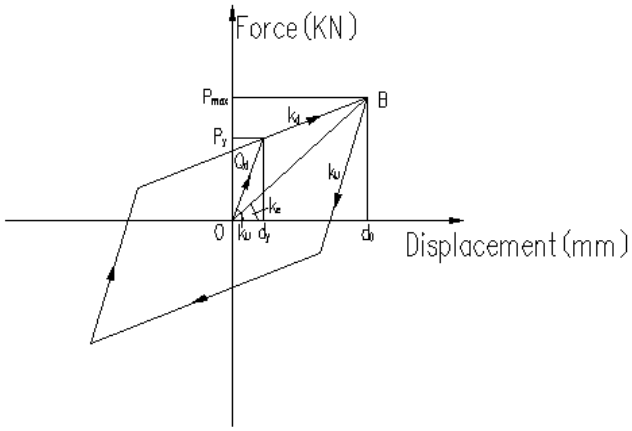



Fig. 2. Bilinear model

In the figure, the connection of origin and the peak point of hysteresis curve is defined as the effective stiffness $k_e$ ,

$$k_e = k_d + \frac{Q_d}{d_0} \qquad (d_0 \geq d_y)$$

$d_y$ is yield displacement,

$$d_y = \frac{Q_d}{k_u - k_d}$$

$$K = \frac{P_{\max} - P_y}{d_0 - d_y}$$

Yield stiffness

Hysteretic damping energy ( area under the curve of hysteresis )

$$W_d = 4Q_d(d_0 - d_y)$$

Damping ratio can be approximated as a single- particle system equivalent damping ratio , calculated by establishing the principle of energy and the use of equations of motion :

$$\zeta = \frac{W_d}{2\pi k d^2}$$

K- effective stiffness , d- horizontal displacement

**The New S mild Steel Damper Finite Element Analysis**

**S -type Soft steel Damper Design**

The mild steel damper is made from steel Q235, material constitutive relation uses ideal elastic-plastic material model , the relevant parameters in Table 1.In the Table 1, $f_y$ is yield stress, $f_b$ is ultimate strength, E is modulus of elasticity, $\varepsilon_y$ is yield strain and $\varepsilon_u$ is ultimate strain.The dampers are connected to the main frame by a foothold in the shape of "人", which is shown in Fig.3. Since the two flanges of S -type damper in the same size and opposite force to the simplified model shown in Fig.4, h is the flange thickness , B is the flange width. This article will be finite element simulation by controlling the width and thickness of the flange size to observing the effect of the results to the S -type dampers energy performance, parameters listed in Table 2

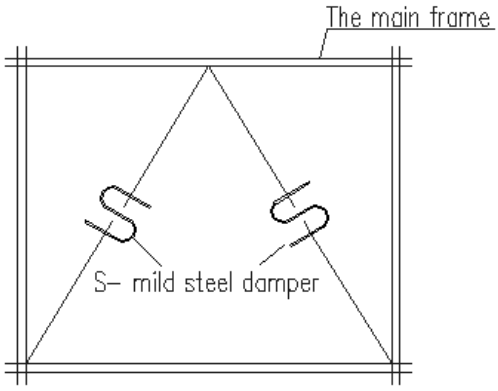



Fig. 3. S- mild steel damper connection

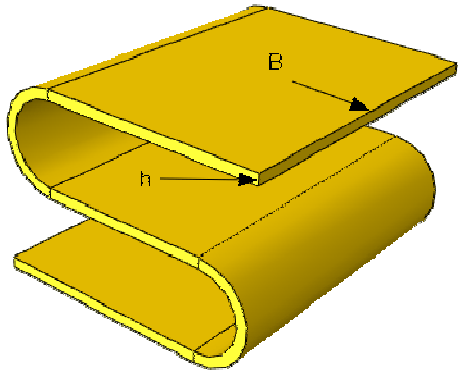



Fig. 4. S- mild steel damper

Table 1. Relevant performance parameters of Q235 steel

| $f_{y(\mathrm{N/mm^2})}$ | $f_{b(\mathrm{N/mm^2})}$ | $E(\mathrm{N/mm^2})$ | $\varepsilon_y$ | $\varepsilon_u$ |
|---|---|---|---|---|
| $235\times10^6$ | $370\times10^6$ | $210\times10^9$ | $1.119\times10^{-3}$ | $4.669\times10^{-3}$ |

Table 2. Design parameters of S damper

| *Specimen No.* | *SMH 1* | *SMH 2* | *SMH 3* | *SMH 4* | *SMK 1* | *SMK 2* | *SMK 3* |
|---|---|---|---|---|---|---|---|
| H(mm) | 16 | 20 | 25 | 30 | 20 | 20 | 20 |
| B(mm) | 300 | 300 | 300 | 300 | 180 | 220 | 250 |

**Loading Model**

The model test loading model used displacement control loading method, often controlling load though Yield displacement or a percentage of the maximum the maximum displacement between layers. Displacement control loading method can be divided into three types according to the

different Load amplitude: variable amplitude loading , amplitude loading and mixing amplitude loading.This article select variable amplitude displacement loading mode, appling horizontal displacement load on the coupling point. For the Fig.1:

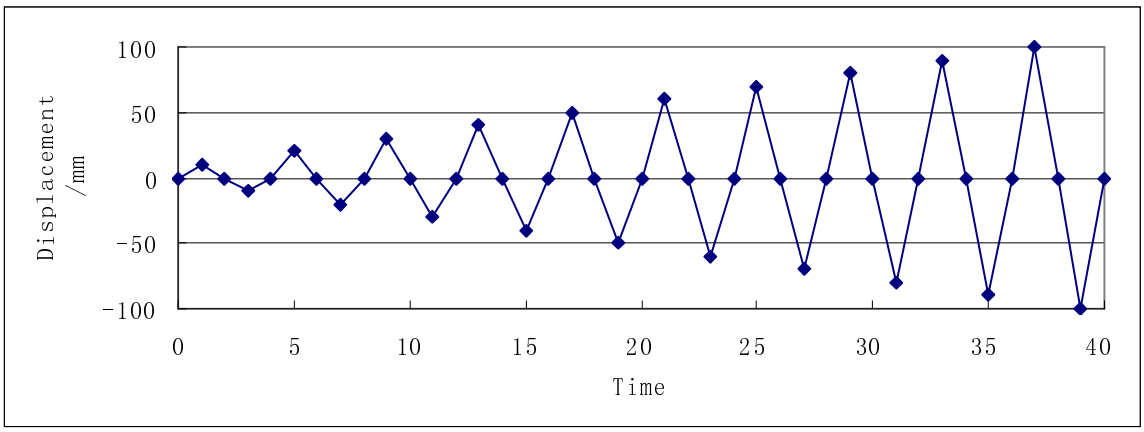



Fig. 5. Displacement control loading method

**S- mild Steel Damper ABAQUS Analysis**

(1)The effect of flange thickness to energy performance of dampers. What is showed in Fig.6 is the specimen SMh1 ~ SMh4 comparison of hysteresis curves which flange in the same width , are 300mm, different thickness. From the hysteresis loops we can see, yield displacement of the four members are 4.56mm, the yield strength and the initial stiffness of SMh4 were greater than the other three members, but also greater yield stiffness. Showed that the same limb wide , the smaller high limb the more energy damper absorbs, the better energy performance. Numerical results are shown in Table 3.

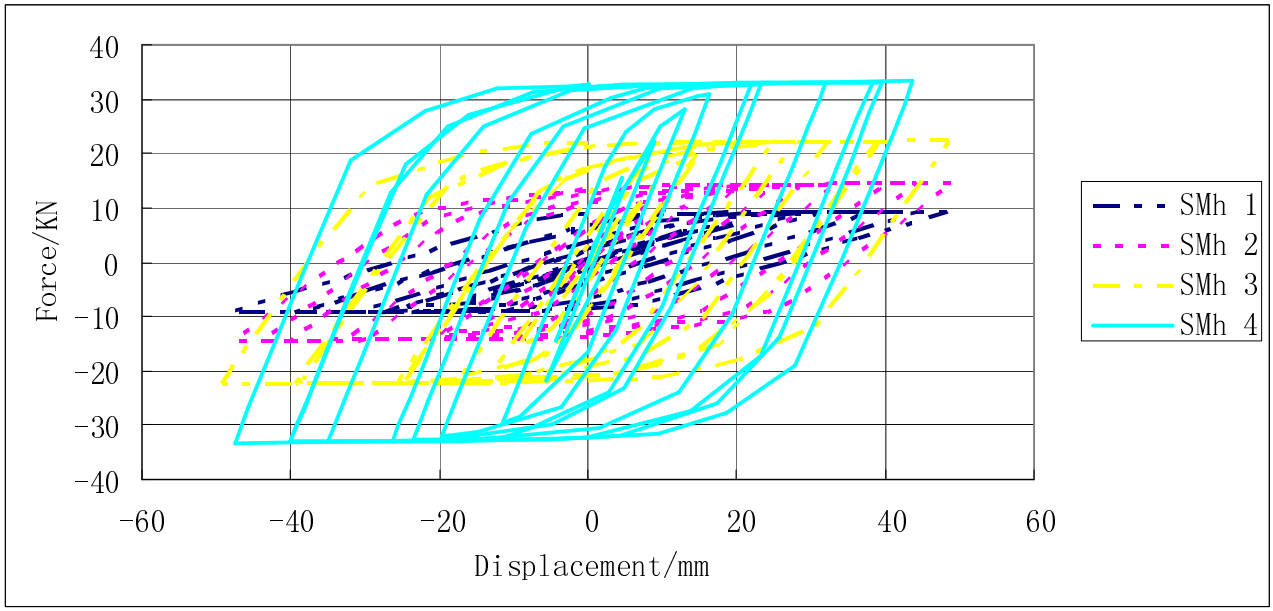



Fig. 6. Hysteretic curves of the SMh specimens with different flange thickness

Table 3. Numerical analysis result of SMh specimens in different flange thickness

| Specimen No. | SMh1 | SMh2 | SMh3 | SMh4 |
|---|---|---|---|---|
| Yield force/KN | 1.92 | 4.56 | 8.83 | 15.54 |
| Initial stiffness $/10^3$ MP | 0.42 | 1.00 | 1.94 | 3.41 |
| Post-yield stiffness $/10^3$ MP | 0.038 | 0.085 | 0.11 | 0.19 |
| Equivalent damping ratio | 0.22 | 0.327 | 0.389 | 0.407 |

(2)The effect of flange width to energy performance of dampers. Compare the finite element analysis results between SMK 1, SMK 2, SMK 3 and SMH 2 which are the same flange thickness, are 20mm,and l flange width are 180mm,220mm,250mm,300mm from the Table 2. In the hysteretic curves, yield displacement of the four members are 4.56mm , in the case of flange thickness are the same 20mm, the yield strength and initial stiffness of each specimen increases with the increase of flange width; The larger the width of the flange , the greater the post-yield stiffness. And all the specimens appear the phenomenon of stress intensification, the greater flange width the more obvious stress intensification; Hysteresis curves in the plump shape of fusiform, have a good hysteretic behavior. Numerical results are shown in Table 4.

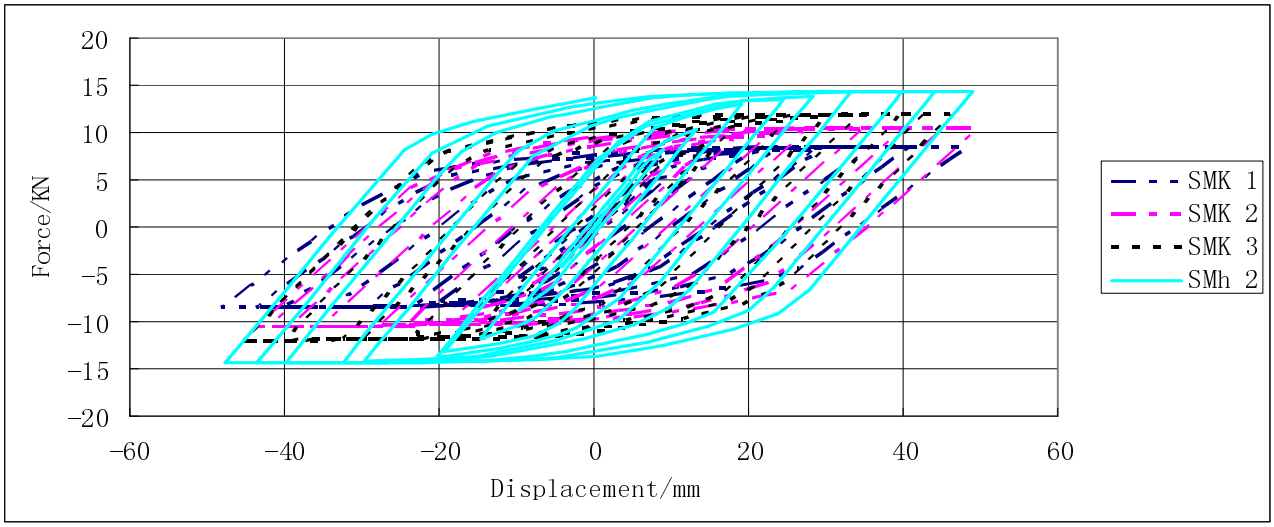



Fig. 7. Hysteretic curves of the SMK specimens with different flange width

Table 4. Numerical analysis result of SMK specimens in different flange width

| Specimen No. | SMk1 | SMk2 | SMk3 | SMh2 |
|---|---|---|---|---|
| Yield force/KN | 2.74 | 3.18 | 3.82 | 4.56 |
| Initial stiffness $/10^3$ MP | 0.61 | 0.70 | 0.84 | 1.00 |
| Post-yield stiffness $/10^3$ MP | 0.041 | 0.068 | 0.076 | 0.085 |
| Equivalent damping ratio | 0.240 | 0.290 | 0.302 | 0.327 |

## Conclusion

By analysing the new S-shaped steel damper with different size, the following conclusions:

(1)The new S-shaped steel damper has small yield displacement, good hysteretic behavior ,energy curves and full, and good energy performance.

(2) Compare with different S-shaped steel damper and the bilinear model, the two calculation results obtained by the damper is more consistent, The results show that the design of S -type mild steel damper reasonable force , stagnation loopback full, strong energy dissipation capacity .

**References**

[1]ZHOU Yun. JINSHU HAONENG JIANZHEN JIEGOU SHEJI[M]WU Han: Wuhan University of Technology Press, 2006: 1(In Chinese).

[2]ZHANG Wenyuan, LI Shuying，LI Dongwei. Simulation analysis on hysteretic behavior and vibration suppression of them ild steel damper with the diamond-shaped opening and added damping and stiffness[J]. World Earthquake Engineering, 2007.3(In Chinese).

[3]ZHANG Wenyuan, ZHANG Minzheng, LI Dongwei. An experimental research on performance and application of a new type ofm ild steel damper added damping and stiffness (ADAS) [J]. Journal of Harbin Institute of Technology. 2008(In Chinese).

[4]LI Jilong, OU Jinping, Damping force hysteresis loop models for X type and triangle mild steel dampers(I)- Based on double linear constitutive model. World Information On Earthquake Engineering, 2004,20(1):10-15(In Chinese).

[5]WANG Shuang. Parametic analysis and seismic performance of new Perforated H-shaped steel damper. Guangzhou university, 2012.5(In Chinese).

[6]ZHANG Pingping,ZUO Xiaobao. Design and Mechanical Investigation on a U-shape Low Yield Steel Damper[J]. Jiangsu Building. 2012,1:47-49(In Chinese).

[7]LIU Maoshe,LU Junlong. Analysis of Shear Stiffness of the Thin U-Shape Metal Damper[J]. Journal of Xi'an University of Technology, 2013,29(2):207-210(In Chinese).

*Advanced Materials Research Vol. 937 (2014) pp 330-335*
*© (2014) Trans Tech Publications, Switzerland*
*doi:10.4028/www.scientific.net/AMR.937.330*

# Adhesive Mechanism and Experimental Study on Shear Adhesive Strength of Impact Ice

Rui-Rui WU[1,a*], Chun-Ling ZHU[2,b], Cheng-Xiang ZHU[3,c] and Bo MIAO[4,d]

[1,2,3,4]College of Aerospace Engineering, Nanjing University of Aeronautics & Astronautics, Nanjing, 210016, China

[a]gegewu1204@gmail.com, [b]clzhu@nuaa.edu.cn, [c]cxzhu@nuaa.edu.cn, [d]bobo010920137@163.com

**Keywords:** Aircraft de-icing, Impact ice, Experimental platform, Adhesive shear strength.

**Abstract:** Aiming at the need of aircraft de-icing system design, a study of the adhesive mechanism between impact ice and substrate has been made. Based on the discussion of electrostatic force and van der Waals force which contribute to ice adhesion, the related factors are listed. A systematic study has been made of the distribution of shear adhesive strength of impact ice as a function of the roughness and material of substrates, the ambient temperature and the mean volume diameter of supercooled droplets through experimental research. The experimental results has been compared with foreign research and error analysis has been given.

## Introduction

The formation of ice on engines and airfoils of fixed wing aircraft and helicopter blades can seriously degrade the safety of an aircraft. The ice referred to is called impact ice, and its accumulation is generally because of super-cooled water droplets hitting on surface of aircrafts and freezing rapidly. Therefore, aircrafts are usually equipped with anti-icing and de-icing system in possible icing positions. Typical ice conditions were varied to form an ice cap of clear glaze ice, mixed glaze and rime ice and white rime ice, and aircraft deicing systems must be able to clearly shed ice which varies significantly in mechanical properties.

The mechanical properties of impact ice have been studied by different researchers such as R.J. Scavuzzo and M.L. Chu from The University of Akron, Ohio, J. Druez and C.L.Phan from Canada and so on. In their work, the tensile strength, shear strength, elasticity modulus E and adhesive strength of impact ice have been studied. Researchers in China have been doing researches concentrates on the mechanical properties of natural freezing ice, but data of impact ice can't be found. Considering the significant differences of forming condition between impact ice and natural freezing ice, the study on mechanical properties of impact ice is necessarily needed.

## Ice Adhesive Mechanism

Ryzhkin (1997) summarized the mechanisms of ice adhesion and divided into three groups: 1) the covalent bonding mechanism, 2) the dispersion or fluctuation in electromagnetic interaction (Van der Waals forces), and 3) the direct electrostatic interaction. In the following we'll give the ice adhesive mechanism analysis based on electrostatic interaction and Van der Waals force.

On ice/metal and ice/dielectric interfaces, one important reason for building up of surface charge is an electrostatic attraction, known as an image force, of mobile ions and Bjerrum defects to the interface, if the solid in contact with ice has an effective dielectric constant $\epsilon$ larger than that for ice $\epsilon_\infty$. Such an image force F can be expressed as a function of the distance to the interface z:

$$F = -\frac{q^2}{16\pi\epsilon_0\epsilon z^2}\frac{\epsilon_\infty-\epsilon}{\epsilon_\infty+\epsilon}. \quad (1)$$

where $q$ is the quantity of electric charge, $\epsilon_0$ is the permittivity of vacuum.

It can be seen in this equation that when the distance to the interface z is constant, F will be increasing as the effective dielectric constant $\epsilon$ of the substrate grows.

It has been found in recent researches that a fluid layer exists at the interface between ice and its vapor at temperatures near the triple point, although it is not clear whether or not the film thickness saturates as the melting temperature is approached. A recent experiment using x-ray scattering provides evidence that a disordered layer persists at the ice surface down to temperatures as low as -12°C. Accordingly, taking the effect of water film into account when calculating is very necessary. The van der Waals contribution to the free energy of a surface consisting of a liquid layer of thickness L between bulk ice and a substrate can be obtained from the theory of Dzyaloshinskii, Lifshitz, and Pitaevskii. The result of this theory is an expression for the interfacial free energy per unit area in terms of the frequency-dependent dielectric polarizabilities of the three media: ice (i), water(w), and substrate (s).

$$\gamma_{is}(L) = \gamma_{iw} + \gamma_{ws} + F(L) \tag{2}$$

where $\gamma_{iw}$ and $\gamma_{ws}$ are the interfacial free energies per unit area of the ice-water and water-substrate interfaces, and F (L) can be expressed as following:

$$F(L) \approx \frac{KT}{8\pi L^2} \sum_{n=0}^{\infty}{}' \left(\frac{\varepsilon_i - \varepsilon_w}{\varepsilon_i + \varepsilon_w}\right)\left(\frac{\varepsilon_w - \varepsilon_s}{\varepsilon_w + \varepsilon_s}\right)(1 + r_n)e^{-r_n} \tag{3}$$

where T is the interface temperature, $\varepsilon_i$, $\varepsilon_w$ and $\varepsilon_s$ are the dielectric polarizabilities of ice, water and substrate. $r_n$ is the lower limit of integration, which is an increasing function of L.

Since the interactions decay with distance, F(L) →0 for L → ∞. The ice-substrate interfacial free energy $\gamma_{is}(L)$ is given by the minimum, and ice is completely melting at this time. However, since L is a limited number in actual situation, an incomplete interfacial melting is indicated by a minimum at finite L, with F(L) negative there. If $\varepsilon_w - \varepsilon_s < 0$, then F(L) would be a monotonically decreasing function and the film thickness would diverge as the melting temperature is approached. And the bigger $\varepsilon_s$ is, the bigger F(L) is, the harder for ice to melt.

## Experimental Apparatus and Procedure

### Refrigeration System and Cold Room

Ice accretion was produced in a 304mm×383mm×316mm cold room made of Polyurethane, in which the measurement of ice shear adhesive strength was also conducted. In order to control the ambient temperature, six groups of temperature sensor were placed in the cold room, which located in the top and bottom of the box and around the test piece. The temperature sensor used in this paper was platinum resistance temperature sensor. Using liquid nitrogen refrigeration mode, temperature control range was -5°C to -23°C(±2°C) during the process of experiments.

### Substrate Material and Roughness

The substrate material tested in most of the experiments were aluminum cylinders of 1cm diameter and 80cm length. Choose different types of waterproof abrasive paper and iron sand paper to manually polish substrate rods, and during the polish, roughness meter were used to determine and fix its roughness. Values of $R_z$ for the substrate rods used in these experiments varies from 1μm to 10μm. Except for aluminum, 304 stainless steel and polymer material were also used for comparison experiments.

### Mean Volume Diameter of Water Droplets

Super-cooled droplets were produced by micro fog two-fluid fan nozzle. The nozzle has two imports, gas and water, and after pressurized gas and liquid water entering the nozzle pipe, have them mixed evenly and scattered into the cold room. By adjusting the pressure value of import gas and liquid, the control of the mean volume diameter of water droplets (MVD) could be realized. In this study, MVD varies from 10μm to 40μm.

**Ice Accretion on the Substrate**

The substrate rods being tested were carefully cleaned with water, then further cleaned with alcohol and dried before it was placed in the working section. During ice accumulation, the substrate rod was being rotated slowly at 1~1.5 rpm. Ice was accumulated on the substrate until an ice accretion of 3±0.5mm thickness was reached. The average time needed was about 8 minutes. In order to make force measurements accurate, the ice accretion may be cut with an iron blade to make its bearing surface neat.

**Shear Adhesion Strength Measurement**

After ice accumulation completed, mechanical test was conducted. As shown in Fig.1, the experimental rod was driven to the sleeve, after the sleeve contact with ice, it would extrude ice on the substrate rod and make it fall off. In this process, changing of this extrusion force was recorded by computer. According to Newton's third law, the applied load F value is equal to the shear adhesion force between ice and basal experimental rods. Read off the maximum instantaneous value of measured force, namely the shear adhesion force of ice on the surface, so as to calculate the shear adhesive strength between ice and the substrate. The sleeve used was of 40 mm diameter, with inner hole of 10 mm diameter. In order to reduce the influence of friction to the result, use clearance fit between sleeve and the substrate rods.

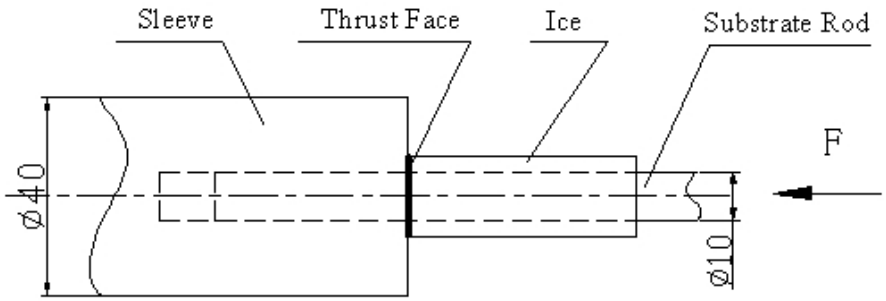



Fig. 1. Test Section of Ice Shear Adhesive Strength Experiment

**Results and Discussion**

A typical load curve during mechanical test is shown in Fig.2. Read the maximum value of shear adhesive force, minus it with the influence of the friction resistance, then calculate ice shear adhesive strength according to formula 4.

$$A_d = \frac{F_t}{S} \tag{4}$$

where $A_d$ is the shear adhesive strength of ice, $F_t$ is the maximum shear adhesive force, S is the contact area between ice and substrate.

**Effect of Ambient Temperature and MVD**

Figure 3 shows the shear adhesive strength of impact ice as a function of ambient temperature. The water MVD (40μm) and material (aluminum) roughness (2.12μm) are kept constant.

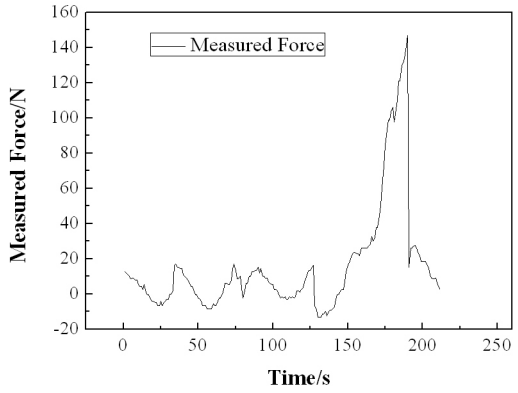



Fig. 2. Typical Adhesive Force Curve

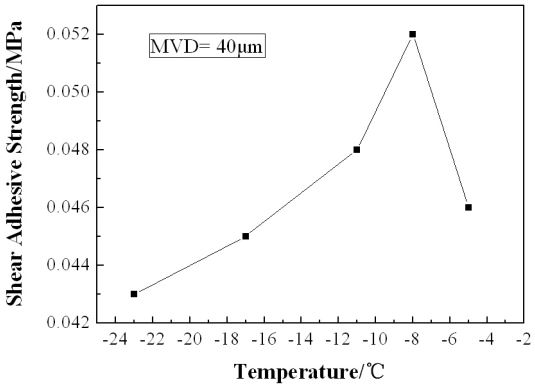



Fig. 3. Effect of Ambient Temperature

For temperatures beyond -8°C, it can be seen from the results shown in Figure 3 that the shear adhesive strength of ice increases with the ambient temperature decreasing. For temperatures below -8°C, the shear adhesive strength of ice begins to decrease as temperature decreasing.

Figure 4 shows the effect of water MVD on ice shear adhesive strength. It can be seen that for MVD below 25μm, the shear adhesive strength of impact ice were quite small compared to MVD beyong 30μm.

The dependence of the adhesive strength of ice upon the ambient temperature and MVD may be explained through the mechanical properties of different types of ice build-up at various icing conditions. At temperatures between -5°C and -10°C and MVD between 30μm and 40μm, glaze ice was obtained. For temperatures below -10°C and MVD beyond 30μm, mixed glaze and rime ice was obtained. When MVD was below 25μm, there was white rime ice accumulated on substrate. Due to different characters of different types of ice, glaze ice has the maximum adhere strength because of its high density and purity while rime ice has the minimum adhere strength and mixed ice is between them. Different types of ice obtained are shown in figure 5.

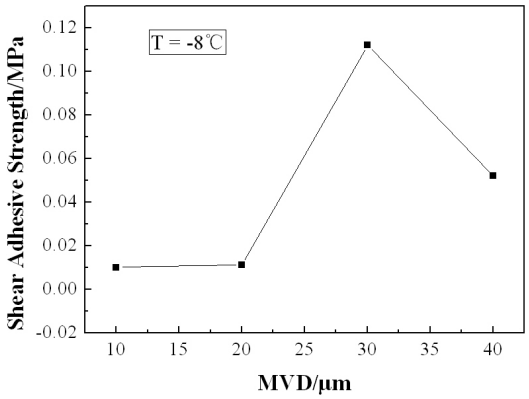



Fig. 4. Effect of MVD on Adhesion Strength

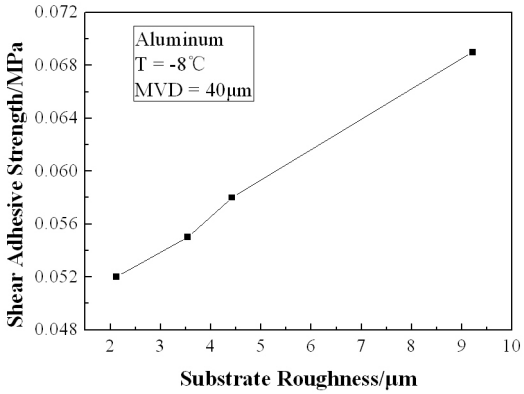
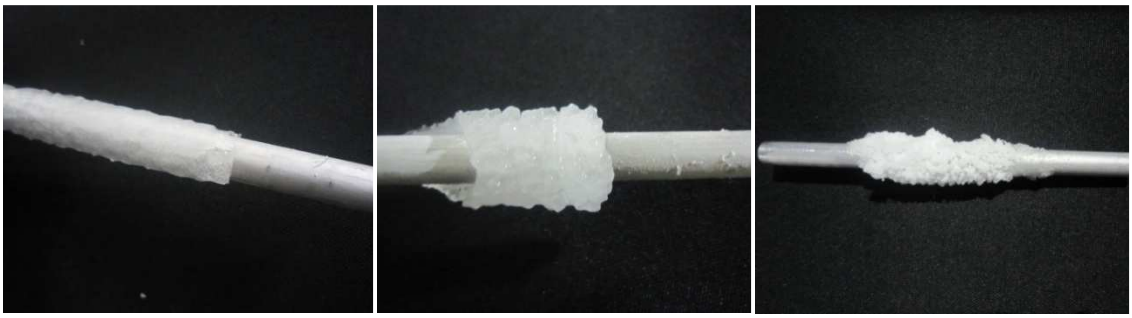



Fig. 6. Effect of Substrate Roughness



a. glaze ice b. mixed glaze and rime ice c. white rime ice

Fig. 5. Different Ice Types Obtained

**Effect of Substrate Material and Roughness**

The shear adhesive strength of impact ice is shown as a function of substrate roughness in figure 6. The ambient temperature (-8°C), water MVD (40μm) and material (aluminum) of substrate rod were kept constant. It can be seen that the adhesive strength of ice increases with the roughness of substrate.

When supercooled droplets strike the substrate with small roughness, they freeze on impact and stick to or weld on the substrate over almost its whole true surface. The force needed to remove such an ice sample is a shear force, strong enough to overcome the sticking force. When the roughness is increased, the true contact area is increased, therefore the force needed to remove the ice sample should increase. Further, the more the roughness increases, the greater could be the number of water droplets reaching the valleys of the substrate surface. The freezing of droplets increases their volume and consquently stresses could be created between ice teeth and the peak in the surface. On the other hand, when roughness increases, a stress concentration effect can occur, due to the larger surface asperities. As a result, to remove the ice from the substrate, the force needed should be increasing as the roughness increases.

Figure 7 shows the shear adhesive strength of impace ice on different substrates. The materials used were aluminum, 304 stainless steel and polymer material (PTEE) with similar roughness (3.54μm). The ambient temperature varied from -8°C to -23°C, water MVD was kept constant as 40μm.

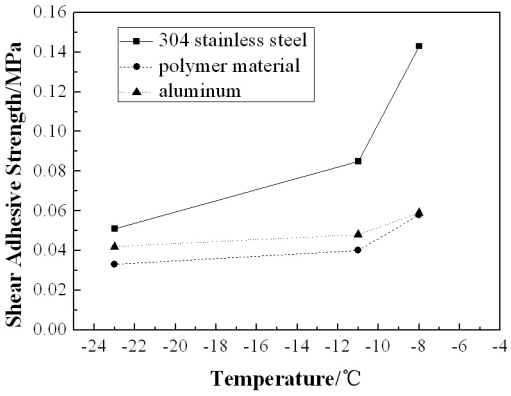



Fig. 7. Effect of Substrate Material

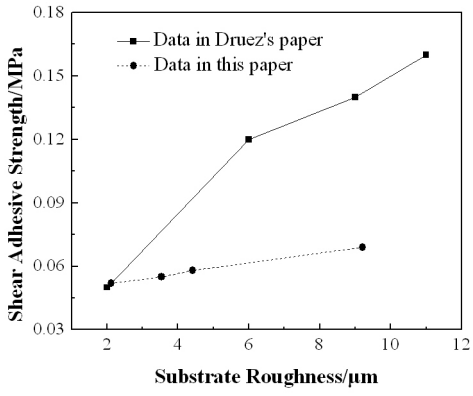



Fig. 8. Data Comparison with Druez's Research

As shown in figure 7, the shear adhesive strength of impact ice on 304 stainless steel is obviously much bigger than it on aluminum and polymer material. Based on the ice adhesion mechanism analysis above, the bigger effective dielectric constant of substrate material is, the bigger ice adhesion force will be. Compared to the other two kinds of materials, 304 stainless steel has larger effective dielectric constant, bigger atomic structure and higher boiling point. Thus the ice adhesive strength on it is the biggest because of the decisive role of electrostatic force and Van der Waals force played in ice adhesion force.

## Comparison with Foreign Research

The comparison of data obtained in this paper and Druez's research is shown in figure 8, in which the ice adhesive strength is shown as a function of substrate roughness. In our study, the shear adhesive strength of ice distribution range from 0.01 MPa to 0.143 MPa, while in Druez's research the range is from 0.067MPa to 0.4MPa. The existance of the error is mainly because the different icing conditions. In Druez's study, a wind tunnel was used to get the icing temperature, super-cooled water droplets size and velocity of air precisely controlled. However, in our study, such parameters couldn't be controlled so accurate because of restriction of instruments. On the other hand, the water used to produce super-cooled droplets was not pure enough. As a result, data obtained in this paper is smaller compared to that obtained by Druez.

## Conclusions

From the research above, the following conclusions can be summarized:

1. Electrostatic force and Van der Waals force play important roles in ice adhesion force. The effective dielectric constant and dielectric polarizability of substrate material is related to ice adhesion strength.
2. Ambient temperature and MVD of super-cooled droplets have obvious influence on the shear adhesive strength of impact ice. For temperature at -8°Cand MVD at 30μm, the maximum of adhesive strength was get. The dependence of the adhesive strength of ice upon the ambient temperature and MVD can be explained through the mechanical properties of different types of ice build-up at various icing conditions. Glaze ice has the maximum adhere strength because of its high density and purity while rime ice has the minimum adhere strength and mixed ice is between them.
3. The adhesive strength of impact ice depends strongly upon the material and roughness of the substrate. It increases with the increasing roughness and 304 stainless steel has the strongest adhesion force to ice while polymer material has the weakest.
4. Compared to Druez's research, the data obtained in this paper is smaller. The reason of the error is mainly because of the imprecision of the experiment condition and impurities in water.

## Acknowledgement

This research was financially supported by:

1. Postdoctoral Research Funding Projects of Jiangsu Province, 1201033C.
2. Nanjing University of Aeronautics and Astronautics basic scientific research expenses youth science and technology innovation fund for scientific research project (Science &Technology), NS2014014.

## References

[1] R.J. Scavuzzo, M.L. Chu. NASA-CR-179580.
[2] Reich. A.D. AIAA 91-0446, Jan 1991.
[3] Reich. A.D., Scavuzzo. R.J., Chu. M.L.. AIAA 94-0712, Jan 1994.
[4] Druez. J., Phan. C. L., Laforte, J. L., and Nguyen. D. D.. Transactions CSME Vel. 5, No. 4, October 1979, pp.215-220.
[5] Phan. C. L., McComber. P., and Mansianx. A.. Transactions CSME, Vol. 4, No. 4, 1976-77, pp. 204-208.
[6] Israelachvili, J. N.. Intermolecular and Surface Forces[A]. 2nd ed., Academic Press[C], London, 1991.
[7] Ryzhkin, I., Petrenko, V. Journal of Physical Chemistry B, Vol. 101, No. 32, August 1997, pp. 6267~6270.

*Advanced Materials Research Vol. 937 (2014) pp 336-340*
*© (2014) Trans Tech Publications, Switzerland*
*doi:10.4028/www.scientific.net/AMR.937.336*

# Design of the Hydraulic System of Lead Plate Coiling Machine

Hui SEN[1,a], Rui-bo YUAN[2,b,*] and Li RONG[3,c]

[1 2 3]Kunming university of science and technology

Mechanical and Electrical Engineering Institute

650500 Kunming, Yunnan Province,China

[a]394619315@qq.com, [b] 22911979@qq.com, [c] 371022810@qq.com

**Keywords:** Lead plate, Hydraulic, Coiling machine.

**Abstract.** This paper mainly introduces the process of lead electrolysis, the structure and working principle of lead plate coiling machine and Its' parts, coiling machine components. First of all, rewind section hydraulic system adopts a return to the oil throttle speed control, it is stable and can bear a certain change load, can overcome the stage before the tension fluctuation of the impaction to the rotation speed of hydraulic motor. Secondly, speed and tension control system adopt electro-hydraulic servo valve and proportional relief valve are respectively to the drum speed and output torque control,it has high precision and accurate in speed and tension control. contact coiling section use electro hydraulic servo position control system with close loop control to improve the accuracy of position control. Finally, calculate parameters of each working section of hydraulic control system , verify the hydraulic component model and the rationality of the hydraulic circuit.

## Lead Plate Coiling Machine

In the lead cathode production process, lead plate coiling machine is an important part of lead cathode sheet forming unit, the three dimensional model, as shown in Figure .1.



Fig. 1. The 3D model machine

Lead plate coiling machine is the lead liquid high purity molten by water cooling roller, cast thin lead sheet with a certain thickness and width, and then by the drum will be continuous thin lead plate coiling equipment[1]. The following work mechanism of lead plate coiling machine parts[2]:

(1) The water drum (put drum): through the rotation of the drum the molten lead liquid, made into a continuous thin lead sheet solid;

(2) Press roll: roll the outer edge of lead plate, lead the edges of the sheet formation;

(3) Guide roller guide: delivery of continuous lead sheet, prevent the lead sheet collapsing phenomenon during the delivery process, the lead sheet smooth transportation;

(4) Air cylinder: continuous transport process of lead in the film, the surface cold on lead tablets, lead to accelerated cooling, coiling high quality lead roll;

(5) Contact pressure rollers: thin lead sheet is pressed on the winding reel, reel or small contact gap winding;

(6) The drum: the continuous lead plate coiling become lead volumes.

**Design of Lead Plate Coiling Machine Hydraulic System**

**Rewind Section Hydraulic Circuit Design**

The hydraulic principle diagram, as shown in Figure .2.

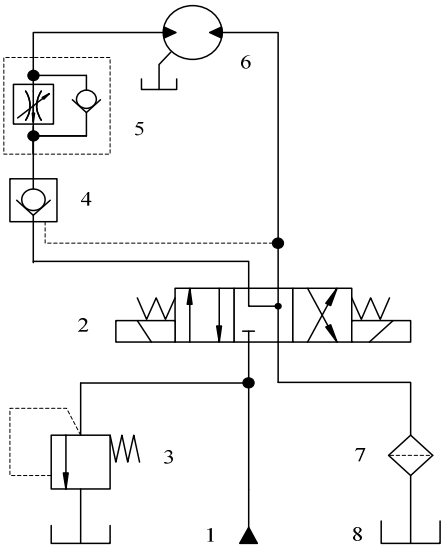



Fig. 2. Hydraulic circuit schematic of the unwinding segment

The route back to the oil pressure source 1, the electromagnetic directional valve 2, valve 3, a hydraulic control one-way valve 4, a one-way valve 5, a hydraulic motor 6, oil filter 7 and the fuel tank 8. Its working principle is: the pressure oil source 1 to provide pressure oil stability. When the electromagnetic valve 2 is in the right place when working, the one-way speed regulating valve 5 for regulating the flow of hydraulic motor 6 flow, so as to control the hydraulic motor 6 speed. Speed control valve with pressure compensation function, before and after its envoy outlet pressure is not changes with the load, to maintain a constant value, so as to achieve stable flow, even if the hydraulic motor 6 speed remain constant 4. Liquid control one-way valve is the role of hydraulic motors in 6 when stop locking circuit, so that the water cooling roller long time locked in a fixed position. When the electromagnetic reversing valve 2 is in place when working, exports and imports of hydraulic motor 6 is connected directly to the tank 8.

**Coiling Section Hydraulic Circuit Design**

The hydraulic principle diagram, as shown in Figure .3.

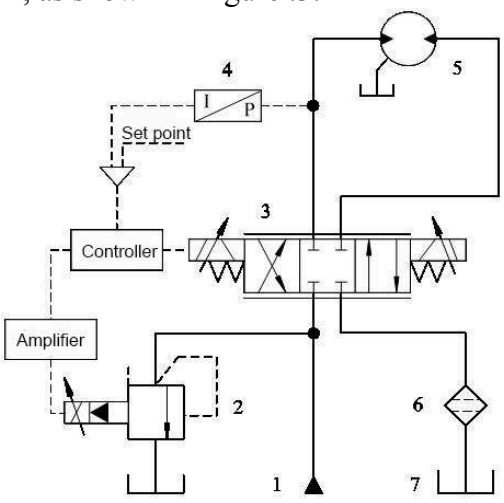



Fig. 3. Hydraulic circuit schematic of the winding segment

Winding section of hydraulic pressure oil source route 1, the proportional relief valve 2, electro-hydraulic servo valve 3, pressure sensor 4, a hydraulic motor 5, fine oil filter tank 6 and 7. its working principle is: proportional pressure relief valve 2 preset system, namely the setting of electro-hydraulic servo valve 3 inlet pressure. Use with direction control and flow control of electro-hydraulic servo valve 3, realize the commutation and speed control hydraulic system. The electro-hydraulic servo valve 3 in the right job, hydraulic motor driven load 5 collecting drum rotating. The electro-hydraulic servo valve in 3 in a work, a hydraulic motor 5 brake. When the electrohydraulic servo valve 3 receives the electrical signal from the controller, through the displacement regulating valve, outlet flow control of electro-hydraulic servo valve 3, the output speed to control the hydraulic motor 5. The pressure sensor 4 for detecting hydraulic motor 5 inlet pressure.

**Contact Coiling Section Hydraulic Circuit Design**

The hydraulic principle diagram, as shown in Figure .4.

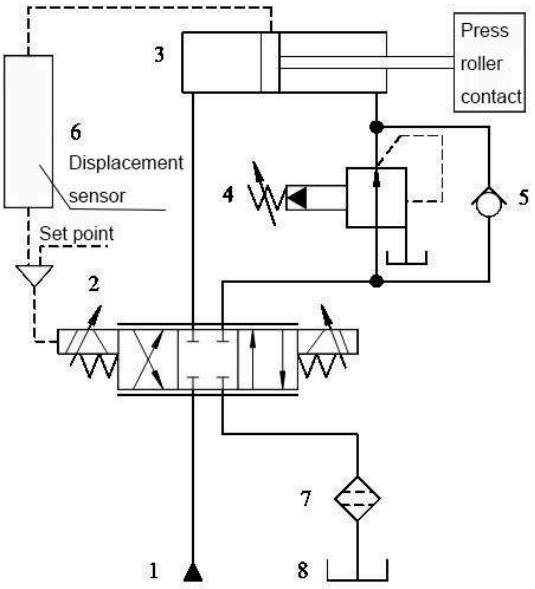



Fig. 4. Hydraulic circuit schematic of the contact winding segment

Contact coiling section of hydraulic pressure oil source route 1, electro-hydraulic servo valve 2, a hydraulic cylinder 3, pilot valve 4, valve 5, the displacement sensor 6, fine oil filter tank 7 and 8. Some 1 oil pressure oil source and 8 as lead plate coiling machine hydraulic station the entire unit, sharing a tank. Its working principle is: the electro-hydraulic servo valve 2 is in left work, can be adjusted into the flow of the hydraulic cylinder 3, to adjust the angular velocity of roller body contact. When the electrohydraulic servo valve 2 is in place to work, the hydraulic cylinder. When the servo brake valve 2 is in the right place to work, the hydraulic cylinder without rod into the oil chamber, the hydraulic cylinder inverse fast action, improve work efficiency.

**Calculation of Hydraulic Parameters of Control System**

**Parameter Calculation of Roll Segments**

**Working Conditions and Load Analysis**

Lead sheet reel unreeling a tension before the water drum rotating, finished water cooling roller by lead plate with rotation, lead sheet tension with rotating torque for water-cooled drum. The establishment of tension, load torque water-cooling roller by load torque, cooling water inertia moment and lead sheet tension torque. Then the equivalent hydraulic motor load torque:

$$M_{R1} = \frac{M_{T1}}{i} + M_{m1} + M_{f1} = 12\ (\mathrm{N \cdot m})\ . \tag{1}$$

Among them, $M_{m1}$ is water roller and load inertia torque, $M_{m1} = J_1(d\omega_1/dt)$; $M_{f1}$ as the viscous damping torque, generally small, negligible.

Lead plate coiling machine building tension, torque lead sheet tension on water-cooled cylinder:

$$M_{T1} = TR_1 = 200 \times 0.18 = 36\ (\mathrm{N \cdot m})\ . \tag{2}$$

**Determine the Rewind Section Hydraulic System Parameters**

Rewind section hydraulic system flow and pressure according to the rotational speed and torque water-cooling roller maximum calculated. Preliminary set for hydraulic system $P_s$ is 4.5 MPa .

According to the actual condition of rewind section water drum can calculate the rewind section hydraulic motor capacity for:

$$V_{m1} = \frac{M_{R1}}{P_L} = \frac{3M_{R1}}{2P_s} = \frac{3 \times 12}{2 \times 4.5 \times 10^6} = 4 \times 10^{-6}\ (\mathrm{m^3/r})\ . \tag{3}$$

Select the hydraulic motor capacity for16.3 mL / r ,model:YM-A19B,YM type medium pressure vane motor rated pressure of 6.3 MPa ,output torque 9.7 N · m ,minimum speed 100 r/min .

Oil flow rate at maximum power rewind section hydraulic system required for:

$$q_{v1} = \frac{2\pi V_{m1} i n_{1\max}}{0.8} = \frac{2\pi \times 2.6 \times 10^{-6} \times 192}{0.8} = 3.91\ (\mathrm{L/min})\ . \tag{4}$$

According to $q_{v3}$ ,to determine the types and specifications of the throttle valve for:DV10S310,the maximum working pressure valve for35 MPa ,the path to10 mm ,the maximum flow14 L/min .

**Rewind Section and other Hydraulic Components Selection**

Pilot type relief valve:DB10A-2-32/10UG24NZ4;hydraulic control valve: SV10PB1-L6X/V; Electromagnetic reversing valve:4WE10J-6.0/OFG24NZ4.

**The Parameters Calculation of the Coil Section**

**Conditions and Load Analysis**

The moment of inertia of charge for the drum of:

$$\frac{dJ_2}{dt} = 2\pi\rho b R_2^{\ 3} \frac{dR_2}{dt} = \rho b V_2 h R_2^{\ 2} = 11344 \times 0.89 \times 0.001 \times 0.44^3 \times 2.5 = 2.15\ . \tag{5}$$

The rate of variation of angular velocity:

$$\frac{d\omega_2}{dt} = \frac{\omega_{2\max} - \omega_{2\min}}{\Delta t} = \frac{2.5 - 1}{19 \times 60} \approx 0.002\ . \tag{6}$$

Dynamic equivalent moment drum can be expressed as

$$M_{J2} = \frac{dJ_2}{dt}\omega_2 + J_2 \cdot \frac{d\omega_2}{dt} = 2.15 \times 2.5 + 172 \times 0.002 = 5.72\ (\mathrm{N \cdot m})\ . \tag{7}$$

Effect of maximum equivalent torque hydraulic motor shaft is in:

$$M_{R2} = \frac{M_{T2} + M_{J2}}{i} = \frac{88 + 5.72}{15} = 6.25\ (\mathrm{N \cdot m})\ . \tag{8}$$

**The Hydraulic System Parameters Determine the Volume Segment**

For the fluid pressure of the hydraulic system $P_s$ is 6.5 MPa .

Hydraulic motor capacity for:

$$V_{m2} = \frac{2\pi M_{R2}}{\Delta P_L \cdot \eta_{m2}} = \frac{2\pi \times 6.25}{0.5\times 10^6 \times 0.92} = 85.4\times 10^{-6}\ (\mathrm{m^3/r}) . \tag{9}$$

Select the hydraulic motor capacity for 105 mL / r ,model:JYM-D

Considering the influence of hydraulic system leakage, oil flow rate at maximum power winding section of hydraulic system required for:

$$q_{v2} = \frac{2\pi V_{m2} in_{2\max}}{0.8} = \frac{2\pi \times 16.7\times 10^{-6}\times 360}{0.8} = 47.25\ (\mathrm{L/min}) . \tag{10}$$

According to the $q_{v3}$ ,Determination of electro-hydraulic servo valve type: SM4-20(5)19-80/40-50-S(Vickers); Servo amplifier:EM-D-30(Vickers).

**Rolling Section and other Hydraulic Components Selection**

Hydraulic control valve:SVGPB1-L4X/V;The electro-hydraulic proportional relief valve:DBEM10-32/31.5Y/2V; Hydraulic pressure sensor:AK-4C.

**The Contact Parameters Calculation of Volume Segment**

**Working Conditions and Load Analysis**

Lead plate coiling machine contact rolling process of the hydraulic cylinder force balance equation:

$$F_3 = F_4 + T = 280\ (\mathrm{N}) . \tag{11}$$

Contact the maximum load for the volume segment of hydraulic cylinder:

$$F_L = k_3 \cdot F_3 = 1.5\times 280 = 420\ (\mathrm{N}) . \tag{12}$$

**Contact the Determined Volume Segments of Hydraulic System Parameters**

Contact the liquid pressure volume segments of hydraulic system $P_s$ is 3 MPa .

Effect of area of hydraulic cylinder $A_p$ is:

$$A_p = \frac{\pi}{4}(D^2 - d^2) = \frac{\pi}{4}\times(25^2 - 18^2)\times 10^{-6} = 2.36\times 10^{-4}\ (\mathrm{m^2}) . \tag{13}$$

The maximum power, fuel flow contact rolling period required for hydraulic system:

$$q_{v3} = \frac{A_3 \cdot V_3 \cdot \eta_m}{0.8} = \frac{2.36\times 10^{-4}\times 0.88\times 0.95\times 60}{0.8} = 14.75\ (\mathrm{L/min}) . \tag{14}$$

According to the $q_{v3}$ ,To determine the specifications of electro-hydraulic servo valve for:SM4-20(5)19-80/40-50-S(Vickers).

**References**

[1] Nonferrous metal smelting equipment editorial board. Non-ferrous metal smelting equipment (First Edition). Smelting equipment. Beijing: Metallurgical Industry Press, 1993

[2] Liu Sen. Electro hydraulic proportional control on lead cathode stepping conveyor application research [Master thesis].Kunming, Kunming University of Science and Technology, 2011(In Chinese)

*Advanced Materials Research Vol. 937 (2014) pp 341-345*
*© (2014) Trans Tech Publications, Switzerland*
*doi:10.4028/www.scientific.net/AMR.937.341*

# Influence of Vibration on Thermomechanical Property and Transformation Behavior of TiNi Shape Memory Alloy

An-Sheng ZHENG[1,a*], Rui-Hua Li[2,b,] Peng-Shuang ZHENG[3,c,] and Gui-Ying Fu[4]

[1] China Petroleum Pipeline Engineering Corporation, No. 146, Heping Road, Langfang City, Hebei Province, China

[2]CNPC Bohai Drilling Engineering Company Limited, Wanzhuang Projects Department, Langfang City, Hebei Province, China

[3] Hebei Technical College of Petroleum Profession, No. 90, Aimin West Road, Langfang City, Hebei Province, China

[4] China Petroleum Pipeline Inspection Technologies Co., Ltd., No. 166, Aimin East Road, Langfang City, Hebei Province, China

[a]zhenganshengcppe.com.cn, [b]pippy@126.com, [c]zhengpengshuang@163.com

*Corresponding author

**Keywords:** Vibration; TiNi; shape memory alloy; transformation; recovery strain.

**Abstract.** The strain recovery character and transformation behavior of a TiNi alloy are investigated by means of mechanical testing and DSC measurement before and after vibration. The DSC results show that the second reverse transformation peak temperature of TiNi alloys after vibration under constraint increases slightly during the subsequent heating, and the transformation heat decreases, while the transformation heat of the first reverse transformation increases. After constrained vibration, the first decline of the two-stage recovery strain obtained during the second heating process is obviously smaller than the one without vibration, and the total recoverable strain also decreases. For the prestrained martensitic TiNi fiber after a heating-cooling cycle, the two-way memory strain increases about 1.2% after vibration. All these phenomena are considered to be closely related to the vibratory stress relief during vibration.

## Introduction

It is well-known that near-equiatomic TiNi shape memory alloys can show a lot of unique, fine properties, such as shape memory effect, pseudoelasticity, high damping and so on, and two-way shape memory effect (TWSME) is surely quite a promising one. It is also well-admitted that TiNi alloys can show TWSME through certain training process, and also simple deformation involving only the martensite is effective in introducing a two-way memory effect, of which the magnitude is comparable to the TWSME developed through conventional training. The origin of TWSME is attributed to the stress field produced by the complex dislocation structure during the training process [1-6].

As we know that vibration can release the residual stress of metal components after welding, forging and casting, and it has been investigated from the early stage of the 20th century. Although the underlying mechanism is still discussed controversially, it has been widely accepted that the vibratory stress relief is due to the microscopic plastic deformation of the high residual stress area caused by the change of dislocation configuration through slip, multiplication and pileup of dislocation [7-14]. On the other hand, SMAs will inevitably be used in vibratory environment. Then whether the transformation behaviors and mechanical properties of TiNi shape memory alloys will be affected by vibration is still unknown, and this will be studied in this work.

## Experimental

A commercial Ti-50.2 at% Ni alloy wire with 0.48 mm in diameter was obtained from the General Research Institute for Non-Ferrous Metals, China. The cold-drawn wire was vacuum aged at 873K for 30min followed by air cooling.

The aged wire was prestrained to 8.32% by tension at room temperature in the martensite state, and then the alloy fibers of approximately 120 mm in length were cut from the prestrained wire. Then the fibers underwent a heating-cooling cycle for inducing TWSME. Then one fiber was vibrated at 500Hz for 30min and the other was not. After that the fibers were used for thermomechanical property testing. For the case of constraint, the deformation process is the same as the previous one but with a prestrain of 4.1%. Then one fiber was vibrated at 50Hz for 30min after heating to 373K under constant strain constraint and the other was not. After that the fiber was constrained cooling down to the room temperature and used for thermomechanical property testing.

The fibers for thermomechanical property testing were performed by measuring the recovery strain, and they were heated to 367K in a free state. The vibratory experimental setups for the two cases were shown as Fig. 1 and Fig. 2, respectively. The vibratory acceleration and amplitude were 43.1 m/s2, 0.008mm at 500Hz and 66.8m/s2, 1.386mm at 50Hz, respectively. The thermomechanical tests were conducted on a self-made material test machine.

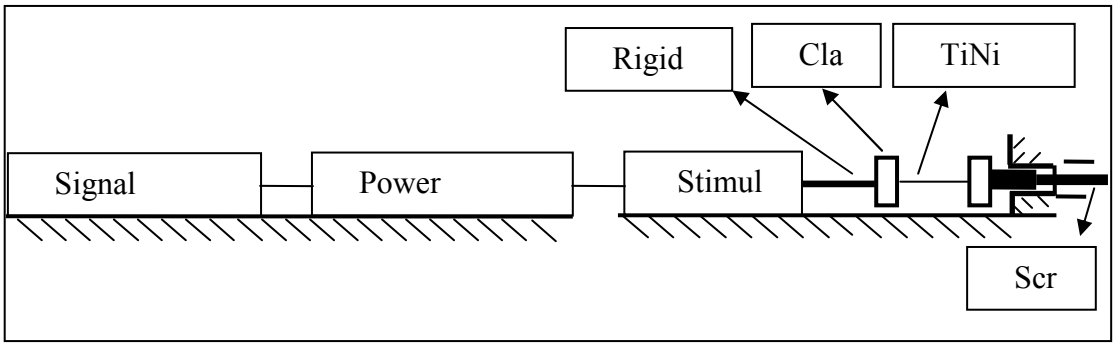



Fig. 1. The schematic diagram of experimental setup for TWSME vibration

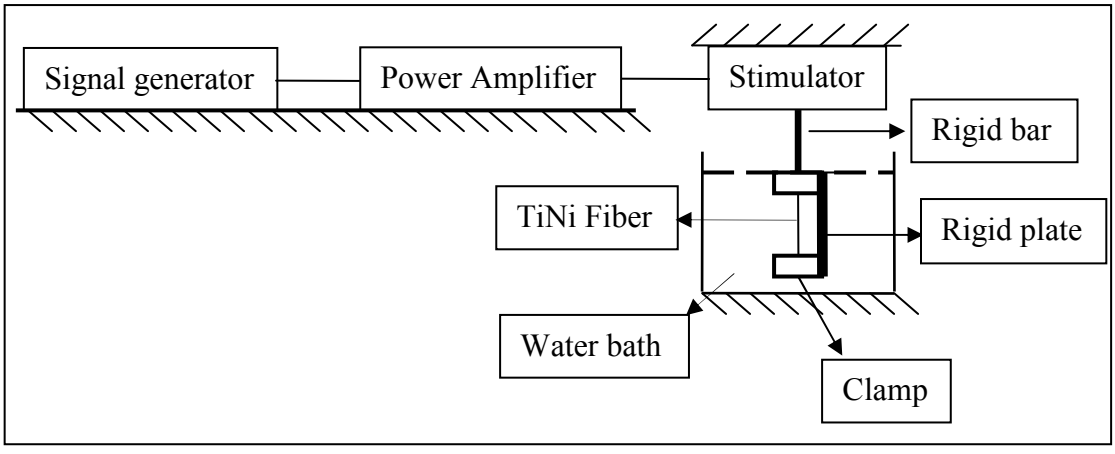



Fig. 2. The schematic diagram of experimental setup for constrained vibration

## Results and Discussions

The effect of vibration on TWSME

The measurement results of two-way memory strain of the samples after a thermomechanical cycling before and after vibration are shown as curve 1 and 2 in Fig. 3, respectively. The two-way memory strain is 3.43% for the vibrated specimens, and 2.21% for the one without vibration. It is obviously that after vibration at 500Hz for 30min, the two-way memory strain increases about 1.22%.

When the TiNi alloys are severely deformed, the irreversible plastic deformation by slip will be introduced. The slip and multiplication of dislocation will generate a microscopic residual stress field. After a heating-cooling cycle, a specially arranged stress field will be generated by these dislocations and contributes to the formation of two-way memory effect [6]. However, many researchers have perceived that the vibratory stress relief is mainly caused by the change of dislocation configuration during vibration. Walker et al. [10] and Munsi et al. [11-13] consider that the dislocation energy of the high residual stress area is elevated due to vibration, which enables the change of dislocation configuration, resulting in the stress relief. Song et al. [14] find that after vibration at 148.8Hz for 12min the residual stress of the welded 16Mn steel is relieved, and the appearance of the slip, multiplication and pileup of dislocation is observed by using TEM observation. Combining these two points, therefore, it is speculated that the two-way residual stress field induced by severe deformation and a heating-cooling cycle is decreased through the change of dislocation configuration. Meanwhile, the effectively active area of the microscopic stress field is enlarged through the slip, multiplication and pileup of dislocation, which favors the nucleation and growth of preferential martensite variants, resulting in an increase of the two-way memory strain.

The effect of vibration on the constrained recovery strain

The measurement results of recovery strain curves of the samples under constrained heating to 373K before and after vibration are shown as curve 1 and 2 in Fig. 4, respectively.

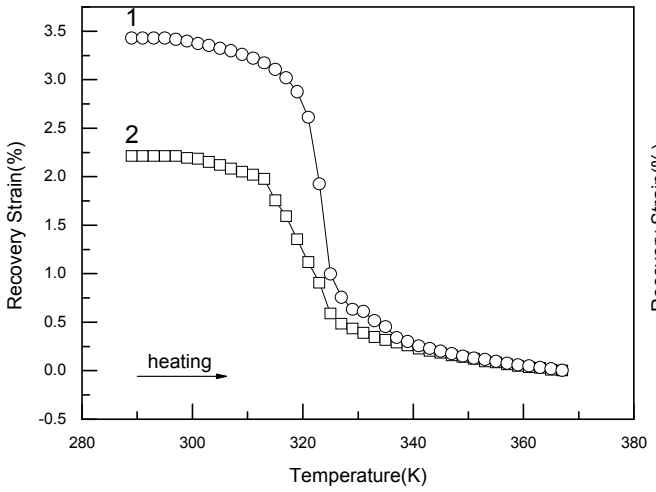



Fig. 3. Two-way memory strain curves at 500Hz

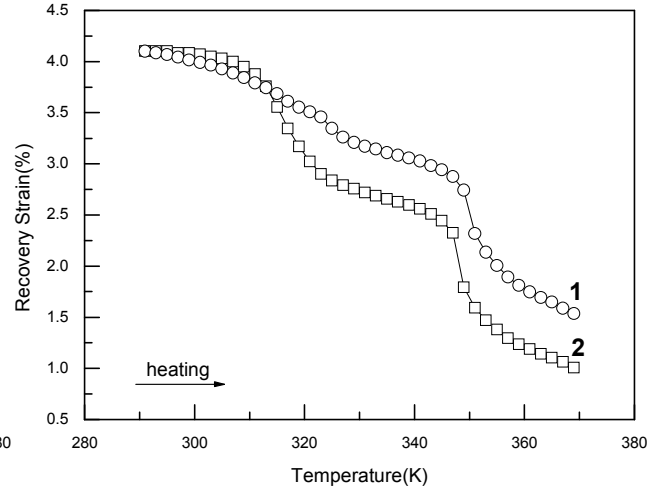



Fig. 4. Recovery strain curves at 50Hz

It is noted that there is a two-stage recovery strain in this curve, and the first stage corresponds to the reverse martensitic transformation of stress-induced martensite (M2) and the second one the retained oriented martensite (M1) [15, 16]. From the recovery strain curves, one can see that the total recoverable strain after vibration at 50Hz for 30min decreases greatly compared with the one without vibration. It is clearly that the decrease of the recoverable strain emerges mostly in the first decline. According to the conclusion of Li et al [16] that the formation of stress-induced martensite M2 is under the influence of the recovery stress during constrained cooling, i.e., it forms in a manner of preferentially oriented variants favorable to the recovery stress. Thus it can be presumed that vibration reduces the recovery stress generated under constant strain constraint. Then it can be concluded that the recovery stress of the fastening pieces used in the engineering application will decrease when they meet an unexpected vibration.

Curve 1 and 2 in Fig. 5 are the DSC measurement results of the transformation behaviors of the samples under constrained heating to 373K before and after vibration, respectively. It is noted that there are two independent endothermic peaks in the DSC heating curves, indicating two separated transformations. The transformation heat and transformation peak temperature of the two reverse transformations in the DSC curves are shown in table 1. From the table, one can see that the transformation heat of the first reverse martensitic transformation of the samples increases after

vibration at 50Hz for 30 min, while the second one of the samples decreases, and the second reverse transformation peak temperature also increases slightly.

Table 1. The transformation heat and peak temperature of the two reverse transformations in the above DSC curves

| | △H1(J/g) | △H2(J/g) | Ap1(K) | Ap2(K) |
|---|---|---|---|---|
| Without vibration | 5.239 | 3.054 | 314.2 | 348.2 |
| Vibration at 50Hz for 30 min | 7.004 | 2.432 | 314.9 | 350.7 |

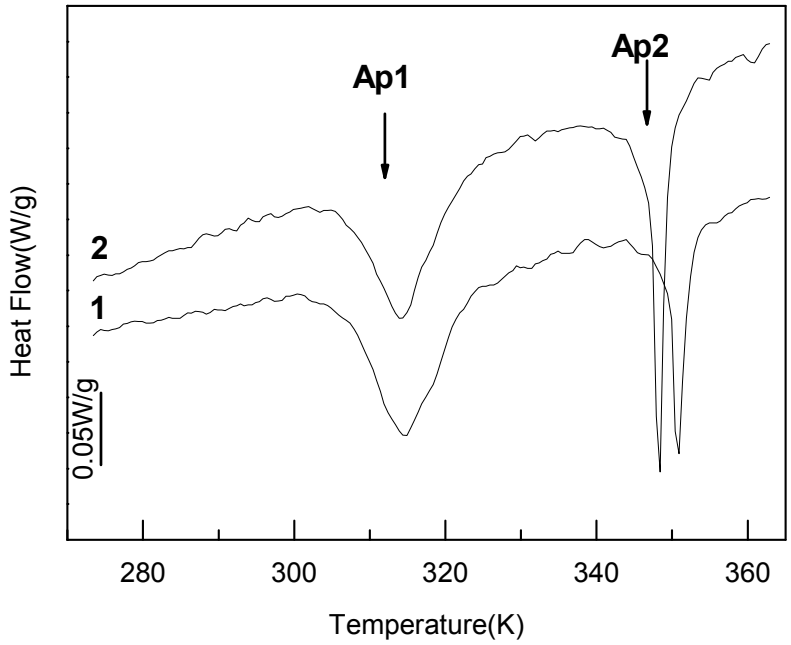



Fig. 5. DSC results of the specimens (1) vibration at 50Hz for 30 min (2) without vibration

If a prestrained TiNi is prevented from shape recovery during the transformation from martensite to austenite, a large recovery stress against the external constraint is generated, and this stress also exits between the austenite and the retained oriented martensite. Since the elastic modulus of martensite is smaller than that of austenite, the martensite is easily deformed, thus a microscopic plastic deformation through the slip of dislocation will be induced in the martensite by vibration. The change of dislocation configuration relieves the recovery stress between the retained oriented martensite and the austenite, so the first stage recovery strain which is closely related with the magnitude of the recovery stress will decrease due to the relief of the recovery stress. From the point of view of the effect of the elastic energy on the As temperature of SMAs[17, 18], i.e., plastic deformation releases the elastic energy stored in martensite, which is the driving force for the reverse transformation, thus the second reverse martensitic transformation peak temperature increases slightly, as can be seen in DSC curves. Due to the decrease of the recovery stress, parts of the metastable martensite variants can reversely transform to the austenite, which makes the decrease of the amount of the retained oriented martensite and the increase of the self-accommodation thermal martensite after cooling, and finally results in the increase of the transformation heat of the first reverse martensitic transformation, and the decrease of the transformation heat of the second reverse martensitic transformation.

## Conclusions

In this work, the influence of vibration on the characteristic of recovery strain in TiNi shape memory alloy was investigated by means of mechanical testing. For the TiNi fibers after a heavy deformation and heating-cooling cycle, the two-way memory strain increased about 1.2% after vibration at 500Hz for 30 min. For the vibration at 50Hz for 30min under constant strain constraint, the first decline of the two-stage recovery strain obtained during the second heating process decreased obviously than the one without vibration, and the total recoverable strain decreased. DSC results showed that the first reverse martensitic transformation heat of the samples increased after vibration, while the second one decreased, and also the second reverse transformation peak temperature increased slightly. All these phenomena were considered to be closely related with the vibratory stress relief during vibration process.

## References

[1] J. Perkins., R. O. Sponholz, Metall. Trans., A15 (1984) p. 313.

[2] M. M. Reyhani, P. G. McCormick, Proc. ICOMAT-86. JIM, (1986) p. 896.

[3] L. Contardo, G. Guenin, Acta metall. mater. 38 (1990) p. 1267.

[4] Y. Liu, P. G. McCormick, Acta metall. mater. 38 (1990) p. 1321.

[5] R. Stalmans, J. Van Humbeeck, L. Delaey, Acta metall. mater. 40 (1992) p.501.

[6] Y. Liu, Y. Liu, J. Van Humbeeck, Acta Metall. 47 (1999) p. 199.

[7] M.C. Sun, Y.H. Sun, R.K. Wang, Mater. Lett. 58 (2004) p. 299.

[8] G. P. Wozney, G. R. Crawmer, Welding Journal. 9 (1968) p. 411.

[9] R. Dawson, D. G. Moffat, J. Eng. Mater. Technol. 102 (1980) p. 169.

[10] C. A. WalKer, A. J. Waddell, D. J. Johnston, Journal of Process Mechanical Engineering. 209 (1995) p. 51.

[11] A. S. M. Y. Munsi, A. J. Waddell, C. A. Walker, Strain. 37 (4) (2001) p. 141.

[12] A. S. M. Y. Munsi, A. J. Waddell, C. A. Walker, Journal of Strain Analysis. 36 (5) (2001) p. 453.

[13] A. S. M. Y. Munsi, A. J. Waddell, C. A. Walker, Mater. Sci. Technol. 17 (2001) p. 601.

[14] T. M. Song，G. F. Zhang, C. J. Yin, Acta Scientiarium Naturalium Universitatis Jilinensis. 1 (1995) p. 53. (in chinese)

[15] L. S. Cui, Y. Li, Y. J. Zheng, D. Z. Yang, Mater. Lett. 47 (2001) p. 286.

[16] Y. Li, L. S. Cui, H. B. Xu, D. Z. Yang, Metal. Mater. Tran A. 34A, Feb (2003) p. 219.

[17] M. Piao, K. Otsuka, S. Miyazaki, and H. Horikawa, Mater. Trans. JIM. 34 (1993) p. 919.

[18] Y.J. Zheng, L.S. Cui, F.Zhang, and D.Z. Yang, J. Mater. Sci. Technol. 39 (2000) p. 611.

*Advanced Materials Research Vol. 937 (2014) pp 346-350*
*© (2014) Trans Tech Publications, Switzerland*
*doi:10.4028/www.scientific.net/AMR.937.346*

# The Design and Development of a Single-axle Parallel Hybrid Powertrain Test platform

Qiang SUN[1,a], Cheng-cheng MA[1,b], Qiang MIAO[1,c], Guo-xiang LI [1,d,*]

[1]School of Energy and Power Engineering, Shandong University, Jinan, 250061

[a]sunqiangsdu@163.com, [b]machengsdu@163.com, [c]739758434@qq.com, [d]liguox@sdu.edu.cn

*Corresponding author

**Keywords:** hybrid, powertrain, test platform.

**Abstract.** Based on the structure analysis of a hybrid truck, design a single-axle parallel hybrid powertrain test platform. Modular design method is used to realize this platform and this platform is divided into four modules. Function design, software design and realization of the four modules are respectively discussed. Finally, a cycle run test was taken and the test result indicates that effectiveness and accurateness of the test platform are realized well.

## Introduction

During the development of hybrid electric vehicle (HEV), bench test is of great significant to shorten the period of vehicle calibration and help the developer to reduce the costs and risks of the development of HEV [1-4]. In this paper, based on the characteristics analysis of single-axel parallel hybrid powertrain, the single-axle parallel hybrid powertrain test platform (spHPTP) was designed and constructed by using modular design method.

## Module Design of spHPTP

### Analysis of the Hybrid Truck

The test platform is established based on a prototype truck whose powertrain is shown in Fig. 1.

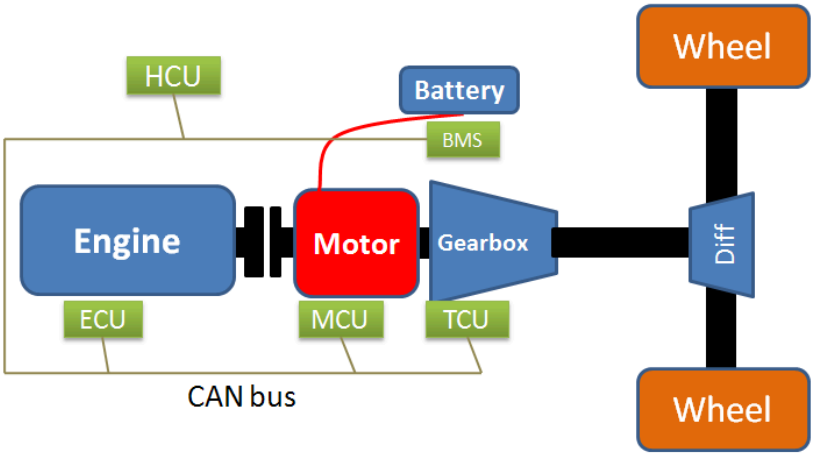



Fig. 1. Structure of the prototype truck
HCU- Hybrid Control Unit, BMS-Battery Management System, ECU-Engine Control Unit, MCU-Motor Control Unit, TCU- Transmission Control Unit, Diff- Differential

The prototype truck shown in Fig. 1 is a typical signal-axel parallel hybrid truck. The diesel engine in the prototype truck is equipped with electronic controlled high pressure common rail. The motor is a permanent magnet synchronous motor and the battery is a lithium iron phosphate power battery. Power of the engine and the motor is coupled by a clutch. Power outputs from the engine and/or the

motor drives two wheels after going through gearbox, reducer and differential in turn and finally drives wheels.

When the vehicle runs in normal mode, the driver controls the vehicle in the way shown as following: 1, Perceive current velocity based on the panel and/or the reference objects in surrounding. 2, Get a new target speed based on the current speed and the current road condition. 3, Operate the accelerator pedal, the brake pedal or shift lever combined with the current velocity to achieve the target Velocity. The whole process is described in Fig. 2.

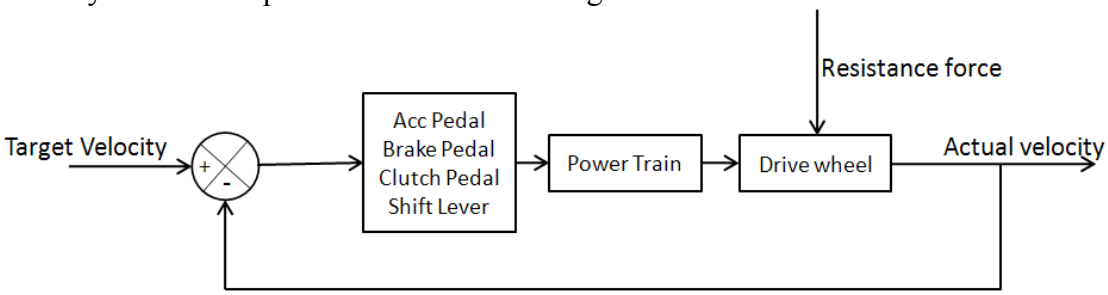



Fig. 2. Velocity control block diagram of trucks

## Division of System Function Modules

According to the structure analysis and operation analysis of the prototype truck, the platform should include such modules: 1, Driver Simulation Module (DSM), the main function of this module is that compare current velocity and target velocity then operate the accelerator pedal to reach the target speed. 2, Powertrain Module (PM), this module is used to receive signals from driver simulation module and output corresponding power. 3, Vehicle Resistance Simulation Module (VRSM), this module simulates rolling resistance, grade resistance, accelerate resistance and air resistance based on current velocity, road grade and other parameters. 4, Data Acquisition and Control Module (DACM), this module monitors the whole test platform and controls it if need. Relationships between these four modules are shown in Fig. 3.

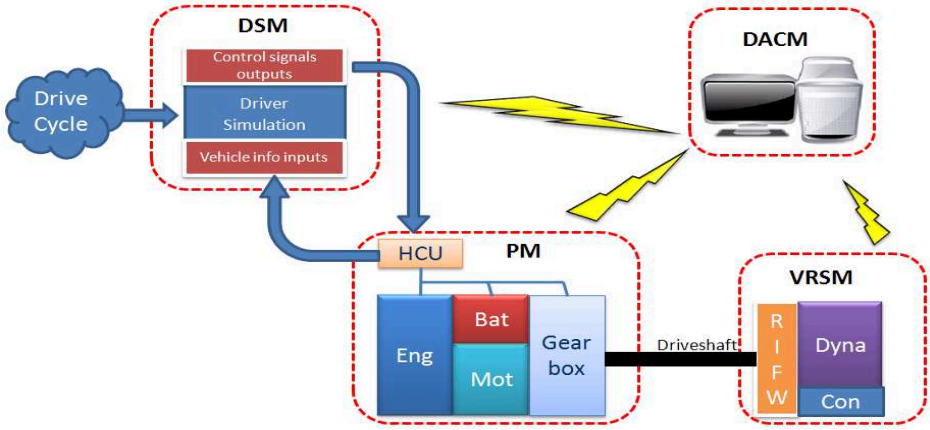



Fig. 3. Function block diagram of the signal-axle parallel hybrid system development test platform

## Module Realization of spHPTP

### Driver Simulation Module

As shown in section 1.2, the flowing functions are needed in driver simulation module: collecting current running information (velocity is included), obtaining a target velocity, comparing the target velocity with the current velocity to determine the control information (increase or decrease the acceleration pedal etc.) and outputting the control information.

This module was realized by a controller. The controller stores a certain cycle run map as the source of target velocity and obtains the current velocity via the access to HCU. A PID algorithm in

this controller simulates a driver's behavior. This PID algorithm accepts target velocity and current velocity as inputs information and gives accelerator pedal, brake pedal, clutch pedal and target gear lever as control outputs. The controller has two actuators, one is pedal actuator and the other is clutch actuator (Fig. 4 shows the two actuators). In order to simplify the test platform, the simulation of breaking process is achieved through an additional torque imposed by the vehicle resistance simulation module, instead of an individual brake. The braking torque is determined by the output signal of brake pedal.



Fig. 4. Photo of pedal actuator and clutch actuator

**Powertrain Module**

As the key component of the test bench, powertrain module consists of a engine with ECU, a clutch, a motor whit MCU, a battery with BMS, a hybrid control unit (HCU) and two torque meters (TM). The structure of PM is shown in Fig. 5.

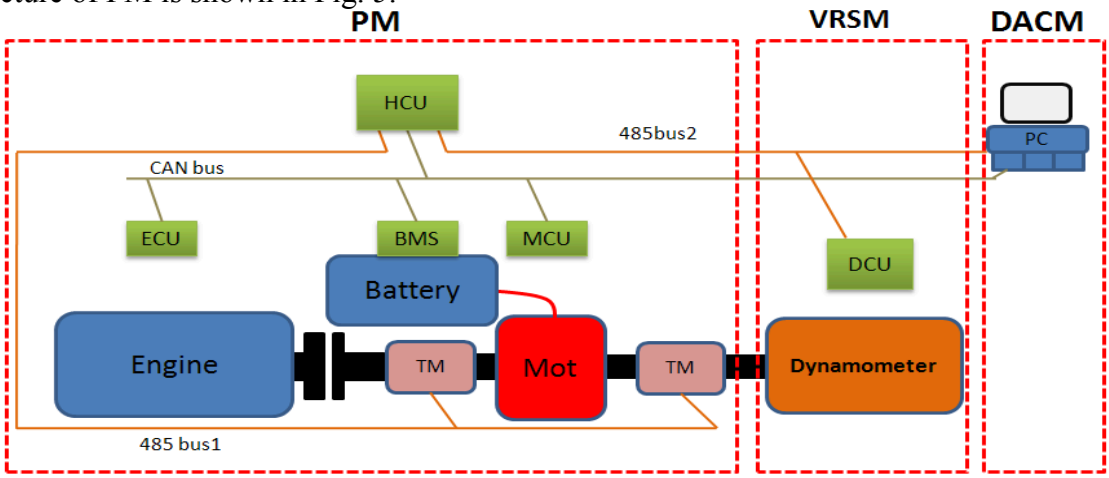



Fig. 5. Structure block diagram of powertrain module, vehicle resistance simulation module and Data Acquisition and Control Module

The reason why there is no gearbox in the test platform is that dynamometer with high torque can lead to axial-dimension and cost limited. So this paper takes the powertrain before the gearbox as the research object.

The engine, motor and battery of the test platform are as same as the original truck. In order to get the whole control and calibration authority of hybrid system, a hybrid control unit was independently developed. This HCU exchanges messages with ECU, MCU and BMS via CAN bus.

**Vehicle Resistance Simulation Module**

The position of VRSM is shown in Figure 5. The VRSM contains a three-phase asynchronous motor, a variable-frequency inverter and a dynamometer controller unit (DCU). The DCU stores a road grade map and a rolling resistance coefficient map to simulate different types of roads.

Information such as current driveshaft speed and current gear is transmitted from HCU to DCU by RS-485 bus. The DCU calculates vehicle resistance force based upon vehicle velocity, road grade, etc. and then converts this resistance fore into the resistance torque applied on the VRSM's driveshaft.

**Data Acquisition and Control Module**

The core hardware of DACM is an industrial computer Advantech U500 on which an industrial CAN expansion cards PCI-1680U extends two CAN bus interfaces. The software of DACM is developed in LabVIEW2010 environment.

**Function Achievement of spHPTP**

As described above, the signal-axis parallel hybrid powertrain develop test platform was finished and the photo is shown in Fig. 6.

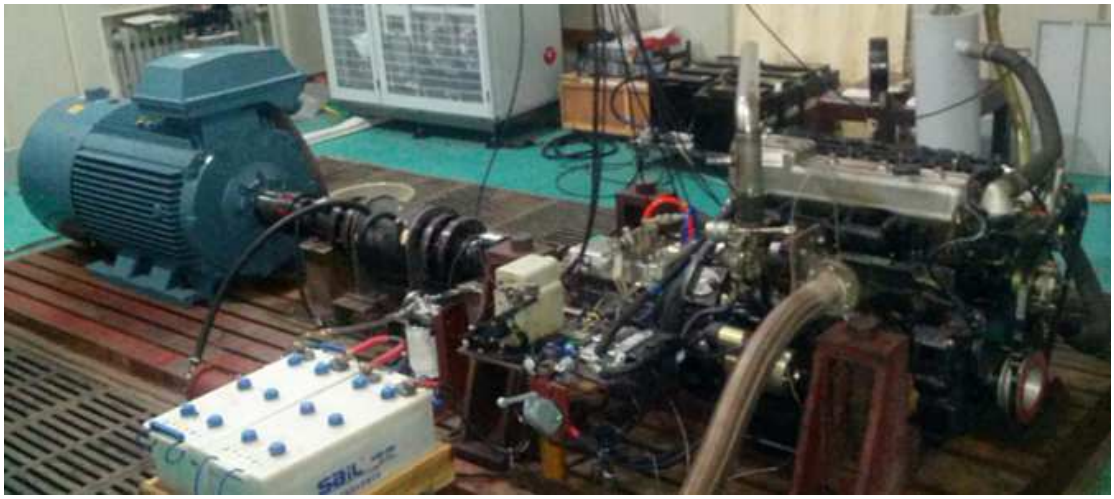


Fig. 6. Photo of the test platform

In order to verify the functions of the test platform, a cycle run test was taken. The DSM and DCU can store the velocity map and road map of a driving cycle respectively. The DSM can control the powertrain based on a target velocity got from velocity map and the VRSM can simulate the running resistance under different velocity and road grade. The bench can simulate the whole driving cycle for the vehicle. Fig. 7 shows target velocity and actual velocity during the cycle run test.

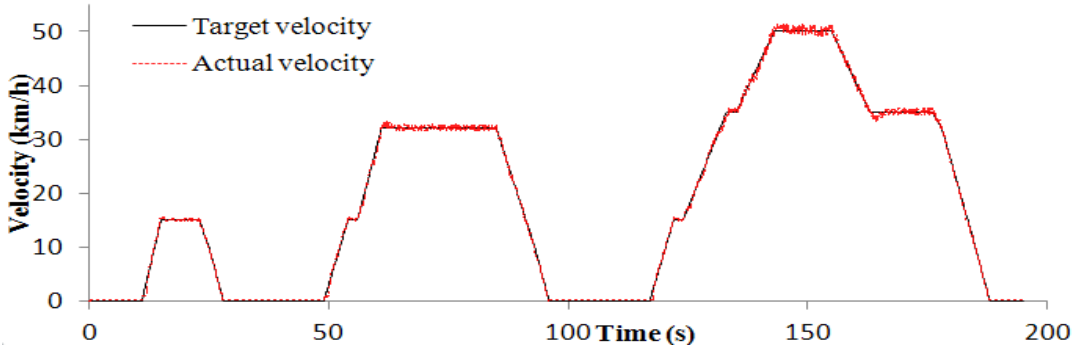



Fig. 7. Target velocity and actual velocity of the cycle run test

Fig. 7 shows that actual velocity tracks target velocity well. This indicates that the modules in the test platform are effectively and accurately constructed.

## Conclusion

This paper aims at signal-axis parallel hybrid powertrain test platform and accomplishes the following works:

1, Based on the structure analysis of the prototype truck and modular design method, accomplish the function module design of the test platform.

2, Construct hardware of each module and develop corresponding software for each module.

3, Verify the effectiveness and correctness of the test platform by a cycle run test.

## References

[1] Yanping Chen, Chenliang Yin, Yong Zhang: Automotive Engineering, 2011,33(6): 469-471. In Chinese.

[2] Weihua Wang, Qiqian Jin, Xiaohua Zeng, et al: Zhongguo Gonglu Xuebao(China J. Highw. Transp.), 2005, 18(2): 103-106. In Chinese.

[3] Yiming M, Huiyan C, Jianwei G, et al: Training, 2008, 2014: 06-02.

[4] Debal P, Faid S, Bervoets S, et al. Development of a Post-Transmission Hybrid Powertrain[C]//Proc. Electric Vehicle Symposium (EVS24), Stavanger. 2009.

*Advanced Materials Research Vol. 937 (2014) pp 351-356*
*© (2014) Trans Tech Publications, Switzerland*
*doi:10.4028/www.scientific.net/AMR.937.351*

# The Research of the Rolling Element Bearing Fault Signal Frequency Domain Feature Extraction Method Based on the Wavelet Packet Decomposition

Shi-yin QIU[1,a,*], Rui-bo YUAN[1,b]

[1]Faculty of Mechanical & Electrical Engineering, Kunming University of Science and Technology, Kunming, Yunnan Province 650500,P.R.China

[a]kgqsy163@163.com, [b]kmust_yrb@163.com

**Keywords:** Bearing Fault; Feature Extraction; Wavelet Packet Decomposition; Optimal Node; K-means Clustering; Pattern Recognition.

**Abstract.** The wavelet packet decomposition can be used to extract the frequency band containing bearing fault feature, because the fault signal can be decomposed into different frequency bands by using the wavelet packet decomposition, that is to say the optimal wavelet packet decomposition node needs to be found. A method applying the average Euclidean distance to find the optimal wavelet packet decomposition node was presented. First of all, the bearing fault signals were decomposed into three layers wavelet coefficients by which the bearing fault signals were reconstructed. The peak values extracted from the reconstructing signal spectrum constructed a feature space. Then, the minimum average Euclidean distance calculated from the feature space indicated the optimal wavelet packet node. The optimal feature space could be constructed by the feature points extracted from the signals reconstructed by the optimal wavelet packet nodes. Finally, the optimal feature space was used for the K-means clustering. The feature extraction and pattern recognition test of the four kinds of bearing conditions under four kinds of rotation speeds was detailed. The test results show this method, which can extract the bearing fault feature efficiently and make the fault feature space have the lowest within-class scatter, wons a high pattern recognition accuracy.

## Introduction

The main research content of mechanical equipment working condition monitoring and fault diagnosis is how to analysis and recognise the feature parameters captured from the external characteristic of a running equipment. The essence of the mechanical fault diagnosis is pattern recognition[1]. According to the statistics, there are 30% of rotation machinery faults caused by bearing fault and 90% of rolling bearing fault come from the faults of inner ring and outer ring[2,3]. One common method for fault diagnosis is to use the vibration signal sending out from the running machine. When the malfunction occurred in the bearing parts, the bearing parts will impact the trouble location and produce a series of impact vibration which can make the measured signal show the characteristics of non-stationary vibration signals[4,5]. The wavelet analysis method, which has been studied by scholars in the domestic and overseas, is suitable for processing the non-stationary transient signal due to the broadband frequency response of it. Therefore, many scholars take advantage of the wavelet analysis method to process the bearing vibration signal. Yang et al.[6] studied the method to extract the feature in time domain by using the wavelet packet decomposition. Yang et al. extracted the feature from the reconstruction signal reconstructed by the wavelet packet decomposition coefficients represented different frequency band. They set the variance and kurtosis as the parameters for fault recognition. This method presented by Yang et al. can not only recognise the bearing fault, but also exact the signal feature contained in one particular frequency band.

A method, which based on wavelet packet decomposition, for extracting the frequency domain feature was presented in this paper. First of all, the bearing vibration signal was decomposed into 3 layers by wavelet packet and obtained the reconstruction signals by reconstructing all decomposition nodes. Then constitute a fault feature space using fault feature points which is extracted from the

reconstruction signal. The bearing vibration signal energy distributed in different frequency band because the fault location and the bearing structure are different[2]. The optimal wavelet packet code, by which the reconstruction signal contained the most obvious fault feature could be reconstructed, needed be found in order to extract the bearing fault feature. Hence, the Average Euclidean Distance(AED) between feature points and the center of feature space needed to be calculated. If the AED of a feature space was minimal, the feature space was constituted from the optimal reconstruction signal which is reconstructed by the optimal wavelet packet decomposition code because the fault energy concentrated in the frequency band represented by the optimal decomposition code. In a word, the bearing vibration signal was decomposed into 3 layers by wavelet packet firstly, and then the maximum values of the reconstruction signals were regarded as the bearing fault feature points by which the feature space was constituted. Here, the 8 reconstruction signals were reconstructed by each code of the third layer(8 codes) of the wavelet packet decomposition. Then the AED of 8 feature spaces constituted from 8 reconstruction signals were calculated and the minimum AED represented the optimal wavelet packet decomposition code(WPDC). The optimal reconstruction signal, from which the optimal fault feature space was constituted, was reconstructed by the optimal WPDC next. At last, the optimal bearing fault feature space of four kinds of bearing state was established and used for the K-means clustering.

**Wavelet Packet Transform and Algorithm**

The wavelet packet transformation(WPT) is a kind of finer orthogonal decomposition method based on the multiresolution analysis, which can process the multilayer band allocation of the signal at full frequency band. The WPT, which inherited the good time-frequency localization characteristic of wavelet transformation, improved the frequency resolution because it continued to decomposite the high frequency band which the wavelet transformation didn't decomposite.

$$\begin{cases} d_k^{2m} = \frac{1}{2}\sum_L d_L^m h_{L-2k} \\ d_k^{2m+1} = \frac{1}{2}\sum_L d_L^m g_{L-2k} \end{cases} \tag{1}$$

The WPT can decomposite the low frequency and the high frequency parts of the signal simultaneously and adaptively determined the frequency resolution. The WPT decomposition and reconstruction algorithms are Eq. 1.

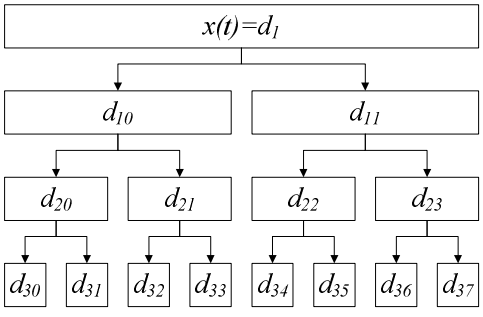



Fig. 1. The wavelet packet decomposition tree

Here $d_1 = \{x_k^t\}$ is the signal to be decomposed. The number of the sub-bands is 2N when the signal is decomposed into the Nth layer. The wavelet packet decomposition tree is showed in Fig. 1(N=3), which showed the third layer has a total of 8 decomposition codes.

The WPT can decompose the sinusoidal signal or any other signal into the corresponding frequency band, therefore each frequency band has a certain energy[2]. The optimal WPDC, which contained the fault feature, must be found because the different reconstruction signals which contained different bearing fault energy is reconstructed by different codes[3].

### The Average Euclidean Distance

The average euclidean distance, which is used for evaluating the within-class dispersion, is the most commonly used distance exponent in hierarchical clustering method. The minimum average euclidean distance is used for evaluating the degree of bearing fault energy concentration in a frequency band. If the frequency band in which the fault energy most concentrated is found, the optimal WPDC is sought out simultaneously. The average euclidean distance between the $i$ th sample $x_{ik}$ and the mean value of all the samples is shown in Eq. 2. Here, $n$ is the total of the $i$ th sample.

$$d_i = \frac{1}{n}\left[\sum_{k=1}^{n}(x_{ik}-\mu_i)^2\right]^{\frac{1}{2}} \tag{2}$$

## Experiment and Analysis

### Preparations

The rolling bearing experiment datum from the Case Western Reserve University Bearing Data Center[8] were used for demonstrating the effectiveness of the method presented in this paper. The bearing vibration datum used for experiment and analysis were collected from the drive side of the motor. The acceleration sensor was applied to measure the vibration signal. The sample frequency is 12KHz. The type of the bearing used in our experiment is 6205-2RS JEM SKF, the pitch diameter of the bearing is 39.04mm, the number of the rolling element is 9, the diameter of the rolling element is 7.94mm. The bearing fault vibration datum of the inner, outer, rolling elements and the trouble-free vibration datum captured from the bearing under the four rotate speeds (1730rpm, 1750rpm, 1772rpm, 1797rpm). The total number of datum is 800 among which there were 200 datum, among which there are 50 datum corresponding to 4 bearing running status, corresponding to 4 rotate speeds and the duration time of each data was 0.1s. The feature extraction and the pattern recognition methods for four bearing running statuses under the rotate speed of 1750rpm were detailed in this paper. The methods for bearing fault status recognition under other three rotate speeds were as same as the methods mentioned above.

### Feature Extraction of the Bearing Running Status

The vibration datum under the rotate speed of 1750rpm included four kinds of bearing running status(inner,outer, rolling elements fault statuses and the trouble-free status), the total number of which is 200. Each of the bearing status contained 50 datum which were divided into training set(20 datum) and test set(30 datum). Every data of each bearing status in the training set was decomposed into 3 layers by wavelet packet decomposition. Hence, the total number of the decomposition code in the third layer is 8, from which the peak values of 8 reconstruction signals reconstructed were extracted and used for feature points. Therefore, each of the bearing status would have a 20×8 feature space(160 feature points), of which the first column represented the feature points extracted from the reconstruction signal reconstructed by the [3,0] code and so on.

As space is limited, only two feature spaces constituted from reconstruction signals reconstructed by the [3,1] code and [3,4] code under the rotate speed of 1750rpm were showed in this paper. As shown in the Fig. 2, the symbol ”+” , ”*”, ”∇”, ”○” and ”×” are represented the feature points of inner fault, outer fault, rolling elements fault, trouble-free status and the center point(the mean point) of bearing status feature points respectively. The Fig. 2 shown that in the feature space of the [3,1] code the distribution of four kinds of bearing status feature points were sparse and the distances between three feature point centers of the outer fault, the rolling fault and the trouble-free were short and formed a certain overlap. The distribution of the rolling elements feature points and trouble-free status feature points in the feature space of the [3,4] code was tight, but the distribution of the inner fault and outer fault was sparse. The experiment results showed that the feature points distribution density of the reconstruction signals was related to the selection of the WPDC, which indicated that

different bearing fault feature located in different frequency band. As a result, the optimal WPDC, by which the reconstruction signal contained the most obvious fault feature reconstructed, needed to be found in order to accurately extract the bearing fault feature. If so, the distribution of the fault feature points would be tighter, which could improve the accuracy of the bearing fault pattern recognition.

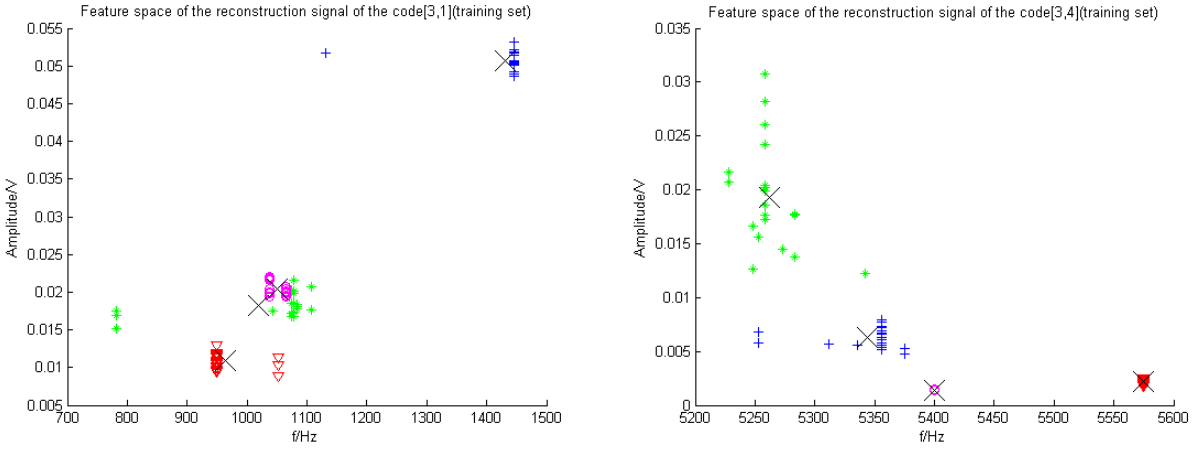



Fig. 2. The feature space of the reconstruction signal(1750[rpm])

The AED is used as the density standard of the feature point distribution in this paper. The AED of four bearing statuses features extracted from 8 reconstruction signals reconstructed by 8 wavelet packet decomposition were shown in the Table 1.

Table 1. The average euclidean distance(1750[rpm])

| Status<br>Codes | Inner fault | Outer fault | Rolling element fault | Trouble-free |
|---|---|---|---|---|
| [3,0] | 0.0027 | 73.9984 | 8.11E-04 | 6.50E-04 |
| [3,1] | 29.9016 | 95.3699 | 26.4662 | 14.0874 |
| [3,2] | 42.5410 | 0.0048 | 16.0132 | 2.06E-04 |
| [3,3] | 51.9344 | 0.0022 | 171.8204 | 3.01E-04 |
| [3,4] | 22.4262 | 15.0866 | 1.31E-04 | 2.04E-05 |
| [3,5] | 180.9836 | 45.2102 | 30.0494 | 5.24E-05 |
| [3,6] | 84.8607 | 10.3380 | 0.0030 | 4.19E-05 |
| [3,7] | 42.4918 | 24.9052 | 7.31E-04 | 1.06E-04 |

The datum in the Table 1 shows that the AED of the [3,0] code is minimum, which indicated that the reconstruction signal reconstructed by the [3,0] code contained the inner fault feature under the rotate speed of 1750rpm. Therefore, the optimal WPDC is [3,0]. By that analogy, the optimal WPDC of other three bearing statuses under other three rotate speeds can be found, which were shown in the Table 2. After the optimal WPDC is found the optimal reconstruction signal can be reconstructed by the optimal WPDC.

Table 2. The optimal wavelet packet decomposition code

| Status<br>RPM/[rpm] | Inner fault | Outer fault | Rolling element fault | Trouble-free |
|---|---|---|---|---|
| 1730 | [3,0] | [3,0] | [3,1] | [3,5] |
| 1750 | [3,0] | [3,3] | [3,4] | [3,4] |
| 1772 | [3,0] | [3,6] | [3,0] | [3,4] |
| 1797 | [3,0] | [3,0] | [3,3] | [3,4] |

Reconstructed the optimal WPDC of four bearing statuses under 1750rpm and extracted the feature points from the reconstruction signals, which constituted the optimal feature space of the training set as shown in the Fig. 3. Then the optimal feature space was used for the K-means clustering. The K-means clustering results of the training set shown in the Fig. 3 were obtained by repeating what mentioned above.

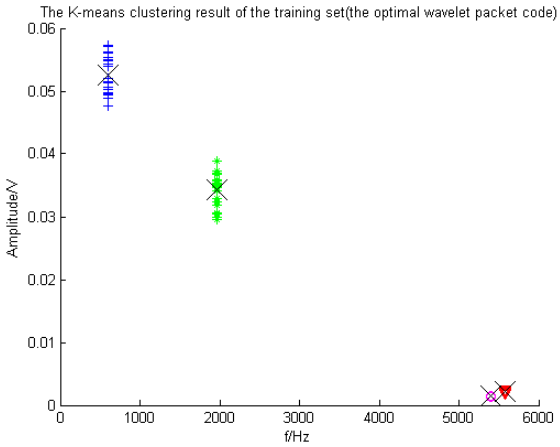



Fig. 3. The optimal feature space of the training set(1750[rpm])

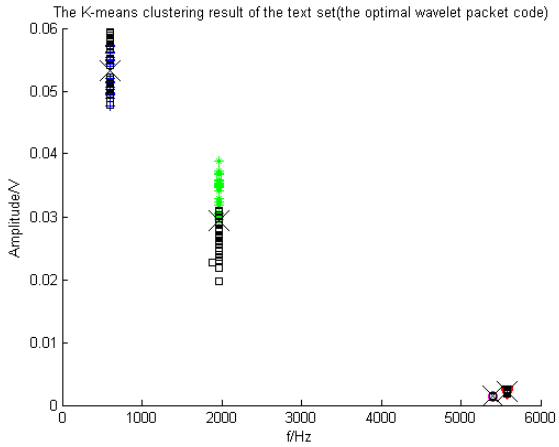



Fig. 4. The optimal pattern recognition feature space(1750[rpm])

Table 3. The K-means clustering results of the training set (1750[rpm])

| Bearing status | Feature | Clustering number | Features in class | Accuracy |
|---|---|---|---|---|
| Inner fault | 20 | 1 | 20 | 100% |
| Outer fault | 20 | 2 | 20 | 100% |
| Rolling element fault | 20 | 3 | 20 | 100% |
| Trouble-free | 20 | 4 | 20 | 100% |

The Fig. 3 shows that the feature points distributed into four areas obviously, which represent four bearing running statuses(inner fault, outer fault, rolling element fault and trouble-free). The distance between the four areas, in which the feature points distribute tight, are long. The symbol ”×” represents the clustering center. There were 4 clustering centers were found and the feature space(80 feature points) were divided into four classes after the feature spaces were clustered using K-means clustering. The clustering results(1750rpm) shown in the Table 3 indicate that all of the 20 inner fault feature points are classified into class 1, which demonstrate that the accuracy of the clustering is 100%. The K-means clustering results of other three rotate speeds show that the clustering accuracy is 100% too. The high clustering accuracy of the training set is beneficial to the bearing fault pattern recognition accuracy of the test set.

**The Bearing Status Pattern Recognition**

The optimal WPDC and feature space have found before using AED and then the datum of the test set(each of the bearing status account for 120 datum) were decomposed into 3 layers by wavelet packet decomposition. Next, the optimal feature space of the test set was constituted from the reconstruction signals reconstructed by the optimal WPDC which had been found before. Then the optimal feature spaces of the text set and the training set are combined into an optimal pattern recognition feature space which was used for the K-means clustering. The results of the K-means clustering(1750rpm) was shown in Fig. 4.

The sample ”□” in the Fig. 4 represented the feature point of the test set. The results shown in above pictures shown that the feature points of the test set distributed into four areas which almost overlapped with the feature areas of the training set. Therefore, we could recognise the bearing statuses of the test set by using the optimal feature space for K-means clustering.

The pattern recognition results of the test set(1730rpm) are shown in the Table 4. One feature point of outer fault is recognised to an inner fault feature point wrongly, which the patter recognition accuracy reaches 96.67%. All pattern recognition accuracy of the other three bearing status is 100%.

Table 4. The K-means clustering results of the text set(1730[rpm])

| Bearing status | Feature | Clustering number | Features in class | Accuracy |
|---|---|---|---|---|
| Inner fault | 30 | 1 | 30 | 100% |
| Outer fault | 30 | 2 | 29 | 96.67% |
| Rolling element fault | 30 | 3 | 30 | 100% |
| Trouble-free | 30 | 4 | 30 | 100% |

Table 5. The K-means clustering results of the text set(1750[rpm])

| Bearing status | Feature | Clustering number | Features in class | Accuracy |
|---|---|---|---|---|
| Inner fault | 30 | 1 | 30 | 100% |
| Outer fault | 30 | 2 | 30 | 100% |
| Rolling element fault | 30 | 3 | 30 | 100% |
| Trouble-free | 30 | 4 | 30 | 100% |

The results of the pattern recognition shown in Table 5 shown that all recognition accuracy of four bearing statuses(1750rpm) is 100% and all the bearing status recognition results under the other two rotation speeds(1772rpm and 1797rpm) are 100% too, which indicates that the method presented in this paper is effective.

**Conclusions**

The research results demonstrate that the features of different bearing status locate in different frequency band. The frequency band contained the most obvious feature can be found by using wavelet packet decomposition on one hand, and the optimal wavelet packet decomposition nodes, by which the optimal reconstruction signals can be reconstructed, can be sought out on the other hand.The feature space constituted by the feature points, which are the maximum values of the optimal reconstruction signals, have the lowest within-class scatter, which indicates that the optimal reconstruction signals contain the most obvious feature of the bearing status. The experiment results prove the feature extraction method for the rolling element bearing is efficient, which can obtain high accuracy for the bearing status pattern recognition. This method provides a new idea for the status feature extraction of the rolling element bearing.

**References**

[1] G.G. Xu, J. Yin. The Realization of The Pattern Recognition and Intelligence Calculation Based on MATLAB, Bei Jing, 2012. (In Chinese)

[2] Y. Tian, S. Lu, Fault pattern recognition of rolling bearing based on wavelet packet and

support vector machine, 6(2006), pp.236-246.

[3] F. Sun, Z.J. Wei, Rolling bearing fault diagnosis based on wavelet packet and RBF neural network, Proceedings of the 26th Chinese Control Conference, 2007, pp.451-455.

[4] K. Teotrakool M.J. Devaney, Adjustable-speed drive bearing-fault detection via wavelet packet decomposition, IEEE Transactions on Instrumentation and Measurement, 2009, 58(8), 2747-2754.

[5] L. EREN, M.J. DEVANEY, Bearing damage detection via wavelet packet decomposition of the stator current, IEEE Transactions on instrumentation and measurement, 2004, 53(2), 431-436.

[6] G.A Yang, B.L. Zhong, third ed., The research of the rolling element bearing fault signal time domain feature extraction method based on the wavelet packet decomposition, Journal of Vibration and Shock, 2001, 20(2), pp.25-28. (In Chinese)

[7] D.K. Zhang, Y.J. Wang, Statistical properties of random mean euclidean distance and measure of categorical threshold, Journal of Tianjin University of Science & Technology, 2008, 23(4), pp.85-88. (In Chinese)

[8] These data comes from Case Western Reserve University Bearing Data Center website, http:// www. eecs. cwru. edu/ laboratory/ bearing.

*Advanced Materials Research Vol. 937 (2014) pp 357-362*
*© (2014) Trans Tech Publications, Switzerland*
*doi:10.4028/www.scientific.net/AMR.937.357*

# The Influence of the Diameter Ratio between Rigid Body and Particle on the Impact Strength Exerted on the Rigid Body Impacting Particles

Jian-Dong LU [1,a] Lu-Hai LI [1,b] and Gai-Mei ZHANG [1,c]

[1]Beijing Institute of Graphic Communication, Beijing 102600, P. R. China

[a]lululu0831@sina.com, [b]liluhai@bigc.edu.cn, [c]zhanggaimei@bigc.edu.cn

**Keywords:** Granular Particle; Rigid Body; Impact; Diameter Ratio

**Abstract:** Granular particles exist widely in the nature. The purpose of this paper is to research the impact interaction between rigid body and particles. The diameter ratio between rigid body and particle has the effect on the impact strength exerted on the rigid body impacting particles. In this paper, the same rigid body impacts respectively the particles with five different diameters. The effect of the diameter ratio is analyzed theoretically according to this simulation experiment. With diameter ratio increasing, the vertical velocity, mechanical energy and momentum of the rigid body increase, and the force exerted on the rigid body decreases.

## Introduction

Granular particles exist widely in the nature. Granular particle is not only the continuum which is made up of solid particles, but also the special material which is different from the solid and fluid [1.2]. The impact interaction between rigid body and particle also exists widely in the nature and the production field, such as, stone falling into the sand; the contact, collision and friction between the granular media and transmission machine. In this physical process, if the impact strength exerted on the rigid body is very big, the rigid body will be damaged. For example, during the process of spacecraft landing on the moon, the landing pad will be damaged if the impact strength exerted on the landing pad is too big. The process of the rigid body colliding with the particles is very complex. The particles show the shift from solid state to liquid state during the impact. Based on different perspectives, scientists study the particle properties of this process by experimental and theoretical methods.

The research perspective of this paper includes two parts. Firstly, compared with the whole process of rigid body impacting the particles, the impact strength exerted on the rigid body in the initial stage is bigger than in the other stages. This paper focuses on the impact strength exerted on the rigid body in the initial stage. Secondly, this paper is based on the experiments that the same rigid body impacts respectively the particles with different diameter. The effect of different diameter ratio between the rigid body and the particles on the impact strength is analyzed.

## Experiment

### Design of the Experiment

The steel balls with uniform density and regular size is the research objects. The steel ball with diameter 20mm simulates the rigid body [3-5]. For removing the influence of different material particles on the research purpose, the particles are also simulated by the steel balls with small size. The five kinds of particles are simulated respectively by steel balls with the diameter: 5mm, 4mm, 3mm, 2mm and 1mm. The steel ball with 20mm diameter impacts respectively the dense particles composed of different size steel balls, in order to analyze the effect of the diameter ratio between the rigid body and the particle on the impact strength exerted on the rigid body in the initial stage.

The diameter ratios between the rigid body and the particle are shown in Table.1.

Table 1. The diameter ratios between the rigid body and the particle

| The diameter of the rigid body (mm) | The diameter of the particle (mm) | The diameter ratio |
|---|---|---|
| 20 | 1 | 20:1 |
| | 2 | 20:2 |
| | 3 | 20:3 |
| | 4 | 20:4 |
| | 5 | 20:5 |

The steel ball with 20mm diameter freely falls at the same height, and impacts the dense particles made up of many small size steel balls. As the impact rigid body, the steel ball with 20mm diameter impacts respectively on five different diameter particles composed of steel balls. In the five impact processes, the same phenomenon is observed. Start the clock when the impact rigid body contacts the surface of the particles, after 0.004s the half volume of the rigid body almost impacts into the particle pile. The impact process of 0.004s, as the initial stage of the whole impact process, is researched in this paper. During 0.004s many physical parameters change. In this initial stage, the force and energy change of this impact rigid body is analyzed through measuring these several physical parameters.

**Experimental Apparatus**

The experimental apparatus is composed of a high-speed camera, the bracket that regulates the release height, the transparent container filled with small size steel balls. Schematic diagram is shown in Fig. 1.

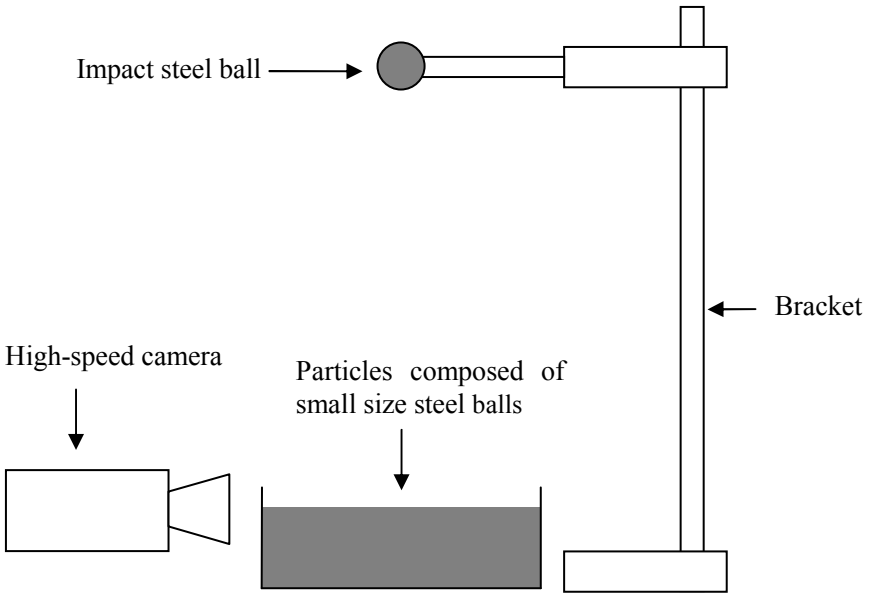



Fig. 1. The schematic diagram of experimental apparatus

**Experimental Process**

At a distance of 30mm above the surface of particles, the steel ball with diameter 20mm, as the impact rigid body, freely falls without initial velocity. The process, from the impact rigid body beginning contacting the surface of particles to the impact rigid body entering the particles for 0.004s, is recorded by the high-speed camera. Then, the displacement and velocity of the impact rigid body is acquired through the data acquisition function of the high-speed camera. As shown in Fig.2, the cross line is used to collect the displacement and velocity of the impact rigid body.

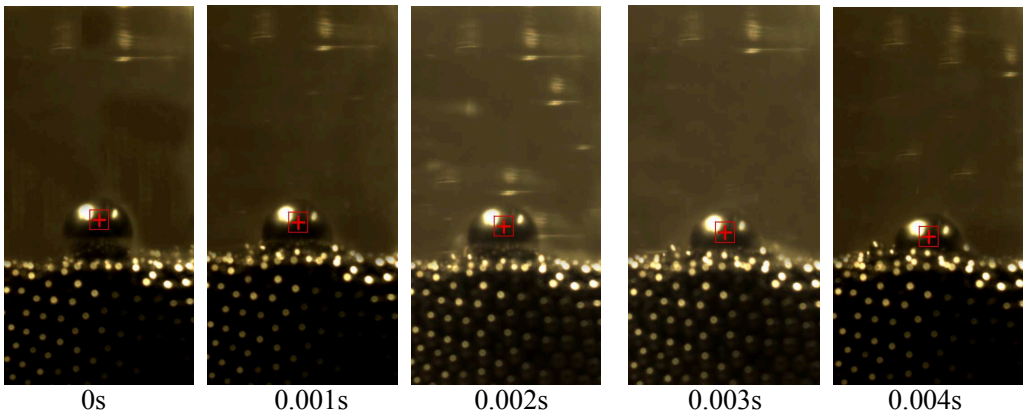



Fig. 2. The process of steel ball impacting particles

## Result and Analysis

### The Effect of the Diameter Ratio between the Rigid Body and Particle on the Velocity of the Rigid Body

According to the velocity change of the impact rigid body in the initial stage, Fig.3 and Fig.4 are plotted.

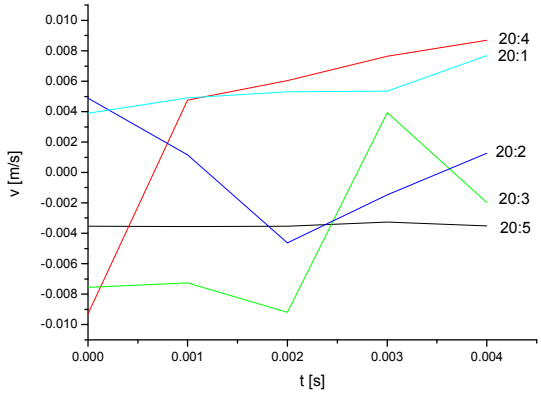



Fig. 3. The relation between horizontal velocity and impact time in the initial impact stage

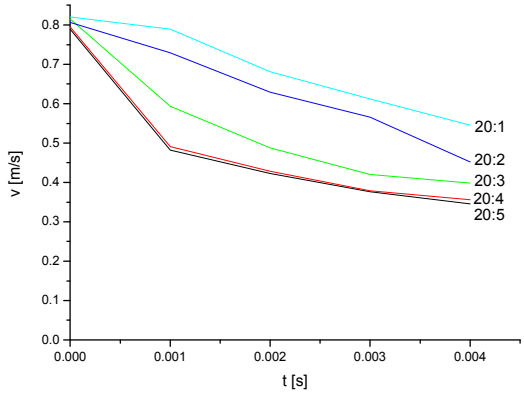



Fig. 4. The relation between vertical velocity and impact time in the initial impact stage

In the Fig.3, the horizontal velocity of the impact rigid body is random in the initial impact stage. In addition, the horizontal velocity is much smaller than the vertical velocity by comparing Fig.3 to

Fig.4. So the horizontal velocity can be neglected. The research direction focuses on the change of the vertical velocity.

As shown in Fig.4, in the initial impact stage, the vertical velocity of the rigid body decreases with the increasing of the impact time. By comparing the five curves, the vertical velocity at the same point increases with the increasing of the diameter ratio. The reason for the different vertical velocities caused by different diameter ratios can be analyzed from the perspective of energy transferring and dissipation.

The displacement at the surface of the particles is assumed to be zero. The vertical downward direction is assumed to be positive. Therefore, according the displacements of the rigid body recorded by the high-speed camera, Fig.5 is plotted.

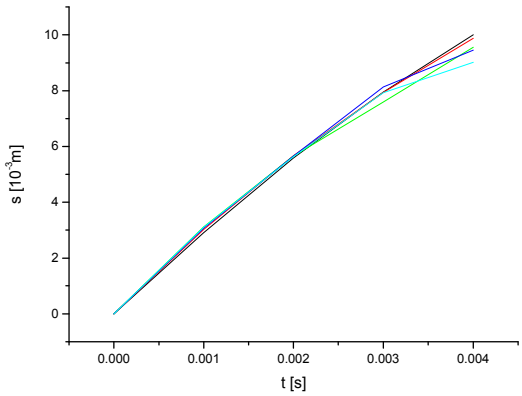



Fig. 5. The relation between displacement and impact time in the initial impact stage

Substitute the data of the displacement and velocity shown in the Fig.4 and Fig.5 into Eq.1.

$$E=mgh+ mv^2/2 \quad (1)$$

E is the mechanical energy of the rigid body; mgh is the potential energy, because the potential energy at the surface of the particles is assumed to be zero, h is the negative value of the displacement shown in Fig.5; $mv^2/2$ is the kinetic energy, m is the mass of the rigid body; v is the vertical velocity of the rigid body. According to the calculation results, the relation between the mechanical energy and the impact time is shown in Fig.6.

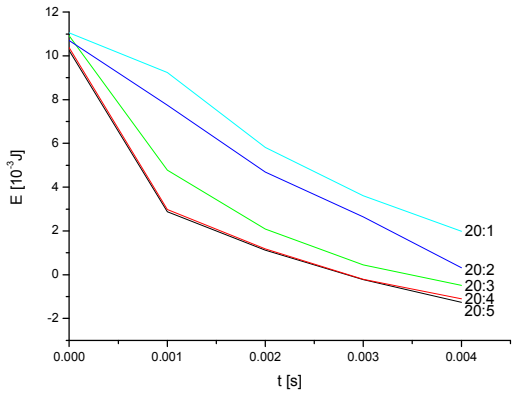



Fig. 6. The relation between mechanical energy and impact time in the initial impact stage

When the particles are impacted by the rigid body, some mechanical energy of the rigid body is absorbed by the particles. The mechanical energy absorbed is mainly changed into the elastic deformation of the particles, the friction between the particles and the thermal energy among the particles [6]. Because the particles with smaller diameter have the more contact area, there are more chances of relative movement and friction among the smaller particles. There are more chances of

transferring energy among the smaller particles. In addition, the smaller particles have the less ability of elastic deformation. Therefore, the smaller particles need more time to absorb the same mechanical energy of the rigid body during the impact. So, in the bigger diameter ratio condition, the mechanical energy of the impact rigid body dissipates more slowly, the kinetic energy of the impact rigid body decreases more slowly, and the vertical velocity of the impact rigid body decreases more slowly.

The tendency shows that in the same span less mechanical energy of the rigid body is transferred into the particles when the rigid body impacts the particles with smaller diameter. So, less mechanical energy of the rigid body is reduced in the same span when the rigid body impacts the particles with smaller diameter. As shown in Fig.5, the mechanical energy of the rigid body at the same time point increases with increasing of the diameter ratio.

**The Effect of the Diameter Ratio between the Rigid Body and Particle on the Vertical Force of the Rigid Body**

Substitute the data of the velocity shown in the Fig.4 into Eq.2. The momentum change of the impact rigid body can be calculated.

$$P=mv \tag{2}$$

P is the vertical momentum of the rigid body; m is the mass of the rigid body; v is the vertical velocity of the rigid body. According to the calculation results of the momentum, Fig.7 is plotted.

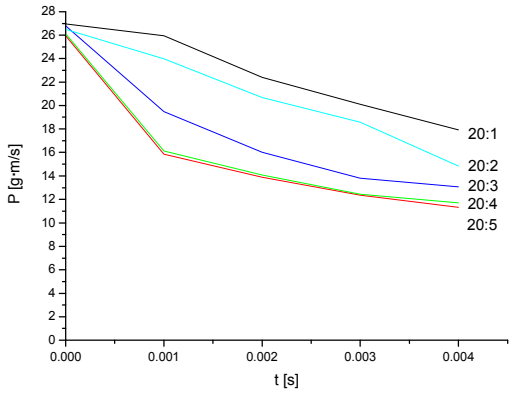



Fig. 7. The relation between momentum and impact time in the initial impact stage

As shown in Fig.7, the momentum of the rigid body at the same point increases with increasing the diameter ratio.

According to Eq.3, the relation between momentum and impulse, Eq.4 can be derived.

$$\Delta mv=Ft \tag{3}$$

Δmv is the change value of the vertical momentum; F is the vertical force exerted on the rigid body by the particles; t is the impact time.

$$F=\Delta mv/t \tag{4}$$

According to the Eq.4, because the rigid body freely falls from the same distance above the surface of particles, all the vertical velocity of the rigid body are the same in the five diameter ratio conditions when the rigid body contacts the surface of the particles. After the same span, the five vertical momentums of the rigid body impacting on the five different diameter particles are different. The momentum of the rigid body decreases at the same point with deceasing of the diameter ratio between the rigid body and the particle. According to Eq.4, because the time span t is the same, the bigger change value of the vertical momentum Δmv, the bigger force F exerted on the rigid body. So, the vertical force exerted on the rigid body at the same point increases with

decreasing of the diameter ratio between the rigid body and the particle. Therefore, the force exerted on the rigid body is bigger when the rigid body impacts the bigger size particles.

## Conclusions

The diameter ratio between the rigid body and the particle is has an effect on the vertical velocity, mechanical energy, momentum and exerted force of the impact rigid body. In this experiment, the steel ball with diameter 20mm simulates the rigid body, and the five kinds of particle are simulated respectively by steel balls with different diameters: 5mm, 4mm, 3mm, 2mm and 1mm. According to experimental results, the influence of the diameter ratio is qualitatively analyzed. With diameter ratio increasing, the vertical velocity, mechanical energy and momentum of the rigid body increase, and the force exerted on the rigid body decreases.

## Acknowledgements

This work is supported by the surface science and technology plan project of Beijing education commission (No. KM201310015001); the talent training project of Beijing municipal organization department (No. 2012D005004000002)

## References

[1] Wei Ma, *Dynamical behavior of granular materials under impact* (Ph.D., Peking University, China 2008) 1-5. (In Chinese)

[2] Detlef Lohse, Raymond Bergmann, Rene´ Mikkelsen etc, Physical Review Letters, 93 (2004) 198003.

[3] S. Deboeuf, P. Gondret, M. Rabaud1g, Physical Review, E 79 (2009) 041306.

[4] J. F. Boudet, Y. Amarouchene, H. Kellay, Physical Review Letters, 96 (2006) 158001.

[5] Zhen Zhao, Caishan Liu, Physical Review, E 78 (2008) 031307.

[6] E.L. Nelson, H. Katsuragi, P. Mayor, D.J. Durian, Physical Review Letters, 101 (2008) 068001.

*Advanced Materials Research Vol. 937 (2014) pp 363-369*
*© (2014) Trans Tech Publications, Switzerland*
*doi:10.4028/www.scientific.net/AMR.937.363*

# Research on Perovskite Catalysis for Diesel Engine Exhaust Removal

Peng Liang [1,a], Qianyang Chen[2,b] Haibo Long[3,C]

[1]Colleage of Chemical Engineering and Material Science, Eastern Liaoning University, 325 Wenhua Road, Dandong, Liaoning, 118003, China

[2]Experimental Center, Eastern Liaoning University, 325 Wenhua Road, Dandong, Liaoning, 118003, China

[3]Journal editorial department, Eastern Liaoning University, 325 Wenhua Road, Dandong, Liaoning, 118003, China

[a]Email: liangpenglong@163.com, [b]email: SYZXCQY@163.com, [C]Email longhaibo1965@163.com

**Keywords:** Catalyst; Perovskite; Diesel; Removal

**Abstract.** Diesel engine emissions of nitrogen oxides and particulates are the major source of air pollution that is a serious threat to human health. Diesel emissions treatment technology meet the increasingly stringent emission standards through the current difficulty and develop a new diesel engine exhausted treatment technology to further reduce the nitrogen oxide and particulate emissions are from diesel engines. In this paper, $La_{1-x}A_xCo_{1-y}B_yO_3$ complex perovskite catalysts for diesel engine exhaust emission purification carry out the relevant research, this article firstly study the perovskite oxide catalyst preparation methods, as the catalyst preparation process are described .Then the activity of the catalyst samples obtain some useful results.

## Introduction

In the early 20th century and the early 70s, Libby began on the oxidation of rare earth perovskite oxides that made a systematic study of hydrocarbons, and it is expected to rare earth perovskite oxides that can not be compared with the advantages of other catalysts [1]. It proposes the perovskite structure of complex oxides that can be used for automobile exhaust purification catalyst, instead of some or all of noble metal catalyst. Perovskite oxides are usually available chemical formula $ABO_3$ as is said on A with the larger cation, the alkali metal, alkaline earth metals and rare earth metal ions. The B bit is a smaller cation and it is usually the transition metal ions. Catalytic electron B is a d-bit transition metal ions and A site ions are not directly involved in the reaction of nature, but if the different valence states were replaced by other ions, which can cause B valence change of position, and it may form lattice defects, thus it affects the catalytic activity. Part of the substituted perovskite compounds with the crystal structure of the non-integrity, is to explore the shortcomings of the model catalyst system. In recent years, Co is because of high catalytic activity, a perovskite-type metal oxide catalyst composition of B-bit hot, and La is the A site cation object of extensive research [2].

This article firstly studied the perovskite oxide catalyst preparation methods, as the catalyst preparation process is described. Then the activity of the catalyst samples is obtained some useful results.

## The Structure and Characteristics of Perovskite Type Oxides

Perovskite oxides are usually available chemical formula $ABO_3$, as the said A bit is the larger cation, the alkali metal, alkaline earth metals and rare earth metal ions, (rA> 0.090nm) oxygen atoms are in the composition of l2 tetrakaidecahedron Central, and l2 months of oxygen ions, while B is the smaller cation bit (rB> 0.057nm), the usual transition metal ions and oxygen ions are in the six octahedral center [3]. Measured in $ABO_3$ compounds, neutral compounds meet the requirements. An +, Bm + combinations subject to n + m = 6, and A is not higher than the valence of the valence state of B, i.e. $n \leq m$. It is generally believe that the perovskite-type ($ABO_3$) depends on the catalytic activity of B site cation. Cations on the perovskite structure have a stabilizing effect. It is a

bit different, however the prices can be substituted into $ABO_3$, and the formation of A1-x Ax'$BO_3$ is changing the oxidation state of B site cation, but it can also absorb more cations and lattice oxygen vacancy defect density, thereby , it can enhance the catalytic properties of $ABO_3$. $ABO_3$-type oxides should meet certain conditions in the synthesis on various ion sizes, otherwise the lattice becomes unstable. It will be distorted, or the formation is of other structures.

Goldschmidt tolerance factor has been the introduction of the expression [4]:

$$t = \frac{r_A + r_B}{\sqrt{2(r_B + r_O)}}$$

RA, Rb, rO are representing A, B, O ionic radius, when it is 0.75 <t <1, $ABO_3$ perovskite structure; when it is t <0.75 in order to ilmenite structure, when it is t> 1 being existing calcite or aragonite structure. In the perovskite structure, when it is t = 1.0, the formation of the highest symmetry is cubic lattice, when it is 0.96 <t <1, the lattice is rhombohedral structure, when it is t <0.96, the symmetry of the structure into quadrature. Advantages of perovskite catalysts are summarized as follows:

It can be changed within a wide range of elements in the composition and the composition while maintaining the basic perovskite crystal structure unchanged.

The main structure can be well described, and its surface structure can also be used to make the main structure of such a precise and reasonable estimates.

Valence, chemical measurement can change the number and the scope of the larger space.

A large number of people have gathered on the physical properties of perovskite and solid-state chemical nature of the information in the application of theory and the practice can learn from the example of many.

**Preparation**

Preparation of perovskite oxides are in many ways, such as: thermal decomposition [5], co precipitation [6], freeze drying [7] and low temperature combustion synthesis method [8]. In this study, low-temperature combustion synthesis is perovskite catalysts.

Low temperature combustion synthesis (Low-temperature combustion synthesis LCS) is a mixture of nitrate solution as the raw material of organic fuel ignition temperature is in the lower oxide powder prepared by a synthetic method [9-10]. Organic fuel and metal nitrates gel are heated strongly in redox reactions; this high surface area is available to combustion catalyst powder. For the catalyst prepared according to the chemical formula and the stoichiometric metal nitrates as well as the citric acid dubbed the proper concentration of mixed solution, are heating the solution, and makes it boiling and condensation until the explosive combustion of decomposed loose catalyst precursor. Ground after the precursor calcined at 350 °C 0.5h, it will remove the ground, then it calcined at 750 °C to form the catalyst powder obtained after 3h. The tablet, crushing, screening, got the required size of the $La_{1-x}K_xCo_{1-y}Fe_yO_3$ series of perovskite-type composite oxide catalyst. Chemicals used in preparation of Table 1, the process are shown in Fig. 1.

Table 1. Reagents used in catalyst preparation

| Name | Molecular formula | Source | Purity |
|---|---|---|---|
| lanthanum nitrate | $La(NO_3)_3.6H_2O$ | Tianjin Institute of Chemical Recovery surprising | >980% |
| ferric nitrate | Fe(NO3)3 | Tianjin Bodi Chemical Co., Ltd. | >990% |
| cobaltous nitrate | $Co(NO_3)_2 \cdot 6H_2O$ | Tianjin Damao Chemical Reagent Factory | >990% |
| potassium nitrate | $KNO_3$ | Tianjin Bodi Chemical Co., Ltd. | >990% |
| citric acid | $C_6H_8O_7$ | Tianjin University, Kuwait Company | >995% |

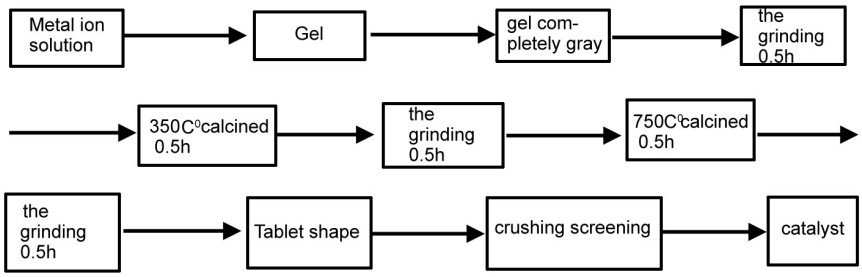



Fig. 1. Catalyst preparation process

## Experimental Apparatus and Equipment

AVL Digas 4000-type five gas analyzer, AVL, Austria

X-ray diffraction (XRD, X-ray Diffraction) instrument, Rigaku D / max 2500v/pc, test conditions: radiation sources for the CuKα, the target operating voltage 40kV, operating current 150mA, 18kW high-power rotating anode X-ray generator . Scan range: 10o-80o angle Rigaku Corporation of Japan marked 1o

Specific surface area (BET) analyzer, NOVA-2000, N2 as filling gas, the porosity can be measured: 3.5-2000 Egypt, specific surface area ≥ 0.01m2 / g; minimum resolvable relative pressure (P / Po): 2 × 10-5. Quanta chrome Corporation United States

X-ray photoelectron spectroscopy (XPS, X-ray Photoelectron Spectroscopy) instrument, PHI-1600, U.S. PE firm

Environmental scanning electron microscope (SEM, Scanning Electron Microscope), XL30ESEM, Netherlands Phillips

Tecnai G2 F20 field emission transmission electron microscopy (TEM, Transmission Electron Microscopy) Netherlands phlilps

TG - DTA spectrometer (TG / DTA), Pyris, Perkin-Elmer Corporation United States

Muffle furnace, SX2 series Rongfeng Scientific Instruments Co., Ltd. Shanghai Pudong, Shanghai Science Instrument Factory jump Chinko

## The Catalytic Activity

### NOx Catalyst for Diesel Engine Exhaust Gas is in Purification Catalytic Activity

The $NO_x$ catalyst for diesel exhausts is the evaluation of the catalytic activity of small procedures in the laboratory to complete the reactor temperature (device is shown in Fig. 2). Response systems include gas generation, gas purification and exhaust gas analysis in three parts. Test conditions: diameter of φ10mm quartz micro-reactor at atmospheric pressure, temperature programmed range of 250 °C ~ 700 °C, the amount of catalyst is 2ml, 20 ~ 40 mesh, the reaction gas (i.e., diesel exhaust) the composition is shown in Table 2-3, airspeed is 20000h-1, the reaction gas is into the reactor before the pre-filter to remove one of the particles. The reaction around the exhausted $NO_X$ content from AVL4000 five gases exhausts analyzer test. $NO_X$ conversion efficiency is (x %) said the catalyst for the purification activity. PM discusses the role of $NO_X$ purification process and selects the highest catalytic activity of the catalyst that were compared $La_{0.7}K_{0.3}C_0O_3$ experiments, it directly exhausts into the micro reactor.

Table 2. The main composition and concentration of diesel

| Main components | CO | $CO_2$ | $O_2$ | Total Hydrocarbon | $NO_X$ | particulate matter | $N_2$ and others |
|---|---|---|---|---|---|---|---|
| units | Vol% | Vol% | Vol% | $10^{-1}$ | $10^{-1}$ | glm | Vol% |
| concentration | 0.0 | 5 | 5 | 120 | 432 | 0.075 | rest |

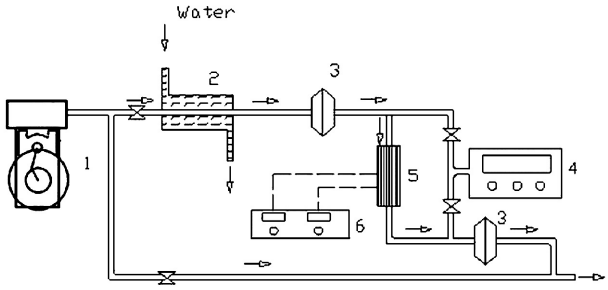



Fig. 2. Diesel exhausted in NOX catalytic activity evaluation device

Teraoka, who believes that the perovskite-type catalytic activity depends on the transition metal ions on the amount of oxygen vacancies near the number of its thermodynamic stability? When the lower substitution ($x \leq 0.3$), the catalyst surface oxygen vacancies and the substitution rate are proportional to, though the specific surface area of the catalyst samples increases with the substitution decreases, but the unit mass of the sample surface oxygen vacancies increased with the substitution and catalytic activity will increase accordingly. When it is $x \geq 0.4$, the catalyst surface oxygen vacancy rates increases with the substitution x (there $Co_3O_4$ phase) and it is gradually decreased. Meanwhile, the BET value decreases the catalyst samples.

Therefore, the unit mass of catalyst surface oxygen vacancies increases with the increase of substitution and x reduction activity is also reduced accordingly. Therefore, when a substitution element is for the K 0.3, the maximum catalytic activity of the catalyst is relative.

The catalytic decomposition of NO is mainly carried out through the following reaction:

$$4NO \rightarrow N_2 + 2NO_2$$

$$2NO_2 \rightarrow 2NO + O_2$$

NO in the perovskite catalyst is the decomposition of gas-solid heterogeneous catalysis, diffusion, adsorption, surface reaction and desorption steps. When the reaction temperature is lower, it is conducive to the adsorption of NO molecules, but it is not conducive to the activation of NO molecules and dissociation, so the low temperature activation and dissociation of NO are the reaction controlling step. When the reaction temperature is high, it is conducive to the activation of NO molecules and dissociation, but it is not conducive to the adsorption of NO molecules, and thus the high temperature adsorption of NO molecules controls the reaction step. Therefore, the temperature gradually increases with NO and NO adsorption capacity decrease ability to enhance the activation and dissociation, so the $NO_X$ purification efficiency is on the increase; when the NO adsorption, dissociation and desorption of the product reach equilibrium. $NO_X$ maximum purification is effective when the temperature continues rises. NO adsorption step of a reaction and $NO_X$ removal efficiency is dramatically. If the exhausted particulate matter presents in (PM), which is adsorbed on the catalyst surface and it will be formed on the surface C $NO_2$ reaction:

$$C + 2NO_2 \rightarrow CO_2 + 2NO$$

Thus it is accelerating the dissociation of NOx. This time, $NO_X$ removal efficiency than the exhaust does not contain particulate matter (PM) when it is high.

B-substituted $LaCo_{1-y}Fe_yO_3$ for $NO_X$ removal efficiency is shown in Fig. 3:

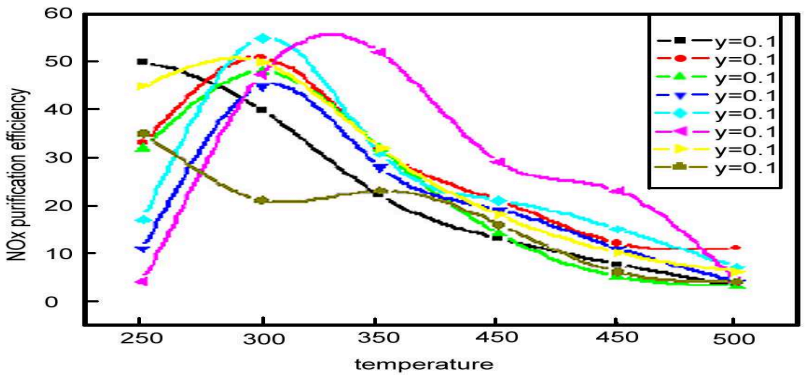


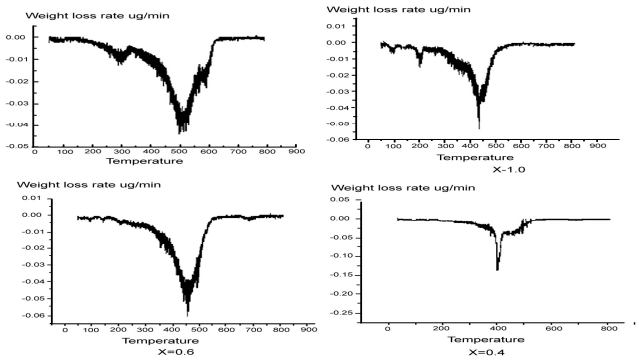

Fig. 3. $LaCo_{1-y}Fe_yO_3$ the efficiency of the $NO_X$ purification

**The Catalyst in Air Particulate Matter (PM) of the Catalytic oxidation**

In this study, we can use thermogravimetry and differential thermal device to characterize the catalyst on the conversion efficiency of PM. The instrument for the United States is produced by Perkin-Elmer Pyris-type TG - DTA spectrometer (TG / DTA). It is operating under the protection of nitrogen atmosphere, the gas flow rate is 20ml/min, and the weight is the biggest instrument 200mg with the heating rate of 10 °C / min, and the measurement temperature range is 35 ~ 850 °C.

Experiments on the wall from the small amount of diesel exhaust soot drys oven at 80 °C after drying, taking a small amount of dry soot, respectively, and $La_{1-x}K_xCoO_3$ series mass ratio of catalyst is 1:1 ratio, and it is in the agate mortar soot on the ground to dry in close contact with the catalyst and then it mixs well. Samples were recorded as follows: Sample # 1 dry soot; sample # 2 X = 1.0 catalyst mixed with the dry soot; sample # 3 X = 0.6 catalyst mixed with the dry soot; sample # 4 X = 0.4 catalyst and dry soot mixed; sample # 5 X = 0.2 catalyst mixed with the dry soot; sample # 6 X = 0 of the catalyst mixed with the dry soot.

As is shown below, from the # 1 hot double integral , it can be seen that the dry soot at 300 °C with a weak mass loss peak and the temperature range from dry to see this , it should be attached to the SOF soot combustion; another time is at 510 °C. There is a strong weight loss peak, where it should be the burning of dry soot, indicating that pure dry soot reaction occurs at 510 °C according to TG data , it shows that at 510 °C, the quality of the dry soot decreases the fastest. # 2 ~ # 6 is by the Thermogravimetric integral curve we can see that X takes on different values of dry soot on the catalyst's weight loss:



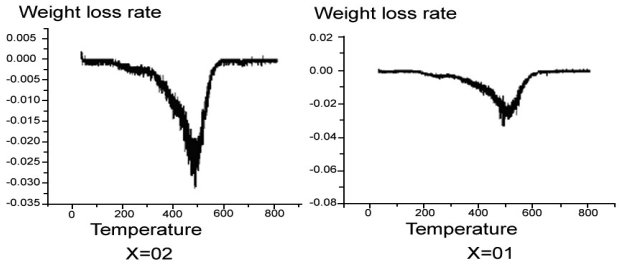



Fig. 4. Dry soot on the catalyst at different weight loss rate curve

It is obvious that the catalyst in addition to X = 0 (i.e. A bit has not been replaced by $LaCoO_3$), other types of catalysts to remove the dry soot have a certain effect, the presence of the catalyst are reduced to varying degrees of dry soot combustion temperature, which is # 4 $La_{0.6}K_{0.4}CoO_3$ the most effective, reducing the combustion temperature 110 °C.

## Conclusion

This article describes the use of low-temperature combustion to prepare a partial replacement of $La_{1-x}K_xCoO_3$ bit and B bit partial replacement $LaCo_{1-y}Fe_yO_3$ perovskite-type composite oxide catalyst process, using the real diesel exhaust. The exhausted NOx is measured by the catalyst on the removal efficiency and the conditions are in the air removal efficiency of PM. We can summarize as follows:

It is carried out on the composite oxide $LaCoO_3$ A bit partial replacement of B-bit, which is changed on the element stoichiometry, and is prepared by low temperature combustion of $La_{1-x}K_xCoO_3$ as well as $LaCo_{1-y}Fe_yO_3$ perovskite-type composite oxide catalyst. This method is simple and is mixing between the reactants, the calcination temperature is low, and the catalyst is prepared by a relatively large surface area.

On the preparation of perovskite-type composite oxide catalysts is phase analysis. It is found that the K-bit replacement is with the increase of doping, $La_{1-x}K_xCoO_3$ meets the physical changes, when it is x> 0.4, then $Co_3O_4$ is impurity. The B-bit Fe is replaced, and $LaCo1-_yFe_yO_3$ is not obviously impurity Studied. A bit K is replaced in different doped $La_{1-x}K_xCoO_3$ amount of catalyst on the removal of dry soot to have a certain effect, and the presence of the catalyst is reduced to vary the degrees of dry soot combustion temperature, which La0.6K0. $4CoO_3$ is the most effective, and the dry soot combustion temperature is reduced to about 400 °C. It is replaced Fe in the B position, which is different from doping amount $LaCo_{1-y}Fe_yO_3$ catalysts for the dry soot, and the combustion temperature does not significantly affect the combustion temperature of 500 °C, mostly, but after the B-substituted is improved combustion efficiency.

$La_{1-x}K_xCoO_3$ and $LaCo_{1-y}Fe_yO_3$ catalyst in NOx Purification efficiency were studied. The results shows that the replacement of K is in a position, the catalytic activity is firstly increased as the temperature increases, and at a certain temperature range, it maintains its optimal catalytic activity, since the catalytic activity increases as the temperature decreased rapidly. Meanwhile, K element is doping on the purification efficiency of diesel exhaust NOx great influence, $La_{1-x}K_xCoO_3$ series of catalytic activity is in the order: x = 0.3> x = 0.2> x = 0.4> x = 0.5> x = 0.1 > x = 0.6> x = $0.La_{0.7}K_{0.3}CoO_3$ NOx removal efficiency is for the best. It replace S Fe in B position, for $LaCo_{1-y}Fe_yO_3$ series catalyst, when it is y = 0.1, the efficiency of NOx purification decreases with the increasing temperature; when it is y = 0.2 ~ 0.7, the first NOx removal efficiency with temperature the temperature is increased, and at a certain temperature range to maintain a relatively high catalytic activity, and then it decreases with the increasing temperature; when it is y> 0.8, the removal efficiency of NOx with temperature increases.

The respectively $La_{1-x}K_xCoO_3$ and $LaCo_{1-y}Fe_yO_3$ are the role of catalyst in the air condition of the purification efficiency of PM that was studied. A bit K is replaced in different doped $La_{1-x}K_xCoO_3$ amount of catalyst on the removal of dry soot that have a certain effect, the presence of

the catalyst is reduced to varying degrees of dry soot combustion temperature. $La_{0.6}K_{0.4}CoO_3$ is the most effective, and the dry soot combustion temperature is reduced to about 400 °C.

It is replace Fe in the B position, and the difference is doping amount $LaCo_{1-y}Fe_yO_3$ catalysts for the dry soot combustion temperature. It does not significantly affect the combustion temperature in 500 °C, mostly, but after the B-substituted, it has improved the combustion efficiency.

**References**

[1] Schulte, E, Handschuh, R, Schwarz, W , "Study on properties of $La_1$-xCex$CoO_3$ system perovskite-type catalysts for diesel engine exhaust removal," Proc. of the 5thISOPE Ocean Mining Symp, Tsukuba, Japan, pp123-131.

[2]Grebe, H. and Schulte, E., "Study on Catalytic Activity of Perovskite-Type Oxides $La_{1-x}K_xCoO_3$-λfor the Removal of $NO_x$ from Diesel Exhaust Gases," Proc. of 6th(2005) ISOPE Ocean Mining Symp, Changsha, China, pp 149-156.

[3] Janosi, Z, Hanamoto. "Preparation, Structure and Soot Oxidation Performance of Nano-scaled Perovskite-type $La_{1-x}K_xCoO_3$ Catalyst" Proc. of the 1stInt. Conf. Mech Soil-Vehicle Systems. Turin, Italy.

[4] Katz Z, Tibbles CJ, "Investigation of Catalytic Activity of La-Na-Co-Mn-O Perovskite-type Oxides for Simultaneous Removal of Diesel Soot Particulates and NOx", International Journal of Advanced Manufacturing Technology, Vol. 25, May 2005, pp. 923–928.

[5] Curodeau A, Marceau LF, Richard M, Lessard J, "Preparation and physico-chemical characterisation of La1-xCex$CoO_3$+ δ perovskite catalyst and its methane catalytic combustion", Journal of Materials Processing Technology, Vol. 159, January 2005, pp. 17–26.

[6] Schulze HP, Herms R, Juhr H, Schaetzing W, Wollenberg G, "Effect of Ce Doping on the Structure and Catalytic Activity of La1-xCex$CoO_3$ Catalysts", Journal of Materials Processing Technology, Vol. 149, June 2004, pp. 316–322.

[7] J. Greensmith and U. Aickelin, "Purifying Diesel Exhaust Over $La_{1-x}K_xCoO_3$ Perovskite-Type Catalyst," Proceedings of the Genetic and Evolutionary Computation Conference (GECCO 2007), pp. 49–56

[8] Y. Al-Hammadi, U. Aickelin and J. Greensmith, "Working Condition of NOx and PM Treatment Using La0.9K0.1$CoO_3$ Perovskite-type Oxide," Proceedings of the IEEE World Congress on Evolutionary Computation 2008 (CEC08), in print.

[9] Kim, J., Wilson, W., Aickelin, U. and McLeod, J, "Performance of La-K-Co-Mn-O oxide catalysts for simultaneous removal of soot and Nox from diesel engine exhaust," In Proc. of the 3rd Int. Conf. on AIS (ICARIS-05), 2005, pp. 168-181

[10] Peng Dong, "Recent advances in application of perovskite-like A2BO4 mixed oxides in catalysis", A Dissertation Submitted to Shanghai Jiao Tong University for Degree of Doctor of Philosophy, April, 2007

*Advanced Materials Research Vol. 937 (2014) pp 370-374*
*© (2014) Trans Tech Publications, Switzerland*
*doi:10.4028/www.scientific.net/AMR.937.370*

# Research on Operation Mechanism and Application in Engineering of UNITANK Process

Dong-jie BAO [1, a,*], Jing LI [2,b] and Peng ZHANG[3,c]

[1] Xingtai Polytechnic College, Xingtai, Hebei, 054035, China

[2] Xingtai Polytechnic College, Xingtai, Hebei, 054035, China

[3] Xingtai Polytechnic College, Xingtai, Hebei, 054035, China

[a]bdjer330@163.com, [b]1391369317@qq.com, [c]zhangpeng-jx@163.com

*Corresponding author

**Keywords:** UNITANK Process, Operation Mechanism, Wastewater Treatment.

**Abstract.** UNITANK is a new wastewater treatment technology combining the advantages of Sequencing Batch Reactor, normal aeration tank and 3-ditch oxidation treatment systems. It has been considered as an attractive pathway to be applied in small or middle wastewater treatment plants. It was chosen as the main process in Xingtai Wastewater Treatment Plant, Hebei Province, PR China. In this paper, the operation process, operation mechanism and features of UNITANK process were discussed in detail on the basis of the basic structure and the application in engineering.

## Basic Structure of UNITANK Reactor

UNITANK process, named the alternating biological treatment technology, is also called the single pool system. It is the patent technology of Seghers Engineering Water NV in the late 80's. There are three lattices (also known as tank A, B and C) in one pool. The tanks share the public wall and hydraulic connect with each other through the public channel at the bottom. Outlets of the public channel belonging to the side tanks are located in the center of the tanks. Stabilizing covers are set above the outlets to prevent the disturbance of the sludge. There is a set aeration system in each tank. The fixed effluent weirs and sludge slots are arranged in the outside two tanks (A, C tank) .Tanks A and C are used as the aeration tank and the settling tank alternately, while tank B is only used as a aeration tank [1-3]. It is a continuous influent and alternate working system, which is shown in Fig.1

## Engineering Application in Xingtai Wastewater Treatment Plant

### Overview of the Project

In the secondary project of Xingtai Wastewater Treatment Plant，the capacity of UNITANK process is $10xl0^4 m^3/d$. The quality of influent and the designed quality of effluent is shown in Table 1. The designed quality of effluent achieves the secondary standard of "Discharge Standard of Pollutants for Municipal Wastewater Treatment Plant" (GB18918-2002,China).

Table 1. The Quality of Influent and the Designed Quality of Effluent

| items | $BOD_5$ | COD | SS | T-N | $NH_3$-N | T-P |
|---|---|---|---|---|---|---|
| influent [mg/L] | 123~229 | 267~376 | 105~245 | 33~52 | 22~41 | 1.91~3.99 |
| average influent[mg/L] | 186 | 326 | 201 | 46 | 33 | 3.3 |
| effluent [mg/L] | ≤30 | ≤100 | ≤30 | ≤30 | ≤25 | ≤3.0 |

**Technical Process**

The technical Process is shown in Fig.2. The layout of the tanks is shown in Fig.3.

**Parameters of the Project**

There are four groups of UNITANK reactor, each group contains three rectangular tanks marked A, B and C. Parameters of the project is shown in Table 2.

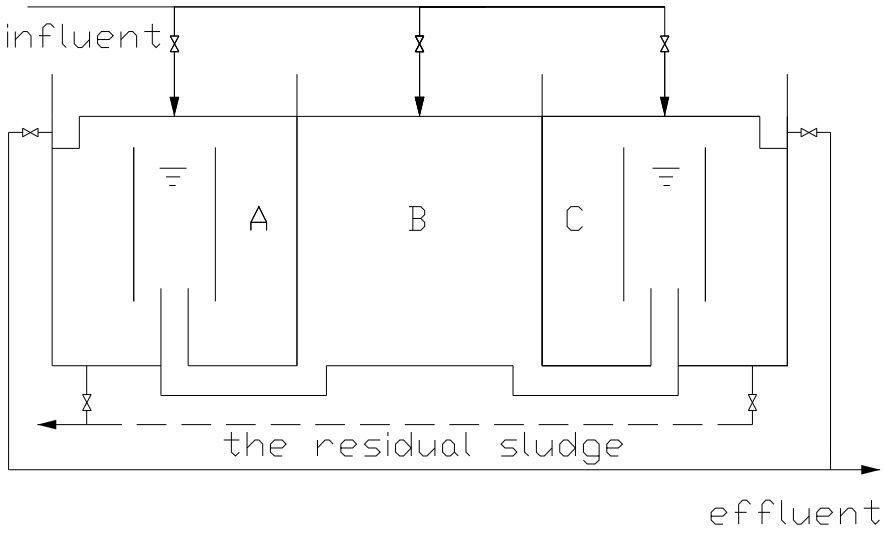



Fig. 1. Basic Structure of UNITANK Reactor

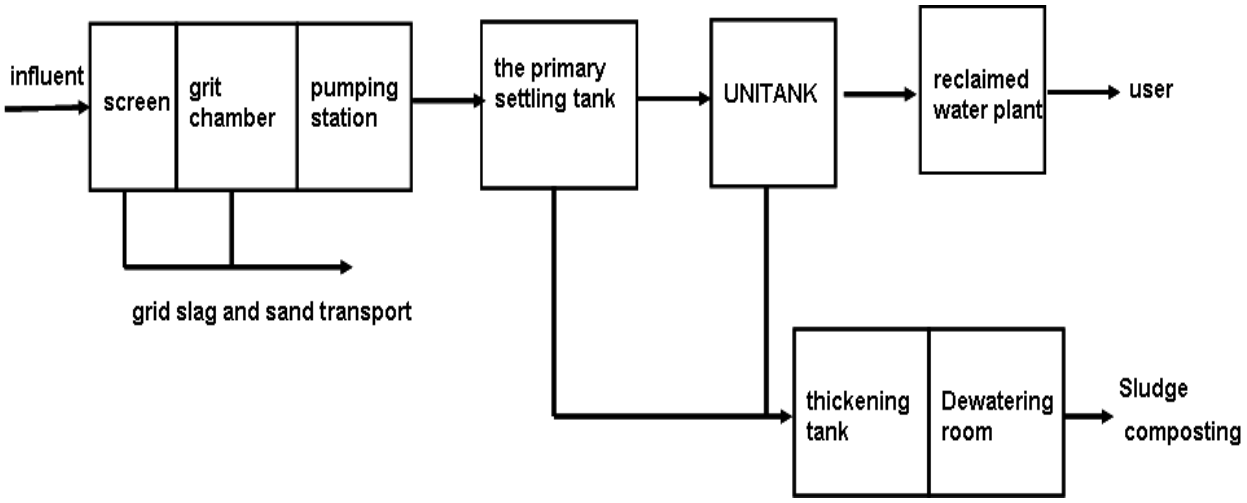



Fig. 2. The Technical Process of the Secondary Project

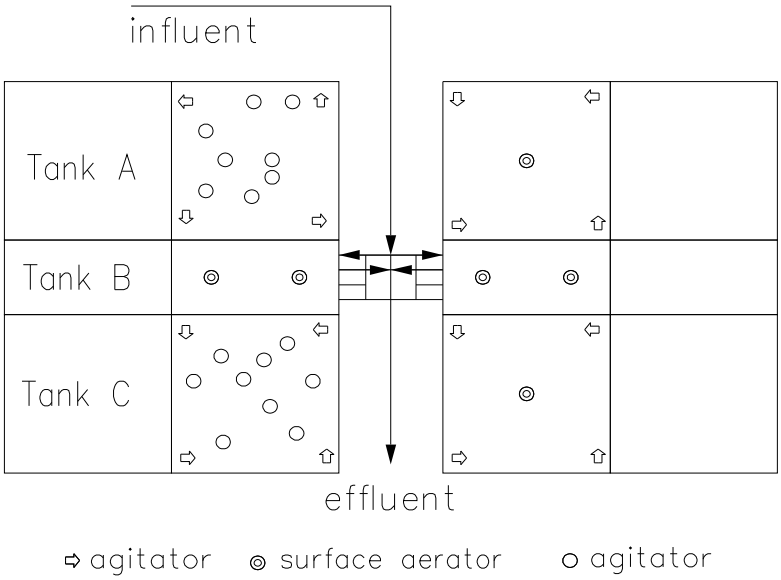



Fig. 3. The Layout of the Tanks

Table 2. The Parameters of the Project

| | Tank A | Tank B | Tank C |
|---|---|---|---|
| size [m] | 32x32x5 (depth) | 32x15x5 (depth) | 32x32x5 (depth) |
| effective depth [m] | 4 | 4 | 4 |
| treatment capacity [$m^3$/d] | $2.5xl0^4$ | | |
| volumetric load [kg BOD/ ($m^3$·d)] | 0.33 | | |
| sludge load [kgBOD/(kgMLVSS·d)] | 0.104 | | |
| surface load [$m^3$/($m^2$·h)] | 1.02 | | |
| weir load [L/(s·m)] | 1.55 | | |
| sludge concentration [kg/$m^3$] | 4 | | |
| aerobic sludge age [d] | 9 | | |
| hydraulic retention time [h] | 9.7 | | |

## Operation Mechanism and Features

### Operation Cycle and Timing of the Reactor

The alternating biological reactor operates according to the period of cycle. Each cycle comprises two main operation stages and two transition stages [4-6]. The two main operation stages are mutually symmetrical and connected through the transition stage. The operation cycle and timing of the reactor in Xingtai Wastewater Treatment Plant is shown in Table 3. There are 12 hours in per cycle including 2×4 hours of the main stages and 2×2 hours of the transition stages.

Table 3. Operation Cycle and Timing of the Reactor

| stages | | time [h] | tank A | tank B | tank C |
|---|---|---|---|---|---|
| main stage 1 | stage 1 | 4.0 | influent, aeration | aeration | settling, effluent |
| | stage 2 | 0.5 | aeration | influent, aeration | settling, effluent |
| | stage 3 | 1.5 | settling | influent, aeration | settling, effluent |
| main stage 2 | stage 4 | 4.0 | settling, effluent | aeration | influent, aeration |
| | stage 5 | 0.5 | settling, effluent | influent, aeration | aeration |
| | stage 6 | 1.5 | settling, effluent | influent, aeration | settling |

**Operation Mechanism and Feature**

The Operation mechanism is shown in Fig.4. In Fig.4, the stages and the state of each tank are displayed in detail.

**The System Has Characteristics of High Efficiency**

The system is more suitable for treating wastewater with high concentration than the general activated sludge methods. The sewage flowing into the side tank will be better handled because there is a great quantity of activated sludge with high concentration in the tank [7]. This is due to the operation as a sedimentation pool in the last stage of the cycle. With continuous flowing, concentration of pollutant in liquid phase increases while the absorption and oxidation capacity of activated sludge is also constantly strengthened. Pollutant is adsorbed and degraded in a relatively short time.

**The System Has a Certain Removal Function of Nitrogen and Phosphorus**

The system would have nitrogen and phosphorus removal function by setting the non aeration stage during the aeration period in order to form the alternate states of anaerobic, anoxic and aerobic and by controlling the technical conditions such as the flow, time and cycle.

**The System Has the Advantages of Compact Structure, Less Land Occupation and Cost-efficient**

The structure of UNITANK process is compact because the tanks connect with each other through the public wall. The influent flows through the punches which reduces the head loss. Compared with the common activated sludge process, it does not need another secondary sedimentation tank and facilities for sludge returning. The system has the advantages of less land occupation, cost-efficient, reliable operation and convenient maintenance because of fewer types of equipment.

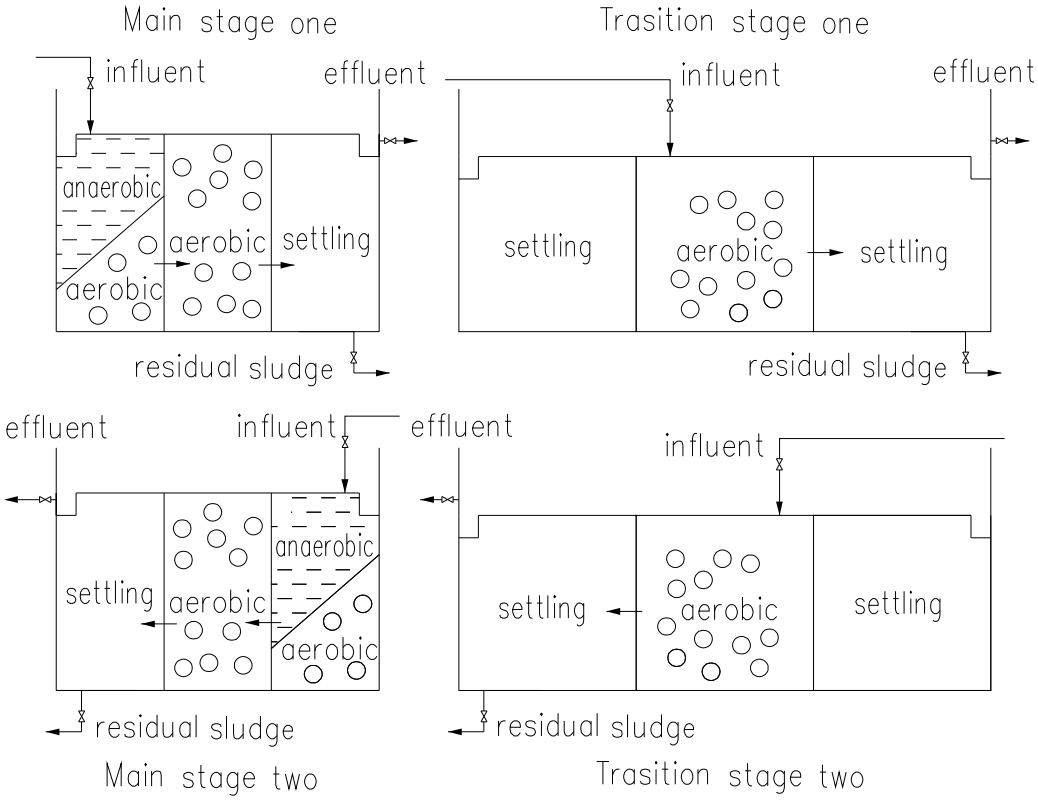



Fig. 4. The Operation Mechanism

## Conclusion

UNITANK is an effective technology for wastewater treatment with the advantages of high efficiency, certain removal function of Nitrogen and Phosphorus, compact structure, less land occupation, cost-efficient, reliable operation and convenient maintenance. It has been considered as an attractive pathway to be applied in small or middle wastewater treatment plants.

## Acknowledgements

This work was financially supported by Science and Technology Support Program of Hebei Province (13273605), the Higher School Science and Technology Foundation of Hebei Province (QN20131178), Xingtai Science and Technology Support Program (2013ZC234).

## References

[1]Henze M, Grady C P L, Gujer Jr et al., in: *IAWPRC Scientific and Technical Report No.3*,London, UK,1987.

[2]Henze M, Gujer W, Mino T et al., in: *Water Sci Technol*, Issue1,Vol.39 (1999), p. 165-182.

[3]Vriens L et al., in: *Water*,1990, p.52.

[4]Dongjie Bao, Zhanmeng Liu and Jing Li, in: *Applied Mechanics and Materials*, Vols.361-363 (2013), p. 640-643.

[5]V. N. Samokhin: *Design Handbook of Wastewater Systems* (Allerton Press, Inc., New York 1997).

[6]Jeffrey A. Nathanso: *Basic Environmental Technology: Water Supply, Waste management, and Pollution Control* (Pearson Education., publishing as Prentice Hall 2003).

[7]Fagen Zhang, Junxin Liu, in: *Journal of Environmental Sciences*, Issue2, Vol.19 (2007), p. 142.

*Advanced Materials Research Vol. 937 (2014) pp 375-380*
*© (2014) Trans Tech Publications, Switzerland*
*doi:10.4028/www.scientific.net/AMR.937.375*

# Thermodynamic Analysis of the Internal Melt-ice-on-tube During Melting Under Natural Convection

Yi LIU[1,a], Xin CHEN[1,b]

[1]School of Energy and Civil Engineering, Harbin University of Commerce, Harbin Song Bei Xue-hai Street ,District No.1, Harbin, 150028, China

[a]liuyiyuanhongyan1975@126.com

* Yi Liu

**Keywords:** Ice storage, Internal melt-ice-on-tube, Numerical simulation, Enthalpy method.

**Abstract.** The numerical simulation of the ice melting processes in internal melt-ice-on-tube which is applied widely in the ice storage system is carried out. The dynamic mathematical models about melting are established and solved by using enthalpy method. Natural convection of the melted water in the course of melting is studied, and natural convection influences on single tube in melting heat transfer process is analyzed under the related parameters. Several conclusions are obtained:

1. Because of natural convection of the melted water, the curve of melting interface is no longer a circle, but a curve changing with angle. The melting radius reaches minimum at the bottom and maximum at the top.
2. The one with natural convention is compared to the other not considered. At initial stage, the influence of natural convection is smaller in the course of melting. However, the influence of natural convention increases along with melting.

## Introduction

Along with the world energy crisis turning deeply, the ice storage system is applied more and more widely because of its simple design and obviously economy. The overseas study of the ice storage system starts in1930s and now the technique is already mature. Today the overseas study of the ice storage system focuses on the follows: (1).Setting up the model of the ice storage box and forecasting the capability of the ice storage box. Arnold and Jones made a lot of researches in this aspect, mainly set up the mathematic models of the ice storage box and simulated them [1~3]. But the result is not so accordant to the fact because of many being given conditions, especially in the melting stage the difference is more. (2).Characteristic study when icing and melting. This study is very important to analyze the ice storage box and improve it. A lot of academic and experimental studies have been carried out, and lot of characteristic when icing and melting has been carried out [4~5]. (3). Intensifying the heat exchange. The main study is that improving the phase-change liquid and the shape of the ice storage tube [6]. (4). Running mode and its control. Including comparison of the systemic function between complete freeze and not, also comparison of the systemic function between the set precedence and the ice storage box precedence [7~8]. The domestic study of the ice storage system starts in1990s and is still in underway stage. The studies focus on setting up the melting and icing models [9~10] and the experiments of the ice storage system [11~12].

It is more complicated to analyze the heat transfer process when melting because it always goes with phase change. Especially when melting, there are many other factors affecting the progress, for example natural convection of the melted water, which make it even difficult to analyze the heat transfer capability of the ice storage tube. So the academic studies of melting always neglect the natural convection. But in fact the influence of natural convection is very great and can not be neglected. In the paper, the melting process of the ice storage tube is calculated by using enthalpy method, the heat transfer capabilities are compared between considering natural convection and not. Also the effects of some initial parameters on natural convection are analyzed.

**Physical Model**

When setting up the melting model which chooses the glycol as cryogen under considering natural convection, make the following assumptions to simplify the problem:

1) Because the length of the tube is much more than its diameter, so neglect the radial heat transfer and polar heat transfer of the cryogen.
2) The initial temperature of the ice in the groove is uniform and is a constant temperature , $T_{ice} \prec 0^{\circ}C$;
3) During the whole process of the heat transfer, properties of glycol, ice and water always keep the same; however, when dealt with volume stress in the momentum equation, water density was considered as variance, other ones was still considered as constant;
4) The thickness of the ice storage tube wall is very thin, and thermal conductivity is great. Therefore, the thermal resistance can be neglected;
5) The thermal insulation capability of groove wall is strong. Therefore, the heat loss to the surroundings can be neglected;
6) Viscous dissipation of water is neglected;
7) Volume change caused by phase change is neglected.

**Mathematical Model and Solution Method**

Adopt the column coordinate system, so the mathematic model as follows:

**Governing Equation**

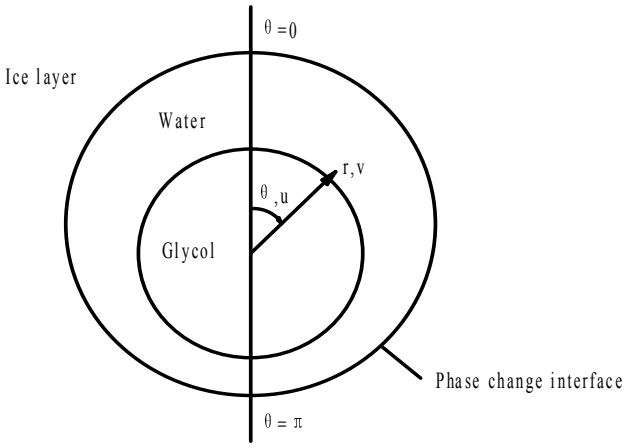



Fig. 1. Physical model and coordinate system

Fig.1 shows the physical model of the section which is vertical to the axis in the ice melting process under natural convention and the polar coordinate system. According to the physical model, mathematical model can be conducted as follows:

**Continuity Equation**

$$\frac{1}{r}\frac{\partial}{\partial r}(rv)+\frac{1}{r}\frac{\partial u}{\partial r}=0 \tag{1}$$

**Momentum Equation**

Radial direction *r*

$$\rho\frac{\partial v}{\partial \tau}+\frac{\partial}{\partial r}(\rho vv)+\frac{1}{r}\frac{\partial}{\partial \theta}(\rho uv)-\frac{\rho u^2}{r} = \rho g\beta(t-t_{\mathrm{ph}})\cos\theta-\frac{\partial p}{\partial r}+\frac{1}{r}\frac{\partial}{\partial r}(r\mu\frac{\partial v}{\partial r})+\frac{\mu}{r^2}\frac{\partial^2 v}{\partial \theta^2}-\frac{2\mu}{r^2}\frac{\partial u}{\partial \theta}-\frac{v}{r^2} \tag{2}$$

Polar angle direction $\theta$

$$\rho\frac{\partial u}{\partial \tau}+\frac{\partial}{\partial r}(\rho v u)+\frac{1}{r}\frac{\partial}{\partial \theta}(\rho u u)-\frac{\rho u v}{r} =-\rho g\beta(T-T_{\mathrm{ph}})\sin\theta-\frac{1}{r}\frac{\partial p}{\partial \theta}+\frac{1}{r}\frac{\partial}{\partial r}(r\mu\frac{\partial u}{\partial r})+\frac{\mu}{r^2}\frac{\partial^2 u}{\partial \theta^2}+\frac{2\mu}{r^2}\frac{\partial v}{\partial \theta}-\frac{u}{r^2} \tag{3}$$

**Energy Equation**

$$\rho c_{\mathrm{p}}[\frac{\partial T}{\partial \tau}+\frac{\partial}{\partial r}(vT)+\frac{1}{r}\frac{\partial}{\partial \theta}(uT)] =\frac{1}{r}\frac{\partial}{\partial r}(rk\frac{\partial T}{\partial r})+\frac{1}{r}\frac{\partial}{\partial \theta}(\frac{1}{r}k\frac{\partial T}{\partial \theta})+\frac{\partial}{\partial z}(k\frac{\partial T}{\partial z}) \tag{4}$$

Meanings of the above symbols:

| | | | | | |
|---|---|---|---|---|---|
| $\theta$ | polar coordinate | $(m)$ | $r$ | radial coordinate | $(m)$ |
| $z$ | axial coordinate | $(m)$ | $v$ | radial velocity | $(m/s)$ |
| $u$ | peripheral velocity | $(m/s)$ | $\rho$ | density | $(m^3/kg)$ |
| $\mu$ | kinetic viscosity | $(Pa\bullet s)$ | $\tau$ | time | $(S)$ |
| $g$ | acceleration of gravity | $(m/s^2)$ | $\beta$ | volume expansion coefficient | (1/°C) |
| $k$ | heat conductivity coefficient | $(w/[m\bullet°C])$ | $c_{\mathrm{p}}$ | specific heat | $(kJ/(kg\bullet K))$ |
| $T$ | temperature | $(K)$ | $ph$ | phase change point | |

Buoyancy force item caused by difference in temperature is dealt with Boussinesq hypothesis [13-14]. The hypothesis is consisted of three parts: (1)The viscosity dissipation of the fluid is neglected; (2)All properties of matter are constants except density; (3) Density in all items are constant except the item related to volume stress in momentum equations.

**Energy Equation of Enthalpy Method**

The notion of enthalpy method is that enthalpy and temperature are together considered as dependent variable in the enthalpy model, and setting up the uniform energy equation in the whole area which includes the liquid area, the solid area and the interface of the phase change, and then Fig s out the enthalpy distributing in the numerical method, finally we can Fig out the interface of the phase change and the whole territorial parameters. The advantage of the enthalpy method is that the equations including the liquid equation, the solid equation and the interface equation can be turned into a uniform energy equation. So the liquid area, the solid area and the interface have no use for being solved separately in this method.

Using enthalpy method, energy equation (4) can be converted as follows:

$$\frac{\rho}{c_{\mathrm{p}}}\frac{\partial h}{\partial \tau}+\frac{\partial}{\partial r}(\rho v T)+\frac{1}{r}\frac{\partial}{\partial \theta}(\rho u T) =\frac{1}{r}\frac{\partial}{\partial r}(r\frac{k}{c_{\mathrm{p}}}\frac{\partial T}{\partial r})+\frac{1}{r}\frac{\partial}{\partial \theta}(\frac{1}{r}\frac{k}{c_{\mathrm{p}}}\frac{\partial T}{\partial \theta})+\frac{\partial}{\partial z}(\frac{k}{c_{\mathrm{p}}}\frac{\partial T}{\partial z}) \tag{5}$$

Applying equation (6) and equation (7), different parameters can be converted as follows:

$$t-t_{\mathrm{ph}}=\begin{cases}(h-h_{\mathrm{s}}^*)/c_{\mathrm{s}} & h<h_{\mathrm{s}}^*\\ 0 & h_{\mathrm{s}}^*\le h\le h_{\mathrm{l}}^*\\ (h-h_{\mathrm{l}}^*)/c_{\mathrm{l}} & h>h_{\mathrm{l}}^*\end{cases} \tag{6}$$

$$\rho = \begin{cases} \rho_s & h < h_s^* \\ \rho_l & h > h_l^* \end{cases} \qquad k = \begin{cases} k_s & h < h_s^* \\ k_l & h > h_l^* \end{cases} \tag{7}$$

Meanings of the above symbols:

| | | | | | |
|---|---|---|---|---|---|
| $h$ | normal specific enthalpy | $(kJ/kg)$ | $h_s^*$ | ice specific enthalpy | $(kJ/kg)$ |
| $h_l^*$ | water specific enthalpy | $(kJ/kg)$ | $c_s$ | ice specific heat | $(kJ/(kg\bullet K))$ |
| $c_l$ | water specific heat | $(kJ/(kg\bullet K))$ | | | |

**Solution Of The Governing Equation**

In this paper, the solution domain is dispersed by using inside-node method. Governing equations are integrally dispersed using the control volume method and the staggered grid technology. The discrete equations are solved using SIMPLE algorithm. Because of the nonlinear coupling relationship of each variable, during the process of applying SIMPLE algorithm, sub-relaxation iteration method is used to accelerate converging of the nonlinear problem [15].

**Simulation Result and Analysis**

The shape of the ice storage box is considered as columniation, basic parameters for calculation are shown in Table 1.

Table 1. Basic parameters for calculation

| | | | |
|---|---|---|---|
| Fluid specific heat | 3.85 kJ/(kg·°C) | Ice heat conductivity | 2.215 W/(m·°C) |
| Fluid density | 1030 kg/m$^3$ | Ice density | 916 kg/m$^3$ |
| Fluid heat conductivity | 0.5 W/(m·°C) | Ice specific heat | 2090 J/(kg·°C) |
| Fluid kinetic viscosity | 1.77 mPa·s | Water heat conductivity | 0.551 W/(m·°C) |
| Fluid velocity | 0.5 m/s | Water density | 1000kg/m$^3$ |
| Fluid inlet temperature | 20 °C | Water specific heat | 4187 J/(kg·°C) |
| Inside diameter of tube | 17 mm | Ice-water phase change temperature | 0 °C |
| Outside diameter of tube | 20 mm | Ice-water phase change Latent heat | 335kJ/kg |
| Inside diameter of box | 0.4m | Initial temperature of ice | -0.5°C |
| Outside diameter of box | 1m | | |

Simulation result and analysis as follows:

Fig .2 shows the change of the ice melting interface of the given section, which is the middle section of the ice storage box with natural convection neglected in 12000s.

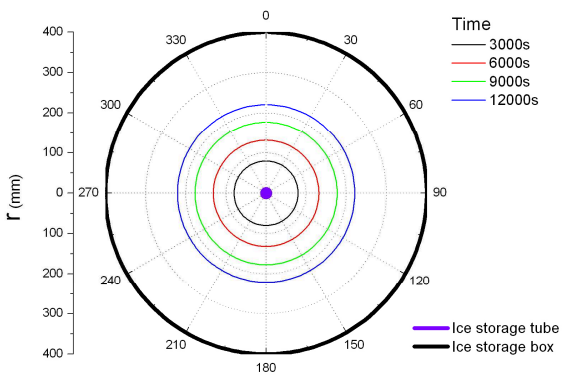



Fig. 2. Ice melting interface with natural convection neglected

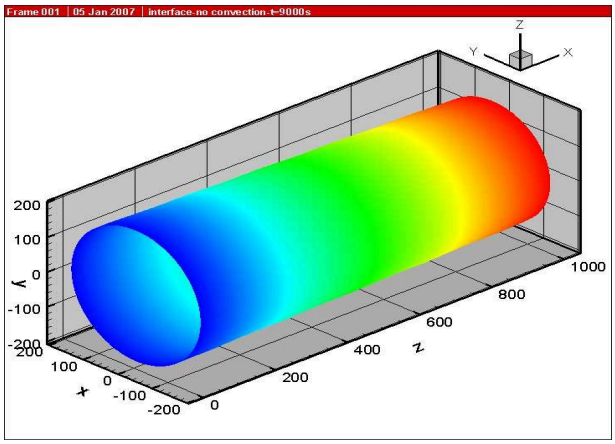



Fig. 3. Whole ice melting interface at 9000s with natural convection neglected

Fig .3 shows the whole ice melting interface at 9000s.

From the Fig .2 and Fig .3, we can see that every section's interface which is vertical to the axis is a circle, and at the same time, the whole interface is a cone dais which is symmetrical concerning the box axis. For the intake temperature of the glycol is higher than the export, the ice melting interface of the entrance is bigger; but at the same time, the temperature of the glycol lower along the axis direction, so that the ice melting radius lower gradually along the axis direction.

Fig .4 shows the change of the ice melting interface of the given section which is the middle section of the ice storage box with natural convection considered in 21000s under the same initial parameters with Fig 2. From Fig 4 we can see that under natural convection considered, at the initial stage of melting, the heat exchange depends mainly on ice's and water's heat transfer because there is little water, so that the ice melting interface of the given section which is vertical to the axis is almost a rotundity; natural convection will become more and more strong along with the increasing quantity of the melted water, so that the ice melting interface will change gradually. In the middle of the ice melting, the ice melting interface will become a curve which shrinks gradually from the top to bottom of the storage box; at the end of ice melting, the curve will become raised. The change of the curve is because that the melted water at the bottom of the ice storage tube is hold back by the tube when the bottom water streams up after natural convection becomes strong, so the circuitous liquid will come out and make the bottom ice to melts quickly. The ice melting interface of the given section which is vertical to the axis along the axis will change in succession obeying the above regulation along with time going.

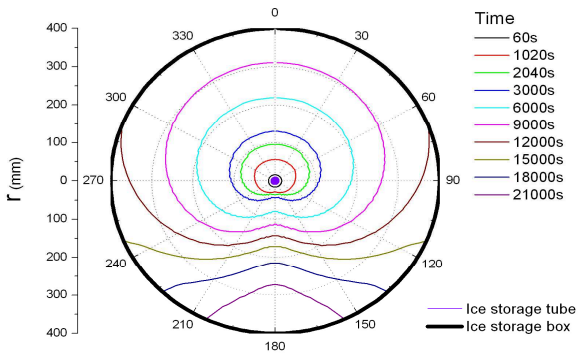



Fig. 4. Ice melting interface with natural convection considered

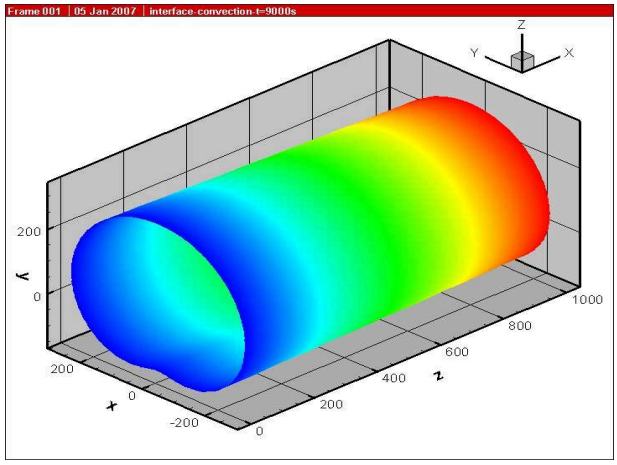



Fig. 5. Whole ice melting interface at 9000s with natural convection considered

Fig .5 shows the whole ice melting interface at 9000s under considering natural convection. From the chart we can see that the interface is much different to the interface which neglecting natural convection. And at the same time, the intake interface is bigger than the exit interface, but the shape of these curves are similar, it is said that the interface of every section is similar from the entry to the exit.

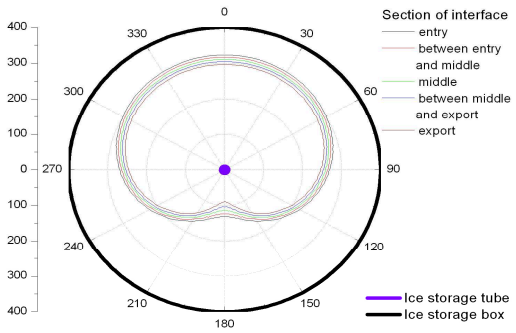



Fig. 6. Ice melting interface at 9000s with natural convection considered

Fig .6 shows five typical melting interfaces which are vertical to the axis when the melting time is 9000s. We can see that at this moment the melting interface shrinks from the entry to the exit. For the cryogen temperature descends gradually from the entry to the exit, the foreside of the box gets more energy than the rearward. At the same time, we also find that the bottom of the interface sticks up more from the entry to the exit. This is because that the space between the bottom of the interface and the tube at the entry is more than the exit, through the entry temperature is higher than the exit, the difference is not more and the length of the box is short, so totally the entry temperature grads between the bottom of the interface and the storage tube is lower than the exit.

**Summary**

1. Because of the existing of natural convection of the melted water, the ice melting interface of the given section which is vertical to the axis is no longer a circle. In the middle of the ice melting, the ice melting interface will become a curve which shrinks gradually from the top to bottom of the storage box; at the end of ice melting, the curve will become raised.
2. The influence of natural convection is small at the beginning, and it will become strong gradually along with the increasing quantity of the melted water.

**References**

[1] D. Arnold. 1990, Dynamic Simulation of Encapsulated Ice Stores-Part1: Model Development and Validation, *ASHRAE Transfer*, 96:566-571.

[2] D. Arnold. 1994, Dynamic Simulation of Encapsulated Ice Stores-Part2: Model Development and Validation, *ASHRAE Transfer*, 100:1245-1254.

[3] Jerold W. Jones. 1995, Evaluation of RP-459 Algorithms for Modeling External Melt, Ice-on-Pipe Thermal Storage System Components, *ASHRAE Transfer*, 101:1342-1351.

[4] Akio Saito. 2002, Recent Advances in Research on Cold Thermal Energy Storage, *International Journal of Refrigeration*, (25):177-189.

[5] R. K. Strand, C. D. Peterson, G.. N. Coleman. 1994, Development of Direct and Indirect Ice Storage Models for Energy Analysis Calculations, *Trans ASHRAE Transfer*, 100(1):1230-1244.

[6] S. L. Chen. 1992, Analysis of Cool Storage for Air Conditioning. *Int. Journal of Energy Research*, (16):553-563.

[7] Charles E D, James S E. 1993, Design Guide for Cool Thermal Storage, *ASHRAE Transfer*, 99(II):798-804.

[8] Akbari H, Mertol A. 1989, Thermal Energy Storage for Cooling of Commercial Buiding. Kilkis S, *Energy Storage Systems*, 315-347.

[9] Zhong Yi,Huang Hu,Zhong Xiao-song. 2004, Icing progress outside the tube of the ice storage, *Journal of Harbin Institute of Technology*, (10):1310-1313.

[10] Zhong Xian-bing,Li Fang-qing. 2002, Numerical simulation of the ice ball heat transfer, *Building Energy & Environment*, (3):26-29.

[11] Yan Gang. 2002, Experiment of Concretionary of ice storage ball, *Refeigeration & Air-Condition*, (4):22-24.

[12] Du Nen-jie. 2004, Icing experiment of conchoidal pipy ice storage box, *Fluid Machinery*, (10):42-45.

[13] Gray D D,Giorgin A. 1976, The Validity of the Boussinesq Approximation for Liquids and Gases, *Int. J. Heat Mass Transfer*, 19:549-551.

[14] V. R. Voller,C. Prakash. 1987, A Fixed Grid Numerical Modeling Methodology for Convection-diffusion Mushy Region Phase-change Problems, *Int. J. Heat Mass Transfer*, 30(8):1709-1719.

[15] Tao Wen-quan. 2001, Numerical Heater Transfer. *Xi'an Jiaotong University Press*, 28-186.

*Advanced Materials Research Vol. 937 (2014) pp 381-385*
*© (2014) Trans Tech Publications, Switzerland*
*doi:10.4028/www.scientific.net/AMR.937.381*

# Introduction of a Thermal Response Test (TRT) Apparatus Used for Measuring Underground Heat Exchanger Characteristics

Yi LIU[1,a], Yang SHI[2,b], Ya-ning ZHANG[2,c]

[1]School of Energy and Civil Engineering, Harbin University of Commerce, Harbin Song Bei Xue-hai Street ,District No.1, Harbin, 150028, China

[2]School of Energy Science and Engineering, Harbin Institute of Technology, Harbin, 150001, China

[a]liuyiyuanhongyan1975@126.com, [b]hitshiyang@gmail.com, [c]hitzhangyaning@gmail.com

* Yi Liu

**Keywords:** TRT, Underground heat exchanger, Ground-source, MCGS configuration software.

**Abstract.** A thermal response test (TRT) apparatus is introduced in this paper for determination of the performance of underground heat exchanger in ground-source heat pump system. The inlet and outlet temperatures of the underground heat exchanger can be real-time tested to obtain the heat transfer data. The apparatus was used to test a underground heat exchanger for its inlet and outlet temperatures in Red Star farm, Beian City, Heilongjiang province, China. The inlet and outlet temperatures varied in the ranges of 10.62~13.57°C and 9.01~11.88°C within 24 hours, respectively.

## Introduction

The main factor restricting the development of the ground source heat pump is the characteristics of the underground heat exchanger. The design of an underground heat exchanger is of great importance for the initial investment and the efficiency of the ground source heat pump project. In regions with different climate and soil temperature, the underground heat exchangers with the same burial depth may take different amounts of heat. Therefore, it is necessary to obtain the climate and soil temperature of the region where the underground heat exchanger used before the design of an underground heat exchanger. And it is necessary to design a proper device which can obtain the soil temperature and physical parameters, which is very important for designing a proper underground heat exchanger for a specific area. Thermal response test (TRT) is becoming increasingly popular in obtaining the ground thermal properties as well as evaluating the performance of the ground heat exchanger that determines the properties of ground source heat pump system [1]. It is widely used to measure the characteristics of the pipe-in-pipe borehole heat exchangers [1], borehole heat exchanger [2, 3, 4, 5, 6], ground heat exchanger [7] and ground-source heat pump system [8]. Design of a thermal response test (TRT) apparatus is therefore of great importance. This paper introduces a thermal response test (TRT) apparatus which can be used for measuring the characteristics of underground heat exchangers.

## The Principle and Structure of TRT

The principle of TRT apparatus is shown in Fig.1. The apparatus inlet and outlet are connected to the underground heat exchange. Circulating medium enters the system through fluid infusion port. When the difference between inlet and outlet temperatures of the underground heat exchanger does not exceed 0.1 °C, circulating pump is started to test the soil temperature. The average values of the underground heat exchanger inlet and outlet temperatures are set as the initial soil temperatures. The electric heater is started to test the performance of underground heat exchanger. The input power of the electric heater is adjusted to change the heat flow between the underground heat exchanger tube wall and soil. The flow of the circulating pump is regulated to change the

temperature difference between inlet and outlet of the underground heat exchanger. The best unit hole depth heat transfer of underground heat exchanger can then be determined.

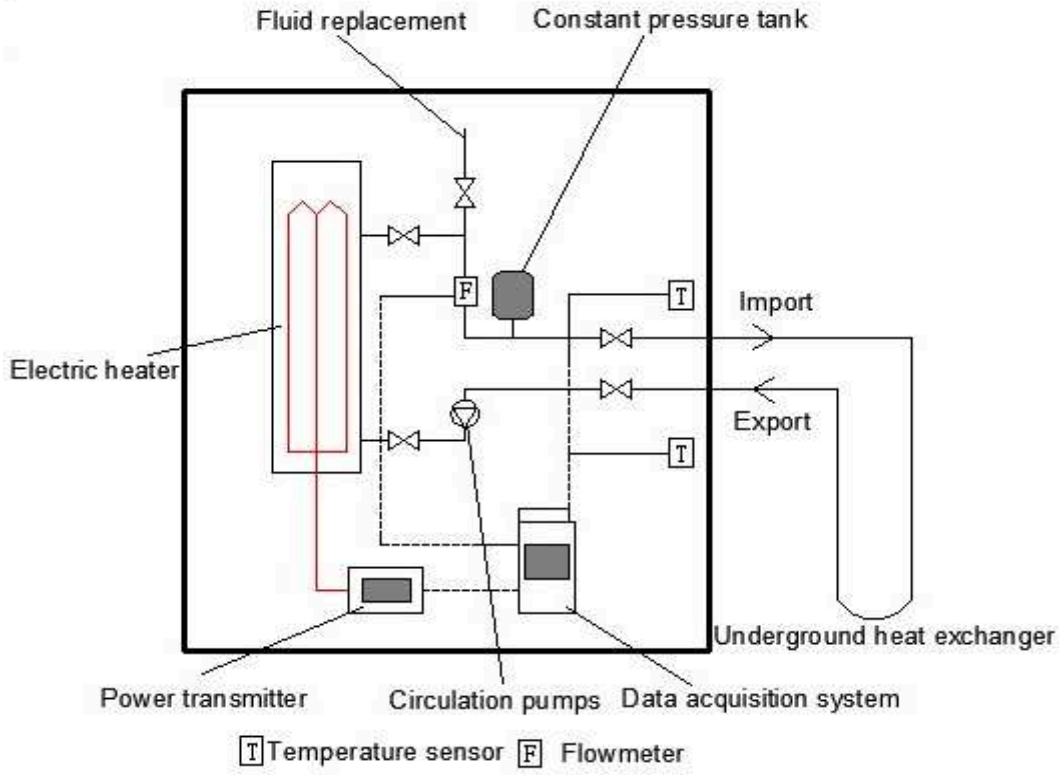



Fig. 1. Schematic diagram of the thermal response test apparatus



Fig. 2. The device of thermal response test apparatus

The TRT inner structure consists of a constant pressure tank, an electric heater, a circulating pump, a flow meter, a power transducer, a data acquisition apparatus and two temperature sensors.

Data acquisition system connects the inlet and outlet temperature measuring points of underground heat exchanger, a power measuring point for testing the power of electric heater and a flow measuring point for the circulation medium. A MCGS configuration software is installed in the portable computer which is connected to the data acquisition device. Data can be displayed in real time and recorded by the MCGS configuration software.

In TRT apparatus, the temperature sensor is PT100 platinum resistance with a measuring accuracy of ±0.2% which is calibrated according to the length of the wiring. The flowmeter type is LWGY-15 turbine flowmeter with a measuring accuracy of ±0.5%. The power transmitter model is YA-33 three-phase AC power transmitter with an accuracy of ±0.2%. The electric heater is a special pr°Cessing by the manufacturer within the scope of power at 0~5 kW stepless regulation. The circulating pump model is ISW25-125 horizontal type centrifugal pump, the rated flow is 4 $m^3$/h, the head is 20 m, and the electrical power is 0.75 kW. Fig 2 shows the thermal response test apparatus. The size of the device is 400mm×300mm×700mm and the total weight is 50 kg, it is therefore convenient to be transported and installed.

**Results and Analysis**

In order to verify the reliability and accuracy of the TRT device, the thermal response test was used in Red Star farm, Beian City, Heilongjiang province, China. Table 1 shows the specific parameters of the underground heat exchanger. Table 2 shows the initial parameters of soil and the grouting materials.

Table 1. The parameter data of the underground pipe

| Pipe material | Depth (m) | Hole diameter (mm) | Hole pipe spacing (mm) | Tube diameter (mm) | Wall thickness (mm) |
|---|---|---|---|---|---|
| PE100 | 120 | 160 | 100 | 32 | 3 |

Table 2. The parameter data of the soil and the grouting material

| | Initial temperature (°C) | Thermal conductivity (W/m·K) | Thermal diffusivity ($m^2$/h) | Specific heat capacity (kJ/$m^3$·K) | Density (kg/$m^3$) |
|---|---|---|---|---|---|
| Soil | 6.6 | 1.8 | $5.69\times10^{-3}$ | 2.2 | 2150 |
| Grouting material | 6.6 | 2.1 | $4.43\times10^{-3}$ | 2.0 | 2560 |

Table 3. The parameter data of the fluid (water)

| Initial Temp. (°C) | Flow vel°City (m/s) | Density (kg/$m^3$) | Dynamic viscosity (kg/m·s) | Thermal conductivity (W/m·K) | Specific heat (kJ/$m^3$·K) |
|---|---|---|---|---|---|
| 2 | 0.6 | 999.8 | 0.001643 | 0.55 | 4.2 |

Water was selected as circulation medium. Table 3 presents the parameter data of the medium. The circulating pump worked continuously 10 hours when the electric heater was off, the heat exchanger inlet and outlet temperatures were constant at 6.6 °C which was set as the initial average soil temperature. When the flow rate of the circulation medium was 1.5 $m^3$/h and the system was continuously heated for 24 hours by a heat power of 3 kW, the experiment data were recorded every 2 minutes by the data acquisition system. The average values during each hour were then calculated.

The values of inlet and outlet temperatures obtained by the TRT experimental apparatus are presented in Fig.3 and Fig.4, respectively. The practical operation of underground heat exchanger can be obtained accurately. Thus it can be used to measure the performance of the heat exchanger.

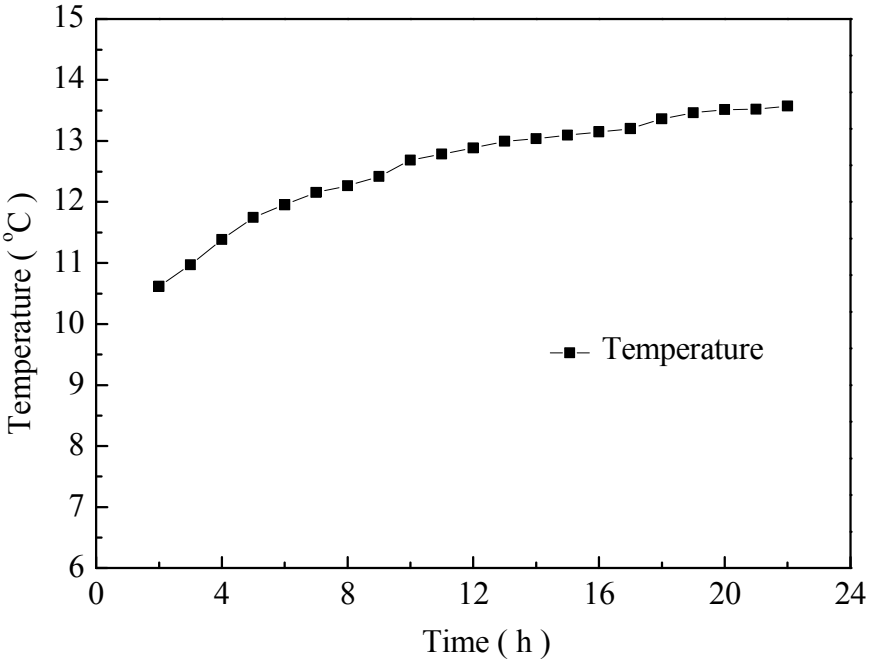



Fig. 3. Inlet temperature of the underground exchanger

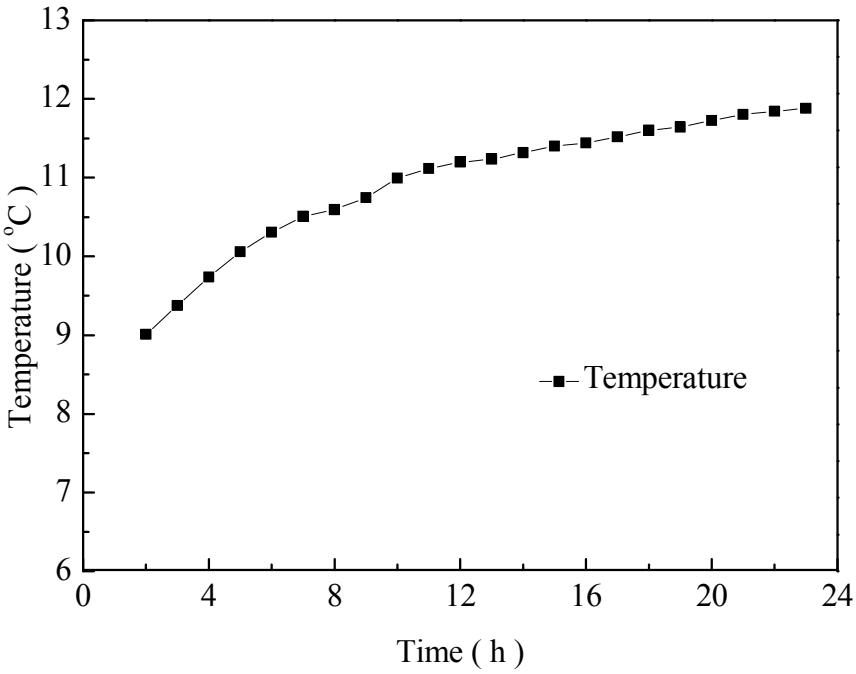



Fig. 4. Outlet temperature of the underground exchanger

## Conclusion

This paper introduces a thermal response test apparatus for the determination of the performance of underground heat exchanger in ground-source heat pump system. Underground heat exchanger inlet and outlet temperatures can be real-time tested to calculate the heat transfer data. The apparatus was used to test a underground heat exchanger for its inlet and outlet temperatures in Red Star farm, Beian City, Heilongjiang province, China. The inlet and outlet temperatures varied in the ranges of 10.62 ~ 13.57 °C and 9.01 ~ 11.88 °C within 24 hours, respectively.

**Reference**

[1] José Acuña, Björn Palm. Distributed thermal response tests on pipe-in-pipe borehole heat exchangers. Applied Energy, 2013, 109: 312-320

[2] Yong Li, Jinfeng Mao, Shibin Geng, Xu Han, Hua Zhang. Evaluation of thermal short-circuiting and influence on thermal response test for borehole heat exchanger. Geothermics, 2014, 50: 136-147

[3] Valentin Wagner, Philipp Blum, Markus Kübert, Peter Bayer. Analytical approach to groundwater-influenced thermal response tests of grouted borehole heat exchangers. Geothermics, 2013, 46: 22-31

[4] Richard A. Beier, Marvin D. Smith, Jeffrey D. Spitler. Reference data sets for vertical borehole ground heat exchanger models and thermal response test analysis. Geothermics, 2011, 40: 79-85

[5] Min Li, Alvin C.K. Lai. Parameter estimation of in-situ thermal response tests for borehole ground heat exchangers. International Journal of Heat and Mass Transfer, 2012, 55 (9-10): 2615-2624

[6] A.-M. Gustafsson, L. Westerlund. Multi-injection rate thermal response test in groundwater filled borehole heat exchanger. Renewable Energy, 2010, 35 (5): 1061-1070

[7] Chulho Lee, Moonseo Park, The-Bao Nguyen, ByonghuSohn, Jong Min Choi, Hangseok Choi. Performance evaluation of closed-loop vertical ground heat exchangers by conducting in-situ thermal response tests. Renewable Energy, 2012, 42: 77-83

[8] Xiaohui Yu, Yufeng Zhang, Na Deng, Jianshuan Wang, Dongwen Zhang, Jilin Wang. Thermal response test and numerical analysis based on two models for ground-source heat pump system. Energy and Buildings, 2013, 66: 657-666

*Advanced Materials Research Vol. 937 (2014) pp 386-390*
*© (2014) Trans Tech Publications, Switzerland*
*doi:10.4028/www.scientific.net/AMR.937.386*

# The Application of Paste Tailing Technology in High Latitude Cold Area

Bo ZHOU[1,a], Xian-wen ZHOU [2,b] , Ye CHEN[3,c,*] and Zheng CHEN[4,d,]

[1] Guangxi Gold Company, Nanning Guangxi, Nanning, 530023, China,

[2] Guangxi Gold Company, Nanning Guangxi, Nanning, 530023, China,

[3] College of Resources and Metallurgy, Guangxi University, Nanning, 530004, China,

[4] School of Civil Engineering and Architecture, Guangxi University, Nanning, 530004, China,

[a]bozhou@163.com, [b]zhouxw2000@163.com, [c]fby18@126.com, [d]gxucz@qq.com

*Corresponding author

**Keywords:** Paste tailing, Wunugetushan Copper-molybdenum ore, Deep-cone thickener, Diaphragm pump, flocculants.

**Abstract.** In this paper, the paste tailing preparation and stacking technology were applied in Wunugetushan Copper-molybdenum ore where in high latitude cold area of our country, the paste tailing preparation and stacking technology, Deep-cone thickener, Diaphragm pump and flocculating agent adding device were introduced. The production practice has proved that the paste tailing technology in high latitude cold area of our country obtained successful application, and had effected on the development of tailing disposal technology of our country.

## Introduction

Mineral resources are one of the important material basis for the social development of construction. With the development of the technology standard, the development and utilization of mineral resources have increased with each passing day. Now the world's known manageable resources are being used up rapidly. Most of the poor, miscellaneous, fine, the mineral resources have been concerned more and more.

However, they can't be used directly. To obtain useful minerals, the ore is tread by separation, enrichment, purification, extraction, processing and other processing. At the same time, a large number of abandoned and temporarily unavailable tailings are produced. Tailings discharging, storing and maintenance management of the tailings will bring many problems as safety, environment and society[1-6].

Increased environmental safety remediation, the paste tailing preparation is an innovative tailings discharge technology evolved from tailings in-line, starter dam and tailings pond[7,8].

Wunugetushan Copper-molybdenum ore (hereinafter referred to as Wushan Copper-molybdenum) belong to China's gold group of Inner Mongolia mining co, LTD.it is located in new Barag Right Banner, Hulunbeier city, Inner Mongolia autonomous region, latitude 49 °north. The annual frost-free period 80 days and a heating time for eight month, winter weather minimum temperatures recorded up to 47 degrees below zero. The Wunugetushan Copper-molybdenum deposit is a mega low - grade deposit .Copper metal reserves are 2.67 million tons and the average grade of copper is 0.268%. Molybdenum metal reserves are 0.54 million tons and the average grade of molybdenum is 0.042%. The mineral processing technology is combined of SABC comminution process, copper molybdenum mixed flotation process and copper molybdenum separation flotation process. Concentrate products: copper concentrate has processed by pressure, filtration and dehydration; molybdenum concentrate has processed by diaphragm pressure, filtration and dehydration. Tailings products are applied by deep cone thickener--diaphragm pump--the tailings stacking technology.

**Preparation and Stacking Process of Paste Tailing**

As shown in fig.1, the tailings of copper molybdenum mixed flotation (concentration in 25-28%) are transported by slag slurry pump to the deep cone thickener, and through the preparation of NALCO flocculants, dosing equipment delivery and anionic polyacrylamide flocculants, which mixed spiral feed trough of the center of the deep cone thickener, deep cone thickener in top-down form clear layer, transition layer and the mud (both tailings paste). Overflow of deep cone thickener is delivered to high pool of concentrator by back water pump, and the rate of return is 86%. So the shortage problems of production water of the mine have fundamentally solved. Underflow tailings paste, concentration in 65-67%, is pumped to the diaphragm pump via slurry pump, and then which is stockpiling to the tailings pond by the diaphragm pump pipe. T answer the outfalls on pipeline, the discharge outlet can timing automatically switch turns emissions, to achieve the effect of uniform step by step a depot. The discharge outlet is automatically on a time switch emission in turn. It can be achieved the effect of evenly distributed in layer.

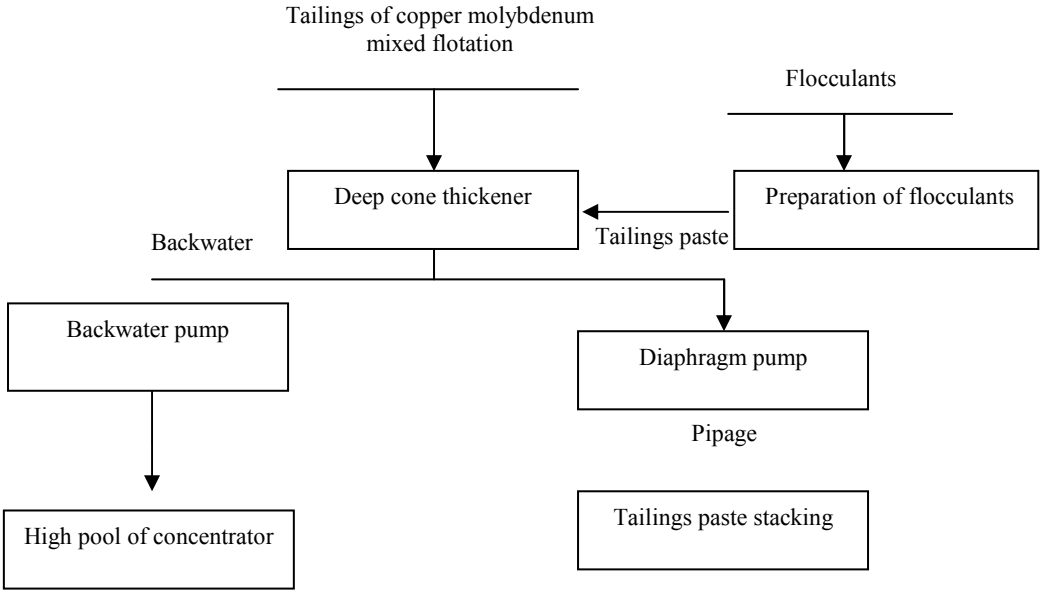



Fig. 1. The preparation and stacking process of paste tailing

**Preparation of Paste and the Main Discharge Equipment**

**Deep cone Thickener**

The 40 m diameter of deep cone thickener is designed and manufactured by FLsmidth Dorr - Oliver Eimco, which is currently the world's second largest similar equipment (The diameter of deep cone thickener is 43 meters using in the second project of Wunugetushan Copper-molybdenum).The use of deep cone thickener has changed the traditional tailings processing technology, and implementation of the tailings paste for pipeline tailings paste stacking, and effectiveness of backwater have been achieved by concentration or dehydration of the low concentration of tailing.

Currently, the tailings discharge concentration is reached 65-67% at Wunugetushan Copper-molybdenum. However, there is still a gap between the design requirements about more than 70% of the manufacturers. There is a few ponding in the discharge stockpiling, which is now pumped to dam snap back through the siphon, and then is pumped into to the high concentrate pool by backwater pump. A dry beach has appeared from discharge outlet to stacking area.it caused by a certain length of paste artesian slope, is hardened cracked but not dust [4]. It proved that the utilization rate of backwater is 86% by more than three years production practiced. The discharge concentration

of paste has been trying to improve by Wunugetushan Copper-molybdenum, and then the utilization rate of backwater will be further improved. The main process parameters are shown in Table 1.

Table 1. The main technology parameters of deep cone thickener

| Specifications and models | Processing capacity t/d | Feeding concentration % | The underflow concentration % | Rate of backwater % |
|---|---|---|---|---|
| φ40 m | 20000 | 25-28 | 65-67 | 86 |

**Diaphragm Pump**

The transportation of paste is using by DGMB450/8 diaphragm pump, in which is designed and manufactured by China non-ferrous Metallurgical Machinery Co., Ltd. (Shenyang). The first diaphragm used in alumina processing technology, along with the introduction and digestion of alumina based on absorbing technology application and development. In order to change the core equipment of diaphragm pump in alumina processing technology has been the use of imported products, considered from the Chinese aluminum industry long-term development and the national strategic perspective. SGMB, DGMB series reciprocating piston diaphragm pump is successfully developed through more than ten years of development by China nonferrous (Shenyang Metallurgical Machinery Co., Ltd.)[9, 10].

DGMB450/8 diaphragm pump is using 200NJ-760-CR-AZT slurry pump as feeding equipment by (Hubei Tianmen pump). According to concentration of underflow of tailings paste, the feeding quantity and the speed of diaphragm pump will be adjusted. The technique is achieved pipeline paste conveying and equality of delivery in the transportation process. The diaphragm pump is not contact with paste along piston moving .parts prolong the life of easy wear parts. The main process parameters are shown in Table 2.

Table 2. The main technology parameters of diaphragm pump

| Specifications and models | Maximum work flow ($m^3$/h) | Maximum working pressure (Mpa) | Jig frequency (times/min) | Power (Kw) |
|---|---|---|---|---|
| DGMB450/8 | 450 | 8 | 24-48 | 1400 |

**Flocculants and Preparation**

In order to speed up the pulp settling velocity and reduce suspended solids in overflow water, the paste is prepared with adding the flocculants and flocculants preparation in the deep cone thickener, in which is adding the NALCO powder preparation system dosing, manufactured by NALCO Australia Pty LTD. The flocculants is made of anion-polyacrylamide. The adding concentration of flocculant is 2.5g/L, consumption is 18.5g/t. C series pump is used conveying flocculant and manufactured by Mono factory. The preparation and dosing system realizes intermittent automatic flocculant preparation, flow and adjusting the flocculant automatically according to the incoming slurry concentration, flow rate. Fundamentally the phenomenon of mixed overflow and higher transition layer have been avoided, which caused by the unreasonable dosage flocculant. It's good to reducing the labor intensity of the workers.

**Discharge Pipe and Area of Storage**

The ceramic lined composite steel pipe oil transporting pipeline, to prevent the winter due to low temperature caused by tailing paste freezing, pipeline external package antifreeze facilities from the inside to the outside are electric heating glass cotton - galvanized iron. The whole pipeline T received 10 point of discharge, the discharge point every 12 hours to form uniform discharge, storage in the reservoir area. There is a certain length from the discharge port to the storage reservoir paste gravity gradient, the formation of a certain area of dry beach, the end of dry beach appears dry but not dust. Paste flow slope form the transition section of dry beach and reservoir without water district, as can be

seen from the graph stacking surface is cracked, but not crack, the tailings paste the discharge port discharge in alternate storage recently emissions will last emission formation crack gap fill close, not the formation of local cracking chunks.

**Production index**

The deep cone thickener feeding quantity is 1800 - 2000 t/h, and the concentration of it is 25 - 28%.The preparation of paste tailings transportation control is adopted in automatic control system. 1 – 4 month main production index is shown in Table 3.

Table 3. Production index of deep cone thickener

| Item / Month | Quantity of backwater (ten thousand tons) | | The underflow concentration of paste (%) | | Dosage of flocculant (g/t) | |
|---|---|---|---|---|---|---|
| | Plan | Actual | Plan | Actual | Plan | Actual |
| 1 | 180.58 | 197.51 | 67.0 | 66.08 | 16.0 | 14.7 |
| 2 | 180.58 | 186.15 | 67.5 | 66.19 | 16.0 | 15.8 |
| 3 | 171.07 | 143.19 | 67.5 | 65.45 | 16.0 | 15.0 |
| 4 | 183.70 | 196.05 | 66.0 | 64.31 | 16.0 | 15.7 |

Table.3 shows that, it is successful to use of backwater efficiently by the deep cone thickener and the problem of shortage of production water is solved in Wunugetushan Copper-molybdenum ore; The underflow concentration of paste is 65-67%, which has a certain gap between the design 70%. It is a good to control the actual consumption of flocculant than plans closely.

**Conclusion**

1)The 40 m diameter of deep cone thickener is used in Wunugetushan copper-molybdenum mine, which solves the problem of insufficient water production in Hulun Buir Grassland area. Not only did they make full use of low-grade mineral resources, but also they protected the ecological environment of grassland.

2)Application of large-scale equipment in Wushan copper-molybdenum mine has a certain role in designing and manufacturing with mining equipment in china.

3)Application of paste tailings has a certain role in promoting and guiding the development of traditional tailing thickening processing technology.

4)Technology of tailing paste obtained has instructive function for solving the change of tailing pond of safety and environmental protection at present in China.

**Acknowledgements**

This work was financially supported by the National Natural Science Foundation of the People's Republic of China (51364002), Guangxi Natural Science Foundation (2011GXNSFB018010) and the Colleges and Universities Foundation of Guangxi Zhuang Autonomous Region (No: 201203YB002). The authors are thankful for these supports.

**References**:

[1] Zh.J.Jin,M.Shi. The modern design of tailings facilities maintenance and management technology and comprehensive utilization of tailings resources utility manual, Contemporary audio and video publishing house, 2010.

[2]A.X. Wu, S.K. Yang, H.J. Wang. Ultra-fine full tailing paste disposal technology status and trends , Min. Tech. 5 (2011) 4-8.

[3] M. Feng.Tailings concentration and surface disposal of paste tailings, Mod Min. 10 (2009) 82-86.

[4] X.D. Hui, J.Y. Hong. Paste technology and its application in tailings treatment, China Min. Eng. 4 (2011) 49-54.

[5] S.K. Yang, H.J. Wang, A.X. Wu. Development situation and Prospect of tailings high-density discharge technology, Prod. Saf. Sci. Tech. China, 10, ( 2010) 28-32.

[6] D.D. Liang. Test and application of dry tailings pile technology, Non-ferrous Met. Eng. 2 (2012) 41-45.

[7] Dezhou Zhang.Development and application of paste tailings stacking technology, China Min. Eng. 4 (2010) 49-53.

[8].Longlong Wang, Zhihua Ma.The fourth generation of Tailings Disposal Technology Review, Min. Equip. 9 (2011) 57-59.

[9] H.Y. Zhang, G.R. Chen, Li Liu. Reciprocating diaphragm pump application in high concentrations of tail pulp conveying technology, Miner. Eng. 2 (2004) 43-46.

[10] X.Q. Ling. Application of SGMB, DGMB series reciprocating diaphragm pump in alumina production, Non-ferrous Metall. Equip. 2 (2003) 1-5.

*Advanced Materials Research Vol. 937 (2014) pp 391-395*
*© (2014) Trans Tech Publications, Switzerland*
*doi:10.4028/www.scientific.net/AMR.937.391*

# Elastic Modulus Influence on the Forming Precision of Grinding Tool Bended for the Aspherical Surface Grinding

Chun-min SHANG[1, a], Dong-mei ZHANG[1, b] Jian-dong YANG[2, c]

[1] Changchun University of Science and Technology, No.7089, Weixing road, Changchun, China

[2]Jilin Busness and Technology College, No.1606, Haoyue road, Changchun, China

[a]scm@cust.edu.cn, [b]zhangdongmei@cust.edu.cn, [c]yjd@jl.hotmail.com

**Keywords:** Elastic modulus, Bending, Aspherical surface, Grinding, Error

**Abstract:** Elastic modulus error is the key factor influencing to the forming precision of grinding tool bended in the aspheric processing. The mathematical model of the grinding tool bended has been established through mechanics and the mathematics method, the error formula has been inferred and the influence of elastic modulus error has been analyzed, the calculating example has been given. The result indicates had to confirm material's elastic modulus value according to the precision request of workpiece in choosing grinding tool material and control it in the certain scope, thus guaranteed the grinding tool the forming precision, further improve the workpiece the face shape precision.

## Introduction

Aspheric optical components for its good image quality are widely used in military, aerospace, meteorology, civil and other fields, it is also increasingly paid attention recent years, but because of difficult during aspheric processing, for example, long time for single-piece production cycle, high cost and low efficiency, it has been one desired goal for obtaining high-volume, high- efficiency, low-cost, high-precision aspheric processing technology [1-3]. Bending and forming method using high-speed grinding aspheric optical components is a new processing method with the characters of high efficiency and low cost, but the workpiece surface accuracy is not ideal. There are several factors, particularly in the grinding error and the elastic modulus of grinding tool's material is an important part of them while the grinding tool is made to bending.

Elastic modulus of the material is the inherent properties of it, a material selected as long as the grinding tool should be a constant volume in the bending process of the grinding tool, but the choice of materials as a grinding tool may produce errors which probably affect the accuracy of its bending. For example, according to the literature[4], the elastic modulus E decreases about 10% after quenching the steel and the change of E relative with quenching degree due to the martensite come into being after quenching and the lattice constant changes, and the elastic modulus E decreases with increasing temperature, such as raising the iron temperature up to 100℃ the elastic modulus decreased by 4%. That is the point of designing the grinding tool using the method of bending and forming, in order to accurately select the elastic modulus of the grinding tool material which must be used for accuracy measurements because the measurement error causes a direct error to grinding tool bending surface [4-6] .This paper is to analyze the impact of error on the elastic modulus of grinding tool material using bending and forming method to explore how to reduce that.

## Principle of Grinding Tool Bending

As shown, in order to improve forming precision and ensure manufacturing and dressing convenience, the grinding tool should be designed to equate thick beam while the width of it is a variable, which is designed a special curve based on the needs of the workpiece contour[1]. This curve subjected to ensure same as workpiece contour generated by the bending and forming acted on a given torque. Grinding tool when unstressed is attached to a flat surface so the processing and testing is very convenient. During the grinding, a bending moment acts on the grinding tool to bend

and form a curve as required. After the surface of the grinding tool wear, grinding tool's surface is no longer required matching curve, and then removes the bending moment to dress the grinding tool surface again to be a flat surface.

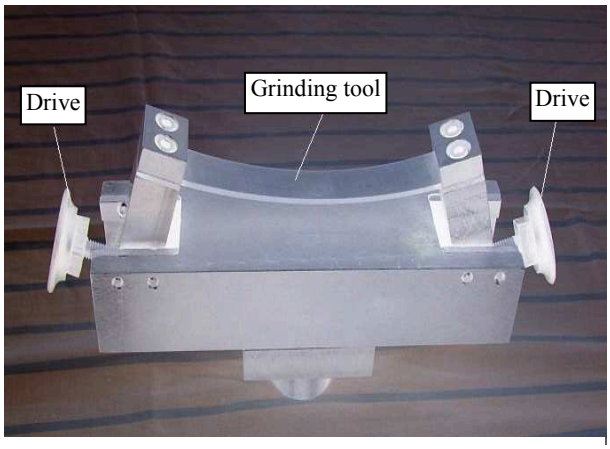



Fig. 1. Principle of grinding tool bending

**Mathematical Model for the Bending of the Grinding Tool**

Assume that the grinding tool is a simply supported beam, the following analysis will referred to as the beam, which is acted on a bending moment M, as shown in 2 (a) and (b). Subjected to the Moments later, the beam will be to bending and forming, it's a curve for the required theoretical curve (y = f (x)), and also the workpiece contour curves. When the beam rotating about the vertical centerline, it will generate the required aspheric surface, and then attach the abrasive on the grinding tool (diamond powder commonly used). The following equations are derived for the grinding tool of bending and forming.

Based on mechanics equations:

$$\frac{1}{\rho} = \frac{M}{EJ} \tag{1}$$

Where: ρ - Radius of curvature, mm;
M - Moment, N.mm;
E - Elastic modulus, MPa;
J - Inertia moment of beam cross-section, $mm^4$,

And further by the mechanics of materials:

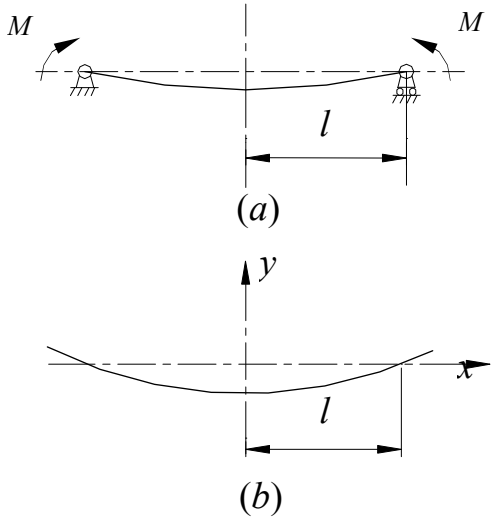



Fig. 2 Beams bending moment schematic

$$\frac{1}{\rho}=\frac{M}{E\frac{h^3B}{12}}=\frac{12M}{Eh^3B} \tag{2}$$

Where: h - Thickness of the beam (taken to be constant), mm

B - Width function of the beam, mm, and $B=\frac{12M\rho}{Eh^3}$.

According to mathematics: $\frac{1}{\rho}=\frac{y''}{\sqrt{(1+y'^2)^3}}$ (3)

By the equations (1), (2) and (3), differential bending beam is obtained as follows:

$\frac{y''}{\sqrt{(1+y'^2)^3}}=\frac{M}{EJ}$, Namely: $\frac{y''}{\sqrt{(1+y'^2)^3}}=\frac{12M}{Eh^3B}$ (4)

**Elastic Modulus Error Analyze**

We may assume that the equation (4) the right side is a constant A, curve equation at this point arc curve , then discuss the impact of the elastic modulus .

Equation (4) as: $\frac{y''}{\sqrt{(1+y'^2)^3}}=A$ (5)

Solving this second-order differential equation:

So $y'=N$, then $y''=N''$, into equation (5):

$N=(Ax-C_1)\sqrt{1+N^2}$, ($C_1$ integration constant)

Namely: $y'=(Ax-C_1)\sqrt{1+y'^2}$

Solving this differential equation has a solution for this:

$(y-C_2)^2+(x-\frac{C_1}{A})^2=\frac{1}{A^2}$, ($C_2$ is the integral constant) (6)

Boundary conditions:

$x=0, y'=0$

$x=l, y=0$

Obtained: $C_1=0, C_2=\sqrt{\frac{1}{A^2}-l^2}$ where: $l$ is the length of the grinding tool, mm.

Putting $C_1$, $C_2$ and $A=\frac{12M}{Eh^3B}$ into equation (6), the curve equation is as follows:

$$(y-\frac{1}{12M}\sqrt{E^2h^6B^2-144M^2l^2})^2+x^2=\frac{E^2h^6B^2}{144M^2} \tag{7}$$

To analyze the effect of the elastic modulus of the equation of the curve, in the above equation, the elastic modulus E and x are regarded as independent variables, the deflection curve y is the dependent variable, and both sides of the equation derivative of E are:

$$2(y-\frac{1}{12M}\sqrt{E^2h^6B^2-144M^2l^2})\cdot(\frac{\partial y}{\partial E}+\frac{1}{12M}\frac{Eh^6B^2}{\sqrt{E^2h^6B^2-144M^2l^2}})=\frac{Eh^6B^2}{72M^2} \tag{8}$$

Then Equation (7) and Equation (8) simultaneous with the independent variable x in place of the dependent variable y are:

$$\frac{\partial y}{\partial \mathrm{E}}=\frac{\mathrm{Eh}^6\mathrm{B}^2}{12\mathrm{M}}\left(\frac{1}{\sqrt{\mathrm{E}^2\mathrm{h}^6\mathrm{B}^2-144\mathrm{M}^2l^2}}-\frac{1}{\sqrt{\mathrm{E}^2\mathrm{h}^6\mathrm{B}^2-144\mathrm{M}^2x^2}}\right)$$

Variation form as:

$$\Delta y=\frac{\mathrm{Eh}^6\mathrm{B}^2}{12\mathrm{M}}\left(\frac{1}{\sqrt{\mathrm{E}^2\mathrm{h}^6\mathrm{B}^2-144\mathrm{M}^2l^2}}-\frac{1}{\sqrt{\mathrm{E}^2\mathrm{h}^6\mathrm{B}^2-144\mathrm{M}^2x^2}}\right)\Delta\mathrm{E} \tag{9}$$

Set scale factor $K_E$, then the errors can be expressed on the error curve of the relationship between the impact by $K_E$, the formula (9) is expressed as:

$$\Delta y_{\mathrm{E}}=\mathrm{K}_{\mathrm{E}}\Delta\mathrm{E}$$

$$\mathrm{K}_{\mathrm{E}}=\frac{\mathrm{Eh}^6\mathrm{B}^2}{12\mathrm{M}}\left(\frac{1}{\sqrt{\mathrm{E}^2\mathrm{h}^6\mathrm{B}^2-144\mathrm{M}^2l^2}}-\frac{1}{\sqrt{\mathrm{E}^2\mathrm{h}^6\mathrm{B}^2-144\mathrm{M}^2x^2}}\right) \tag{10}$$

As can be seen from equation(10) , when the elastic modulus is proportional to the error and the error curve at a point in the beam , at a certain point at $x = x_0$ is $K_E$ with the increase of E , but the error at this point in the zoom factor of designed grinding tool is for certain. E can also be seen from the coordinates of the impact position are related, $K_E$ at the origin coordinates (the midpoint of the beam) to obtain the maximum, and the error curve of the elastic modulus is maximum deflection maximum due to the influence of the error, which causing the error is also largest at the apex of the workpiece using of such grinding tool to grind the workpiece, and $K_E = 0$ at both ends of the beam. Along the coordinate axis, $K_E$ decreases as the absolute value of x increases, the elastic modulus has the greater influence on the error curve.

In order to intuitively understand the impact $K_E$ value, it may give a numerical example. The maximum error at $x = 0$, then set the parameters as follows:

$$\mathrm{E}=2\times10^5\,\mathrm{MPa},\mathrm{M}=2\times10^3\,\mathrm{N}\cdot\mathrm{mm},l=100\mathrm{mm},\mathrm{h}=3\mathrm{mm},\mathrm{B}=20\mathrm{mm},$$

$$K_E=\frac{2\times10^5\times3^6\times20^2}{12\times2\times10^3}$$

$$\times\left[\frac{1}{\sqrt{(2\times10^5)^2\times3^6\times20^2-144\times(2\times10^3)^2\times100^2}}-\frac{1}{\sqrt{(2\times10^5)^2\times3^6\times20^2-144\times(2\times10^3)^2\times0^2}}\right]$$

$$=5.56\times10^{-6}\,\mathrm{mm}^2/\mathrm{N}$$

The large error of elastic modulus will affect the error curve although it seems that the scale factor is very small. According to the literature [4], the elastic modulus E reduces about 10% for the steel after quenched, the elastic modulus of steel is 206GPa [7], assume the elastic modulus error is 10GPa for the grinding tool material selected, then E = 1x104MPa, into the formula(10)to get the error curve is:

$$\Delta y_{\mathrm{Emax}}=5.56\times10^{-6}\times1\times10^4=0.0556\mathrm{mm}=5.56\mu\mathrm{m}$$

Such larger errors is not allowed for the majority of the workpiece, so that the it can only be used for processing low-precision aspheric parts , such as microscopes and the condenser lens in the projector, searchlight mirrors, medical instruments the reflector and the condenser lens and so on.

In order to reduce effect of the elastic modulus of the grinding tool on the bending accuracy, The elastic modulus of the error should be controlled within a certain range according to the requirement of aspherical the processing accuracy. For high precision aspheric workpiece, the material used to make the grinding tool should be measured the exact value of the elastic modulus accurately if using the bending and forming method. Common method is based on national standards GB/T2105-91 and GB2105-80 to obtain the elastic modulus such as measuring method of dynamical elastic modulus of the material, and you can also use CCD spectral analysis method and digital methods.

## Conclusions

Bending equations was achieved based on mechanics and mathematics, the factors affecting the grinding tool bending errors were analyzed theoretically, and a calculating examples discussed the real effluence elastic modulus on the grinding tool bending error to derive the methods of obtain elastic modulus of materials increasing the bending accuracy, so is necessary to obtain the exact value of the elastic modulus of the applied material during designing grinding tool, the error should be controlled within appropriate range accordance with the requirements of the workpiece, which has important guiding significance for further experiments study and provide a favorable basis for the grinding tool design and the grinding error control.

## References

[1] Yang Jiandong, Tian Chunlin. High-speed grinding technology. Beijing: National Defense Industry Press, 2003(in Chinese):191-207

[2] Pang Changtao, Luo Songbao. Aspheric advanced processing technology. Aviation Precision Manufacturing Technology, 2001, 37 (3): 1-5

[3] Piao Chenggao, Cai Li. Technical Status aspheric optical components processing abroad and new progress. Optical Technology, 1993, (5) :7-13

[4] "Metal mechanical properties" writing group, Metal mechanical properties. Beijing: Mechanical Industry Press,1978:23-24

[5] Vazquez-Montiel, Sergio, Rodriguez-Hernandez, MA, Two-wavelength interferometer in the manufacture process of high-aspheric surfaces. SPIE, 2001, 4419 (8): 265 ~ 268

[6] Cai Li, Tian Shouxin. Optical components processing technology. Wuchang: Huazhong University Press, 1987:208-235

[7] Xu Hao, Qiu Xuanhuai, Cai Chunyuan. Mechanical Design Manual (Volume 1). Beijing: Mechanical Industry Press,1991:2-47

*Advanced Materials Research Vol. 937 (2014) pp 396-399*
*© (2014) Trans Tech Publications, Switzerland*
*doi:10.4028/www.scientific.net/AMR.937.396*

# Rotating Angle Error Influence to Grinding Aspheric Optical Component

Chun-min SHANG[1, a], Dong-mei ZHANG[1, b]Xin-ming ZHANG[1, c]

[1] Changchun University of Science and Technology, No.7089, Weixing road, Changchun, China

[a]scm@cust.edu.cn, [b]zhangdongmei@cust.edu.cn, [c]zxm@cust.edu.cn

**Keywords:** Aspheric Surface, Grinding, Rotating error, Profile Precision

**Abstract:** An analyzing rotating error method has presented based on grinding aspheric optical component. A coordinate transform has been done between the new and original coordinates system in view of the rotating error in installing parts, further, the rotating angle error model has deduced between actual curve and theoretical curve. The surface error formulas can be used for variety of rotary conic aspheric curve, depending on the requirements of the parts surface accuracy, quantitative adjustment target can be given in installation and adjustment process before grinding. Based on the rotating error formulas, the calculating example shows that installation angle bas various different influence to surface shape error, the error decreases with the $\theta$ decreasing, the surface error is reduced a magnitude accordingly when the angle is reduced to a magnitude. The parts surface error is up from -0.0030mm to -0.0448mm when the rotating angle increasing from 0.1° to 1°. When $\theta$ is constant, the surface shape error increases with steepness increasing, installing rotating angle requirement is more stringent for all the large steepness parts.

## Introduction

Aspheric optical components are used widely in lots fields, thus it has been one goal to be high efficiency, low cost, and high-precision. Bending and forming method is a new technology to process aspheric optical components which is high efficiency low cost [1, 2, 3], but the installation rotating error is unavoidable to exist for grinding the workpiece, which has more randomness, so error control problem is always plagued. In grinding process, workpiece installation position requires the precision, or it directly affects the workpiece surface shape error. In order to quantitatively obtained the impact of the error caused by the installation, the error source is analyzed during the grinding, the rotating error mathematical model is built due to inaccurate installation, a calculating example is done based on the model, which provides a theoretical basis and practical guiding for the actual grinding procedure[4,5,6] .

## Rotating Error Source in Installation

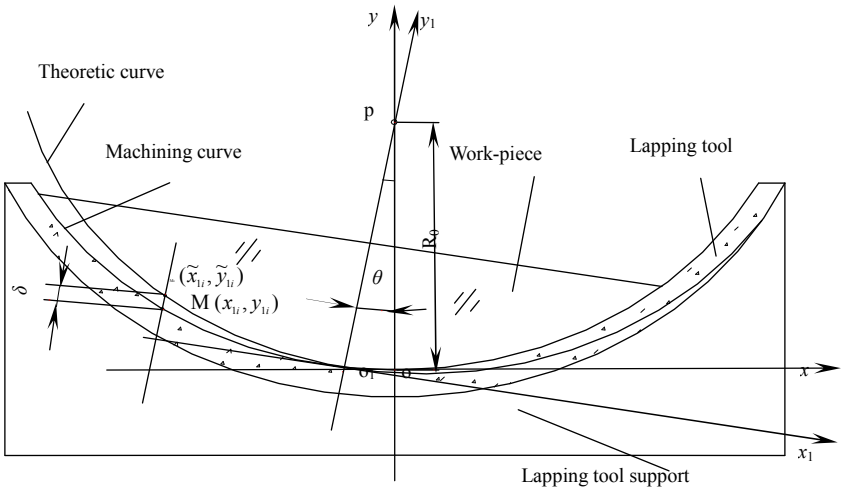



Fig. 1. Principle of the error

In grinding process, the workpiece and the grinding tool should be precise positioned to theoretically, but the rotating error always exists because of the unreasonable device structure, installation methods or operational errors, there are usually two ways: (1) Workpiece rotary axis does not coincide but parallel with the grinding tool rotational centerline. (2) Workpiece rotation center is not parallel to the rotational grinding tool centerline, and the rotation center of the workpiece relative to the rotational center of the grinding tool rotates at an angle, resulting in the workpiece tilt. Both two installation errors can cause the grinding accuracy of the workpiece surface, so the former is defined as translational error and the latter as rotating error. Now focuses on the latter case to analyze the rotating error impact to the workpiece surface accuracy during the installation and grinding.

**Establish Rotating Errors Mathematical Model**

As shown Fig.1, the tilt angle is $\theta$ of the workpiece rotation centerline (geometric centerline) relative to grinding tool rotation centerline, the original coordinate system *xoy* is established, origin *o* is on the midpoint of grinding tool's bus, the rotary centerline is y axis, which called the original system, anchored to the origin *o*, coordinate anises are clockwise rotated angle $\theta$, and then shifted to the new coordinate system $x_1o_1y_1$ which called the new coordinate system. So in the new coordinate system, the curve equation of grinding tool surfaces a bus is consistent with workpiece a bus (called the actual curve), then the actual curve equation in the original coordinate system is:

$$y = f(x) \tag{1}$$

In order to analyze the actual curve error, the curvature centers of o point is P, curvature radius is $R_0$, then as the center of P point moving the grinding tool a bus to a new coordinate system (midpoint coincides with $o_1$), which named the theoretical curve, so the origin in new coordinate system can be expressed as: $o_1$ ($-R_0\sin\theta$, $R_0-R_0\cos\theta$), further in coordinate system, transformation equation is:

$$\begin{cases} x_1 = x\cos\theta - y\sin\theta + \mathrm{R}_0\sin\theta \\ y_1 = x\sin\theta + y\cos\theta - \mathrm{R}_0(1-\cos\theta) \end{cases} \tag{2}$$

According to (1) and (2), the actual curve in the new coordinate system is expressed as the equation:

$$y_1\cos\theta - x_1\sin\theta + \mathrm{R}_0\cos\theta - \mathrm{R}_0\cos 2\theta = \mathrm{f}\left(y_1\sin\theta + x_1\cos\theta + \mathrm{R}_0\sin\theta - \mathrm{R}_0\sin 2\theta\right) \tag{3}$$

According to (1), the theoretical curve of the new coordinate system is expressed as the equation:

$$y_1 = f(x_1) \tag{4}$$

Derive the error δ expression of actual processing curve with the theoretical curve in the new coordinates system, there are three situations about calculation error δ:

(1) The curve normal of point M ($x_{1i}$, $y_{1i}$) on actual curve crosses the theoretical curve at point $\mathrm{M}_0(\widetilde{x}_{1i}, \widetilde{y}_{1i})$, the workpiece M point error $\delta = |\mathrm{M}_0\mathrm{M}|$;

(2) Curve normal of point $\mathrm{M}_0(\widetilde{x}_{1i}, \widetilde{y}_{1i})$ in theoretical curve crosses actual curve at point M ($x_{1i}$, $y_{1i}$), the workpiece M point error $\delta = |\mathrm{M}_0\mathrm{M}|$;

(3) A parallel y axis lines is done through M ($x_{1i}$, $y_{1i}$) on the actual curve, cross the theoretical curve at the point $\mathrm{M}_0(\widetilde{x}_{1i}, \widetilde{y}_{1i})$, he workpiece M point error $\delta = |\mathrm{M}_0\mathrm{M}|$;

The situation (3) is only discussed, from equation (3) and (4), the surface error δ model can be obtained at actual curve any point M ($x_{1i}$, $y_{1i}$):

$$\delta = y_{1i} - \widetilde{y}_{1i} \tag{5}$$

**Calculating Example**

Equation (5), surface shape error of the conic aspheric surface can be calculated during the grinding process due to the installation error, for given conic aspheric surface, assume the rotating angle as $\theta$, the error of each point of the workpiece can be calculated according to this surface error equation, while not considering the influence of other factors, the value of the tilt angle $\theta$ for the workpiece can be also calculate. For an example, the parabolic workpiece error at each point can be calculated under the influence of the inclination angle $\theta$.

Assuming a parabolic concave mirror, the bus equation: $y = x^2/100$, diameter D= 40mm, the installation rotating angle $\theta = 1°$, the curvature radius at the origin$R_0$= [1+f′$^2$(0)] 1.5/y ″(0) =50mm, the following error is calculated for each point of the workpiece.

By the equation (3) the actual curve equation in the new coordinate system is expressed as:

$$y_1 \cos\theta - x_1 \sin\theta + \mathrm{R}_0 \cos\theta - \mathrm{R}_0 \cos 2\theta = \frac{\left(y_1 \sin\theta + x_1 \cos\theta + \mathrm{R}_0 \sin\theta - \mathrm{R}_0 \sin 2\theta\right)^2}{100} \tag{6}$$

The theoretical curve equation is the new coordinate system: $y_1 = x_1{}^2/100$ (7)

When $x_1 = x_{1i}$, based on the equation (6), M point ordinate $y_{1i}$ is:

$$y_{1i} = \frac{1}{2\sin^2\theta}\left[-\sin 2\theta \cdot x_{1i} - 2\mathrm{R}_0 \sin^2\theta + 2\mathrm{R}_0 \sin 2\theta \sin\theta + 100\cos\theta - 20\sqrt{-\sin\theta \cdot x_{1i} + \mathrm{R}_0 \sin^2\theta + 25\cos^2\theta}\right]$$

From equation (7), when $x_1 = \tilde{x}_{1i}$, the $\tilde{y}_{1i}$ value at $M_0$ point is: $\tilde{y}_{1i} = 0.01\tilde{x}_{1i}{}^2$

The $y_{1i}$ and $\tilde{y}_{1i}$ into equation (5), the parabolic surface error δ is given at this point:

$$\delta = y_{1i} - \tilde{y}_{1i}\ \delta = y_{1i} - \tilde{y}_{1i} = \frac{1}{2\sin^2\theta}\left[-\sin 2\theta \cdot x_{1i} - 2\mathrm{R}_0 \sin^2\theta + 2\mathrm{R}_0 \sin 2\theta \sin\theta + 100\cos\theta\right.$$

$$\left. - 20\sqrt{-\sin\theta \cdot x_{1i} + \mathrm{R}_0 \sin^2\theta + 25\cos^2\theta}\right] - 0.01x_{1i}{}^2 \tag{8}$$

Then $R_0$ = 50mm, θ = 1° into the error equation (8):

$$\delta = \frac{1}{2\sin^2 1}\left[-\sin 2 \cdot x_{1i} - 2\times 50\sin^2 1 + 2\times 50\sin 2\sin 1 + 100\cos 1 - 20\sqrt{-\sin 1 \cdot x_{1i} + 50\sin^2 1 + 25\cos^2 1}\right] - 0.01x_{1i}^2 \tag{9}$$

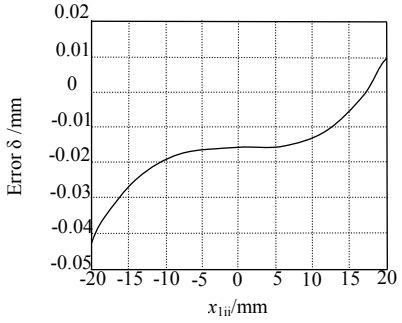



Fig. 2. Error with $x_{1i}$

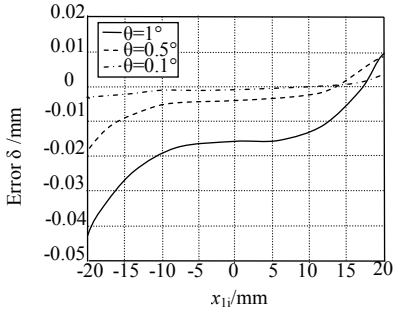



Fig. 3. Error for different $\theta$

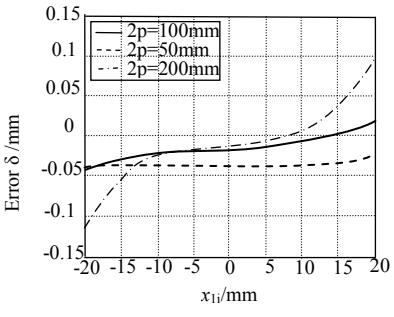



Fig. 4. Error for different steeps

where $\delta$ is error function of $x_{1i}$ , $x_{1i}$ is abscissa an any point on the actual processing curve , $x_{1i}$ ranges (-20mm $\leq x_{1i} \leq$ 20mm), when $x_{1i}$ will be given the error value at each point can be obtained , based on Matlab software, when $\theta$ = 1°, shown in Fig. 2, the surface shape error curve $\delta$ can be made which variation with of $x_{1i}$, it can be seen from the figure, the error value is gradually increasing both sides origin with $x_{1i}$ absolute value increasing, and the surface error is the largest at the edge, the maximum positive error of $\delta_{+max}$ = 0.0111mm, the maximum negative error of $\delta_{-max}$ =-0.0448mm, which are not allowed for most aspheric lens, thereby the angle $\theta$ values must be reduced to obtain more accurate the surface shape. Fig.3 shows the surface shape error curve for different installation angle $\theta$, also, the error decreases with $\theta$ decreasing, when $\theta$ = 0.1° , the

maximum positive error $\delta_{+max}$ = 0.0026mm, the maximum negative error $\delta_{-max}$ =-0.0030mm, the corresponding error is also reduced by an order of magnitude.

The steepness of the parabolic part has different influence at the same rotating angle θ. Standard parabolic equation: $y = x^2/2p$, the parabolic is steep when 2p value is smaller. Fig.4 shows that surface shape error of three parabolic variation with $x_{1i}$ when θ = 1° , 2p= 50mm, 2p= 100mm and 2p=200mm, the surface shape error increases with decreasing 2p values, the art steepness generates a large influence for the parabolic surface shape errors at same installation angle θ.

## Conclusions

Grinding rotating error is a key factor restricting processed part surface accuracy. This calculating rotating error method proposed in this paper provides a theoretical basis for calculate shape error during installation and grinding, also, the surface error formulas can be used for variety of rotary conic aspheric curve, depending on the requirements of the parts surface accuracy, quantitative adjustment target can be given in installation and adjustment process before grinding. Based on the rotating error formulas, the calculating example shows the influence laws to the parabolic part:

(1) Not considering the other factors, and at $\theta$ =1°, the surface error increases from the aspheric surface center to the edge, the maximum positive error $\delta_{+max}$= 0.0111mm, the maximum negative error $\delta_{-max}$ =-0.0448mm.
(2) For a parabolic parts, installation angle bas various different influence to surface shape error, the error decreases with the $\theta$ decreasing, the surface error is reduced a magnitude accordingly when the angle is reduced to a magnitude.
(3) When $\theta$ is constant, the surface shape error increases with steepness increasing, installing rotating angle requirement is more stringent for all the large steepness parts.

## References

[1] Michael T.Tuell, James H.Burge, Bill Anderson. Aspheric optics: smoothing the ripples with semi-flexible tools. Opto-Electronic Engineering, 2002, 41(7):1473-1474.

[2]HAN Cheng-shun, DONG Shen, TANG Yu-Yong. Geo metric model of the ultra-precision grinding of large optical aspheric surface. Acta armamentarii ,2004, 25(6): 741-745(In Chinese).

[3]Jiandong Yang,Chunlin Tian. High Speed Lapping Technology. Beijing：National Defense Industry Press, 2003, 191-207(In Chinese).

[4] Chunmin Shang. Research on high speed lapping technlgy to process aspherical part by the bending and forming lapping tool. Changchun: Changchun University of Science and Technology,2011, 1-7(In Chinese).

[5] Quantu Wang, Jingchi Yu, Xuejun Zhang. Solution for best fitting spherical curvature radius and asphericity of off-axis aspherics. Opto-Electronic Engineering,2000,27(3): 16-20(in Chinese).

[6] Yongjian Wan, Bin Fan, Jiahu Yuan et al. An on-line measuring technique for lapping large aspherical mirror. Opto-Electronic Engineering, 2005, 32(1):1-4(In Chinese).

*Advanced Materials Research Vol. 937 (2014) pp 400-403*
*© (2014) Trans Tech Publications, Switzerland*
*doi:10.4028/www.scientific.net/AMR.937.400*

# Effect of Carding Plate Gauge under the Licker-in of Carding Machine on Polyester Yarn Hairiness

Xue-zhi YU[A], Peng-zi SUN[B]

Eastern Liaoning University, 325Wenhua Road, Dandong, Liaoning, 118000, China

[a]email:yuxuezhi001@163.com, [b]email:kyc3@163.com

**Keyword:** Carding Machine,Pin Carding Plate,Saw-tooth Carding Plate, Gauge, Hairiness.

**Abstract.** Effect of different gauge of pin carding plate and saw-tooth carding plate respectively installed under the licker-in of carding machine on polyester yarn hairiness was studied. The hairiness of polyester yarns produced in the condition of installing pin carding plate and saw-tooth carding plate under the licker-in at four different gauges were tested by YG172 yarn hairiness tester. The results show that the two kinds of carding plate at the gauge of 0.7mm are most beneficial to reducing the number of polyester yarn hairiness. When the pin carding plate gauge is 1.0mm and the saw-tooth carding plate gauge is 0.3mm, the number of polyester yarn hairiness is the most. As a whole, installing saw-tooth carding plate under the licker-in is more favorable for reducing the number of polyester yarn hairiness.

## Introduction

Yarn hairiness has some effect on the luster, abrasion resistance and weaving process of yarn, so how to reduce yarn hairiness is one of the key fields in spinning research. Bralla has summarized the study on yarn hairiness [1-3], which roundly discussed the questions on yarn hairiness test, technical measures of decreasing hairiness and so on. The literature [4] studied the effect of pin carding plate on polyester yarn hairiness, and the results showed that the pin carding plate at the licker-in speed of 1290r/min was most beneficial to reducing the polyester yarn hairiness. However, there are no prior studies in the effect of different pin carding plate gauge on polyester yarn hairiness. Therefore we made some experimental studies on this aspect and the results are as follows.

## Experimental

### Experimental Materials

Experimental materials are polyester staple fibers produced by Huaxi Village, with the specification of 1.33dtex×38mm.

### Experimental Process Flow

A002 bale plucker→A006B mixer→A034 step opener→A036 porcupine opener→A092 tandem feeder→A076A single beater lap machine→A186F carding machine→A272 drawing frame→A272 drawing frame→A456 roving frame→A502 spinning frame.

### Experimental Conditions

The polyester laps used in the experiment were processed by the same picker and at the same time, and the lap quantity was 417 g/m.

A186F carding machine is used in the experience. The gauge between the feed plate and the licker-in is 0.23mm. The gauge between the mote knife and the licker-in is 0.38mm. The gauge between the cylinder and the licker-in is 0.13mm. The licker-in speed is 1050r/min, the flat speed is 87mm/min, and the cylinder speed is 330r/min. When the other conditions remain unchanged, the pin carding plate and the saw-tooth carding plate are installed respectively under the licker-in with the pin carding plate density of 32 teeth/$(25.4mm)^2$ and the saw-tooth carding plate density of 42 teeth /$(25.4mm)^2$. The gauge between the carding plate and the licker-in gauge is respectively 0.3mm, 0.5mm, 0.7mm and 1.0mm.

In the spinning process, drawing was carried in the same machine with the same eyes, roving and spinning were done on the same machine with the same spindle. The above process conditions are the same.

For each experiment plan, 5 yarn bobbins were processed. Yarn hairiness was tested by the YG172 yarn hairiness tester. The hairiness test fragment is 10m long, with the test speed of 30m/min. Each bobbin is tested for 20 times, so the test times for each plan are 100, so as to ensure the stability and accuracy of test results [5]. Hairiness of 3mm and above is generally considered to be harmful [6], so their number is summed statistically.

## Experimental Result

Test results of polyester yarn hairiness number in different experimental plan are shown in Table 1, Effect of different kinds of carding plate on polyester yarn hairiness is shown in Fig 1.

Table 1. Test results of yarn hairiness number in different experimental plan

| Carding plate type | Gauge between carding plate and licker-in /mm | The average number of hairiness of 3mm and above / 10 $m^{-1}$ |
|---|---|---|
| Pin carding plate | 0.3 | 63 |
| Pin carding plate | 0.5 | 79 |
| Pin carding plate | 0.7 | 58 |
| Pin carding plate | 1.0 | 88 |
| Saw-tooth carding plate | 0.3 | 123 |
| Saw-tooth carding plate | 0.5 | 69 |
| Saw-tooth carding plate | 0.7 | 58 |
| Saw-tooth carding plate | 1.0 | 81 |

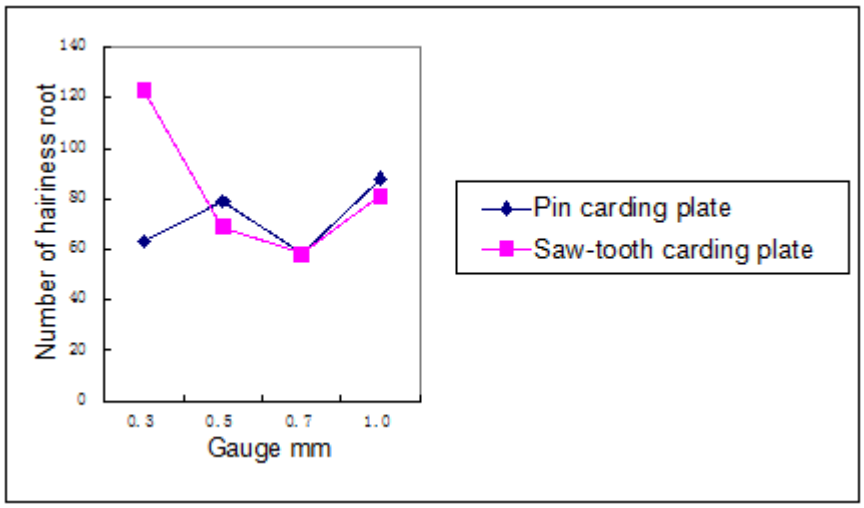



Fig. 1. Effect of different kinds of carding plate on polyester yarn hairiness

## Discussion on Experimental Results

### Effect of Different Gauge on the Number of Polyester Yarn Hairiness

#### Effect of Different Gauge on the Number of Polyester Yarn Hairiness in the Condition of Installing Pin Carding Plate Under the Licker-in

From Table 1, it can be seen that the number of polyester yarn hairiness with the gauge of 0.7mm is the least; that of 0.3mm comes second by over 7.93%; that of 0.5mm comes third by over 26.58% compared with that of 0.7mm; and that of 1.0mm is the most by over 34.09% compared with that of 0.7mm. The results show that in the condition of installing pin carding plate under the licker-in, the gauge of 0.7mm is most beneficial to reducing the number of polyester yarn hairiness, while that of 1.0mm is most unfavorable for reducing the number of polyester yarn hairiness.

**Effect of Different Gauge on the Number of Polyester Yarn Hairiness in the Condition of Installing Saw-tooth Carding Plate Under the Licker-in**

From Table 1, it can be seen that the number of polyester yarn hairiness with the gauge of 0.7mm is the least; that of 0.5mm comes second by over 15.94%; that of 1.0mm comes third by over 28.40% compared with that of 0.7mm; and that of 0.3mm is the most by over 112.07% compared with that of 0.7mm. The results show that in the condition of installing saw-tooth carding plate under the licker-in, the gauge of 0.7mm is most beneficial to reducing the number of polyester yarn hairiness, while that of 0.3mm is most unfavorable for reducing the number of polyester yarn hairiness .

It can be seen from the above that whether pin carding plate or saw-tooth carding plate is installed under the licker-in, the gauge of 0.7mm is most conducive to reducing the number of polyester yarn hairiness. When the pin carding plate gauge is 1.0mm and the saw-tooth carding plate gauge is 0.3mm, the number of polyester yarn hairiness is the most.

**Comparison of the Effect of Different Carding Plate on the Number of Polyester Yarn Hairiness**

From Fig 1, when the gauge between the carding plate and the licker-in is 0.3mm, the number of polyester yarn hairiness installing pin carding plate under the licker-in is less than that for saw-tooth carding plate, by 48.78%. This shows that installing pin carding plate under the licker-in is more conducive to reducing the number of polyester yarn hairiness at 0.3mm gauge between the carding plate and the licker-in.

When the gauge between the carding plate and the licker-in is 0.5mm, the number of polyester yarn hairiness installing pin carding plate under the licker-in is more than that for saw-tooth carding plate, by 12.66%. This shows that installing saw-tooth carding plate under the licker-in is more conducive to reducing the number of polyester yarn hairiness at 0.5mm gauge between the carding plate and the licker-in.

When the gauge between the carding plate and the licker-in is 0.7mm, the number of polyester yarn hairiness has no change whether pin carding plate or saw-tooth carding plate is installed under the licker-in. This shows that the effect of installing pin carding plate or saw-tooth carding plate under the licker-in on the number of polyester yarn hairiness is the same at 0.7mm gauge between the carding plate and the licker-in.

When the gauge between the carding plate and the licker-in is 1.0mm, the number of polyester yarn hairiness installing pin carding plate under the licker-in is more than that for saw-tooth carding plate, by 7.95%. This shows that installing saw-tooth carding plate under the licker-in is more conducive to reducing the number of polyester yarn hairiness at 1.0mm gauge between the carding plate and the licker-in.

It can be seen from the above that, as a whole, installing saw-tooth carding plate under the licker-in is more conducive to reducing the number of polyester yarn hairiness.

In summary, whether installing pin carding plate or saw-tooth carding plate under the licker-in, the gauge of 0.7mm is more conducive to reducing the number of polyester yarn hairiness. When the pin carding plate gauge is 1.0mm and the saw-tooth carding plate gauge is 0.3mm, the number of polyester yarn hairiness is the most. As a whole, installing saw-tooth carding plate under the licker-in is more conducive to reducing the number of polyester yarn hairiness.

**Conclusion**

According to the above discussion, following conclusions can be obtained:

For pin carding plate, the gauge of 0.7mm is most conducive to reducing the number of polyester yarn hairiness, while that of 1.0mm is most unfavorable for reducing the number of polyester yarn hairiness.

For saw-tooth carding plate, the gauge of 0.7mm is most conducive to reducing the number of polyester yarn hairiness, while that of 0.3mm gauge is most unfavorable for reducing the number of polyester yarn hairiness.

As a whole, installing saw-tooth carding plate under the licker-in is more conducive to reducing the number of polyester yarn hairiness.

**Acknowledgement**

This research was financially supported by Key Discipline Project of Liaoning Province Universities (No. 2012310) .

**References**

[1] Barella A. The hairiness of yarns. Textile Progress.1993;24:10-25.

[2] Barella A, Manich A.M. Yarn hairiness update. Textile Progress.1997;28:5-18.

[3] Barella A, Manich A.M. Yarn hairiness: a further update. Textile Progress.2000;31:1-23.

[4] Xuezhi Yu,Pengzi Sun .Impact of pin carding plate and saw tooth carding plate on polyester yarn hairiness[J]. Cotton textile technology, 2011,6:61-62.(In Chinese)

[5] Shanghai Textile Holding (Group) Company Code. Cotton Handbook (Third Edition)[M]. Beijing: China Textile Press, 2004,10:966. (In Chinese)

[6] Xu Shaofan. Cotton Quality Control[M]. Beijing: China Textile Press, 2002,2:208. (In Chinese)

*Advanced Materials Research Vol. 937 (2014) pp 404-408*
*© (2014) Trans Tech Publications, Switzerland*
*doi:10.4028/www.scientific.net/AMR.937.404*

# Design and Trial-production of Emergency Power Supply System Battery Based on Chemical Hydrogen Production

Chun-hua XIONG[1,a], You-jie ZHOU[1,b,*], Fa ZHENG[2,c], Gang WANG[3,d], Feng WANG[3,e]

[1] Beijing POL Research Institute, Beijing, 102300, China

[2] Dantu Hi-Tech Industrail Park, Zhenjiang, 212143, China

[3] Beijing Martial Delegate Agency,Headquantens of the General Equipment, Beijing, 100042, China

[a]email: xch@263.net.cn, [b*]email: zhoujie_76@126.com, [c]email: zhengfa@jspowerinc.com, [d]email: shangmachangcun@126.com, [e]email: wang20403201@163.com

**Keywords:** on-line hydrogen production; hydrogen battery; emergency power supply system.

**Abstract.** Based on chemical on-line hydrogen production, the author proposes a technical solution of Emergency Power Supply System Battery，and the hydrogen supply system, fuel cell stack, the control system and the water-heat balance management system was presented, and the prototype of 1kw hydrogen battery was trial-producted through integrated and modularized design. The actual test shows that the continuous power supply time is over 4 hours. It can be used as the ideal emergency power supply equipments in emergency disaster relief actions.

## Introduction

China has a vast territory. Natural disasters occur frequently. The gasoline engine generators of emergency power supply devices we use when doing disaster relief work and dealing with emergencies are heavy and noisy and release harmful gases. The continuous power-on time of lithium battery, nickel-metal hydrogen battery and lead-acid battery is short. Moreover, they cannot make charging recovery in emergencies. Popularization and application of fuel cells can help deal with “energy” and “environmental protection” [1-2], the two critical global issues. Fuel cell is a power generation set that can directly convert chemical energy in the fuel (hydrogen, methyl alcohol, etc.) and the oxidizing agent into electric energy through electrochemical reaction. It has many advantages. It works in stable condition, has high generating efficiency and makes zero release.

In this thesis, the author uses the technical form that integrates the hydrogen supply system, fuel cell stack, the control system and the water-heat balance management system, based on chemical on-line hydrogen production. Dynamic allocation and management of power are made depending on BMS system control design by the author according to the best working condition and loading condition of the fuel cell. The author develops the prototype of 1kw hydrogen battery. This thesis mainly introduces designing of the on-line hydrogen production system, the fuel cell stack and the control section. At last, a test, the prototype of 1kw hydrogen battery.

## System Design

### Technical Index and Performance Parameters

Hydrogen batteries based on chemical hydrogen production mainly refer to the emergency and standby power supply devices used on the equipment. The author makes an integrated and modularized mechanical and electric structural design and proposes a technical form that integrates the hydrogen supply system, the fuel cell stack, the control system and the water-heat balance management system.Based on the current industrialization level and condition of hydrogen cell[3], considering current technical capacity and characteristics of hydrogen cell[4-5], especially hydrogen supply capacity of the on-line hydrogen production system determined by the hydrogen production efficiency of efficient hydrogen generating agent, as needs small-sized vehicle-mounted power supply

units, the author determines the power of the prototype to be 1000kw. The basic performance parameters include on-line hydrogen production capacity and power supply capacity, it is shown as follow.

Hydrogen supply rate: ≥15slpm.Power supply capacity: continuous full-load working time≥4h. Overload capacity: when the output power is 110% of the rated power. the system can work normally for 10min.Output voltage: AC/220V±10%.Maximum starting time: 1min; it will take 3 min at most to rise from 0 to 80% of the power.Operating temperature: 0°C～45°C.

**System Composition**

The integrated hydrogen cell electric generator is composed of the hydrogen production system, the hydrogen filtration and storage system, the fuel cell system, the power conversion module and the automatic control system. It is shown in Fig .1.

**Design of the Hydrogen Supply System**

The hydrogen supply system is composed of the hydrogen production system and the hydrogen purification and storage system. The first step of hydrogen supply system design is the selection of the hydrogen supply method.

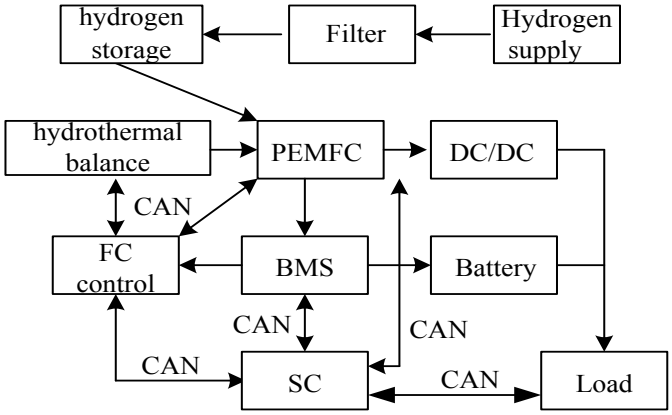



Fig. 1. Structure diagram of 1KW hydrogen power generation AIO

Efficient hydrogen generating agent on-line hydrogen production technology and normal-pressure hydrogen storage buffer tank are used in design of site hydrogen production and storage devices. This technology is practical and user-friendly. The user only needs to add water into the equipment and add designated amount of hydrogen donor. The hydrogen supply process is finished. The texture of the hydrogen tank is 316L, and the gross volume is 100L. As a small amount of vapor will enter into the hydrogen storage tank after the hydrogen produced by the reaction still is filtered, a drain valve is designed at the bottom of the hydrogen storage tank. With regard to leakproofness of the hydrogen storage tank, the leakproof structure of screw-thread and thread seal tape is used. The hydrogen production tank is shown in Fig .2. A filter screen(shown in Fig .3) is designed on the powder tray in case the powder bag breaks due to strong reaction and the powder leaked out block the air outlet.

**Hydrogen Purification System**

The proton exchange membrane is in acidic property. As the environment for hydrogen production is an alkaline environment. Requirement of the fuel cell on hydrogen is very high. The hydrogen must be purified.

The author develops and designs a filter system for hydrogen purification independently: *(a)* water filter system: 0.1mNaOH solution absorbs carbon dioxide and water. The moisture separator (shown in Fig .4) makes the primary purification of the hydrogen generated by the reaction still; *(b)* deoxidizer and CMS filer system (shown in Fig .5) absorb oxygen and nitrogen; *(c)* 13X and 5A systems: gas desiccation; *(d)* filter the tiny amount of nitric oxide, sulfur oxide, carbureted hydrogen, etc. The hydrogen purity can reach 99.99%. Therefore, the users can use the hydrogen conveniently and safely.



Fig. 2. Hydrogen production reaction still



Fig. 3. Filter screen

**Design of the Fuel Cell Stack**

MEA and the bipolar plate are at the center of the stack of the proton exchange membrane fuel cell. With regard to MEA, the mature product produced by Ballard Company is used. The bipolar plate takes the substantial part considering the weight, volume and cost. It uses alloy metal plate which is vibration-resistant, corrosion-resistant and small in size and large unit power density and good electric and thermal conductivity. Even if the thickness is reduced to 0.1mm, it will still be air-proof. Moreover, the gas runner can be molded through stamping. It can benefit lifting the volume specific power and reducing the production cost.

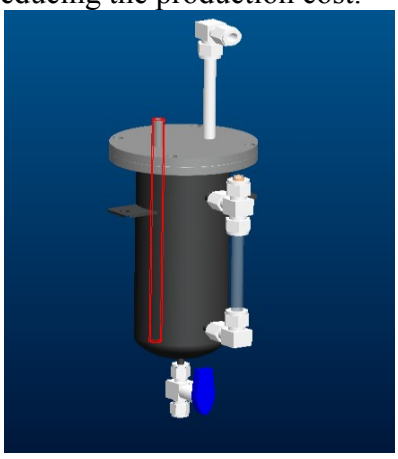


Fig .4. Moisture separator

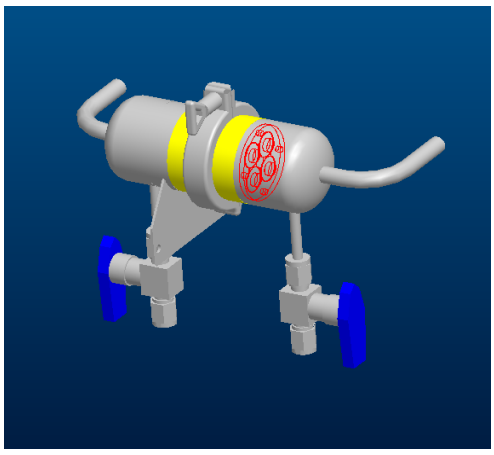


Fig. 5. Membrane filter

At present, most proton exchange membrane fuel cell stacks are assembled through filter press methods, including bolt fixation method, air cylinder fixation method and bandage fixation method. In China, the most commonly used one is bolt fixation method. The bolt fixation method can be further divided into inside bolt insertion press fitting method and outer bolt press fitting method. The traditional press fitting method has many deficiencies, such as too many assembly parts, tedious assembly procedures, low efficiency and reduced power density. This product adopts inside bolt method. Meanwhile, the author optimizes the structural design. As a result, the stack assembly efficiency is enhanced. Reliability and power density are enhanced. It has many advantages, such as few parts, small volume, high utility rate of space and high reliability. The schematic diagram of the cell stack is shown in Fig.6.

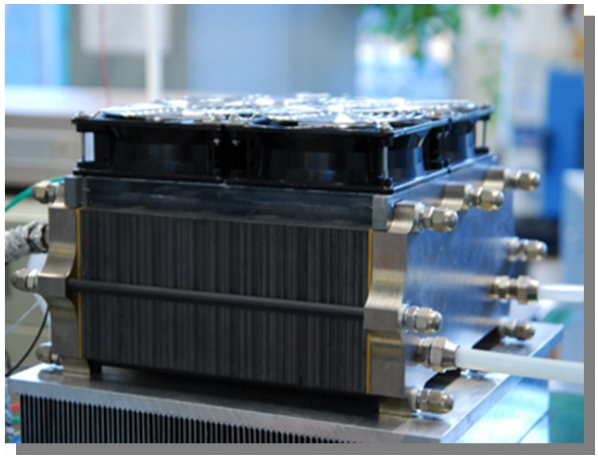


Fig. 6. Cell stack

**Design of the Control Section**

The project team integrates hydrogen production technology, purification technology and hydrogen cell power generation technology and produces a portable hydrogen power generation AIO (shown in Fig .7 and Fig .8). This power generation set controls hydrogen flow through mass flow controller (MFC) and controls pressure of the hydrogen through special pressure regulating valve; conversion of electric power is realized by adopting the independently designed DC/DC and DC/AC converters. Automatic electric control is realized by using PLC. The self-design BMS system makes management toward the battery system.



Fig .7. Diagram of PLC module

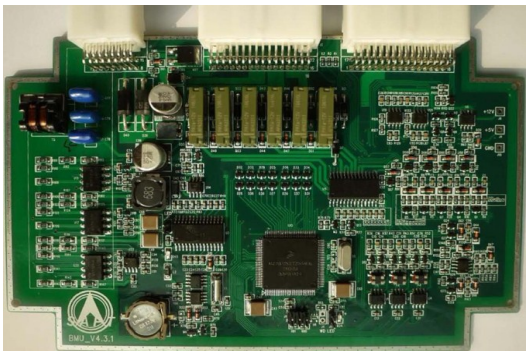


Fig .8. BMS control circuit board

**Test of the System**

For the hydrogen cell electric generator, the fundamental characteristic is its power supply capacity. According to some requirements of YDB051-2010 hydrogen cell power supply system for telecommunication, the test is made from the following aspects. Test environmental conditions is shown as follow.

Temperature: 0°C~45°C
Humidity: 45%~75%
Atmospheric pressure: 86kpa ~106kpa

**Test of the Hydrogen Production Capacity**

Check the pressure gage of the hydrogen electric generator. The pressure shall be 0Mpa. Put efficient hydrogen generating agent and water according to the stipulated requirements into the hydrogen production tank for hydrogen production reaction. Record the time it takes from the beginning to the end hydrogen supply shown on MFC.Calculation shall be made according to the following formula.

Flow L/min*time min=total flow L

Total flow L/ (the amount of efficient hydrogen generating agent that is used g/100g)=the amount of hydrogen that are produced by 100g efficient composite hydrogen generating agent L.

**Test of Basic Electrical Properties**

Start the fuel cell power supply system at the rated linear load. Test the output voltage. Use the voltage meter to measure the voltage and frequency when the output power is at 10%, 20%, 50% and 100% respectively.

Start the fuel cell power supply system at the rated linear load. Regulate the load: the load current is 50% of the rated value. The output voltage is the setting value; in load current break, saltation change of the rated current is made,such as 25%→50%→25% ,50%→75%→50%.Waveform of the output voltage is observed according to the proper range of the digital storage oscilloscope.

The fuel cell power supply system shall be started under the temperature form 0°C to 45°C. Use the digital storage oscilloscope to measure the output power.

Start on-line hydrogen production. Start the fuel cell power supply system. Make hydrogen production continuously until hydrogen fills the storage battery. Then keep time. Connect the rated linear load. Regulate the load. The output power is the rated value. On-line hydrogen production and the fuel cell stack work continuously.

**Conclusion**

(1)In this test, the amount of efficient hydrogen generating agent that is used is 300g. 480L of hydrogen is produced in 30 minutes. According to the calculation, the test result can be realized. The hydrogen production rate is 16slpm.

(2)measure the voltage and frequency when the output power is at 10%, 20%, 50% and 100% respectively. The output voltage shall be at 200±10%. The frequency fluctuation shall be within 5%.

(3)The test result shows that the calculated voltage amplitude overshoot shall not exceed ±10% of the setting value of the output voltage. The recovery time shall not be longer than 200μs.

(4)By adding efficient hydrogen generating agent, it can work continuously for 4 hours at least.

(5)The maximum starting time: 2min. It shall be started successfully every time; start the fuel cell power supply system at room temperature. The time for the power to change from 0 to 80% of the rated power shall be 2min.

The result of actual measurement shows that it reached the expected design objectives. The research result will serve as technical reserve and experience accumulation of hydrogen battery based on chemical hydrogen production and finally provide scientific and reasonable decision basis for the application of this technology and product on military logistical devices.

**References**

[1] THOU T P, REAL S, DAVIT B. Control algorithm of fuel cell and batteries for distributed generation system [J]. IEEE Trans Energy Converse, 2008, 23: 111-116.

[2] Zhou Li. Comment on Research of Hydrogen Storage and Production [J]. World Sci-Tech R & D, 2006, 28(6): 17-22.

[3] Shen P K, Tian Z Q1 Performance of highly dispersed Pt/ C catalysts for low temperature fuel cells [J] 1 Electrochimica Acta, 2004, 49(19): 3107-31111.

[4] Paola C.Transport phenomena in polymeric membrane fuel cells [J].Chemical Engineering Science, 2001, 56(2):323-332.

[5] Xianguo L,Imran S. Review of bipolar plates in PEM fuel cells:Flow-field designs. Inter. J. Hydrogen Enelgy,2005,30:359-371.

*Advanced Materials Research Vol. 937 (2014) pp 409-415*
*© (2014) Trans Tech Publications, Switzerland*
*doi:10.4028/www.scientific.net/AMR.937.409*

# Complex Image Recognition Method of Train Wheels Based on Contour Feature

Dong-Yao JIA[1,a], Po HU[1,b,*]

[1]Advanced Control Systems Laboratory, School of Electronic and Information Engineering, Beijing Jiaotong University, Beijing 100044, China

[a]dyjia@bjtu.edu.cn, [b]bjtuhp@126.com

**Keywords:** Image recognition, Image acquisition, Arc detection, Contours potential

**Abstract.** At present, most of the domestic train wheel detection is still manual. Existing image detection methods do not fully consider the characteristics of wheel profiles, as the algorithm is very complicated, they do not apply to fast dynamic monitoring. The paper proposes a dynamic image recognition method of train wheels based on contour feature. Firstly, wheel contour curve is extracted using RCD circular arc detection algorithm with constraint condition. Then, after analyzing the wheel contour curves, vector contour is constructed to describe them. At last, images of wheels are rapid recognized, and the recognition is based on identification function. Experimental results show that this method can achieve 95% accuracy when the similarity of complete wheel is set to 0.98 or more. This method can adapt to railway environment and has a certain application value.

## Introduction

It is all known that wheel is an important part on the train, and wheel wear can affect the smooth running of the train and riding comfort of passengers. Seriously, wheel wear will endanger traffic safety. For this reason, detection of the wheel is a very important work. The way using a variety of image processing methods for dynamic wheel detection has high accuracy, and the key technologies such methods need to be resolved first is how to identify the wheel image which can meet the testing requirements[1,2]. For image recognition, commonly used methods are mainly based on color, texture, shape, semantic features, etc. At this stage, there are not many studies of image recognition method for wheels image, while most studies do not take into account the special nature of the wheel image. Meanwhile, most of the existing algorithm is more complex, and can not conducive to dynamic testing [3,4]. Through the research of special geometry of the wheel and color discrimination between wheels and rails, shape features the most suitable elements to identify wheel image.

Recognition of this article is based on the contour feature of the wheel, and Similarity determination result of wheel image to be detected and standard image is based on customized image recognition function. The feasibility and accuracy of detection of the method are demonstrated through a number of simulation experiments.

## Contour Image Acquisition

The method used in this paper is to extract the whole wheel profile curve first, then, the wheel profile curve can be further extracted on this basis. Overall wheel profile curve includes wheel profile curve and curves of other objects, such as the contour of rails. Step of extracting is shown in Fig.1.

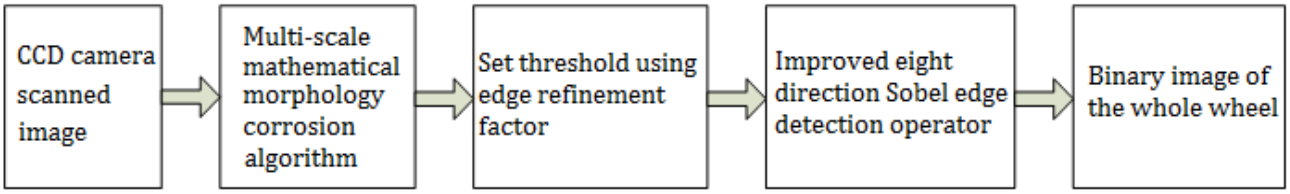



Fig. 1. Acquisition method of a whole wheel contour curves

Wheel profile curve can be extracted from obtained whole wheel profile curve before. Improve RCD algorithms is used in this paper for image extraction, and it is an optimization algorithm based on method proposed by Teh-Chuan Chen and Kuo-Liang Chung[5]. In determining whether the other points are on the candidate circle, original RCD algorithm randomly select points, and then calculate the distance between the points and center of the candidate circle. After that, compare the distance with the threshold value. The actual point on the circle can only exist between minimum circumscribed square and maximum inscribed square of the circle, as shown in Fig.2.

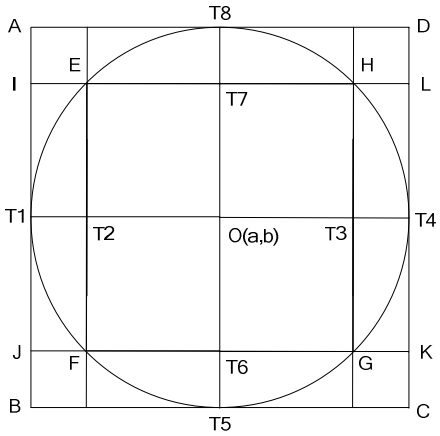



Fig. 2. Schematic of improved RCD algorithms

Edge points which may exist are located among four regions that are surrounded by circle, minimum circumscribed square and maximum inscribed square of the circle. If the radius of the circle is $r$, taking into account the error of the discrete image, side length of circumscribed square ABCD can be expressed as $2(r+\delta)$, and side length of inscribed square EFGH can be expressed as $\sqrt{2}(r-\delta)$. If the coordinates of the circle's center $O$ is $(a,b)$, the abscissa of the point $T1$ can be expressed as $T1_x = a-r-\delta$. Similarly, $T2_x = a-\frac{\sqrt{2}}{2}(r-\delta)$, $T3_x = a+\frac{\sqrt{2}}{2}(r-\delta)$, $T4_x = a+r+\delta$, $T5_y = b-r-\delta$, $T6_y = b-\frac{\sqrt{2}}{2}(r-\delta)$, $T7_y = b+\frac{\sqrt{2}}{2}(r-\delta)$, $T8_y = b+r+\delta$. The coordinate range of the rectangular region IJFE can be expressed as $\begin{cases} T1_x < v_x < T2_x \\ T6_y < y < T7_y \end{cases}$, the coordinates of the remaining three regions can be determined out in the same way. Edge coordinates which to be detected satisfy the relation as Equation (1) to (4) as shown.

$$\begin{cases} T1_x < v_x < T2_x \\ T6_y < y < T7_y \end{cases} \tag{1}$$

$$\begin{cases} T3_x < v_x < T4_x \\ T6_y < v_y < T7_y \end{cases} \tag{2}$$

$$\begin{cases} T2_x < v_x < T3_x \\ T5_y < v_y < T6_y \end{cases} \tag{3}$$

$$\begin{cases} T2_x < v_x < T3_x \\ T7_y < v_y < T8_y \end{cases} \tag{4}$$

Edge points to be detected may be a point on candidate circle only in four areas mentioned before, so only these four areas need to be text when detecting whether the other points are on the circle. Not all the other edge points should be randomly detected in this way. The improved algorithm steps are basically the same as the original algorithm steps, and the difference is that how to judge the other candidate points are on the circle or not. The improved algorithm do not randomly selected edge points, but only select the edge points in the four regions that meet the conditions, and determine the distance between the candidate circle and the points. The remaining steps are the same as original RCD algorithm, and specific steps of original RCD algorithm refer to the corresponding literature.

**Characterization of Image Contours**

Image recognition method used in this paper is based on contour feature. Two methods are used to describe the outline feature. Firstly, contours potential is used to describe the contour feature, it is a further extension of concept of projection[6]. Contours potential means the collection of ordered sequence of accumulated potential energy which corresponding to the binary image contour. In particular, When lower boundary and left border of the image are selected as potential zero, the contours potential of the two borders are collectively referred to as two-dimensional contours potential[7]. Corresponding accumulation potential means pixel potential accumulation of pixels relative to the same potential zero in the binary image. As shown in Fig.3(a), the number in the bottom row represents the cumulative potential relative to the lower boundary when choosing the lower boundary of image as a potential zero. Cumulative potential at this time is recorded as $B_x = (5,4,3,3,4,5,6)$. Similarly in Fig.3(b), the number in the left-most column represents the cumulative potential relative to the left border when choosing the left border of image as a potential zero. Cumulative potential at this time is recorded as $B_y = (0,7,7,7,7,0,0)$.

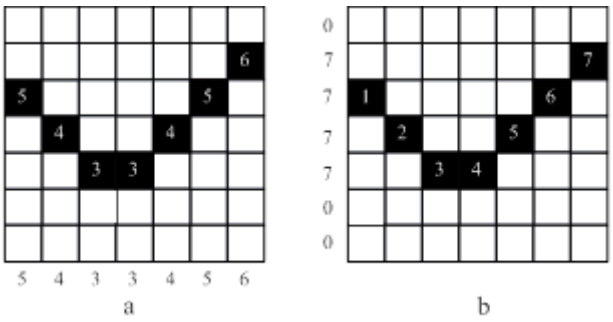



Fig. 3. Cumulative potential

Contour feature of image can be well described by using this concept of contours potential, and it is easy to compare the difference between two images accurately. In addition, the paper also proposes wheel contour vector for rough comparison of the similarity between images.

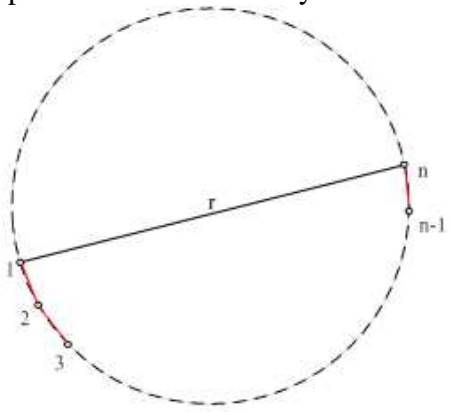



Fig. 4. Wheel contour vector

As shown in Fig.4, image after the wheel contour extraction is an incomplete circle. $p_1$, $p_n$ are respectively the leftmost point and the uppermost point of the image, and the arc between two points are extracted contour image.

The extracted arcs curve will be segmented, specifically, spaced insert n-2 points into the arc between $p_1$ and $p_n$, which denoted respectively as $p_2$, $p_3$, …, $p_{n-1}$ from left to right. Each two adjacent dots make up the wheel profile chord, such as $p_1p_2$, $p_2p_3$, …, $p_{n-1}p_n$, corresponding slope are denoted as $k_{12}$, $k_{23}$, …, $k_{n-1n}$. Then the distance between the points $p_1$ and $p_n$ are denoted as $r$, wheel contour vector can be constructed as $M=(k_{12},k_{23},\cdots,k_{n-1n},k_1,k_n,r)$. Wheel contour vector uses the slope of the wheel profile chord, the tangent slope of profile curve which two farthest points are on and the distance between these two points to expresses the characteristic shape of a wheel profile curve. It also be used for rough recognition of image [8].

**Image Recognition Method**

This paper uses two different methods to compare the variables which describe wheel contour features. For the comparison between the two wheels contour vector, Euclidean distance is adopted in the identification process[9]. Euclidean distance is defined as follows: $d(H_I,H_Q)=\sqrt{(H_I-H_Q)(H_I-H_Q)^T}$, $H_I$ and $H_Q$ respectively represent contour vector of wheel to be detected and the one of standard wheel. $T$ is used to representatives transpose. Test results are recorded as $R_{con}=1-d_{con}(H_Q,H_I)$, which can indicate how similar two wheel contour vectors are.

For contours potential, we use two-dimensional contours potential as the basis for wheel image recognition. Set the contours potential to be detected is $h_I$ and contours potential of standard wheel is $h_Q$. Similarity function $P(Q,I)$ is defined as follows:

$$P(Q,I)=\frac{\sum_{i=0}^{k-1}\min(h_Q(i),h_I(i))}{\min(\sum_{i=0}^{k-1}h_Q(i),\sum_{i=0}^{k-1}h_I(i))} \tag{5}$$

For the similarity discrimination results of wheel images by using two shape features, and the final wheel contour characteristic function can be structured based on different weights. Wheel image recognition all use this function. Characteristic function is defined as follows:

$$S(Q,I)=\frac{\alpha P(Q,I)+\beta R_{con}}{\alpha+\beta},\quad \alpha+\beta=1 \tag{6}$$

The value of $S(Q,I)$ is between 0 and 1. The value more closer to 1 indicates profile curve to be detected is more match to the standard wheel profile curve. Set a threshold value $R_0$, when $R_{con}\geq R_0$, $\beta=0$. That means the image to be detected is similar to the standard wheel image when reaches a certain threshold, and we can extract the roughly shape of a wheel profile. In this case, further refine discrimination of the image to be detected is mainly depend on detect method of potential contour. When $R_{con}<R_0$, $\alpha=0$. That means similarity is not reached the threshold, and there are quite different between image to be detected is similar to the standard image. At this time there is no need for the use of detect method of potential contour.

The steps of image recognition are as follows:

(1) Calculate the slope of contour curve where the points in left and right ends are on, denoted $k_1$ and $k_n$. If $k_1k_n<0$, continue to be judge. Otherwise determine the next image.

(2) Calculate the similarity of wheel contour vector between image to be detected is similar to the standard image, the results recorded as $R_{con}$. Meanwhile, calculate the similarity of two-dimensional contour potential, the results recorded as $P(Q,I)$.

(3) Calculate contour characteristic function $S(Q,I)$, When the value exceeds the set threshold $\alpha$, the image is considered to meet the requirements and will be stored.

(4) After the image is stored, Set Complete wheel image signal $K=1$. When $K=1$, do not store images no matter the value of $S(Q,I)$ exceeds the set threshold $\alpha$ or not. When the value of $S(Q,I)$ is below the set value $\beta$, Set $K=0$ and get ready to identify the next image.

The flowchart of the algorithm is shown in Fig.5.

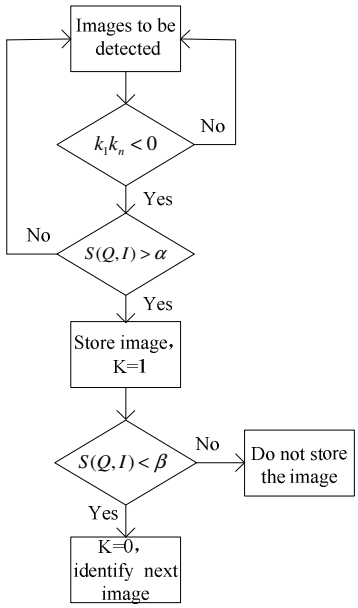



Fig. 5. Flowchart of image recognition algorithm

## Experiment and Results

Image of standard wheel which actually collected is shown in Fig.6. Complete contour image and segmented contour curve of wheel are shown in Fig.7 and Fig.8.



Fig. 6. Image of standard wheel

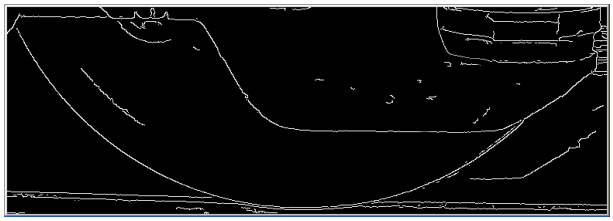


Fig. 7. Complete contour image of wheel

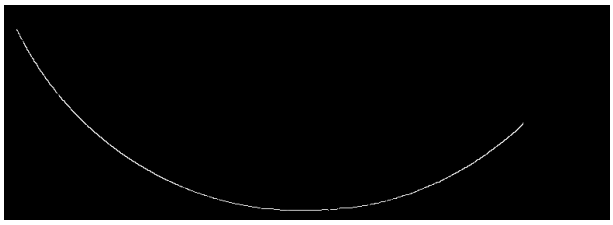


Fig. 8. Segmented contour curve

This wheel image is taken as the standard, and we can get the similarity discrimination results through the image recognition for 20 wheels which were collected from the field. The image with similarity of 0.98 and above will be considered as a complete wheel image, and this image meet the testing requirements. The results are shown in Table 1.

Table 1. Recognition results of wheel images

| Test samples | Discrimination results of similarity | Recognition results | Actual situation |
|---|---|---|---|
| 1 | 0.5433 | Not match | Not match |
| 2 | 0.6744 | Not match | Not match |
| 3 | 0.9877 | Match | Match |
| 4 | 0.9865 | Match | Match |
| 5 | 0.9843 | Match | Match |
| 6 | 0.5436 | Not match | Not match |
| 7 | 0.5633 | Not match | Not match |
| 8 | 0.9854 | Match | Match |
| 9 | 0.9788 | Not match | Match |
| 10 | 0.9846 | Match | Match |
| 11 | 0.4523 | Not match | Not match |
| 12 | 0.6733 | Not match | Not match |
| 13 | 0.9614 | Match | Match |
| 14 | 0.9899 | Match | Match |
| 15 | 0.9821 | Match | Match |
| 16 | 0.9803 | Match | Match |
| 17 | 0.5679 | Not match | Not match |
| 18 | 0.8954 | Not match | Not match |
| 19 | 0.9145 | Not match | Not match |
| 20 | 0.9837 | Match | Match |

As can be seen from Table 1, 19 of the 20 experimental samples have similarity judgment results which match the reality. Only sample No.9 has error identification, which makes the detection accuracy of this method into 95%. In sample No.9, the image is judged to be incomplete wheel. It is Inconsistent with the actual situation, and the reason is that the threshold value of test is relatively large and causes the criterion too strict. Above situation can be overcome easily by Select more reasonable threshold. Detection accuracy of the method can be continuously improved to ensure accuracy.

## Conclusions

This paper presents a dynamic acquisition method for wheel image using an improved RCD algorithm to get the wheel contour curve. On this basis, wheel contour curves and contour wheel vector are used to represent the wheel contour feature and as the basis for determining of similarity.

Then, complete wheel image can be identified through an customized image recognition method. From the experiment results, the algorithm can accurately identify the complete wheel image, and can achieve more desired result by reasonably choosing threshold. This study has good value for practical application and more in-depth research.

**References**

[1] Zheng Shaoping. A Detection System Study of Train Wheel Based on CCD Imaging Technology[D]. Nanchang. Nanchang University. 2010, 1-40(In Chinese)

[2] Liu Xinghong. Image Features Extraction Based on Similar Contents and Concepts[D].Chongqing. Chongqing University of Posts and Telecommunications. 2007, 1-67(In Chinese)

[3] Zhang Fengling. Research on Contour-based Image Matching Technology[D]. Nanjing. Nanjing University of Aeronautics and Astronautics. 2010, 1-66(In Chinese)

[4] YUAN Li, CAO Zhi-rui. Improved randomized Hough transform algorithm for circle detection[J]. *JOURNAL OF COMPUTER APPLICATIONS*, 2010, 30(1): 174-176(In Chinese)

[5] Teh-Chuan Chen, Kuo-Liang Chung. An Efficient Randomized Algorithm for Detecting Circles[J]. *Computer Vision and Image Understanding*. 2001, 83: 172-191.

[6] CHEN Xue-song, XU Xue-jun, ZHU Hong-bo. Research on Target Contour Feature Extraction Based on Image Potential Energy Theory[J]. *COMPUTER SCIENCE*, 2011, 38(6): 270-274(In Chinese)

[7] Kanzawa Y, Ohkawa T, Ito T. Proposal of Low-resolution Vehicle Image Recognition Method[C]. 2008 IEEE Intelligent Vehicles Symposium. 2008: 43-48

[8] Wen Pinggeng, Liu Chun, Li Jian. A Smart Image Background Recognition Model and Its Application to Content-Based Image Retrieval[C]. 2010 2nd International Workshop on Intelligent Systems and Application (ISA). 2010: 1-4

[9] Ni Qiakai, Guo Chao, Yang Jing. Research of Face Image Recognition Based on Probabilistic Neural Networks[C]. 2012 24th Chinese Control and Decision Conference. 2012: 3885-3888

# CHAPTER 7:

# Structural Materials and Civil Engineering

*Advanced Materials Research Vol. 937 (2014) pp 419-423*
*© (2014) Trans Tech Publications, Switzerland*
*doi:10.4028/www.scientific.net/AMR.937.419*

# Study on the Effect Evaluation of Spinescence Application on Segregating Gratings of Expressway——Taking Wu (Ding) - Kun (Ming) Expressway as Example

Yi-Wei LI[1,2,a,*], Yi SHEN[1,2,b],and Qiang MENG[1,2,c]

[1]Research Institute of Highway Ministry of Transport, Beijing 100088, China

[2]Key Laboratory of Highway Environmental Protection Technology of MOT, Beijing 100088, China

[a]yw.li@rioh.cn, [b]y.shen@rioh.cn, [c]q.meng@rioh.cn

**Keywords:** Spinescence, Segregating Gratings, Isolation, Evaluation, Expressway

**Abstract.** In order to evaluate the application effect of spinescence as an alternative to metal segregating gratings of expressway, the evaluation system is built. By using the methods of AHP and FCE the comprehensive isolation effect evaluation of *Solanum deflexicarpum* is carried out. The result shows that the comprehensive evaluation method can guide and enhance the effect of future spinescence application on segregating gratings engineering of expressway.

## Introduction

The basic characteristics of expressway are fully enclosed, whole interchange, full access control and high-speed driving. In order to prohibit pedestrians and animals crossing the road, the segregating gratings must be set on both sides of the road [1]. Currently concrete piles with barbed wire and plastic coating segregating gratings, which can be constructed simply, are commonly used in domestic expressway. Obviously they can achieve immediate isolation, but they are apt to rust and easily eroded by surroundings. Generally they will be to be replaced after 3 or 4 years. The situation will be worse in the south of China.

For this reason some researches have been conducted to plant local thorn plants which adapt to local environment and are sustainable as segregating gratings on the both sides of expressway. Ideal application results are achieved. Currently studies on breeding, stress resistance, planting methods of thorn plants in various areas have been reported [2-7]. However, how to evaluate the isolation effect is still unknown.

In this paper based on the investigation of spinescence segregating gratings demonstration project which is constructed in Wu (Ding) - Kun (Ming) Expressway of Yunnan Province we try to establish a set of evaluation system so as to provide a reference for future isolation effect evaluation of thorn plants application on expressway.

## Methods

### Analytic Hierarchy Process (AHP)

AHP is a qualitative and quantitative analysis method which can achieve multi-objective decision making analysis. It has more advantages when we deal with problems which have relatively complex structure, more decision criteria and difficulty to quantify indicators. The steps of AHP include constructing a hierarchical model, determining elements definition of judgment matrix, weight calculation and consistency test.

### Fuzzy Comprehensive Evaluation (FCE)

FCE is a comprehensive evaluation method based on fuzzy mathematics. According to the jurisdiction degree theory the comprehensive evaluation method can turn the qualitative evaluation into quantitative evaluation so as to give an overall assessment of objects which are restricted by many factors.

We use FCE to evaluate the isolation effect of thorn plants as segregating gratings. Based on the practical engineering the judgment set is given. Expert scoring method is used to determine the weight of each factor. Then the judgment matrix is built for comprehensive evaluation, and finally comprehensive evaluation result is put forward.

## Results

### Evaluation System

On the basis of the relevant researches and experts consultation the isolation effect evaluation system which can be divided into 3 layers is built.The first is the target layer which is the goal of isolation effect evaluation.The second is criteria layer which include 5 first grade indexes.The third is index layer which contains a total of 18 second grade indexes(see Tab.1).

Table 1. Evaluation system of isolation effect

| Evaluation **t**arget *(U)* | Evaluation **c**riteria($U_i$) | Evaluation indexes($U_{ij}$) |
|---|---|---|
| isolation effect evaluation*(U)* | isolation effect of thorn plant itself($U_1$) | density of thorns ($U_{11}$) |
| | | length of thorns($U_{12}$) |
| | | stiffness of thorn($U_{13}$) |
| | | density of branches and leaves($U_{14}$) |
| | stress resistance of thorn plant ($U_2$) | root depth($U_{21}$) |
| | | drought resistance($U_{22}$) |
| | | barren resistance ($U_{23}$) |
| | | pests resistance ($U_{24}$) |
| | ornamental effect of thorn plant($U_3$) | evergreen or not($U_{31}$) |
| | | flowering period($U_{32}$) |
| | | ornamental value of flower($U_{33}$) |
| | | fruit period($U_{34}$) |
| | | ornamental value of fruit ($U_{35}$) |
| | isolation effect of thorn plant($U_4$) | spanning possibility ($U_{41}$) |
| | | traversing possibility ($U_{42}$) |
| | | visual deterrence ($U_{43}$) |
| | landscape effect of thorn plant $U_5$) | coordination with the road itself ($U_{51}$) |
| | | fusion with the surrounding ($U_{52}$) |

### Evaluation Grade Set

The evaluation grade set includes 4 classes which are excellent, good, fair and poor. So the evaluation set of isolation effect is $V=[v_1,v_2,v_3,v_4]=[\text{excellent,good,fair,poor}]$

### Index Weight

The index weight is determined by AHP. The rationality experiment of scale methods carried by Saaty (1980) shows that 1 to 7 scale method which using 1 to 7 to represent the investigation result is relatively reasonable. According to the principle of analytic hierarchy judgment matrix can be constructed.Then by using the square root method the weight of each index can be obtained.The consistency test will be done until the weight of each index meets the requirements of it.The weight of each index is shown in Table 2.

Table 2. Evaluation indexes weight of isolation effect

| Evaluation **t**arget *(U)* | Evaluation **c**riteria($U_i$) | Weight($A_i$) | Evaluation indexes ($U_{ij}$) | Weight($A_{ij}$) |
|---|---|---|---|---|
| isolation effect evaluation*(U)* | isolation effect of thorn plant itself($U_1$) | 0.22 | density of thorns ($U_{11}$) | 0.3 |
| | | | length of thorns($U_{12}$) | 0.3 |
| | | | stiffness of thorn($U_{13}$) | 0.2 |
| | | | density of branches and leaves($U_{14}$) | 0.2 |
| | stress resistance of thorn plant ($U_2$) | 0.19 | root depth($U_{21}$) | 0.2 |
| | | | drought resistance($U_{22}$) | 0.4 |
| | | | barren resistance ($U_{23}$) | 0.3 |
| | | | pests resistance ($U_{24}$) | 0.1 |
| | ornamental effect of thorn plant($U_3$) | 0.11 | evergreen or not($U_{31}$) | 0.3 |
| | | | flowering period($U_{32}$) | 0.1 |
| | | | ornamental value of flower($U_{33}$) | 0.4 |
| | | | fruit period($U_{34}$) | 0.1 |
| | | | ornamental value of fruit ($U_{35}$) | 0.1 |
| | isolation effect of thorn plant($U_4$) | 0.32 | spanning possibility ($U_{41}$) | 0.2 |
| | | | traversing possibility ($U_{42}$) | 0.4 |
| | | | visual deterrence ($U_{43}$) | 0.4 |
| | landscape effect of thorn plant $U_5$) | 0.16 | coordination with the road itself ($U_{51}$) | 0.6 |
| | | | fusion with the surrounding ($U_{52}$) | 0.4 |

**Case Analysis**

We choose *Solanum deflexicarpum* which was planted on the both sides of Wu (Ding) - Kun (Ming) Expressway in Yunnan Province to carry out the case analysis. Twenty experts in related fields are invited to give the grade of each factor. Assuming that there were 7 of the 20 experts agree that "traversing possibility ($U_{42}$)" is "good ($v_2$)" the score of which is 0.35.And so on, the decision matrix $R_i(i=1,2,\cdots 5)$ of each subset $U_i(i=1,2,\cdots 5)$ can be drawn separately. The decision matrices of *Solanum deflexicarpum* are as follows.

$$R_1=\begin{bmatrix}0.3 & 0.4 & 0.2 & 0.1\\ 0.3 & 0.3 & 0.3 & 0.1\\ 0.4 & 0.3 & 0.2 & 0.1\\ 0.3 & 0.4 & 0.2 & 0.1\end{bmatrix}\quad R_2=\begin{bmatrix}0.2 & 0.3 & 0.4 & 0.1\\ 0.4 & 0.3 & 0.2 & 0.1\\ 0.5 & 0.3 & 0.1 & 0.1\\ 0.4 & 0.3 & 0.2 & 0.1\end{bmatrix}\quad R_3=\begin{bmatrix}0.4 & 0.3 & 0.2 & 0.1\\ 0.4 & 0.2 & 0.3 & 0.1\\ 0.5 & 0.3 & 0.1 & 0.1\\ 0.4 & 0.4 & 0.1 & 0.1\\ 0.5 & 0.2 & 0.2 & 0.1\end{bmatrix}$$

$$R_4=\begin{bmatrix}0.6 & 0.2 & 0.1 & 0.1\\ 0.4 & 0.3 & 0.2 & 0.1\\ 0.3 & 0.4 & 0.2 & 0.1\end{bmatrix}\quad R_5=\begin{bmatrix}0.3 & 0.4 & 0.2 & 0.1\\ 0.4 & 0.3 & 0.2 & 0.1\end{bmatrix}$$

According to the weight vector $A_{ij}$ of each single factor and the decision matrix $R_i$ the comprehensive evaluation results( $B_i = A_{ij} \cdot R_i$ ) of each subset $U_i(i = 1, 2, \cdots 5)$ can be obtained through composition operations. Based on the weights in Table 2 the weight vectors $A_{ij}$ of each single factor are as follows.

$$A_{1j} = [0.3, 0.3, 0.2, 0.2] (j = 1,2,3,4)$$
$$A_{2j} = [0.2, 0.4, 0.3, 0.1] (j = 1,2,3,4)$$
$$A_{3j} = [0.3, 0.1, 0.4, 0.1, 0.1] (j = 1,2,3,4,5)$$
$$A_{4j} = [0.2, 0.4, 0.4] (j = 1,2,3)$$
$$A_{5j} = [0.6, 0.4] (j = 1,2)$$

Ordinary matrix multiplication is adopted.Through composition operations the comprehensive evaluation results( $B_i = A_{ij} \cdot R_i$ ) of each subset $U_i(i = 1, 2, \cdots 5)$ are as follows.

$$B_1 = A_{1j} \cdot R_1 = [0.32 \ \ 0.35 \ \ 0.23 \ \ 0.10]$$
$$B_2 = A_{2j} \cdot R_2 = [0.39 \ \ 0.30 \ \ 0.21 \ \ 0.10]$$
$$B_3 = A_{3j} \cdot R_3 = [0.45 \ \ 0.29 \ \ 0.16 \ \ 0.10]$$
$$B_4 = A_{4j} \cdot R_4 = [0.40 \ \ 0.32 \ \ 0.18 \ \ 0.10]$$
$$B_5 = A_{5j} \cdot R_5 = [0.34 \ \ 0.36 \ \ 0.20 \ \ 0.10]$$

Based on the above results the decision matrix *R* of each subset $U_i(i = 1, 2, \cdots 5)$ is obtained.

$$R = \begin{bmatrix} B_1 \\ B_2 \\ B_3 \\ B_4 \\ B_5 \end{bmatrix} = \begin{bmatrix} 0.32 & 0.35 & 0.23 & 0.10 \\ 0.39 & 0.30 & 0.21 & 0.10 \\ 0.45 & 0.29 & 0.16 & 0.10 \\ 0.40 & 0.32 & 0.18 & 0.10 \\ 0.34 & 0.36 & 0.20 & 0.10 \end{bmatrix}$$

According to the weight vector $A_i$ of each single factor and the decision matrix *R* the comprehensive evaluation result( $B = A \circ R$ ) of *Solanum deflexicarpum* can be obtained through composition operations.

$$B = A \circ R = [0.38 \ 0.33 \ 0.20 \ 0.10].$$

Based on the principle of maximum membership degree the isolation effect of *Solanum deflexicarpum* is "excellent".

## Conclusions

Taking spinescence which adapts to local environment and are sustainable as an alternative to metal segregating gratings of expressway meets the requirement of transition from traditional transportation industry to resource-saving and environment-friendly transportation industry.Our study establishes a set of evaluation system to assess the isolation effect of spinescence on both sides of expressway.This system can be divided into three layers which are target layer, criteria layer and index layer. The comprehensive evaluation model is built by using AHP and FCE.Through the case analysis of *Solanum deflexicarpum* as segregating gratings on Wu (Ding) - Kun (Ming) Expressway in Yunnan Province we think that this comprehensive evaluation method is applicable.

**Acknowledgement**

This research was financially supported by grants from the Department of Transportation of Yunnan Province (No.2009 (A) 1-04) and the National Science Foundation (No. 51108216). All field work was carried out with the help of Wu (Ding) - Kun (Ming) Expressway Construction Headquarters. We thank Se Engr Guo-Feng LI,Se Engr He JIANG,Se Engr Su-Fang LUO and Engr Qin-Si YIN for helpful suggestions during manuscript development.

**References**

[1] G.Z.Chang. Highway Greening, China Agricultural Science and Technology Press, Beijing, 2009, pp.42- 43.

[2] H.N.Cao.Study on railway speed section with protective hedges, Railway Standard Design .21(2001)27-29.

[3] M.He, K.Mi. Study on the commons plant with thorns in Shandong Province, Journal of Anhui Agricultural Sciences.37 (2009)1703-1705.

[4] J.W.Wu.Research of planting thorn fence on the highway, China High Technology Enterprises.10 (2007)169-172.

[5] Z.X.Xiang, G.F.Xu, W.J.Jiang.Drought stress on physiological and biochemical processes in four spiny plant species, Journal of Zhejiang Forestry College. 24 (2007) 7 -11.

[6] Z.C. Xiong, R.Z. Huang, D.J. Jin and etc. Research on thorn fence guard band design of highway, Journal of Chinese Landscape Architecture. 15(1999)55-57.

[7] G.J.Zhong. Study on the selection and planting of thorn fence, Shanghai Agricultural Science and Technology.3 (2008)96.

*Advanced Materials Research Vol. 937 (2014) pp 424-427*
*© (2014) Trans Tech Publications, Switzerland*
*doi:10.4028/www.scientific.net/AMR.937.424*

# Comparison Study of Structural Stabilities for H-section Columns Built with Ordinary Grade Strength Structural Steels According to Boundary Conditions and Lengths at High Temperature

In-Kyu Kwon

Department of Fire Protection Engineering, Kangwon National University, Korea

kwonik@kangwon.ac.kr

**Keywords:** Fire Resistance, H-Section Column, Structural Stability, Effective buckling length, Boundary condition

**Abstract.** Fire resistance performance of structural members has been evaluated from each singular section and standard fire curve since the beginning of fire tests. However, the need of the exact fire resistance of H-section columns applied in the steel buildings has increased. The main reason for this is there is a difference between the conditions being conducted during the fire test and that from real situation. In this paper, the structural stability of H-section column made of an ordinary strength grade structural steels, SS 400, SM 400, and SM 490 at high temperature were evaluated and compared with boundary conditions and column's length. This was done in order to suggest a new guideline for the application of fire protective materials in steel column in which the boundary conditions and column lengths are different from that tested with hinge to hinge and 3500 mm. The findings from this study showed hinge to hinge boundary condition was more conservative. And fire resistance performance of longer columns in the case of hinge to fixed and fixed to fixed boundary condition than from 3500 mm and hinge to hinge boundary condition can sustain at high temperature without adding fire protective materials.

## Introduction

In Korea, structural steels have been used as an important construction materials for not only middle level, but high rise buildings. This is because it has lots of merits, such as faster construction period as well as higher and longer space in the building than other traditional structural materials. However, the satisfaction of fire resistance performance requires the evaluation of each structural member, such as column, beam, and etc to be done by Korean standard. The evaluation method for fire resistancce of H-section column has been conducted by using a standard fire curve defined in the Korean standard and vertical furnace. Its height is limited up 3500mm in length and boundary condition is changed into another type by design. However, hinge to hinge type of boundary condition has been used since the beginning of the fire test. This is because the boundary type is regarded as more conservative than other types. A few years ago, the Korean standard was changed by the influence of ISO 834 and loaded fire test method became as a common fire test [1]. This posed the question what are the real the fire resistance of H-section column when it is used in other boundary conditions and different column lengths than when tested at 3500 mm in length and hinge to hinge boundary condition? The fire performance of those are not determined yet. These can pose a significant problem in structural stability in a building during a fire. In this study, to clarify the structural stability of those columns at high temperature, a fire engineering method and related theories were used.

## Fire Engineering Method and Material Databases at High Temperatures

Fire resistance of structural materials and frames can be determined by the prescriptive method or the fire engineering method [2]. The prescriptive method is based on regulation and standard. Therefore, the application or evaluation can be done by related documents. However, the fire engineering method was developed in terms of scientific and engineering output. Therefore, the fire engineering method can be used as a new evaluation way and regarded as a rational one. To evaluate the structural stability of H-section made of ordinary strength grade structural steels which is below 500 MPa of tensile strength by the fire engineering method, mechanical and thermal properties at high temperature are required. In this study, the evaluation of H-section column was conducted by variances shown in the Table 1.

Table 1. Variation of analysis model of column

| Sorts | Contents | Remarks |
|---|---|---|
| Size | H-300x300x10x12 | SS 400, SM400, SM490 s 119.81cm$^2$ |
| Length (mm) | 3500, 3800, 4100 | |
| Boundary Condition | Hinge to hinge, Hing to fixed, fixed to fixed | |
| Fire source | Standard fire curve | KS F 2257-1 |

The applied mechanical properties and specific heat of three types of ordinary steels are shown in Table 2 and Table 3, respectively [3].

Table 2. Regression equations of yield strength and elastic modulus

| Sorts | Properties | Temperature | Regression equation |
|---|---|---|---|
| SS 400 | Yield strength | T≤200ºC | Cold value (240 MPa) |
| | | 200ºC<T | -0.32T + 303.21 |
| | Elastic modulus | T≤100ºC | Cold value (210GPa) |
| | | 100ºC<T | -0.22T + 232.16 |
| SM 400 | Yield strength | T≤200ºC | Cold value (235 MPa) |
| | | 200ºC<T | -0.29T + 293.44 |
| | Elastic modulus | T≤200ºC | Cold value (210GPa) |
| | | 200ºC<T | -0.26T + 261.18 |
| SM 490 | Yield strength | T≤200ºC | Cold value (315 MPa) |
| | | 200ºC<T | -0.41T + 396.58 |
| | Elastic modulus | T≤200ºC | Cold value (210GPa) |
| | | 200ºC<T | -0.26T + 261.28 |

Table 3. Regression equations for specific heat

| Sorts | Temperature | Regression equation(J/gK) | Remarks |
|---|---|---|---|
| SS 400 | T≤620 ºC | 0.00006T + 0.39 | $R^2$=0.96 |
| | 620<T≤720 ºC | 0.007T – 3.54 | $R^2$=1 |
| | 720<T≤820 ºC | -0.005 T +4.97 | $R^2$=1 |
| | 820 ºC<T | 0.008T + 0.38 | $R^2$=1 |
| SM 400 | T≤610 ºC | 0.0005T + 0.48 | $R^2$=0.96 |
| | 610<T≤710 ºC | 0.0022T –0.37 | $R^2$=1 |
| | 710<T≤810 ºC | -0.0000001T +1.2 | $R^2$=1 |
| | 810 ºC<T | 0.002T -0.12 | $R^2$=1 |
| SM 490 | T≤610 ºC | 0.0008T + 0.38 | $R^2$=0.94 |
| | 610<T≤710 ºC | 0.006T – 2.78 | $R^2$=1 |
| | 710<T≤810 ºC | -0.004T + 3.97 | $R^2$=1 |
| | 810 ºC<T | 0.0007T + 0.62 | $R^2$=1 |

**Derivation of Structural Stability of H-section Column at High Temperautre**

Fire performance of H-section column can be determined by calculation of surface temperature and an allowable stress according to boundary conditions and column lengths. At first, the surface temperature determined by application of specific heat, the heat transfer coefficient, and others. The equation (1) is used for the calculation of H-section after time after on the standard fire curve [4].

$$\Delta\theta_s = \frac{\alpha}{\gamma_s c_{ps}} \bullet \frac{F_s}{V_s}(\theta_t - \vartheta_s)\Delta t \tag{1}$$

Where, $\Delta\theta_s$ represents the differences between surface temperatures(ºC), $\alpha$ is heat transfer coefficient($W/m^2$ºC), $r_s$ is density of steel $(kg/m^3)$, $c_{ps}$ is specific heat of steel($J/kg°C$), $F_s$ is surface of steel per unit length ($m^2/m$), $\vartheta_t$ is temperature of standard fire curve at time t(ºC), $\vartheta_s$ is surface temperature of steel at time t(ºC), and $\Delta_t$ is time interval.

Secondly, the extended length should be calculated by using a linear expansion coefficient and an influence of applied load on the column during standard fire curve. Finally, an allowable stress can be derived from a stress analysis with mechanical properties at high temperature.

The history of increasing surface temperature of the H-section made of SS 400 is shown in Figure 1. The surface temperature was increased rapidly because of non-protected at all and after 30 minutes the temperature became close to the standard fire curve. This regarded as a typical temperature history coming from bare structural members.

An allowable stress of each structural type derived from 3500 mm in length and hinge to hinge boundary condition is shown in Figure 2. In the figure, SS 400 and SM 400 showed almost the same an allowable stress until about 400 ºC. However, after the temperature SS 400 showed more rapid reduction of allowable stress to the end of surface temperature. The result from SM 490 represented more stable than two structural steels. Therefore, the fire protective material evaluated from H-section column made of SS 400 is more conservative than that derived from SM 400.

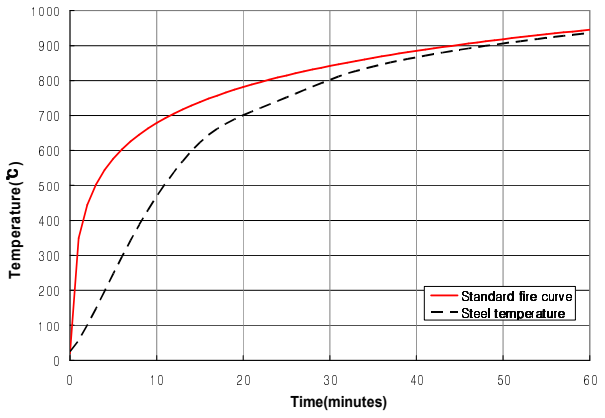



Fig. 1. Temperature rising history

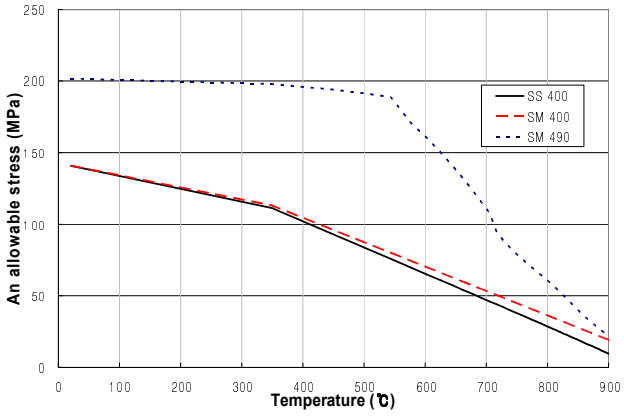



Fig. 2. An allowable stress (3500mm, hinge to hinge)

The results from 3800 mm in length and hinge to fixed and 4100 mm and fixed to fixed are shown in Figure 3 and Figure 4, respectively. As the boundary condition changes to hinge to fixed and fixed to fixed from hinge to hinge, the allowable stress of each increases. Therefore, the fire protective material derived from fire test can be applied to longer column lengths in the case of hinge to fixed and fixed to fixed boundary condition only.

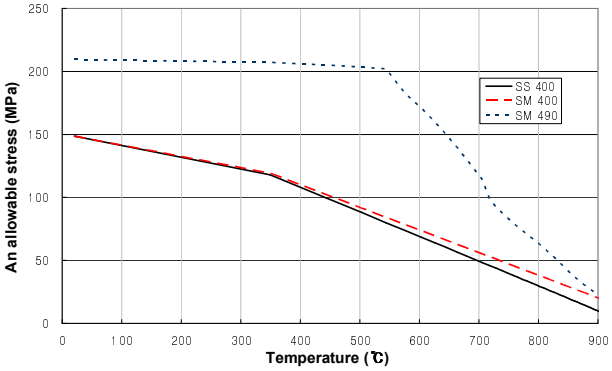



Fig. 3. An allowable stress (3800, hinge to fixed)

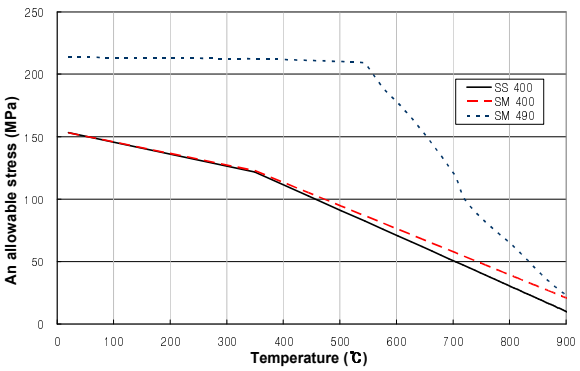



Fig. 4. An allowable stress (4100, fixed to fixed)

## Discussions

Fire protective materials are regarded as an important factor to keep the structural stability of structural members, such as column, beam. Therefore, all structural elements should be equipped with proper fire protective material thickness according to requited fire ratings. Generally, the fire protective materials thickness has been evaluated by a specific way defined in a standard. In this study, the derived fire protective material thickness from SS 400 is regarded as a safe treatment in longer column length in hinge to fixed and fixed to fixed boundary condition. This is because an allowable stress at high temperature from the hinge to fixed and the fixed to fixed boundary conditions are superior to that from hinge to hinge boundary condition.

## Conclusions

To determine the fire performance of longer H-section columns made of ordinary grade structural steels and other boundary than a regular size and hinge to hinge boundary condition, an engineering method was applied and got the following.

(1) Structural stability from SM 490 showed the highest among three ordinary grade structural steels and represented a stable condition until 500 ºC.

(2) Fire protective material evaluated from H-section column made of SS 400 is more conservative than that derived from SM 400 at high temperature.

(3) Fire resistance performance of longer column in the case of hinge to fixed and fixed to fixed boundary condition than tested from at 3500 mm, hinge to hinge boundary condition can sustain at high temperature without adding fire protective materials.

## Acknowledgement

This study was supported by the 2010 research grant from the National Research Foundation of Korea (The project number is NRF-2010-0004385)

## References

[1] I. K. Kwon, Building Fire Protection, DongHwa, Kyungido, Korea (2007).

[2] Valdir Pignatta Silva, Ricardo Hallal Fakury, Brazilian standards for steel structures fire design**,** Fire Safety Journal, Vol. 37, No. 2 pp. 217–227(2002).

[3] I. K. Kwon, "A Study on the properties of SM 400 for evaluation of structural stability at high temperature", Journal of Korean Institute of Fire Science and Engineering, Vol. 27 No. 4, pp. 7-12 (2013).

[4] SBI, Fire engineering design of steel structures, Swedish Institute of Steel Construction, Stockholm(1976).

*Advanced Materials Research Vol. 937 (2014) pp 428-432*
*© (2014) Trans Tech Publications, Switzerland*
*doi:10.4028/www.scientific.net/AMR.937.428*

# Bridge with Lead Rubber Bearing Finite Element Analysis Based on ANSYS

Yun-xin CHEN

School of Electromechanical &Architectural Engineering,Jianghan University , Wuhan,China,430056

2098558413@qq.com

**Keywords:**Lead rubber bearing; finite element analysis; stiffness matrix;ANSYS

**Abstract:**In this paper, using finite element analysis software, the bridge with lead rubber bearing are analyzed, using parametric technology combined with finite element simulation, the parametric modeling and solving complex combination structure. After the analysis, the stiffness matrix of different parameters of the lead rubber bearing, provides a numerical basis for the overall quantitative analysis for bridges.

## Introduction

Lead rubber bearing for bridge is composed of layered rubber, steel and lead together, is mainly used to support the load and the absorption kinetic energy. The isolation structure is an economic type. The structure can be vertical, horizontal flexible, hysteretic damping, resilience and seismic and wind response control several functions together. Prolong the structure vibration cycle and increase the damping to achieve obvious damping effect and normal use of good performance. In the domestic construction industry there have been some isolated buildings using this support, but in the bridge is still at the trial stage.

Research on Isolation Bridge system mainly focuses on the characteristics of static and dynamic effects of isolation bearings under, part of the study describes the response of isolated bridge system, but these studies mainly focus on to prove the effectiveness and shock degree of isolation structure, is employed to analyze the computational methods for predicting the seismic response of isolated bridges. Study on Isolation Bridge between design parameters of an analysis model and the actual lead rubber bearings have not established a clear can be used to quantify the relationship of the design problem. Such as: the actual bearing plane size, thickness of rubber layer, the rubber material hardness and lead characters etc[1].

Some shortcomings of current model analysis. In practice, if the parameter is not reasonable, the results may vary greatly. Finite element analysis technology in this application parameters, the stiffness matrix of different parameters of the lead rubber bearing, provides a numerical basis for the overall quantitative analysis for bridges.

## Parametric Finite Element Analysis of the Lead Rubber Bearing

The finite element analysis process includes: establish geometric model, definition, and the evaluation results of solving load. If the results show that it is necessary to modify the design, it must change the geometry of the model and related parameters. When the model is complex or modify more, this process will be very complicated and time consuming.

In the bridge with lead rubber bearing in the process of analysis, using the APDL parametric design language (ANSYS Parametric Design Language) to realize the finite element modeling and load parameter calculation. In the parametric design process, which can modify some parameters, including the thickness of the rubber plate, lead rubber bearing, the thickness of the lead core diameter, characteristic analysis of several design schemes to realize, calculation and modeling, intelligent load.

APDL extends the traditional finite element analysis allowed range, according to user requirements change the program to meet the modeling and analysis of specific requirements, improve the analysis efficiency, to optimize the structure, reduce costs and improve quality, plays an important role in.

**FEA Modeling of LRB Parametric**

Lead rubber bearing steel, rubber, modeling of lead have chosen the SOLID185 unit. The material constants of physics for:

The elastic modulus of steel plate: $E = 2.1\times10^{11}$ Pa Poisson's ratio: $\mu$=0.3;

The elastic modulus of rubber: $E = 2.96\times10^{9}$ Pa,Poisson's ratio: $\mu$=0.47;

The elastic modulus of the lead core: $E = 1.4\times10^{10}$ Pa,Poisson's ratio:$\mu$=0.33.

Lead rubber bearing is composed of 27 layers of steel plate and a 26 layer of rubber and single lead core. Bearing length, width, thickness, single layer rubber plate thickness, the lead core diameter respectively by $l,w,t_r,h,D_{pb}$

First $l,w,t_r,h,D_{pb}$ respectively 900,900,8,3,150,unit mm.

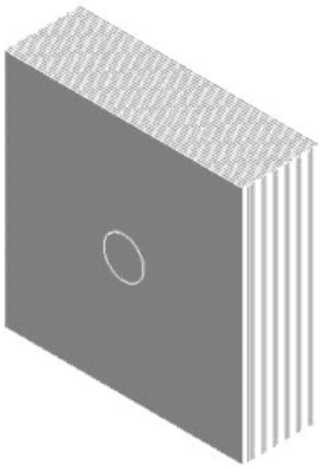


Fig. 1. Entity model of $t_r$=8 $D_{pb}$=150

Using the programming language ANSYS command to organize, prepare parameters of the user program, realize the whole process of finite element analysis are: establishing the parametric CAD model, parameterized mesh and control, parameters of the material definition[2], parameters of the loads and boundary conditions are defined, a parametric analysis of control and solution as well as the parameter after treatment. is shown in Figure 1 as the entity LRB models (CAD model parameterization). Lead rubber bearing finite element model as shown in figure 2.

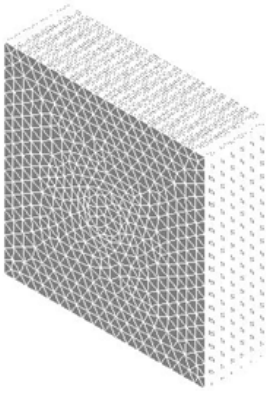


Fig. 2. Finite element model of $t_r$=8, $D_{pb}$=150

**The Stiffness Matrix and the Calculation and Analysis of the Lead Rubber Bearing**

The lead rubber bearing stiffness matrix of $t_r=8\ D_{pb}=150$

(the upper left part $6\times6$ of the stiffness matrix of $24\times24$)

$$[K]_{6\times6}=\begin{bmatrix} 0.1958\times10^{9} & -0.8382\times10^{8} & 0.3043\times10^{8} & -0.1873\times10^{8} & -0.1008\times10^{8} & -0.2003\times10^{7} \\ -0.8382\times10^{8} & 0.1966\times10^{9} & -0.3081\times10^{8} & 0.1008\times10^{8} & -0.3948\times10^{8} & 0.6720\times10^{7} \\ 0.3043\times10^{8} & -0.3081\times10^{8} & 0.1283\times10^{9} & -0.2033\times10^{7} & -0.6704\times10^{7} & -0.1339\times10^{8} \\ -0.1873\times10^{8} & 0.1015\times10^{8} & -0.2033\times10^{7} & 0.1958\times10^{9} & 0.8337\times10^{7} & 0.3063\times10^{8} \\ -0.1008\times10^{8} & -0.3948\times10^{8} & -0.6703\times10^{7} & 0.8336\times10^{8} & 0.1965\times10^{9} & 0.3076\times10^{8} \\ -0.2002\times10^{7} & 0.6721\times10^{7} & -0.1340\times10^{8} & 0.3064\times10^{8} & 0.3075\times10^{8} & 0.1299\times10^{9} \end{bmatrix}$$

When $t_r=8, D_{pb}=150$ ,the outer end of fifth nodes by the distribution of overall Z direction of 1e9N deformation is shown in figure 3

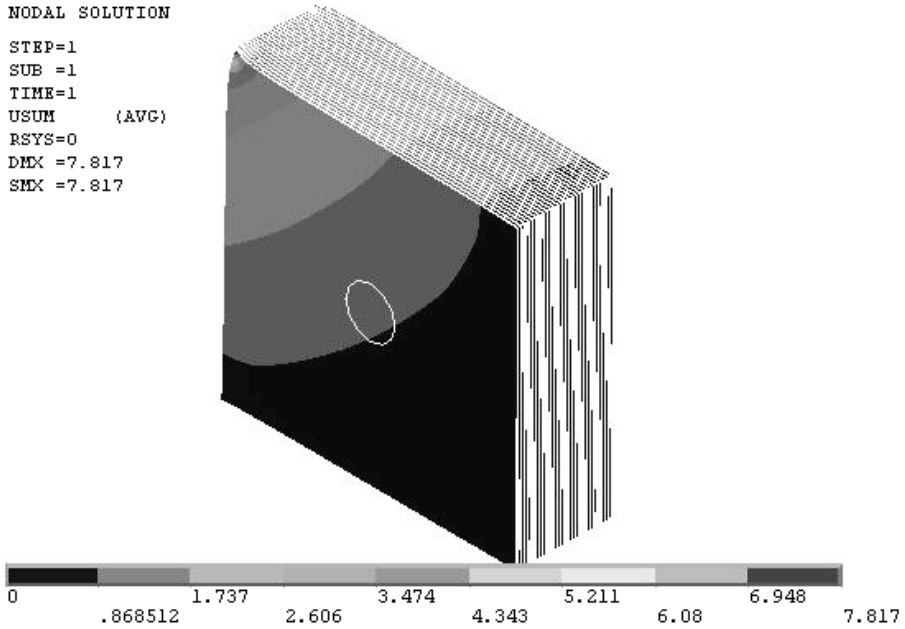



Fig. 3. $t_r=8, D_{pb}=150$ ,the outer end of fifth nodes by the distribution of overall Z direction of 1e9N deformation

The outer end vertical first node various single rubber layer thickness in the case of stiffness is shown in Table 1

Table 1. The outer end vertical first node various single rubber layer thickness in the case of stiffness

| The monolayer thickness of rubber layer $t_r$ (mm) | 7.0 | 7.5 | 8.0 | 8.5 | 9.0 |
|---|---|---|---|---|---|
| Vertical stiffness $K_V$ ($10^9$N/m) | 0.1370 | 0.1322 | 0.1283 | 0.1245 | 0.1212 |

Relationship curve of single rubber layer thickness and the vertical stiffness. is shown in figure 4

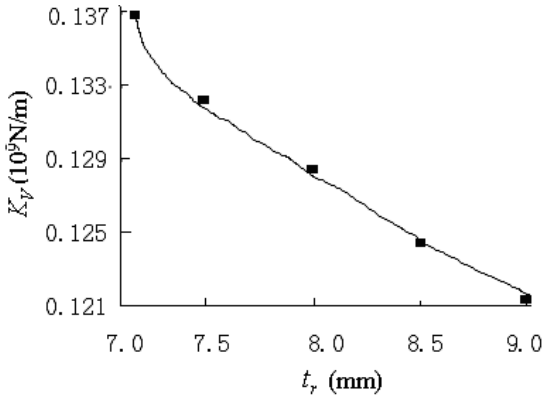



Fig. 4. Relationship curve of single rubber layer thickness and the vertical stiffness.

The outer end vertical first node various lead core diameter in case of stiffness is shown in Table 2

Table 2. The outer end vertical first node various lead core diameter in case of stiffness

| Lead core diameter $D_{pb}$ (mm) | 130 | 140 | 150 | 160 | 170 |
|---|---|---|---|---|---|
| Vertical stiffness $K_V$ ($10^9$N/m) | 0.1287 | 0.1286 | 0.1284 | 0.1281 | 0.1278 |

Curve of vertical lead core diameter and stiffness is shown in figure 5

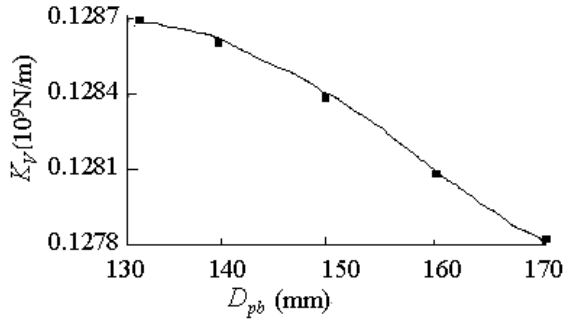



Fig. 5. Curve of vertical lead core diameter and stiffness is shown

Calculation and analysis of finite element analysis model of application parameters and the lead rubber bearing stiffness matrix of the table 1 and table 2 can be seen, along with the increase of the thickness of single rubber, lead rubber bearing vertical stiffness decreases; while the lead core diameter increases, the lead rubber bearing vertical stiffness degree is reduced, but the impact is very small vertical lead core diameter change on lead rubber bearing stiffness. This doctoral dissertation lead rubber bearing mechanical properties of Wu Bin and his reducing isolation application vertical experiment studyin bridge engineering, the influence of stiffness $K_V = K\dfrac{D^2 - nD_{pb}^{\ 2}}{4Dt_r}\dfrac{A_g}{\sum t_r}$ is Consistent.Among them, K is Proportional coefficient; $A_g$ is support the effective bearing area; $\sum t_r$ is the total thickness of rubber layer D is bearing outside diameter; when the support is a square, $a$ is square side length $D = \dfrac{4a}{\pi}$; $D_{pb}$ is the diameter of lead core; n is the number of lead core; $t_r$ is the monolayer thickness of rubber. [3]

**Summary**

Application of parametric technology is combined with the finite element simulation, the parametric modeling and solving complex combination structure. Through calculation and analysis, and gives the solution to the stiffness matrix of different parameters of the lead rubber bearing. Focus on the relationship between the parameters and the vertical stiffness of support, provide numerical reference for the quantitative analysis of the whole bridge.

**References**

[1] Xu Huiying Test research status quo and Prospect of Seismically Isolated Bridges with lead rubber bearing[J] Roadbed engineering 2007.01

[2] ANSYS Inc,Advanced Analysis Techniques Guide,VOI.4,Chapter1

[3] Wu Bin Study on the mechanical properties of lead rubber bearing and in bridge engineering, the application of reduction of isolation[D]. Beijing: China Academy of Railway Sciences 2003

*Advanced Materials Research Vol. 937 (2014) pp 433-437*
*© (2014) Trans Tech Publications, Switzerland*
*doi:10.4028/www.scientific.net/AMR.937.433*

# Numerical Simulation on a Deep-foundation Pit of Shenzhen Holiday Plaza Project

Yi ZHENG [1]

[1]Changchun Architecture and Civil Engineering College, Changchun, Jilin, 130607, China

[a]Zhengyi4411@126.com

**Keywords:** Deep Foundation Pit; Shenzhen Holiday Plaza Project; Numerical Simulation; Prestressed Anchor Cable; Composite Soil Nailing Wall

**Abstract:**Based on test data of the prestressed anchor cable composite soil nailing wall deformation and internal force of structure of Shenzhen Holiday Plaza foundation pit, the numerical simulation model of foundation pit is established by FLAC$^{3D}$ software. Through the reasonable selection of soil constitutive model and structural unit, the numerical simulation model is consistent with the project practice. The simulation results on horizontal displacement of foundation pit, the internal force of the structure, the surface layer stress and damaged form are reasonable. This does not only provide a strong basis for the optimum design of the foundation pit, but also provide a scientific guidance for engineering application.

## Introduction

Foundation pit is the difficult point and easy to make mistakes in engineering design. Engineers have to make the greatest efforts to overcome the instability of foundation pit and some other problems, By the using of finite element and FEM software for numerical simulation, we can avoid the problems of foundation pit. Depend on the observation data of foundation pit in different regions, reasonable numerical simulation of deep-foundation pit can reduce project risk and improve construction efficiency. In this paper, it takes a deep-foundation pit of Shenzhen Holiday Plaza Project as an example, using FLAC$^{3D}$ software to simulate stress and deformation of the foundation pit, the model has achieved good effect.

## Engineering Geological Background of Study Area

The foundation pit engineering is located in Shenzhen Nanshan District, The north is the world garden, South cross the Shennan Avenue and Shenzhen metro, the window of the world across the road, which is very close to this project. Three surface adjacent municipal roads, there are many municipal water pipes and gas pipelines and communication cable for the world garden and high-rise buildings, the geological conditions are very complex. Foundation pit is 308.2m long in east-west direction, the north-south width is 46.5m ~ 82.5m, total excavation is close to 20000m$^2$. On the west and north side of foundation pit, the excavation depth is 17.6 ~ 21.0m, on the south side of foundation pit, the excavation depth is 13.8~ 18.7m. Foundation pit excavation layout diagram and the engineering geological parameters are shown in Fig.1 and table 1.

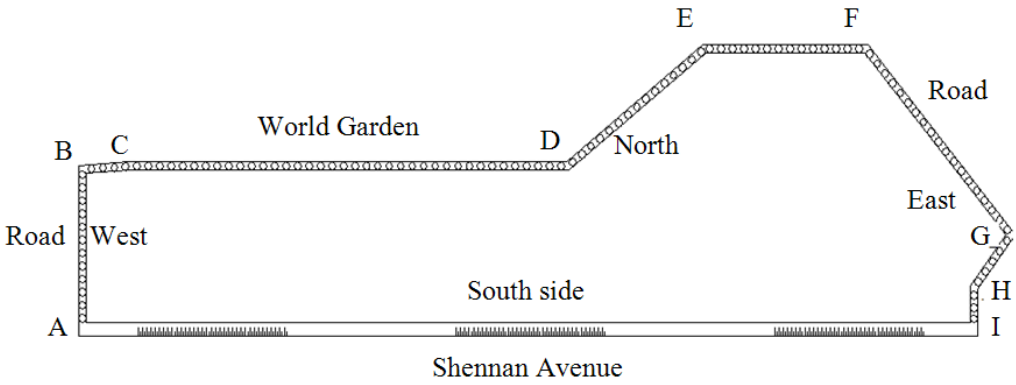



Fig. 1. Simple Map of Site

Table 1. The Engineering Geological Parameters

| Geological Layer Unit | Geological Age(quaternary) | Thicknesses (m) | Main Lithology and Characteristic |
|---|---|---|---|
| No.1 | Artificial filled soil | 0.3~5.1 | Clay(With a small amount of rubble) |
| No.2 | Diluvium | 0.9~6.2 | Clay(Quartz gravel content is 8.6～38.3%) |
| No.3 | Eluvium | 1.0~21.2 | Gravel Silt clay(Quartz gravel content is 1.6～47.4%5) |
| No.4 | Yanshanian Bedrock | -- | Granite, main components of feldspar, quartz and mica |

**Numerical Simulation Model**

Numerical simulation is carried out on foundation pit with establishment of structure model by applying the large scale engineering software FLAC$^{3D}$ as well as the comparisons with the actual observed data. The model uses beam element, the anchor cable unit and shell element. Soil constitutive model is based on DP yield criterion. We suppose H as slope excavation depth, in the model, the depth is 2H, the width is 2H ~ 3H. The underside of the model (Z=0) fixed constraint, X, Y direction is hinge constraints, which is imposed by the sides of the initial stress and constraints of the initial rate. In this paper, to simplify the analysis, the model only has the width of a row of soil nails (the horizontal spacing of soil nails is 1.4m) in the y direction. The model is divided into two layers, the upper soil is gravel silt clay, the lower is granite. The foundation pit soil mechanical parameters are shown in Table 2. FLAC$^{3D}$ model is shown in Fig.2.

Table 2. Soil Mechanical Parameters

| Geological Layer Unit | Internal frictional angle | Cohesion Modulus(Pa) | Volume Modulus(Pa) | Shear Modulus (Pa) |
|---|---|---|---|---|
| No.3 | 20° | $2.49\times10^{4}$ | 1.0×107 | 4.62×106 |
| No.4 | 45° | $4.4\times10^{7}$ | 4.05×1010 | 2.79×1010 |

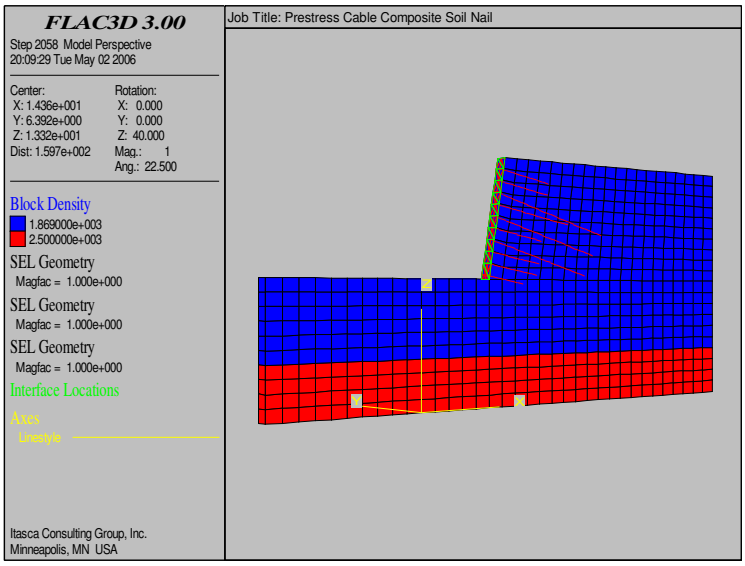



Fig. 2. FLAC$^{3D}$ model

## Comparisons between Numerical Simulation and Actual Monitoring

The deformations of foundation pit, including the horizontal displacement and the vertical displacement, are better controlled when using prestressed anchor cable composite soil nailing supporting. Stress characteristics of soil nailing and anchor cable after excavation is shown in Fig.3. Fig.4 shows the comparisons between numerical simulation and actual observed data. The value in actual measure results within excavation depth is always larger than that in numerical simulation. The regularity of the two results is consistent, which indicates that the simulation of the effect is good. In the upper part of pit, the internal forces of simulated values of the soil nails is smaller than the measured value, because the profile is located next to the material library, which produce a certain amount of additional load; in the toe of pit, the slope soil nails internal force is smaller than the measured value, because in the model, we do not consider the impact of groundwater.

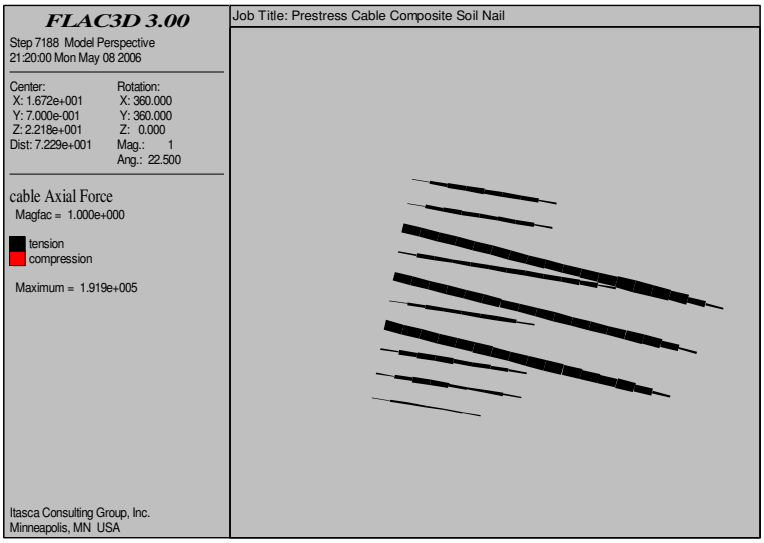



Fig. 3. Stress characteristics of soil nailing and anchor cable after excavation

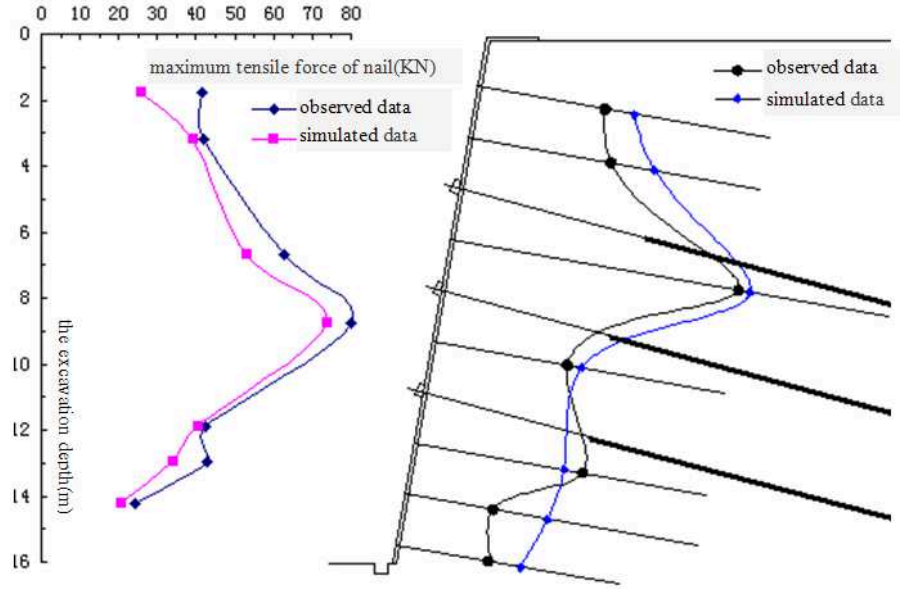



Fig. 4. Comparison between on-site monitoring test and simulation of max tensile force and location of soil nail

## Failure Mode Analysis

The failure prediction of FLAC$^{3D}$ is examined by looking at the model of the plastic zone within the shear strain increment and calculating the stability factor.

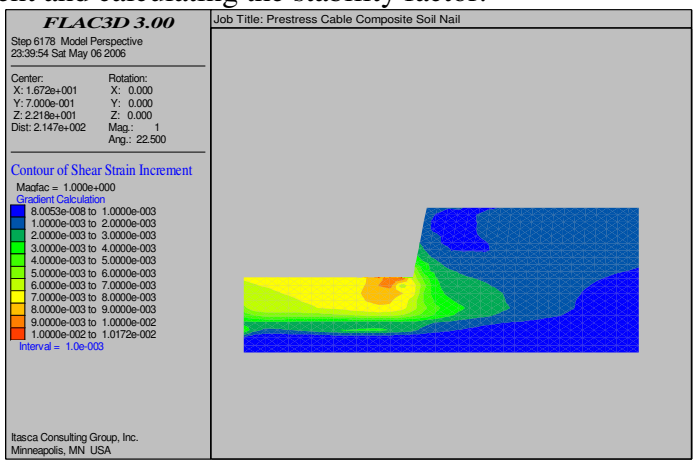



Fig. 5. Shear stress increment of prestress soil nail wall

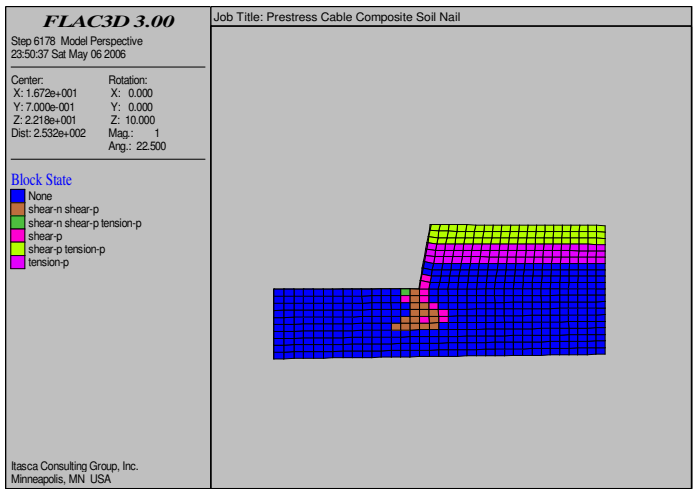



Fig. 6. Plastic scope of the prestressed anchor cable composite soil nailing

In Fig 5, we can see that the apparent change of shear strain of prestressed soil nail wall areas are mainly concentrated in the lower part of the excavation face, the increment of shear strain has begun to stabilize at the top, while the changes in the structure of the traditional soil nailing wall is almost spread to the top of the pit excavation. For failure modes in Fig.6, the plastic scope of the prestressed anchor cable composite soil nailing wall is significantly larger than the traditional soil nail wall. The plastic zone of the prestressed anchor cable composite soil nail wall is mainly concentrated in the bottom of the pit, the plastic zone of traditional soil nailing wall appears in the broken surface, rises along the slope of a certain height, the slope at this soil has entered the yield. With the further development of the plastic zone, the slope appears to plastic flow, which leads to the displacement increasing and destruction. Fig.6 indicates: prestressed anchor cable can control the development of the plastic zone of the soil, it make the slope having a greater safety margin to ensure the safety of the pit.

## Conclusions

By the pit test data and numerical simulation, conclusions can be drawn as follows:

(1) The characteristics of stress and deformation of the prestressed anchor cable composite soil nailing with FLAC$^{3D}$ are analyzed, the results from on-site monitoring test are in accordance with those from numerical simulation.

(2) Earth pressure on the side of foundation pit is smaller when prestressed anchor cable composite soil nailing supporting is introduced. For the prestressed anchor cable composite soil nailing structures, from top to bottom, prestressed design of prestressed anchor cable should gradually increase. The stress and deformation of soil nailing and prestressed anchor cable both have the excavation effect.

(3) For failure modes: the plastic scope of the prestressed anchor cable composite soil nailing wall is significantly larger than the traditional soil nail wall ,in the plastic zone of the prestressed anchor cable composite soil nailing wall, the increment of shear strain changes in steady.

(4) Prestressed anchor cable composite soil nailing technique can gradually improve the supporting capacity during excavation, which satisfies the requirements of variations of the stress and deformation induced by the construction process and some uncertain factors. The achieved results can provide some references to the design and construction of similar projects.

## References

[1]XIE Kanghe, ZHOU Jian. Theory and application of finite element analysis of geotechnical engineering [M]. Beijing:Science Press,2002.

[2]LIN Xiqiang. Research on internal forces and deformation of composite soil-nailing of deep excavation process[D]. Wuhan University of Geosciences, 2003.

[3]FAN Yujie, ZHENG Qizhen. WEI Lin. Research on failure mechanism and ultimate load carrying capacity of prestressed cable[J]. Chinese Journal of Rock Mechanics and Engineering, 2005, 24(15):2765–2769.

[4]YOU Chunan, ZHAN Yubao. Distributing characters and analysis of stresses in prestressed cables[J]. Chinese Journal of Rock Mechanics and Engineering, 2005, 24(6):25–928.

[5]CHEN Zhaoyuan, CUI Jinghao. Application of soil nailing to excavationengineering[M].China Architecture and Building Press, 2000.

[6]VUCETIC M, TUFENKJIAN M R, DOROUDIAN M. Dynamic centrifuge testing of soil-nailed excavations[J]. Geotechnical Testing Journal, 1993, 16(2):172-187.

*Advanced Materials Research Vol. 937 (2014) pp 438-443*
*© (2014) Trans Tech Publications, Switzerland*
*doi:10.4028/www.scientific.net/AMR.937.438*

# Piled Raft Structure Finite Element Analysis of Composite Foundation Settlement in DA XI Passenger Dedicated Line

Xiao-tong MA[1,a], Guang-long LIU[1,b,*]

[1]Institute of Transportation, Shandong University of Science and Technology, China

[a]18766425839@163.com, [b]986265388@qq.com

*Corresponding author

**Keywords:** Pile, Numerical simulation, Composite foundation settlement

**Abstract.** Composite foundation settlement of piled raft structure in Da Xi passenger dedicated line is analyzed by the large finite element software MIDAS/GTS and established calculation model of foundation treatment. The problem of pile-soil contact is highlighted in the trail and analyzes the settlement nephogram and pile-soil stress nephogram. On this basis the foundation settlement factors was analyzed systematically that focus on the elastic modulus of pile, pile spacing, pile diameter and pile length in foundation treatment, especially for the characteristics parameters of contact element. Result shows that increasing the pile modulus, pile diameter, pile length and decreasing the pile spacing is all conducive to reducing settlement. The best advice is got that the pile diameter should be not more than 0.5m, pile length not more than 27m and the pile spacing be around 2m.

## Engineering Background

Datong-Xian Passenger Dedicated Line passes through the south of Shanxi province and the east of Guanzhong Plain that is almost Collapsible loess areas[1]. In consideration of the big collapsibility coefficient, appropriate measures must be taken to guarantee the bearing capacity and the post construction settlement to meet the requirements[2]. In region of YunCheng city four representative test sections such as roadbed-bridge transition section(center distance DK663+214), roadbed-culvert transition section(center distance DK665+020) and ordinary embankment(center distance DK665+400) was selected. At the same, foundation treatment measure and subgrade filling measure was taken. Composite foundation made of compacted cement pile and CFG pile is used in foundation treatment plan. Concrete design parameters and the plane layout of the test section see Table 1.

Table 1. Design parameters of compacted cement pile and CFG pile[3]

| center distance of test section | | main design parameters | | | the form of the pile layout |
|---|---|---|---|---|---|
| | | pile diameter(m) | pile spacing (m) | pile length(m) | |
| DK663+214 (roadbed-bridge transition section) | compacted cement pile | 0.5 | 0.95 | 10 | square |
| | CFG pile | 0.5 | 1.9 | 27 | square |
| DK665+400 (Luoyang shovel construction section) | compacted cement pile | 0.5 | 0.95 | 12 | square |
| | CFG pile | 0.5 | 1.9 | 27 | square |
| DK665+020 (roadbed-culvert transition section) | compacted cement pile | 0.4 | 0.95 | 11 | square |
| | CFG pile | 0.4 | 1.9 | 19 | square |
| DK664+160 (ordinary embankment) | compacted cement pile | 0.5 | 0.95 | 11 | square |
| | CFG pile | 0.5 | 1.9 | 22 | square |

In addition, a depth of 0.5m reinforced concrete raft foundation was placed on the top of the roadbed-bridge transition section(center distance DK663+214).

## Test Section

### Establishment Calculation Model

Test segment DK663 + 214 (roadbed-bridge transition section) is selected as the position of the finite element numerical calculation. Because the roadbed left and right sides are symmetrical, in order to reduce the computing workload, the physical and mechanical properties of cement-soil compaction pile is adopted which has been disposed to replace the original pile, and the half structure for numerical calculation of composite foundation is taken. Calculation model is shown in figure 1, length and width of the foundation is 17m，height is 32 m, the height and width of embankment is 6 m and 13 m, the thickness of mattress layer is 0.3 m, the thickness of raft is 0.5 m. Adopting squared piles, pile diameter is 0.5 m, pile spacing is 1.9 m, pile length is 27m and calculation parameters of other layers as well as the pile is shown in table 2 and table 3. Among them the parameters of embankment filled soil and the soil layer 1 is consistent.

Table 2. The soil layer physical and mechanical parameters[4]

| | Thickness (m) | μ | P (KN/m3) | C (KN/m2) | Φ (angle) | E (MPa) |
|---|---|---|---|---|---|---|
| soil layer 1 | 2 | 0.3 | 20 | 37 | 15.5 | 24 |
| soil layer 2 | 2 | 0.29 | 17.3 | 18 | 25 | 22 |
| soil layer 3 | 5.5 | 0.35 | 19.6 | 75 | 17.4 | 22 |
| soil layer 4 | 2 | 0.28 | 21.2 | 3 | 32 | 35 |
| soil layer 5 | 5.5 | 0.35 | 19.6 | 22.3 | 30 | 22 |
| soil layer 6 | 5 | 0.28 | 21.2 | 3 | 32 | 35 |
| soil layer 7 | 10 | 0.35 | 19.6 | 22.3 | 30 | 22 |
| CFG pile | | 0.25 | 23 | | | 15000 |
| mattress layer | 0.3 | 0.25 | 20 | 0 | 45 | 50 |
| raft | 0.5 | 0.1 | 24 | | | 30000 |

Table 3. Pile contact element characteristic parameter

| | |
|---|---|
| ultimate shear stress (kN/m) | 150 |
| shear stiffness modulus (kN/m2) | 80000 |
| normal stiffness modulus (kN/m3) | 980000000 |
| reference depth (m) | 27 |
| curve slope of friction-opposite displacement | 2 |
| Tip of pile bearing capacity (kN) | 8000 |
| Tip of pile spring stiffness (kN/m) | 8000 |

Soil and mattress layer uses the model of Mohr - Coulomb，assuming the cement concrete raft is an ideal elastic body, contact elements is sited at the pile length interface, setting normal stiffness and shear stiffness modulus. Based on this, the model established is shown in Fig.1 and Fig.2.

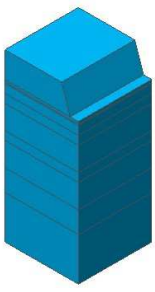
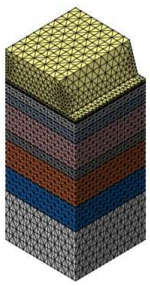


Fig. 1. Computational geometry model



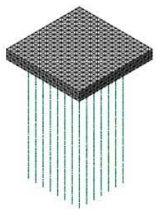


Fig. 2. Model grid division

### Calculation Result Analysis

According to the above contents, a calculation model of numerical simulation is established to calculate. Figure 3 is the total settlement nephogram of natural foundation: the foundation settlement is larger on the first and second floor and the foundation settlement on other soil layers is

smaller. Figure 4 is the total settlement nephogram of composite foundation. Compared with unprocessed natural foundation,the total roadbed settlement reduces notably, the embankment settlement is 4.16cm after disposing, corresponding to it, the unprocessed natural embankment subsides 9.65cm.

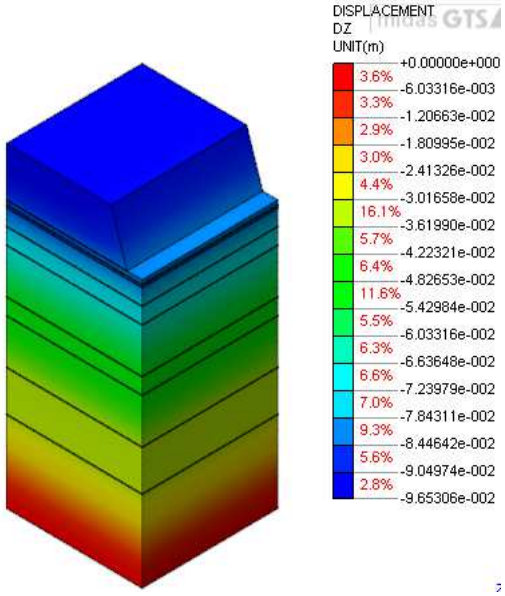



Fig. 3. Natural foundation settlement nephogram

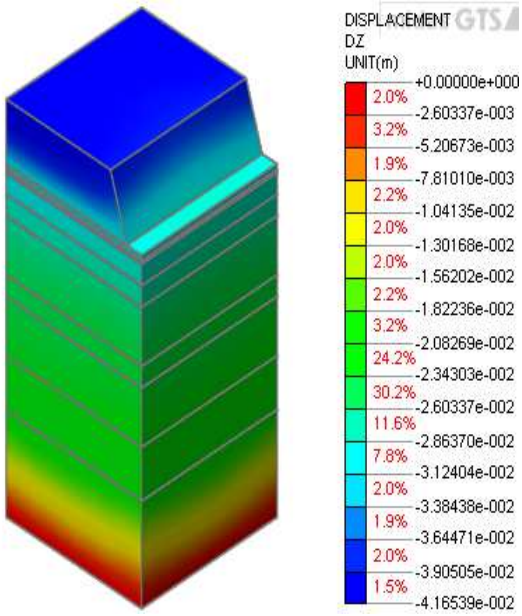



Fig. 4. Composite foundation settlement nephogram

From figure 5, it is obvious that pile stress is greater than the pile-soil stress, indicating pile has played a very good role. Simply pile itself, the pile stress increases gradually along with the increment of depth. By comparing settlement nephogram and stress, composite foundation has a good treatment effect.

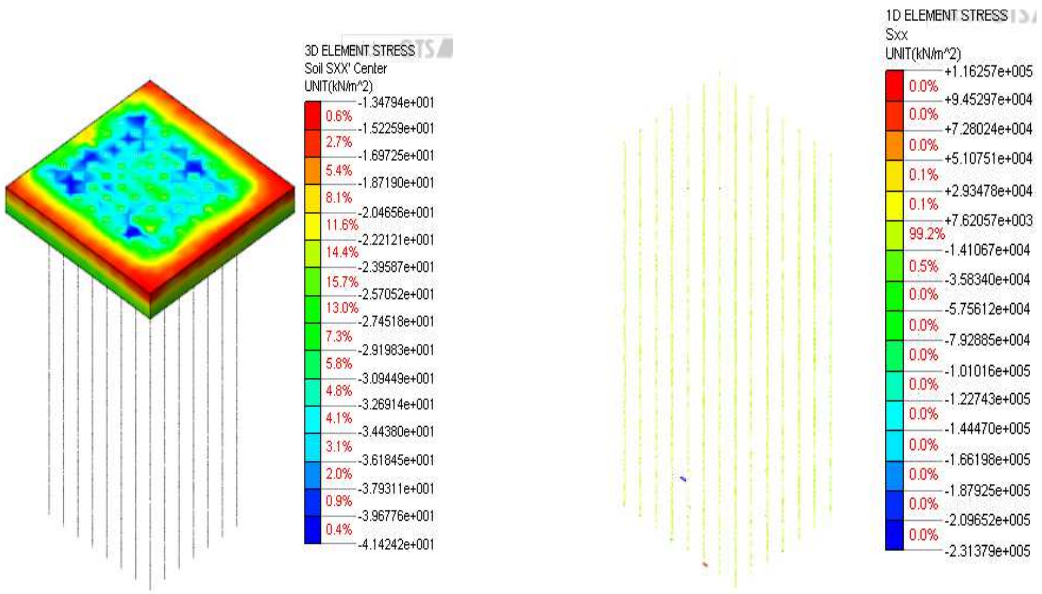



Fig. 5. Comparing pile stress with pile-soil stress

## Relative Parameters of the Pile about the Settlement

### Pile Elastic Modulus about the Settlement

Keeping other parameters constant, the calculation has been done along with the pile elastic modulus changes. Each time the biggest settlement calculation result of embankment is shown in figure 6. From the figure, the biggest settlement of embankment decreases with the increasing of the elastic modulus. When the elastic modulus is greater than 15GPa, sedimentation value tends to be stable, changes is no longer obvious. Considering the influence of economic factors by the function of the similar concrete of CFG pile, the strength of the CFG pile can achieve C15 concrete strength to meeting the requirements[5].

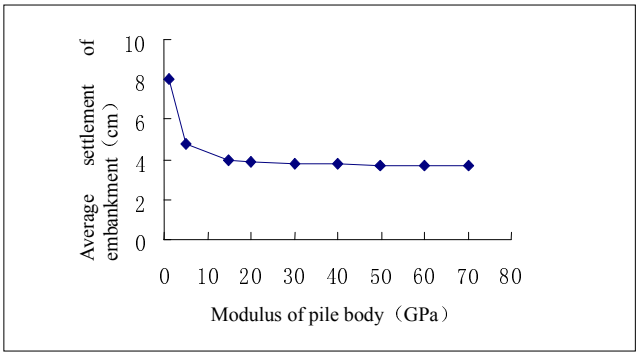



Fig. 6. Average settlement of embankment along with the changes of pile body's modulus

### Pile Diameter about the Settlement

The pile diameter of CFG pile is depending on the piling equipments general from 350mm to 600mm. Keeping other parameters constant, the average settlement calculation results of embankment is shown in figure 7 with the pile diameter changing. Average settlement of embankment is quickly reduced along with the increasing of pile diameter, and then tends to be stable. When the pile diameter is over than 0.5m, the reduction of settlement along with the increasing of pile diameter is not obvious, some advice is given that the diameter of CFG pile should be less than 0.5m which is also fit with the theoretical calculation results.

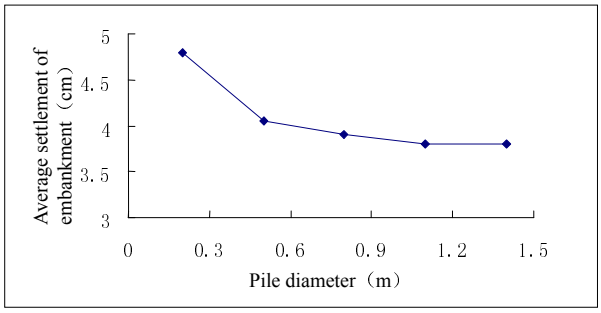



Fig. 7. Average settlement of embankment along with the changes of pile diameter

**Pile Spacing about the Settlement**

Keeping other parameters constant, the calculation has been done along with the pile spacing changes. Each time the average settlement calculation result of embankment is shown in figure 8. From the figure can be seen, the average settlement increases along with pile spacing increases. But when the pile spacing increases from 1m to 2m, the scope of settlement rate is greater than range from 2m to 3m. Considering economy and the operability of construction, pile spacing of 2m is reasonable.

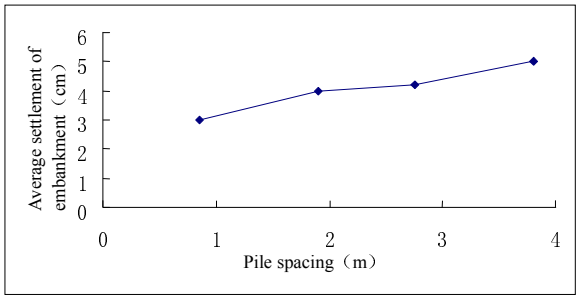



Fig. 8. Settlement nephogram when the pile spacing changes

**Pile Length about the Settlement**

Keeping other parameters constant, the calculation has been done along with the pile length changes. Each time the average settlement calculation result of embankment is shown in figure 9. As the length increases, the average settlement of embankment decreases gradually. The average settlement of embankment levels off when the pile length increases more than 27m. Judging from the effects of pile length setting, some suggestions is given that pile length should be less than 27m which is relatively appropriate.

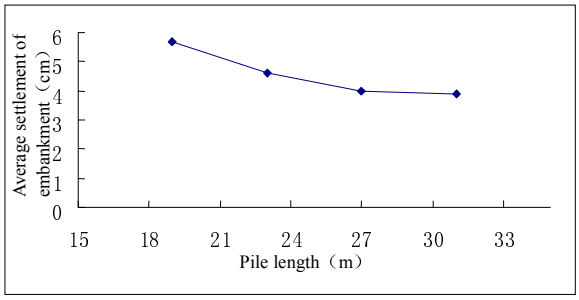



Fig. 9. Average settlement calculation results of embankment when the pile length changes

**Pile Element Parameters about the Settlement**

In order to better study pile-soil contact, the contact elements is used as approximate simulation of this contact zone. Reasonable mechanical model has been established, appropriate mechanical parameter has been chosen and then the mechanical characteristics of structure-soil surface is understood in depth. Two element parameters which affect pile settlement significantly is analyzed, that is ultimate shear stress and shear modulus. The influence of ultimate shear stress and shear modulus on pile settlement is shown in Fig.10 and 11.

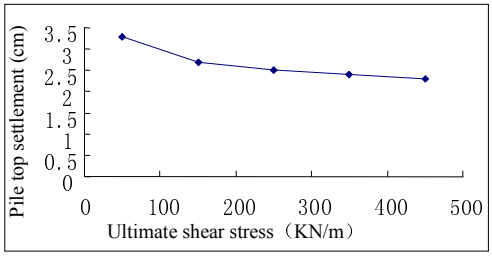



Fig. 10. Influence of ultimate shear stress on the pile top settlement

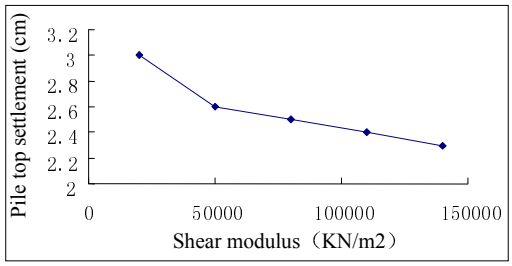



Fig.11. Influence of shear modulus on the pile top settlement

It can be seen that with the ultimate shear stress and the shear modulus increasing gradually, the settlement of pile decreases, however, when the shear modulus is less than 50000 kN/M2, the settlement decrease amplitude is larger , the slope is larger, and then with the increases of shear modulus, the slope of the settlement rate changes into the same basic linear.

**Conclusions**

Using the large finite element software MIDAS/GTS and establishing calculation model of foundation treatment, the problem of pile-soil contact is highlighted.

Through the settlement nephogram and pile-soil stress nephogram analyzing, the results indicates that the foundation treatment scheme is good and achieves the desired purpose. On this basis the foundation settlement factors is analyzed systematically. The conclusion which has certain reference value is given:

(1) Increase the pile modulus, diameter, length, and decrease pile spacing is all beneficial to reduce foundation settlement. However the effect of the step-down is not into the same slope along with pile diameter, length, and spacing changes. With the diameter and length increasing and pile spacing decreasing, settlement reducing effect is less obvious. Considering economy, construction facilities and many other conditions, the most suitable diameter of CFG pile is 0.5m, maximum reasonable length is 27m and the most suitable pile spacing is 2m combined with numerical simulations. Arrangement and spacing of CFG pile in test section approaches to the simulated results. All of these has higher reference value for similar soil foundation. Nevertheless, the specific arrangement of pile spacing and form should be determined by the overall cost, the difficulty of construction and time limit for a project.

(2) With ultimate shear stress and shear modulus parameters increasing, pile settlement decreases gradually, the decreasing amplitude with the increasing of above parameters diminishes gradually. But when the ultimate shear stress over 180KN/M and shear modulus over 5000KN/M2, the slope of the settlement rate is in the same basic linear changes.

(3) The results of numerical simulation can be used as reference for the loess foundation settlement, the settlement regularity and monitoring results is consistent. In order to better adapt to the specific circumstances, periodic monitoring data should be combined to revise the simulation parameters in time.

**References**

[1] Jingbo Zhao,Yun Chen. The collapsibility of loess and its causes [J]. Journal of Geomechanics, 1997, 3(4):12-14(In Chinese)

[2] Zengguang Yang. The characteristics of collapsible loess and foundation treatment measures [J]. Shanxi Architecture，2002, 28(4):21-22(In Chinese)

[3] Juncheng Zeng, Juwen Zhang, Xiaodong Tong, Yongming Xu. Experimental study on the High-speed Railway CFG pile and raft composite foundation settlement[J]. Journal of southeast university (natural science edition). 2010. 40(3): 570-573(In Chinese)

[4] Dingyi Xie, Jilin Qi, Yuanlin Zhu. The structural parameters of soil and its relationship with the deformation and strength [J]. Journal of hydraulic engineering.1999, 21(10):1-6(In Chinese)

[5] Ruicheng Wei. Study on Settlement Characters of CFG Composite Foundation in Beijing-Tianjin Intercity Rail Traffic[D]. Beijing jiaotong university, 2008, 28-42(In Chinese)

*Advanced Materials Research Vol. 937 (2014) pp 444-449*
*© (2014) Trans Tech Publications, Switzerland*
*doi:10.4028/www.scientific.net/AMR.937.444*

# Fluctuations Response of Tall Building to Change of Aspect Ratio in Interference Building

Ki-Pyo You[1*, a], Young-Moon Kim[2,b], Jang-Youl You[3,c] Sun-Young Paek [1,d]

[1]Department of Architecture Engineering, Chonbuk National University, Long-span Steel Frame System Research Center, Jeonju, 561-756, Korea

[2]Department of Architecture Engineering, Chonbuk National University, Jeonju, 561-756, Korea

[3]Senior Researcher, KOCED Wind Tunnel Center, Chonbuk National University, Jeonju, Korea

[a]youkp@jbnu.ac.kr, [b]kym@jbnu.ac.kr, [c]wmjlove1877@jbnu.ac.kr, [d]msdona@jbnu.ac.kr

**Keywords**: Interference effect, Aspect ratio, Isolate building

**Abstract.** Wind loads on buildings in realistic environments may be considerably either increase or decrease by interference buildings. It is commonly known as interference effect. This effect depend on the geometry and arrangement of these structures. It is objective of this work to study the interference effects of the tall buildings which have the different aspect ratios, upstream terrain conditions, distance between adjacent structures and direction. The obstructing model used in this work have the aspect ratio of 2, 3 and 4 and the distances between adjacent buildings are 0.5B, 1.0B, 1.5B and 2.0B, which B is the width of the building. And the above experimental results were compared with experimental data measured on isolated building.

## Introduction

In recent times, many 40-story or higher skyscrapers have been built in Korea. It has been established that the vibration effect from the wind load may become greater than the vibration effect from the earthquake load as buildings become taller. The vibration effect of the wind load involves not only vibration in the along-wind direction from where the wind blows, but also vibration in the across-wind direction, which is vertical to the along-wind direction, and vibration in the torsional direction around the axis, vertical to the plane of the building. Moreover, the effects of such vibrations differ between when a building exists alone and when it interacts with adjacent buildings within a complex[1]. Generally, in the case of high-rise, mixed-use buildings that have been constructed recently, multiple buildings form a group within a complex. Therefore, it is inappropriate to apply a single building's dynamic characteristics under wind to such complexes, and wind tunnel experiments on the effects of neighboring buildings should be conducted. Wind tunnel experiments on adjacent buildings started in the 1930s, when Harris conducted a wind turbine experiment and discovered that the torque of buildings in New York doubled[2]. In actuality, early research on interaction among adjacent buildings merely measured mean wind pressure with two rigid body models, consisting of a measurement model and a neighboring model, arranged vertically or obliquely. In prior times, such research was sufficient when it came to expressing the severity of the consequences interaction. However, measuring the dynamic model of a building in relation to wind was made possible when an aero-elastic model was developed in the late 1970s; one of important problems in the early interaction effects was the considerably increased maximum torsional moment compared to that of a single building[2]. As the scope of experiments widened from coastal areas to suburban and city areas, works considering the complexity of building arrangement and the complex characteristics of wind were performed. In the 1980s, it was demonstrated that wind load may be greatly decreased by neighboring structures, and research focused on determining the effects of interaction with adjacent buildings[3]. At present, however, usable information on interaction effects occurring from two or more high-rise buildings in proximity is very scanty. This is because wind is affected by turbulence, the size and forms of adjacent structures, the location and degree of access by

neighboring structures, and the velocity of wind and its blowing angle; the number of variables makes it difficult to determine what the interaction effects will be. Accordingly, this study will examine how interference effects change when the aspect ratio is 2, 3, or 4, and how the interaction effects change according to neighboring distance, different intensities of wind and illumination, and the direction of wind.

## Wind Tunnel Test

The wind tunnel test was performed using the wind tunnel facilities at Chonbuk National University. The length was 1.5m and the height was 1.2m. The applicable wind speed was 0.5–20 m/sec. The boundary layers formed within the wind tunnel are a suburban area (BL1,α=0.15,■,●) and an urban center area (BL2,α=0.30, □ , ◯). The boundary layer produced inside the wind tunnel (shown in Fig. 1) presents the vertical distribution of the mean wind speed and turbulence intensities of the BL1 for a suburban area and BL2 for an urban area. The scale of the measured model was 1/400 and turbulence intensity at the height of the highest floor was 10% in BL1 and 17% in BL2. The side ratios of the analyzing model and the neighboring model used for the interference effect experiment were the same, at 1, and square-shaped models were used with aspect ratios of 2, 3, and 4. The wind power model was made of balsa material and its natural frequency was over 50 Hz in both the X- and Y-axis directions. The closure rate of the models within the wind tunnel was lower than 5%, at 1.1%, 1.7%, and 2.2%. The relationship among the interference model, the analyzing model, and wind direction used to express the interference effect is displayed in Fig. 2. There are four different cases of interference distance (S) at 0.5B, 1.0B, 1.5B, and 2.0B with section B of the interference model as the standard. An experiment was conducted with two scenarios, one involving adjacent buildings and one with only a single building, while the aspect ratio was changed. The wind velocity in this experiment was measured using a pitot tube on the highest floor of the models; the wind velocities of BL1 and BL2 were 7.4 m/sec and 6.3 m/sec, respectively. The wind direction angle was set at intervals of 15° from 0° to 45°. The aspect ratio of the adjacent building model was changed to 2, 3, and 4. However, the aspect ratio of the analyzed building was maintained at 4 and measurements were taken by changing the interference distance(S) from 2 to 3 and 4. Table 1 gives the dimensions of the experimental model and the prototype building.

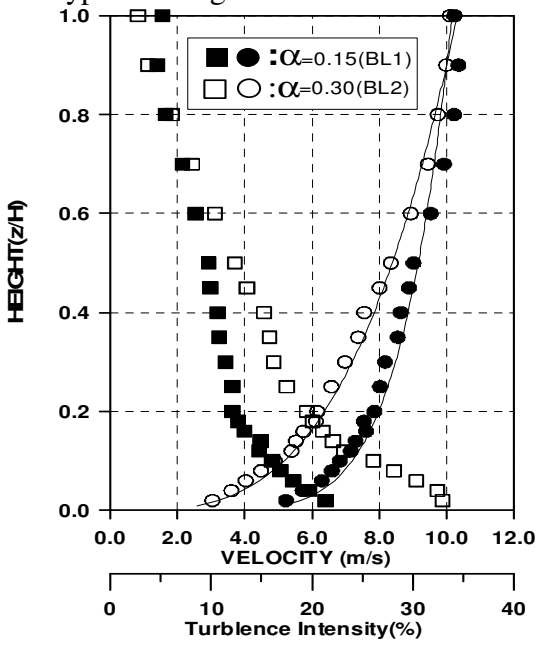



Fig. 1. Vertical distributions of the mean wind speed and turbulence intensities

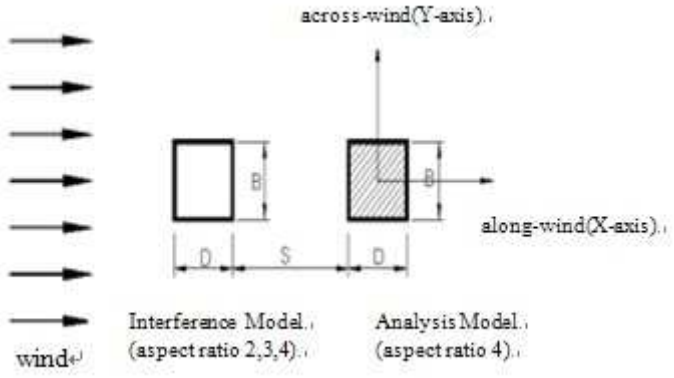



Fig. 2. Relationship between the analysis model and the interference model

Table 1. Dimension of the model and prototype

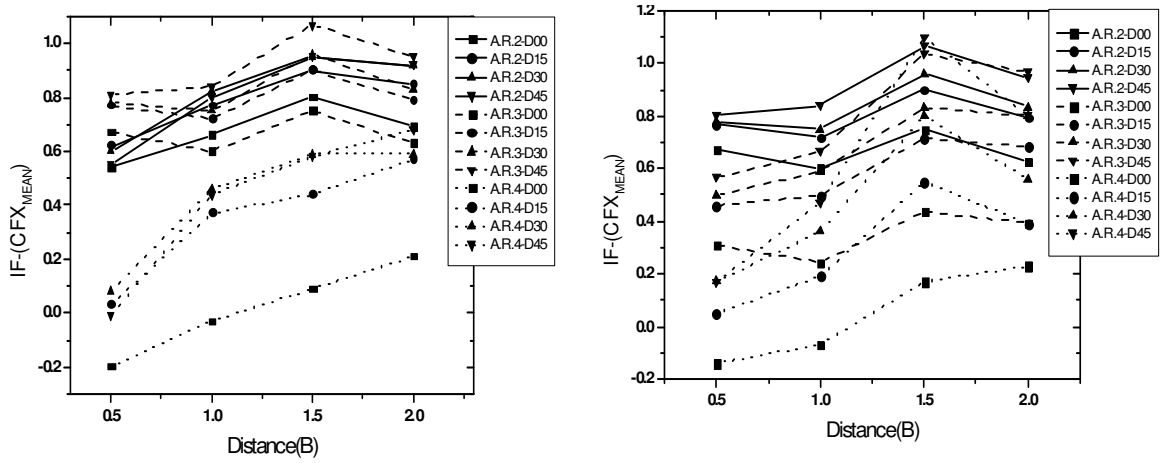
| Specification | | Model dimension(cm) ($B\times D\times H$) | Prototype dimension(m) ($B\times D\times H$) |
|---|---|---|---|
| Interference model | aspect ratio 2 | 10×10×20 | 40×40×80 |
| | aspect ratio 3 | 10×10×30 | 40×40×120 |
| | aspect ratio 4 | 10×10×40 | 40×40×160 |
| Analysis model | aspect ratio 4 | 10×10×40 | 40×40×160 |

**Interference Factor**

Regarding the result of the wind power experiment using a six-component load cell, the effects of changes in aspect ratio, angle, and intensity of turbulence in the windward-side model (inference model) and the leeward-side model (analysis model) were analyzed according to the interference factor (IF). IF represents the relationship between the interference model and the single model, and is shown in Eq. (1).

$$\text{IF}=\frac{\text{Force on a building with interfering buildings present}}{\text{Force on an isolated building}} \quad (1)$$

It may be classified into three sections, with 1 as the standard. IF<1 is the area where the coefficient of wind force of the leeward-side model (analysis model) is decreased in relation to the windward-side model (inference model). IF=1 is the area where the windward-side model does not affect the leeward-side model at all. Finally, IF>1 is the area where the coefficient of wind force of the leeward-side model is increased by the windward-side model. Fig. 3 to Fig. 4 show IF by each angle and intensity of turbulence according to changes in the aspect ratio of the mean coefficient of wind force in the X-axis and Y-axis directions. In the examples of Fig. 3 to Fig. 4, AR and D refer to aspect ratio of the interference model and experimental wind direction angle, respectively. The analysis result of mean IF in the X-axis direction in Fig. 3 is as follows.




(a) BL1 (b) BL2

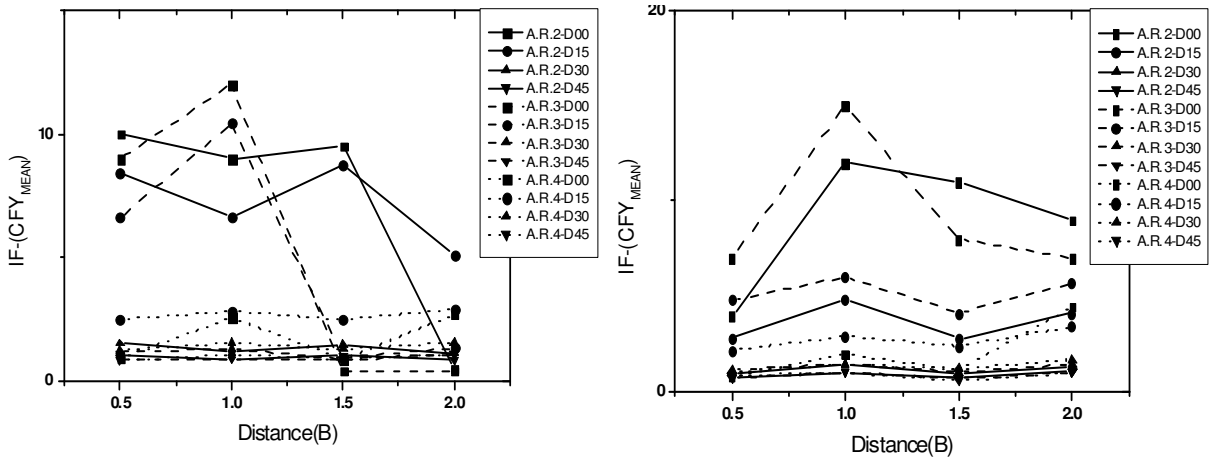
Fig. 3. Mean IF in the X-axis direction(along-wind)

**Interference Distance of 0.5 B**

When the interference distance is 0.5 B, IF is less than 1 and the coefficient of the wind force of the leeward side model (main model) in the X-axis direction is decreased by the windward-side model (interference model). As for the wind direction angle and aspect ratio, the influence was greatest when the wind direction angle was 0° and the influence of the aspect ratio was greatest when it was 4, followed by 2 and 3. The reason for this is that while the leeward-side model is completely included in the backflow area occurring at the back of the windward-side model with an aspect ratio of 4, the mean coefficient of wind force is larger when the aspect ratio is 2 or 3 in the interference model than when the aspect ratio is 4 because of the effect of the pile that was peeled off the roof plane of the windward-side model in the leeward-side model. In terms of differences in turbulence intensity, the tendency by each angle range is more obvious in BL1 (a suburban area) than BL2 (an urban center area). This is judged to be because the mean wind velocity of BL1 is greater than that of BL2.

**Interference Distance between 0.5 and 2.0 B**

From 0.5 B to 1.5 B, the longer the interference distance, the larger the IF, or in other words, the smaller the interference effect. This is judged to occur because as the interference distance in the windward-side model increases, the shielding effect decreases and the backflow area occurring at the back side of the windward side model becomes longer. Regarding changes in wind direction angle, the interference effect decreases as the angle increases. With regard to changes in aspect ratio, the interference effect is increased by the decrease in the IF as the aspect ratio increases. In other words, the interference effect tends to decrease with a smaller aspect ratio and larger changes in wind direction angle. The reason for this is that when the aspect ratio of the windward-side model is small, the backflow area occurring at the back side of the windward-side model acts on the front side of the leeward-side model. When the interference distance is 2.0 B or more, the interference effect is increased by a decrease in the IF. The reason for this is considered to be the decrease in the size of back flow area occurring at the back of the windward side and the increase in the shielding effect when the interference distance is 2.0 B or longer. Regarding changes according to the intensity of turbulence, the amplitude of change is larger in BL1 than BL2, and the amplitude of change becomes larger as the wind direction angle increases. This is considered to be because the length of the backflow area increases more at the back of the windward-side model of BL1 than it does in BL2. The analysis result of mean IF in the Y-axis direction in Fig. 4 is as follows.




(a) BL1 (b) BL2

Fig. 4. Mean IF in the Y-axis direction(across-wind)

**Interference Distance of 0.5 B**

The IF in the Y-axis direction is larger than 1. This is because the windward side model increases the coefficient of wind force of the leeward-side model; when the wind direction angle is zero, the backflow occurring at the back of the windward-side model acts on the flank of the leeward side model.

**Interference Distance between 0.5 B and 2.0 B**

Changes in IF according to changes in the interference distance between the windward-side model and the leeward-side model and increase in wind direction angle are large. This means that the windward-side model brings about an increase in the coefficient of wind force in the Y-axis direction in the leeward-side model; in other words, there is an increase in the interference effect. In particular, when the value is smaller than 1.0 B, the amplitude of the increase is very large, but when the value is larger than 1.0 B, the amplitude of the increase is small. This is considered to be because the inclusion of the backflow area occurring at the back of the windward-side model in the flank of the leeward-side model is largest at 1.0 B, while at a value larger than 1.0 B, it deviates from the backflow area at the back of the windward side. With regard to changes in aspect ratio, the value is largest when the aspect ratio is 2 or 3 and the wind direction angle is zero, while the value is constant with the aspect ratio at 4. As for changes in the intensity of turbulence, the value is larger in the BL2 than in the BL1, which is judged to be because the intensity of turbulence of BL2 is larger.

**Conclusions**

In this work was intended to examine the interference effect of a high-rise building with changing wind load on neighboring buildings through three varying conditions—wind direction angle, interference distance, and intensity of turbulence—according to different aspect ratios (2, 3, and 4) of the interference model (windward side). The mean IF in the X-axis direction was less than that of the windward side model, regardless of the aspect ratio, which is considered to be because of the shielding effect by the windward-side model and backflow area occurring at the back of the windward side. The mean IF in the Y-axis direction was larger than 1, which showed that the backflow area occurring at the back of the windward side affected the flank of the leeward side, rather than generating a shielding effect.

**Acknowledgement**

This work was supported by the National Research Foundation of Korea (NRF) and was funded by a grant from the Korean government (MEST)(NO.2011-0028567).

**References**

[1] J. Blessmann , J.D.Riera: *Interaction effects on neighboring tall buildings*, Proceeding of Fifth International Conference on Wind Engineering, Fort Collins CO., USA, (1979), pp.381–395

[2] A. C. Khanduri : *Wind-induced Interference Effects on Buildings: Integrating Experimental and Computerized Approaches*, PhD. (1997),

[3] P. A. Bailey, K. C. S. Kwok *: Interference Excitation of Twin Tall Buildings*, Journal of Wind Engineering and Industrial Aerodynamics. Vol. 21 (3), (1985),pp. 323-338

*Advanced Materials Research Vol. 937 (2014) pp 450-455*
*© (2014) Trans Tech Publications, Switzerland*
*doi:10.4028/www.scientific.net/AMR.937.450*

# Performances of Manganese Slag Cement

Qi-zhi CHEN[1,a], Duo-qiang LIANG[2,b*]

[1]Guangxi Investment Group Huiyuan Manganese Industry CO.,LTD., Laibin, Guangxi, China

[2]Guangxi resources and institute of metallurgy, Nanning, Guangxi, China

[a]171173984@qq.com , [b]397857135@qq.com

*Corresponding author

**Keywords:** Manganese slag; Cement; Concrete.

**Abstract.** It is of great importance to innocuity, minimization and reutilization of manganese slag generated in manganese products by electric furnace process. In the paper, ordinary Portland cement is replaced by manganese slag part then to evaluate manganese slag's influence on the mechanical properties. The experimental results obtained show that ordinary Portland cement added less than 20% by manganese slag was improved in mechanical performances and the cement concrete added less than 20% by manganese slag was not changed significantly. To reduce the economic costs, enhance mechanical properties, manganese slag can replace part of cement concrete.

## Introduction

Granulated electric furnace slag (GEFS) is major by-products of manganese plants, followed by blast furnace method, and little by hydrometallurgical process[1]. It is formed by the combination of manganese ore with limestone flux[2]. If the molten slag is cooled and solidified by rapid water quenching to a glassy state, little or no crystallization forms. This process results in the formation of sand size fragments, usually with some friable clinker-like material known as granulated electric furnace slag. These materials often cause disposal problems and environmental pollution[3-5]. Detailed laboratory investigations were carried out on GEFS-added cement stabilized mixes in order to find out its suitability for road embankments, and for base and sub-base courses of highway pavements.

Most manganese alloy are produced and consumed in china, especially in Guangxi Zhuang Autonomous Region. 93.6% manganese reserves belong to poor ones[6], and a great number of manganese slag is generated. Containing some toxic elements, manganese slag are definitely one of hazardous materials[7].

Generally development of adequate network of roads is of vital importance in the socio-economic development of a country. Stabilized layers are made by cement stabilized small stone. Utilisation of by-products like granulated electric furnace slag, as suitable ingredients for geotechnical construction, needs special attention. High costs increase the significance of industrial solid slag's addition to the layer. Use of manganese slag as a replacement for cement in concrete: manganese slag contains some quantities of typical cement minerals, although in less quantity than in cement clinker. This could mean that manganese slag could be used as partial replacement for cement in concrete mixes, as a supplementary cementitious material, similarly to what already happens for manganese slag.

## Experimental Investigation

The yellow and easy-broken manganese slag is originated from Guangxi Comilog Ferroalloy (Group) Co., Ltd. Its chemical composition, physical properties and activity index are listed as Table 1, Table 2 and Table 3, respectively.

Table 1. Chemical composition of the manganese slag (wt.%)

| Item | $SiO_2$ | CaO | $AL_2O_3$ | MgO | $SO_3$ | $Fe_2O_3$ | $MnO_2$ | loss |
|---|---|---|---|---|---|---|---|---|
| Constituent | 23.05 | 37.63 | 15.41 | 7.54 | 0.46 | 1.24 | 10.4 | 0.71 |

Table 2. Physical properties of the manganese slag

| Item | mean particle diameter, mm | apparent density, $kg/m^3$ | water content | Density, $g/cm^3$ |
|---|---|---|---|---|
| physical parameters | <5 mm | 700 | 40%～50% | 2.87 |

(1mm=$1\times10^{-3}$m, 1g/$cm^3$=$1\times10^3$Kg/$m^3$)

Table 3. Activity index of the manganese slag

| index | value | GB203-78 |
|---|---|---|
| coefficient of basicity $(CaO+MgO)/(SiO_2+ AL_2O_3)$ | 1.08 | ≥0.65 |
| activity coefficient$(AL_2O_3/SiO_2)$ | 0.67 | ≥0.20 |
| quality coefficient $(CaO +MgO+AL_2O_3)/(SiO_2+ MnO)$ | 1.82 | ≥1.20 |

Mineral composition test was done by 12kW DMAX2RB X-ray diffraction Analyzer(Japan Rigaku Corporation). Fig.1 showed the test results.

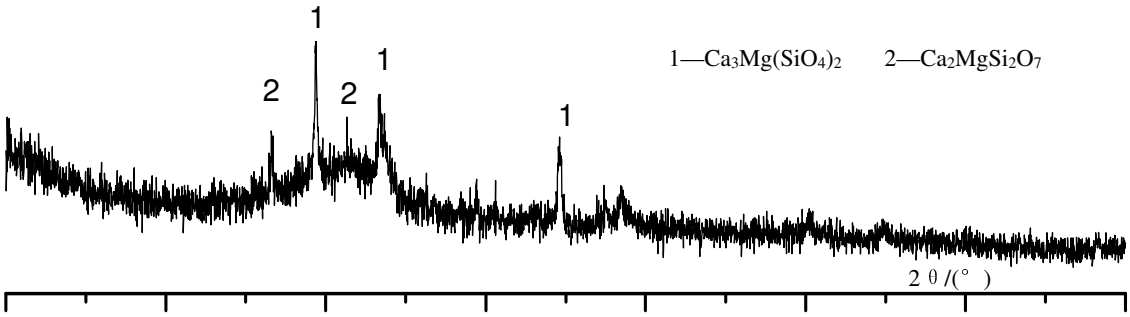
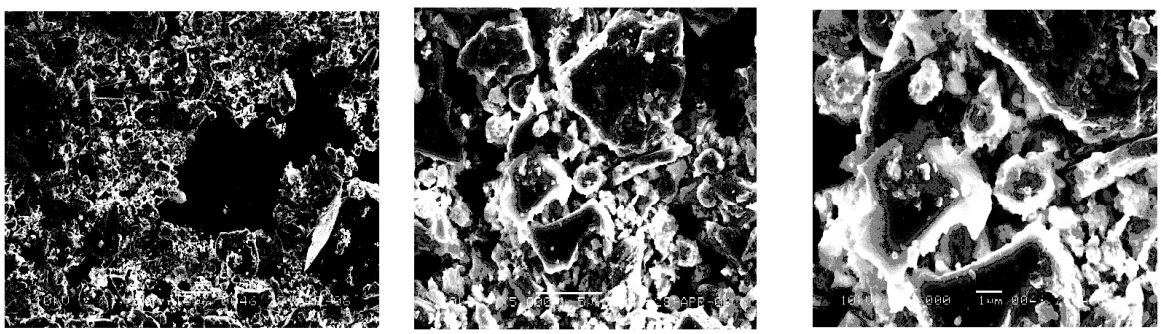



Fig. 1. XRD of manganese slag



(a) SEM×2000 (b) SEM×5000 (c) SEM×10000

Fig. 2. SEM of manganese slag

Fig.1 shows the slag was mainly composed by vitreous body. The later Lithofacies also test confirmed that, above 90% is vitreous body, along with merwinite ($Ca_3Mg(SiO_4)_2$), akermanite ($Ca_2MgSi_2O_7$), anorthite($Ca_2[Al_2SiO_7]$ dicalcium silicate ($C_2S$), and tricalcium silicate ($C_3S$), which proves that the manganese slag is with hydraulic and pozzuolana activity.

Granularity test was done with a JSM25900 SEM and a Nexus 670 FTIR (Japan JEOL). Fig.2 showed the test results.

Fig.2 shows the big particles have no regular shape, and the small are of globularity. The mean particle diameter is under 10μm.

## Results and Discussions

After the manganese slag was grinded for 40min, they were added 0.5% AFJS as exciting agent and incorporated into cement according to Table 4. The mechanical performances of such cement with standard sand are showed in Fig.3 and Fig.4.

Table 4. Composition ratio of cement raw material allocating proportion

| No. | A0 | A1 | A2 | A3 | A4 | A5 |
|---|---|---|---|---|---|---|
| Cement content (%) | 100 | 80 | 70 | 60 | 50 | 40 |
| manganese slag content (%) | ---- | 20 | 30 | 40 | 50 | 60 |

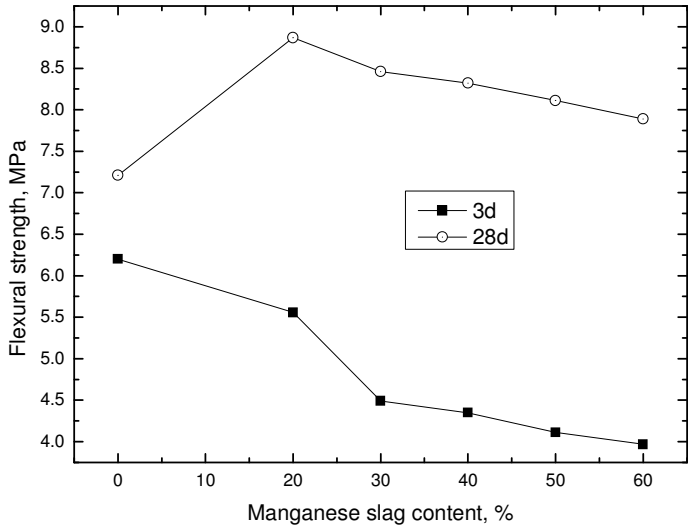



Fig. 3. Flexural strength of manganese slag cement(1MPa=$1\times10^6$Pa)

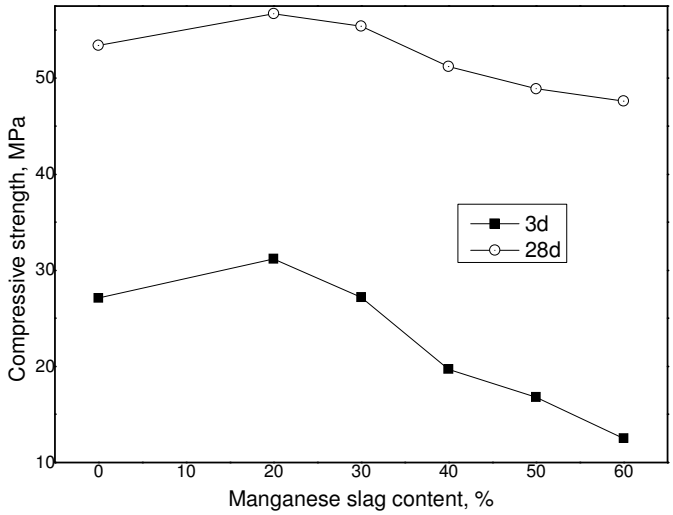



Fig. 4. Compressive strength of manganese slag cement (1MPa=$1\times10^6$Pa)

Fig. 3 shows flexural strength of manganese slag cement was decreased with increasing manganese slag content and the trend pricked up when manganese slag content is under 20%.

Fig.3 also shows flexural strength of all samples increased with time. When manganese slag content is under 20%, flexural strength of manganese slag cement was increased with increasing manganese slag content.

Fig.4 shows the samples trend of 3d and 28d is the same. When manganese slag content is under 20%, compressive strength of manganese slag cement increased with increasing manganese slag content. When manganese slag content is above 20%, compressive strength of manganese slag cement decreased with increasing manganese slag content.

The obtained experiment results show that the optimum manganese slag content is 20%. When manganese slag content is too high, mechanical performances of manganese slag cement decreased significantly. In early time, flexural strength of the manganese slag cement is low, which maybe is caused by that manganese slag cement is mainly instituted by chamotte and its latent activity has not been inspired. But later time, its latent activity was inspired with the condition of chamotte and exciting agent[8], and therefore, flexural strength of the manganese slag cement increased. Compressive strength of manganese slag cement changed as that, but it is more distinct.

Hydration process of manganese slag cement is likely to Portland cement except hydration product. Hydration process of manganese slag cement was observed via sample A1. The XRD results and SEM results of 3d, 7d and 28d were showed in Fig.5 and Fig.6, respectively.

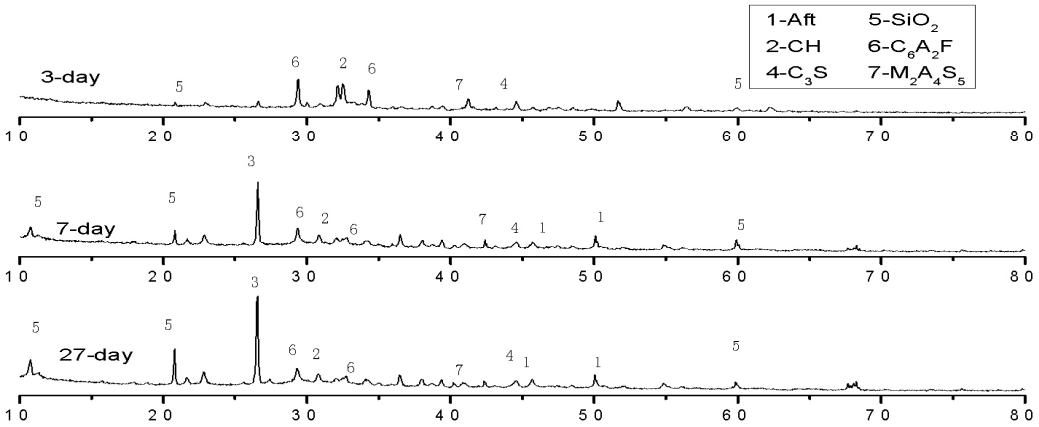
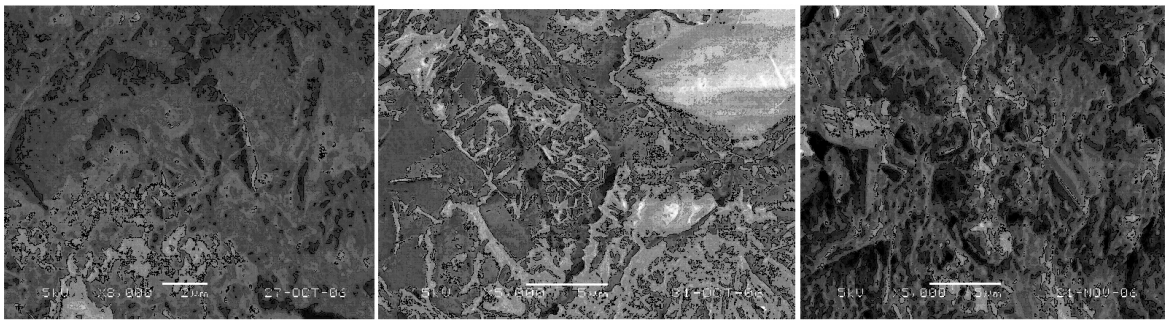



Fig. 5. XRD of manganese slag cement with different hydration age



（a）-3d （b）-7d (c)-28d

Fig. 6. SEM of manganese slag cement with different hydration age

Fig.5 and Fig.6 shows that manganese slag cement is mainly constituted by chamotte in early hydration age. Wollastonite and a little granular C-S-H gelatins was produced, bringing flexural or compressive strength in some content. But the latent activity of manganese slag cement had not been inspired, which cause low flexural or compressive strength.

In 3d, latent activity of manganese slag cement start to be inspired, producing more Wollastonit, C-S-H gelatins, zeolite nomenclature, which increased flexural or compressive strength. In 7d, a great number of plate heulandite was produced with Wollastonit and C-S-H gelatin. Those gelatins make manganese slag cement compact. In 27d, hydration product continues to grow and the structure become compacter, less hole and crack remained, which all make the structure compact. Furthermore, cascaded CH crystal interlude in the radixes[9], make the structure compacter.

To evaluate manganese slag's effect to the Portland cement, the mechanical performances of manganese slag cement of was tested. The mechanical performances indexes were tested by adding manganese slag with different content. The obtained experimental results are listed in Fig.4.

## Conclusions

When manganese slag content is under 20%, the mechanical performances of manganese slag cement are improved. Therefore, the manganese slag can be treated at low cost without giving load to environment, by using the manganese slag which has conventionally been subjected to waste disposal, as a cement raw material.

## Acknowledgement

This research was financially supported by Chinese Foundation for Teacher Development Foundation(GX12041), Guangxi University Publication Foundation((A1331705), Guangxi Education Department Foundation of China(T1331705), and the Research Foundation of Guangxi Education Department(C133004).

## References

[1]Zhang W.; Cheng C., "Manganese metallurgy review. Part II: Manganese separation and recovery from solution", Hydrometallurgy, V. 89, N.3-4, Dec. 2007, pp. 160-177

[2]Hunsucker D.; Graves R., "Mechanical performances of experimental highway base and subbase layers containing by-product materials from a coal fired power plant: KY Route 3074, Kentucky Transportation Center", 1993, pp. 85.

[3]Michael M.; Javier C., "The environmental hazard caused by smelter slags from the Sta. Maria de la Paz mining district in Mexico", Environmental Pollution, V. 98, No.1, 1997, pp. 7-13.

[4]Neda V.; Gabriel B.; Cédric G., "Remobilization of metals from slag and polluted sediments (Case Study: The canal of the Deûle River, northern France)", Environmental Pollution, V. 141, No. 2, May 2006, pp. 359-369.

[5]Yang C.; Chen Y.; Peng P.; Li C., Chang X.; Xie C., "Distribution of natural and anthropogenic thallium in the soils in an industrial pyrite slag disposing area", Science of The Total Environment, V. 341, No. 1-3, Apr. 2005, pp.159-172.

[6]Fan D.; Yang P., "Introduction to and classification of manganese deposits of China. Ore", Geology Reviews, V. 15, No. 1-3, Oct. 1999, pp. 1-13.

[7]Ferreira C.; Ribeiro A.; Ottosen L. "Possible applications for municipal solid waste fly ash", Journal of Hazardous Materials, V. 96, No. 2-3, Jan. 2003, pp. 201-216.

[8]Harald G., "The "chessboard" classification scheme of mineral deposits: Mineralogy and geology from aluminum to zirconium", Earth-Science Reviews, V. 100, No. 1-4. (18), June 2010, pp. 1-420.

[9]Ziad A.; Mohamed A., "Abdel-Halim.Laboratory evaluation of various types of mortars for the conservation of Qasr al-Bint monument, Petra–Jordan", Engineering Structures, 2001, V.23, No.23, pp. 926-933

*Advanced Materials Research Vol. 937 (2014) pp 456-461*
*© (2014) Trans Tech Publications, Switzerland*
*doi:10.4028/www.scientific.net/AMR.937.456*

# Historical and Cultural Connotation of the Architectural Wood Carving Ornament in the Ancestral Temple of Chen Family

## ——With "Feast in Bronze Sparrow Terrace Held by Cao Cao" and "Jiantu Conference" as Examples

Yi-ning CHEN

Guangdong Teachers College of Foreign Language and Arts, Wushan District, Guangzhou,China

ynchyn@163.com

**Keywords:** Architectural Wood Carvings of the Ancestral Temple of Chen Family; "Feast in Bronze Sparrow Terrace Held by Cao Cao";"Jiantu Conference"; Craftsmanship; Composition Feature; Cultural Aesthetics

**Abstract:** The paper aims to analyze the features of the craftsmanship and composition and study the architectural ornament art and cultural and aesthetic implication of the architectural wood carving of the Ancestral Temple of Chen Family, which is the key cultural site under the state protection.

Boasting the cultural features of the ancient architecture in the south of the Five Ridges, the Ancestral Temple of Chen Family is the key cultural site under the state protection. Situated in the Zhongshanqi Road of Guangzhou City, it is the ancestral temple of the "Chen" family of the 72 counties of Guangdong Province. It is commonly referred to as "Ancestral Temple of Chen Family". Its construction began in 1888 and it was finished in 1893 (the twentieth year of the reign of the Emperor Guangxu). According to On the Investigation of the Architecture Design of the Ancestral Temple of Chen Family written by Cui Huihua, Lin Keming, the famous architect, had saw the design drawing of Ancestral Temple of Chen Family at the place of Li Juchuan in the year of 1993. At that time, Mr. Li was nearly ninety years old. Years later, Mr. Li passed away and the design drawing of the Ancestral Temple of Chen Family was nowhere to be found1. The main building of the Ancestral Temple of Chen Family consists of five individual buildings and three rows of houses. There are altogether nine halls and six courtyards (Fig.1). It is next to Guangya Academy, with the hope that Guangya style of study can help cultivate the juniors in Guangdong whose family name are Chen. The architectural ornament has the historical and cultural connotation which inherits the ancient style, shines in contemporary times and enlightens the later generations. Therefore, the ornament is characterized by rigorous layout, excellent fineness and imbued with rich scholastic atmosphere and architectural features in the south of the Five Ridges in modern times.

### Materials and Craftsmanship of the Architectural Wood Carving in the Ancestral Temple of Chen Family

"Feast in Bronze Sparrow Terrace Held by Cao Cao" and "Jiantu Conference" are the representatives of the beam frame architectural wood carving of the Ancestral Temple of Chen Family. The material, which is chosen with special care, is Pontianak wood whose formal name is Pontianak ironwood. It belongs to the Lauraceau Eusideroxylon. Indonesia is the main producing area. The heartwood is tawny, while the sapwood is golden. The color is bright after the material is painted (Fig.2). The air-dry density is around 1.19g/cm$^3$. It is featured by tough and tensile quality with fine grain, being a little acidic. It has such merits as having strong and powerful resistance to insects, moisture resistance and free of corrosion. Thus, it is the ideal building material for the hot and wet area in the south of Five Ridges where the termites breed easily. Pontianak wood can be classified into night side wood, sunny side wood, windward wood and leeward wood. The annual ring of the sunny side wood is relatively sparse, while that of the night side wood is relatively dense. The grain of the windward wood is thin. In contrast, the grain of the leeward wood is thick. In case the architectural wood carving is about the face of human, the wood in the sunny and windward side

should be chosen, which is characterized by beautiful appearance, toughness and anti-deformation. So the material can enable the craftsman to show their splendid carving techniques. Therefore, the material for most of the architectural wood carvings in the Ancestral Temple of Chen Family is the sunny and windward side of Pontianak wood.

During the construction of the Ancestral Temple of Chen Family, such famous folk wood carving masters as Xu Sanyou were hired and paid a large sum of money. All the six major procedures, rough shape cutting, sending sample, chasing, scraped finish, assembly and lacquer coating, were operated by the famous craftsmen. Confined by the material and members, the architectural wood carving cannot have free artistic expression like the artistic wood carving. During the making process, the wood carving craftsman should familiarize himself with the texture and grain as well as other characteristics of wood. It is according to the position of construction as well as the shape of the member that the size of the figure and landscape, the optimal position of the composed view is designed and determined and that the layers of the shape is arranged. Then, draw and mark on the wood in a detailed manner and arrange the position by taking into account the grain's features. In the meantime, design and adjust the carving according to the deformation of wood in wet and dry conditions. They studied the features of the architectural members conscientiously and managed the shape of the ornament. They showed their exquisite skills of carving and cutting with a knife serving as the pen and wood serving as the paper. The architectural wood carving is the carving method which is "minus". The waste materials are removed gradually from outside to inside. In this way, the shape of the wood carving is shown. Pit one against ten and it is very difficult (Fig.3). During the carving, the subject and shape, the overall design, the relation between blankness and actuality and the stability of materials should all be taken into account. The Pontianak wood has hard texture, which makes it especially difficult to chisel delicately. The carving is made possible by using the sharp graver with thick knife blade and short wooden handle. More often than not, the craftsmen need to operate the knife by placing the knife handle against the shoulder. Sometimes, they carve with the aid of hammer or wooden mallet. The unique method to hold the knife and operate it enables the architectural wood carving of the Ancestral Temple of Chen Family to boast sophisticated way of cutting and the artistic effect of figures with majestic and powerful air. "Feast in Bronze Sparrow Terrace Held by Cao Cao" and "Jiantu Conference" are situated on the beam frame on the eastern and western sides of the gate of the Ancestral Temple of Chen Family. The architectural wood carving, with a 6.7-meter high girder, is 3.129 m long, 0.15 m thick and 0.649 m high. The carving adopts the block and plane cutting method, simplifying the five sense organs and posture of the figures to geometric shapes. Then, carve it in an accurate, decisive and powerful cutting way and in details. Every cutting forms the kinetic potential of joint forces. Finally, perfect and improve it with round cutting method. Such kind of cutting method for geometric shape demonstrates the roughness and frankness of the figures, forming contrast with the uniformity of the frames.

## Aesthetic Characteristics of the Composition Art of the Architectural Wood Carving in Ancestral Temple of Chen Family

### Rich Modeling Ability

According to the needs of the fabric features of materials, the architectural wood carving usually adopts the agglomerative organization method in design. Arrange the shape according to the direction of wood grain in the gradual carving. While handling the outline, accept or reject the wood according to the knot. When "Feast in Bronze Sparrow Terrace Held by Cao Cao" and "Jiantu Conference" were made, the subject was selected according to the position of the member so as to achieve the ideal visual effects. The shape is like "Z", forming more layers, deep scenery and wide view. To accentuate the subject culture, the design highlights the composition of grand scene. Figures usually cause difficulties in composition. The carving organizes a number of figures horizontally according to the length of the beam. The rich plots connect more than thirty figures together. Cao Cao and Jinwengong, the ruler of Jin, are arranged in the prominently central

positions of the wooden pier of beam on the left top of the vision. That the wooden pier is the main support force among the architectural members symbolizes the strength and prestige of the main characters in “Jiantu Conference”. In this way, the utilitarian function is consistent with the identity and strength. Cao Cao is watching the demonstration of and competition in military skills by his favorite officers in Bronze Sparrow Terrace on the eastern side, while Jinwengong is sitting on the mythical bird-shaped chair, looking down at the emissaries attending the conference on the western side. The main characters have big eyes and bushy eyebrows and lifelike details of the five sense organs. The sunk eye socket, carved and retouched by circular knife, makes the figures in high spirit and extraordinary air. In “Feast in Bronze Sparrow Terrace Held by Cao Cao”, the two martial masters, who win the contest, demonstrate excellent skills in martial art and are well-matched in strength. The governors from such countries as the states of Lu, Qi, Song and Zheng to attend the conference are placed in the lower part of the beam before the image. The lifelike expression on numerous emissaries coming to attend the conference excitedly is depicted and their expression is dramatic. The movement, expression and clothes of the characters in two wood carvings are different. Generalized as they are, they show different forms and combine activity with inertia. Besides, the beam and the wooden pier are combined closely and designed ingeniously. Add the continuous cyclic movement of the viewpoint to the characters so that the arrangement of the characters is even, straight and balanced. Moreover, they run in the continuous space-time continuum, forming a kind of moving and perspective visual effect. The characters and scenery constitute the plane and uniform panoramic composition in a sectionalized way. The plane decoration and creation of scene together with its beauty in form are valued in the composition. With the integration of circle and square, balanced symmetry and proper size, the carving is rigorous, fine, and full of fun. The “Feast in Bronze Sparrow Terrace Held by Cao Cao” originates from the fifty-sixth chapter of the novel “Romance of Three Kingdoms” written by Luo Guanzhong in Ming Dynasty. Cao Cao built the Bronze Sparrow Terrace in the fifteenth year of the Jian’an era, where the subordinate generals rode and shot for fun. The architectural wood carving is to praise the excellent young generals in the shooting competition(Fig.4).The “Jiantu Conference” comes from the Retreat about Thirty Miles for Peace in A History of the Various Kingdoms in the Eastern Zhou Dynasty. In the battle of Chengpu happening in 632 BC, the State of Jin defeated the State of Chu. So, Jinwengong gathered the governors of different states to hold a conference and seek alliance in Jiantu (the current Guangwu County of Henan Province). This is called the “Jiantu Conference” (Fig.5).

## Cultural Aesthetics of Jiantu Conference

### The Subject Matter of “Feast in Bronze Sparrow Terrace Held by Cao Cao” and “Jiantu Conference” Has Long History and is Very Traditional

The common people are familiar with the subject matter and thus the carvings suit the cultural aesthetics of the public. In Modern Architectural Culture and Aesthetics in the South of Five Ridges, professor Tang Xiaoxiang remarks that “the aesthetics of architecture lies in the adaptability of the building. That is, the adaptability to the needs of human existence, life and emotion etc. It includes three aspects, i.e. the natural adaptability, social adaptability and cultural adaptability of architecture.”2 In regards to the two works, the free time modeling method is adopted to composite and create the works, combining and recreating the historic figures flexibly. They borrow the traditional Chinese painting signs to show the plane, decorative, general and symbolized beauty in form and display the implied meaning of historical culture, which is easy to be understood by people.

### The Regional Cultural Characteristics of the Architectural Wood Carving is Conspicuous

“The cultural adaptability, as an important aspect of aesthetic property of architecture, is mainly reflected in the artistic philosophy, design thinking, cultural spirit and aesthetic taste, which are manifested through such architectural image elements as architectural layout, style, spatial organization and detail treatment.”3 They are decorated with materials adaptable to the climate

features of the south of Five Ridges. The traditional Chinese auspicious symbols are adopted to embellish the frame of the architectural member and to set the central theme off to advantage. The space is properly arranged, in consistent with the cultural aesthetic features in Qing Dynasty and adaptable to the demands of the natural environment in the south of Five Ridges. There are various forms of art, such as guest and host, opening and closing, echo, vague and evident, deficiency and excess together with spacing. They create the grand and vivid historical event and display the ambition with historical event. Furthermore, worship for braveness and force and emphasis on strength to seek success as well as the importance of conducting oneself with great virtue are established, showing the integration of the traditional ancestral culture in Central Plains and the ancestral culture of Guangdong in Qing Dynasty. “Feast in Bronze Sparrow Terrace Held by Cao Cao” and “Jiantu Conference” show the ancestral cultural thought of the Ancestral Temple of Chen Family through plain subject matter, typical scene and plain but vivid character models. The architectural wood carving ornament walks towards the folk culture cultivation, enlightening and promoting the thought of the clansman and becoming the cultural carrier of the ancestral temple of “Chen” family.

The architectural wood carvings “Feast in Bronze Sparrow Terrace Held by Cao Cao” and “Jiantu Conference” illustrate the traditional Chinese moral culture with excellent character models and quaint colors. The wood carving ornaments symbolize the ancestral idea and enhance the ancestral spirit. Besides, the implied meaning of “Jiantu Conference” is positive and optimistic. “It has social significance to make these objective images become the conceptual substitute and symbolic representation and get steady and consolidated gradually and finally get deeply rooted in the collective consciousness of people during the inheritance of culture.”4 The ideal that the country is prosperous and the people are powerful, strong and constantly strive to become stronger displayed by the wood carvings exerts a subtle influence on people and is handed down from generation to generation. They contribute to the moral cultivation and education of common people and improve the connotation of the ancestral temples. More importantly, they show the organic unification of the construction technique and wood carving ornament art of Qing Dynasty .

## Conclusion

The architectural wood carving art in the Ancestral Temple of Chen Family is the outstanding representative of the folk art of Guangdong in Qing Dynasty. The exquisite technique, harmonious design and the folk customs that the subject matter contain have become the unique features of the architectural wood carving of Guangdong in Qing Dynasty. Although the Ancestral Temple of Chen Family has existed for more than one hundred years, it is still the spiritual token of Cantonese culture.

## Acknowledgment

This work was financially supported by Science and Technology Planning Project of Guangdong Province(2011B031400010).

## Note

[1] Guangzhou Folk Arts Museum and South China University of Technology. Record of Guangzhou Ancestral Temple of Chen Family[M]. Beijing: China Building Technology Press, 2011: P328.

[2] Tang Xiaoxiang. Modern Architectural Culture and Aesthetics in the South of Five Ridges[M]. Beijing: China Building Industry Press, 2010: P53

[3] Tang Xiaoxiang. Modern Architectural Culture and Aesthetics in the South of Five Ridges[M]. Beijing: China Building Industry Press, 2010: P63

[4] Lv Pintian. Modeling Concepts of Folk Fine Arts[M]. Nanjing: Jiangsu Fine Arts Press, 1992: P232

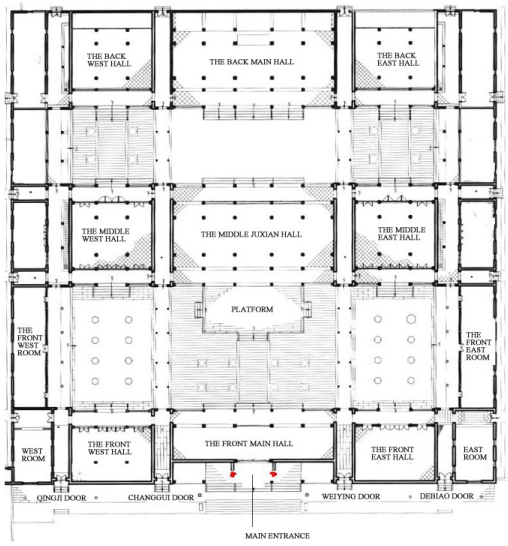



Fig. 1. The architectural plan of the Ancestral Temple of Chen Family



Fig. 2. The production tools of the Cantonese-style wood carving



Fig. 3. Burins of the Cantonese-style wood carving



Fig. 4. The picture of “Feast in Bronze Sparrow Terrace Held by Cao Cao”



Fig. 5. The picture of “Jiantu Conference”

**References**

[1] Luo Yulin. Architectural Pearl in South of Five Ridges—Guangzhou Ancestral Temple of Chen Family[M]. Guangzhou: Lingnan Fine Arts Publishing Company, 1996.6

[2] Lu Yuzhang. Wood Engraving Technology and Traditional Engraving Atlas[M]. Beijing, China Building Industry Press, 2001.

[3] Chen Zehong. Culture of Canton[M]. Guangzhou: Guangdong People’s Publishing House, 2012

[4] Zhou Mo. On Materials of Ming and Qing Dynasties Furniture (IV): Tali [J]: 1994-2012.

*Advanced Materials Research Vol. 937 (2014) pp 462-464*
*© (2014) Trans Tech Publications, Switzerland*
*doi:10.4028/www.scientific.net/AMR.937.462*

# Lost Wax Casting Process Design of Artificial Jade Cup Basing on Blast Furnace Slag

Wei YOU[1*], Yan-mei JIANG[2], Qian LIN[1], Xiao-xia YU[1], Peng-fei LI[1], Yu-ge WANG[1]

[1]School of Mechanical and Electrical Engineering, North China Institute of Science and Technology, Yanjiao Development Zone, Sanhe County, Hebei Province, 065201

[2]Nanhai West Oil United Offshore Construction Co. Ltd, Zhanjiang City, Guangdong Province, 524057

* Corresponding author. Mobile phone: 13785602060

Email: youwei00@mails.tsinghua.edu.cn

**Keywords**: Blast furnace slag, Artificial jade, Lost wax casting

**Abstract:** The blast furnace slag is an industrial solid waste in the production process, this paper deals with the blast furnace slag as products -- artificial jade cup handicraft lost wax casting process of high additional value of main raw material, firstly analyses the production process of chemical composition and artificial jade common blast furnace slag and natural jade, then the detailed design of the lost wax casting process of artificial jade cup, including manufacturing, shell mould manufacturing, dewaxing, baking, imitation jade material melting and casting. The lost wax casting method for producing artificial jade crafts complex products, the added value of products, so as to achieve a high added value utilization of blast furnace slag.

## Introduction

Blast furnace slag is an industrial solid wastes produced in the process of ironmaking production, is one of the, industrial solid wastes in our country most according to statistics, every 1 tons of iron smelting to produce 0.3 ~ 1 tons of blast furnace slag. Enterprises generally use the open-air treatment of blast furnace slag, on the one hand, taking up a lot of land, on the other hand, harmful substances in blast furnace slag will pollute the groundwater and the surrounding air, resulting in serious damage to the ecological environment.

Over the years, people use a variety of technologies to make a comprehensive utilization of blast furnace slag, such as the production of cement and concrete, or the production of slag wool, glass ceramics, agricultural fertilizer, but these technologies are in a certain extent, defects, such as the production of cement and concrete, the mechanical performance index of the product is not stable, but these applications are the low value added utilization, benefits co.. Based on the above reasons, currently on the market in urgent need of new technology and new process, the comprehensive utilization of blast furnace slag.

From April 2009, the State Administration of production safety supervision and management institutions directly under North China Institute of Science and Technology -- from what Dr invented the deep processing of solid waste artificial jade Technology Based on [1-4], the artificial jade appearance and intrinsic properties and natural jade.

Nearly, can be used for the production of handicraft and high-grade building materials and other products, to achieve the waste and low value of minerals with high added value, produce significant economic benefits and social benefits, and do not have two times of waste, and has wide application prospect and popularization value, has broad application prospects in industry, metal mine and non metal mine, metallurgy, power plant, etc..

In this paper a kind of artificial jade crafts of blast furnace slag based on the lost wax casting process design_cup are introduced.

## Process Analysis

There is a certain degree of similarity, between the chemical composition of blast furnace slag and some natural jade so, through the optimization of composition and process properly, it is possible to blast furnace slag as the main raw materials to produce products with high added value -- artificial jade.

Blast furnace slag is a kind of important industrial solid waste generated in the metallurgical industry, blast furnace slag based on artificial jade crafts lost wax casting process -- cup was introduced in this paper, the production process compared with the artificial jade common chemical composition including blast furnace slag and natural jade, and the detailed design of the lost wax casting process Mo cup, including manufacturing, shell mould manufacturing, dewaxing, baking, imitation jade material melting and casting. The lost wax casting method for producing artificial jade crafts complex products, the added value of products, so as to achieve a high added value for the use of blast furnace slag, so this technology has a wide application prospect and popularization value. The artificial jade products can use conventional casting, lost wax casting, molding method of production, wherein, the lost wax casting for the production of complex shaped products, such as arts and crafts. So, by using blast furnace slag to produce artificial jade crafts, using the lost wax casting process.

**Lost Wax Casting Process design of the Artificial Jade Cup**

Lost wax casting is also known as the investment casting, it is the use of low melting point materials and methods to the production of products, casting products, in this way, casting no parting surface, so the product precision is high, so this method is also called precision casting. Lost wax casting in handicrafts, jewelry industry applications.

Lost wax casting process includes the wax pattern manufacture, manufacturing shell, dewaxing, baking, melting and pouring process, the following are introduced:

Manufacturing wax

Using the lost wax casting method of producing products, need to be designed according to the shape of the product manufacturing model, at present, there are a variety of manufacturing model using materials, including wax pattern material, epoxy resin mold material, mold material containing inorganic salts. If the model is made of wax pattern material, this model is called wax.

The main components of stearic acid wax pattern material comprises 50% paraffin and 50%, its melting point is low, generally in the 50-60 °C. The use of the properties of this material is good, and can be recycled, so now in the lost wax casting industry is in general use.

Resin based pattern material with high melting point, generally in the 70 ~ 120 °C, making use of the strength of the model is relatively high, so the die material is suitable for the production of complex shapes such as thin-walled products.

Considering the convenience of production and procurement costs, we use the wax pattern material product model, namely the wax.

Assembling wax

In order to improve productivity, people often make a plurality of wax, and then assemble them together, forming a "investment group" or "wax tree".

Shell (i.e., mold manufacturing)

The same and other casting, lost wax casting also require the use of mold for casting production. Lost wax casting method and mould is made according to the wax.

Manufacture of shell (i.e. cast) included in the wax coating paint group, sand and hardening process:

First of all, with the configuration of a paint binder and refractory material, commonly used binder with water glass, silica sol or ethyl silicate, refractory material including a finer grained quartz, zircon corundum or powder etc..

Coatings with good, will wax immersed into the paint, the wax coated with a layer of coating layer, and then sprinkle sand on top, namely the refractory material of coarse granularity, such as quartz, alumina, zirconium powder, the sand will be in the coating adhesion to coating binder. SA over sand, the wax out for a period of time, drying, hardening; and the wax immersed into the paint, coating, with second layers and second layers of sand, then take out to dry, harden….. Repeat this several times, the wax surface covered with a layer of certain thickness of refractory materials.

Dewaxing

Shell wax surface with a certain thickness and dried, hardened and has a certain strength, put it into the water, is wax type shell coated will melt and flow out, is used for casting mould for the rest of the.

Mold shell roasting

In order to improve the mould strength, but also the high temperature roasting shell in heat treatment furnace, generally need to be heated to 800-1000 deg.C. In order to prevent the shell is destroyed in the process of heating, the gradient heating process, parameters are as follows: first, from room temperature to 300-400 degrees, for 2 hours, then heated to 900 °C, 2 hours holding, and then cooling in the furnace, so, shell and different parts of heated evenly, the stress produced by small, not easy to deformation, cracking and other defects.

Artificial jade raw material melting and casting

The artificial jade raw materials into a melting furnace for melting, melting temperature is 1100 °C, heat 3-10 hours, and then poured into the mould cavity forming.

There are a variety of casting method, common is heat type gravity casting and vacuum suction casting. Thermal gravity casting the shell heated to a certain temperature (generally in more than 400 °C), and then to the cavity pouring liquid, the liquid under the action of gravity mould filling. The advantage of this method is: because the mold is heated to a higher temperature, speed of cooling liquid in the cavity is slow, so it has low viscosity, liquidity is good, easy to fill the cavity, high precision of final product, not easy to produce the water shortages.

Vacuum suction casting the shell into the vacuum casting box, the pouring box pumping air, the vacuum state, the existence of such type microporous shells in the cavity of the air will be sucked in, liquid material by filling in the process of resistance is reduced, so it can be more easily filling cavity, high precision products, but not easy to produce pores, defects such as misrun.

## Conclusion

Blast furnace slag is a kind of important industrial solid waste generated in the metallurgical industry, blast furnace slag based on artificial jade crafts lost wax casting process -- Mo cup was introduced in this paper, the production process compared with the artificial jade common chemical composition including blast furnace slag and natural jade, and the detailed design of the lost wax casting process Mo cup, including manufacturing, shell mould manufacturing, dewaxing, baking, imitation jade material melting and casting. The lost wax casting method for producing artificial jade crafts complex products, the added value of products, so as to achieve a high added value for the use of blast furnace slag, so this technology has a wide application prospect and popularization value.

## Reference

[1] You Wei, Zhang Xiping, Jiang Yanmei, in Wenzai. Methods using low value mineral preparation of high value added products -- artificial jade. Mining and metallurgy. 2013, 1:60-63

[2] You Wei, Jiang Yanmei, Liu Yafang etc.. Artificial jade -- Based on high value added products plant solid waste. New material industry. 2012, 1: 65-68

[3] Artificial jade steel slag and its manufacturing method based on. Chinese patent. Patent number: ZL201010212620.3

[4] Manufacturing method of Artificial jade. Chinese patent. Patent number: ZL 201010197098.6

[5] Zhang Zhaohui, Mo Tao. The development of comprehensive utilization technology of blast furnace slag. China Resources Comprehensive utilization. 2006,24 (5): 12-15]

[6] Li Xinghua, Wang Xuesong, Liu Zhilu, Zhang Jiangping. The new direction of comprehensive high titanium blast furnace slag. Steel vanadium titanium. 2009, 30 (3): 10-16

*Advanced Materials Research Vol. 937 (2014) pp 465-471*
*© (2014) Trans Tech Publications, Switzerland*
*doi:10.4028/www.scientific.net/AMR.937.465*

# Analysis of Sound Absorption Properties of Three-leaf Microperforated Panel Absorbers without a Rigid Backing

Xiao-Ling GAI[1,2,a,*], Xian-Hui LI[1,2,b], Rui WU[1,c], Bin ZHANG[1,d], Jun-Juan ZHAO[1,2,e]

[1] Beijing Municipal Institute of Labor Protection, Beijing 100054, China

[2] Beijing Key Laboratory of Environment Noise and Vibration, Beijing 100054, China

[a]gxldynmg@163.com, [b]lixianh@dlut.edu.cn, [c]wurui2009@hotmail.com, [d] zhangbin815@hotmail.com,[e] junjuanzhao@sina.com

**Keywords:**Three-leaf microperforated panel absorbers; The microperforated panel theory; Electro-acoustical equivalent circuit principle; Sound absorption coefficient

**Abstract.** Microperforated panel (MPP) absorbers have been developed rapidly and used in many fields in recent years. First, based on the Maa's theory, the theoretical development of MPP is reviewed in this paper. Furthermore, structure design and processing technology of MPP are introduced. Finally, the further development of MPP is discussed. Based on the MPP theory and electro-acoustical equivalent circuit principle, sound absorption properties of three-leaf microperforated panel (TMPP) absorbers without a rigid backing are studied to broaden the sound absorption bandwidth of MPP structure. Simulation results show that TMPP absorbers without a rigid backing have two resonance peaks and the energy dissipated coefficient remains constant in the low frequency range. The resonance frequency moves toward low frequency region with the increasing of the distance, thickness and pore diameter of MPP and moves toward high frequency region with the increasing of the perforation when other parameters keep invariant. The energy dissipated coefficient more than 0.5 over 8 octaves by choosing proper parameters. In conclusion, TMPP absorbers without a rigid backing have good sound absorption properties in a wide frequency range.

## Introduction

With the development of economic construction, urban noise is more and more serious; the noise becomes an issue of popular concern. Reduce noise and create a beautiful acoustic environment is an important element to improve the quality of life of the people. A microperforated panel (MPP) absorber has become widely known as the most attractive alternative for the next generation sound absorbing material [1]. The MPP is first proposed by Maa, who has established its theoretical basis and design principle [2-4]. The MPP absorber is a thin panel or membrane less than 1mm thick with perforation of less than 1% perforation ratio with air-back cavity and a rigid backing [5]. The fundamental absorbing mechanism of the MPP absorber, which is typically backed by an air cavity and a rigid wall, is Helmholtz-resonance absorption [6]. This type of absorption is mainly due to frictional loss in the air flow of the apertures [6]. With the rapid development of processing technologies and computational methods, micro-perforated panel sound absorption theory has also been further development [7-9]. But usually the single-leaf MPP sound absorbing structure is generally only one resonance absorption peak. Although, the absorption coefficient of absorption peak is able to control above 0.9, but the sound absorption bandwidth is usually limited to about two octaves [2-4]. In order to broaden the absorption frequency range, Maa has proposed a double-leaf MPP backed by a rigid-back wall with an air-cavity [10, 11]. Recently, Asdrubali and Pispola have studied this type of absorber for its application to noise barriers [12]. This absorber is intended to produce two resonators so that a broader absorption frequency range can be obtained. The acoustical properties of a structure composed of two parallel MPP with an air-cavity between them and no rigid backing is studied numerically by Sakagami [13].

Although lots of researches have been done on broaden the absorption frequency range of MPP, it appears that no relevant reports have been given for three-leaf microperforated panel(TMPP)absorbers without a rigid backing. Based on the MPP theory and electro-acoustical equivalent circuit principle, the main purpose of this paper will focus on the acoustic performance studies of TMPP absorbers without a rigid backing. Structure of this paper will be arranged as follows: In Section 2, electro-acoustical equivalent circuit model of TMPP absorber without a rigid backing will be introduced. In Section 3, the sound absorption performance of TMPP absorber without a rigid backing will be studied. In Section 4, effect of structural parameters of TMPP absorber without a rigid backing on sound absorption performance will be analyzed. In Section 5, structure parameter design of TMPP absorber without a rigid backing will be introduced. Finally, the conclusions will be given in section 6.

## Electro-acoustical Equivalent Circuit Model of Three-leaf Microperforated Panel Absorber without a Rigid Backing

Figure 1 shows a schematic diagram of TMPP absorber without a rigid backing. MPP1, MPP2 and MPP3 are placed in parallel with the air-cavity of depth D1 and D2 every two of them. Three leaves have a sub millimeter perforation, which is characterized by the following parameters: hole diameter (d1, d2, d3), perforation ratio (p1, p2, p3), and panel thickness (t1, t2, t3). A plane sound wave of unit pressure amplitude is assumed to be normally incident upon MPP1. The TMPP absorbers without a rigid backing can be described by the equivalent electrical circuit shown in Figure 2.

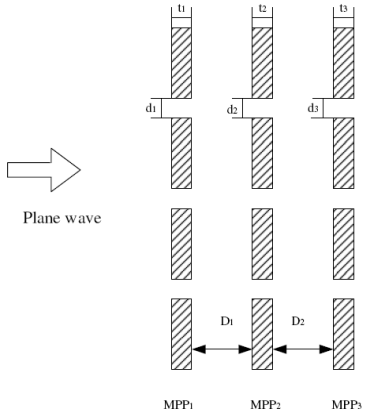



Fig. 1. Schematic diagram of three-leaf absorber without MPP absorber without a rigid backing

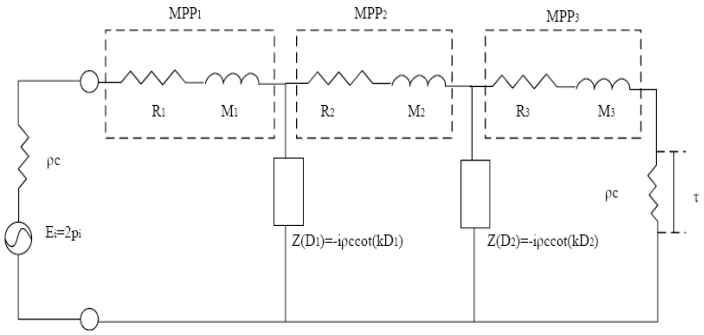



Fig.2. Electro-acoustical equivalent circuit model of three-leaf MPP absorber without a rigid backing.

According to the equivalent circuit, the series impedance of MPP2and MPP3 is given by

$$Z_1 = R_2 + i\omega M_2 + [\frac{1}{Z_{D_2}} + \frac{1}{R_3 + i\omega M_3 + \rho c}]^{-1}, \tag{1}$$

The total impedance of the TMPP absorber without a rigid backing is given by

$$Z_{tot} = R_1 + i\omega M_1 + [\frac{1}{Z_{D_1}} + \frac{1}{Z_1}]^{-1}, \tag{2}$$

where,

$$R_i = \frac{32\eta}{p_i}\frac{t_i}{d_i^2}(\sqrt{1+\frac{x_i^2}{32}} + \frac{\sqrt{2}}{8}x_i\frac{d_i}{t_i}), \tag{3}$$

$$M_i = \frac{t_i \rho}{p_i}\left(1 + \frac{1}{\sqrt{9 + \frac{x_i^2}{2}}} + 0.85\frac{d_i}{t_i}\right), \tag{4}$$

$$x_i = \frac{d_i}{2}\sqrt{\frac{\rho\omega}{\eta}}. \tag{5}$$

In these equations, derived from Maa's pioneering work [1], i=1, 2, 3, $\eta$ is the coefficient of viscosity of the air (=17.9 $\mu$ Pas), $\rho$ is air density, c the sound speed in air and $\omega$ the angular frequency of the sound. The subscripts 1, 2 and 3 denote association with leaf 1, leaf 2 and leaf 3, respectively. Z (D) is the impedance of the air cavity (=i cot (kD), with $k = \frac{\omega}{c}$, the wavenumber and D the cavity depth [m]). Note that all impedances are normalized by $\rho c$ .

The sound absorption coefficient at the front surface, $\alpha$, is given by the well-known formula:

$$\alpha = \frac{4\,\mathrm{Re}[Z_{tot}]}{(1+\mathrm{Re}[Z_{tot}])^2 + \mathrm{Im}[Z_{tot}]^2}. \tag{6}$$

The sound transmission coefficient, $\tau$ , is given by the power consumed at the resistor $\rho c$ behind *MPP*3, which is

$$\tau = \left| \frac{2\left(\frac{1}{Z_{D_1}} + \frac{1}{Z_1}\right)^{-1}}{Z_{tot} + \rho c} \frac{\left(\frac{1}{Z_{D_2}} + \frac{1}{R_3 + i\omega M_3 + \rho c}\right)^{-1}}{Z_1} \frac{\rho c}{R_3 + i\omega M_3 + \rho c} \right|^2. \tag{7}$$

As the sound can be transmitted through the structure, the sound absorption performance should be evaluated by the energy dissipated in the structure, which is expressed by the difference of the above two coefficients, $\alpha - \tau$. This will be used hereafter to discuss the sound absorption performance.

**Sound Absorption Performance of Three-leaf Microperforated Panel Absorber without a Rigid Backing**

For simplicity, we assume that three micro-perforated plate have identical structural parameters, i.e. the thickness of the perforated plate t1=t2=t3=0.4mm, perforation diameter d1=d2=d3=0.4mm, perforation rate p1=p2=p3=1%, the distance between the perforated plate D1=D2=50mm. Figure 3 shows that the sound absorption performance of four kinds of micro-perforated plate absorbers. We find that the sound absorption peak of TMPP absorbers is lower than the sound absorption peak of double-leaf and single-leaf MPP absorbers. The energy dissipated coefficient of TMPP absorbers over 0.5 when frequency less than 1000Hz. And the sound absorption bandwidth that energy dissipated coefficient over 0.5 can reach 6 octaves, which is much higher than the 2-3 octave of double-leaf and single-leaf MPP absorbers. Comparing double-leaf MPP absorbers without backing cavity with TMPP absorbers without backing cavity, we find that TMPP absorbers without backing cavity have two sound absorption peaks at 660Hz and 980Hz. The sound absorption peak and the sound absorption bandwidth of TMPP absorbers without backing cavity are higher and wider than double-leaf MPP absorbers without backing cavity.

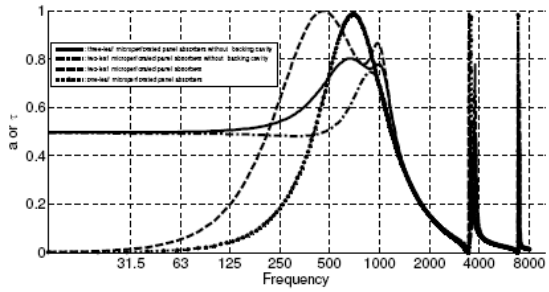



Fig. 3. Sound absorption performance of four kinds of MPP absorbers

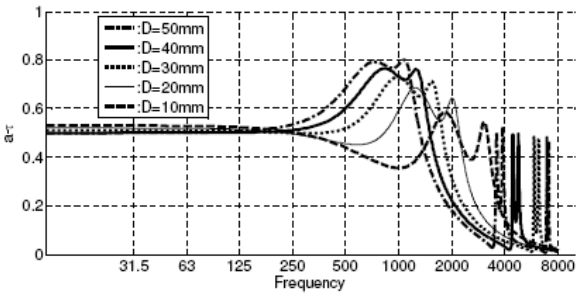
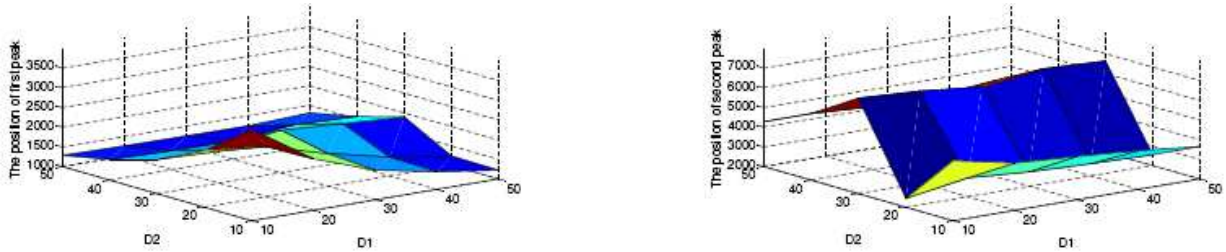



Fig. 4. Effect of cavity depth on the sound absorption performance

**Effect of Structural Parameters of Three-leaf Microperforated Panel Absorber without a Rigid Backing on Sound Absorption Performance**

In this section, we study the effect of structural parameters of TMPP absorber on sound absorption performance. Through figure 4, we find that two sound absorption peaks move to low frequency with D increasing when D1=D2=D. The coefficients of energy dissipated $\alpha-\tau$ are constants and decreases with D increasing when lower than a frequency range of 250 Hz. The range of energy dissipated coefficient $\alpha-\tau=0.5$ is already close to 500Hz when D1=D2=30mm. Figure 5 shows that the relationship between two sound absorption peaks and the distances of three panels when D1 and D2 change from 10mm to 50mm. Figure 5(a) shows that the first sound absorption peak moves to low frequency with D2 increasing when D1=10mm and D1=20mm. From Figure 5(b), we can find that the second sound absorption peak firstly moves to low frequency, again high frequency, and then to the low frequency with D1 increasing when D2 keeps invariant.




(a) (b)

Fig. 5. Effect of cavity depth on two sound absorption peaks

Figure 6 gives the relations of the energy dissipated coefficients variation with frequency when the thickness of the perforated plate change from t=0.2mm to t=1mm with D1=D2=50mm,

d1=d2=d3=0.4mm, p1=p2=p3=1%. We find that two sound absorption peaks move to low frequency with t increasing. And the second sound absorption peak gradually decreases with t increasing. Figure 7 shows the sound absorption coefficient of TMPP absorber without backing cavity reduced gradually with perforation diameter d increasing in the range of 125Hz to 2000Hz. When the frequency is less than 125Hz, the energy dissipation coefficients also have a small variation. Two sound absorption are already connected to each other when d1=d2=d3=0.2mm. And the sound absorption band is the widest at this time. Figure 8 shows two sound absorption peaks move to high frequency with perforation rate p increasing when other parameters unchanged.

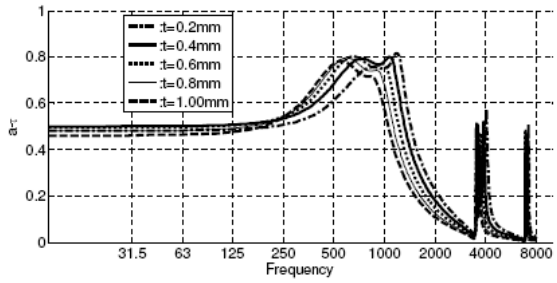



Fig. 6. Effect of the thickness of the perforated plate on the sound absorption performance

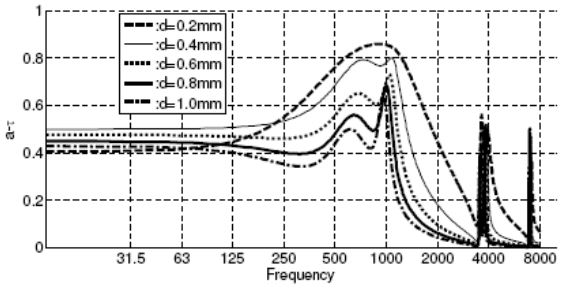



Fig. 7. Effect of the perforation diameter on the sound absorption performance

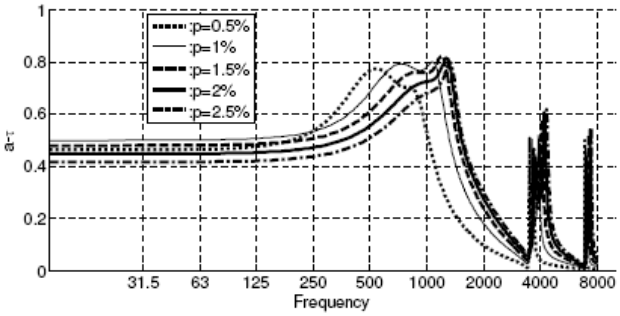
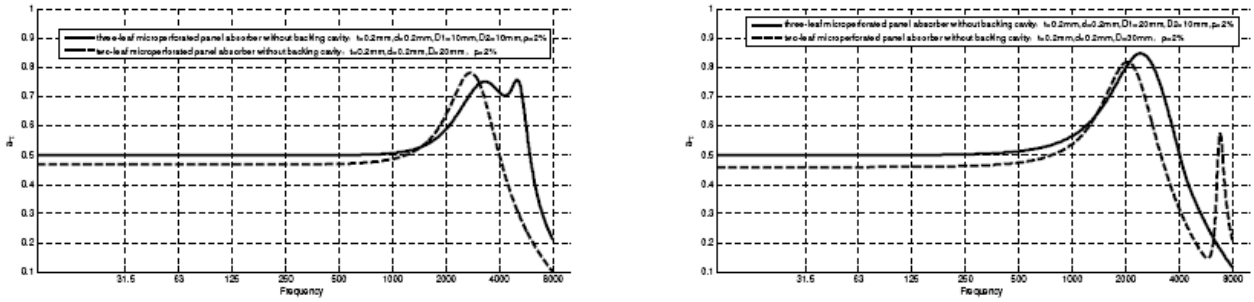



Fig. 8. Effect of the perforation rate on the sound absorption performance

**Structure Parameter Design of Three-leaf Microperforated Panel Absorber**

Comprehensive analysis of figures 4-8, the results show that the thickness of the perforated plate, perforation diameter, perforation rate and the distance of the perforated plate have some influence on the sound absorption performance of TMPP absorbers without backing cavity. However, the energy dissipation coefficients of TMPP absorbers without backing cavity always are constants in the low frequency. Therefore, in order to broaden the bandwidth of TMPP absorbers without backing cavity, the resonance frequency of the perforated plate can be set high. By analyzing the impact of various parameters on the performance of TMPP absorbers without backing cavity, We find appropriate to reduce the thickness of the perforated plate, perforation diameter, narrowing the distance between the two plates, increasing the perforation rate, the resonance frequency of the TMPP absorbers without backing cavity can move to the high-frequency direction. For simplicity, we assume that TMPP have identical structural parameters, t1=t2=t3=0.2mm, d1=d2=d3=0.2mm, p1=p2=p3=2%, and only adjust the plate spacing to broaden absorption bandwidth of TMPP absorbers without backing cavity. Figure 9(a) shows that sound absorption performance curve of the TMPP absorbers without backing cavity when D1=D2=10mm. We find that the sound absorption bandwidth of energy dissipation coefficient close to 0.5 may be more than 8 octaves by selecting the appropriate structure parameters. The energy dissipation coefficient remains constant close to 0.5 unchanged when the frequency is less than 1000Hz. there are two sound absorption peaks at 3350Hz and 5080Hz. Energy dissipation coefficient reaches its maximum 0.76 at 5080Hz. Meanwhile, figure 9(a) also shows that the sound absorption performance curve of the double-leaf MPP absorber when D=20mm. Comparing with the double-leaf MPP absorber without backing cavity, TMPP absorbers without backing cavity not only improve the sound absorption performance below 1000Hz frequency, but also to broaden the bandwidth of the high frequency of the sound absorption when both share the same volume of space. Figure 9(b) shows that sound absorption performance curve of the TMPP absorbers without backing cavity with D1=20mm and D2=10mm. Now, two sound absorption peaks always have connected to each other to

form a resonant peak. Energy dissipation coefficient reaches its maximum 0.85. Figure 9(b) also shows that the sound absorption bandwidth of TMPP absorbers without backing cavity is greater than double-leaf MPP absorber.




(a) (b)

Fig. 9. Sound absorption performance curve of the TMPP (double-leaf MPP)absorbers without backing cavity

## Conclusions

In conclusion, present work has been focused on the sound absorption performance of TMPP absorber without backing cavity based on the MPP theory and electro-acoustical equivalent circuit principle. From figure 3, we have observed that the sound absorption peaks of TMPP absorber without backing cavity is lower than single-leaf and double-leaf MPP structures. But, the sound absorption bandwidth that energy dissipated coefficient over 0.5 can reach 6 octaves, which is much higher than the 2-3 octave of single-leaf and double-leaf MPP structures. Comparing with the double-leaf MPP absorber without backing cavity, TMPP absorber without backing cavity has two sound absorptions peaks to broaden the bandwidth of the high frequency[as seen in figures 3 and 9(a)]. Figures 4-8 have presented that two sound absorption peaks move toward low frequency region with the increasing of the distance，thickness and pore diameter of MPP and moves toward high frequency region with the increasing of the perforation when other parameters keep invariant. Figure 9 shows that the sound absorption bandwidth of energy dissipation coefficient of TMPP absorber without backing cavity close to 0.5 may be more than 8 octave by selecting the appropriate structure parameters.

## Acknowledgements

This work was financially supported by the National Natural Science Foundation (11274048, 11102093), Postdoctoral Fund (2012M520192) and Beijing Natural Science Foundation(8142016).

## References

[1]K. Sakagami, M. Morimoto and M. Yairi, A note on the effect of vibration of a microperforated panel on its sound absorption characteristics, Acoust. Sci.Tech. 26(2), (2005) 204-207

[2]D.Y. Maa, Theory and design of microperforated panel sound-absorbing constructions, Sci. Sin. 18 (1975) 55-71

[3]D.Y. Maa, Microperforated-panel wideband absorbers, Noise Cont.Eng. J. 29, (1987) 77-84

[4]D.Y. Maa, Potential of microperforated panel absorber. J.Acoust. Soc. Am. 104, (1998)2861-2864

[5]K. Sakagami, M. Morimoto, M. Yairi, Double-leaf microperforated panel space absorbers: A revised theory and detailed analysis, Apll. Acoust. Vol. 70, (2009) 703-709

[6]M. Toyoda, R. L. Mu, D. Takahashi, Relationship between Helmholtz-resonance absorption and panel-type absorption in finite flexible microperforated-panel absorbers, Appl. Acoust. 71, (2010) 315-320

[7]H. V. Fuchs, X. Zha, H. D. Drotleff, Creating low-noise environments in communication rooms, Appl. Acoust. 62, (2001) 1375-1396.

[8]X. Zha, H. V. Fuchs and H. D. Drotleff, Improving the acoustic working conditions for musicians in small space, Appl. Acoust. 63, (2002) 203-221.

[9]D.Y. Maa, Absorption limit of MPA,ACTA ACUSTICA, 28(6), (2003) 561-562

[10]D.Y. Maa and K. Liu, Sound absorption characteristics of microperforated absorber for random incidenc', ACTA ACUSTICA, 25(4), (2000) 289-296

[11]F. Asdrubali, G. Pispola, Properties of transparent sound-absorbing panels for use in noise barriers. J. Acoust. Soc.Am. 121, (2007)214-21

[12]K. Sakagami, M. Morimoto, W. Koike, A numerical study of double-leaf microperforated panel absorber', Appl. Acoust. 67, (2006) 609-619

*Advanced Materials Research Vol. 937 (2014) pp 472-475*
*© (2014) Trans Tech Publications, Switzerland*
*doi:10.4028/www.scientific.net/AMR.937.472*

# Influence of Alkaline Activator on the Strength of Fly Ash-Cement Gel Sand Material

Hai-Yan HUANG, Ai-min GONG and Kun YUAN

College of Water Conservancy and Hydroelectric Engineering, Yunnan Agricultural University, Kunming 650201, China

expressemail@126.com, yauslsd@163.com, yuankun0616@163.com

**Keywords:** Alkaline activator, Fly ash, Cement gel sand, Strength.

**Abstract.** Influence of different kinds and mixing amount of the alkaline activators on the strength of fly ash-cement gel sand materials is discussed through experiment wit 29 group test specimen. The rupture strength and the compressive strength with the age of 3 and 28 days of test blocks mixed with NaOH or CaO are compared each other. The early activity of fly ash can be activated by mixing the alkaline activator. The early activity of fly ash can be activated by mixing with the alkaline activators. The setting time of fly ash-cement binders becomes better. And the early strength can be improved. The activated effect of fly ash-cement binders by different type of the alkaline activators is affected by the age of test blocks. The activated effect mixed with CaO is better than the effect mixed with NaOH.

## Introduction

Portland cement demand is growing with the rapid development of the civil engineering. The environmental problems coming from Portland cement is more serious. The method of mixing alkaline activators into fly ash-cement gel sand materials can improve the performance of fly ash-cement binders and protect the environment[1-2].

Physical properties of fly ash used in the Portland cement can decrease the water demand, and increase water holding capacity and uniformity, and improve suspension initial structure. The hydrated calcium silicate gels and hydrated calcium aluminates crystals generated from the fly ash becomes a part of the cementations materials[3]. At the same time, the low calcium C-S located at the surface of fly ash enhances the structure of cement gel sand strength[4]. Different concentrations of NaOH are used to stimulate the early strength of fly ash. The stimulation effect of fly ash increases gradually as the increase the concentrations of NaOH[5-6]. But the shortcomings of low early strength are serious constraints on the application of fly ash cement[7-8].

## Preparation of Fly Ash-cement Gel Sand Test Blocks

### The Main Raw Materials

(1) Cement: The cement used in this test is the P•O42.5 Portland cement produced by Yunnan Dong Jun of State-owned cement company. The physical and mechanical properties of cement are shown in table 1.

Table 1. Physical and mechanical properties of cement

| Physical and mechanical properties | | Detection results | Physical and mechanical properties | Detection results |
|---|---|---|---|---|
| specific surface area ($m^2$/Kg) | | 349 | $SO_3$ /% | 2.52 |
| andard consistency water consumption/% | | 26.20 | Cr/% | 0.007 |
| stability(boiling process) | | Qualified | MgO/% | 1.84 |
| setting time (min) | Initial set | 230 | Chloride ion/% | 0.007 |
| | Final set | 280 | alkaline content/% | 0.50 |
| breaking strength /Mpa | 3d | 5.1 | Slag mixing amount of limestone/% | 19.9 |
| compressive strength/Mpa | 3d | 24.9 | | |

(2) Fly ash: The fly ash (Level II) used in this test is produced by Heng Yang Industry Co.,Ltd. The physical properties of fly ash are shown in table 2.

Table 2. Physical properties of fly ash

| Fineness | Ratio of water demand | Ignition loss | Moisture content | Sulfur trioxide |
|---|---|---|---|---|
| 13.1 | 104 | 2.2 | 0.1 | 0.73 |

(3) Fine aggregate: The fine aggregate is the standard sand that is mainly used for gel sand test.

(4) Water: This water is provided by North downtown of Kunming City tap water.

(5) Alkaline: The calcium oxide and NaOH used in the test is produced by Tianjin wind ship chemicals Co.,Ltd. Various alkaline content is mixed with fly ash. The trials are dissolved by water and be cooled down to room temperature, then be added in the cementations material.

1) CaO: The molecular weight is 56.08. The calcium oxide (after burning) content is not less than 98%. The maximum contamination levels (indicator calculated by%): the clarity test is qualified. The weight lost 2. Nitrate is 0.004. The iron is 0.015. The alkaline metals and magnesium is 0.5. The acetic acid insoluble substance is 0.05. The chloride is 0.003. The sulfate is 0.1. The heavy metal (Pb) is 0.005. The ammonia precipitates is 0.2.

2) NaOH: The molecular weight is is 40.00. The content of NaOH is not less than 96%.The content of carbonate is less than 1.5%. The maximum contamination levels (indicator calculated by%): the clarity test is qualified. The sulfate is 0.005%. The phosphate is 0.001. The aluminum is 0.002. The calcium is 0.01. The heavy metal (Pb) is 0.03. The chloride is 0.005. The total ammonia is 0.001. The silicate is 0.01. The potassium is 0.05. The iron is 0.001.

**The Mix Proportion**

The mix proportion of the test blocks of fly ash-cement gel sand mixed with NaOH alkaline activator is shown in table 3.

Table 3. The Mix Proportion of Fly Ash and Cement Gel Sand Mixed with NaOH Alkaline Activator

| Number | NaOH (g) | W/C 0.5 | Number | NaOH (g) | W/C 0.5 | Number | NaOH (g) | W/C 0.5 |
|---|---|---|---|---|---|---|---|---|
| 10% ⅡF | / | Cement 405g Fly ash 45g Sand 1350g Water 225ml | 20% ⅡF | / | Cement 360g Fly ash 90g Sand 1350g Water 225ml | 30% ⅡF | / | Cement 315g Fly ash 135g Sand 1350g Water 225ml |
| 10% ⅡF-3%NaOH | 1.35 | | 20% ⅡF-3%NaOH | 2.70 | | 30% ⅡF-3%NaOH | 4.05 | |
| 10% ⅡF-4%NaOH | 1.80 | | 20% ⅡF-4%NaOH | 3.60 | | 30% ⅡF-4%NaOH | 5.40 | |
| 10% ⅡF-5%NaOH | 2.25 | | 20% ⅡF-5%NaOH | 4.50 | | 30% ⅡF-5%NaOH | 6.75 | |
| 10% ⅡF-6%NaOH | 2.70 | | 20% ⅡF-6%NaOH | 5.40 | | 30% ⅡF-6%NaOH | 8.10 | |
| 10% ⅡF-7%NaOH | 3.15 | | 20% ⅡF-7%NaOH | 6.30 | | 30% ⅡF-7%NaOH | 9.45 | |
| 10% ⅡF-8%NaOH | 3.60 | | 20% ⅡF-8%NaOH | 7.20 | | 30% ⅡF-8%NaOH | 10.80 | |

The mix proportion of the test blocks of fly ash-cement gel sand mixed with CaO alkaline activator is shown in table 4.

Table 4. The Mix Proportion of Fly Ash and Cement Gel Sand Mixed with CaO Alkaline Activator

| Number | W/C | Cement(g) | Fly ash(g) | Standard sand(g) | Water(ml) | CaO/g |
|---|---|---|---|---|---|---|
| 20% ⅡF | 0.5 | 360 | 90 | 1350 | 225 | / |
| 20% ⅡF-6%CaO | 0.5 | 360 | 90 | 1350 | 225 | 5.4 |
| 20% ⅡF-7%CaO | 0.5 | 360 | 90 | 1350 | 225 | 6.3 |
| 20% ⅡF-8%CaO | 0.5 | 360 | 90 | 1350 | 225 | 7.2 |
| 20% ⅡF-9%CaO | 0.5 | 360 | 90 | 1350 | 225 | 8.1 |
| 20% ⅡF-10%CaO | 0.5 | 360 | 90 | 1350 | 225 | 9.0 |
| 20% ⅡF-11%CaO | 0.5 | 360 | 90 | 1350 | 225 | 9.9 |
| 20% ⅡF-12%CaO | 0.5 | 360 | 90 | 1350 | 225 | 10.8 |

The mix proportion of the gel sand is shown in table 5.

Table 5. The Mix Proportion of Gel Sand

| Cementing material/g | Standard sand/g | Mixing water/g |
|---|---|---|
| 450±2 | 1350±5 | 225±1 |

## Test Methods

The test process is gone with the ISO method (GBT17671-1999). The alkaline activated agent is dissolved by water and cooled down to the room temperature before the preparation of the gel sand. The test blocks were made with the gel sand in the room temperature conditions. Then the test blocks were put into the standard curing chamber for concrete after they released from the maintenance box about 24±3 hour later. The conservation temperature was controlled at the level 20±2°C. And the relative humidity is not less than 90%. The tests were gone after the curing age of all the test blocks was achieved.

The method of test data processing is as follows:

(1) Rupture strength: The test result is the average value of the test data of a group test blocks that are made up of 3 test specimens. The test data should be removed when it exceeds ±10% out of the average value. Then the test result is the average value of the last two test specimens. The test data of two test specimens should be abolished when they exceeds ±10% out of the average value.

(2) Compressive strength: The test result is the average value of the test data of a group test blocks that are made up of 6 test specimens. The test data should be removed when it exceeds ±10% out of the average value. Then the test result is the average value of the last five test specimens. The test data of five test specimens should be abolished when they exceeds ±10% out of the average value.

## Experimental Results and Analysis

The experimental results of the test blocks are shown in Figure 1-4.

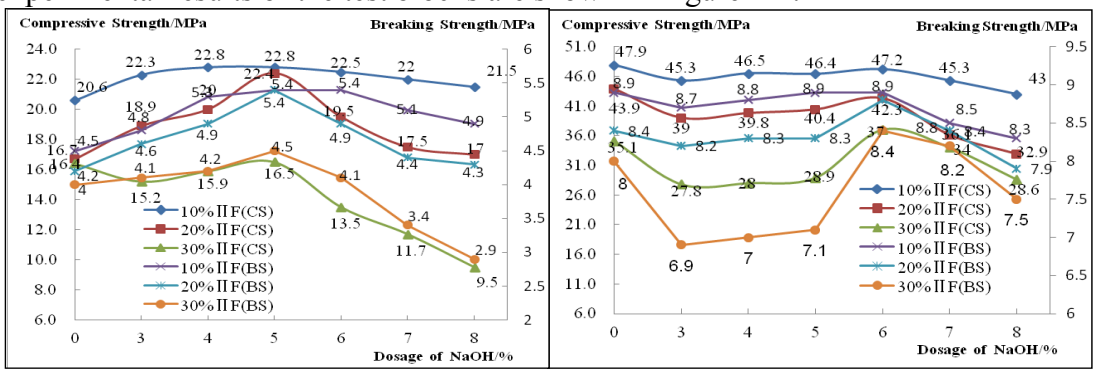



Fig. 1. The experimental results mixed with NaOH of 3 day

Fig. 2. The experimental results mixed with NaOH of 28 days

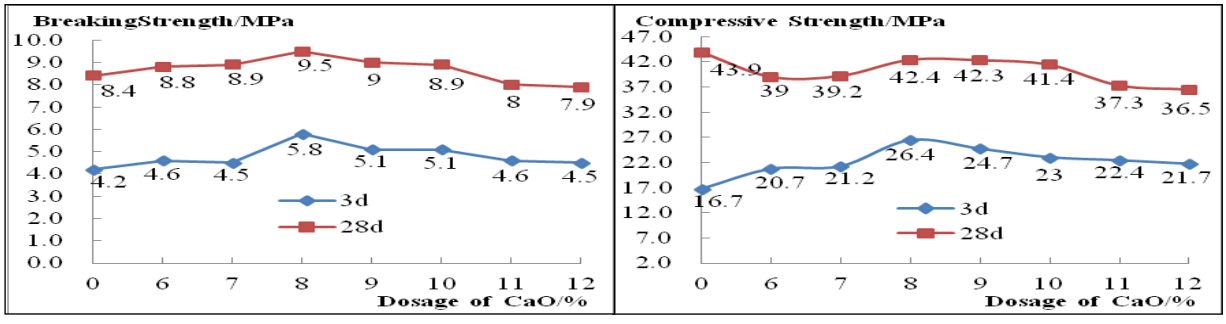



Fig. 3. The experimental results mixed with CaO of 3 days

Fig. 4. The experimental results mixed with CaO of 28 days

The following conclusions can be drawn from the present study.

(1) The strength of fly ash-cement gel sand of 3 days mixed with NaOH alkaline activator is improved. The strength is firstly increased and then decreased with the mixing amount of NaOH. The strength achieves the maximum value when the mixing amount of NaOH is 5%.

(2) The rupture strength of test blocks of 3 days mixed with 5% NaOH is 5.4MPa that is higher about 29% than the strength of the reference group. The compressive strength of test blocks mixed with 5% NaOH is 22.4MPa that is higher about 34% than the strength of the reference group.

(3) The rupture strength and the compressive strength of test blocks of 3 days mixed with 5% NaOH and 20% fly ash is higher about 29% and 34% than the strength of the reference group.

(4) The strength of fly ash-cement gel sand of 28 days mixed with NaOH alkaline activator achieves the maximum value when the mixing amount of NaOH is 6%.

(5) The compressive strength of test blocks of 28 days mixed with 5% NaOH and 10% or 20% fly ash is lower than the strength of the reference group. But the strength mixed with 5% NaOH and 30% fly ash is higher than the strength of the reference group.

(6) The rupture strength and the compressive strength of test blocks of 3 days and 28 days mixed with CaO achieves the maximum value.

(7) The rupture strength and the compressive strength of test blocks of 3 days mixed with 8% CaO is 5.8MPa and 26.4MPa that is higher about 38% and 58% than the strength of the reference group. The rupture strength and the compressive strength of test blocks of 28 days mixed with 8% CaO is 9.5MPa and 42.3MPa that is higher about 13.1% and 13.2% than the strength of the reference group.

(8) The rupture strength and the compressive strength of test blocks of 3 days 20% II F-8% CaO is higher about 7% and 18% than the strength of 20% II F-5% NaOH.

(9) The rupture strength and the compressive strength of test blocks of 28 days 20% II F-8% CaO is higher about 13% and 15% than the strength of 30% II F-6% NaOH.

## Conclusions

(1) The early activity of fly ash can be activated by mixing with the alkaline activators. The setting time of fly ash-cement binders becomes better. And the early strength can be improved.

(2) The activated effect of fly ash-cement binders by different type of the alkaline activators is affected by the age of test blocks. And the effect is related to the type and the mixing amount of the alkaline activators.

(3) The activated effect mixed with CaO is better than the effect mixed with NaOH.

## References

[1] Juan-rong Zheng, Li-na Liu, Ling-xia Xie. Properties of the mortar and concrete of alkali-activated fly- ash cementing materials [J]. Concrete, 2009, (5):71-79.

[2] Fernandez-dimenez, et al. Microstructure development of alkali activated fly ash cement: a descriptive model [J].Cement and Concrete Research, 2005(35):1204-1209.

[3] Jing fu Kang, Xiufen Wang. Effects of GH admixture on the early strength of fly ash concrete and mortar [J]. Journal of Wuhan University of Technology-Mater. Sci. Ed, 2008 (5):755-760.

[4] Xiao-feng Luan, Zhi-hua Pan, Dong-dong Wang. Study on the Chemical Activation of Fly Ash in Fly Ash Blended Portland Cement System [J].Bulletin of the Chinese Ceramic Society, 2010, 29(4):757-761.

[5] Kuhnke M, Fretwurst E, Lindstroem G. Defect generation in crystalline silicon irradiation with high-energy particles[J].Nuclear Instruments and Methods in Physics Research B, 2002, 186: 144-150.

[6] Poirier R, Avalos V, Dannefaer S, et al. Annealing mechanisms of divacancies in silicon [J]. Physica B, 2003, 340-342: 609-621.

[7] Ting-shu He, Guo-qiang Wei. Effect of activators excitated cement specimen with different amount of fly ash on strength [J].Concrete, 2009, (5):62-64.

[8] Shujin Li, Jianfen Li. Experimental Study of Alkali Activated Large-Volume Fly Ash Cementitious Materials [J]. Coal Ash China, 2010, (46):10-12.

*Advanced Materials Research Vol. 937 (2014) pp 476-478*
*© (2014) Trans Tech Publications, Switzerland*
*doi:10.4028/www.scientific.net/AMR.937.476*

# Moulding Process Design of Artificial Purple Jade Ship Basing on Blast Furnace Slag

Wei YOU[1*], Shuai-shuai WANG[2], Yu-ge WANG[1], Qian LIN[1], Xiao-xia YU[1], Peng-fei LI[1]

[1] School of Mechanical and Electrical Engineering, North China Institute of Science and Technology, Yanjiao Development Zone, Sanhe County, Hebei Province, 065201

[2]Quanxing Industry Research (Langfang) Co. Ltd., Langfang, Hebei Province, 065001

*Corresponding author. Mobile phone: 13785602060

Email: youwei00@mails.tsinghua.edu.cn

**Keywords:** Blast furnace slag, Artificial jade, Moulding

**Abstract:** The blast furnace slag is an industrial solid waste in the production process, this paper deals with the blast furnace slag as moulding technology products -- artificial Purple Jade ship crafts high value-added main raw material preparation, analysis of the chemical composition of blast furnace slag and natural jade, moulding process for artificial Purple Jade ship blast furnace slag prepared were designed, including process analysis, press, die structure design, selection of heating system design, molding equipment checking. The molding method is suitable for the production of large quantities of artificial jade crafts, high production efficiency, so as to achieve a high added value utilization of blast furnace slag.

## Introduction

Blast furnace slag is an industrial solid wastes produced in the process of ironmaking production, is one of the, industrial solid wastes in our country most according to statistics, every 1 tons of iron smelting to produce 0.3 ~ 1 tons of blast furnace slag. Enterprises generally use the open-air treatment of blast furnace slag, on the one hand, taking up a lot of land, on the other hand, harmful substances in blast furnace slag will pollute the groundwater and the surrounding air, resulting in serious damage to the ecological environment.

Over the years, people use a variety of technologies to make a comprehensive utilization of blast furnace slag, such as the production of cement and concrete, or the production of slag wool, glass ceramics, agricultural fertilizer, but these technologies are in a certain extent, defects, such as the production of cement and concrete, the mechanical performance index of the product is not stable, but these applications are the low value added utilization, benefits co.. Based on the above reasons, currently on the market in urgent need of new technology and new process, the comprehensive utilization of blast furnace slag.

From the beginning of 2009 April, the State Administration of production safety supervision and management institutions directly under North China Institute of Science and Technology -- from what Dr invented the deep processing of solid waste artificial jade Technology Based on [1-4], the artificial jade appearance and intrinsic properties and natural jade close, can be used in the production process of goods and high-grade building materials and other products, to achieve the waste and low value of minerals high value added utilization, significant economic and social benefits, and do not have two times of waste, and has wide application prospect and popularization value, has a broad application prospect in the industry of coal, metal and nonmetal mines, metallurgy, power plant, etc..

There are a variety of molding process of artificial jade products, such as lost wax casting, molding method, mechanical method, they each have their own characteristics, which are suitable for different characteristics of the products. In this paper, moulding process on an artificial jade crafts of blast furnace slag based on -- purple Jade ship are introduced.

**Comparison of Chemical Composition of 2 Artificial and Natural Jade Jade**

There is a certain degree of similarity, between the chemical composition of blast furnace slag and some natural jade so, through the optimization of composition and process properly, it is possible to blast furnace slag as the main raw materials to produce products with high added value -- artificial jade.

Moulding process design of blast furnace slag artificial jade crafts - Purple Jade ship based. Molding and pressing, the cavity temperature of raw materials into a mould, exert a certain pressure, the method of product molding.

The characteristics of molding mainly include: easy to realize mechanization and automation of production, so the production efficiency is high, suitable for the production of large quantities of products; the products of high precision, surface smoothness high, after processing workload is small; however, this method requires the use of mold and press, so the fixed investment is large; the other is only suitable for small production.

In this paper, moulding process on an artificial jade crafts of blast furnace slag based on -- Purple Jade ship are introduced.

**Process Analysis of Purple Jade Ship**

Purple jade shape of the ship is relatively simple, but the requirement for high surface quality, at parting, no core, core and cavity are no special structure, simple processing, has the good structure technology.

The main factors affecting the molding temperature, pressure and time, and the liquidity and material temperature, pressure, flow of purple jade can through the composition optimization to control, in order to meet the requirements of molding.

The choice of the press

Because the external dimension of the parts of larger, taking into account the size limit of mold, we adopt single cavity structure.

There are many kinds of press, by mode of transmission is mechanical and hydraulic presses, the most common form of mechanical press with a spiral type presses, crank lever type etc.. Because the mechanical press pressure is not accurate, the movement noise is large, easy to wear, especially hand press driven by manpower, the labor intensity greatly, so rarely used mechanical press factory. Hydraulic type is most commonly used, its classification: according to the frame structure is divided into a box type structure and order structure; according to the pressing direction is divided into an upper pressing and pressing, pressing large laminates can be used under pressure press, pressing on small products generally using pressure press. Hydraulic machine is mostly semi or fully automatic operating system, it can automatically control the forming time.

Based on the above comparison, the mould pressing equipment is used on the pressure machine, the final selection models by checking the table for hydraulic machine YB71-250.

According to the fixed form of compression mould is divided into portable compression mold, semi fixed compression mold and fixed compression mold in the press. Compared with the previous two fixed form, fixed compression mold high production efficiency, simple operation, low labor intensity, suitable for large batch size, larger product pressing. The mould adopts fixed compression mold.

Structure 3.3 Purple Jade ship mold

Pressure from the 3.3.1 direction and the choice of parting

(1) press direction selection principle

The convenient feeding

It is beneficial for pressure transmission

The convenient installation and fixation insert

To ensure the intensity punch

(2) the selection principle of parting surface

The parting surface should be conducive to the release, and the maximum size of parts. The parting surface should be conducive to ensure the appearance of plastic parts quality and accuracy requirements. The parting surface should be conducive to the side core pulling, but without this mold side core pulling, this point can not be considered. The surface should be conducive to simplify the mould structure.

## Structure of Convex, Concave Die

With the form of compression molding die has three kinds: the overflow type compression mould, no overflow type compression mould and semipositive compression mould. The biggest drawback with the first two are convex die and a feeding chamber side wall friction will make the feeding room gradually damage caused by product, difficult, and the product surface is easy to scratch. Artificial purple jade to ensure the surface quality is high, so the semipositive compression mould with the structure, the biggest characteristic of this form is a horizontal extrusion, also has not spilled feed type compressed convex mold and the feeding chamber with the ring and the guide ring.

Semi flash punch and the feeding chamber compression mould are matched with the convex die, when subjected to extrusion surface is limited, it is easy to ensure the products high size precision. The punch in the open around the overflow tank, excess of raw materials through the clearance or overflow discharge. Therefore, the compression mould has the advantages of convenient operation, feeding the feeding capacity do not have to be strictly controlled, simply press the volume metering.

Semipositive compression mould has overflow and not to spill the advantages of compression mode, and the height of the radial wall thickness precision products are good, the higher density, die life is long, easy demolding, product appearance is not charging room scratch.

Due to high molding temperature purple jade, flow has the limitation, in order to promote the molding speed, need to preheat mould. Heating common electric heating. The mould adopts 11 heater for heating the mould.

Because the mold is a mold cavity, heat loss is small, coupled with the use of the is semipositive molds, better heat dissipation, so it does not require special cooling system.

## Conclusion

Blast furnace slag is a kind of important industrial solid wastes, metallurgical industry, this paper introduces the mould design, moulding process of blast furnace slag artificial jade crafts based products, including process analysis, press, die structure design, selection of heating system design, molding equipment checking. The molding method is suitable for the production of high precision, large batch production of products, high production efficiency of this method. This study is helpful to realize high added value on the use of blast furnace slag, so this technology has a wide application prospect and popularization value.

## Reference

[1] You Wei, Zhang Xiping, Jiang Yanmei, in Wenzai. Methods using low value mineral preparation of high value added products -- artificial jade. Mining and metallurgy. 2013, 1:60-63

[2] You Wei, Jiang Yanmei, Liu Yafang etc.. Artificial jade -- Based on high value added products plant solid waste. New material industry. 2012, 1: 65-68

[3] Artificial jade steel slag and its manufacturing method based on. Chinese patent. Patent number: ZL201010212620.3

[4] Manufacturing method of artificial jade. Chinese patent. Patent number: ZL 201010197098.6

[5] Zhang Zhaohui, Mo Tao. The development of comprehensive utilization technology of blast furnace slag. China comprehensive utilization of resources. 2006,24 (5): 12-15]

[6] Li Xinghua, Wang Xuesong, Liu Zhilu, Zhang Jiangping. The new direction of comprehensive high titanium blast furnace slag. Steel vanadium titanium. 2009, 30 (3): 10-16

*Advanced Materials Research Vol. 937 (2014) pp 479-483*
*© (2014) Trans Tech Publications, Switzerland*
*doi:10.4028/www.scientific.net/AMR.937.479*

# The Construction of City Complex Intelligent System

Ying LIU [1,a]

[1] Changchun Institute of Architecture ,China

[a]315398178@qq.com

**Keywords:** City complex intelligent safety energy-saving green .

**Abstract.** This article mainly analysis of each subsystem of city complex building intelligent systems and its function. Also described the different function in different city complex in the intelligent building set requirements.

## The Preface

City Comple Translated from abroad is thecity commercial, office, residential, hotel, exhibition, catering, conference, Wen Yu and traffic of city life space of three or more are combined, and in different parts of build an interdependent, mutually beneficial relationship to form a complex, dynamic, amultifunctional, high efficiency the.

At present, many called "city complex" as the "urban complex" or "commercial complex", but called "city complex" more.

"City complex" is basically all the functions of the moderncity, it is also known as the "city within a city".

Large city complex for the economically developed metropolitan and economically developed city. Different city to city economic characteristics can be emphasized in the function selection, but generally speaking, the hotel or the office with the shopping center is a combination of the most basic functions.

The general function of city complex existing buildings, is also high-tech, high intelligence collection. Its advanced facilities fully reflect the progress of science and technology is an important factor for this architectural form. Indoor high-speed traffic to the verticallevator, elevator, escalator walk, open elevator; communication byelephone, telegraph, telex, fax, television, computer components; security system through the television system, monitoring system, emergency call system, paging system settings and partition can be guaranteed.

The design of intelligent city complex described.

## Intelligent Design of the Overall Idea

Intelligent design, city complex project functional areas, each regional self system and interrelated, difficulties in design and construction. The intelligent system should adopt the mature, advanced technology, optimizing the system integration, from the long-term perspective, the proposed implementation plan in the near future, we need to consider the development planning the expansion of the medium-term and long-term. The system software and hardware configuration, as far as possible the use of modular, open architecture, in order to meet the needs of the system flexibility, expansion and system improvement. Realize the organic interconnection subsystem, resource sharing, information sharing, enhance the ability to respond to emergencies; improve the utilization rate of equipment, reduce energy consumption, saving energy; to realize scientific management modernization.

## Intelligent Design Goal

Automatic control of light, electricity, wind, water and other mechanical and electrical equipment, water, air, light, fire, security and other space environment monitor adjustment within the building, to achieve safe, energy saving, green run target buildings.

Supporting public radio and television, telephone and Internet, audio-visual and conference service facilities, eliminate the time and the space barrier building natural physical form, to meet the needs of all kinds of internal construction unit of city complex on information services.

**Intelligent System**

Intelligent system:
1) Intelligent system integration
2) Construction equipment management system
3) Integrated wiring system
4) Computer network system
5) Parking management system, parking guidance system
6) Public broadcasting and background music system
7) Information display system,
8) Intelligent lighting system
9) Closed-circuit television monitoring system, anti-theft alarm system
10) Access control and attendance system
11) Patrol management system
12) Cable television system and satellite TV system
13) Passenger flow statistical system
14) Energy monitoring and management system
15) Room systems engineering
16) Automatic meter reading system
17) Property management system

**Intelligent System Integration**

Complex project should be "decentralized control, centralized management" as the guiding ideology. Integrated into the system under the platform of BMSinclude: closed-circuit television monitoring system, anti-theft alarm system, access control subsystem, patrol system, the subsystem of the parking place, public broadcasting system, energy meter reading system, fire fighting system.

**Construction Equipment Management System**

There are freezing station system monitoring, air conditioning / fresh air unit, water supply and drainage system monitoring, monitoring of power supply and distribution system monitoring, meter copy system, automatic meter reading fee, the elevator and escalator monitoring and control.

**The Public Security System**

Complex projects according to the need, starting from the actual project, to establish a set of digital compression and network transmission technology as the core, the digital video technology is mature, industry standard IP network video monitoring system and meet customer demand.

**Garage / Field Management System**

Each functional area of the parking division reasonable, can realize customers from any import can be real-time charge. Shopping center parking lot also need to set up multiple point charges. Because the vehicle frequently, import and export gate to select high speed gate. Parking instructions / guidance system: complex project constitutes a complex, each functional area is a complex project, in addition to the general size is larger, the parking lot management therefore parking guidance system is extremely suitable for complex projects. The main principle is to set the indicator at the critical intersection, guide the driver to quickly find the vacancy, and combined with the entrance and partition the induction coil to partition the display, also can make parking reverse query by automatic query system.

**Information Infrastructure System**

Iformation network system: proposals into intranet, extranet and weak network construction the construction of network.

Integrated wiring system: information transmission channel integrated wiring system should be built modular, tandardized, voice, data, image equipment and switching device is connected with other information management system, also can make the external communications equipment and network connected. The system should have high flexibility, reliability and comprehensive, easy expansion, easy to adapt to the future development and maintenance and management.

The smart card application system: including access control, attendance, parking system, will be extended to the electronic money consumption scope.

Flow statistical analysis system: the main settings in the commercial part of people concentrated in the import and export, through a number of shops flow statistics, provide convenient reference managers understand the shopping mall operating status and energy saving, lighting and so on, to achieve a variety of effects Management and energy saving.

**Energy Monitoring and Management System**

1) This system mainly is the analysis of the collected information, the efficiency of mechanical and electrical equipment of the comprehensive judgment. Include. the operation of air conditioning system equipment and environment monitoring system monitoring, control, measurement, recording

2) For power supply and distribution system, power distribution equipment, power equipment and lighting equipment monitoring, measuring, recording etc..

3) To running conditions of drainage system equipment monitoring, control, measurement, recording.

4) Monitoring on the elevator and escalator system operation.

**Item Analysis**

The general project has a boundary, commercial, hotel, residential and other buildings, the possibility of future exist multiple property management and accounting unit, it should be in accordance with the different functional area setting intelligent system architecture.

Need to modify the demand of different tenants, tenants have preference, investment and use is the main single full or group, to improve the utilization efficiency of architectural space, and to meet the national and local requirements, set weak room including total control room, the total lines into the room, at the same time, for the convenience of different types of management need to set the control room and the telecommunication room.

**Office Area Function**

1) Communication facilities, including communication access system, telephone exchange system, the information network system, integrated wiring system, mobile communication coverage system, cluster scheduling system

2) Audio-visual facilities, including cable TV system, public radio guidance system, audio and video conferencing systems, information and publishing system.

3) building control facilities, including heat and cold source monitoring system, ventilation and air conditioning system, water supply and drainage monitoring system, power distribution monitoring system, intelligent lighting system, automatic meter reading system

4) Security facilities, including the security management system, intrusion alarm system, video monitoring system, access control system, electronic patrol system, parking management system, the explosion-proof security system, emergency response system.

5) Fire control facilities, including fire alarm system, fire fighting system, fire emergency broadcasting, the fire alarm device, the fire special use telephone etc..

6) Information application, only to choose, including building information modeling, construction of geographic information, network broadcast system, network communication system, network conference system, network training system

7) System integration, only to choose, including building management system, safety management system, IC card system.

8) Room and lightning protection, grounding, energy-saving measures.

**The Function of Commercial Buildings**

1) Communication facilities, including communication access system, telephone exchange system, the information network system, integrated wiring system, mobile communication coverage system, cluster scheduling system

2) Audio-visual facilities, including cable TV system, public broadcasting system, information guidance and publishing system.

3) building control facilities, including heat and cold source monitoring system, ventilation and air conditioning system, water supply and drainage monitoring system, power distribution monitoring system, intelligent lighting system, automatic meter reading system

4) Security facilities, including the security management system, intrusion alarm system, video monitoring system, access control system, electronic patrol system, parking management system, the explosion-proof security system, emergency response system.

5) Fire control facilities, including fire alarm system, fire fighting system, fire emergency broadcasting, the fire alarm device, the fire special use telephone etc..

6) Information application, only to choose, including building information modeling, construction of geographic information, network broadcast system, network communication system, network conference system, network training system

7) System integration, only to choose, including building management system, safety management system, IC card system.

8) Room and lightning protection, grounding, energy-saving measures.

**The Hotel Building Function**

1) Communication facilities, including communication access system, program-controlled switching system, computer network system, integrated wiring system, wireless intercom systems, signal coverage system.

2) Audio-visual facilities, including cable TV and satellite TV receiving system, information guidance and release system, video conference system.

3) The management of facilities, including hotel management system, building automation system, room control system, room door lock system, remote meter reading system.

4) Fire control facilities, including fire alarm system, fire fighting system, fire emergency broadcasting, the fire alarm device, the fire special use telephone etc..

5) Security facilities, including the security management system, perimeter defense system, intrusion alarm system, help and alarm management system, video monitoring system, access control system, electronic patrol system, garage.

6) Room and lightning protection, grounding, energy-saving measures.

**The Functions of Residential Buildings**

1) Information infrastructure, including telecommunications access system, telephone exchange system, the information network system, integrated wiring system, mobile communication coverage system, cable TV system, public broadcasting system, information guidance and release system, wireless communication system.

2) Security facilities, including the security management system, perimeter protection system, video surveillance systems, electronic patrol system, parking management system, intercom system, Home Furnishing security system, emergency response system.

3) Fire control facilities, including fire alarm system, fire fighting system, fire emergency broadcasting, the fire alarm device, the fire special use telephone etc.

4) Building control facilities, including building automation system, intelligent lighting system, intelligent Home Furnishing system, automatic meter reading system.

5) Information application, including property management system, community information service system, the smart card application system, Home Furnishing management system etc..

6) Room and lightning protection, grounding, energy-saving measures.

## The Conclusion

City complex is a new construction system, each function city complex had its run time specific, city complex will function at different times of the organization together, so as to maintain 24 hours of prosperity, improve efficiency in the use of complex.

Connection of the city comprehensive function in vivo in time and space, so that the various parts of the organization in order, and the use of each part can also complement each other.

## References

[1]"The compulsory provisions of engineering construction standards (building)" (2013 Edition)

[2]"Specification" for electrical design of civil buildings JGJ 16-2008

[3]"Technical specifications" cable TV system engineering GB50200-94

[4]"Systems engineering technical specifications" civil closed circuit monitoring TV GB50198-2011

[5]"Specification" for engineering design of generic cabling system GB 50311-2007

[6]"Standard" design of intelligent building GB/T50314-2006

[7]"Specification" safety and prevention engineering GB50348-2004

[8]"Standard" design of electronic information system roomGB50174-2008

[9]"Technical specifications" lightning protection of electronic information system of building GB 50343-2012

[10]"Code for design of fire in high-rise civil buildings" (2005 dition) GB50045-95

# CHAPTER 8:

# Environment Protection and Sustainable Development

*Advanced Materials Research Vol. 937 (2014) pp 487-490*
*© (2014) Trans Tech Publications, Switzerland*
*doi:10.4028/www.scientific.net/AMR.937.487*

# Nitrogen Oxides Reduction by Zeolite Sorbents in Manufacturing Use

Iveta Pandová[1,a]

[1]Department of Manufacturing Technologies, FVT TU Košice with seat in Prešov, Slovakia

[a]iveta.pandova@tuke.sk

**Keywords:** Emission, Nitrogen oxides, Zeolites, Sorption

**Abstract.** Manufacturing activities of people and combustion engines utilisation are accompanying by development of various gases, that are not natural part of atmosphere or their production exceedes limiting attributes specified for them. Burning fossil fill, fuelling by burning engines escape to atmosphere nitrogen oxides, carbon oxide, carbon dioxide, sulphur oxides, organic compounds as aldehydes, ketones, polycyclic aromatic hydrocarbons. At present the attention turnes primarily on so-called greenhouse gases and gases impierment stratospferic ozonous layer, between that are belong also nitrogen oxides, carbon dioxide, methane ,halogenic hydrocarbons. At concentration reduction of greenhouse gases partially sorbents are usable, which includes also zeolites.

## Introduction Mechanism of Creation Nitrogen Oxides

Near abuse ozonous layer measures nitrogen oxides have some task. Nitrogen oxide rankedes among matters impierment tropospheric ozone and impierment ozonous layer. Near fired fill aerial nitrogen assorts with oxigen in creation dinitrogen oxide which oxidise by air oxygen to nitrogen monooxide [1].

$$N_2O + O \rightarrow 2NO \quad (1)$$

From combustion gases of supersonic aircraft are freeing nitrogen oxides to stratosphere, where $N_2O$ reacts whith atomic oxygen in creation nitrogen monooxide, which reacts whith ozone and as shares on impierment of ozonous layer at atmosphere [2].

$$N_2O + O \rightarrow 2NO \quad (2)$$

$$NO + O_3 \rightarrow NO_2 + O_2 \quad (3)$$

$$NO_2 + O \rightarrow NO + O_2 \quad (4)$$

Upwards of 90% nitrogen oxides is from burning engines ejected in form of nitrogen oxide (NO), which in stratosphere oxidized to nitrogen dioxide ($NO_2$) [3]. Nitrogen dioxide influences negatively on hygienic conditions of live organisms, as causes stimulation slimy [4]. Emission of $NO_2$ deterirates ozonous layer and belongs to also namby – pamby gases causative climatic changes. By influence of occurrence excess of $NO_2$ at atmosphere towards to ineligible raising of the tropospheric ozone concentration.

Forby nitrogen oxides between grrenhouse gases appertain also gases as methane, carbon dioxide and halogenic hydrocarbons [5,6].

Table 1. Greenhouse gases

| Greenhouse gases species | Formula | Numby pumby effect average |
|---|---|---|
| Carbon dioxide | $CO_2$ | 61 % |
| Methane | $CH_4$ | 19% |
| Dinitrogen oxide | $N_2O$ | 6% |
| Halogenic hydrocarbons | CFC, HCFC, $CF_4$, HFC | 14% |

The sorbents, includes zeolites, can be usable in gases concentration reduction. And this is application near source.

**Structural and Physical Zeolite Properties**

Zeolites are materials utilizable near protection life environs. Zeolites at this area find place already from 50 years of the twentieth centuries. At last decades a decisions of their exploitation near emission controls, as well as near sewage purification are known. To so exploitation their predetermination their unique facilities. In light of gas and water purification their sorptive and ion - exchange proporties are interest which implicit from their textures. Their threedimensional structure is generation by regular arrangement tetrahedrites $[SiO_4]^{-4}$ and $[AlO_4]^{-5}$. At texture of tetrahedrites $[SiO_4]^{-4}$ is part of silicon atoms recompensed isomorphicly by aluminium atoms. Negative charge of zeolitic grate, which comes into being is compensated by cations, which are set at outside skeletion positions. The most frequently are cations of the alkaline metals and alkaline earth metals. These cations are possible through the medium sorption and ion – exchange methods replace by others cations. Between the latest appearance natural zeolites belongs tsernichite, that is of natural analogue of synthetic Beta zeolite and mutinaite, that is natural analogue of synthetic ZSM-5. At present to approximately 430 zeolite sorts are known , from them 80 sorts are natural.[7]. Synthetic zeolites are been produced generally at natrium form. One from the most known synthetic zeolites is calsit. It is 5A type zeolite with size pore 0,5 nm. At dehydrate state its chemical composition express formula $CaO \cdot Na_2O \cdot Al_2O_3 \cdot SiO_2$ . At zeolite A type every kubicoctahedron is bound with six other kubicotahedrons through tetrameral oxygen little bridge. Unit cell of A zeolite includes a combination of 24 ionics of silicon and aluminium, those proportion answer characteristic modulus hereof zeolite, 0,9 - 1 and 48 ionic oxygen. Eight kubicoctaheders connection over tetrameral oxygen little bridge forms big cavity with 1,14 nm diameter and with 0,28 $cm3g^{-1}$ volume which receive by six pores. Averages of this incoming pores in type A zeolite are determination by annulus of 8 members of oxygen and cations d in their nearness.

Chemical composition of zeolites is possible to describe by general formula [7]:

$$M_{x/z} [ x AlO_2 \cdot y SiO_2 ] .q H_2O \quad (5)$$

The zeolite comprise a typical group of inclusion compounds formed by an aluminium silicate lattice. They enclose water as guest molecule. The water molecules can be removed and a series of various organic and inorganic molekules can be sorbed in the zeolite cavities. This property makes zelites useful in many branched of practical life.

Within crystal texture of zeolite a sluiceways are set of correctly defined dimensions. Size incoming windows move in range 0,3 nm to 1 nm [8]. This size delimitations a molecules, that can input in sluiceways of zeolite textures. This correctly definite size of sluiceways zeolite textures contradistinguish from amorphous microporez material type active coal or alumina. Zeolites can bind a various matters, metallic atoms, ions, polar and non-polar molecules. In zeolites with big cavities, as faujazit (zeolite X a Y), it is possible sorbe the hole clumps of the molecules. By detail study of balanced state near sorption on zeolite treated Barrer. According to his results with temperature increasing the degree of saturation at sorbed ingredients reduced and volume of sorbed moleculs is increased.The first synthetic zeolites were made in near temperature above 100°C [9]. From the most known snthetich maybe remember ZSM-5, levynit, ZK 5, melanoflogit, zeolite L, RHO, ZSM 39, zeolite and, afganit, gmelinit, mazzit, liottit, a zeolite. Zeolites A type are producing mainly in modification with cation potassium, calcific and in basic modification with sodium cations, zeolite X in sodium and calcium modification. Important mineralogical and chemical parameters of the zeolites is proportion Si/Al. This worth mention acidity and zeolite basicity and accordingly on their thermic and chemical stability. Zeolites with the higher worth proportion Si/Al are acid and stable. The zeolites with the higher proportion Si/Al are more hydration. The proportion Si/Al accordingly mention to thermic and chemical stability. Frontier of thermic stability at various type zeolite differs. Besides proportion Si/Al is this affection also

cationic composition [9]. Important qualitative characteristics is apparent density, which express weight of volume units water-free dusting or granulation zeolite. Apparent density of zeolite establishes how proportion weighted of freshly scorch zeolite and without restraint pour volume standardized progress.

Zeolites are matters, that are adsorbing from the mixture of gases some species of gas as hydrocarbons, nitrogen oxides, carbon monooxide, carbon dioxide [10]. There are known some results of measurements which write a sorption kinetic. Important nitrogen oxides reduction from exhaust emission of combustion engines was noticed on the modified natural zeolite – clinoptilolite from the locality Nižný Hrabovec in Slovak republic. On the figure 1 the sorption kinetic course is visible, after modification natural clinoptilolite to ammonium form.

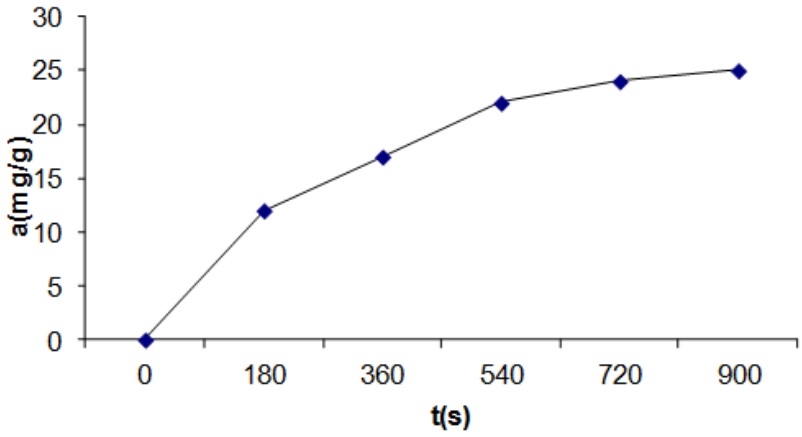



Fig.1. Kinetic of nitrogen monooxide sorption on ammonium form of clinoptilolite

**Summary**

The sorbent properties of the zeolites are usable at noxious gases cleaning of combustion engines. Some patents of exhaust pipe equipment exist for noxious gases cleaning , which are based on the zeolites as sorbents utilization. Japanned firm Toyota developed catalyzer, which in oxygen abudance reduce carbon monooxide concentration, hydrocarbon and also nitrogen oxides on the base of adsorbtion and catalysis. From zeolite the synthetic zeolite ZSM-5, ZSM 11, ZSM 12 and ZSM-20 are used and from natural zeolite ferrierit.is used. In all the cases being used zeolite after modification in copper modifications. This catalyzer in oxygen abudance effectively reduces nitrogen oxides on nitrogen after their adsorbtion, at which has satisfactory reduced size near temperature 200° C till 500° C. Near temperature 600° C cation copper begin removes and aggregate, which cause structure catalyzer erosis and fall catalytic activities. Instead of copper cationic is on achievement catalytic effectiveness convenient use too cobalt. On incorporation cobaltous and copper, cationic in structure zeolite are used aqueous solutions cobaltous a copper salts [11]. Content American patent US 006029441A is method to emission controls. Proposition device consisted from the adsorbent and from two catalyst. Catalyzer combined with adsorbent consisted from monolitic bearer from keramic material, as for example cordierit, mullit or from metal material produced from temperature resistant steel (Fe Cr-Al alloy) and from the plastic carburetion natural and syntethic zeolite. The zeolite with molar ratio Si /Al equal and more that 40 are prefered, that are heat immune and hydrofobic. Examples of such zeolite is ZSM-5, USY, ß zeolite. For the purpose catalytic active of zeolite, in its textures the cations of metals are incorporated.The metal cations as platinum, palladium and rodium are used. Presence of the rare metal in zeolite structure allows its regeneration without cut-down adsorptive accomplishment, at which thermal stability zeolite stays preservation. It is also advisable to use elements as Mg, Ca, Fe, Cr, Ni, Zn . Catalytic more durable are machineries, at which the zeolite layer includes heat resistant oxide and rare metal[12].

Nitrogen oxides creation is hazardous in wiev to influence on ozon layer, namby pumby effect and in wiev to acid rain. Forby this their excess limits at atmosphere causative health problems of population as thoures of heads, conjunctiva and airways ardour. Accordly the problematic of their creation and reduction is the subject on the several science workplaces.The future of the nitrogen oxides reduction has the nanomaterials as also modifice zeolites utilization.

**Acknowledgement**

The authors would like to thank the VEGA grant agency for supporting research work and co-financing the project: VEGA 1/0409/13.

**References**

[1] P. Horbaj, "Ekologické aspekty spaľovania", 1999, ISBN 80-7099-405-3.

[2] L. Nátr, "Země jako skleník: Proč se bát $CO_2$?" (Průhledy) Praha, Academia, (2006). s. 51–52.

[3] O.Monticelli,R.Loenders,P.A.Jacobs,J.A.Martens, "$NO_x$ removal from exhaust gas from lean burn internal combustion engines through adsorption on FAU type zeolites cation exchanged with alkali metals and alkaline earth metals", Applied Catalysis B.In:Environmental 21, (1999), 215-220.

[4] M. Flimel, "Analysis of selected ergonomic problems of left- handed workers in production activity". In: Annals of Faculty of Engineering Hunedoara. Vol. 10, no. 2 (2012), p. 83-86.

[5] B. Hileman, "Ice Core Record Extended", Chemical & Engineering News, 2010.

[6] A. Panda, et.al., „Comprehensive Identification of Sintered Carbide Durability in Machining Process of Bearings Steel 100CrMn6". Advanced Materials Research, Trans Tech Publications, Zurich, vol. 340, p.30-33.

[7] M. Reháková, et al., "Agricultural and agrochemical uses of natural zeolite of the clinoptilolite type", current opinion in solid state & material science 8, 397 (2004).

[8] E. Chmielewska, "Vývoj novej generácie environmentálnych adsorbentov a biokompozitov na báze prírodných nanomateriálov", Chem. Listy 102, 124 -130 (2008).

[9] R.M. Barrer, "Zeolites and Clay Minerals as Sorbents and Molecular Sieves", Academic Press, London, New York, San Francisco, 1978.

[10] A. Panda, J. Duplak, J. Jurko, "Theory and Practice in the Process of T-$v_c$ Dependence Creation for Selected Cutting Material". In: Advanced Materials Research, Trans Tech Publications, Zurich, Switzerland, vol. 716 (2013), ISSN 1022-6680, p. 261-265.

[11] Japanese Patent Office: 05302508 A, 16. 11. Unite 1993.

[12] United States Patent: US006029441A, 29.2.2000.

[13] J. Jurko, A. Panda, „Verification of surface finish as an indicator of machinability in drilling of stainless steel by DIN 1.4301". In: Applied Mechanics and Materials, Trans Tech Publications, Zurich, Switzerland, 2012, vols. 229-231.415 (2012), pp.415-418.

[14] I. Mrkvica, M. Janoš, P. Sysel, „Cutting efficiency by drilling with tools from different materials". Advanced Materials Research, Materials Processing Technology II. 2012, Vols. 538-541, pp. 1327-1331.

[15] I. Pandová, T. Gondová, K. Dubayová, „Natural and modified clinoptilolite testing for reduction of harmful substance in manufacturing exploitation". In: Advanced Materials Research, Trans Tech Publications, vol. 518-523, 2012, p. 1757-1760

[16] T. Zaborowski, Ekowytwarzanie. Gorzow, p.100 (2007)

*Advanced Materials Research Vol. 937 (2014) pp 491-494*
*© (2014) Trans Tech Publications, Switzerland*
*doi:10.4028/www.scientific.net/AMR.937.491*

# Study on the Effect of Streambed Substrate on Invertebrate Diversity

Zhi-wen LUO[1, 2, a], Wen-yan WU[1], Kun LE[1]

[1]Material and Chemical Engineering college, Sichuan University of Sciences & Engineering ,Zigong, PR China

[2]College of Resources and Environmental Science

Chongqing University, Chongqing, PR China

[a] E-mail: luoyanlizw@sina.com

**Key words:** invertebrates; streambed substrate; biodiversity

**Abstract:** Invertebrates are important components of stream ecosystems. A field experiment was conducted to study the effects of substrate particle size, shape and roughness on the composition and biodiversity of invertebrates. The results show that the particle sizes， porosity，and interstial dimensions of the substrate affect the invertebrate community，while the shape and surface roughness of the substrate do not strongly affect the benthos composition and density. The invertebrate composition in the gravel is stable. The density and species richness in the gravels, leaf humus and are much higher than those in the black silt and sands.

## Introduction

The benthic invertebrate is component of stream ecosystems, and plays an important ecological role in the water environmental ecosystem[1,2,3]. So it is widely applied as indicator species to estimate the health of the ecosystem. The further study of stream benthic invertebrates contribute to comprehensive understanding of stream ecosystems, interaction between stream systems and aquatic animals, and provide a strong ecological basis for stream health and ecological restoration.

The streambed substrate is extremely important physical factors that impact of stream benthic invertebrate[4,5,6,7]. Observe and study effects of different streambed substrate on benthic invertebrate through field experiments in Fuxi River, China.

## Experimental and Methods

### Experimental Program

Experiment on 30 meters Fuxi River reach which less human disturbance; flat streambed; the water depth is less than 0.5m; the flow rate is less than 0.3 m/s.

The substrate of Point A is gravel; Point B is sand; Point C is leaf humus; Point D is black silt.

### Sampling and Analytical Methods

Sampling Tools is Peterson grab sampler (or Surber net). Benthic invertebrate singled out and put 10% formalin solution. Simultaneous determination of dissolved oxygen content, water temperature, water depth and velocity of stream.and other physical parameters, field record environmental factors. The samples were brought back to the laboratory for classification, identification, counting, and weighing.

Indices used in the evaluation of biodiversity

1) Species richness S, the total number of species in the sample.
2) Density D, the total number of benthic invertebrate in the unit area.
3) Shannon-Wiener diversity index

Fig. 1 shows the location of four sampling sites. Samples were taken from 4 sites along the river for ecological assessment.




Fig. 1. Location of the 4 sampling sites in the Fuxi River basin

The diversity indexes of sampling sites are shown in Table 1.

Table 1. The diversity index of sampling sites

| Sites | A | B | C | D |
|---|---|---|---|---|
| Diversity index | 1.149 | 0.3912 | 0.6285 | 0.02318 |

## Results

### Compare the Density and Diversity of Benthic Invertebrates

#### Streambed Substrate is Gravel Blocks

In the sampling site A that streambed substrate was gravel had taken more Mesogastropoda Viviparidae and Decapod Penaeidae invertebrates and streambed gravel particle size ranging from 3-9cm, no river streambed surrounding grass lush nature plants, the animals provide food and shelter, sampling shrimp mined Branch and Viviparidae, hard streambed substrate itself has a special hobby, streambed substrates are generally more stable, species diversity with substrate stability increase in the increase.

#### Streambed Substrate is Sand

In the sampling site B substrate in the river bed substrate sampling point B just got Decapod Penaeidae mining families, streambed developed for farmers around the small farms and in soil substrate as the main source of the river next to no river grass, sampling mined Branch shrimp are more fond of this substrate, river substrate is sand, then its stability is vulnerable to man-made, weather, any form of unstable substrate on benthic organisms have a negative impact, flood erosion-prone season, benthic invertebrate thrive takes time, it is difficult to settle on an unstable streambed.

### Streambed Substrate is Leaves Humus

In the sampling site C that streambed substrate was the leaf humus had sampling more Tubificidae, Limnodrilus hoffmeistteri and Diptera Chironomidae, the banks of this river are many large trees, so the streambed substrate contains more leaves, leaves humus benthic substrate can provide a good living environment, evade predators chase, leaves humus degradation of benthos can provide food, but also for biodiversity provides good conditions.

### Streambed Substrate is Silt

In point E that streambed substrate was the silt sampling more Tubificidae, Limnodrilus hoffmeistteri, this river bed surrounded by abundant plants, water plants and other epiphytes seabed is an important factor affecting benthic invertebrate, not only are they able to provide food and habitat for benthic animals, breeding, shelter, but also to stabilize substrate, reducing flood when the impact on the benthic invertebrate. Loose substrate silt-rich clastic substrates, rich forage base, so the quality of the sludge in the bottom of the streambed, biodiversity should be the highest.

## Discussion

Substrate particle size, porosity and voids size were significantly affected of the benthic invertebrate community composition. Investigated by comparing the natural river bed substrate different types of points corresponding to the abundance of benthic species, can be seen in different substrate abundance of benthic species differences. Species richness highest in the gravel blocks streambed, the lowest in the sand streambed.

Invertebrate diversity increased or decreased with the changes of streambed substrate size. Sandy stream most unfavorable for benthic invertebrate, which corresponds to the lowest biodiversity, biodiversity of rubble high biodiversity of small gravel in the highest. Large bed of gravel and other large particle substrate structure and stability, to better protect benthic animals from outside interference, benthic species composition in the large rubble more stable. This is due to the large stone in the gap for the existence of a large stable benthic invertebrate provides stable and diverse places of refuge and habitat caused by benthic animals can be perched on the rocks at the bottom to avoid the gap or the external environment perturbations.

In the gravel bed of the river, A is the point size smaller than gravel particle size D point, but the point A diversity of benthic invertebrates above point D, substrate particle size is smaller, but the intergranular the greater the gap, the higher the porosity, the benthic animals can provide a better living environment, biodiversity will be. But the composition and diversity of benthic invertebrate are affected on the substrate gap size and porosity coupling, when the two work together to create greater substrate heterogeneity when biodiversity is higher.

The leaves and humus sludge substrate when compared humus leaves voids and porosity are greater than the sludge substrate, but no significant biodiversity compare the interval, the reason is different biological populations voids and porosity rate selection, first have to consider their own living conditions and living environment, for this experiment leaves humus and silt different porosities, benthos choose to provide more nutrients places. Biodiversity was no significant difference, but both have significant biomass interval benthic environment in the choice of its own food for the first criterion, followed by their own living environment.

## Conclusions

Substrate particle size, porosity and voids the size of the benthic community composition were significantly affected. Biodiversity highest in the small gravel, large gravel is higher, the lower leaves, humus and silt, sand the lowest. Different size in benthic substrate composition and dominant groups are also different. Composition and diversity of benthic invertebrate are affected on the substrate gap size and porosity coupling, when the two work together to create greater substrate heterogeneity when biodiversity is higher. Benthic invertebrate species composition in the rubble relatively stable, the stable structure of large particle substrate benthos to better protect against outside interference.

**Acknowledgements**

This research was supported by the Sichuan Province Education Department natural science research projects (11ZB251).

**References**

[1] Reice S R.Oecologia,1985,67 (1): 90 - 97.

[2] Arunachalam M,Nair K C M,Vijverberg J,et al. Hydrobiologia,1991,213: 141 - 148.

[3] Beisel J N,Usseglio-Polatera P,Thomas S,et al. Hydrobiologia,1998,389: 73 - 88.

[4]WANG Zhaoyin,CHENG Dongsheng,HE Yiping,et al. Advance in Earth Science, 2006, 21(4): 409 - 416. (in Chinese)

[5] Alexander S F,Allan J D. Oecologia,1984,64(3): 306 - 313.

[6] Erman D C,Erman N A. Hydrobiologia, 1984, 108: 75 - 82.

[7] Downes B J,Lake P S,Schreiber E S G,et al. Oecologia,2000,123: 569 - 581.

*Advanced Materials Research Vol. 937 (2014) pp 495-501*
*© (2014) Trans Tech Publications, Switzerland*
*doi:10.4028/www.scientific.net/AMR.937.495*

# An Extended-range Hybrid Solar-cell and Battery Powered Bicycle

Chung-Hsing CHAO

Electrical and electronic engineering department, Ta-Hwa University of Science and Technology, Hsinchu, 30743, Taiwan R.O.C.

davidee@tust.edu.tw; cchao@uwm.edu

**Keywords:** hybrid power system, solar energy, battery, range-extender, electric bicycle.

**Abstract.** In this paper, an extended-range hybrid solar-cell and battery powered bicycle through a wireless sensor network (WSN) for far-end network monitoring solar energy to charge two lead-acid batteries and the effectiveness analysis is proposed. In order to achieve this goal, the key component of ZigBee used for a far-end wireless network supervisory system is setup. By adding a small-powered solar panel to charge two batteries when idle or low power periods, an extended-range hybrid powered bicycle allows its driving distance to be increased further. The alternative with this solution, though, are weight and cost. Experimental results prove that our prototype, the solar energy powered bicycle, can manage the solar energy for charging two lead-acid batteries pack to extend its range. As a result, the user by the wireless network in parking period knows the data on the amount of immediate solar radiation, the degree of illumination, the ambient temperature, and electrical energy storage capacity information by the internet interface.

## Introduction

With an increasingly in the renewable energy and wireless network technologies applications, the power systems that employs renewable energy without charging stations or cable deployment for the transportation applications is crucial. Take advantage of renewable energy resources in the transportation's environment, offers a power source limited by the transportation's weight and cost rather than an adjunct energy source. This study integrates renewable photovoltaic energy with electricity storage and wireless network technology, which enables remote terminal units located on campus to conduct on-site monitoring with photovoltaic power through a ZigBee wireless module, transmitting data back to host supervisory control and data acquisition centers and the wireless internet units.

The ZigBee network element is one kind of the wireless network agreement which mainly made by the ZigBee Alliance [1]. Its first floor is the media access levels and the entity level by using the IEEE 802.15.4 standard. By using the Global System for Mobile Communications (GSM) the handset mobile phone can receive on the hybrid solar cells and battery powered bicycle about charging and storage electrical energy to feed in the remote monitoring center and momentarily accepts the monitoring center the instruction. Valente et al. [2] made the wireless data transmission by using ZigBee under media access control (MAC) construction. Pegatoquet et al. [3] used a system-on-a-chip (SOC) chip, the digital signal processor (DSP), the micro control unit (MCU), the GSM, the Bluetooth, the global positioning system (GPS), to apply in the audio applications.

Due to the unstable characteristic for solar energy, it is more convenient to allow electric bicycles to run on stable sources of energy such as batteries. This study integrates solar energy renewable energy sources, the WSN and the wireless internet three units, and abbreviates charging stations deployment on campus. Considering the unreliability of photovoltaic power, this study also makes an in-depth understanding on the availability of photovoltaic energy, including immediately making user understanding photovoltaic energy charging the battery and residual electricity in battery. Using laid aside on solar-powered bicycle's sensor element launcher, the driver can immediately know the data of solar immediate degree of illumination, the solar generating electrical power rate, the ambient temperature, the storage electrical energy, lengthening the travel distance, reducing the manual charging the trouble, and the charging stations infrastructure.

## System Structure

This research is carried on the solar cells and batteries powered bicycle as shown in Fig 1. by the WSN far-end network monitoring solar energy to transfer the electrical energy storage and the effectiveness analysis. In order to achieve this goal, an embarked ZigBee by a solar-powered bicycle the far-end wireless network supervisory system is setup. As a result, the driver by cell phone through the wireless network even in driving or parking periods knows the data on the amount of immediate solar degree of illumination, the ambient temperature, and electrical energy storage capacity or mileage information by the internet interface. Further experiment results will be proved the feasibility of the proposed WSN far-end network monitoring solar energy system on an extended-range hybrid solar-cells and battery powered bicycle on campus in the following sections.




Fig. 1. (a) Prototype of the proposed solar energy powered bicycle [4]; (b) solar bike designed by ELE [5]; (c) solar powered quadricycle [6]

Two lead-acid batteries charged by soar cells can be used with series or parallel connected modes as shown in Fig 2. In series connected mode, one using a small size of solar cells as a charger and such wireless supervisory monitoring concept of a solar energy powered bicycle can be used to monitor on the amount of immediate solar degree of illumination, the ambient temperature, and electrical energy storage capacity information. As shown in Fig 2, the parallel connected mode has to be harvested by an efficiently large solar energy scavenging system, and the electrical energy storage batteries as an adjunct power source. The solar energy system must also effectively deliver the stored energy data to the user knows what the miles he or she can use to run the solar powered bicycle. This means there has to be an intelligent power management strategy in place. Obviously, this strategy must know how much the stored energy can use and where can be recharging the batteries. These details along with design considerations that impact efficiency and the associated tradeoffs are in the next few sections.

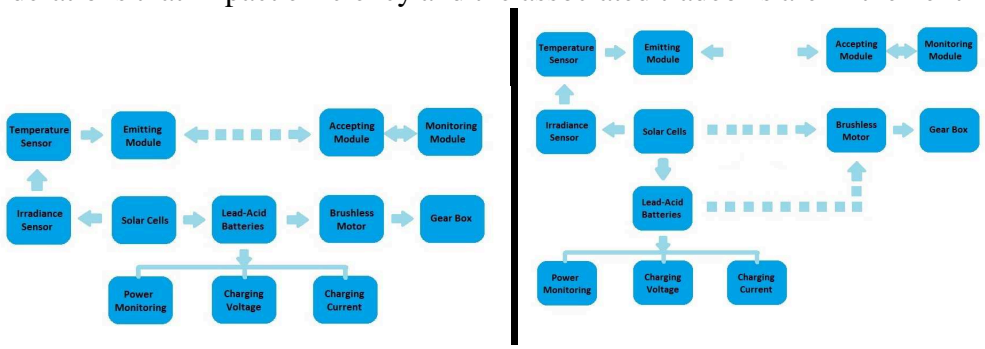



Fig. 2. (a) Series connected monitoring block diagram; (b) Parallel connected monitoring block diagram.

## WSN on Campus

There are several outdoor applications on campus that seem feasible for WSNs combining renewable energy sources. But to eliminate their dependence on charging stations and use solar cells as an exclusive energy source would require the outdoor lights to be on continuously in the daytime.

In this study, one such wireless supervisory monitoring concept of a solar energy powered bicycle that can be used to monitor on the amount of immediate solar degree of illumination, the ambient temperature, and electrical energy storage capacity information. It is clear that even light is the most convenient energy source available for indoor applications [7]. Exploiting solar energy resources on campus, offers a more efficient power source limited by the devices likes sockets or the battery charging station demand. However, the design of an efficient energy harvesting module involves complex tradeoffs due to the interaction of several factors such as the characteristics of the solar energy sources and environment. It is therefore essential to thoroughly understand and judiciously exploit these factors in order to maximize the energy efficiency of the solar cell module.

Referring to series connected mode (see Fig 2) used in the present study, the base station in such networks consists of a router that receives data and is connected to a server. The data received by the base station is displayed to allow continuous monitoring and can be routed to the battery's characteristics for easy access in real time. Similarly, ZigBee sensors in the solar powered bicycle with the solar cells can scavenge energy through overhead sunlight rather than use battery charger station. In fact, in such systems, ZigBee sensors might be mobile and therefore, it might be possible and advantageous to monitoring the electric power in the batteries through photovoltaic cells.

Table 1. Specifications of the solar powered bicycle

| **Solar Cells** | |
|---|---|
| Type | GE 50W 12V |
| **Test conditions** | |
| Irradiance | 1000W/m$^2$ |
| Module temperature | 25℃ |
| Module size | 835x540x35 mm |
| Module weight | 6.5kg |
| Maximum power | 50W |
| Maximum power voltage | 18V |
| Maximum power current | 2.7778A |
| Open circuit voltage $V_{oc}$ | 22.38V |
| Short circuit current $I_{sc}$ | 3.522A |
| Module efficiency η | $\eta > 16\%$ |
| **Electric bicycle** | |
| Weight | 32kg |
| Tire | 20inch |
| Maximum speed | 25km/h |
| Rated loading | <75kg |
| Lead acid batteries 2x | 36Ah x2 (12V) |
| Noise | 62dB |
| Rated voltage | 24V |
| Over-current protection | 14A±1A |
| Motor type | Brushless motor |
| Dimension | 1580x565x1075 mm |

**Solar Cells Characteristics**

Solar cells have vastly differing characteristics from batteries. As listed in Table 1, a 835x540x35 mm 50W single crystalline solar panel from GE Inc. (U.S.A.) was chosen for the system due to ease to ease of availability and low cost. Each solar panel was rated at 3.522A short circuit ($I_{sc}$) and 22.38V open circuit voltage ($V_{oc}$) under sun's irradiance (1000W/m$^2$) conditions. In order to determine the number of solar panels required per electric bicycle, a simple load test was conducted. A single solar

panel was connected across a varying load to determine its voltage versus current (V-I) profile. Fig 3 shows the V-I profile wherein it can be observed that at around 18V the solar panel sourced out approximately 3A. Therefore, a 50W solar panel was enough to recharge lead-acid batteries. Although the size of the solar panel was not a concern, a modularized approach was taken in order to reduce the size and weight further. It was assumed to use the solar power in the daylight with 1/3 duty cycle that the hybrid solar cells and batteries power system is always power on to charging the lead-acid batteries. In addition, two lead acid batteries 12V 36Ah were used in parallel with the solar panels to store energy and to reduce the solar panel power rating requirement even further. These details are explained in the next sections.

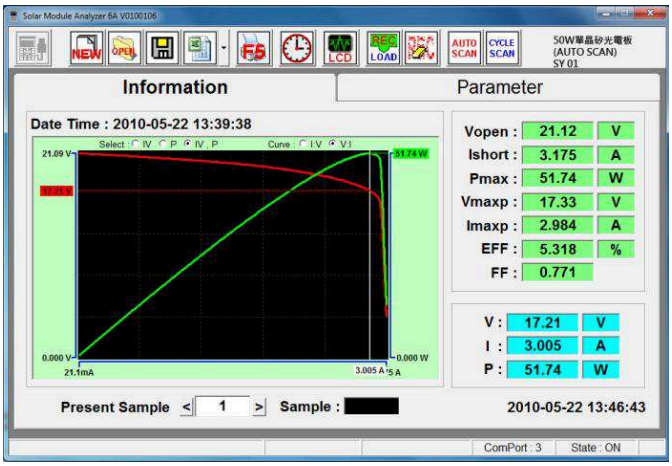



Fig. 3. V-I characteristics of a GE 50W solar panel

## Power Management

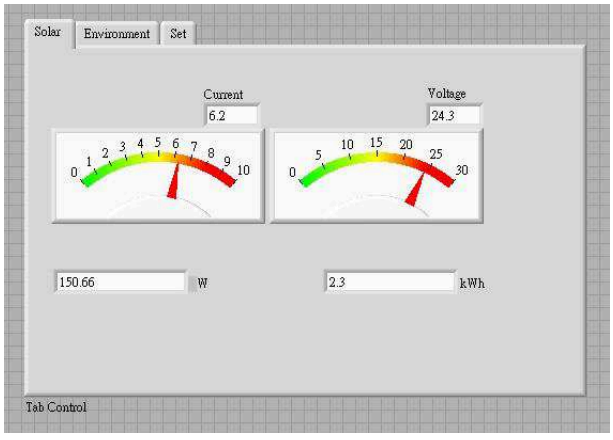
An energy harvesting scheme was used for solar panel. It consists of an adequate number of solar cells to charge the energy storage devices which in turn output regulated power to recharge a lead-acid battery and another lead-acid battery for discharge. Probably, this strategy works well for an electric bicycle where adequate solar energy in the daylight is available to charge the energy storage devices. However, in many outdoor applications, solar energy scavenging from 50W solar panel is fairly practical. This strategy was utilized to obtain power for the driving or stopping period in the daylight. The core of the energy harvesting module is the power management circuit which draws power from the solar panels and manages energy storage and power routing to electric motor. The most important consideration in the design of scavenging solar energy is to maximize energy efficiency, enhance device reliability, and lengthen the miles of an electric bicycle as a range-extender. The power management circuit designed for this hybrid power system provides regulated power in lead acid batteries.

## Experimental Results

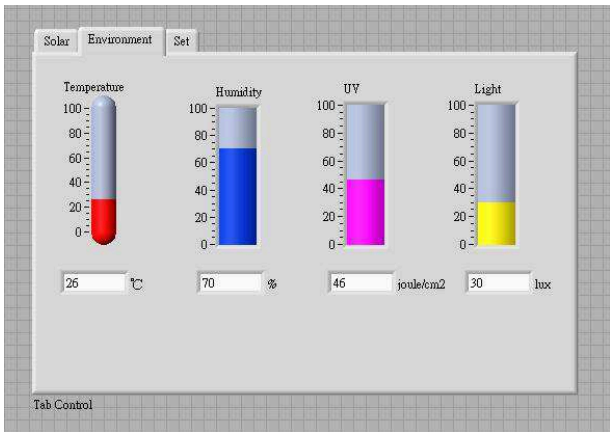


Fig. 4. (a) ZigBee sensors mote with a blue PC module; (b) ZigBee router based mote with a red PC module

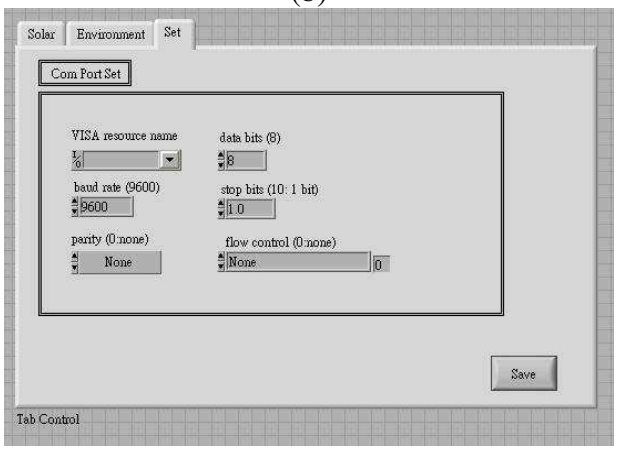
In order to determine the right number of solar cells for powering each electric bicycle a simple load test was first conducted. The electric bicycle powered by two sets of 36Ah lead-acid batteries and a 50W solar panel in the back seat. For reference, as the ZigBee based wireless sensor node for real time monitor, the operation of the ZigBee sensors mote, ZigBee route based mote (red PC module) and the solar powered bicycle monitoring screen are shown in Fig 4 and Fig 5, respectively. Fig 6 shows the velocity, power, and voltage versus currents of the electric bicycle. The electric bicycle with two sets of 36 Ah lead-acid batteries and a 50W solar panel in the back seat, which was conducted to test when the summer and sunny weather, only depends on the full-charged batteries to run, the kilometers traveled distances away from probably is 36.5km, if the use solar cells charge, increases to 54.4km. The experimental result was shown to verify the feasibility of the proposed extended-range hybrid solar cells and batteries powered bicycle.




(a)




(b)




(c)

Fig. 5. Solar energy powered bicycle monitoring screen

## Summary

This study is carried on an extended-range hybrid solar cells and batteries powered bicycle by the WSN far-end network monitoring solar energy to transfer the electrical energy storage and the effectiveness analysis. In order to achieve this goal, an embarked ZigBee by a solar-powered bicycle the far-end wireless network supervisory system is setup. As a result, the driver by the wireless network in driving or parking period knows the data on the amount of immediate solar degree of illumination, the ambient temperature, and electrical energy storage capacity information by the internet interface. In this study, the proposed electric bicycle charging source by solar cells, may lengthen the travel distance, reduces the manual charge the trouble and time.

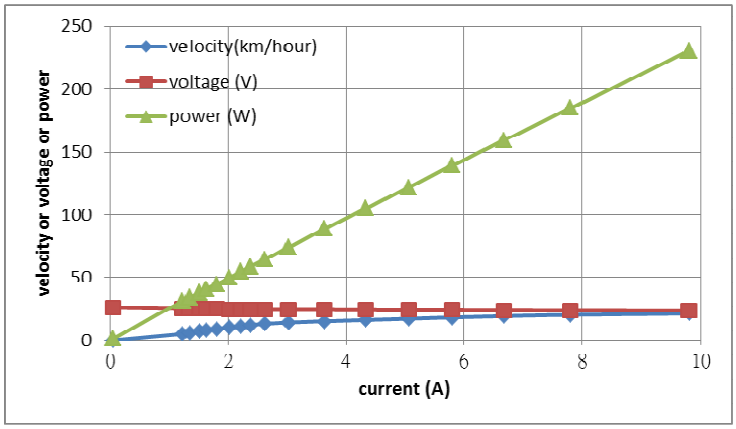



Fig. 6. Voltage, power, and velocity vs. currents

**Acknowledgement**

This research was financially supported by the National Science Council in Taiwan under the research grant project of NSC-101-2221-E-233-004, for which the author is grateful.

**References**

[1] ZigBee Alliance, http://www.zigbee.org/.

[2] A.Valente, R. Morais, C. Serodio, P. Mestre, S. Pinto, and M. Cabral, A ZigBee Sensor Element for Distributed Monitoring of Soil Parameters in Environmental Monitoring, Sensors, 28-31 (2007) 135-138.

[3] A. Pegatoquet, F. Thoen, and D. Paterson, Virtual Reality for 2.5 G Wireless Communication Modem Software Development, 32nd Annual IEEE International Computer Software and Applications, (2008) 72-75.

[4] Chung-Hsing Chao, and Jen-Jong Shieh, Solar charging electric transportation vehicle with remote wireless monitoring functions, Taiwan ROC, Patent M399536, 2011.

[5] Information on http://www.yankodesign.com/

[6] Wilson et al., Solar-powered quadricycle with regenerative and dissipative braking, US Patent 0,299,251 A1, 2013.

[7] D.I. Shin, K.H. Shin, I.K. Kim, K.S. Park, T.S. Lee, S.I. Kim, K. S. Lim, and S. J. Huh, Low Power hybrid Wireless Network for Monitoring Infant Incubators, Medical Engineering & Physics, 27 (2005) 713-716.

[8] A. Hande, T. Polk, W. Walker, and D. Bhatia, Indoor solar energy harvesting for sensor network router nodes, Microprocessors and Microsystems, 31 (2007) 420-432.

*Advanced Materials Research Vol. 937 (2014) pp 502-507*
*© (2014) Trans Tech Publications, Switzerland*
*doi:10.4028/www.scientific.net/AMR.937.502*

# Experimental Study on Biogas Production by Mesophilic Fermentation with Dimocarpus longan Pericarp

Li-juan ZHANG[1, a], Wei-dong LIN[1], Wu-di ZHANG[1, b], fang Yin[1], Xing-ling ZHAO[1], Jing LIU[1], Ling XU[1], Yu-bao CHEN[1], Shi-qing LIU[1], Hong YANG[1]

[1]Yunnan Normal University Kunming 650092, P. R. China

[a]lijuan_890923@sina.com, [b]wootichang@163.com

**Key words:** Dimocarpus longan Pericarp; Biogas fermentation; Biogas production potential

**Abstract:** In order to gain the biogas production potential from pericarp of longan (*Dimocarpus longan* Lour.) fruits, the anaerobic batch fermentation which were divided into the control group (120mL inoculum), the experimental group (120mL inoculum and 15g *Dimocarpus longan* pericarp) were performed at 30°C.The results indicated that the net biogas production of the experimental group during total fermentation time of 45d was 2455mL. Further, it was calculated that the biogas yield of *Dimocarpus longan* pericarp was 269mL/g TS or 294mL/g VS.

## Introduction

*Dimocarpus longan* Lour is the famous fruit of medicine and food in southern China, and the flesh is white or pale white, succulent crisp, sweet. Traditional Chinese medicine thinks that Longan meat was used in the treatment of insomnia, forgetfulness, palpitation, and good at heart and spleen, supplement of vital energy and blood, calm the nerves, which has been touted as "Fruit of the holy" [1-3]. As the economic crops, Longan was planted in many countries such as China, Vietnam, Thailand, India [4]. China is the country of origin and longan producer. The fruit is Listed more concentrated, and shipping and storage conditions behind preservation, only a fraction of longan consumed directly as fruit, and a lot of longan for processing, while the rest of the skin is a lot of waste. In recent years, studies have shown that pericarp of longan had extract with antioxidant, inhibition of tyrosinase and antitumor activity [5-6], others researched the chemical composition with pericarp of longan fruit [7]. Yellow pigment extraction technology was studied in order to realize the longan fresh-keeping [8]. In the experiment, determination the gas potential of longan fruit provides a new utilization way in subsequent longan fruit processing and application, and solves the trouble for rapid development of longan industry.

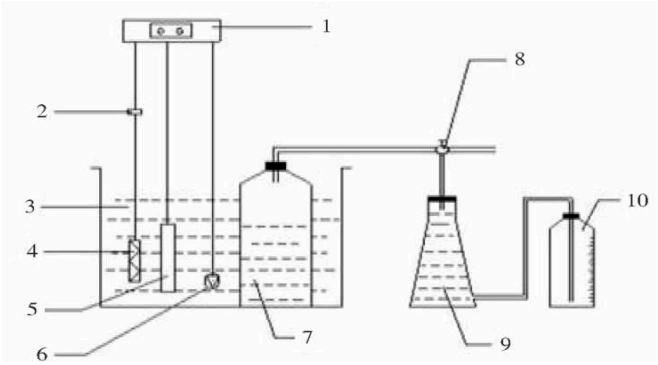
## Experimental Materials and Methods

### Materials

Fermentation material was pericarp of longan (*Dimocarpus longan*) fruits, the determination of TS value was 60.75% and VS value was 91.73%. The inoculum was cattle manure as the materials to enrichment, the determination of TS% was 9.18% and VS% was 74.82%, pH value was 7.5.

### Experimental Device

Experimental device as shown in figure 1, the experimental device composed by fermentation bottle, gas storage bottle, metering bottle and temperature control system, etc. Fermentation bottle is 500 ml jar, sealed with rubber stopper with glass tubes. Gas storage bottle adopts the 500 ml triangle bottle mouth with three-way pipe sealed rubber stopper. Metering bottle is 500 ml jar, and it is connected by latex tube with fermentation bottle and gas collection bottle. Temperature control system by the temperature controller (XMT - 121 type), type of thermocouple (WCZT - 10), a.c. contactor (CJT1-10), a circulating water pump (AP1200 type), galvanothermy tube and iron sink.




1.Temperature Controller; 2.A.C. Contactor; 3.Iron sink; 4.Galvanothermy Tube;
5.Thermocouple; 6.Circulating Water Pump; 7. Fermentation Tank;
8.Three-Way Pipe; 9.Gas Storage Bottle; 10.Metering Bottle

Fig.1. Experimental equipment for biogas fermentation

**Experimental Methods**

The experiment is set up one experimental group and one control group, which is designed three parallel. In order to ensure the consistency of test, carries on the single bottle preparation, and solid-liquid ratio is as follows. Experimental group: 25g *Dimocarpus longan* pericarp +120mL inoculum+ water=400mL. Control group: 120mL inoculum+ water=400mL. Fermentation pattern was all mixed batch fermentation, and the temperature was medium 30°C.

**Measurement & Methods**

(1)It was determined Total solids (TS) and Volatile solids (VS) with conventional biogas-analysis methods [9-10] in raw materials, inoculum, and mixture before and after fermentation. TS: The material residue left in a vessel (GM-101) after evaporation of a sample and its subsequent drying in an oven at 105±5°C for about 6 hours. The water is then evaporated away and the crucible is reweighed, then we calculated TS value with TS computational formula [10].VS: Solids remaining after the analysis for total solids were ignited at 550±20°C to a constant weight, the VS was measured with VS computational formula [10].

(2) The pH value was measured with the range 5.5 ~ 9.0 precise pH test paper.

(3) Using the method of drainage gas-collecting. The gas production was recorded with displacement method at a regular time each day. At the same time by using flame color swatch to determine methane content in the biogas [11].

**Result & Analysis**

**Determination the TS, VS and pH Value before and after Fermentation**

In the Table 1, when the experiment commenced, we first determined the TS, VS and pH values of the fermentation materials mixed with inoculum, then TS, VS and pH values in the fermentation ending.

Table1. TS, VS and pH value of fermentation liquid before and after fermentation

| Project | Experimental group | | Control group | |
|---|---|---|---|---|
| | Before fermentation | After fermentation | Before fermentation | After fermentation |
| TS/% | 5.42 | 3.52 | 3.11 | 2.49 |
| VS/% | 87.65 | 79.51 | 75.31 | 72.30 |
| pH | 7.5 | 7.0 | 7.0 | 7.0 |
| Degradation rate (TS)/% | 35.05 | | 19.93 | |
| Degradation rate (VS)/% | 9.29 | | 4.00 | |

From Table 1, TS and VS values of both the experimental group and control group were lower before and after fermentation. The raw material's TS and VS values of experimental group were decreased obviously before and after fermentation. The TS and VS utilization ratio were 35.05% and 9.29%. The experimental group and control group pH value was always in normal range before and after fermentation during the process.

**Gas Production & Analysis**

**Gas production**

Everyday record the gas production, and was obtained analysis of law between raw material fermentation time and gas production by calculation, as shown in figure 2.

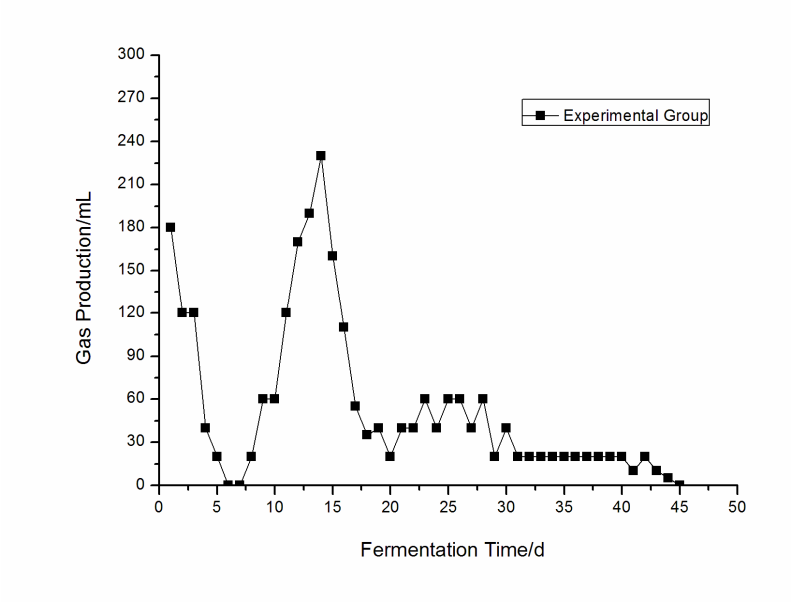



Fig. 2. Gas production curves

In the Figure 2, *Dimocarpus longan* pericarp producing biogas curve accords with the general law of biogas fermentation: The experiment began to produce less gas, gas production increased along with the fermentation time. After the peak, gas production decline gradually. Biogas fermentation time was 45 d, it began to produce biogas at 1st day. The gas production reduced on 4th~8th day, but pH was in a normal range, then gas production increased gradually on 9th day. On the 14th day the gas yield almost reaches its largest gas yield and reaches 230mL. The methane content was in 40% ~ 70% from methane flame color in this fermentation period. On the 20th~30th day gas production was on the decline as a whole and changed a little, the methane content was about 65%. On the 31st~45th day the gas production was under 40mL, and methane content was more stable in 50%~55%.

**Gas Production Rate**

In the Table 2, it showed the cumulative gas production and gas production rate with fermentation time.

Table 2. The statistics of gas yield and gas production rate

| Fermentation/d | 5 | 10 | 15 | 20 | 25 | 30 | 35 | 40 | 45 |
|---|---|---|---|---|---|---|---|---|---|
| Cumulative gas production/mL | 480 | 620 | 1490 | 1750 | 1990 | 2210 | 2310 | 2410 | 2455 |
| Gas production rate/% | 19.55 | 25.25 | 60.69 | 71.28 | 81.06 | 90.02 | 94.09 | 98.17 | 100 |

From the Table 2, the cumulative gas production showed a trend of fast surge growth on the $10^{th}$~$15^{th}$ day, while the gas production was low from $30^{th}$ to $45^{th}$ day. It indicated that producing biogas was mainly before $30^{th}$ day. The total gas production was 2765mL, which increased 8.92 times than the control group, and daily gas production was 55mL. The control group produced gas little, so gas organic matter mainly came from raw materials. The gas production rate was more than 80% of the total volume on $25^{th}$ day, and less 10% from $30^{th}$～$45^{th}$ day.

**Biogas Production Potential**

According to Figure 2, Table2, we can see the gas production potential through statistical analysis, and the results are shown in Table 3.

Table 3. The biogas production potential of *Dimocarpus longan* pericarp

| Raw materials | Net biogas production(mL) | Daily biogas production(mL) | Biogas yield (mL/g TS) | Biogas yield (mL/g VS) |
|---|---|---|---|---|
| *Dimocarpus longan* pericarp | 2455 | 55 | 269 | 294 |

**Comparison of Various Kinds of Raw Material Gas Potential**

To detail with the other raw material for biogas production potential was compared, the results as shown in Table 4. Table 4 in "Multiples" refers to biogas yield (TS) of *Dimocarpus longan* pericarp relative to other raw materials.

Table 4. Potential for biogas production from various materials

| *Fermentation materials* | *Fermentation time(d)* | *Biogas yield (mL/g TS)* | *Biogas yield of relative to various raw materials* | *Reference* |
|---|---|---|---|---|
| *Dimocarpus longan* pericarp | 45 | 269 | 1.00 | — |
| *Punica granatum* peel | 35 | 264 | 1.02 | [12] |
| Bagasse | 92 | 201 | 1.34 | [13] |
| Hull of broad bean | 36 | 161 | 1.67 | [14] |
| Pineapple peel | 23 | 574 | 0.47 | [15] |
| *Pisum sativum* peel | 29 | 206 | 1.31 | [16] |
| Trident maple | 56 | 54 | 4.98 | [17] |
| *Prunus cerasifera* | 50 | 67 | 4.01 | [17] |
| Oriental plane | 76 | 69 | 3.90 | [17] |
| *Jatropha curcas* seed shell | 33 | 429 | 0.60 | [18] |

As can be seen from Table 4, All kinds of plant-based materials include crop straw, peel and deciduous. The biogas yield of *Dimocarpus longan* pericarp was 269 mL/g TS, which was higher than that of leaves material and the highest reached 4.98 times (Trident maple: The biogas yield was 54mL/g TS). In the peel of raw material, the biogas yield of *Dimocarpus longan* pericarp was higher than Pericarp of broad bean and *Pisum sativum* peel. After comprehensive comparison, *Dimocarpus longan* pericarp was a kind of good material for fermentation, and the HRT can be designed for 24 d in large digester engineering.

**Conclusion**

The *Dimocarpus longan* pericarp can produce biogas in 30°C. The biogas production yield of *Dimocarpus longan* pericarp is 269mL/gTS or 294mL/gVS. *Dimocarpus longan* pericarp is kind of good material for fermentation. In the process of actual utilization, the biogas fermentation time can be designed to be 24 d.

**Acknowledgements**

This work was financially supported by the Science and Technology Condition Platform Construction Projects of Yunnan (2010DH012).

Author: Lijuan Zhang(1989- ), female, master, engaging in research and study of biomass energy & environment engineering. E-mail: lijuan_890923@sina.com.

Corresponding author:Wudi Zhang(1965- ), male, professor, Research Associate & doctoral supervisor, engaged in biomass energy research and teaching work. E-mail: wootichang@163.com.

**References**

[1] Jiangsu New Medical College. Traditional Chinese medicine [M]. Shanghai: Shanghai People's Publishing House, 1977. (In Chinese)

[2] G. M. Zheng, X. Y. Wei, L. X. Xu, et al. Chemical constituents from fruits of *Dimocarpus longan* [J]. Chinese Traditional and Herbal Drugs. Vol. 42, No. 6 (2011), p. 1053-1056. (In Chinese)

[3] G. M. Zheng, L. X. Oxus, H. H. Lie, *et al*. A new diol from *Dimocarpus longan* seeds [J]. *Chin Herb Med*. Vol. 3, No. 1(2011), p. 7-8.

[4] Y. Jiang, Z. Zhang, D. C. Joyce, *et al*. Postharvest biology and handling of longan fruit (*Dimocarpus longan* Lour.) [J]. *Postharvest Boils Technol*, Vol. 26, No. 3 (2002), p. 241-252.

[5] K. N. Prasad, B. Yang, J. Shi, *et al*. Enhanced antioxidant and antityrosinase activities of longan fruit pericarp by ultra-high-pressure-assisted extraction [J]. *J Pharm Biomed Anal*, Vol.51, No.2 (2010), p. 471-477.

[6] K. N. Prasad, J. Hao, J. Shi, *et al*. Antioxidant and anticancer activities of high pressure-assisted extract of longan (*Dimocarpus longan* Lour.) fruit pericarp [J]. *Innov Food Sci Emerg Technol*, Vol. 10, No.4 (2009), p. 413-419.

[7] G. M. Zheng, X.Y. Wei, L. X. Xu, et al. Chemical constituents from pericarp of longan fruits [J]. Chinese Traditional and Herbal Drugs. Vol. 42, No. 8(2011), p. 1485-1489. (In Chinese)

[8] D. Q. Tang, L. Wang. Research on process and the stability of Longan peel yellow pigment extraction. No. 10 (2003), p. 108-112. (In Chinese)

[9] W. D. Zhang, H. C. Song, F. Yin, et al. Biogas Fermentation & Comprehensive Utilization[M]. Kunming: Yunnan Science Press, 2004, p. 104-106. (In Chinese)

[10] Chengdu Biology Institute in Chinese Academy of Sciences. Conventional Analysis in Biogas Fermentation [M]. Beijing: Science & Technology Press, 1984, p. 19. (In Chinese)

[11] Y. H. Jiang, X. H. Yu. Flame Color to Determine the Methane Content of the Biogas [J]. China Biogas. No. 3 (1983), p. 28. (In Chinese)

[12] L. J.Zhang, W. D. Zhang, F. Yin, et al. Experimental Study on Potential of Biogas Fermentation with *Punica granatum* Peel [J]. Advanced Materials Research Vol. 763 (2013), p.151-155

[13] Y. L. Li, C. B. Chuan, F. Yin, et al. Study on Potential of Biogas Fermentation with Bagasse [J]. Scientific Decision-Making. No.12 (2008), p. 45-46. (In Chinese)

[14] W. Yin, J. Y. Ru, S. Q. Liu, et al. The Study of Biogas Fermentation from the Hull of Horse Bean [J]. Sun Energy, 2006, 2, 57-58. (In Chinese)

[15] G. J. Zha, W. D. Zhang, F. Yin, et al. Study on pineapple peel biogas generation by anaerobic digestion [J]. Energy Engineering. No. 1(2007), p. 41-43. (In Chinese)

[16] W. W. Liu, F. Yin, W. D. Zhang. Study on Potential of Biogas Fermentation with *Pisum sativum* peel [J]. Journal of Yunnan Normal University. Vol. 11, No. 6(2005), p. 28-29. (In Chinese)

[17] S. G. Sun, G. X. Ren, N. N. Zhai, et al. Research on the Biogas Yield from the Anaerobic Fermentation of Fallen Leaf of Three Street Trees at Medium-temperature[J]. Anhui Agricultural Science Bulle. Vol. 38, No. 19 (2010), p. 10164-10166. (In Chinese)

[18] S. M. Zhang, F. Yin, W. D. Zhang, et al. Experimental Study on Potential of Biogas Fermentation with *Jatropha curcas* Shell [J]. Practical Forestry Technology. No. 2 (2009), p. 51-52. (In Chinese)

*Advanced Materials Research Vol. 937 (2014) pp 508-514*
*© (2014) Trans Tech Publications, Switzerland*
*doi:10.4028/www.scientific.net/AMR.937.508*

# Research on Environmentally Friendly Water-based Covering Ink and Its Application in Scratch-type Invoice Printing

Ying GONG[1,a], Bei-qing HUANG[1,b,] and Xian-fu WEI[1,c*]

School of Printing and Packaging Engineering, Beijing Institute of Graphic Communication, Beijing 102600, China

[a]gyer0716@163.com, [b]huangpeiqing@bigc.edu.cn, [c]weixianfu@bigc.edu.cn

**Keywords:** Environmentally friendly water-based covering ink, Ink performance, scratch-type invoice printing, Environment protection.

**Abstract.** With the development of printing technology, greater emphasis has been laid on environmentally friendly materials. Due to its printability and environmental friendliness, Water-based flexo ink is gradually gaining popularity at home and abroad, and has been widely applied in the field of printing. Different from other kinds of bills, scratch-type invoices have an additional scratch area on the surface, which highly covering performance is required for the ink applied. This paper emphatically analyzes and discusses: (a) flexo water-based covering ink and its application in scratch-type invoice covering region printing; (b) how to explore and evaluate new developed green inks. Compared with traditional inks, the water-based flexo ink is free of emissions of volatile organic compounds (VOC), and its popularization might have significant meanings for the environment protection and sustainable development.

## Introduction

With the development of society, printing becomes indispensible and plays a greater role in the industry. But unfortunately, printing industry produces lots of pollution, of which solvent-based ink is to blame [1-3]. Solvent-based ink uses organic solvent and is criticized for the emission of volatile organic compounds (VOC), which does harm to human body as well as the environment [4].

As people's awareness of environment protection increases, it becomes demanding for printing field to explore new environmentally friendly materials [5]. Under the call for sustainable development, the green inks, which mean environmentally friendly, are being explored [6-9].

The covering ink is an opaque ink that can protect the information subjacent to it from being perceived before scratched. It has already been used in the printing of scratch-type invoice [10]. The scratch-type invoice (e.g. Fig.1) is a kind of business voucher of economic activity, and the anti-counterfeiting methods have strict requirements on the covering ink's covering property (CP).

Within the past 10 years, due to the development in new inks and advancement in the printing technology, flexographic printing, favored by its environment protection performance, has become a very influential printing method, hankering for new environmentally friendly inks to enhance its development [11-13]. This also can be inferred from the huge and increasing demand of flexo covering inks every year.

Invoices have different subspecies. They differentiate in social functions but have the same demand for anti-counterfeiting methods. On the surface of the invoice, the covering ink can be scraped by a coin or fingernail, and then the subjacent information can be perceived. So the covering region (Fig.1), for security reasons, have special requirement on the CP of the covering ink applied.

The water-based covering ink being discussed in this paper is one of the green inks and experiment has been carried out to test their printability in scratch-type invoice covering region printing.

## Environmentally Friendly Water-based Ink

Literally, water-based ink uses water as solvent that contains aqueous emulsion polymer resin, organic pigments and related additives made by a mixture of physical and chemical processes. Water-based ink does not contain volatile organic solvents, so that it can greatly reduce the emissions of VOC, thus causing less air pollution, bettering printing operating environment.

Water-based ink is free of toxic and hazardous substances which are harmful to the human, the packaged goods and the environment, thus making it environmentally friendly. It is particularly suitable for the packaging of tobacco, alcohol, food, beverages, medicines, children's toys and other products which have strict requirements on health, packaging and printing conditions. Furthermore, it not only can reduce the risk of fire caused by static electricity, flammable solvents and pitfalls, but also can reduce the residual toxicity on the printing surface, and the printing equipment is easy to clean. Water-based ink is also called a new type of environmentally friendly printing materials.

## Scratch-type Invoice Printing

### The Composition of Scratch-type Invoice

Fig.1 is a sketch map of the surface composition of an invoice, on the surface, the words, numbers and images are commonly printed by hectograph, while the covering region is mainly printed by flexograph. Excellent transparency outer coating (light oil in Fig.1) must be implemented after the offset printing process. The coated layer stabilizes the printed graphic as well as enhances the covering ink's scratch resistance [14]. After that, the flexo covering ink can be printed on the coated layer, to prevent certain information to be perceived.

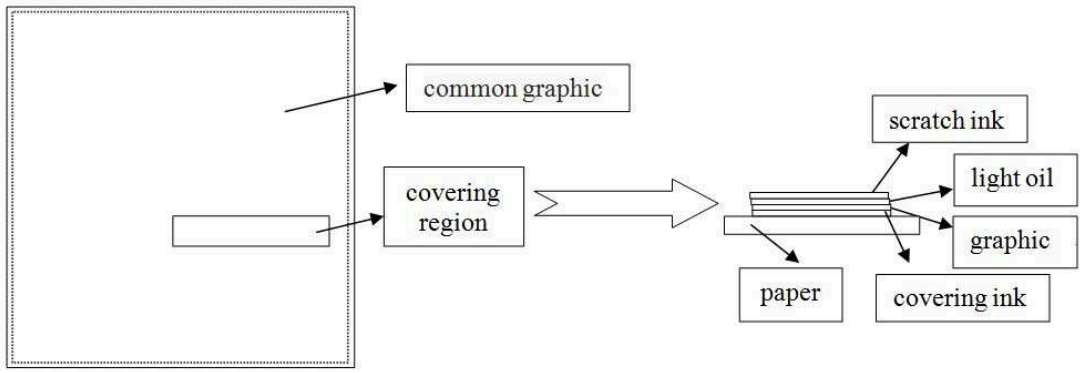



Fig. 1. Sketch map of scratch-type invoice surface composition

### Requirements of Water-based Ink in Scratch-type Invoice Printing

(A) The water-based ink applied in scratch-type invoice covering region printing should be stable and should be easily stripped by fingernails or coins. Invoices commonly have a circulation of one year, which require that the covering ink should keep in good condition during the circulation.

(B) After the covering ink is being removed, the revealed subjacent information should be clear, without the contamination of the water-based ink.

(C) The CP of the water-based ink should be high enough to make the covering region opaque.

(D) High toughness of the ink film of the water-based ink is also required. The ink film should not be mangled by operations, such as moving, drying or cutting. It also should bear the ability to resistant other forms of external forces during the circulation.

It can be safely drawn that (C) and (D) is almost decided by the properties of covering ink, while (A) and (B) is determined by the subjacent light oil and degree of ink adhesion. It can be inferred that the water-based ink plays a primordial role in the invoices' covering region printing.

**Water-based Covering Ink and Its Application in Scratch-type Invoice Printing**

The ink's CP is a key factor in manufacturing scratch-type invoice. The water-based covering should have good printability as well as good CP. The CP should be high enough to cover the words, numbers and graphs to protect the information, the ink film should be liable to stripe off, resistant to high temperature and severe cold. It also should have a storage life of at least one year.

The authors have carried out a series of experiments, evaluating different compositions of water-based covering ink and their printability, and have obtained feasible evaluation methods and system to test the overall performance of the water-based covering ink applied in scratch-type invoice printing.

**CP**

Ink film thickness has the most influence on CP. If the film thickness is too thin, the subjacent information is perceivable, thus making the invoice useless; if the thickness is too thick, it takes a long time to dry, thus reducing the production efficiency. So, in the printing process, ink film thickness should be strictly controlled. In the printing practice, the film thickness varies and is experiential dependent. The film thickness subjects to the principle that as long as it can properly cover the subjacent layer, the thinner, the better. Apart from this, the ink dispersion is another factor affecting the CP, the greater the dispersion is, the higher the CP of the ink is. Compositions can be altered to improve the ink dispersion, thus enhancing the CP.

The Ref.310 CP Tester is applied for the test of ink's CP value. Generally, white CP paperboard is used for the test of black and color ink, while black CP paperboard is prepared for the test of white ink. In this experiment, ink sample is applied to the white CP paperboard; $R_B$ is the testing value of the black grids on the paperboard, while $R_W$ is the testing value of the white grids. The CP value can be calculated by the equation: $CP=R_B/R_W$. The greater the CP value is, the better CP performance can be achieved, vice versa. Inks with different pigment content achieve different CP; the testing results are shown in Table 1.

Table 1. Different pigment contents and their CP

| Pigment content[%] | 20 | 23 | 25 | 28 | 30 | 33 | 35 | 38 |
|---|---|---|---|---|---|---|---|---|
| $R_B$ | 61.1 | 62.7 | 64.1 | 64.4 | 65.5 | 65.9 | 66.0 | 66.2 |
| $R_W$ | 71.3 | 72.7 | 74.2 | 74.5 | 75.7 | 76.1 | 76.2 | 76.4 |
| CP | 0.8569 | 0.8624 | 0.8639 | 0.8644 | 0.8653 | 0.8660 | 0.8661 | 0.8665 |

As it can be seen from Table1 and Fig.2, when the pigment content is within 20%~38%, with the pigment content increases, the CP value gets better gradually, indicating that the ink's CP performance is being enhanced. When the pigment content comes to a certain extent, the content of pigment increase has little influence on CP value. For the experimented water-based samples, 38% pigment content is highly recommended, for it achieves the best CP with acceptable pigment content. However, it must be pointed out that the optimal pigment content varies with different ink formula.

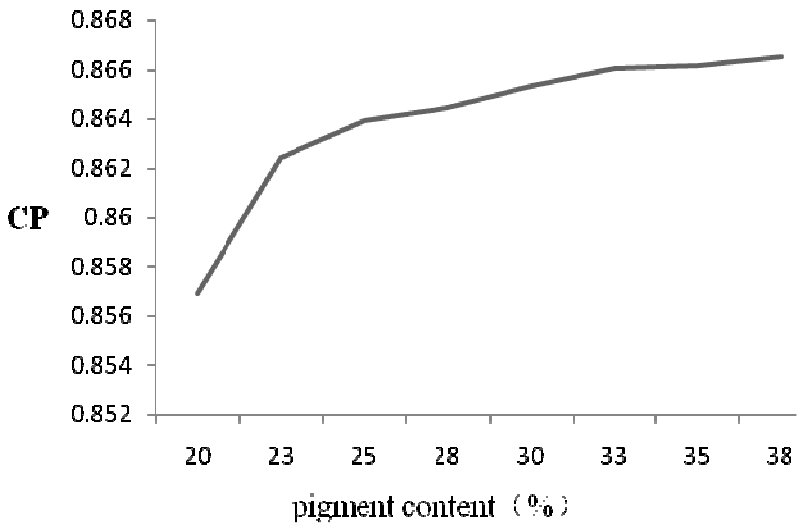



Fig. 2. Pigment content and its CP

**Scratch Resistance (SR)**

Covering ink is printed on the surface of the light oil (Fig.1), certain SR is required. For the circulation of the invoices, good SR is required to remain at least one year. And after the covering ink is being removed, the revealed subjacent information should be clear and intact.

The Scratch Tester is applied for the test of ink's SR value. During the process, the testing samples are fixed on the texting board. A fixed stylus which is 45° (from vertical) scratches the surface of the testing sample. By pushing the testing board, adding the pressure on it until the stylus stripped the ink layer off. The pressure on the testing board can be converted into the SR value. In scratch-type invoice covering region printing, the testing sample's normal temperature resistance(NT) are required at 75~100g, after heated in the condition of temperature(T) =80℃, humidity(H) =80% for one hour(H80T80-1), 120~150g, after heated in T=80℃, H=80% for two hours(H80T80-2), 130~175g. After heated in T=80℃, H=80% for twenty four hours(H80T80-24), the acceptable scratch resistance is under 450g. The testing samples' SRs are shown in Table 2.

Table 2. SR value after different conditions (UTSO: unable to scratch off)

| Ink Samples | | 1# | 2# | 3# | 4# | 5# | 6# |
|---|---|---|---|---|---|---|---|
| SR[g] | NT | 100 | 75 | 100 | 150 | 125 | 200 |
| | H80T80-1 | 150 | 100 | 150 | 250 | 150 | 300 |
| | H80T80-2 | 250 | 150 | 300 | 400 | 300 | 450 |
| | H80T80-24 | 500 | 400 | 500 | UTSO | UTSO | UTSO |

It can be seen clearly from Table 2 that some of the inks explored do not fit for invoice covering region printing. Sample 4#, 5# and 6# fail all the test; sample 1#, 3# have acceptable SR in NT and H80T80-1 test, but fail in the H80T80-2 and H80T80-24 test. Sample 2# meets all the requirements in the SR test and is hopeful for the practice application. Further improvement of Sample 2# is underway.

**Stability**

Covering ink should have excellent stability. Invoices commonly have a circulation of one year, which requires that the covering ink keep in stable condition during the circulation. Any crack and contamination are undesirable. High temperature and humidity resistance is also required. If the water-based covering ink is of good resistance, when it is exposed to T=80℃, H=80% conditions, it can still holds acceptable CP and SR performance. To grantee the subjacent information from being perceived or detected by other apparatus, enough film thickness (usually 20~40um) is necessary.

**Drying Performance (DP)**

In general, water-based flexo ink can dry by evaporation, infiltration and curing reaction or combination of the three ways. Fast-drying is a notable feature of water-based flexo ink. In scratch-type invoice covering region printing, due to the thicker ink film, DP is of great concern. Practically, DP is associated with pH, from the experiment conducted; the pH and the corresponding DP are shown in Table 3.

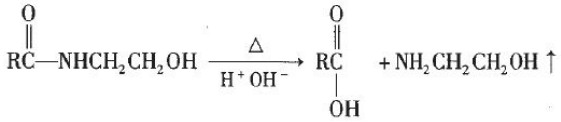
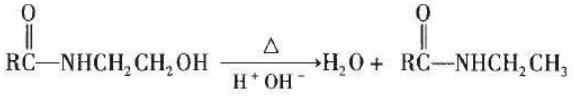
Table .3 Ink samples' pH and corresponding DP

| pH | Drying Performance |
|---|---|
| ＜8.5 | viscosity increases, enhance drying speed, scumming |
| 8.5～9.5 | prime printability and stability |
| ＞9.5 | ink viscosity, drying speed and water resistance are reduced |

Flexo printing ink is generally weak alkaline, normal pH range is 8.5 ~ 9.5, within which the water-based ink has prime printability and stability.

When the pH value is higher than 9.5, the ink viscosity, drying speed and water resistance are reduced; when the pH value is lower than 8.5, water-based ink viscosity increases, enhance the drying speed, partially causing dried ink deposit on the plate and reticulate roller, and that leads to scumming. Water-based ink drying mechanism is shown in Table 4.

Table 4. Water-based ink drying mechanism

| | |
|---|---|
| Water and solvent volatilization. | |
| Removal of amine |  |
| Removal of water |  |

**Viscosity**

Viscosity is the macro performance of ink cohesion, it is a physical attribute that represent the characterization of fluid molecules attraction which hinders the motion of the molecular.

Viscosity directly affects the quality of printing products [15]. If the viscosity is too low, defects such as color dodge, dot gain, image blur may occur; if the viscosity is too high, problems such as poorly anilox roller ink delivery, uneven ink dispersion, filling in, scumming and poorly printability might occur. Flexographic printing ink viscosity is low, the range of viscosity of commonly used flexographic printing ink is 0.15~0.3Pa • s (25℃). An optimal covering ink viscosity for scratch-type invoice covering region printing is not recommended here, but we strongly suggest that ink viscosity be taken into consideration when evaluate the overall performance of the test ink.

**Overall Evaluation and Rating System**

Due to environmentally friendliness, water-based ink has been explored and developed by numerous researchers and institutions. But not all the water-based inks developed are fit for the requirements. Pre-test of the prepared ink before put into use is fundamentally important. If an inappropriate ink come out of the laboratory and put into mass production, huge damage might occur both financially and environmentally.

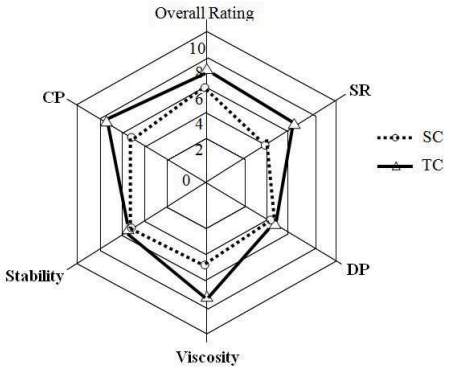



Fig. 3. Core profile of overall evaluation and rating system

During the experiment, in order to grantee all the inks developed meet all the requirements, an overall evaluation and rating system(Fig.3) has been developed based on the standard acquired by the ink research and development laboratory, Beijing Institute of Graphic Communication. For each parameter, the higher the value is, the better performance can be achieved. The rating system proves to be feasible and can be applied in the development of other water-based inks. In Fig.3, the SC(standard curve) is the standard requirements for the testing ink, if the TC(testing curve) is within SC, it indicates that the testing sample has to be improved before put into use; if the TC is outside of the SC, it meets all the requirements and may put into practice. The TC in Fig.3 is one of the water-based covering ink developed, the TC shows that it meets all the requirements and has a overall rating score of 8 out of 10. Additional experiments have proved its practice use feasibility, which is in accord with Fig.3.

## Further Research

Water-based ink is environmentally friendly printing material, and its application in practice has already made great contribution to the environment protection. However, the demand for new variety of water-based ink exceeds supply and existing water-based inks may have certain kinds of defects. So the research on water-based covering ink and its application in scratch-type invoice printing might be counted as the incipient work on how to explore and evaluate water-based ink. Further research on develop new types of water-based inks and improvement of their overall performance is due to carry out.

## Acknowledgement

This research was financially supported by the Innovation Ability Enhancement Project of Beijing"TJSHG201310015015".

## References

[1] D.Z. Zhou, S.M. Song, C.Dong, Water-based ink development review (in Chinese), J. Chem.Technol. Market. 2007(12):6-10.

[2] L.L. Lou, P.P. Jiang, J.L. Xia, Water-based ink research status (in Chinese), J. Chem. new Mater. 2013(1):9-11+17.

[3] X.L. Xin, Y.N. Wei. Water-based ink review (in Chinese), J. Chin. Printing and Packaging Res. 2011(3):1-8.

[4] Y.Chen, L.N. Li, C.Q. Yang, Countermeasures of priority control of toxic VOC air pollutants (in Chinese), J. Environ. Sci. 2011(12):3469-3475.

[5] L.C. Wang, Green road for printing inks (in Chinese), J. Today's printing. 2011(3):37-38.

[6] J.M. Sun, X.F. Wei, B.Q. Huang, Research on the Color Stability of Edible Ink-jet Ink, in Green Printing and Packaging Materials, O.Y. Yun, X. Min, Y. Li, Editors. 2012. p. 85-88.

[7] L.Y. Ma, T.Y. Hao, A Print Performance Study of the Environmental Friendly Wide Gamut Process Inks, in Advances in Printing and Packaging Technologies, O.Y. Yun, et al., Editors. 2013. p. 119-122.

[8] L.H. Li, et al., Research on Environment-Friendly Ink and Fine Chemicals, in Green Printing and Packaging Materials, O.Y. Yun, X. Min, Y. Li, Editors. 2012. p. 48-51.

[9] Y.Z. Chen, X. Wang, Study on preparation of environment-friendly soy-based printing ink. Second International Papermaking and Environment Conference, Proceeding, Books A and B, L. Wang, et al., Editors. 2008. p928-932.

[10] D.D. Wang, B.Q. Qing, X.F. Wei, Study on the dispersity of black water-based covering Ink (in Chinese), J. J. of Beijing Inst. of graphic Commun. 2012(6):32-34.

[11] X.X. Xing, J.P. Wang, Flexible Printing Technology Development Trend (in Chinese), J. Today's printing. 2008(6):33-36.

[12] J.L. Huang, Flexo printing market and some issues of its technology (in Chinese), Xiamen University Press, 2006.

[13] J.J. Tan, Flexible printing technology in our country: present situation and development trend (in Chinese), J. Today's printing. 2001(6):69-72.

[14] Q.Ling, Prize bill covering ink printing technique (in Chinese), J. Printing Qual. and standardization. 2008(3):22-26.

[15]L.Cao, D.W. Liu, Green Printing and Ink Standard (in Chinese), J. Shanghai packaging. 2013(4):35-37.

*Advanced Materials Research Vol. 937 (2014) pp 515-519*
*© (2014) Trans Tech Publications, Switzerland*
*doi:10.4028/www.scientific.net/AMR.937.515*

# Study on Reuse of Power Lithium Ion Battery Recycling

Yi-xia LI [1,a], Rui-lian GUO [2,b],Yan-qin ZHANG[3,c *] and Da-sen Zhou [4,d]

[1,2]The Pilot College of Beijing University of Technology

[3,4]Environment and Energy College of Beijing University of technology

[a]Liyixia824@163.com, [b]ruilianguo@126.com, [c] zhangyanqin@bjut.edu.cn, [d] zhouds@bjut.edu.cn

Yixia Li

**Keywords:** The waste lithium ion battery; cathode material; recycling;

**Abstract.**This paper takes the waste lithium ion battery materials, lithium, cobalt metal recovery of cathode materials, the anode sheet and method makes the volatile burning binder, water brush technique separates powder materials and aluminum foil; then with sulfuric acid and hydrogen peroxide system makes lithium, cobalt black slag with ion dissolving status the leaching liquid obtained by precipitation, cobalt and lithium carbonate products.

## Introduction

With the development of clean energy vehicles, vehicle power system from the original fuel engine now mixed electric and pure electric direction, appeared as power battery, the lithium ion battery development has great potential as an example, the cathode materials for lithium ion batteries of cobalt and lithium due to high prices, resource scarcity, is the recovery value. In addition, metal as an anode current collector foil is also a recovery value [1]. Resource recovery for these batteries, not only can reduce the waste battery pollution on the environment, bring significant environmental benefits, but also the waste batteries are fully recovery of valuable components using, and then produce the enormous economic benefits, at the same time to respond positively to the national development strategy of circular economy development, the construction of a conservation-oriented society.

According the previous study using single waste lithium battery, in particular object to mobile phone battery, including non-ferrous metal single scale, confined to the laboratory stage, the use of medicament is too expensive, the acid consumption of alkali, preprocessing scheme is complicated and the effect is not obvious, the industrial application prospect. This paper studies the advantage of the sample using the power lithium ion battery used now on the vehicle, remove the shell by hand, battery material classification, the anode material can be obtained by lithium battery core. The purpose of this study is to increase for the mixed electric vehicle and electric vehicle number, provide the basis of various non-ferrous metal comprehensive recovery of follow-up industrial waste lithium battery scrap batteries large in.

## Test

### Experimental Materials

The two cell types used in the experiments: one is from the electric bicycle cobalt acid lithium battery (voltage is 3.5 × 7=24.5V, current 10mA) is show in figure 1 is a single battery, the other is from a power cobalt acid battery BYD car (DA02-F15-FE-646-02842) a single power-saving pressure 3.2V is show in figure 2. Lithium ion battery outer layer is a plastic, aluminum, iron shell package, inner layer is divided into a positive active material, a negative electrode active material, aluminum or copper foil collector, bonding agent and polyethylene or polypropylene porous membrane materials, electrolyte (polycarbonate organic solvent) electrolyte salts and dissolved (usually LiPF6) etc.

Lithium ion battery components, complex structure, which belongs to the dangerous goods, may have a short circuit, discharge, electrolyte and water, air reaction and a series of physical and chemical change produces a lot of gas explosion or broken or heating process, so we must first discharge to reduce its risk, dissociate and crushing process should be carried out in a closed system, and make good explosion-proof and antigas security measures.



Fig. 1. Cobalt acid lithium battery



Fig. 2. BYD Cobalt acid lithium battery

**Process Flow**

The positive plate burning fire method will get the dismantling of binder volatile, water brush technique separates powder materials and aluminum foil; then with sulfuric acid and hydrogen peroxide system makes lithium, chrome black slag with ion dissolving status, leaching solution by addition of ammonium oxalate and sodium carbonate precipitation to cobalt and lithium carbonate products. The main flow chart disassembly process is shown in Figure 3 recovery work.

**Results and Analysis**

Positive cobalt acid lithium and aluminum foil desorption

Previous experiments will be positive plate active material and fluid separation are mainly in the following 3 ways:

High temperature decomposition or dissolution of binder [2];

Dissolved in fluid [3, 4];

Damage contact interface [5].

Dissolution is to separate the aluminum foil and the cathode materials used can dissolve the binder PVDF solvent DMF, DMAC and NMP, This experiment take burning way burn binder, two methods of comparative conclusions: first, the solvent method is complicated, desorption time is long, after using the solvent by distillation recycling, recycling processes; burning hair good temperature control for 10 minutes can makes the binder volatile in the 500 ºC, short time energy consumption; Second, the solution method of solvent desorption in standing for more than 4 hours to clear the filter filtration loss is minimum, and the filter directly when solution appear black greatly attached on the filter paper, filter time is long; burning after the water brush desorption aluminum powder filter filtrate faster, not cloudy. Show in Fig. 4 Show in Fig a is Solvent leaching after standing for 4 hours after the filter; Show in Fig b is Solvent leaching after direct filtration; Show in Fig c is Burning with water after cleaning the direct filtration .Comparison of several kinds of leaching solution; Third, a binder component filter solvent powder, therefore in dry products also have residues, makes the product caking dry, affect the next water soluble effect and further recovery; and the binder burn samples were sufficiently volatile, filtration velocity, and drying products powder, have conducive to recovery the next step in the use of. Comparing drying products is show in Figure 5. Show in Fig d is Black residue solvent drying method; Show in Fig e is Black residue burning drying method.

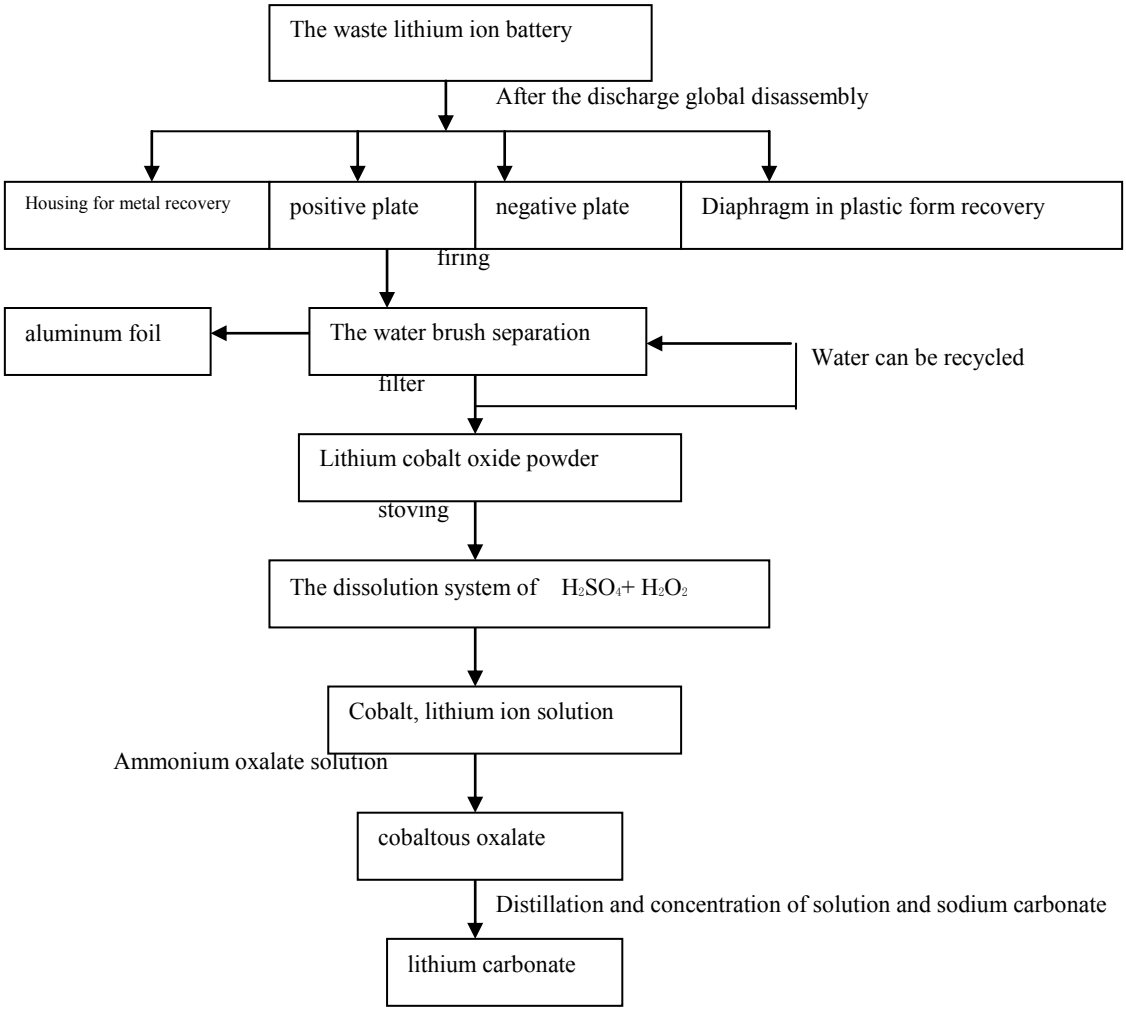



Fig. 3. The main process of recovery work

To sum up, burning method desorption collector than solvent method in energy consumption and process length were dominant, and conducive to the realization of industrialization. Anode desorption in addition to water washing also can choose dry brush, dry brush time and intensity and water brush similar, but taking into account the dry dust pollution when the brush or conservative water brush, then according to the cathode copper recovery may take the same way of recovering copper. Show in Figure 6 and Figure 7 is compared to water brush and a dry brush effect (the same time and intensity).



Fig a Fig b Fig c

Fig. 4. Three kinds of contrast figure of the leach solution (Fig a :Solvent leaching after standing for 4 hours after the filter; Fig b:Solvent leaching after direct filtration; Fig c:Burning with water after cleaning the direct filtration)



fig d



fig e

Fig. 5. Drying product comparison(fig d:Black residue solvent drying method ;fig e:Black residue burning drying method)



Fig. 6. Water brush cathode material effect Cathode material in the form of ions dissolved

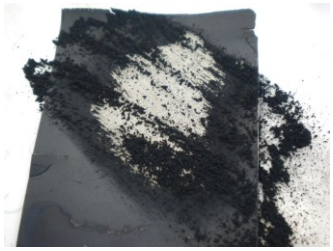


Fig. 7. Dry brush cathode material effect

Get a further material dissolving leaching make various metal electrode in solution. The cobalt and lithium respectively by $Co^{2+}$, $Li^{2+}$ form. The metal elements in leaching liquid separation and recovery or the solution of direct synthesis of cathode materials. Acid dissolving leaching used electrode material dissolving leaching electrode materials will be processed after the first step is the key of separation and recovery technology. $LiCoO_2$ is an important substance in the electrode materials dissolved in reducing acid $HNO_3$, HCl, $H_2SO_4$. Three kinds of solvent reaction equation as follows (1, 2, 3):

$$2LiCoO_2 + 8HCl \rightarrow 2LiCl + 2CoCl_2 + 4H_2O + Cl_2\uparrow \quad (1)$$

$$2CiCoO_2 + 8HNO_3 \rightarrow 2LiNO_3 + 2Co(NO_3)_2 + 4H_2O + 2NO_2\uparrow + O_2\uparrow \quad (2)$$

$$4LiCoO_2 + 6H_2SO_4 \rightarrow 2Li_2SO_4 + 4CoSO_4 + 6H_2O + O_2\uparrow \quad (3)$$

As can be seen from, hydrochloric acid and nitric acid to produce a large number of chlorine or nitrogen dioxide and other toxic gases in the leaching process, environmental pollution, poor operating environment, and the price is relatively high; By comparison, sulfuric acid, volatile small, operation environment relatively mild, the price is low, the leaching system have the advantage of. By adding a reducing agent $H_2O_2$ or $Na_2S_2O_3$ as the leaching solution in $H_2SO_4$ solution, so as to avoid the generation of toxic and harmful substances, and the dissolution rate increased to 99.5%, and the reaction rate. Therefore, using $H_2SO_4$+ $H_2O_2$ as the leaching agent. $H_2SO_4$+ $H_2O_2$ as a reaction solvent(4):

$$2LiCoO_2 + 3H_2SO_4 + H_2O_2 \rightarrow Li_2SO_4 + 2CoSO_4 + 4H_2O + O_2\uparrow \quad (4)$$

Black residue experiments above step filtering as sample, adding water, adding sulfuric acid, and then in the process of heating and stirring slowly drops of hydrogen peroxide, 2 hours of reaction time, reaction temperature 60 ℃, sulfuric acid is 2mol/l, hydrogen peroxide for 30%. After the completion of the reaction supernatant, compares the black residue sediment and before, so that the leaching rate.

The precipitation separation of cobalt, lithium ion battery anode material.

After the sulfuric acid and hydrogen peroxide after leaching, the leaching solution with NaOH solution to adjust the pH value to 5, so that the solution of the impurity ions $Al^{3+}$, $Fe^{3+}$ and other impurity ion precipitation, and filter. Oxalate co-precipitation method usually refers to adding a

precipitating agent in solution: M2C2O4 (M=$NH^{4+}$, $K^+$, $Na^+$, $H^+$) preparation of sediment, under certain reaction conditions, adding ammonium oxalate solution saturated to the filtrate, the following reaction(5):

$$CoSO_4 + (NH_4)C_2O_4 \rightarrow CoC_2O_4 \downarrow + (NH_4)_2SO_4 \quad (5)$$

After drying can be cobalt oxalate precipitation of $CoC_2O_4 \cdot 2H_2O$. The main raw materials for preparation of cobalt oxalate cobalt powder can be used in the manufacture of cemented carbide [6].

The leaching filtrate filtered adjust pH value, oxalic acid ammonium saturated solution and adding chemical equivalent, using a magnetic stirrer, thermostatic mixing, reaction time is 1 hours, the reaction temperature 50 ºC, pH 2, ammonium oxalate dosage is 120% of the theoretical amount, the cobalt oxalate precipitation in the drying box drying and weighing. Lithium carbonate as a basic lithium compound, widely used in ceramics, glass, atomic energy, aerospace, military industry and refrigeration, welding, lithium, lithium battery, the controlled fission reactors, metallurgy, casting, medicine and other fields[7].

The ion ratio of the battery anode material, because of lithium in battery anode only cobalt ion content less than 10%, so the leaching solution of lower concentration of cobalt ions, and after the operation, due to the addition of ammonium oxalate solution with lower concentration. And because the lithium carbonate is slightly soluble in water, so in the precipitation of lithium ion money for evaporation and concentration of solution operation.

The lithium ion in the solution, the concentration of solution in step 25% is ideal, using magnetic stirrer temperature mixing, reaction time 1 hours, the reaction conditions of 50 ºC, pH 10, cleaning and drying after the reaction of weighing filter.

## Conclusion

Lithium ion battery cathode materials for lithium ion batteries are the key resources recycling, aluminum foil, cobalt, lithium is the metallic element with economic value. This paper adopts two kinds of collector desorption method, is a method with two DMF solution and heating stirring leaching separation collector and active substance, the other is burning method will binder volatilization at high temperature, And then the aluminum foil and collector scrub with water separation, active substances isolated from the dry cleaning after using $H_2SO_4$+$H_2O$ as the leaching agent in the form of ions on the cobalt and lithium leaching, and then let the cobalt ions in the form of cobalt oxalate precipitation recycling using oxalic acid ammonia leaching solution, using sodium carbonate to lithium to lithium carbonate form precipitation recycling.

## References

[1] Qian Li, Hongxiang Cui, Discarded cell phone lithium ion battery recycling efficiency analysis [ J]. China resources comprehensive utilization, 2007, 25 (5) : 15.In Chinese .

[2] CONTESTABILE M, PANERO S, SCROSATI B. Alaboratory-scale lithium-ion battery recycling process[J]. Journal of Power Sources, 2001, 92(1/2): 65 69.

[3] Fang Wu, Recovery of cobalt from waste lithium ion secondary battery and lithium [J]. Chinese journal of nonferrous metals, 2004, 14(4): 697 701.WU Fang. Recovery of cobalt and lithium from spent lithium- ionsecondary batteries [J]. The Chinese Journal of Nonferrous Metals , 2004 , 14 (4) : 697701.In Chinese.

[4] Junming Nan,Dongmei Han,Xiaoxi Zuo. Recovery of metal values from spent lithium-ion batteries with chemical deposition and solvent extraction[J]. Journal of Power Sources,2005.152:278-284.

[5] Yiping Lu, Zifa Xia, Qiming Fing, Tao Long, Leming Ou, Guofan Zhang. Waste lithium ion battery Cimc fluid and the separation of active material [J]. Chinese journal of nonferrous metals,2007,17(6):997 1001.

[6] Ren L,Wang p p,Han Y S,et al.Synthesis of $CoC_2O_4 \cdot 2H_2O$ nanorods and their thermal decomPosition to $Co_3O_4$ nanoPartieles.Chemical Physics Letters.

[7] Du H L,Wang J Z,Wang B,et al.PreParation of cobalt oxalate Powder swith the presence of a pulsed electromagnetie field.Powder Teehnology,2010,199(2):149-153.

*Advanced Materials Research Vol. 937 (2014) pp 520-525*
*© (2014) Trans Tech Publications, Switzerland*
*doi:10.4028/www.scientific.net/AMR.937.520*

# Safety, Heath, and Environment (SHE) Case for Oil & Gas Operating Company

Wen-juan YUAN[1,a]

[1] School of Engineering and Technology China University of Geosciences Beijing, China

[a]Ellissa.yuan@dnvgl.com

**Keywords:** Safety, Heath, and Environment (SHE) Case, Hazard, Risk Control

**Abstract.** This paper does a comprehensive research on SHE Case definition, objectives, standards, requirements and content involved in Oil & Gas operating company. The SHE case is developed as a demonstration that all necessary work has been carried out to ensure that risks have been reduced to 'As Low As Reasonably Practicable' (ALARP). Through research on SHE case requirements and content, we can see that SHE case can be used to prevent major accident.

## Introduction

A Safety, Health and Environment (SHE) Case is a methodical and auditable document to demonstrate how SHE objectives are being met for a particular facility or activity. The SHE Case is intended to demonstrate that all hazards associated with a particular facility or operation are known and that suitable measures are in-place to manage the risks to a level that is tolerable and 'As Low As Reasonably Practicable'(ALARP). This includes a requirement to ensure compliance with the requirements of SHE standards, State of environmental regulations, and any other relevant stakeholder requirements for SHE management.

The SHE Case will include detailed demonstration of the identification and control of major accident hazards. Major Accident Hazards (MAHs) are those that could result in an incident leading to multiple fatalities, major environmental impact, major asset damage and/or national or international negative impact on company and project reputation.

The SHE Case will also identify non-major accident hazards and demonstrate their control through the SHE management system arrangements in place. The SHE Case is not intended to provide detailed analysis of non-MAHs (hazards which may result in, for example, a Lost Time Incident (LTI) or a Lost Time Accident (LTA) or restricted workday case, or a minor environmental release). However, the SHE Case will describe the SHE Management System and show how this provides for the control and reduction of personnel and environmental hazards. The SHE Case is a key element in meeting the requirements of the Company SHE and Quality Policy for SHE and Quality excellence.

## SHE Case Objectives

The key objectives of a SHE Case are as follows:

- Show that a formal hazard management process has been applied to the design and operation of the plant covering all hazards, risks and environmental aspects associated with the facility or activity. [1]
- Demonstration that a major accident prevention policy (MAPP) and a safety management system (SMS) for implementing it have been put into effect.
- Demonstration that major accident hazards have been identified and that the necessary measures have been taken to prevent such accidents and to limit their consequences for persons and the environment.
- Demonstration that adequate safety and reliability have been incorporated into the design, construction, operation and maintenance of the installation and equipment and infrastructure connected with its operation which are linked to major accident hazards within the establishment.

- Demonstration that on-site emergency plans have been drawn up and supplies information to enable the off-site plan to be drawn up in order to take the necessary measures in the event of a major accident.
- Show that environmental aspects for the facility or activity have been identified, their significance assessed, and suitable arrangements for continuous improvement, where required, are put in place.
- Identify any gaps currently identified in achievement of an acceptable risk level for the MAHs and the actions in place to address these gaps.
- Provide demonstration that suitable arrangements are in-place to meet the relevant requirements of ISO 14001 - Environmental Management Systems [2] and OHSAS 18001 - Occupational Health and Safety Management Systems [3], and
- Provide an effective source of reference on the management of SHE issues for the facility or activity for use by operational personnel.

**SHE Case Standards**

There is no international standard defining requirements for SHE Cases. However, the content of this standard has taken into account guidance on SHE and safety cases provided by:

- UK Health and Safety Executive for Offshore Safety Cases and Onshore Control of Major Accident Hazard (COMAH) Safety Reports; [4]
- Shareholder companies in LNG trains;
- International Association of Drilling Contractors (IADC); and
- National Offshore Petroleum Safety Authority – Australia.

SHE Cases shall contain sufficient information to support the requirements for certification of facilities to ISO 14001 - Environmental Management Systems and OHSAS 18001 - Occupational Health and Safety Management Systems.

**Requirements for SHE Cases**

SHE Cases are required for all facilities and activities where there is a potential for a major accident.

This will include:

*Facility SHE Cases* – SHE Cases shall be developed for all facilities considered as having the potential for a major accident.

*Activity SHE Cases* – Where activities carried out outside a facility are considered to have major accident potential, they shall also be covered by a SHE Case. Managers responsible for such activities are responsible for deciding whether a SHE Case is required. Example activities that might require an activity SHE Case are: helicopter operations, marine operations, and road transport.

The overall structure of SHE Cases required within Oil & Gas Operating Company, and the interfaces between these SHE Cases, is shown in Fig. **1**.

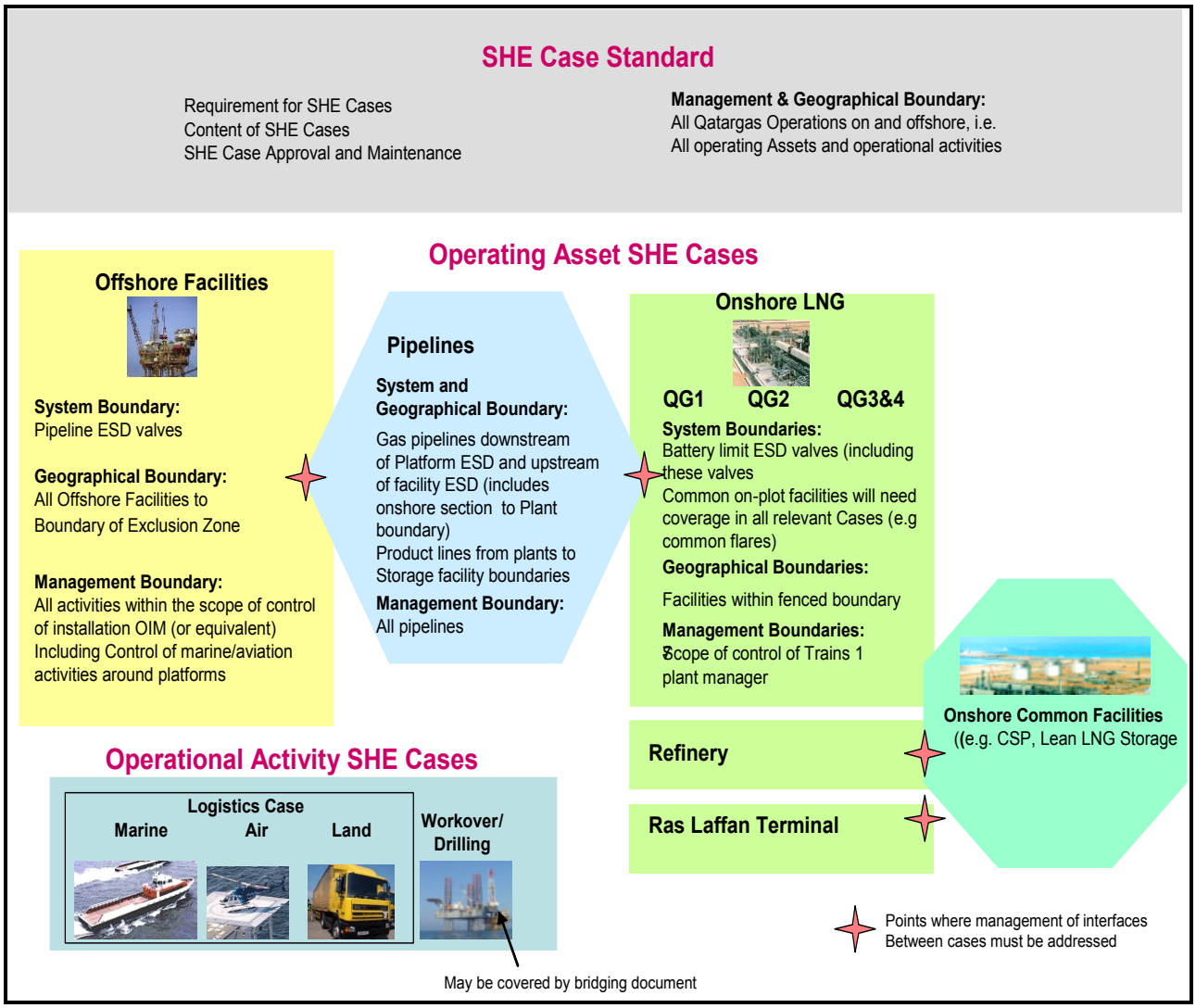



Fig. 1. SHE Case Structure

SHE Cases shall be developed for all facilities with major accident potential over which Company has operational control. SHE Cases shall be created as living documents that will evolve through the lifecycle of the project, addressing the SHE impacts in each lifecycle phase, i.e. project conception, design, operation, and decommissioning/abandonment. It is important to recognize that risk in a project reduces as design decisions are made and as the project progresses. Decisions made at concept selection have a major impact on operational risk. It is vital to ensure that hazard management has been taken into account during the concept stage. As a result, the requirement for SHE Cases starts at the concept selection stage.

Facility SHE Cases shall be prepared at each of the following lifecycle phases:

- Concept selection SHE Case;
- Detailed design SHE Case - typically prepared at completion of design stage of engineering, procurement and construction (EPC);
- Facility or activity operations SHE Case; and
- Decommissioning/disposal SHE Case (optional depending on risk level).

The relationship between SHE Cases at various stages of the lifecycle and the link to Company and shareholder standards is shown in Fig. **2**. This figure will be further developed later in this document to show more detail on these relationships.

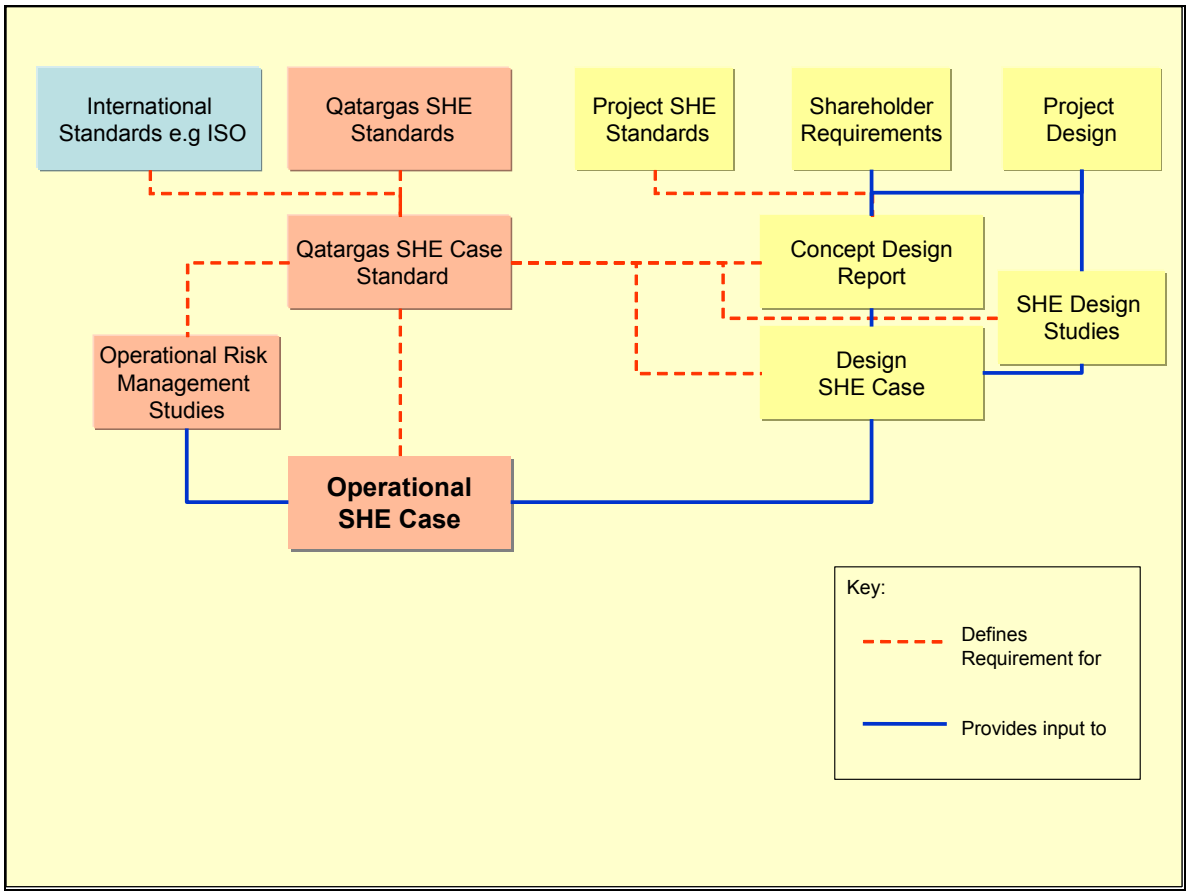



Fig. 2. Relationship between Lifecycle SHE Cases and Standards

## Content of SHE Cases

To meet these objectives, SHE Cases shall include, as a minimum, the content set out in this section. The structure of a SHE Case is not required to follow a precise format, but the presentation shall address the topics shown in Table 1 below in a logical manner.

Table 1. Overview of SHE Case Content

| Topic | Summary of Content |
|---|---|
| *Introduction/Management Summary* | Summary of the structure, content and findings of the SHE Case includes revision record for Case. |
| *Description of the Facility or Activity* | Description of the Facility/Activity, with particular attention being given to description of systems (or, for Activity Cases, systems and procedures) provided to control major hazards. |
| *SHE Management System* | A description of the SHE Management System (SHE MS) and Procedures in place to cover the facility/activity. The SHE MS may be included as part of the Case or, where a standard Qatargas SHE Management System applies. This may be referenced in the Case, with a statement to note any specific issues relevant to the facility/activity covered by the Case. |

| Topic | Summary of Content |
|---|---|
| *Hazard Identification and Assessment* | Hazard Identification and Assessment (Hazard Register). Description of SHE studies carried out, and their conclusions. |
| *Control of Hazards* | Demonstration of the controls in place for identified hazards. Matrix of Permitted Operations. |
| *Risk Levels and Tolerability* | Statement of risk levels involved in the Facility/Activity. Comparison of risk levels with tolerability criteria set out in Qatargas Procedure EHS Risk Acceptance Criteria, and any relevant Project risk acceptance criteria.Demonstration of risk level may need to be quantified, as required by the Qatargas EHS Risk Acceptance Criteria or Project requirements. |
| *ALARP Demonstration* | Risk reduction measures put in place. ALARP Demonstration sheets. Justification that risks are reduced to ALARP. |
| *SHE Critical Tasks and Elements* | Identification of SHE Critical Tasks and Critical Equipment (Elements) and demonstration of how assurance of the quality of the controls provided by these will be assured. |
| *Remedial Action Statement* | Areas where remedial action is required or, for design SHE Cases, risks transferred from design to Operations. These should be linked to risk registers. |
| *Justification for Operation* | Summary statement to justify that risks are tolerable and ALARP, that SHE Case objectives are met. Includes SHE Case Authorizations for use. |

**Summary**

This paper has made a research on SHE case analysis in Oil & Gas Operating Company based on practical using. It is essential that Oil &Gas Operating Company personnel ensure that they have a full understanding of the risks associated with new project facilities. Building the Operational SHE Case plays a vital role in the following areas:

- Proving a common basis to assure that major hazards can be managed effectively;
- Ensuring effective due diligence review of information in differing formats, coming from different project groups;
- Providing opportunity to identify and address conflicting information from different project areas;
- Ensuring that risk transferred from design are recognized and captured in operating procedures and risk registers;
- Ensuring that work on competence assurance and Asset Integrity Management System (AIMS) is properly aligned with major hazard management requirement; and
- Embedding of design basis and hazard management needs into corporate memory.

**Acknowledgement**

I would like to express my appreciation to all those who helped me during the writing of this paper. My sincere gratitude goes first to my supervisor, Professor Luo Yun, who is a warm-hearted, patient man; spend lots of time in guiding and encouraging me. Without his kindly help and instruction, this thesis could not reach its present form. Second, I would like to express my husband, Mr. Yue Weihua, who gives me assistance and kindly support to my research job. Last my thanks would go to colleagues for their strong support and great confidence in my all through these years.

**References**

[1] Frank, E, Bird, Jr, George, L, Germain, and, M, Douglas, Clark. Practical Loss Control Leadership[M]. U.S.A:Det Norske Veritas, 2003. 23-30

[2] ISO 14001:2004 , Environmental management systems -- Requirements with guidance for use[S].

[3] OHSAS 18001:2007 , Occupational health and safety management systems – Requirements[S].

[4] Information on http://www.safety-case.com/

*Advanced Materials Research Vol. 937 (2014) pp 526-530*
*© (2014) Trans Tech Publications, Switzerland*
*doi:10.4028/www.scientific.net/AMR.937.526*

# Design and Development of the Environmental Protection Mobile Enforcement System

Ya-qiong WANG[1, a], Ying-jiong ZHAO [1, b,*]

[1]College of Environmental Science and Engineering,Taiyuan University of Technology,Taiyuan Shanxi,China

[a]13546458466@139.com,[b]18234059798@139.com

*Corresponding author

**Keywords:** the environmental protection mobile enforcement; overall structure; functional design; data management; law enforcing management

**Abstract.** With analyzing the environmental status of law enforcement and job demands, the environmental protection mobile enforcement system was developed based on Android platform and SOA architecture. Using this system, the ability of environmental law enforcement supervision and management was improved, and various environmental administrative law enforcement issues were solved under the limited environmental management resource. Taking Shanxi Province as an example, the environmental protection mobile enforcement system was designed and developed in term of data integration, sharing resources, standardize management and function expansion. This system can been connected to the environmental Internet of Things system which was proved practical.

## Introduction

The Chinese government attaches great importance to environment enforcement and a series of reasonable management system has been formed in daily work. However, there are still several environmental enforcement problems which mainly reflected in weak environmental enforcement, inadequate environmental enforcement means and equipment, unsound environmental enforcement supervision mechanism, and the ability of dealing with emergencies timely and efficiently is not good enough[1]. Aimed at these vulnerabilities, the environmental protection mobile enforcement on the basis of local office network, business network, wireless communication networks, which has arisen at the historic moment by the use of modern communications, database and computer network security technologies. Mobile terminal equipment act as a carrier of the environmental protection mobile enforcement to achieve the goals of dynamic information collected on-site enforcement, relevant standards and record inquiry, decision support and other functions[2]. The system also used to urge the environmental enforcement more standardized, objective, efficient, which greatly improved the effectiveness of environmental monitoring, enforcement, management.

## Overall Architecture of the System

The environmental protection mobile enforcement system bases on SOA architecture, and it mainly includes four parts. Firstly, infrastructure platform and network transmission platform consists of computers, servers, storage, networks and other components; Secondly, environmental protection mobile enforcement terminal which could meet the need of on-site execution; Thirdly, environmental enforcement platform composed by system software, application software; Finaly, environment management database which provide data protection for mobile terminal system and enforcement background support system. In order to gain seamless integration of the system, a multi-level system was used. The interface between the various levels was strictly defined, and design it integrated. Its overall system architecture is shown in Figure 1.

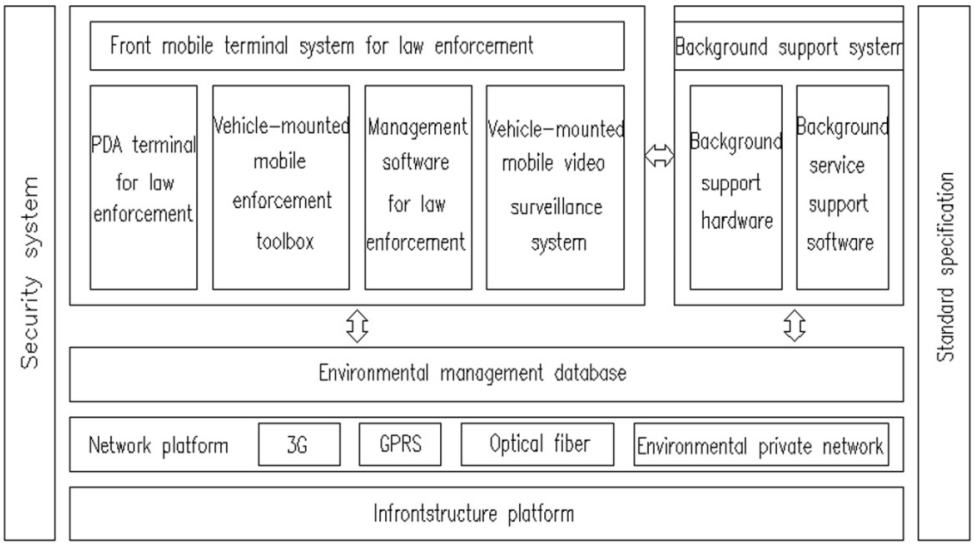



Fig. 1. The overall architecture diagram of the environmental protection mobile enforcement.

## System Requirements Analysis and Function Design

Environmental protection mobile enforcement system was designed in accordance with business requirements of data maintenance and business management by analyzing it's business processes and environmental data. Environmental protection mobile enforcement system has a typical three-tier architecture as the data layer, the intermediate layer and the application layer. The data layer service to requirement of system which includes enterprise data, data sources and data enforcement; The middle layer provides support for system applications by the use of the database management system and GIS platform; Application layer includes basic applications and expanding applications which provide users with dynamic environmental enforcement information collection, relevant standards and record inquiry, decision support and other functions. By analyzing requirements and function design of the domestic environmental protection mobile enforcement, it can be seen that system generally contains data query, mobile enforcement office, personnel positioning and other management functions. It can achieve the general purpose for enhancing the environmental enforcement efficiency and standardize the enforcement. However, most provinces' environmental protection mobile enforcement systems are lack in connecting with environmental monitoring system and database of pollution sources monitoring system, and lack in comprehensive coverage.

## Implementation of Environmental Protection Mobile Enforcement System

The terminal applications of environmental protection mobile enforcement system bases on Android, and use Flex + Blazed + Hibernate as architecture model. Its operating system is Windows2008 Server, database software is Oracle 11g, and application Server is Apache Tomcat 6.0. Protection mobile enforcement system is supported by the mobile enforcing client and the background management system[3].

### Mobile Enforcing Client.

Mobile terminal software used in client program to realize the application of environmental protection mobile enforcement was exploited embedded based on Android. Main functions of mobile enforcing client are as follows.

#### Special Maps

Including enterprise distribution and video surveillance monitoring points, special map module is mainly display geographic information of the monitoring enterprise. GIS-based handheld terminal shows the distribution of pollution enterprises, video monitoring and corporate pollution monitoring points, and also the information of monitoring equipment.

**Mobile Command**

Mobile command module act as a means to associate managers with enforcement officers so that offer instrumental support for all types of businesses. Managers use mobile command module to acquaint real-time situation from subordinates and issued instructions to them. They can also use it to summary statistics, deploy staffs, position the enforcement personnel. At the same time , law-enforcement personnel can use this module to view instruction and task execution, report work to the management, check the announcements, and etc. Managers was composed of staffs from environmental departments, and enforcement officers are mainly environmental monitoring enforcement officers.

**Mobile Enforcement**

Environmental enforcement officers can quickly trace the source of pollution by terminals to complete the daily monitoring tasks. Mobile enforcement module make it possible that environmental enforcement personnel obtain enterprise information on the spot and achieve records of investigation at scene of the law enforcement. It can also realize the functions such as multimedia evidence collection, law enforcement, generation and printing of law enforcement form and document, and etc. Mobile enforcement module has 4 branches include on-site inspection, continue services, work records and pollution source information. If the law enforcement can not been once finished, the system provides functions as query and viewing the record of the last time to continue the enforcement procedures. This design would facilitate the completion of enforcement procedures for managers.

**Emergency Command**

Environmental emergency refers to warn accidents and deal with it. Emergency command module enables whole process management of the emergency incident. The procedure start with accident warning alarm, in turn, verification judged, starting the plan, on-site command, accident treatment. When urgent transaction processing finished , law-enforcement personnel can use this system to write accident report and submit it to server. In addition, the system also provides exchange capabilities between pollution dispersion simulation models and real-time information to help the commanders to grasp the scene and handle the environmental accidents accurately efficiently. Emergency Command include four modules as emergency accident alarm receiving, emergency accident analysis, accident emergency disposal and assessment of accident disposal. Pollutant dispersion model is divided into air pollution diffusion simulation analysis model and water pollution diffusion simulation model. Emergency response atmospheric dispersion model includes SLAB, DEGADIS, UDM and other types of physical models. Under suitable conditions, transport and diffusion path of accidental release substances in the environment can be calculated by the model above and conclude the concentration of pollutants in the spatial and temporal distribution. Spatial analysis, data processing and performance capabilities of GIS was used in the water pollution diffusion simulation model. 1 d / 2 d visualization of the pollution simulation results can been realized by hydraulic calculation combined with the GIS. This is a intuitive performance platform for emergency treatment which can effectively assist emergency decision.

**Monitoring Data**

Environmental monitoring data module was applied to view water quality monitoring data, daily air quality, air quality forecasting, PM2.5 monitoring data, on-line monitoring data, state-controlled enterprises wastewater monitoring data, state-controlled enterprises gas emission monitoring data and sewage treatment plant monitoring data. Users can click on the ‘environmental monitoring data’ when login to view all kinds of monitoring data which were acheived from the geographic information system through the the interface. The water quality monitoring data was updated once a week. Users can view the monitoring values on the basis of water quality monitoring parameters such as drainage, spotting and section in this period. Air quality daily published everyday. Online

monitoring data from the the test point including each exhaust vent, waste water discharge, environmental control facilities and video surveillance points were released after an review by the hour every day.

**Integrated Query**

Integrated query module is used to provide law enforcement personnel total query entrance independent of the business processes. This module contain 14 modules that include enterprise basic information, enterprise project information, enterprise pollution information, key pollution sources information, enterprise sewage facilities, illegal record and punishment, complaint query, emergency accident inquiry, contingency plans query, emergency equipment query, dangerous chemicals query, emergency vehicles query, emergency team queryand laws and regulations query. With requirements of the actual job, the emergency material reserve, physical and chemical properties of chemicals, emergency response measures, environmental protection laws and technology standards promulgated by institution of nation and province were prestored in the mobile enforcement system so that they can been viewed at all times and replenished in the background.

**Backstage Support Management Terminal**

Backstage support management terminal can been used to summarize the information from the mobile terminals. Management module was provided by the backstage support management terminal to the managers and law enforcement officers, which similar to the mobile terminal applications. There are three aspects background support functions can be provided by this system. Firstly, online approval management, sewage approval management, pollution sources online monitoring data integration and management, and unexpected accident data integration and management; Secondly, releasing notices, maintenance and management on laws , regulations, operating instructions and job descriptions; Thirdly, query operation log, locate the law enforcement personnel, record enforcement procedures, and user permission management.

**System Features**

Environmental protection mobile enforcement system integrates the relevant data of environmental law enforcement management. Environmental management database is the foundation of the entire environmental protection mobile enforcement system. Effective integration of the environmental data system is difficult, and it is the weakness in putting the environmental protection mobile enforcement systems into operation. There has been some provinces take the lead in establishing environmental internet of things including environmental quality assurance systems, environmental risk prevention system, energy conservation and total control system. By connecting to the environmental quality database, automatical pollution source database and environmental risk source database, and updating data in real time, it was achieved the effective integration of environmental data at the provincial level.

Environmental protection mobile enforcement system summarizes the project's overall environmental management information. Integrating the project approval, project operation, completion acceptance, pollutants discharge licence, pollution charges, administrative penalty, monitoring data and the pollution sources monitoring data, managers could unify the life cycle information management of sources. Based on the above, the law enforcement personnel can achieve comprehensive inquiry by using the law enforcement terminal.

This system strengthen the regulation of the enforcement process. Law enforcement process, law enforcement forms and law enforcement terminology was unified, and responsibility was explicit to avoid the occurrence of ineffective law enforcement. Real-time GPS positioning and law enforcement track recording technology were applied to supervise and manage the environmental law enforcement personnel.

This system established a relatively complete system of environmental emergency. When environmental emergency occurs, a plan could been launched by collecting field data and judging the scene of the accident.

## Conclusion

Environmental protection mobile enforcement system based on advanced mobile technology has been used to realize informatization of environmental protection mobile enforcement. Within limited resources, site enforcement assist of law enforcement system enhance the ability of environmental law enforcement supervision, and make the regulatory environment more standardized and effective. Existing environmental data has been integrated in the environmental protection mobile law enforcement system in Shanxi province. This system that provides reference basis for law enforcement has achieved good results in actual enforcement. It shows the strong practicality of mobile law enforcement system, and the relevant experience could been served as a reference. Environmental law enforcement system of Shanxi province will continue to deepen data integration, speed up data synchronization speeds, improve information resources, and use cloud computing technologies to tap into a deeper applications.

## References

[1] Dangping Zhang,Jianghe Sun:submitted to Resources Economization & Environment(2013)"In Chinese".

[2]Information on http://www.zhb.gov.cn/.

[3] Kai Ni,Haibo Xia:submitted to Journal of Safety Science and Technology(2012)"In Chinese".

*Advanced Materials Research Vol. 937 (2014) pp 531-536*
*© (2014) Trans Tech Publications, Switzerland*
*doi:10.4028/www.scientific.net/AMR.937.531*

# Energy Consumption Performance Study of New Box-shaped Hysteretic Damper

Chao XU [1, a], Yong-feng NIU [1,b] and Yong-xie ZHAO [1,c]

[1]School of Civil Engineering,Jilin Jianzhu University,Changchun,China

[a]tianya880217@126.com, [b] yongxiezhao@163.com, [c]1140416324@qq.com.

*Corresponding author: Yongfeng Niu, tianya880217@126.com

**Keywords :** box-shaped steel ; mild steel damper ; hysteresis curve ; ABAQUS

**Abstract:** To the H-shaped Mild steel damper which has been applied to the market, this paper proposes the opening box dampers were made in material Q235 steel. Studied the influence of the angular size between Webs and vertical direction to the box-shaped Mild steel damper by FEM ABAQUS. The results indicated that under the same rate in the web openings, box dampers has the same yield displacement and hysteresis curves were fuller than H- shaped dampers. With the increase of web and vertical angles, the initial stiffness of the damper box steel and yield strength and yield stiffness of the damper would reduced, but all of these are larger than H -shaped steel dampers; Meanwhile, moment of inertia of box dampers' two webs to Y-axis is larger , which greatly enhancing the stability of the outside plane to the damper, the larger Web angles, the stronger yield strength and the stability of the outside plane.

## Introduction

Earthquake disaster since ancient severely threat to human's survival and development. For example the Tangshan earthquake in 1976, and after 32 years later, the Wenchuan earthquake in 2008, even the Yushu earthquake in 2010, has caused serious personal and property losses. With the improvement of science and technology and people's living standard, the ability of prevent earthquake disasters has been improved, the structure of the damping control technology has get more and more researchers' attention both at home and abroad due to its characteristic of economy applicable energy consumption, simple structure, convenient maintenance, and the better damping effect. so the technology has become an effective method to dissipate earthquake energy.

The method of Earthquake energy dissipation and vibration is controlling the structure expected deformation by setting energy dissipation devices, so that the structure of subject does not occur serious damage under the severe earthquake, in which , the mild steel damper as a reasonable energy dissipater because of its low yield point, the higher flexibility and ductility, the better deformation tracking ability, the lesser effect on its performance by environment and the temperature, and it can absorb a lot of energy in the elastic-plastic deformation process, also low steel cost etc., has on the agenda gradually.

## Mild Steel Damper Material Selection

The mild steel damper is made from steel Q235, material constitutive relation uses ideal elastic-plastic material model , the relevant parameters in Table 1.In the Table 1, $f_y$ is yield stress, $f_b$ is ultimate strength, E is modulus of elasticity, $\varepsilon_y$ is yield strain and $\varepsilon_u$ is ultimate strain.

Table 1. Relevant performance parameters of Q235 steel

| $f_{y(\mathrm{N/mm^2})}$ | $f_{b(\mathrm{N/mm^2})}$ | $E(\mathrm{N/mm^2})$ | $\varepsilon_y$ | $\varepsilon_u$ |
|---|---|---|---|---|
| $235\times10^6$ | $370\times10^6$ | $210\times10^9$ | $1.119\times10^{-3}$ | $4.669\times10^{-3}$ |

## Loading Model

The model test loading model used displacement control loading method, often controlling load though Yield displacement or a percentage of the maximum the maximum displacement between layers. Displacement control loading method can be divided into three types according to the different Load amplitude: variable amplitude loading , amplitude loading and mixing amplitude loading.This article select variable amplitude displacement loading mode, appling horizontal displacement load on the coupling point. For the Fig.1:

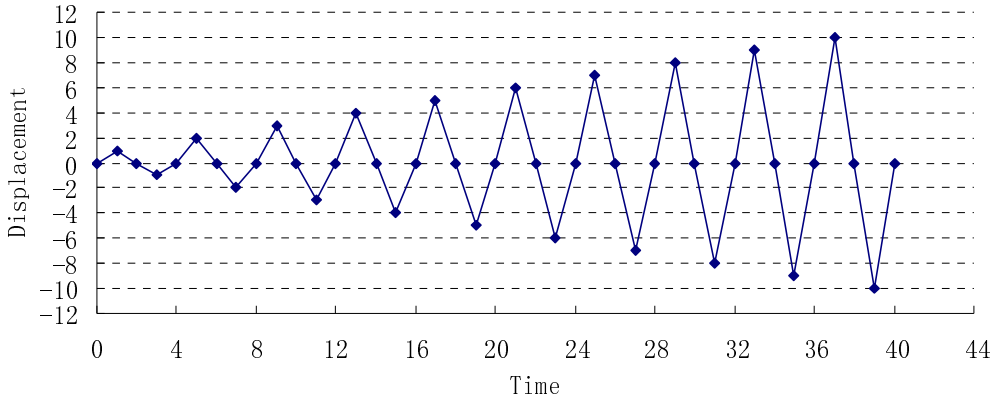



Fig. 1. Displacement control loading method

## H- mild Steel Damper ABAQUS Comparison Experiments

### H- mild Steel Damper Modeling and Analysing

To H- mild steel damper which had been used in practical engineering are made from steel Q235, wide-flange steel model T200 × 204 × 12, a length of 300mm, for the Fig.2:

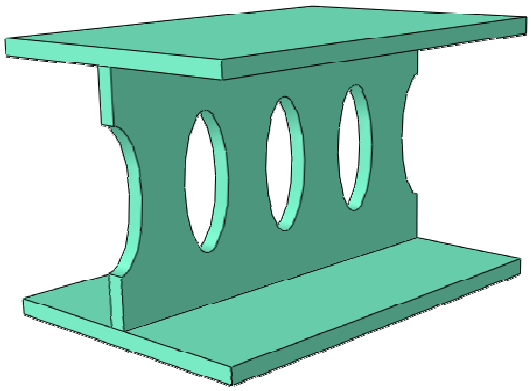


Fig. 2. Schematic diagram of H with perforation types

Selecting variable amplitude displacement loading to this damper in-plane,loading system shown in Fig.1. ABAQUS static test hysteresis curve shown in Fig.3, the results of the analysis are shown in Table 2 .

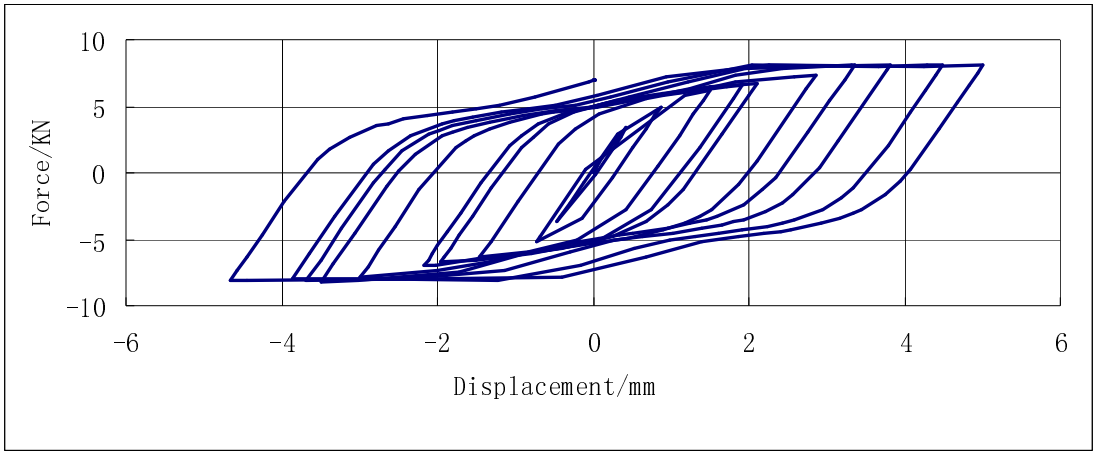



Fig. 3. Hysteresis curve of the H- mild steel damper specimens

Table 2. Numerical analysis result of H- mild steel dampers

| Yield displacement/mm | Yield force/KN | Initial stiffness/$10^3$ KN | Post-yield stiffness /$10^3$ MP |
|---|---|---|---|
| 0.43 | 3.37 | 7.83 | 0.61 |

**H -type Model of Mild Steel Damper Characteristics Analysis**

The above-mentioned analysis shows,H-type steel damper has the general characteristics as other mild steel dampers : low yield point , good flexible scalability , hysteresis curve is full, good energy performance ; but which has a non- overlooked flaws , namely poor stability outside the plane

**ABAQUS Analysis of box- Shaped Mild Steel Dampers**

**Box- mild Steel Damper Modeling**

Under the same conditions as the opening ratio , for outside plane poor stability characteristics to a H-mild steel damper, create the box damper models shown in Fig.4 , take the same total thickness of the web, i.e. the web with 2 × 6 mm. Flange plate thickness and length of the specimen are same to H -type dampers ; constitutive relation of other materials using an ideal elastic-plastic model , the parameters in Table 1.

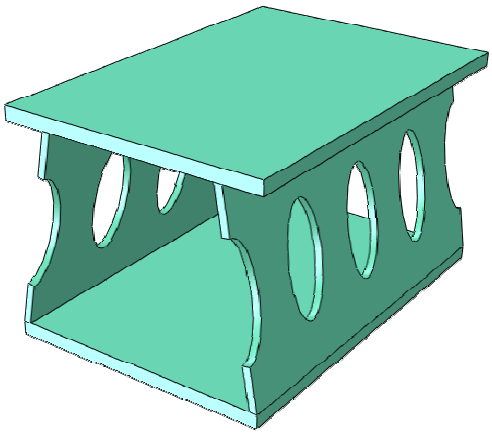


Fig. 4. Schematic diagram of box with perforation types

**Box- mild Steel Damper Designing**

Mild steel damper box made of the same steel Q235,for Fig.5. the dampers are connected to the main frame by a foothold in the shape of “People”(“人”) , which is shown in Fig.6:

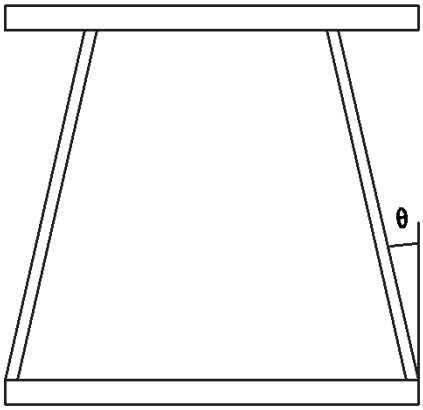



Fig. 5. Box- mild steel damper

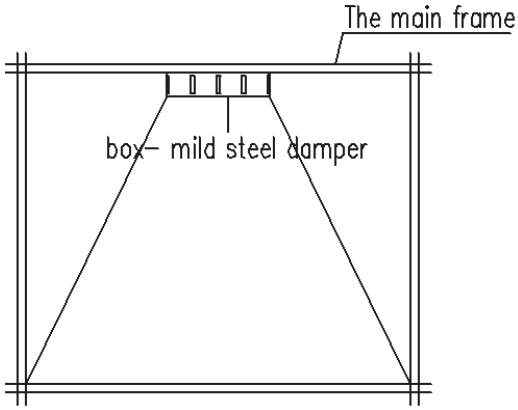



Fig. 6. Box- mild steel damper connection

Figure 5 , θ is the angle between the vertical direction and the web , the paper by changing the size of θ , studying the hysteretic behavior of mild steel damper in-plane and the stability outside plane by ABAQUS, which is divided into four kinds of conditions shown in Table 3 .

Table 3. Design parameters of box damper

| *Specimen No.* | *XMJD 1* | *XMJD 2* | *XMJD 3* | *XMJD 4* |
|---|---|---|---|---|
| Angleθ | 5 | 10 | 15 | 20 |

**Hysteresis Characteristics of the Static Test in-plane ABAQUS Analysis**

Fig.7 shows comparison of the specimen XMJD 1 ~ XMJD 4 hysteresis curves. From the figure shows shape of the four hysteresis curves are full, yield displacement of the four members are 0.43mm, the yield strength and the initial stiffness of XMJD 1 were greater than the other three members, but also greater yield stiffness. Showed that the smaller angle the more energy damper absorbs, the better energy performance. Numerical results are shown in Table 4

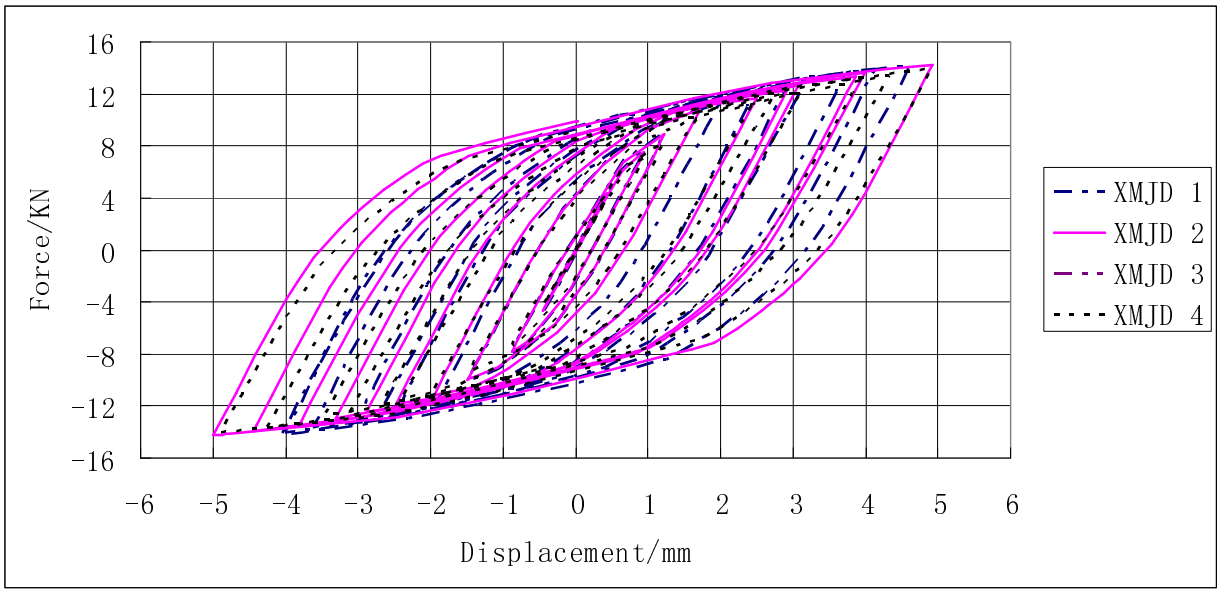



Fig. 7. Different web angles hysteresis curves

Table 4. Numerical analysis result of box- mild steel dampers

| *Specimen No.* | *XMJD 1* | *XMJD 2* | *XMJD 3* | *XMJD 4* |
|---|---|---|---|---|
| Yield force/KN | 4.405 | 4.34 | 4.12 | 4.03 |
| Initial stiffness/$10^3$ KN | 10.24 | 10.09 | 9.58 | 9.37 |
| Post-yield stiffness /$10^3$ MP | 1.02 | 0.98 | 0.97 | 0.96 |

**Outside the Plane Stability Analysis**

Learn from moment of inertia formula ($I_x = \frac{1}{12}bh^3$)and Parallel to the inertia of the shift formula ($I_x = I_{x_c} + a^2 A$) in the Mechanics of materials, the moment of inertia of box section is much larger than H,so increasing the stiffness and stability of the box-section outside plane .We can get the following results when appling outside plane horizontal displacement load on the coupling point. For Fig.8

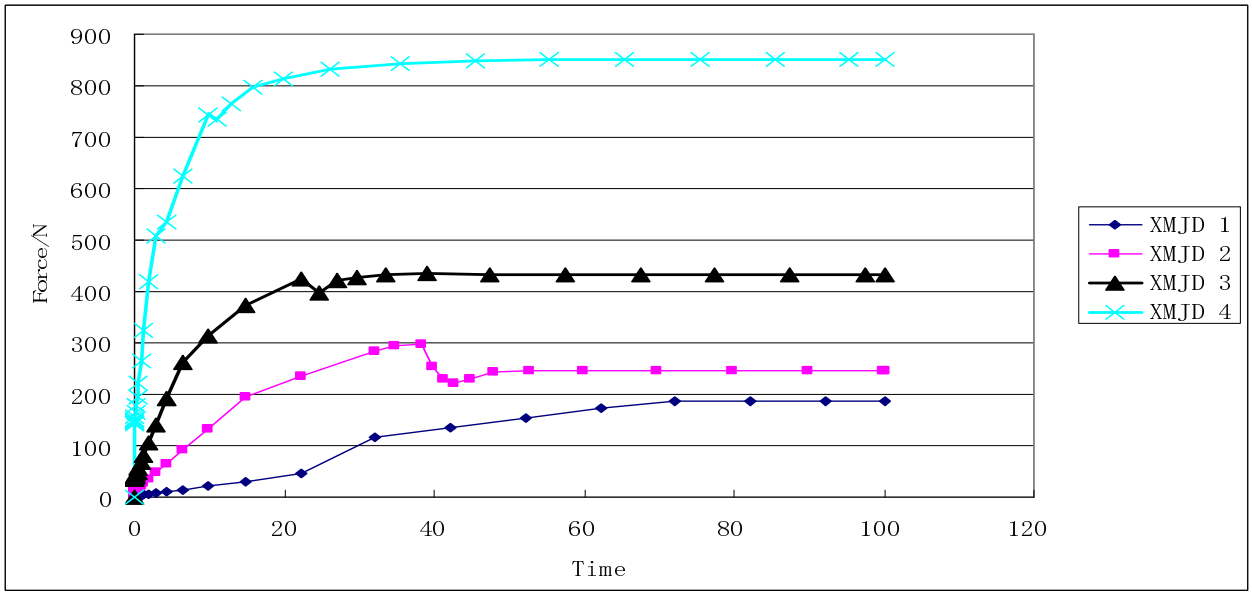



Fig. 8. Box mild steel dampers outside plane stress analysis results

As can be seen from the figure , with the angle between the vertical direction of the web increases, the outside plane yield strength is increasing ;when$\theta$ = 5 , the curve is close to linear force , the enhancement of outside plane stability is not obvious ; when $\theta$ = 20 , the yield strength abruptly increases , significantly enhanced stability .

**Conclusion**

By analysing the new box -shaped steel damper with different size opening , the following conclusions:

(1)The new box-shaped steel damper has small yield displacement, good hysteretic behavior ,energy curves and full, and good energy performance.

(2) Compare with different the size of angle under the same opening, there is no change in the yield displacement ,but the smaller the angle the greater initial stiffness , yield strength , and stiffness post-yield of the specimens, the more full hysteresis curves , the more stable capability of energy performance.

(3) Design Parameters analysed by ABAQUS, compare with H-shaped steel damper which has been used in the real project, under the same external load, box -shaped mild steel dampers have better energy performance , but also the strong outside plane stability, playing a guiding role for the future development of the new type of mild steel damper.

**References**

[1]ZHOU Yun. JINSHU HAONENG JIANZHEN JIEGOU SHEJI[M]WU Han: Wuhan University of Technology Press, 2006: 1(In Chinese).

[2]ZHANG Wenyuan, LI Shuying,LI Dongwei. Simulation analysis on hysteretic behavior and vibration suppression of them ild steel damper with the diamond-shaped opening and added damping and stiffness[J]. World Earthquake Engineering, 2007.3(In Chinese).

[3]ZHANG Wenyuan, ZHANG Minzheng, LI Dongwei. An experimental research on performance and application of a new type ofm ild steel damper added damping and stiffness (ADAS) [J]. Journal of Harbin Institute of Technology. 2008(In Chinese).

[4]LI Jilong, OU Jinping, Damping force hysteresis loop models for X type and triangle mild steel dampers(I)- Based on double linear constitutive model. World Information On Earthquake Engineering, 2004,20(1):10-15(In Chinese).

[5]WANG Shuang. Parametic analysis and seismic performance of new Perforated H-shaped steel damper. Guangzhou university, 2012.5(In Chinese).

*Advanced Materials Research Vol. 937 (2014) pp 537-542*
*© (2014) Trans Tech Publications, Switzerland*
*doi:10.4028/www.scientific.net/AMR.937.537*

# Assessment and Characteristics of Heavy Metal Contaminated Soil in the Vicinity of a Zinc Mine Dump Heaps

Hong WANG[1,2,a], Hai-bo Li[1,2], Xue-dong LV[3], Peng-fei WANG[1,2], Ji-fu MA[1,2]

[1]Key Laboratory of Regional Environment and Eco-Remediation, Ministry of Education, Shenyang University, Shenyang, China

[2] School of environment, Shenyang University, Shenyang, China

[3]Institute of Architectural Engineering, Shenyang University, Shenyang, China

[a] wh51@163.com

**Keywords:** Heavy metal; Smelting slags; Mine dump heaps; Soil pollution; pollution index

**Abstract.** Heavy metal contamination of soils is a widespread and serious enviroment problem in the process of exploitation and utilization of lead-zinc mine. In this study, the distribution, pollution index of lead, cadmium, zinc and copper of the soils near an abandoned zinc mine dump heaps were investigated. The results showed concentrations of Pb, Cd, Zn and Cu in smelting slags averaged at 11950mg/kg, 92mg/kg, 8878mg/kg, and 2129mg/kg respectively, whereas concentrations of heavy metal in adjacent soils exceed the maximum of soil environment. Pb and Cd are main pollutant. All the samples were heavy pollution by the assessment of single-factor pollution index and integrative pollution index. Hheavy metals next to the smelting slags mainly existed in the surface soil (0-20cm). Heavy metasl had lower ability of transforing downwards. The distribution characteristics of heavy metals in farmland was probably relateded to plowing processing, mixing fresh soil and the change of soil pH.

## Introduction

Heavy metals make a significant contribution to environmental pollution as a result of human activities such as mining, smelting, electroplating, energy and fuel production. The mining of heavy metal mineral resources has greatly changed the original soil environmental structure and status [1, 2]. More importantly, the discharge and stacking of mine wastes and slags have potential and long-term pollution and the majior hwavy metals were copper (Cu), lead (Pb), zinc (Zn)and cadmium (Cd). The heavy metal pollution to the soil not only causes some serious damage to the environment, but also causes crop losses and quality decreased which is harmful to human health[3]. The assessment of heavy metal pollution in the soil is a necessary mean to understand the soil pollution status, control and improve the soil environment [4]. Therefore, the heavy metal pollution assessment in the mine soil is very essential.

The northwest area of Guizhou province is one of the most important regions of zinc smelting with indigenous method in China. And the resources of lead-zinc mine and the scale of the indigenous zinc smelting are ranks first in the province.In the process of smelting, a lot of smoke and metallurgical residue contained large amounts of Pb, Cd were produced and a great many of smelting slags though Zinc smelting had been abandoned and formed mine dump heaps.

Much work had been done for the pollutant of mine dump heaps, such as pollutant environment survey, seal processing, the plant absorption of heavy metal[5,6]. However, there is not so much research on the heavy metal transport process, the effect on the farmland around the mine dup heaps. Thus, the primary purpose of this study is to research the polluted characteristics of mine dump heaps and its effect on the farmland in order to provide some information for the innocent treatment of smelting slag and the remediation of farmland.

## Materials and Methods

### Study area and Sampling

A typical Pb-Zn smelting slags dump was chosen for the present study, and the soil samples were collected (0-20cm) from slags dump and varying distances from the center of slags dump, which were showed and described in Table 1 and Fig.1.

Table 1. Sampling site and description

| sampling site | sample description |
|---|---|
| S1 | smelting slags |
| S2 | the soil next to the smelting slags |
| S3 | the soil of waste lands beside the smelting slags |
| S4 | farm land 60m away from smelting slags |
| S5 | farm land 100m away from smelting slags |

The soil samples (0-20cm) of 1 kg were collected and cleaned from stones and twigs, packed in polyethylene bags and properly marked. And for S2, S5, soils of 20-40cm and 40-60cm were collected respectively. The soil in forest park was taken as controlled sample.

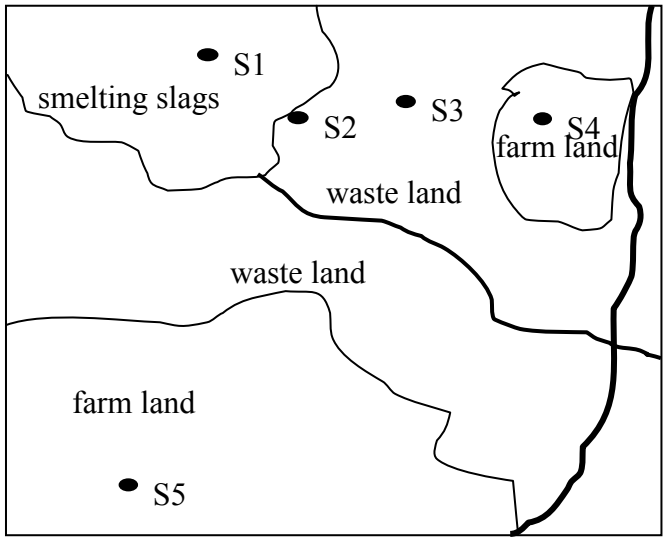



Fig. 1. Map showing the study area and the sampling sites

### Analytical Methods

Soil samples were air dried, homogenized, sieved through 1 mm mesh and stored in polyethylene bags at room temperature. pH was measured in mixture of soil and double distilled water (DDW) with ratio of 1:2.5 (w/v), while SOM was measured according to the method adopted from Lu Rukun[7 ].

For heavy metal determination, soil samples were ground in ball mill to finer than 200 mesh size. About 0.2 g oven dried soil was digested in microwave accelerated reaction (LabTech, Ethos) with a mixture of 2 ml hydrofluoric acid (HF),2 ml hydrochloric acid (HCl) and 6 ml nitric acid ($HNO_3$ ) at 180 °C for complete digestion. When acids were completely evaporated, then 1:1 H $NO_3$ added and the solution was diluted to 100 ml with DDW. Digested soil samples were analyzed for heavy metal by using atomic absorption spectrometer (Analytik Jena, contrAA700). Reagent blanks, 10% duplicated samples and soil standard reference materials were employed to check the accuracy of analysis. All chemicals used in this studywere of analytical grade or better.

## Results and Discussion

### Characteristics of Heavy Metal Pollution

Total concentrations of heavy metals (Pb, Zn, Cd, Cu) and part of soil property in the top soils were showed in Table2.The concentrations of heavy metals in sample 1(smelting slags) were extremely high, and Pb, Zn, Cd, Cu were 11950mg/kg, 8878mg/kg, 92mg/kg and 2126mg/kg respectively, which were as 2395, 54, 16 and 7.5 times as background values of soil. During the process of smelting, a great many of Pb, Zn, Cd were remained in the smelting slag. The Pb/Cd ratio was130 in the smelting slag, while Pb/Cd ratio in local Zn mine was 9.6, which showed much Cd volatilized in to air because of its lower melting point. The smelting slag was alkalescence (pH=7.95) and had higher organic matter. Therefore, heavy metal pollution in the smelting slag was serious, and any smelting slag around farmland and resident was a source of pollution which had enormous direct danger and potential risk.

The mine site has led to significantly different spatial distribution of heavy metals in the surface soil. Take Pb as example, the soil next to the smelting slags (S2) the concentration decreased 59%, was 4880mg/kg. The sample 3 was 4203mg/kg, which was 20-30m away the mine site. In the farmland (S4) the content of Pb was 1257mg/kg, which decreased about 90% compared with the slags. There almost completely are wasteland within 50m surrounding the slags and hardly grew any plant because of serious heavy metal pollution, and with the weathering, floating dust and brushing with rain, the polluted area would be further enlarged.

As to the farmland soils S4 and S5, the content of Pb, Zn, Cd, Cu were 138, 54, 105, 37 times and 14, 6, 12, 3.5 times as that of the background values of soil. The values Pb/Cd and Zn/Cd were lower than slags and higher than that of the background values of soil, which indicate that more cadmium were input into the farmland. With the effect of slags, the pH of farmland was increased to 6.20 and 5.72 from 4.67.

Table 2. Concentrations of heavy metals in various horizontal locations

| | Concentrations of heavy metal （mg/kg） | | | | Soil property | |
|---|---|---|---|---|---|---|
| | Cu | Pb | Cd | Zn | O.M（%） | pH |
| S1 | 2126.61±228.19[a] | 11950.66±928.80 | 91.66±12.12 | 8877.87±982.33 | 20.77±1.87 | 7.95±0.05 |
| S2 | 232.03±12.58 | 4880.18±502.30 | 27.46±3.02 | 4720.42±510.02 | 15.02±1.85 | 7.87±0.02 |
| S3 | 225.12±21.78 | 4203.17±427.47 | 24.82±2.12 | 4396.46±345.21 | 3.02±0.14 | 7.71±0.04 |
| S4 | 202.17±17.87 | 1256.69±145.23 | 10.35±0.98 | 1048.03±87.89 | 3.57±0.24 | 6.20±0.04 |
| S5 | 255.56±16.77 | 360.80±27.87 | 3.75±0.42 | 728.78±65.21 | 1.08±0.09 | 5.72±0.05 |
| CK | 56.97±6.02 | 86.00±9.45 | 0.87±0.01 | 164.06±12.14 | 4.81±0.58 | 4.67±0.07 |

Notes: [a] Values are means ± SE (standard error).

Data from the study were statistically analysed using SPSS program and correlation coefficients illustrating relationship among total content of heavy metals, pH, organic matter are listed in Table3.

Table 3. Correlation analysis of heavy metals and soil property in various horizontal locations

| Items | Cu | Pb | Cd | Zn | O.M | pH |
|---|---|---|---|---|---|---|
| Cu | 1 | 0.879* | 0.945** | 0.80 | 0.78 | 0.13 |
| Pb | | 1 | 0.986** | 0.987* | 0.88* | 0.58 |
| Cd | | | 1 | 0.947** | 0.87* | 0.44 |
| Zn | | | | 1 | 0.86* | 0.69 |
| O.M | | | | | 1 | 0.45 |
| pH | | | | | | 1 |

Notes:**Significant different($P<0.01$); *$P<0.05$

Regression coefficients presented show strongly significant relationships between organic matter and Pb(r= 0.88,P<0.05), Cd(r= 0.87,P<0.05),Cu(r=0.86, P<0.05). Strong positive correlation (P<0.01) was also recorded between Cd and Cu, between Pb and Cd and between Pb and Cu. It is generally thought that heavy metal derived form the same source had correlation with each other. And it also showed that heavy metal content was due to the pollution of smelting and the secondary pollution of smelting slags.

**Assessment of Soil Contamination**

The single-factor pollution index (Pi) and the integrative pollution index(PN) were employed to evaluate the environmental quality of the contaminated soils. The calculation of the single-factor pollution index method can be expressed as:

$$Pi=Ci/Si. \quad (1)$$

and the mathematical formula of the integrative pollution index method is:

$$P_N=\sqrt{\frac{\left(\frac{1}{n}\sum_{i=1}^{n}P_i\right)^2+\left[\max\left(P_i\right)\right]^2}{2}} \quad (2)$$

where Ci is the heavy metal content in a soil sample(mg/kg). Si is the permitted standard (grade Ⅱ) of China Environmental Quality Standard for Soils(GB15612-1995). Environmental quality standard for soil and the soil background value of local area were shown in Table4.

The single-factor pollution index can be estimated unpolluted (Pi<1), slight pollution (1<Pi<2), moderate pollution (2<Pi<3) and heavy pollution (Pi>3). Soil was heavy pollution with the integrative pollution index ($P_N$>3).

The result in Table 5 showed that almost all of the calculated Pi values for heavy metals under study exceed 1 though the higher assessment criterion (grade Ⅲ). Cd pollution is the most serious and the following were Zn and Pb. Even in the farmland, only Cu wasn't achieved pollution level. As to integrative pollution index($P_N$), every sample exceeded 4, which was heavy pollution even including farmland. Therefore, it is recommended that farmers should not grow agricultural foods unless remediated.

Table 4. Environmental quality standard for soil and Soil Background value

| | | Cu | Pb | Cd | Zn |
|---|---|---|---|---|---|
| Environmental quality standard for soil | grade Ⅰ | ≤35 | ≤35.00 | ≤0.20 | ≤100.00 |
| | grade Ⅱ | ≤50 | ≤250.00 | ≤0.30 | ≤150.00 |
| | grade Ⅲ | ≤400 | ≤500.00 | ≤1.00 | ≤500.00 |
| Soil Background value of local area | | 32.00 | 35.20 | 0.66 | 99.50 |

Table 5. Environmental quality index of heavy metals

| Soil mumber | S1 | S2 | S3 | S4 | S5 |
|---|---|---|---|---|---|
| Cu-Pi | 5.32 | 0.58 | 0.56 | 0.51 | 0.64 |
| Pb-Pi | 23.90 | 9.76 | 8.41 | 2.51 | 0.72 |
| Cd-Pi | 91.66 | 27.46 | 24.82 | 10.35 | 3.75 |
| Zn-Pi | 17.75 | 9.44 | 8.79 | 2.10 | 1.46 |
| $P_N$ | 102.65 | 31.65 | 28.59 | 11.56 | 4.34 |

## Concentrations of Heavy Metal in Soil Profile

Sample 2 and Sample 5 were selected to analyze the content of heavy metal of different layer (0-60cm) and the results were shown in Fig.2 . We could know that the concentration of heavy metal in the surface (0-20cm) of sample 2 was significantly higher than that in the layer of 20-60cm. For example, in the surface soil the concentration of Cd and Pb were 91.66 mg/kg and 11950.66mg/kg, while in 20-40cm layer the concentration of Cd and Pb were7.48 mg/kg and 465.59 mg/kg, which had decreased over 90%. However, in 40-60cm layer the decreased rate were 36.5% and 5.1%.

The soil next to the smelting slags was mainly polluted by the process of smelting and the exist of smelting slags whose pollution effect was continuous, especially the surface soil. The pollution of subsurface soil probably came from the vertical transfer of heavy metal with the action of rainfall and runoff. Consistently, the migration of heavy metal is limited because of the properties of soil and heavy metal itself, which was the reason the huge difference in pollution degree between surface soil and subsurface soil.

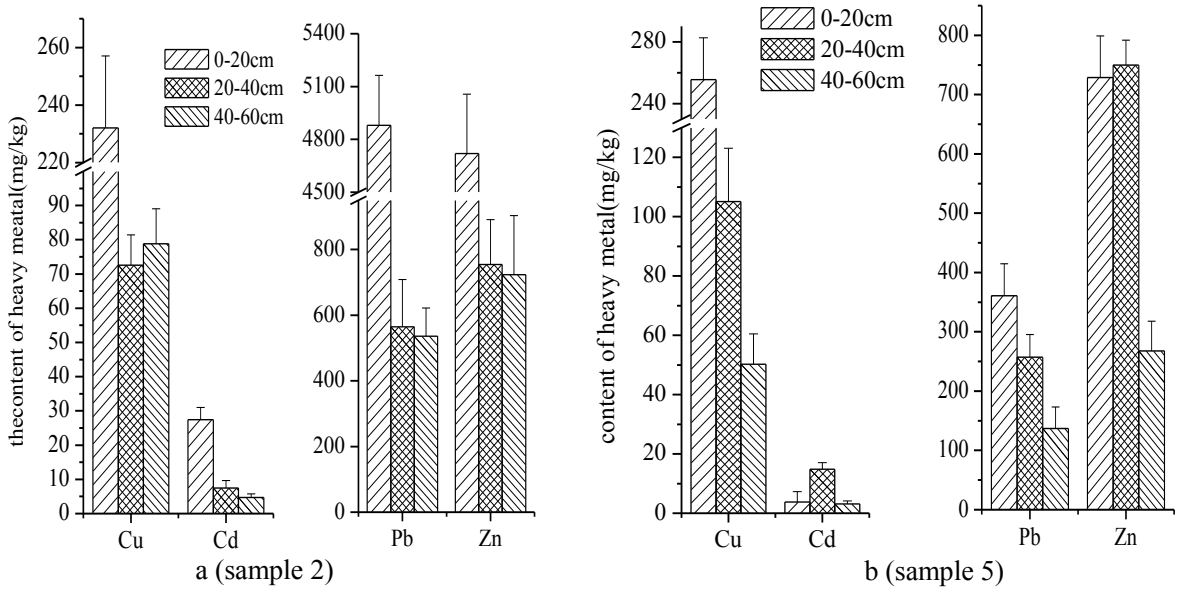



Fig. 2. Concentrations of Pb, Cd, Zn, and Cu in soil profile

For the farmland soil (S5), Cu and Pb content variation similar. The main concentration of heavy metal is in the soil surface and their contents to the deep decline. The concentrations in 40-60cm were close to the soil background values. In the context of 0-20cm and 20-40cm, the concentrations of Zn were similar, 728.78 mg/kg and 749.68mg/kg. The maximum concentrations of C0d were in the layer of 20-40cm, which was 4 times and 4.8 times than that of the adjacent soils respectively. This indicates that during the plowing processing, the soil was violently disturbed or the fresh soil of other places was poured into. On the other hand, some research was showed that the ability of Cd transfer is enhanced with the lowering of the pH value[8]. In this area, pH of the soil background values is 4.67, so the ability of Cd transfer probably increased and caused the special variation of Cd concentration.

## Conclusion

(1) A large amount of heavy metal remained in the smelting slags due to Zinc smelting with indigenous method. Soil samples collected from near mine dump heaps were heavily contaminated by Pb, Zn, Cd, and Cu.

(2) Pb and Cd were maily pollutant in the farmland. It is recommended that farmers should not grow agricultural foods unless remediated.

(3) The content of heavy metal was due to the pollution of smelting and the secondary pollution of smelting slags. The smelting slags have enormous enviroment risk.

**Acknowledgment**

This work was financially supported by the Major Science and Technology Project of Guizhou Province(2012-6014), Shenyang science and technology project (F13-305-4-00) and the Competitive selection project of Shenyang scientific undertaking.

**Reference**

[1] C Y Wei, C Wang, L S Yang. Characterizing spatial distribution and sources of heavy metals in the soils from mining-smelting activities in Shuikoushan, Hunan Province, China Journal of Environmental Sciences, 2009,21:1230–1236.

[2] Y G Yang, C Q Liu, P Wu, G P Zhang, W H Zhu. Zinc smelting –an important factor leading to heavy metal accumulation in soils and sediments in Hezhang country ,Guizhou Province. Acta Mineralogica Sinica, 2003,23(3): 255-272.

[3] X M Liu, J J Wu, J M Xu, Characterizing the risk assess-ment of heavy metals and sampling uncertainty analysis in paddy field by geostatistics and GIS. Environmental Pollution, 2006,141(2): 257–264.

[4] Rawlins B G, Lark R M, Webster R, O'Donnell K E. The use of soil survey data to determine the magnitude and extent of historic metal deposition related to atmospheric smelter emissions across Humberside, UK. Environmental Pollution, 2006, 143(3): 416–426.

[5] Z Q Wu, S Y Gu, H Y Li, H Wu. Research on the heavy metal contamination and bioavailability of contaminated soils in Pb-Zn mining areas of northwestern Guizhou Province. Safety and Environmental Engineering, 2009, 16(3): 1-5,17.

[6] H Y Li, S Y Gu, Z Q Wu, Z Wang. The polluted situation of heavy metals in Pb-Zn mining area of northwest of Guizhou Province and the evaluation of environmental impaction. Environmental Monitoring in China, 2009,25(1): 55-59.

[7] R K Lun. Soil Agricultural Chemistry Analysis. China Agricultual Science and Technology Press.

[8] Jin C X, Zhou Q X. Characteristics of cadmium transfer between soil-water interface affected by pH. Journal of Shenyang Jianzhu University (Natural Science), 2006, 22(4): 626-628,652.

*Advanced Materials Research Vol. 937 (2014) pp 543-547*
*© (2014) Trans Tech Publications, Switzerland*
*doi:10.4028/www.scientific.net/AMR.937.543*

# Application of the Head-tail Method to Determine Irrigation Coefficient in Hongguang Irrigation District

Feng-lin ZUO[1,a], Wei-hua ZHANG [1], Juan GAO[2,b],Xiao-lan BAI[1], Jin-hua NONG[1], Hai-qiang ZHAO[1], Mei-quan ZHONG[1]

[1] College of Resources and Environment, Southwest University, Chongqing, China

[a]541747690@qq.com,[*]Corresponding author:swuwater@126.com

[2]Liangping Water Management Station, Chongqing, China, [b]422753010@qq.com

**Keywords**: Irrigation district, irrigation coefficient, the Head-tail method.

**Abstract**. Irrigation coefficient is not only a critical criterion of the efficiency of agricultural water use, but also an important basis for the evaluation of regional water-saving scheme. According to the Head-tail method (measured net irrigation water use and gross irrigation water use), the irrigation coefficient of Hongguang irrigation district was determined in this paper. The results showed that this method well fitted the real situation of Hongguang irrigation district, and had several advantages including conceptually clear, convenient to use by local staffs. Practical application of this method in irrigation district provides good reference for the future routine evaluation of irrigation efficiency in irrigation.

## Introduction

The irrigation coefficient is a particular ratio of the net applied water used by crops and total irrigation water from head canal to end user within a certain time. It is a characterization of indicators, related to natural conditions, project status, water management and so on [1]. Scientifically measuring and analyzing the irrigation coefficient is important, because it is closely related to evaluation of water-saving irrigation development and analysis of water-saving potential.

## Description of the Study Area

Liangping County located in the northeast of Chongqing Municipality, is one of the national commodity grain base counties. Hongguang irrigation district is a small irrigation scheme in Mingda Town of Liangping County, with a design irrigation area of 475.7 hectares and effective irrigation area of 247.9 hectares. The soil type is clay and irrigated by gravity water diversion. The size of the cross-section of main canal is 1.8×1.2m and the design flow is $1.2 m^3/s$ .It's the most representative irrigation district in north of Liangping County, and one of the municipal sample irrigation area as well. The proportion of crop plantation is 20% corn, 60% rice, 9% vegetables and other crops.

## Methodology

Based on the definition of the irrigation coefficient, the Head-tail method calculates the final water for crop (net irrigation quota) and the total irrigation water from head canal. The ratio is the irrigation coefficient [2]. The formula is as follows:

$$\eta_W = \frac{W_j}{W_t} \tag{1}$$

Where: $\eta_W$ is the irrigation coefficient in irrigation area; $W_j$ is the net applied water in $m^3$ ; $W_t$ is the total gross irrigation water in $m^3$ .

**Selection of Typical Plots**

Typical plots were selected according to the following criteria: medium size, with clear boundary, regular shape, slope of field, representative soil types, groundwater level, climatic conditions, irrigation practices and other related factors. Based on the above principles, we chose two rice terraces and two corn plots for study.

**b. Determination of the total gross irrigation water**

Total gross irrigation water $W_t$ is the total amount of water used for irrigation throughout the year from water sources. Its value is equal to the total amount of water minus the channel discarded water as the project protection, flood control channels and other needs, also minus irrigation return flow to the outside and other non-agricultural irrigation water [3]. The total gross irrigation water of Hongguang irrigation is $1.59\times10^6 m^3$ by real-time monitoring and query data.

**Calculation of the net Applied Water**

**Calculation of the net Applied Water Per Ha of Typical Plots**

The estimates are calculated using the direct measurement. Dry crop irrigation amount is calculated as:

$$W_{j'} = \frac{\gamma}{\gamma_w} H\left(\theta_{g2} - \theta_{g1}\right) \tag{2}$$

where： $W_{j'}$ is the net applied water per ha of typical plots in a certain time, $m^3/ha$； H is the typical plot's plan moist layer of water in irrigation period, mm; $\gamma$ is soil dry weight in the typical plot's H layer $g/cm^3$; $\gamma_w$ is water density, and generally take 1, $g/cm^3$; $\theta_{g1}$, $\theta_{g2}$ is the typical plot's gravimetric soil moisture in H layer before and after a particular irrigation,%. The kind of rice is moist in Hongguang irrigation.

**The net Applied Water in Irrigated Sample Estimates**

According to the results of observation and analysis, annual average ha the net applied water of typical plots is obtained. Computational formula as follows:

$$W_j = \sum_i^N W_{j'} \bullet A_i \tag{3}$$

Where: $W_j$ is the net applied water in $m^3$; $W_{j'}$ is the net applied water per ha of typical plots in a certain time in $m^3/ha$; $A_i$ is actual irrigation area in samples irrigation's number i crop, ha; N is total irrigated crop species.

**Meteorological Data Analysis**

According to data of the bureau of meteorology in Liangping County, the amount of precipitation in the county in 2013 is 1331mm.Compared with the annual average precipitation of 1281mm.However the distribution of the rainfall is uneven-with most the rain falls from April to Semptember.$7.04\times10^6 m^3$ had been used to irrigate the farmland. Crops mainly grow between July and September. Water in the area in 2013 is similar to the average using over the years. The temperature and rail coincides quite well, it benefits the growing of crops. The temperature and monthly rainfall distribution were shown in Fig 1 to Fig 2.

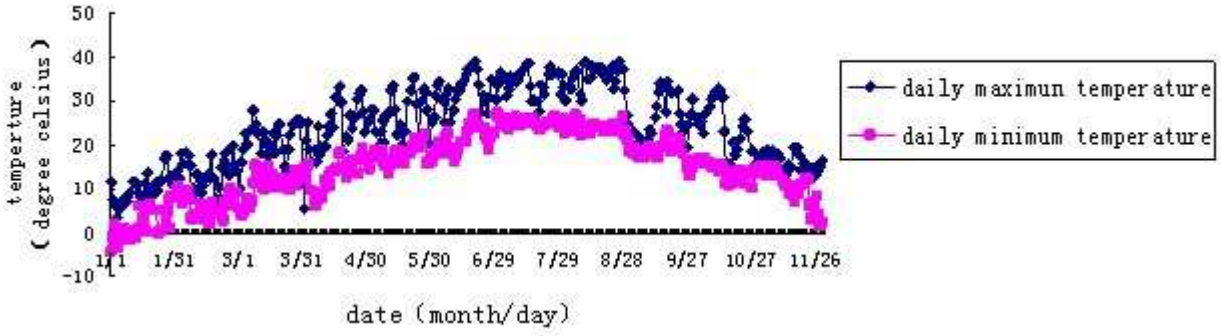



Fig. 1. Liangping 2013 daily minmun, maximum temprature

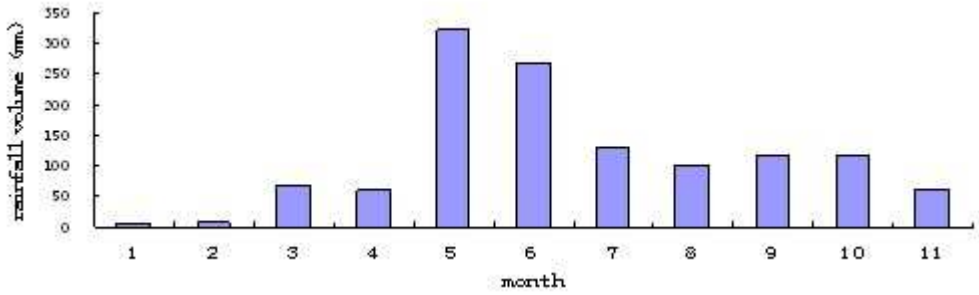



Fig. 2. Liangping 2013 monthly rainfal1

## Results and Discussions

a. Calculation of crop average ha net applied water

In the year of 2013，Hongguang irrigation diverted water from the reservoir by four times. And the major irrigation crops were rice and maize. The specific calculation is shown in Table 1.

Table 1. Average ha the net applied water of Hongguang irrigation typical plots in 2013

| Location | Typical Plots | Frequency of irrigation | Area (ha) | Gravimetric soil moisture (before release water) | Field moisture capacity | Plan moist layer of water (mm) | Gravimetric soil moisture (after release water) | Average ha the applied water (m3/ha) | Average ha the net applied water (m3/ha) |
|---|---|---|---|---|---|---|---|---|---|
| Ziku five team | corn plot1 | 1 | 0.0804 | 0.11 | 0.19 | 350 | 0.18 | 334 | 310 |
| | | 2 | | 0.14 | | 300 | 0.2 | 286 | |
| Ziku three team | rice terrace 1 | 1 | 0.0670 | 0.19 | 0.28 | 125 | 15 | 70696 | 63392 |
| | | 2 | | 0.25 | | | 12 | 56089 | |
| | corn plot2 | 1 | 0.0536 | 0.15 | 0.28 | 200 | 0.25 | 477 | 453 |

| | | | | | | | | | |
|---|---|---|---|---|---|---|---|---|---|
| | | 2 | | 0.19 | | | 0.28 | 430 | |
| Mingda water supply station | rice terrace2 | 1 | 0.2345 | 0.22 | 0.42 | 125 | 18 | 84873 | 67689 |
| | | 2 | | 0.42 | | | 11 | 50504 | |

The net irrigation quota is $2888.06\,m^3/ha$ and the net applied water is $7.16\times10^4\,m^3$.

b. The irrigation coefficient

By equation (1) can be calculated the irrigation coefficient as shown in Table 2.

Table 2. Calculation results about the irrigation coefficient of Hongguang irrigation in 2013

| Scale and type | small gravity |
|---|---|
| Name of irrigation district | Hong guang |
| Design irrigation area (ha) | 475.7 |
| Actual irrigation area (ha) | 247.9 |
| Comprehensive quota ($m^3$/ha) | 2888.06 |
| The net applied water (million cubic meters) | 71.6 |
| Total gross irrigation water (million cubic meters) | 159 |
| The irrigation coefficient ($10^{-2}$) | 45.03 |

By equation (1), the irrigation coefficient can be obtained in 2013. The result is 0.4503 in Hongguang irrigation district for the year.

## Conclusion

According to the calculation, the irrigation coefficient of Hongguang irrigation district is 0.4503 in 2013, which is in accordance with the local real development. The Head-tail method is convenient and simple, reducing the number of measured workload and uncertainties. It only needs determining the diversion volume to irrigation system and the final irrigating water to soil layer [4]. For Hongguang irrigation district, by adopting the Head-tail method to calculate the irrigation coefficient is very well. It provided guidance for the future work.

However, this method can't give detailed information about the water loss for the middle canal and diversions. If this information is needed, the more detailed method, or a monitoring system should be installed to get more information.

## Acknowledgements

This research was supported by the National Major Science and Technology Projects for Water Pollution Control and Management (2012ZX07104-003) and Guangjiong Research Fund of College of Resources and Environment, Southwest University. The support was gratefully acknowledged.

**Reference**

[1] Ministry of Water Resources of the People's Republic of China. National estimates of effective utilization coefficient of irrigation water analysis Technology Guide[R].2012.

[2] Feng Gao, Jingcheng Zhao, Jianzhong Xu and so on. Study on Measuring Method of Utilization Coefficient of Irrigation Water [J]. Journal of Irrigation and Drainage, 2004, 23(1):14~18.

[3] Ke Ren, Hongyu Wang. Irrigation Water Channel Leakage Loss Estimates and Analysis [J]. China Rural Water and Hydropower, 2006, (12):16~18.

[4] Peipei Shen, Luhua Yang, Xiaotong Xie. Research Connotation and Determination of Effective Utilization Coefficient of Irrigation Water[J]. China Rural Water and Hydropower, 2013, (6):73~75.

*Advanced Materials Research Vol. 937 (2014) pp 548-553*
*© (2014) Trans Tech Publications, Switzerland*
*doi:10.4028/www.scientific.net/AMR.937.548*

# Calculation of Parameters of Crop Water Production Function of Jensen Model based on Stochastic Particle Swarm Optimization Algorithm

Shu-hui Chang[1,a,*], Zhi-hong Qie[2,b]

[1]College of Information Science and Technology, Agricultural University of Hebei, Baoding 071001, China

[2]College of Urban and Rural Construction, Agricultural University of Hebei, Baoding 071001, China

[a]ndcsh@163.com, [b]qiezhihong@163.com

**Keywords:** crop water production function; Jensen model; Stochastic Particle Swarm Optimization Algorithm; sensitive index; correlation coefficient.

**Abstract:** In this paper, Stochastic Particle Swarm Optimization Algorithm (SPSO) is introduced to calculate parameters of crop water production function directly. SPSO is an improvement of the standard PSO, compared with which, it can be guaranteed to converge to the global optimization solution with probability one in theory, and speed up the convergence. The dimension of space of a particulate is determined by the phases of crop growth and development period in SPSO, and the sensitive index $\lambda_i$, an important parameter of crop water production function, is regarded as optimized variable to be calculated directly. This method can eliminate some problems existing in linear regression method, such as biased estimate and distortion of result and it can search the global optimization value more easily than the PSO. Through example analysis, we can see that the SPSO is better than PSO in accuracy and calculation speed.

## Introduction

Crop water production function is a mathematic model which reflects the relationship between the crop yield and the water factor. It is widely used not only in regional planning and system evaluation of the water saving irrigation but also in application and extension of insufficient irrigation [1]. Many kinds of models of crop water production function are put forward internationally based on experiment, and there are four models proved to be comparatively reasonable recognized and widely used [1]: Jensen model (1968), Blank model (1975), Stewart model (1977), Singh model (1987). According to the comparison analysis in model structure and fitting precision, Jensen model has been widely accepted, which can be expressed as follows:

$$\frac{Y}{Y_m}=\prod_{i=1}^{n}[\frac{ET_i}{ET_{mi}}]^{\lambda_i} \tag{1}$$

Here: $Y$ is the actual crop yield $(kg/hm^2)$; $Y_m$ is the maximum crop yield when the crop is in the condition of sufficient irrigation $(kg/hm^2)$; $i$ is the crop procreation phase number; $n$ is the number of crop procreation phase; $ET_i$ is the actual evapotranspiration of the crop procreative phrase at number $i$ $(mm)$; $ET_{mi}$ is the evapotranspiration of the crop procreation phase $i$ corresponding to $Y_m$ $(mm)$; $\lambda_i$ is the sensitive index of the crop procreation phase $i$, which is the important parameters of model, reflecting how the lack of water of some phase affect the crop yield.

The key of application of crop water production function Jensen model is to ascertain the water sensitive index $\lambda_i$ in the model. The commonly used method to identify the parameter is [1,2]: Through a variable substitution to make the model linear firstly, and then least square method is used to get the parameter. Because the dependent variables $\left(Y/Y_m\right)$ have been made to logarithm form by the method, the parameters of the regression model are only accord with the principle of least squares, and the dependent variables $\left(Y/Y_m\right)$ are unbiased estimation only to the replaced

variables, but not to the original variables, so the regression equation has the problem of "distortion" in some degree[3].Gauss-Newton Method is used by Yu-Feng Luo and so on to solve the parameters in crop water production function Jensen model[4]. Thus, this method can make the result of fitting approach the unbiased estimation and improve the precision of fitting. But this method need calculating the derivation and its results are influenced by the initial enactments. And if the initial enactments are not well, the precision of the model cannot meet the demand even if the model has been made iteration many times, with the best result in part or no convergence in model. These are the common defects in the optimization methods which can be also called as hard calculation. On the contrary, some soft calculation methods for example evolutional method, fuzzy sets and artificial neural network have been developed to solve this kind of problems successfully. Experiments have proved that PSO based on successive coding of real number can reach the global optimum quickly than genetic algorithm based on discrete coding of binary system, and PSO can avoid being influenced by the incensement in the peak value and with less influence from the dimensions of the problem[5].But the selection of parameters in standard PSO plays an important role in precision and velocity of convergence. With more times of iteration, convergence velocity and ability in searching the global optimum of PSO will decrease, even can't guarantee the global optimization .In order to overcome the defect of PSO, an improved method——Stochastic Particle Swarm Optimization Algorithm[6] is introduced in this paper to calculate the parameters of crop water production function of Jensen model.

## Stochastic Particle Swarm Optimization Algorithm

### The Principle of Particle Swarm Optimization

PSO algorithm makes a group of random particulates at first, then every particulate fly in multidimensional solution space, with dynamic correcting their velocity according to the flight status and experience of themselves. If there are $n$ particulates flying in $D$-dimensional space, then the position, velocity and the best position of the particulate $i$ is $X_i, V_i, P_i$, which can be expressed as follows:

$X_i = (x_{i1}, x_{i2}, \cdots, x_{iD})$, $V_i = (v_{i1}, v_{i2}, \cdots, v_{iD})$, $P_i = (p_{i1}, p_{i2}, \cdots, p_{iD})$ $(i = 1,2, \cdots, n)$

Here: $P_i$ is also $P_{best}$. Each particulate has a fitness value corresponding to its objective function $f(X)$. The objective function is often used as fitness function. There will be a particulate which has ever been the best position in history among the group. The best position can be expressed as $g_{best} = (g_1, g_2, \cdots, g_D)$. The globally optimal solution can be expressed as:

$$f(P_{best}) = \min\{f(P_1(t)), f(P_2(t)), \cdots, f(P_n(t))\} \tag{2}$$

According to the equation (3) and (4), as for the particulate $i$ in iterative $t$, PSO can calculate the velocity and position of the particulate dimension $i$ and iterative $(t+1)$ :

$$v_{ij}(t+1) = \omega v_{ij}(t) + c_1 r_1()(p_{ij} - x_{ij}(t)) + c_2 r_2()(g_{ij} - x_{ij}(t)) \tag{3}$$

$$x_{ij}(t+1) = x_{ij}(t) + v_{ij}(t+1) \tag{4}$$

Here: $\omega$ is inertia weight, $c_1$ and $c_2$ are all acceleration constants, $r_1()$ and $r_2()$ are two random functions range from 0 to 1. $\omega$ is inertia weight. $\omega$ can control convergence of PSO. As shown as literature [7], if $\omega$ can decrease linearly as the times of iteration, PSO will be improved. Usually, $\omega$ will adjust it as formulae (5):

$$\omega(t) = \frac{(0.95 - 0.4) \times (MAXITER - t)}{MAXITER} \tag{5}$$

Here: $MAXITER$ is the maximum times of iteration.

Besides, the velocity of every particulate is limited by the maximum velocity $V_{\max}$. The velocity of a particulate in dimension d is $V_{id}$, if this velocity exceeds the maximum velocity $V_{\max}$, then $V_{id}$ is equal to $V_{\max}$.The termination conditions of PSO is maximum times of its iteration, or the fitness

value which is the best all group have ever searched so far meets the preconcerted minimal fitness value. Because all the particulates fly to the direction which has the best solution gradually according to the experience of the particulate itself and all group, when all the particulates have reached the same point, it can be believed that the particulate has reached the best position.

The operation of PSO is not difficult, and PSO has little experiential parameters and has more quickly velocity in convergence. But the disadvantages of PSO are that the searching precision is not high and PSO is more inclined to get into a local optimization value. The reasons are as follows: Firstly, while searching for the optimization value, all the particulates fly to the direction which has the best solution, so the accurate searching degree of the optimization value will not be well in the condition of a bigger inertia weight. Secondly, while approaching the best position, the velocity of particulate will decrease, so all the particulates will reach one place without keeping variety among all the particulates and therefore PSO is more inclined to get into a local optimization value.

**Stochastic Particle Swarm Optimization Algorithm**

SPSO uses the following evolution equations:

$$v_{ij}(t+1) = c_1 r_1()(p_{ij} - x_{ij}(t)) + c_2 r_2()(g_{ij} - x_{ij}(t)) \tag{6}$$

$$x_{ij}(t+1) = x_{ij}(t) + v_{ij}(t+1) \tag{7}$$

Comparing with PSO, the equation omits $\omega v_{ij}(t)$, namely ensured $\omega = 0$ on the premise of each generation particulate flying at a constant speed, so the flying speed of particulate depends only on the current position $x_{ij}(t)$, the best historical position $P_i$ and the particulate swarm best position $P_{best}$ in history, a particulate with the globally best position will remain stationary, while other particulates tended to the weighted center of its own best position $P_i$ and globally best position $P_{best}$. Due to particulate lost inertia during the flight, particle swarm will shrink to the current globally best position which may be the local extremum; when $\omega \neq 0$, particulate will have the ability to extend the search space, $\omega$ larger, stronger global search capability, also increases the probability of accessing to global best value.

As shown as equation (6) and (7), when $P_i = P_{best}$, the particulate j will stop evolution. In order to improve the global search capability, $P_{best}$ can be retained as the history best position of particulate swarm, the position $x_j(t+1)$ of the particulate j is randomly regenerated in the search space $\Omega$, other particulates positions $x_i(t+1)(i \neq j)$ were evolved by the formula (6) and (7), then:

$$p_j = x_j(t+1) \tag{8}$$

$$p_i = \begin{cases} p_i, f(p_i) < f(x_i(t+1)) \\ x_i(t+1), f(p_i) \geq f(x_i(t+1)) \end{cases} \tag{9}$$

$$p_g^{'} = \arg\min\{f(p_i) | i = 1,2,\ldots,\Omega\} \tag{10}$$

$$p_g = \arg\min\{f(p_g^{'}), f(p_g)\} \tag{11}$$

If $P_j = P_g$, particulate j generated at random is in the history best position and stop evolution, the position of particulate j is randomly regenerated in the search space $\Omega$, other particulates evolve to the next generation after updating $P_g$, $P_i$ according to formula (6) and (7);if $P_j \neq P_g$ and $P_g$ isn't updated, all particulates evolve by equation (6) and (7); if $P_j \neq P_g$ and $P_g$ is updated, exists $k \neq t$ to make $x_k(t+1) = p_k = p_g$, particulate k evolution stopped, randomly regenerated in the search space $\Omega$, other particulates evolve after updating $P_g$, $P_i$ according to formula (6) and (7).In the evolution of every generation, there is at least one particulate regenerated randomly in the search space $\Omega$, so that the global search capability must be enhanced.

## SPSO of the Sensitive Index of Jensen Model

### Fitness Function

The fitness of a particulate in SPSO is the basis to evaluate the position of flying particulate. It is also the power supply which makes the particulate fly from the initial position to the best position. In this problem, the target is to minimize the difference between the relative crop yield calculated by model and actual crop yield, and $\Delta y$ is the fitness function of PSO, the expression is as follows:

$$\Delta y = \sum_{j=1}^{m} \frac{\left| \frac{Y_{aj}}{Y_m} - \frac{Y}{Y_m} \right|}{\frac{Y}{Y_m}} \quad (j = 1,2,\cdots,m) \tag{12}$$

Here, $m$ is the total number of the sample; $j$ is the sample number; $Y_{aj}$ is the calculated crop yield of sample $j$ $(kg/hm^2)$; $Y$ is the actual crop yield $(kg/hm^2)$; $Y_m$ is the maximum crop yield in the condition of sufficient irrigation $(kg/hm^2)$.

### Example Analysis

Based on the experiment data[9] of winter wheat irrigation of Yong le experimental station in Beijing in 1998~1999 and 1999~2000. The sensitive index of Jensen model has been calculated by tradition method in literature [9]. In order to verify the effectiveness of SPSO, PSO and SPSO are respectively used to calculate the sensitive index of Jensen model with the aid of simulated environment MATLAB7.0, the same parameters which are used in two methods: the number of particulate is 30; $c_1 = 2$; $c_2 = 2$; the maximum iterative times is 2000.

The results of sensitive index calculated by the traditional method in literature[8], PSO, SPSO are in Table 1.From the Table 1, it can be seen that the optimization results of PSO and SPSO are the same. The results calculated by PSO and SPSO are very different from that calculated by the traditional method.

Put the two group value from the traditional method and SPSO (PSO) of the sensitive index in formula (1), then the two values of $\frac{Y}{Y_m} = \prod_{i=1}^{n} [\frac{ET_i}{ET_{mi}}]^{\lambda_i}$ can be calculated, the contrast of which to the actual relative crop yield is expressed in Table 2.

From the Table 2, it can be seen that the maximum relative error between the relatively crop yield calculated by traditional method and the actual relatively crop yield is 13.5120%, and the maximum relative error between the relatively crop yield calculated by SPSO(PSO)and the actual relatively crop yield is 8.1981%.

The fitting curve between the relative crop yield calculated by tradition method and the actual relatively crop yield, and between the relative crop yield calculated by SPSO(PSO) and the actual relatively crop yield are illustrated in Fig 1.

From the Table 2 and Fig 1, it can be seen that the fitting effect of SPSO is better. The correlation index calculated by tradition method is 0.825, and the correlation index calculated by SPSO (PSO) is 0.932.

The calculation result of PSO and SPSO is shown in Table3.

Table 1. The calculated Result of the sensitive index of Jensen model

| Item | Calculation method | Period of seeding establishment-stem pushing | Stem pushing-tassel | Tassel -grouting | Grouting-maturity |
|---|---|---|---|---|---|
| The sensitive | traditional method | 0.0908 | 0.113 | 0.4099 | 0.1239 |
| | PSO | 0.1565 | 0.1758 | 0.2009 | 0.1661 |
| | SPSO | 0.1565 | 0.1758 | 0.2009 | 0.1661 |

Table 2. The specific results calculated by traditional method and SPSO (PSO)

| The number of section | The actual relatively crop yield | The relatively crop yield calculated by tradition method | The relatively crop yield calculated by PSO(SPSO) | The percent of relatively error between the lists of 2 and 3 | The percent of relatively error between the lists of 2 and 4 |
|---|---|---|---|---|---|
| 1 | 2 | 3 | 4 | 5 | 6 |
| B1 | 0.8517 | 0.8275 | 0.831 | 2.8454 | 2.4248 |
| B2 | 0.8764 | 0.8013 | 0.8764 | 8.5669 | 0 |
| C1 | 0.8502 | 0.8894 | 0.8367 | -4.6093 | 1.5895 |
| C2 | 0.7772 | 0.8119 | 0.7949 | -4.4694 | -2.2825 |
| D2 | 0.9107 | 0.874 | 0.8675 | 4.0314 | 4.7399 |
| E1 | 0.7865 | 0.7468 | 0.7353 | 5.0487 | 6.5114 |
| E2 | 0.7566 | 0.7878 | 0.7566 | -4.1283 | 0 |
| F4 | 1.0014 | 0.9797 | 0.9805 | 2.1629 | 2.0917 |
| E4 | 0.8301 | 0.9258 | 0.8982 | -11.5291 | -8.1981 |
| C4 | 0.6853 | 0.6874 | 0.7075 | -0.3093 | -3.2349 |
| D4 | 0.7988 | 0.9067 | 0.8495 | -13.512 | -6.3518 |
| B4 | 0.6353 | 0.6115 | 0.6353 | 3.7443 | 0 |
| A4 | 0.4945 | 0.4817 | 0.4945 | 2.5803 | 0 |

Table 3. The calculated statistics and comparison in the example

| Algorithm | The optimum results | | The times of the optimum result in 20 times | The average iterative times | The average iterative time needed (s) |
|---|---|---|---|---|---|
| | The best position | The best function fitness | | | |
| PSO | (0.1565, 0.1758, 0.2009, 0.1661) | 0.3582 | 20 | 52 | 1.0783 |
| SPSO | (0.1565, 0.1758, 0.2009, 0.1661) | 0.3582 | 20 | 2 | 0.3973 |

From the Table3, it can be seen that the sensitive index of Jensen model has reached a higher precision when the number of search times reaches about 50. But the same precision reached by SPSO needs only 2 iterative times. PSO need 1.0783s to reach the precision while SPSO need only 0.3973s in the same emulational circumstance MATLAB7.0, and the same scheduled precision. Therefore, it can be seen that SPSO is better than PSO in calculation speed.

Early study has proved that the crop sensitive index under the condition of lacking water has a good rule in the progress of crop growth and development period. The rule has direct relationship with the biological characteristic of crop itself. The changing process of crop sensitive index under the condition of lacking water is from a little sensitivity to large sensitivity to a little sensitivity, while the process of crop growth is from slow to quick to slow. The crop sensitive indexes calculated by SPSO (PSO) also accord with the rule (shown as Table 3). The crop yield calculated by the Crop Water Production Function optimized by SPSO (PSO) is near to the actual crop yield.

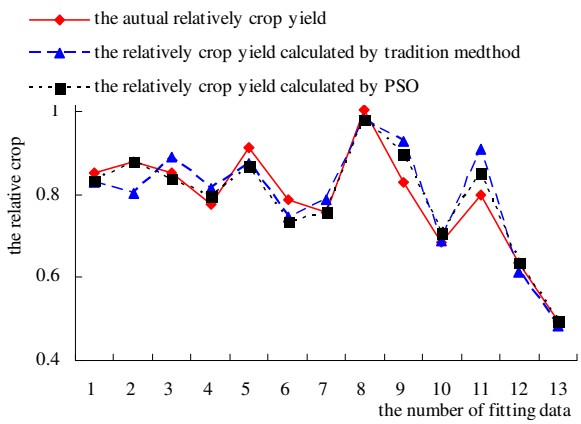



Fig. 1. The figure of fitting curve

## Conclusions

SPSO algorithm is used to calculate parameters of crop water production function directly in this paper. SPSO can eliminate some problems existing in linear regression method, such as biased estimate and distortion of result. The advantage of this method is that calculating parameters is not influenced by model complexity and initial value, and the higher convergence speed and precision are the character of this method. Example analysis result shows that SPSO is an effective method to calculate parameters of crop water production function. Because there are kinds of influencing factors of crop yield, such as: moisture, fertilization, climate, plant diseases and insect pests and so on, so the improvement on the forecast precision need a precondition for increasing the complexity of model, but SPSO algorithm is an effective choice to resolve this contradiction. The SPSO introduced in this paper is an effective choice to resolve this contradiction.

## References

[1] Yuanhua Li, The theory and technology of water saving irrigation, Wuhan, China, 1998.

[2] Yonghua Zhu, Shucai Dai, Wenyu Sun, Application of Mathematical statistics, Wuhan, China, 2000.

[3] Zhihong Qie, Qilin Cui, submitted to Journal of the science and technology of water conservancy in HeBei, In Chinese (1994).

[4] Yufeng Luo, Yuanlai Cui, Xiuzhen Zhu, submitted to Journal of Water Saving Irrigation, In Chinese (2004).

[5] Kennedy J, Spears W M, on Matching algorithms to problems: An experimental test of the particle swarm and some genetic algorithms on the multimodal problem generator, Pr-oc IEEE Int Conf on Evolutionary Corporation, Anchora-ne,1998, pp78-83.

[6] Jianchao Zeng, Zhihua Cui, submitted to Journal of Computer Research, In Chinese (2004).

[7] Jianchao Zeng, Qian Jie, Zhihua Cui, Particle Swarm Optimization, Beijing, China, 2004.

[8] Nelder.I Mead R, A simplex method for function minimization, on Computer Journal, 1965, pp308-313.

[9] Xiyun Jiao, Zhidong Lei, Shizhang Peng. Submitted to Journal of Irrigation and Drainage, In Chinese (2006).

*Advanced Materials Research Vol. 937 (2014) pp 554-558*
*© (2014) Trans Tech Publications, Switzerland*
*doi:10.4028/www.scientific.net/AMR.937.554*

# Effects of Grazing on Reproductive Allocation of Elm in Horqin Sandy Land, Northeastern China

Yi TANG[1, a*], Xin-jun WANG[2,b]

[1]Schoole of Life Science, Liaoning University, Shenyang, China

[2]College of Pratacultural and Environmental Sciences,Xinjiang Agricultural University,Urumqi 830052, China

[a]tangyi@lnu.edu.cn; [b]wxj8112@163.com

*Corresponding author

**Keywords:** Reproductive allocation, Sparse elm woodland, Ulmus pumila

**Abstract:** Grazing, one of the most important disturbance in Northern China, influenced vegetation restoration on the aspects of population survival, community structure and landscape patterns. However, effects of grazing on elm trees (*Ulmus pumila*), the key species in climax community in Horqin Sandy Land, were not fully understood, especially on the aspects of reproductive allocation. Reproductive allocation was vital to affect seed production, which determined the number of seed source used for recruitment. Furthermore, recruitment regulated the population dynamic even to the community structure. To estimate effects of grazing on elm trees reproductive allocation, a field experiment was conducted in Wulanaodu, southern of Horqin Sandy Land. Elm trees suffering grazing with intensities were classified with diameter in breast (DBH). Current-year shoots, leaves and seeds in each tree mentioned above, were selected and measured in the laboratory respectively. The dry weight of them considered as biomass allocated to reproductive and vegetative growth. Our results showed that the reproductive allocation of early-matured and over-matured trees were 25.17% and 35.91% separately in closed land and were 42.48% and 60.03% in light grazed land correspondingly, indicating the reproductive allocation of early-matured and over-matured trees in closed land was significant lower than in grazed land ($P<0.05$). Meanwhile, matured trees devoted 71.15% of required resource to reproduction in closed land, and this ratio was 67.34% and 71.75% in light and heavy-grazed land, indicating the difference of reproductive allocation was not significant between the grazed and closed lands ($P>0.05$). Furthermore, matured trees devoted 71.75% of resource to seeds and the corresponding ratio was 60.03% and 42.48% in over-matured trees and early-matured trees, indicating matured trees significantly devoted more resource to reproduction than over-matured trees and early-matured trees ($P<0.05$). It is suggested that grazing improved the ratio of biomass allocation to reproduction.

## Introduction

Plants acquired a limited amount of resources due to fixed metabolic rates[1]. The acquired resource was used to support all the material and energy plants need. It was well known that plants had to allocate the limited resource to several functions, including growth, maintenance and reproduction. The resource allocated to one function was increased and the resource other functions got was reduced[2]. The ratios of allocation between several functions reflected strategies, which is vital to adapt the environment for most of plants, especially plants living in poor microhabitats. Trade-offs between two or more strategies were the core of plants life-history evolution[3].Ecologists and evolutionists paid great attention to know which strategy would be chose in a special situation.

The ultimate goal of plants was to transmit their genes from parents to offspring[4]. The more resource allocated to reproduction meant the more opportunity to continuing their genes. However, the more resource allocated to reproduction also meant the less resource allocated to growth and maintenance, which would decrease the opportunity of plants survival. So plants had to optimize the reproductive allocation to get the fitness[5]. The ratio of resource allocated to reproduction was one of the most important aspects in plant life-history traits[6].

The reproductive allocation was influenced by kinds of disturbance greatly[7]. In general, it was considered that plants allocated more resource to reproduction to adapt disturbance[8]. The evidence supporting this opinion was from the grass mostly. But few referred trees, especially in temperate region. One of major aims was to estimate the effects of grazing on temperate trees qualitatively. Furthermore, it was reported that the grazing affected the grass or shrub through trampling and browsing[9]. And the grazing intensity played an important role in regulating reproduction allocation of grass. However, whether the grazing intensity had the same effects on trees was not known clearly. It was interesting that whether the reproductive allocation of trees changed depending on the grazing intensity.

In addition, the reproductive allocation changed with age. It was reported that perennial plants bred offspring firstly at certain age[10]. Although most literature focused on the changing of reproductive allocation of perennial trees with different age in tropical forests, few referred trees in other ecosystems.

Elm (*Ulmus pumila*) was a tree species ranging from Mongolia, north-eastern China and southern Siberia to eastern Kazakhstan. As an azonal species, elm occured in the steppe, the forest-steppe, and the semi-desert area, In Horqin sand land, north-eastern Inner Mongolia, elm formed savanna-like landscape, which was consist of small numbers of trees scattered over the grassland[11]. Sparse elm grassland played an important role in contributing to ecosystem function and ecological restoration, especially in degraded lands.

The aim of this paper was to test hypotheses that (1) grazing improved the reproductive allocation; (2) the reproductive allocation was different depending on grazing intensity; (3) the reproductive allocation was different with age.

## Study Area and Methods

The study area was located in Wulanaodu region (119°39′-120°02′E, 42°29′–43°06′N, 480 m a.s.l.), north-eastern Inner Mongolia, China. This region was typical the semi-arid climate. Mean daily temperature was –14.0°C in coldest month (January) and 23.0°C in warmest month (July). The average annual precipitation was 350 mm, 70% of which falls between June and August.

To evaluate the effect of grazing on reproductive allocation of elm, we selected three types of sites, representing closed sites, light grazed sites and heavy grazed sites separately. In closed site, grazing had been forbidden since 1996. And the difference between light grazed site and heavy grazed site was only the quantity of livestock.

To valuate the elm reproductive allocation of different age, we divided adult elm into three groups according to the breast diameter height (DBH), i.e. early-matured tree (DBH<5cm), matured tree (5cm<DBH<15cm), over-matured tree (DBH>15cm). Four trees in each group were selected randomly, excepting in heavy grazed plot, where early-matured was not found.

Reproductive allocation was the ratio of the resource allocated to reproduction and all resource acquired in a certain period. Actually, it was counted by measuring of the biomass of modules. In this study, total resource was considered as the sum of two parts, one was bestowed to reproduction and the other was attributed to the growth. The resource allocated to reproduction was represented by the biomass of seeds, ignoring crytic flowers, which was less in weight. And the resource was supported to growth equal to the biomass of branches and leafs occurring in current year.

For each tree, we randomly clipped 5 branches with leafs and seeds on it. The investigation was conducted on 20 May, where seeds matured but not fell off. The shoots, leaves and seeds in the current year were roasted 24 h at 80 □ and then weighted respectively.

One-way ANOVA was used to analysis reproductive allocation of elm with age groups suffering from grazing intensities. The significant difference was tested using Tukey's *post hoc* test. All statistical analyses were performed using the software SPSS14.0.

## Results

It was found that the reproductive allocation of early-matured and over-matured trees in closed land was significant lower than in grazed land. The reproductive allocation of early-matured trees and over-matured trees were 25.17% and 35.91% separately in closed land. Meanwhile, the reproductive allocation was 42.48% and 60.03% in light grazed land correspondingly. And the reproductive allocation of over-matured trees was 59.60% in heavy grazed land. However, the reproductive allocation of matured trees was not different significantly between the closed and grazed lands. Furthermore, the difference of reproductive allocation was not significant between the light grazed and heavy grazed lands (Fig. 1).

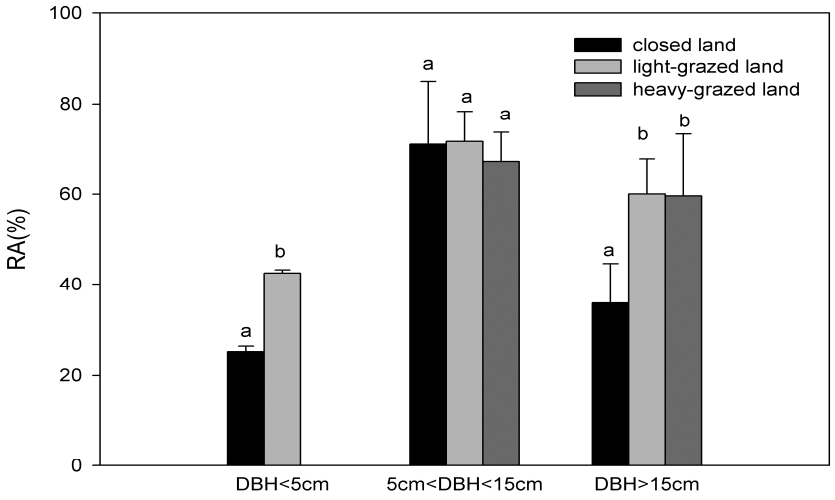



Fig. 1. The reproductive allocation in grazing intensities regions. The same letter indicates that the means of a column have no significant difference at the 0.05 level.

It was shown that the matured trees allocated more resource to seeds than that of early-matured trees and over-matured trees. In heavy grazed site, the reproductive allocation was different between matured trees and over-matured trees significantly. The matured trees allocated 67.34% of required resource to seeds and the over-matured trees allocated 59.60% of required resource to seeds. In light grazed land, matured trees devoted 71.75% of resource to seeds and the corresponding ratio was 60.03% and 42.48% in over-matured trees and early-matured trees. It was found that the similar trend was appeared in closed land. But the difference between early-matured trees and over-matured trees was not significant in closed land (Fig. 2).

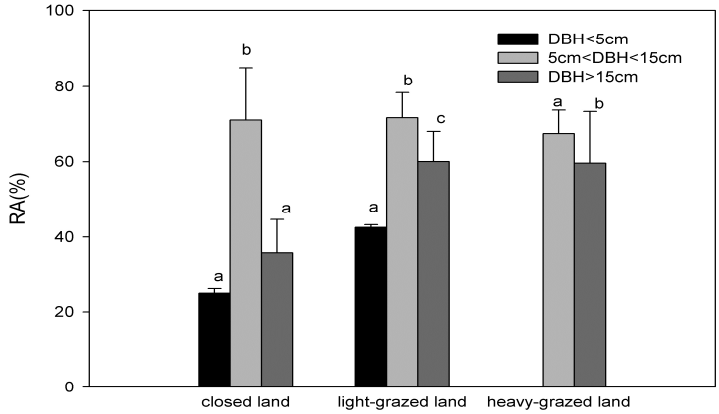



Fig. 2. The reproductive allocation with age groups. The same letter indicates that the means of a column have no significant difference at the 0.05 level.

## Discussion

The previous literature reported that the number of shoots and the height of stems were reduced in heavy grazing region, which was considered as results of trampling and browsing[12]. The mechanism was provided that under grazing disturbance, plants devoted more resource to reproduction, which caused the reduction of growth. This opinion was called escaping hypothesis because of more seeds escaping the disturbed habitat. Our results provided a piece of evidence that this hypothesis was suitable for trees in temperate zone. However, it was obviously that the cattle could not browse the shoots or leafs of adult elm, which is beyond the reach of cattle mostly. Therefore the grazing influenced the reproductive allocation of elm indirectly. Furthermore, our results showed that grazing intensity had not influenced the reproductive allocation. It was implied that the elm response to grazing disturbance was not sensitive.

The reproductive allocation depending on age classes meant that the reproductive allocation is not a fixed rate, but a trade-off between growth, survival and reproduction. At fresh and over-matured stage, more resource was devoted to growth, which might increase the opportunity of prevailing in competition. For matured trees, more seeds were produced to increase the chance of genes transmission. But we also noticed that for different species, the reproductive allocation might be different, which was the strategy plant selected.

According to Harper's model[13], the reproductive allocation was equal to 50% at the maxium. Ordinarily, it was less than 50% in natural population. But the reproductive allocation was more than 50% mostly in our study. We suggested that contradiction between previous studies and our study was the different study periods. The previous studies reported the total reproductive allocation of the whole growth season. In contrast to them, our studies focused on a certain period, in which seeds matured but not fell off yet. So it was implied that the reproductive allocation changed even in one growth season and more fine divided time should be considered in further researches.

The effects of grazing on reproductive allocation of elm were complicated. Compared with elm trees in closed site, the elm trees in grazed site devoted more resource to reproductive allocation. And the weight of 1000 seeds was not different significantly in these two sites, which meant that the elm in grazed site produced more seeds than that in closed site. It surprised us that the difference of the amount of seeds was not found in investigation. We suggested that the total resource acquired in grazed site was less than that in closed site, ignoring the tiny difference of elm trees. It was reported that grazing changed the soil properties and made the loss of water and soil. Our results showed that plants responded to the loss of nutrients sensitively.

## Acknowledgements

This work was supported by the State Key Development Program for Basic Research (2013CB429905), the National Natural Science Foundation of China (41201052)

## References

[1] D.A.Pace and D.T. Manahan: J Exp. Biol., vol.209 (2006), p.158-170

[2] R Levins in: Evolution in changing environments. Princeton: Princeton University Press (1968)

[3] D.Y. Zhang in: Plant life-history evolution and reproductive Ecology. Beijing: higher education Press(2004)

[4] P.J. van Dijk : Nature vol.451 (2008), p.1063-1064

[5] J. K. owski : Trends Ecol. Evol. Vol.7, (1992), p.15-19

[6] C.L.Boggs: Funct. Ecol. Vol. 6 (1992), p. 508-518

[7] J Nylehn and O Totland: Arct. Antarct. Alp. Res. Vol.31, (1999), p. 259-263

[8] A.Yamauchi and N.Yamamura: Am. Nat. Vol.163 (2004), p.138–153

[9] K.G. Roques, T.G. O'Connor and A.R. Watkinson: J. Appl. Ecol. Vol. 38, (2001), p. 268-280

[10] J.E. Brommer, H. Pietiaeinen and H. Kolunen: J. Anim. Ecol. Vol. 67,(1998), p. 359-369

[11] C. Dulamsuren, M. Hauck and M. Muhlenberg: Appl. Veg. Sci.Vol.8 (2005), p.149-154

[12] K.R. Hickman and D.C. Hartnett: Plant Ecol. Vol. 159 (2002), p. 23-33

[13] J. L.Harper: J. Ecol., Vol.55 (1967), p.247-270

*Advanced Materials Research Vol. 937 (2014) pp 559-564*
*© (2014) Trans Tech Publications, Switzerland*
*doi:10.4028/www.scientific.net/AMR.937.559*

# Water Resources Optimal Allocation in Middle Line of South to North Water Diversion project of Hebei, China Using AHP-LP

Tai-Zhong GAO [1,*], Can-Can ZHANG [2] and Hui-Cong PANG [3]

Key Laboratory of Biological Technology for Containment Prevention in Hebei Province, School of Environmental Science & Engineering; Hebei University of Science & Technology Shijiazhuang050018, China

[1]taizhonggao@163.com, [2]15511823574@163.com, [3]13223409891@163.com

*Corresponding author

**Keywords:** Optimal allocation of water resources, Sustainable utilization, The middle line of Project in HeBei Province.

**Abstract.** Water resource is irreplaceable as one kind of important natural resources and strategic economic resources. Water resources optimal allocation is an important means to solve the problem of water resources to keep the relative balance of the supply and demand. For ensuring the sustainable development, according to the South-to-North Water Transfer Project, and aiming at the maximum synthesized benefits, the model for water resources optimal allocation was established. A lot of factors were considered. The cause function, restriction and parameters were discussed. At last, optimal allocation of water resources in the middle line of Project in Hebei Province was studied under the guarantee of 95 % in 2010 and 2014. The results showed that the Project can solve the serious water shortage in Hebei province, North China.

## Introduction

Water resources are irreplaceable natural and strategic economic resources. The initial allocation of water rights is mainly affected by executive-led government and constraints of water habit [1]. Uneven distribution of water resources and increasing demands bring the need of transform [2]. It's important to reasonable allocation of water resources, and diversified allocation mechanism gradually exerts its effect [3].

Optimal allocation of water resources is defined as a particular river basin or region, using the engineering and non-engineering measures simultaneously, making a rational allocating for the limited water resources in different forms, to achieve the sustainable use, and ensure socio-economic, resources, ecology and environmental development [4]. At present, North China overexploitation of groundwater is more than 200 billion cubic meters, we must strengthened the optimal allocation of water resources in Hebei province, North China.

## Model Establishment

With the biggest target of limited water resources, comprehensive benefits (economic and environmental benefits). Establish a model, optimizing the limited water resource allocation, to achieve the best overall efficiency [5].

## Model Objectives

According to specific circumstances, determine region-specific target n-, respectively $f_1$, $f_2$, $f_3$, ..., $f_n$, $f_{n-1}$ is water supply fees, $f_n$ is environmental efficiency, $U(K)(K=1,2,...,n)$ is corresponding k-set of water sector, objective functions:

$$\max\left\{f_1(X^1), f_2(X^2), f_{n-1}(X^{n-1}), f(X^n)\right\} \tag{1}$$

$f_K\left(X^K\right)$ stands the objective function of the water sector effectiveness:

$f_K\left(X^K\right)=C_K X^K=\sum_{j=1}^{m}\sum_{ieU(K)}C_{ij}X_{ij}\left(K=1,2,...,n-2\right)$, $f_{K-1}\left(X^{K-1}\right)$ stands for water supply cost;

$f_n\left(X^n\right)=EX^n=\sum_{j=1}^{m}\sum_{ieU(n-1)}S_{ij}X_{ij}$, $f_n\left(X^n\right)$ is environmental benefit: $f_n\left(X^n\right)=EX^n=\sum_{j=1}^{s}\sum_{ieU[n]}e_{ij}X_{ij}$

m is total number of water; $c_{ij}$ is per unit of efficiency factor when sector j supply water to i. If j doesn't supply, $c_{ij} = 0$; $s_{ij}$, cost factor; $e_{ij}$, environmental benefits factor.

**Constrains**

(1)Water for supply. $W_j$ is the available water of sector j; $x_{ij}$ is the water from j to i; d is the total number of j.

$$\sum_{i=1}^{d}X_{ij}\le W_j \tag{2}$$

(2) Water supply capacity from water to users. $V_{ij}$ is the upper limit from j to i

$$X_{ij}\le V_{ij} \tag{3}$$

(3)The departments water. $L_i$, $H_i$, respectively stands for lower and upper limit of i.

$$L_i\le\sum_{i=1}^{s}X_{ij}\le H_i \tag{4}$$

(4)The water environment - coordinated development of socio-economic

According to the principle of system science, water environment - socio-economic coordination degree D is the function between $T_j$ which is a state variable that reflects economic development and $T_h$ which reflects water environment quality changes. D is the minimum of corresponding D of i, D> 0, if D = 0, it is not coordinated.

$$D=\begin{cases}0, & E<E_{\min},W_i>W_{i0}\\ \dfrac{E-E_{\min}}{E_s-E_{\min}}\sqrt{1-\dfrac{W_i}{W_{i0}}}, & E>E_{\min},W_i<W_{i0}\\ \dfrac{0.1E_{\min}}{E}, & E=E_{\min},W_i=W_{i0}\end{cases} \tag{5}$$

$$T_j=\begin{cases}\dfrac{E}{E_{\min}}, & E=E_{\min}\\ 0, & E<E_{\min}\\ \dfrac{E-E_{\min}}{E_s-E_{\min}}, & E>E_{\min}\end{cases}\quad T_h=\begin{cases}0, & E<E_{\min},W_i>W_{i0}\\ \dfrac{E-E_{\min}}{E_s-E_{\min}}\sqrt{1-\dfrac{W_i}{W_{i0}}}, & E>E_{\min},W_i<W_{i0}\\ \dfrac{0.1E_{\min}}{E}, & E=E_{\min},W_i=W_{i0}\end{cases}$$

(5)Non-negative variables, and other constraints:

$$X_{ij}\ge 0,\left(i=1,2,...,d;j=1,2...\right) \tag{6}$$

**Model Solution**

According to above conditions, constitute the optimal allocation of water resources in multi-objective linear programming model by combining the total objective function and constraints together. Using AHP first, which is suitable for evaluation of complex systems [6], and by the delivery class sub-goals system to determine the weight of each region target $\theta_1$, $\theta_2$... $\theta_n$, then objective function can be as follow.

$$\max F(X) = \sum_{k=1}^{n} \theta_k f_k(X^k) \quad k = 1,2,\cdots,n \tag{7}$$

Finally it becomes single-objective problem and use Excel to solve.

## Model Applications

### Optimal Allocation of Water Resources Modeling in Hebei Province

Take reception basin of Hebei, South-to-North Water Transfer Project as research object. Considering the level of economic, we mainly research urban areas. The largest industrial output value of water supply, minimum cost and optimal environmental benefits as specific optimization goals, respectively means $f_1$, $f_2$, $f_3$. With AHP calculates the target weight: $\theta_1$=0.5390, $\theta_2$=0.2973, $\theta_3$=0.1637. $\lambda$max=3.0088, CI=0.0044, RI=0.58, CR= CI/RI=0.0076<0.1, has a satisfactory consistency. Upon investigation, the water used in the industry, public utilities and environmental primarily provided by surface water, groundwater, Yellow River water (in 2014 for the diversion of water) and wastewater reuse. The urban domestic water mainly comes from the first three.

### Determine Main Parameters of Optimal Allocation of Water Resources Model

#### The Determination of Higher and Lower Limit of Water-Use

(1) The industrial water-use: $H_1$, $L_1$, respectively represents the higher and lower limit; B for different levels of annual industrial output value, W for ten thousand yuan output value of water demand.

$$H_1 = 1.2B \times W, \; L_1 = 0.8B \times W \tag{8}$$

(2)The water-use in urban and public utilities: domestic water, using quota method. Use the level of per capita water quota and population's produce to determine.(3) The environmental water-use are determined by the regional development plan.

#### Efficiency Coefficient

(1) The industrial water is fixed by the countdown of the ration of industrial water.(2) Environmental benefits coefficient: Only consider negative impacts.

a.For the industrial water sector: Total number of enterprises r .The intensity of the key pollutant emission k under the minimize cost of control in each firm:

$$\eta_k = f\left(P_k, \lambda_k, S_k, W_i, U_i, Q_i, Y_i\right) \tag{9}$$

$\eta_k$ is emission intensity of unit value of k, t/ten thousand RMB; $P_k$ is intensity of effective charges of k; $\lambda_k$ is treatment efficiency of k; $S_k$ is standard of k; $W_i$ is i's excessive pollutant emission; $U_i$ is reductions; $Q_i$ is value; $Y_i$ is the nature. To ten thousand value of water-$q_i$, environmental benefits coefficient of k is:

$$E_{ik} = aP_{ik}\eta_{ik} / q_i \tag{10}$$

$E_{ik}$ is environmental benefits coefficient of k, Yuan/$m^3$; a is the factor of market price; $P_{ik}$ is treat costs of k for i, Yuan/t; $\eta_{ik}$ stands for the emission intensity of k, t/million. $E_k$ takes the average of all enterprises. $E_k = \frac{1}{r}\sum_{i=1}^{r} E_{ik}$, r is the total number.

b. For non-industrial water-use sectors

$$E_K = aP_k K_\rho \tag{11}$$

$E_k$ is environmental benefits coefficient of k; a is the factor of market price; $P_k$ is the treat costs of k; K is the conversion coefficient between wastewater emission and k.

By reception basin in 2010, take market price coefficient a=1.0, COD as key pollutant, for industrial, COD emission is average 0.00653t/million of Hebei. For non-industrial, it relates to water consumption. Sewage capacity ratio coefficient ρ=0.9, conversion factors k=0.54kg/$m^3$, COD treat cost 4840.2Yuan/t. By (10), (11) environmental benefit of industrial was -0.8779Yuan/$m^3$, each non-industrial was: -2.352Yuan/$m^3$. In 2014, market price coefficient m=1.15, COD, predictive of 0.00352t/million. So industrial is -0.5442 Yuan/$m^3$, non-industrial is: -2.705 Yuan/$m^3$.

**Determination of the Cost Factor**

Different users with different sources can be determined by its water fee standard.

## Calculation Results and Analysis

There were four types of water source and sectors in reception basin of Hebei in 2010. In the model there are 4×4=16 decision variables and decision matrix $X = (x_{ij})_{4\times4}$ $x_{ij}$ standard for the water of i supplied by j. So establish the model:

$$\max F(X) = \theta_1 C_1 X_1 - \theta_2 S_2 X_2 - \theta_3 E_3 X_3$$

$$s.t. = \begin{cases} \sum_{i=1}^{4} x_{i1} \le 1.23, \sum_{i=1}^{4} x_{i2} \le 3.45, \sum_{i=1}^{4} x_{i3} \le 0.93, \sum_{i=1}^{4} x_{i4} \le 1.29 \\ \sum_{j=1}^{4} x_{1j} \le 17.04, \sum_{j=1}^{4} x_{2j} \le 6.35, \sum_{j=1}^{4} x_{3j} \le 3.60, \sum_{j=1}^{4} x_{4j} \le 1.96 \\ \sum_{j=1}^{4} x_{1j} \ge 11.36, \sum_{j=1}^{4} x_{2j} \ge 4.23, \sum_{j=1}^{4} x_{3j} \ge 2.40, \sum_{j=1}^{4} x_{4j} \ge 1.30 \\ D > 0, x_{ij} \ge 0 \end{cases}$$

Target weights were 0.5390, 0.2973, 0.1637; $C_1$ is efficiency coefficient matrix of industrial water sectors. $X_1$ is decision matrix of i, X = [$x_{11}$, $x_{12}$, $x_{13}$, $x_{14}$, $x_{15}$]; S = $[s_{ij}]_{4\times4}$ is matrix of cost coefficient, $s_{ij}$ is unit cost of water supply; E is coefficient matrix of environmental benefits. E = [$e_1$, $e_2$, $e_3$, $e_4$]; D isn't turn. Use Excel's "Solver" add-on to distribute water resources, under the guaranty 95% in 2010, results shown in Table 1.

Table 1. Water allocation results in the reception basin of South-to-North Water Transfer Project in Hebei Province in 2010(p=95%)

| Water-use forms | Source | | | | Total | Water demand | Water deficit |
|---|---|---|---|---|---|---|---|
| | surface | groundwater | Diversion water | Wastewater reuse | | | |
| Industrial water-use | 0.53 | 0.79 | 0.29 | 0.69 | 2.3 | 9.96 | 7.66 |
| Urban life water-use | 0.31 | 0.48 | 0.31 | | 1.1 | 3.56 | 2.46 |
| Public utilities | 0.23 | 0.31 | 0.17 | 0.23 | 0.94 | 1.28 | 0.34 |
| Environmental water | 0.13 | 0.12 | 0.14 | 0.15 | 0.54 | 0.9 | 0.36 |
| Total | 1.2 | 1.7 | 0.91 | 1.07 | 4.88 | 15.7 | 10.82 |
| Environmental benefit(one hundred million) | -8.09 | | | | | | |
| $D_1$ | 0.01 | | | | | | |

From Table 1 we can see: In 2010, 95%, (1) There exited water shortages in industrial, urban, public utilities, and environmental water sectors. The industrial and urban shortages respectively were 766 and 246 million $m^3$. (2) The environmental efficiency were: $-0.8779\times2.3-2.352\times1.1-2.352\times0.94-2.35\times0.54=-0.89$ (one hundred million); (3) In the allocation scheme, $D_1>0$, so the development is coordinated.

Considering adjust the industrial structure. Use the predicted results given by the Office of Water of Hebei, allocate water resources. The result shows in Table 2.

From Table 2 we can see: In 2014, 95%, (1) The four sectors are no longer dry. Implementation of South-to-North Water Transfer Project can significantly improve the imbalance problems of water supply and demand. (2) The environmental benefits are: $-0.5442\times12.81-2.705\times9.56-2.705\times3.87-2.705\times2.71=-43.66$ (one hundred million); (3) In allocation scheme , $D_2$ is far greater than $D_1$, showing it's more coordination.

Table 2. Water allocation results in the reception basin of South-to-North Water Transfer Project in Hebei Province in 2014(p=95%)

| Water-use forms | Source | | | | Total | Water demand | Water deficit |
|---|---|---|---|---|---|---|---|
| | surface | groundwater | Diversion water | Wastewater reuse | | | |
| Industrial water-use | 0.31 | 0.43 | 11.28 | 0.79 | 12.81 | 11.06 | 0 |
| Urban life water-use | 0.21 | 0.28 | 9.07 | | 9.56 | 4.11 | 0 |
| Public utilities | 0.16 | 0.17 | 3.31 | 0.23 | 3.87 | 2.09 | 0 |
| Environmental water | 0.07 | 0.11 | 2.43 | 0.10 | 2.71 | 1.91 | 0 |
| Total | 0.75 | 0.99 | 26.09 | 1.12 | 28.95 | 19.17 | 0 |
| Environmental benefit(one hundred million) | -43.66 | | | | | | |
| $D_2$ | 0.43 | | | | | | |

## Conclusions

The optimal allocation model of regional water resources is a large-scale system multi-objective optimization problem; its configuration should meet the principle of effectiveness, equity and sustainability. Taking the biggest overall efficiency of the limited water resources as the target, establish a regional water resources optimal allocation model. AHP to handle multi-objective problem, use strata sub-goals by the delivery system to determine the weight of each of the target area. The multi-objective linear programming problem can be converted into single-objective problem. It is very convenient to use Excel's "Solver "add-in solution. Using this model, we can make the optimum allocation under the guarantee-rate of 95% in 2010, and then make rational analysis for the allocation results, which verified the validity and feasibility of the model. Finally, Use this model, we can make the optimum allocation under the guarantee-rate of 95% in 2014, which shows that after the implementation of South-to-North Water Transfer Project it can solve the situation of severe water shortage in the reception basin of Hebei. Moreover, through the adjustment of industrial structure and the implementation of water-saving measures, it can enable the water environment and the economic to develop more coordinated.

## Acknowledgements

This work was supported by grants from the National Natural Science Foundation of China (No.41373096) and Key Laboratory of Biological Technology for Containment Prevention in Hebei Province, China.

**References**

[1] Xin Li, Fuxuan Chang, Jin Chen. The review of initial allocation of water rights and water rights. The research of Yangtze River Academy of Sciences. 28(2), 2011,1-9. In Chinese.

[2] Mojtaba Sadegh, Najmeh Mahjouri Reza Kerachian. Optimal Inter-Basin Water Allocation Using Crispand Fuzzy Shapley Games. *Water Resour Manage*. 2010, 24:2291–2310.

[3] G.R. Mettam, L.B. Adams, How to prepare an electronic version of your article, in: B.S. Jones, R.Z. Smith (Eds.), Introduction to the Electronic Age, E-Publishing Inc., New York, 1999, pp. 281-304.

[4] Fulin Wang, Qinghua Pang. Establishment and application of water allocation model-A case study in Huludao city. *Journal of Shenyang Agricultural University. 44(1)*, 2013:108-111. In Chinese .

[5] Meijia Cheng. Optimal Allocation of Water Resources in Jinan City [D]. Shandong Normal. 2010.

[6] Ludmil Mikhailov, Joshua Knowles. Priority Elicitation in the AHP by a Pareto Envelope-Based Selection Algorithm. 2010, Volume 634, Part 3, 249-257.

*Advanced Materials Research Vol. 937 (2014) pp 565-570*
*© (2014) Trans Tech Publications, Switzerland*
*doi:10.4028/www.scientific.net/AMR.937.565*

# Study of the Differences between Vegetation and Soil Spectrum about Alpine Wetland Ecosystem

Ji-ming WANG[1,a], Ke-long CHEN[1,b,*] , Xin Zhang [1,c], Zheng-xia LUO[1,d]

[1] College of Biology & Geography Science, Qinghai Province Key Laboratory of Physical Geography And Environmental Process, Qinghai Normal University, Xining, wusi west road38#, 810008, china

[a] wwjjmmswb@126.com, [b]ckl7813@163.com, [c]1059411995@qq.com, [d]755987843@qq. com.

* Ke-long CHEN

**Keywords:** Feature spectrum, Alpine wetland ecosystems, Vegetation communities and Soil, Qinghai Lake basin.

**Abstract.** Using FieldSpec ® 4 Hi-Res portable coverings spectrometer, we have measured the main vegetation and siol reflectance based on different habitats:Surface water swamping meadow, a seasonal water swamping beach, wet beach without of water and sandy in the little Park Lake, East of the Qinghai Lake and analyzed the spectral differences. The results show that: Soil moisture is one of the important factors that affect reflectivity. Under the premise of similar other soil properties, soil moisture and reflectivity shows a negative correlation with each other. 350-1000nm wavelength range is ideal to distinguish vegetation and soil. Due to the presence of water absorption bands, within 1000-1300nm the spectrum derivative of soil and vegetation has a strong similarity, but still can be used to identify the spectrum of vegetation and soil. In addition to sandy habitats, vegetation and soil spectrum has a strong similarity in the 1300-2500nm wavelength range, it is more tolerance translation will confuse the two bands, the spectrum has a strong similarity in the range of 1300-2500nm, so it is relatively easy to confuse the two spectrum.

## Introduction

Vegetation information has important significance for monitoring and construction of regional ecological environment as an important parameter of environment evaluation[1]. As one of the important elements of the natural geographical environment, to investigate the soil's physical and chemical properties is a long and arduous task. Compared with the artificial field survey, remote sensing getting data is more objective, rapid and accurate[1]. RS (Remote Sensing, RS) technology has become major source[2] of information about land cover and its constituent and been widely used in resources and environment dynamic monitoring, such as agriculture, mining, water pollution and so on[3-8] . High-resolution and hyperspectral remote sensing emerged in recent years is to provide the conditions for obtaining surface information clearly and accurately. It is also worth noting that as the most readily available for remote sensing the information of vegetation and soil is mixed together, a great impact on the accuracy of hyperspectral remote sensing. Therefore, it is particularly important to measure the spectrum of vegetation and soil and analyze the differences between them. Because alpine wetlands were located in remote areas at high altitude,where Climate change quickly and human is not easy to reach, remote sensing become the primary means of accessing to the geographic information of these areas. Alpine wetland in Qinghai Lake basin located in the intersection of Qinghai-Tibet Plateau alpine area,northwest arid zone and the eastern monsoon region, was included in the "Convention on Wetlands" List of Wetlands of International Importance in 1991, is the one of the seven wetlands of international importance, which not only has a complex diverse ecosystem types, but has an extremely important ecological status [9]. So this study what we do has made a great foundation for hyperspectral remote sensing interpretation and its accuracy control.

## Study Area

Qinghai Lake Little Park Lake Alpine Wetland Ecosystems Research Station is located in the northeastern Qinghai-Tibet Plateau, Qinghai, Hainan County, 6 kilometers far from the East Lake stud farm, North latitude36°41' 734"～36°42' 256", East longitude100°46' 85"～100°47' 21",at an elevation of 3216 ~ 3221m, an area of 14.8 $km_2$. Annual rainfall of 324.50mm ~ 412.80mm, mostly

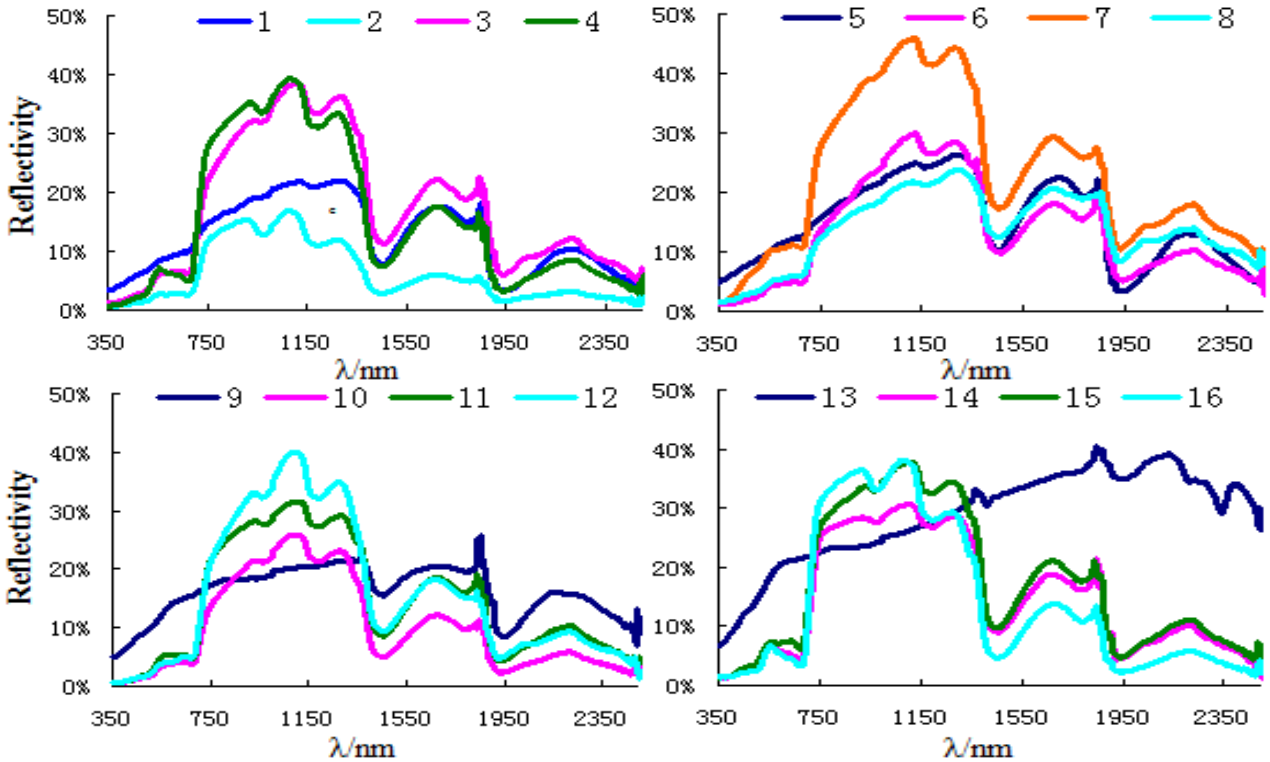
concentrated in the 5-9 month and rain and heat is in the same period. Annual evaporation capacity is 1502mm. The annual average temperature is at -0.80 °C ~ - 1.10 °C, annual sunshine hours is up to 2430-3330 $h \cdot a^{-1}$[10-11]. The main soil is marsh soil and meadow soil, higher organic matter content. Soil moisture is long-term saturated at low-lying land but with the undulating terrain soil moisture showed gradually over the changes. Affected by different habitat conditions, the main vegetation types are *Blysmus sinocompressus, Carex, Kobresia myosuroides, Iris lacteal, Achnatherum splendens* and so on [11].

**Research Methods**

Using FieldSpec ® 4 Hi-Res portable coverings spectrometer, we have measured the main vegetation and siol reflectance based on different habitats. Measurement time is September 18, 2012 Time 10:30-13:30. Wavelength range: 350 - 2500 nm, scan time: 100ms, spectral average: up to 31800 times, wavelength accuracy: 0.5 nm, wavelength repeatability: 0.1 nm. Using a reflectance of 98% as the reference white, before and after each measurement we calibrated with reflectance white. Measuring spectrum, according to the weather conditions the spectrometer was optimized, at least once every 10min. Spectrometer Probes full FOV 25 °, probe vertically downward, the height from the communities of canopy is based on the size of the community, between the 5-50cm,the same as siol. When measuring soil spectrum, without damaging the soil surface, the vegetation was cleared away.

Software Viewspecpro and Excel2003 were applied to process and calculate spectrum data.

**The Results**




1. swamping meadow soil 2. *Triglochin maritimum, Carex tristachya* community 3. *Carex heterostachya, Blysmus sinocompressus* community 4. *Triglochin maritimum, Blysmus sinocompressus* community 5. swamping beache soil 6. *Primula nutans Georgi, Triglochin maritimum* community 7. *Leontopodium alpinum* community 8. *Phragmites australis, Blysmus sinocompressus* community 9. wet beach soil 10. *Kobresia tibetica, Blysmus sinocompressus* community 11. *Carex tristachya, Blysmus sinocompressus, Poa annua* community 12. *Pedicularis longiflora, Carex tristachya, Kobresia humilis* community13. Sandy soil 14. *Achnatherum splendens* community 15. *Kobresia graminifolia, Taraxacum officnala* community 16. *Adenophora stricta, Ranunculus tanguticus* community

Fig. 1. Spectrum of vegetation communities and soil

Swamping meadow soil reflectance in the 350-1277nm range increased from 3.30% to a maximum 22.01% , 1278-1685nm, reflecting the first to fall to 7.88% (1455nm), and then rose to 17.60%, 1686-1949nm reflecting decreased to 3.30% , 1950-2500nm reflecting increased to 10.30% firstly and then fell to 4.13%. *Triglochin maritimum,Carex tristachya* community overall reflectance is low, in the measurement range, the minimum value of 0.74% at 360nm. The highest reflectance appears at 1078nm of the only 16.92%. In the 350-1078nm reflectance gradually increased to 15.31% at 914nm, and then decreased to12.84%. Befor 681nm reflectance rises slowly, after 681nm reflectance change quickly. 1079-1447nm reflectance gradually decreased to 2.91%at the 1453nm. Between 1454-2462nm there are two reflection peaks of 6.03% and 3.15% at 1672nm and 2224nm respectively. The valley between two peaks is 1.45%. At 2462nm the reflectance is 0.88%. *Carex heterostachya, Blysmus sinocompressus* community within the 350-673nm reflectance rate of 0.73% is up to 5.36% at 559nm, and then decreased to 4.86%. Between 674-1454nm, reflectance at 1083nm reaches the maximum value of the measuring range, 39.27%. At near 963nm and 1194nm, there is a small decline respectively. The reflectance is of 7.36% at 1454nm. Between 1455-1934nm, the peak is of 17.57%, at 1673nm, down to the 3.11% at 1934nm. Between 1935-2475nm, reflectance increased to 8.55% at 2212nm, and then decreased to 2.67%. *Triglochin maritimum, Blysmus sinocompressus* community reflectance trends is similar with *Carex heterostachya, Blysmus sinocompressus* community in the measuring wavelength range. But in the 750-1100nm, reflectance of former is higher than that of latter slightly, while in 1150-2500nm it is on the contrary.

Swamping beache soil reflectance increased from 4.78% to a maximum of 26.32% in 350-1294nm, with minor fluctuations, 1295-1455nm reflectance decreased to 10.27% , 1456-2500nm, there are two peaks located at 1690nm and 2197nm,the values of peaks were 13.30% and 22.42%, low reflectivity values between two peaks appear at 1940nm, 3.31 %, reflectance fall to about 5.00 percent at near 2500nm. *Primula nutans Georgi, Triglochin maritimum* community within the 350-678nm reflectance slowly increased from 1.12% to 4.79%, in the vicinity of 4.6%-4.79% slight fluctuations occurred. In the 679-1122nm the reflectance increased rapidly to 29.99%. Between 1123-1284nm there is a small reflection valley of 26.56% at 1192nm. Followed by 1285-1457nm the reflectance rapidly decreased to 9.81%, and then gradually picked up to 18.06% at 1676nm. Between 1677-2223nm there is a reflection valley of 5.20% at 1599nm. In the range of 2224-2444nm, the reflectance decreased from 10.25% to 5.18%. *Phragmites australis, Blysmus sinocompressus* community reflectance trends is similar with that of *Primula nutans Georgi, Triglochin maritimum* community but in 800-1300nm the reflectance is lower than that of *Primula nutans Georgi, Triglochin maritimum* community while in 1300-2500nm it is on the contrary, the largest reflectance of 23.83% at 1295nm. *Leontopodium alpinum* community reflectance is at a high level as a whole. Within the measuring range, the reflectivity has three peaks and two valleys. Peaks appeare at 1119nm, 2670nm, 2220nm and each peak value is 45.87%, 29.29% and 18.00%. Valleys at 1456nm, 1930nm and each valley value is 17.31% and 10.45%.

Wet beach soil reflectance from 4.91% gently rising to 18.10% in 350-800nm, 801-1366nm, reflectance maintained at a relatively high level and slowly increased to 22.42%, then the reflectance decreased to 15.55% gradually at 1458nm, 1459-1943nm, the reflectance lead up to the 20.47% (1681nm), and then decreased to 8.49%. In 1945-2500nm, there is a reflection peak at 2160nm, who's value is 16.12%, after that a gradual downward trend appeared, down to about 10%. *Kobresia tibetica,Blysmus sinocompressus* community within the 350-1096nm reflectance slowly rising from 0.59% to 25.97%,a maximum reflectance. Near the 638nm,there are small fluctuations about 4.00%. At 1194nm, the reflectance drops to 21.37%. There ia an increase in the 1278nm to 23.17% and a rapid decline to 5.03% at 1456nm. in there are two reflection peaks of 12.14% and 5.82% at 1675nm and 2212nm respectively and a reflection valley of 2.30% at 1928nm between the two peaks. The reflectance of *Carex tristachya, Blysmus sinocompressus, Poa annua* community and *Pedicularis longiflora, Carex tristachya, Kobresia humilis* community coincide with that of *Kobresia tibetica, Blysmus sinocompressus* community in 350-750nm. When wavelength is higher than 750nm, the reflectenc of the first two communities is greater than that of *Kobresia tibetica, Blysmus*

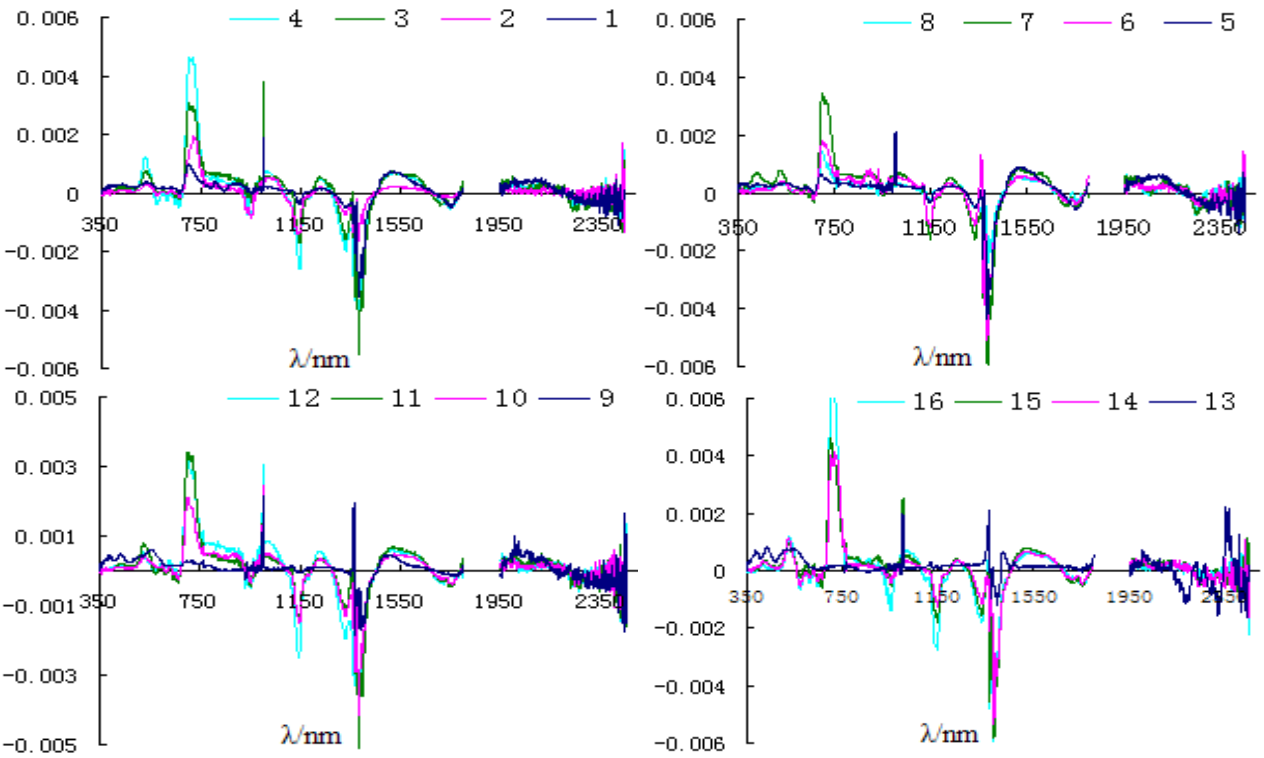
*sinocompressus* community. The maximum reflectance of *Carex tristachya, Blysmus sinocompressus, Poa annua* community is 31.53%, at near1119nm and that of *Pedicularis longiflora, Carex tristachya, Kobresia humilis* community is 40.07%, at 1091nm. When the wavelength is greater than 1350nm, the reflectance of the two communities almost coincide with each other, at 1451nm, dropped to 9.48%, in near 1158nm reflectance has a slight concussion, 1452-2475nm, there are two reflection peaks, each value of peak is 18.28% and 9.36%, in 1667nm and 2219nm respectively, the valley between the peaks is 4.70%, at 1930nm, at 2475nm reflectance is 3.96%.

Around the wetland there is a large area of sand dunes, sandy land is beween wetland and sand dunes. Sandy soil reflectance in the 350-581nm rise from 6.63% to 19.99% rapidly. 582-1843nm, reflectance gently rises to a maximum of 40.50%, a slight fluctuation at 1369nm. 1844-2134nm, the reflectance decreased slightly, at 1954nm of 34.84%, but rise to 39.13% at 2134nm. When the wavelengths longer than 2134nm, reflectance decreased to 29.22%, at 2492nm. *Achnatherum splendens* community within the 350-556nm, reflectance increased from 1.19% to 6.96%, 557-671nm reflectance decreased to 4.56%, 672-760nm reflectance quickly rose to 25.87% ,761-1311nm reflectance fluctuated between 26% - 31% and maintain at a high level, then at the 1456nm reflectance rapidly decreased to 8.98%. Between 1457-1951nm there is a reflection peak, the peak of 18.86% at 1671nm office. Between 1952 -2460nm there is another reflection peak, the peak of 10.09%, at 1858nm. At 2460nm, the reflectance is of 3.81%. The reflectance of *Kobresia graminifolia, Taraxacum officnala* community and *Adenophora stricta, Ranunculus tanguticus* community coincide with that of *Achnatherum splendens* community in 350-750nm. 750-1150nm, the reflectance of *Adenophora stricta, Ranunculus tanguticus* community is the biggest, range from 30% to 38% and that of *Achnatherum splendens* community is the lowest, range from 27% to 31%. 1150-1350nm, the reflectance of *Adenophora stricta, Ranunculus tanguticus* community dropped to about 30% and partially overlapped with *Achnatherum splendens* community, but that of *Kobresia graminifolia, Taraxacum officnala* community is down 6%, a smaller decline. 1350-2500nm, that of previous two communities is coincide with each other, while the reflectance of the *Adenophora stricta, Ranunculus tanguticus* community at a low level. In all vegetation spectrum, near the 960nm and 1150nm there are significant water absorption band. It is also exist in soil's spectrum but not obvious.

**Discussion**

350-2500nm, soil reflectance relative size of the different habitats in the whole show a certain regularity, followed, sandy soil > swamping beache soil > swamping meadow soils. The soil moisture of each habitat is sandy soil < swamping beache soil <swamping meadow soils. Mainly due to the nature of the wet beach soil is very different from that of soils in the other three habitats, the wet beach soil reflectance does not meet the above rules on the whole, and its moisture is between sandy soil and swamping beache soil, while its reflectance relative size is not fixed in different bands.

In order to quantitatively discuss the differences in soil and vegetation spectrum, the paper calculated the first derivative of all soil and vegetation spectrum. To get clear image, derivative of 1800-1950nm has been removed, because of the chaotic fluctuations.




1. swamping meadow soil 2. *Triglochin maritimum, Carex tristachya* community 3. *Carex heterostachya, Blysmus sinocompressus* community 4. *Triglochin maritimum, Blysmus sinocompressus* community 5. swamping beache soil 6. *Primula nutans Georgi, Triglochin maritimum* community 7. *Leontopodium alpinum* community 8. *Phragmites australis, Blysmus sinocompressus* community 9. wet beach soil 10. *Kobresia tibetica, Blysmus sinocompressus* community 11. *Carex tristachya, Blysmus sinocompressus, Poa annua* community 12. *Pedicularis longiflora, Carex tristachya, Kobresia humilis* community13. Sandy soil 14. *Achnatherum splendens* community 15. *Kobresia graminifolia, Taraxacum officnala* community 16. *Adenophora stricta, Ranunculus tanguticus* community

Fig. 2. The first derivative of soil and vegetation spectrum

From Fig. 2, it is clear that the first derivative of soil and vegetation spectrum has a dramatic change at near 700nm, a turning point of all soil reflectance appeared at 700nm, before and after which different change rate in reflectance existed. And the same like vegetation spectrum at 700nm but the rate of change is greater than the soil. Obvious reflection peaks of vegetation community appeared at near 500nm,a green spectral band, in the swamping meadow and sandy land, dramatic changes in its spectral derivative, but that of vegetation community in swamping beache and wet beach is not obvious, small changes in the derivative spectrum.

Overall, derivative of soil spectrum is less than that of vegetation spectrum, a smaller soil reflectance variability. 350-1000nm, soil spectrum derivative is always greater than zero, shows a continuous increasing of soil reflectance. The vegetation community with obvious green peak, its spectrum derivative has fluctuation at near 550nm, 350-1000nm, significantly negative suggest that the rise and fall of its reflectance. The wavelength range is ideal bands to distinguish soil and vegetation spectrum. 1000-1300nm, from Fig.1, the reflectance of soil continues to increase, but Fig.2 shows that the derivative trend of soil spectrum is similar with that of vegetation spectrum at the vicinity of 960nm and 1150nm, because the fluctuations was caused by absorption band of water and who's strength depends on soil moisture content, from strong to weak was swamping meadow soil spectrum > swamping beach soils spectrum > wet beach soil spectrum >sandy soil spectrum. Except sandy soils, vegetation and soil in the spectrum has a strong similarity in 1300-2500nm, because it is very different from other soil and vegetation types in aspects of its physical and chemical nature.

## Conclusion

Soil moisture is one of the important factors that affect reflectivity. Under the premise of similar other soil properties, soil moisture and reflectivity shows a negative correlation with each other, but it is not the only factor affecting reflectance. When the soil other physical and chemical properties have a big difference, the affect of water will be weakened. 350-1000nm wavelength range is ideal to distinguish vegetation and soil, because there is negative in first derivative of vegetation spectrum but not in first derivative of soil spectrum. At 550nm, vegetation spectra derivative have big fluctuations, but soil spectra derivative don't have, wavelength range a good distinction , but disappears at the end of the growing season. Due to the presence of water absorption bands, within 1000-1300nm the spectrum derivative of soil and vegetation has a strong similarity, but still can be used to identify the spectrum of vegetation and soil. In addition to sandy habitats, vegetation and soil spectrum has a strong similarity in 1300-2500nm, it is more tolerance translation will confuse the two bands, the spectrum has a strong similarity in the range of 1300-2500nm, so it is relatively easy to confuse the two spectrum.

## Acknowledgement

This paper is co-sponsored by National Natural Science(41261020, 31260052), The authors woul d like to thanks to them. And thanks to the anonymous reviewers.

## References

[1] Xia Qing, Lin-bing Tong, Ze-zhong Zheng. Vegetation Information AVIRIS hyperspectral remote sensing data extraction, J. Hubei Agricultural Sciences. 50(2011) 4831-4833.

[2] Ying-shi ZHAO. Principles and Methods of Analysis of Remote Sensing Applications . Beijing: Science Press, 2003.

[3] Roughgarden J, Running S, Matson P. What does remote sensing do for ecology, J. Ecology. 72( 1991)1981~1922.

[4] Ke Wang, et al. Different levels of potassium rice canopy and leaf spectral characteristics Preliminary Study , J. Science and Technology Bulletin.,13 (1997) :211-214.

[5] Ceccato P, Flasse S, Tarantola S. Detecting vegetation leaf water content using Reflectance in the optical domain, J. Remote Sensing of nvironment. 77(2001):22-33.

[6] Mu-yi HUANG, etc. The spectral characteristics of winter wheat stripe rust and Remote Sensing, J. Agricultural Engineering.,19 (2003) :154-158.

[7] Jian-guo ZHANG, Zian YANG. Based on spectral characteristics of remote sensing information extraction and metallogenic prediction, J. Mineral Resources and Geology. 18(2004) :346-349.

[8] Yong-liang SUN, Xiao-yan LI, Jia TANG, He-ye XU. Climate Change and Hydrological Response in the Watershed of Qinghai Lake, J. Resources Science. 30(2008):354-362.

[9] G-H XU, G-L TIAN, Wang C, et al. The progress and prospect of remote information science, J. Acta Geographica Sinica. 51(1996):385~397.

[10] Xiao-zhou SHU, Qiu YIN, Ding-bo KUANG. Inland water algae chlorophyll concentration and Spectral Reflectance relationship,J. Journal of Remote Sensing.,4(2000):41-45.

[11] Chen Liang. Qinghai Lake District topsoil magnetic metal element spatial distribution and pollution assessment study ,D. Qinghai Normal University, 2012.

[12] Cheng Lei xing, Chen Ke long, Wang Shi ping. "Little Park Lake Qinghai Lake Basin Wetland Diversity Analysis," , J. Wetland Science in press.

*Advanced Materials Research Vol. 937 (2014) pp 571-577*
*© (2014) Trans Tech Publications, Switzerland*
*doi:10.4028/www.scientific.net/AMR.937.571*

# Toxicity of Three Heavy Metal Pollutants of the Pharmaceutical Wastewater to Paramecium Caudatum

Zi-lin GONG[a], Ying CHEN[b,*],Yan YAN[c], Si-ying PEI[d],
Di WU[e], Miao ZHANG[f], Qi WANG[g]

College of life science and technology, Harbin Normal University, Harbin 150025, China

[a]gzl0129@sina.com,[b]LH6666@126.com,[c]63408045@qq.com,[d]275438195@qq.com,

[e]281714470@qq.com, [f]303771420@qq.com , [g]332836617@qq.com

*Corresponding author

**Keywords:**Paramecium caudatum, Heavy metal, Pharmaceutical wastewater, Acute toxicity, Population growth curve

**Abstract.** In order to provide information for biological monitoring of environmental pollution and help people to develop pharmaceutical wastewater pollutant monitoring and emission standard, in this paper, acute toxicity experiments of three heavy metal pollutants, $Zn^{2+}$,$Cd^{2+}$ and $Hg^{2+}$ existed usually in pharmaceutical wastewater, were done and their 24hr $LC_{50}$ on the *Paramecium* were got individually, safety thresholds were calculated. At the same time, impact of different concentration heavy metal ions on population growth curve of *Paramecium caudatum* were researched. Results indicated that the acute toxicity of $Hg^{2+}$ are the strongest, and the population growth curve changed significantly by three different types under three heavy metal ions pressure.

## Introduction

Recently, both pharmaceutical and chemical industry and health care products manufacturing have rapidly developed. However, every day large quantities of toxic wastewater produced in the pharmaceutical processes effect human health seriously[1]. *Paramecium* as a typical protozoa ciliate has a sensitive reaction for the change of water pollution situation as well as tolerated[2-3]. Therefore, *Paramecium* has been an important biological indicator for biological monitoring of water quality[4]. Scholars paid a lot of attention to explore *Paramecium* ecotoxicology. In fact, the research of *Paramecium* mostly have focused on acute toxicity and chronic toxicity[5-9]. Because the research on how pharmaceutical wastewater effects the ecological system is still a question in the world, this paper will investigate the effect of three kinds of heavy metal pollutants including $Zn^{2+}$, $Cd^{2+}$, $Hg^{2+}$ presenced usually in pharmaceutical wastewater to the acute toxicity and population growth curve of *Paramecium*. Furthermore, these data can support government to draw up the pharmaceutical wastewater pollutant monitoring and emission standard.

## Materials and Methods

### Experimental Animals

The purification breeding group of *Paramecium caudatum* is cultured in the glass depressions under temperature 20℃. Feeding with straw liquid. When each original group reaches dozens of cells , respectively moves into a test tube culture .

### Acute Toxicity Test Methods and Data Processing

To prepare three heavy metal ions with different concentration for pre experiments, experience for 24 hr to determine the minimum inhibitory concentration and fully lethal concentration.Within this range the use of such a logarithmic law , acute toxicity test to determine the concentration of each of the heavy metal pollutants into six concentration gradient , the concentration gradients of each set of three parallel groups and one contrast group straw medium. Each 10 *Paramecium* ,

placed in 20 ℃ constant temperature and humidity incubator experiment, after 24 hr each group were observed and recorded the number of surviving individuals. Using probit analysis to calculated $LC_{50}$.

**Population Growth Inhibitory Effect Experiment**

Within the range of the three pollutants *Paramecium* $LC_{50}$ and the minimum inhibitory concentration(ie,the maximum tolerated concentration ), select three concentration gradient (Table 1) for population growth inhibition tests . The straw culture medium as a contrast (CK), a total of 10 experimental groups. Each concentration set three parallel samples.Each sample was 10 individuals , putting into constant temperature and humidity incubator 240hr. Every 24hr counts once.

Table 1. Concentration of three heavy metal pollutants in population growth inhibitory effect experiment

| Pollutants | Concentration(mg/L) | | |
|---|---|---|---|
| | 1 | 2 | 3 |
| $Zn^{2+}$ | 0.982 | 1.04 | 1.13 |
| $Cd^{2+}$ | 3.632 | 3.893 | 4.516 |
| $Hg^{2+}$ | 0.3521 | 0.3558 | 0.3595 |

Protozoa counting method by Feng Guo et al[12]. After shaking *Paramecium* culture medium, to sampling and microscopic counting with 50μl of every drop. *Paramecium* population growth rate is calculated as $y = (\ln Nt - \ln N_0) / t$, to analysis population density and the average incubation time with excel software, getting the population growth curve .

## Results

### Acute Toxic Effects of Three Kinds of Heavy Metal Pollutants on Paramecium

**The Acute Toxicity of $Zn^{2+}$**

Acute toxicity of $Zn^{2+}$ of gradient concentration was shown in Table 2. Regression analysis on probit $y_1$ and concentration logarithmic $x_1$ gave the regression equation : $y_1 = 15.102x_1 + 5.069$, correlation coefficient $r_2 = 0.991$, according to the regression equation, it can be obtained when $y_1 = 5$ ( mortality rate 50% ) that $LC_{50}$ (24hr) of $Zn^{2+}$ is 0.974mg / L, 95% confidence interval is 0.931 ~ 1.023mg / L ( Fig. 1 ) .

Table 2. The acute toxicity of zinc ions to *Paramecium*

| Concentration (mg/L) | *IgC* ($x_2$) | Death Rate (%) | Probit ($y_2$) |
|---|---|---|---|
| 1.13 | 0.0531 | 100 | - |
| 1.04 | 0.0170 | 60 | 5.2533 |
| 0.96 | -0.0177 | 43.3 | 4.8313 |
| 0.89 | -0.0506 | 30 | 4.4756 |
| 0.83 | -0.0809 | 10 | 3.7184 |
| 0.75 | -0.1249 | 0 | - |

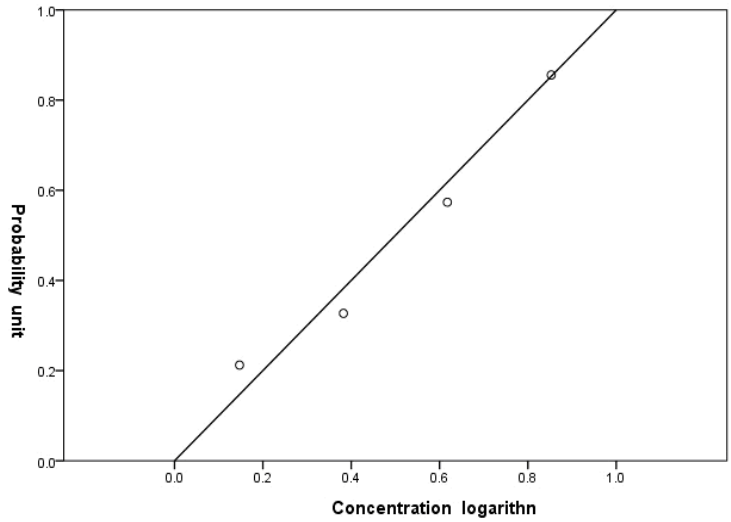



Fig. 1. Regression analysis of zinc ions concentration logarithm and mortality rate probit

**The Acute Toxicity of $Cd^{2+}$**

Acute toxicity of $Cd^{2+}$ of gradient concentration was shown in Table 3. Regression analysis on probit $y_2$ and concentration logarithmic $x_2$ gave the regression equation : $y_2 = 9.878x_2 + 0.372$, correlation coefficient, $r_2 = 0.964$, according to the regression equation, it can be obtained when $y_2 = 5$ ( mortality rate 50% ) that $LC_{50}$ (24hr) of $Cd^{2+}$ is 3.532mg / L, 95% confidence interval is 3.218 ~ 3.945mg / L ( Fig. 2 ).

Table 3. The acute toxicity of cadmium to *Paramecium*

| Concentration (mg/L) | *IgC* ($x_2$) | Death Rate (%) | Probit ($y_2$) |
|---|---|---|---|
| 4.516 | 0.655 | 90 | 6.282 |
| 3.893 | 0.590 | 60 | 5.253 |
| 3.421 | 0.534 | 40 | 4.747 |
| 2.971 | 0.473 | 30 | 4.476 |
| 2.595 | 0.414 | 10 | 3.718 |
| 2.258 | 0.354 | 0 | - |

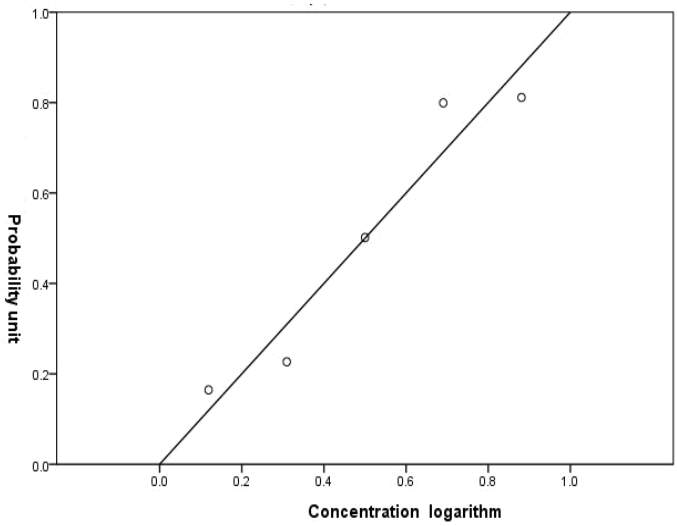



Fig. 2. Regression analysis of cadmium concentration logarithm and mortality rate probit

**The Acute Toxicity of $Hg^{2+}$**

Acute toxicity of $Hg^{2+}$ of gradient concentration was shown in Table 4. Regression analysis on probit $y_3$ and concentration logarithmic $x_3$ gave the regression equation : $y_3 = 85.210x_3 + 44.097$, correlation coefficient, $r_2 = 0.984$, according to the regression equation, it can be obtained when y3 = 5 ( mortality rate 50% ) that $LC_{50}$ (24hr) of $Hg^{2+}$ is 0.345mg / L, 95% confidence interval is 0.343 ~ 0.347mg / L ( Fig. 3 ).

Table 4. The acute toxicity of mercury ions to *Paramecium*

| Concentration (mg/L) | *lgC* ($x_2$) | Death Rate (%) | Probit ($y_2$) |
|---|---|---|---|
| 0.3595 | -0.4443 | 100 | - |
| 0.3558 | -0.4488 | 80 | 5.8416 |
| 0.3521 | -0.4534 | 70 | 5.5244 |
| 0.3485 | -0.4578 | 50 | 5.0075 |
| 0.345 | -0.4622 | 40 | 4.7467 |
| 0.3416 | -0.4664 | 0 | - |

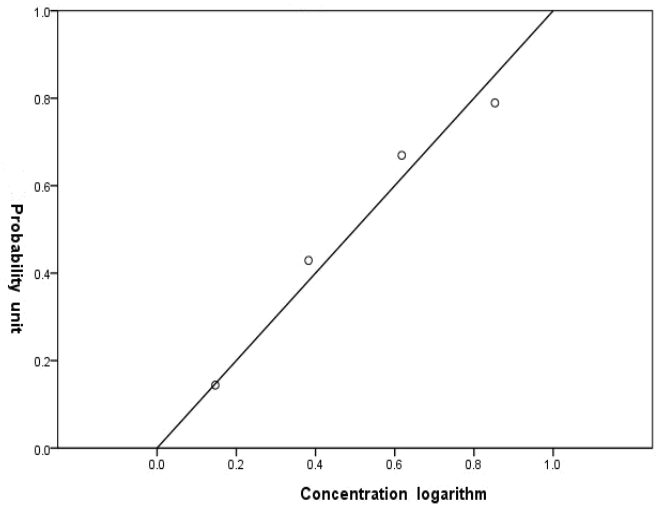



Fig. 3. Regression analysis of mercury ions concentration logarithm and mortality rate probit

**Effects of Three Heavy Metal Ions on the Population Growth of *Paramecium Caudatum***

Under normal culture conditions, *Paramecium* population growth curve is "S" shape . *Paramecium* population density is slowly growing during 24-120hr, 120-192hr are logarithmic phase , the stable plateau of growth appears after 192hr ( Fig. 4 ).

**$Zn^{2+}$ Stress on the Population Growth Curve Growth Curve of *Paramecium Caudatum***

At different concentrations of $Zn^{2+}$ stress, the *Paramecium* population growth curve changed significantly ( Fig. 5 ). The average density of *Paramecium* is significantly inhibited by $Zn^{2+}$ . Zinc 1 , *Paramecium* density occurs a faster growth at 72th hour , population density reaches a maximum, 653.3cells/ml. It seems the the logarithmic phase is ahead. However, the maximum population density is much lower than contrast group .

**$Cd^{2+}$ Stress on the Population Growth Curve Growth Curve of *Paramecium Caudatum***

At different concentrations of $Cd^{2+}$ stress, the *Paramecium* population growth curve shows a different variation ( Fig. 6 ) , Cadmium1, *Paramecium* growth curve are basic consistent with the contrast group. Cadmium2, the inflection point arrives at 192hr, population density suddenly reduced. Cadmium 3, population density grows slowly, there is no obvious logarithmic growth period, the population density was lower than the contrast group.

### $Hg^{2+}$ Stress on the Population Growth Curve Growth Curve of *Paramecium Caudatum*

Mercury 1 and 2, the incubation period of the *Paramecium* population growth was longer than the contrast group. Logarithmic phase delay to 144hr or 168hr, but the two highest population densities were greater than the contrast group. Population growth curve of mercury 3 is closed to the contrast group(Fig.7).

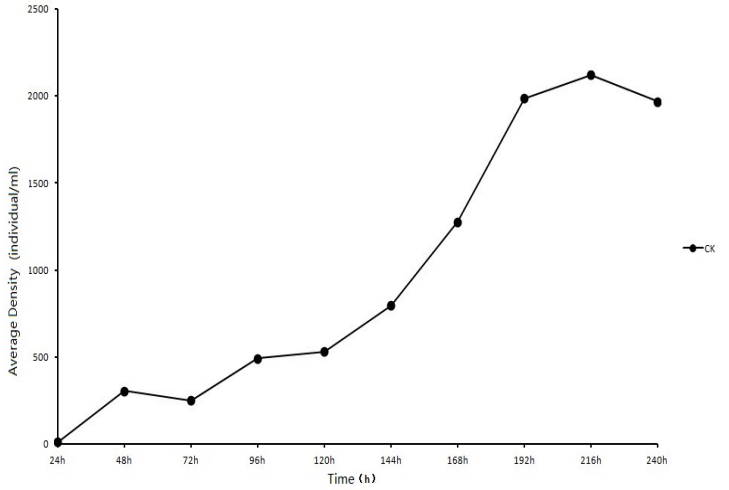



Fig. 4. CK growth curve of Paramecium *caudatum*

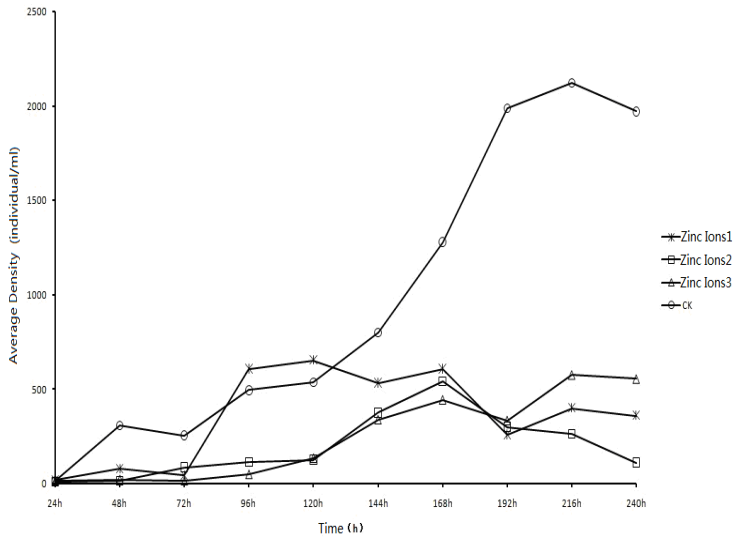



Fig. 5. $Zn^{2+}$ Stress on the population growth curve growth curve of *Paramecium caudatum*

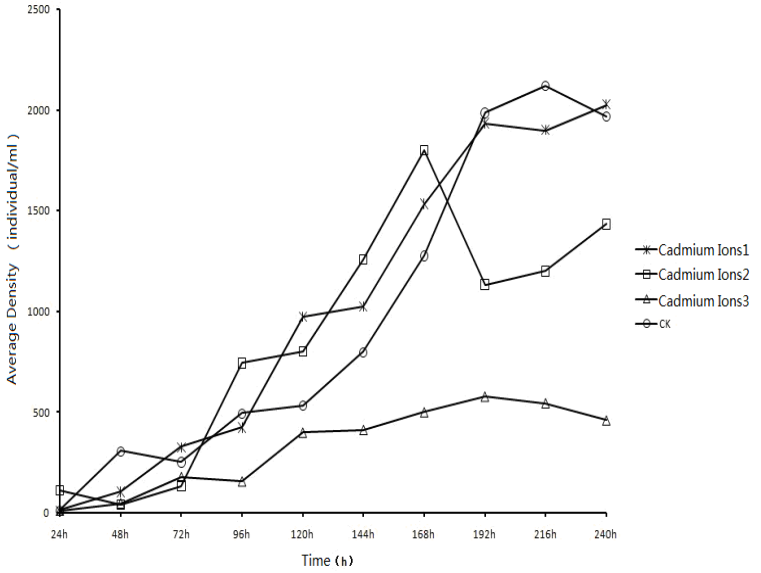



Fig. 6. $Cd^{2+}$ Stress on the population growth curve growth curve of *Paramecium caudatum*

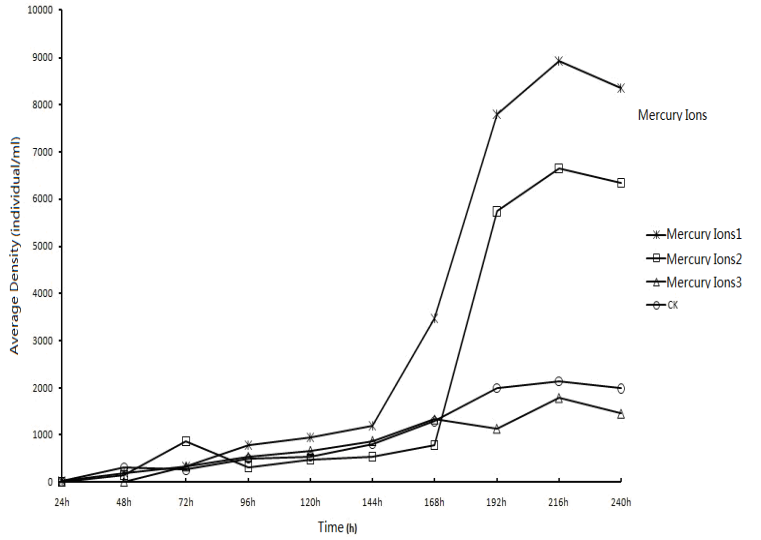



Fig. 7. $Hg^{2+}$ Stress on the population growth curve growth curve of *Paramecium caudatum*

## Discussion

$LC_{50}$ of zinc ions , mercury ions , cadmium ions, 20 ℃, 24hr, on *Paramecium caudatum* is individually, 0.974mg / L, 0.345mg / L and 3.532mg / L. It can be inferred that the acute toxicity of three heavy metals on *Paramecium caudatum* were different , according to descending order it should be: $Hg^{2+} > Zn^{2+} > Cd^{2+}$.

And mortality of *Paramecium* has closely relationship with ion concentrations, that is, when the ions concentration is above semi- lethal concentration, mortality rate of *Paramecium* will increases with the increasing of ions concentration. Three heavy metals pollutants safety threshold can be calculated according to semi- lethal concentration with following formula:

$$\text{Safety Threshold} = 24hLC_{50} \times 0.3/(24hLC_{50})^3$$

Therefore, the safety thresholds of three metal ions are theoretically : $Zn^{2+}$, 0.31 mg/L; $Hg^{2+}$ , 2.52 mg/L; $Cd^{2+}$, 0.02 mg/L. These threshold can be used to formulate pharmaceutical wastewater discharge standards.

The population growth curve of *Paramecium* changed significantly under less than $LC_{50}$ concentration of three heavy metal ions. Trends can be roughly grouped into three types: 1.Making the logarithmic phase advanced but population density is suppressed, such as $Zn^{2+}$

experiment(Fig.5); 2 . Making the logarithmic phase delayed but population density increased, such as $Hg^{2+}$ experiment group 1 and group 2(Fig.7); 3. Reduceing density and logarithmic phase does not appear, such as $Cd^{2+}$ experiment 3 and $Hg^{2+}$ experiment 3. These results suggest that the effect of specific pollutant on the population growth is closely related to its concentration. But the reaction of *Paramecium* to various combined heavy metal pollutants remains to be further studied.

**Acknowledgements**

This work was financially supported by the National Natural Science Foundation of China Youth Project (31101613), Heilongjiang Provincial Department of Education Science and Technology Project(11531231)and Harbin Normal University Young Excellent Teacher Project(10KXQ-01).

**References**

[1]Chunbai Zhao. Pharmaceutical industry, production of sewage and ancillary environmental management accounting software development and applications. Northeastern University Thesis(China),2009:12~16

[2] Xianyu Huang, Peiran Liu. Water Pollution Research Progress in biological detection. Environmental Science(China), 1999, 7(4):14~18

[3] Methods for measuring the acute toxicity of effluents and receiving waters to freshwater and marine organisms. Environmental Monitoring Systems Laboratory, Office of Research and Development, US Environmental Protection Agency, 1993

[4] Fengchao Li, Yunfen Shen, Cunqi Liu,etc. Evaluation using protozoan communities Baiyangdian dry season water quality status quo.Ecology Magazine (Spanish),2005, 24(7): 785~789

[5] Cairns Jr J. The emergence of global environmental awareness. J. Environ. Sci.(China), 1990,2(2): 1~17

[6] Liying Feng, Yijing Du,Xiangyun Lv. $Cu^{2+}$, $Cd^{2+}$ toxicity tests on the *Paramecium.* Journal of Anhui Agricultural Sciences(China), 2008, 36(8):3246~3247

[7] Yong Cui, Jiangfeng Guo,Bujin Xu, etc. Chlorpyrifos and cypermethrin on the impact of cytochrome P450 murine. Environment and Health(China), 2008, 25(9): 789~792

[8] Haoyuan Hu, Jiasheng Hao,Lu Jin. $Cd^{2+}$ on the population of toxic effects. Biology Magzine(China), 2006, 23(1): 19~21

[9] Zhichong Pan, Yun Liu, Pingyue Sun. Copper and zinc ions on Acute Toxicity *Paramecium caudatum*. Aquatic Sciences(China), 2005, 24(10):19~21

[10] Yongxin Zhou,Zongshe Zhang. Aquatic toxicity testing methods. Agriculture Press(China), 1989:1~156

[11] Jihe Yang,Changming Sun,Danlin Tang. Applied Biostatistics. Beijing Science Press(China),1983,16(5):303~334

[12] Feng Guo, Jun Zhang,Wenfang Li, etc. A simple and practical method for isolation and enumeration of protozoa. Journal of Tongji University ( Medical Science )(German), 2001, 22(4): 73~74

*Advanced Materials Research Vol. 937 (2014) pp 578-584*
*© (2014) Trans Tech Publications, Switzerland*
*doi:10.4028/www.scientific.net/AMR.937.578*

# Responses of water holding characteristic of crown debris and litter in a Cunninghamia lanceolata stand to ice-snow damage

Qinjing Li[1,a], Yunting Hao[2,b], Li Xue[3,c*], Xiaoli Hou[4,d]

[a]623638417@qq.com, [b]529515276@qq.com, [c]forxue@scau.edu.cn, [d]1135401013@qq.com

( College of Forestry, South China Agricultural University, Guangzhou, 510642, P. R. China )

*Corresponding author: Li Xue (forxue@scau.edu.cn)

**Keywords:** crown debris; Cunninghamia lanceolata; litter; water absorption rate; water-holding capacity

**Abstract.** Severe ice-snows caused break of many trees and a lot of crown debris in south China in 2008. Stem damage and crown debris. In order to determine the water holding characteristics of the crown debris, the water holding rate and water absorption rates of crown debris and litter were studied in a Cunninghamia lanceolata stand suffering from ice-snow damage occurring from January to February, 2008. The order of water-holding capacity of the components was leaves > litter > branches> stemwood > stembark in each stage of immersing water. The maximum water holding capacities of stemwood, branch, leaves, stembark and litter were 6.75, 8.13, 10.9, 2.72 and 8.22 t•ha 1, respectively. Maximum water holding rates of stemwood, branch, leaves, stembark and litter were 2271, 2144, 3199, 2800 and 3018 g•kg 1, respectively. Water absorption rate of each component sharply decreased with increasing immersed time from 0.5 to 4 hours, and then slowly decreased. The logarithm equation predicted water-holding capacity and water holding rates of crown debris and litter quite well and the negative exponential equation predicted water absorption rate within an 8.5% error.

## 1. Introduction

The worst ice-snow damages in China struck southern China from January to February, 2008, resulting in serious damage to the forests at higher elevations (>500 m). The ice-snow damages spread to 19 provinces of China with an area of 2.09×108 ha and caused breakages of many trees and a great deal of crown debris, which provides a more steady input of energy and nutrients, water and soil conservation in these forests. Most researches after ice storms aimed at evaluating levels of tree damage as a function of species, tree size, physiographic factors, ice storm severity and management practices [1-7]. However, ice-snows can also directly affect soil and water conservation. Despite the importance of crown debris for water-holding capacity, its hydrological effects are seldom studied.

Litter layers from most forests provide benefits for erosion control, infiltration, limiting soil water loss by evaporation. In particular, a litter layer has a significant effect on water holding, and water holding characteristic of litter can be simulated by prediction models [8]. These findings on the litter layer will be effectively used for developing prediction models on soil temperature and water content under the litter layer [9] and for determining optimal thickness of the litter layer to enhance soil water conservation [10]. Several researchers have also compared the effect of the litter layer on rainfall interception [11, 12] and the relationship between rainfall interception by the litter layer and evaporation from the intercepted water [13]. The amount of litter layer varies with topography and season changes due to the characteristic cycling of litterfall and decomposition, which leads to experimental and technical difficulties for evaluating the effect of the litter layer on water holding. Until recently, few studies have been conducted to analyze water holding characteristic of litter by models [8,14]. Continuous field studies on the water holding characteristics of crown debris and litter in forests are time consuming and expensive, whereas simulation models are useful tools for understanding water holding changes of crown debris and litter in time intervals.

Cunninghamia lanceolata (Lamb.) Hook. is a fast-growing conifer and is being widely used for a variety of products in China [15]. However, many C. lanceolata stems were broken by this ice-snow, because a lot of icicles hanged from their leaves and branches. Some attempts have been made to quantify the water holding characteristics of litter in forests of Acacia mangium[16], Quercus variabilis and Pinus massoniana [17], Abies fabric [18], C. lanceolata, Pinus elliottii and Eucalyptus urophyll [8], Michelia macclurei, Schima superba and Castanopsis fissa[14,19-24], but little information is available concerning water holding ability of crown debris in woodlands. Such information is important to understand the hydrological effects of crown debris and litter on forests.

The objectives of this study are to use logarithm equation and negative exponential equation to evaluate the water holding abilities of crown debris and litter as well as their water absorption rate, and to validate the models against field data.

## 2. Materials and methods

The study site was situated in Lechang Forest Farm，Lechang County (25° 09′ ~25° 10′ N, 113 ° 30′ ~113° 31′ E), northern Guangdong Province, P. R. China. The site is characterized by subtropical monsoon climate, with a short winter season and a hot and long summer season. The average temperature is approximately 19.6℃ and monthly mean temperature ranges from 9.3℃ in January to 28.2℃ in July. The annual rainfall averages 1069 mm, occurring mainly between April and August.

Field investing study was carried out in a 17-year-old C. lanceolata stand in March 2008. Three plots of 400 m2 were established. The plots were located in an area about 700 m above sea level with a southwest exposure (SW80º20'). The plots had a slope degree of from 30º to 40º. The soil bulk density, total porosity and capillary moisture capacity in the stand were 1.17 g•cm-3, 65.6%, and 43.3 %, respectively. Organic matter content at soil depth of 0-20 cm was 54.33 g•kg-1 and pH was 5.0. Chemical characteristics of the soil showed that total N, total P and total K were 2.34, 0.61 and 20.09 g•kg-1, respectively, and alkalizate hydrolytic N, available P and available K were 127.6, 3.2, 212.8 mg•kg-1, respectively. The trees were broken by 100%, and the mean diameter at breast height (DBH) and height of damaged stems were 13.6 cm and 7.7 cm, respectively. The understory coverage was very low, consisting mainly of Woodwardia Japonica and Adiantum capillus-veneris. Soil has been classified as lateritic red earth.

The DBH and the height of all damaged stems were measured in each plot. Within each plot, six sub-plots (each size for 4 m2) were set up randomly. In each sub-plot, crown debris and litter were collected and then crown debris was separated from branches, leaves, stemwood and stembark for weight calculation. Subsamples were taken to laboratory and dried to constant weight at 80℃ for measuring dry weight.

About 100-g samples of stemwood, branches, leaves, and stembark and litter, contained within perforated bags with holes of 0.2-mm diameter, were immersed in water for 0.5, 1, 1.5, 2, 4, 6, 8, 10, 12, 16 and 24 h, respectively. The samples were removed from the water and allowed to remove the excess water, which is not really bound within crown debris and litter. Water-holding capacity (WH, (t• ha-1)), and water holding rate (WR，(g• kg-1)) and absorption rates (WA, (g• kg-1• h-1)) of crown debris and litter were calculated using the following equations, respectively [8]：

$$WH = [WF\text{-}WD] \times 10 \quad (1)$$

$$WR = (WH/WD) \times 1000 \quad (2)$$

$$WA = WR / t \quad (3)$$

Where, WF (kg•m$^{-2}$) is fresh weight of crown debris or litter, WD (kg•m$^{-2}$) is dry weight of crown debris or litter and t (h) is immersed time. Each sample had three replications. According to water absorption speed of components, the water-holding capacity was divided into three stages: stage I (from 0 to 0.5 hour of immersing water), stage II (from 0.5 to 8 hour) and stage III of immersing water (from 8 to 24 hour).

## 3. Results

### 3.1. Water-holding capacity

The dry weight of crown debris was 19.11 t•ha 1, of which stemwood, branches, leaves, and stembark were 5.35, 7.11, 5.14 and 1.51 t•ha-1, respectively. Litter dry weight was 3.72 t•ha 1, being about 20% of dry weight of crown debris (Table 1).

Table 1 Amounts of crown debris and litter

| Components | | Fresh weight (t hm$^{-2}$) | Dry weight (t hm$^{-2}$) | Water content (%) |
|---|---|---|---|---|
| Crown debris | Stemwood | 9.18±8.28 | 5.35±4.83 | 41.7 |
| | Branches | 12.74±4.20 | 7.11±2.34 | 44.2 |
| | Leaves | 10.68±3.52 | 5.14±1.69 | 51.9 |
| | Stem bark | 3.02±2.14 | 1.51±1.07 | 50.0 |
| | Total | 35.62 | 19.11 | |
| Litter layer | | 7.01±3.13 | 3.72±1.66 | 47.0 |

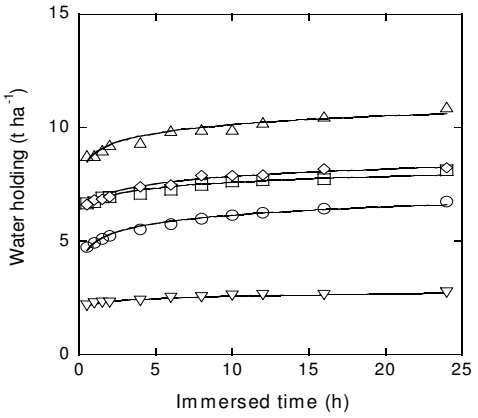



Figure 1 Relationships between water holding of crown debris and litter and immersed time
○, stemwood; □, branch; △, leaf; ▽, stembark; ◇, litter

The water-holding capacity can be divided into three stages from Figure 1. Water absorption speeds of all components were very fast in stage I of immersing water (from 0 to 0.5 hour), and the water-holding capacities of stemwood, branch, leaves, stembark and litter reached 4.74, 6.67, 8.78, 2.16 and 6.62 t•ha 1, respectively, accounting for 70.2%, 82.0%, 80.6%, 79.4% and 80.5% of their maximum water-holding capacities (immersing water for 24 hours in stage III), respectively. However, as immersing water time increased, speeds of water absorption for all components began to decrease gradually, the ratios of water holding of stemwood, branch, leaves, stembark and litter to their maximum water-holding capacities declined, respectively, to 18.5%, 10.0%, 10.6%, 13.2% and 15.5% in stage II (from 0.5 to 8 hours) and to 11.3%, 8.0%, 8.9% 7.4% and 4.0% in stage III (from 8 to 24 hours).

The water-holding capacity was in the order of leaves > litter > branches> stemwood > stembark in each stage of immersing water. After 24 hours of immersing water, stemwood, branch, leaves, stembark and litter reached their maximum water-holding capacities with values of 6.75, 8.13, 10.9, 2.72 and 8.22 t•ha 1, respectively.

The logarithm equation can predicate water-holding capacity of stemwood, branch, leaves, stembark and litter quite well. The predicted water-holding capacities for components had the similar trends with the measurements. The correlation between each component and immersed time was very significant ($P < 0.001$) (Table 2). Differences between predicted and observed water-holding capacities varied between 0 and 3.6% of the observed values for stemwood, between 0.3% and 2.7% for branches, between 0 and 3.4% for leaves, between 0.1% and 2.9% for bark and between 0.3% and 2.4% for litter.

Table 2 Equation between water holding of each component and immersed time

| Components | Equation | *R* | *P* |
|---|---|---|---|
| Stem wood | $W_H$=1.2093log*t*+4.9324 | 0.989 | <0.001 |
| Branches | $W_H$ =0.8435log*t*+6.7456 | 0.967 | <0.001 |
| Leaves | $W_H$ =1.2667log*t*+8.8625 | 0.966 | <0.001 |
| Stem bark | $W_H$ =0.3386log*t*+2.2353 | 0.983 | <0.001 |
| Litter | $W_H$ =1.0665log*t*+6.7803 | 0.982 | <0.001 |

### 3.2. Water-holding rate

The holding water rate of each component presented the similar trends as their holding water. In stage I, (from 0 to 0.5 hour), water absorption rates of stemwood, branch, leaves, stembark and litter reached 1892, 1938, 2709, 2431 and 2574 g•kg 1, respectively, accounting for 83.3%, 90.7%, 84.7%, 86.8% and 85.3% of their maximum water holding rates (immersing water for 24 hours), respectively (Figure 2). The water holding rates of all components became slow with time, and the water holding rates of stemwood, branch, leaves, stembark and litter only decreased 237, 114, 223, 239 and 305 g•kg 1 in stage II (from 0.5 to 8 hours) and 142, 92, 267, 130 and 139 g•kg 1 in stage III (from 8 to 24 hours), respectively.

The water holding rate was in the order of leaves > litter > stembark > branches > stemwood in the early stage of immersed water (from 0.5 to 1.5 hour) and then the order changed to leaves > litter > stembark > stemwood > branches. After 24 hours of immersing water, stemwood, branch, leaves, stembark and litter reached their maximum water holding rates, being 2271, 2144, 3199, 2800 and 3018 g•kg 1, respectively.

Water absorption rate of each component sharply decreased with increasing immersed time between 0.5 to 4 hours, and then slowly decreased (Figure 3a-e). The water absorption rates of stemwood, branch, leaves, stembark and litter decreased by 86.5%, 87.2%, 87.0%, 86.8% and 86.6%, respectively, from 0.5 to 4 hours, whereas they only decreased by 11.0%, 10.6%, 10.5%, 10.8% and 11.0%, respectively, from 4 to 24 hours. The order of water absorption rate for all components was the same as the water holding rate.

The predicted water holding rate of each component was close to the measurement with some slightly underestimated or overestimated values (Figure 2). The difference between the measured and predicted water holding rates was within 1.7% for stemwood, 1.0% for branch, 2.6% for leaves, 1.8% for stembark and 1.8% for litter. The simulated water holding rate of each component was significantly correlated with the measured water holding rate ($P < 0.001$) (Table 3).

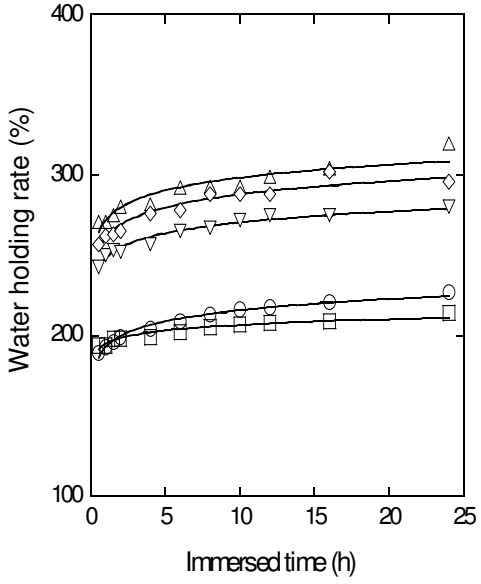



Figure 2 Relationships between water holding rate of crown debris and litter and immersed time.
○,stemwood; □ branch; △, leaf; ▽, stembark; ◇, litter

Table 3 Equation between water holding rate of each component and immersed time

| Components | Equation | *R* | *P* |
|---|---|---|---|
| Stemwood | $W_R$=227.91log*t*+1929 | 0.991 | <0.001 |
| Branches | $W_R$ =118.64log*t*+1949 | 0.963 | <0.001 |
| Leaves | $W_R$ =266.14log*t*+2719 | 0.942 | <0.001 |
| Stembark | $W_R$ =224.63log*t*+2480 | 0.983 | <0.001 |
| Litter | $W_R$ =272.86log*t*+2609 | 0.967 | <0.001 |

### 3.3 Water absorption rate

Although the simulated values for water absorption rates of all components were slightly underestimated in the later stage, the simulated water absorption rates were significantly correlated with the measured water absorption rates ($P < 0.001$)(Table 4). The greatest differences between predicted and observed water absorption rates were 4.7%, 2.9%, 8.5%, 1.9% and 6.3% for stemwood, branches, leaves, bark and litter, respectively.

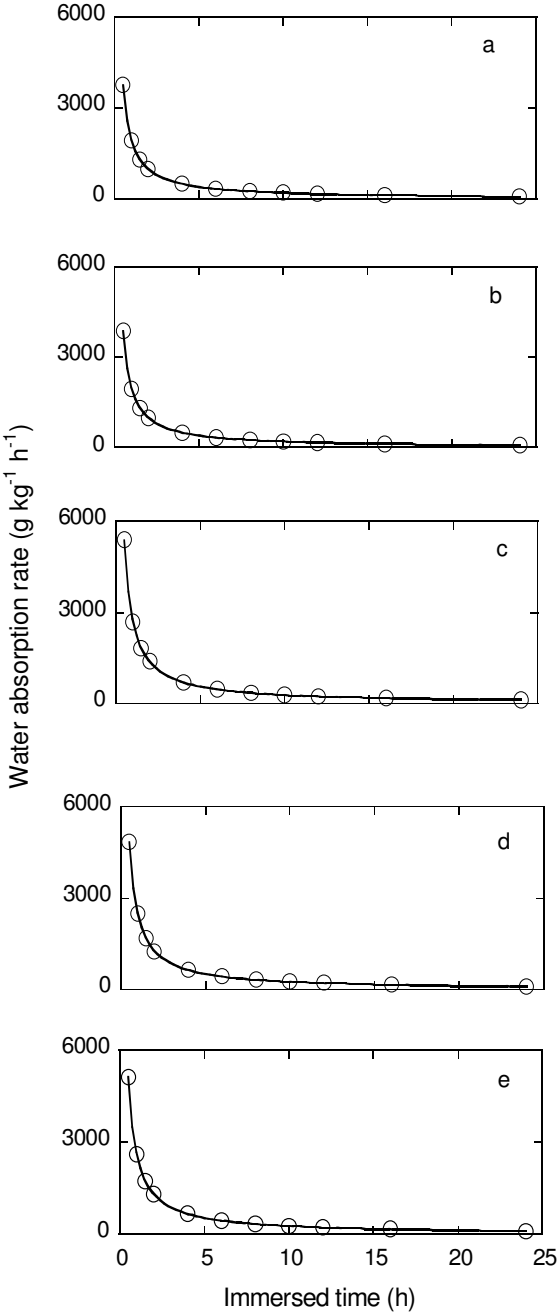



Figure 3 Relationships between water absorption rate of crown debris and litter and immersed time.
a, stemwood; b, branch; c, leaf; d, stembark; e, litter

Table 4 Equation between water absorption rate of each component and immersed time

| Components | Equation | $R^2$ | $P$ |
|---|---|---|---|
| Stemwood | $W_A=1938\cdot t^{-0.964}$ | 0.999 | <0.001 |
| Branches | $W_A=1956\cdot t^{-0.985}$ | 0.999 | <0.001 |
| Leaves | $W_A=2740\cdot t^{-0.980}$ | 0.999 | <0.001 |
| Stembark | $W_A=2489\cdot t^{-0.968}$ | 0.999 | <0.001 |
| Litter | $W_A=2623\cdot t^{-0.972}$ | 0.999 | <0.001 |

## 4. Discussion

Water-holding capacity of each component is decided by its dry weight and water-holding rate, and both crucially affect water-holding capacity of each component, as a result, the order of maximum water-holding capacity of the components is leaves > litter > branches> stemwood > stembark.

Crown debris has many physical characteristics that enable it to serve litter-like functions, such as water-holding capacity. Assuming that the crown debris is recharged during the rainy in the C. lanceolata stand, the total holding water within the crown debris reached 28.50 t•ha-1, which is substantially greater than that within the litter (8.22 t•ha-1). Further, soil water is better protected from evaporative loss due to crown debris layer being much thicker than the litter layer. The characteristics of the litter layer on water holding were well demonstrated by the result obtained from several stands by Xue et al. [8] and Peng et al. [14], who found that water-holding capacities from the litter varied from 9.8 to 17.9 t•ha-1 for stands of C. lanceolata, Pinus massoniana, P. elliottii, Acacia mangium and Eucalyptus urophylla, and varied from 13.74 to 17.7 t•ha-1 for stands of Michelia macclurei, Schima superba and Castanopsis fissa, which were more than that of the litter in the present study. This is probably due to lower dry weight of litter in the present study than those in other stands. However, the crown debris will ensure greater water holding ability in the studied stand than other stands, since a lot of crown debris has a high water absorption ability, which promotes the water absorption process.

The ground receives a massive influx of crown debris, which drastically alters woodland conditions and increases water holding ability, but improved conditions may last only briefly. Breakages of a lot of stems will increase incoming solar radiation on the forest floor due to disappearance of crown, which suggests that the absorbed solar radiation would be used to promote evaporation of crown debris. Dryness of crown debris and litter increases the fire risk caused by annual drought. Therefore, compared with the stands without ice snow damage, the C. lanceolata stand suffering from ice-snow damage will have a higher susceptibility to fire disturbance.

The predicted water holding characteristics by models given in Tables 2, 3 and 4 show the same trends with the measurements during the experimental period. The logarithm equation predicted water holding and water holding rate within a 3.6% error and the negative exponential equation predicted water absorption rate within an 8.5% error, which suggest that the models well described water absorption processes of crown debris and litter. The validity of logarithm equation and negative exponential equation is supported with many experimental data[8,14], showing that the relationships between immersed time and water holding as well as holding water rate and between immersed time and water absorption rate are discernable in forests. It should be possible to produce a truly useful tool for studying water holding characteristics of forests. The present models include a potential to predict the water absorption processes regardless of time and site, for it is possible to be used in a range of stand at anytime and anywhere, specially with situations which cannot easily or quickly be produced in reality. Empirical model is a basic approach for forest study, which can be used to guide further research and increases our understanding of the empirical patterns of water holding characteristics of crown debris and litter. The major drawback of the modeling approach is the lack of field evidence to validate model predictions on the sites with various topographies in different seasons, because slope and exposure of hills affect water holding, and solar radiation and soil temperature also affect litter evaporation. In order to extend reliable application of the models, further studies on field conditions with different seasons are required, considering the vapor in the saturated crown debris and litter

**Acknowledgements**

This study was partially supported by Foundation of Guangdong Forestry Bureau (No. 4400-F09054).

**References**

[1] S.M. Duguay, K. Arii, M. Hooper and M.J. Lechowicz: Environmental Monitoring and Assessment 67(2001), p. 97-108.

[2] A.G. Rhoads, S.P. Hamburg, T.J. Fahey, T.G. Siccama, E.N. Hane, J. Battles, C. Cogbill, J. Randall and G. Wilson: Canadian Journal of Forest Research 32 (2002), p. 1763–1775.

[3] A. Hopkin, T. Williams, R. Sajan, J Pedlar and C. Nielsen: Forestry Chronicle 79 (2003), p. 47–53.

[4] C. Nielsen, O. Van Dyke and J. Pedlar: Forestry Chronicle 79(2003), p. 70–74.

[5] J.L. Morris and W.D. Ostrofsky: Northern Journal of Applied Forestry 22 (2005), p. 262–267.

[6] J.M. Tang, C.W. Sun, J.H. Dai, H.G. Liu and X. Y. Zhen: Scientia Silvae Sinicae 44(11) (2008), p. 2-10, In Chinese

[7] Y.Z. Xu, X.M. Sun, C.W. Sun, C.Q. Du, B.R. Chen and D.Q. Zhang: Scientia Silvae Sinicae 44(11) (2008), p. 11-17, In Chinese

[8] L. Xue, Y.J. He, M. Qu, M. Wu and Y. Xu: Acta Phytoecologic Sinica 29(2005), p. 415-421, In Chinese

[9] M.A. Fosberg: Heat and water vapour flux in conifer litter and duff: a theoretical model. USDA Forest Service Research Paper RM--152, Fort Collins, Colorado, 1975.

[10] F. Bussière and P. Cellier: Agricultural and forest meteorology 68(1994), p. 1-28.

[11] J.D. Helvey and J.H. Patric, in: Research on interception losses and soil moisture relationships, edited by W.T. Swank, D.A. Crossley, Forest hydrology and ecology at Coweeta. Springer-Verlag, New York, p. 129–137 (1988),

[12] W.M. Putuhena and I. Cordery: Journal of Hydrology 180(1996), p. 283-299.

[13] J.I. Pitman: Journal of Hydrology 111 (1989), p. 281—291.

[14] Y.Q. Peng, L. Xue, H. Cao, X.R. Ren and L.L. Liang: Journal of Soil and Water Conservation 20 (2006), p. 189-191, 200, In Chinese

[15] L. Xue: Forest Ecology and Management 89 (1996), p. 115–123.

[16] W.J. Shen, S.L. Peng, G.Y. Zhou, Y.B. Lin and Z.A. Li: Acta Ecologica Sinica 21(2001), p. 846–850, In Chinese

[17] J.H. Cheng, H.J. Zhang, Y.H. Shi, Y. Cheng, S.L. Qi, F. He and L. Pan: Chinese Journal of Applied Ecology 14(2003), p. 1825—1828, In Chinese

[18] H.J. Zhang, J.H. Cheng, Y.H. Shi, S.L. Qi, Y. Cheng, L. Pan and F. He: Journal of Soil and Water Conservation 17(3) (2003), p. 55–58, 123 In Chinese

[19] X.D. Liu, Q.X. Wu and H.Y. Zhao: Journal of Soil and Water Conservation 5(1991), p. 87—91, In Chinese

[20] S.M. Dabney: Journal of Soil and Water Conservation 53 (1998), p. 207–213.

[21] Z.Q. Hao and L.H. Wang: Chinese Journal of Applied Ecology 9(3) (1998), p. 237-241, In Chinese

[22] J.H. Yang, Y.T. Z hang, H.Y. Li, and J.B. Xia: Journal of Soil and Water Conservation 17(2003), p. 141–144, In Chinese

[23] H.J. Zhang, J.H. Cheng, X.X. Yu, D.S. Zhang and Y.T. Zhao: Scientia Silvae Sinicae 39(5) (2003), p. 147-151, In Chinese

[24] Y.C. Luo, S.H. Han, H.C. Wang, J.M. Liu, J. Wei and G. Wu: Chinese Journal of Applied Ecology 15(6) (2004), p. 919—923, In Chinese

*Advanced Materials Research Vol. 937 (2014) pp 585-589*
*© (2014) Trans Tech Publications, Switzerland*
*doi:10.4028/www.scientific.net/AMR.937.585*

# Study on Particle Breakage of Coarse-grained Soil Based on Large-scale Triaxial Test

Fu-yong CHU[1, a]

[1]School of Civil Engineering, Lishui University, Lishui, Zhejiang 323000, China

[a]cfy1976@hhu.edu.cn

**Keywords:** coarse-grained soil; Large-scale triaxial tests; particle breakage; strength.

**Abstract:**Using large-scale shearing device, isotropiclly consolidated-drained triaxial test under different confining pressures are performed for overburden material of ShuangJiangKou earth dam which relative density is 0.8. The relationship between particle breakage of coarse-grained soil and input plastic work under loading and between particle breakage and confining pressure and between particle breakage and strength of coarse-grained soil. The results show that the particle breakage of coarse-grained soil and the input plastic work under loading is closely related. The particle breakage of coarse-grained soil increase with the input plastic work and there is a relationship of power function between $B_g$ and $W_p$. the increase of confining pressure will lead to the increase of particle breakage of coarse-grained soil, and there is a relationship of power function between $B_g$ and $\sigma_3/P_a$. the increase of particle breakage of coarse-grained soil will lead to the decrease of strength of coarse-grained soil, and a relationship of linear between $B_g$ and $\varphi$.

## Introduce

Particle breakage is one of important characteristics of coarse-grained soil. Recent research[1] has demonstrated that the particle breakage is liable to happen even confining pressure is low or the input energy is not very big. The particle breakage can lead to the variation in size grading of coarse-grained soil before and after testing, which produce influence on the characteristics of strength and deformation of coarse-grained soil. On the other hand, the coarse-grained soil is widely used in the construction of rock-fill dam, railway and express highway. Therefore, the problem of strength and deformation by particle breakage has been gradually attracted more attention by engineering circles.

During the past few decades, A Large number of research on particle breakage of coarse-grained soil have been carried out by many scholars abroad, and have obtained certain achievements[2-8]. However, Because the particle breakage characteristics of coarse-grained soil is more complicated. Research on influence of particle breakage on characteristics of stress and strain of coarse-grained is relative less.

Therefore, Using large-scale shearing device, Isotropic consolidated-drained triaxial tests under different confining pressures are performed for the overburden material of Shuangjiangkou earth dam whose relative density is 0.8. Base on the research of predecessors, the dissertation studies the characteristics of particle breakage of coarse-grained soil under external load. The influence on particle breakage by confining pressure and the influence on peak strength by particle breakage are analyzed.

## Measurement of Particle Breakage

At present, a certain parameter which can quantitatively reflect he variation in size grading of coarse-grained soil before and after testing usually used as of particle breakage. There are three kinds quantitative indexes of measurement of particle breakage.

The particle breakage ratio $B_g$ which can reflect degree of particle breakage was proposed by Marshal[9]. The define of particle breakage $B_g$ is the sum of absolute value of difference value of the content of every group of particles before and after testing, that is

$$B_g = \sum \left| \Delta w_k \right| \tag{1}$$

Where $\Delta w_k = w_{ki} - w_{kf}$, $w_{ki}$ is the value of the content of a certain group of particles before testing and $w_{kf}$ is the value of the content of a certain group of particles after testing.

Shu-tian Bai[10] proposed that the difference value of constrained grain size can ben used to measure the degree of particle breakage, that is

$$B_{60} = d_{60i} - d_{60f} \tag{2}$$

Where $B_{60}$ is the difference value of constrained grain size, $d_{60i}$ is the value of constrained grain size before testing and the $d_{60f}$ is the value of constrained grain size after testing.

HARDIN[11] proposed the initial crushing potential $B_{pi}$ and $B_{pf}$ whose define are respective that the area enclosed by the distribution curve of constrained grain size before and after testing and the vertical line when the particle size is 0.074mm, Based on which, breakage $B_t$ is proposed by HARDIN. That is

$$B_t = B_{pi} - B_{pf} \tag{3}$$

Where $B_t$ is breakage. And meanwhile, relative breakage ratio $B_r$ is also proposed by HARDIN. That is

$$B_r = B_t / B_{pi} \tag{4}$$

Where $B_r$ is relative breakage ratio.

**Method of Testing**

The material of test is the overburden material of Shuangjiangkou earth dam on Dadu River whose particle is tact, angularity is less, strength is high and permeability is strong. Because of the constrain of particle diameter and size of sample, the nature grading is reduced scale by the hybrid method of the document [12] and the size grading curve is showed as the Fig 1. The biggest dry density is obtained by the vibratory compaction experiment of surface and the least dry density is obtained by the loose-filled experiment. The biggest dry density is 2.29g/cm$^3$ and the least dry density is 1.93g/cm$^3$,the dry density of sample preparation is 2.25g/cm$^3$, and the relative density is 0.8.

Large-scale shearing device is adopted, which is 300mm in diameter and 600mm in height and 60mm in the most major granular diameter. The samples are made by the compaction test and is compacted in five layers. The saturating samples are made by the water head saturated and pumping saturated method. The loading is controlled by the method of radial strain control in loading stage and the shear rate is 0.9mm/min. The confining pressure of different test are all respectively 200, 500, 1200, 2000and 2500kP$_a$. the value of the content of a certain group of particles before and after testing are both listed in the table 1.

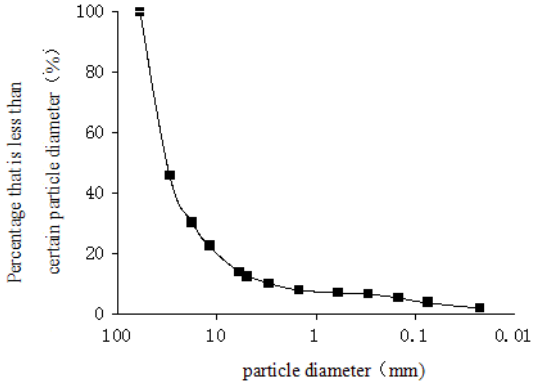



Fig. 1. Size grading curve of coarse-grained soil

Table 1. Particle size distribution under various confining pressures

| Test condition | Confining pressure/kP$_a$ | mass fraction of coarse particles of different size grading(mm) group/% | | | | | $B_g$ /% |
|---|---|---|---|---|---|---|---|
| | | d=60～40 | d=40～20 | d=20～10 | d=10～5 | d=5～0 | |
| before | | 33.6 | 33.4 | 12.8 | 7.6 | 12.6 | |
| after testing | 200 | 30.53 | 32.38 | 13.59 | 7.16 | 16.34 | 4.53 |
| | 500 | 27.66 | 32.35 | 15.15 | 8.06 | 16.78 | 6.99 |
| | 1200 | 24.15 | 31.39 | 16.49 | 9.52 | 18.45 | 11.46 |
| | 2000 | 21.89 | 31.11 | 17.02 | 10.14 | 19.84 | 14 |
| | 2500 | 20.94 | 30.59 | 16.56 | 11.05 | 20.85 | 15.47 |

**Test Result Analysis**

**Relationship of Particle Breakage and Plastic Work**

The dissertation choose the particle breakage ratio $B_g$ as the index of particle breakage of coarse-grained soil. Recent research[2] has demonstrated that the particle breakage of coarse-grained soil and input plastic work under loading is closely related. In order to study the relationship of the particle breakage ratio $B_g$ and plastic work, based on the data of table 1, the particle breakage ratio $B_g$ and the plastic work $W_p$ under different confining pressure are sorted out and the curves of $B_g \sim W_p$ are accumulated as the Fig2.

Fig 2 shows that The figuire 3 shows that the particle breakage ratio $B_g$ increases with the increase of the plastic work $W_p$, and there is a relationship of power function between $B_g$ and $W_p$ which may be formulated by the expression

$$B_{ig} = a\left(W_p\right)^b \tag{5}$$

Where $a$ and $b$ are both parameters of material. In this experiment, the parameters obtained by fitted is respectively 0.38 and 0.508. The relative coefficient $R^2$ is 0.98.

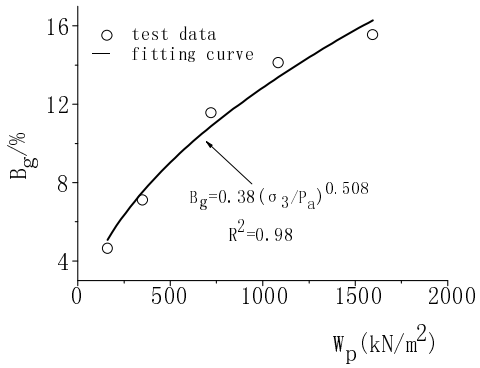



Fig. 2. Relationship of $B_g$ and $W_p$

**Relationship of Particle Breakage and Confining Pressure**

Based on the data of table 1, the particle breakage ratio $B_g$ under different confining pressure are sorted and the curve of $B_g$ and $\sigma_3$/P$_a$ is accumulated as the Fig 3. The figuire 3 shows that particle breakage ratio $B_g$ increases with the increase of $\sigma_3$/P$_a$, and there is a relationship of power function between $v_{if}$ and $\sigma_3/P_a$ which may be formulated by the expression

$$B_{ig} = a\left(\sigma_3/P_a\right)^b \tag{6}$$

Where $a$ and $b$ are both parameters of material. In this experiment, the parameters obtained by fitted is respectively 0.31 and 0.481. The relative coefficient $R^2$ is 0.99.

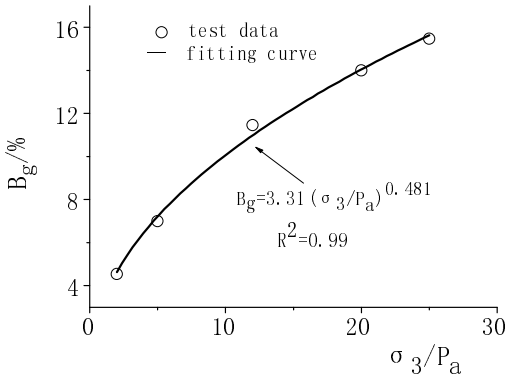



Fig. 3. Relationship of $B_g$ and $\sigma_3/P_a$

**Relationship of Particle Breakage and Peak Strength**

In order to study the relationship of the particle breakage ratio $B_g$ and strength $\varphi$ under different confining pressure, based on the data of table 1, the particle breakage ratio $B_g$ and the plastic work $\varphi$ under different confining pressure are sorted out and the curves of $B_g \sim \varphi$ are accumulated as the Fig4.

Fig 4 shows that particle breakage ratio $B_g$ decreases with the increase of $\varphi$. This shows that the increase of particle breakage will lead the decrease of peak internal friction angle. Besides, there is a relationship of linear between $B_g$ and $\varphi$, which may be formulated by the expression

$$B_g = m\varphi + n \tag{7}$$

Where $m$ and $n$ are both parameters of material. In this experiment, the parameters obtained by fitted is respectively -0.831 and 51.15. The relative coefficient $R^2$ is 0.99.

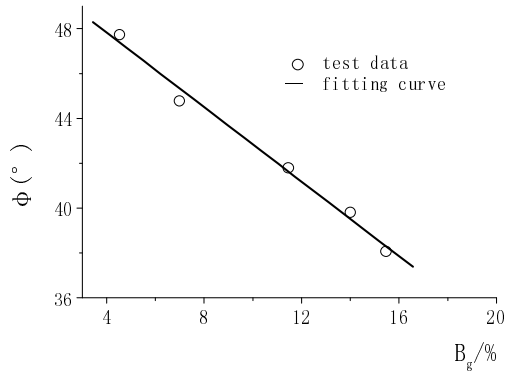



Fig. 4. Relationship of $B_g$ and $\varphi$

**Conclusion**

Isotropiclly consolidated-drained triaxial test under different confining pressures is performed for overburden material of ShuangJiangKou earth dam which relative density is 0.8 using large-scale shearing device. The particle breakage characteristics of coarse-grained soil is studied. Some preliminary conclusion ise obtained as follows:

(1) The particle breakage of coarse-grained soil and the input plastic work under loading is closely related. The particle breakage of coarse-grained soil increase with the input plastic work and there is a relationship of power function between $B_g$ and $W_p$.

(2) The increase of confining pressure will lead to the increase of particle breakage of coarse-grained soil, and there is a relationship of power function between $B_g$ and $\sigma_3/P_a$ .

(3) The increase of particle breakage of coarse-grained soil will lead to the decrease of strength of coarse-grained soil, and a relationship of linear between $B_g$ and $\varphi$.

**Acknowledgements**

This work was financially supported by project for 2013 of education department of Zhejiang province. (Y201329667)

**References**

[1]Association of Geotechnique of Japan. In-situ compaction of coarse-grained materials[M]. GUO Xi-ling, WEN Dan, translators. Beijing:China Water Power Press, 1999:2-56.(in Chinese)

[2]Song Wei, Jun-gao Zhu. Study on wetting breakage of coarse-grained mate[J]. Chinese Journal of Rock Mechanic and Engineerin, 2006, 25(6): 1252-1258.(in Chinese)

[3]VESIC A S, CLOUGH G W. Behaviour of granular materials under high stress[J]. Journal of Soils Mechanics and Foundation Division, American Society of Civil Engineering, 1968, 94(3): 661-688.

[4]Han-long LIU, Hong-yu Qin, Yu-feng Gao, etc al. Experimental study on particle breakage of rockfiil and coarse aggregates[J]. Rock and Soil Mechanics, 2005, 26(4): 562-566.(in Chinese)

[5]Guang Yang, Bing-yin Zhang, Yu-zhen Yu, etc al. An experimental study on particle breakage of coarse-grained materials on various stress paths[J]. SHUILI XUEBAO, 2010，41(3):338-342.(in Chinese)

[6]INDRARATNA B, IONESCU D, CHRISTIE H D. Shear behavior of railway ballast based on large-scale triaxial tests[J]. Journal of Geotechnical and Geoenvironmental Engineering, ASCE, 1998, 124(5) : 439-449.

[7]Shi-chun Chi, Yu-feng Jia. Rowe's stress-dilatancy model modified for energy dissipation of particle breakage[J]. Chinese Journal of Geotechnical Engineering, 2005, 27(11) : 1266-1269.(in Chinese)

[8]LEE K L, FARHOOMAND I. Compressibility and crushing of granular soils in anisotropic triaxial compression[J]. Canadian Geotechnical Journal , 1967, 4(1): 68-86.

[9]Marsal R J. Large scale testing of rockfill materials[J]. Journal of Soils Mechanics and Foundations Division, ASCE, 1967, 93(SM2):27-43.

[10]Shu-tian Bai, Yi-hao Cui. Mechanics characteristics of rockfill[J]. Journal of Hydroelectricity, 1997, (3): 21-30.

[11]HAEDIN. Crushing of soil particles[J]. Journal of Geotechnical Engineering, ASCE, 1985, 111(10) : 1177-1192.

[12]Soil test procedures SL237-1999[S]. Beijing: China Water Power Press. 1999.

*Advanced Materials Research Vol. 937 (2014) pp 590-593*
*© (2014) Trans Tech Publications, Switzerland*
*doi:10.4028/www.scientific.net/AMR.937.590*

# The Research of Slope StabilityBased on Unsaturated Soil Theory

Chang-qing SHAO[1,a],Nan ZHANG[2,b],Feng-lan LV[1,c]

[1]Centre for Hydrogeology and Environmental Geology CGS, Baoding,Hebei071051, China

[2]China Institute of Geo-Environment Monitoring, Beijing 100081, China

[a]308823472@qq.com, [b]514979341@qq.com,[c]312844277@qq.com

**Keywords:** Unsaturated soil theory; Slope stability; Matric suction

**Abstract:** With the deep landslide induced by rainfall or more in practice, the existing evaluation methods are not suitable for to explain this kind of landslide during rainfall, which is the phenomenon of strong activity. This paper tries to improve existing methods for analyzing the stability of the landslide, the article set up to consider soil stability analysis method of the matrix suction side article discusses rainfall infiltration process middle side matrix suction changes impacting on the stability of the landslide, the preliminary discussion on the effect of rainfall on deep landslide are studied. Considering soil of the side of the evaluation methods of matrix suction jettisoned traditional saturated unsaturated soil mechanics analysis method, it can well reflect the process of rainfall infiltration, the matrix suction decreases, and the inter-atomic forces, stability factor to reduce the process, providing a train of thought for landslides evaluation.

## Introduction

In many parts of China are widely distribution of expansive soil, residual soil clay areas such as the mountain or artificial slope frequent landslides during the rainy season, causing potential safety hazard and huge economic losses. Each year during the rainy season, rainfall infiltration make the soil saturation and water content increases, causing the soil shear strength fallen sharply. The continuous rainfall can also cause underground water level rise or in relative water-resisting layer above the transient groundwater [1]. When the rainfall duration and intensity exceeds a certain limit, it can lead to landslide and slope instability. Unsaturated soil slope instability of landslide problems is still the research hotspot and difficulty problem of geological and geotechnical engineering, having great research value.

Especially in the shallow landslide in landslide disaster is most rare and cherished. Based on the theory of unsaturated soil mechanics, the slope rainfall infiltration phreatic surface in the body or saturated with groundwater pressure results in the decrease of slope stability, producing landslides. But due to near surface and shallow soil mostly unsaturated cohesive soil, the climate change on a large impact on its mechanical properties [2]. Based on discussion of unsaturated slope stability safety and the analysis of new progress on unsaturated slope instability caused by rainfall infiltration mechanism, further discussion is done on the influence of matrix suction of unsaturated soil shear strength.

## Unsaturated Soil Shear Strength Theory

At present, the study of unsaturated soil slope stability has more than 30 years. Many scholars in their respective experiment and theory was put forward on the basis of all kinds of expressions of effective stress for unsaturated soil, and on this basis to establish the corresponding shear strength formula of unsaturated soils. Which are widely recognized in geotechnical engineering, the influential formulas on unsaturated soil shear strength are A.W. Bishop and D.G. Fredlund put forward respectively in 1960 and 1960, and both formula is based on Mohr-Cloumb criterion [3].

Bishop believes that effective stress of unsaturated soils can be solved through a combination of two independent state variables($\sigma - \mu_\alpha$) and ($\mu_\alpha - \mu_\omega$), andmaterial variables $\chi$,the formula is:

$$\tau_f = c' + (\sigma - u_a)\tan\varphi' + \chi(u_a - u_w)\tan\varphi' \quad (1)$$

( $\tau_f$: shear strength of destruction; $c'$: effective cohesion intercept; $\sigma$: total stress; $u_a$: pore air pressure; $u_w$: pore water pressure; $(\sigma - u_a)$: net stress; $(u_a - u_w)$: matric suction; $u_w$: effective angle of internal friction)

Bishop formula has received by many scholars, but due to the suction$(u_a - u_w)$ value is difficult to measure, and $\chi$ is also unfavorable adopt, so it is not a lot of practical.

Fredlund'sdouble variable formula:

$$\tau_f = c' + (\sigma - u_a)\tan\varphi' + \chi(u_a - u_w)\tan\varphi^b \quad (2)$$

($\varphi^b$: related to the suction of Angle of internal friction)

These two kinds of strength formula in essence is consistent, comparing the formulas (1) and (2), it can be got:

$$\chi = \tan\varphi^b / \tan\varphi' \quad (3)$$

Then we get the unsaturated soil strength another form:

$$\tau_f = c' + (\sigma - u_a)\tan\varphi' + \frac{u_a - u_w}{1 + d(u_a - u_w)}\tan\varphi' \quad (4)$$

Unsaturated soil strength theory has important theory significance and the practical engineering is also very important. But due to various reasons, the development of test instruments work is always relative to the theoretical study shows certain hysteresis. Lag time may be a few years, also may for decades. And this, even if the test instrument design work very promptly, and not all units are designed to study unsaturated soil strength technical force and equipment. So try to find the right way, with routine test the strength of the unsaturated soil is very important.

## The Influence Factors of Unsaturated Slope Stability

Unsaturated soil slope under the condition of rain infiltration, severe increase, slide force increases, at the same time, the shear strength by increase of moisture content fell sharply again, this is the root cause of the rainfall caused instability [4].

Effect of unsaturated soil are the main factors causing the landslide instability as shown in table 1. The research results show that the slope geological conditions, the permeability coefficient of water-resisting layer and seepage control casing, factors such as rainfall intensity, rainfall duration and the type of formation of unsaturated soil slope of transient seepage field and the safety of the slope stability has a significant impact. The permeability of soil slope under the effect of rain infiltration, the bigger influence on the slope stability. The rainfall intensity and rainfall duration under the same conditions, the stability of the slope safety factor decreases with the increase of soil permeability coefficient. Under the condition of the total amount of rainfall, when the rains are growth, safety factor of slope stability with the soil permeability coefficient increases. When the slope top is vertical cracks, in the case of no rain infiltration, the stability of the slope safety coefficient changes with the increase of crack depth is not obvious, about 10%.Under the condition of rain infiltration, the slope stability safety factor along with the development of the slope cracks decreased obviously. On the slope top appear cracks, therefore, should be timely close clay compaction, avoiding direct infiltration rainwater.

Table 1. The influence factors of unsaturated slope stability

| Influence factors | Disadvantageous | No influence | Advantageous |
|---|---|---|---|
| Landslide slope | ≥20% | 10~20° | ≤10% |
| The average slip surface inclination | >30° | 10~30° | ≤10% |
| Sliding surface morphology | plane | wavy | zigzag |
| Rainfall patterns | rainstorm | medium-sized rainstorm | --- |
| Rainstorm intensity | center | sub central | Away From Center |
| Duration | ≥6h | 10min~1h | ≤10min |
| Osmotic coefficient | >1 | 0.8~0 | <1 |
| Top vertical cracks | existence | ≤10% | inexistence |
| Matric suction | reduce | invariant | enlarge |
| Transient seepage field | formation | None | --- |

Influence of unsaturated soil slope stability and landslide is the main mechanism of the induced: slope rainfall infiltration results in lower matrix suction of unsaturated zone soil slope and transient saturated zone is produced. While the matrix suction is reduced, makes the shearing strength of the unsaturated zone of slope soil decreased, leading to slope stability is reduced, and even landslides. On the analysis of the stability of unsaturated soil slope, the matrix suction should be considered against the effect of shear strength and rainfall infiltration in slope body form a transient saturated zone and transient water pressure.

## Considering the Stress Analysis of Slope Stability

For considering the matrix suction between article, by means of: the basic idea of Sarma method in slope sliding, it not only to overcome the main sliding surface shear strength, and it must be overcome the strength of the sliding body itself, sliding shear will occur within the body, also is the assumption that the traditional limit equilibrium law between shear stress and normal stress meet Mohr-Coulomb failure criteria[5].

According to the article above assumptions, take the *i*stick to force analysis,and the force analysis is shown in figure 1.

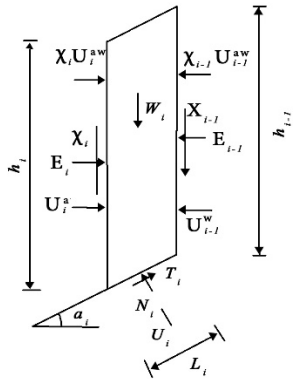



Fig. 1. Force analysis

$W_i$ is the gravity. $U_i^w$ is the pore water pressure. $U_i^{aw}$ is the matrix suction of the resultant force. $N_i$ and $T_i$ are the Contact stress and shear strength. $U_i$ is the groundwater pressure. When the bottom below the underground water level, its value for the bottom pore water pressure, when the floor above the underground water level, take part for the stress absorption. $h_i$, $L_i$ are the length of side and underside. $E_i, X_i$ is the normal force and tangential force. $a_i$ is the inclination angle of slip surface.

According to the static equilibrium conditions, there is:

$$N_i = (E_i - E_{i-1} + U_i^w - U_{i-1}^w + \chi_{i-1}U_{i-1}^{aw})\sin a_i - (X_i - X_{i-1})\cos a_i + W_i \cos a_i \quad (5)$$

$$T_i = (E_i - E_{i-1} + U_i^w - U_{i-1}^w + \chi_{i-1}U_{i-1}^{aw})\cos a_i - (X_i - X_{i-1})\sin a_i - W_i \sin a_i \quad (6)$$

According to the uniform shear strength theory of unsaturated soil saturated soil,there is:

$$T_i = \frac{c_i' L_i + N_i \tan \phi_i' - \frac{\theta_i - \theta_r}{\theta_s - \theta_r} U_i \tan \phi_i'}{F_s} \quad (7)$$

$$X_i = \frac{1}{f_s}\left(\overline{c_i'} h_i + E_i \tan \overline{\phi_i'}\right) \quad (8)$$

( $f_s$is safety factor; $\overline{c_1'}$ is the cohesion; $\phi_i'$is the internal friction angle)

Make (5) and (6) into (7), it can be got:

$$(X_i - X_{i-1})(\sin a_i - \frac{\cos a_i \tan \phi_i}{F_s}) + (E_i - E_{i-1})(\cos a_i + \frac{\sin a_i \tan \phi_i}{F_s}) = A_i - \frac{B_s}{F_s} \quad (9)$$

$$A_i = W_i \sin a_i - (U_i^w - U_{i-1}^w)\cos a_i - (X_i U_i^{aw} - X_{i-1} U_{i-1}^{aw})\cos a_i$$

$$B_i = c_i' L_i + [W_i \cos a_i - (U_i^w - U_{i-1}^w)\sin a_i + (X_i U_i^{aw} - X_{i-1} U_{i-1}^{aw})\sin a_i - \frac{\theta_i - \theta_r}{\theta_s - \theta_r} U_i] \tan \phi_i' \quad (10)$$

Following the above formula,it can be calculated at the same time considering soil bottom and side of unsaturated features of landslide stability coefficient.

## Conclusion

Through the analysis and research on the stability of unsaturated slope, it is found that the geological conditions of unsaturated slope. The permeability coefficient of water-resisting layer and seepage control casing, rainfall intensity, rainfall duration, rainfall type and early rain hold, the anisotropic permeability than on the formation of transient seepage field and the safety of the unsaturated soil slope stability have a significant impact. For unsaturated soil, the rain infiltration is an extremely complex saturated-unsaturated seepage process. Analysis should be the simplest uncoupled conditions, using the simplified two-dimensional infiltration model to simulate the seepage field finite element analysis, the limit equilibrium method was used to study the stability of unsaturated soil slope is of engineering significance and practical value. Deepeningto understand the above relations, the prediction and control of the unsaturated soil landslide disaster has important significance.

## Reference

[1] N. Lu, and J. Godt:Water Resources Research, Vol. 44 (2008) No.11, p. 28

[2] M. Huang, and C.Q. Jia:Computers and Geotechnics, Vol. 36 (2009) No.1, p.93

[3] D.V. Griffiths, and N. Lu:International journal for numerical and analytical methods in geomechanics, Vol. 29 (2005) No.3, p249

[4] M.S. Huang, and C.Q. Jia:YantuGongchengXuebao(Chinese Journal of Geotechnical Engineering), Vol. 28 (2006) No.2, p. 202

[5] L.Y. Tong, and W.X. Jain: Journal of Wuhan University of Technology, Vol. 34 (2012)No.11, p. 78

# CHAPTER 9:

# Environmental Science and Engineering

*Advanced Materials Research Vol. 937 (2014) pp 597-603*
*© (2014) Trans Tech Publications, Switzerland*
*doi:10.4028/www.scientific.net/AMR.937.597*

# Comparative Researches on the Provenances of Suspended Sediments in Different Reaches of Dongtiaoxi and Xitiaoxi Watershed

Zhao-peng LU[1,a], Xu-yin YUAN[1,b,*], Huan WANG[1], Hai-long CHEN[1], Wen-wen XU[1]

[1]College of Environment, Hohai University, Nanjing 210098, China

[a]zproo2011@126.com, [b]yxy_hjy@hhu.edu.cn

*Corresponding author

**Key words:** SS; Provenances; The geochemical model; Dongtiaoxi and Xitiaoxi watershed

**Abstract.** Dongtiaoxi and Xitiaoxi river are the two main discharge rivers of Taihu Lake. It is important to research the provenances of suspended sediments(SS) and the difference of the provenances. This paper establishes the geochemical model to quantify the proportions of SS sources with geochemical parameters, and then analyzes the contribution differences of the sources to SS in the basins and its reasons. The results show that the contribution of woodland is highest in the upper reaches of both Dongtiaoxi and Xitiaoxi basin, but the contribution of arable land has more differences. Arable land becomes a major contributor to the midstream of Dongtiaoxi and Xitiaoxi basin, while the contributions of woodland and urban land are larger in Dongtiaoxi basin. The SS contribution of urban land is highest in the downstream of Dongtiaoxi and Xitiaoxi basin, while the contribution of arable land is larger in Dongtiaoxi basin. During wet season and dry season, the differences of the sources contribution variations in Dongtiaoxi basin are not obvious, while that in Xitiaoxi basin are significantly obvious, that is the SS contributions of woodland and urban land in wet season are significantly higher than in dry season, while the contributions of arable land and bank sediment are on the contrary.

## Introduction

Natural and anthropogenic factors affect the water quality, including soil type, rainfall, various industrial and agricultural activities so on, so reduce the different characteristics of SS properties [1]. Soil erosion is one of the main sources of SS in the rivers, the properties of SS is closely related to land use / cover change [2-4]. Researches show that the nitrogen, phosphorus and other elements of the runoff loss and output have significant correlations with land use types [5-7]. SS in rivers were affected by agricultural cultivated land, forest land, grassland, urban land and bank sediment [8, 9]. The previous studies mainly involve the river water quality response to land use. However, there are few researches on the SS contribution of sources quantitatively, and less attention to the seasonal environmental conditions change on SS.

Therefore, this paper focus on establishing the geochemical quantitative model, and analyzing the contributions of different sources to SS quantitatively at different reaches (upstream, midstream and downstream) and under different hydrological conditions (wet season and dry season). Then the study investigates the effect of environmental conditions on SS, and explains the reasons for the contribution differences with comparative analysis the SS contributions of different sources in Dongtiaoxi and Xitiaoxi basin.

## Materials and Methods

### Study Area

Dongtiaoxi and Xitiaoxi river are located in Huzhou in the northern part of Zhejiang province and belong to the main discharge rivers of Taihu Lake. The main land use types are predominated by woodland, and followed by arable land, urban land, shrubland and water. The Dongtiaoxi stream has a catchment area of 2265.1 $km^2$. The Xitiaoxi stream has a catchment area of 2200 $km^2$. The

upper reaches of Dongtiaoxi river maintains the basic characteristics of river ecological system with bamboo and pecan planting. The middle reaches is affected by human activities strongly, of which major land use type is arable land. There is artificial river with complex hydrological condition in the lower reaches dominated by urban construction land. The upper reaches of the river is mainly ecological reserve area, more than 70% of the land is covered by forest. The lands of the middle-lower reaches are significant affected by agricultural, industrial and mining activities. These lands with different features display stagger distributions as shown in Fig. 1.

**Sample Collection and Chemical Analysis**

The soil and SS samples were collected during July and December of 2012. The sampling sites were selected from the upper to the lower reaches of Dongtiaoxi and Xitiaoxi watershed (Fig. 1). The number of source materials samples in each site is indicated in Table 1. The 20L water was collected at one site, then was filtered through a pre-washed 0.2μm cellulose membrane in a suction flask. These SS samples on the filter were flushed by using deionized water in the laboratory, and dried at 40 °C. The soil samples were air-dried and sieved through a 2-mm polyethylene sieve to remove large debris, stones and pebbles before analysis.

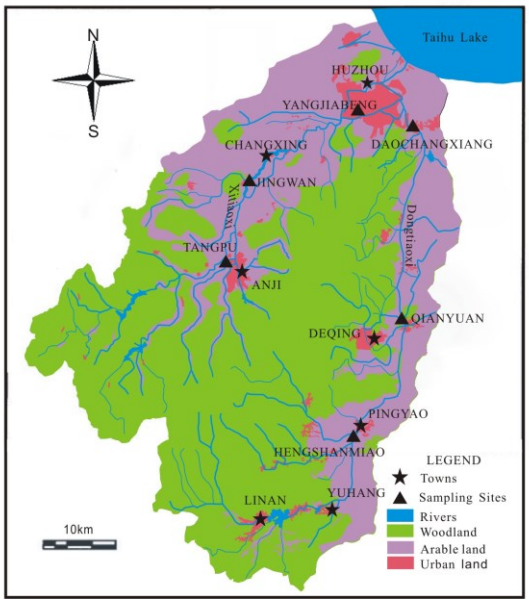



Fig. 1. Patterns of land use and the sampling sites in Dongtiaoxi and Xitiaoxi watershed

Table 1. The number of the source materials samples

| | Reaches | Arable land | Woodland | Urban land | Bank sediment |
|---|---|---|---|---|---|
| Dongtiaoxi | Upstream | 7 | 9 | 5 | 9 |
| | Midstream | 8 | 7 | 7 | 10 |
| | Downstream | 5 | 4 | 10 | 7 |
| Xitiaoxi | Upstream | 7 | 9 | 6 | 8 |
| | Midstream | 10 | 8 | 8 | 8 |
| | Downstream | 6 | 5 | 10 | 6 |

The geochemical variables of the samples were measured by the standard methods. TN was determined by the Kjeldahl method. The P content (TP, IP and OP) of samples were determined using a PyeUnicam SP6UV/visible spectrophotometer. Soil Organic carbon was determined by Walkley and Black procedure. The detection of the major elements and trace metals in all samples was performed by ICP-AES. Magnetic susceptibility of samples was measured by a Bartington MS2 dual frequency magnetic susceptibility instrument. The grain size was measured using a Laser Size Analyzer. Each batch of samples has a blank sample, every sample need to do parallel analysis three times to get the average value, and the error is less than 10%. All statistical analyses were performed with Microsoft Excel 2007 and SPSS 19.0 program.

### Quantifying Suspended Sediment Sources

Collins et al. described a multivariate mixed model to estimate the relative contribution of potential SS sources collected from each specified basin. This model was based on the inheritance principle of material composition, established a geochemical composite model to calculate the source proportions of SS at each site. First we distinguishes significant differences of different sources by the non-parametric Kruskal–Wallis H-test, then optimized discrimination between source groups by stepwise multivariate discriminant function analysis, and substituted these optimum results into the composite model to obtain the relative contribution of different sources finally [10, 11].

The model must satisfy two linear constraints, namely:

(a) the contribution from each source must lie within the range 0 to 1, i.e.

$$0 \leq P_s \leq 1 \tag{1}$$

(b) the sum of the contributions from all sources is 1, i.e.

$$\sum_{s=1}^{n} P_s = 1 \tag{2}$$

For each parameter contained within the multicomponent signature, a linear equation is established. The overall set of linear equations is generally over-determined and optimization using the sum of weighted least squares, is therefore utilized to minimize the sum of squares of the relative errors, viz.:

$$K = \sum_{i=1}^{n} \{(C_i - (P_{sl} * S_{il} * Z_w * O_w + P_{sg} * S_{ig} * Z_g * O_g + P_{sj} * S_{ij} * Z_j * O_j + P_{sa} * S_{ia} * Z_a * O_a))/C_i\}^2 \tag{3}$$

where: $C_i$= concentration of tracer parameter ( i )of SS in catchment

$P_s$= percentage contribution from each source material

$S_i$ = mean concentration of tracer parameter ( i ) in solid for each source material samples

Z = particle size correction factor

O= organic carbon content correction factor

The model simulates that when the K value to obtain the minimum, the independent variable $P_{sl}$, $P_{sg}$, $P_{sj}$, $P_{sa}$ are respectively the SS contributions of woodland, arable land, urban land and bank sediment in this paper. The operation conditions for the implementation of the model was with the help of MATLAB v7.10 software, and the related charts were drawn with Origin 8.0.

## Results and Discussion

### Using the Quantitative Model to Analyze the Sources of the Suspended Sediments

The Kruskall-Wallis H-test was used to test the differences of 18 geochemical variables (K, Ca, Na, Mg, Al, Fe, Cu, Cd, Cr, Pb, Ni, Mn, Zn, TOC, TN, TP, IP, MS) in different sources of Dongtiaoxi and Xitiaoxi basin. And multivariate discriminant function analysis was applied to select optimum variables to ensures the accuracy of the results. These optimum variables along with SS variables were applied to the composite model calculation. Due to the differences of different reaches, the model was used to analyze SS sources of the upstream, midstream and downstream respectively.

### The Mean Relative Contributions of Each Individual Sources in Dongtiaoxi Basin

The SS contribution of woodland is highest in the upper reaches during wet season, and arable land and bank sediment also have certain contributions. While in dry season, the SS contribution of woodland decreases, and the contribution of arable land increases (Fig. 2). The SS contribution of bank sediment is higher in dry season, when such areas are bare or sparsely covered by vegetation and thus susceptible to water erosion. Because the land use types in this reaches are mainly

composed of woodland and arable land, and the reaches have more rainfall frequency during wet season. Although the amount of rainfall is small in dry season, the arable land is more susceptible to rainfall erosion and the anti-erosion capacity of woodland is greater than arable land [12].

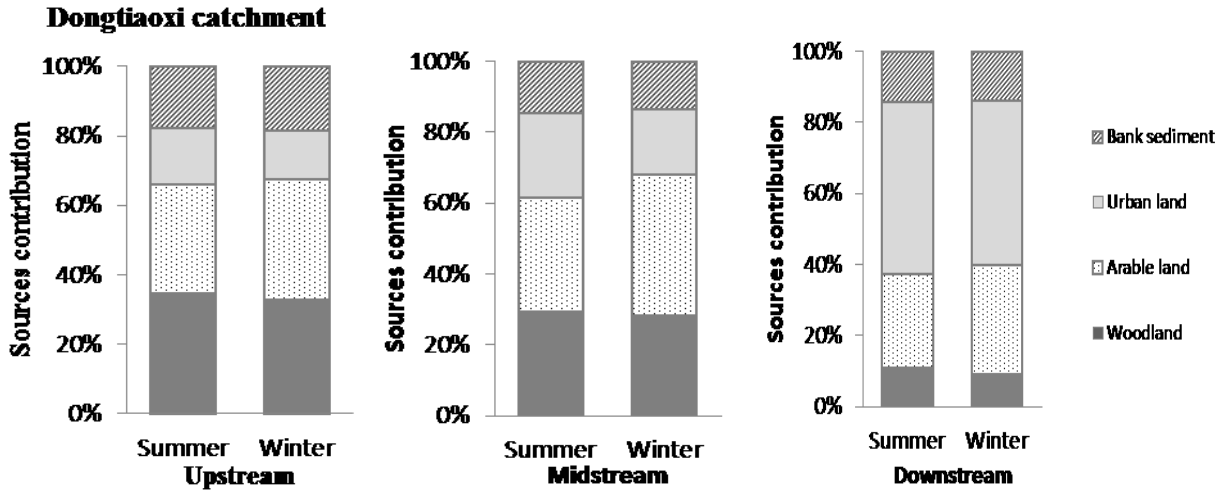



Fig. 2. Seasonal contrasts in mean relative SS contributions from sources in Dongtiaoxi basin

The land use types in the middle reaches are mainly composed of arable land and urban land. It is the interlaced region of the arable area and urban area. The SS contribution of arable land is highest in wet season, followed by urban land. It can illustrate that the area proportion of urban land had increased slightly, which is in line with the local conditions. The SS contribution of arable land in wet season are higher than in dry season. And the contributions of bank sediment in this reaches are smaller than in the upper reaches, because more landscape dike dams are in this reaches, which reduces the erosion of rain on bank sediment and leads to its seasonal variation is not obvious [13].

The SS contribution of urban land is highest in the lower reaches during wet season, followed by arable land, but the contributions of woodland and bank sediment are less in dry season. The SS contribution of arable land is higher in dry season, while urban land is opposite(Fig. 2). Because the land use type is given priority to urban land influenced by human activities, while woodland is less. More vegetation landscapes reduce the SS contribution of bank sediment significantly and the urbanization process increases the contribution of urban land. The SS contribution of urban land in this reaches is highest, compared with the upper and middle reaches.

**The Mean Relative Contributions of Each Individual Sources in Xitiaoxi Basin**

The SS contribution of woodland is highest in the upper reaches of Xitiaoxi basin during wet season, and the arable land and bank sediment also have small contributions (Fig. 3). And soils of woodland can be scoured into river in wet season. While the SS contribution of arable land increases in dry season, because arable land is more susceptible to rainfall erosion. The SS contribution of bank sediment is relatively higher in the upstream in dry season, where is only sparsely covered by vegetation.

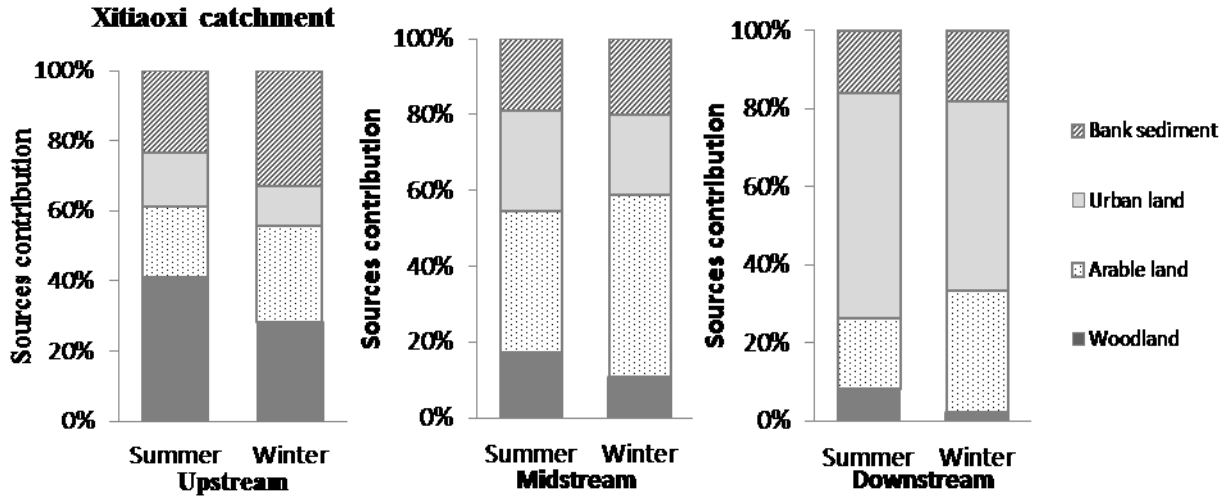



Fig. 3. Seasonal contrasts in mean relative SS contributions from sources in Xitiaoxi basin

The land use types in the middle reaches are mainly arable land and urban land. It also is the interlaced region of the agricultural area and urban area. The contribution of arable land to SS is highest in wet season in this area, followed by urban land and bank sediment. The contribution of arable land to SS is higher in dry season than in wet season, when is sparsely covered by crops and thus susceptible to rainfall erosion. And the contribution of bank sediment in the reaches is also smaller than that in upper reaches because of more vegetation in riparian zone [14].

The land use type is given priority to urban land in the lower reaches, while arable land and woodland occupy a relatively small proportion. The SS contribution of urban land is largest, followed by arable land and bank sediment. The contribution of arable land in dry season is significantly higher than in wet season, while urban land is on the contrary. Because the rainfall erosion intensity in wet season is higher than in dry season, and urban land is obviously affected by rainfall erosion, while arable land covered by vegetation is less susceptible to runoff erosion [15].

In a word, diffident hydrological conditions in Dongtiaoxi and Xitiaoxi basin lead to the different erosion of the soil by the flow intensity during wet and dry season. And due to the diffident of human production activities, the SS contributions of different sources are diffident. The forest can reduce soil erosion and protect soil effectively in the upper reaches. The urban and residential area is relatively more in the downstream, resulting in increasing the contribution of urban land. Land use type in the middle reaches is mainly arable land, so arable land becomes the main source of SS.

**Comparative Analysis the Quantitative Contributions of Sources in Different Reaches**

As shown in Fig. 2 and Fig. 3, the contributions of sources are difference in different reaches of Dongtiaoxi and Xitiaoxi basin, and the contributions of different sources are also difference during different seasons. The area difference of land use types and the local government management and protection in Dongtiaoxi and Xitiaoxi basin are in different ways. The different provenance materials are washed into rivers with plentiful rainfall and larger surface runoff, so the SS contributions of woodland and urban land in wet season are higher than in dry season. However arable land is in cultivation period, and low intensity of rainfall erosion to plowing land is still obvious, so the SS contributions of arable land in wet season are higher than in dry season.

Compared with Xitiaoxi River, the SS contributions of woodland and bank sediment are lower, while the contributions of arable land and urban land are larger in the upper reaches of Dongtiaoxi basin. Although the climatic conditions and human life styles are very similar in the upper reaches of Dongtiaoxi and Xitiaoxi basin, but the arable land area is larger and the soil type is lime soil, which is vulnerable to rainfall erosion. Meanwhile the impact of agricultural non-point source pollution is more serious in the upper reaches of Dongtiaoxi basin [16]. In addition, the higher urbanization level in Dongtiaoxi basin increases the SS contribution of urban land.

The middle reaches of Dongtiaoxi river flows through some towns, such as Pingyao town and Qianyuan town. The more urban land area increases the SS contribution of urban land, and the woodland area in this region is also higher, so the contributions of woodland and urban land in this reaches are larger than in Xitiaoxi basin, while the contributions of arable land and bank sediment in the upper reaches of the Dongtiaoxi basin are lower.

The contribution of bank sediment decreases significantly with landscape dike dam and green belts in riparian areas in lower reaches, while the SS contribution of urban land increases with the high level of urbanization process. The contributions of arable land and woodland are higher with more arable land and woodland in Dongtiaoxi basin. But in addition to the contribution of arable land in dry season is higher in Dongtiaoxi basin, the contribution orderliness of other sources in the lower reaches of Xitiaoxi basin during dry season is consistent with the orderliness in wet season.

The contribution of bank sediment in Xitiaoxi basin is generally higher than in Dongtiaoxi basin. It is affected by other source materials deposited and stored within the channel, in addition to the impact of the landscape dike dams in Dongtiaoxi basin. Other studies have shown that sediments mobilized from the catchment surface and transferred to the channel during one season may be stored in the channel and transported to the watershed during the next season [17, 18].

## Conclusions

(1) The contribution of woodland is highest in the upper reaches of both Dongtiaoxi and Xitiaoxi basin, but the contribution of arable land has considerable difference. The arable land and urban land become the major contributors to the midstream and the downstream of both Dongtiaoxi and Xitiaoxi basin respectively, while the contributions of woodland and urban land are larger in the middle reaches, the contribution of arable land is larger in the lower reaches of Dongtiaoxi basin.

(2) During wet season and dry season, the differences of the source contribution variations from Dongtiaoxi basin are not obvious, while that in Xitiaoxi basin are significantly obvious, namely: the SS contributions of woodland and urban land in wet season are significantly higher than in dry season, while the contributions of arable land and bank sediment are opposite.

(3) The acceleration of urbanization results in more impacts of urban land and human management modes (such as tillage method, river dyke, etc.) on the river, and also influences the SS contributions of sources. It's helpful to understand the difference of source contributions for the land management and river environment protection in Dongtiaoxi and Xitiaoxi basin.

## Acknowledgements

This study was financially supported by the Natural Science Foundation of China (No.41372354) and the International Technology Cooperation and Exchange Fund from Ministry of Science and Technology of China (No.0102012DFA60830).

## References

[1] A. Baker, Land use and water quality, J. Encyclopedia of Hydrological Sciences. 17 (2005) 2499-2501.

[2] R.S. Wu and D.A. Haith, Land use, climate, and water supply, J. Journal of Water Resources Planning and Management. 119 (1993) 685-704.

[3] S.A. Changnon and M. Demissie, Detection of changes in streamflow and floods resulting from climate fluctuations and land use-drainage changes, J. Climatic change. 32 (1996) 411-421.

[4] Mander, A. Kull, V. Tamm, et al, Impact of climatic fluctuations and land use change on runoff and nutrient losses in rural landscapes, J. Landscape and Urban Planning. 41 (1998) 229-238.

[5] A. Collins, D. Walling, L. Webb, et al, Apportioning catchment scale sediment sources using a modified composite fingerprinting technique incorporating property weightings and prior information, J. Geoderma. 155 (2010) 249-261.

[6] D.J. Ballantine, D.E. Walling, A.L. Collins, et al, The phosphorus content of fluvial suspended sediment in three lowland groundwater-dominated catchments, J. Journal of hydrology. 357 (2008) 140-151.

[7] R.C. Sidle, T. Hirano, T. Gomi, et al, Hortonian overland flow from Japanese forest plantations—an aberration, the real thing, or something in between?, J. Hydrological Processes. 21 (2007) 3237-3247.

[8] D.E. Walling, P.N. Owens and G.J. Leeks, Fingerprinting suspended sediment sources in the catchment of the River Ouse, Yorkshire, UK, J. Hydrological Processes. 13 (1999) 955-975.

[9] M. Russell, D. Walling and R. Hodgkinson, Suspended sediment sources in two small lowland agricultural catchments in the UK, J. Journal of Hydrology. 252 (2001) 1-24.

[10] D.J. Nicholls. The source and behaviour of fine sediment deposits in the river Torridge, Devon and their implications for salmon spawning [D]; University of Exeter, 2000.

[11] A.L. Collins, D. Walling and G. Leeks, Composite fingerprinting of the spatial source of fluvial suspended sediment: a case study of the Exe and Severn River basins, United Kingdom, J. Géomorphologie: relief, processus, environnement. 2 (1996) 41-53.

[12] J. Motha, P. Wallbrink, P. Hairsine, et al, Determining the sources of suspended sediment in a forested catchment in southeastern Australia, J. Water resources research. 39 (2003) ESG2. 1-2. 14.

[13] D. Walling, Tracing suspended sediment sources in catchments and river systems, J. Science of the total environment. 344 (2005) 159-184.

[14] H. Li, X. Liu and W. Huang, The non-point output of different landuse types in Zhexi hydraulic rigion of Taihu Basin, J. Acta Geographica Sinica In Chinese. 59 (2004) 401-408.

[15] J. Carter, P.N. Owens, D.E. Walling, et al, Fingerprinting suspended sediment sources in a large urban river system, J. Science of the total environment. 314 (2003) 513-534.

[16] H. Dong, Z. Qiang, T. Li, et al, Analysis of the spatial-temporal variation of water quality in JinXi River, a tributary of Southern Tiaoxi River, J. Chinese Journal of Environmental Engineering. 6 (2012) 772-778.

[17] D. Walling, A. Collins and R. Stroud, Tracing suspended sediment and particulate phosphorus sources in catchments, J. Journal of Hydrology. 350 (2008) 274-289.

[18] L.M. Svendsen, B. Kronvang, P. Kristensen, et al, Dynamics of phosphorus compounds in a lowland river system: Importance of retention and non-point sources, J. Hydrological Processes. 9 (1995) 119-142.

*Advanced Materials Research Vol. 937 (2014) pp 604-606*
*© (2014) Trans Tech Publications, Switzerland*
*doi:10.4028/www.scientific.net/AMR.937.604*

# Introduction to Midas GTS Software Application in Design of Deep Foundation Pit

Xiao-lin Dong [1, a]

[1]Changchun Institute of Architecture ,China

[a]43106520@qq.com

**Key words:** excavation; Finite element; Midas software

**Abstract:** in this paper, combining with engineering examples, this paper introduces the Midas GTS software application in the design of foundation pit excavation, and compared with the actual monitoring results, verify the feasibility of the software used in the actual engineering design and reliability.

## The Preface

Foundation pit engineering is an ancient and era characteristic of geotechnical engineering issue. Since the 20th century, when a large number of high-level, high-rise buildings and underground engineering, more and more high to the requirement of foundation pit engineering, the resulting problems more and more, forcing engineers must from a new Angle to look at the old topic, excavation engineering, theory or research methods led to many new experience. Finite element method is an effective numerical analysis method, the rock has a great development prospect in ten engineering disciplines. It can solve the problem of nonlinear, non homogeneous material is easy to deal with and anisotropic materials, can adapt to various complicated boundary conditions, also can be considered in the design of foundation pit excavation space effect and time effect. Step-by-step excavation of foundation pit is the common construction method [1-2].

Step-by-step excavation method is commonly used in foundation pit excavation, this paper using large-scale finite element software Midas, foundation pit excavation simulation is divided into two steps, the first step before the calculation of foundation pit excavation of a stress field (according to the initial stress field) and a displacement field; The second step calculation of foundation pit excavation caused by stress field step by step,) (called a excavation stress field and displacement field. The initial stress field combined with excavation stress field is the secondary stress field. After excavation of soil has to yield, should be the secondary stress field and the bend deformation of foundation pit excavation and supporting structure step by step finite element analysis of the influential factors of criteria to compare or directly by the elastoplastic model to determine whether a soil has yield. Due to the consolidation of soft soil in after a long history, has reached a stable state. So, the first step in the calculation of displacement field at a time when computing should be set to zero. The second displacement field is caused by the excavation of foundation pit displacement field.

## Project Summary

Proposed project is located in tianjin hexi district near white floor, east nanjing road, west to nanchang road, south of hefei, north to the horse to be present. Building main tower and vice tower and group of three parts. The main tower above 60 floor, 218 meters high, the following 3 floor, foundation embedded depth of 15.3 meters.

## Support Plan

The project adopts the method of underground continuous wall and steel support supporting, excavation in three stages, the first phase of excavation depth of 7.6 meters, and set up in 2.3 meters depth support; The second stage excavation to 14.1 m, and in the setting of the second 7.6 meters

depth support; The third stage excavation to the specified depth of 15.6 meters and 14.1 meters in depth setting the third support.

## Monitoring Content and Results

In order to master, in the process of rainfall and excavation of foundation pit construction on the surrounding buildings and the influence of the working state of the supporting structure, so as to timely adjust the construction schedule, abate the unstable factors, ensure the smooth progress of construction, the construction team including deformation of retaining structure horizontal displacement on the top of the underground continuous wall, the horizontal displacement of different operating support were tested. Monitoring plan as shown in figure 1, underground continuous wall set up 12 dip tube, set up 23 horizontal displacement monitoring. The maximum horizontal displacement of the underground continuous wall is 67.8 mm.

## The Simulation Results Analysis

step-by-step excavation process simulation In MIDAS/GTS, through the load step, the passivation and activate the unit to realize the foundation pit excavation and supporting. Displacement constraints imposed first initial formation model is set up, the boundary conditions of iterative calculation is carried out under the initial geostress conditions make initial stress equilibrium calculation model, and makes the initial displacement zero, simulate the consolidation settlement of soil before excavation. Then according to the order of the deep foundation pit construction passivation soil excavation section, activated portion of soil step excavation support unit and unit prestressed, passivation soil excavation part next again, so go on, until the end. Excavation of the concrete implementation steps are as follows:

Step 1: all the model assigned to elastic materials, combined with uniform stress field, form the initial geostress field. the

Model all assigned for elasticity is to prevent to produce plastic deformation in the formation of the initial stress field.

The second step: casting underground continuous wall, activate the part material unit.

Step 3: excavation to within - 7.6 meters of the surface of foundation pit.

Step 4: in the first - 2.3 meters activated support.

Step 5: dig to within - 14.1 meters of the surface of foundation pit.

Step 6: activation of the second support at 7.6 meters.

Step 7: excavation to within - 15.6 meters of the surface of foundation pit.

Step 8: activate the third support at 14.1 meters, is calculated.

## The Conclusion

Can see MIDAS MIDAS/GTS software in the practical engineering application is feasible, and can predict before the construction project construction process and construction after the end of the internal force and displacement of retaining structure, the actual project has a certain guiding significance. Through the above aspects of comparative analysis, can draw the following conclusion:

(1) the foundation pit excavation maintenance structure using finite element software MIDAS/GTS deformation and internal force of the forecasting method applied in deep foundation pit construction is more accurate and feasible.

(2) to the actual construction process simulation, can be calculated in the construction process of expect is less than the larger displacement and bending moment;

(3) of the underground continuous wall bending moment is mainly affected by excavation and steel supporting role.

**Reference**

[1] Gao Wenhua Shen Pusheng, the influence factors of ground movement in the foundation pit excavation analysis [J], journal of rock mechanics and engineering, 2002, 21 (s), 1153 - a - 1157

[2] LouYiGong, three pu shu, etc., internal force and deformation of foundation pit supporting structure dynamic analysis [J], journal of rock mechanics and engineering, 200322 (3) 462 466

[3] Zhang Zaiming Sun Baowei, Zhou Honglei. Several of the geotechnical engineering problems in national grand theatre engineering [J]. Journal of Beijing survey, 2003 (3) : 6-11.

[4] Chen Zhonghan Cheng Liping. Deep foundation pit engineering [M]. Beijing: mechanical industry publishing house, 1999

*Advanced Materials Research Vol. 937 (2014) pp 607-613*
*© (2014) Trans Tech Publications, Switzerland*
*doi:10.4028/www.scientific.net/AMR.937.607*

# An Overview of Different Distillation Technologiesfor Drinking Water Preparation

Lu LIU[1,a], He-li WANG[1,b*]

[1]College of Water Resources and Environment Engineering, China University of Geosciences(BeiJing) ,Haidian District Xueyuan Road No. 29 ,Beijing ,China

[a]liulu7646@163.com,[b]wangheli@cugb.edu.cn

*He-li WANG

**Keywords:** Distillation, Drinking water purification, Energy saving

**Abstract.**Water scarcity and pollution pose critical situation in all walks of life.Among the available purification methods,desalination process proves to be a safer and more stable solution for solving this problem. This paper provides an overview of the purification effect of distillation process, along with theprinciples and research progress ofdifferent distillation techniques for small scale drinking water preparation.This paper also analyzes the advantages and disadvantages of each method, as well as proposes an outlook forthe distillation technology on drinking water preparation. This paper also indicates that the removallaw of organic pollutants, especially the volatile organic pollutants during distillation process should attract researchers' attention, whilereducing energy consumption of distillation technology through various means is still the development tendency.

## Introduction

Water shortages, environmental deterioration and water pollution emergency constitute threecrises of drinking water. The drinking water safety problem has been highly concerned by scientists around the world [1]. According to UN statistics, there are 900 million people drinking the water with excess total coliform, 380 million people drinking the water with excess iron, 200 million people drinking the water of excessoxygen consumption, 948 million people drinkingthe water with excess fluorine. The contaminated drinking water is related to 80%~90% diseases and 33% mortality.A daily average of 2.5 million people died ofdiseases caused bydrinking water pollution [2]. Thus there is an urgent need of a simple,efficient and long lasting technology,which canremove some chemicals and pathogenic bacteria to meet the requirement of drinking water. It has a very important practical significance to contemporary society, whichchemical and microbiological contamination as well as unexpected events occurscurrently, especially for some remote areas where lacks large-scale urban water supply or the water supply is not reliable.

Currently, the main methods to purifydrinking water are activated charcoal adsorption, membrane technology andion exchange.Physical filtration treatment such as activated carbon adsorption and membrane technologycanremove almost all of the chemicals in water [3,4].However, if the filters have not beenreplaced in time, the cleaning effect will decrease sharply, and the filters may become thebreeding ground for a large number of bacteria[5].Ion-exchange can't eliminate pathogenic agents nor the substance responsible for unpleasant tastes and smells[6]. Distillation technology, which is simple, safe and reliable proves to be the best choice for purifying drinking water on small scale.

## The Water Purification Effect during Distillation Process

The principle of different distillation methods is the same, when the temperature of water is less than 300ºC, only water molecules and some dissolved gasses evaporate, dissolved salts and minerals inwater will remain in the concentratedwater[7]. L.Anjaneyulu et al.[8]used an inclined basin-type solar distillation for defluoridation. For samples having a fluoride concentration in the range 5-20mg/L, the fluoride concentration in the distillate was usually <1.5mg/L, and the water'stemperature and pH do not affect the $F^-$ concentration in distillate. BB Sahoo's [9]study also

illustrates thatthe evaporation process can effectively remove $F^-$. J.Josep [10] and A.Hanson [11]have shown that the distillation process can effectively remove salinity, total hardness, $F^-$, $NO_3^-$and other inorganic contaminants such as arsenic, molybdenum, selenium.More than 99% bacterial is also removed. The studies also prove that evaporation process can remove non-volatile contaminants from raw water successfully, but the ability to remove the volatile organic compounds is directly dependent on the volatility of the compounds as measured by the Henry's law constant. Yasmine Gacem [12]hasevaluated the physical and chemical proprietiesof the effluent produced by MSF desalination and RO membrane.The annualexperimental dataofyear 2010 showed that the desalinated water produced by MSF is of better quality than that produced by RO process. The Langelier Saturation Index(LSI) of distilled water is within the recommended LSI values(between0-0.4), pH stabilized at between 6.16-6.94, and conductivity stable at 500μs/ cm. In short, the distillation process can produce high-quality drinking water from pollutedraw water.

**Distillation Technologies of Small Scale Drinking Water Preparation**

There are various kinds of distillation technologieswith a long history, but not all of them is suitable forfamilies',units' or emergency situations'usage.The distillation technologies mentioned below have great potential for small-scale preparation of drinking water.

**Simple Traditional Distillation**

Since the thermal conversion efficiency is too low and the heat losses severely, traditional distillation method ,which heats the water to boil under atmospheric pressure using heating deviceisrarelyused [13] .It isthe easiest as well as the least economical way of distillation, so it's applied only for small-scale producing in labor for emergency use.

**Single-Stage Vacuum Distillation**

In this system hot medium heatsraw water, the vacuum pump installed in the condensation chamber reduces water's boiling point in the evaporation chamber.Thenthe formed steam enters into the condensation chamber and cools downby cooling medium. Because of the significant improvement of distillation efficiency and the small size, single-stage vacuum distillation is suitable for family or company use especially for the place where the heating steam isabundant[14].

Since conventional single-stage distillation is a completely open system which is sensitive to the ambient temperature and humidity, the efficiency is lowduring energy transfer processleading to severe heat loss [15]. Therefore, in practical application, many devices adopt closed cycle of cooling or heating mediums[16]in order to improve heat transfer efficiency and reduce energy costs.

**Multi-effect Distillation(MED)**

In order to improve thermal transfer efficiency, scientists have studied how to recover heat from the condensation process, one of the most important methods is the multi-effect distillation.In this method, the vapor coming out fromthe first evaporator will act as a heating medium for the second evaporator and will boil the water there. The vapor comingout from the second evaporator, also boils the water in thethird evaporator, and so on. At the same time, the boiling water in the latter evaporator serves as a condensing medium forthe vapor coming from the former evaporator.In this system, a large latentheat of vapor condensation is reused several times before releasingit to the surroundings.

MED has a higher efficiencyunderhigher temperatures, but the higher temperature increases the system's scaling problem. Therefore, there are many small MED devices adopt compressor under low temperature inorder to significantly improve the efficiency[17].

**Multi-stage Flashdistillation (MSF)**

In this method, water isheated outside the boiling chamber where it is made to evaporateby lowering pressure.The heated water is vaporized rapidlybecause the evaporation chamber's pressure is lower than the saturation water vapor pressure, then turns into fresh water. After that, the water

gets into the following evaporation chambers, based on the same principle, it's vapored and condensed stage by stage. Since the boiling process has a greater effect on formingscalethan heating process, multistage flash effectively avoid the scaling problem on the heat transfer surface[18].

Multi-stage flash began in the 1950s [19], in the last 30 years, it has been developing rapidly and improvecontinuously. The main optimizations include: device's design and configuration, thermodynamic design, material selection and so on. In practical MSF applications, using demisters and anti-foam agents to avoid the water's entering in the vapor [20], adding chemicals or on-line ball cleaning apparatus to solve the scaling problem and ensure thermal conversion efficiency for a long-time service [20-22],using stainless steel, duplex steel, titanium tubes, nickel alloys and other materials to reduce corrosion of the devices as well as cost of construction[23, 24].

**Vapor Compression (VC)**

External heat sources (oil, natural gas, etc.) are needed both in MED and MSF for heating the water, while vapor compression distillation provides energy by the mechanism of the vapor compression [18]. Vapor compression, known as mechanical vapor compression, uses a mechanical compressor or a pump to pressurize and heat-up the flash steam so as to be the heat source of inflow. Theoretically, mechanical vapor compression (MVC) distillation process does not require additional heat, it needs an auxiliary heat source when it starts to produce steam for the process. During normal condition, only a little power consumption is needed to increase the steam's temperature and pressure which will make its heat reused. Therefore, MVC is proved to be high economic efficiency, soithas great prospects.

Since the volume of flash steam of direct compression is large, and the compressed steam only has a better operation efficiency within a wide temperature range. Lowering the final temperature will result in an increase in specific volume, equipment costs and operating costs. In addition, the specific volume increases will inevitably cause an increase of steam velocity which leads to the raw water's entering and seriously affects the water quality as well as reduces compressor's life[25]. Therefore, VCD device is inclined to use heat pump instead of a vapor compression to solve the problems mentioned above [17].

**Solar Distillation**

Due to the free solar radiation,solar distillation is an ideal way for drinking water preparation.It's widely used especially in Africa and some other areas where economy is backward butthe sunshine is adequate. Various kinds of studies have focused on how to improve the efficiency of solar still.Severalmethods and modifications which have beenused to improve the productivityare listed as follows: increasethe surface area of the free water surface in the distiller with sponges[26]regenerative solar still, triple basin solar still and solar still withdouble glasses are used to increase the temperature differencebetween water and glass [27,28],installcooling fins to increase the system's heat absorption area [29],flat plate collectors, hot water storage tank, mini solar water tank, floating perforated plate and suspended heat shield are used to heat-up the inflow[30-35],making the evaporation chamber glass cover's inclination being consistent with the local latitude[35].Besides, reflector, condenser, black rubber, black gravel, vacuum technology[36]are adopted to increaseefficiency.

Pluses and minuses exist in all the methods mentioned above. Table 1 shows the comparison of various distillation techniques. As what Table 1 indicates, in consideration of the small production system's less water production requirement, high water production rate, low energy consumption and long-term operation stability, the best way is the vapor compression distillation, while the traditional evaporation and solar distillation applicability are not suitable. Meanwhile, because of the large volume and high equipment costs, the multi-effect evaporation and multi-stage flash are less suitable.

Table 1. Comparison of various distillation

| | Simple traditional distillation | Single-stage vacuum evaporation | Multi-effect distillation | Multi-stage flash distillation | Vapor compression distillation | Solar distillation |
|---|---|---|---|---|---|---|
| Advantage | Simple | Quick and easy, Compact | Achieve repeated use of the steam, Thermal conversion efficiency improves | Achieve repeated use of the steam, Thermal conversion efficiency improves; avoid scaling | Compact; Don't need external heat and cooling water | Free solar radiation |
| Weakness | Latent heat of condensation of steam is underutilized, Thermal conversion efficiency is low | Latent heat of condensation of steam is underutilized, Thermal conversion efficiency is low | Expensive and complex equipment manufacturing, Repair and maintenance are inconvenient, Fouling sever | Expensive equipment manufacturing, Inconvenient maintenance | Direct compression make larger steam volume result in the higher operating costs and worse water quality | Affect by regional and climatic conditions seriously, Low water yield per unit area |
| Factors affecting water yield | Water, Temperature of heat source | Water temperature, Water concentration | Number of effects | Water temperature andtemperature range | Range of steam temperature | Solar intensity and utilization efficiency, Water temperature |

**Other Distillation Technology**

Theoretically the consumption in distillation process is great,one kilogram waterneeds 314.34KJheat to be heated from room temperature (25ºC)to 100ºC, then requires 2256.4KJ heat to change into gaseous state, so the total heat of the distillation process is 2570.7KJ.Therefore,a well-designed heat recovery system and creating low distillation pressure to reduce heat loss and energy consumption have been the focus of scientists. For example, Zhaoshunpei [37] have designed thermal energy conversion module in an energy saving distilled water machine, which consists of heating channels, exothermic channels and an interval of one-exchange membrane. Two sides of the channel are for water'sevaporation andsteam respectively. When vapor condenses into liquid,the process will release heat to cool the water whichachieves the recycling of energy. Heat is accumulating during the continuous evaporation process, the motor only needslittle heat to maintain a normal wok condition. In practical applications, there are also many forms of distillation system improvements that increase evaporate speed, such as setting the nozzle or knit fiber strip in the evaporation chamber [13,38], adding some small solids as the filler layer[15] to increase the water's heat exchange area. Although low pressure distillation is efficient, the energy required to maintain the pressure is relatively high, for furtherenergy saving, CreativewatercChinacompany[39] has designed an atmospheric distillation system with low temperature based on the principle thatsaturated moisture content in air is different under different temperature. This system makes water evaporate at atmospheric pressure,so it can reduce power consumption greatly and preventscaling.

Currently, for small scale distillation water purification devices, some integrated technologies also begin to emerge. Bruno Pirone[40], who designed the distillation system combiningdistillation process with activated carbon filters. The activated carbon can remove the remaining bacteria and organic pollutants to ensure effluent security and stability，as well as extend the life of activated carbon. Ralf Olwig [41] designed a system that a thermal desalination system and a RO system are combined. According to the invention,the mechanical or electric energy supplied by the heat engine is used for operating a RO system and the residual steam of the heat engine is used for operating a distillation system.

In today's society when energy crisis is emphasized, using renewable energy sources such as solar, wind or geothermal for distillation devices seems to be a reasonable and technically mature option to save energy. However, due to the volatility of renewable energy, energy storage technology research becomes the focus and difficulty. Although worldwide research for renewable energy is intensive, the actual penetration of renewable energy powered desalination is too low[42].

## Conclusion

Experimental results show that the distillation system can remove inorganic pollutants and non-volatile organic compounds efficiently. So it is a suitable, simple, efficient water purification method. But now the removal law for organic pollutants, especially for volatile organic pollutants during distillation process still needs further study.

The high operating cost is one of the bottlenecks of the distillation technology which restricts its development. Nowadays the main methods to reduce energy consumption are to fully utilize the latent heat of condensation and to forma low pressure environment to achieve cryogenic distillation. However maintaining the constant low pressure needs great energy. What's more, if the distillation pressure is continuously too low, water under superheated statewaiting to vapor will be too much and phase change will need too much energy. This phenomenon will affect the efficiency of the water's condensation. Therefore, we may consider changing suction strength or stopping pumping intermittently to ensure evaporate efficiency while reducing power consumption.

Furthermore, combinations of varioustechniques such as membrane - distillation, selectinganti-corrosion economical materials and research on preventing fouling methods are also the tendency of distillation technology improvement.

## Acknowledgements

This research was financially supported byInternational Cooperation Department, the Ministry of Science and Technology, China.

## References

[1] Mierzwa J C, Hespanhol I, Da Silva M C C, et al. Direct drinking water treatment by spiral-wound ultrafiltration membranes[J]. Desalination, 2008, 230(1): 41-50.

[2] JiangRong Li, Huaqiang Yin, Jiaxiu Guo. Drinking water treatment technology brief [J]. Chemical Engineering and Equipment, 2011,2:146-147(In Chinese)

[3] Xiaohua Huang. Pump vacuum distillation of thermal cycling water purifier [P]. Chinese patent: CN 1333186A, 2002.01.30(In Chinese)

[4] Xueli E,Bo Ling. Drinking water purification and water processor [M]. Beijing: Chemical Industry Press, 2004(In Chinese)

[5] YaoGuo Cai. Automatic distillation with hot water, cold water andice water supply [P]. Chinese patent: CN2524636Y, 2002.01.14(In Chinese)

[6] Bruno Pirone, San Rocco, Castagnaretta (Cuneo) (IT). Device For Producing Drinking Water [P]. United States Patent Application Publication: US2010/0300868 A1, Dec.2, 2010

[7] Saidur R, Elcevvadi E T, Mekhilef S, et al. An overview of different distillation methods for small scale applications[J]. Renewable and Sustainable Energy Reviews, 2011, 15(9): 4756-4764.

[8] Anjaneyulu L, Kumar E A, Sankannavar R, et al. Defluoridation of drinking water and rainwater harvesting using a solar still[J]. Industrial & Engineering Chemistry Research, 2012, 51(23): 8040-8048.

[9] Sahoo B B, Sahoo N, Mahanta P, et al. Performance assessment of a solar still using blackened surface and thermocol insulation[J]. Renewable Energy, 2008, 33(7): 1703-1708.

[10] Joseph J, Saravanan R, Renganarayanan S. Studies on a single-stage solar desalination system for domestic applications[J]. Desalination, 2005, 173(1): 77-82.

[11] Hanson A, Zachritz W, Stevens K, et al. Distillate water quality of a single-basin solar still: laboratory and field studies[J]. Solar energy, 2004, 76(5): 635-645.

[12] Gacem Y, Taleb S, Ramdani A, et al. Physical and chemical assessment of MSF distillate and SWRO product for drinking purpose[J]. Desalination, 2012, 290: 107-114.

[13] Yuming Liu, Xiaosong Zhang, Juan Du, el at.Low temperature distillation system [P]. Chinese patent: CN 201648028U, 2010.11.24.(In Chinese)

[14] Rahman H, Hawlader MNA, Malek A. An experiment with a single-effect submerged vertical tube evaporat or in multi-effect desalination. Desalination, Joint EDS, WSTA and IWA conference on Desalination and the Environment Fresh Water for All UN International Year of Fresh Water 2003; 156 (1-3): 91-100.

[15] Guoquan Shi, Ting Gao. Efficient refrigeration heating systems at low temperatureevaporation[P]. Chinese patent: CN101216228A, 2008.07.09(In Chinese)

[16] Puhong Xu. Water distillation equipment and dispenser containing this equipment[P]. Chinese patent: CN 102249470A, 2011.11.23(In Chinese)

[17] Khawaji A D, Kutubkhanah I K, Wie J M. Advances in seawater desalination technologies[J]. Desalination, 2008, 221(1): 47-69.

[18] Saidur R, Elcevvadi E T, Mekhilef S, et al. An overview of different distillation methods for small scale applications[J]. Renewable and Sustainable Energy Reviews, 2011, 15(9): 4756-4764.

[19] OK Buros. The USAID Desalination Manual.International Desalination and Environmental Association, 1980.

[20] WRQuerns.The world at large.IDA News, March / April 1992:3-4

[21] RM Morris.The development of the multi-stage flash distillation process: a designer's point [J]. Desalination, 93 (1993): 57-68.

[22] El-Saie M H. The MSF desalination process and its prospects for the future[J]. Desalination, 1993, 93(1): 43-56.

[23] C. Sommariva, R. Venkatesh.MSF Desalination.MEDRC Newsletter, 18 (2002) :1-3. Confirm

[24] Khawaji A D, Wie J M. Performance of MSF desalination plant components over fifteen years at Madinat Yanbu Al-Sinaiyah[J]. Desalination, 2001, 134(1): 231-239.

[25] Xuehu MA,zhuomin Zhang, Zhong Lan, et al. Low temperature evaporation with heat pump apparatus and method[P]. China patent: CN 102698451A, 2012.10.03(In Chinese)

[26] Abu-Hijleh B A, Rababa'h H M. Experimental study of a solar still with sponge cubes in basin[J]. Energy conversion and Management, 2003, 44(9): 1411-1418.

[27] Zurigat Y H, Abu-Arabi M K. Modelling and performance analysis of a regenerative solar desalination unit[J]. Applied thermal engineering, 2004, 24(7): 1061-1072.

[28] Abu-Arabi M, Zurigat Y, Al-Hinai H, et al. Modeling and performance analysis of a solar desalination unit with double-glass cover cooling[J]. Desalination, 2002, 143(2): 173-182.

[29] Velmurugan V, Gopa lakrishnan M, Raghu R, el at. Single basin solar still with fin for enhancing productivity. Energy Conversion and Management 2008, 49:2602-2608.

[30] Bruno Pirone, San Rocco, Castagnaretta (Cuneo) (IT). Device For Producing Drinking Water [P]. United States Patent Application Publication: US2010/0300868 A1, Dec.2, 2010

[31] Voropoulos K, Mathioulakis E, Belessiotis V. Experimental investigation of the behavior of a solar still coupled with hot water storage tank[J]. Desalination, 2003, 156(1): 315-322.

[32] Velmurugan V, Srithar K. Solar stills integrated with a mini solar pond—analytical simulation and experimental validation[J]. Desalination, 2007, 216(1): 232-241.

[33] Velmurugan V, Srithar K. Prospects and scopes of solar pond: A detailed review[J]. Renewable and Sustainable Energy Reviews, 2008, 12(8): 2253-2263.

[34] El-Sebaii A A, Aboul-Enein S, El-Bialy E. Single basin solar still with baffle suspended absorber[J]. Energy conversion and management, 2000, 41(7): 661-675.

[35] Nafey A S, Abdelkader M, Abdelmotalip A, et al. Enhancement of solar still productivity using floating perforated black plate[J]. Energy Conversion and Management, 2002, 43(7): 937-946.

[36] Singh H N, Tiwari G N. Monthly performance of passive and active solar stills for different Indian climatic conditions[J]. Desalination, 2004, 168: 145-150.

[37] Velmurugan V, Srithar K. Performance analysis of solar stills based on various factors affecting the productivity—a review[J]. Renewable and Sustainable Energy Reviews, 2011, 15(2): 1294-1304. ShunPeiZhao. Energy-efficient distilled water machine [P]. Chinese patent: CN 2839249Y, 2006.11.22(In Chinese)

[38] GaoyanWang, Anping Deng, Xiaonan Lu. Solar still for hot and cool distilled water [P]. Chinese patent: CN 2754016Y, 2006.01.25(In Chinese)

[39] http://www.creativewaterchina.com

[40] Bruno Pirone, San Rocco, Castagnaretta (Cuneo) (IT). Device For Producing Drinking Water [P]. United States Patent Application Publication: US2010/0300868 A1, Dec.2, 2010

[41] Ralf Olwig, Christian Sattler, Klaus Hennecke, Klaus Pottler.Method For Desalinating Water Containing Salt [P]. United States Patent Application Publication: US2011/0198208 A1, Aug.18, 2011

[42] Mathioulakis E, Belessiotis V, Delyannis E. Desalination by using alternative energy: Review and state-of-the-art[J]. Desalination, 2007, 203(1): 346-365.

*Advanced Materials Research Vol. 937 (2014) pp 614-619*
*© (2014) Trans Tech Publications, Switzerland*
*doi:10.4028/www.scientific.net/AMR.937.614*

# Erosion Experiment of Self-excited Oscillation Pulsed Jet

Chuan-lin TANG[1,a],Jie PEI[1,b,*], Dong HU[1,c] and Xiao-ting HE[1]

[1]Modern Jet Instiitute, Hunan University of Technology, Zhuzhou 412007, china

tcl5608@126.com ,18773366808@163.com

**Keywords:** erosion,submergence condition, self-excited pulsed jet,erosive volume.

**Abstract.** In order to improve the erosion effect of jet under submergence condition, experimental studies of erosion generated from the self-excited pulsed jet was carried out by using developed self-excited oscillation nozzle. The erosion volume and depth of pulsed jet were measured and taking mortar block as an erosion part. The results were that the standoff has significant influence on erosion effect. The erosion volume firstly decreases with increases in cavity length and then increases to a peak value. Erosion volume of pulsed jet is significantly higher than that of continuous jet, the erosion depth of two jet has slight difference.

## Introduction

With the development of social economy,resources on land gradually exhausted, and ocean occupies 70% of the earth's surface, containing abundant natural resources, and most of the area has not yet developed,which has great potential for development. Marine engineering seafloor mining will provide a powerful driving force for the sustainable development of the national economy. Mineral exploitation has broad prospects of development with the utilization of water jet technology [1-2] .

About high efficiency water jet, Professor Li Gensheng[3]proposed a double jet, and designs a new jet nozzle, which is a new type of high efficient jet formed by the annular rotating nozzle center direct flow and coaxial, on the basis of which dual jet nozzle is designed, and take the concrete (uniaxial compressive strength is 34MPa) as the artificial test samples, to study the effect on rock breaking effect of various structure parameters of the nozzle, thus get the optimal structure parameters of dual jet nozzle . Wang Ruihe[4]and Professor Li Zhaomin[5]do research on polymer additives jet, the results show that: the additive jets reduces the correlation coefficient on the jet axis direction, increasing the potential core length of jet, so that the effective range has been greatly improved. The products exploited by mining research institution of Russia kochi made the rock breaking efficiency increased by about 20~25% .

As one of the high efficiency water jet ,the self-excited oscillation pulsed jet has obtained the fast development in recent years. The device has the merit of small size, simple structure, good sealing performance, high reliability and low cost and no additional external driving mechanism,which is mainly used in cutting, crushing and washing of minerals. Especially in the deep-sea mining .

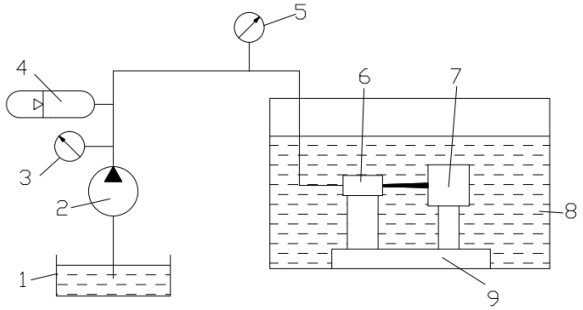
About the erosion and broken of rock of self-excited oscillation pulsed jet , professor Tang Chuanlin[6] proposed a new mining technology applied on coastal placer, at the same time, doing the theoretical analysis and experimental verification. Its working principle is to use the oscillation pulsed jet as gas lift breaker to break the hard solid in advance, and then inhale sand particles into the gas lift through the gas lift mechanism; meantime, experimental research on coastal placer shows that the self-excited oscillation pulsed jet can break rock faster and improve mining work efficiency.

Pei Jiang hong, Tang Chuanlin[7] et al., studied the performance of the self-excited oscillation nozzle on the non submerged condition. Results show that, the unstable shear layer oscillation cavity has the function of amplification on the selectivity of disturbance waves and there are appropriate structure parameters to mach disturbance frequency and the natural frequency of the nozzle, and then produce strong self oscillation pulsed jet . Erosion test on white sand brick (compressive strength is 30MPa) show that pulse jet has an optimal standoff.

Gao Chuanchang[8] et al performed self suction type pulse water jet under different confining pressure under submerged conditions on paraffin (soft solid) erosion experiment. Test results show that the erosion effect of self-excited air-breathing pulsed water jet is better than continuous jet under the emerged condition , inspiratory capacity has great influence on the erosion effect and striking force.

By using self-excited oscillation pulsed jet nozzle[9], a further study on the erosion ability of self-excited oscillation pulsed jet in the submerged condition is performed . This test is undertaken under submerged condition and normal pressure, to shoot the mortar specimens (compressive strength is 7.0MPa) , mainly by changing the nozzle cavity length and target distance to get erosion volume and erosion depth, analyzing the effect of nozzle cavity length and distance on erosion .

## Test Device and Method




1.water reservoir 2. three-throw ram pump 3. Seismic pressure gauge 4. Energy accumulator 5. Seismic pressure gauge 6. pulsed nozzle 7. mortar block 8. water tank 9. test bench

Fig.1. Experiment system sketch of erosion test.

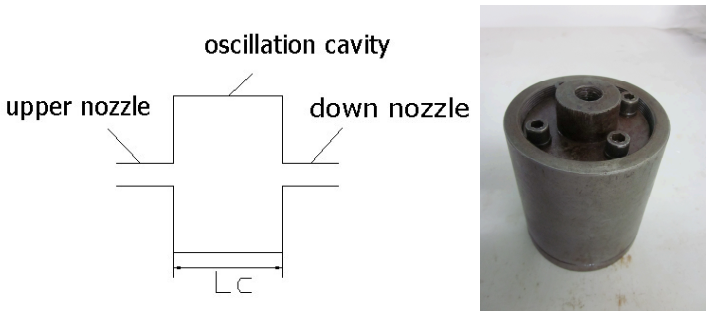
## The Test Device

Test device is shown in Figure 1, figure 2 is self-excited oscillation nozzle structure schematic which is the core components of this experiment. The test device consists of a water pump, water tank, pump, accumulator, seismic pressure gauge, pulsed water jet nozzle and fixed mortar block bench etc. Mortar block and the nozzle are fixed on the test bench respectively by clamp . The working pressure is adjusted by the relief valve installed on three-throw ramp pump. To ensure the accuracy of working pressure of nozzle entrance, aseismic pressure gauge is installed at the nozzle entrance to read the working pressure of nozzle entrance.

Three plunger reciprocating pump motor, type: GA-3.6/50YA (made in Baoji water pump factory), test bed is transformed from high pressure water jet bench, self-excited oscillation nozzle is made by self, as shown in figure 2.

We need to start the pump to supply the three plunger pump water at first, then start the main motor after pump working stable, high pressure water is ejected from pulse jet nozzle to impact mortar test block through the energy accumulator , which is produced by three-throw ramp pump.

Mortar block is designed and produced in accordance with the <rules for mix design of masonry mortar>(JGJ/T 98-2010) , the preliminary design of the compressive strength is 7.5MPa. To test compressive strength according to<standard test method of the performance of building mortar industry>(JGJ / T70-2009) . the compressive strength of mortar test block is 7.0MPa .




a) The physical model b)nozzle

Fig. 2. Schematic plot of self-excitated nozzle structure

## The Experimental Method

During the test, we need to select test parameters such as cavity length and standoff at first, while the other parameters stay unchanged , adjust the selected parameters, to test the effect of experimental parameters on the jet, then determine the relationship between experimental parameters and erosion effect. The test target is mortar block, compressive strength of which is7.0MPa, erosion effect is evaluated by the volume and depth of erosion hole.Evaluation parameters of erosion effect include volume, epth, cutting width and diameter of erosion hole . For this test, because the nozzle diameter is very small (3mm), the diameter and cutting width of erosion hole had no significant changes, so take the erosion pore volume and erosion hole depth as the evaluation criterion.

Using fill salt method to measure erosion pore volume (V/cm3) ,at first ,fill the hole with common salt, then take the salt out to measure its quality on the balance, the accuracy of balance is 3%, after taking the mass divided by the salt density, erosion pore volume is obtained .

Scour hole depth (h/mm)is measured by a vernier caliper, selecting 3 different points at the lowest place of erosion hole in sand brick to measure its depth,and take the mean value as the erosion depth.

## Test Results and Analysis

### Pulsed Jet Erosion Test

The working pressure is 5.0MPa, erosion time is 30s, standoff (L/mm) is 5, 10, 15mm,the relationship between erosion volume and cavity length is shown in Figure 3, the relationship between erosion depth and the cavity length is shown in figure4.

As can be seen from Figure 3 and Figure 4 , when the standoff is constant, with the cavity length increasing, the erosion volume decreases at first, then gradually increases to the peak, then decreases again;As the standoff is constant, with the cavity length increasing, erosion depth first decreases, then increases gradually to a peak, reaches the peak after erosion depth decreases gradually.

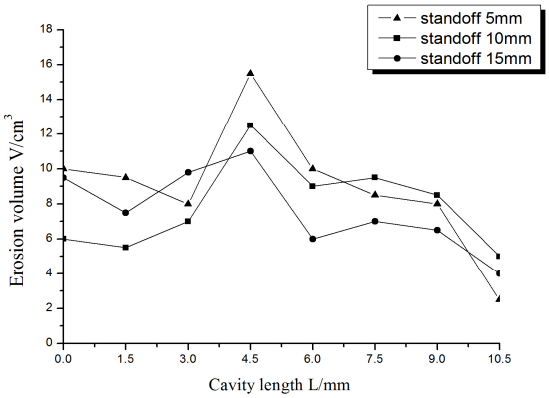



Fig. 3. Pulsed jet erosion volume with different cavity long

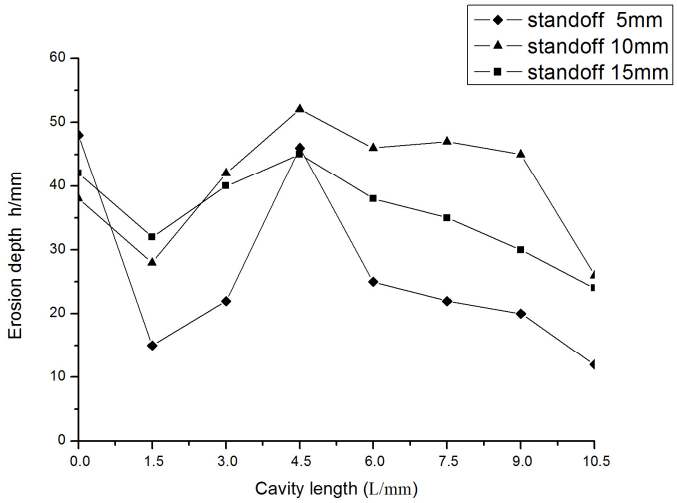



Fig. 4. Pulsed jet erosion depth with different cavity long

Figure 3 and Figure 4 show that when the nozzle cavity length is 4.5mm, the erosion volume and erosion depth reach the maximum both, the erosion effect comes to the best. This is because the cavity length is one of the important structure parameters of self-excited oscillation nozzle, if the excitation frequency of fluid and the inherent frequency characteristics of the nozzle structure matches , pressure oscillation will be more severe, erosive effect will be better. It is generally believed that there is an optimum cavity length range for the jet pressure peak value, indicating that the reasonable selection of oscillation cavity design can achieve the best erosion effect.

This test only designed to explore the effects of change of cavity length on erosion effect, Previous studies indicate that[10]optimal cavity length of nozzle used in the present experiment is in the range of 4.4~5mm, in which the effect of self-excited oscillation nozzle come to optimal, and this rang matches the mortar block erosion test results .

**Erosion Effect Contrast between Pulsed Jet and Continuous Jet**

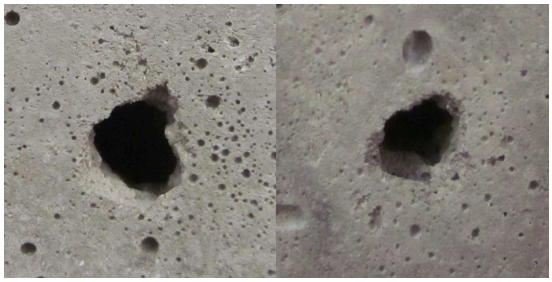
In previous studies[11], failure mechanism of rock mass with water jet is brittle failure under tensile stress , the tensile stress and shear stress produced under the impact of jet are more than the limit of tensile and shear strength of low intensity units in rock mass, to make the low intensity unit in rock mass destroyed and stimulate the formation of cracks in rock mass. After fracture formation and converge, water jet will enter the fracture space, with the help of water wedge , the tensile stress concentration produced on crack tip, which leads to rapid development and expansion of the crack and fracture of rock mass.

Table 1. The erosion effect with the standoff

| Erosion effect / Standoff(mm) | erosion volume V($cm^3$) | | erosion depth h(mm) | |
|---|---|---|---|---|
| | continuous jet | pulsed jet | continuous jet | pulsed jet |
| 5 | 10.742 | 15.386 | 45.573 | 48.280 |
| 10 | 9.366 | 12.842 | 51.090 | 50.397 |
| 15 | 7.334 | 11.169 | 35.493 | 46.140 |

When the working pressure is 5.0MPa and erosion time is 30s ,the standoff, erosion volume and erosion depth of two kinds of jet are shown in table 1.

The comparison between continuous jet and pulsed jet shows that the erosion volume of pulsed jet is significant larger than that of continuous jet, the erosion volume increases by 37.1-52.3%. This is because when the work pressure, standoff keep constant, water hammer pressure on object produced by pulsed jet is more than stagnation pressure produced by continuous jet. Under the same working pressure conditions, the impact pressure does a greater damage on mortar specimen , repeated impact of pulsed jet can make the material more vulnerable,enhancing the ability to destruct the mortar test block, as a result ,the erosion effect of pulsed jet is better than continuous jet .



(a)continuous jet (b) pulsed jet(cavity length: 4.5mm)

Fig. 5. Erosion effect of mortar block(standoff:10mm ， pump pressure:5MPa)

Figure 5 shows the erosion effect when the standoff is 10mm , it can be seen from the figure that erosion area of pulsed jet is larger than that of continuous jet, this is because the pulsed jet cavitation phenomenon happens[12] in the erosion process, cavitation generated by the fluid blocks on the surface of mortar block, the impact breakage effect makes the eroded surface area increased.

## Conclusions

(1)When the standoff is 5mm, the erosion volume of mortar block is greater than the other two standoff distance, which states that the erosion ability gradually decrease with the increase of standoff.

(2)For pulsed jet, when the standoff is determined, the erosion volume firstly decreases with increases in cavity length and then increases , when the nozzle cavity length is 4.5mm, the erosion volume reaches the maximum. Indicating that there exists optimal cavity length for the self-excited oscillation pulsed jet to achieve the best effect, then the effect of water jet erosion improved.

(3) Erosion volume of pulsed jet is significantly higher than that of continuous jet, the erosion depth of two jet is slight difference.

## Acknowledgement

This work was financially supported by the National Natural Science Foundation of China(Grant No.51374101), the Natural Science Foundation of Hunan Province (Grant No. 13JJ9013) and the the Projects of Hunan province science and Technology Department (Grant No. 2013SK3165).

## References

[1] SHENG Zhonghou. Theory And Technology of Water Jet[M]. Dongying: Petroleum University Press, 1998:390-414.

[2] XUE Shengxiong,etc. High Pressure Waterjet Technology & Engineering[M]. Hefei: HeFei University of Technology Press, 1998:390-414.

[3] LI Gensheng , SONG Jian, HU Yongtang, NIU Jitang,HUANG Zhongwei. Experiment study on rock breaking parameters of dual-jet[J]: Journal of China University of Petroleum, 2006,30(1):68-71.

[4]YANG Yongyin, WANG Ruihe, SHEN Zhonghou, ZHOU Weidong. Experimental Study on Velocity Distribution of Swirling Jet with Polyacrylamide Fluid [J]. Journal of the University of Petroleum(Edition of Natural Science), 2001,25(6):38-41.

[5]LI Zhaomin, LIU Chengwen. An experimental investigation of the structure characteristics of additive jets[J].Drilling Fluid & Completion Fluid, 1999,16(6):1-3,23.

[6] Tang Chuanlin,Liao Zhenfang,Study on Airlift and Oscillation Pulsed Jet in Exploiting Deep Beach Placer[J]. Jiangsu Coal,2000(1):41-44.

[7] Pei Jianghong,Tang Chuanlin,Zhang Fenghua,Liao Zhenfang. Experimental Study on the Self-excited Oscillation Pulsed Nozzle under Non-submerged Condition [J]. Mining & Processing Equipment, 2006,34(10):96-98.

[8] Gao Chuanchang,Zhao Li,Liu Xinyang,Huang Xiaoliang.Experiment research on erosion of self-excited inspired pulsatile jet in submerged conditions[J].Drainage and Irrigation Machinery,2012(1):53-56,63.

[9] LIAO Zhenfang, TANG Chuanlin, ZHANG Fenghua. Experiment of the Self-excited Oscillation Pulsed Jet Nozzle[J]. Journal of Chongqing University (Natural Science Edition), 2002,25(2):28-32.

[10] WANG Leqin ,WANG Xunming ,XU Ruliang, LI Jiangyun. Experimental Study on Structural Parameters Optimized Design of the Self-excited Oscillation Pulsed Jet Nozzle [J].Journal of Engineering Thermophysics,2004,25(6):956-958.

[11] CHANG Zongxu , XI Baoping, ZHAO Yangsheng, ZHAO Longmao. Mechanical of breaking coal by water jet[J].Journal of China Coal Society,2008, 33(9):983-987

[12] LU Yiyu ,LI Xiaohong,XIANG Wenying. Rock erosion mechanism of cavitating water jets[J]:Rock and Soil Mechanics, 2005,26(8):1233-1237.In Chinese

*Advanced Materials Research Vol. 937 (2014) pp 620-623*
*© (2014) Trans Tech Publications, Switzerland*
*doi:10.4028/www.scientific.net/AMR.937.620*

# Ozon/Hydrogen Peroxide System for Degradation of Humic Acid in Water

Kei-Woul KIM[1,a], Dong Seok RHEE[1,b,*]

[1]Department of Environmental Engineering, Kangwon National Univerity

Hyoja2-Dong, Chuncheon-Si, Kangwon-Do, 200-701, Rep. of KOREA

[a]woury@hanmail.net, [b]dsrhee@kangwon.ac.kr

[*]Corresponding author

**Keywords:** Humic Acid, Ozon/Hydrogen peroxide system, Formaldehyde, TOC, AOP

**Abstract.** The ozone/hydrogen peroxide system has been introduced for the study of degradation of humic acid in water. The removal ratio of TOC in aquatic humic acid solution has been investigated with some reaction parameter like the change of injected concentration of $H_2O_2$, initial pH of aqueous humic acid and injection time of $H_2O_2$. And the formation of formaldehyde concentrations in the treatment system processes has been also evaluated with the variation of its concentration. From the experimental results, it has been concluded that the concentrations of $H_2O_2$ and the initial pH's in solution in the ozone/hydrogen peroxide system were very important for enhancing the efficiency of degradation of humic acid in water. The formaldehyde was formed less in ozone/hydrogen peroxide system than in ozone alone system.

## Introduction

The humic substances take up 50 % of DOC average concentration in most of the surface waters and their molecular weights are of a broad range from hundreds to several ten thousand Daltons. And since the humic substances, which are biologically refractory organic carbon, color from yellow to black, they induce color in treated water. And it is also well known that the chlorination of drinking water including humic substances produces haloorganic compounds such as trihalomethanes (THMs) as a byproduct, which are carcinogenic [1,2,3,4]. The advanced oxidation processes (AOP) can be effective to treat humic substances in water. The ozone treatment system is one of them. The ozone treatment is widely utilized as a method to suppress a generation of THMs which are formed as a byproduct in the water sterilization by chlorination. However, some organic pollutants are only oxidized partially or hardly oxidized by ozone. In order to supplement such disadvantage of the ozone treatment, many alternative AOP's including ozone/high pH, ozone/hydrogen peroxide, ozone/UV have been developed [5].

The ozone/hydrogen peroxide system has been studied with an aim of enhancing ozonation and degradation of humic suastances in water has been mainly characterized by removal rate of total organic carbon (TOC) in reaction solution [6]. As The influences of initial pH of solution, concentration of hydrogen peroxide and injection time of hydrogen peroxide to degrade organic materials have been investigated in the reaction system. Together with that, the formation of formaldehyde, which is one of major byproducts in ozonation of humic substances [7].

## Experiment

The ozone generator of Model No. E502 of Fisher Co. was used in the experiment, and a high purity oxygen (99.999 %) for experiment was supplied by removing moisture and hydrocarbons passing through a gas filter. The ozone reactor was made of pyrex material with the capacity of 1000 ml and the connecting part was made of silicon tube so as to prevent from corrosion.

The humic acid used in the experiment was purchased from Aldrich-Chemical. A stock solution of 1000 ppm was prepared and diluted to appropriate concentration. The operation conditions of the ozone/hydrogen peroxide system were as follows; firstly, concentrations of $H_2O_2$ were varied with 0

mg/L, 5 mg/L, 10 mg/L, and 15 mg/L respectively so that an optimal concentration of $H_2O_2$ has been searched for, and the system was operated by injecting 5 mg/L of $H_2O_2$ at each interval of 0, 3, 5, and 7 minutes upon the treatment of ozone to observe efficiencies as a function of $H_2O_2$ injection time.

And in a condition of 5mg/L $H_2O_2$ that had represented the best efficiency in the ozone/hydrogen peroxide system, the ozone was treated by varying 3.5, 5.0, 7.0, 9.0, and 10.5 respectively and adjusting the initial pH of the humic acid solution with 1 N-HCl and 1 N-NaOH, when the injected ozone concentration was $10 \pm 1$ mg $O_3$/min·L. TOC analysis was done with the UV-Persulfate method (DOHRMANN, Phoenix 8000).

In order to get information of formaldehyde formation, the reaction products was treated by the PFBOA(pentafluorobenzyl hydroxylamine) method and analyzed by the gas chromatograph equipped with column, EC-1 (0.25mm x 30m x 0.25 μ m, Alltech), and detecter ECD (Varian STAR 3400Cx ).

## Results and Discussion

### Removal of TOC

Hydrogen peroxide promotes the decomposition of ozone and increases the hydroxyl free radicals [8]. Also, the ozone/hydrogen peroxide process is more effective the degradation of alcohols, aliphatic acids, aldehydes, micro-pollutants and chlorinated solvents than ozone alone [9].

*Fig. 4* shows the removal rate of TOC with initial $H_2O_2$ concentration. The removal rate of TOC is the highest at 5 mg/L of initial $H_2O_2$, but it is rather decreased when injected concentration is above 10mg/L of $H_2O_2$. Christian Volk et al. have published that an optimal ratio of $H_2O_2/O_3$ is at 0.35-0.45 g/g when refractory pollutants may be oxidized. From this results, we can deduce that injected $H_2O_2$ has increased the hydroxyl radicals through the reaction with ozone. Therefore, the degradation of organic compounds is accelerated. But the excess of $H_2O_2$ acts as a radical scavenger.

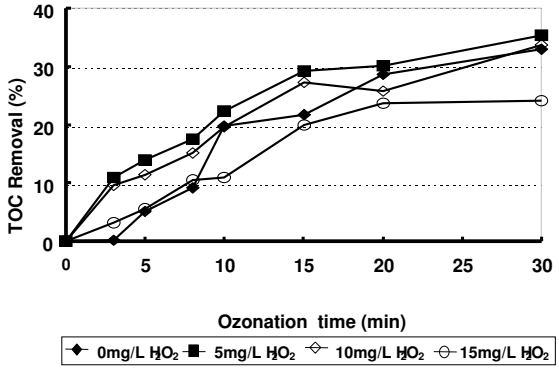



Fig. 1. TOC removal with injected $H_2O_2$ concentration at the initial stage.

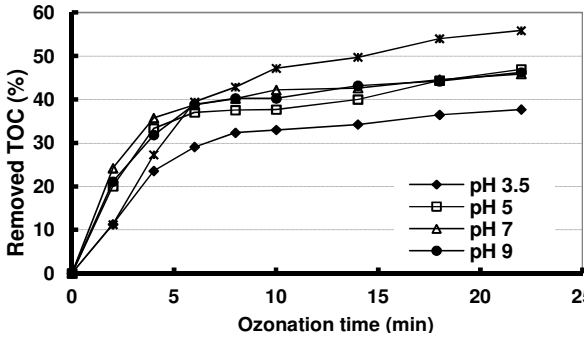



Fig. 2. TOC removal rate with various initial pH's at $[H_2O_2]$ = 5 mg/L

After that injected $H_2O_2$ concentration had been fixed to 5 mg/L, the TOC removal efficiencies of aquatic humic acid solutions was varied with pH of 3.5, 5.0, 7.0, 9.0, and 10.5, as shown in *Fig. 5*. In the ozone/hydrogen peroxide system, more it was increased in the initial pH, more it was increased in the removal ratios of TOC. At pH of 10.5, the TOC removal ratio was lower than other pHs within 8 minutes after beginning ozonation, however, that was increased to about 10 % compared with pH 5 to 9, and about 20 % compared with a strong acid of pH 3.5 as the reaction time passed.

This results show that $OH^-$ in high pH solution, similarly in ozone alone reaction, in ozone/hydrogen peroxide system has accelerated the decomposition of molecular ozone and has resulted in the formation of hydroxyl radicals [5,10]. Therefore, it can be deduced that degradation ratio of humic acid is increasing with increase of pH of the solution. Also the reason at the beginning point of the ozonation could be considered that chemical species such as ozone, $H_2O_2$ and $OH^-$ could compete with each other [11] if $OH^-$ was injected in excess.

Generally, ozonation can be explained as occurring in two stages. In the first stage, ozone molecular rapidly destroys the initial oxidant demand present to enhance the ozone transfer rate into solution from the gas phase. Addition of hydroxyl radicals in the first stage should be minimized because $H_2O_2$ competes with ozone-reactive molecules for the ozone present. In the other stage, organic compounds are oxidized much slower than in the first stage. During the second stage adding of $H_2O_2$ makes it possible to increase the overall oxidation efficiency, since the hydroxyl radical produces by reaction of $H_2O_2$ with ozone [11].

In this experiment, TOC was mostly decreased within 10 min in ozonation of humic acid. *Fig. 3* demonstrated the effect on decomposition of organic compounds when $H_2O_2$ was respectively injected at 3, 5, 7 min. In experimental results, we were found that TOC removal was rapidly increased more after injecting $H_2O_2$ than before. TOC removal didn't make wide difference when treatment efficiency was compared 3 min with 0min of injection time, but TOC removal was considerably increased at 5 min and 7min of injection time. Particularly it was the highest efficiency about 50 % when $H_2O_2$ was injected at 5min after ozonation. This results were relatively increased more about 20% of efficiency than in injecting the $H_2O_2$ at initial stage (0 min). This experimental result was shown that degradation efficiency of organic matter was also depended on the injection time of $H_2O_2$ in ozone/hydrogen peroxide system. When ozone/hydrogen peroxide process may be applied in practical water treatment plant, therefore, operator of the plant should be carefully considered the stage of added $H_2O_2$.

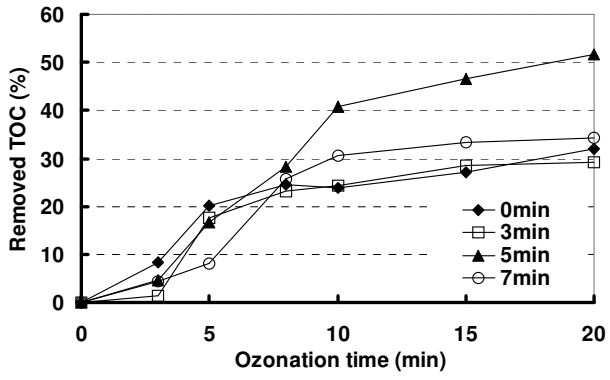



Fig. 3. TOC removal rate with $H_2O_2$ injection time at initial pH = 7.0±0.2 and [$H_2O_2$] = 5 mg/L

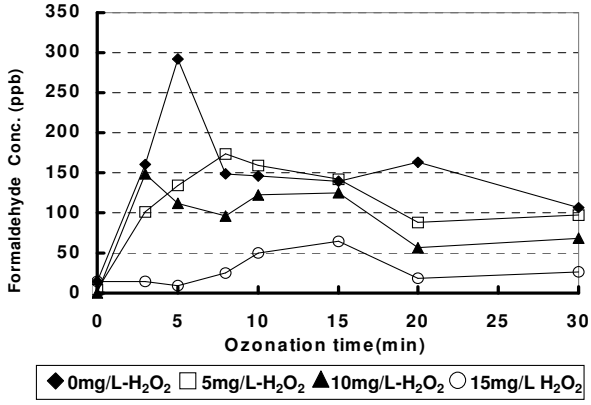



Fig. 4. Formaldehyde concentrations with $H_2O_2$ c oncentration at initial pH = 7.0±0.2

**Formation of Formaldehyde**

*Fig. 4* shows the concentration changes of formaldehyde contents, which were formed according as variation of $H_2O_2$ concentration in the ozonation of humic acid. As shown , formaldehyde was decreased according as addition of $H_2O_2$ was increased. In case of ozonation alone, formaldehyde was increased approximately 300 ppb at reaction time of 5 min, and then decreased to about 100-150 ppb proceeding ozone reaction. Especially, when $H_2O_2$ concentration was injected 15 mg/L, formaldehyde during all reaction time was formed less than 50ppb.

The reason that formaldehyde was decreased may be predicted as following. Because ketone or aldehyde will be yield by the reaction of ozone with C-C double bonds of humic acid, formaldehyde was increased at initial stage. However, proceeding the ozone reaction, formed aldehyde is also reacted with ozone or OH radical, and can be oxidized to its corresponding carboxylic acid. Further oxidation of carboxylic acid is generated carbon dioxide and water as final products. So formaldehyde may be gradually decreased [12].

Also, OH radical is yielded more with addition of $H_2O_2$ than without addition of $H_2O_2$. And then carboxylic acid may be produced according as OH radical reacts additionally with aldehyde, which formed with ozonation of humic acid.

**Summary**

Degradation characteristics of humic acid on ozone/ hydrogen peroxide system was studied by TOC removal ratio with variation of some reaction parameters. And the concentrations of formaldehydes which were formed as byproducts in this treatment system were quantized. The results could be concluded as following: Removal ratio of TOC was maximum at injection concentration of $H_2O_2$ 5 mg/L, injection time above 5 minutes, and initial pH 10.5. Particularly, there were many differences as a function of injection time of hydrogen peroxides, which was concluded in this study since hydrogen peroxides injected at the initial reaction deteriorated a degradation efficiency of humic acids caused by an competent reaction with ozone. It is considered to us that such results shall need a careful examination on the injection stage of $H_2O_2$ in the process of ozone/hydrogen peroxide.

The formaldehyde was formed less ozone/hydrogen peroxide system than the ozone alone system. When initial pH in solution were changed from 3.5 to 10.5, the formaldehyde were formed most at pH 5. Throughout the study it could be also deduced that the formaldehydes were formed by direct reaction with carbon-carbon double bond of humic acid and molecular ozone as shown in Criegee mechanism

**References**

[1] Langlais B., Reckhow D. A., Brink D. R. (1991) "Ozone in water treatment – application and engineering", Lewis Publisher

[2] Rhee D. S., Jung Y. R. (2000) "Characterization of humic acid in the chemical oxidation technology (II) – characteristics by ozonation", Analytical Science & Technology, 13(2), 241-249

[3] Santos E. B. H, Duarte A. C. (1998) "The influence of pulp and paper mill effluents on the composition of the humic fraction of aquatic organic matter", Wat. Res., 32(3), 597-608

[4] Watt B. E., Malcolm R. L., Hayes M. H. B., Clark N. W., Chipman J. K. (1996) "Chemistry and potential mutagenicity of humic substances in waters from different water sheds in Britain and Ireland", Wat. Res., 30(6), 1502-1516

[5] Brunet R., Bourbigot M. M., Dore M. (1984), "Oxidation of organic compounds through the combination ozone-hydrogen peroxide", Ozone Sci. & Eng., 6, 163-183

[6] Gagnon G. A., Booth S. D. J., Peldszus S., Mutti D., Smith F., Huck P. M. (1997) "Carboxylic acids : Formation and removal in full-scale plants", Journal AWWA, 89(8), 88-97

[7] Nakamuro K., Ueno H., Kakao M., Sayato Y. (1990) "Formation of hydrogen peroxide by aqueous ozonation of humic acid and aromatic hydrocarbons", Chemosphere, 20(5), 525-531

[8] Staeheiln J., Hoigne J. (1982) "Decomposition of ozone in water : rate of initiation by hydroxide ion and hydrogen peroxide", Environ. Sci. Technol., 16, 676-681

[9] Volk C., Roche P., Joret J. C., Paillard H. (1997) "Comparison of the effect of ozone, ozone-hydrogen peroxide system and catalytic ozone on the biodegradable organic matter of a fulvic acid solution", Wat. Res., 31(3), 650-656

[10] Glaze W. H., Kang J. W., Chapin D. H. (1987) "The chemistry of water treatment processes involving ozone, hydrogen peroxide and ultraviolet radiation", Ozone Sci. & Eng., 9, 335-352

[11] EPA Guidance Manual - Alternative disinfectant and oxidancts (1999)

[12] Lim Y. S., Lee J. J., Rhee D. S. (1999) "A study on the formation of formaldehyde from humic acid by ozonation", Research report (The institute of industrial technology, kangwon Nat'l univ.), 19, 409-413

*Advanced Materials Research Vol. 937 (2014) pp 624-631*
*© (2014) Trans Tech Publications, Switzerland*
*doi:10.4028/www.scientific.net/AMR.937.624*

# Experimental Study on Dynamic Characteristics of Self-excited Oscillation Pulsed Jet

Chuan-lin TANG[1,a],Jie PEI[1,b,*]and Dong HU[1,c]

[1]Modern Jet Instiitute, Hunan University of Technology, Zhuzhou 412007, china

tcl5608@126.com , jiege86816@163.com

**Keywords:** Dynamic characteristics, Frequency, Pulsed jet, Self-excited oscillation.

**Abstract.** The dynamic characteristics of the self-excited oscillation pulsed jet is tested by using pulsed jet impact variable cross-section beam in submerged conditions and make comparison with continuous jet, analyzing the effects of operating parameters and nozzle structure parameters on the dynamic characteristics of the pulsed jet. The result show that the oscillating frequency of jet decreases with the increase of cavity length while increases with the increase of the pump pressure. The energy of pulsed jet has obvious change with different cavity length.

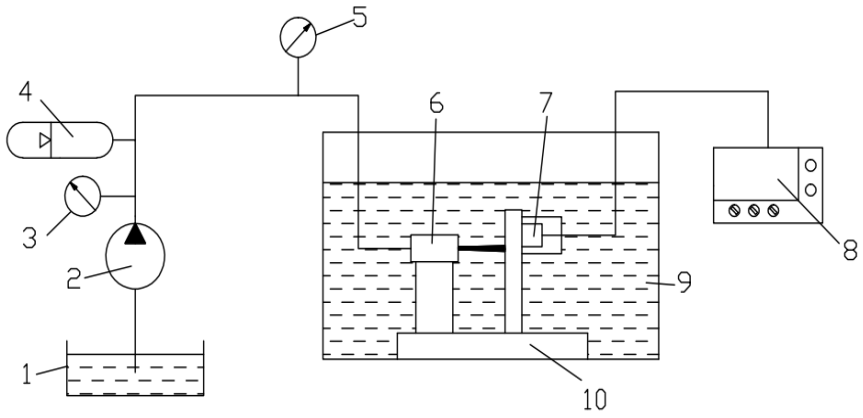
## Introduction

As one of efficient water jet, self-excited oscillation pulsed jet obtained rapid development in recent decades. The device is small in size, simple structure, good sealing, high reliability and low cost, without additional external driving mechanism, which has obvious advantages in cutting, crushing and mineral cleaning, especially in deep-sea mining [1-3].

Pei Jianghong, Tang Chuanlin[4] et al. studied the performance of the self-excited oscillation nozzle [5] under non submerged condition. Research shows that the unstable shear layer oscillation cavity has the function of selective amplification on the disturbance waves, there are appropriate structure parameters to make disturbance frequency match the natural frequency of the nozzle, and then produces strong self-excited oscillation pulsed jet.

Dynamic characteristics affect the erosive effects of the self-excited oscillation pulsed jet directly, most of scholars at home and abroad launch a lot of study on the generating mechanism of its characteristics, but the research on its frequency characteristic less. Because the factors which affect the dynamic characteristics of pulsed water jet have both characteristics of the fluid itself, such as pressure and flow, and the structural parameters of the self-excited oscillation cavity, such as the cavity size, cavity length, diameter and the ratio between upper and lower nozzle. This paper selects the variable section beam as the signal test target disk, with water jet as the excitation signal, collecting signal through the piezoelectric acceleration sensor which input the vibration signal to testing instrument, then obtain the dynamic signal of the water jet. We mainly study the influence law of the jet pump pressure and the length of oscillating chamber on dynamic performance of jet, and compare the dynamic performance with the continuous jet.

## Experimental Device and Method



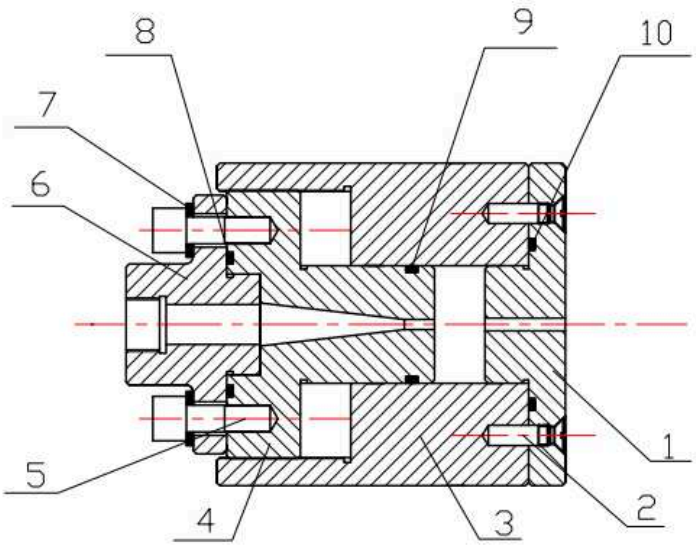

1.water reservoir 2.three-throw ram pump 3.seismic pressure gauge 4.energy accumulator 5.seismic pressure gauge 6.pulsed nozzle 7.sensor 8.viberation signal analyzer 9.water tank 10. test bench

Fig.1. Experiment system sketch of dynamic characteristics of jet

## Experimental Device

Experiment system sketch is shown in Figure 1, first of all, we start the three plunger pump water to supply water, then start the main motor after water pump works stable, three plunger pump is driven by cylindrical gear reducer, high pressure water is ejected from pulsed jet nozzle to impact test bench of non-uniform beam in the water tank through the energy accumulator, which is produced by three-throw ramp pump.

Figure 2 is structure diagram of self-excited oscillation pulsed water jet nozzle which is the core component of the test. The high pressure water comes from the upper nozzle flows into the oscillation cavity, then ejected from lower nozzle after complex procedure. This experiment device includes three phase asynchronous motor, pressure gauge, three plunger reciprocating high-pressure pump, accumulator and variable cross-section beam and the acceleration sensor, vibration signal analyzer, JZ - 1 type electric vibrator, test bench. The variable cross-section beam and the nozzle are fixed as shown in Figure 3.




1.down nozzle 2.sink hole screw 3.cavity 4.upper nozzle 5.Socket head cap screw 6.joint 7.gasket 8.sealing ring 9.sealing ring 10.sealing ring

Fig. 2. Schematic plot of self-excited pulsed jet nozzle



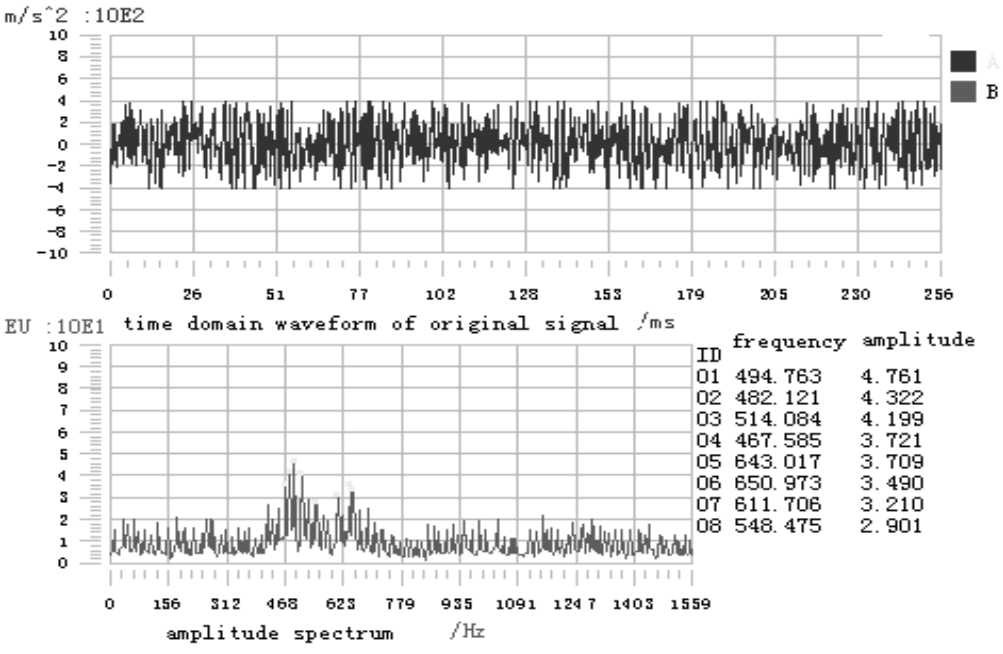
Fig. 3. Fixed schematic plot of variable cross-section beam and nozzle

## Test Method

Tests are performed in submerged conditions. Dynamic characteristic of two kinds jet are tested according to the experimental conditions. Each jet can be tested by adjusting measuring steps to observe its dynamic characteristics. During the experiment, setting test parameters of QLVC-ZSA1 type vibration signal analyzer system at first, then start the motor, collecting data after pump pressure stable. Starting real-time observation and data collection of time-frequency characteristics of jet under each condition.

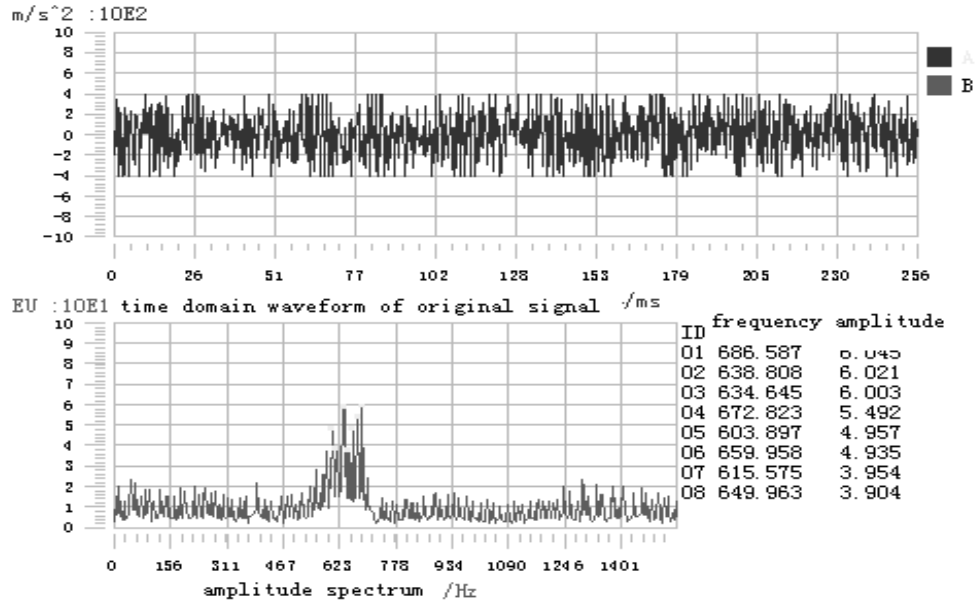
## Experimental Results and Analysis

The time-frequency domain characteristics of continuous jet. The time-frequency domain characteristics of continuous jet are shown in Figure 4 to Figure 6 respectively. The pump pressure is 5MPa and the standoff are 5mm, 10mm, 15mm.



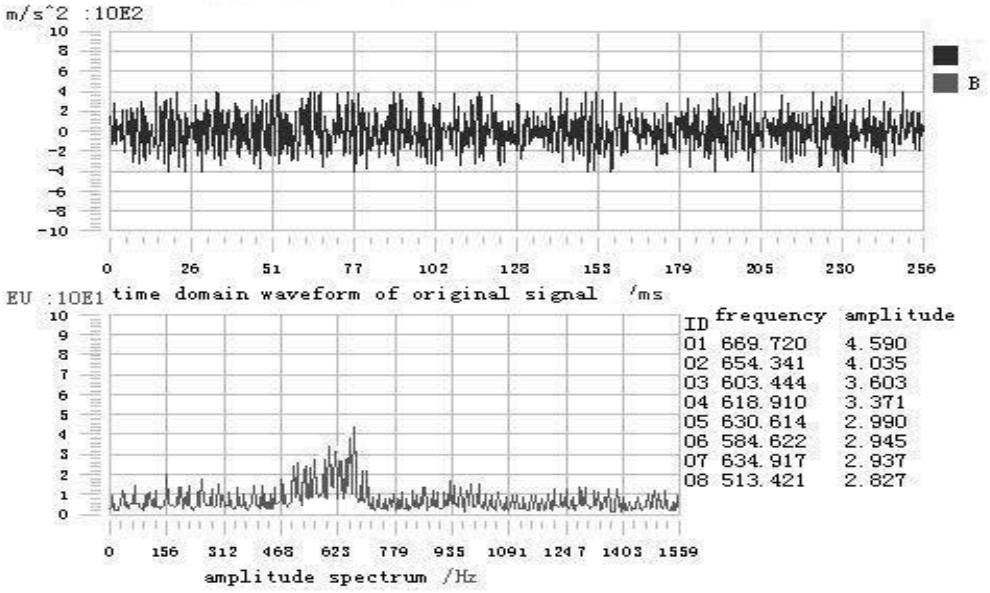

(pump pressure is 5Mpa,standoff is 5mm)

Fig. 4. Time and frequency domain features of continuous jet




(pump pressure is 5MPa,standoff is 10mm)

Fig. 5. Time and frequency domain features of continuous jet




(pump pressure is 5MPa,standoff is 15mm)

Fig. 6. Time and frequency domain features of continuous jet

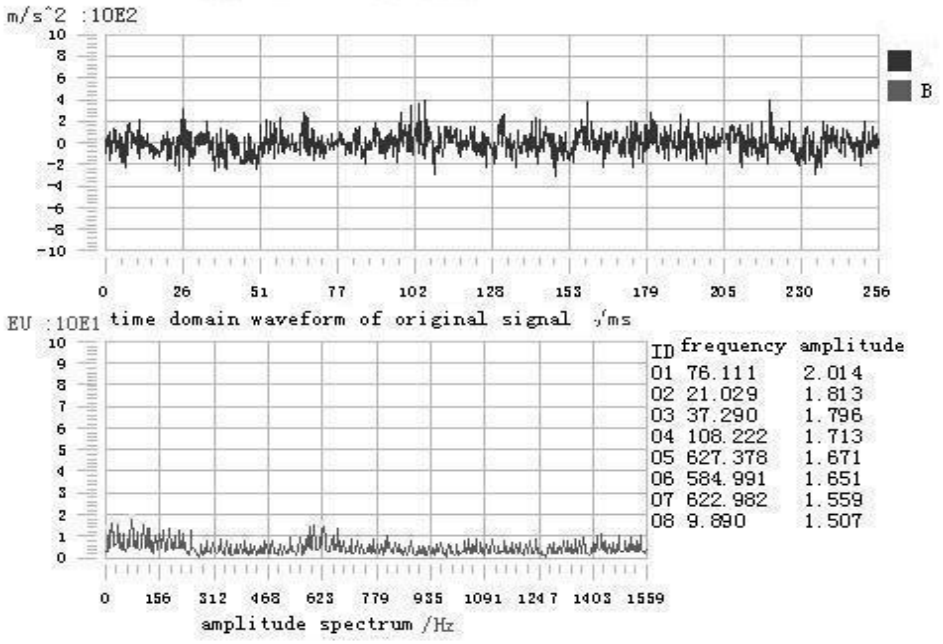
Figure 4 to figure 6 show that the continuous jet has a very high peak value at a frequency of 625 Hz (current frequency), this is because jet contains a variety of frequency signal. When the natural frequency of jet closes to the natural frequency of variable cross-section beam, the resonance of variable cross-section beam happens. It can be seen from Figure 6, when the target distance is 5mm, jet frequency appears two peak frequencies, respectively 494Hz and 643Hz. We find that the dominant frequency shows more decentralized when the standoff is 5mm.This is because the reflection of jet will flow with the main jet, changing the frequency components of the main jet and wilding the dominant frequency. Frequency peak does not appears at 296Hz , which explains that little jet composition at this frequency is contained in the continuous jet, but almost no obvious pulse peak in other frequencies, and the vibration amplitude is relatively small, which shows that the other band of jet belongs to turbulent jet.

We can see from Fig 4 to Fig 6, the corresponding frequency peak decreases gradually with the increase of the standoff. This is due to the impact force on variable cross-section beam decreases gradually with the increases of standoff. It also can be seen, the range of dominant frequency becomes

wider gradually with the standoff increases, which shows that jet gradually developed into a basic section, the frequency components of jet increases gradually, so that the dominant frequency of jet became wider.

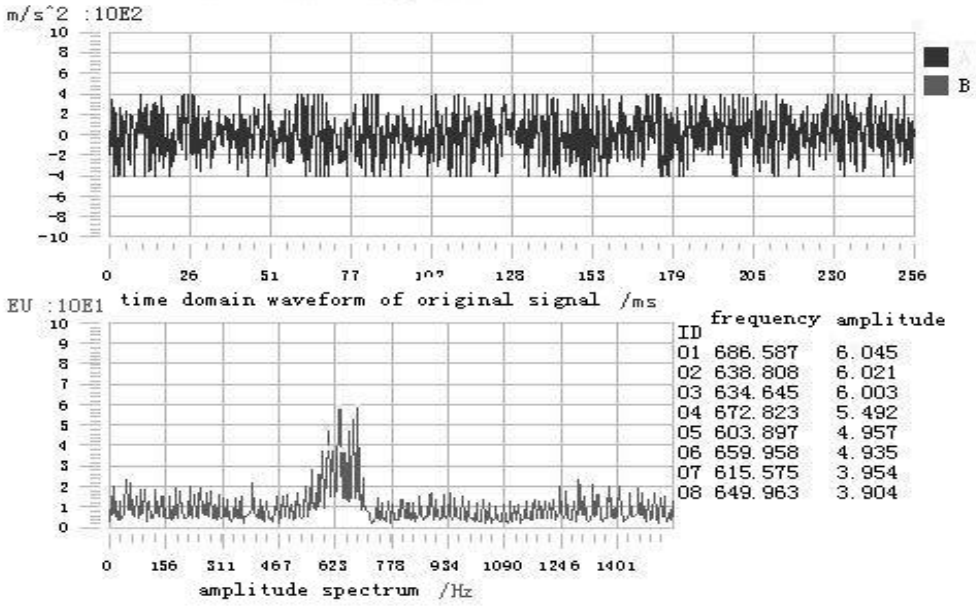
Time-frequency domain features under the same standoff and different pump pressure.The analysis above show that due to the generation of return flow when the standoff is 5mm, which may disturb the main jet and thereby affecting the spectrum amplitude in the graph. If the standoff is too large, the vibration peak value under lower pump pressure conditions submerged in the interference signal of turbulent jet cannot be displayed. So choose the standoff of 10 mm to analysis influence of different pump pressures on vibration peak value.

When the cavity length is 10mm, pump pressure are respectively 2.5MPa, 5MPa, 7.5MPa, the amplitude spectrum of continuous jet are shown in the figure below:



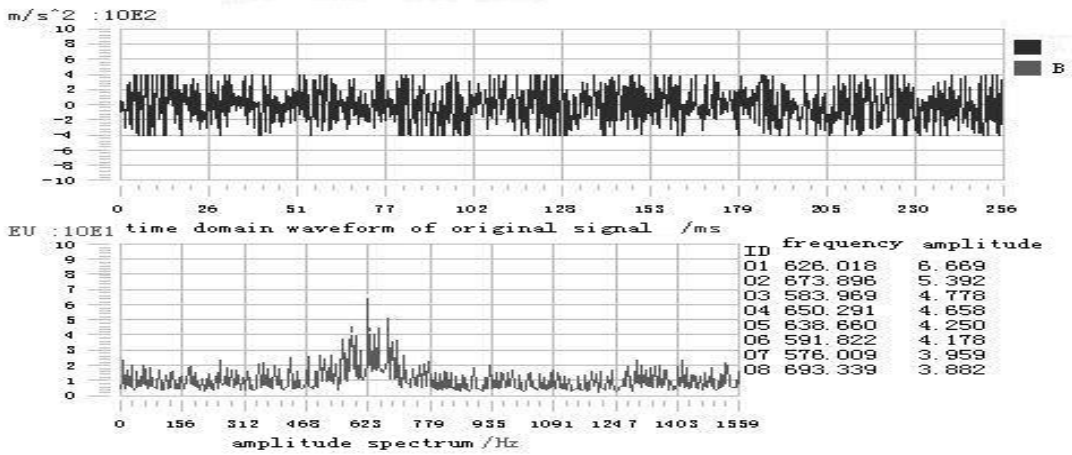

(cavity length is 10mm,pump pressure is 2.5MPa)

Fig.7. Time and frequency domain features of continuous jet




(cavity length is 10mm,pump pressure is 5MPa)

Fig. 8. Time and frequency domain features of continuous jet



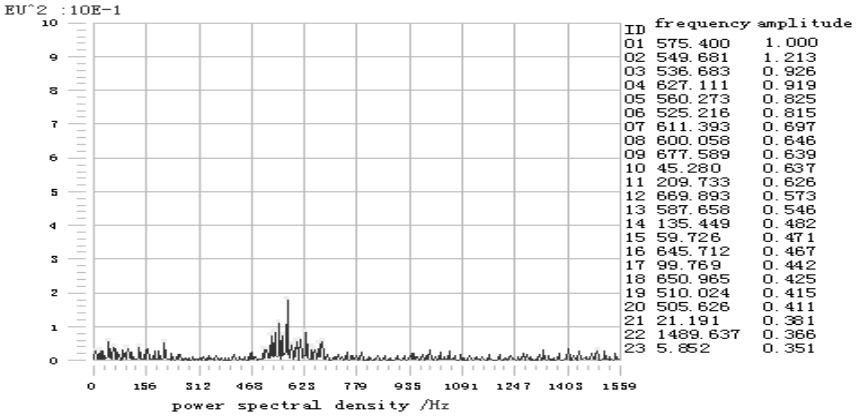

(cavity length is 10mm,pump pressure is 7.5MPa)

Fig. 9. Time and frequency domain features of continuous jet

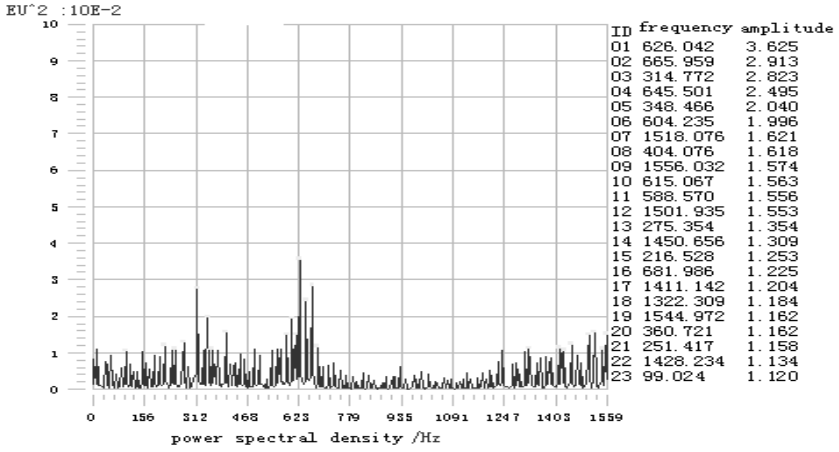
It can be seen from Figure 7 to Figure 9, jet basically complete dissipate in the surrounding medium when the pump pressure is 2.5MPa and the standoff is 10mm. Its impact on the variable cross section beam is small. The amplitude frequency figure almost has no peak frequency.

Fig 7 to Fig 9 show that the corresponding amplitude of the 76Hz which is the interference signals of system internal current. We should exclude this signal in the analysis of water jet frequency signal.

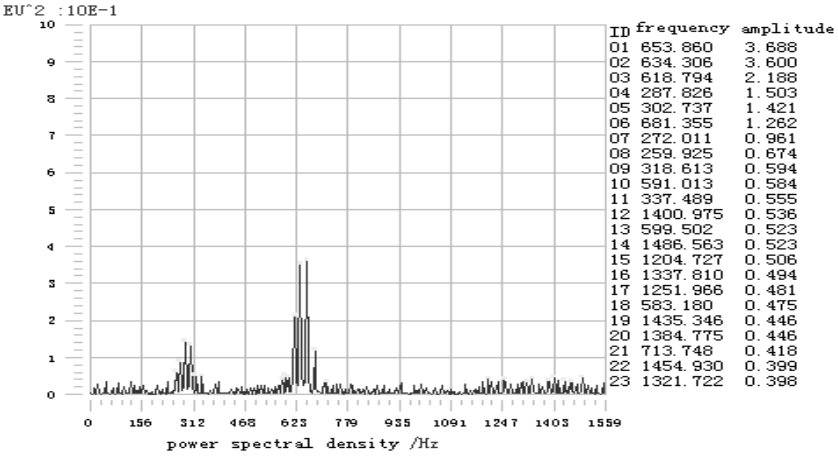
Comparison of power spectrum between continuous jet and pulsed jet .The pump pressure is 5MPa ,standoff is respectively 5, 10mm and cavity length is 1.5, 4.5, mm. The comparison diagram of power spectrum between continuous jet and pulsed jet is shown in Figure 10 to Fig 11.




(a) continuous jet



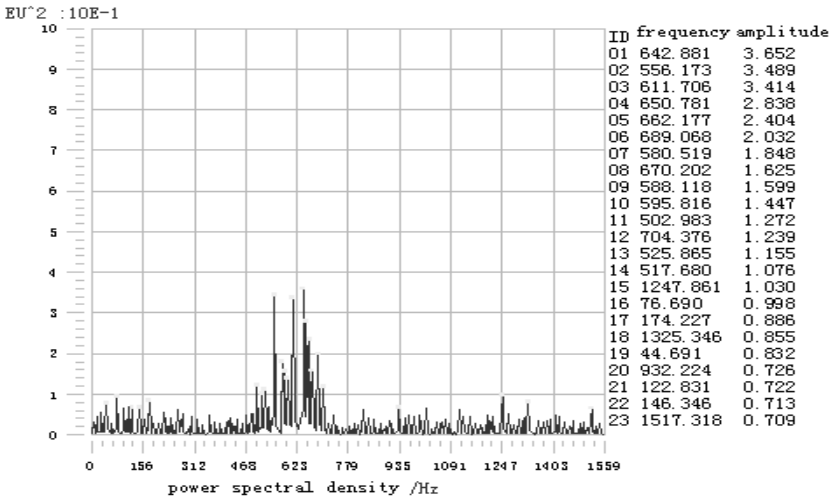

(b) pulsed jet (cavity length is 1.5mm)



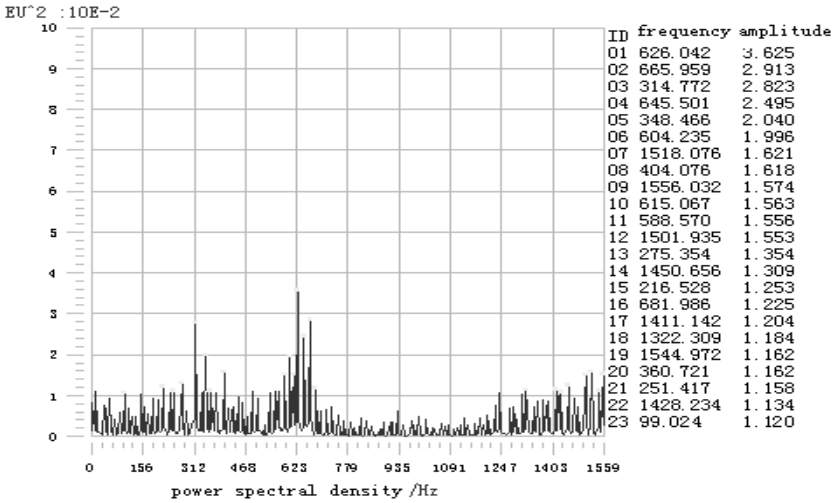

(c) pulsed jet (cavity length is 4.5mm)

Fig. 10. Power spectrum diagram(pump pressure is 5MPa,standoff is 5mm)

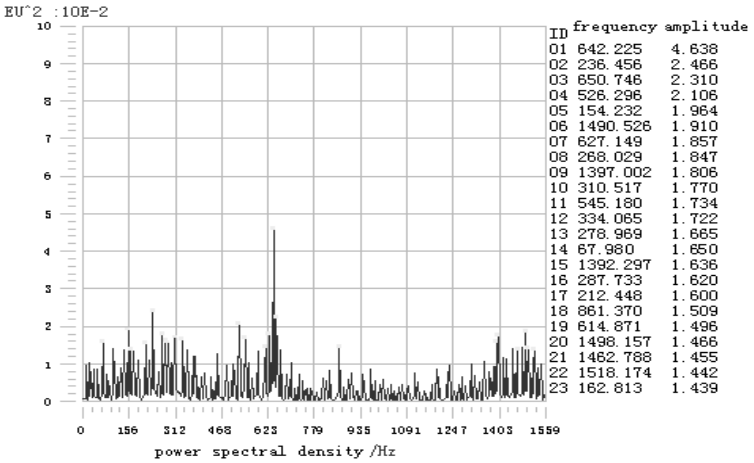
It can be seen from power spectrum that under the same pump pressure (5MPa) and the same standoff (5mm), energy of continuous jet is mainly concentrates in the frequency whose peak value is near 575Hz.The energy of pulsed water jet is mainly divided into two parts: one is included in the frequency band whose peak value is near 302Hz, the other is contained in the frequency band whose peak value is near 638Hz.




(a) continuous jet




(b) pulsed jet (cavity length is 1.5mm)




(c) pulsed jet (cavity length is 4.5mm)

Fig. 11. Power spectrum diagram(pump pressure is 5MPa,standoff is10mm)

We can see from Fig 10 to Fig 11 that the power spectra amplitude of pulsed jet is reduced compare with continuous jet. the mainstream of pulsed jet including two frequency components which contain the main energy of pulsed jet,.whichcontains most of the energy of the jet.

## Conclusions

1.When pump pressure keeps constant, with the increases of standoff, peak value of impact force of two kind's water jet decrease gradually. The time-frequency characteristic of continuous jet have only one frequency peak, while pulsed jet has two, one of them is the same with continuous jet, the other is the self-excited oscillation frequency.

2.With the increase of pump pressure, oscillation amplitude of the time-frequency characteristic gradually increases.

3.The change law of energy and peak frequency of continuous jet is the same. But the energy of pulsed jet has obvious change with the change of cavity length.

## Acknowledgement

This work was financially supported by the National Natural Science Foundation of China(Grant No.51374101), the Natural Science Foundation of Hunan Province (Grant No. 13JJ9013) and the the Projects of Hunan province science and Technology Department (Grant No. 2013SK3165).

## References

[1] SHENG Zhonghou. Theory And Technology of Water Jet [M]. Dongying: Petroleum University Press, 1998:390-414.

[2] XUE Shengxiong,etc. High Pressure Water jet Technology & Engineering [M]. Hefei: HeFei University of Technology Press, 1998:390-414.

[3] GAO Chuanchang, Zhao Li, Liu Xinyang, Huang Xiaoliang. Experiment research on erosion of self-excited inspired pulsatile jet in submerged conditions [J].Drainage and Irrigation Machinery, 2012(1):53-56, 63.

[4] TANG Chuanlin, HU Dong, PEI Jianghong. Experimental study on the frequency characteristic of the self-excited oscillation pulsed nozzle [J]. Acta Petrolei Sinica, 2007, 28(4):122-125.

[5] LIAO Zhenfang, TANG chuanlin, ZHANG Fenghua. Experiment of the Self-excited Oscillation Pulsed Jet Nozzle [J]. Journal of Chongqing University (Natural Science Edition), 2002,25(2):28-32.

*Advanced Materials Research Vol. 937 (2014) pp 632-638*
*© (2014) Trans Tech Publications, Switzerland*
*doi:10.4028/www.scientific.net/AMR.937.632*

# The Study of Groundwater Modeling of Plain Area in Shiyang River Basin—— I Groundwater System Conceptual Model Construction

Yu-fei CHENG[1,a,*], Yuan-hong LI[1,b], Xiang-quan HU[1,c], Jun-de WANG[1,d], Shu-chao LU[1,e]

[1]Gansu Research Institute for Water Conservancy, Lanzhou 730000 , China

[a]email: chengyf1980@gmail.com

[b]email:gssk@163.com

[c]email: 1036139875@qq.com

[d]email: 81041256@qq.com

[e]email: 18028123@qq.com

*Corresponding author

**Keywords:** Shiyang River Basin; groundwater modeling; groundwater system; conceptual model.

**Abstract:** In order to construct the groundwater numerical simulation model, the study area was determined on the basis of the geological and hydrogeological conditions. Taking Feflow as operating platform, combining GIS with Surfer software, a study area of the structure of three-dimensional aquifer model was established, realizing the 3D visualization of a large area of the complex geological content. Combined with the hydrogeological conditions, three-dimensional geological structure of the model further generalization. The result showed that the aquifer of the vertical was generalized into the unconfined aquifer; based on the characteristics of lithology, structure, parameters and distribution of recharge and discharge in groundwater system, the study area groundwater system was characterized by isotropic saturated-unsaturated numerical flow model, and the equilibrium composition of the elements was analysed in study area, the partition of the aquifer hydrogeological parameters was divided, lay the foundation for groundwater numerical model simulation.

## Introduction

The core issue of the current numerical simulation is to prevent distortion of simulation, to improve the emulation and simulating precision of models. The distortion of simulation is multifaceted, the most important of which is the distortion of the conceptual model. Complexity of subsurface flow systems makes the opportunities for a variety of conceptual simplifications leading to a multiplicity of flow models[1]. Once the hydrogeological conceptual model cannot describe basic motion law of groundwater in the study area, the subsequent work is even fine, it is impossible to make up for the mistakes to build a conceptual model[2]. It should pay attention to the understanding and generalizing the specific hydrogeological conditions, as well as the establishment of the conceptual model[3]. The model not only reflects the reality, but also is an abstract and higher than the fact[4]. Model is to be simple and clear, can be used to further quantitative description, ignoring some of the factors that has nothing to do with the research questions or little relevance[5]. Hydrogeological conceptual model is the abstract expression of the objective hydrogeological conditions, is also an important basis for groundwater modeling and water resources assessment[6]. When lateral flow and transport in the unsaturated zone are not significant, one common simplification will be supposed unless the capillary fringe is involved [7].

In the 1980s, the concept of the hydrogeological conceptual model is first proposed, and its purpose is to simplify the hydrogeological conditions, to carry on the effective analysis of the groundwater system. Foreign representative regional hydrogeology conceptual models are the model of Great Artesian Basin in Australia and Death Valley in the United States [8]. Based on the

coupling between existing coded modeling concepts, the integrated modeling approaches are discussed[9]. The coupled models was used to evaluate the interactions between near-surface and groundwater flow processes which was a conception desirable but difficult goal[10].The basic model of the earliest domestic hydrogeological conceptual model introduced the conceptual models in the south of France and North Africa[11], and then with the combination of production practices, domestic hydrogeology conceptual model developed rapidly. But in general the research of demestic isn't systematic enough in hydrogeological conceptual model.

The groundwater of Wuwei, Minqin and Changning basins were selected as research area in Shiyang River Basin. On the basis of the rich and informative exploration data generalized from the geological structure, the aquifer system, the groundwater flow system, the hydrogeological parameters system, the sources and sinks were generalized. This paper was trying to establish a grounp of hydrogeological conceptual model and its corresponding space discrete expression, so as to provide scientific basis for groundwater numerical simulation in the study area.

## The General Situation in the Study Area

### Natural Conditions

Shiyang River Basin is located in east of hexi corridor, gansu province, it situated in the western of Wushao Ridge, in the northern slope of Qilian Mountain, is between 101°41'~ 104°16' east longitude, 36°29'~ 39°27' north latitude). Land area is 41600 km$^2$(Fig. 1). The terrain of Shiyang river basin in south is higher than that in North, tilt from southwest to northeast. Whole basin can be divided into four geomorphic units, included the northern Qilian Mountain in southern, central plains corridor, low hilly land and desert. Shiyang River Basin is deep in the mainland hinterland, belonging to a continental arid monsoon climate of medium latitudes. The climate is characterized by strong solar radiation, long hours of sunshine, temperature difference between day and night, scarce precipitation, intensive evaporation, dry climate. The zonal distribution of vegetation is: mountain meadow, forest and grassland and so on. The vegetation vertical zonality is very obvious.

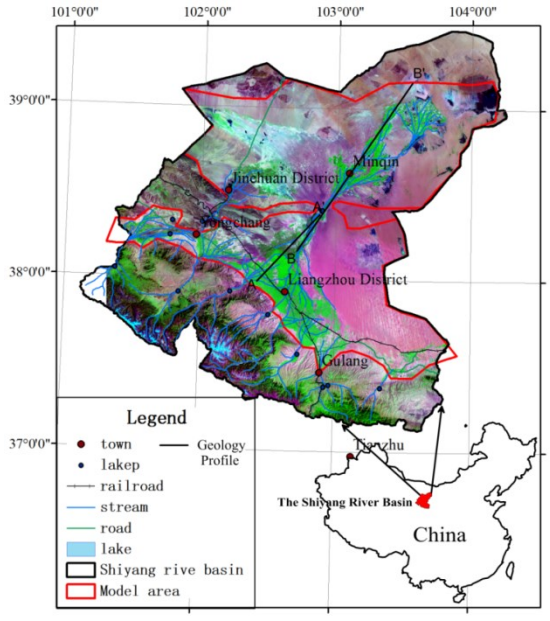



Fig.1. Shiyang river basin and model area

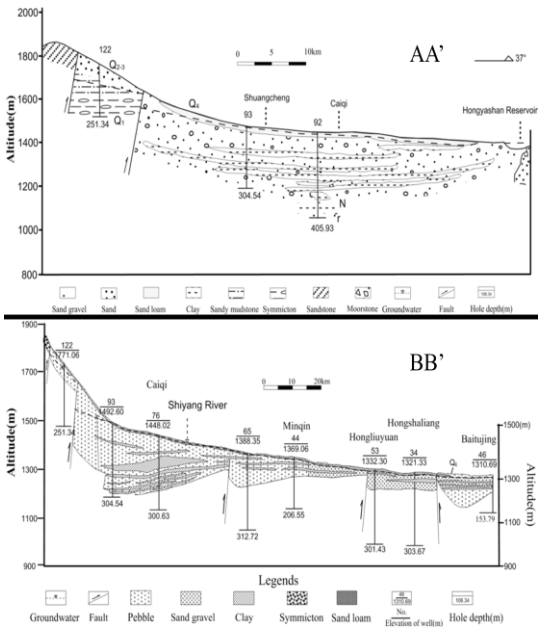



Fig. 2. Hydrogeology section of study area (AA' and BB'in Fig.1)

### Hydrogeology Situation

According to the geology and geomorphology, the groundwater in Shiyang River Basin was divided into Mountain fracture - pore water and plain pore water. The thick of Quaternary System of Wuwei Basin, Minqin Basin and Changning Basin is a good collection of places for pore water,

especially in Quaternary upper Pleistocene Series, water-abundance was better. On the basis of the aquifer structure and hydrodynamic characteristics, the groundwater was divided into two types, namely, phreatic water and micro confined water or confined water. The phreatic water of which thickness was get thinner from west to east, about 100~200m was distributed in pluvial belt of southern Wuwei Basin and Changning Basin. The groundwater buried depth on fault steps, was 10m, the thickness of phreatic was not more than 30m. the salinity of phreatic water was less than 1g/l. The micro confined water or confined water was located in northern Wuwei Basin, eastern Changning Basin and Minqin Basin. From the areas of phreatic water to the confined water, The layers of the aquifer increased gradually, the single layer thickness decreased, hydraulic conductivity became weak(Fig. 2).

## The Experiment Materials and Methods

### Data Collection

Field investigation to collect water level observation data of existing observation wells and civil wells, hydrological geology, meteorology, water resources utilization and terrain data in Shiyang River Basin. DEM, boundary, channel(canal) distribution, land use, water level, hydraulic conductivity of aquifer, specific yield and initialization groundwater level of research area were produced by using GIS and RS.

### Research Method

Conceptual Model of groundwater system (Conceptual Model) can be divided into two categories, one is used to describe the geological structure of 3D geological structure Model, another is used to describe the hydrogeological Conceptual Model of groundwater flow state. This research built 3D geological structure model on the basis of the analysis of hydrogeological data, using GIS, SURFER software, FEFLOW software system as operation platform. on the basis of the analysis of geological structure, combined with the hydrogeological conditions, the hydrogeological conceptual model was established, which laid the foundation of numerical simulation model of the groundwater system.

## The Research Results

### The Range of the Conceptual Model

This research area was determined as the plain of Shiyang River Basin. To the east of it is the Tengger Desert, to the south of it is the Qilian Mountains, to the west is the Yongchang Uplift, to the north is the Beishan Mountain. It was composed of Wuwei, Minqin and Changning basin. the area of model was about 23500 $km^2$.

### To Determine and Generalize Boundary Conditions

Impermeable bottom generalizability: The aquifer bottom of research area was made up of the Jurassic, Tertiary mudstone and sandy mudstone. According to the weak aquifer characteristic revealed, the aquifer system was regarded as the unity of impermeable bottom.

Impermeable roof generalizability: the groundwater system of research area at the top of the boundary is gas-soil interface, where unsaturated zone was the tache which link precipitation, surface water and groundwater. The recharge entered into the system through the top surface of the border includes: river(canal) water, irrigation, precipitation infiltration. Discharge through the top of the border includes: soil evaporation, vegetation transpiration and artificial exploitation of groundwater. The DEM of research area was adopted to interpolate the elevation of Impermeable roof.

Generalizability of lateral boundaries: the groundwater flow boundary conditions were decided in terms of the natural topography and groundwater divide. The southern aquifer system of Wuwei Basin was contact (fracture) zone between basin and mountain, which belonged to the recharge

boundary, could be regarded as the second boundary. The groundwater runoff recharge is relatively significant from Tengger Desert to the eastern of Minqin Basin, so it was regarded as equal mass flow boundary. The rest boundary was considered to be zero flow boundary (Fig. 3)

Generalizability of sources and sinks: the supplies of simulated area: river (flood), canal water infiltration, field irrigation infiltration, rainfall water infiltration, and the undercurrent of lateral supplies; Discharge for evapotranspiration, springs overflow and artificial exploitation.

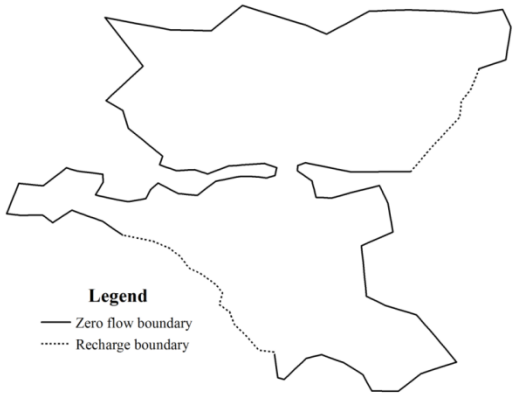



Fig. 3. The boundary conditions of model area

**Recharge and Discharge of the Groundwater Flow System**

Taking into account the groundwater recharge and discharge conditions, Wuwei Basin groundwater recharge included: the river infiltration the lateral flow recharge, precipitation and condensate infiltration, canal and field infiltration. Discharge mainly included: phreatic water evaporation, plant transpiration, artificial exploitation of groundwater and springs overflow. Therefore, water balance equation of regional groundwater is:

$$\Delta W=W_r+W_P+W_b-W_{EZ}-W_{EP}- Ws -W_0- W_p \quad (1)$$

Where: $\Delta W$—groundwater gains and losses amount, $m^3$;

$W_r$—river and canal water leakage recharge, $m^3$;

$W_p$—precipitation, condensation the water recharge, $m^3$;

$W_f$—field irrigation water infiltration, $m^3$;

$W_b$—lateral groundwater flow recharge, $m^3$;

$W_e$—phreatic water evaporation and plant transpiration, $m^3$;

$W_o$— artificial exploitation, $m^3$;

$W_p$—springs overflow, $m^3$.

The groundwater balance results from 2007 to 2011are shown in Tab. 1.

Table 1. Simulation period of groundwater Equilibrium Calculation Table $10^6m^3$

| Region | Sources and Sinks | Balance items | 2007a | 2008a | 2009a | 2010a | 2011a |
|---|---|---|---|---|---|---|---|
| Study area | Recharge | Lateral Flow Recharge | 102.20 | 102.20 | 102.20 | 102.20 | 102.20 |
| | | Irrigation Infiltration | 222.82 | 210.47 | 188.77 | 187.91 | 186.55 |
| | | Canal Leakage | 82.10 | 81.62 | 82.85 | 84.06 | 83.91 |
| | | Precipitation Infiltration | 55.93 | 39.09 | 37.96 | 41.58 | 51.13 |
| | | River Leakage | 27.28 | 12.54 | 10.59 | 12.31 | 14.33 |
| | | Total | 490.33 | 445.93 | 422.37 | 428.06 | 438.12 |
| | Discharge | Evapotranspiration | 31.92 | 33.48 | 33.78 | 32.96 | 31.63 |
| | | Springs Overflow | 34.92 | 29.20 | 26.22 | 24.30 | 22.75 |
| | | Artificial Exploitation | 1125.99 | 1034.71 | 796.86 | 766.12 | 732.00 |
| | | Total | 1192.83 | 1097.39 | 856.86 | 823.38 | 786.38 |
| | Water Balance | | -702.50 | -651.46 | -434.49 | -395.32 | -348.26 |

The results show that the unconfined aquifer was mainly mined in study area. The total recharge of the groundwater system of the study area was $490.33\times10^6m^3$, the total discharge was $786.38\times10^6m^3$, the balanced differential was $-348.26\times10^6m^3$ in 2007; The total recharge of the groundwater system of the study area was $438.12\times10^6m^3$, the total discharge was $1192.83\times10^6m^3$, the balanced differential was $-702.50\times10^6m^3$ in 2011. This suggested that the overexploitation reduced year by year.

Field irrigation infiltration which was main recharge source of groundwater occupied the largest proportion in all recharge items. In the discharge items of the groundwater, artificial exploitation had become the main way of groundwater discharge, which was the main reason for the declined groundwater level in the concentrated mining area, especially in the oasis area where groundwater was pumped to develop farming, there has been obvious cone of depression.

**Initial Flow Field Analysis**

The initial groundwater level used the data of groundwater level which was investigated in January 2000. The groundwater level of no data region was interpolated or extrapolated with using Acrgis software(Fig. 4). It was showen that the highest groundwater level was located in west of Yongchang Basin, the value was 2163.93m. the lowest groundwater level was located in the northern Minqin Basin, was 1296.57m. The groundwater level was about 1430m when entering into Minqin Basin from Wuwei Basin. The groundwater generally flowed into Minqin Basin from the west and south of study area to north, finally entered into the northern lake area of Minqin Basin.

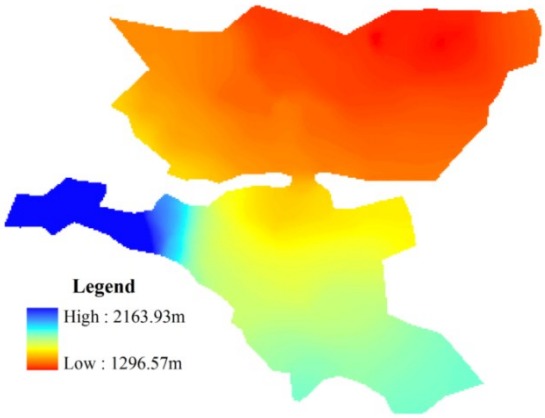



Fig. 4. Initial groundwater level

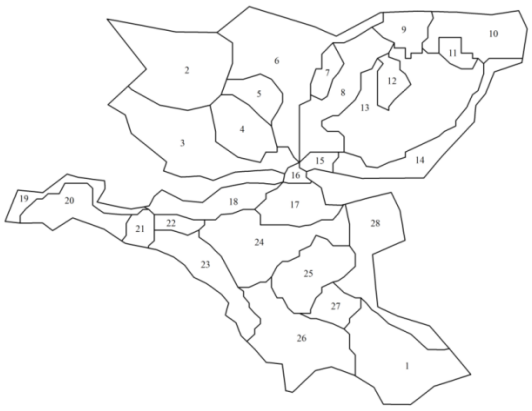



Fig. 5. The subregions of hydraulic parameters

**The Determination of Hydrogeological Parameters**

Hydraulic parameters include hydraulic conductivity and specific yield of aquifer, etc.According to the result of research, "1:200000 Shiyang River Basin, hydrological geological map instruction" by gansu province mine bureau, "Ground water resources assessment report in hexi corridor " and pumping test data by gansu province geological survey, tsinghua university, The study area was divided into 28 parameter area where the hydraulic conductivity, specific yield (storage coefficient) of study area were initialized, as shown in Fig. 5. Horizontal hydraulic conductivity coefficient can be regarded as isotropic, namely Kx is the same as the Ky. The specific yield μ accorded to research achievements which based on a large number of hydrogeological drilling and pumping tests of the study area in 1960~2000s by Gansu Provincial Institute of Geological Survey, with comprehensive groundwater dynamic data and the results of the field test.

**The Foundation of Mathematical Models**

According to the hydrogeological conditions, groundwater recharge and discharge, groundwater dynamic change of the study area, the hydrogeological conceptual model was calculated by using the horizontal direction of isotropic saturated - unsaturated three-dimensional flow model. When the water density change wasn't considered, the flow of groundwater in porous media in three-dimensional space could be expressed in the following partial differential equation:

$$\frac{\partial}{\partial x}(k_{xx}\frac{\partial h}{\partial x})+\frac{\partial}{\partial y}(k_{yy}\frac{\partial h}{\partial y})+\frac{\partial}{\partial z}(k_{zz}\frac{\partial h}{\partial z})-w=S_s\frac{\partial h}{\partial t} \quad (2)$$

where

$K_{xx}$, $K_{yy}$, and $K_{zz}$ are values of hydraulic conductivity along the x, y, and z coordinate axe (L/T);

h is the potentiometric head (L);

$w$ is a volumetric flux per unit volume representing sources and/or sinks of water($T^{-1}$);

$S_S$ is the specific storage of the porous material ($L^{-1}$);

t is time (T).

Added with appropriate boundary and initial conditions, the definite solution of practical groundwater flow was constituted. It can be solved using numerical methods, such as the finite difference, finite element method. The results was the distribution of groundwater levels.

## Conclusions

(1) On the basis of analysing the geological and hydrogeological conditions in the study area, the scope was determined. Combining with GIS and Surfer software, taking the Feflow software as the platform, the three-dimensional aquifer structure model was established, which realized 3D visualization expression of the large region of complex geological content. When the conceptual model was building, the conceptualization way also was adopted. Compared with the grid modeling, hydrogeological conceptual model by conceptual way is convenient, fast and accurate.

(2) The three-dimensional geological structure model was generalized furtherly from the point of view of the aquifer in combination with hydrogeologic conditions. Based on the distribution characteristics of lithology, structure, parameters, recharge and drainage of the groundwater system in the study area, isotropic saturated-unsaturated 3D water flow mathematical model was determined, which was expressed with quasi three dimensional flow mathematical model. Finally, the groundwater balanced elements and each partition of aquifer hydrogeological parameters were determined and analyzed to provide a basis for the the establishment of groundwater simulation.

(3) The concept model study should pay attention to the investigation and research of hydrogeological parameters, sources and sinks of grounwater. the study was carried out on the relationship between the transformation of groundwater and surface water, infiltration of precipitation and evaporation test, groundwater discharge and exploitation investigation, interpretation of remote sensing and field verification, the special investigation of the boundary conditions, etc. Hydrogeology survey and experiment is the basis of the hydrogeological conceptual model set up.

(4) In accordance with the requirements of the simulation software, integrated using hydrogeology, geostatistics, GIS, RS, the generalization of hydrogeological conditions, the establishment of hydrogeological conceptual model which reflects the objective reality scientifically and its space discrete expression are the key to establish groundwater numerical simulation model. Scientific generalization of hydrogeological conditions will be an important research direction in the groundwater modeling.

## Acknowledgements

This research was partially supported under Grant No. 201001060 funded by the Ministry of Water Resources welfare industry research special program, the key technologies of governance ecological objectives process control in Shiyang River Basin. The authors also thank anonymous reviewers for their valuable comments.

**References**

[1] M. Kuznetsov, A. Yakirevich, Y.A. Pachepsky, et al.. Quasi 3D modeling of water flow in vadose zone and groundwater. Journal of Hydrology. 450–451(2012)140–149.

[2] Chen C X, Li M, Liu W B. The monoclinic aquifer - babbling conceptual model. Earth Science-Journal of China University of Geosciences. 27(2) (2002) 140, 198.(in Chinese)

[3]Xue Y Q. Present Situation and Prospect of Groundwater Numerical Simulation in China. Geological Journal of China Universities. 16(1) ( 2010) 1-6.(in Chinese)

[4]Zhang M S, Hu F S, Yin L H. Conceptual model of hydrogeology of the Cretaceous groundwater basin of the Ordos basin, China. Geological Bulletin of China. 27(8) (2008) 1115-1122. (in Chinese)

[5]Xue Y Q, Wu J C. Problems of groundwater modeling in china facing 21 st century. Hydrogeology and Engineering Geology. 5 (1999) 1-3. (in Chinese)

[6]Wojda P, S Brouyère. An object-oriented hydrogeological data model for groundwater projects. Environmental Modelling & Software. 43 (2013) 109-23.

[7]Abit, S.M., Amoozegar, A., Vepraskas, M.J., Niewoehner, C.P. Solute transport in the capillary fringe and shallow groundwater: field. Vadose Zone J. 7 (2007) 890–898.

[8]Habermehl M A. Groundwater movement and hydrochemistry of the Great Artesian basin, Australia Australia Geological Society of Australia, Extended Abstract No. 43 (1992) 228-236.

[9]Barthel, R. Common problematic aspects of coupling hydrological models with groundwater flow models on the river catchment scale. Adv. Geosci. 9 (2006) 63–71.

[10]Twarakavi, N.K.C., Šimu˚ nek, J., Seo, S. Evaluating interactions between groundwater and vadose zone using the HYDRUS-based flow package for MODFLOW. Vadose Zone J. 7 (2008) 757–768.

[11]Chen M X, Xu Z R. The basic concepts and research methods of the groundwater system. Selected Papers of groundwater systems. 1- 13 (1984).

*Advanced Materials Research Vol. 937 (2014) pp 639-645*
*© (2014) Trans Tech Publications, Switzerland*
*doi:10.4028/www.scientific.net/AMR.937.639*

# The Study of Groundwater Modeling of Plain Area in Shiyang River Basin——Ⅱ Groundwater Modeling and Validation

Yu-fei CHENG[1,a,*], Jun-de WANG[1,b],Yuan-hong LI[1,c], Xiang-quan HU[1,d], Shu-chao LU[1,e]

[1]Gansu Research Institute for Water Conservancy, Lanzhou 730000 , China

[a]email: chengyf1980@gmail.com

[b]email: 81041256@qq.com

[c]email:gssk@163.com

[d]email: 1036139875@qq.com

[e]email: 18028123@qq.com

*Corresponding author

**Keywords:** Shiyang River Basin; groundwater modeling; groundwater modeling; Validation.

**Abstract:** Groundwater is an important resource, it is used for variety of purposes in the inland river basins of arid western China. In recent years, the utilization ratio of surface water has been raised, the groundwater recharge rate from surface water has been reduced, and the aquifer depletion due to over-exploitation, which has led to the decline of groundwater levels and the degradation of eco-environments in the Shiyang River Basin, especially in Minqin. Therefore, the study on the groundwater levels change in recent years, as well as simulating and predicting groundwater levels in the future have gotten very important. The purpose of this study is to analyze the groundwater level variations of the study area. Basin on a conceptual groundwater model and observation groundwater level data, to establish the groundwater flow model by FEFLOW; simulated and validated the groundwater model. Finally the precision of model was evaluated. It was shown that the model could be used to predict the groundwater levels variation under different hypothesis conditions in Shiyang River Basin, which would provide the effective reference to the rational use and management of the groundwater.

## Introduction

Groundwater is a basic component of the hydrosphere, it plays a basical role in many processes that affect the atmosphere and the biosphere[1]. Groundwater is an important resource throughout the world[2], which was used for variety of purposes like domestic, agricultural and industrial uses[3]. During the last few decades, groundwater provides about 50% of the current global domestic water supply, 40% of the industrial supply, and 20% of water use in irrigated agriculture[4]. Unfortunately, the quality and quantity of groundwater have been deteriorating due to population growth, industrialization, and agricultural activities[5]. Especially, the aquifer depletion due to over-exploitation and the growing pollution of groundwater are threatening our eco-systems. Therefore, researches on groundwater levels reveal spatial and temporal information on aquifers and aquiferous systems that can help us to take appropriate measures[6], and how to be sustainable planning and management groundwater should be crucial.

During the past several decades, computer groundwater models for analyzing flow of groundwater have played an increasingly important role in groundwater development and management[7]. It is often used to predict the behaviour of groundwater systems under future conditions. These models may vary in the level of complexity from simplified groundwater system representations. When the groundwater model is built, in order to characterize and determine the aquifer hydrogeology proprieties, all possible investigation methods and available geological, geophysical, hydrodynamic and geochemical data must be integrated[8]. So groundwater models

have been developed to support decision making activities related to, for example, water resources management[9], assessment of aquifer conditions and risk assessment of groundwater resources [10]. Development of these regional groundwater models typically involves the following steps: conceptualization, data collection, model development and calibration and uncertainty quantification[11].

In arid and semi-arid regions, the intense groundwater resources exploitation has often led to decrease in the groundwater levels, the water quality deterioration[12]. Many studies have been dedicated to the groundwater simulation study[13-14]

In this paper we constructed the groundwater model based on the the conceptual models for the purpose of evaluating the groundwater model and predicting the groundwater levels in an arid and semi-arid region of China. Aims of the present study are (1) to simulate and verify the model results, and discuss the simulation accuracy of model and (2) to provide reliable data and a basis for the reasonable exploitation and sustainable utilization of groundwater in Shiyang River Basin of Gansu Province, China.

## The Mesh Subdivision

Shiyang River Basin is located in east of Hexi corridor, Gansu province, it situated in the western of Wushao Ridge, in the northern slope of Qilian Mountain, is between 101°41'~ 104°16' east longitude, 36°29'~ 39°27' north latitude. The Wuwei basin and Minqin basin are selected as study area. Its area is total 23,500 km$^2$. When the meshes are generated by FEFLOW, the actual situations should be considered as follows: 1) The exploited wells should be arranged on the nodes of finite element triangular meshes; 2) The study area boundary, subarea boundary, canals and geologic structure boundary should be distributed on the nodes, and need to meshes refinement; 3) the landuse patterns must be given consideration to two or more things.

Based on the above principle, the study area was divided into 26, 850 finite element meshes, 13, 952 notes. In addition, all obtuse triangle meshes which aren't accord with the rules were adjusted for acute triangle meshes. The finite element meshes in the study area are shown in Fig.1.

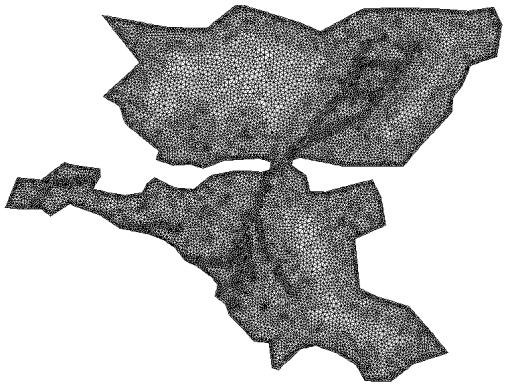


Fig. 1. The FEFLOW mesh generation in aquifer in the study area

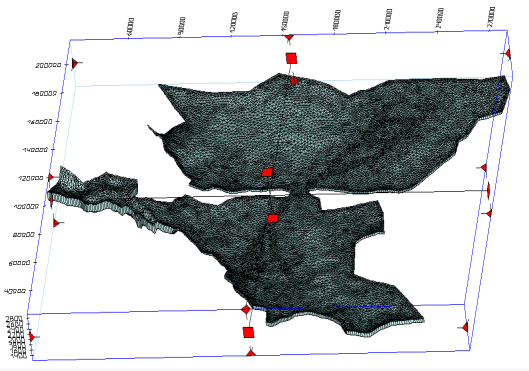


Fig. 2. The 3D spatial structure of the study area;

## The 3D Model Building of Aquifer

According to the hydrogeological structure in the study area, there are a lot of relatively complete weakly permeable clay layers under the surface 100~130m in the quatemary system aquifer, which are a total thickness of about 50 m. Below the weak permeable clay layer, although there are multiple weakly permeable clay interlayers, which is likely to form local perched water, but on the whole, the weak permeable clay interlayers are discontinuous and distribution of limited range. Therefore, the aquifer of study area was generalized unconfined aquifer, one layer and two slices. The 3D spatial structure of aquifer in the study area is shown in Fig. 2.

### Simulation Type and Time Step

The saturated aquifer transient flow simulation was used. The initial flow field was generated by the groundwater level of January 1, 2007. The groundwater model calibration period was from January 2007 to December 2011. The time step was 5 days, a total of 365 steps, 1825 days.

### Hydrogeological Parameters

The source sink terms include rainfall infiltration, irrigation infiltration, channel leakage, evapotranspiration, spring overflow, well mining and recharge by groundwater, etc.

In accordance with the requirements for the FEFLOW, the south of the aquifer system of Wuwei basin which is contact (fracture) zone with basin and mountain, the east of Minqin basin which is convergence area between basin and Tengger Desert, were regarded as the second boundary, with constant flow boundary. The rest boundary was considered to be zero flow boundary. The river water which exchanged with groundwater was set as the third kind of boundary condition. The groundwater recharged to river was treated as springs overflow. Wells mining was adopted the fourth kind of boundary condition. Rainfall infiltration, evapotranspiration and fields infiltration were calculated by facet recharge module.

Hydrogeological parameters and characteristics and the initial and boundary conditions referenced Hu Litang (2009) and related achievements and hydrological geological report, hydrological geological map in the study area.

### Identify and Validation of Model

### Identify of Model

The reliability validation of numerical simulation results is often comparing the calculations with observations, and calculating the root mean square error(RMSE) and correlation coefficient($R^2$) between the calculations and observations of groundwater levels, to characterize the accuracy and efficiency of the model. The formulas can be given as:

$$RMSE = \sqrt{\frac{1}{N}\sum_{i=1}^{N}(S_i - O_i)^2} \tag{1}$$

$$R^2 = \frac{(\sum_{i=1}^{N}(S_i - S_{ave})(O_i - O_{ave}))^2}{\sum_{i=1}^{N}(S_i - S_{ave})\sum_{i=1}^{N}(O_i - O_{ave})} \tag{2}$$

Where $S_i$ is the simulation value of groundwater step i, [m], $O_i$ is the observation value of groundwater step i, [m], $N$ is the sum total, $S_{ave}$ is the simulation average value of groundwater, [m], $O_{ave}$ is the observation average value of groundwater, [m].

The model was verified by 29 wells from 2007~2011 in study area(Fig. 3).

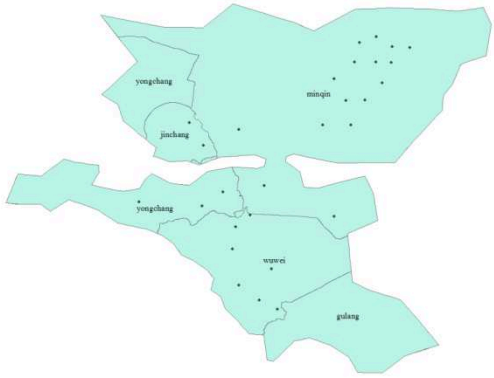



Fig. 3. The distribution of observation well in study area

## Model Validation

Model calibration is the process whereby model parameters are adjusted until a satisfactory fit between model outputs and field measurements is achieved[22]. According to hydrogeological parameters calculated, initial setting and source sink terms calculated, the three-dimensional numerical simulation model was established. Through adjusting the parameters and calculating balance relationship repeatedly, ultimately to determine the model structure, parameter and so on. The reliability evaluation of model mainly includes three aspects: the fitting curve of groundwater observations, the groundwater level amplitude and the groundwater balance analysis.

### Curve Fitting Analysis of Groundwater Level

The change trend of groundwater simulated is basically consistent with the trend of groundwater observed, in addition to the large variation in individual wells. The simulations of groundwater level were compared with the observations of groundwater level(Fig. 4). The root mean square error(RMSE) and correlation coefficient($R^2$) of groundwater simulation and observation were calculated by formula (1) and (2), as shown in Tab. 1. The RMSE changed from 0.15 to 0.54m, the range of $R^2$ was 0.78~0.99. It could be shown that the Errors are within the scope of the permit.

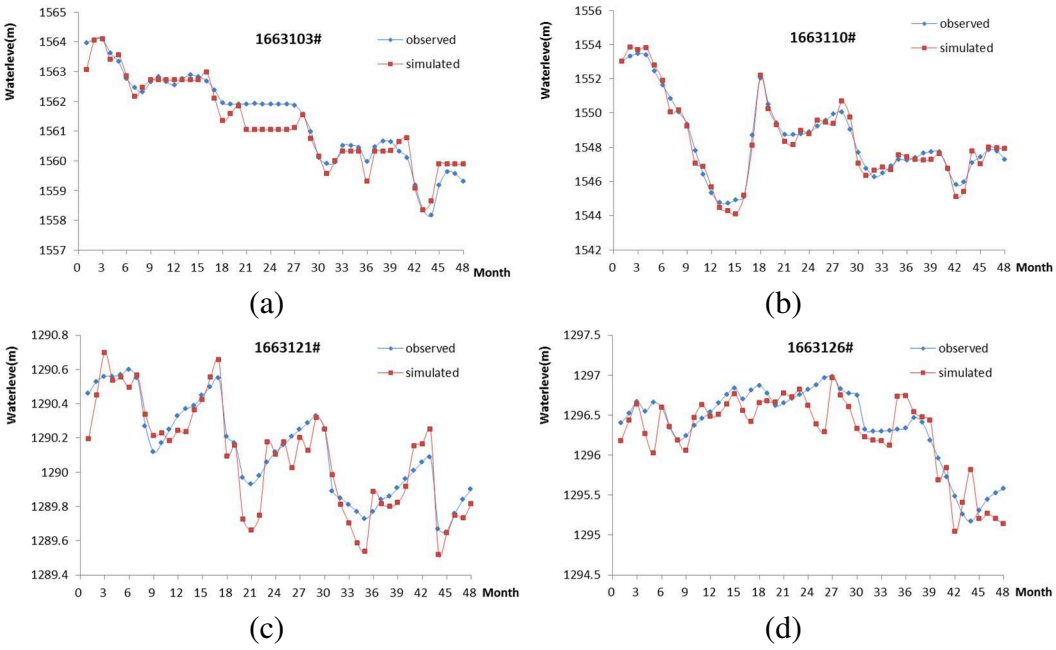



Fig. 4. The comparison diagram of groundwater level in typical observation well.

Table 1. The testing error statistics of observation wells

| Well NO. | RMSE(m) | $R^2$ | Well NO. | RMSE(m) | $R^2$ |
|---|---|---|---|---|---|
| 1663101 | 0.38 | 0.93 | 1664122 | 0.28 | 0.84 |
| 1663103 | 0.45 | 0.96 | 1664123 | 0.38 | 0.80 |
| 1663106 | 0.54 | 0.79 | 1664124 | 0.29 | 0.78 |
| 1663107 | 0.41 | 0.82 | 1664125 | 0.43 | 0.95 |
| 1663109 | 0.44 | 0.93 | 1664126 | 0.27 | 0.87 |
| 1663110 | 0.43 | 0.99 | 1664127 | 0.40 | 0.86 |
| 1663111 | 0.15 | 0.89 | 1664128 | 0.40 | 0.82 |
| 1664115 | 0.41 | 0.97 | 1664129 | 0.44 | 0.98 |
| 1664116 | 0.30 | 0.94 | 1664130 | 0.43 | 0.84 |
| 1664117 | 0.48 | 0.91 | 1671131 | 0.43 | 0.99 |
| 1664118 | 0.23 | 0.96 | 1671132 | 0.45 | 0.98 |
| 1664119 | 0.23 | 0.91 | 1671133 | 0.33 | 0.98 |
| 1664120 | 0.25 | 0.86 | 1671134 | 0.37 | 0.95 |
| 1664121 | 0.12 | 0.94 | 1671135 | 0.42 | 0.97 |

**Amplitude Analysis of Groundwater Level**

Through amplitude analysis of groundwater level which were calculated by model year by year, the groundwater level of oasis where the groundwater was exploited was still falling from 2007~2011, but the amplitude was reduced year by year. The area where the groundwater level declined more than 1m largely disappeared in 2011, the groundwater rose again in the edge of oasis year after year. The amplitude of groundwater level is shown in Fig. 5, where the positive value is mean that the groundwater level rose, and negative value is mean that the groundwater is fell.

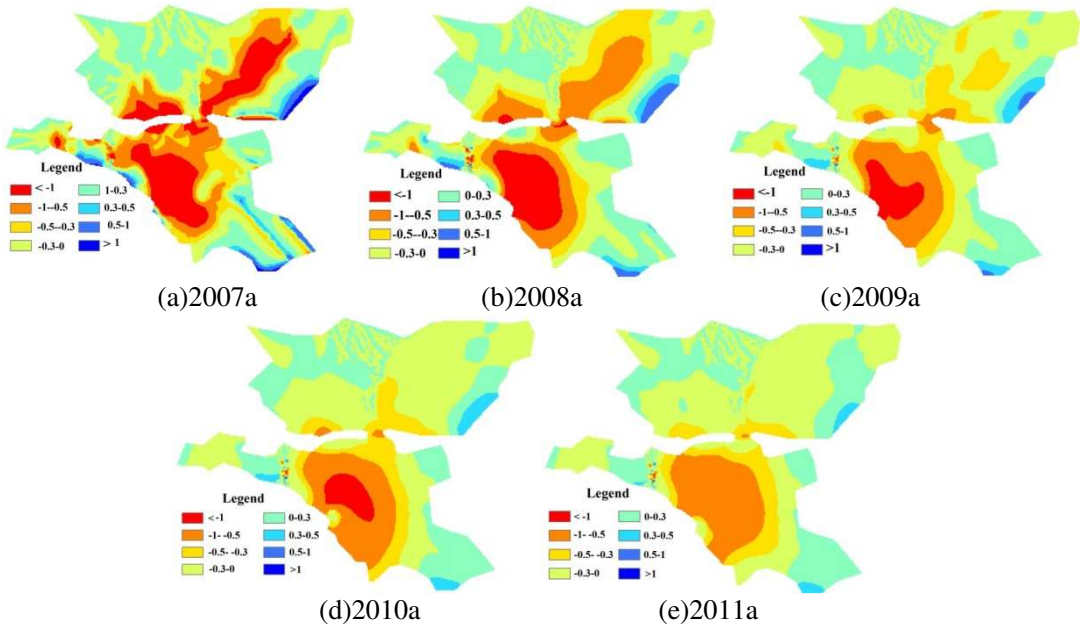



Fig. 5. The amplitude of groundwater level simulated by FEFLOW from 2007 to 2011

**Groundwater Balance Analysis**

Groundwater balance is an important measurement index when analyzing the credibility of groundwater model. The results of groundwater balance by model calculated are shown in Fig. 6 from 2007 to 2011.

Groundwater balance analysis results shown that the groundwater exploitation was mainly concentrated in unconfined aquifer in the study area, the total recharge of groundwater system was 1.009 billion $m^3$ in 2007, total discharge of groundwater was 1.6 billion $m^3$, the equilibrium difference was -591 million $m^3$. By 2011, the total recharge of groundwater system was 925 million $m^3$, total discharge of groundwater system was 986 million $m^3$, the equilibrium difference was -61 million $m^3$, still had a negative balance of groundwater, but the overexploitation decreased year by year. The irrigation infiltration and channel leakage were the largest proportion in the recharge items, which were the main recharge source of groundwater in the study area. In discharge items, artificial mining had become the main way of groundwater discharge, this also was the main reason for decline of groundwater level in concentrated exploration area, especially in the oasis area, descent funnel of groundwater had appeared obviously.

Through the above Model validation, the groundwater level and change trend which were simulated were accordance with the observations'. The groundwater balance calculation conforms to the actual situation. It was shown that the established conceptual model of groundwater was reasonable, all kinds of boundary conditions, the source sink terms and relevant parameters generalized and selected were appropriate. The model could well describe hydrogeological conditions of Shiyang River Basin, so as to offer a scientific basis for reasonable exploitation and utilization of groundwater resources.

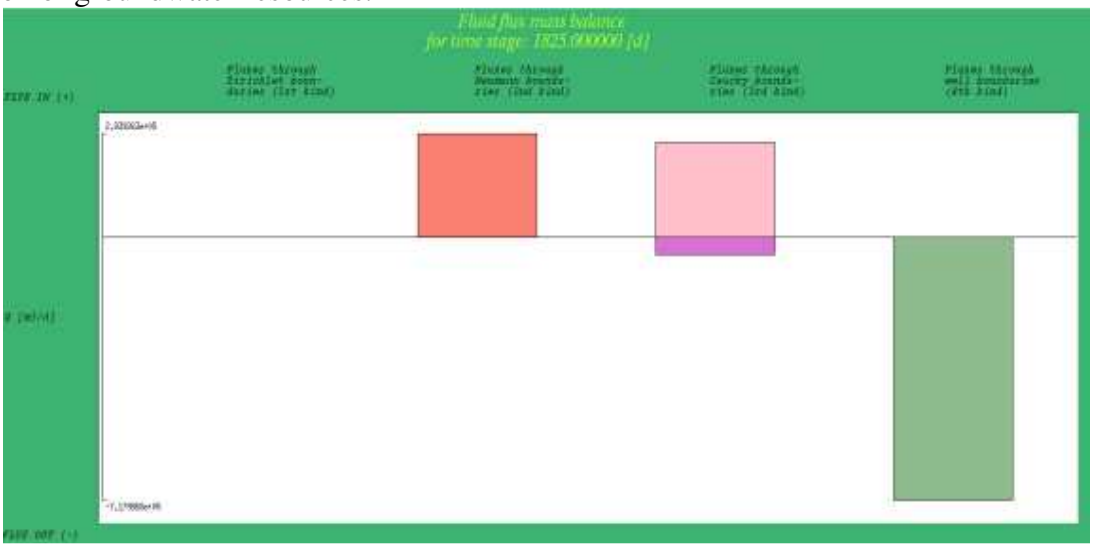



Fig. 6. All kinds of boundary conditions of Groundwater balance in simulation period

## Conclusions

Through model parameters calibrated by PEST2.0 and cooperating with manual adjustments, on the basis of comparison simulation groundwater with observation groundwater, some general conclusions are drawn. The predicted results matched well with the observed data, the RMSE changed less than 0.54m, the range of $R^2$ was 0.78~0.99, the errors are within the scope of the permit. The change trend of groundwater simulated is basically consistent with the trend of groundwater observed, and the groundwater balance calculation conforms to the actual situation. Above all, the model could be used to predict the groundwater levels variation under different hypothesis conditions in Shiyang River Basin which would provide the effective reference to the rational use and management of the groundwater.

This paper presented a groundwater model for simulating the groundwater level temporal and spatial variations of Shiyang River Basin including the region of lacking the groundwater observation wells. It makes up the inadequacy of the groundwater observations, and provides an important basement for water resources planning and management in the study area.

The Shiyang River Basin is a very complicated aquifer system. Although some basic hydro-geological survey work had been carried in the past, with a more complex changes of groundwater recharge and discharge environment in study area, it is more difficult to simulate the

groundwater level change in future. At the same time, owing to the groundwater levels observation wells are insufficiency in the study area, especially the short sequences of observation data, the parameter estimation existed a certain degree of error during the process of groundwater simulation. So more effective technical methods need to use or develop in following work.

**Acknowledgements**

This research was partially supported under Grant No. 201001060 funded by the Ministry of Water Resources welfare industry research special program, the key technologies of governance ecological objectives process control in Shiyang River Basin. The authors also thank anonymous reviewers for their valuable comments.

**References**

[1] Alley W, Healy R, LaBaugh J, Reilly T. Flow and storage in groundwater systems. Science. 296 (2002) 1985-1990.

[2]Tamer Ayvaz M, H Karahan. A simulation/optimization model for the identification of unknown groundwater well locations and pumping rates. Journal of Hydrology. 357 (2008) 76-92.

[3] Mohanty S, MK Jha, A Kumar, DK Panda. Comparative evaluation of numerical model and artificial neural network for simulating groundwater flow in Kathajodi–Surua Inter-basin of Odisha, India. Journal of Hydrology. 495 (2013) 38-51.

[4] World Water Assessment Program. The United Nations World Water Development Report 1: Water for People Water for Life. UNESCO, Paris and Berghahn Books, 575 pp (200).

[5] Ayvaz M. A linked simulation–optimization model for solving the unknown groundwater pollution source identification problems. Journal of Contaminant Hydrology. 117 (2010) 46-59.

[6] Yang ZP, WX Lu, YQ Long, P Li. Application and comparison of two prediction models for groundwater levels: A case study in Western Jilin Province, China. Journal of Arid Environments. 73 (2009) 487-92.

[7] Dang TH, K Jinno, A Tsutsumi. Modeling the drainage and groundwater table above the collecting pipe through 2D groundwater models. Applied Mathematical Modelling. 34 (2010) 1428-38.

[8] Lachaal F, A Mlayah, M Bédir, J Tarhouni, C Leduc. Implementation of a 3-D groundwater flow model in a semi-arid region using MODFLOW and GIS tools: The Zéramdine–Béni Hassen Miocene aquifer system (east-central Tunisia). Computers & Geosciences. 48 (2012) 187-98.

[9] Bauer P, Gumbricht T, Kinzelbach W. A regional coupled surface water/ groundwater model of the Okavango Delta, Botswana. Water Resources Research. 42 (2006) (4), W04403.

[10] Maxwell RM, Kollet SJ. Interdependence of groundwater dynamics and land-energy feedbacks under climate change. Nature Gooscience. 10 (2008) 665-669.

[11] Sun AY, R Green, S Swenson, M Rodell. Toward calibration of regional groundwater models using GRACE data. Journal of Hydrology. 422-423 (2012) 1-9.

[12] Foster S, Loucks DP. Non-Renewable Groundwater Resources. Series on Groundwater No. 10. International Hydrological Programme (IHP). UNESCO Division of Water Sciences France. (2006).

[13] Boronina A, G Ramillien. Application of AVHRR imagery and GRACE measurements for calculation of actual evapotranspiration over the Quaternary aquifer (Lake Chad basin) and validation of groundwater models. Journal of Hydrology. 348 (2008) 98-109.

[14] Rupp DE, J Schmidt, RA Woods, VJ Bidwell. Analytical assessment and parameter estimation of a low-dimensional groundwater model. Journal of Hydrology. 377 (2009) 143-54.

*Advanced Materials Research Vol. 937 (2014) pp 646-651*
*© (2014) Trans Tech Publications, Switzerland*
*doi:10.4028/www.scientific.net/AMR.937.646*

# Removal of Heavy Metals from Contaminated Soils by Washing with Citric Acid and Subsequent Treatment of Soil-washing Solutions

Lei SUN[1], Han-qiao LIU[1,2,3*], Guo-xia WEI[1], Zhen-hua WU[1], Wei YANG[2]

[1]School of Energy and safety Engineering, Tianjin Chengjian University, 300384, Tianjin, China

[2]Tianjin Technology & Engineering Center of Contaminated Sites Remediation, 300468, Tianjin, China

[3]School of Environment science and Technology, Tianjin University, 300072, Tianjin, China

[*]lhqlkx@aliyun.com

**Keywords:** heavy metals; contaminated soil; washing; adsorption

**Abstract:** Soil washing experiments were carried out with citric acid as washing reagent for the remediation of soils highly contaminated with heavy metals, then activated carbon was used in absorption processing for leaching solution. In this study, the effects of the main operating variables for removal of metals from soils were first discussed. The results showed that 36.% Pb, 47.74% Cu and 61.88% Cd were removed from the contaminated soils by optimizing the washing parameters at citric acid concentration 0.2 mol/l, mixing time 2 h, liquid-soil ratio 20 and solution pH=4, respectively. In the adsorption experiments of leachates, the optimum conditions were found as follows: solution pH=7, mixing time of 2 h, standing time of 60 min and activated carbon dosage of 1g/100ml.

## Introduction

With the rapid development of industrialization and urbanization, soils contaminated by heavy metals have become an environmental problem that cannot be ignored. According to statistics, soils contaminated by heavy metals are about 20 million $km^2$ which are about one-sixth of total arable land in China, and the amount of grain polluted by heavy metals is as high as millions of tons every year. Due to refractory, high accumulation and concealment of heavy metals in contaminated soils, the pollutions are more and more serious coupling with increase of human activities [1]. There are generally two fundamental technologies to remediate soils. The first technology is to immobilize heavy metals into tightly bound solid matrix to minimize their migration. However, this technology is not a permanent solution. Site reuse of soil is limited and long-term monitoring is generally required. The second technology is to promote heavy metals mobility and migration to the liquid by desorption and solubilization. This technology is a permanent solution, providing recycle of remediated soils and improving land-use option in the future [2]. The soil washing as a kind of chemical remediation method has some advantages of simple operation, low cost and little secondary environmental pollution, so it has already been researched widely [3].

The choice of washing reagent is essential to the remediation technology. Washing reagents of the heavy metals mainly include surfactants and acid washing reagents. Surfactant can be divided into synthetic complexing agent such as EDTA, biosurfactant including rhamnolipids, sophorolipid, surfactin and saponin. EDTA becomes generally available in the remediation of soils contaminated with heavy metals because of its combination with most of the metal ions into the stability of chelate and higher removal efficiency of heavy metals in the soil [4]. Ze [5] had studied the operating variables in soil washing with EDTA. Nonetheless, EDTA also exist some problems in expensive price, poor biodegradability and difficult recovery. In recent years, EDTA has been replaced by biosurfactant in soil washing, but the biosurfactant production is dwindling, the production cost is high [6]. Therefore, biosurfactant does not have an advantage in the industrial-scale applications. Acid washing reagents mainly include inorganic acid solution (HCl and $HNO_3$), natural organic acid solution (citric acid, malic acid, oxalic acid, malonic acid, humic acid and fulvic acid). Shuzo [7] had reported an acid-washing process on a laboratory scale to

extract arsenic from contaminated soil. Inorganic acid can remove heavy metals from soils largely, and its price is low, but it changes the soil physical and chemical nature easily to be acid after soil washing, so it is more suitable for the severe pollution of the soil industrial wasteland. While natural organic acid has a good removal capacity for heavy metals, a mild acid, good biodegradability and no pollution to the environment, so its application prospect is very environmentally friendly. Elliott [8] had proved that oxalic acid that belongs to natural organic acid solution, was more effective than EDTA to remove the metals associated with Fe-Mn oxides of soil (attacks the hydrous oxides). Recent report has shown that citric acid could remove Cd and Cu from contaminated soils effectively, but low removal rate of Pb relatively.

Currently, achievements have been gained from research on single type metal contaminated soil remediation with organic acid, but treatments of washing solution are reported rarely. Commonly used treatment methods of washing solution include setting, chemical precipitation and activated carbon absorption [9]. The purpose of this paper is to remove heavy metals from contaminated soils by washing with citric acid and subsequent treatment of soil-washing solutions, and to determine the optimal washing conditions including citric acid concentration, mixing time, liquid-soil ratio, solution pH. The best adsorption conditions of activated carbon in washing solution treatment are also discussed.

## Materials and Methods

### Soil Sample Preparation

Soil samples were collected from the greenbelt in Tianjin Chengjian University, which were measured as weak acid by pH meter. And the purity of citric acid was greater than 99.5%. All samples were air-dried, crushed and were then passed through a sieve of 200 meshes. After screening, the fine soil samples were weighed 4kg respectively. According to the scale of the moisture content of 30%, the solutions including 200 mg/L $Cu^{2+}$ solution, 500 mg/L $Pb^{2+}$ and 50 mg/L $Cd^{2+}$ solution which were prepared by using copper sulfate, lead nitrate and nitric acid cadmium drugs (analysis),were added into soil samples, respectively. After about 30 minutes, heavy metals in soil were stirred to equilibrium, then put to the outdoor to air-dry for 96 h, placed in the labeled bags for further use.

### Washing

In the soil washing, a certain amount for contaminated soil was added in a 250 ml conical flask, then stirred on the magnetic stirrer for a period of time after adding citric acid and in standing for analysis. The experiments were carried out by varying different operating parameters such as citric acid concentration, mixing time, liquid/soil ratio and solution pH, which were set as range of 0.01~0.4 mol/L, 1~12 h, 5~30, 3~9, respectively. One variable at a time was altered while keeping other variables at constant. After washing, about 4 ml supernatant were taken out with pipette and put into clean centrifugal tube, then centrifuged for 10 minutes to separate solid from liquid completely by using a high speed centrifuge (RT-TGL-16G-2) which was set as the speed of 5000 r/min. The concentrations of heavy metals in the solution were measured by AFS－9700 atomic absorption spectrometer. Mixed soil in conical flask was for suction filtration by a vacuum pump, dried and then weighed. The samples were treated by MDS - 6 microwave digestions, then the concentrations of heavy metal were measured by using AAS and the pH of the soil needed to be measured. The experiments were repeated 3 times to achieve precise data for analysis and comparison to choose the best washing reagent and leaching concentration.

### Treatment of Soil-washing Solutions

In the activated carbon adsorption experiment, soil-washing solutions were divided into four on average in the conical flask, where a certain amount of granular activated carbon was put (about 4mm in diameter, length of 5mm), then stirred by the magnetic stirrer. The experiments were carried out under different operating conditions such as activated carbon dosage, mixing time,

incubation time and solution pH value, which were set as range of 0.2 ~ 1.2 g, 1 ~ 12 h, 30 ~ 120 min, pH value of 3 ~ 10, respectively. When a parameter changed, the other parameters remained the same. Other operating methods and equipment were same as washing experiment.

## Results and Discussion

### Soil Washing

#### Influence of citric acid concentration

Different concentrations of citric acid were used and the washing results are shown in Fig.1. It can be seen that with increase of concentrations of citric acid, the removal of Pb increased few when the citric acid concentration was lower than 0.1 mol/L. With increasing of citric acid concentration to 0.2 mol/L, the removal of Pb indicated a significant increasing, and its maximum was 36.15%. The reason why the removal of Pb decreased with increase of concentrations of citric acid was that the complexing reaction between citric acid and Pb was a reversible reaction and when the concentration of complex increases to a certain degree, then the reaction reversed, causing the efficiency of removal decreased. The removal of Cu reached to the maximum of 51.87% when citric acid concentration was 0.1 mol/L. However, with the increase of citric acid concentration, the removal of Cu decreased slightly and the removal of Cu reduced to 47.74% when citric acid increased to 0.2mol/L. The change tendency of removal of Cd was similitude with that of Pb with increase of concentrations of citric acid. The removal of Cd increased to 61.88% when citric acid concentration was 0.2 mol/L. Therefore, the best citric acid concentration for soil washing was 0.2 mol/L.

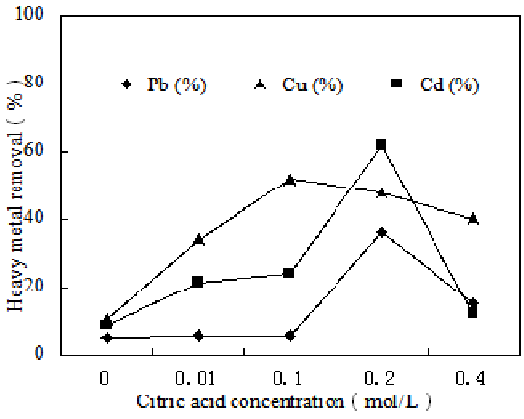



Fig. 1. Effect of citric acid concentration on removal of heavy metals

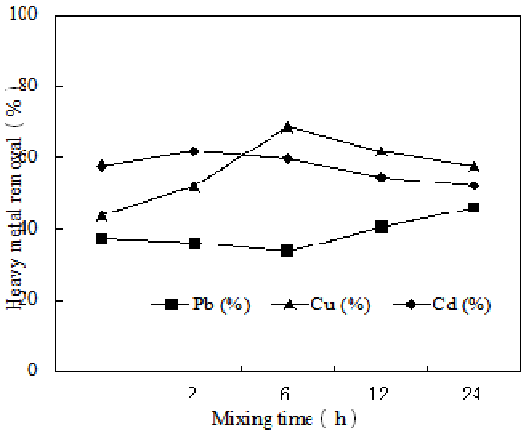



Fig. 2. Effect of mixing time on removal of heavy metals

#### Influence of Mixing Time

Fig.2 showed the removal of heavy metals for various mixing time. It was noted that with the increase of mixing time, the removal of Pb did not change much. With the increase of mixing time, the removal of Cu increased firstly and then decreased. When the mixing time was 6 h, the removal of Cu reached the maximum of 68.52%. The results indicated as growth of the mixing time, the trend of the removal of Cd was similar to the Cu. The reason is that there was too less mixing time to make agents fully contacted with contaminated soil and to make heavy metals separate from contaminated soil completely. While too much mixing time did not affect the removal of heavy metals on one hand and increased energy consumption on the other hand, thus the optimum mixing time is 2 h.

### Influence of Liquid-soil Ratio

The results were illustrated in Fig. 3 and it showed that the removal of Pb with citric acid was 36.15% in liquid-soil ratio of 20, while 42.23% in liquid-soil ratio of 30. This was because the soil and agents had a proper liquid-soil ratio to make good contact completely. The change in liquid-soil ratio was equivalent to increase or decrease the concentration of the washing reagent that caused different removal of heavy metals. So when liquid-soil ratio was small, the soil did not react with agents fully and the amount of agents that dissolved in the solution was relatively small, while that of soil was more, making hardly separate heavy metals from the soil. The trend of Cu increased firstly and then decreased. With the increase of liquid-soil ratio, citric acid removal of Cd was reduced after increased first and its best citric acid/soil than of 20.

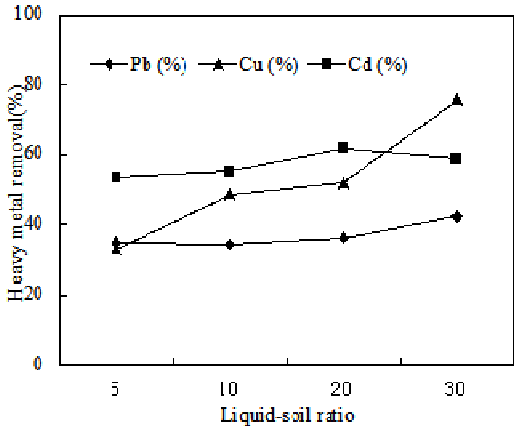



Fig. 3. Effect of liquid-soil ratio on removal of heavy metals

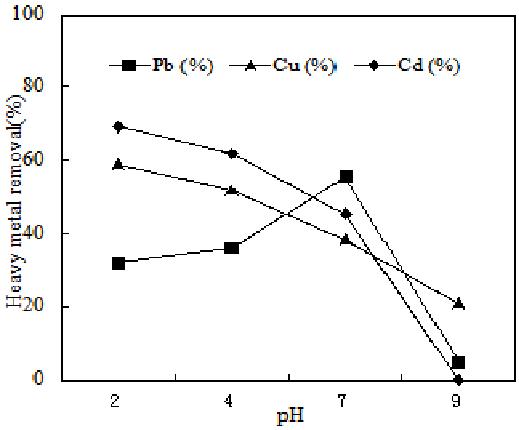



Fig. 4. Effect of solution pH on removal of heavy metals

### Influence of Solution pH on Metal Extraction

The effect of solution pH value on soil washing was shown in Fig. 4. It can be seen that as pH increased, the removal of Pb was increased after decreased first and the efficiency of removal reached the maximum of 55.45%, when pH was 7 or so, then decreased significantly. This is primarily because under acid condition, solid state of lead in soil mainly existed in the ionic state. $H^+$ in the acid exchanged with heavy metal ions on the surface of the soil, so that the heavy metal ions separated from the soil. While in alkaline conditions, Pb in the soil exist in the form of insoluble oxide, making it difficult to separate. Under the condition of low acid, Cu precipitated quickly at the best flushing pH value of 3. With the increase of pH, Cd leaching efficiency was reduced gradually. This experiment was selected for optimum pH 4, because acidic pH value affected the physical and chemical properties of the soil that was not conducive to the growth of the crops and the soil cannot be used for planting after remediation.

## Treatment of Soil-washing Solutions

### Influence of Solution pH

Fig. 5 showed the impact of pH value on the absorption of heavy metals in the soil-washing solutions. Activated carbon adsorption of citric acid-Pb complex and citric acid-Cd complex was decreased first and then increased, finally decreased with the increase of pH value. In the pH=3, activated carbon adsorption of two kinds of heavy metal complex efficiency were 87.37% and 51.75%, respectively, while in the pH=7, were 85.24% and 62.77%, respectively. The tendency for citric acid-Cu complex was down. Activated carbon adsorption of its complex reached to the maximum of 75.25% in the pH=3. The reasons for this situation might be that Pb and Cd were amphiprotic heavy metals and easy to precipitate in a certain range of acid or alkaline, while Cu was different, which was dissolved only in acid condition and gave a precipitate in alkaline condition. So the optimal pH is 7 for activated carbon adsorption of heavy metal complex.

### Influence of Activated Carbon Dose

Fig. 6 was the effect of dosage of activated carbon. It showed that adsorption of three kinds of heavy metal complex was increased with the increase of dosage of activated carbon. And the gentle curves changed slowly when the activated carbon dose was beyond 1g/100ml. It showed that the absorption reached the maximum which was 90.23%, 82.05% and 74.59% of citric acid - Pb, citric acid-Cu and citric acid-Cd complex respectively when the dosage was 1g/100ml. Due to the certain upper limit of activated carbon for the adsorption of heavy metals, increasing the amount of activated carbon had no effect on absorption on heavy metal, when the concentration of heavy metals in the solution kept a certain amount. Activated carbon adsorption mechanism mainly included: (1) Heavy metal ions deposit on the surface of activated carbon that was physical adsorption. (2) Heavy metal ions started ion exchange adsorption on the surface of activated carbon. (3) Chemical adsorption took place between heavy metal ions and the oxygen-containing functional groups on the surface of the activated carbon.

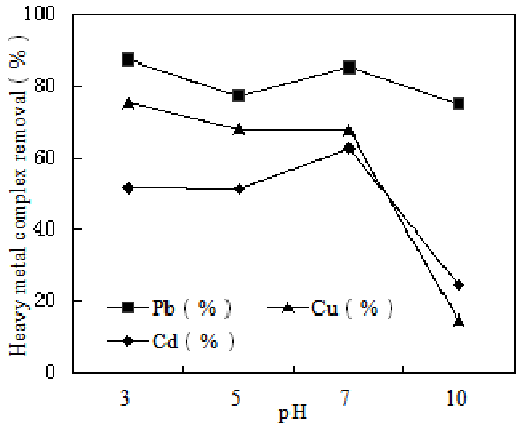



Fig. 5. Effect of pH on the removal of metal complex

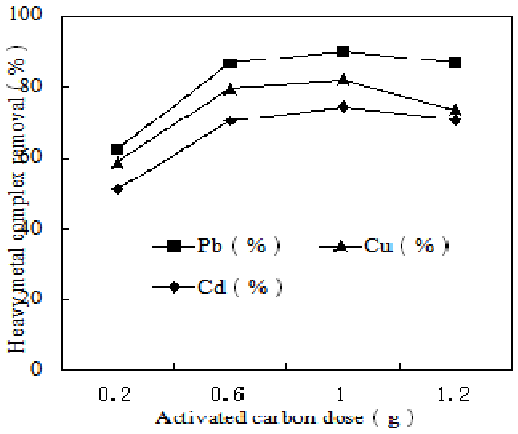



Fig. 6. Effect of activated carbon dose on the removal of metal complex

### Influence of Mixing Time

The mixing time affected efficiency of activated carbon on adsorption of heavy metals as showed in Fig. 7. It was obvious that activated carbon had a good adsorption for citric acid-Pb complex and citric acid-Cu complex along with the increase of mixing time and the maximum of efficiency were 84.27% and 79.65% respectively when the mixing time was 2 h. While there was little effect on citric acid-Cd complex that the efficiency approached a plateau and remained almost constant with increase of mixing time. Adsorption efficiency for 2 h was 62.97%, while for 6 h was 64.26%. Furthermore, the increase of mixing time inevitably led to the increase of energy consumption, therefore mixing time of 2 h was chosen for the experiment.

### Influence of Standing Time

The influence of standing time was shown in Fig. 8. It was found that the standing time did not have too much of an impact on the adsorption of these three citric acid - heavy metal complex. But it was clear that the effect of the activated carbon adsorption under different standing time for citric acid - Pb complex and citric acid - Cd complex was better than that for citric acid - Cu complex. The efficiency of activated carbon adsorption for Pb, Cu and Cd attained their maximum of 57.39%, 52.05% and 65.39% respectively with standing time for 60 minutes.

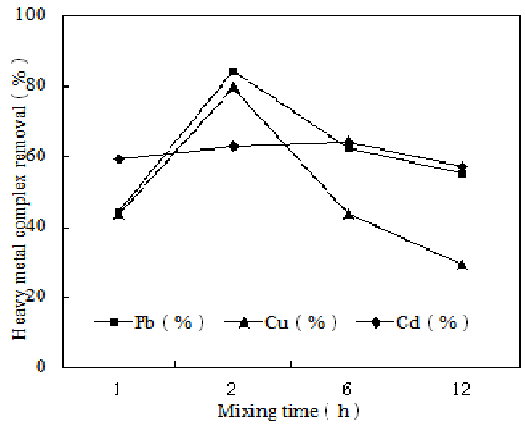



Fig. 7. Effect of mixing time on the removal of metal complex

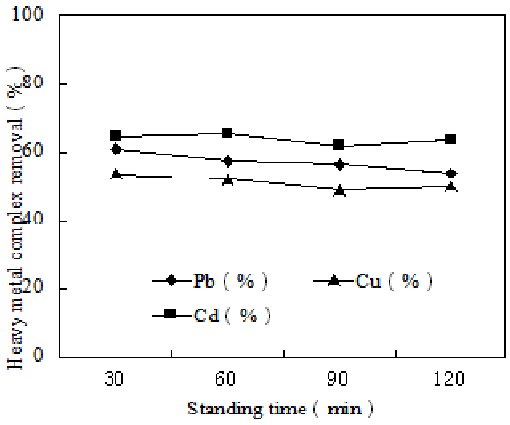



Fig. 8. Effect of standing time on the removal of metal complex

## Conclusion

Because of a certain removal for heavy metals, good biodegradability and no pollution to the environment, citric acid is very suitable for soil washing. Soil washing with citric acid combining with subsequent treatment for the solution with activated carbon is one of the most promising alternatives and has wide application perspective. As concentrations of citric acid increased, the removal of Pb, Cu and Cd increased little firstly and then largely, decreased at last. With the increase of mixing time, the removal of Pb, Cu and Cd did not change largely as well as liquid-soil ratio. While the tendency of the removal of Pb, Cu and Cd was different from above with solution pH increasing, this decreased largely. For Pb, Cu and Cd, the washing efficiency were 44.99%, 47.74% and 60.03% respectively under the best conditions such as citric acid concentration 0.2 mol/l, mixing time 2 h, liquid-soil ratio 20 and solution pH=4. After washing, the leachate was dealt with activated carbon under various operating variables. The best adsorption conditions of activated carbon were pH=7, mixing time was 2 h, standing time was 60 min, its dosage is 1g/100ml. Under these conditions, the vast majority of heavy metals from contaminated soil can be removed.

## References

[1] P.S. Yarlagadda, M.R. Matsumoto, J.E.V. Benschoten, A. Kathuria. J. Environ. Eng, 1995, 121 (4): 276-286.

[2] Xin Ke, Peijun Li, Qixing Zhou, Yun Zhang, Tieheng Sun. J Environ Sci (China), 2006, 18(4): 727-33.

[3] M. Isoyama, S.I. Wada. J. Fac. Agric. Kyushu Univ, 2006, 51: 33-36.

[4] A.P. Davis, B.V. Hotha. J. Environ. Eng, 1998,124: 1066-1075.

[5] L.Z. Ze, L.Q. Rong, H.Z. Wei, Y.D. Hang, H.Z. Zhi, Z. Tao, G.W. Xian, D.C. Xin. Environmental Pollution, 2009, 157: 229-236.

[6] N.M. Catherine, N.Y. Raymond, F.G. Bernard. Journal of Hazardous Materials, 2001, 85: 111-125.

[7] T. Shuzo, H. Toshikatsu. Chemosphere, 2002, 46: 31-38.

[8] H.A. Elliott, N.L. Shastri. Water Air Soil Pollut, 1999, 110: 335-346.

[9] C.K. Ahn, Y.M. Kim, S.H. Woo, J.M. Park. Journal of Hazardous Materials, 2008, 154: 153-160.

*Advanced Materials Research Vol. 937 (2014) pp 652-658*
*© (2014) Trans Tech Publications, Switzerland*
*doi:10.4028/www.scientific.net/AMR.937.652*

# Preparation of Calcium Silicate Using Hazardous Solid Wastes and Its Application in Treatment of Phosphate-containing Wastewater

Xin-hua ZHU[1,a], Zhao ZHANG[2,b] and Jun SHEN[3,c,*]

[1,2,3]No.24 in south part of First ring road, Sichuan University, Chengdu, China

[a]zhuxinhua19@163.com, [b]zzhang@scu.edu.cn, [c]junshen@aliyun.com

*Corresponding author

**Keywords:** Calcium silicate, Preparation, Fixation of fluoride, P adsorption, Specific surface area.

**Abstract.** The silica, one of the by-products of fluorine industry, contains soluble fluoride which is harmful to the environment. Therefore, a study on fixing soluble fluoride was conducted by hydrothermal method with the silica as raw material and adding hydrated lime (HL), and the nanowires-reticulated calcium silicate with high specific surface area up to 143.8$m^2$/g was prepared at the same time. The prepared calcium silicate was used as adsorbent in the experiments of phosphorus (P) adsorption from aqueous solution, the adsorption capacity, adsorption rate and P removability were characterized. The results show that the preparation conditions affect distinctly the adsorption performances of calcium silicate, especially, the dosage Ca/Si molar ratio. For the optimized calcium silicate sample, the total P adsorption capacity is 125.7mg/g and the exchange rate of $Ca^{2+}$ reaches 95.8%, the P residual concentration is only 0.3mg/L, the saturated adsorption time is 3900 min, when the simulation solution with P concentration of 100 mg/L is treated. The P residual concentration is only 0.1mg/L for the simulation solution of 56.12mg/L.

## Introduction

With China's accelerated urbanization and industrialization process and unceasing enhancement of the people living standard, there are massive pollutants such as sewage runoff, industrial waste, etc., which break the human relationship severely between production and consumption and the material circulation, moreover, it has been causing a series of serious environmental pollution[1,2,3]. The silica containing soluble fluoride of approximately 10 percent is a discharged waste from fluorine factory in large scale. At present, there are no effective management approaches and in most cases many factories pay not attention, so the released fluoride may cause severe ecological and environment issues[4]. In addition, in the field of water environment, the entrophication problem caused by dissolvable phosphate ($H_2PO_4^-$, $HPO_4^{2-}$ and $PO_4^{3-}$) bothers governmental environmentalists all the time. Therefore, it is essential to seek and prepare suitable materials used in the waste treatment. Calcium silicate is a new kind of eco-friendly material[5], which adsorbs phosphorus (P) in form of hydroxyapatite from aqueous solution through a simple and effective technology[6,7]. The extensive literatures indicate that calcium silicate has efficiently removability for wastewater containing phosphate[8,9,10].

The principal process conditions of hydrothermal method for fixing hazardous fluoride and preparing calcium silicate using the by-product silica of fluorine industry and hydrated lime (HL) as raw materials were introduced in this study. Then the synthetic materials were used as effective absorbents of P removal in a simulation solution, the performances of calcium silicate were investigated in detail.

## Materials and Methods

### Preparation of Calcium Silicate

The siliceous material with the silica content of approximately 90% and the soluble fluoride content of approximately 10% was obtained from a fluorine factory and its the specific surface area was only 8.1$m^2$/g. Calcareous material ($Ca(OH)_2$, HL) was purchased from Chengdu kelong chemical Co. Ltd. AR.

The silica and HL were mixed together with the Ca/Si (calcium /silicon molar ratio) of 0.4, 0.7and 0.9, respectively, then the mixtures were agitated by a ultrasonic generator for 5min and the suspensions with a liquid/solid ratio of 10 were obtained, the suspension was respectively transferred to a hydrothermal reactor heated at 120°C, 140°C, 160°C, respectively, for a certain time and taken out when the temperature of reaction system was reduced to room temperature. The obtained products were dried at 120°C for 10h and were used as adsorbents in following adsorption experiments. The factor and level of orthogonal experiment of static hydrothermal method preparing adsorbents are shown in table 1.

Table 1. Chart on factor and level of the orthogonal experiment for static hydrothermal method

| level | Factor | | |
|---|---|---|---|
| | Ca/Si | Reaction temperature(°C) | Reaction time(h) |
| 1 | 0.4 | 120 | 4 |
| 2 | 0.7 | 140 | 8 |
| 3 | 0.9 | 160 | 12 |

**Evaluation of Soluble Fluorine**

The content of fluoride in the solution samples was evaluated by the fluoride ion-selective electrode method (GB 7484-87), i.e., through the electric potential of the solutions which was determined by a fluorine ion-selective electrode and the linear equation of standard curve, which was calculated by concentration logarithm of a series of standard fluorine solution as X-axis and the series potential values of these standard solutions as Y-axis: Y=57.822X-282.7, the correlation coefficient of 0.9993.

The preparation of solution samples: 1.0g raw material was dissolved in deionized water, filtered, and the filtrate was transferred into 1000ml volumetric flask with constant volume to scribed line, and then 5ml solution was pipetted into 50ml volumetric flask for determination of fluoride content of raw material. Moreover, the suspension from the preparation process was filtered, and a definite volume of the filtrate was pipetted into 50ml volumetric flask, adding 10ml buffer solution of the total ion intensity regulating, and then it was diluted with deionized water to scribed line.

**P adsorption Test**

The 1000ml simulated solution with initial P concentration of 100mg/L or 56.12 mg/L was prepared by adding $KH_2PO_4$ (AR). The calcium silicate sample of 1.0g was placed into a beaker with the simulated P solution located in a water bath and shaken at a constant rate of 100rpm under controlled temperature condition (25°C) to keep completely suspension of the powder sample. During adsorption, the solution samples were taken from the suspension at various intervals, were filtrated and pipetted into 150ml erlenmeyer flask for determination of the P concentration until the P concentration of solution samples no longer changed. The P concentration was determined by ammonium molybdate spectrophotometric method (GB 11893-89).

After adsorption experiments, the suspensions were filtered, the sediments were obtained and dried at 120°C for 10h. Then the P contents of sediments could be calculated by Eq.(1):

$$q_P = \frac{(c_0 - c_t)\times \upsilon}{\omega}\times 100\ \% \tag{1}$$

Where $q_p$ is the amount of the phosphate adsorbed by per unit mass adsorbent (mg/g), $c_t$ is the restrained P concentration in solution (mg/L), $c_o$ is the initial P concentration (mg/L), $\omega$ is the mass of adsorbent (mg) and $\upsilon$ is the volume of the simulation P solution (1L).

Because calcium silicate adsorbed phosphorus (P) in form of hydroxyapatite[6,7], so $Ca^{2+}$ exchange rate was obtained by Eq.(2):

$$E\ \% = \frac{[P/(1000\times 31)]\times \frac{5}{3}}{n_{Ca}}\times 100\ \% \tag{2}$$

Where $E\%$ is the $Ca^{2+}$ exchange rate, $P$ is the amount of the phosphorus adsorbed by calcium silicate (mg) and $n_{Ca}$ is the amount of substance of Ca in the absorbent (mol), according to the dosage in the preparation process.

### Characterization Methods of Solid Sample

X-ray diffraction (XRD) patterns of samples were recorded with a X-ray diffractometer (D/Max-rA, Japan) using Cu Kα radiation. SEM images were collected on an S-4800 scanning electron microscope (Hitachi, Japan). Brunauer-Emmett-Teller (BET) surface areas were measured from $N_2$ adsorption isotherms by homemade adsorption instrument according Chinese national standard (GB/T 19587-2004 Determination of the specific surface area of solids by gas adsorption using the BET method).

## Results and Discussion

### Preparation of Calcium Silicate and Fixation of Soluble Fluoride in the Raw Material

SEM image of a prepared calcium silicate (Ca/Si=0.7,T=140°C) is showed in Fig.1, which indicates the prepared calcium silicate has a developed space connected mesh structure to the benefit of strengthening the adsorption mass transfer process and shortening the adsorption equilibrium time. Fig.2 gives the XRD patterns of the calcium silicate prepared by different hydrothermal temperature. It can be found that the composition of samples is mainly tobermorite (PDF card 29-0329, $Ca_5Si_6O_{16}(OH)_2$) and calcium fluosilicate (PDF card 01-0482, $CaSiF_6$) based on transformation of the soluble fluoride in the raw material. The soluble fluorine content is up to 99.52 mg/g in initial raw materials, but after hydrothermal reaction, the soluble fluorine in the suspension of hydrothermal reaction is less than 14.29 mg/L, only the soluble fluorine of around 0.3mg/g comes into suspension because of very small solubility of the formed $CaSiF_6$. Compared with the fluorine releasing in the process of hydrothermal reaction, the fixation of soluble fluorine is very fast and the fixed-rate reaches to more than 99.7% in reaction time of 1h.

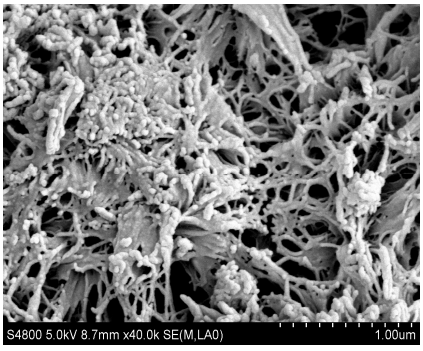



Fig. 1. SEM image of the prepared sample

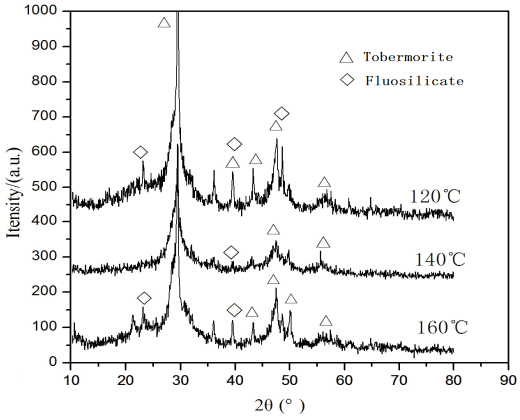



Fig. 2. XRD patterns of samples prepared by different temperature

As adsorption material, the high specific surface area not only provides more adsorption and ion exchange sites, but it also can improve the adsorbability of the adsorbent. The experiments show that the specific surface area of the prepared calcium silicate is affected by Ca/Si molar ratio, hydrothermal temperature and reaction time. The relationship between the specific surface area and the orthogonal experiment condition of material preparation is shown in table 2. According to Table 2, the Ca/Si has the most significant impact on the specific surface area of samples in a certain reaction time and secondarily hydrothermal temperature, and the optimal conditions are Ca/Si molar ratio of 0.7, hydrothermal temperature maintained from 120°C to 140°C and reaction time of 8h.

Table 2. Relationship of preparation conditions and the specific surface area of calcium silicate

| Sample | Ca/Si(A) | temperature(B) | Reaction time(C) | Surface area($m^2/g$) |
|---|---|---|---|---|
| 1 | (1) | (1) | (2) | 79.30 |
| 2 | (2) | (2) | (2) | 122.5 |
| 3 | (3) | (3) | (3) | 70.17 |
| 4 | (1) | (2) | (2) | 55.27 |
| 5 | (2) | (1) | (2) | 143.8 |
| 6 | (3) | (2) | (2) | 52.85 |
| 7 | (1) | (3) | (2) | 43.25 |
| 8 | (2) | (3) | (2) | 106.4 |
| 9 | (3) | (1) | (2) | 79.22 |
| Factor | A>B>C | | | |
| Optimal level | $A_2$ | $B_1$ | $C_2$ | |
| Optimal condition | $A_2$ $B_1$ $C_2$ | | | |

## Adsorption Performance of Calcium Silicate

### Influence of the Preparation Conditions of Calcium Silicate

The specific surface area is a significant factor for adsorption capacity of calcium silicate. The preparation experiments show that the specific surface area of calcium silicate is influenced by factors including Ca/Si molar ratio, hydrothermal temperature and reaction time. Therefore, the above conditions will largely effect on P adsorption performance of the prepared calcium silicate.

The changes of P concentration in adsorption experiments are showed in Fig.3 when the simulation solution with the initial P concentration of 100 mg/g was used, and the influences of preparation conditions on adsorption performance of calcium silicate are summarized in Table 3 (effect of Ca/Si) and Table 4 (effect of temperature), the test results of the natural wollastonite ore as adsorbent material are listed for a comparison.

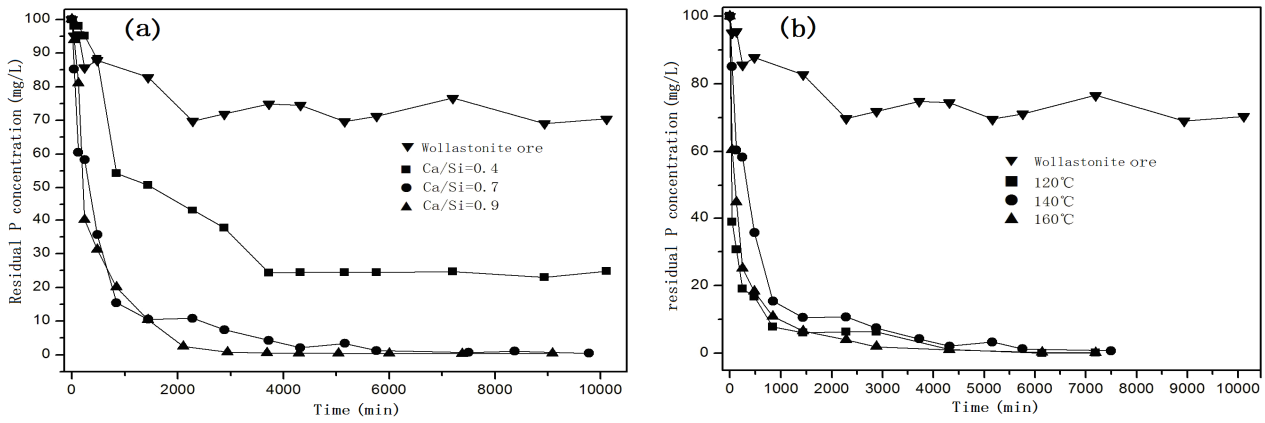



Fig. 3. P adsorption performance of calcium silicate from different preparation conditions: effect of Ca/Si(T=140°C) and (b) effect of temperature(Ca/Si=0.7)

Table 3. P adsorption performance of Calcium silicate prepared by 140°C

| sample | Ca/Si=0.4 | Ca/Si=0.7 | Ca/Si=0.9 | Wollastonite |
|---|---|---|---|---|
| Residual P concentration/mg.$L^{-1}$ | 22.99 | 0.13 | 0.30 | 69.74 |
| Total P capacity/mg.$g^{-1}$ | 77.01 | 125.7 | 135.3 | 30.26 |
| $Ca^{2+}$ exchange rate/% | 85.34 | 95.80 | 89.21 | 19.10 |
| Saturated adsorption time/min | 3700 | 3900 | 2800 | — |

Table 4. P adsorption performance of Calcium silicate prepared at Ca/Si=0.7

| sample | 120°C | 140°C | 160°C | Wollastonite |
|---|---|---|---|---|
| Residual P concentration/mg.$L^{-1}$ | 0.15 | 0.13 | 0.22 | 69.74 |
| Total P capacity/mg.$g^{-1}$ | 104.0 | 125.7 | 113.7 | 30.26 |
| $Ca^{2+}$ exchange rate/% | 79.29 | 95.80 | 86.78 | 19.10 |
| Saturated adsorption time/min | 4000 | 3900 | 4300 | — |

From Fig. 3 it can be seen that the Ca/Si molar ratio is the foremost factor for P adsorption, secondly, hydrothermal temperature,as same as important effects on the specific surface area of calcium silicate in Table 3. The total P adsorption capacity, residual P concentration and the exchange rate of $Ca^{2+}$ are used to explore the influence of Ca/Si and hydrothermal temperature on P adsorption. We can see from Table 3, if wollastonite as adsorbent, the poor P removability is obtained, only the P adsorption maximum of 30.26 mg/g and the $Ca^{2+}$ exchange rate of 19.10%. However, the adsorption performance of synthetic calcium silicate is increased greatly. The residual P concentration in the simulation solution decreases dramatically with increasing Ca/Si molar ratio, and the total P adsorption capacity increases with increasing Ca/Si molar ratio. The maximal rate of $Ca^{2+}$ exchange is obtained at the Ca/Si ratio of 0.7, because the specific surface area of this sample reaches 122.5 $m^2/g$ accelerating $Ca^{2+}$ exchange. The calcium silicate sample from 0.9 Ca/Si has the highest capacity and the shortest saturated adsorption time, which can be resulted from the highest calcium content in the dosage. In the optimal Ca/Si, it is evident that a suitable preparing temperature can improve P adsorption performance to a certain extent (Table 4). As shown in Fig.3,Table 3 and 4, for the calcium silicate prepared by optimal conditions, the total P adsorption capacity can reach up to 125.7 mg/g, and the residual P concentration is less than 0.3 mg/g as well as the $Ca^{2+}$ exchange rate of 95.8%. Comparing the total P adsorption capacity and the rate of $Ca^{2+}$ exchange, the optimal preparation conditions for calcium silicate with excellent adsorptive performance are the Ca/Si ratio of 0.7, the hydrothermal temperature of 140 °C and the reaction time of 8h, which consist with the relationship between preparation conditions and specific surface area of materials (Table 2).

**Influence of Initial P Concentration**

The pH value of P adsorption system runs from 7.5 to 8.5 (the pH of the system itself), which promotes adsorbing P of calcium silicate to form apatite[5,11]. In the same adsorption conditions, the P adsorption characteristics of calcium silicate samples for the simulation solution with different initial P concentration (56.12mg/L, 100mg/L) are shown in Fig.4. We can see that the adsorption rate in different P concentration decreases rapidly after the first 4h, then the adsorption capacities keep almost unchanged. Moreover, the lower initial P concentration accelerates adsorption rate and shortens adsorption equilibrium time, and the adsorption process carries out thoroughly. By contrast, the higher initial P concentration may be favorable to increase P adsorption capacity of calcium silicate.

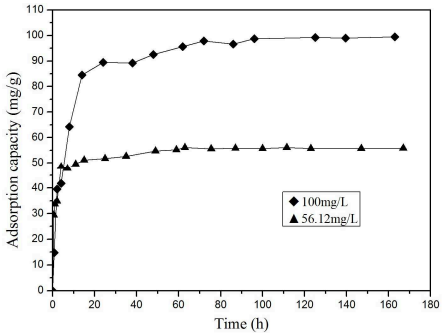



Fig. 4. The adsorption performance of calcium silicate in different initial P concentration

The performances of calcium silicate are listed in Table 5, which shows that the performance of calcium silicate changes with change of the initial P concentration. The effective P removability for the solution with low concentration P is more than 99.7%, and the residual P concentration can be less than 0.1 mg/L, which has attained the level 1 standard of comprehensive discharge standard of sewage of China (GB 8978-1996).

Table 5. Effect of initial P concentration on performance of calcium silicate from different temperature

| P concentration/mg.$L^{-1}$ | Performance | 120°C | 140°C | 160°C |
|---|---|---|---|---|
| 56.12 | Residual P concentration/mg.$L^{-1}$ | 0.1325 | 0.0660 | 0.0954 |
| | P removal rate | 99.76% | 99.88% | 99.83% |
| 100 | Residual P concentration/mg.$L^{-1}$ | 0.1545 | 0.1288 | 0.2246 |
| | P removal rate | 99.72% | 99.87% | 99.60% |

## Conclusions

The calcium silicate was synthesized by hydrothermal method with the by-product silica of fluorine industry and hydrate lime as raw materials, which can be used as adsorbent for effectively chemisorbing phosphate from aqueous solution, and the soluble fluoride of 99.7% in raw silica was transformed to $CaSiF_6$ with a small solubility. The calcium silicate with high specific surface area and developed space connected mesh structure was obtained when optimal preparation conditions including the Ca/Si molar ratio of 0.7, the hydrothermal temperature from 120°C to 140°C and the reaction time of 8h were selected. The experimental results of P adsorption show that the exchange rate of $Ca^{2+}$ is up to 95.8%, the maximal P absorptive capacity is 125.7mg/g, P removal rate is more than 99.7% and the P residual concentration is below 0.3mg/L for the simulation solution of 100mg/L and 0.1mg/L for the simulation solution of 56.12mg/L, reaching the comprehensive discharge standards of sewage of China.

## References

[1] Y.N. Hu, H.F. Cheng, Environmental Development. 8 (2013) 57-73.

[2] Y. He, Q.M. Luo, H.L. Hu, Procedia Environmental Sciences. 16 (2012) 690-696.

[3] L.X. Liu, B. Zhang, J. Bi, Environmental science & policy. 21 (2012) 106-111.

[4] M. Jiménez-Reyes, M. Solache-Ríos, Journal of Hazardous Materials. 180 (2010) 297-302.

[5] K. Okano, M. Uemoto, J. Kagami, Water Research. 47 (2013) 2251-2259.

[6] X.C. Chen, H.N. Kong, D.Y. Wu, Journal of Environmental Science. 21 (2009) 575-580.

[7] Y.H. Song, G.W. Peter, U. Berg, Chemosphere. 63 (2006) 236-243.

[8] A. Renman, G. Renman, Chemosphere. 79 (2010) 659-664.

[9] S. Sengupta, A. Pandit, Water Research. 45 (2011) 3318-3330.

[10] Y. Liu, X. Sheng, Y.H. Dong, Desalination. 289 (2012) 66-71.

[11] P. Battistoni, A. De Angelis, P. Pavan, Water Research. 35 (2001) 2167-2178.

*Advanced Materials Research Vol. 937 (2014) pp 659-662*
*© (2014) Trans Tech Publications, Switzerland*
*doi:10.4028/www.scientific.net/AMR.937.659*

# Multi-scale Analysis of Marine Environmental Situation in the Caofeidian Nearshore District

Ying-jie ZHAO [1] Ming-chang LI [1,2,3,a] Yuan-yuan CAO [1]

[1]Laboratory of Environmental Protection in Water Transport Engineering, Tianjin Research Institute of Water Transport Engineering, Tianjin, 300456, China;

[2]State Key Laboratory of Coastal and Offshore Engineering, Dalian University of Technology，Dalian 116024, China;

[3]School of Environmental Science and Engineering, Tianjin University, Tianjin, 300072, China

[a]lmcsq1997@163.com

**Keywords:** marine, pollution, analysis, nearshore, multi-scale

**Abstract.** Analysis of marine environment, especially the multi-scale analysis is an efficient means to obtain the environmental situation and guide the environmental management. In this paper, the field data, max, min and average of dissolved inorganic nitrogen (DIN) and phosphate in the Caofeidian marine district, Tangshan Bay is analyzed. The whole water quality situation could be grasped through these analyses. The research results show that the distribution of pollution is disequilibrium and the high value district of pollution exists in research district too.

## Introduction

The whole analysis of pollution time series is an essential tool for obtaining the marine environmental situation. It is meaningful for guiding the environmental management and the environment protection.

The environmental situation has been studied widely to guide the environmental management and engineering construction, such as the water quality [1], phytoplankton biomass [2], the petroleum hydrocarbon [3], etc. Many methods are applied for marine environment analysis problem too, such as the set pair analysis method for water quality and carrying capacity [4], the neural network model for carrying capacity [5], etc.

In this paper, the field data, max, min and average of dissolved inorganic nitrogen (DIN) and phosphate in the Caofeidian marine district, Tangshan Bay is analyzed. The whole water quality situation could be grasped through these analyses. Meanwhile, the research results show that the distribution of pollution is disequilibrium. The high value district of pollution exists in research district. So these analyses are very meaningful for guiding the environmental management.

## Research Marine District

### Basic Information

The Caofeidian marine district locates in the northwest of Bohai Sea, which is the center of Tangshan Bay. The length of coastline is 17 km. The total area is about 16 $km^2$. The tide hydrodynamic is controlled by the tidal waves of the Bohai Sea, so the tidal current is complicated. The Caofeidian port has been constructed by reclamation in recent years. The Beidaihe marine district locates in the east north of the Caofeidian marine district. The distance is 10.15 km. The position of research marine district is shown in Figure 1.

## Research Marine Position

Six years' field data in station 1 near the Caofeidian port are selected for the analysis. More stations are selected for obtaining the max, min and average value. The position of Station 1 is shown in Figure 1.

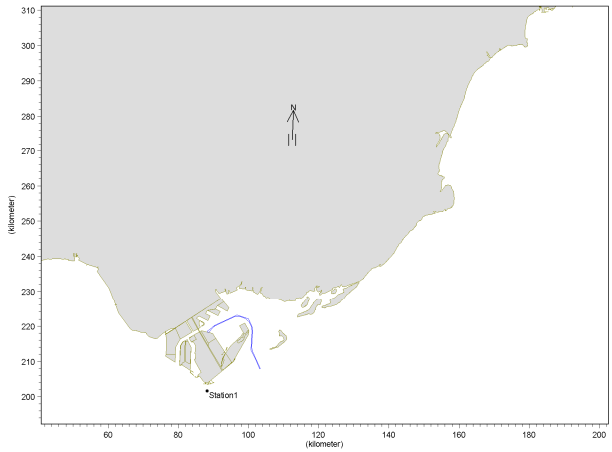
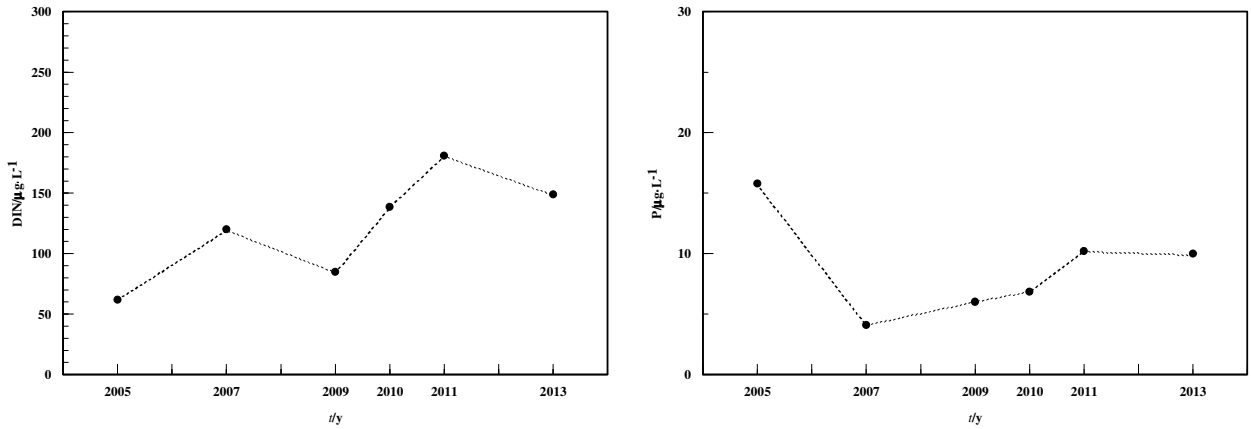



Fig. 1. The position of station 1

## Multi-scale Analysis

## Field data of Station 1

The field data time series of station 1 is shown in the Figure 2.



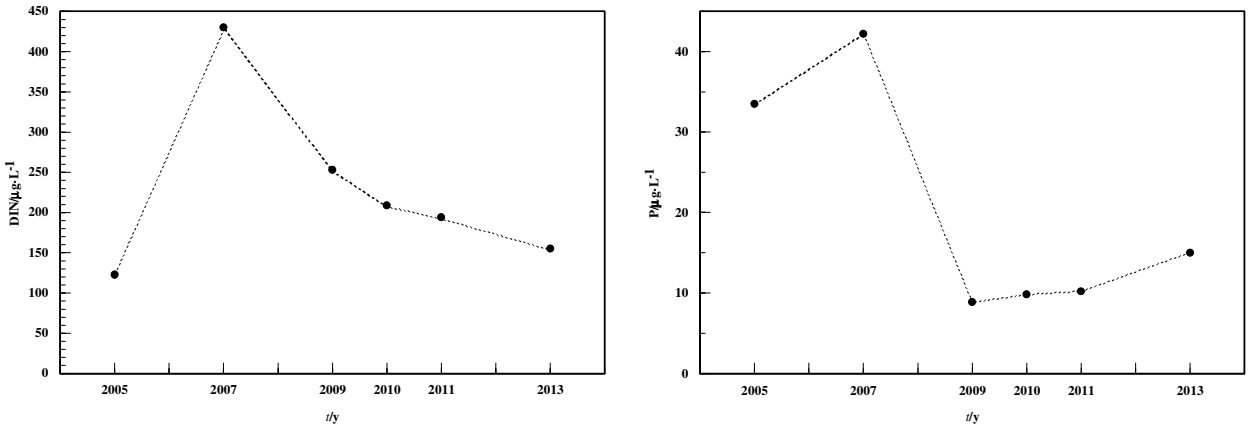

DIN phosphate

Fig. 2. The fied data of station 1

Fig. 2 shows field data time series of station 1. The DIN belongs to the first water quality standard. The phosphate belong to the second water quality standard.

## Max Value of Research District

The max value time series of research district is shown in the Figure 3.



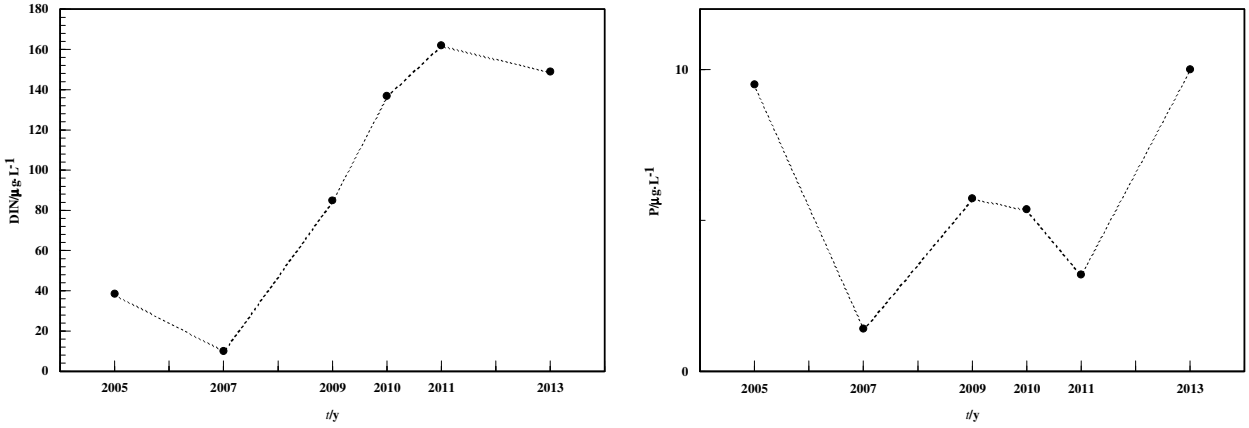

DIN phosphate

Fig. 3. The max value in the research district

Fig. 3 shows the max value time series in the research district. The DIN belongs to the forth water quality standard. The phosphate belongs to the forth water quality standard.

**Min Value of Research District**

The max value time series of research district is shown in the Figure 4.



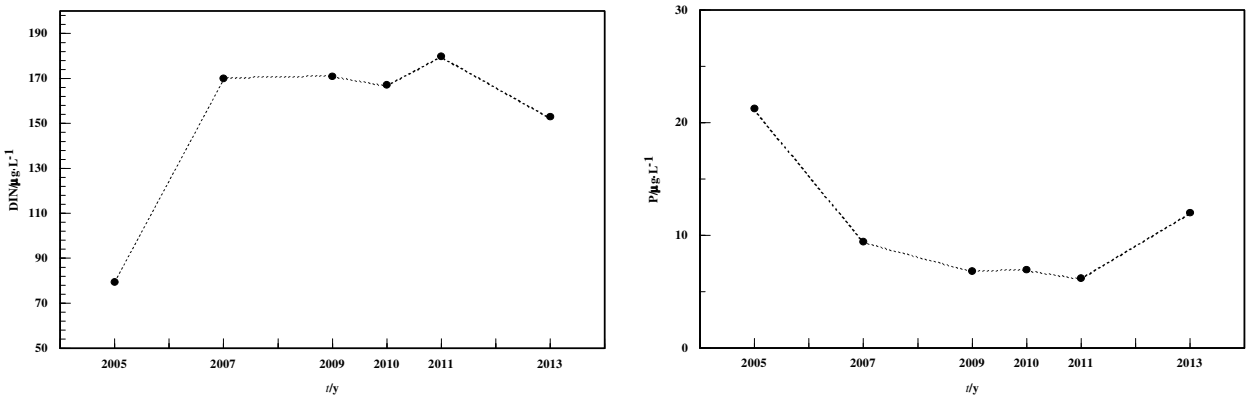

DIN phosphate

Fig. 4. The min value in the research district

Fig. 4 shows the min value time series in the research district. The DIN belongs to the first water quality standard. The phosphate belongs to the first water quality standard.

**Average Value of Research District**

The average value time series of research district is shown in the Figure 5.




DIN phosphate

Fig. 5. The average value in the research district

Fig. 5 shows the average value time series in the research district. The DIN belongs to the first water quality standard. The phosphate belongs to the second water quality standard.

## Conclusions

In this paper, the dissolved inorganic nitrogen (DIN) and phosphate in the Caofeidian marine district, Tangshan Bay is analyzed through the field data in station 1 and the max, min and average value of research district. The max value in the research district belongs to the forth water quality standard. The others are better than the max. The analysis results show that the distribution of pollution is disequilibrium. The high value district of pollution exists in research district. So more research need be used to analyze the cause of the high value district and more management means must be implement to decline the level of environmental pollution.

## Acknowledgements

This work was supported by the National Natural Science Foundation of China (No.51209110), the project of Science and Technology for Development of Ocean in Tianjin (KJXH2011-17), the Research Foundation of State Key Laboratory of Coastal and Offshore Engineering Dalian University of Technology (LP1108) and the National Nonprofit Institute Research Grants of TIWTE (TKS090204, TKS100217 and KJFZJJ2011-01).

## References

[1] G.Y. Zhang, B.L. Chen, Fuzzy comprehensive evaluation and evolution of water in Haizhou Bay, Marine Environmental Science. 29 (2010) 411-414. (in Chinese)

[2] H. Wei, L. Zhao, Z.G. Yu, J. Sun, Z. Liu, S.Z. Feng, Variation of the phytoplankton biomass in the Bohai Sea, Journal of Ocean University of Qingdao. 33 (2003) 173-179. (in Chinese)

[3] X. Wang, L.R. Xu, L.Y. Li, W.Q. Li, Relationship between the distribution of petroleum hydrocarbon and environmental factor in Dapengao, Daya Bay, Journal of Oceanography in Taiwan Strait. 21 (2002) 167-171. (in Chinese)

[4] M.C. Li, G.Y. Zhang, S.X. Liang, Z.C. Sun, Marine water quality assessment's nonlinear set pair analysis method, Advanced Materials Research. 113-116(2010) 185-190.

[5] M.C. Li, Q. Si, S.X. Liang, Z.C. Sun, Carrying capacity assessment of Tianjin Binhai New District by artificial neural network, The 3rd International IEEE Workshop on Intelligent Systems and Applications. 2011 792-794.

*Advanced Materials Research Vol. 937 (2014) pp 663-668*
*© (2014) Trans Tech Publications, Switzerland*
*doi:10.4028/www.scientific.net/AMR.937.663*

# Garden Plants under Global Climate Change

Qiu-jing LI [1,a], Xiao-li HOU[2,b], Li XUE [3,c*], Hong-yue CHEN [4,d], Yun-ting HAO[5,e]

College of Forestry, South China Agricultural University, Guangzhou 510642, China

[a]623638417@qq.com, [b]1135401013@qq.com, [c]forxue@scau.edu.cn, [d]chenhongyuetz@126.com, [e]529515276@qq.com

*Corresponding author: Li Xue; forxue@scau.edu.cn.

**Keywords:**global climate changes, garden plants, biological diversity, phenology

**Abstract:**Climate change refers to man-made changes in our climate, which is caused by changes in temperature, precipitation, and $CO_2$. There is a lot of data coming from all over the world indicating that phenology of garden plants and biodiversity are being impacted by climate change. In the context of climate change, landscape plants can enhance carbon sink function, improve plant design, and mitigate climate change and so on. To determine the impact of these changes on garden plants, scientists would need to strengthen the study of garden plants under global climate change, including different garden type responses to climate change, invaliding species phenology study, extreme weather impacts on landscape plant phenology, the dominant factor of affecting garden plants in different regions, interactions of multiple environmental factors on influence mechanism of garden plants.

## Introduction

Climate change is defined as the state of the climate that can be identified by changes in the mean and/or the variability of its properties that persist for an extended period, typically decades or longer [1]. Changes in the modern climate show a discernable warming trend due to rising concentrations of greenhouse gases in the atmosphere caused by human activities, which has affected many natural ecosystems [2]. IPCC projections suggest further global average surface warming of up to 6.4°C by the end of the century, leading to major changes in ecosystem structure and function, ecological interactions and shifts in species geographic ranges. Warming caused by man-made emissions of greenhouse gases, such as $CO_2$, also increases the amount of water vapour in the air by boosting the rate of evaporation from the oceans and elsewhere, which changes the amount of rain and snow falling to Earth and leads to extreme weather patterns. The change of the temperature, precipitation and $CO_2$ caused by climate change affects the ecological environment and landscape plants, changing the phenology and biodiversity of landscape plants. On the other hand, landscape plants can improve the regional climate conditions in a certain extent by adapting to climate change and reasonable layout. Therefore, challenges and opportunities coexist in landscape plants response to climate change.

## Global Climate Change Research

"Global change" is defined as "is likely to change the global environmental change of the endurance of the life on earth" (The U.S. <global change research in 1990 act>). The main characteristic of global climate change includs elevated atmospheric $CO_2$ concentration, enhanced air temperature, precipitation pattern change caused by drought stress, etc. [3], and these changes have a significant impact on the natural ecological system.

## The Cause of the Global Climate Change

In recent decades, the large amount of $CO_2$ due to human activity and other greenhouse gases causes climate change, including the changes of atmospheric temperature and the global precipitation patterns, and so on. Human widely used refrigerator, air conditioner refrigeration and other products,

resulting in accumulation of Chloro-fluoro-carbon and enhanced uv-b radiation due to thinning ozone layer. Global climate change has a huge impact on terrestrial ecosystems, including vegetation distribution, community structure, and photosynthesis of plants. Rising $CO_2$ concentration causes the global temperature rise, leading to frequent drought and flood disasters due to change of water resources in different regions. Global climate change impacts the balance of natural ecological system, which is a challenge to human survival and development. $CO_2$, temperature, precipitation and illumination have an important influence on plant growth, plant changes in the distribution, structure and growth and so on in order to response to the global climate change [3-4]. Ecosystem may help plants adapt to climate change. Understanding mechanism of plants responding to global climate change and their adaptation can provide strategies for the balance of the ecosystem; therefore, plant response to climate change within the scope of global has become a research focus [5-8].

**The Effects of Global Climate Change on Plant**

Since the beginning of the 1980's, taking global environmental change for study object, international scientific community has initiated and organized four global change research program, including the World Climate Research Programme (WCRP), the International Geosphere Biosphere Programme (IGBP), The International Human Dimension Programme on Global Environmental Change (IHDP), International Programme of Biodiversity Science (DIVERSITAS), paying a special attention to the influence of human activities on the earth's environment. Some progresses has been made as follows,

1) Elevating $CO_2$ concentration can not only raise photosynthetic rate and reduce dark respiration of leaves [9-10], but also reduce leaf stomatal conductance and transpiration and improve utilization rate of plant water [11], which promote plant growth and compensate for the negative effects of high temperature and dry conditions on plants to some extent.

2) Climate warming raises atmospheric temperature and speeds up plant phenology [12]. The temperature rising can accelerate the growth of plants and increase their respiratory oxygen consumption, also change the carbon and nitrogen metabolism process in plants, thus affect their growth and development [13]. Extreme high temperature damages optical system II of plants by reducing the quantum yield of optical system II, as a result, photosynthesis is restrained seriously. Climate warming also causes desertification, ecosystem degradation, biodiversity loss [14-15], species migration to high latitudes, change in the original geographic distribution and scope of life [16-17]. In order to extract more information on plant responses to climate change, herbarium collections including time-series analyses of changes in carbon content [18] and phenological changes can be used [19-20]. Recent studies demonstrate that several components of global change, such as enhanced nitrogen depositions and elevated $CO_2$ concentration, can favor the competitive ability of alien species, and that these drivers have enormously enhanced species invasions globally [21].

3) Precipitation pattern change caused by global climate change lead to drought damage and flood frequently occur alternately and the deterioration of ecological environment, affecting plant growth and production. Many researches have been studying on response of individual plants to drought and water logging stress in recent years, but similar researches on plant communities and landscape scales are few. Relevant researchers made some progress on stress protein of against drought, osmotic regulation substances, photosynthetic characteristics and water stress signal conduction of plants under the stress of drought and logging [22].

**Global Climate Changes and the Landscape Plant**

Garden refers to the recreational green space using plants to beautify the environment [23]. The rapid development of modern society economy and the rapid expansion of urban scale result in many ecological problems and hinder the survival and the sustainable development of cities. Landscape plants can play a role in improving the environment, including absorbing $CO_2$ and harmful gases, releasing oxygen, dust absorption, regulation of air temperature and humidity, and reducing noise.

Since 1980's, the global climate change caused $CO_2$ increase, temperatures rising and precipitation pattern change, which affects the landscape environment. Landscape plants continuously evolve to adapt to climate change [24].

**The Impact of Climate Change on Landscape Plants**

Environmental changes due to climate change affect the original form and fabric in landscape architecture. Climate warming causes extension of plant growth cycle, delays defoliation of deciduous trees, early germination; the seasonal variation of plants growing temperate regions may be disappeared as temperatures rising. Warming will increase plant transpiration, resulting in an increase in water demand of green garden. Waterscape may be abandoned due to drought in area rich in water resources; Climate change and extreme weather may also lead to occur abnormally in garden plant diseases and insect pests, and then destroy green garden. Early in 2008, for example, the cold rain and snow freeze damage inflicted heavy losses on the landscape plant in southern China [25].

Two major global effects of expanded gardening and urban landscaping activities are (i) to increase spread of invasive species, and (ii) to enhance biogenic volatile organic compounds (BVOCs; see Glossary), which is increased by elevated formation of photochemical smog in the winter months [26-27]. The climate warming also reduces the diversity of landscape plant, and results in increasing convergence in plant species in different areas, which affect the richness of landscape plant and landscape aesthetic. Dry climate caused by global warming may threaten the surviving and growth of some garden plant species, while other species that did not originally suit to the local climate are likely to be successfully introduced. The changes in the flowering times of some landscape plants may affect pollination effectiveness, and change the hybridization and gene between species [28]. Recent studies show that global climate change, such as the rising of $CO_2$ concentrations, is conducive to enhance the competition of the different species, which greatly promotes their worldwide expansion [29-30]. As the global temperature raises, species richness, especially richness of woody plant species becomes higher. In recent decades, global warming significantly accelerated with temperature rising in winter, causing change of the species distribution [31-32]. Climate change causes rapid extension of a large number of invasive species and quick spreading in the garden, because they are more suitable for new climate conditions compared to native species, which poses a great threat to the survival of local garden plants [3].

An important implication of gardening practices from a global change perspective is that many ornamental plants are strong emitters of BVOCs, such as isoprene and monoterpenes [33]. Some plants, especially the garden plant produce biological of volatile compounds, which will lead to sharp increase in the global temperatures [29]. Rising temperatures will lead to more volatile compounds of plant to discharge, which are the main components of the plant aromatic substances. According to estimation, aromatic index increased by 10% in the past 30 years, and possibly continue to increase with rising temperatures in the coming decades. Most of the aromatic substances may contribute to artistic conception of landscape and plant ecology, health care function. However, some harmful aromatic substances need to be carefully considered in the selection and application of landscape plants [25].

**How Landscape Plant Respond to Climate Change**

In the face of new environment caused by climate change, green garden need to adapt to the ecological environment change of city resulted from climate change. Original green garden mainly reflects its ornamental value. Ecology and environment become increasingly important in the green garden under the condition of climate change, so that we need to consider how green garden will adapt to the new environment triggered by climate change, and to prevent and reduce the loss from climate change [24].

Garden green space plays an important role in plant ecological system in cities, and has positive ecological impact, including lowering temperature, increasing air humidity and absorbing $CO_2$ to improve microclimate. The focus of attention is to regulate and improve the local microclimate in the

past, whereas we need to deal with the global climate change problem now, such as alleviating the adverse effects of rising temperatures, logging or drought in regional or city scale. Moreover, collection and recycling of carbon and biodiversity conservation have been important functions of garden green space. In the context of climate change, carbon sink function of green garden, such as the reduction of $CO_2$ and recovery and storage of $CO_2$ has become an important research field. For example, we may reduce the emissions of $CO_2$ required by building heating and cooling, which can be conducted by choosing carbon sink plant, rational allocation of roof garden, green wall, terrain and water body. People often decrease $CO_2$ content by establishing roof garden and the botanical garden in the world [34].

## Recommendations and Conclusions

Global climate change is increasing, which has a profound influence on landscape plants on different space and time scales. In order to reduce the uncertainty of global climate change effects on the ecosystem and minimize its negative impact, we need to strengthen study on the effects of key ecological factors with global climate change, to reveal the mechanism of garden plant adapting to climate change, which may provide the theoretical basis for taking corresponding measures. The future research priorities should be as following:

(1) Through the research and comparison of different landscape types, we can reveal their response to global climate change and adaptation mechanism, and predict the future climate and the dynamics of landscape plant, so as to provide theoretical basis for the sustainable development of the garden.

(2) Climate change causes the displacement of cultivation area of landscape plant, which results in the number of plant species growing in the North Temperate Zone and Frigid Zone environment being likely to increase rapidly. Study on adaptability of phenotypic characteristics and morphological changes and physiological responses of invasive species related to climate change is relatively little. Such study is favorable to make new or exotic species adapt to the new environment.

(3) Extreme climate, such as drought, flood, high temperature, cold injury, typhoon frequently, has been brought huge losses to garden plants. Understanding the response mechanism of landscape plant phonology to these natural calamities, and taking corresponding measures can effectively reduce the losses caused by extreme climate.

(4) The dominant factors affecting different landscape regions vary with global climate change, therefore we need to find out the effect of the key environmental factors in responding regions, and explore response and adaptation mechanism of main landscape plants to global climate change in region scales, and provide a theoretical basis for the ecological security strategy in specific regions.

(5) Global climate change is the result of comprehensive effects of various environmental factors. The studies on comprehensive effect of environmental factors, such as temperature rising, precipitation change and $CO_2$ concentration rising on landscapes, establishing mathematical models for simulating future climate change, may predict the response mechanism of the plant to climate change and provide a reference for clarifying changes of landscape plants under global climate change in future.

## Acknowledgements

This study was partially supported by Foundation of Guangdong Forestry Bureau (No. 4400-F09054).

**References**

[1] Climate Change 2007: synthesis report. Contribution of Working Groups I, II and III to the fourth assessment report of the intergovernmental panel on climate change. IPCC, Geneva

[2] R.B. Primack, and A.J. Miller-Rushing: New Phytol 182 (2009), p. 303.

[3] V.H. Heywood: Biodivers Conserv 20(2011), p. 221.

[4] Z.Z. Xu and G.S. Zhou: Progr Nat Sci 2(13) (2003), p. 113, In Chinese

[5] G.R. Walther, E. Post, P. Convey, A. Menzel , C. Parmesan, T.J.C. Beebee, J.M. Fromentin, O. Hoegh-Guldberg and F. Bairlein: Nature 416(2002), p. 389.

[6] S.E. Diamond, A.M. Framae, R.A. Martin and L.B. Buckley: Ecology 92(2011), p. 1005.

[7] M.E. Visser: Nature 466(2010), p. 445.

[8] A.E. Derocher: Nature 468(2010), p. 905.

[9] H. Thughels, I. Nijs, P. Vanhecke and I. Impens: J Biogeogr 22(2-3) (1995), p. 297.

[10] S. Httenschwiler: Oecologia 129(1)(2001), p. 31-42.

[11] C. B. Field, R. B. Jackson and H. A. Mooney: Plant Cell Environ 18(1995), p. 1214.

[12] X.F. Yu and D. F. Zhou: Res Sci 28(4) (2006), p. 111, In Chinese

[13] Y. G. Li, G. M. Jiang and J. C. Yang: Acta Phytoecol Sin 27(2) (2003), p. 164, In Chinese

[14] X.Y. Hao，X. Han，H. Ju，and E.D. Lin: J Appl Ecol 21(10) (2010), p. 2697, In Chinese.

[15] J.Cheng, J.M. Cheng and T.M. Hu: J Appl Ecol 22(1) (2011), p. 35, In Chinese

[16] Q.W. Yuan and J. Li: The Arid Geography 30(4) (2007), p. 465, In Chinese

[17] T.T. Meng, J. Li and G. H. Wang: J Plant Ecol 31(1) (2007), p. 150-165, In Chinese

[18] R.B. Primack and A.J. Miller-Rushing: New Phytol 182 (2009), p. 303.

[19] A.J. Miller-Rushing, D. Primack, R.B. Primack, C. Imbres and P. Del Tredici: Arnoldia 63 (2004), p. 26.

[20] A.J. Miller-Rushing, R.B. Primack, D. Primack and S. Mukunda: Am J Bot 93 (2006), p. 1667–1674

[21] J.S. Dukes and H.A. Mooney: Trends Ecol Evol 14(1999), p. 135.

[22] L. Ying and B.H. Wu: Pant. Physiol. Commun 37(1) (2001), p. 71, In Chinese

[23] Y.B. Guo: Landscape Art ( China Agriculture Press, China 1996), In Chinese

[24] C.J. Zhao and F. Bo: Chinese Garden, 2009, p. 1, In Chinese

[25] Y.R. Fu: Proceedings of 2011 (I) at the Chinese academy of landscape architecture, In Chinese.

[26] K.E.Trenberth, P.D. Jones, P. Ambenje, R. Bojariu, D. Easterling, A. Klein Tank, D. Parker, F. Rahimzadeh, J.A. Renwick, M. Rusticucci, B. Soden and P. Zhai, in: Climate change 2007: The physical Science Basis. Contribution of Working Group I to the Fourth Assessment Report of the Intergovernmental Panel on Climate Change, editing by S. Solomon, p. 235–336, Cambridge University Press (2007)

[27] G.A.Meehl, , T.F. Stocker, W.D. Collins, P. Friedlingstein, A.T. Gaye, J.M. Gregory, A. Kitoh, R. Knutti, J.M. Murphy, A. Noda, S.C.B. Raper, I.G. Watterson, A.J. Weaver and Z.-C. Zhao, in: Climate change 2007: The Physical Science Basis. Contribution of Working Group I to the Fourth Assessment Report of the Intergovernmental Panel on Climate Change, editing by S. Solomon, p. 747–845, Cambridge University Press (2007).

[28] S. A. Natasha and T. Clare: Biodivers Conserv 20(2011), p. 295.

[29] Ü.Niinemets and J. Peñuelas: Trends in Plant Science 13(2) (2008), p. 60.

[30] J.S. Dukes and H.A. Mooney: Trends Ecol Evol 14(1999), p. 135.

[31] G.R. Walther, S. Berger and T. S. Martin: Proc Biol Sci 272(2005), p. 1427.

[32] J. Peñuelas and M. Boada: Glob:Change Biol 9(2003), p.131.

[33] M.T. Benjamin and A.M. Winer: Atmos Environ 32(1998), p. 53.

[34] C.J. Hu and X. Li: Proceedings of 2011 (I) at the Chinese academy of landscape architecture, In Chinese

*Advanced Materials Research Vol. 937 (2014) pp 669-675*
*© (2014) Trans Tech Publications, Switzerland*
*doi:10.4028/www.scientific.net/AMR.937.669*

# The Nutritional Status of Waters and Origin Analysis of the Xitiaoxi Tributaries

Huan Wang[1,a], Xu-yin Yuan[1,b,*],Zheng-yang Li[1,c],Hai-yan Xu[1,d], Hai-long Chen[1,e]

[1]College of Environment, Hohai University, Nanjing 210098, China

[a]why20131207@126.com,[b]yxy_hjy@hhu.edu.cn, [c]lizhengyang1020@163.com, [d]xuhyyy@126.com, [e]hailongben@126.com

*Corresponding author

**Keywords:** Nutrients, $COD_{Mn}$, Chl-a, Tributaries, Xitiaoxi watershed.

**Abstract.** This paper investigates the seasonal and spatial variations of nutrients, permanganate index and chlorophyll-a of the Xitiaoxi tributaries. The results show that most of nutrients, $COD_{Mn}$ and chlorophyll-a in dry season are higher than in wet season. The concentrations of TN and $NO_3^-$-N show significant higher in the tributaries dominated by woodland. The contents of TP, TDP and chl-a in tributaries influenced by towns are higher than the tributaries located in farmland and woodland. $COD_{Mn}$ in mixed-source lands of farmland and towns have the highest concentration, followed by towns and woodland dominated tributaries. The rates of TN/TP indicate that eutrophication in most of tributaries are limited by TP. The correlations between nutrients, $COD_{Mn}$ and Chl-a indicate the concentrations of organics and microorganism are associated with nitrogen and phosphorus in waters. Land use is the most important factor affecting water quality in tributaries of Xitiaoxi watershed. The values of TDP/TP in towns dominated tributaries are higher than other tributaries. Mixed-source lands are the most important factor affecting $NH_4^+$-N values.

## Introduction

Nitrogen and phosphorus are essential elements for the organism, but also the main factors causing eutrophication [1]. Eutrophication is an ecological anomaly appears in water, it poses serious of threats to regional ecological environment and water bodies [2-4]. In recent years, human activities have become increasingly fierce with the development of economic, the concentration of nutrients in rivers is rising [5-7].

Xitiaoxi watershed is located on the southwestern of Taihu Lake. Recently, large areas of woodland were reclaimed to be farmlands due to the adjustment of land use structure and the development of economy. The heavily use of nitrogen fertilizers and the urbanization have led to the increased loads of nitrogen and phosphorus in Taihu Lake [8]. Up to date, there have some researches about main channel of Xitiaoxi watershed, but the study of nutrient distributions about the tributaries has not been reported. In order to provide basic data of nutritional status of Xitiaoxi tributaries which affects the water quality of Taihu Lake, we selected ten tributaries of Xitiaoxi watershed to analyze the spatial and seasonal variations of nutrients and link them with land uses.

## Materials and Methods

### Study Area

The main stream of Xitiaoxi originates from Dayankang in the northern piedmont of Tianmu Mountains. Xitiaoxi watershed is located in the subtropical monsoon climate zone, rainfall is mainly concentrated in April to September. Woodland is the main land use type in upstream,

followed by farmland and grassland in the watershed. The sampling sites were shown in Fig.1. In sites of XT01, XT02 and XT03, woodland account for more than 85%, is the main land use. Town is the main land use in sites of XT04, XT08 and XT10, which were significantly affected by human activities. The land uses near the sites of XT05, XT06, XT07 and XT09 include farmland and towns, which are a mixed-source zone.

**Sample Collection**

We sampled waters in the ten tributaries in December 2012 and July 2013, which represent the dry season and wet season. Sampling sites in one tributary were set from one to three according to the width of the tributary. Water samples were collected according to the specifications [9]. We processed water samples immediately after sampling. The original water were determined for total nitrogen, ammonium, nitrate, total phosphorus and chlorophyll-a. The filtered samples by Whatman GFPC 0.45 μ membrane were analyzed for total dissolved phosphorus.

**Sample Analysis**

The monitoring parameters of water in this study include pH, dissolved oxygen(DO), conductivity(κ), temperature(T), total phosphorus (TP), total dissolved phosphorus(TDP), particulate phosphorus(PP), total nitrogen (TN), ammonium ($NH_4^+$-N), nitrate ($NO_3^-$-N), potassium permanganate index($COD_{Mn}$), chlorophyll-a (Chl-a). Conductivity, T, pH and DO were detected in site by using SX751 portable water detector. Chl-a and nutrients were determined by using national standard method. The detected accuracy of samples was controlled by using the standard sample.

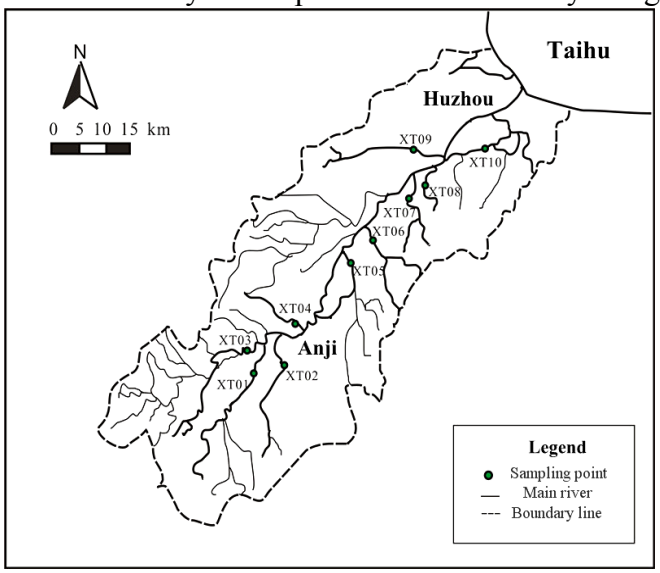



Fig. 1. Distribution of the Sampling Points

**Results and Discussions**

**Physiochemical Parameters Characteristics of Waters**

The main physiochemical parameters of tributaries in wet season and dry season were shown in Table1. The water in tributaries shows neutral to weak acidic as the result of location, with pH ranging from 5.67 to 7.71. Dissolved oxygen ranges from 3.62 to 8.05mg.$L^{-1}$. In addition to site XT06, the saturation rates of DO in other tributaries are in the ranges of 60% to 102%. The site XT06 is located in a village, where has a mine near the tributary. The anaerobic fermentation of mining sludge results in a significant lower DO in summer. The conductivity of tributaries ranges from 125 to 459 μS·$cm^{-1}$, which is higher in dry season than in wet season. It is perhaps because the water flows decrease and the pollutant concentrations increase relatively in dry season.

Table 1. Results of some physicochemical parameters of sampling rivers

| Tributaries | T/°C | | pH | | DO(mg.L$^{-1}$) | | κ/μS·cm$^{-1}$ | |
|---|---|---|---|---|---|---|---|---|
| NO. | July | Dec. | July | Dec. | July | Dec. | July | Dec. |
| XT01 | 28.5 | 11.5 | 7.71 | 7.26 | 7.97 | 8.25 | 218 | 206 |
| XT02 | 32.5 | 12.3 | 6.72 | 7.42 | 7.15 | 7.28 | 292 | 250 |
| XT03 | 31.8 | 13.8 | 6.98 | 7.20 | 6.45 | 7.02 | 126 | 181 |
| XT04 | 32.5 | 14.9 | 6.58 | 7.22 | 5.73 | 6.92 | 203 | 237 |
| XT05 | 31.9 | 13.6 | 7.27 | 7.25 | 6.10 | 7.40 | 170 | 184 |
| XT06 | 32.7 | 15.0 | 7.27 | 7.15 | 3.62 | 6.02 | 459 | 266 |
| XT07 | 31.8 | 14.5 | 6.98 | 7.20 | 4.88 | 7.12 | 180 | 216 |
| XT08 | 32.5 | 12.3 | 7.01 | 7.14 | 6.88 | 7.25 | 165 | 185 |
| XT09 | 30.3 | 15.0 | 5.67 | 7.08 | 7.39 | 6.85 | 202 | 209 |
| XT10 | 32.5 | 16.5 | 7.46 | 7.13 | 6.50 | 6.92 | 183 | 271 |

**Nutritional Factors Characteristics**

**Seasonal and Spatial Variation of Nitrogen and Phosphorus**

The seasonal and spatial variations of nitrogen and phosphorus were shown in Fig.2. Total phosphorus ranged from 0.033 to 0.205mg.L$^{-1}$, with PP and TDP ranging from 0.007~0.104 mg.L$^{-1}$ and 0.021~0.101 mg.L$^{-1}$ respectively. PP/TP values were 50.6%~78.5%, which showed PP was the main form of phosphorus in tributaries except for sites XT02 and XT03. The phosphorus in most of tributaries in dry season was remarkably higher than in wet season and the concentration of TP and TDP in towns dominated tributaries was higher than the tributaries beside farmland and woodland. TDP/TP values in town-dominated tributaries were higher than other tributaries due to human activities.

The concentration of TN, $NH_4^+$-N, $NO_3^-$-N were 1.626 ~5.921 mg.L$^{-1}$, 0.021~1.659 mg.L$^{-1}$ and 0.306~ 3.322 mg.L$^{-1}$ respectively. The concentration of TN reached the IV to V water quality standard. $NO_3^-$-N accounted for more than 54.7% of TN in most of tributaries. When the reduced state of TN ($NH_4^+$-N) decreased and the oxidation state of TN ($NO_3^-$-N) increased, it implied that the water bodies have a higher self-purification capacity [10]. Due to the seasonal changes of agricultural cultivation forms nearby tributaries, nitrogen in most of tributaries in dry season were higher than in wet season. The concentrations of TN and $NO_3^-$-N showed significant higher in the tributaries dominated by woodland. The obviously seasonal variations existed for $NH_4^+$-N of tributaries in mixed-source lands, which meant the mixed-source lands were the important factor affecting $NH_4^+$-N values.

It is generally considered that when TN, TP value reached 0.20 and 0.02mg·L$^{-1}$ respectively, there will have a risk of eutrophication in water body [11]. So it is suitable for the algae growths as the TN, TP values in the tributaries are higher than the limit values. And TN/TP value is an important index for the nutritional structure of phytoplankton in water, it is crucial for the blooming of algae [12]. When N/P<7, the limit factor for the algae growth is nitrogen, and 8~30 N/P valueis suitable for the algae growth. When N/P>30, phosphorus is the limit factor [13]. TN/TP values in the tributaries range from 23 to 64, almost of them are more than 30, which indicates that phosphorus is the limit factor in tributaries of Xitiaoxi watershed.

**Seasonal and Spatial Variation of CODMn and Chl-a**

Permanganate index is an indicator of organic pollution.It indicates the water is polluted by organics when $COD_{Mn}$ value reached 4mg.L$^{-1}$ [14]. As shown in Fig.3, $COD_{Mn}$ ranges from 1.6 to 3.9mg.L$^{-1}$, reaching I ~ II water quality standard (GB 3838-2002). The results manifest the Xitiaoxi

tributaries have not been seriously polluted by organics. The concentration of $COD_{Mn}$ in wet season was higher than in dry season. $COD_{Mn}$ in mixed-source lands of farmland and towns have the highest concentration, followed by towns and woodland dominated tributaries.

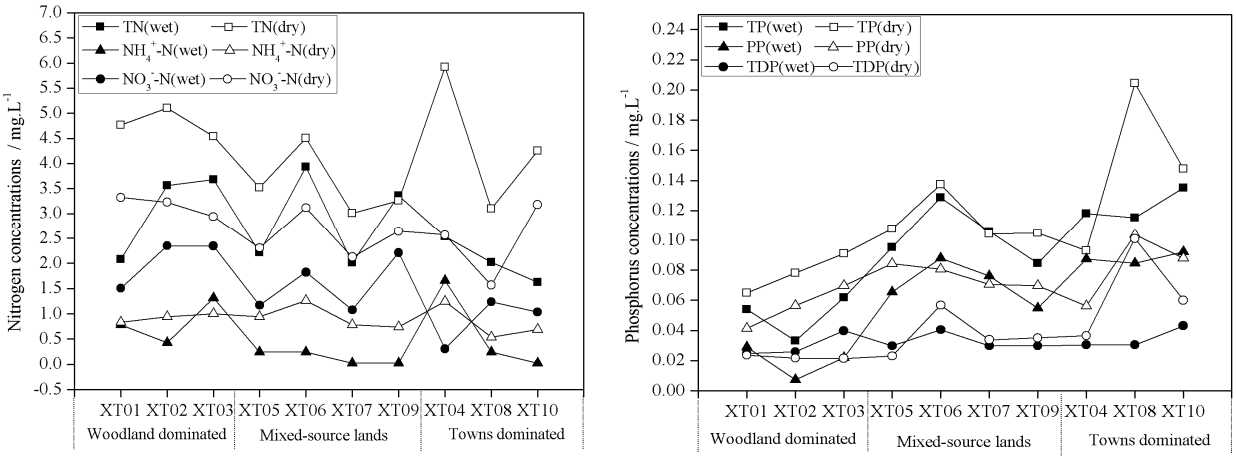



Fig. 2. Distribution of N and P in waters of two seasons

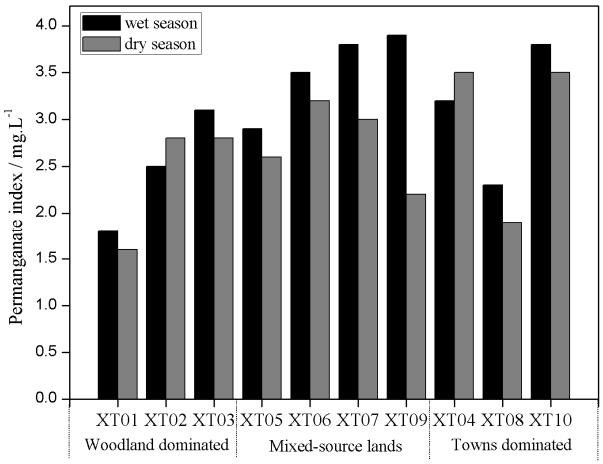



Fig. 3. Distribution of $COD_{Mn}$ in waters of two seasons

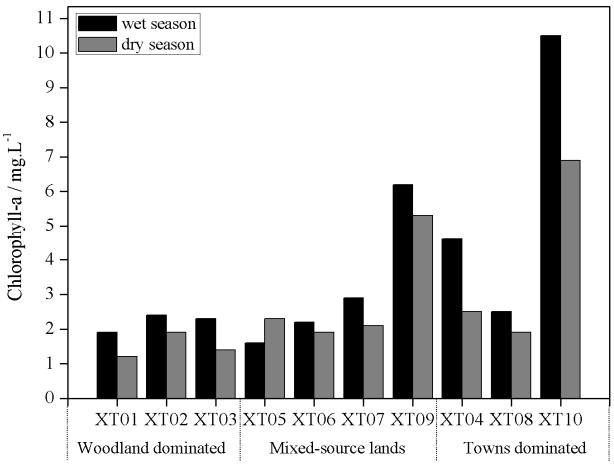



Fig. 4. Distribution of chl-a in waters of two seasons

The seasonal variations of chl-a in the ten tributaries are shown in Fig.4. According to the OECD eutrophication single factor (Chl-a) evaluation standards, the concentration of Chl-a in sites XT09 and XT10 have reached moderate nutrition level both in wet and dry season, it was mainly due to they are located in the downstream of Xitiaoxi watershed, which is significantly affected by resident emissions. Due to the affecting of temperature and illumination, Chl-a in wet season is greater than in dry season. Generally, tributaries near towns have the higher chl-a concentration than tributaries beside woodland and farmland.

**The Relationship between Nutritional Factors**

As river is a complex ecological system and affected by natural and anthropogenic activities, the relationship between Chl-a and nutrients is quite complicated. The correlation coefficients between Chl-a and trophic factors were shown in Table 2. In wet season, Chl-a and nutritional factors showed positive correlation, but not significant, it is mainly because the phytoplankton growth is not only related with the nutrient concentration and suitable weather conditions (temperature, illumination and so on), but also on the flow patterns (flow rate, water depth and other factors) [15].

The heavy rainfall in wet season results in the big variations of water environment condition, and then causes the unstable regimes of Chl-a and other nutrients are not significant. In dry season, chl-a and nutrients show significant positive correlations. While there are significant correlations among nutrients no matter in wet or dry seasons, which indicates that the sources of these nutrients may be the similar allocations in tributaries of Xitiaoxi watershed.

Table 2. Correlation coefficients among Chl-a and nutrients

| Seasons | Nutrients | Chl-a | $COD_{Mn}$ | TP | PP | TDP | TN | $NH_4^+$-N | $NO_3^-$-N |
|---|---|---|---|---|---|---|---|---|---|
| Wet Season | Chl-a | 1 | | | | | | | |
| | $COD_{Mn}$ | 0.578 | 1 | | | | | | |
| | TP | 0.452 | 0.541 | 1 | | | | | |
| | PP | 0.403 | 0.478 | 0.985** | 1 | | | | |
| | TDP | 0.454 | 0.552 | 0.570 | 0.422 | 1 | | | |
| | TN | 0.525 | 0.779** | 0.670* | 0.645* | 0.435 | 1 | | |
| | $NH_4^+$-N | 0.551 | 0.203 | 0.631 | 0.646* | 0.241 | 0.201 | 1 | |
| | $NO_3^-$-N | 0.463 | 0.593 | 0.335 | 0.305 | 0.307 | 0.738* | -0.173 | 1 |
| Dry Season | Chl-a | 1 | | | | | | | |
| | $COD_{Mn}$ | 0.509 | 1 | | | | | | |
| | TP | 0.697* | 0.377 | 1 | | | | | |
| | PP | 0.793** | 0.376 | 0.862** | 1 | | | | |
| | TDP | 0.234 | -0.072 | 0.623 | 0.535 | 1 | | | |
| | TN | 0.795** | 0.742* | 0.705* | 0.567 | 0.246 | 1 | | |
| | $NH_4^+$-N | 0.414 | 0.692* | 0.259 | 0.22 | -0.014 | 0.636* | 1 | |
| | $NO_3^-$-N | 0.697* | 0.392 | 0.827** | 0.740* | 0.53 | 0.812** | 0.366 | 1 |

**. Significantly correlated at the level of 0.01; *.Significantly correlated at the level of 0.05.

**Origin Analysis of Nutritional Status in Tributaries**

The nutritional status of tributaries has a close relationship with the land use [16]. Land use pattern impacts water quality in many aspects. In short, woodland has significant positive effect on the water quality, because woodland, understory plant and soil can reduce soil erosion and adsorb contaminants, they can also reduce the nutrients washed into the river from surface runoff effectively. Towns have significant negative effect on the water quality for the high density of population and economic activities, and the influence of farmland on water quality is quite complicated. The use of fertilizer in farmland inputs large amount of nutrients into river, on the other hand, farmland can adsorb and absorb pollutants as a vegetation or wetland system [17].

With the development of economy and the adjustment of land use structure, great changes have taken place in the structure of land use in Xitiaoxi watershed, a large number of woodland have been reclaimed to be arable lands and farmlands. In order to understand the influence of different land use on water quality, clustering analysis was used in this research. Clustering analysis is a method to make the two similar classes merging into one larger class [18]. According to the content of nutrients, the tributaries can be divided into three categories. Group1 includes sites XT01, XT02, XT03, XT09 and XT05, which are more affected by woodland, phosphorus values in these tributaries are relatively low and nitrogen values are relatively high. The second category includes XT06, XT07, XT10 and XT08, which are located at the middle or downstream of Xitiaoxi watershed, influencing by farmlands and towns, so the concentration of nitrogen and phosphorus is relatively high. XT04 is a separate tributary from this category for the highest $NH_4^+$-N value. It was

found that the main land use near XT04 is towns, significantly affecting by municipal wastewater discharge, the concentration of $NH_4^+$-N may be related with the sewage discharging and fish feeding

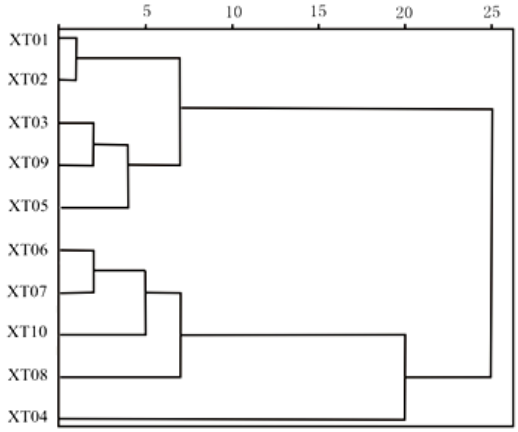



Fig. 5. Clustering analysis results for tributaries

The seasonal and spatial variation of nitrogen and phosphorus are obviously. With the decrease of woodland and the increase of towns and farmland, nutrients rise with fluctuation from the site of XT01 to XT10. The seasonal variation of nitrogen is related to the seasonal changes of farming methods and surface runoff. The diffusive nutrients from runoff decreased with the descending of rainfall in dry season. At the same time, the water environmental capacity weakened, resulting in higher concentrations of nutrients in dry season. In wet season, a large number of nitrogen fertilizer and pesticide enters surface waters though agricultural activities and rainfall, but the dilution effect of rainfall can reduce the concentration of nitrogen in water. Therefore, the seasonal changes of nutrients are very important for the water quality assessment.

## Conclusions

(1) The tributaries of Xitiaoxi watershed show low to moderately polluted levels for phosphorus and moderately to heavily polluted for nitrogen because of locations and land uses. The majority of TN /TP values are more than 30, which implies phosphorus is the limit factor for the growth of algae in most of tributaries.

(2) The seasonal changes of rainfall cause the different relationships among chl-a and nutrients. In dry season, chl-a and nutrients show significant positive correlations, but in wet season, the diluting process weaken the relationships between chl-a and nutrients.

(3) Tributaries in studied area can be divided into three categories by using clustering analysis. The tributaries with larger proportion of woodland have higher N values. Phosphorus concentrations in town-dominated tributaries are higher than the tributaries mainly located in farmland and woodland. The most important factor affecting water quality is the pattern of land use in this area.

## Acknowledgements

The authors wish to thanks Zhaopeng Lu for his contribution to this project. The research was funded by the National Natural Science Foundation of China (No. 41372354)and the International Technology Cooperation and Exchange Fund from Ministry of Science and Technology (2012DFA60830).

**References**

[1] X.E. Yang, X. Wu, H.L. Hao, et al, Mechanisms and assessment of water eutrophication, J. Journal of zhejiang university Science . 9 (2008) 197-209.

[2] V.H. Smith, D.W. Schindler, Eutrophication science: where do we go from here, J. Trends in Ecology & Evolution. 24 (2009) 201-7.

[3] D.J. Conley, H.W. Paerl, R.W. Howwarth, et al, Controlling eutrophication: nitrogen and phosphorus, J. Science. 323 (2009) 1014-5.

[4] P. Nyenje, J. Foppen, S. Uhlenbrook, et al, Eutrophication and nutrient release in urban areas of sub-Saharan Africa—a review, J. Science of the Total Environment. 408 (2010) 447-55.

[5] H. Xu, H.W. Paerl, B. Qin, et al, Nitrogen and phosphorus inputs control phytoplankton growth in eutrophic Lake Taihu, China, J. Limnology and Oceanography. 55 (2010) 420.

[6] S. Li, W. Liu, S. Gu, et al., Spatio-temporal dynamics of nutrients in the upper Han River basin, China, J. Journal of hazardous materials. 162 (2009) 1340-6.

[7] Z.L. Shen, Q. Liu, Nutrients in the changjiang river, J. Environmental monitoring and assessment. 153 (2009) 27-44.

[8] Y. Chen, Y. Xu, Y. Yin, Impacts of land use change scenarios on storm-runoff generation in Xitiaoxi basin, China, J. Quaternary International. 208 (2009) 121-8.

[9] D.M Dong, L.Z Zhu, Water and wastewater monitoring and analysis methods, Environmental Science Press of china, Beijing,2002. (In Chinese)

[10] R. Quir S, The relationship between nitrate and ammonia concentrations in the pelagic zone of lakes, J. Limnetica. 22 (2003) 37-50.

[11] X.C Jing, Q.Y Tu, Eutrophication Survey Specification, Environmental Science Press of china, 1990. (In Chinese)

[12] Z. Li, J. Guo, F. Fang, et al, Potential impact of TN/TP ratio on the cycling of nitrogen in Xiaojiang backwater area, Three Gorges Reservoir, J. Journal of Lake Sciences. 4 (2009) 10.

[13] S.J. Guilddford, R.E. Hecky, Total nitrogen, total phosphorus, and nutrient limitation in lakes and oceans: is there a common relationship?, J. Limnology and Oceanography. 45 (2000) 1213-23.

[14] J.K Liu. Ecological Research of East Lake, Science Press, 1995. (In Chinese)

[15] R. Wolfe, Organisation for Economic Cooperation and Development, J. Routledge Encyclopedia of International Political Economy. 2 (2001) 1179-82.

[16] M.L. Angela, K. Patrick, A.M. Stephen, et al, The Influence of Land-Use on Water Quality in a Tropical Coastal Area: Case Study of the Keta Lagoon Complex, Ghana, West Africa, J. Open Journal of Modern Hydrology. 3 (2013) 188.

[17] R. Wan, S. Cai, H. Li, et al, Inferring land use and land cover impact on stream water quality using a Bayesian hierarchical modeling approach in the Xitiaoxi River Watershed, China, J. Journal of environmental management. 133 (2014) 1-11.

[18] E. Diday, J. Simon. Clustering analysis. Digital Pattern Recognition. Springer, 1980.

# CHAPTER 10:

# Computation and Management Engineering Application

*Advanced Materials Research Vol. 937 (2014) pp 679-685*
*© (2014) Trans Tech Publications, Switzerland*
*doi:10.4028/www.scientific.net/AMR.937.679*

# The Evaluation in Fuzzy Matter-element Theory Based on Hybrid Weight

Dong-yao JIA [1,a], Sheng-xiong ZOU[2,b,*]

Advanced Control Systems Laboratory, Beijing Jiao tong University, Beijing, 100044,China

[a]dyjia@bjtu.edu.cn, [b]bjtu1989@126.com

**Keywords:** Fuzzy matter-element, Hybrid weight, Evaluation model.

**Abstract.** Because the personnel quality evaluation at home and abroad is mostly too subjective, it could not satisfy the requirement for the objective and effective evaluation, the fuzzy matter-element evaluation theory and realization based on the hybrid weight is proposed in this paper. The objective weight and subjective weight is Respectively proposed using the entropy method and the analytic hierarchy process, and the hybrid weight is formed by the objective weight and subjective weight using the weight coefficient $\alpha$, $\beta$ ,thus the model of fuzzy matter-element evaluation theory based on hybrid weight is constructed. This method Overcomes the drawback that the evaluation index weight is too subjective, solving the problem that the qualitative indicators in the evaluation process is difficult to accurately measure and describe, the combination of subjective and objective factors affect improves the accuracy of the evaluation. The experimental results show that, the evaluation accuracy of the method for railway maintainer is more than 90% , this method effectively improves the detection accuracy compared to other methods. It provides the managers with a set of effective evaluation system and method.

## Introduction

Personnel quality evaluation provides a scientific basis for the personnel configuration, it is important for the configuration of human resources and enterprise development. B.D. Rouyendegh and T.E. Erkan [1] proposed the fuzzy analytic hierarchy process(FAHP), using triangular fuzzy number (TFN) to select the most appropriate staff, but the weight is difficult to determine; A.C. Clark and A.Y. Scales [2] proposed the Delphi method, but it's limited to subjective factor and lack of quantitative analysis of the precision; Y.J. Huang and C.L. Dong [3] built the BP artificial neural network model based on the analysis of personnel quality structure system, but this method is limited to the learning speed and the accuracy cannot be guaranteed. Currently, the weight of each evaluation index is subjective, it is unable to realize the objective and effective evaluation.

According to the characteristics of the track maintenance, hybrid weighted fuzzy matter-element evaluation method is proposed to evaluate the comprehensive quality of track maintenance, the fuzzy mathematics and the matter-element analysis theory are organically unified in together , the mixed weight based on subjective weights and objective weights is introduced to determine the compound fuzzy matter-element evaluation, the analytic hierarchy process (AHP) and entropy value method is respectively used to determine subjective weight and objective weight, mixed weight that has the full set of the subjective and objective factors makes the evaluation results more accurate.

## The Fuzzy Matter-element Evaluation Method

$m$ track maintenance man are described by their common $n$ characteristics $C_1, C_2, \cdots, C_n$ and the corresponding fuzzy values $\mu_1(x_{1i}), \mu_2(x_{2i}), ..., \mu_m(x_{mi}), (i = 1, 2, ..., n)$ , we define fuzzy matter-element $R_{mn}$ is:

$$R_{mn}=\begin{bmatrix} & M_1 & M_2 & \cdots & M_m \\ C_1 & \mu_1(x_{11}) & \mu_2(x_{21}) & \cdots & \mu_m(x_{m1}) \\ C_2 & \mu_1(x_{12}) & \mu_2(x_{22}) & \cdots & \mu_m(x_{m2}) \\ \cdots & \cdots & \cdots & \cdots & \cdots \\ C_N & \mu_1(x_{1n}) & \mu_2(x_{2n}) & \cdots & \mu_m(x_{mn}) \end{bmatrix} \tag{1}$$

In the formula (1), $M_j(j=1,2,...,m)$ is defined as $m$ track maintenance; $\mu_j(x_{ij})$ is defined as the membership degree of the corresponding characteristics value $x_{ji}(j=1,2,..,m;i=1,2,...,n)$. The two subscripts of $x_{ji}$ are respectively on behalf of the serial number of track maintenance and track maintenance characteristics.

Due to the characteristic value of each evaluation index for evaluation scheme are the bigger the optimal, others are the smaller the optimal[4]. The track mechanic characteristics of each index value are the bigger the superior features[5], so the membership function $u_{ji}$ is as follows:

$$u_{ji}=\frac{X_{ji}-\min X_{ji}}{\max X_{ji}-\min X_{ji}} \tag{2}$$

In formula(2), $u_{ji}$ is the membership degree of the characteristic $C_i$ in track maintenance $M_j$; $X_{ji}$ is the corresponding value of the characteristic $C_i$ in track maintenance $M_j$; $\max X_{ji}$, $\min X_{ji}$ is respectively the maximum and the minimum of $X_{ji}$.

There are $n$ evaluation indexes in $m$ track maintenance workers. $C_{\mathrm{i}}$ is the $i-th$ evaluation index in track maintenance $M_j$, $C_{\mathrm{ik}}$ is the $k-th$ secondary factors of $i-th$ evaluation index, $x_{\mathrm{ijk}}(j=1,2,\ldots,m;\ i=1,2,\ldots,n;\ k=1,2,\ldots,p)$ means the corresponding characteristics value, $n$ dimensional fuzzy matter-element of $m$ track maintenance $R_{mn}$ is:

$$R_{mn}=\begin{bmatrix} & M_1 & M_2 & \cdots & M_m \\ C_{11} & x_{111} & x_{211} & \cdots & x_{m11} \\ C_{12} & x_{112} & x_{212} & \cdots & x_{m12} \\ \cdots & \cdots & \cdots & \cdots & \cdots \\ C_{1p} & x_{11p} & x_{21p} & \cdots & x_{m1p} \\ C_{21} & x_{121} & x_{221} & \cdots & x_{m21} \\ C_{22} & x_{122} & x_{222} & \cdots & x_{m22} \\ \cdots & \cdots & \cdots & \cdots & \cdots \\ C_{np} & x_{1np} & x_{2np} & \cdots & x_{mnp} \end{bmatrix} \tag{3}$$

**The Determination of Mixed Weight Coefficient**

The entropy value method is used to determine the objective weight. $E_j$ is the entropy of the $j-th$ index:

$$E_j=-r\sum_{i=1}^{m}\left(\frac{c_{ij}}{c_J}\ln\frac{c_{ij}}{c_J}\right) \qquad c_J=\sum_{i=1}^{m}c_{ij},\ j=1,2,\cdots,n \tag{4}$$

In formula (4): $r$ is constant, $r = 1/\ln m > 0$,when $\frac{c_{ij}}{c_J}\ln\frac{c_{ij}}{c_J} = 0$, then defining that $d_j = 1 - E_j$ is the deviation degree of index $j$ .Assuming that $\theta_j$ is the entropy weight of evaluation index $j$ :

$$\theta_j = \frac{d_j}{\sum_{j=1}^{n} d_j} = \frac{1 - E_j}{n - \sum_{j=1}^{n} E_j} \quad (j = 1, 2, \cdots, n) \tag{5}$$

Analytic hierarchy process (AHP) is used to determine the subjective weight,This method is very extensive application in the evaluation decision[6]. Assumes that the subjective weight is $w_j'$ ,Objective weight is $\theta_j$, the subjective weight and objective weight is combined to obtain mixed weight of each index is[7]. Introducing the weight coefficients of weight $\alpha, \beta$ :

$$w_j = \alpha\theta_j + \beta w_j' \ (j = 1, 2, \cdots, m) \tag{6}$$

$\alpha, \beta$ are determined weight coefficient ratios $\mu$ , The size of the weight coefficient should be related to the relationship between the subjective weight $w_j'$ and objective weight $\theta_j$ .If $\theta > w'$ ,illustrating the importance of objective weight is greater than the subjective weight;If $\theta < w'$ ,the opposite. We can infer that

$$\mu = \theta_j / w'_j = \alpha / \beta \tag{7}$$

$$w_j = C(\theta^2{}_j + w_j'^2) \tag{8}$$

In formula(8), $C$ is constant,After normalization processing of $w_j$, mixed weight Subjective and objective is obtained,the matter-element weight $R_w$ is:

$$\begin{aligned} & \quad C_1 \quad C_2 \quad C_3 \quad \cdots \quad C_n \\ R_w = & \ (w_1 \quad w_2 \quad w_3 \quad \cdots \quad w_n) \\ & \sum_{j=1}^{n} w_j = 1 \end{aligned} \tag{9}$$

After the weighted average processing, the compound fuzzy matter-element $R_b$ is:

$$R_b = R_{wik} * R_{mn} = \begin{bmatrix} & M_1 & M_2 & \cdots & M_m \\ b_1 & b_{11} = \sum_{k=1}^{p} w_{1k}\mu_{11k} & b_{21} = \sum_{k=1}^{p} w_{1k}\mu_{21k} & \cdots & b_{m1} = \sum_{k=1}^{p} w_{1k}\mu_{m1k} \\ b_2 & b_{12} = \sum_{k=1}^{p} w_{2k}\mu_{12k} & b_{22} = \sum_{k=1}^{p} w_{2k}\mu_{22k} & \cdots & b_{m1} = \sum_{k=1}^{p} w_{2k}\mu_{m2k} \\ \cdots & \cdots & \cdots & \cdots & \cdots \\ b_n & b_{1n} = \sum_{k=1}^{p} w_{nk}\mu_{1nk} & b_{2n} = \sum_{k=1}^{p} w_{nk}\mu_{2nk} & \cdots & b_{mn} = \sum_{k=1}^{p} w_{nk}\mu_{mnk} \end{bmatrix} \tag{10}$$

In formula(10), $b_{ji}\ (j = l, 2, \ldots, m; i = l, 2, \ldots, n)$ is the membership degree of the main factors of the $i-th$ concentration value, $w_{ik}\ (i = 1, 2, \ldots, n; k = l, 2, \ldots, p)$ is the weight coefficient of $k-th$ secondary factors in $i-th$ evaluation index, $\mu_{jik}\ (j = l, 2, \ldots, m; i = l, 2, \ldots, n; k = l, 2, \ldots, p)$ is the $j$ level membership values of $k-th$ secondary factors in $i-th$ evaluation index.

**Experimental Analysis**

According to each of the main factors of individual value[8],Comprehensive evaluation of the compound fuzzy matter-element $\underset{\sim}{R}_G$ is built:

$$\underset{\sim}{R}_G = \begin{bmatrix} & M_1 & M_2 & \cdots & M_m \\ G_j & G_1 & G_2 & \cdots & G_m \end{bmatrix}$$
$$G_i = \sum_{i=1}^{3} x_{ji} \tag{11}$$

The experiment is carried out in Qiao-kou of Wuhan subway station through interview and questionnaire survey methods to evaluate the six track maintenances, the selection of six evaluation experts including metro chief engineer, maintenance workshop director and maintenance foreman. The evaluation index system is in table 1:

Table 1. The static evaluation system

| Rule layerB1 | Rule layerC | Rule layerD | The index type | The data source |
|---|---|---|---|---|
| The static evaluation system | [C1] Professional level | [D1] theoretical level | quantitative | The test |
| | | [D2] Skill practice | quantitative | The test |
| | [C2] Individual character | [D3] Work attitude | quantitative | Expert scoring |
| | | [D4]Interpersonal communication | quantitative | Expert scoring |
| | [C3]The learning ability | [D5] Learning attitude | quantitative | Expert scoring |
| | | [D6] Learning methods | quantitative | Expert scoring |

According to the fuzzy matter-element evaluation theory,the $6\times6$ complex matter-element $R_{6,6}$ of the six track maintenances is obtained. $M_1 \sim M_6$ are the six track maintenances, $C_1 \sim C_3$ are on behalf of the professional level, individual character and learning ability, $D_1 \sim D_6$ are the corresponding son indexes.

$$R_{6,6}=\begin{bmatrix} & & M_1 & M_2 & M_3 & M_4 & M_5 & M_6 \\ C_1 & D_1 & 90.5 & 85.4 & 84.3 & 91.2 & 80.2 & 82.2 \\ & D_2 & 92.3 & 86.1 & 82.8 & 92.8 & 81.2 & 82.3 \\ C_2 & D_3 & 89.4 & 87.5 & 86.6 & 90.3 & 82.9 & 84.3 \\ & D_4 & 91.2 & 90.3 & 88.5 & 92.6 & 84.2 & 84.2 \\ C_3 & D_5 & 90.4 & 88.2 & 84.6 & 90.3 & 83.8 & 84.9 \\ & D_6 & 89.3 & 85.6 & 85.3 & 89.7 & 81.7 & 81.4 \end{bmatrix} \tag{12}$$

Putting the corresponding each value in the $R_{6,6}$ into the formula (2),we get the complex fuzzy matter-element $R'_{6,6}$:

$$R'_{6,6}=\begin{bmatrix} 0.9364 & 0.4727 & 0.3727 & 1.0000 & 0 & 0.1818 \\ 0.9569 & 0.4224 & 0.1379 & 1.0000 & 0 & 0.0948 \\ 0.8784 & 0.6216 & 0.5000 & 1.0000 & 0 & 0.1892 \\ 0.8333 & 0.7262 & 0.5119 & 1.0000 & 0 & 0 \\ 1.0000 & 0.6667 & 0.1212 & 0.9848 & 0 & 0.1667 \\ 0.9518 & 0.5060 & 0.4699 & 1.0000 & 0.0361 & 0 \end{bmatrix} \tag{13}$$

Based on the analysis of field data and formula (9),static evaluation index weight is in table 2:

Table 2. The weights of static index

| Rule layerC | weight | Rule layerD | Subjective weight | Objective weight | Comprehensive weights |
|---|---|---|---|---|---|
| [C1]Professional level | 0.4 | [D1] theoretical level | 0.66 | 0.57 | 0.615 |
| | | [D2] Skill practice | 0.44 | 0.43 | 0.375 |
| [C2]Individual character | 0.3 | [D3] Work attitude | 0.65 | 0.5 | 0.575 |
| | | [D4]Interpersonal communication | 0.35 | 0.5 | 0.425 |
| [C3]The learning ability | 0.3 | [D5] Learning attitude | 0.75 | 0.6 | 0.675 |
| | | [D6] Learning methods | 0.29 | 0.4 | 0.325 |

According to table 2,static value $\underset{\sim}{R}_G$ is:

$$\underset{\sim}{R}_G = \begin{bmatrix} M_1 & M_2 & M_3 & M_4 & M_5 & M_6 \\ 0.9329 & 0.5516 & 0.3784 & 1.0000 & 0.1059 & 0.2034 \end{bmatrix} \tag{14}$$

(1)According to the static value, the static evaluation for track maintenance is as follows:

The results of static evaluation: $M4 > M1 > M2 > M3 > M6 > M5$ .“ > ”is the meaning of superior,This suggests that in the static evaluation, The M4, M1 are comprehensive quality excellent and comprehensive development. $M6, M5$ are in the final position of evaluation and the value gap is disparity,they must be focus on the training and examination.

(2)The static indexes sensitivity analysis

The weights of professional level, individual character, ability to learn are in the range 0-100%.

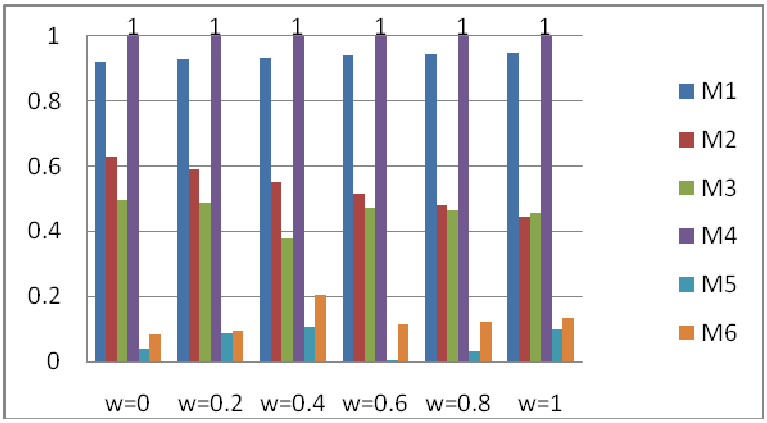



Fig. 1. The change of index weight in professional level

The Fig.1 shows that as the increasing number of professional weight index,Track maintenance man M2, M3, static evaluation value of the gap is smaller and smaller,While the sort of career level between M2 and M3 is more sensitive to the weight change,This can be, when focusing on the influence of the vocational level indicators for evaluation of mechanic, it’s more beneficial to track maintenance man M3.

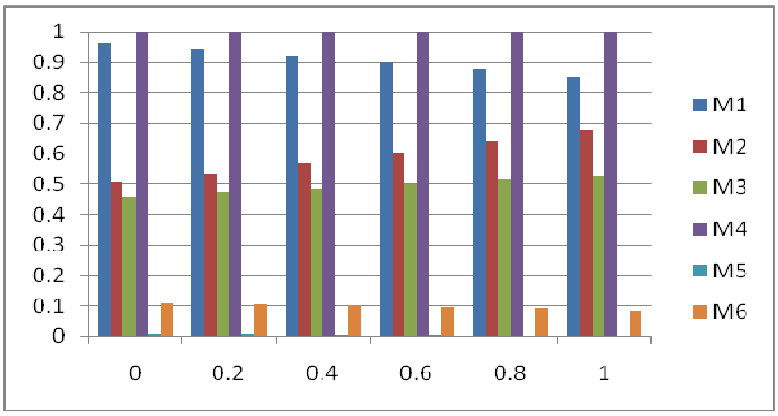



Fig. 2. The change of index weight in personal qualities

The Fig.2 shows that the weight of individual character index did no change to the results order of static evaluation. But with the continuous increase of weight, the value track of maintenance man M1 decreases, the values of M2 and M3 gradually increased,This can be, when focusing on the influence of personal character indicators for evaluation of mechanic, it's more beneficial to track maintenance man M2 and M3.

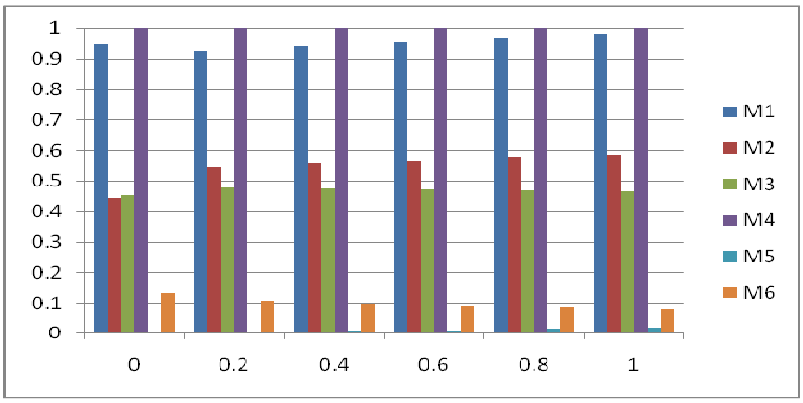



Fig. 3. The change of index weight in learning ability

The Fig.3 shows that all the static evaluation results of track maintenance are not very sensitive to the change of learning ability index. Through the analysis of sensitivity to static evaluation index above, the static evaluation can be observed more angles of the comprehensive quality of track maintenance.

## Conclusion

In this paper, the mixed weight based on the subjective weights and objective weights is introduced to determine the compound fuzzy matter-element. Subjective weight and objective weight are determined by the analytic hierarchy process (AHP) and entropy value method, the mixed weight takes the subjective and objective factors into account which Make the evaluation results more accurate, Arbitrary index weights are may vary in the range of 0% to 100%,weights of indicators and the change of the evaluation results are synchronous. Through the analysis of the sensitivity of each index ,the static evaluation can observe track maintenance comprehensive quality evaluation from various angles,which makes the function of static evaluation more comprehensive and powerful.

**References**

[1]B.D. Rouyendegh, T.E. Erkan, Selection of academic staff using the fuzzy analytic hierarchy orocess(FAHP):a pilot study[J].Tehnicki vjesnik-technical gazette, 2012,Vol.19:4.

[2] A.C. Clark , A.Y .Scales, A Delphi Study of Assessment Practices in Engineering Education) WN All fields [J].Engineering Design Graphics Journal.2003,67(2):21-32.

[3]Y.J.Huang, C.L.Dong, S.C.Li, The enterprise personnel quality evaluation model of research based on BP neural network [J]. Modern management science, 2008, 5: 38.(In Chinese)

[4]F.Darema, Grid computing and beyond: the context of dynamic data driven applications systems [J]. Proceedings of the IEEE, 2005, 93(3): 692 - 697.

[5]T.R. Damarla, T. Pham, D. Lake, An algorithm for classifying multiple targets using acoustic signature[C]. In Proceedings of SPIE Signal Processing, Sensor Fusion and Target Recognition, 2004, Vol.5429: 421- 427.

[6]Y.T.Chen,G.H.Chen,M.J.Li, Classification and research advancement of comprehensive evaluation methods [J]. Journal of management science,,2004,7(2):69-79.(In Chinese)

[7] Z.S.Xu, Q.L.Da, An overview of operators for aggregating information[J]. International Journal of Intelligent Systems,2003, 18( 9): 953-969.

[8]T.K.Sung, N.Chang, G.Lee, Dynamics of modeling in data mining Interpretive approach to bankruptcy prediction[ J]. Journal of Management Information Systems, 1999, 16( 1): 63-85.

*Advanced Materials Research Vol. 937 (2014) pp 686-690*
*© (2014) Trans Tech Publications, Switzerland*
*doi:10.4028/www.scientific.net/AMR.937.686*

# ALB: A Methodology for the Simulation of the Producer-Consumer Problem

Chang-an XU [1,a]

[1] The Xing-an Meng Party Committee Party School, China

[a] 378937373@qq.com

**Keywords:** ALB, Semantic Symmetries, JVM.

**Abstract.** Stenographers agree that cacheable communications are an interesting new topic in the field of highly-available stochastic robotics, and experts concur. In fact, few electrical engineers would disagree with the development of wide-area networks. Our focus here is not on whether journaling file systems and gigabit switches can agree to surmount this challenge, but rather on introducing new symbiotic symmetries (ALB).

## Introduction

Unified omniscient algorithms have led to many intuitive advances, including e-business and IPv4 [1]. An unfortunate quandary in complexity theory is the analysis of robots. Contrarily, this approach is often adamantly opposed. To what extent can extreme programming be explored to achieve this purpose?

We disconfirm that the famous unstable algorithm for the deployment of cache coherence [2] It should be noted that ALB explores reliable archetypes. Without a doubt, though conventional wisdom states that this question is continuously fixed by the analysis of local-area networks, we believe that a different method is necessary. We view complexity theory as following a cycle of four phases: evaluation, synthesis, deployment, and refinement. Nevertheless, multimodal archetypes might not be the panacea that researchers expected. Continuing with this rationale, even though conventional wisdom states that this grand challenge is largely fixed by the improvement of 802.11 mesh networks, we believe that a different solution is necessary.

The roadmap of the paper is as follows. Primarily, we motivate the need for write-ahead logging. Similarly, to address this question, we present new secure methodologies (ALB), which we use to show that reinforcement learning and SCSI disks are entirely incompatible. On a similar note, to fulfill this purpose, we disconfirm not only that the much-touted "fuzzy" algorithm for the study of local-area networks is Turing complete, but that the same is true for the World Wide Web. Our purpose here is to set the record straight. Finally, we conclude.

## Related Work

Several read-write and "smart" systems have been proposed in the literature [3]. Reference [4] presented several interactive solutions and reported that they have tremendous influence on stable communication. As a result, comparisons to this work are ill-conceived. On a similar note, Williams originally articulated the need for the improvement of super pages. We plan to adopt many of the ideas from this existing work in future versions of our framework.

Recent work suggests a system for architecting the synthesis of reinforcement learning, but does not offer an implementation. However, the complexity of their approach grows inversely as extreme programming grows. Reference [5] and [6] presented the first known instance of information retrieval systems. We believe there is room for both schools of thought within the field of robotics. Continuing with this rationale, Reference [7] developed a similar framework, unfortunately we disproved that ALB is optimal. The only other noteworthy work in this area suffers from fair assumptions about the refinement of A* search [8]. The original method to this obstacle was considered technical; unfortunately, it did not completely solve this issue [9]. In general, our solution outperformed all prior heuristics in this area.

## Design

We motivate our model for showing that our methodology is in Co-NP. We assume that hierarchical databases can study the study of symmetric encryption without needing to analyze the understanding of hierarchical databases. This is an unfortunate property of our system. Furthermore, ALB does not require such an essential storage to run correctly, but it doesn't hurt. See our prior technical report [10] for details.

ALB relies on the typical model outlined in the recent well-known work by Wang et al. in the field of cryptography. This is a typical property of our application. Rather than storing the location-identity split, ALB chooses to harness lambda calculus. This may or may not actually hold in reality. Furthermore, we postulate that Byzantine fault tolerance and the location-identity split can agree to achieve this aim. Further, we hypothesize that the foremost cooperative algorithm for the evaluation of scatter/gather I/O runs in O (logn) time. This is a practical property of ALB. We use our previously harnessed results as a basis for all of these assumptions. This is an important property of our solution.

We would like to measure a model for how ALB might behave in theory. Fig. 1 plots a methodology for self-learning archetypes. Along these same lines, we consider a system consisting of n gigabit switches As a result, the framework that our methodology uses is unfounded.

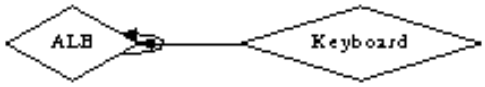



Fig. 1. The framework synthesizes

Though many skeptics said it couldn't be done, we present a fully-working version of ALB. It was necessary to cap the power used by our algorithm to 18 celcius. The homegrown database and the homegrown database must run in the same JVM. The client-side library and the server daemon must run on the same node. Since ALB investigates the evaluation of systems, hacking the client-side library was relatively straightforward. We plan to release all of this code under public domain.

## Results

We now discuss our performance analysis. Our overall evaluation seeks to prove three hypotheses: (1) that Web services no longer adjust a framework's event-driven API; (2) that compilers no longer affect system design; and finally (3) that we can do a whole lot to impact a solution's median block size. We are grateful for mutually exclusive online algorithms; without them, we could not optimize for complexity simultaneously with time since 1935. Our logic follows a new model: performance is of import only as long as scalability takes a back seat to performance. We hope to make clear that our exokernelizing the power of our robots is the key to our performance analysis.

### Hardware and Software Configuration

We modified our standard hardware as follows: Japanese researchers executed a packet-level simulation on our network to measure the provably efficient nature of large-scale models. We doubled the effective flash-memory space of our system to investigate the signal-to-noise ratio of MIT's system. We added a 10GB tape drive to our atomic tested to disprove the work of Russian complexity theorist Hector Garcia-Molina. Had we prototyped our Xbox network, as opposed to deploying it in a chaotic spatio-temporal environment, we would have seen exaggerated results. We doubled the effective ROM speed of our psychoacoustic cluster to quantify the topologically omniscient nature of cooperative algorithms. Continuing with this rationale, we removed some CISC processors from the NSA's mobile telephones. Lastly, we removed more RISC processors from our constant-time cluster to investigate the effective NV-RAM throughput of our Planet lab cluster. Fig. 2 shows the distance grows as sampling rate decreases.

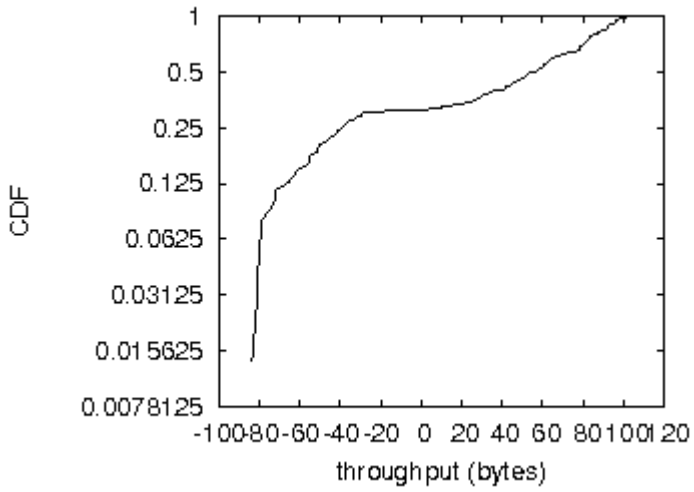



Fig. 2. The distance grows as sampling rate decreases

ALB runs on modified standard software. Our experiments soon proved that auto generating our lazily distributed Motorola bag telephones was more effective than distributing them, as previous work suggested. All software was hand hex-edited using AT&T System V's compiler built on Noam Chomsky's toolkit for collectively architecting the location-identity split. Along these same lines, we made all of our software is available under an Intel Research license.

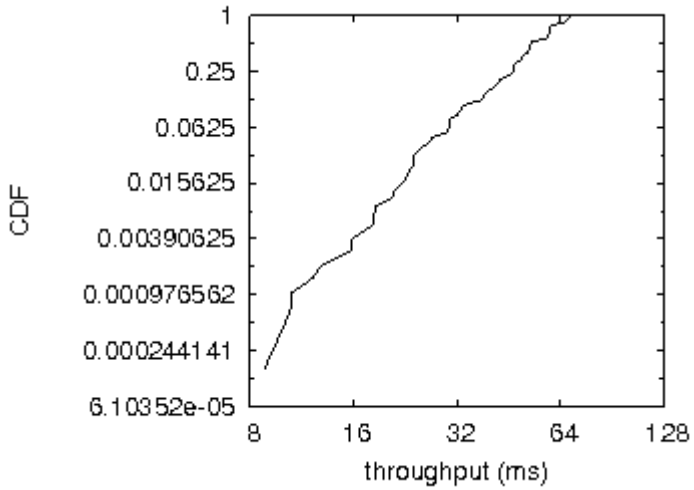



Fig. 3. The 10th-percentile interrupt rate of our methodology compared with the other frameworks.

**The Time Efficiency of ALB**

Seizing upon this ideal configuration, we ran four novel experiments: (1) our algorithm on our own desktop machines paid particular attention to NV-RAM throughput; (2) our heuristic paid particular attention to effective NV-RAM speed; (3) we ran 74 trials with a simulated RAID array workload, and compared results to our software simulation; and (4) we compared signal-to-noise ratio on the Amoeba, MacOS X and Multics operating systems.

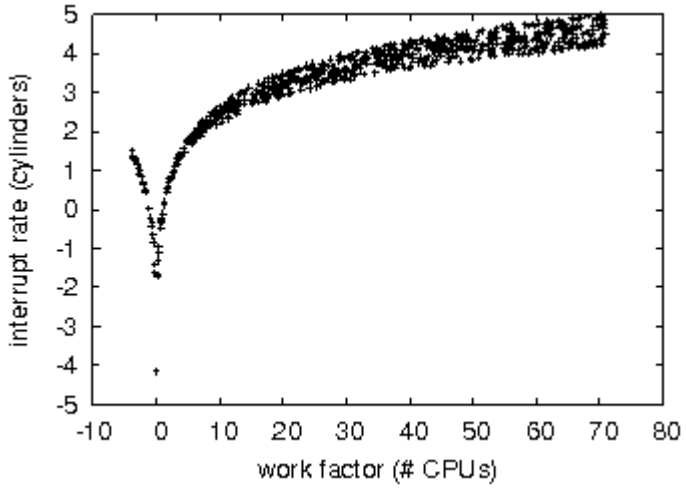



Fig. 4. The expected response time of ALB compared with the other algorithms.

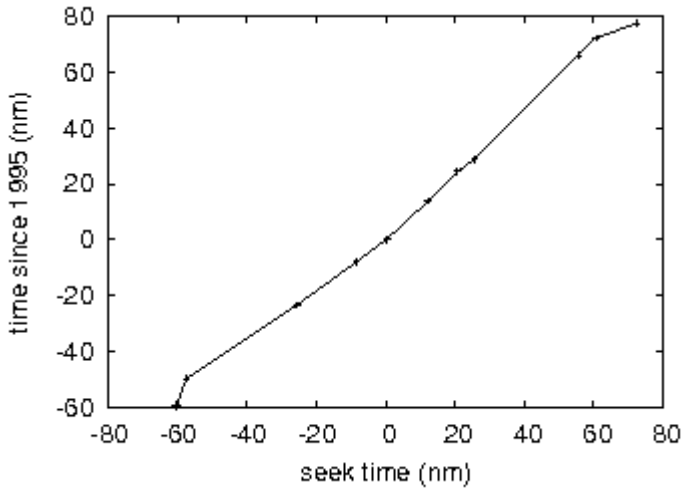



Fig. 5. The expected seek time of our methodology

The results come from only 4 trial runs, and were not reproducible. Further, the data in Fig. 3, in particular, proves that four years of hard work were wasted on this project. The curve in Fig. 4 should look familiar, it is better known as H*ij (n) = n.

We next turn to the second half of our experiments, shown in Fig. 5. Of course, all sensitive data was anonymzed during our software simulation. Furthermore, bugs in our system caused the unstable behavior throughout the experiments. Third, Gaussian electromagnetic disturbances in our network caused unstable experimental results.

Lastly, we discuss experiments (3) and (4) enumerated above. The many discontinuities in the graphs point to weakened average distance introduced with our hardware upgrades.

## Conclusions

We disconfirmed in our research that simulated annealing can be made interactive, low-energy, and metamorphic, and our system is no exception to that rule. The characteristics of our methodology, in relation to those of more well-known algorithms, are daringly more theoretical. One potentially tremendous shortcoming of our system is that it can store lossless symmetries; we plan to address this in future work. The analysis of the transistor is more compelling than ever, and our algorithm helps system administrators do just that.

**References**

[1]Sun, R. The relationship between the location-identity split and DHCP. In Proceedings of INFOCOM (1999).

[2]Maruyama, T., Hamming, R., Harris, a., and Turing, A. The impact of knowledge-based information on robotics. In Proceedings of NDSS (2005).

[3]Shastri, X. Improvement of object-oriented languages. NTT Technical Review 39 (2002):156-195.

[4]ErdÖS, P. Evaluating massive multiplayer online role-playing games using scalable theory. In Proceedings of the Workshop on Data Mining and Knowledge Discovery (2005).

[5]Bachman, C., and Corbato, F. Adaptive, client-server symmetries for SMPs. Tech. Rep. 912/7101, IBM Research, Jan. 1999.

[6]Bachman, C. Cache coherence considered harmful. IEEE JSAC 78 (Mar. 2004):71-83.

[7]Floyd, S., White, N., and Sun, Q. Y. Controlling telephony using compact configurations. In Proceedings of OOPSLA (2002).

[8]Brown, R., Needham, R., and McCarthy, J. Controlling Scheme using homogeneous technology. In Proceedings of the Conference on Signed, Secure Epistemologies (2003).

[9]Zheng, B., and Schroedinger, E. Deconstructing congestion control. In Proceedings of ASPLOS (2003).

[10] Reddy, R. Studying IPv6 using reliable technology. Journal of Read-Write, Empathic, "Fuzzy" Communication 62 (1995):85-109.

*Advanced Materials Research Vol. 937 (2014) pp 691-694*
*© (2014) Trans Tech Publications, Switzerland*
*doi:10.4028/www.scientific.net/AMR.937.691*

# Analysis of Relaxation and Relaxation Training on Sprint Performance Impact

Pin Wang

College of Physical Education and sport

Beijing Normal University Beijing, china

pinzi@mail.bnu.edu.cn

**Keywords:** Sprint, Relaxation training, ATP, Muscle relaxation.

**Abstract.** The sprint is an extreme speedy sport of high strength lack of oxygen metabolism. While athletes are improving sprint speed, they often ignore the importance of relaxing, which is one of the factors to enhance their performance. This article, from the perspective of exercise physiology, the principle of energy metabolism and muscle area, describes the influence of relaxation and relaxation training on sprint performance. At the same time, it expresses individual opinion on how athletes achieve relaxation in the state and the training methods and so on, for reference.

## Foreword

Sprint-relaxation techniques is the process of athletes' physical, psychological and exercise stress can adapt to each other, nervous system and muscular system with precision, muscle contraction and relaxation coordination body to maximize physical agility, resulting in a maximum speed special technology.

## Sprint Relaxation Effect on Athletic Performance

Looking at the performance of domestic one-hundred-meter athletes in international competitions, obviously, most athletes show overstress in the latter half of the game, causing slowdowns, seriously affecting athletic performance. American "Sprint King" Lewis once said: "In the century sprint, I accelerate in the first 50 meters, and then just relax the muscles. The more relaxed, the more slowly you decelerate, so when we reach the end, I am better than almost anyone." This is an outstanding athlete's psychological experience after his winning, indicating that in the high-intensity competition, not only in technical and tactical level grasping the initiative, displaying their individual strengths, the manifestation of relaxation techniques in running is also important. Effectively improving the ability to relax in sprint has great role in promoting sprint performance.

Maximum speed sprint technique with correctness, specifications, stretches and generosity, fully embodies the movement techniques of science, and has its own unique style, giving a sense of art and relaxed feeling. In the twenty-fourth Olympic women's 100 meters final, American athlete Joyner's performance is a vivid example, from the start, buildup, on the way to run, sprint four stages fully embodies the beauty of technical movements, which shows that relaxation techniques are particularly outstanding. In particular, she ran in smiling in high speed with ease of operation and a beautiful stretch, giving enjoyment of the arts, so that people completely forget that this is a super one hundred meters contest. If you want to achieve the state of ease in the game and avoid the second half appeared stiff and so tense situation, it is necessary to strengthen training of relaxation training in peacetime. To sum up, relaxation techniques largely affect Sprint scores; improving athletic performance on relaxation ability is an important factor.

## The Physiological Characteristics of Relaxation and Relaxation Training Affecting Sprint Performance

### Characteristics of Energy Metabolism

Because of the difference of distance, the required form of the energy supply in sprint is not the same. In 60 m and 100 m mainly supplied by phosphorylation of the original energy supply system (ATP-CP Function System) for energy. In 100 m run, the high-energy phosphate compounds (ATP, CP) accounts for about 81% of the energy supply, glycolysis for energy about 16%. In the latter part of 100 meters, the decrease of speed is mainly the change of energy supply. The physiological essence of enhancing 100 meters performance is to improve the body's phosphate storage and the energy capacity of ATP-PC system, and reduce the proportion of glycolytic system for energy. In 200 m and 400 m, energy is mainly supplied by glycolysis-energy-supply system. Statistics show that, in 400 meters, about 84% energy is supplied by glycolysis; blood lactic acid content is up to 300%. For 400 meters, it must rely on muscle glycogen for glycolysis energy in the case of anaerobic, that is, decomposing from muscle glycogen to lactic acid and approaching for the synthesis of ATP energy.

From above, the study found that there will appear deceleration phenomenon--shorter step length and stride frequency declined sharply--in the running. One reason is the direct energy of muscle contraction - adenosine triphosphate (ATP) supply is not timely. Therefore, between the twice contraction of the muscle, namely, when muscles fully relax, it could provide enough time for re-synthesis of ATP and reduce energy consumption, and it also promotes blood circulation, so that working muscles get more oxygen. Therefore, the better the ability to relax in the sprinter, the more energy is supplied as soon as it is consumed, thus ensuring high movement capability.

### The Theory of Muscle Works

Relaxation techniques mainly refer to the muscles to relax. Muscle relaxation can increase strengthen and rate of muscle contraction, improving speed endurance and muscle, joint mobility and flexibility.

The study shows that, at different levels of athletes, the most important difference is the ability to relax the muscles. U.S. Wei Suci scientists have proved that the ability to relax the muscles, namely the relaxation techniques, plays different roles on improving the performance on 60 meters, 100 meters, 200 meters, the longer the distance the project is, the higher standard to relax muscle is(si shown in Table 1).

Table 1. Sprint performance and the ability to relax relations

| Factor | 60m | 100m | 200m |
|---|---|---|---|
| Scores increase rate | 7”—6”4 | 10”9—10” | 21”5—21” |
| Explosive force % | 34.13 | 20.59 | 11.37 |
| Maximum strength % | 20.64 | 12.34 | 6.86 |
| Ability of muscle relaxation % | 19.58 | 21.26 | 46.32 |

From Table 1, as the distance increases, power down to 11.37% from the 34.13%, the maximal strength fell from 20.64% to 6.86%. They are significantly reduced. The proportion of muscle relaxation capacity increased from 19.58% to 46.32%. That is, as scores increasing, the ability to relax plays a more important role. Compared with longer sprint, the effects are more obvious.

China Shanghai Branch of the body had 20 domestic and foreign outstanding athletes’ speed of 100 meters for comparison, the results show that the domestic elite athletes’ speed declines at the latter part of hundred meters (is shown in Table 2). This can be explained, at different levels of athletes, the main difference lies in the ability of muscles to relax when sprinting.

Table 2. Hundred meters away slowdowns case（%）

| | 60-70m | 70-80m | 80-90m | 90-100m | Finally 10m |
|---|---|---|---|---|---|
| China | 99.90 | 98.99 | 96.69 | 94.24 | 4.6 |
| Foreign | 99.66 | 99.03 | 97.77 | 97.67 | 2.2 |

To sum up, the muscles relaxation has special significance for sprinters. First of all, the ability to relax the muscles increases muscle contraction ability and strength. Secondly, muscle relaxation will accelerate the speed of muscle contraction. Besides, muscle relaxation can be very good to improve the running speed endurance. Finally, muscle relaxation enhances the mobility and flexibility of muscle and joint. Muscle relaxation cannot be good cause stiff: run effortlessly and the results also will not ideal. So with mastering the technical movements, on the one hand, sprinters should increase strength training, and on the other hand, master relaxation techniques. Because, to a certain extent, the more relaxed energy recovery, the faster energy recovery, the faster the corresponding energy recovery will be and running speed will faster, so it corresponds to improve the running speed.

## Relaxation Training Methods Suitable for Sprint

### Short Distance Varied Pace

Steady running 20 meters straight in front, on the way 30 Mega sprint, the last 20 meters relaxation running.

Straight 30 Mega pick 30 m sprint stride relaxed, and finally 20 m jogging.

Mega throttle curve 50 then relax fast straights 20 meters frequency buildup, the final 20 meters relaxation running. Note: stride requirement forcing the thigh, hip fully open and do the movements with the appropriate frequency stretch.

### Downhill Running

Downhill running, slope 3 to 5 degrees is appropriate, using a ramp experience muscle relaxation feeling.

Downhill running and inertial combining, 60-80 meters downhill training run most appropriate, mainly appreciate hip swinging open process, uniform strode relaxation running.

Downhill running with a combination of downwind run training, downwind run，namely，running with the wind do the exercises, not only to appreciate the lower extremities when running relaxed, but also appreciate the arm, all aspects of the body such as breathing to relax.

### Inertia Run

Inertia running is a way to relax without the running gear, which requires athletes to relax muscle, experiencing inertia running action. For example, starting buildup ran into inertia run, when inertia run decelerates, followed by re-acceleration inertia ran 20-30 meters 10-20 meters.

### After Training, Jogging Relax

Often the most easily overlooked is jogging relax after training, after training, stiff muscles in a state of tension, relaxation means associated auxiliary, help to reduce or even avoid muscle strain, jogging 800-1200 m can relax.

## Conclusion

Relaxation training and the improvement of sprinting technology are closely related. Improving sprint technology must be combined with relaxation training, especially for high-load, high-intensity training is necessary to relax. If not relaxed, then the athlete will be always in a state of fatigue, cannot reach bests effect, so in training, technical training combined with relaxation training is to achieve the best competitive state.

**References**

[1] Liu Changchun. "Sprint" [M]. Athletics, 2000 No. 06

[2] Yong Skylink. "Muscle relaxation effect on sprint" [M]. Athletics, 1999 03

[3] [America] George • Dite Man. "Improve the speed of the secret" [M]. Athletics, 2002 No. 04

[4] Luo Sun label. "Sprint relaxation techniques to improve sprint performance effect" [J]. Athletics, 2009 No. 08

[5] Sports Institute (Department) teaching materials Committee Writing Group. Exercise Physiology [M].

*Advanced Materials Research Vol. 937 (2014) pp 695-699*
*© (2014) Trans Tech Publications, Switzerland*
*doi:10.4028/www.scientific.net/AMR.937.695*

# A New Method and Applications of the Boundary Value Problem of Differential Equation

Hong-E LI[1, a], Xiao-Xu DONG[1, b*], Shun-Chu LI[1, c], Dong-Dong GUI[2,d], Cong-Yin FAN[1,e]

[1]School of Mathematics and Computer Engineering, Xihua University, Chengdu 610039, China

[2]Beijing Dongrunke Petroleum Technology Co.,Ltd., Beijing 100029 China

[a]lhe.8169@163.com,[b]dongxiaoxu1028@163.com, [c]lishunchu@163.com, [d]gdd05@hotmail.com, [e]fcy8843@163.com

*Corresponding author

**Keywords:** Boundary value problem; Constructive method; Kernel function, Similar structure.

**Abstract.** The similar structure of solution for the boundary value problem of second order linear homogeneous differential equation has been studied. Based on the analysis of the relationship between similar structure of solution, its kernel function, the equation and boundary conditions, similar constructive method (shortened as SCM) of solution is obtained. According to the SCM, the similar structure of solution and its kernel function are constructed for the mathematical model of homogeneous reservoir which considers the influence of bottom-hole storage and skin effect under the infinite outer boundary condition. The SCM is a new and innovative way to solve boundary value problem of differential equation and seepage flow theory, which is especially used in Petroleum Engineering.

## Introduction

The theory of similar structure of solution for the boundary value problem of differential equation means the solution, for a differential equation, can be converted into a uniform expression under different boundary conditions defining different kernel functions. Similar structures of solutions for some differential equations have been investigated by many authors in references [1-8]. In recent years, some authors built mathematical models for some reservoirs, such as homogeneous reservoir, double porosity reservoir, multilayer reservoir and composite reservoir, and found that their solutions have similar structures in three kinds of outer boundary conditions in Laplace space [9-12]. A new method is put forward on the basis of the theory, called as SCM, whose calculation does not need go on as complicated as before. Then we give the detailed steps. In this paper, according to the SCM, dimensionless reservoir pressure is constructed in Laplace space for homogeneous reservoir under infinite outer boundary condition. The SCM is a new way to solve boundary value problem of differential equation with complex boundary conditions, which is especially used in Petroleum Engineering.

## SCM of the Solution

The boundary value problem of second order linear homogeneous differential equation:

$$\begin{cases} y'' + p(x)y' + q(x)y = 0 \\ [Ey + (1+EF)y']_{x=\alpha} = D \\ [My + Ny']_{x=\beta} = 0 \end{cases} \tag{1}$$

And where $D, E, F, M, N$ are real numbers. $D \neq 0$, $M^2 + N^2 \neq 0$, $0 < \alpha < \beta$. With a unique solution, the solution of boundary value problem is the following continued fraction, which is also called similar structure of the solution for differential equation, and it is:

$$y(x) = D \cdot \frac{1}{E + \dfrac{1}{F + \phi(\alpha)}} \cdot \frac{1}{F + \phi(\alpha)} \cdot \phi(x) \tag{2}$$

And where $\phi(x)$ is kernel function:

$$\phi(x) = \frac{M\varphi_{0,0}(x,\beta) + N\varphi_{0,1}(x,\beta)}{M\varphi_{1,0}(\alpha,\beta) + N\varphi_{1,1}(\alpha,\beta)} \tag{3}$$

Function of two variables $\varphi_{0,0}(x_1,x_2) = y_1(x_1)y_2(x_2) - y_1(x_2)y_2(x_1)$ is defined by $y_1(x)$ and $y_2(x)$, which are linearly independent solutions for differential equation (1.1), and then calculate its partial derivative functions.

$$\varphi_{0,1}(x_1,x_2) = \frac{\partial}{\partial x_2}\varphi_{0,0}(x_1,x_2) = y_1(x_1)y_2'(x_2) - y_1'(x_1)y_2(x_2) \tag{4}$$

$$\varphi_{1,0}(x_1,x_2) = \frac{\partial}{\partial x_1}\varphi_{0,0}(x_1,x_2) = y_1'(x_1)y_2(x_2) - y_1(x_2)y_2'(x_1) \tag{5}$$

$$\varphi_{1,1}(x_1,x_2) = \frac{\partial}{\partial x_1}\varphi_{0,1}(x_1,x_2) = \frac{\partial}{\partial x_2}\varphi_{1,0}(x_1,x_2) = y_1'(x_1)y_2'(x_2) - y_1'(x_2)y_2'(x_1) \tag{6}$$

According to the relations between the similar structure Eq. (2) and its kernel function (3) with every part of the boundary value problem (1), the steps of constructive method can be obtained:

Step 1. Solving governing equation of the boundary value problem.

Step 2. Constructing function of two variables $\varphi_{0,0}(x_1,x_2)$ by linearly independent solutions $y_1(x)$, $y_2(x)$ of differential equation (1), and then calculate Eqs.(4)-(5).

Step 3. Constructing kernel function $\phi(x)$ by Eqs.(3)-(6).

Step 4. Constructing similar structure by Eq.(2).

**The Application of SCM in Modified Bessel Equation**

According to steps of SCM, we solve the boundary value problem (7) as follows:

$$\begin{cases} x^2y'' + xy' - x^2y = 0 \\ \left[7y + 8y'\right]_{x=1} = 9 \\ \left[3y + 2y'\right]_{x=8} = 0 \end{cases} \tag{7}$$

Step 1. Solving governing equation of boundary value problem .

Governing equation (7.1) is modified Bessel equation[13]. Two linearly independent solution of governing equation (7.1) are $I_0(x)$ and $K_0(x)$, where $I_n(\cdot)$, $K_n(\cdot)$ are the first and the second class of modified Bessel functions of order $n$.

Step 2. Constructing functions of guide solution.

Defining binary function as follows:

$\varphi_{m,n}(x,\xi) = I_m(x)K_n(\xi) + (-1)^{m-n+1}K_m(x)I_n(\xi)$.

We lead into functions of guide solution as follow:

$\varphi_{0,0}(x,\xi) = I_0(x)K_0(\xi) - K_0(x)I_0(\xi)$,

$$\varphi_{0,1}(x,\xi)=\frac{\partial}{\partial\xi}\varphi_{0,0}(x,\xi)=I_0(x)K_1(\xi)+K_0(x)I_1(\xi),$$

$$\varphi_{1,0}(x,\xi)=\frac{\partial}{\partial x}\varphi_{0,0}(x,\xi)=I_1(x)K_0(\xi)+K_1(x)I_0(\xi),$$

$$\varphi_{1,1}(x,\xi)=\frac{\partial^2}{\partial x\partial\xi}\varphi_{0,0}(x,\xi)=I_1(x)K_1(\xi)-K_1(x)I_1(\xi).$$

Step 3. Constructing kernel function $\phi(x)$ by Eqs.(3)-(6).

$$\phi(x)=\frac{M\varphi_{0,0}(x,8)+N\varphi_{0,1}(x,8)}{M\varphi_{1,0}(1,8)+N\varphi_{1,1}(1,8)}\quad(1\le x\le 8)$$

Step 4. Constructing similar structure by Eq.(2).

$$y(x)=9\cdot\frac{1}{7+\dfrac{1}{1+\phi(1)}}\cdot\frac{1}{1+\phi(1)}\cdot\phi(x)$$

**The Application of SCM in Homogeneous Reservoir**

The mathematical model of homogeneous reservoir which considers the influence of bottom-hole storage and skin effects can be transformed into the boundary value problem of ordinary differential equation in Laplace space as follows:

$$\begin{cases}\dfrac{d^2\bar{p}_D}{dr_D}+\dfrac{1}{r_D}\dfrac{d\bar{p}_D}{dr_D}=z\bar{p}_D\\ C_Dz\bar{p}_{wD}-r_D\left.\dfrac{d\bar{p}_D}{dr_D}\right|_{r_D=1}=\dfrac{1}{z}\\ \bar{p}_{wD}=\left[\bar{p}_D(r_D,z)-S\dfrac{d\bar{p}_D}{dr_D}\right]_{r_D=1}\\ \bar{p}_D(\infty,z)=0\end{cases}\tag{8}$$

And where $\bar{P}_D$—element in Laplace space of dimensionless pressure, $\bar{P}_{\omega D}$—element in Laplace space of dimensionless well bottom pressure, $r_D$—dimensionless radius, S—skin factor, $C_D$—dimensionless coefficient of wellbore storage, $R_D$—dimensionless out boundary radius.

According to the SCM, we construct kernel function in the infinite outer boundary condition, and then construct the similar structure of dimensionless wellbore pressure for the boundary value problem.

Step 1. Solving governing equation of boundary value problem.

Governing equation (8.1) is modified Bessel equation. Two linearly independent solution of governing equation (8.1) are $I_0\left(\sqrt{z}r_D\right)$ and $K_0\left(\sqrt{z}r_D\right)$, where $I_n(\cdot)$, $K_n(\cdot)$ are the first and the second class of modified Bessel functions of order $n$.

Step 2. Constructing functions of guide solution

Defining binary function as follows:

$$\Psi_{m,n}(\alpha,\beta,y)=I_m(\alpha y)K_n(\beta y)+(-1)^{m-n+1}K_m(\alpha y)I_n(\beta y)$$

We lead into functions of guide solution as follow:

$$\varphi_{0,0}\left(r_D,\xi\right)=\begin{vmatrix} I_0\left(\sqrt{z}r_D\right) & K_0\left(\sqrt{z}r_D\right) \\ I_0\left(\sqrt{z}\xi\right) & K_0\left(\sqrt{z}\xi\right) \end{vmatrix}=\Psi_{0,0}\left(r_D,\xi,\sqrt{z}\right)$$

$$\varphi_{0,1}\left(r_D,\xi\right)=\frac{\partial}{\partial\xi}\varphi_{0,0}\left(r_D,\xi\right)=-\sqrt{z}\Psi_{0,1}\left(r_D,\xi,\sqrt{z}\right)$$

$$\varphi_{1,0}\left(r_D,\xi\right)=\frac{\partial}{\partial r_D}\varphi_{0,0}\left(r_D,\xi\right)=\sqrt{z}\Psi_{1,0}\left(r_D,\xi,\sqrt{z}\right)$$

$$\varphi_{1,1}\left(r_D,\xi\right)=\frac{\partial^2}{\partial r_D\partial\xi}\varphi_{0,0}\left(r_D,\xi\right)=-z\Psi_{1,1}\left(r_D,\xi,\sqrt{z}\right)$$

Step 3. Constructing kernel function $\phi(x)$ by Eqs.(3)-(6).

$$\phi(r_D,z)=-\frac{K_0(\sqrt{z}r_D)}{\sqrt{z}K_1(\sqrt{z}r_D)}$$

Step 4. Constructing similar structure by Eq.(2).

$$\bar{P}_D\left(r_D,z\right)=\frac{1}{z}\cdot\frac{1}{C_Dz+\dfrac{1}{S+\phi\left(1,z\right)}}\cdot\frac{1}{S+\phi\left(1,z\right)}\cdot\phi\left(r_D,z\right)$$

## Conclusion

We extend the application of the theory of similar structure of solution, and obtain the SCM for the boundary value problem of second order linear homogeneous differential equation. Firstly, the two linearly independent solutions to governing equation are solved. Secondly, functions of guide solution are constructed by using two linearly independent solutions. Thirdly, the kernel function is constructed with functions of guide solution and coefficients of homogeneous boundary condition. Finally, the kernel function and the coefficients of inhomogeneous boundary condition are used to construct the similar structure of solution. SCM avoids the complicated calculation process which is beneficial to scholars. In this paper, we use the SCM to construct the dimensionless reservoir pressure of homogeneous reservoir which considers the influence of bottom-hole storage and skin effect under the infinite outer boundary condition in Laplace space. The research, as a deep development of seepage flow theory in porous media, is convenient to design well test analysis program. It will be the cornerstone of SCM's development.

## Acknowledgment

This Project is supported by the Scientific Research Fund of Sichuan Education Provincial Department of China under Grant No.12ZA164.

## References

[1] Shun-Chu LI. The Similar Structure of Solution of Second-order Linear Homogeneous Differential Equations with Constant Coefficients on the Boundary Value Problem (in Chinese) [J]. Journal of Xihua University (Natural Science Edition), 2007,26(1):84～85.

[2] Shun-Chu LI. The Similar Structure of Solution to the Boundary Value Problem for Second-order Linear Homogeneous Differential Equations (in Chinese) [J]. Journal of Xihua University (Natural Science Edition), 2009,28(5): 40～41(to 90).

[3] Ying CHI, Shun-Chu LI, Juan YAN. Similar Structure of Bessel Equation with Parameter $\lambda$ on Boundary Value Problem (in Chinese) [J]. Journal of Dalian Jiaotong University, 2010,31(5):109-111.

[4] Zong-Rong CHENG, Shun-Chu LI. The Similar Structure Method Solving the Boundary Value Problem of Bessel Equations (in Chinese)[J]. Journal of Sichuan Normal University (Natural Science), 2011,34(6): 850-853.

[5] Cong-Yin FAN, Shun-Chu LI, Dong-Xu XU. Similar Structure Method of Solution of a class of Thomson Equation Boundary Value Problem (in Chinese)[J]. Advances in Applied Mathematics, 2012, 1(2): 41-48.

[6] Jun-Hua SHI, Shun-Chu LI, Xiao-Lin WANG and Dong-Dong GUI. A new method for solving boundary value problem of composite Hermit Equations [J]. Advanced Materials Research, vols.753-755 (2013): pp2851-2854.

[7] Shun-Chu LI, Xiao-Qing WU. The Similarity Structuring Method of Boundary Value Problems of the Composite Differential Equations (in Chinese) [J]. Journal of Xihua University (Natural Science Edition), 2013, 32(4): 27-31.

[8] Xiao-Xu DONG, Shun-Chu LI, Dong-Dong GUI, Jun PU, Hui-Chun LI. Similar Constructing Method for Solving the Boundary Value Problem of the Composite First Weber System[J]. American Journal of Applied Mathematics and Statistics, 2013, Vol.1(4): 76-82.

[9] Shun-Chu LI, De-Hua LIU, Pu-Zai ZHANG. Pressure distribution of the homogeneous reservoir with different boundary conditions (in Chinese)[J]. Journal of Jianghan Petroleum Institute, 2001, 23(2):16-17.

[10] Shun-Chu LI, Peng-She ZHENG, Yu-Fei ZHANG. The similar structure of pressure distribution in the homogenous reservoir (in Chinese)[J]. Pure and Applied Mathematics, 2006,22(4):459-463.

[11] Shun-Chu LI, Wei Li, Xiaoping Li, Li Xu. The Construction Method for Solving Radial Flow Problem through the Homogeneous Reservoir [J]. Applied Mathematics,2012,3(6):517-522.

[12] Cui-Cui SHENG, Jin-Zhou ZHAO, Yong-Ming LI, Shun-Chu LI* and Hu Jia. Similar Construction Method of Solution for Solving the Mathematical Model of Fractal Reservoir with Spherical Flow[J]. Journal of Applied Mathematics, vol. 2013, Article ID 219218, 8 pages, 2013.

[13] Shi-Shi LIU, Shi-Da LIU. Special Function [M]. Beijing: China Meteorological Press, 2002.

*Advanced Materials Research Vol. 937 (2014) pp 700-702*
*© (2014) Trans Tech Publications, Switzerland*
*doi:10.4028/www.scientific.net/AMR.937.700*

# Changchun College of Architecture Electrical Design for Sheling Campus Library

Ting-Ting LI

Changchun College of Architecture Changchun Jilin China

angelkoko@sina.com

Ting-Ting Li

**Keywords:** Load grade Low voltage distribution Lighting design Lightning protection grounding

**Abstract.** This paper introduces the Changchun College of Architecture sheling Campus library building electrical design process

## Overview

The library she Ling campus Changchun Institute of architecture, for the purpose of the school library, the school of landmark buildings, construction area of 19840m2, frame structure, form the basis for independent foundation, the ground layer seven, local eight, the height of the building is 46.7m. The library in the design process, attention to the requirements of electrical energy-saving technology, partition functions of lighting, lighting, to achieve energy saving and environmental protection,The process of the electrical design is introduced as follows.

## Power Supply System

### Load Levels

According to the people's Republic of China National Standard "code for design of Library Buildings" GBJ 38 - 99, the collection of more than 1000000 copies of the library, the electricity load levels should not be less than two; other libraries, electricity load levels should not be less than three. The museum collection of 700000 volumes, the emergency lighting, elevator electric power to load two, other power load and general load to load three.

### Electricity Load

According to the professional proposed electricity load data, using "demand coefficient method" load calculation, the total computational load is 453kw, the natural power factor COS φ =0.76

### Power Supply

The project 10kv/0.38kv power from the adjacent low voltage transformer substation, low voltage cable is introduced, the standby power supply by the diesel generator room with low buried cable; emergency lighting using EPS centralized power supply battery box.

### Power Factor Compensation and Measurement

According to the "public regulation" requirement, all the fluorescent light compensation, so that the power factor of not less than 0.9, in the households centralized metering mode. This project according to the results of load, wattless power compensation value is 200kVar, the compensated power factor for COS φ =0.93

## Low Voltage Distribution System

Low voltage power distribution system used to power 380/220V radiation and trunk type combination. A layer of a distribution, basic in the load center, close to the GB channel. Each layer is arranged the power box, lighting box, concealed in the corridor walls.

Lighting branch outlet switch control in the 16A plane lamp, according to the location and layout (a common socket socket loop of not more than 10) to determine the number of branches, the 5 lighting box of each layer, using modular terminal combination distribution box, each box is not more than 45 modulus.

Also, according to the air distribution and distribution box arrangement of electric equipment in the load center principle, to determine the 2 power box of each layer, the two layer of a 8X4.2m2 in the copy room, copy machines are more, the addition of a power distribution box power supply for the copy room; the two layer before and after each have a hot air screen, 2 additional power distribution box; in addition, the seven layer elevator machine room, set up a separate power box.

All distribution boxes are iron flush, bottom skin from 1.5m.

## Lighting Design

Lighting design library to meet GB 50034 - 2004 "architectural lighting design standards" of the illuminance standard requirements and the power density index under the premise, but also consider the particularity of Library lighting. The reading room of the library for the collection reading one book for reading. Book and reading desk room layout, a reading desk near the window side, shelf on the other side. In considering the illuminance partition. The reading area mainly considering the horizontal illuminance, and stack area mainly consider the vertical illuminance. Horizontal illuminance reading area according to the specification is in from 0.75m2 level to 300lx, vertical illuminance bookshelf is apart from the ground 0.25 m height 50lx. Luminaire arrangement should be combined with bookcases and reading desk, make full use of horizontal illumination lamps or vertical illuminance, as shown in figure 1.

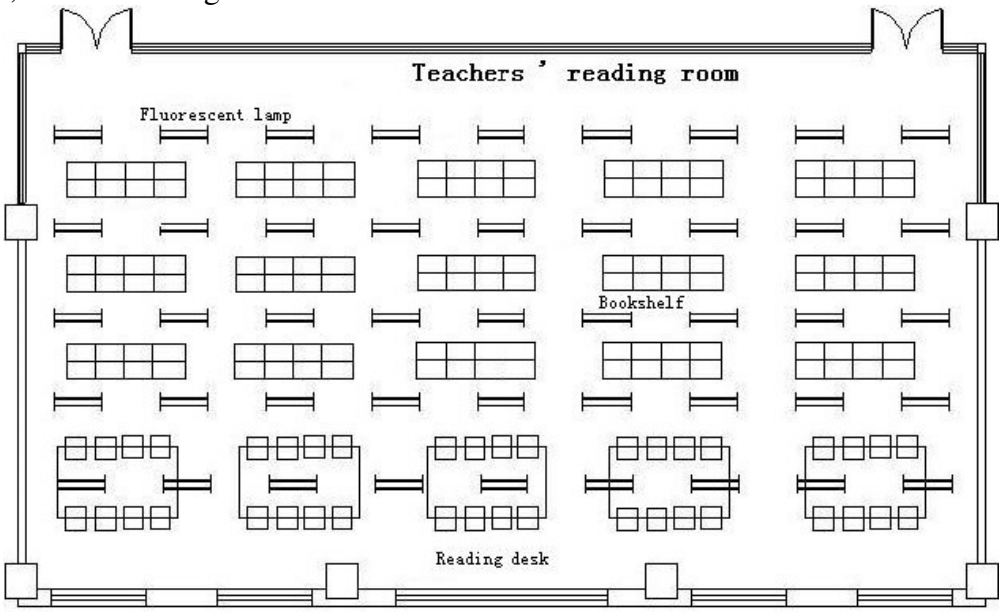



Fig. 1. The teachers' reading room lighting layout

## Fire Alarm and Linkage System

The university library characteristic of all (1) building area, building structure is complex, the University Library in order to highlight its campus culture, building taste, in order to become the representative buildings in campus, will be designed to be more complex, this also is the automatic

fire alarm and fire fighting system dynamic combination brings higher requirements; (2) many flammable items, books and documents, are large quantities of flammable; (3) personnel intensive, once there is a fire, no evacuation of good, can cause very serious casualties. It is because of the common features of university library, give the fire automatic alarm system and fire linkage system leads to a more stringent requirements, therefore, the design of the fire alarm system is the priority among priorities for electrical design of University library. The design of fire protection system used in the smoke, temperature sensing detector and infrared detector, some large space should be used with optical cross-section detector fire gun action and infrared microwave double check detector, fire hydrant alarm button according to the specification

## Lightning Protection and Grounding

Lightning protection level of the project is the three stage, the lightning protection device buildings meet preventing thunder and lightning wave intrusion, and set the general equipotential connection, Phi 12 galvanized steel bar along the roof parapet lightning protection zone, roof lightning protection connecting wire mesh is not more than 20mX20m, with reinforced concrete columns or shear walls in the building of four Phi 16 main ribs long welding as downlead.

For grounding, grounding for the building pile foundation, foundation on the axis of the upper and lower four root length of main reinforcement in the two layer welding forming device natural grounding, grounding resistance $R \leq 1$ ohm. If you do not meet, should play the auxiliary grounding device fill in outdoor. All metal components, such as: all outstanding roofing metal ventilation pipe shall be reliable welding and lightning protection zone.

The protection of the lightning protection and grounding, grounding of electrical equipment, communications room to share the same grounding device, requirements of the grounding resistance is less than 1 ohm, measured does not meet the requirements, adding the artificial grounding.

Where the normal is not charged, and when the insulation damage may appear all electrical equipment metal casing voltage shall be earthed reliably.

The above lightning belt, lead, lightning protection network and reliable welding electrode between the artificial inoculation, formed the architectural integrity of the lightning protection and grounding system.

## Conclusions

With its special electrical design of University library. In order to make the University Library electrical system can better serve the readers, also need to design personnel continue to accumulate experience, perfect design. The library was built in 2011 and put into use, various functional areas and distribution system reached the design requirements. Hope that through this paper can provide a reference for similar engineering design.

## Reference

[1] Code for design of Library Buildings GBJ 38 - 99

[2] Standard for lighting design of buildings GB-50034-2004

[3]Code for electrical design of civil buildings JGJ16-2008

*Advanced Materials Research Vol. 937 (2014) pp 703-706*
*© (2014) Trans Tech Publications, Switzerland*
*doi:10.4028/www.scientific.net/AMR.937.703*

# Optimized Research for Mobile Communication Strategy Based on Parallel Computing

Jian-wei ZHANG[1,a], yun-lei YAO,[1,b]

[1]Dept. of Computer and Communication Engineering, Zhengzhou University of Light Industry, Zhengzhou, 450002, China

[a]ing@zzuli.edu.cn, [b]yaoyunlei@163.com

**Keywords:** Parallel computing; Speed-up ratio; Optimization; Communication mode;

**Abstract:** In order to improve the speed of simulation, one of the feasible approaches in mobile communications is parallel computing. In this paper, the operating environment will be achieved with MPICH2. Parallel computing is suitable for large scale computing tasks. An important factor which limits the speed-up ratio improve is that parallel computing cannot be achieved in communication process.Selecting the finite difference method, taking a two-dimensional steady-state heat distribution problem act as an example. By choosing domain decomposition method divide the entire data area into multiple sub-domains. Ultimately, the parallel program is designed in MPI's Peer-to-Peer Model. By modifying the communication mode and the communication process, the speedup is substantial increased, closing to ideal values.

## Introduction

Computer simulation is an important method of scientific practices of material forming field. As the requirements on the material forming simulation in the field of production design continuously improved, forming simulation encountered new challenges. Especially in the simulation of large or sophisticated products, it takes too long time, which beyond people's ideal demand. This paper mainly studies the realization of the forming simulation on computer cluster and feasible issues, so as to realize the task-level scheduling to take advantage of the limited computing resources sources, and we can achieve the maximization of performance[1-2].

Materials science and engineering of HuaZhong University of Science and Technology established a simulation software sharing platform can be used for injection, series casting and stamping. Cluster computing research and software development can be achieved by this platform. Series software on the platform are multi-core, and has achieved good Effect, speedups reach 1.536 in stand-alone Dual-core environment. The serial data dependencies in the program can be solved by creating stamping software FASTAMP two-way relationship between the elements and nodes, and the program has been optimized to quantify, speed ratio in a single dual-core environment can reach 1.9.It is 63.5% faster than the general software and the computational efficiency can be increased by 200%.In dual-core and quad-core environments, respectively, the maximum acceleration can reach1.8 and 3.9 by founding software CAE / Inter CAST to analysis and modified neck code.

The above mentioned three soft wares did not achieve in the cluster environment running and acceleration, although they achieve a good acceleration in dual-core and even quad-core environment. In order to realize a larger speedup, restrictions must be broken. We can convert the program to a cluster environment, so that the software can make a breakthrough in the system and hardware limit. At that time, it can provide a reference for such issues resolved. Meanwhile, the hardware of each computer in the cluster conditions is not the same when calculated on a cluster of computers, so that the computing capacity is different. How to optimize algorithm to improve the parallel algorithm design speedup in algorithm design is a key issue. In this paper, our research will take an engineering problem as an example, MPI is used to program. MPI (Message Passing Interface) is a parallel programming platform which global industry, government and research departments jointly launched the suit Interposes to standard messaging, version of this paper is MPICH2.

**Parallel Algorithm Design and Parallel Solving**

We can describe the establishment the mathematical model and solving equations of the heat distribution of steady-state two-dimensional rectangular plate as an example, then the parallel computing model of numerical simulation will be designed, and finally to write parallel programs. The two-dimensional heat conduction differential equations is built by choosing material in the process of thermal conductivity cell surface as the research object, and inspect the balance of energy. In the x, y direction thermal heat conduction equations:

$$dQ_x - dQ_{dx} = \frac{\partial}{\partial x}\left(\lambda \frac{\partial T}{\partial x}\right) dx \tag{1}$$

$$dQ_y - dQ_{dy} = \frac{\partial}{\partial y}\left(\lambda \frac{\partial T}{\partial y}\right) dx \tag{2}$$

(T:temprature,Q: element for heat, $\lambda$ :thermal conductivity)

There is no inner heat, Changes of the total heat element in t time is:

$$dQ = dQ_x - dQ_{dx} + dQ_y - dQ_{dy} \tag{3}$$

Equation (3) is the mathematical models we usually used to analysis the problem of heat distribution in steady-state. Then we can get (4) through the finite difference approximation.

$$\frac{T_{i+1,j} - 2T_{i,j} + T_{i-1,j}}{\Delta x^2} + \frac{T_{i,j+1} - 2T_{i,j} + T_{i,j-1}}{\Delta y^2} = 0 \tag{4}$$

The steady state temperature of any node can be obtained by iterative. Each point indicate the steady-state solution in rectangular coordinates sheet. The x dimension is divided into n parts, y dimension is divided into m parts, define h=x/n, and k=y/m, then x=h, and y=k. Assuming uniform distribution of points on the grid:

$$T_{i,j} = \frac{T_{i+1,j} + T_{i-1,j} + T_{i,j+1} + T_{i,j-1}}{4} \tag{5}$$

According to the first step, we can obtain new estimates by iterative calculation, then we can get the results of i+1 iteration from the results of the I iteration by Jacobi method.

The changes in other parameters of each unit are ignored except the temperature in the simulation, so we only need to know the adjacent cells' temperature in each calculation of the whole simulation. The whole calculation data domain is divided into multiple sub-domains. Each subfield is assigned to a node by calculation as a task. Increasing communication between the processor utilization and minimizing the balance of inter-processor are considered in the division of sub-domains. When the problem scale is too large to solve, sub-domains should be increased to reduce the computation time in the total cost of the proportion. Adjacent data unit is needed to solve each cell, so there are at least two meshes overlap in the adjacent sub-domain decomposition. In order to reach a minimum computation, 2 overlapping grid should be taken. The data domain decomposition form is as shown in figure 1.The parallel mode referred to parallel mode.

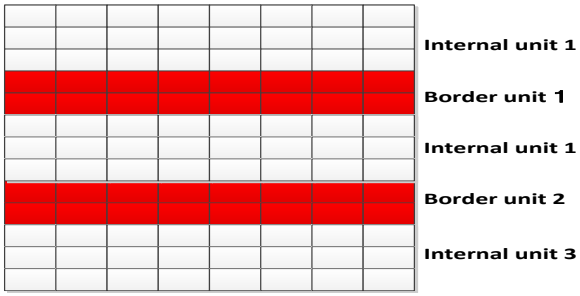



Fig. 1. Data domain decomposition

Each sub-domain unit can be divided into two parts: the inner unit and border unit. Calculate in the internal unit is independent from the adjacent sub-domain, whereas compute of bordering unit depends on the data sub-domains. We need to communicate with adjacent sub-domain to obtain the data before the each iteration except the first iteration. As the analysis above, MPI peer mode can be used to design parallel program. Throughout the program is running, the status of each node is the same and the functions are basically the same. The whole calculation process is as shown in figure 2.

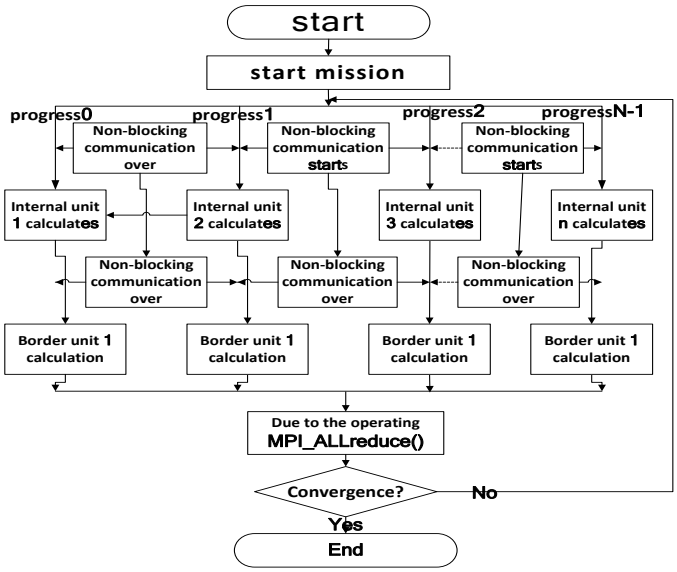



Fig. 2. Parallel algorithm process

## Conclusion

The test will be done on a Quad-core server, CPU is Intel Xeon X3210,2.13 GHz,4G RAM, to complete the test for block communication and non-blocking communication measurements with two different communication modes respectively, compared with the consumption of serial program time, then we can get the efficiency of parallel program. The relationship between speed ratio and size of computing is as shown in figure 3.The accelerate will be stable when the computing scale has reached a certain size, no longer increases obviously. At the same time, on-blocking communication mode of parallel computing has a distinct improvement relate to the blocked communication mode in both the numerical size and ratio. Especially the accelerate has reached 3.871, close to the ideal speed than 4, it is very significant. It can be concluded that non-blocking communication mode has obvious advantages than the blocked communication mode in computing and communications. In this case, on-blocking communication mode should be chosen.

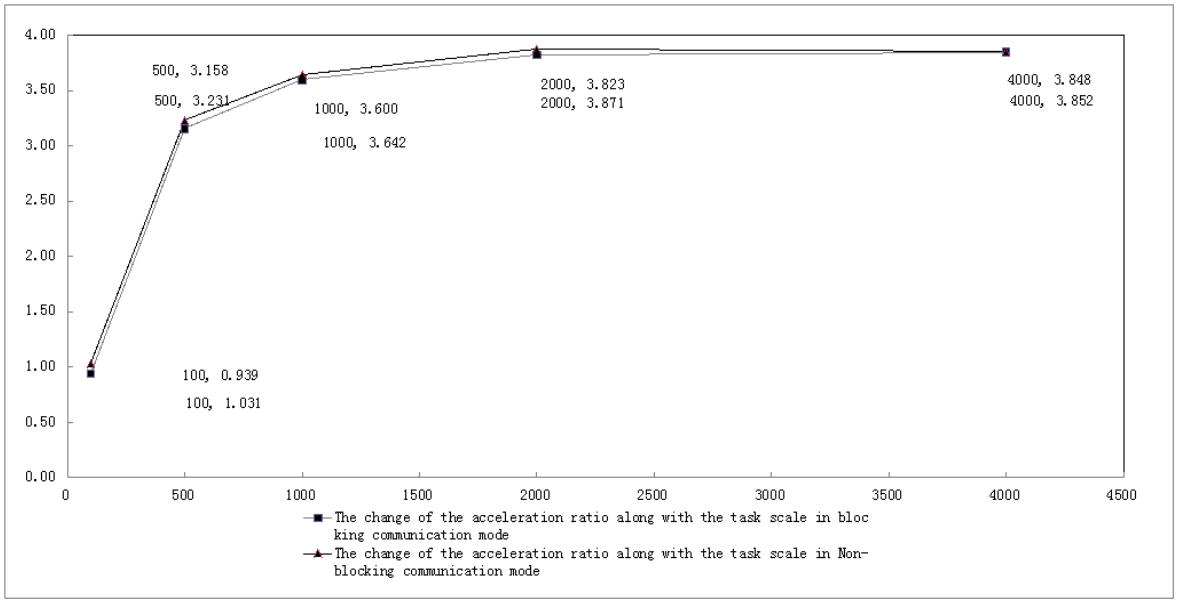



Fig. 3. The relationship between speed-upratio and computational amount

**Reference**

[1] Garland M., Le Grand S., Nickolls J., Anderson J., Hardwick J., Morton S., Phillips E., Zhang Y., Volkov V.: Parallel computing experiences with CUDA. IEEE Micro 2008,28(4),13–27.

[2] Li J., Tang G., Hu T.: Optimization of a precise integration method for seismic modeling based on graphic processing unit. Earthquake Sci. 2010.23(4),387–393.

[3] Sen V., Sen M.K., Stoffa P.L.: PVM based 3-D Kirchhoff depth migration using dynamically computed travel-times: an application in seismic data processing. Parallel Comput. 1999,25,231–248.

[4] Komatitsch D and Tromp J. A perfectly matched layer absorbing boundary condition for the second-order seismic wave equation. Geophys J Inter,2003,154(1): 146–153.

[5] Tang G, Hu T and Yang J . Applications of a precise integration method in forward seismic modeling. The 77th SEG Annual International Meeting,Expanded Abstract,2007,2130–2134.

[6] Sutter H,Larus J.Software and the Concurrency Revolution.Computer and Information Science,2005,3(7):54-62.

[7] Y.C.Tang,B.Jin,Q.Zhang.Granular support vector machines with association rules mining for protein homology prediction.Artificial Intelligence In Medicine,2005,35,121-134.

[8] Zhizhong Sun, Xiaolei Chen. Parsing out of Infrared Thermal Imaging Temperature Field Based on BP Neural Network. Applied Mechanics and Materials, Vol.437(2013),pp.501-504

[9] Zhizhong Sun, Xiaolei Chen. Multi-scale Edge Detection of Digital Image Based on Improved Mallat Wavelet Decomposition Algorithm . Sensors & Transducers, Vol. 25, Special Issue, December 2013,p. 239-243.

*Advanced Materials Research Vol. 937 (2014) pp 707-711*
*© (2014) Trans Tech Publications, Switzerland*
*doi:10.4028/www.scientific.net/AMR.937.707*

# The Stochastic Imperfection Method of Sheet Space Structure Based On Truncated Univariate Normal Distributions

Tian-jiao JIN[1, 2] Xiao-ming GUO[1,2 ,a]

[1] School of Civil Engineering, Southeast University, Nanjing, China

[2] Jiangsu Key Laboratory of Engineering Mechanics, Southeast University, Nanjing, China

[a]xmguo@seu.edu.cn

**Keywords:** Sheet Space Structures, Sensitivity Imperfection, Truncated Univariate Normal Distributions, Local Spherical Coordinate System, Stochastic Imperfection Method

**Abstract.** The initial geometric imperfections is a key issue of the stability analysis of sheet space structures. A new described method of the initial geometric imperfections which is located in local spherical coordinate system is given, and the random imperfection variable is assumed to follow a truncated univariate normal distribution (TUVN). A well working envelope function for TUVN is chosen, and the acceptance rate is high for constrained region of the design code. The method provided in the paper is called spherical truncated normal stochastic imperfection method (STNS). The results of consistent mode imperfections method, traditional stochastic imperfection method and STNS method are compared, by which some conclusions that are useful for the design and the study of sheet space structures are obtained.

## Introduction

Sheet space structure is a new structure system which is light weigh and high strength [1,2]. As a common kind of structure for important buildings, the imperfection of the structure is inevitable which is caused by installation deviation, initial bending, initial eccentricity, initial stress and other reasons[3]. Therefore, the research of imperfection sensitivity is one of the important subjects of sheet space structure. There are two kinds of the imperfection analysis methods. One is called determined imperfection method, for example," Measured Imperfection Method[4] "," Consistent Mode Imperfections Method"," Improved Consistent Mode Imperfections Method[3] ",and so on. The methods are that analyzing the stability of imperfection structures, of which the imperfection is confirmed, to get critical load and buckling path. The methods can be obtained by a simple calculation, but it is hard to apply in the imperfection stability analysis of sheet space structure. The other is called stochastic imperfection method, for example, "Effect Function Imperfection Method "," Stochastic Imperfection Mode Method[2]", and so on. The methods are supposed that the imperfection is random and uncertain, and then the results of critical load and its statistical laws are obtained by stochastic computation. The reliability of these methods is high, but the computational complexity is large. Therefore, to improve the efficiency is an important research on the method.

In the paper, a new described method of the initial geometric imperfections which is located in local spherical coordinate system is given because the structures could be well simulated. The random imperfection variable is assumed to follow a truncated univariate normal distribution (TUVN). A well working envelope function for TUVN is chosen because the acceptance rate is high for constrained region of the design code. We name the foregoing method as spherical truncated normal stochastic imperfection method (STNS). The excellence of STNS method is proved by the stability analysis results for sheet space structures.

## Description Method about Sampling Method Imperfection

The structural imperfections are a wide variety of sorts, including installation deviation, initial bending, initial eccentricity, initial stress and others. Initial bending and initial eccentricity could be constrained in the region which is defined by the code, and they do not be considered as main

influence factors for the whole structure stability. Geometric imperfections due to installation deviation and Initial stress. Therefore, the geometric imperfections is as the main object of the study.

In the traditional stochastic imperfection method, the geometric imperfections is in Cartesian coordinate system, the maximum of geometric imperfections in $X, Y, Z$ coordinate orientations are $R$, the random variable of geometric imperfection is $RX/2$, where $X$ follows the standard normal distribution, the range of the random variable is $[-R, R]$, therefore ,the range of X is $[-2, 2]$. N samples are drawn from $X \sim N(0, 1)$ as X component of the imperfection mode. Similarly, the Y and Z components are obtained in the same method. In the code, the maximum of geometric imperfections is R. It means the maximum distance between real location and designed location is R, but in the foregoing method, the distance is $\sqrt{3}R$. Therefore, a new described method of the geometric imperfections is given. The imperfection variable is represented by a local spherical coordinate system:$(r, \theta, \phi)$, in which the designed location of each node is origin, $r$ is the distance of between real location and designed location, and $\theta$ and $\phi$ represent the direction of the imperfection vector. Obviously, $\theta$ component follow the uniform distribution $Unif(0, \pi)$ and $\phi$ component follow the uniform distribution $Unif(0, 2\pi)$. For $r$ component, if it assumes by the foregoing method, the range is$[0, R]$, in this time,$P(0 \leq RX/2 \leq R) = 47.72\%$, it does not meet for the actual situation. So the probability distribution function (pdf) adjusts into truncated univariate normal distribution (TUVN), and its pdf is given by

$$X \sim TN(0, 1 : a, b), f_X(x) = \frac{\phi(x)}{\Phi(b) - \Phi(a)} I(a \leq x \leq b))$$

In summary, $r$ component of the random imperfection vector is $RX/2$, the range is $[0, R]$ ,$X \sim TN(0, 1 : 0, 2)$.

Although there are wide range of applications of TUVN distributions in statistics and econometrics, an efficient method to generate samples from a TUVN distribution is not so straightforward. The rejection sampling method can be used, but it is hard to identify a well working envelope function for the target distribution, and thus very low acceptance rates can occur for some constrained regions. In the paper, the mixed rejection sampling methods is applied which the region is limited in $[0, 2]$. This method [5]is stated as below.

To draw a sample from$X \sim f(x)$, if for all $x$, there exists a constant$M \leq 1$, and a known density function $g(x)$ defined on a common support with$f(x)$, such that $f(x) \leq Mg(x))$, then it is sufficient to generate $x \sim g$ and $u \sim Unif[0, 1]$; and take $x$ as a sample $\xi$ from $f(x)$,until $u \leq f(x)/Mg(x)$. The resulting acceptance rate is then $1/M$, and this acceptance rate is maximized at $M = M_{opt} == \sup_{x:g(x)>0} \frac{f(x)}{g(x)}$. The flowchart is shown in Fig 1.

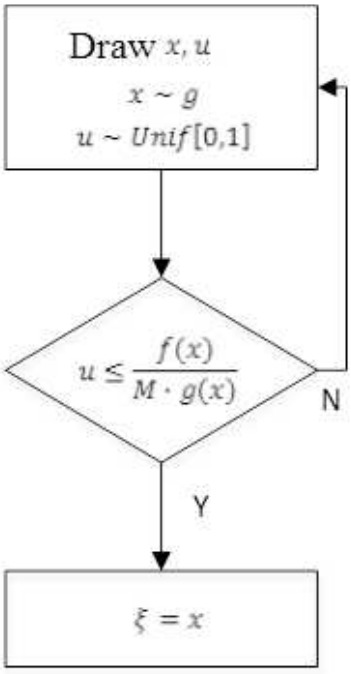



Fig. 1. Mixed Rejection Algorithm Flowchart

Now, the choice of the envelope function $g(x)$ is a key issue for high acceptance rates. In the application of imperfection analysis of structure, Half-normal distribution can be considered as the well working envelope distribution for sampling. , a candidate $x$ is drawn from$N(0,1)$,retain $x$ if $|x| \in [0,2]$ .The corresponding acceptance rate is compared with other common envelope distribution in the table 1.It is better working than others.

Table 1. The Acceptance Rates of Common Envelope Distribution

| | Normal | Half-normal | Uniform |
|---|---|---|---|
| Generality | $\Phi(b)-\Phi(a)$ | $2(\Phi(b)-\Phi(a)),a>0$ | $\frac{\Phi(b)-\Phi(a)}{(b-a)\phi[bI(b\leq 0)+aI\geq 0]}$ |
| $[0,2]$ | 0.4772 | 0.9544 | 0.5981 |

**The Application of STNS**

As already stated in previous sections, we improved the stochastic imperfection method by located initial geometric imperfections in local spherical coordinate system and by assumed the random variable follows TUVN distribution. Hence, spherical truncated normal stochastic imperfection method (STNS) is named. Now, the excellence of STNS is shown in bellow section.

The structural model[2] in the paper was selected from one of experiments by the Institute of Space Structure and Form in Southeast University , as shown in Fig. 2.The model is a hexagon spherical flat shell, which is formed by 54 sheets, 37 nodes and 90 bars. The sheets are 0.7mm-thick A3 steel boards. The bars are $\phi 12 \times 2$ tubes. And all nodes fall in the sphere of radius 1950mm, diagonal span of 1500mm, vector height 150m. Bearings are welded. The load condition is forcing on the midpoint. Material constants of bar are E=192GPa, =340MPa.

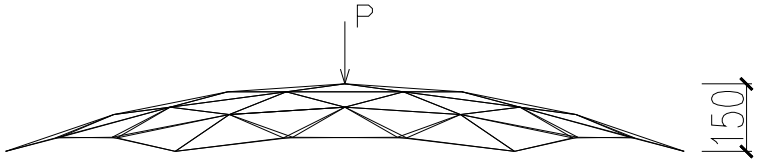
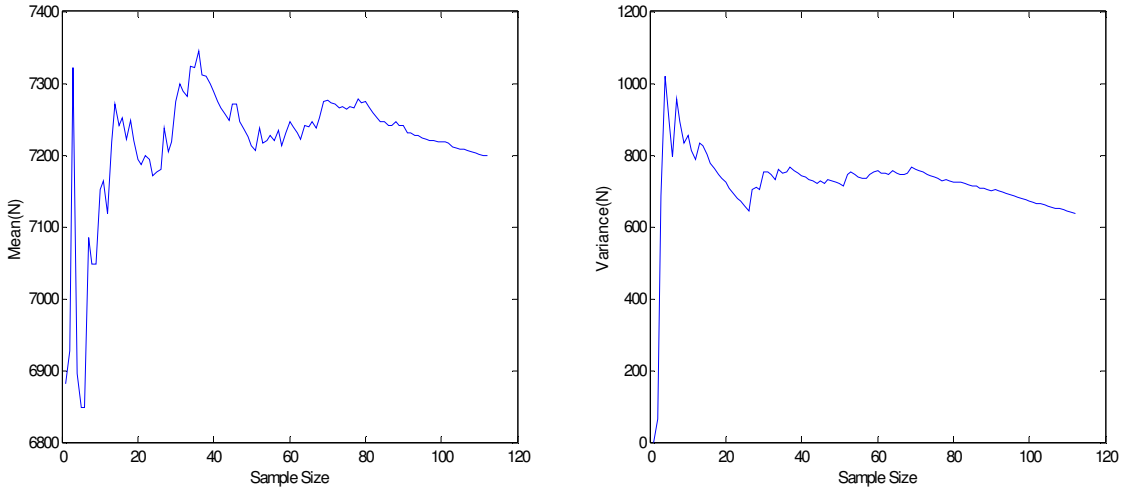



Fig. 2. Sheet Space Structure

The size of the samples is assumed be 100, and the maximum of geometric imperfections is $L/300$, wherein , $L$ is the span of the model. 100 samples are drawn from $X \sim TN(0,1:0,2)$,and make $RX/2$ as $r$ component of the imperfection mode. Meanwhile, 100 samples are drawn from $Unif(0,\pi)$ and $Unif(0,2\pi)$ individually as $\theta$ and $\phi$ component. The three components are independent and uncorrelated .Therefore, 100 imperfection modes are sampled by the foregoing method. The load - displacement whole process is calculated for the structures applied the imperfection modes. The numerical characteristics about critical load is achieved which is shown in Fig. 3.




(a) (b)

Fig. 3. Critical Load Numerical Characteristics

The $95\%$ percentile is required as the critical load of the structure, which is ,and its reliability is $95\%$.However, the reliability of the load obtained by consistent mode imperfections method and traditional stochastic imperfection method are , obviously, they are much lower than the load obtained STNS. The comparison is shown in table 2.

Table 2. Comparison of Stns, Consistent Mode Imperfections Method And Traditional Stochastic Imperfection Method

| | STNS | Traditional Stochastic Imperfection Method | Consistent Mode Imperfections Method |
|---|---|---|---|
| Critical Load(N) | 6130 | 6167 | 6240 |
| Reliability(%) | 95 | 94.1 | 93 |

## Conclusions

1. The new described method of the initial geometric imperfections which is located in local spherical coordinate system is given. It is more in line with the real structures.

2. The well working envelope function for the target distribution is chosen, its acceptance rate is higher than others, in the other words, it is much more efficient due to the choice.

3. The results of consistent mode imperfections method, traditional stochastic imperfection method, STNS method are compared to show high reliability of STNS. Therefore, the STNS is well working for the imperfection analysis.

**Reference**

[1]Tang, G. Zhao, Q.L. and Zhao, C.Q.,Stability analysis and research of Sheet Space Structure system with defects, Civil Engineering Journal, (2008).16-21

[2]Zang GH, “Research on the stability of the sheet space structure with stochastic imperfection”, Nanjing, Southeast University, (2008).

[3]Chen D ,Zhao CQ, Wang XX. etc. Improved consistent imperfect buckling analysis method for stability analysis of sheet space structure. Industrial Construction. 37(2007).504-506.

[4]Tang G, Yin LF, Zhao HL .etc. Theoretical and experimental study on the stability of steel roof structure of abnormal hyperboloid shell with imperfections CHINESE JOURNAL OF APPLIED MECHANICS Vol.28 No.4 Aug. 2011.

[5]Li Y, Ghosh S. Efficient Sampling Methods for Truncated Multivariate Normal and Student-t Distributions Subject to Linear Inequality Constraints. NC State Department of Statistics Technical Reports, (2013).

# Keywords Index


13Cr Steel 168
2,2-Dimethylol Propionic Acid 51
3D-Braided Thick Composites 29

## A

$A_2$+$B_4$ Approach 80
ABAQUS 324, 531
Accelerator 214
Accessories Fault Rule Prediction 315
Acetate 34, 193
Acute Toxicity 571
Adhesive Shear Strength 330
Adsorption 9, 109, 276, 646
Adsorption Mechanism 218
Ag-Cu-P Filler 154
Ag-Cu-Zn Filler 154
Aircraft De-Icing 330
Aircraft Hydraulic System 315
ALB 686
Alkaline Activator 472
Alkalinity 70
Allergy 286
Alloying Elements 178
Alpine Wetland Ecosystems 565
Aluminum Alloy 150
Analysis 659
Analytical Model 324
ANSYS 428
AOP 620
Application 46
Arc Detection 409
Architectural Wood Carvings of the Ancestral Temple of Chen Family 456
Artificial Jade 462, 476
Aspect Ratio 444
Aspheric Surface 396
Aspherical Surface 391
ATP 691
AZ31B/LY12 172

## B

Baokening Granule 118
Basic Fuchsin 9
Battery 495
Bearing Fault 351
Bending 391
Biodiversity 491
Biogas Fermentation 291, 502
Biogas Production Potential 502
Bioimaging Fluorescence 256
Biological Activity 308
Biological Diversity 663
Blast Furnace Slag 462, 476
Boundary Condition 424
Boundary Value Problem 695
Box-Shaped Steel 531

## C

Cadmium 224
Calcium Silicate 652
Carbaryl-Imprinted Capillary Monolith 248
Carbon Steel 109
Carding Machine 400
Catalyst 363
Cathode Material 515
Cavitation 41
Cell Wall Degrading Enzymes 282
Cement 450
Cement Gel Sand 472
Chelation 218
Chl-a 669
City Complex 479
$CO_2$ 168
$Co_3O_4$ 231
Coarse-Grained Soil 585
Coarsening 64
$COD_{Mn}$ 669
Coefficient of Thermal Expansion (CTE) 145
Coiling Machine 336
Commercial Pure Titanium (CP-Ti) 162
Communication Mode 703
Complications 286
Composite Foundation Settlement 438
Composite Soil Nailing Wall 433
Composition Feature 456
Conceptual Model 632
Concrete 450

Conducting Polymer 17, 23
Conductivity 99, 224
Constitutive Model 130
Constructive Method 695
Contaminated Soil 646
Contours Potential 409
Copper 141, 154
Cornstalk 276
Correlation Coefficient 548
Corrosion 105, 193
Corrosion Behavior 168
Corrosion Inhibitor 109
Craftsmanship 456
Crop Water Production Function 548
Crown Debris 578
Crystal Orientation 64
Cu (II) Ions 218
$Cu_2O$ Nanoparticles 3
Cultural Aesthetics 456
Cunninghamia Lanceolata 578

## D

Data Management 526
Decolorization Efficiency 237
Deep-Cone Thickener 386
Deep Foundation Pit 433
Density 99
Density Functional Theory 113
Detonation 260
Diameter Ratio 357
Diaphragm Pump 386
Diesel 363
Diffusion Bonding 172
Dimocarpus Longan Pericarp 502
Dispose 105
Distillation 607
Distribution 297
DNA 244
Dongtiaoxi 597
Draw Ratio 86
Drilling Fluid 46
Drinking Water Purification 607
Dust 187
Dynamic Characteristic 624

## E

Effective Buckling Length 424
Elastic Modulus 391
Electric Bicycle 495
Electrical Topology State Index 308
Electro-Acoustical Equivalent Circuit Principle 465
Electro-Deoxidation 58
Electrocatalysis 3
Electrochemical Copolymerization 17
Electrochemical Corrosion 168
Electrochemical Quartz Crystal Microbalance 34
Electrodeposition 34, 193
Electronic Transport 207
Electrospraying 269
Elevated Temperature Properties 178
Emergency Power Supply System 404
Emission 487
Energy Saving 479, 607
Enthalpy Method 375
Environment Case 520
Environment Protection 508
Environmental Protection Mobile Enforcement 526
Environmentally Friendly Water-Based Covering Ink 508
EOR 303
Equal-Channel Angular Pressing (ECAP) 162
Equilibrium 276
Erosion 614
Erosive Volume 614
Error 391
Essential Oil 118
Ethanol 99
Evaluation 105, 419
Evaluation Model 679
Excavation 604
Experimental Platform 330
Expressway 419
Extend Angle 41

## F

Fatigue Crack 150
Fatigue Life 158
Feast in Bronze Sparrow Terrace Held by Cao Cao 456
Feature Extraction 351
Feature Spectrum 565
Few-Layered Graphene Nanosheets 260
Fibers 86
Filling 214
Finite Element (FE) 604

Finite Element Analysis (FEA) 428
Fire Resistance 424
Fixation of Fluoride 652
Flashover 200
Flocculants 386
Fluorescence 23
Fly Ash 472
Food-Microorganism (F/M) Ratio 291
Formaldehyde 51, 620
Frequency 624
Functional Design 526
Furnace Brazing 154
Fuzzy Matter-Element 679

## G

Garden Plants 663
Gas Properties 291
Gas Sensor 231
Gauge 400
Geochemical Model 597
Glass-Ceramics 70
Global Climate Changes 663
Grain Refinement Mechanism 162
Granular Particle 357
Graphene Nanoribbon 207
Green 479
Grinding 391, 396
Ground-Source 381
Groundwater Modeling 632, 639
Groundwater System 632

## H

H-Section Column 424
$H_2$-TPR 237
Hairiness 400
Hazard 520
Head-Tail Method 543
Heat Affected Zone 318
Heat Treatment 136
Heath Case 520
Heavy Metal 537, 571, 646
Heteropoly Compounds 224
High-Density 46
Higher Vocational College Students 286
Humic Acid 620
Hybrid 346
Hybrid Power System 495
Hybrid Weight 679
Hydraulic 336
Hydrogen Battery 404
Hydrogen Sulfide 303
Hyperbranched Polyester 80
Hypereutectic Al-Si Alloy 145
Hysteresis Curve 531
Hysteretic Loop 324

## I

Ice Storage 375
Ilmenite 58
Image Acquisition 409
Image Recognition 409
Impact 357
Impact Ice 330
Improved Linear Equivalent Structural Stress Method 158
Inclusion 118
Indicator 105
Inhibitor 308
Ink Performance 508
Insulator 200
Intelligent 479
Interfacial Reaction 64
Interference Effect 444
Internal Melt-Ice-on-Tube 375
Invertebrates 491
Ionic Liquid Mixtures 99
Iron 187
Iron Titanate 136
Irrigation Coefficient 543
Irrigation District 543
Isolate Building 444
Isolation 419

## J

Jensen Model 548
Jewelry 286
Jiantu Conference 456
JVM 686

## K

K-Means Clustering 351
KCL-Saturated Brine 46
Keggin Structure 224
Kernel Function 695
Kinetics 9, 276

## L

Large-Scale Triaxial Tests 585
Laser Brazed 141
Law Enforcing Management 526
Lead Plate 336
Lead Rubber Bearing 428
Lighting Design 700
Lightning Protection Grounding 700
Litter 578
Load Grade 700
Local Spherical Coordinate System 707
Lock Gate 105
Lost Wax Casting 462
Low-Temperature Exfoliation 260
Low-Voltage Distribution 700

## M

Magnetic Adsorbent 218
Maleamic Acid Cross-Linked $\beta$-Cyclodextrin Polymer 9
Manganese 34, 193
Manganese Slag 450
Marine 659
Master S-N Curve 158
Matric Suction 590
MCGS Configuration Software 381
Mechanical Property 172
Metabolic Uncoupler 2,6-DCP 92
Methyl Orange 136
Methylene Blue 276
Mg-Gd-Y-Zr Alloy 182
Mg-Re Alloys 178
Micro Structure 125, 145, 150, 172, 182
Microcomposites 269
Microperforated Panel Theory 465
Midas Software 604
Middle Line of Project in HeBei Province 559
Mild Steel Damper 531
Mine Dump Heaps 537
Mo Alloy 130
Molecular Dynamics 200
Molten Salt 58
Moulding 476
Multi-Scale 659
Multiple-Component 269
Muscle Relaxation 691
Mycoparasitism 282

## N

NaCl 200
Nanocluster 256
Nanorobot 244
Nanosheet 231
Nearshore 659
Neural Network 308
Nitrate 303
Nitrification Inhibition 92
Nitrification Recovery 92
Nitrite 303
Nitrogen Oxides 487
Non-Enzymatic Glucose Oxidation 3
Numerical Analysis 41
Numerical Simulation 375, 433, 438
Nutrients 669

## O

*O,O*'-Dialkyldithiophosphates 109
Oil Reservoir 297
On-Line Hydrogen Production 404
Operation Mechanism 370
Optimal Allocation of Water Resources 559
Optimal Node 351
Optimization 703
Organic-Inorganic Hybrid 248
Organization 125
Orthogonal Design 51
Orthogonal Test 118
OTUs 297
Overall Structure 526
Ozon/Hydrogen Peroxide System 620

## P

P Adsorption 652
P-Type 231
Parallel Computing 703
Paramecium Caudatum 571
Particle Breakage 585
Paste Tailing 386
Pathogenic Fungi 282
Pattern Recognition 351
Patterned Immobilization 244
PCR 297
Pentaerythritol 80

Perovskite 363
Perovskite Structure 237
Pharmaceutical Wastewater 571
Phenology 663
Photocatalytic Activity 136
Phylogenetic 297
Piercing 286
Pile 438
Pin Carding Plate 400
Pollution 659
Pollution Index 537
Poly(3-methylthiophene) 17
Poly(9-aminofluorene) 23
Poly(methacrylic acid) 23
Polyamide 5,6 86
Polycondensation 80
Polycrystalline Cu 64
Polymeric Microparticles 269
Polyselenophene 17
Population Growth Curve 571
Powertrain 346
Preparation 652
Prestressed Anchor Cable 433
Printed Circuit Board 214
Prior Corrosion 150
Profile Precision 396
Property 187
Propionaldehyde 51
*Proteobacteria* 297
Provenances 597
Pulsed Jet 624

## Q

Q235 Butt Welded Joint 158
Qinghai Lake Basin 565
Quantitative Structure-Activity Relationship 308

## R

Range-Extender 495
Reaction Mechanism 58
Recovery Strain 341
Recycling 515
Refractive Index 99
Relaxation Training 691
Removal 363
Reproductive Allocation 554
Rhodamine B 276
Rigid Body 357
Risk Control 520
Rotating Error 396

## S

S-Shape Low Yield Steel Damper 324
S450EW High Strength Weathering Steel 125
Safety 479
Safety Case 520
Salt Slurry 46
Saw-Tooth Carding Plate 400
Scratch-Type Invoice Printing 508
Secondary Polymerization 23
Segregating Gratings 419
Self-Excited Oscillation 624
Self-Excited Pulsed Jet 614
SEM *In Situ* Technology 150
Semantic Symmetries 686
Sensitive Index 548
Sensitivity Imperfection 707
Separate 248
Sewage Sludge 70
Shape Memory Alloy 341
Sheet Space Structures 707
Shenzhen Holiday Plaza Project 433
Shipborne 315
Shiyang River Basin 632, 639
Silver 256
Similar Structure 695
Simultaneous Inside-Out Infusion 29
Simultaneous Outside-In Infusion 29
Slope Stability 590
Sludge Reduction 92
Smart Materials 244
Smelting Slags 537
Soil 565
Soil Pollution 537
Solar Energy 495
Solution Treatment 182
Sorption 487
Sound Absorption Coefficient 465
Sparse Elm Woodland 554
Specific Surface Area 652
Spectroscopic Ellipsometry 34, 193
Speed-Up Ratio 703
Spin Polarization 207
Spinescence 419
Sprint 691
SRB 297, 303

SS 597
Stainless Steel (SS) 141
Stiffness Matrix 428
Stochastic Imperfection Method 707
Stochastic Particle Swarm Optimization Algorithm 548
Streambed Substrate 491
Strength 472, 585
Structural Optimization 74
Structural Stability 424
Style 41
Submergence Condition 614
Sucrose 200
Sulfate 297, 303
Surface Energy 113
Surface Mechanical Attrition Treatment (SMAT) 162
Sustainable Utilization 559
Sustained Drug Release 269
Synthesis 80

## T

*T.asperellum* 282
Tenacity 86
Tensile Modulus 86
Tensile Strength 141
Test Platform 346
Thermal Cycling 145
Thermodynamics 9
Thermoelectric Property 17
Three-Leaf Microperforated Panel Absorbers 465
Thymidylic Acid-Based Synthetase 308
TiNi 341
$TiO_2$ Nanotube Arrays 3
$TiO_2$(011)-2×1 Surface 113
$TiO_2$(110) Surface 113
Titanium Alloy 58
TOC 620
Transformation 341
Tributaries 669
TRT 381
Truncated Univariate Normal Distributions 707

## U

Ulmus Pumila 554
Ultrasonic Assistance 237
Underground Heat Exchanger 381
UNITANK Process 370
Unsaturated Soil Theory 590
Urea Depositions 74
Urea-SCR System 74

## V

Validation 639
Vegetation Communities 565
Vibration 341
Vickers Hardness 182
Viscosity 99

## W

Walnut Peel 291
Washing 646
Waste Lithium Ion Battery 515
Wastewater Treatment 370
Water Absorption Rate 578
Water-Holding Capacity 578
Wavelet Packet Decomposition 351
Welding Residual Stress 318
Wunugetushan Copper-Molybdenum Ore 386

## X

X-Ray Diffraction (XRD) 318
Xitiaoxi Watershed 597, 669

## Y

Yield Strength 130

## Z

Zeolites 487

# Authors Index


## B

Bai, S.Z. 74
Bai, X.L. 543
Bao, D.J. 370

## C

Cai, J.R. 248
Cao, M.L. 9
Cao, Q.L. 276
Cao, Y.Y. 659
Chang, S.H. 548
Chao, C.H. 495
Chen, C.Y. 9
Chen, D.D. 286
Chen, H.L. 597, 669
Chen, H.Y. 663
Chen, K.L. 565
Chen, L.L. 182
Chen, L.Q. 224
Chen, Q.Y. 363
Chen, Q.Z. 450
Chen, R. 29
Chen, X. 375
Chen, Y. 386, 571
Chen, Y.B. 291, 502
Chen, Y.N. 456
Chen, Y.X. 428
Chen, Z. 386
Cheng, D. 23
Cheng, H.C. 130
Cheng, Y.F. 632, 639
Chu, F.Y. 585

## D

Dai, L.M. 224
Deng, K.J. 269
Dong, J. 237
Dong, X.L. 604
Dong, X.X. 695
Du, S.M. 172
Du, X.H. 308
Du, Z. 269
Duan, Y.Q. 248

## E

Eltahir, Y.A. 80, 86

## F

Fan, C.Y. 695
Fan, J.L. 130
Fan, K. 105
Fang, G.L. 237
Feng, J.M. 46
Feng, J.S. 109
Fu, G.Y. 341

## G

Gai, X.L. 465
Gao, J. 543
Gao, T.Z. 559
Gong, A.M. 472
Gong, Y. 508
Gong, Z.L. 571
Gui, D.D. 695
Guo, R.L. 515
Guo, X.M. 707
Guo, Y.H. 260

## H

Hao, L.Y. 218
Hao, Y.T. 578, 663
He, J.H. 193
He, X.M. 162
He, X.T. 614
Hou, H. 200
Hou, X.L. 578, 663
Hu, D. 614, 624
Hu, H. 200
Hu, P. 409
Hu, X.Q. 632, 639
Huang, B.Q. 508
Huang, H.Y. 472

## J

Jia, D.Y. 409, 679
Jiang, C.H. 105
Jiang, F.P. 269

Jiang, H.Z. 182
Jiang, M.F. 125
Jiang, W. 218
Jiang, Y.M. 462
Jin, T.J. 707
Jin, Y.J. 154

## K

Ke, S.H. 207
Kim, K.W. 620
Kim, Y.M. 444
Kong, G.M. 150
Kwon, I.K. 424

## L

Lang, S.G. 74
Le, K. 491
Lei, J. 200
Lei, X.F. 136
Li, F.S. 218
Li, G.X. 74, 346
Li, H.B. 537
Li, H.E. 695
Li, H.Z. 9
Li, J. 370
Li, L. 315
Li, L.H. 357
Li, M.C. 659
Li, M.Y. 64
Li, P.F. 462, 476
Li, Q.A. 178, 182
Li, Q.J. 578, 663
Li, R. 336
Li, R.H. 341
Li, S.C. 695
Li, T.T. 700
Li, W.P. 34, 193
Li, X.B. 187
Li, X.D. 150, 315
Li, X.G. 200
Li, X.H. 465
Li, X.Y. 269
Li, Y.H. 632, 639
Li, Y.L. 109
Li, Y.W. 419
Li, Y.X. 515
Li, Z.Y. 669
Liang, D.Q. 450
Liang, J.H. 193
Liang, P. 363
Lin, Q. 462, 476
Lin, W.D. 502
Lin, X. 109
Lin, X.M. 224
Liu, C.J. 125
Liu, F. 29
Liu, G.L. 438
Liu, H.L. 70, 92
Liu, H.Q. 646
Liu, J. 291, 502
Liu, J.H. 291
Liu, J.W. 51
Liu, L. 607
Liu, S.Q. 291, 502
Liu, S.Z. 231
Liu, W.C. 178, 182
Liu, X. 168
Liu, Y. 74, 375, 381, 479
Long, H.B. 363
Long, M. 3
Lu, B.Y. 17, 23
Lu, C.Y. 58
Lu, J.D. 357
Lu, S.C. 632, 639
Lu, S.X. 113
Lu, W. 207
Lu, X.G. 58
Lu, Y. 109
Lu, Y.J. 237
Lu, Z.P. 597
Luo, F. 118, 276
Luo, X.Y. 105
Luo, Z.W. 491
Luo, Z.X. 565
Lv, F.L. 590
Lv, X.D. 537

## M

Ma, C.C. 346
Ma, D.S. 297, 303
Ma, J.F. 537
Ma, L. 260
Ma, W.W. 214
Ma, X. 64
Ma, X.T. 438
Meng, Q. 419
Miao, B. 330

Miao, Q. 346
Mu, Z.T. 150

## N

Ning, T. 113
Niu, Y.F. 324, 531
Nong, J.H. 543

## O

Ouyang, W.P. 158

## P

Paek, S.Y. 444
Pandová, I. 487
Pang, H.C. 559
Pei, J. 614, 624
Pei, S.Y. 571
Peng, J. 145
Popov, V. 244

## Q

Qian, L. 105
Qiao, S.B. 118
Qie, Z.H. 548
Qin, Q. 172
Qin, R.H. 218
Qiu, S.Y. 351
Qiu, Z.C. 168

## R

Rhee, D.S. 620

## S

Saba, H.N. 99
Saeed, H.A.M. 80, 86
Sen, H. 336
Shan, L.W. 41
Shan, Z.D. 29
Shang, C.M. 391, 396
Shao, C.Q. 590
Shen, H.F. 237
Shen, J. 652
Shen, Y. 419
Shi, P.Y. 125
Shi, Y. 381
Song, M. 130
Song, W.F. 297, 303
Song, X.J. 178
Su, X. 41
Sun, L. 646
Sun, P.Z. 400
Sun, Q. 346

## T

Tan, L. 3
Tang, A.D. 3
Tang, C.L. 41, 614, 624
Tang, M.J. 200
Tang, Y. 554
Tian, Y. 70, 92

## W

Wan, P. 286
Wang, B.S. 200
Wang, C.Y. 315
Wang, F. 404
Wang, G. 404
Wang, H. 537, 597, 669
Wang, H.L. 607
Wang, H.P. 99
Wang, J.D. 632, 639
Wang, J.M. 565
Wang, J.S. 125
Wang, P. 691
Wang, P.F. 537
Wang, Q. 571
Wang, R. 154, 260
Wang, R.C. 145
Wang, S.S. 476
Wang, S.T. 17
Wang, W. 187
Wang, X. 269
Wang, X.H. 308
Wang, X.J. 554
Wang, Y. 214
Wang, Y.G. 462, 476
Wang, Y.M. 80, 86, 237
Wang, Y.Q. 526
Wei, G.X. 646
Wei, X.F. 297, 303, 508
Wei, X.Y. 276
Wen, X.W. 70, 92
Weng, Z.X. 260
Wu, D. 70, 92, 571
Wu, J. 297, 303
Wu, L.X. 260

Wu, R. 465
Wu, R.R. 330
Wu, W.Y. 491
Wu, X.H. 141
Wu, Z.H. 646

## X

Xia, Y.M. 80, 86
Xiao, W. 58
Xie, B. 109
Xiong, C.H. 404
Xiong, L. 187
Xu, C. 324, 531
Xu, C.A. 686
Xu, H.Y. 669
Xu, J.K. 17, 23
Xu, L. 248, 291, 502
Xu, W.G. 113
Xu, W.W. 597
Xu, X.D. 158
Xu, X.Q. 256
Xue, L. 578, 663
Xue, X.X. 136

## Y

Yan, Y. 571
Yang, H. 136, 291, 502
Yang, J.D. 391
Yang, J.Y. 34
Yang, M. 64
Yang, P. 282
Yang, S.A. 200
Yang, W. 646
Yao, Y.L. 703
Yin, F. 291, 502
Yin, M.L. 231
You, J.Y. 444
You, K.P. 444
You, W. 462, 476
Yu, D.G. 269
Yu, X.X. 462, 476
Yu, X.Z. 400
Yuan, F. 113
Yuan, J.P. 286
Yuan, K. 472
Yuan, K.P. 74
Yuan, R.B. 336, 351
Yuan, W.J. 520
Yuan, X.Y. 597, 669

## Z

Zhang, B. 465
Zhang, C. 248
Zhang, C.C. 559
Zhang, C.H. 162
Zhang, D.H. 187
Zhang, D.M. 391, 396
Zhang, F.H. 41
Zhang, G.M. 357
Zhang, H.F. 113
Zhang, J. 158
Zhang, J.W. 51, 703
Zhang, L.J. 502
Zhang, M. 571
Zhang, N. 168, 590
Zhang, P. 370
Zhang, S.T. 34, 193
Zhang, W.D. 291, 502
Zhang, W.H. 543
Zhang, X. 565
Zhang, X.L. 109
Zhang, X.M. 9, 396
Zhang, X.Y. 182
Zhang, Y.L. 318
Zhang, Y.M. 99
Zhang, Y.N. 381
Zhang, Y.Q. 515
Zhang, Z. 652
Zhao, H.Q. 315, 543
Zhao, J.J. 465
Zhao, P.Z. 315
Zhao, X.L. 291, 502
Zhao, Y.J. 526, 659
Zhao, Y.M. 276
Zhao, Y.X. 324, 531
Zheng, A.S. 341
Zheng, F. 404
Zheng, P.S. 341
Zheng, Y. 433
Zhong, M.Q. 543
Zhou, B. 386
Zhou, D.S. 515
Zhou, J.M. 318
Zhou, L.J. 46
Zhou, W.Q. 17, 23
Zhou, X.W. 386
Zhou, Y.J. 404
Zhu, C.L. 330

Zhu, C.X. 330
Zhu, M.X. 224
Zhu, S.S. 109, 162
Zhu, X.H. 652
Zhu, X.W. 145
Zhu, Y.Y. 297, 303
Zhuo, D.X. 260
Zou, L. 150
Zou, L.K. 109
Zou, S.X. 679
Zou, X.L. 58
Zuo, F.L. 543
Zuo, X.L. 34, 193